

# nature

THE INTERNATIONAL WEEKLY JOURNAL OF SCIENCE



## Rising tide

A 500-year model of Antarctica's contribution  
to future sea-level rise **PAGE 591**

### PARTICLE ACCELERATORS

#### OPEN ALL HOURS

*A day in life of the  
synchrotron that never sleeps*

**PAGE 564**

### NAVIGATION

#### LOST IN SPACE

*GPS and satnav have  
dulled our sense of place*

**PAGE 573**

### METROLOGY

#### FEEL THE FORCE

*Tiny drone-ready gravimeter  
prepares for take-off*

**PAGES 585 & 614**

**NATURE.COM/NATURE**

31 March 2016 £10

Vol 531, No. 7596



9 770028 083095

13b



# Play nicely

Attempts by digital companies to curb unpleasant behaviour online could make the Internet a more welcoming and useful space.

30 March 2016

Article tools

There are standard operating instructions for the Internet and you've probably heard them before: don't feed the trolls, stay away from certain social-networking sites and whatever you do, however much they call to you, never read the comments at the bottom of the page. Many of the most popular features and facets of the online world, the ones that allow for the kind of community and broad conversation and idea sharing that only the Internet can provide, also have a reputation as an open sewer of vitriol — of racist, sexist, xenophobic, homophobic, threatening and just plain offensive language and activity.

## Related stories

- [Can a video game company tame toxic behaviour?](#)
- [Misjudgements will drive social trials underground](#)
- [A 61-million-person experiment in social influence and political mobilization](#)

How did it get to be this way? Social psychologists have a few ideas about the factors that might contribute. One is the disinhibition effect. The Internet is a place where people can be anonymous, invisible and part of a very large crowd. With users separated by physical distances and free from authority, consequences or social cues, the norms encoded into most face-to-face interactions fall away.

Many who watched the early days of the Internet remember seeing how the culture emerged and norms solidified. There were the early Usenet flame wars: fierce and seemingly endless arguments about topics both important and banal. There were jokesters and pranksters who took pleasure in pushing people's buttons and upsetting debates by voicing irrational, unpopular or downright nasty opinions. By the early 1990s, this activity had a name: 'trolling'. The trolls were aided and abetted by a sort of bystander apathy. Many believed that someone else, surely, would speak up about what was going on — few did.

That silence effectively gave the small number of trolls the ability to set the cultural standards for all. You hear it all the time: they're



a part of the digital fabric. You can't do anything about it. Just ignore it.

But online toxicity and cyberbullying have grown out of control in the ever-connected world of social media and gaming. And their rancid fruits have spilled beyond the confines of digital space: reputations have been ruined, privacy invaded and other real harms inflicted.

Online toxicity poses complex problems for companies whose networks host open forums and social interaction. Facebook and Twitter, for example, are private owners of what many deem to be public spaces, places where bullying and harassment can happen, but also where protest, civic action and calls for social justice take place. The question is open as to what extent these companies should be held accountable — whether they should protect targets of abuse, punish abusers and provide ways for society's malcontents to assemble.

**“Online toxicity and cyberbullying have grown out of control.”**

Promisingly, many companies seem to have accepted that efforts to control behaviour, although difficult, are worth it. Research on those who inhabit these online spaces and how they interact can reveal ways to tackle the complexities, but much of this useful work goes on behind the scenes. One of the companies most public about its efforts is Riot Games of Los Angeles, California, the maker of the popular online game *League of Legends*. The company has tackled a formidable problem with toxicity by asking players to help set the game's cultural norms. Its efforts are evidence-based and supported by classic psychological theory. And, as we [explore in a News Feature](#), it is collaborating with academic scientists, who may be able to inject new ideas into its work.

For the company, its actions serve the bottom line. *League of Legends* has a problem with toxicity that drives some people away. But many observers think that the sense of responsibility that Riot projects is sincere.

The company is to be lauded for sharing what it has learnt and for collaborating openly and transparently. Games and social networks can provide a rich seam of behavioural data free from the artificiality of laboratory work, and the number of participants is incredible. There are certainly risks involved for the companies. Many users are unaware of the extent to which digital companies already manipulate and experiment with their individual experiences, as revealed in the backlash to a Facebook study (A. D. I. Kramer *et al.* *Proc. Natl Acad. Sci.*



*USA* 111, 8788–8790; 2014). And, of course, experiments designed to get people to spend more money or more time on the Internet will probably never be palatable to every user. But if the citizens of the Internet are willing to participate in the right kinds of studies and experiments, it could lead to a friendlier, more-productive space.

*Nature* 531, 549 (31 March 2016) doi:10.1038/531549a



# Time out

Artificial fixes to make the most of summer time may do more harm than good.

30 March 2016

Article tools

## Rights & Permissions

Last week, Europe joined the United States in shifting the clocks forward an hour. Who doesn't look forward to 'summer time', with its promise of long, warm evenings for strolling, al fresco dining and working the fields? Circadian biologists don't; many of them greet the new time with a seasonal chorus of 'Foul!'

### Related stories

- [How do you sleep?](#)
- [Clock-gene variants linked to diabetes](#)
- [Restless nights, listless days](#)

### More related stories

For many, the time shift known as daylight saving is a burdensome disruption. Some people do not adjust well at all, as witnessed by reports of increased incidence of heart attacks and traffic accidents the day after the change. Our 'chronotype' — whether we are early-to-rise larks or committed night owls — is set in our genes, and chained to the light - dark cycle of the Sun. It is not going to be that easily deceived by the hands of our watches and clocks, which now only loosely attach to true astronomical time, and to true biological time.

In fact, the very notion of an agreed time at which we should all wake and pay attention — to bosses, teachers and traffic — is misplaced. A huge research effort at the Ludwig Maximilian University of Munich known as the [human sleep project](#) has shown the hopelessness of trying to alter preferred wakefulness patterns.

The project began in 2000 with the launch of a web-based questionnaire about sleep and wake times on working days and free days. A quarter of a million individuals around the globe have since participated. It provides a rich source of research data, and one mined with particular glee by those chronobiologists who are natural owls and have a grudge



against a society that habitually imposes inflexible school and work times.

A landmark study of the data showed that late and early chronotypes have a bell-curve distribution across all populations. And within their own chronotype, all individuals are, relatively speaking, earlier risers as children, become much later as adolescents and then become slowly earlier as adults (T. Roenneberg *et al. Curr. Biol.* **14**, R1038 – R1039; 2004).

Another study, which considered data from across Germany, demonstrates the unrelenting power of the Sun (T. Roenneberg *et al. Curr. Biol.* **17**, R44 – R45; 2007). The country spans nine degrees of longitude, so the Sun rises 36 minutes earlier at its most easterly point compared with its most westerly. Whatever their individual chronotype, physical and biological time for these people diverges on average by an extra four minutes with each longitudinal step.

**“We need flexibility not in the time displayed by the clock, but in our attitude to it.”**

The discomfort that some of these chrono-victims feel is magnified across the vast geographical swathe of Central European Time. In summer, midnight on the clock is, astronomically speaking, actually 11 p.m. in the Czech capital, Prague, but barely 9.30 p.m. in the western Spanish outpost of Santiago de Compostela. The Spanish habit of dining at 10 p.m., when many Czech restaurants have long since closed, starts to make sense.

Other studies have shown the power of biological time. Night owls, including adolescents who are driven sulking from their beds to attend school long before they are truly awake, spend large parts of their weekends ‘catching up’ on missed sleep (M. Wittmann *et al. Chronobiol. Int.* **23**, 497 – 509; 2006).

And placing activity meters on wrists to monitor movements 24 – 7 shows that, although people will adjust their bedtimes to daylight-saving time, peaks and slumps in their activity remain ruled by their separate, fixed, biological clocks (T. Kantermann *et al. Curr. Biol.* **17**, 1996 – 2000; 2007).

Whereas the power of astronomical and biological time remains, modern life weakens the light – dark cycle that connects them. City dwellers tend to spend most of their days working indoors, where lighting levels can be 40 times weaker than average daylight. Night time is no longer

particularly dark thanks to electric lighting both indoors and in the streets. Camping experiments in the mountains, in which people have to live outside during daylight hours and have no source of light beyond the campfire, show that night owls quickly become much earlier chronotypes.

Daylight-saving time is far from universal. And experience in other countries shows that it is not necessary. Japan and South Korea, like most Asian countries, see no need for it. Most African countries don't either. Ukraine observes it — but after annexation by Russia in 2014, Crimea chose to align its time with Moscow, which does not observe daylight saving.

In Europe, some politicians, prodded by data on the counter-productivity of enforcing inflexible social timetables across an entire population, and also by evidence that shift workers who live against their biological clocks have a higher incidence of metabolic diseases, have opened a debate on the value of making the change every six months.

Fixing time will not fix its problems. To do that, we need flexibility not in the time displayed by the clock, but in our attitude to it. One high school in Germany this year decided to allow its older students the option of beginning classes at 8.50 a.m. instead of 8 a.m., anticipating that the adolescents would be more alert and capable of learning by then. Britain is looking at changes too. Perhaps more of society should wake up to the opportunities.

*Nature* **531**, 549 – 550 (31 March 2016) doi:10.1038/531549b



# Honey trap

Psychology drives some overindulgence — and it could help us to resist.

29 March 2016

Article tools

[Rights & Permissions](#)

Take a look at the chocolate spilling from your cupboard shelves, the left-over Easter eggs and the fondant-filled bunnies. How do you feel? Do you recognize that combination of wanting to do something and yet knowing that perhaps you shouldn't?

## Related stories

- [Sugar tax could sweeten a market failure](#)
- [High-fat diets raise risk of obesity in offspring](#)
- [Neuroscience: What drives sugar addiction](#)

## More related stories

If you can conquer the call and ignore the stimulus, walk away without indulging, then well done you. Everyone else: you may feel bad as you wolf it down, but please don't feel too bad. You are merely feeling what it means to be human. You are Hamlet, agonizing over the pros and cons of a single goal: to eat or not to eat.

Psychologists call this particular form of internal torture approach-avoidance conflict. The outcome is binary, but the cognitive processing that goes into the decision is oscillatory. Should I or shouldn't I? As we near the goal (reach for the chocolate) we feel the pull of the bathroom scales, and so we back away again to avoid the guilt that eating it causes. As we do so, we imagine the taste in our mouth and approach the chocolate once more. In a very human way, this back-and-forth means that, whatever we decide, the effort is stressful and the outcome unsatisfying.

One theory of addiction suggests a severe imbalance in this 'push-me-pull-me' dynamic. Most people who have an addiction, from gambling and smoking to substance use, are aware of the damage their habit causes. But they find it easier — pathologically so — to approach their goal than to avoid it.

Can their balance be restored? Some research indicates that it can. Studies involving people with alcohol dependence suggest that physical

actions to represent the conflict — pushing away repeated pictures of alcohol to make them smaller or pulling them closer to make them larger — can be manipulated to change the amount a person consumes. (The pushing mimics avoidance and encourages less drinking.) The effect seems to translate to the clinic, with people being treated for alcohol dependence more likely to abstain from drinking if this computerized task is included in their therapy.

Could the same idea work for chocolate? And, on a larger scale, could it help to address the growing obesity crisis? As [nations such as Britain introduce sugar taxes](#), could a little psychological nudge help to blunt our collective sweet tooth too?

Some research suggests so. In one study, students who spent some time being tricked to push away pictures of chocolate — they thought that they were responding to the shape of the image, not its content — ate less of a chocolate muffin than did colleagues who pulled the images closer (S. E. Schumacher *et al. Appetite* **96**, 219–224; 2016). The problem is that other research has found contrasting results. In one experiment, students who were trained to avoid chocolate images actually went on to eat more of the real stuff (D. Becker *et al. Appetite* **85**, 58–65; 2015).

There are psychological subtleties to unwrap here. Existing motivation to avoid chocolate, and cravings to approach it, might be influencing the results. As always, more research is needed, and shouldn't be too difficult to arrange. One study advertised for volunteers with the phrase: do you like chocolate? And who could avoid that?

*Nature* **531**, 550 (31 March 2016) doi:10.1038/531550a

DAVID FISHER



## Sugar tax could sweeten a market failure

*Britain has announced a tax on sugary drinks. Countries should go further and target foods that have large carbon footprints, says Adam Briggs.*

Health campaigners and political observers got a surprise in the United Kingdom's latest budget. This month, Chancellor of the Exchequer George Osborne announced a sugar tax in the form of a levy on sugary-drinks manufacturers.

This is a bold and welcome move from a Conservative government that has often been criticized for not standing up to industry. It demonstrates that officials and policymakers have heeded advice and now recognize that sugar is a public-health problem that needs legislative control. The tax has potential implications not just for public health and the global soft-drinks industry, but also for the ability of all governments to act on market failures in food.

Britain will not be the first place to introduce a sugar-drink tax. Mexico, France, Hungary and Finland, among others, have taxed sugary drinks; South Africa, the Philippines, Indonesia and India are considering doing so. Hungary and Finland have also taxed some unhealthy foods.

Scientists, campaigners and policymakers around the world will watch the reaction of both the British public and soft-drinks companies to the tax with interest (there are already reports of potential legal challenges). Britain has a reputation as an international leader in working with industry to reduce salt in food through reformulation, and the government's latest policy is designed to force soft-drinks manufacturers to do the same.

The risks to health from sugar have become apparent in recent years. There is growing evidence that it causes tooth decay, diabetes and heart disease, and it has been implicated as a leading cause of the global obesity epidemic. Public-health campaigners around the world have targeted soft drinks as a focus of their attention. And with good reason: sugary drinks directly harm health, they have no beneficial nutrients, healthier substitutes are available, and they can be neatly defined by legislators.

The UK policy is an example of taxes being used to correct a negative externality: that is, a market failure in which the full cost of a product to individuals and society is not included in the price. Adverse health outcomes that arise from drinking soft drinks are a prime example.

Mexico's law (and a similar model used in Berkeley, California) also tries to correct this negative externality. The taxes there are not explicitly designed to raise revenue, but instead to shift behaviour and improve public health. An analysis of the Mexican tax in *The BMJ* suggests that it is working. The study showed that purchases of sugary drinks fell by 12% at the end of the first year after a 10% price rise, with greater declines among those who were less well off (M. A. Colchero *et al. Br. Med. J.* 352, h6704; 2016).

The UK government has a similar goal. The tax is aimed at reducing childhood obesity, and revenue will be allocated to schools to expand

breakfast clubs and increase sport provision.

But Britain is trying to do it slightly differently. Rather than being a sales tax that directly raises the price of sugary drinks (as called for by the public-health community and found in other countries), it is instead a tax levied on the manufacturer. From April 2018, soft-drinks companies will be required to pay 18p (25¢) for every litre of sugary drink with 5–8 grams of sugar per 100 millilitres sold in Britain, and 24p for every litre with more than 8 grams of sugar (2 teaspoons) per 100 millilitres. Coca-Cola contains 10.6 grams of sugar per 100 millilitres.

The fine details will be determined in the coming months, with the timing of the levy's introduction designed to give soft-drink companies enough time to reduce the sugar content of their products and change advertising strategies if they wish. Once introduced, it will then be up to the companies to decide how they change the price of their taxed (and untaxed) products, if at all.

The global implications are significant. If effective, substantial product reformulation to reduce sugar content would be an important public-health victory. It would provide a model for other countries that may be unwilling to implement a tax without giving industry the opportunity to adapt beforehand. Equally, industry may choose to keep the sugar content of its drinks the same and either absorb the tax or pass it onto the consumer across their product ranges. This would mean no relative price increase on sugary drinks and so probably no drop in consumption.

The rising popularity of taxes on unhealthy foods and drinks suggests that a similar intervention is possible for another major negative

externality in food: greenhouse-gas emissions.

Agriculture is responsible for up to 30% of the world's greenhouse-gas emissions, yet is often overlooked in climate discussions and was barely mentioned at December's United Nations climate talks in Paris.

Taxing food that is responsible for high greenhouse-gas emissions when it is produced and transported could benefit the health of both people and the planet. An obvious place to start is red meat, including beef and lamb. Research in our group suggests that a climate tax to address this externality would see its price rise by 5–45%, depending on the cut and quality. Consumption could fall by up to 20%. Along with smaller price changes to other carbon-intensive foods, this could shrink UK emissions by nearly 19 million tonnes of carbon dioxide equivalent per year—about the same as 85,000 Boeing 747 flights between London and New York. Sugar is a good start, but we can aim higher. ■

Adam Briggs is a public-health researcher at the University of Oxford, UK.  
e-mail: adam.briggs@dph.ox.ac.uk

REVENUE WILL BE  
ALLOCATED  
TO SCHOOLS  
TO EXPAND  
BREAKFAST CLUBS  
AND INCREASE  
SPORT  
PROVISION.

➔ NATURE.COM  
Discuss this article  
online at:  
[go.nature.com/qii4n1](http://go.nature.com/qii4n1)

# RESEARCH HIGHLIGHTS

Selections from the  
scientific literature

## GENETICS

### Genes linked to diabetes risk

Variations in two genes have been linked to both type 1 and type 2 diabetes in mice and in humans.

Type 1 diabetes occurs when the immune system attacks insulin-producing  $\beta$ -cells in the pancreas, whereas type 2 diabetes is caused by metabolic changes that make cells resistant to insulin. Adrian Liston of the University of Leuven in Belgium and his colleagues studied a mouse model of type 1 diabetes and found that variations in two genes, *Xrcc4* and *Glis3*, promote diabetes. The variants made  $\beta$ -cells prone to programmed cell death and senescence.

Pancreatic cells taken from people with type 2 diabetes showed reduced expression of the GLIS3 protein compared to that in healthy cells. Expression of *XRCC4* was normal, but levels of an important partner of this protein were reduced. The findings suggest a mechanistic link between the two forms of diabetes.

*Nature Genet.* <http://doi.org/bdnd> (2016)

## ASTRONOMY

### Protoplanet imaged in infancy

Astronomers have captured images of a young star system in the earliest stages of planet formation.

Researchers in 2014 used the Atacama Large Millimeter/submillimeter Array (ALMA) in Chile to image the star HL Tau and its dusty disk, some 138 parsecs (450 light years) from Earth. They found distinct gaps in the disk, where developing planets were thought to be collecting material along their orbits as

they grew. To study the system further, Carlos Carrasco-González of the National Autonomous University of Mexico in Morelia and his colleagues used the Very Large Array in New Mexico, which is more sensitive to the disk's inner region than ALMA. It revealed that part of the innermost ring of dust seems to be clumping together into a planet that is 3–8 times the mass of Earth, suggesting that planets are forming in the rings rather than in the gaps.

This is the first time that planetary formation has been observed at such an early stage, the authors say.

*Astrophys. J. Lett.* in the press; preprint at <http://arxiv.org/abs/1603.03731> (2016)



## DEVELOPMENTAL BIOLOGY

### Zebrafish skin in myriad colours

Researchers have created a transgenic zebrafish with skin that fluoresces in thousands of colours — enabling them to track the behaviour of hundreds of individual cells in real time.

Kenneth Poss at Duke University Medical Center in Durham, North Carolina, and his colleagues adapted a 'brainbow' technique published in 2007, which engineered neurons to express different mixtures of fluorescent proteins. The team made the skin cells of zebrafish express the proteins so that cells

could appear in one of around 5,000 different colours. About 70 could be distinguished clearly through a microscope — enough for most cells to be made distinct from their neighbours (pictured).

Using this 'skinbow' method, the team found that skin cells responded in three ways to fin amputation: cells from nearby regions migrated in to cover the new tissue; new skin cells were created; and some skin cells grew in size.

*Dev. Cell* 36, 668–680 (2016)

## CANCER

### How tumour cells lie in wait

Researchers have worked out how certain cancer cells go into hiding in the body and emerge later to cause the disease to recur.

Cancer can reappear and spread through the body years after the primary tumour has been surgically removed. To find out more about this latent period, Joan Massagué at Memorial Sloan Kettering Cancer Center in New York and his colleagues isolated cells from human lung and breast cancers that formed tumours only months after being injected

into mice. The team found that these cells entered a quiescent, slow-dividing state by inhibiting a signalling pathway driven by the protein WNT. The cells also expressed high levels of the stem-cell genes *SOX2* and *SOX9*, which enabled the cells to grow into new tumours under certain conditions.

Moreover, the cells downregulated the expression of molecules that are recognized by immune cells called natural killer cells, allowing the latent cancer cells to hide from immune surveillance until conditions permitted them to form metastases.

*Cell* <http://dx.doi.org/10.1016/j.cell.2016.02.025> (2016)

CHEN ET AL./DEV. CELL (2016)



## ECOLOGY

## Pesticides alter bee foraging

Bumblebees that have been exposed to neonicotinoid pesticides are slower to learn how best to collect pollen from wildflowers than are their unexposed counterparts.

Neonicotinoids are widely used insecticides, and their application has been restricted in some countries because of their negative impact on bees. To study the effects of the chemicals on bee foraging, Dara Stanley at Royal Holloway University of London in Egham, UK, and Nigel Raine at the University of Guelph, Canada, observed individual bumblebees (*Bombus terrestris*) while the insects foraged on two species of wildflower. Bee colonies that had been dosed with the neonicotinoid thiamethoxam released more foragers, and these bees collected pollen more often than did controls. But unexposed bees required fewer visits to flowers to learn how to collect pollen efficiently.

The results suggest that environmental exposure to this insecticide at sub-lethal levels probably changes how well bees forage and pollinate in the wild, say the authors. *Funct. Ecol.* <http://doi.org/bdn8> (2016)

## GENETICS

## Feathery feet are more like wings

Some bird feet are covered by feathers (pictured) instead of scales and show greater similarity to wings than to legs at the molecular level.



Michael Shapiro at the University of Utah in Salt Lake City and his colleagues crossed breeds of domestic pigeon (*Columba livia*) that had feathery or scaly feet and analysed the offspring to identify genomic regions that contribute to this unusual trait. They also compared the genomes of 15 feather-footed and 28 scale-footed pigeons.

They found that the hind limbs of birds with feathery feet showed gene-expression patterns that resembled those of wings, or fore limbs. In pigeon and chicken embryos, a gene called *Tbx5* that normally regulates forelimb outgrowth and identity was expressed in the developing legs of birds with feathery feet. Furthermore, the expression of *Pitx1*, a hindlimb gene, was lower in these birds than in those with scaly feet.

*eLife* 5, e12115 (2016)

## GEOLOGY

## Warm weather sets rocks loose

Rockfalls in steep terrain could be triggered by warm weather.

Precipitation, earthquakes and freeze–thaw cycles are known to increase the risk of rockfalls, but some falls have no known cause. Brian Collins of the US Geological Survey in Menlo Park, California, and Greg Stock of the US National Park Service in El Portal, California, attached ‘crackmeters’ to a 500-metre cliff in California’s Yosemite National Park.

They found that a crack behind a slab in the cliff widened every day as the rock expanded in the heat, and closed up at night. It was also wider during the summer than in the winter. Over 3.5 years, the crack steadily opened up, and the authors say that such rock slabs could eventually fall, even without stresses such as an earthquake or heavy rain.

The study suggests that warm summer afternoons are most likely to see such

## SOCIAL SELECTION

Popular topics on social media

### Mammals face off in Twitter battle

While US basketball fans nationwide have been cheering on Badgers and Wildcats in the NCAA college-level tournament this month, scientists and animal enthusiasts have been riveted by pandas, bison and other furry combatants in Mammal March Madness. The Twitter-based competition, organized by four biologists, features hypothetical battles that are based on the real-life strengths and vulnerabilities of the contestants. In the final battle on 24 March, the tundra wolf defeated the forest hog. Since its debut in 2013, the month-long tournament has attracted a passionate base of fans who try to predict the results of each round and root for their favourite animals, while discussing online the biology of the mammals. Laura Huenneke, an ecologist at Northern Arizona University in Flagstaff, summed up the

➔ **NATURE.COM**  
For more on popular papers:  
[go.nature.com/cg6cxf](http://go.nature.com/cg6cxf)

drama on Twitter: “Unlike NCAA, March Mammal Madness #2016MMM has equal appeal for 3 yr olds, pro biologists...unbearable cuteness AND total geek curiosity.”

rockfalls, which matches records at Yosemite and other places around the world. *Nature Geosci.* <http://dx.doi.org/10.1038/ngeo2686> (2016)

## ANTHROPOLOGY

## Ancient genomes from tooth plaque

Hardened plaque from 700-year-old teeth has yielded complete mitochondrial genomes for six people.

Calcified dental plaque, or calculus, is often preserved on ancient teeth, and studies have identified human and bacterial proteins in the build-up. A team led by Christina Warinner at the University of Oklahoma in Norman sequenced DNA in the calculus on 700-year-old remains from a cemetery in Illinois. The samples contained enough DNA to reconstruct full mitochondrial genomes.

The calculus can be useful when analysing remains that are considered to be sacred and that cannot be sampled using destructive methods, the authors note.

*Am. J. Phys. Anthropol.* <http://doi.org/bdnb> (2016)

## VIROLOGY

## Zika’s arrival in Americas tracked

The Zika virus probably entered the Americas between May and December 2013, more than a year before it was first detected in Brazil.

A team led by Pedro Vasconcelos at Brazil’s Ministry of Health in Ananindeua sequenced the genomes of seven Zika viruses isolated from patients and linked to the current outbreak of the disease in Brazil. They found little diversity among the viruses, indicating that they are all related to a single root virus that entered the country in 2013.

At that time, a growing number of passengers were arriving in Brazil by air from Zika-endemic areas such as the Pacific Islands, which experienced Zika outbreaks between 2012 and 2014.

*Science* <http://dx.doi.org/10.1126/science.aaf5036> (2016)

➔ **NATURE.COM**  
For the latest research published by Nature visit:  
[www.nature.com/latestresearch](http://www.nature.com/latestresearch)

# SEVEN DAYS

The news in brief

## EVENTS

### Space silence

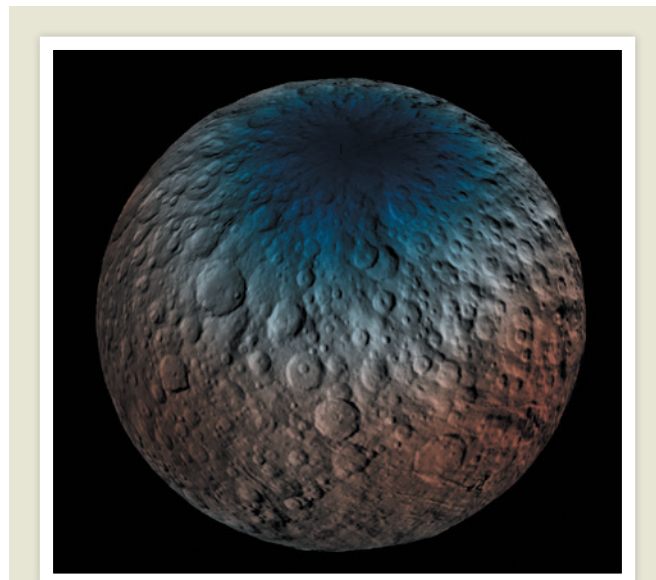
The Japan Aerospace Exploration Agency (JAXA) lost contact with its flagship X-ray astronomical satellite, Hitomi — previously known as ASTRO-H — on 26 March. Launched on 17 February, it had been going through initial tests and calibrations. Hitomi's status remains unknown, but JAXA engineers are working to regain communication. The US Joint Space Operations Center, which tracks space debris, reported five objects near the spacecraft around the time that it went silent, which it characterized as pieces of a “break-up”. On 28 March, unconfirmed reports said that telescopes had seen the satellite tumbling. See [go.nature.com/jlkhvg](http://go.nature.com/jlkhvg) for more.

### Japan's whaling

Japan's Institute for Cetacean Research has confirmed that 333 minke whales were killed by the country's controversial ‘scientific’ whaling initiative in the Antarctic, which started last year. In a 24 March statement, the institute said that 103 males and 230 females — many of which were pregnant — were caught between December last year and March. In 2014, an international court declared that Japan's whaling programme was not scientific, and the country has struggled to convince the International Whaling Commission to approve a revised programme (see A. S. Brierley and P. J. Clapham *Nature* **529**, 283; 2016; J. Morishita *Nature* **531**, 35; 2016).

### Philippines satellite

The Philippines's first micro-satellite was successfully launched on 22 March from Cape Canaveral, Florida. The craft, Diwata-1 — a collaboration between the



## Hydrogen on Ceres

The northern polar region of the dwarf planet Ceres contains lots of hydrogen and probably water, as revealed in an image taken by NASA's Dawn spacecraft and released on 22 March. Dawn scientists compiled this false-colour map using data from the spacecraft's neutron-counting instrument, which scans the uppermost metre of Ceres's surface material. Red indicates high neutron counts, and blue shows low counts. Fewer neutrons near the north pole indicate the presence of hydrogen there, probably in the form of water ice.

University of the Philippines Diliman, the Philippine Department of Science and Technology and Japan's Tohoku and Hokkaido universities — is part of a resupply mission to the International Space Station, from where it will be placed into orbit. The satellite will beam back images of weather patterns and land and water resources, and represents “a giant leap for Philippine science and technology”, said Jose Cuisia, the country's US ambassador.

## FUNDING

### Frontier science

Microsoft co-founder Paul Allen has pledged US\$100 million over 10 years

to transformative bioscience projects and investigators. The first grants from the Paul G. Allen Frontiers Group in Seattle, Washington, were announced on 23 March. Four scientists will receive \$1.5 million each: Ethan Bier at the University of California, San Diego; James Collins at the Massachusetts Institute of Technology, Cambridge; Jennifer Doudna at the University of California, Berkeley; and Bassem Hassan at the Brain and Spine Institute, Paris. Two universities, Stanford in California and Tufts in Medford, Massachusetts, will each receive \$30 million, from the Allen group and partners, over 8 years. Competitions for additional investigators and

research centres will be held periodically.

### Russian funding

Concerns have been raised over future support for civilian basic research under a science and technology strategy that the Russian government plans to launch this year. Despite mounting budget pressure, the government's overall spending on military and civilian science is to remain stable, deputy prime minister Arkady Dvorkovich told the Russian Academy of Sciences last week. But scientists told *Nature* that they fear that priority research programmes set to be introduced by the end of the year will favour commercial research over fundamental science. Recipients of Russian grants have already lost substantial purchasing power owing to the rapid decline of the rouble.

### Fetal research

A US Congress committee is preparing to subpoena 17 universities and research institutions for data on their use of human tissue from aborted fetuses, according to media reports on 24 March. This is the second round of subpoenas from the House Select Investigative Panel on Infant Lives, which was created in October 2015 to investigate allegations that reproductive health-care provider Planned Parenthood was illegally selling fetal tissue to researchers — charges that the non-profit group denies. The committee's chair, Representative Marsha Blackburn (Republican, Tennessee), is seeking the names of researchers who work with fetal cells and tissue.

### Canadian science

Canada's government will boost funding for science and technology, finance minister Bill Morneau announced on

NASA/JPL-CALTECH/UCLA/ASI/INAF

**INTEL** 22 March. Science-granting agencies will receive an extra Can\$76 million (US\$58 million) annually from the 2016–17 fiscal year, plus Can\$19 million for indirect costs at academic institutions that undertake federally sponsored research. The government also plans to spend up to Can\$2 billion over 3 years on a new science infrastructure, and Can\$800 million over 4 years on a series of “innovation networks and clusters” that aim to foster research and development ties with the private sector.

## PEOPLE

**Macchiarini affair**

The Karolinska Institute announced on 23 March that it has rescinded its contract with controversial surgeon Paolo Macchiarini. Macchiarini, formerly a visiting professor at the institute in Stockholm, had been internationally fêted for his pioneering transplants of artificial windpipes — but allegations of scientific and ethical misconduct began to emerge almost two years ago. The institute’s disciplinary board now says that he “engaged in conduct and research that is incompatible with a position of employment”. Macchiarini says that he rejects the board’s findings. See [go.nature.com/qqeikq](http://go.nature.com/qqeikq) for more.

**Intel icon dies**

Andrew Grove, the legendary chairman and chief executive of semiconductor giant Intel, died on 21 March aged 79, the company has announced. Grove (pictured) was the first engineer to be hired by Intel’s founders in 1968. He later had a crucial role in management as the company, based in Santa Clara, California, drove down the cost of computer chips and boosted their power, both at an exponential rate. Born into a Jewish family in Hungary, Grove survived the Holocaust; in the mid-1950s, he escaped through the Iron Curtain and emigrated to the United States.

## FACILITIES

**Solo observatories**

Two US radioastronomy observatories will branch out on their own following a funding crunch, the National Radio Astronomy Observatory (NRAO) in

Charlottesville, Virginia, announced on 24 March. The Green Bank Telescope in West Virginia will become the independent Green Bank Observatory, and the Very Long Baseline Array — a set of ten dishes stretching from Hawaii to the US Virgin Islands — will be the Long Baseline Observatory. The changes come as the US National Science Foundation, which funds the NRAO, looks to save money by offloading some of its astronomy facilities.

## RESEARCH

**Asymmetry pegged**

The LHCb experiment at CERN’s Large Hadron Collider near Geneva, Switzerland, has improved the accuracy of a crucial measurement of the difference in behaviour between matter and antimatter. At a meeting in La Thuile, Italy, physicist Matthew Kenzie of CERN, Europe’s particle-physics lab, reported on 23 March that one indicator of asymmetry — called  $\gamma$  and measured through the decay of  $B$  mesons and their antiparticles — in the behaviour of quarks had been determined with a precision of about 10%, twice that of previous experiments. One of three angles of a triangle,  $\gamma$  encodes the asymmetries

## COMING UP

**31 MARCH–1 APRIL**

US President Barack Obama hosts the last of four summits on nuclear security in Washington DC. [go.nature.com/4fq3gj](http://go.nature.com/4fq3gj)

**1–2 APRIL**

Robotics experts gather in Coral Gables, Florida, to wrestle with the legal and policy questions surrounding robots. [go.nature.com/sc4fuc](http://go.nature.com/sc4fuc)

**6–7 APRIL**

The Astroparticle Physics European Consortium holds a meeting in Paris to discuss updating its global-initiatives road map. [app2016.in2p3.fr](http://app2016.in2p3.fr)

in quark behaviour; LHCb physicists hope to measure all three angles with a precision that is better than 1%.

## POLICY

**Call for drug reform**

Drug policy needs to be shorn of ideological bias and based on better science, according to the Johns Hopkins–Lancet Commission on Public Health and International Drug Policy. In a 24 March report, the group calls for decriminalization of minor drug offences including use and possession, regulated drug markets and a focus on harm reduction rather than prevention of use (J. Csete *et al.* *Lancet* <http://doi.org/bdp2>; 2016). The commission also says that current global policies are causing huge health problems, and that a more diverse source of funders is needed to provide “non-ideological” science on drug policy and reform.

**NATURE.COM**

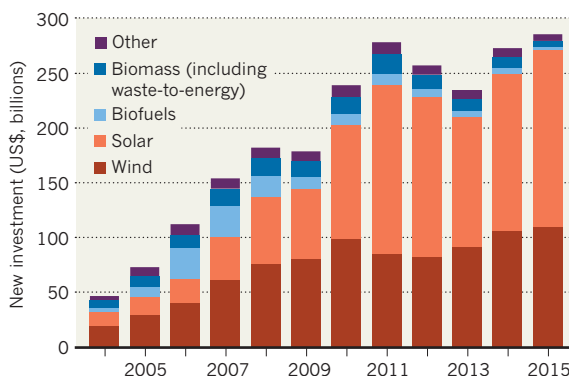
For daily news updates see: [www.nature.com/news](http://www.nature.com/news)

## TREND WATCH

Global investments in renewable energy rose to a record US\$286 billion in 2015, more than double the investment in coal and gas-fired power generation, the United Nations Environment Programme (UNEP) announced on 24 March. The world added 134 gigawatts of renewable-energy capacity in 2015 — up 26% from 2014. Most investment went into solar and wind power. For the first time, UNEP reported, investments by developing countries surpassed those of developed countries.

**RENEWABLES INVESTMENTS RISE**

Solar and wind power are the main beneficiaries of increased global investment in renewables, which rose to record levels in 2015.



# ‘Minimal’ cell raises stakes in race to harness synthetic life

Craig Venter’ s creation comes as CRISPR gene-editing methods provide alternative ways to tinker with life’ s building blocks.

- [Ewen Callaway](#)  
24 March 2016  
Article tools

[Rights & Permissions](#)

*Michael Lewis/Corbis Outline*

Synthetic biologist Craig Venter, whose team embarked on its quest to whittle life down to its bare essentials two decades ago.

Genomics entrepreneur [Craig Venter](#) has created a synthetic cell that contains the smallest genome of any known, independent organism. Functioning with 473 genes, the cell is a milestone in his team’ s 20-year quest to reduce life to its bare essentials and, by extension, to design life from scratch.

Venter, who has co-founded a company that seeks to harness synthetic cells for making industrial products, says that the feat heralds the creation of customized cells to make drugs, fuels and other products. But an explosion in powerful ‘gene-editing’ techniques, which enable relatively easy and selective tinkering with genomes, raises a nagging question: why go to the trouble of making new life forms when you can simply tweak what already exists?

*Thomas Deerinck and Mark Ellisman/NCMIR/UCSD*

Each cell of JCVI-syn3.0 contains just 473 genes, fewer than any other independent organism.

Unlike the [first synthetic cells](#) made in 2010<sup>1</sup>, in which Venter’ s team at the J. Craig Venter Institute in La Jolla, California, copied an existing bacterial genome and transplanted it into another cell, the genome of the minimal cells is like nothing in nature. Venter says that the cell, which is described in a paper released on 24 March in *Science*<sup>2</sup>, constitutes a brand new, artificial species.



“The idea of building whole genomes is one of the dreams and promises of [synthetic biology](#),” says Paul Freemont, a synthetic biologist at Imperial College London, who is not involved in the work.

The design and synthesis of genomes from scratch remains a niche pursuit, and is technically demanding. By contrast, the [use of genome editing is soaring](#) — and its most famous tool, [CRISPR - Cas9](#), has already gained traction in industry, agriculture and medicine, notes George Church, a genome scientist at Harvard Medical School in Boston, Massachusetts, who [works with CRISPR](#). “With much less effort, CRISPR came around and suddenly there are 30,000 people practising CRISPR, if not more.”

#### Related stories

- [Genomics: DNA's master craftsmen](#)
- [Researchers start up cell with synthetic genome](#)
- [Sizing up the 'synthetic cell'](#)

#### [More related stories](#)

Microbiologists were just starting to characterize the bacterial immune system that scientists would eventually co-opt and name CRISPR when Venter's team began its effort to whittle life down to its bare essentials. In a 1995 *Science* paper, Venter's team sequenced the genome of *Mycoplasma genitalium*, a sexually transmitted microbe with the smallest genome of any known free-living organism<sup>3</sup>, and mapped its 470 genes. By inactivating genes one by one and testing to see whether the bacterium could still function, the group slimmed this list down to 375 genes that seemed essential.

One way to test this hypothesis is to make an organism that contains just those genes. So Venter, together with his close colleagues Clyde Hutchison and Hamilton Smith and their team, set out to build a minimal genome from scratch, by joining together chemically synthesized DNA segments. The effort required the development of new technologies, but by 2008, they had used this method to make what was essentially an [exact copy of the \*M. genitalium\* genome](#) that also included dozens of non-functional snippets of DNA ‘watermarks’<sup>4</sup>.

But the sluggish growth of natural *M. genitalium* cells prompted them to switch to the more prolific *Mycoplasma mycoides*. This time, they not only synthesized its genome and watermarked it with their names and with famous quotes, but also implanted it into another bacterium that had been emptied of its own genome.

The resulting ‘JCVI-syn1.0’ cells were unveiled<sup>1</sup> in 2010 and hailed — hyperbolically, many say — as the dawn of synthetic life. (The feat prompted US President Barack Obama to launch a bioethics review, and the Vatican to question Venter’s claim that he had created life.) However, the organism’s genome was built by copying an existing plan and not through design — and its bloated genome of more than 1 million DNA bases was anything but minimal.

*Thomas Deerinck and Mark Ellisman/NCMIR/UCSD*

JCVI-syn1.0 cells were hailed as the dawn of synthetic life in 2010.

In an attempt to complete its long-standing goal of designing a minimal genome, Venter’s team designed and synthesized a 483,000-base, 471-gene *M. mycoides* chromosome from which it had removed genes responsible for the production of nutrients that could be provided externally, and other genetic ‘flotsam’. But this did not produce a viable organism.

So, in a further move, the team developed a ‘design-build-and-test’ cycle. It broke the *M. mycoides* genome into eight DNA segments and mixed and matched these to see which combinations produced viable cells; lessons learned from each cycle informed which genes were included in the next design. This process highlighted DNA sequences that do not encode proteins but that are still needed because they direct the expression of essential genes, as well as pairs of genes that perform the same essential task — when such genes are deleted one at a time, both mistakenly seem to be dispensable.

Eventually, the team hit on the 531,000-base, 473-gene design that became known as JCVI-syn3.0 (syn2.0 was a less streamlined intermediary). Syn3.0 has a respectable doubling time of 3 hours, compared with, for instance, 1 hour for *M. mycoides* and 18 hours for *M. genitalium*.

“This old Richard Feynman quote, ‘what I cannot create, I do not understand’, this principle is now served,” says Martin Fussenegger, a synthetic biologist at the Swiss Federal Institute of Technology (ETH) in Zurich, Switzerland. “You can add in genes and see what happens.”

With nearly all of its nutrients supplied through growth media, syn3.0’s essential genes tend to be those involved in cellular chores such as making proteins, copying DNA and building cellular membranes. Astoundingly, Venter says that his team could not identify the function of 149 of the

genes in syn3.0' s genome, many of which are found in other life forms, including humans. "We don' t know about a third of essential life, and we' re trying to sort that out now," he says.

*Thomas Deerinck and Mark Ellisman/NCMIR/UCSD*

Syn3.0 cells double once every 3 hours.

This has blown Fussenegger away. "We' ve sequenced everything on this planet, and we still don' t know 149 genes that are most essential for life!" he says. "This is the coolest thing I want to know."

Syn3.0' s lasting impact on synthetic biology is an open question. "I think it' s kind of a George Mallory moment," says Church, referring to the English mountaineer who died in 1924 trying to become the first person to climb Mount Everest. " 'Because it' s there' was the excuse he gave for climbing Everest."

Church says that genome-editing techniques will remain the go-to choice for most applications that require a small number of genetic alterations, whereas genome design will be useful for specialized applications, such as recoding an entire genome to incorporate new amino acids. Fussenegger thinks that genome editing will be the favoured approach for therapies, but that writing genomes from scratch will appeal to scientists interested in fundamental questions about how genomes evolve, for instance.

Even Venter acknowledges that syn3.0' s genome, although new, was designed by trial and error, rather than being based on a fundamental understanding of how to build a functioning genome. But he expects fast improvements, and thinks that genome synthesis from scratch will become the preferred approach for manipulating life. "If you want to make a few changes, CRISPRs are a great tool," he says. "But if you' re really making something new and you' re trying to design life, CRISPRs aren' t going to get you there."

*Nature* **531**, 557 – 558 (31 March 2016) doi:10.1038/531557a

## POLITICS

# Scientists say 'no' to UK exit from Europe in *Nature* poll

Most researchers in Britain and the wider EU think that the union benefits science.

BY DANIEL CRESSEY

The charged question of whether the United Kingdom should stay in the European Union — to be put to a national referendum on 23 June — splits the general population almost evenly. But most scientists want the country to stay in, according to a *Nature* poll of nearly 2,000 researchers living in the EU, both inside and outside the United Kingdom (see 'Scientists speak on a Brexit').

Most of the polled researchers also think that a British exit, or 'Brexit', would harm science in the nation and in the EU at large.

Political debate concerning a Brexit has revolved heavily around immigration, the economy and infighting in the country's ruling Conservative Party. Prime Minister David Cameron supports the 'in' camp, but several high-profile members of his party want out.

However, science is making inroads into the discussion. "Research and innovation are actually coming more into the debate," says Mike Galsworthy, co-founder of the advocacy group Scientists for EU. "It's going to get more heated around that issue." On 10 March, *The Times* newspaper published a letter extolling the benefits to science of EU membership, signed by more than 150 researchers at the University of Cambridge who are fellows of the Royal Society. "I think in the sciences, it's clearly overwhelmingly in favour of staying in," says lead signatory Alan Fersht, a Cambridge chemist.

Scientists in favour of staying note that UK universities receive around 16% of their total research funding directly from the EU, and that membership allows researchers to move freely between member states and to work with no restrictions (see *Nature* 530, 15, 2016).

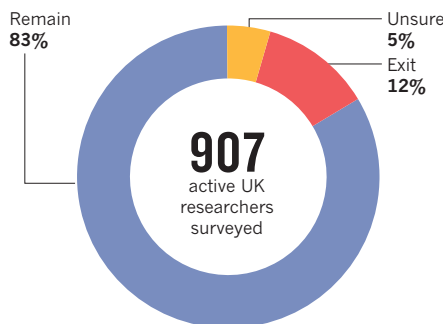
But pro-Brexit Conservative justice minister Michael Gove has suggested that money that the United Kingdom currently gives to the EU as part of its membership could be invested in science if the country leaves. And cancer researcher Angus Dalgleish — who is campaigning for the United Kingdom to leave the union — complained about EU regulation of science on the television programme *Newsnight* on 10 March. The campaign to leave is making science a major point of its activities, says Jamie Martin, an advocate for the leave side and a former special adviser to Gove. ■

## SCIENTISTS SPEAK ON A BREXIT

*Nature* surveyed researchers in the United Kingdom and the wider European Union on the impact of a British exit from the EU.

### UK RESEARCHERS

Should the UK exit the EU or remain?



When only the 666 who plan to vote in the referendum are included, the figures shift slightly — to 80% remain and 14% exit.

**€17 BILLION (US\$19 BILLION)**  
Approximate annual UK contribution to the EU budget.

**€1.4 BILLION**  
Funding received by UK researchers from EU since 2014.

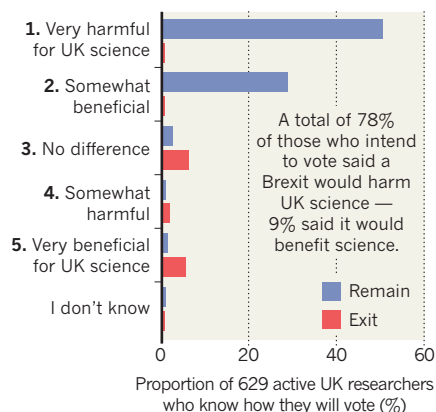
*"The UK is too small to sustain a world-class scientific programme in isolation."*

RESEARCHER WHO WILL VOTE TO REMAIN

*"We could be more open to researchers coming from outside the EU who are currently discriminated against."*

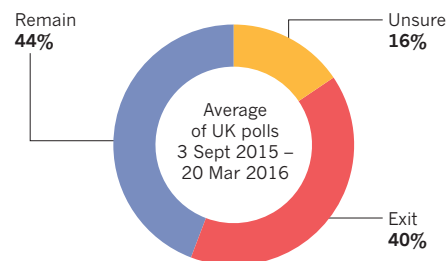
RESEARCHER WHO WILL VOTE TO EXIT

What impact would a UK exit from the EU have on UK science?



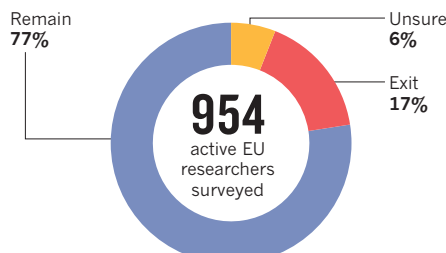
### UK POPULATION

Should the UK exit the EU or remain in the EU?

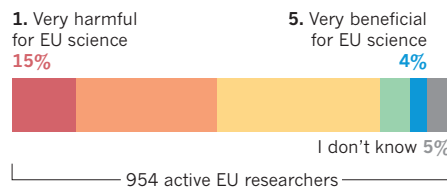


### EU RESEARCHERS EXCLUDING UK

Should the UK exit the EU or remain?



What impact would a UK exit from the EU have on the rest of EU science?



Most scientists think that, if the United Kingdom left the EU, science in the nations left behind would suffer, albeit less than UK science.

Responses to the poll were solicited by e-mail from people who had registered their addresses with *Nature*; on social media; and through a pop-up on its website. The full survey can be found at: [go.nature.com/oxlugl](http://go.nature.com/oxlugl)





Under current guidelines, transgender teenagers are advised to wait until 16 to begin hormone treatment.

#### MEDICAL RESEARCH

# Transgender youth study kicks off

*Scientists will track psychological and medical outcomes of controversial therapies to help transgender teens to transition.*

BY SARA REARDON

For transgender children who think their bodies are the wrong sex, puberty can be terrifying. To alleviate this psychological trauma, physicians are increasingly giving transgender adolescents drugs to block puberty until their bodies — and decision-making abilities — are mature enough to begin cross-sex hormone treatment, typically at age 16.

But the side effects of such therapy are largely unknown, and researchers and clinicians are still trying to determine how to treat children who question the gender they were assigned at birth. A US study set to begin recruiting participants in May could offer some clarity.

Funded by the US National Institutes of Health (NIH), the US\$5.7-million project will be not only the largest-ever study of transgender youth, but also only the second to track the psychological effects of delaying puberty — and the first to track its medical impacts. It comes as the NIH and others have begun to spend heavily on research related to the health of transgender people, says Robert Garofalo, a paediatrician at Ann and Robert H. Lurie Children's Hospital of Chicago, Illinois, and a leader of the study. "We seem to really be at a tipping point," he adds.

Garofalo and his colleagues aim to recruit 280 adolescents who identify as transgender,

and to follow them for at least five years. One group will receive puberty blockers at the beginning of adolescence, and another, older group will receive cross-sex hormones. Their findings could help clinicians to judge how best to help adolescents who are seeking a transition.

About 75% of children who question their gender identify as the gender assigned at birth by puberty. But those who identify as transgender in adolescence almost always do so permanently. Denying them the ability to transition is unethical, says bioethicist Simona Giordano of the University of Manchester, UK. "Not treating adolescents is not being neutral," she says. "It means exposing children to a lot of harm."

#### AGE OF CONSENT

Still, there is no clear age at which children can consent to irreversible treatments, including to hormones. To allow more time to decide and to let their bodies mature, transgender children on the cusp of adolescence are often given drugs called GnRH agonists that block the effects of sex hormones. This is "the safest way to relieve transgender adolescents at the worst time of their life," says Wylie Hembree, an endocrinologist at Columbia University in New York City.

Only one study, published in 2014, has examined the psychological effects of such treatment. Child psychiatrist Annelou de Vries

and her colleagues at VU University Medical Center in Amsterdam monitored a group of 55 transgender adolescents who received puberty blockers at around age 13, cross-sex hormones at about 16 and gender-reassignment surgery at around age 20. They found study participants — now in their 20s — to be as mentally healthy as their non-transgender peers (A. L. de Vries *et al. Pediatrics* **134**, 696–704; 2014).

Less is known about how postponing puberty affects physical health. GnRH agonists have been used for decades to treat children who start to mature too early. But some scientists worry that putting off puberty in older children may disrupt bone and brain development, reducing bone density and leading to cognitive problems.

Later this year, the Endocrine Society will update its guidelines for treating transgender youth. Stephen Rosenthal, a paediatric endocrinologist at the University of California, San Francisco (UCSF), and a leader of the new study, anticipates two major changes. One is to discontinue blanket advice to withhold cross-sex hormone therapy until age 16, to allow flexibility on the basis of when a child enters puberty.

The other change addresses a more controversial topic: whether to allow prepubescent children to live as the gender they identify with. Because most children who question their gender do not do so past adolescence, many psychologists discourage "socially transitioning" until the teenage years. Other clinicians use a "wait and see" approach.

But encouraging children to live as the gender they identify with is an increasingly popular choice. "There's been a real sea change," says Diane Ehrensaft, a psychologist at UCSF. She reports seeing more prepubescent patients recently who have already transitioned socially.

Many transgender-rights activists support this model, and liken any other approach to gay-conversion therapy. "You're telling a kid, 'I don't believe you,'" says Asaf Orr, staff attorney at the National Center for Lesbian Rights in San Francisco. The best strategy, he says, is "to affirm a child's gender exploration, regardless of what the end result is going to be".

The debate is so heated — and evidence so sparse — that the authors of the American Psychiatric Association's 2013 *Diagnostic and Statistical Manual of Mental Disorders (DSM-5)* were unable to reach a consensus. "People are making declarations of knowledge that are their belief systems, that aren't also backed up by empirical research," says Jack Drescher, a psychiatrist at the William Alanson White Institute in New York City.

Nevertheless, several US states and Ontario, Canada, have banned transgender-conversion therapy, which may include any practices that do not actively help children to live as the gender they identify with. No matter the approach, Giordano says, clinicians and families should help children to understand what they are experiencing. "Going through the social and physical transition is a long journey," she says. ■

ANDREW SPEAR/EVINE

## FUNDING

# Biological collections threatened

*Hiatus in US National Science Foundation funding could hamper research.*

BY ANNA NOWOGRODZKI

The cabinets of the Field Museum in Chicago hold a collection of eggs that led to one of the most famous conservation discoveries of the twentieth century: that the pesticide DDT was causing widespread nesting failures in birds of prey.

But such specimen troves — which are used to identify species, track diseases and study climate change — have lost a valuable means of support. On 16 March, the US National Science Foundation (NSF) announced that it would indefinitely suspend a programme that provides funding to maintain biological research collections. The agency will honour current grants, but it is not accepting new proposals.

“It’s surprising and disheartening,” says Christian Sidor, a palaeontologist at the University of Washington in Seattle and a curator at the Burke Museum of Natural History and Culture, also in Seattle. “It rattled

through the entire museum yesterday.”

He and other researchers are worried because the NSF is one of the only public providers of funds to maintain specimen collections. It awards between US\$3 million and \$5 million a year in grants for such collections, equivalent to roughly 0.06% of the agency’s \$7.5-billion budget for the 2016 fiscal year.

Although the phrase ‘biological collections’ might call to mind images of dusty museum drawers, these resources are as likely to include jars of fish larvae collected last week as they are pressed plants from 100 years ago. “Our fish collection, for example, is the repository for NOAA for the north Pacific,” said Sidor. NOAA — the US National Oceanic and Atmospheric Administration — uses the specimens collected each year to assess fish abundance and to set fishing quotas.

The NSF says that it is evaluating the collections grant programme, and is thus unable to say whether the funding hiatus is temporary

or permanent. “That depends on the results of the evaluation,” says Muriel Poston, director of the NSF’s Division of Biological Infrastructure.

That doesn’t satisfy scientists. “What gives?” tweeted Felisa Smith, an ecologist at the University of New Mexico in Albuquerque. “Biological collections are the bedrock of a lot of contemporary science!”

Comparing modern plants or animals to preserved specimens can help scientists to understand how the climate is changing and provide evidence of a species’ historical range, which can illuminate whether a modern population is endangered or threatened.

Many museums are pushing to digitize their collections, which improves global access to information. But “there’s no point digitizing if we don’t take care of the collections themselves”, says Barbara Thiers, director of the William and Lynda Steere Herbarium at the New York Botanical Garden. “You certainly can’t get any DNA out of an image.” ■



Recent studies suggest that the Antarctic ice sheet is much less stable than scientists once thought.

## CLIMATE

# Trigger seen for Antarctic collapse

*Continued growth of greenhouse-gas emissions this century could raise sea levels more than 15 metres by 2500.*

BY JEFF TOLLEFSON

Choices that the world makes this century could determine the fate of the massive Antarctic ice sheet. A study published online this week in *Nature*<sup>1</sup> finds that continued growth in greenhouse-gas emissions over the next several decades could trigger an unstoppable collapse of Antarctica's ice — raising sea levels by more than a metre by 2100 and more than 15 metres by 2500.

"That is literally remapping how the planet looks from space," says study co-author Rob DeConto, a geoscientist at the University of Massachusetts Amherst. The good news, he says, is that it projects little or no sea-level rise from Antarctic melt if greenhouse-gas emissions are reduced quickly enough to limit the average global temperature rise to about 2 °C.

The findings add to a growing body of research that suggests that Antarctic ice is less stable than once thought. In its 2013 report<sup>2</sup>, the Intergovernmental Panel on Climate Change estimated that Antarctic melting would contribute just a few centimetres to sea-level rise by 2100. But as scientists develop a better understanding of how the ocean and atmosphere affect the ice sheet, their projections of the continent's future are growing more dire.

DeConto and co-author David Pollard, a palaeoclimatologist at Pennsylvania State University in University Park, developed a climate model that accounts for ice loss caused by warming ocean currents — which can eat at the underside of the ice sheet — and for rising atmospheric temperatures that melt it from above. Ponds of meltwater that form on the ice surface often drain through cracks; this can set off a chain reaction that breaks up ice shelves and causes newly exposed ice cliffs to collapse under their own weight.

They found that by including all of these processes, they could better simulate key geological periods that have long puzzled scientists. Before the last ice age began 130,000–115,000 years ago, for instance, sea levels were 6–9 metres higher than today — yet atmospheric carbon-dioxide levels were about 30% lower. And 3 million years ago, when CO<sub>2</sub> levels roughly equalled today's, the oceans may have been 10–30 metres higher.

Incorporating the physics of ice melt driven by atmospheric warming, along with cliff collapse, helped DeConto and Pollard to reproduce these key periods with their model. "That

***"That was sort of an epiphany that maybe we were on to something."***

was sort of an epiphany that maybe we were on to something," DeConto says. Ultimately, he and Pollard tested how well different versions of their model simulated the past, and then used the ones that performed best to project future sea-level rise. They found that over time, atmospheric warming would become the main driver of ice loss.

"I think their processes are still a bit speculative, but it's good work," says Nick Golledge, an ice-sheet modeller at the Victoria University of Wellington in New Zealand. His research, published in *Nature* in October<sup>3</sup>, suggests that Antarctic ice melt driven by rising greenhouse-gas emissions could boost global sea levels by up to 39 centimetres by 2100, and by as much as 3 metres by 2300.

Still, Golledge cautions, scientists know little about how the atmosphere and ocean affected ancient glaciers. "We don't really have a great handle on what the climate was like in the past," he says.

A third *Nature* study, published in December<sup>4</sup>, suggested that Antarctic melting was unlikely to produce more than 30 centimetres of sea-level rise by 2100. But its authors noted that newly identified processes such as surface melting and the collapse of ice cliffs could increase ice loss. As such, DeConto and Pollard's projections "are consistent with our recent study", says co-author Tamsin Edwards, a physicist at the Open University in Milton Keynes, UK.

Glaciologists are already aware of the destructive power of the atmospheric-warming and cliff-collapse mechanisms that DeConto and Pollard's model simulates. A string of unusually warm summers caused the sudden collapse of Antarctica's Larsen B ice shelf in 2002. And scientists have witnessed the basic physics of ice-cliff collapse during calving events on the Jakobshavn and Helheim glaciers in Greenland.

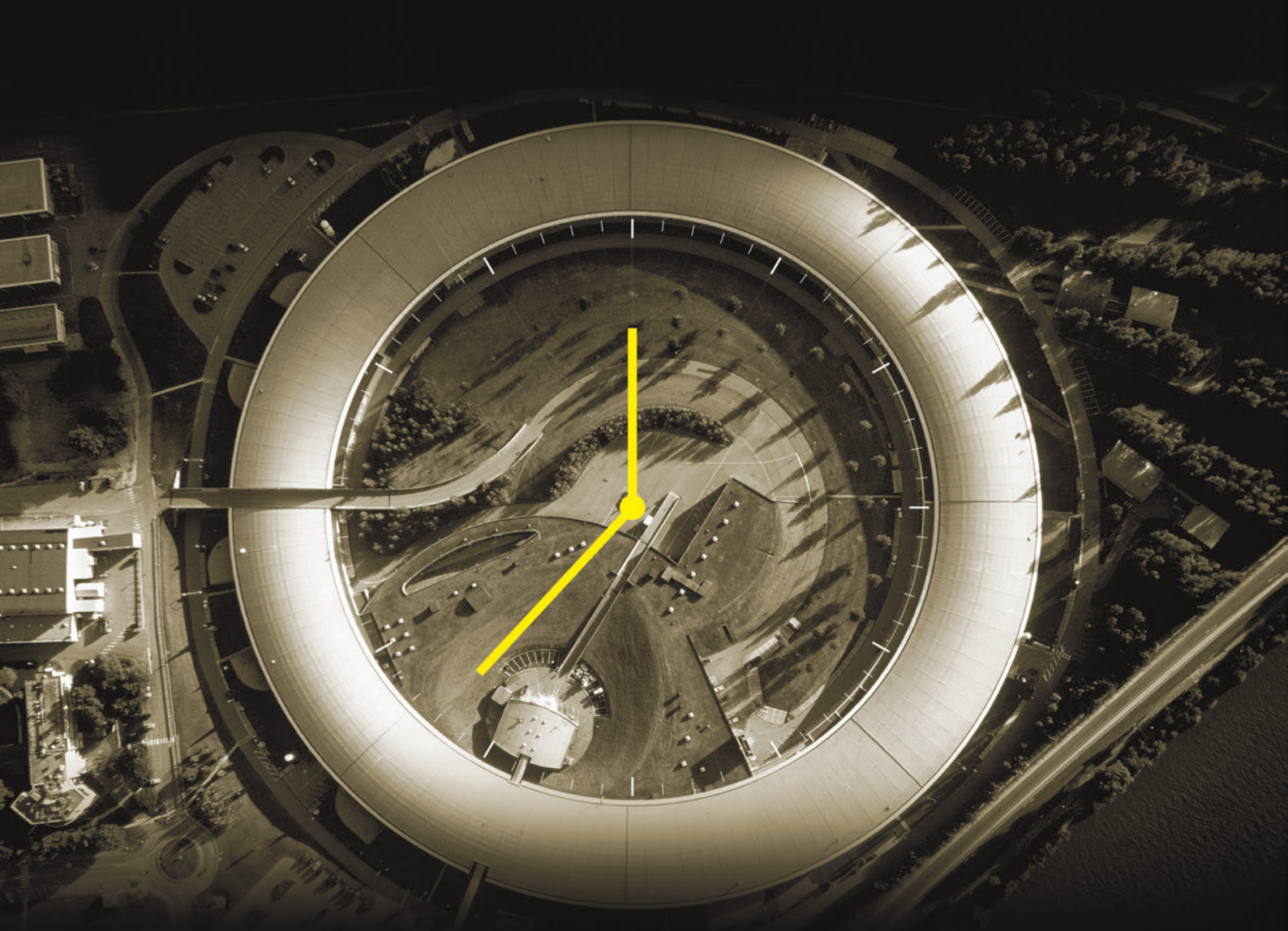
"On the observational side, I see the things they are talking about," says David Holland, a physical-climate scientist at New York University. "There's a lot of observation and modelling to go, but they are adjusting people's thinking in a very scientific way."

For DeConto, the new model results underscore the choice that humanity is facing. If he and Pollard have the physics correct, this process of ice-shelf disintegration, followed by ice-cliff collapse, will be nearly impossible to stop once it gets under way.

"Once the ocean warms up, that ice will not be able to recover until the oceans cool back down," he says — a process that could take thousands of years. "It's a really long-term commitment." ■

1. Pollard, D. & DeConto, R. M. *Nature* <http://dx.doi.org/10.1038/nature17145> (2016).
2. Church, J. A. et al. in *Climate Change 2013: The Physical Science Basis. Contribution of Working Group I to the Fifth Assessment Report of the Intergovernmental Panel on Climate Change* (eds Stocker, T. F. et al.) 1137–1177 (Cambridge Univ. Press, 2013).
3. Golledge, N. R. et al. *Nature* **526**, 421–425 (2015).
4. Ritz, C. et al. *Nature* **528**, 115–118 (2015).





# *24 hours at the X-ray factory*

Life in a synchrotron — a massive laboratory that runs day and night.

BY RICHARD VAN NOORDEN

**B**y half past four in the morning, PhD student Warren Stevenson has been awake for 22 hours. “I’m tired — but we work now or we don’t work at all,” he says, leaning back on his swivel chair and staring resolutely at two computer screens. “We plan to take a nap at 6 a.m. and wake up at 8. It’ll be intense.”

Stevenson’s intensity is warranted: he has just a few precious hours to collect data crucial for his PhD about the structure of liquid crystals. And he is not the only scientist determined to defy sleep on this freezing November night. Nearby, in rooms positioned around a vast circular chamber, workers are simultaneously conducting 28 separate

The European Synchrotron Radiation Facility in Grenoble, France.

ESRF experiments. This is the European Synchrotron Radiation Facility (ESRF) in Grenoble, France — a giant science factory that, for 24 hours a day and as many days a year as its engineers can safely manage, pulses out the most intense high-energy X-ray beams in the world.

The teams who come here work in different fields: some study fossils, others batteries, still others proteins, minerals, artwork or archaeological treasures. But each visits for the same reason: to examine the structure of material by exposing it to light with the short wavelength that's needed to reveal details at the scale of atoms. Work hours are long: most of the current visitors arrived yesterday and have been granted only a few 8-hour shifts to collect their data. And competition to use the machine is so fierce — around 45% of requests are granted — that the facility operates around the clock to fit in as many as possible.

Altogether, some 8,000 scientists visit here each year, conducting upwards of 2,000 experiments and producing the raw material for around 1,800 papers. In the past seven years, two Nobel prizes have been awarded for discoveries made at the synchrotron. It is a non-stop, international, interdisciplinary laboratory — which is why *Nature* spent 24 hours walking its tunnels to observe a slice of contemporary science as it unfolds (see 'The synchrotron that never sleeps').

"Our time here is precious. It will be months before our next visit — or it could be a year if we aren't lucky," says Xiangbing Zeng, Stevenson's PhD supervisor. Some visitors have teams large enough to rotate in shifts; many others will return home with dark circles under their eyes. But the scientists don't mind. They value the opportunity to bury themselves in data collection while escaping the rest of life. "For the week after, you feel jet-lagged," says biochemist Andrea Schmidt. "It doesn't get any easier. But it's always exciting to come here."

**10:00** Schmidt is already looking harried. She and two colleagues flew in yesterday from the Charité medical university in Berlin, bringing with them 120 precious protein crystals frozen in a flask of liquid nitrogen. The German biochemists have just 24 hours to deduce the structure of their crystal — a bacterial protein that has been engineered to fluoresce when hit by red light and that is used to tag and study structures in living tissue. What's not clear is how such proteins work at the level of atoms and molecules. It would be an "important publication" if the team can explain it, says Schmidt.

Synchrotrons are the workhorses of structural biology. There are around 50 of them in the world, and the vast majority of the 6,000 or so atomic-resolution protein structures reported by scientists last year were solved at

these facilities, by examining the diffraction patterns formed when high-power X-rays are fired at crystallized proteins. At the ESRF, working quarters consist of a small office opening onto a cramped experimental room called a hutch, which is where Schmidt and her colleagues will analyse their crystals — each less than a hair's width across, and trapped in frozen solvent in the centre of a half-millimetre loop of nylon.

As soon as Schmidt's team arrived this morning, the researchers began sticking tape over every visible light they could find. Light

**"For the week after, you feel jet-lagged. But it's always exciting to come here."**

could cause molecules in the protein crystal to wiggle, making it impossible to capture an atomic-resolution picture. Schmidt flicks the light switch on and off, checking to see whether the rigged-up room is now completely dark. "It's MacGyver-like stuff," grins her PhD student Dennis Kwiatkowski.

**10:23** Inside the 844-metre central ring of the synchrotron, electrons are circling at nearly the speed of light and spitting out X-rays like water flicking from a spinning car wheel. The X-rays are channelled through thin pipes to as many as 43 stations, called beamlines, around the ESRF ring, with a hutch and office attached to each.

Earlier this morning, specialist engineers injected fresh bunches of accelerated particles into the ring because the machine had been off for maintenance the day before. Each beamline has its own dedicated ESRF scientist who calibrates the X-ray beam for that day's experiment, and often sits with the team all day. "There are a lot of critical components and a lot of possible modes of failure," says David von Stetten, the support scientist for Schmidt's team. "It's important to check it every day."

**10:46** Stevenson, Zeng and a third member of the team, PhD student Huanjun Lu, have started their day by preparing samples of the liquid crystals that they want to image. The group, from the University of Sheffield, UK, wants to work out how molecules are aligned inside the crystals, which are similar to those found inside LCD televisions. The work might one day lead to improved screens that can flicker on and off at higher rates.

The team is one scientist down: a Chinese national couldn't get his visa in time, so it's impossible for the rest to pair up in shifts as they had planned. There won't be any chance to leave the building, says Stevenson, but he shrugs. "It's just the work ethic. We never see Grenoble when we come here."

**12:15** In a hutch 200 metres away, PhD student Annalisa Chieli is using a microtome to painstakingly cut ultra-thin slivers of dry paint from a block. It is her first time at the synchrotron. Yesterday, at home with her parents in Perugia, Italy, she watched a YouTube video about it. Now she is here, she says, "you can feel the research in the air".

Chieli, from the University of Perugia, is preparing to shine X-rays at samples taken from one of the four versions of *The Scream*, a painting by the famously melancholic Norwegian artist Edvard Munch, as well as samples from Jackson Pollock's *Alchemy*. Yellowish hues in both artworks have faded over time, and museum curators are not sure why. The synchrotron work could help to explain it, and perhaps protect the art.

Today is prep work, explains team leader Letizia Monico, from the Institute of Molecular Science and Technology of Perugia: they are scanning various samples of yellow paint to build up a reference library showing how pigments of different elemental composition absorb X-ray light and how that changes with age. Tomorrow, precious flakes from the real paintings will be scanned and compared with this gallery to decipher how the compounds in them have changed with time.

Like most of the researchers here, Monico and Chieli need pay nothing to visit. Twenty-one countries have signed up as partners of the synchrotron, contributing a combined €110 million (US\$124 million) to operate it each year. The cash covers all the food and accommodation expenses for three members of each team visiting from a partner nation.

**13:17** Because the clientele is international, the two canteens have to be, too. The larger one is buzzing as visitors and staff scientists tuck into a selection of meat, fish, pizza, pasta, desserts, cheese, yogurt — and a choice of wines (often French). Altogether, the canteen doles out some 1,000 meals a day. The working language of the ESRF is English, but here the multilingual chatter is like a session at the United Nations.

Monico's team picks the quieter, upper canteen. "For me, salad, and lots of vegetables," says Monico, a small, brown-haired Italian who gesticulates animatedly as she explains the chemistry of the cadmium sulfide yellow pigment that she expects to find in Munch's work. "Art is my passion," she says. The third member of the group, Frederik Vanmeert, of the University of Antwerp in Belgium, says his passions lie elsewhere. "I'm interested in the techniques," he says.

**14:00** Back at her hutch, Schmidt's expression grows — if possible — slightly more anxious. The team is behind schedule: half the day has been spent setting up everything for the



experiment on the light-sensitive protein. “If you don’t have a good method to overcome frustration, then you are in the wrong field,” she says, staring at a magnified computer-screen image of her frozen sample.

Schmidt and her group leader, Patrick Scheerer, want to get a picture with better than 2.8-ångström resolution to distinguish the separate amino-acid side chains of the protein. But Schmidt is on the 9th sample out of 100, and hasn’t seen a discernible image yet. “Ninety per cent of the experiments go wrong,” she says, as she moves her mouse to decide where to aim the X-ray beam next.

She clicks the mouse button — and throws up her hands in frustration. “Aah, 4.85 ångströms. You can only see a sheet or a helix, nothing else. Patrick will kill me if I don’t collect the data.”

Schmidt knows she could be in for a slog.

crystals into a sample-changer at the beginning of the day, but doesn’t need to intervene regularly: researchers who send in samples to be analysed are informed of results by automated e-mails. The best part? It keeps Bowler’s hours regular: he works from 8 a.m. until 6 p.m. each day. “I’m going to pick up my daughter from a piano lesson, then I’m done for the day,” he says.

**18:50** Nearby, Alexey Nikulin and Natalia Lekontseva are filling up a vacuum flask at a liquid-nitrogen dispenser. They flew in from the Institute of Protein Research in Pushchino, near Moscow, on Monday, and depart at the end of the week. “Hamburg’s synchrotron doesn’t work at the moment, and Berlin’s is full up,” says Nikulin, as the two trundle the full, heavy vessel back to their hutch. The liquid nitrogen will be used to keep their crystals,

McCarthy, who’s in charge of the ESRF’s user programme. “In the olden days, you prepared your samples for measurement and went off to have dinner in town,” she says.

**21:00** The synchrotron’s electrons are tiring out. The lead-lined pipe is not a perfect vacuum, and occasional collisions with air molecules make the tightly focused bunches of electrons spread out slightly and lose energy, causing the flux of each X-ray beam to drop. Engineers pump replacements into the synchrotron’s storage ring to maintain the beams through the night.

**21:36** In hutch ID22, the computer emits a gong sound — an alert signifying that the most recent measurement has ended. The team of five scientists, led by Boaz Pokroy from the Technion in Haifa, Israel, applied for time here

## THE SYNCHROTRON THAT NEVER SLEEPS

Because of high demand, the European Synchrotron Radiation Facility runs day and night, pulsing out high-energy X-ray beams to 43 experimental stations to explore the atomic structure of samples ranging from proteins to portraits.

For a video of 24 hours in the synchrotron, see [go.nature.com/2frnrx](http://go.nature.com/2frnrx)



When US structural biologist Brian Kobilka used the ESRF’s tightly focused beamline in 2007 to take the first picture of a G-protein-coupled receptor — a structure that would win him the 2012 Nobel Prize in Chemistry — his team worked through 1,043 crystals before it hit the jackpot.

**16:00** Next door, Matthew Bowler is looking relaxed. He has already scanned 80 crystal samples, couriered in from Helsinki the day before, and has successfully determined 3 protein structures without breaking a sweat.

Bowler hasn’t done this all by himself. Rather, he works on one of the world’s only automated X-ray crystallography beamlines. The robot, which Bowler built with other ESRF staff scientists, loads up crystal samples, scans each frozen blob, decides where to fire the X-rays for best results, collects data sets and then moves on to the next one. “It does this 24 hours a day, and it doesn’t get tired,” Bowler says with pride. The robot has processed 15,000 crystals over the past year. (Unfortunately for Schmidt, the specialized light conditions required by her protein make it impossible for the robot to handle.)

Bowler supervises the machinery and loads

of an RNA-binding protein, frozen until they are ready for use.

**19:10** Out in the corridor, Magnus Larsson walks past, on his way home for the day. He’s easily identifiable as a non-researcher from his suit. Larsson is an industrial liaison officer who is visiting from the MAX IV synchrotron in Lund, Sweden, the world’s first ‘fourth-generation’ machine, which promises to produce tighter, brighter beams of X-rays when it opens in June. He has been visiting to get tips on how the ESRF works with industry researchers, who pay their own way but are allowed no more than 10% of the synchrotron’s beamtime.

After he’s gone, the synchrotron’s grey corridors are empty. The air conditioning clanks and hums. Although each group works just a minute or two’s walk away from its neighbours, the teams rarely interact.

As darkness falls outside, researchers begin drifting back towards the synchrotron’s canteen for dinner. The superior intensity of the X-rays generated by modern machines — which collect data in minutes, where older ones took hours — means that scientists who come to synchrotrons now have less time away from their hutches, says Joanne

eight months ago. It was worth the wait, Pokroy says: “The ESRF is, no question, the best synchrotron on this Earth.”

The researchers are here in the name of materials science: they are examining the crystals that form when biological molecules, such as amino acids, are mixed with inorganic minerals such as copper oxide, so that the two crystallize together in a composite. The team is exploring whether this changes the electronic properties of the minerals in predictable ways, Pokroy says, perhaps leading to semiconductors with new properties.

Carlotta Giacobbe, their Italian staff-support scientist, points to a closed-circuit-television picture on the computer monitor, which shows a tall yellow robotic arm dipping to remove some tubes of powdered crystalline samples from the X-ray beam. “There are a lot of sounds,” Giacobbe says: “there’s a train whistle when the measurement starts, a gong when it stops and a scream if there’s a problem with data backup.” (There’s also a donkey bray and the sound of laughter, which play when the scientists make mistakes.)

**22:19** The researchers in Monico’s team are finishing their paint analyses and are

ESRF (LEFT IMAGE), NATURE

about to retire to the ESRF's guesthouse, which has 173 rooms and is full up tonight. Vanmeert is entering code on the computer, instructing a robot to move a sample of pigments slowly through the X-ray beam while they're gone.

"If you make a single error, you lose the night," warns ESRF beamline scientist Marine Cotte. Vanmeert is careful, but he is also looking forward to bed. "I will read a book and dream about beamlines," he says.

**23:00** At Pokroy's beamline, things aren't going so well. The gong sounds, and Giacobbe looks at the camera, expecting the yellow arm to move towards a fresh array of samples. Nothing.

"No ... shit. Wait, it didn't work," she sighs. "OK. This means that the night will be longer than expected."

won't know the protein's full shape until the researchers can analyse the data later on.

"If we have exciting results like these, we don't need any coffee to stay up," says Schmidt's colleague, Bilal Qureshi. Qureshi says he likes the single-minded focus the team can achieve on a synchrotron visit. "We generate a lot of ideas, and we don't think about much else."

**2:00** The synchrotron is emptying — but where samples can't be changed by robot or need careful supervision, dozens of experimenters remain in their hutches. One of them is Stefan Mebs, a cheery German chemist from the Free University in Berlin; he and his colleague Peer Schrapers have elected to do night shifts for the next two weeks, because their samples must be changed every half-hour by hand. "On the day shift, you can sleep at normal times — but the experiments are

visitors, who can't imagine how else one would stay up. "Sometimes people jog around the inside of the tunnel," Villanova says. "Though there's a nice river not far away."

**5:00** Despite their earlier success, Schmidt and her team have come unstuck because of a broken sample holder. After half an hour trying to fix it, they give up for the night. With 30 crystals not yet analysed, they creep wearily back to the guesthouse for 5 hours' sleep before they fly back to Germany. Schmidt will be back in two weeks to do it all again.

**6:45** Stevenson and Zeng have been up for well over 24 hours, but they have managed to obtain results on two liquid crystal samples. "I'm as pleased as I can be in the present circumstances," Stevenson says. "I think I'll just pass out, eventually."



Pokroy leans over. "The robot is shy? Why didn't it change?"

"I don't know," Giacobbe says, rapidly typing in commands.

She and Pokroy go inside the hutch and fish around at cables, while the rest of the team looks concerned. Pokroy finds a possible culprit — a red cable that appears to have been cut. But no-one is sure of the problem, and it is too late to call in a technician, so data collection will stop. "We will lose a night," Giacobbe says, looking downcast. The six scientists put on their coats, pick up their bags, and leave for the guesthouse. Behind them, the robot is still.

**23:13** The guesthouse is so full that some scientists couldn't get rooms. Georgios Kalantzopoulos and Erik Glesne, two materials scientists from the University of Oslo, set out to walk the 40 minutes into Grenoble for a hotel they have booked there instead. It's raining, and by the time they arrive, they are drenched.

**00:00** At last, a breakthrough. By slogging through dozens of crystals, Schmidt's team has managed to get a 2.5-ångström-resolution picture of the light-sensitive protein — enough for the core of a research paper, although they

more stressful," says Mebs. "At night, it's more relaxed. It's quite calm."

This group is blasting X-ray pulses at haemoglobin — the oxygen-carrying protein in red blood cells — in the hope of working out exactly how oxygen molecules bind to its iron-atom core. The team wants to examine this at room temperature as well as the sub-zero conditions that are usual for working with crystals, to see whether the binding is different at each, says Mebs.

**3:00** On the far side of the synchrotron, three scientists are still up — although they have installed a sofa in their office in case they have time to catch a nap, says Julie Villanova, the ESRF staffer on the beamline. "When people come here, they are really motivated, and they push us all," she says. Her two users for the day — Peter Joergensen and Salvatore De Angelis of the Technical University of Denmark in Kongens Lyngby — are taking pictures of tiny pits in electrodes from different samples of solid oxide fuel cells to see how they have degraded over time.

Villanova makes an espresso in a kitchen nearby, although she does not drink it herself — something that impresses the Danish

**8:00** With the night shift ending, cleaners mop and vacuum the tunnels before a new tide of scientists pours into the synchrotron. Giacobbe returns early with two colleagues to try to sort out last night's problem. "We thought it was the wires, but it was actually a software fault," she says. "I feel relieved. It's nice when you discover what the problem is and fix it."

The gong sounds, and then the train whistle, and in the hutch beyond, a robotic arm whisks around to pick up a sample. Giacobbe smiles. "It's OK to lose one shift. They can recover the time."

**9:00** Two fresh-faced researchers walk into the office just vacated by Schmidt's group and put down their bags. Theodoras Goulas and Mariana Castrillo Bricenyo have just arrived from the Institute of Molecular Biology in Barcelona, Spain — and now, like their predecessors, they have 24 hours in the hutch. Goulas is looking forward to the long day ahead. "I'm pretty sure we'll get something," he says. ■

**Richard Van Noorden** is a senior news editor for Nature.





BY BRENDAN MAHER

# GOOD GAMING

**SCIENTISTS ARE HELPING TO TAME  
TOXIC BEHAVIOUR IN THE WORLD'S  
MOST POPULAR ONLINE GAME.**

**NEXT STOP — A KINDER INTERNET?**

**I**t took less than a minute of playing *League of Legends* for a homophobic slur to pop up on my screen. Actually, I hadn't even started playing. It was my first attempt to join what many agree to be the world's leading online game, and I was slow to pick a character. The messages started to pour in.

"Pick one, kidd," one nudged.

Then, "Choose FA GO TT."

It was an unusual spelling, and the spaces may have been added to ease the word past the game's default vulgarity filter, but the message was clear.

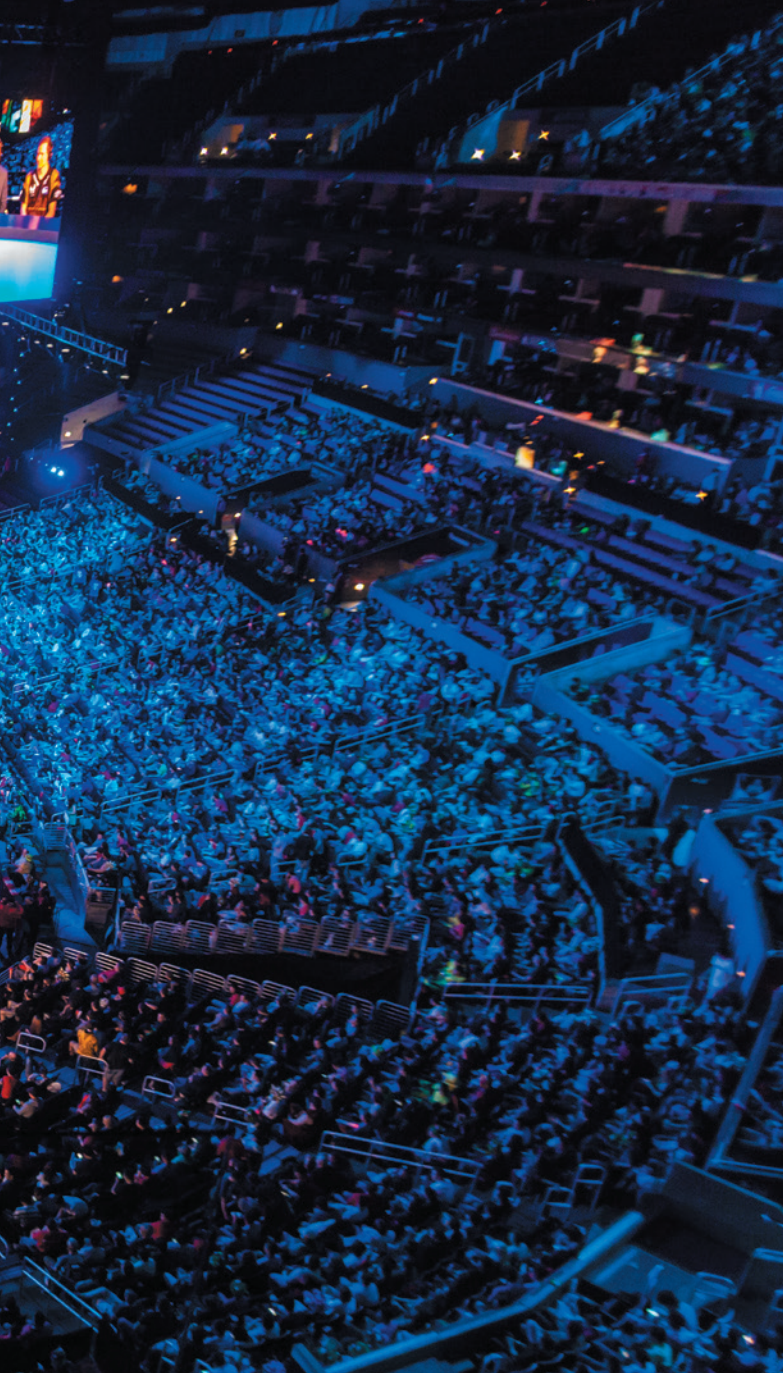
Online gamers have a reputation for hostility. In a largely consequence-free environment inhabited mostly by anonymous and competitive young men, the antics can be downright nasty. Players harass one another for not performing well and can cheat, sabotage games and do any number of things to intentionally ruin the experience for others — a practice that gamers refer to as griefing.

Racist, sexist and homophobic language is rampant; aggressors often threaten violence or urge a player to commit suicide; and from time to time, the vitriol spills beyond the confines of the game. In the notorious 'gamergate' controversy that erupted in late 2014, several women

**➔ NATURE.COM**

To hear more about taming gaming behaviours, visit [go.nature.com/m9pbcq](http://go.nature.com/m9pbcq)





MARY WATSON

involved in the gaming industry were subjected to a campaign of harassment, including invasions of privacy and threats of death and rape.

*League of Legends* has 67 million players and grossed an estimated US\$1.25 billion in revenue last year. But it also has a reputation for toxic in-game behaviour, which its parent company, Riot Games in Los Angeles, California, sees as an obstacle to attracting and retaining players. So the company has hired a team of researchers to study the social — and antisocial — interactions between its users. With so many players, the scientists have been able to gather vast amounts of behavioural data and to conduct experiments on a scale that is rarely achieved in academic settings.

Whereas other game companies have similar research teams, Riot's has been remarkably open about its work — with players, with other companies and with a growing collection of academic collaborators who see multiplayer games as a Petri dish for studying human behaviour. "What's most interesting with Riot is not that they're doing it but that they're publicizing it and have an established way of sharing it with academics," says Nick Yee, a social scientist and co-founder of Quantic Foundry, a video-game-industry consulting firm in Sunnyvale, California.

Riot's findings have helped to reveal where the toxic behaviour comes

**A team from South Korea won the 2013 *League of Legends* world championship in Los Angeles.**

from and how to steer players to be kinder to each other. And some say that the work may translate to digital venues outside the game. "The work they do is extensible to thinking about big questions," says Justin Reich, an education researcher at the Massachusetts Institute of Technology in Cambridge, "not just how do we make online games more civil places, but how do we make the Internet a more civil place?"

## BIG BUSINESS

Jeffrey Lin, the lead designer of social systems at Riot, is the public face of its research programme. He has been playing video games online since he was about 11 years old and had long wondered why so many of his fellow gamers put up with toxic behaviour. "Everybody you talk to thinks of the Internet as this hate-filled place," he says. "Why do we think that's a normal part of gaming experiences?"

In 2012, Lin was finishing a PhD in cognitive neuroscience at the University of Washington in Seattle and was working for the game company Valve in nearby Bellevue when a friend and fellow gamer introduced him to the co-founders of Riot, Marc Merrill and Brandon Beck. They had recognized that toxic behaviour was a major drag on players' experience, and they wanted to solve the problem with science. So they hired Lin as a game designer, essentially giving him the keys to a juggernaut in the online gaming world.

*League of Legends*, Riot's only game, was released in 2009 and currently attracts 27 million players each day. It is by far the most popular of a growing segment of games referred to as eSports, a world in which elite players form professional teams, win university scholarships and take part in million-dollar tournaments in sporting arenas. The final of *League of Legends*'s 2015 world championship in Berlin drew 36 million viewers online and on television, rivalling the audience of the finals of some traditional sports.

The game can be intimidating to newcomers. Players control one of more than 120 characters called champions, each of which has specific abilities, weaknesses and roles. Teams are usually made up of five players, who must cooperate to kill monsters and opponents, collect gold to purchase magical items, capture territory and eventually destroy the other team's base.

Matches last about half an hour on average, so having a poorly performing player on a team can be aggravating. And the game requires coordination between players, for which it provides an in-game chat function. If someone makes a mistake, he or she will generally hear about it fast. Players can report their teammates for being toxic, and this can result in a temporary or permanent ban from the game. But working out how to distinguish a few frustrated grumbles or good-natured trash talk from the kind of vitriol that is worthy of punishment is a difficult task.

To tackle it, Lin needed to make sure that he had a good picture of where such toxicity was coming from. So he got a team to review chat logs from thousands of games each day and to code statements from players as positive, neutral or negative.

The resulting map of toxic behaviour was surprising. Common wisdom holds that the bulk of the cruelty on the Internet comes from a sliver of its inhabitants — the trolls. Indeed, Lin's team found that only about 1% of players were consistently toxic. But it turned out that these trolls produced only about 5% of the toxicity in *League of Legends*. "The vast majority was from the average person just having a bad day," says Lin. They behaved well for the most part, but lashed out on rare occasions.

That meant that even if Riot banned all the most toxic players, it might not have a big impact. To reduce the bad behaviour that most players experienced, the company would have to change how players act.

Lin borrowed a concept from classic psychology. In late 2012, he initiated a massive test of priming, the idea that imagery or messages presented just before an activity can nudge behaviours in one direction or another.

The Riot team devised 24 in-game messages or tips, including some that encourage good behaviour — such as "Players perform better if you give them constructive feedback after a mistake" — and some that discourage bad behaviour: "Teammates perform worse if you harass them after a mistake". They presented the tips in three colours and at different times during

the game. All told, there were 216 conditions to test against a control, in which no tips were given. That is a ridiculous number of permutations to test on people in a laboratory, but trivial for a company with the power to perform millions of experiments each day.

Some of the tips had a clear impact. The warning about harassment leading to poor performance reduced negative attitudes by 8.3%, verbal abuse by 6.2% and offensive language by 11% compared with controls. But the tip had a strong influence only when presented in red, a colour commonly associated with error avoidance in Western cultures. A positive message about players' cooperation reduced offensive language by 6.2%, and had smaller benefits in other categories. Riot has released just a few of these analyses, so it is hard to make broad generalizations.

From a scientific standpoint, says Lin, the results from the priming experiments were "epic", and they opened the doors to many more research questions, such as how various tips and colours might influence players from different cultures. But the behavioural improvements were too modest and too fleeting to change the culture of the game. Lin reasoned that if he wanted to make the community more civil, then players would have to have a say in devising the norms. So Riot introduced the Tribunal, which gives players a chance to serve as judge and jury to their peers. In it, volunteers review chat logs from a player who has been reported for bad behaviour, and then vote on whether the offender deserves punishment.

The Tribunal, which started in 2011, gave players a greater sense of control over establishing community norms, says Lin. And it revealed some of the things that triggered the most rebukes: homophobic and racial slurs. But players who were banned from the game were often unsure why they had been punished, and continued to act negatively when the bans were lifted. So Lin's team developed 'reform cards' to give feedback to banned players, and the company then monitored their play. When players were informed only of what kind of behaviour had landed them in trouble, 50% did not misbehave in a way that would warrant another punishment over the next three months. When they were sent reform cards that included the judgements from the Tribunal and that detailed the chats and actions that had resulted in the ban, the reform rate went up to 70%.

But the process was slow; reform cards might not show up until two weeks to a month after an offence. "If you look at any classic literature on reinforcement learning, the timing of feedback is super critical," says Lin. So he and his team used the copious data they were collecting to train a computer to do the work much more quickly. "We let loose machine learning," Lin says. The automated system could provide nearly instantaneous feedback; and when abuse reports arrived within 5–10 minutes of an offence, the reform rate climbed to 92%. Since that system was switched on, Lin says, verbal toxicity among so-called ranked games, which are the most competitive — and most vitriolic — dropped by 40%. Globally, he says, the occurrence of hate speech, sexism, racism, death threats and other types of extreme abuse is down to 2% of all games.

"If the numbers they put out there are correct and true, it seems to be working well," says Jamie Madigan, an author in St Louis, Missouri, who writes about the psychology of gamers. And that's because the reprimands are specific, timely and easy to understand and act upon, he says. "That's classic psychology 101."

## OPEN DATA

Riot's research team is constantly experimenting with other ways to improve interactions in the game. Sportsmanlike behaviour can earn players honour points and other rewards. Tinkering with chat features

helped, too. And the team is planning to use the Tribunal to train the game's algorithms to detect sarcastic and passive-aggressive language in chats — a major challenge for machine learning.

From the start, Riot has also made much of its data available for others to investigate. Jeremy Blackburn, an avid gamer and computer scientist who works at Telefonica Research and Development in Barcelona, Spain, mined data on 1.46 million Tribunal cases to develop his own machine-learning approach for predicting when player behaviours would be deemed toxic. Together with Haewoon Kwak at the Qatar Computing Research Institute in Doha, he found that the most important factor — beyond the specific words used in the toxic messages — was how well the opposing team performed<sup>1</sup>. Blackburn, who is interested in studying cyberbullying, hopes to look more at how different cultures judge behaviour. Some evidence, he says, suggests that it is common for Korean gamers to gang up on and berate the poorest-performing players, for example. League data may bear this out. "We saw there was a lot more pardon for this verbal-abuse category."

Rachel Kowert in Austin, Texas, is a research psychologist on the board of the Digital Games Research Association. She is impressed by the work and especially by Blackburn and Kwak's unfettered access. "It's awesome for the researchers. You can't put a price on real data," she says.

Other companies also have data that scientists would like. Blizzard Entertainment in Irvine, California, makes the popular online fantasy game *World of Warcraft*, which many regard as a treasure trove for data on complex social interactions. But few people outside the company have been able to work with the data, and most of those who do are subject to stiff non-disclosure agreements. (Blizzard did not respond to *Nature's* requests for comment.)

By contrast, Riot talks about its data at gaming conferences, and when it collaborates with researchers there are few restrictions on publishing. It also has an outreach programme, visiting universities to establish collaborations. And last May, Lin presented data at the annual meeting of the Association for Psychological Science in New York City to drum up more interest.

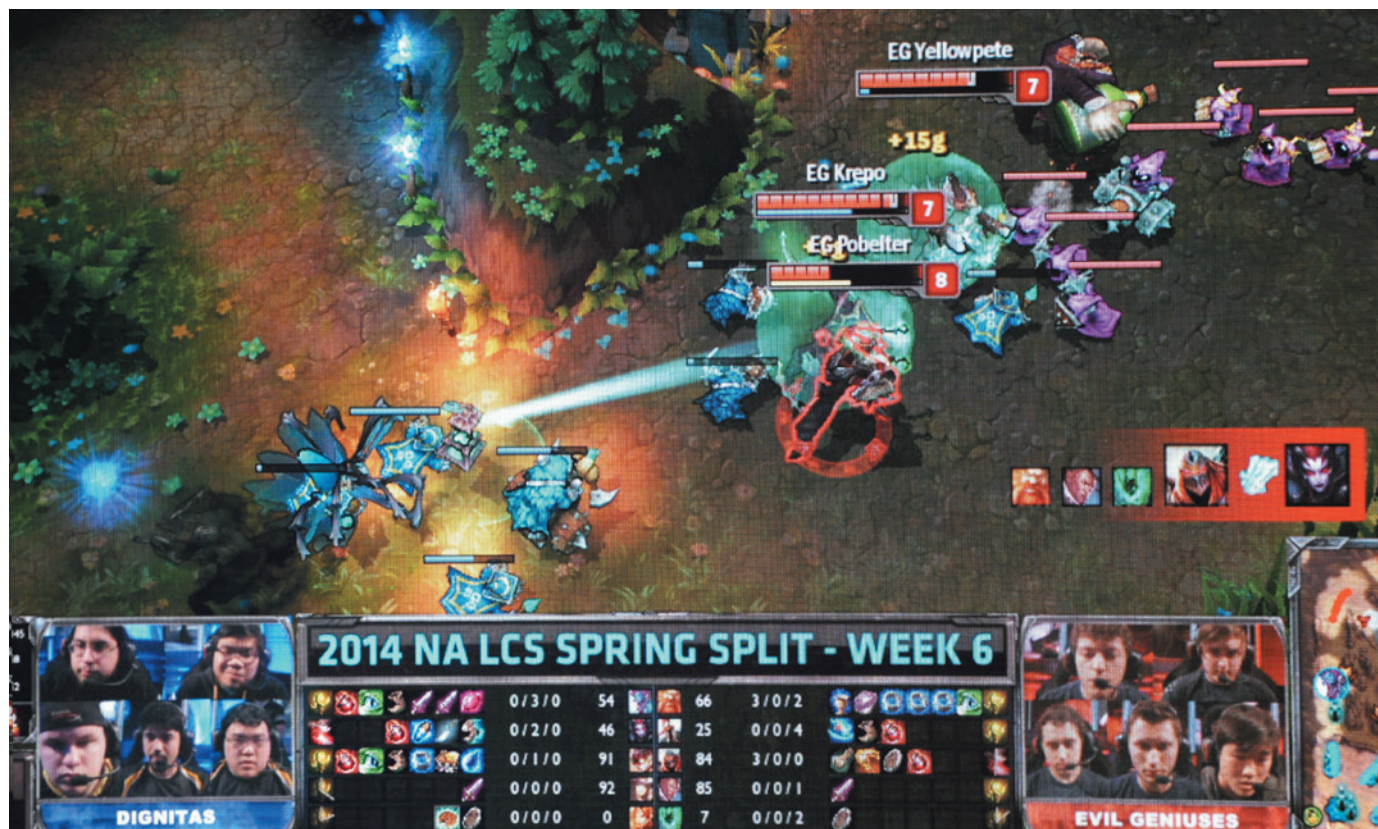
Even with those efforts, the company's research has yet to achieve broad recognition among behavioural scientists. "Hopefully they will come to more conferences where people are studying behaviour," says Betsy Levy Paluck, a social psychologist at Princeton University in New Jersey. Although she was not familiar with Riot, she says that the company seems to be working out how to do high-powered, big-data research in psychology, which has been a major challenge.

Daphné Bavelier, a cognitive neuroscientist at the University of Geneva in Switzerland, met Lin at the conference in New York City. Her research has suggested — to the joy of many gamers and the agony of their parents — that some games, particularly fast-paced first-person shooters, can improve a handful of cognitive abilities, such as visual attention, both within and outside the games<sup>2</sup>. She plans to collaborate with Riot to study how players tackle the steep learning curve in *League of Legends*.

The team-based nature of the game could also be useful to scientists. Young Ji Kim, a social scientist at the Massachusetts Institute of Technology's Center for Collective Intelligence, was able to recruit 279 experienced teams from *League of Legends* to fill out surveys and work together on a battery of online tests that were designed to explore team dynamics and the factors that make teams successful. (By providing an in-game incentive worth about \$15, Riot helped her team to get thousands of sign-ups in a couple of hours, she says.) The preliminary results suggested that the teams' rank in the game correlates with their collective intelligence — a measure that generally tracks with things such as social perceptiveness and taking equal turns in conversation.

**"IT'S AWESOME FOR THE RESEARCHERS. YOU CAN'T PUT A PRICE ON REAL DATA."**





The enthusiasm that players show for participating in experiments such as these may be attributable to Lin, who writes frequently about Riot research and can often be found answering players' questions on Twitter and other social media. Being upfront and public about the efforts is important, says Bavelier. Although most digital companies run experiments on users, they are often less transparent. Facebook, for example, published a study about how behind-the-scenes tinkering with news feeds can manipulate user emotions<sup>3</sup>, and received significant backlash from users. "We need to learn from some of the mistakes of others to make sure that the users are aware of what we're doing," says Bavelier.

Riot has an internal institutional review board that evaluates the ethics of all its experiments. Although not a conflict-free arrangement, it at least suggests that the research is being reviewed with an eye towards participant protection. Academic collaborators also need to get approval from their local boards.

### VIRTUAL VIOLENCE

Lin has lofty goals for his teams' research and interventions. "Can we improve online society as a whole? Can we learn about how to teach etiquette?" he asks. "We're not an edutainment company. We're a games company first, but we're aware of how it could be used to educate."

Parents, lawmakers and some scientists have fretted for decades that video games, particularly violent ones, are warping the minds of children. But James Ivory, a communication scientist at Virginia Polytechnic Institute and State University, in Blacksburg, says that much of the attention on violence has missed the biggest impact that games have. "Researchers are slowly starting to wise to the idea that it may not be as important to think of what it means for someone to pretend to be a soldier than whether they're spending their time spewing racial or homophobic slurs."

By the age of 21, the average young gamer will have logged thousands of hours of playing time. That fact alone makes dichotomies such as 'real world' and 'digital world' ring false — for many, game-playing is the real world. And, says Ivory, "the strongest influence these games have on people is how they interact with other people".

**League of Legends requires teammates to communicate and cooperate.**

Some researchers are cautious about trying to apply lessons from the game to other settings. Dmitri Williams, a social scientist and founder of Ninja Metrics, an analytics company in Manhattan Beach, California, warns that games have very specific incentive structures, which could limit how well these experiences map to the wider world. "People behave well in real life because if they offend someone or screw up, they have to deal with the consequences." So, the manipulations that work to curb bad behaviour in *League* may be meaningless elsewhere.

And there are still considerable challenges for Riot. Players continue to complain about toxic behaviour or what they deem to be unwarranted punishments. And a blog called 'League of Sexism' argues that the suggestive portrayal of female characters in the game contributes to a strong current of sexism in the player community. "It's difficult for players to identify sexist behaviour when sexism is built into the game's very imagery," says a representative for the blog, who wished to remain anonymous. Although Lin's efforts are "admirable and likely industry-leading", the representative says, many games are still "awash with verbal harassment, grieving and overall negative behaviour from teammates and opponents". Lin says that Riot artists are aware of these concerns and that they have made efforts to portray female characters in a stronger and more-powerful way.

Although Riot boasts that serious toxic behaviour infects only 2% of games, somehow I managed to experience it within a minute of playing for the first time. But immediately after "FA GO TT" popped up on my screen, something interesting happened. Another player chimed in with, "Calm down". Perhaps it was a sign that Lin's efforts to engineer a more civil, self-policing digital space is starting to work. Or maybe it was just a friendly teammate reminding us all that it's just a game. ■ **SEE EDITORIAL P.549**

**Brendan Maher** is a features editor with Nature.

1. Blackburn, J. & Kwak, H. Preprint at <http://arxiv.org/abs/1404.5905> (2014).
2. Green, C. S. & Bavelier, D. *Nature* **423**, 534–537 (2003).
3. Kramer, A. D. I., Guillory, J. E. & Hancock, J. T. *Proc. Natl Acad. Sci. USA* **111**, 8788–8790 (2014).



# COMMENT

**MATHEMATICS** Biopic charts the challenges faced by Indian maths giant Ramanujan **p.576**

**PSYCHOLOGY** How we view the passage of time affects our decisions **p.577**



**GENDER** Institutional changes are necessary to gain equality **p.579**

**HEALTH** Preventing Alzheimer's transmission after surgery **p.580**

PAUL GROGAN/PHOTOPUS MAGAZINE VIA GETTY IMAGES



The paths of vehicles along Regent Street in London, revealed by long-exposure photography.

## Use or lose our navigation skills

Automatic wayfinding is eroding natural abilities, warns **Roger McKinlay**.

In 1984, I was part of a team that was developing a receiver for a satellite-navigation system. After weeks of debugging, the blur of random digits settled on a location. We grabbed a map and plotted the point. The pencilled cross landed exactly on the building that we were in. More than 30 years later, the amazement that I felt still remains. The technology we use is the same — just smaller. But our dependence on knowing exactly where we are has changed.

Navigation has invaded our dreams of the future. Fleets of driverless cars will transport us around cities. As you are driven past the shop that you viewed online, the mannequin wearing the dress that you clicked on will wave and call your name. Or you could stay at home and let a drone deliver your goods. This is the vision with which innovative companies such as Google and Amazon tempt us.

The days of being lost should be over. Access to satellite navigation is ubiquitous, and 80% of the adult population worldwide is likely to own a smartphone by 2020. But it is still not easy for people or machines to find their way around. Satellite navigation is unreliable because it does not work well indoors or in built-up areas. When your phone tells you where you are in a shopping centre, for example, it will actually be a guess based on ground-based WiFi networks. That is because signals from satellites are weak (similar to viewing a 20-watt light bulb from almost 20,000 kilometres away), prone to error and easily disrupted.

More satellites are being launched to improve coverage. By 2020, 30 orbiters from Galileo, the European satellite-navigation system, will complement the US Global Positioning System (GPS) and the Russian GLONASS network. China has just launched the twenty-first satellite in its BeiDou system.

Successful navigation indoors will need other solutions, such as a combination of wall-mounted antennas and WiFi. Quantum physics could come to the rescue. Although the technology is still in its infancy and will take more than a decade to develop, small and super-sensitive quantum sensors might pinpoint our location to within centimetres by picking up tiny changes in Earth's gravitational or magnetic fields.

But navigation is about more than knowing your position. When I followed my satellite-navigation system to a country house, ►

► I found my way blocked by a gate with a notice attached: 'No access, GPS wrong!' I was not lost — my satellite-navigation system knew my position accurately. But it did not understand roads. Newspapers regularly pick up 'satnav' disaster stories — such as a lorry bound for the Mediterranean that arrived at Gibraltar Point near Skegness in the United Kingdom. A sense of direction, a sense of scale and a map are essential. And knowledge of where you want to go also helps. The disappearance in 2014 of Malaysia Airlines flight MH370 is a reminder of the vastness of our world.

Mobility will not become intelligent unless we break two bad habits. First, we must recognize that digital navigation tools do not come for free. They rely on expensive infrastructure — satellites or ground stations — that governments have to pay for. The United States invested more than US\$10 billion to put the GPS satellites in place and spends around \$1 billion each year to maintain the service.

Second, we should make better use of our innate capabilities. Machines know where they are, not the best way to get to a destination; it might be more reliable to employ a human driver than to program an autonomous car to avert crashes. If we do not cherish them, our natural navigation abilities will deteriorate as we rely ever more on smart devices.

## USE OR LOSE

Human spatial memory is outstanding. In Ancient Greece, orators visualized their speeches as a mansion, placing topics in each room, then retrieving them while taking an imagined route through the building. Memory champions still do the same.

But navigation is a 'use-it-or-lose-it' skill. Drivers in a simulator who follow satellite-navigation instructions find it more difficult to work out where they have been than those who use maps. Instructed drivers also fail to notice that they have been led past the same point twice. Mountain-rescue teams are tired of searching for people with drained smartphone batteries, no sense of direction and no paper map.

As we age, our spatial knowledge and our capabilities for route learning and recall also decline. Loss of spatial orientation is an early indicator of dementia. Those who are affected are often moved to unfamiliar places such as care homes, which can exacerbate disorientation. The minimalist interiors of hospitals lack signposts: in a 2015 study<sup>1</sup>, nearly half of junior doctors reported that they had got lost in hospitals on the way to a call in which a patient's life was in danger.

The solution might lie in designing buildings that are easy to navigate<sup>2</sup> — rather than in gadgets. Repeated and mirrored layouts cause confusion; cluttered corridors overload the mind. Placement of simple, memorable

and unique landmarks such as pictures can help with orientation.

The human brain has everything that a hill walker might put in a rucksack. Behavioural neuroscientist Kate Jeffery at University College London describes how mental activity moves from the brain's striatum to the hippocampus when we leave familiar routes<sup>3</sup>. Studies in rats have revealed three types of cell that enable navigation: place cells, which fire at certain locations; head-direction cells, which track the orientation of the head; and grid cells, which set up a coordinate system for assessing scale and distance.

Learning the layout of the streets of London — known as the Knowledge — has been shown to increase the size of part of a taxi driver's hippocampus, and a similar effect has been observed in musicians<sup>4</sup>. While improvising music, a friend who is a free-jazz saxophonist 'sees' a landscape of notes to navigate.

Fresh locational cues can conflict with the maps in our brains. So it is unsurprising that it takes time to reorient when we emerge from an underground station or that the voice of the in-car satellite-navigation system grates on us. Our brains must decide whether to accept the new information and rejig our internal maps or to reject it as being wrong. A simple, reliable cue — such as a north-facing arrow at the top of an escalator — can help to speed up reorientation.

## SIX NINES

Accurate position fixing using satellites is fallible. Out in the open, GPS has good horizontal accuracy — to within about 3 metres. Positions are determined by calculating the time that the signal takes to reach the receiver, and not from any information that is being carried in the signal. Indoors or in built-up areas such as cities, signals can bounce around and give false information.

Intentional disruptions are on the rise. In 2009, engineers who were testing a GPS-based system at Newark airport in New Jersey experienced a daily interruption that was traced to a passing truck. The driver had fitted a GPS jammer to his vehicle to stop his employer from tracking him. Thieves use such jammers to defeat the trackers in luxury cars.

For wayfaring purposes, positions must be aligned to a worldwide reference map. GPS uses the World Geodetic System 1984, for example. In the 1980s, few locally used charts followed this standard, causing mariners to collide with unexpected rocks. The maps of today are vast digital databases, such as the Ordnance Survey MasterMap, which contains 450 million geographic features and is updated continually.

**"When it comes to choosing routes, humans outwit machines."**

When it comes to choosing routes, humans outwit machines. Yet it is the instinct of designers to make smarter machines — such as satellite-navigation systems that are aware of traffic. A better option would be to make it easier for the user to plan their route. Although a computer program can find the shortest or fastest path through a database of roads, in reality, time of day, level of traffic and personal preference also play a part. The driver of a high-sided vehicle needs to know whether a route is passable.

If there is no driver, the consequences of errors in position, mapping or routing could be serious. The information given to the vehicle has to be accurate, always available and reliable and of high integrity.

Often, these requirements can be met only using simple navigation systems. Aircraft rely on radio-based aids that date back to the 1940s. These measure distances from or bearings to known locations on the ground. Since the mid-1960s, aircraft have been able to land automatically in fog by flying down a radio beam that is generated at the end of the runway.

Such systems aim to meet what engineers call the 'six nines' — they work correctly for 99.9999% of the time. It must also be clear who is responsible for maintaining them and the processes that must be followed.

Satellite-navigation systems will meet this standard only if helped by reliable terrestrial-based systems. Plans to develop the Wide Area Augmentation System and the European Geostationary Navigation Overlay Service were put in place more than 20 years ago. But they are yet to make satellite navigation good enough to replace the conventional terrestrial systems used by aviation. For ships, a new terrestrial navigation system called eLORAN is being considered, with signals that are one million times more powerful than those used in GPS.

## NAVIGATION AIDS

Why do we need tools for navigation? Like most animals, our dominant sense is vision. The combination of eyes and our internal map can do an outstanding job. But we need to see at night and in fog, and be aware of out-of-sight landmarks. Pigeons use magnetoreceptors to sense Earth's magnetic field<sup>5</sup>. If humans could 'see' Earth's gravitational or magnetic fields, we might have no need for expensive satellites, radio beacons or even vision.

Aircraft, ships and submarines have for decades used inertial sensors on gyro-stabilized platforms to determine their positions. These systems accurately measure motion with respect to a known starting point but accumulate errors as they cover distance. By the end of the 1960s, aircraft inertial systems could remain accurate to within 25 nautical miles (about 46 kilometres) after a 10-hour





A lorry wedged between houses in Bruton, UK, after its driver followed satellite-navigation instructions.

flight, allowing aircraft to stay within prescribed air lanes during oceanic crossings. But such equipment is bulky and expensive.

Quantum gravitational systems are being developed that might detect changes in force as small as those caused by the gravitational pull of someone standing about one metre away. These systems rely on quantum superposition, in which particles exist in many states simultaneously and are very sensitive to time and electric and magnetic fields.

But all sensors have their own equivalent of fog. Compasses can be confused by magnetic rocks. The Moon landings were affected by the density of rocks in the lunar seas. A robust solution could involve a combination of many sensors. As with satellite navigation, we will need new standards and new maps.

The technical challenges are huge. Cooling sensor atoms to near absolute zero to reduce thermal noise involves bulky lasers and elaborate optics that fill a room. Miniaturization will take time, but within a decade a system that is small enough to fit on a train could map structures, cables and pipelines that lie under the tracks — work that at present is slow and costly.

The impact on robots and autonomous vehicles will be great. Drones will be able to avoid collisions over long distances in the dark. Autonomous operation makes sense where there is plenty of space — in the ocean or the sky.

But on congested roads, efficiency and safety stem from cooperation. Rules and common standards are important. Mallards in tight formation tend to face either north or south when landing. Because vision alone cannot prevent collisions between these

high-speed flyers, the ducks use sensors in their eyes, beaks and ears to align themselves to Earth's magnetic field<sup>6</sup>. Aircraft are confined to air corridors. Navigation conflicts need to be resolved and a controller must decide who gets priority.

Fully autonomous cars will not work without an agreed set of rules and communication between vehicles, which requires an infrastructure. Slow 'hop-on, hop-off' cars might be able to cruise safely around a shopping centre, but hundreds of independent, driverless vehicles roaming city streets, or flocks of drones in urban skies would be impractical. The cost of making such systems safe could be prohibitive. Legal and institutional issues — liability and insurance — must also be addressed.

Even without full automation, sensors and links could make cars easier to drive and safer. Satellite navigation could turn every road into a toll road. Travel history logged in the car could be used to charge drivers for actual road usage, rather than having a flat-rate road tax. When a congestion charge to reduce traffic flow in central London was introduced in 2003, the only available compliance option was number-plate recognition.

#### NEXT STEPS

Governments must invest in research, infrastructure, rules and regulations. Improving navigation cannot be left to companies alone. A trustworthy network of ground stations that would improve satellite navigation enough to guide driverless

***"The solutions lie around the next bend, just over the hill."***

vehicles could present a country of the size of the United Kingdom with an annual maintenance bill of the same order as a global satellite-navigation system. Cars that are capable of doing tasks by themselves — some are already able to park — could appear within a few years, but fundamental changes in the way that our road networks operate will take decades to implement.

In the meantime, three practical steps should be taken.

First, improve the science. We need to understand how systems that include — or lack — people work in practice. Cognition research can tell us where ergonomics and systems engineering will help or hinder human abilities. Increased funding for quantum technology research is welcome, such as the United Kingdom's allocation of £270 million (US\$386 billion) in 2013. And billions of pounds more will be needed to build infrastructure.

Second, engineers must acknowledge the complexity of these systems. They must use quantitative models of how people navigate and drive and should incorporate findings from neuroscience. Basic mistakes need to be avoided — such as relying on satellite-navigation systems to open doors in the impenetrable zones of stations and railway cuttings, as one train company in the United Kingdom did in 2014.

Third, invest in education. Schools should teach navigation and map reading as life skills. The introduction of computers and calculators has not removed the need to understand numbers. The US Navy has started to teach celestial navigation again as a backup skill.

Navigation is where complex systems meet capable users. Marrying them to enable truly intelligent transport will position us to get the best out of people and technology across many fields. The solutions lie around the next bend, just over the hill. ■

**Roger McKinlay** is a satellite communication and navigation consultant based in Leatherhead, UK, a former president of the Royal Institute of Navigation, and a former head of engineering at Thales UK. He sits on the EPSRC Quantum Technology Strategic Advisory Board.  
e-mail: [roger.mckinlay@ntlworld.com](mailto:roger.mckinlay@ntlworld.com)

1. Brown, M., Shaw, D., Sharples, S., Le Jeune, I. & Blakey, J. *BMJ Open* **5**, e006102 (2015).
2. Wiener, J. The effects of typical and atypical ageing on orientation and spatial navigation. *Proc. CogNav 2015* (2015).
3. Jeffery, K. Making a map in the brain using neurons. *Proc. CogNav 2015* (2015).
4. McGuire, E. A., Woollett, K. & Spiers, H. J. *Hippocampus* **16**, 1091–1101 (2006).
5. Wiltschko, W. & Wiltschko, R. *J. Navig.* **46**, 174–191 (1993).
6. Hart, V. *et al. Front. Zool.* **10**, 38 (2013).



WARNER BROS. PICTURES

Dev Patel stars as Srinivasa Ramanujan in *The Man Who Knew Infinity*.

FILM

# In search of Ramanujan

Andrew Robinson marvels afresh at the self-taught mathematical genius in a new biopic.

**T**he story of the Indian mathematician Srinivasa Ramanujan (1887–1920) is improbable. Self-taught, he made many seminal discoveries in number theory and power series — most famously concerning the partition of numbers into a sum of smaller integers — that continue to fascinate mathematicians and intrigue physicists studying black holes and quantum gravity. In *The Man Who Knew Infinity*, director Matthew Brown dramatizes the purest of mathematics for a general audience, and explores the strange personal life of Ramanujan, who died at 32, at the height of his powers, probably from tuberculosis. Based on the compelling biography of the same name by Robert Kanigel (Scribner, 1991), the film took more than ten years to create. It is worth the wait.

Ramanujan's career was 'made' by British mathematician G. H. Hardy, a fellow of Trinity College, Cambridge. In 1913, while working as an accounts clerk in what is now Chennai, Ramanujan sent Hardy startling, entirely unproven, theorems out of the blue. "They must be true," wrote Hardy, "because, if they were not true, no one would have the

imagination to invent them." Hardy lured Ramanujan to Cambridge, even though foreign travel was considered an offence against Hindu caste purity. They collaborated intensively throughout the First World War. Ramanujan had no university degree, but in 1918, Hardy ensured that he was elected a fellow of the Royal Society — the first Indian to receive the honour after it was restricted to scientists — and of Trinity College. They encountered considerable opposition, some of it racially motivated.

Hardy's relationship with Ramanujan holds the film together. Convincing performances by Jeremy Irons as Hardy and Dev Patel as Ramanujan were carefully refined by the film's Japanese-American mathematics adviser, Ken Ono, whose academic career has been dedicated to exploring Ramanujan's theorems. Irons and Patel animate both the consuming passion for mathematics shared by the two, and their astonishing lack of

**The Man Who Knew Infinity**  
WRITTEN AND  
DIRECTED BY  
MATTHEW BROWN  
Edward R. Pressman  
Films/Animus Films:  
2016.

personal intimacy; Hardy, for instance, had only a faint idea of Ramanujan's growing depression, which led to a suicide attempt on the London Underground. Irons, however brilliant, is a generation older than Hardy was in 1914, and Patel is taller and nattier than the more corpulent Ramanujan, who was ill at ease in Western dress.

Much of the action — and mathematics — takes place in the handsome precincts of Trinity College, which opened its doors to a feature film for the first time. In Hardy's room and the quadrangles, Ramanujan persistently resists Hardy's demands for proofs of his tantalizing theorems. An excited Ramanujan infuriates a lecturer by failing to take notes and then quickly chalking a correct formula: a very special integral due to Carl Friedrich Gauss, which Ramanujan knew through a method of his own devising. And in an evocative scene in Trinity's Wren Library, the famously atheistic Hardy tells his Indian protégé that the greatest honour "is to have a

➔ **NATURE.COM**

For more on science  
in culture see:  
[nature.com/  
booksandarts](http://nature.com/booksandarts)



legacy at Wren once we are gone. In this very library are the Epistles of St Paul, the poems of Milton, Morgan's Bible and, in my estimation as a man of numbers, the *pièce de résistance*, Newton's *Principia Mathematica*." Ramanujan's 'lost notebook' — which contains important mathematical discoveries made in India in 1919–20 and was neglected until 1976 — is, fittingly, in the Wren Library.

Scenes in India are no less ravishing. We see Ramanujan in flowing Indian clothes with Brahminical caste marks, chalking endless equations on the floors of a highly decorated Hindu temple. His dominating mother Komalatammal and wife Janaki provide a glimpse of domestic life. Indian and British colonial figures come and go (with a cameo by Ramanujan admirer Stephen Fry). But the film struggles to shed light on the origins of Ramanujan's prodigious gift. Biographers have had the same problem with Gauss and many other mathematicians. As India's great film director Satyajit Ray put it: "This whole business of creation, of the ideas that come in a flash, cannot be explained by science."

Hardy, too, was dazzled and puzzled. On a 0–100 scale of natural mathematical ability, he gave himself a score of 25 and Trinity colleague John Littlewood (a fellow supporter of Ramanujan) 30, compared with 80 for influential mathematician David Hilbert and 100 for Ramanujan. "The limitations of his knowledge were as startling as its profundity," Hardy wrote after Ramanujan's death. "All his results, new or old, right or wrong, had been arrived at by a process of mingled argument, intuition and induction, of which he was entirely unable to give any coherent account."

Ramanujan has inspired many. Christopher Sykes's pioneering UK television documentary, *Letters from an Indian Clerk*, was screened in 1987. The play *A Disappearing Number*, devised by Théâtre de Complicité, was produced in Britain in 2007 (see *Nature* **449**, 25–26; 2007). A biographical novel by David Leavitt, *The Indian Clerk* (Bloomsbury), was published in 2007.

Now, the film has spawned an intriguing, moving autobiography by Ono, *My Search for Ramanujan* (Springer, 2016), written with science writer Amir Aczel, who died before publication. Ono interweaves Ramanujan's life and work with his own fight to become a mathematician — including a suicide attempt — in the shadow of his distinguished mathematician father, Takashi Ono. After years of estrangement, the Onos realized that they were united by admiration and affection for the university drop-out Ramanujan. Here is yet another example of how this enigmatic Indian's unique achievements continue to reverberate nearly a century after his death. ■

**Andrew Robinson** is the author of *Genius and Satyajit Ray: The Inner Eye*.  
e-mail: [andrew@andrew-robinson.org](mailto:andrew@andrew-robinson.org)

## PSYCHOLOGY

# Time piece

**Hedderik van Rijn weighs up an erudite but idiosyncratic survey of how we perceive life passing.**

**T**he sense of time passing plays a pivotal part in decision-making — from choosing chicken or pasta on a long-haul flight to deciding whether to propose marriage to a long-term partner. Although the temporal resolution in these scenarios differs by orders of magnitude, *Felt Time* by psychologist Marc Wittmann (first published in German as *Gefühlte Zeit*; C. H. Beck, 2014) argues that the experiences are closely related.

Wittmann marshals a wealth of behavioural and neuroscience results, as well as references to the arts, literature and philosophy, to argue that how we subjectively experience time determines whether we are able to seize the day and live happy and fulfilled lives, or struggle to finish our daily chores. He urges us to strive to slow down subjective time and to live in the here and now. Inspired by the Roman Stoic philosopher Seneca, his suggestion for cultivating presence is to abstain from busywork — to get rid of the "unconditional work ethic" that drives us back to our desks on sunny Sunday afternoons to finish yet another grant proposal instead of relaxing. Another, more pragmatic, proposal for slowing down subjective time is 'mindfulness'. By using meditation



**Felt Time: The Psychology of How We Perceive Time**  
MARC WITTMANN  
(TRANSLATED BY ERIK BUTLER)  
MIT Press: 2016.

techniques such as a focus on breathing, Wittmann argues, we become more aware of our inner body states, more "mentally present"; this slows down our subjective time, resulting in more fulfilling in-the-moment experiences.

I am not convinced that mindfulness can help in all contexts discussed in *Felt Time*, because Wittmann

defines time very loosely. He links the perception of seconds with perception over months or years. He elides the effects of circadian rhythm and chronotype (whether someone is a 'morning' or 'evening' person), youthful impatience, the observation that years seem to pass faster as we age, and the prospect of dying — the ultimate time limit. Although all of these are associated with our perception of life passing, each has a distinct aetiology: circadian rhythms are driven by well-known biological circuits, for example. But the change in subjective time with age is attributed to experiencing fewer unfamiliar (and therefore memorable) events, something that could be more easily influenced than circadian rhythms.

I do, however, strongly agree with Wittmann's implicit arguments for a more inclusive study of time. Beyond simple laboratory studies of temporal cognition tasks, Wittmann makes the case that science should explore how perceived time affects everyday activities, as well as how everyday activities influence our perception of time. But rather than conducting lab work in which participants must estimate the duration of intervals marked with clear start and end points, we should consider timing as a continuative process: every task we do is timed, irrespective of whether we know at the start that time might become important.

*Felt Time* is divided into two parts. In the first, Wittmann introduces the important role of time in many aspects of everyday



**Perceived and measured time may not always match.**

► life, from speech perception and production to experiencing and memorizing what he terms the “best moments of life”. Here he presents an elegant selection of the often confusing, sometimes contradictory academic literature, with a clear emphasis on his own work and that of collaborators and mentors such

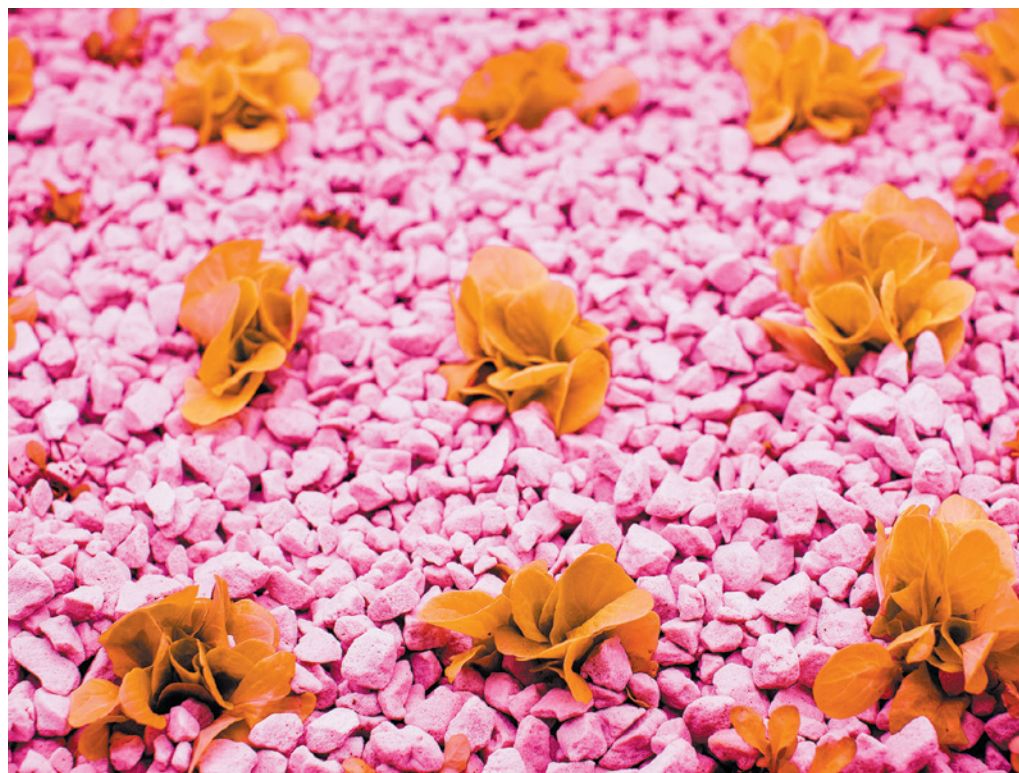
**“Science should explore how perceived time affects everyday activities, as well as how everyday activities influence our perception of time.”**

as functional neuroanatomist Bud Craig and psychologist and neuroscientist Ernst Pöppel.

In the last two chapters, Wittmann advances a theory of how temporal perception is directly linked to the self-consciousness of bodily states. His idea is grounded in the observation that during timing tasks, the brain’s insular cortex (a part of the cerebral cortex associated with the integration of physiological input such as heartbeat) is active. Wittmann suggests that the heart might act as an ‘internal clock’, because accuracy in counting heartbeats correlates with how accurately someone can estimate the duration of an interval. Although there are correlational studies that link sensing heartbeat with timing accuracy, Wittmann unfortunately ignores prominent alternative proposals for the brain mechanisms that underlie the internal clock. For example, there is ample evidence that corticostriatal circuits — neural pathways that link the basal ganglia with the neo-cortex — are key to the accurate timing of duration in the range of seconds to minutes. Such work is better covered in other books or special journal issues on the neurobiology of timing (for example, H. Merchant and V. de Lafuente (eds) *Neurobiology of Interval Timing* (Springer, 2014) and R. B. Ivry and W. H. Meck *Curr. Op. Behav. Sci.* 8; 2016) — but these are aimed at experts.

Although idiosyncratic at times, *Felt Time* eloquently sketches out the importance of time, both in the darkness of the lab and in the full light of everyday behaviour. ■

**Hedderik van Rijn** is professor of cognitive science and neuroscience at the University of Groningen in the Netherlands. He studies how temporal constraints influence cognitive processing, and how the brain keeps track of time.  
e-mail: hedderik@van-rijn.org



In the installation *AQUA*lab, plants purify water for fish, which provide fertilizer for the plants.

#### AGRICULTURE

## Future farming

**Anthony King** views video games for pigs and urban ‘aquaponics’ at Science Gallery Dublin’s latest show.

**T**he visible face of intensive agriculture is supermarkets bulging with vegetables, meat and milk. Yet behind the scenes, as Science Gallery Dublin’s latest exhibition reveals, factory farming’s reliance on energy-intensive fertilizer manufacture and vast amounts of water raises big questions about sustainability. No one solution is on offer in *Field Test*, which is curated by the Center for Genomic Gastronomy, an artist-led global think tank devoted to imagining a more just, biodiverse food system. But visitors can feast on prototypes, research, revolutionary agronomy manifestos, innovative and imagined farm technologies and speculative cuisines. “We’re asking how we can get more from less,” explains acting gallery director Lynn Scarff.

Meat, for instance, is a Western penchant now spreading around the world. The Food and Agriculture Organization of the United Nations estimates that demand will increase by more than two-thirds over the next 40 years, despite sky-high costs — it takes 15,000 litres of water to produce a kilogram of beef. The curators’ *Farmstand Forecast*

**Field Test: Radical Adventures in Future Farming**  
Science Gallery Dublin  
Until 5 June 2016.

looks at alternatives: attractively packaged insect-based foods, and historical ‘miracle’ crops such as breadfruit and *Chlorella* algae. An exhibition strand dubbed ‘Farm Cyborgs’ features animal-husbandry innovations including *Silent Herdsman*, a smart collar for tracking data on bovine health. *Playing With Pigs: Pig Chase* is a video game for alleviating porcine boredom, designed by researchers at the HKU University of the Arts Utrecht and the Wageningen University and Research Centre, both in the Netherlands. A pig uses its snout to manipulate a virtual ball on a touch-sensitive display, while a person uses a finger to do the same on a tablet computer. The reward for moving the ball in harmony is colourful ‘fireworks’.

Imagination-tickling as this is, it does not probe the central issue — demand and supply. That dilemma is framed in ‘Grow House’. Does the plastinated leftover of physician Mark Post’s 2013 *in vitro* burger, made by culturing beef cells, represent a viable solution?



## SOCIETY

# Inching towards equality

**Athene Donald** weighs up a survey of workplace changes designed to avoid gender bias.

Bioartist Oron Catts thinks not. “The real price of growing meat in a lab is hidden,” he notes. Muscle cells are macerated in huge quantities of fetal bovine serum obtained by slaughtering pregnant cows — half a litre of serum yields just 5 grams of meat, says Catts. His speculative *Stir Fly* is a sleek prototype bioreactor co-created by artist Ionat Zurr and designer Robert Foster to grow fly cells in bovine serum. The mix could be siphoned off and eaten as soup, or drained to form insect ‘meat’.

Closed-loop urban agriculture systems offer a time-honoured sustainable alternative. *AQUAlab*, by Dublin-based agricultural start-up firm URBANFARM, harnesses aquaponics — a system in which waste from fish raised for food fertilizes salad and herbs, which in turn purify the water for the fish. (Plants and fish will eventually be harvested as a tasty proof of concept.) The ‘Open Ag Lab’ showcases another city-farming trend — beekeeping. In the *The Dublin Honey Project*, Irish black bees do their stuff in six apiaries across the city, and ecologist Jane Stout from Trinity College Dublin will be identifying pollen from the honey to determine foraging sources. Counter-intuitively, the project argues that cities can be relatively clean for bees because of stringent controls on pesticides. Stout argues, too, for ecological intensification — replacing artificial inputs by optimizing ecosystem services and fostering crop diversity. In service to that vision, botanists at Trinity focus on the microbiome. For *Endophyte Club*, Trevor Hodgkinson, Brian Murphy, Anna Kaja Hoeyer and Anindita Lahiri have extracted the microbiome of wild barley and plated the microorganisms that live in the plant out on agar plates. They show how sprinkling seeds with such endophytes can boost yields, potentially reducing fertilizer use.

The show points out that consumer choices can determine how and what is grown. ‘LOCI Food Lab’ is a cart peddling personalized snacks made from Irish foods, digitally selected on a tablet device using criteria such as biodiverse, traditional or delicious. My attempts yielded sweet-salty yogurt, shoots and leaves, mushroom dust and dillisk seaweed: a locavore’s dream nibble.

Field Test has dug up an assortment of agricultural advances, idealistic prototypes and thought experiments. But the quirkiness on show spurs questioning even as the discoveries framed rouse hope. A coordinated solution to our hungry future remains elusive. ■

**Anthony King** is a writer based in Dublin.  
e-mail: anthonyking@gmail.com

In the 2013 *Lean In* (Knopf), Sheryl Sandberg wrote, “The promise of equality is not the same as true equality.” Sandberg, chief operating officer of Facebook, purported to show women in corporate America how to succeed. I thought she put too much emphasis on the individual woman to ‘man up’. The book that we need to redress the indubitable gender imbalance across many sectors, including science, is one that tells organizations how to reconfigure for equality.

*What Works* by Iris Bohnet is intended as such a book. Sadly, I found it little more use than *Lean In* for working out how to transform labs and universities. Bohnet is a behavioural economist; her profession sets out to find design principles that nudge others to do the right thing, or approach it. But ‘what works’ in one place or situation does not necessarily work elsewhere. Take her discussion of a 1993 Indian law to increase the share of women in local government. It is hard to relate that to increasing the number of female engineering professors anywhere. By trying to cover all sectors and many nations, the book overwhelms with examples rather than solutions.

*What Works* is a curious mix of self-help for organizations and a semi-scholarly review. Bohnet’s 70-odd pages of notes and bibliography are a voluminous resource of model and real-world studies. Her writing is accessible. Yet, I was often left puzzling over what message an admonition was meant to convey. I was particularly confused about same-sex teams versus mixed ones. Sometimes Bohnet says that homogeneity is advantageous — for example, when “a task involves coordination”, which many do. But in general, she thinks that diversity is the ideal, notably when “collective problem-solving” is involved. So what do you do when you need a coordinated solution to a collective problem, such as finding the Higgs boson?

The biggest problem is the structure. Most of the book — the three sections entitled ‘The Problem’, ‘How to Design Talent Management’ and ‘How to Design School and Work’ — mingles solutions and studies. This, I found, made it hard to extract workarounds. Each chapter

ends in bullet points listing things to do, but these often seem too distilled. For example: “Prevent gender bias from having an impact: use gender-neutral designs.” I am not sure that the typical head of department would be much the wiser.

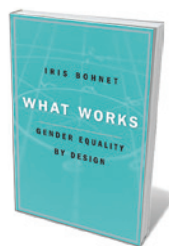
There is little specifically about research and not a great deal pertaining to higher education. Most of the studies deal with politics and business. International comparators are illuminating in an abstract way, but not when it comes to practical advice for a principal investigator or dean. No explicit help is provided for drafting a job advertisement that demands excellence without putting off the less self-confident; nor is there anything on constructing departmental policies to encourage inclusivity among individuals competing for resources. Many of the organizations that Bohnet discusses have tens of thousands of employees. So their strategies for recruitment and promotion are very different from those for hiring a single tenure-track professor.

That said, readers will learn about some approaches that have worked or failed. I found the idea of reframing job specifications useful: for instance, offering flexibility as the norm that anyone can ask for, rather than that tricky thing that pesky women want. Another simple, but key, step is to purge gendered language from all advertisements. For instance, by saying that salaries are negotiable, the advertisement can help both men and women to feel comfortable opening that dialogue; without it, many women are more reticent, and the gender pay gap opens up.

But I didn’t find drawing out the three easy wins for my university very easy. Quotas are helpful, unless there is a backlash because of the idea that less-well-qualified people from under-represented groups have been allowed in. Role models are important, except when people decide ‘problem solved’ and go back to not thinking about them at all. The book is pervaded with caveats — and justifiably so, because equality is a hard problem to solve.

Bohnet hasn’t cracked it because her advice is too broad. But her examples do embody an important point: the path to equality lies in retooling our institutions, not ourselves. ■

**Athene Donald** is professor of experimental physics and former gender-equality champion at the University of Cambridge, UK. She is master of Churchill College, Cambridge.  
e-mail: amd3@cam.ac.uk



**What Works: Gender Equality by Design**  
IRIS BOHNET  
Belknap: 2016.

# Correspondence

## Counter the risk of Alzheimer's transfer

You urgently call for sterilization procedures that can destroy possible protein 'seeds' of Alzheimer's disease on medical instruments (*Nature* **531**, 294–297; 2016). In fact, a proof of principle for such technology is in place and promises to allay fears of surgical transmission.

The process entails adapting an assay for the transmission risk of pathological prion proteins that are deposited on instruments after surgery. A team at the Robert Koch Institute — a governmental body that safeguards public health — used this approach to develop precautionary sterilization procedures (see M. Beekes *et al. Acta Neuropathol.* **128**, 463–476; 2014) against protein aggregates known to be associated with Alzheimer's and Parkinson's pathologies (A. Thomzig *et al. Acta Neuropathol. Commun.* **2**, 151; 2014).

The researchers tested different experimental or commercial instrument cleaners that are effective against prions, followed by steam sterilization. They found that in crude human-brain suspensions that were attached to steel-wire grids acting as instrument surrogates, this treatment combination removed amyloid- $\beta$ , tau and  $\alpha$ -synuclein protein aggregates, as indicated by western blotting.

**Michael Beekes, Achim Thomzig**  
Robert Koch Institute, Germany.  
beekesm@rki.de

## Fanning the flames of Australian wildfires

Climate change will increase the frequency, intensity and scale of Australian bushfires, at huge cost to its population and unique biota. Yet the government-funded science agency, CSIRO, plans to cut at least 100 jobs in climate research. Australia urgently needs political leadership on climate action and investment in climate science (see also D. Lindenmayer

*Nature* **531**, 305; 2016).

For example, fires last year burned an estimated 90% of the habitat occupied by the critically endangered marsupial Gilbert's potoroo (*Potorous gilbertii*) and the western ground parrot (*Pezoporus flaviventris*; go.nature.com/ogriue). The affected areas also contain six other endemic threatened plant and animal species. Their already small and isolated remnant populations are now even more vulnerable.

In Victoria alone, 4.3 million hectares of eucalypt forest burned in 2003–14, comparable to the entire area destroyed over the previous 50 years (T. A. Fairman *et al. Int. J. Wildland Fire* <http://doi.org/bdkt>; 2015). Moreover, modelling for southeastern Australia predicts 5–25% increases in fire risk by 2050 compared with 1974–2003 (see go.nature.com/xmpj8z).

Australia's ill-advised reduction of its climate-science capacity will severely compromise its ability to respond to this growing threat.

**Tim S. Doherty** Deakin University, Victoria, Australia.  
**Martine Maron** The University of Queensland, Brisbane, Australia.  
tim.doherty.0@gmail.com

## EU cash goes to the sticky and attractive

Winning European research money does not depend only on a well-funded research base (G. Parisi *Nature* **530**, 33; 2016). We find that it is also contingent on national governments' ability to retain their own scientists ('stickiness') and to attract others from abroad ('attractiveness').

We analysed statistical indicators of EU scientists' mobility for 2007–14 (<http://erc.europa.eu> and go.nature.com/bpeylu) to determine the stickiness and attractiveness of different countries. We quantified attractiveness and stickiness as the relative difference between the numbers of incoming or remaining researchers, respectively, and of outgoing ones.

For both measures, we found that the higher the value, the better were that country's chances of securing European research funding. The United Kingdom and Sweden are examples of high scorers in both; Italy is among the lowest (see go.nature.com/wyvtls).

We conclude that there is a 'rich-get-richer' effect for countries that have high attractiveness and stickiness scores. Those nations also boast a high gross domestic product per capita and tend to invest more in research and development. This means that they can lure and retain the best researchers by providing competitive salaries and a guaranteed future in research.  
**Manlio De Domenico,**  
**Alex Arenas Rovira** I Virgili University, Tarragona, Spain.  
manlio.dedomenico@urv.cat

## One of animal-study criteria backfires

Applications for animal studies in the European Union have become weightier and more informative since the EU's animal protection act was adopted in 2010. Because applications are now more challenging to review, researchers in some German states are charged a processing fee. This seems to run counter to the act's unifying approach, because no fee is levied from animal researchers in other EU countries.

Fees vary according to the burden of reviewing. For example, the charge for a 30-page application, which currently takes 3–4 months to review, might be €1,000 (US\$1,130) or more — irrespective of whether or not it is successful. German scientists are in effect being penalized for complying with the act by submitting more-detailed applications as part of the 'refinement' of animal research — one of the '3Rs' criteria (see [www.nc3rs.org.uk/the-3rs](http://www.nc3rs.org.uk/the-3rs)).

Such fees could push scientists to conduct their work abroad or deter them from doing animal

experiments at all. This would be a disaster: the freedom of scientific research in Germany is as highly regarded as animal protection (Articles 5 and 20 of the Fundamental Law).

**Michele Boiani, Alexandra Buehler** Max Planck Institute for Molecular Biomedicine, Münster, Germany.  
mboiani@mpi-muenster.mpg.de

## Too many mining disasters in Brazil

Another mining dam collapsed in Brazil last month, bringing the country's total of these human and environmental disasters to more than 80. With at least 600 mining dams still operating, the government urgently needs to evaluate the associated risks, tighten its mining code and enforce its safety law for dams.

The environmental effects reach beyond the pollution of fresh water, soils and coastal systems. Such accidents eradicate rare endemic species and disrupt ecological interactions, ecosystem functions and evolutionary processes (M. Lambertz and J. A. Dergam *Nature* **528**, 39; 2015; J. Massante *Nature* **528**, 39; 2015).

Those responsible for these dam accidents still go unpunished (R. Meira *et al. Biodivers. Conserv.* **25**, 407–409; 2016). In our view, the most pervasive and systematic threats to Brazil's biodiversity are rooted in weak official policies and poor monitoring, management and legislation.

Three mining companies in Brazil have set up a US\$1.1-billion foundation to mitigate social, environmental and economic effects on the Rio Doce basin. But without policy reform, the ecological and social issues could dash Brazil's hopes of meeting the 2020 Aichi biodiversity targets (M. Di Marco *et al. Conserv. Biol.* **30**, 189–195; 2016).

**Alison Gonçalves Nazareno** University of São Paulo, Brazil.  
**Jean Ricardo Simões Vitale** Federal University of Paraná, Brazil.  
alison\_nazareno@yahoo.com.br

## FORUM Cell biology

# Calcium contradictions in cilia

Organelles called primary cilia that protrude from cells have been thought to sense the surrounding environment through calcium-channel proteins that respond to force. Two scientists discuss the implications for developmental biology and kidney disease of a study that challenges this hypothesis. [SEE LETTER P.656](#)

### THE PAPER IN BRIEF

- The primary cilium is a hair-like projection that is often regarded as the cell's signalling antenna.
- It harbours a calcium-channel protein that was thought to open when the cilium was bent by the force of fluid flow, allowing calcium ions ( $\text{Ca}^{2+}$ ) to enter the cell (Fig. 1a).
- On page 656 of this issue, Delling *et al.*<sup>1</sup>

report that they have engineered mice to express a sensor protein that fluoresces in response to  $\text{Ca}^{2+}$  influx into primary cilia, and measured  $\text{Ca}^{2+}$  signals after applying a mechanical force.

- They find no evidence of force-driven  $\text{Ca}^{2+}$  influx (Fig. 1b), and therefore conclude that these structures are not involved in calcium-based mechanosensation.

## Asymmetric implications

DOMINIC P. NORRIS

Although human bodies show left–right asymmetry externally, internal organs are asymmetrically located — our heart and stomach, for example, are on the left side of the body. This asymmetry is established at the time when the embryo comprises a flat disc of cells, in which a small pit called the node transiently forms. Each node cell has a primary cilium that rotates clockwise, somehow driving extracellular fluid from right to left to establish asymmetry<sup>2</sup>. Mounting data<sup>3–5</sup> have supported the idea that cilia on the left of the node directly sense and respond to fluid flow through PKD2  $\text{Ca}^{2+}$ -channel proteins, which open to produce a left-biased ciliary  $\text{Ca}^{2+}$  signal. Delling and colleagues' evidence that this is not the case could have a profound impact on our understanding of left–right patterning.

Debate about how cells in the embryo perceive flow goes back almost 20 years, and several explanatory models have been developed<sup>6</sup>. One posits that a secreted signalling molecule called a morphogen becomes enriched on the left side of the node in response to flow. Another argues that vesicles containing morphogens travel leftward, delivering their cargo unilaterally. A third, the mechanosensation model, suggests that the leftward force itself is perceived by cilia in crown cells that surround the node. Although no model has been proved or disproved, over time, the mechanosensation

hypothesis gained the most traction.

The authors' cilium-specific  $\text{Ca}^{2+}$  sensor allowed them to test this hypothesis directly. Validating the sensor was challenging, but, luckily, the authors found that it was expressed not only in primary cilia, but also in cilium-like structures on hair cells in the inner ear, which are known to respond to force through  $\text{Ca}^{2+}$ -based mechanosensation<sup>7</sup>. Delling and colleagues applied a flow of fluid onto the hair cells and found that the sensor reliably reported  $\text{Ca}^{2+}$  signals in response to physiological levels of force.

Next, the researchers isolated mouse embryos at the ages at which left–right asymmetry is established, and applied fluid flows to either the left or right side of the node for up to 10 seconds. This consistently failed to elicit a ciliary  $\text{Ca}^{2+}$  response. Similarly, the authors failed to detect  $\text{Ca}^{2+}$  signals in the cilia of bone cells.

Delling *et al.* endeavour to explain how their study contradicts so much previous work. First, they propose that previous studies might have misinterpreted imaging artefacts that arose when flow moved the cilium out of the plane of focus, causing changes in fluorescence. Second, they argue that imaging speed is key, because the cilium can become rapidly infused with  $\text{Ca}^{2+}$  that flows in from the cell body, and this might be mistaken as originating in the cilium.

These results seem to discount the mechanism by which mechanosensation has been proposed to act during the establishment of left–right asymmetry. However, the authors are careful to state that they have tested only whether the nodal primary cilium is a  $\text{Ca}^{2+}$ -responsive mechanosensor, not whether force detection plays any part in asymmetry.

Mechanosensation could, for instance, occur through the cell body or through cilia in a calcium-independent manner. Morphogen-dependent mechanisms also remain possible. Whatever the mechanism, it must explain why PKD2 is essential for crown-cell cilia to detect flow — a fact that is now unexplained.

As with all potentially revolutionary findings, possible caveats are likely to be tested in depth by other laboratories. The authors openly lay out some of the limits of their data. But, importantly, left–right patterning of an embryo occurs over hours rather than seconds, and inside the mother rather than in a Petri dish. The extent to which the real-life situation has been modelled in the current study is likely to be questioned.

**Dominic P. Norris** is in the Mammalian Genetics Unit, MRC Harwell, Harwell Campus OX11 0RD, UK.  
e-mail: d.norris@har.mrc.ac.uk

## Signals straightened out

PETER K. JACKSON

The hypothesis<sup>8</sup> that forces generated by urinary flow elicit ciliary mechanosensation in the kidney dates to 2001, and defects in this process have been proposed to cause adult polycystic kidney disease. A technical tour de force has allowed Delling *et al.* to question this long-standing model. The strength of their argument lies in their use of recently developed  $\text{Ca}^{2+}$ -signalling reporters (described above) and their ability to rapidly visualize  $\text{Ca}^{2+}$  signalling while controlling for ciliary movement.

The past few years have seen a renaissance in the study of primary cilia, thanks to genetic studies<sup>9</sup> in model organisms. Another rich source of information comes from the many human-gene mutations that cause ciliary dysfunction, which have allowed researchers to identify structural and trafficking components of cilia, and ciliary signalling mechanisms<sup>10</sup>.



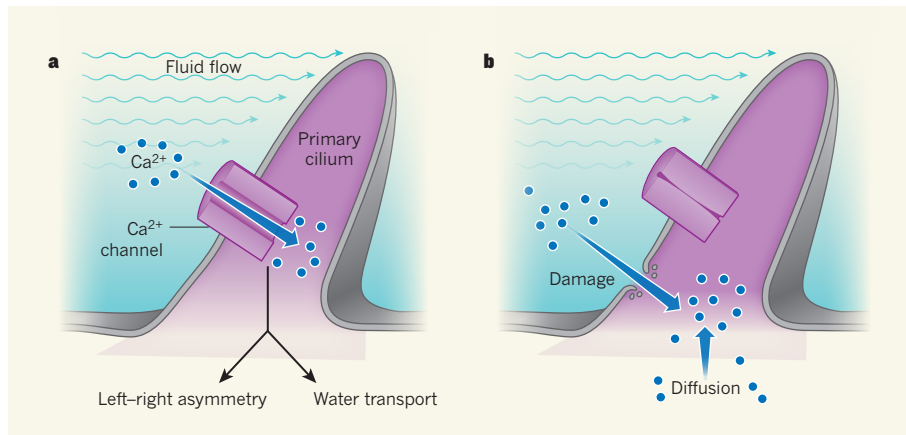


**Figure 1 | The mechanosensation hypothesis.** **a**, Much research suggested that cells' primary cilia respond to force through mechanosensation. In this original model, fluid flow pushes the cilium, which triggers the opening of calcium-sensitive channel proteins and so allows calcium ions ( $\text{Ca}^{2+}$ ) to enter the cilium. Intracellular signalling cascades are activated by the  $\text{Ca}^{2+}$  influx, leading to altered gene expression on the left side of the embryo, or promoting water transport in the kidneys. **b**, Delling *et al.*<sup>1</sup> find that, contrary to this hypothesis, ciliary bending in response to force does not open  $\text{Ca}^{2+}$  channels. Instead, the authors propose that the  $\text{Ca}^{2+}$  influx observed in previous experiments might have been due to diffusion from the cell body, or to damage to cilia in response to extreme levels of force.

Several analyses support the model that cilia are involved in specialized  $\text{Ca}^{2+}$  signalling. First, work<sup>11</sup> by the group that performed the current study indicates that  $\text{Ca}^{2+}$  signals in primary cilia are as strong as  $\text{Ca}^{2+}$  influxes that trigger signalling cascades in other cell types. Second, cilia contain many  $\text{Ca}^{2+}$ -binding proteins, including adenylate cyclase III — an enzyme that is located only in cilia, is vital for several cell-regulatory roles (including limiting cystic growth in kidneys) and is  $\text{Ca}^{2+}$ -dependent. Third, the childhood kidney cystic disease nephronophthisis can be caused by mutations in genes that encode calcium-dependent ciliary proteins; similarly, adult polycystic kidney disease has been linked<sup>10</sup> to mutations in the *PKD1* gene and in the gene that encodes its binding partner, the PKD2  $\text{Ca}^{2+}$  channel. However, another study<sup>12</sup> by the current group indicates that the strong  $\text{Ca}^{2+}$  signals observed in cilia do not require PKD1 or PKD2, but rather the related proteins PKD1L1 and PKD2L1, underscoring the fact that we understand neither the breadth of ciliary  $\text{Ca}^{2+}$  signalling nor the fundamental pathways in which channel proteins such as PKD2 function.

Cells of the proximal collecting duct make up the kidney tubules involved in antidiuretic (urination-reducing), hormone-stimulated water transport. Malfunction of cilia in these cells is thought to be involved in water-transport-driven swelling of the collecting ducts and cysts in cystic kidney diseases. Delling *et al.* examined collecting-duct cilia using a flow chamber to approximate urinary flow rates and to cause varying degrees of ciliary bending, but observed no effects on  $\text{Ca}^{2+}$  signalling. Occasionally,  $\text{Ca}^{2+}$  signals were generated by damaging the cilia, and this would explain the discrepancy between these data and older work. Indeed, without modern sensors and control markers,

measurement of bona fide ciliary signals in past work would have been difficult.

For the  $\text{Ca}^{2+}$ -mechanosensation model to make sense physiologically, the location and timing of  $\text{Ca}^{2+}$  influx would connect an observed signal to the physiological effect. For example, observations of fluid flow, ciliary bending,  $\text{Ca}^{2+}$  influx and water transport in the collecting duct would have to be temporally and spatially linked. Delling and colleagues find no evidence of either the mechanical changes or the appropriate  $\text{Ca}^{2+}$  signals in this setting, thus disputing this model. Although it is hard to categorically disprove a signalling hypothesis, the quality of the authors' work sets a high bar for any future study that supports ciliary mechanosensation.

Researchers must now find another

explanation for how collecting-duct cilia function. An attractive alternative is that urinary flow provides a flux of molecules, possibly metabolites or toxins, that signal through other ciliary receptor proteins to control water retention or to direct toxin clearing. G-protein-coupled receptors are a particularly attractive class of potential receptor, but channels such as PKD2 and PKD2L1 are also candidates, because little is known about potential ligands that activate them. The key regulatory output of ciliary signalling in collecting ducts — calcium-dependent or otherwise — and how this signal impinges on physiology and cystic diseases, remain to be defined. Further study of cilia could help to find a broader explanation of how kidneys regulate water balance without retaining toxic metabolites. ■

**Peter K. Jackson** is in the Departments of Microbiology & Immunology and Pathology, and in the Baxter Laboratory, Stanford University School of Medicine, Stanford, California 94305, USA.  
e-mail: pjackson@stanford.edu

1. Delling, M. *et al.* *Nature* **531**, 656–660 (2016).
2. Nonaka, S., Shiratori, H., Saijoh, Y. & Hamada, H. *Nature* **418**, 96–99 (2002).
3. McGrath, J., Somlo, S., Makova, S., Tian, X. & Brueckner, M. *Cell* **114**, 61–73 (2003).
4. Yoshida, S. *et al.* *Science* **338**, 226–231 (2012).
5. Yuan, S., Zhao, L., Brueckner, M. & Sun, Z. *Curr. Biol.* **25**, 556–567 (2015).
6. Norris, D. P. *BMC Biol.* **10**, 102 (2012).
7. Schwander, M., Kachar, B. & Müller, U. *J. Cell Biol.* **190**, 9–20 (2010).
8. Praetorius, H. A. & Spring, K. R. *J. Membr. Biol.* **184**, 71–79 (2001).
9. Goetz, S. C. & Anderson, K. V. *Nature Rev. Genet.* **11**, 331–344 (2010).
10. Hildebrandt, F., Benzing, T. & Katsanis, N. *N. Engl. J. Med.* **364**, 1533–1543 (2011).
11. Delling, M., DeCaen, P. G., Doerner, J. F., Febvay, S. & Clapham, D. E. *Nature* **504**, 311–314 (2013).
12. DeCaen, P. G., Delling, M., Vien, T. N. & Clapham, D. E. *Nature* **504**, 315–318 (2013).

This article was published online on 23 March 2016.

#### CANCER IMMUNOTHERAPY

## Killers on sterols

**Increasing cholesterol levels in the cell membranes of killer T cells boosts the cells' ability to mount an immune response against tumour cells in mice. Such a strategy might be valuable in anticancer immunotherapies. [SEE LETTER P.651](#)**

**MICHAEL L. DUSTIN**

**T**he dream of stimulating the body's immune response to fight cancer has become a reality in the past decade. Several potent drugs have been clinically approved that block inhibitory checkpoints in the immune system, boosting the ability of the system's T cells to mount responses against a range of cancers<sup>1</sup>. Furthermore, patients' own

T cells have been successfully genetically engineered to attack blood-cancer cells<sup>2</sup>. Although these studies have established the immune system as a powerful ally in cancer therapy, there are still many challenges to overcome, and further advances would increase the number of people who stand to benefit from immunotherapy. In this issue, Yang and colleagues<sup>3</sup> (page 651) propose a way to boost the function of antitumour T cells, using a metabolic trick

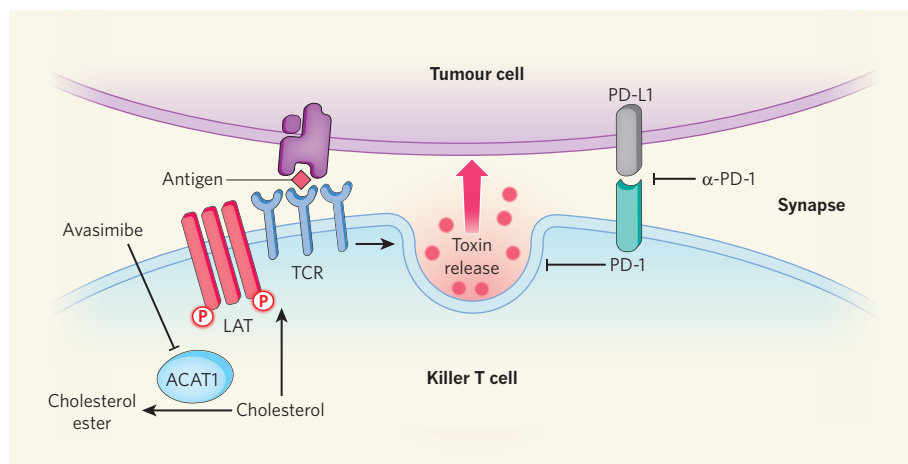


**Figure 1 | Synergy at the immunological synapse.** Yang *et al.*<sup>3</sup> used the drug avasimibe to inhibit the protein acetyl-CoA acetyltransferase 1 (ACAT1), which converts cholesterol to cholesterol ester. This inhibition increases cholesterol levels in the cell membrane of killer T cells, promoting clustering of T-cell receptors (TCRs) that bind to antigens presented on the surface of tumour cells. Higher levels of membrane cholesterol also promote activating phosphorylation (P) of an adaptor protein called linker of activated T cells (LAT), which acts with TCRs to transduce the tumour-cell signal and increases the speed at which the T cell and tumour cell form a point of embrace called the immunological synapse. Together, these factors promote the release of toxin molecules that trigger tumour-cell death. The T-cell protein PD-1 acts as an inhibitory checkpoint of this immune response by interacting with the tumour-cell protein PD-L1 to attenuate synapse formation. The authors found that avasimibe acts additively with  $\alpha$ -PD-1 antibodies that block this checkpoint to reduce tumour growth and prolong survival in mouse cancer models.

to increase the level of cholesterol in the cells' membranes.

T cells sense foreign invaders, including tumour cells, through nanoclusters of T-cell receptor (TCR) proteins on the cell surface. With the help of proteins called adaptors, TCRs then initiate an intracellular signalling cascade that leads to T-cell activation. The ability of cholesterol to enhance this activation has long been known, and probably arises from the sterol's role in organizing the cell membrane in which TCRs are embedded<sup>4</sup>. Cholesterol synthesis can be a limiting factor for T-cell growth, and increasing cholesterol biosynthesis enhances T-cell responses<sup>5</sup>. However, there are currently no therapies that increase cellular cholesterol.

The enzymes acetyl-CoA acetyltransferase 1 (ACAT1) and ACAT2 generate cholesterol esters that are used for storage and intercellular transport of the sterol, rather than contributing to cell membranes<sup>6</sup>. The liver and gut express ACAT2, whereas most cells, including T cells, express ACAT1. Yang *et al.* genetically modified mice such that their T cells lacked ACAT1. T cells developed normally in these mice — a finding that might be explained by the fact that developing T cells express higher levels of ACAT2 than do mature cells<sup>7</sup>.

Surprisingly, one subset of T cells — CD8<sup>+</sup> T cells, or killer T cells, which release toxins that trigger the death of cells that have foreign or mutated proteins — upregulated cholesterol-biosynthesis enzymes in response to the loss of ACAT1, leading to an increase in cell-membrane cholesterol levels. That this seemingly paradoxical response occurred

only in killer T cells and not in CD4<sup>+</sup> T cells is fortuitous, because subsets of the latter are linked to potentially harmful side effects of immunotherapy and local immune suppression in the tumour microenvironment.

Yang *et al.* went on to show that the TCR nanoclusters on the surface of sterol-enhanced killer T cells were larger than those in wild-type cells. Formation of the immunological synapse — the point of embrace between the T cell and tumour cell — also occurred more quickly in enhanced cells than in wild-type cells, as did the release of toxins into the synapse. Immunological-synapse formation is necessary for the destruction of the tumour and its associated infrastructure<sup>8</sup>, and rapid synapse formation enhances the impact of toxin release<sup>9</sup>.

The authors found that several signatures of T-cell activation, in particular phosphorylation of an adaptor protein called linker of activated T cells (LAT), were enhanced in ACAT1-deficient killer T cells. LAT has a lipid modification that ensures that it attaches to cholesterol-rich membrane regions, forming nanoclusters that join with TCRs to create signalling microclusters<sup>10</sup>. Increased cholesterol levels boosted the size of these signalling assemblies and thus enhanced T-cell responsiveness in ACAT1-deficient mice (Fig. 1).

Yang *et al.* transferred antitumour, ACAT1-deficient killer T cells into a mouse model of cancer — an approach similar to adoptive immunotherapy approaches used in the clinic. Compared with wild-type killer T cells, the sterol-enhanced T cells provided the host with greater protection against the

tumour. This result suggests that genetically engineering killer T cells from patients to delete ACAT1 might be a useful component of future immunotherapy approaches.

Can pharmacological inhibition of ACAT with a small molecule achieve similar benefits to genetic mutation? Avasimibe is a non-selective ACAT inhibitor that has been proven safe for short-term treatment in humans<sup>11</sup>. However, it failed to treat cardiovascular disease, for which it was originally developed, and so has yet to be approved for widespread human use. Nonetheless, it can be used in clinical trials, and has the advantage of being administered in a convenient pill. Yang *et al.* found that the effects of avasimibe mimicked those of ACAT1 deletion *in vitro*, and the drug significantly increased survival in mouse models of melanoma and lung cancer.

Yang and colleagues next combined avasimibe with a clinically approved checkpoint-blockade antibody called  $\alpha$ -PD-1, which enhances immunological-synapse formation<sup>12</sup>. Drugs based on the  $\alpha$ -PD-1 antibody have been approved for use in humans to treat lung cancer, kidney cancer and melanoma<sup>13</sup>. Avasimibe acted additively with  $\alpha$ -PD-1 in the authors' animal models, indicating that the two drugs promote synapse formation and tumour destruction through different and complementary mechanisms (Fig. 1).

Many people with cancer fail to respond to checkpoint-blockade drugs, so there is still room for improvement of this breakthrough therapy. Therefore, it is exciting to speculate that Yang and colleagues' basic observations and preclinical data might be a first step towards a pill for boosting killer T cells as part of anticancer and antiviral therapies. ■

**Michael L. Dustin** is at the Kennedy Institute of Rheumatology, University of Oxford, Oxford OX3 7FY, UK.

e-mail: michael.dustin@kennedy.ox.ac.uk

1. Korman, A. J., Peggs, K. S. & Allison, J. P. *Adv. Immunol.* **90**, 297–339 (2006).
2. Porter, D. L., Levine, B. L., Kalos, M., Bagg, A. & June, C. H. *N. Engl. J. Med.* **365**, 725–733 (2011).
3. Yang, W. *et al. Nature* **531**, 651–655 (2016).
4. Xavier, R., Brennan, T., Li, Q., McCormack, C. & Seed, B. *Immunity* **8**, 723–732 (1998).
5. Buck, M. D., O'Sullivan, D. & Pearce, E. L. *J. Exp. Med.* **212**, 1345–1360 (2015).
6. Chang, T.-Y., Li, B.-L., Chang, C. C. Y. & Urano, Y. *Am. J. Physiol. Endocrinol. Metab.* **297**, E1–E9 (2009).
7. Mingueneau, M. *et al. Nature Immunol.* **14**, 619–632 (2013).
8. Dustin, M. L. *Cancer Immunol. Res.* **2**, 1023–1033 (2014).
9. Beal, A. M. *et al. Immunity* **31**, 632–642 (2009).
10. Lillemeier, B. F. *et al. Nature Immunol.* **11**, 90–96 (2010).
11. Tardif, J. C. *et al. Circulation* **110**, 3372–3377 (2004).
12. Yokosuka, T. *et al. J. Exp. Med.* **209**, 1201–1217 (2012).
13. Robert, C. *et al. N. Engl. J. Med.* **372**, 320–330 (2015).

This article was published online on 16 March 2016.



## APPLIED PHYSICS

# Gravity measurements on chips

**Gravimeters have applications ranging from oil exploration to the detection of underground tunnels, but size and lack of portability have limited their field use. A device the size of a postage stamp promises fresh opportunities. [SEE LETTER P.614](#)**

HAZEL RYMER

When an apple fell from a tree onto Isaac Newton's head, or so the story goes, he realized that a force was pulling it down towards Earth. His law of universal gravitation followed, and still provides an excellent first approximation for describing gravity. But measuring the acceleration due to gravity has proved challenging, and is usually solved using enormously expensive and cumbersome instrumentation. The ability to measure gravity using a microchip, as reported on page 614 of this issue by Middlemiss *et al.*<sup>1</sup>, is therefore a major breakthrough.

Seismometers measure movements of Earth's surface, and the earliest was reputedly designed by the polymath Zhang Heng<sup>2</sup> in AD 132. It consisted of a pendulum inside an urn that responded to earthquakes by sending a ball out through a sculpted dragon's mouth and into a toad's in the rough direction of the epicentre (Fig. 1). Seismometers have been miniaturized and digitized since then, and free apps can be downloaded that use the accelerometer inside smartphones to measure vibrations, including those caused by earthquakes.

Seismic signals are produced over a range of frequencies, and 'broadband' seismometers have been developed that typically detect those in the region of 0.01 to 50 hertz. Earth's longer-period oscillations are the domain of gravimeters, rather than seismometers. Gravimeters can measure the change in *g* (the acceleration due to gravity) as it varies over time at a single site because of the relative movement of the Sun and the Moon. This variation is called the Earth tide, and is an oscillation of Earth's surface for which the dominant periods are diurnal and monthly.

Gravimeter development expanded in the 1940s after the physicists Lucien LaCoste and Arnold Romberg made modifications to their zero-length spring<sup>3</sup> — in effect, a seismometer that can detect signals with very long periods. The instruments developed by their company and others dominated geophysical prospecting for decades. Such instruments can be used not only to measure Earth tides, but also to produce maps of gravity.

Gravimeters are now used on ships and aircraft, on land, on the seabed and even in

boreholes to produce maps of the relative value or of the vertical gradient of gravity. These maps can be interpreted in terms of subsurface mass anomalies in applications such as oil prospecting. When changes in gravity through time are measured, applications extend to cavity detection beneath structures such as railway tracks and even to the monitoring of magma and fluid movement beneath active volcanoes.

Portable gravimeters suitable for field use have been around for more than 50 years, but even the smallest one weighs several kilograms and is the size of a small car battery. Although these devices' drift characteristics (relaxation of the spring can lead to apparent drift in the value of gravity) and general usability have improved greatly over time, their basic operating mechanism hasn't changed: a mass on a spring moves in response to gravity, and a series of levers allows the operator to determine the difference in gravity between the point of interest and a reference position.

These relative gravity meters can determine

the difference in gravity between points (which can then be monitored over time) to about 1 microgal, or  $10^{-8} \text{ m s}^{-2}$ , equivalent to variations in the eighth decimal place of *g*. Absolute gravimeters provide a value for *g* to the same accuracy, but take longer to set up and are more suitable for the laboratory than for field use. Other types of instrument — such as falling-mass and pendulum absolute gravimeters, and quantum gravimeters — are also commercially available.

All of these instruments are to some degree cumbersome and awkward to use, but the main problems are their size and price. If either or both of these factors could be reduced, gravimetry applications would increase, just as the reduction in size and price of magnetometers has made beachcombing with metal detectors an easy and affordable pastime. We are still a long way from a smartphone app that can measure gravity to any usable accuracy for prospecting, but Middlemiss and colleagues' device is an important step towards this goal.

Their gravity meter on a chip uses the same sort of technology (microelectromechanical systems, or MEMS) that is now ubiquitous in the accelerometers found in games controllers and smartphones. Its stability and sensitivity represent real breakthroughs. It is about 1,000 times more sensitive than devices used in 'everyday' sensors, such as those in car airbags and games controllers, and more stable than previously developed MEMS devices of similar sensitivity — as the authors prove by using it to measure Earth tides.

At present, their gravimeter needs to be



**Figure 1 | The beginning of gravimetry.** This instrument was designed by Zhang Heng in AD 132, and responded to earthquakes by dropping a ball from a dragon's mouth into the mouth of a toad in the rough direction of the epicentre. Middlemiss *et al.*<sup>1</sup> report a modern-day version of this ancient seismometer — a silicon chip that can measure seismic vibrations of very low frequency, such as changes in gravity.

carefully set up under laboratory conditions to measure Earth tides. But after further development, it will be a field-worthy, portable instrument sensitive enough to detect the small changes in  $g$  needed for surveying and monitoring. On land, such an instrument could monitor  $g$  so that, for example, the rate of change of subsurface mass related to drainage from a reservoir could be quantified. It could also be used to study water tables and magma

levels within volcanoes, or oil and gas reserves if used at the seabed. Airborne instruments — which would be small enough to be carried by drones — could survey large areas in search of gravitational anomalies related to geological formations, or to detect human-made subterranean features. Once these instruments become commercially available, the applications will be limited only by the user's imagination. ■

**Hazel Rymer** is in the Department of Earth, Environment and Ecosystems Science, The Open University, Milton Keynes MK7 6AA, UK.  
e-mail: hazel.rymer@open.ac.uk

1. Middlemiss, R. P. *et al.* *Nature* **531**, 614–617 (2016).
2. Hsiao, K.-H. & Yan, H.-S. *J. Adv. Mech. Des. Syst.* **3**, 179–190 (2009).
3. LaCoste, L. *Leading Edge* **7**, 20–21 (1988).

## RESPIRATORY DISORDERS

# Ironing out smoking-related airway disease

**Lack of the protein IRP2 in mice prevents organelles called mitochondria from accumulating toxic levels of iron in response to smoke exposure. This discovery links environmental and genetic risk factors for a chronic lung disease.**

THOMAS J. MARIANI

Since 2008, chronic lower-respiratory diseases have been the third most common cause of death in the United States<sup>1</sup> — the most prevalent of these being chronic obstructive pulmonary disease (COPD). The name COPD encompasses a complex range of traits associated with irreversible airflow obstruction. These include destruction of the lungs' alveoli (emphysema), excessive mucus production in the airways (chronic bronchitis) and defects in a process called mucociliary clearance, in which cellular protrusions called cilia move mucus out of the lung, along with entrapped irritants. Initially thought to be a smokers' disease,

many risk factors for COPD are now known, both environmental and genetic<sup>2–4</sup>. Writing in *Nature Medicine*, Cloonan *et al.*<sup>5</sup> reveal how one genetic risk factor, increased expression of iron-responsive element-binding protein 2 (IRP2), contributes to disease by modulating iron levels in organelles called mitochondria, ultimately affecting the ability of cilia to protect the lungs from environmental pollutants and pathogens.

Some smokers gradually lose lung function and develop COPD, whereas others do not<sup>6</sup>. Inherited deficiency of the  $\alpha$ -1-antitrypsin protein has long been known<sup>7</sup> to significantly increase susceptibility to emphysema, although this accounts for no more than 10% of COPD cases<sup>8</sup>. In the 1990s, the development

of tools for studying genetic variation stimulated investigation into additional genetic risk factors for COPD. Genome analysis of one group of families that had severe, early-onset COPD revealed several locations containing genes that contribute to disease risk<sup>9</sup>, including a region on chromosome 15 that contains the gene encoding IRP2 (ref. 10).

IRP2 is a key regulator of iron homeostasis in mammals, and exerts a wide range of effects by binding to messenger RNAs that encode proteins involved in iron metabolism. IRP2 expression is increased in people with COPD, although the relevance of this to disease progression has been unclear. In addition, smoking-related increases in lung iron content have been reported<sup>11</sup>. To investigate these observations further, Cloonan *et al.* modelled COPD in mice lacking IRP2, by chronically exposing the animals to cigarette smoke. After smoke exposure, these mice failed to develop many of the complications associated with COPD, including inflammation, emphysema and apoptotic cell death.

The authors went on to explore the mechanism by which IRP2 acts in COPD. High-throughput sequencing of the RNA bound to IRP2 in human cells indicated that this protein might control the function of mitochondria — the main source of cellular energy, and a key regulator of whether cells undergo apoptosis. Analysis of gene expression in human lung tissue, and in lung cells from mice lacking IRP2, further suggested that this protein regulates mitochondrial function in COPD. These findings are consistent with the known role of mitochondria in cellular iron metabolism<sup>12</sup>, and with the fact that mitochondrial dynamics are altered in COPD<sup>13</sup>. The authors next showed that exposure of mice to cigarette smoke raised mitochondrial iron levels, which in turn increased the activity of the protein cytochrome *c* oxidase (COX) — both of which lead to mitochondrial dysfunction (Fig. 1). Furthermore, genetic manipulations that increase mitochondrial iron loading or reduce COX activity worsened or alleviated experimental COPD, respectively.

Finally, the researchers found evidence that targeting mitochondrial iron loading might provide therapeutic benefit in COPD. The drug deferiprone, which can bind to excess iron and block its effects in mitochondria,

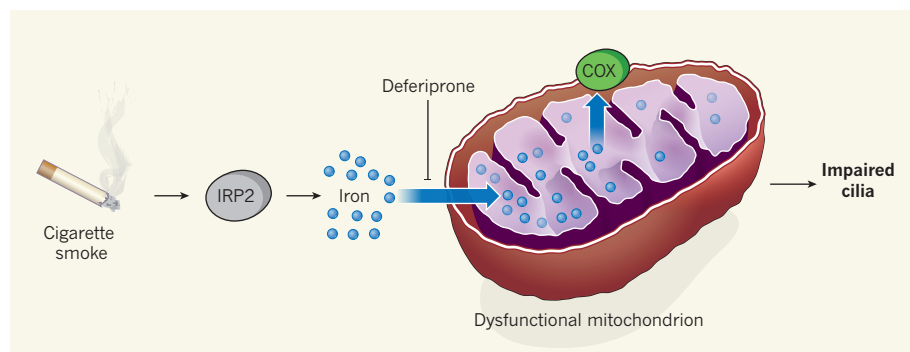


**Figure 1 | Regulation of mucociliary clearance in chronic obstructive pulmonary disease (COPD).**

Smoking increases the risk of COPD, during which airways in the lungs become obstructed by mucus. Cloonan *et al.*<sup>5</sup> report that expression of the iron regulatory protein IRP2 contributes to this process. Specifically, their data indicate that exposure to smoke leads to increased IRP2 levels, which promotes iron accumulation in mitochondria. This increased iron loading in turn increases the activity of the protein cytochrome *c* oxidase (COX), and, together, these factors lead to mitochondrial dysfunction in lung cells. Compromised mitochondrial function reduces the ability of cellular protrusions called cilia to perform their normal role in clearing mucus. The drug deferiprone, which blocks the toxic effects of excess iron in mitochondria, preserves ciliary function in smoke-exposed mice.



maintained or reversed smoke-induced inhibition of mucociliary clearance in mice. Deferiprone has been approved for human use by the US Food and Drug Administration. However, although targeting the iron-loading pathway is of great interest, deferiprone has been associated with reduced white-blood-cell counts and increased risk of infection. These side effects could limit the drug's potential, particularly because periodic lung infections are a major cause of illness in people with COPD.

Another limitation of Cloonan and colleagues' study is that it does not provide clear insight into how IRP2-mediated mitochondrial dysfunction contributes to specific COPD-associated traits. In fact, IRP2 and mitochondrial iron loading are associated with many COPD-related traits in smoke-exposed mice.

One particularly interesting aspect of the study is the apparently direct effect of iron loading and mitochondrial function on the ciliary activity required for mucus clearance. The beating of cilia requires substantial production of energy-carrying ATP molecules by mitochondria. However, I know of no previous reports of a direct association between mitochondrial iron levels and mucociliary clearance. Future studies should identify the cellular processes by which mitochondrial iron loading impairs human lung function. Also unexplored is the relationship between IRP2, cigarette-smoke-induced mitochondrial iron levels and cancer. The genetic region on chromosome 15 that harbours *IRP2* has been repeatedly implicated in susceptibility to lung cancer<sup>14</sup>.

It remains likely that many individual genes each contribute small components of risk to discrete COPD traits. Ultimately, a better understanding of the various risk factors, combined with improved clinical analysis of the traits in each patient, will help to identify the best possible, personalized interventions. Cloonan and colleagues' report represents just one chapter in our improved understanding of the interaction between the genetic and environmental risk factors associated with chronic lung disease. Nonetheless, it is an exciting chapter, because it reveals that smoke-induced mitochondrial iron loading has an unexpected role in COPD, which may serve as a bona fide therapeutic target. ■

**Thomas J. Mariani** is in the Division of Neonatology and the Pediatric Molecular and Personalized Medicine Program, University of Rochester Medical Center, Rochester, New York 14642, USA.  
e-mail: tom\_mariani@urmc.rochester.edu

1. Johnson, N. B., Hayes, L. D., Brown, K., Hoo, E. C. & Ethier, K. A. *MMWR Suppl.* **63** (Suppl. 4), 3–27 (2014).
2. Gordon, S. B. et al. *Lancet Respir. Med.* **2**, 823–860 (2014).
3. Islam, J. Y., Keller, R. L., Aschner, J. L., Hartert, T. V. & Moore, P. E. *Am. J. Respir. Crit. Care Med.* **192**, 134–156 (2015).

4. Weiss, S. T. *Nature Genet.* **42**, 14–16 (2010).
5. Cloonan, S. M. et al. *Nature Med.* **22**, 163–174 (2016).
6. Burrows, B., Knudson, R. J., Cline, M. G. & Lebowitz, M. D. *Am. Rev. Respir. Dis.* **115**, 195–205 (1977).
7. Laurell, C.-B. & Eriksson, S. *Scand. J. Clin. Lab. Invest.* **15**, 132–140 (1963).
8. Lieberman, J., Winter, B. & Sastre, A. *Chest* **89**, 370–373 (1986).
9. Silverman, E. K. et al. *Am. J. Hum. Genet.* **70**, 1229–1239 (2002).
10. DeMeo, D. L. et al. *Am. J. Hum. Genet.* **85**, 493–502 (2009).

11. Ghio, A. J. *Biochim. Biophys. Acta* **1790**, 731–739 (2009).
12. Chen, C. & Paw, B. H. *Biochim. Biophys. Acta* **1823**, 1459–1467 (2012).
13. Aravamudan, B., Thompson, M. A., Pabelick, C. M. & Prakash, Y. S. *Expert Rev. Respir. Med.* **7**, 631–646 (2013).
14. Dubey, S. & Powell, C. A. *Am. J. Respir. Crit. Care Med.* **179**, 860–868 (2009).

This article was published online on 9 March 2016.

## PHYSICAL CHEMISTRY

# A close-up view of coupled molecules

**Processes such as photosynthesis depend on the interplay between the electric dipoles of chromophore molecules. Yet these dipole–dipole interactions have not been visualized at the atomic level — until now. [SEE LETTER P.623](#)**

**GUILLAUME SCHULL**

**I**nteractions between the electric dipoles of molecules have a key role in many biological and photonic processes, but have been difficult to study at the atomic scale. On page 623 of this issue, Zhang *et al.*<sup>1</sup> report the optical properties of two individual molecules separated by a few nanometres, which they probed in real space using a method based on scanning tunnelling microscopy. The resulting highly resolved images provide an unprecedented visualization of the dipole–dipole interactions between the molecules.

Chromophores are a class of molecule that can absorb and re-emit visible light. The colour of the absorbed and emitted photons is intimately linked to the chemical structure of these molecules, but also depends crucially on their immediate environment. In this context, dipole–dipole interactions are key — they have a central role in photosynthesis, for example, transferring the energy harvested from sunlight by one molecule to another molecule that converts it into chemical energy.

Such intermolecular interactions can be viewed, to a first approximation, as an exchange of information mediated by electromagnetic waves. A fascinating consequence of this is that chromophore states may exhibit strong entanglement — a quantum phenomenon in which a group of objects must be considered as a whole to be understood, rather than as a sum of individual components — even when separated in space by several nanometres<sup>2</sup>. The optical properties of chromophores are therefore strongly influenced by the number, distance, arrangement or orientation of their neighbours. Determining the impact of these different parameters is highly desirable, both for fundamental reasons

and for potential applications, but requires methods capable of manipulating and probing the optical properties of chromophores with atomic-scale resolution. Such resolution has been out of reach, even with the best optical set-ups<sup>3</sup>.

Zhang and colleagues overcame this problem by using electrons, rather than photons, to excite the chromophores. Electrons can be confined to atomic-scale pathways using a scanning tunnelling microscope. In such experiments, an extremely thin metallic tip is brought towards a molecule deposited on a metallic surface. Electrons jump from the tip to the molecule when the separation reaches approximately one nanometre, thanks to a quantum effect called tunnelling. A few of these electrons (about 1 in 10,000) lose some of their energy during this process, causing light to be emitted. By precisely scanning the molecule with the tip, the spatial variation of the emitted light intensity can be visualized at a resolution that beats any all-optical approach.

This method was first used to obtain atomic-scale optical maps of fullerene molecules (buckyballs) deposited on gold surfaces<sup>4</sup>. But the optical signal in those experiments was not directly related to the light emission (luminescence) of the molecules, because the direct contact between the fullerenes and the gold surfaces enabled electrons to relax from excited states through a mechanism that is faster than luminescence. This quenching of luminescence can be prevented by separating chromophores from the metallic substrate using a thin, electrically insulating layer of oxide — as reported in a pioneering paper<sup>5</sup> that provided the first evidence that electrons can be used to study single-molecule luminescence. Similar experiments have since been

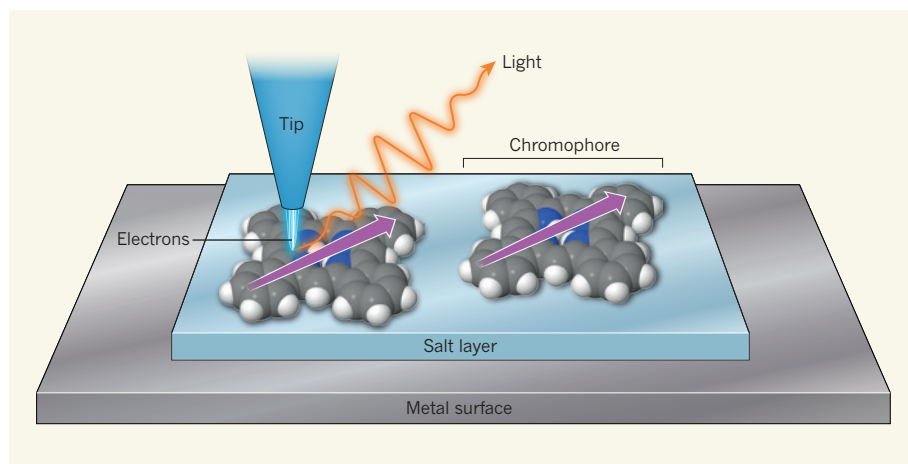


**Figure 1 | Visualizing dipole-dipole interactions.** Zhang *et al.*<sup>1</sup> brought the metallic tip of a scanning tunnelling microscope towards two chromophore molecules on a thin layer of salt, which was deposited on a metallic surface. Electrons jump from the tip to a molecule when the separation reaches about 1 nm, causing the molecule to emit light. By precisely scanning the molecules with the tip, the authors visualized the spatial variation of the emitted light's intensity at atomic resolution. The resulting map is a visualization of the interactions between the chromophores' dipoles (purple arrows).

performed for molecules separated from the surface by chains of organic molecules<sup>6</sup> and for molecules directly suspended between the tip and the surface<sup>7</sup>.

Zhang *et al.* adopted a similar decoupling strategy: they used the metallic tip of a microscope to move two chromophores towards each other on a thin layer of salt, and monitored the spectra emitted by the molecule as they did so. The results are impressive. The authors observed a change in the main emission line of the molecules' luminescence spectra when the distance between the chromophores reached about 3 nm. The line eventually split into multiple peaks as the distance was further reduced.

The authors reconstructed atomically resolved maps of the emitted light by scanning the two chromophores with the tip of the microscope (Fig. 1). The patterns in these photon maps are different for each of the peaks in the luminescence spectrum of the molecules. Backed up by a theoretical analysis, Zhang and colleagues suggest that the data indicate hybridization of the excited states of the two molecules. The maps therefore correspond to a direct visualization of the dipole-dipole coupling between the chromophores.

The researchers went on to use their technique to study how the optical emissions changed in chains of chromophores (in which the molecules are close enough for dipole-dipole interactions to occur) as the number of chromophores increased from two to four. The emission spectra and the photon maps of these systems revealed delocalization of the excited states across the whole chain, which strongly hints that the molecules' states are entangled — although the authors did not measure entanglement in their experiments.

Zhang and colleagues' findings suggest that they could construct, chromophore by

chromophore, a small J-aggregate — a kind of dye whose emission intensity increases quadratically with the number of molecules of which it is composed. However, the observed increase in emission intensity is lower than expected for chains composed of four molecules, indicating that the authors' model of excitation and relaxation mechanisms

in the chromophores needs to be refined.

Future work should also examine the influence of the angle between molecular dipoles, or focus on more-complex arrangements of chromophores. Another exciting prospect is that energy transfers between individual donor and acceptor molecules could one day be investigated directly using the authors' technique. Probing the statistics of the emitted photons<sup>8</sup> — determining the average time between the emission of successive photons — should eventually reveal whether the chromophore chains behave as entangled photon sources, potentially opening up thrilling opportunities for quantum-information experiments. ■

**Guillaume Schull** is at the *Institut de Physique et Chimie des Matériaux de Strasbourg, UMR 7504 (CNRS–Université de Strasbourg), 67034 Strasbourg, France.* e-mail: schull@unistra.fr

1. Zhang, Y. *et al.* *Nature* **531**, 623–627 (2016).
2. Hettich, C. *et al.* *Science* **298**, 385–389 (2002).
3. Yang, B., Trebbia, J.-B., Baby, R., Tamarat, Ph. & Lounis, B. *Nature Photon.* **9**, 658–662 (2015).
4. Berndt, R. *et al.* *Science* **262**, 1425–1427 (1993).
5. Qiu, X. H., Nazin, G. V. & Ho, W. *Science* **299**, 542–546 (2003).
6. Zhu, S. E. *et al.* *J. Am. Chem. Soc.* **135**, 15794–15800 (2013).
7. Chong, M. C. *et al.* *Phys. Rev. Lett.* **116**, 036802 (2016).
8. Merino, P., Große, C., Rosławska, A., Kuhnke, K. & Kern, K. *Nature Commun.* **6**, 8461 (2015).

## NEUROSCIENCE

# Making risk-takers settle

**In rats, individual differences in risk preference and in sensitivity to gains compared with losses are controlled by a specific neuronal population, stimulation of which neutralizes risk-seeking behaviour. [SEE LETTER P.642](#)**

NICK G. HOLLON & PAUL E. M. PHILLIPS

**T**he world is rife with uncertainty, affecting everything from financial investments to animals' foraging decisions. Many individuals find uncertainty intrinsically aversive, choosing to settle for a sure thing even if it means forgoing the possibility of a better outcome. But some seek out the chance of a big win, even if it comes with the risk of getting next to nothing in return. In this issue, Zalocusky *et al.*<sup>1</sup> (page 642) report that driving the activity of a specific population of neurons can sway risk-seeking animals to make more risk-neutral decisions.

Although the term risk is often used colloquially to imply impending danger, in several subdisciplines of economics the formal

definition simply describes the variance in the value or desirability of possible outcomes. Zalocusky *et al.* characterized rats' behaviour in a decision-making task that involved two options, each of which paid out the same sugar reward on average, but which differed in risk. The risky choice yielded either a large or a small reward, whereas the safe option yielded a guaranteed intermediate-sized reward. When choosing the risky option, a rat that received a large reward had made a relative gain, whereas a small reward was a relative loss compared with both the average value of that risky gamble and the certain reward of the safe option.

As a group, the rats' decisions were influenced by recent gains and losses. Like humans, however, not all individuals made the same pattern of choices (Fig. 1). Many rats selected

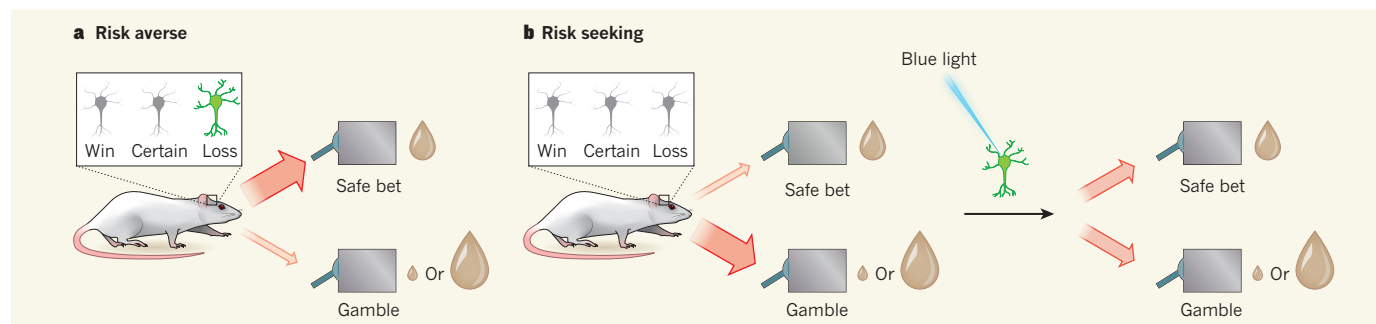


**Figure 1 | Neutralizing risk seeking.** Zalocusky and colleagues<sup>1</sup> tested rats on a decision-making task that involved a choice between two levers. Pressing one lever yielded a guaranteed, intermediate-sized sugar reward, whereas the other produced either a small or a large reward. **a**, Some rats were risk averse, choosing the safe bet more often than the gamble. When these animals made their choice, neurons in the brain's nucleus accumbens that expressed

the D2 receptor protein were more active (blue) following a losing gamble than following a win or a certain outcome. **b**, By contrast, some rats sought out risk — they more often took the gamble, and showed blunted elevation in D2-expressing neuron activity following a loss. Artificially increasing the activity of the D2-expressing neurons using a protein activated by blue light caused risk-seeking rats to make fewer risky choices.

the safe option for most trials, but a subset selected the risky option more than half the time, and these individual differences were stable across days of repeated testing. The likelihood of a rat taking another risk immediately after a winning gamble did not differ between these subgroups. However, there were marked differences in behaviour following a loss — risk-averse rats were more likely to switch to the sure bet, whereas risk-seeking rats were just as likely to gamble again as they were to opt for the certain intermediate reward.

What neural mechanisms account for these differences? A human study<sup>2</sup> implies that how well individuals learn to avoid losses is modulated by diversity in genes that encode D2-subtype receptor proteins for the neurotransmitter molecule dopamine. Moreover, clinical observations<sup>3</sup> indicate that pathological gambling can be a side effect of dopamine-related medications — particularly drugs such as pramipexole (used to treat Parkinson's disease) that directly activate D2 and D3 dopamine-receptor subtypes, which suppresses neural activity.

Previous studies in rodents have used various decision-making tasks to assess risky choices, but pharmacological manipulations of dopamine receptors have produced inconsistent effects<sup>4</sup>. Nonetheless, Zalocusky *et al.* found that treating rats with pramipexole caused a dose-dependent increase in risk-seeking decisions, in agreement with the human clinical data. The authors replicated this effect by infusing the drug directly into the rats' nucleus accumbens, a brain region in the ventral striatum that receives dense input from dopamine-producing neurons and is linked to risky choices<sup>5</sup>.

Next, the authors selectively targeted D2-expressing neurons in the nucleus accumbens, engineering these neurons to express either a genetically encoded calcium indicator to monitor neuronal activity or a light-sensitive ion channel that can be used to promote activity. This is in itself a technical feat, improving our ability to analyse these

cells in wild-type animals. Zalocusky *et al.* found that, at the time when rats were presumably deciding which reward option to select, activity in the D2-expressing cell population was higher when the previous outcome was a loss than after either gain or safe-choice outcomes. The magnitude of this difference predicted an animal's risk preference — those with greater relative D2-cell activity during decisions that followed losses exhibited risk aversion, whereas those in which D2-cell activity showed little difference following each of the various outcomes exhibited risk-seeking behaviour. Moreover, selectively and briefly activating the D2-expressing cells during the decision period reduced gambling in risk-preferring rats, but had no effect on risk-averse rats.

Behavioural economics has described many ways in which actual human behaviour deviates from the predictions made by long-dominant economic theories, ostensibly owing to emotional and cognitive biases that affect our judgement and decisions. For example, prospect theory<sup>6</sup>, a pre-eminent behavioural economic framework, highlights the idea that losses loom larger than gains — a behavioural phenomenon known as loss aversion. Within this framework, Zalocusky and colleagues' behavioural analyses highlight that individual differences in loss sensitivity might underlie variations in risk preference, and the authors' neural recordings and manipulations suggest a plausible mechanism that links loss and risk aversion. Other components of prospect theory that should be considered when interpreting the current data include differences in how individuals subjectively weight probabilities, and in how they determine their basis for comparison when appraising a given outcome as a gain or a loss.

Caveats of the current study involve the neural circuitry of the nucleus accumbens. In other, closely related regions of the striatum, D2-expressing neurons are mostly distinct from D1-expressing neurons, and the neuronal subsets feed into relatively segregated output

pathways<sup>7</sup>. This segregation makes interpreting the functions of discrete neuronal circuits fairly straightforward<sup>8</sup>. However, the output pathways of D1- and D2-expressing neurons in the nucleus accumbens might be less segregated<sup>9</sup>. The authors also acknowledge that analysing an entire population of D2-expressing cells obscures potential differences in the information conveyed by discrete ensembles within this population, as occurs in other neural populations<sup>10</sup>.

Nevertheless, Zalocusky *et al.* have identified specific neural signatures that predict risk preferences, and demonstrated that the activity of these neurons at specific time points contributes to animals' decisions. These findings offer a potential biological substrate for loss aversion and its contribution to risk attitude. As such, the study represents a success for neuro-economics — a field that strives to link economic models to brain function. ■

**Nick G. Hollon** is in the Molecular Neurobiology Laboratory, Salk Institute for Biological Studies, La Jolla, California 92037, USA. **Paul E. M. Phillips** is in the Department of Psychiatry & Behavioral Sciences and the Department of Pharmacology, University of Washington, Seattle, Washington 98195, USA. e-mails: nhollon@salk.edu; pemp@uw.edu

1. Zalocusky, K. A. *et al.* *Nature* **531**, 642–646 (2016).
2. Frank, M. J., Moustafa, A. A., Haughey, H. M., Curran, T. & Hutchison, K. E. *Proc. Natl Acad. Sci. USA* **104**, 16311–16316 (2007).
3. Dodd, M. L. *et al.* *Arch. Neurol.* **62**, 1377–1381 (2005).
4. Orsini, C. A., Moorman, D. E., Young, J. W., Setlow, B. & Floresco, S. B. *Neurosci. Biobehav. Rev.* **58**, 147–167 (2015).
5. Kuhn, C. M. & Knutson, B. *Neuron* **47**, 763–770 (2005).
6. Kahneman, D. & Tversky, A. *Econometrica* **47**, 263–292 (1979).
7. Gerfen, C. R. & Surmeier, D. J. *Annu. Rev. Neurosci.* **34**, 441–466 (2011).
8. Kravitz, A. V. *et al.* *Nature* **466**, 622–626 (2010).
9. Kupchik, Y. M. *et al.* *Nature Neurosci.* **18**, 1230–1232 (2015).
10. Jin, X., Tecuapetla, F. & Costa, R. M. *Nature Neurosci.* **17**, 423–430 (2014).

This article was published online on 23 March 2016.



# Contribution of Antarctica to past and future sea-level rise

Robert M. DeConto<sup>1</sup> & David Pollard<sup>2</sup>

Polar temperatures over the last several million years have, at times, been slightly warmer than today, yet global mean sea level has been 6–9 metres higher as recently as the Last Interglacial (130,000 to 115,000 years ago) and possibly higher during the Pliocene epoch (about three million years ago). In both cases the Antarctic ice sheet has been implicated as the primary contributor, hinting at its future vulnerability. Here we use a model coupling ice sheet and climate dynamics—including previously underappreciated processes linking atmospheric warming with hydrofracturing of buttressing ice shelves and structural collapse of marine-terminating ice cliffs—that is calibrated against Pliocene and Last Interglacial sea-level estimates and applied to future greenhouse gas emission scenarios. Antarctica has the potential to contribute more than a metre of sea-level rise by 2100 and more than 15 metres by 2500, if emissions continue unabated. In this case atmospheric warming will soon become the dominant driver of ice loss, but prolonged ocean warming will delay its recovery for thousands of years.

Reconstructions of the global mean sea level (GMSL) during past warm climate intervals including the Pliocene (about three million years ago)<sup>1</sup> and late Pleistocene interglacials<sup>2–5</sup> imply that the Antarctic ice sheet has considerable sensitivity. Pliocene atmospheric CO<sub>2</sub> concentrations were comparable to today's (~400 parts per million by volume, p.p.m.v.)<sup>6</sup>, but some sea-level reconstructions are 10–30 m higher<sup>1,7</sup>. In addition to the loss of the Greenland Ice Sheet and the West Antarctic Ice Sheet (WAIS)<sup>2</sup>, these high sea levels require the partial retreat of the East Antarctic Ice Sheet (EAIS), which is further supported by sedimentary evidence from the Antarctic margin<sup>8</sup>. During the more recent Last Interglacial (LIG, 130,000 to 115,000 years ago), GMSL was 6–9.3 m higher than it is today<sup>2–4</sup>, at a time when atmospheric CO<sub>2</sub> concentrations were below 280 p.p.m.v. (ref. 9) and global mean temperatures were only about 0–2 °C warmer<sup>10</sup>. This requires a substantial sea-level contribution from Antarctica of 3.6–7.4 m in addition to an estimated 1.5–2 m from Greenland<sup>11,12</sup> and around 0.4 m from ocean steric effects<sup>10</sup>. For both the Pliocene and the LIG, it is difficult to obtain the inferred sea-level values from ice-sheet models used in future projections.

## Marine ice sheet and ice cliff instabilities

Much of the WAIS sits on bedrock hundreds to thousands of metres below sea level (Fig. 1a)<sup>13</sup>. Today, extensive floating ice shelves in the Ross and Weddell Seas, and smaller ice shelves and ice tongues in the Amundsen and Bellingshausen seas (Fig. 1b) provide buttressing that impedes the seaward flow of ice and stabilizes marine grounding zones (Fig. 2a). Despite their thickness (typically about 1 km near the grounding line to a few hundred metres at the calving front), a warming ocean has the potential to quickly erode ice shelves from below, at rates exceeding 10 m yr<sup>-1</sup> °C<sup>-1</sup> (ref. 14). Ice-shelf thinning and reduced backstress enhance seaward ice flow, grounding-zone thinning, and retreat (Fig. 2b). Because the flux of ice across the grounding line increases strongly as a function of its thickness<sup>15</sup>, initial retreat onto a reverse-sloping bed (where the bed deepens and the ice thickens upstream) can trigger a runaway Marine Ice Sheet Instability (MISI; Fig. 2c)<sup>15–17</sup>. Many WAIS grounding zones sit precariously on the edge of such reverse-sloped beds, but the EAIS also contains deep

subglacial basins with reverse-sloping, marine-terminating outlet troughs up to 1,500 m deep (Fig. 1). The ice above floatation in these East Antarctic basins is much thicker than in West Antarctica, with the potential to raise GMSL by around 20 m if the ice in those basins is lost<sup>13</sup>. Importantly, previous ice-sheet simulations accounting for migrating grounding lines and MISI dynamics have shown the potential for repeated WAIS retreats and readvances over the past few million years<sup>18</sup>, but could only account for GMSL rises of about 1 m during the LIG and 7 m in the warm Pliocene, which are substantially smaller than geological estimates.

So far, the potential for MISI to cause ice-sheet retreat has focused on the role of ocean-driven melting of buttressing ice shelves from below<sup>16,18–20</sup>. However, it is often overlooked that the major ice shelves in the Ross and Weddell seas and the many smaller shelves and ice tongues buttressing outlet glaciers are also vulnerable to atmospheric warming. Today, summer temperatures approach or just exceed 0 °C on many shelves<sup>21</sup>, and their flat surfaces near sea level mean that little atmospheric warming would be needed to dramatically increase the areal extent of surface melting and summer rainfall.

Meltwater on ice-shelf surfaces causes thinning if it percolates through the shelf to the ocean. If refreezing occurs, the ice is warmed, reducing its viscosity and speeding its flow<sup>22</sup>. The presence of rain and meltwater can also influence crevassing and calving rates<sup>23</sup> (hydrofracturing) as witnessed on the Antarctic Peninsula's Larson B ice shelf during its sudden break-up in 2002<sup>24</sup>. Similar dynamics could have affected the ice sheet during ancient warm intervals<sup>25</sup>, and given enough future warming, could eventually affect many ice shelves and ice tongues, including the major buttressing shelves in the Ross and Weddell seas.

Another physical mechanism previously underappreciated at the ice-sheet scale involves the mechanical collapse of ice cliffs in places where marine-terminating ice margins approach 1 km in thickness, with >90 m of vertical exposure above sea level<sup>26</sup>. Today, most Antarctic outlet glaciers with deep beds approaching a water depth of 1 km are protected by buttressing ice shelves, with gently sloping surfaces at the grounding line (Fig. 2d). However, given enough atmospheric warming above or ocean warming below (Fig. 2e), ice-shelf retreat can outpace its dynamically accelerated seaward flow as buttressing is lost and

<sup>1</sup>Department of Geosciences, University of Massachusetts, Amherst, Massachusetts 01003, USA. <sup>2</sup>Earth and Environmental Systems Institute, Pennsylvania State University, University Park, Pennsylvania 16802, USA.

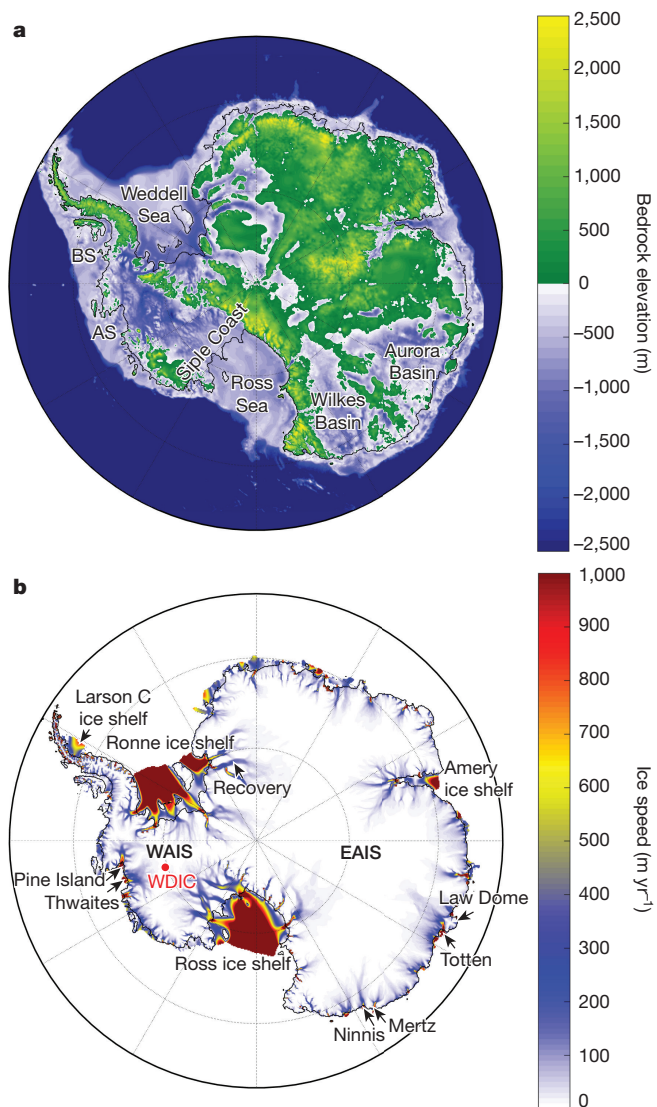


**Figure 1 | Antarctic sub-glacial topography and ice sheet features.** **a**, Bedrock elevations<sup>13</sup> interpolated onto the 10-km polar stereographic ice-sheet model grid and used in Pliocene, LIG, and future ice-sheet simulations. **b**, Model surface ice speeds and grounding lines (black lines) show the location of major ice streams, outlet glaciers, and buttressing ice shelves (seaward of grounding lines) relative to the underlying topography in **a**. Features and place names mentioned in the text are also shown. AS, Amundsen Sea; BS, Bellingshausen Sea; WDIC, WAIS Divide Ice Core. The locations of the Pine Island, Thwaites, Ninnis, Mertz, Totten, and Recovery glaciers are shown. Model ice speeds (**b**) are shown after equilibration with a modern atmospheric and ocean climatology (see Methods).

retreating grounding lines thicken<sup>15</sup>. In places where marine-terminating grounding lines are thicker than 800 m or so, this would produce >90 m subaerial cliff faces that would collapse (Fig. 2f) simply because longitudinal stresses at the cliff face would exceed the yield strength (about 1 MPa) of the ice<sup>26</sup>.

More heavily crevassed and damaged ice would reduce the maximum supported cliff heights. If a thick, marine-terminating grounding line began to undergo such mechanical failure, its retreat would continue unabated until temperatures cooled enough to reform a buttressing ice shelf, or the ice margin retreated onto bed elevations too shallow to support the tall, unstable cliffs<sup>25</sup>. If protective ice shelves were suddenly lost in the vast areas around the Antarctic margin where reverse-sloping bedrock is more than 1,000 m deep (Fig. 1a), exposed grounding-line ice cliffs would quickly succumb to structural failure, as is happening

in the few places where such conditions exist today (the Helheim and Jakobsavn glaciers on Greenland and the Crane Glacier on the Antarctic Peninsula), hinting that a Marine Ice Cliff Instability (MICI) in addition to MISI could be an important contributor to past and future ice-sheet retreat.

Our three-dimensional ice sheet–ice shelf model<sup>25,27</sup> (Methods) predicts the evolution of continental ice thickness and temperature as a function of ice flow (deformation and sliding) and changes in mass balance via precipitation, runoff, basal melt, oceanic melt under ice shelves and on vertical ice faces, calving, and tidewater ice-cliff failure. The model captures MISI (Fig. 2a–c) by accounting for migrating grounding lines and the buttressing effects of ice shelves with pinning points and side-shear. To capture the dynamics of MICI (Fig. 2d–f), new physical treatments of surface-melt and rainwater-enhanced calving (hydrofracturing) and grounding-line ice-cliff dynamics have been added<sup>25</sup>. Including these processes was found to increase the model's contribution to Pliocene GMSL from +7 m (ref. 18) to +17 m (ref. 25). The model formulation used here is similar to that described in ref. 25, but with improvements in the treatment of calving, thermodynamics, and climate–ice–ocean coupling (Methods).

### The Antarctic Ice Sheet in the Pliocene

The warm mid-Pliocene and LIG provide complementary targets for model performance, via the ability to produce ~5–20 m and ~3.5–7.5 m GMSL from Antarctica, respectively. These two time periods highlight model sensitivities to different processes, because Pliocene summer air temperatures were capable of producing substantial surface meltwater, especially during warm austral summer orbits<sup>28</sup>. Conversely, LIG temperatures were cooler<sup>29</sup>, with limited potential for surface meltwater production. Instead, ocean temperatures<sup>30</sup> could have been the determining factor in LIG ice retreat<sup>31</sup>.

To simulate Pliocene and LIG ice sheets, we couple the ice model to a high-resolution, atmospheric regional climate model (RCM) adapted to Antarctica and nested within a global climate model (GCM; see Methods). The RCM captures the orographic details of ice shelves and adjacent ice-sheet margins, which is critical here because the new calving and grounding line processes are mechanistically linked to the atmosphere.

High-resolution ocean modelling beneath time-evolving ice shelves on palaeoclimate timescales exceeds existing capabilities. Instead, we use a modern ocean climatology<sup>32</sup> interpolated to our ice-sheet grid, with uniformly imposed sub-surface ocean warming providing melt rates on sub-ice-shelf and calving-front surfaces exposed to sea water. The RCM climatologies and imposed ocean warming are applied to quasi-equilibrated initial ice-sheet states, with atmospheric temperatures and the precipitation lapse-rate corrected as the ice sheet evolves.

As in ref. 25, the Pliocene simulation uses a RCM climatology with 400 p.p.m.v. CO<sub>2</sub>, a warm austral summer orbit<sup>28</sup>, and 2 °C imposed ocean warming to represent maximum mid-Pliocene warmth (Extended Data Fig. 1). The model produces an 11.3-m contribution to GMSL rise, reflecting a reduction in its sensitivity of about 6 m relative to the formulation in ref. 25, but within the range of plausible sea-level estimates<sup>1,7</sup>. Pliocene retreat is triggered by meltwater-induced hydrofracturing of ice shelves, which relieves backstress and initiates both MISI and MICI retreat into the deepest sectors of WAIS and EAIS marine basins.

### The Antarctic Ice Sheet during the LIG

Summer air temperatures in the RCM are slightly warmer at 116 kyr ago than 128 kyr ago, but remain below freezing in both cases, with little to no surface melt (Extended Data Fig. 2). As a result, substantial oceanic warming >4 °C is required to initiate WAIS retreat at 128 kyr ago, which occurs once an ocean-melt threshold is reached in the stability of the Thwaites grounding line (Extended Data Fig. 3a and d). Allowing two-way coupling between the RCM and the ice-sheet model

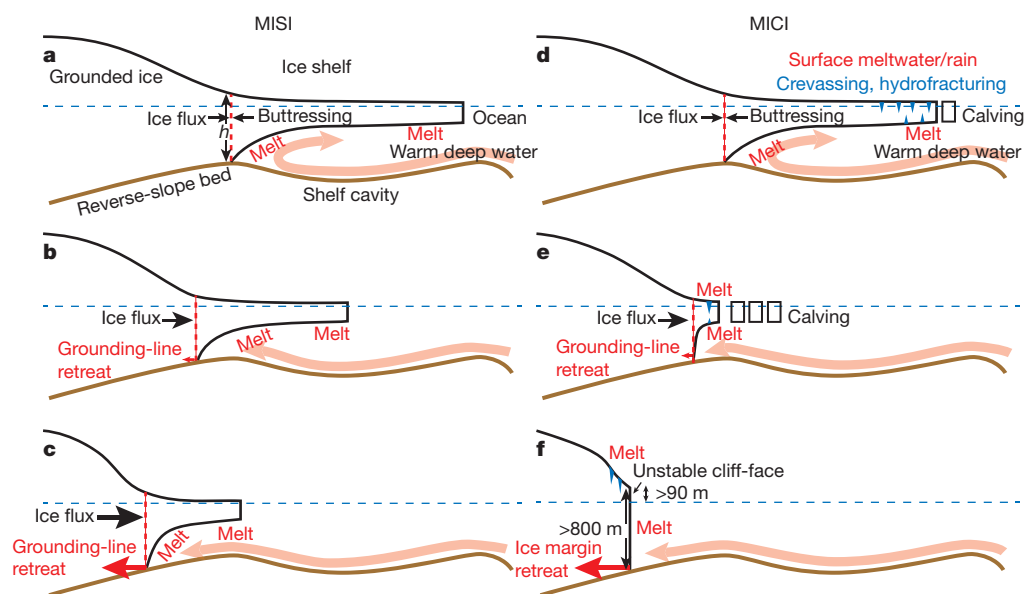


**Figure 2 | Schematic representation of MISI and MICI and processes included in the ice model.** Top-to-bottom sequences (a–c and d–f) show progressive ice retreat into a subglacial basin, triggered by oceanic and atmospheric warming. The pink arrow represents the advection of warm circumpolar deep water (CDW) into the shelf cavity. **a**, Stable, marine-terminating ice-sheet margin, with a buttressing ice shelf. Seaward ice flux is strongly dependent on grounding-line thickness  $h$ . Sub-ice melt rates increase with open-ocean warming and warm-water incursions into the ice-shelf cavity. **b**, Thinning shelves and reduced buttressing increase seaward ice flux, backing the grounding line onto reverse-sloping bedrock. **c**, Increasing  $h$  with landward grounding-line retreat leads to an ongoing increase in ice flow across the grounding line in a positive runaway feedback until the bed slope changes. **d**, In addition to MISI (a–c), the model physics used here account for surface-meltwater-enhanced calving via hydrofracturing of floating ice (e), providing an additional mechanism for ice-shelf loss and initial grounding-line retreat into deep basins. **f**, Where oceanic melt and enhanced calving eliminate shelves completely, subaerial cliff faces at the ice margin become structurally unstable where  $h$  exceeds 800 m, triggering rapid, unabated MICI retreat into deep basins.

(Methods) captures dynamical atmospheric feedbacks as the ice margin retreats. This enhances retreat (Extended Data Fig. 3b, e), but still requires  $>4^{\circ}\text{C}$  of ocean warming to produce a  $>3.5\text{ m}$  increase in GMSL. We find that by accounting for the additional influence of circum-Antarctic ocean warming on the RCM atmosphere (Methods), the GMSL contribution increases to  $>6.5\text{ m}$  with just  $3^{\circ}\text{C}$  sub-surface ocean warming (Extended Data Fig. 3c and f), despite the cooler orbit of the Earth 128 kyr ago. The ocean-driven continental warming at 128 kyr ago agrees with ice core records<sup>29</sup> and supports a Southern Ocean control on the timing of ice-sheet retreat<sup>30,31</sup>, possibly through Northern Hemisphere influences on the ocean meridional overturning circulation<sup>33</sup>.

Alternative simulations (Fig. 3) use time-evolving atmospheric and oceanic climatologies (Methods) based on marine and ice-core proxy reconstructions<sup>29</sup>. These time-continuous simulations produce GMSL contributions of 6–7.5 m early in the interglacial, followed by a prolonged plateau and rapid recovery of the ice sheet beginning around 115 kyr ago. This result matches the magnitude, temporal pattern, and rate of LIG sea-level change in ref. 3 (Fig. 3a), and the simulated recovery of the WAIS satisfies the presence of ice  $>70\text{ kyr}$  ago at the bottom of the WAIS Divide Ice Core<sup>34</sup>.

Combined with estimates of Greenland ice loss<sup>11,12,35</sup> and ocean thermal effects<sup>10</sup>, the simulated, Antarctic contributions to Pliocene and LIG sea level are in much better agreement with geological estimates<sup>2–4</sup> than previous versions of our model<sup>18,27</sup>, which lacked these new treatments of meltwater-enhanced calving and ice-margin dynamics, suggesting that the new model is better suited to simulations of future ice response.

## Future simulations

Using the same model physics and parameter values as used in the Pliocene and LIG simulations, we apply the ice-sheet model to long-term future simulations (Methods). Here, atmospheric forcing is provided by high-resolution RCM simulations (Extended Data Fig. 4)

following three extended Representative Carbon Pathway (RCP) scenarios (RCP2.6, RCP4.5 and RCP8.5)<sup>36</sup>. Future circum-Antarctic ocean temperatures used in our time-evolving sub-ice melt-rate calculations come from matching, high-resolution ( $1^{\circ}$ ) National Center for Atmospheric Research (NCAR) CCSM4 simulations (ref. 37, Extended Data Fig. 5). The simulations begin in 1950 to provide some hindcast spinup, and are run for 550 years to 2500.

The RCP scenarios (Fig. 4) produce a wide range of future Antarctic contributions to sea level, with RCP2.6 producing almost no net change by 2100, and only 20 cm by 2500. Conversely, RCP4.5 causes almost complete WAIS collapse within the next five hundred years, primarily owing to the retreat of Thwaites Glacier into the deep WAIS interior. The Siple Coast grounding zone remains stable until late in the simulation, thanks to the persistence of the buttressing Ross Ice Shelf (see Supplementary Video 2). In RCP4.5, GMSL rise is 32 cm by 2100, but subsequent retreat of the WAIS interior, followed by the fringes of the Wilkes Basin and the Totten Glacier/Law Dome sector of the Aurora Basin produces 5 m of GMSL rise by 2500.

In RCP8.5, increased precipitation causes an initial, minor gain in total ice mass (Fig. 4d), but rapidly warming summer air temperatures trigger extensive surface meltwater production<sup>38</sup> and hydrofracturing of ice shelves by the middle of this century (Extended Data Fig. 4). The Larsen C is one of the first shelves to be lost, about 2055. Around the same time, major thinning and retreat of outlet glaciers commences in the Amundsen Sea Embayment, beginning with Pine Island Glacier (Fig. 4h), and along the Bellingshausen margin. Massive meltwater production on shelf surfaces, and eventually on the flanks of the ice sheet, would quickly overcome the buffering capacity of firn<sup>39</sup>. In the model, the meltwater accelerates WAIS retreat via its thermomechanical influence on ice rheology (Methods) and the influence of hydrofracturing on crevassing and structural failure of the retreating margin. Antarctica contributes 77 cm of GMSL rise by 2100, and continued loss of the Ross and Weddell Sea ice shelves drives WAIS retreat from three sides simultaneously (the Amundsen, Ross, and Weddell seas), all with



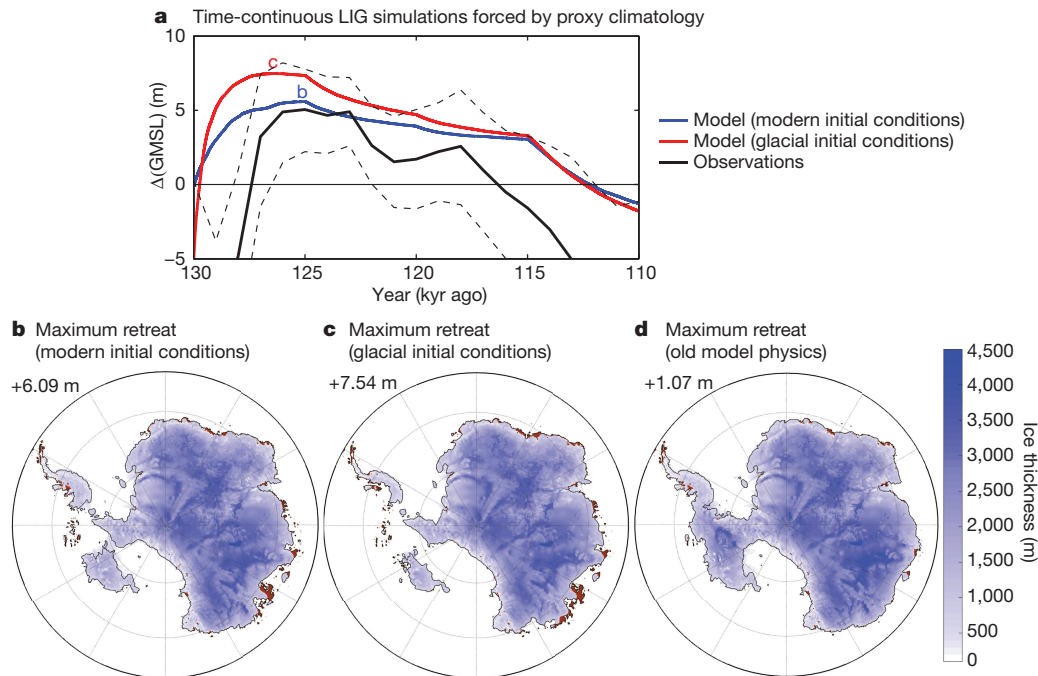


**Figure 3 | Ice-sheet simulations and Antarctic contributions to GMSL through the LIG driven by a time-evolving, proxy-based atmosphere–ocean climatology.** **a**, Change in GMSL in LIG simulations starting at 130 kyr ago and initialized with a modern ice sheet (blue) or a bigger LGM ice sheet representing glacial conditions at the onset of the LIG (red). A probabilistic reconstruction of Antarctica's contribution to GMSL is shown in black<sup>3</sup> with uncertainties (16th and 84th percentiles) as dashed lines. **b**, **c**, Ice-sheet thickness at the time of maximum retreat using

modern initial conditions (**b**) and using glacial initial conditions (**c**). Ice-free land surfaces are brown. The bigger sea-level response when initialized with the 'glacial' ice sheet is caused by deeper bed elevations and the ~3,000-yr lagged bedrock response to ice retreat<sup>50</sup>, which enhances bathymetrically sensitive MISI dynamics. **d**, The same simulation as **b** without the new model physics accounting for meltwater-enhanced calving or ice-cliff failure<sup>27</sup>. GMSL contributions are shown at top left.

reverse-sloping beds into the deep ice-sheet interior. As a result, WAIS collapses within 250 years. At the same time, steady retreat into the Wilkes and Aurora basins, where the ice above floatation is >2,000 m thick, adds substantially to the rate of sea-level rise, exceeding 4 cm yr<sup>-1</sup> (Fig. 4c) in the next century, which is comparable to maximum rates of sea-level rise during the last deglaciation<sup>40</sup>. At 2500, GMSL rise for the RCP8.5 scenario is 12.3 m. As in our LIG simulations, atmosphere–ice sheet coupling accounting for the warming feedback associated with the retreating ice sheet adds an additional 1.3 m of GMSL to the RCP8.5 scenario (Fig. 4b).

The CCSM4 simulations providing the model's sub-ice-shelf melt rates (Extended Data Fig. 5) underestimate the penetration of warm Circum-Antarctic Deep Water into the Amundsen and Bellingshausen seas observed in recent decades<sup>41</sup>. As a result, the model fails to capture recent, 21st-century thinning and grounding-line retreat along the southern Antarctic Peninsula<sup>42</sup> and the Amundsen Sea Embayment<sup>43</sup>. Correcting for the ocean-model cool bias along this sector of coastline improves the position of Pine Island and Thwaites grounding lines relative to observations<sup>42,43</sup> (Fig. 4h) and increases GMSL rise by 9 cm at 2100 (mainly due to the accelerated retreat of Pine Island Glacier), but the correction has little effect on longer timescales (Extended Data Table 1). Ocean warming is important to the behaviour of individual outlet glaciers early in the simulations, but we find that most of the long-term sea-level rise in RCP4.5 and RCP8.5 scenarios is caused by atmospheric warming and the onset of extensive surface meltwater production, rather than ocean warming as implied by other recent studies<sup>44–46</sup>. Without atmospheric warming, the magnitude of RCP8.5 ocean warming in CCSM4 is insufficient to cause the major retreat of the WAIS or East Antarctic basins; and even with >3 °C additional warming in the Amundsen and Bellingshausen seas it takes several thousand years for WAIS to retreat via ocean-driven MISI dynamics alone (Extended Data Fig. 6). We note that despite the 10-km grid resolution, the model simulates major ice streams well (Fig. 1), including

their internal variability<sup>18</sup>. However, during drastic subglacial-basin retreat the internal variability is quickly overtaken as grounding lines recede into deep interior catchments (see Supplementary Video 10).

### Large Ensemble analysis

To better utilize Pliocene and LIG geological constraints on model performance, we perform a Large Ensemble analysis (Methods) to explore the uncertainty associated with the primary parameter values controlling (1) relationships between ocean temperature and sub-ice-shelf melt rates, (2) hydrofracturing (crevasse penetration in relation to surface liquid water supply), and (3) maximum rates of marine-terminating ice-cliff failure. The combination of Pliocene and LIG sea level targets is ideal, because Pliocene retreat is dominated by processes associated with (2) and (3), while the LIG is dominated by process (1).

Both Pliocene and LIG ensembles are run with combinations of widely ranging parameter values associated with the three processes, and the combinations are scored by their ability to simulate target ranges of Pliocene and LIG Antarctic sea-level contributions (Methods). The filtered subsets of parameter values capable of reproducing both targets are then used in ensembles of future RCP scenarios (Extended Data Table 2), providing both an envelope of possible outcomes and an estimate of the model's parametric uncertainty (Fig. 5). Importantly, the ensemble analysis supports our choice of 'default' model parameters used in the nominal Pliocene, LIG, and future simulations (Fig. 4, Extended Data Table 2). The lack of substantial ice-sheet retreat in the optimistic RCP2.6 scenario remains unchanged, but the Large Ensemble analysis substantially increases our RCP4.5 and RCP8.5 2100 sea-level projections to 49 ± 20 cm and 105 ± 30 cm, if higher (>10 m instead of >5 m) Pliocene sea-level targets are used. Adding the ocean temperature correction in the Amundsen and Bellingshausen seas (Fig. 4d and h) further increases the 2100 projections in RCP2.6, RCP4.5 and RCP8.5 to 16 ± 16 cm, 58 ± 28 cm and 114 ± 36 cm, respectively (see Methods and Extended Data Tables 1 and 2).

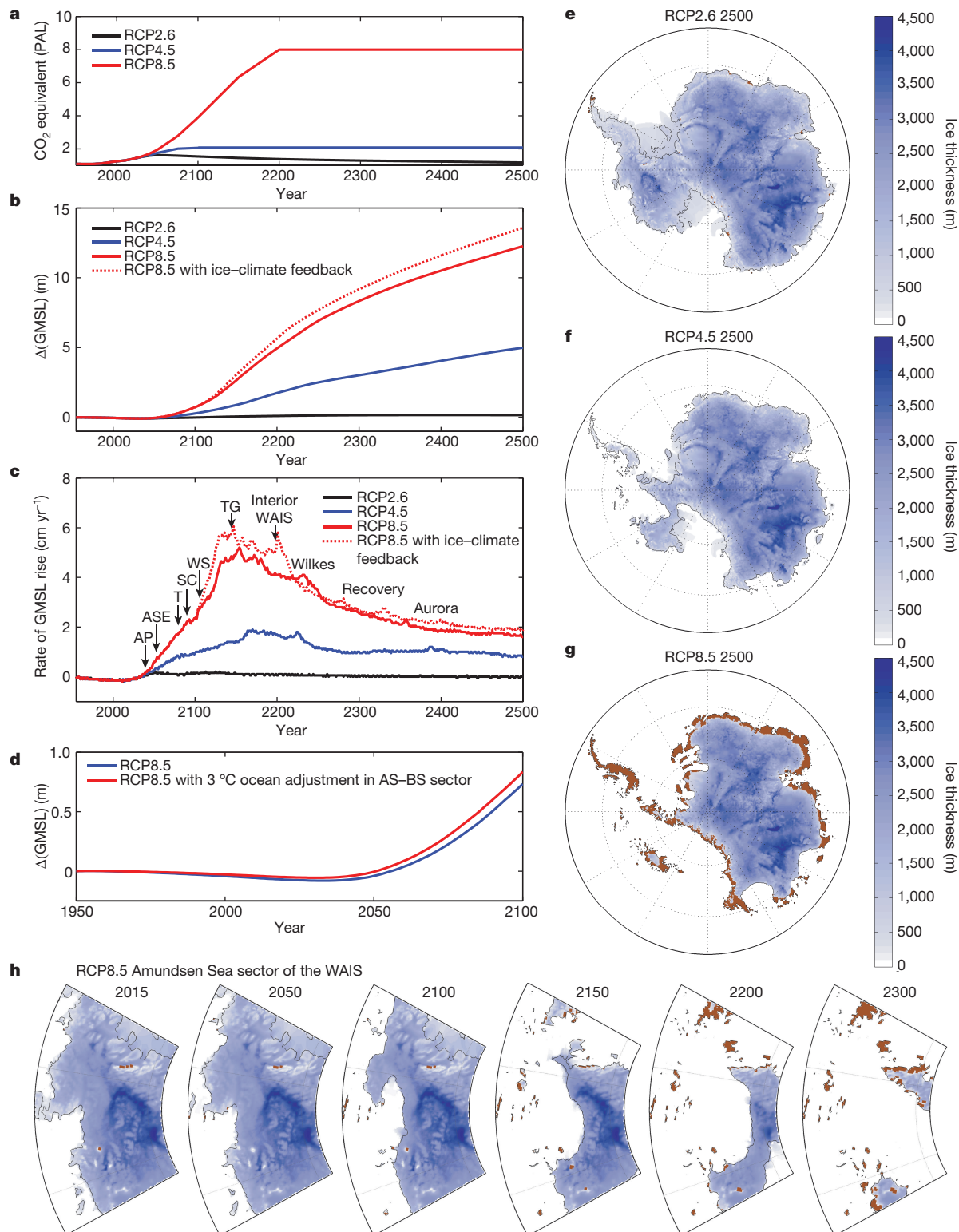


**Figure 4 | Future ice-sheet simulations and Antarctic contributions to GMSL from 1950 to 2500 driven by a high-resolution atmospheric model and 1° NCAR CCSM4 ocean temperatures.** **a**, Equivalent CO<sub>2</sub> forcing applied to the simulations, following the RCP emission scenarios in ref. 36, except limited to  $8 \times \text{PAL}$  (preindustrial atmospheric level, where 1 PAL = 280 p.p.m.v.). **b**, Antarctic contribution to GMSL. **c**, Rate of sea-level rise and approximate timing of major retreat and thinning in the Antarctic Peninsula (AP), Amundsen Sea Embayment (ASE) outlet glaciers, AS–BS, Amundsen Sea–Bellingshausen Sea; the Totten (T), Siple

Coast (SC) and Weddell Sea (WS) grounding zones, the deep Thwaites Glacier basin (TG), interior WAIS, the Recovery Glacier, and the deep EAIS basins (Wilkes and Aurora). **d**, Antarctic contribution to GMSL over the next 100 years for RCP8.5 with and without a +3 °C adjustment in ocean model temperatures in the Amundsen and Bellingshausen seas as shown in Extended Data Fig. 5d. **e–g**, Ice-sheet snapshots at 2500 in the RCP2.6 (**e**), RCP4.5 (**f**) and RCP8.5 (**g**) scenarios. Ice-free land surfaces are shown in brown. **h**, Close-ups of the Amundsen Sea sector of WAIS in RCP8.5 with bias-corrected ocean model temperatures.

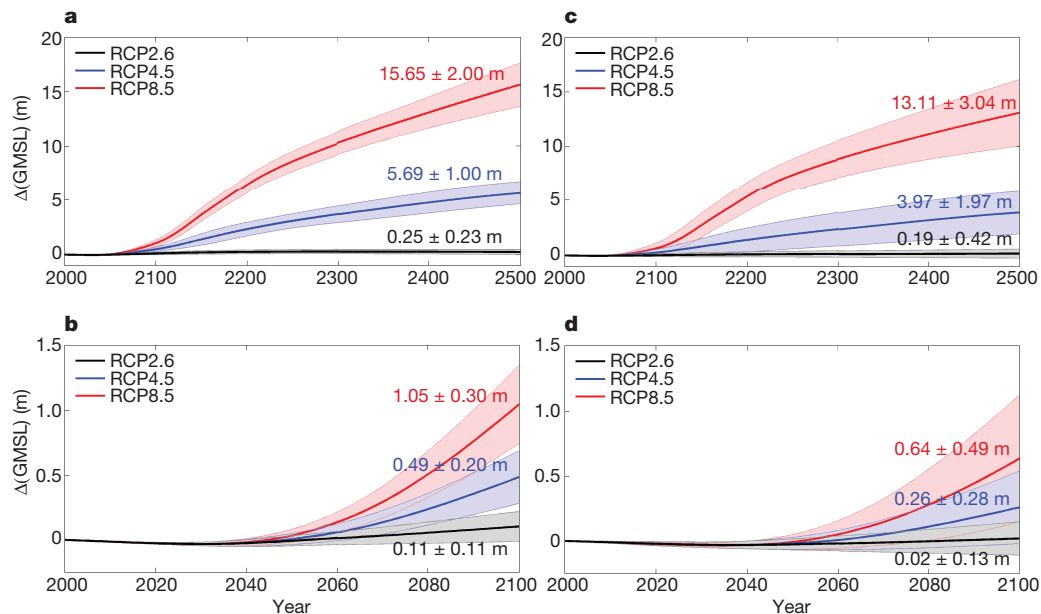


**Figure 5 | Large Ensemble model analyses of future Antarctic contributions to GMSL. a,** RCP ensembles to 2500. **b,** RCP ensembles to 2100. Changes in GMSL are shown relative to 2000, although the simulations begin in 1950. Ensemble members use combinations of model parameters (Methods) filtered according to their ability to satisfy two geologic criteria: a Pliocene target of 10–20 m GMSL and a LIG target of 3.6–7.4 m. **c** and **d** are the same as **a** and **b**, but use a lower Pliocene GMSL

### Long-term commitment to elevated sea level

Ocean warming alone may be limited in its potential to trigger massive, widespread ice loss, but the multi-millennial thermal response time of the ocean<sup>47</sup> will have a profound influence on the ice sheet's recovery. In simulations run 5,000 years into the future, we conservatively assume no ocean warming beyond 2300 and simply maintain those ocean temperatures while the atmosphere cools assuming different scenarios of CO<sub>2</sub> drawdown beginning in 2500 (Methods). For RCP8.5 and natural CO<sub>2</sub> drawdown, GMSL continues to rise until 3500 with a peak of about 20 m, after which the warm ocean inhibits the re-advance of grounding lines into deep marine basins for thousands of years (Extended Data Fig. 7). Even in the moderate RCP4.5 scenario with rapidly declining CO<sub>2</sub> after 2500, WAIS is unable to recover until the global ocean cools, implying a multi-millennial commitment to several metres of sea-level rise despite human-engineered CO<sub>2</sub> drawdown.

Given uncertainties in model initial conditions, simplified hybrid ice dynamics, parameterized sub-ice melt, calving, structural ice-margin failure, and the ancient sea-level estimates used in our Large Ensemble analysis, the rates of ice loss simulated here should not be viewed as actual predictions, but rather as possible envelopes of behaviour (Fig. 5) that include processes not previously considered at the continental scale. These are among the first continental-scale simulations with model physics constrained by ancient sea-level estimates, simultaneously accounting for high-resolution atmosphere–ice sheet coupling and ocean model temperatures.

However, several important processes are lacking and should be included in future work. In particular, the model lacks two-way coupling between the ice sheet and the ocean. This is especially relevant for RCP8.5, in which >1 Sv of freshwater and icebergs would be supplied to the Southern Ocean during peak retreat (Extended Data Fig. 8). Rapid calving and ice-margin collapse also implies ice mélange in restricted embayments that could provide buttressing and a negative feedback on retreat. The loss of ice mass would also have a strong effect on relative sea level at the margin owing to gravitational and solid-earth deformation effects<sup>48</sup>, which could affect MISI and MICI dynamics

target of 5–15 m. Solid lines are ensemble means, and the shaded areas show the standard deviation ( $1\sigma$ ) of the ensemble members. The  $1\sigma$  ranges represent the model's parametric uncertainty, while the alternate Pliocene targets (**a** and **b** versus **c** and **d**) illustrate the uncertainty related to poorly constrained Pliocene sea-level targets. Mean values and  $1\sigma$  uncertainties at 2500 and 2100 are shown.

because of their strong dependency on bathymetry. Future simulations should include coupling with Earth models that account for these processes. Improved ancient sea-level estimates are also needed to further constrain model physics and to reduce uncertainties in future RCP scenarios (Fig. 5).

Despite these limitations, our new model physics are shown to be capable of simulating two very different ancient sea-level events: the LIG, driven primarily by ocean warming and MISI dynamics, and the warmer Pliocene, in which surface meltwater and MICI dynamics are also important. When applied to future scenarios with high greenhouse gas emissions, our palaeo-filtered model ensembles show the potential for Antarctica to contribute >1 m of GMSL rise by the end of this century, and >15 m metres of GMSL rise in the next 500 years. In RCP8.5, the projected onset of major ice-sheet retreat occurs sooner (about 2050), and is substantially faster ( $>4$  cm yr<sup>-1</sup> after 2100) and higher (Figs 4 and 5) than implied by other recent studies<sup>44,45,49</sup>. These differences are mainly due to our addition of model physics linking surface meltwater and ice dynamics via hydrofracturing of buttressing ice shelves and structural failure of marine-terminating ice cliffs. In addition, we use (1) freely evolving grounding-line dynamics that preclude the need for empirically calibrated retreat rates<sup>49</sup>, (2) highly resolved atmosphere and ocean model components rather than intermediate-complexity climate models<sup>45</sup> or simplified climate forcing<sup>44</sup>, and (3) calibration based on major retreat during warm palaeoclimates rather than recent minor retreat driven by localized ocean forcing.

As in these prior studies, we also find that ocean-driven melt is an important driver of grounding-line retreat where warm water is in contact with ice shelves, but in scenarios with high greenhouse gas emissions we find that atmospheric warming soon overtakes the ocean as the dominant driver of Antarctic ice loss. Surface meltwater may lead to the ultimate demise of the major buttressing ice shelves (Supplementary Videos 8 and 9) and extensive grounding-line retreat, but it is the long thermal memory of the ocean that will inhibit the recovery of marine-based ice for thousands of years after greenhouse gas emissions are curtailed.



**Online Content** Methods, along with any additional Extended Data display items and Source Data, are available in the online version of the paper; references unique to these sections appear only in the online paper.

**Received 27 May 2015; accepted 12 January 2016.**

- Rovere, A. *et al.* The Mid-Pliocene sea-level conundrum: glacial isostasy, eustasy and dynamic topography. *Earth Planet. Sci. Lett.* **387**, 27–33 (2014).
- Dutton, A. *et al.* Sea-level rise due to polar ice-sheet mass loss during past warm periods. *Science* **3491**, <http://dx.doi.org/10.1126/science.aaa4019> (2015).
- Kopp, R. E., Simons, F. J., Mitrovica, J. X., Maloof, A. C. & Oppenheimer, M. Probabilistic assessment of sea level during the last interglacial stage. *Nature* **462**, 863–868 (2009).
- O'Leary, M. J., Hearty, P. J., Thompson, W. G., Raymo, M. E. & Mitrovica, J. X. Ice sheet collapse following a prolonged period of stable sea level during the last interglacial. *Nature Geosci.* **6**, 796–800 (2013).
- Raymo, M. E. & Mitrovica, J. X. Collapse of polar ice sheets during the stage 11 interglacial. *Nature* **483**, 453–456 (2012).
- Seki, O. *et al.* Alkenone and boron-based Pliocene pCO<sub>2</sub> records. *Earth Planet. Sci. Lett.* **292**, 201–211 (2010).
- Miller, K. G. *et al.* High tide of the warm Pliocene: implications of global sea level for Antarctic deglaciation. *Geology* **40**, 407–410 (2012).
- Cook, C. P. *et al.* Dynamic behaviour of the East Antarctic ice sheet during Pliocene warmth. *Nature Geosci.* **6**, 765–769 (2013).
- Lüthi, D. *et al.* High-resolution carbon dioxide concentration record 650,000–800,000 years before present. *Nature* **453**, 379–382 (2008).
- McKay, N. P., Overpeck, J. & Otto-Bliesner, B. The role of ocean thermal expansion in Last Interglacial sea level rise. *Geophys. Res. Lett.* **38**, L14605 (2011).
- NEEM community members. Eemian interglacial reconstructed from a Greenland folded ice core. *Nature* **493**, 489–494 (2013).
- Stone, E. J., Lunt, D. J., Annan, J. D. & Hargreaves, J. C. Quantification of the Greenland ice sheet contribution to Last Interglacial sea level rise. *Clim. Past* **9**, 621–639 (2013).
- Fretwell, P. *et al.* Bedmap2: improved ice bed, surface and thickness datasets for Antarctica. *Cryosphere* **7**, 375–393 (2013).
- Shepherd, A., Wingham, D. & Rignot, E. Warm ocean is eroding West Antarctic Ice Sheet. *Geophys. Res. Lett.* **31**, L23402 (2004).
- Schoof, C. Ice sheet grounding line dynamics: steady states, stability, and hysteresis. *J. Geophys. Res.* **112**, F03S28 (2007).
- Favier, L. *et al.* Retreat of Pine Island Glacier controlled by marine ice-sheet instability. *Nature Geosci.* **7**, 874–878 (2014).
- Mercer, J. H. West Antarctic Ice Sheet and CO<sub>2</sub> greenhouse effect—threat of disaster. *Nature* **271**, 321–325 (1978).
- Pollard, D. & DeConto, R. M. Modeling West Antarctic Ice Sheet growth and collapse through the last 5 million years. *Nature* **458**, 329–332 (2009).
- Pritchard, H. D. *et al.* Antarctic ice-sheet loss driven by basal melting of ice shelves. *Nature* **484**, 502–505 (2012).
- Joughin, I., Smith, B. E. & Medley, B. Marine ice sheet collapse potentially under way for the Thwaites Glacier basin, West Antarctica. *Science* **344**, 735–738 (2014).
- Tedesco, M. & Monaghan, A. J. An updated Antarctic melt record through 2009 and its linkages to high-latitude and tropical climate variability. *Geophys. Res. Lett.* **36**, L18502 (2009).
- Phillips, T., Rajaram, H. & Steffen, K. Cryo-hydrologic warming: a potential mechanism for rapid thermal response of ice sheets. *Geophys. Res. Lett.* **37**, L20503 (2010).
- Nick, F. M., Van der Veen, C. J., Vieli, A. & Benn, D. I. A physically based calving model applied to marine outlet glaciers and implications for the glacier dynamics. *J. Glaciol.* **56**, 781–794 (2010).
- Banwell, A. F., MacAyeal, D. R. & Sergienko, O. V. Breakup of the Larsen B Ice Shelf triggered by chain reaction drainage of supraglacial lakes. *Geophys. Res. Lett.* **40**, 5872–5876 (2013).
- Pollard, D., DeConto, R. M. & Alley, R. B. Potential Antarctic Ice Sheet retreat driven by hydrofracturing and ice cliff failure. *Earth Planet. Sci. Lett.* **412**, 112–121 (2015).
- Bassis, J. N. & Walker, C. C. Upper and lower limits on the stability of calving glaciers from the yield strength envelope of ice. *Proc. R. Soc. Lond. A* **468**, 913–931 (2012).
- Pollard, D. & DeConto, R. Description of a hybrid ice sheet-shelf model, and application to Antarctica. *Geosci. Model Dev.* **5**, 1273–1295 (2012).
- DeConto, R. M., Pollard, D. & Kowalewski, D. Modeling Antarctic ice sheet and climate variations during Marine Isotope Stage 31. *Glob. Planet. Change* **96–97**, 181–188 (2012).
- Capron, E. *et al.* Temporal and spatial structure of multi-millennial temperature changes at high latitudes during the Last Interglacial. *Quat. Sci. Rev.* **103**, 116–133 (2014).
- Duplessy, J. C., Roche, D. M. & Kageyama, M. The deep ocean during the Last Interglacial period. *Science* **316**, 89–91 (2007).
- Overpeck, J. T. *et al.* Paleoclimatic evidence for future ice-sheet instability and rapid sea-level rise. *Science* **311**, 1747–1750 (2006).
- Levitus, S. *et al.* World ocean heat content and thermosteric sea level change (0–2000 m), 1955–2010. *Geophys. Res. Lett.* **39**, <http://dx.doi.org/10.1029/2012GL051106> (2012).
- Galaasen, E. V. *et al.* Rapid reductions in North Atlantic Deep Water during the peak of the Last Interglacial period. *Science* **343**, 1129–1132 (2014).
- Fudge, T. J. *et al.* Onset of deglacial warming in West Antarctica driven by local orbital forcing. *Nature* **500**, 440–444 (2013).
- Koenig, S. J., DeConto, R. M. & Pollard, D. Impact of reduced Arctic sea ice on Greenland ice sheet variability in warmer than present climate. *Geophys. Res. Lett.* **41**, 3933–3942 (2014).
- Meinshausen, N. *et al.* The RCP greenhouse gas concentrations and their extensions from 1765 to 2300. *Clim. Change* **109**, 213–241 (2011).
- Gent, P. R. *et al.* The Community Climate System Model Version 4. *J. Clim.* **24**, 4973–4991 (2011).
- Trusel, L. D. *et al.* Divergent trajectories of Antarctic surface melt under two twenty-first-century climate scenarios. *Nature Geosci.* **8**, 927–932 (2015).
- Munneke, P. K., Ligtner, S. R. M., van den Broeke, M. R. & Vaughan, D. G. Firn air depletion as a precursor of Antarctic ice-shelf collapse. *J. Glaciol.* **60**, 205–214 (2014).
- Carlson, A. E. & Clark, P. U. Ice sheet sources of sea level rise and freshwater discharge during the last deglaciation. *Rev. Geophys.* **50**, RG4007 (2012).
- Schmidtke, S., Heywood, K. J., Thompson, A. F. & Aoki, S. Multidecadal warming of Antarctic waters. *Science* **346**, 1227–1231 (2014).
- Wouters, B. *et al.* Dynamic thinning of glaciers on the Southern Antarctic Peninsula. *Science* **348**, 899–903 (2015).
- Rignot, E., Mouginot, J., Morlighem, M., Seroussi, H. & Scheuchl, B. Widespread, rapid grounding line retreat of Pine Island, Thwaites, Smith, and Kohler glaciers, West Antarctica, from 1992 to 2011. *Geophys. Res. Lett.* **41**, 3502–3509 (2014).
- Golledge, N. R. *et al.* The multi-millennial Antarctic commitment to future sea-level rise. *Nature* **526**, 421–425 (2015).
- Winkelmann, R., Levermann, A., Ridgwell, A. & Caldeira, K. Combustion of available fossil fuel resources sufficient to eliminate the Antarctic Ice Sheet. *Sci. Adv.* **1**, e1500589 (2015).
- Feldmann, J. & Levermann, A. Collapse of the West Antarctic Ice Sheet after local destabilization of the Amundsen Basin. *Proc. Natl Acad. Sci.* **112**, 14191–14196 (2015).
- Li, C., von Storch, J.-S. & Marotzke, J. Deep-ocean heat uptake and equilibrium climate response. *Clim. Dyn.* **40**, 1071–1086 (2013).
- Gomez, N., Pollard, D. & Holland, D. Sea-level feedback lowers projections of future Antarctic Ice-Sheet mass loss. *Nature Commun.* **6**, 8798, <http://dx.doi.org/10.1038/ncomms9798> (2015).
- Ritz, C. *et al.* Potential sea-level rise from Antarctic ice-sheet instability constrained by observations. *Nature* **528**, 115–118 (2015).
- Huybrechts, P. *The Antarctic Ice Sheet and Environmental Change: a Three-dimensional Modelling Study* PhD thesis, <http://epic.awi.de/1463/>, Vrije Univ. Brussel (1992).

**Supplementary Information** is available in the online version of the paper.

**Acknowledgements** We thank C. Shields at NCAR for providing CCSM4 ocean model data. NCAR is sponsored by the NSF. We also thank R. Kopp for providing LIG sea-level data, and R. Alley, A. Dutton, and M. Raymo for discussions. This research was supported by the NSF under awards OCE 1202632 PLIOMAX project and AGS 1203910/1203792.

**Author Contributions** R.M.D. and D.P. conceived the model experiments, developed the models, and wrote the manuscript.

**Author Information** Reprints and permissions information is available at [www.nature.com/reprints](http://www.nature.com/reprints). The authors declare no competing financial interests. Readers are welcome to comment on the online version of the paper. Correspondence and requests for materials should be addressed to R.M.D. ([deconto@geo.umass.edu](mailto:deconto@geo.umass.edu)).

## METHODS

**Ice sheet–ice shelf model.** We use an established ice-sheet model, with hybrid ice dynamics following the formulation described in ref. 27, and an internal condition on ice velocity at the grounding line<sup>15</sup> that captures MISI (Fig. 2a–c) by accounting for migrating grounding lines and the buttressing effects of ice shelves with pinning points and side shear. Bedrock deformation under changing ice loads is modelled as an elastic lithospheric plate above local isostatic relaxation. A grid resolution of 10 km is used for all simulations, the finest resolution computationally feasible for long-term continental simulations. The model includes newly added treatments of hydrofracturing and ice cliff failure (Fig. 2d–f) described in ref. 25 and extended here. Basal sliding coefficients are determined by an inverse method<sup>51</sup>, iteratively matching ice-surface elevations to observations until a quasi-equilibrium is reached. In this case, inverted sliding coefficients are derived from a modern (preindustrial) surface climatology, using the same RCM used in our Pliocene, LIG, and future simulations.

In addition to the Pliocene and LIG targets highlighted here, the ice sheet–ice shelf model has been shown capable of simulating: (1) the modern ice sheet, including grounding-line positions, ice thicknesses, velocities, ice streams, and ice shelves (Fig. 1b), (2) the Last Glacial Maximum (LGM) extent<sup>27</sup>, (3) the timing of post-LGM retreat<sup>18</sup>, and (4) the ability of the ice sheet to regrow to its modern extent following retreat<sup>25</sup>.

**Calving and hydrofracturing.** Calving depends on the combined penetration depths of surface and basal crevasses, relative to total ice thickness<sup>23,26,52,53</sup>. Crevasse depths are parameterized according to the divergence of the ice velocity field<sup>52</sup>, with an additional contribution depending on the logarithm of ice speed that crudely represents the accumulated strain history (ice damage) along a flow path<sup>25</sup>. Rapid calving is imposed as ice thickness falls below 200 m for unconfined embayments. The 200-m criterion is decreased in confined embayments according to  $200 \times \max[0, \min[1, (\alpha - 40)/20]]$ , where  $\alpha$  is the 'arc to open ocean' (in degrees), crudely representing the effects of ice mélange in narrow seaways. The unconfined onset thickness of 200 m was increased from its value of 150 m in ref. 25 in order to improve modern Ross and Weddell Sea calving-front locations. A similar dependence on  $\alpha$  is imposed for oceanic sub-ice-shelf melt rates, as described below.

Surface crevasses are additionally deepened (hydrofractured) as they fill with liquid water, which is assumed to depend on the grid-scale runoff of surface melt and rainfall available after refreezing<sup>23,53</sup>. The crevasse-depth dependence on surface runoff plus rainfall rate  $R$  (in metres per year) has been modified slightly for low  $R$  values. The  $R$  used in equation (B.6) of ref. 25 is changed to:

$$\begin{aligned} 0 & \quad \text{for } R < 1.5 \text{ m yr}^{-1} \\ 4 \times 1.5 \times (R - 1.5) & \quad \text{for } 1.5 \text{ m yr}^{-1} < R < 3 \text{ m yr}^{-1} \\ R^2 & \quad \text{for } R > 3 \text{ m yr}^{-1} \text{ (as before)} \end{aligned}$$

This supposes that minimal hydrofracturing occurs for relatively small  $R$  values. The linear segment between  $1.5 \text{ m yr}^{-1}$  and  $3 \text{ m yr}^{-1}$  intersects the  $R^2$  parabola as a tangent at  $R = 3$ . This modification prevents small amounts of recession in some East Antarctic basins for modern conditions, where small amounts of summer melt and rainfall occur.

**Structural failure of ice cliffs.** To account for structural ice-cliff failure<sup>26,54</sup> (MICI in Fig. 2), a wastage rate of ice  $W$  is applied locally to the grid cell adjacent to tide-water grounding lines with no floating ice, if the required stresses at the exposed cliff face exceed the yield strength of ice. This condition depends on the subaerial cliff height at the interpolated grounding line relative to the maximum ice thickness that can be supported, modified locally to account for any meltwater-enhanced crevasse penetration (hydrofracturing), and any reductions in crevasse caused by backstress. For dry crevasse at an ice margin with no hydrofracturing and no buttressing (backstress), the maximum exposed cliff height is 100 m, assuming an ice yield strength of  $1 \text{ MPa}$ <sup>25,26</sup>. The formulation of  $W$  results in a steep ramp in wastage rates of  $0\text{--}3 \text{ km yr}^{-1}$ , where exposed ice cliffs ramp from 80 m to 100 m. The maximum wastage rate of  $3 \text{ km yr}^{-1}$  used as our default is conservatively chosen, based on recent observations of the Jakobshavn Isbrae Glacier (up to  $\sim 12 \text{ km yr}^{-1}$ ) and the Crane Glacier ( $\sim 5 \text{ km yr}^{-1}$ ) following the loss of their ice-buttressing shelves<sup>55–57</sup>.

**Other modifications to ice-sheet model physics.** The model is modified from ref. 25 to include a more physically based parameterization of the vertical flow of surface mobile liquid water (runoff and rainfall) through moulins and other fracture systems towards the base<sup>22,58</sup>, which affects the vertical temperature profiles within the ice sheet. Vertical sub-grid-scale columns of liquid water are assumed to exist, through which the water freely drains while exchanging heat by conduction with the surrounding ambient ice that cools and can freeze some or all of the liquid water within the ice interior.

We use uniform parameter values everywhere: we set the fractional area of sub-grid columns to overall area to be 0.1, and the horizontal scale of drainage elements to be 10 m ( $R$  in ref. 22, used in the calculations of conductive heat exchange with ambient ice). The fractional area includes both large moulins and any downward movement of liquid water in crevasses or cracks of all scales, which would be prevalent in the future melting scenarios investigated here. Offline sensitivity tests show low sensitivity of our model behaviour to these values, but further investigation is warranted.

For reasonable numerical behaviour, the horizontal heat exchange needs to be part of the time-implicit vertical diffusive heat solution for ambient ice temperature in the main model. To avoid an iterative procedure in cases where all liquid water is frozen before reaching the bed, a time-explicit calculation of the water penetration is made first, and one of the following measures is applied in the time-implicit ice-temperature step: (1) the conductive heat exchange coefficient at all levels is reduced by a constant factor for the column, so that the liquid penetrates to the lowest layer but no further; and (2) the conductive coefficient is set to zero below the depth of furthest penetration. Both methods give very similar results in idealized single-column tests; method (1) was used for all runs here. In cases with greater surface liquid flux, there is no reduction of coefficients and some water reaches the base.

A minor bug fix is corrected in the calculation of vertical velocities within the ice ( $w'$  in ref. 27), which previously did not account for the removal of ice at the base due to oceanic melting. This only affects advection of temperature in ice shelves, and has negligible effects on results.

**Ice-sheet initial conditions.** Ice-sheet initial conditions and basal sliding coefficients are provided by a 100-kyr inverse simulation following the methodology in ref. 51, using mass-balance forcing provided by a bias-corrected RCM climatology and modern observed ocean temperatures (described below). In the inverse procedure, basal sliding coefficients under modern grounded ice are adjusted iteratively to reduce the misfit with observed ice thickness, with grounding-line positions fixed to observed locations. The LIG simulation using 'glacial' initial conditions (Fig. 3) uses the same basal sliding coefficients (along with a relatively slippery value for modern ocean beds), but initialized from a previous simulation of the LGM with a prescribed, cold glacial climate representing conditions at  $\sim 20 \text{ kyr}$  ago. The total ice volume in the modern and glacial ice sheets is  $26.55 \times 10^6 \text{ km}^3$  and  $32.30 \times 10^6 \text{ km}^3$ , respectively, equivalent to bedrock-compensated GMSL values of 56.80 m and 62.28 m.

**Atmospheric coupling.** Atmospheric climatologies providing surface mass-balance inputs to the ice model are provided by decadal averages of meteorological fields from the RegCM3 RCM<sup>59</sup>, adapted to Antarctica with a polar stereographic grid and small modifications of model physics for polar regions. The RCM uses a 40-km grid, over a generous domain spanning Antarctica and surrounding oceans, nested within the GENESIS v3 Global Climate Model<sup>60,61</sup>. The GCM and RCM share the same radiation code<sup>62</sup> and orbitally dependent calculations of shortwave insolation, important for the Pliocene and LIG palaeoclimate simulations.

Anomaly methods are used to correct a small  $<2^\circ \text{C}$  Antarctic cold bias in the RCM:

$$\begin{aligned} T &= T_{\text{exp}} + T_{\text{obs}} - T_{\text{ctl}} \\ P &= P_{\text{exp}} \times P_{\text{obs}} / P_{\text{ctl}} \end{aligned}$$

where  $T$  is monthly surface air temperature and  $P$  is monthly precipitation. Subscripts 'exp', 'obs' and 'ctl' refer to model experiment, observed modern climatology, and model modern control, respectively. A modern (1950) RCM simulation is used for the model modern control, and the ALBMAP data set<sup>63</sup> is used for observed modern climatology.

In the climatic correction for the difference between the ice-model surface elevation and the interpolated elevation in the climate model or observational data set<sup>27</sup>, precipitation is now corrected as well as temperature. As before, air temperature  $T$  (in degrees Celsius) is shifted by  $\Delta T = \gamma \Delta z$ , where  $\gamma = -0.008^\circ \text{C m}^{-1}$  is the lapse rate (that is, the decrease in atmospheric temperature with respect to altitude) and  $\Delta z$  is the elevation difference. Now, precipitation  $P$  is multiplied by a Clausius–Clapeyron-like factor:

$$P \times 2^{\Delta T/10}$$

Rates of surface snowfall and rainfall are now consistently multiplied by a factor  $\rho_w/\rho_i \approx 1.1$ , where  $\rho_w$  and  $\rho_i$  are the densities of liquid water and of ice respectively. This consistently converts between the units of most climate models and climatological databases (metres of liquid water equivalent per year) and the ice-model surface budget terms (metres of ice equivalent per year).

**Oceanic sub-ice shelf and calving-face melt rates.** Direct coupling of high-resolution ocean models and ice sheets remains challenging. For present-day simulations we use a parameterization of sub-ice shelf melt rates, similar to that

used by other model groups<sup>64</sup>. The parameterization<sup>27</sup> links oceanic melt rates to the nearest observed (or modelled) ocean temperatures:

$$OM = \frac{K_T \rho_w C_w}{\rho_i L_f} |T_0 - T_f| (T_0 - T_f)$$

where  $T_0$  is ocean temperature interpolated from the nearest point in an observational (or ocean model) gridded data set,  $T_f$  is the local freezing-point temperature at the depth of the ice base, and  $C_w$  is the specific heat of ocean water. The transfer factor  $K_T = 15.77 \text{ m yr}^{-1} \text{ } ^\circ\text{C}^{-1}$  results in a combined coefficient ( $K_T \rho_w C_w / \rho_i L_f$ ) of  $0.224 \text{ m yr}^{-1} \text{ } ^\circ\text{C}^{-2}$ . The depth dependence on  $T_f$  produces higher melt rates at the grounding line, as observed, and the dependence on  $T_0 - T_f$  is quadratic<sup>65</sup>. Although spatially coarse observational data sets and standard GCM ocean models fail to capture detailed ocean current systems below ice-shelf cavities, this approach (Extended Data Fig. 6e and f) is preferable to the *ad hoc* prescription of single temperatures and transfer coefficients along individual sectors of the Antarctic margin as in ref. 27.

The effects of confined geography on ocean currents are represented by reducing basal melting depending on the total arc to open ocean  $\alpha$ , representing the concavity of the coastline<sup>25</sup>. The melt rate computed from ocean temperatures as above is multiplied by the factor:

$$\max[0, \min[1, (\alpha - 20)/20]]$$

This effect, combined with the reduction of thin-ice calving with a similar dependence on  $\alpha$  described above, allows ice to expand into interior basins during cool-climate recovery after major retreats of marine-based ice, as presumably occurred many times in West Antarctica over the last several million years<sup>66</sup>.

Melting of vertical ice surfaces in direct contact with ocean water is derived from the oceanic melt rate (OM) of surrounding grid cells, but is increased by a scaling factor of 10, producing more realistic calving front positions and in better agreement with hydrographic melt rate observations and detailed modelling<sup>67</sup>. Present-day sub-ice shelf and calving-face melt rates described here use the 1° resolution World Ocean Atlas<sup>32,68</sup> temperatures at 400-m depth, interpolated to the time-evolving ice model grid and propagated under ice-shelf surfaces using contiguous neighbour iteration to provide  $T_0$ . The depth of 400 m represents typical observed levels of Circum-Antarctic Deep Water, a main source of warm-water incursions into the Amundsen Sea Embayment today<sup>69</sup>.

**Pliocene simulation.** Our default Pliocene simulation uses the same nested GCM-RCM climatology used in a prior study<sup>25</sup>, with 400 p.p.m.v. CO<sub>2</sub> and a generic warm austral summer orbit<sup>28</sup> (Extended Data Fig. 1). Ocean temperatures are increased uniformly by 2°C everywhere in the Southern Ocean. The resulting Antarctic contribution of 11.3 m GMSL implies >15 m GMSL rise if an additional ~5 m contribution from Greenland<sup>70</sup> and the steric effects of a warm Pliocene ocean are also considered. This result is ~6 m less than in ref. 25, reflecting a reduction in the sensitivity of the model with the changes described above.

**LIG simulations.** The LIG spans a ~20-kyr interval with greenhouse-gas atmospheric mixing ratios comparable to the pre-industrial Holocene<sup>9</sup>. Opportunities for Antarctic ice-sheet retreat within this interval include a peak in the duration of Antarctic summers coeval with a boreal summer insolation maximum at 128 kyr ago, and an Antarctic summer insolation maxima one half-precession cycle later at 116 kyr ago (Extended Data Fig. 2). We target these two orbital time slices because they contrast radiatively long and weak (128 kyr ago) versus short and intense Antarctic summers (116 kyr ago), both of which have been postulated to be important drivers of ice volume on glacial-interglacial timescales<sup>71</sup>.

LIG simulations that include climate-ice sheet feedback asynchronously couple the GCM-RCM and the ice-sheet model. In this case, the nested RCM land (ice) surface boundary conditions are updated at the end of the initial retreat at ice model-year 5000 and the ice-sheet model is rerun using the updated climatology. This improves the representation of ice-climate feedbacks via albedo, ocean surface conditions (sea surface temperatures and sea ice), and dynamical effects of the changing topography on the atmosphere. We find that explicitly including climate-ice feedbacks improves model performance, relative to simple lapse-rate adjustments.

LIG simulations (Extended Data Table 1; Extended Data Fig. 3d, e) apply anomaly-corrected RCM mass-balance forcing at each LIG time slice, using the appropriate greenhouse gas<sup>9,72</sup> and orbital values<sup>73</sup> in the nested GCM-RCM. Ocean temperatures are provided by the World Ocean Atlas data set<sup>32</sup>, with incremental warming of 1–5°C applied uniformly over the Southern Ocean grid domain.

To allow the RCM atmosphere to respond to a warmer Southern Ocean in addition to applying elevated ocean temperatures to the ice model, we increase the southward ocean-heat convergence in the nested GCM-RCM using the methodology described in ref. 28, effectively warming the Southern Ocean sea surface

temperatures by ~2°C and reducing sea-ice extent. Accounting for the effect of a warmer Southern Ocean on the overlying atmosphere produces more LIG ice-sheet retreat for a given ocean warming, improving our model-data fit. With this technique, only 3°C of assumed sub-surface ocean warming is required to produce >6 m GMSL rise from Antarctica at either LIG orbital time slice, reinforcing the notion of a dominant oceanic control on LIG ice-sheet retreat.

The two time-continuous LIG simulations using prescribed climatologies (Fig. 3) use bias-corrected, present-day RCM climatologies with a uniform, time-evolving perturbation derived from the average of Antarctic ice-core climatologies compiled in ref. 29. Southern Ocean temperatures are treated similarly, with World Ocean Atlas temperatures<sup>32</sup> increased according to the average of circum-Antarctic LIG anomalies<sup>29</sup>. Only records from marine drill-cores poleward of 45°S are used in the averages, but we note that there is considerable uncertainty in the proxy sea surface temperature estimates (>2°C)<sup>29</sup>. This approach also assumes that the proxy sea surface temperatures reflect changes at sub-surface depths (~400 m), which is uncertain. The resulting anomalies are applied to the ice sheet model at 130 kyr ago, 125 kyr ago, 120 kyr ago, and 115 kyr ago and the ice-sheet model is run continuously from 130 kyr ago to 115 kyr ago. The pairs of air and ocean temperature perturbations applied at each 5-kyr LIG timestep are 1.97° and 1.70°, 1.41° and 1.51°, 0.83° and 1.09°, –1.57° and 0.31°, respectively.

The time-continuous LIG simulations are initialized from either a present-day initial ice state (Fig. 1b), or from a prior Last Glacial Maximum simulation with  $5.76 \times 10^6 \text{ km}^3$  more ice than today. The latter initial condition may better represent the ice sheet at the onset of the LIG and leads to a greater potential sea-level rise owing to the deeper bed conditions early in the deglaciation, which enhances the bathymetrically sensitive MISI dynamics.

The proxy-forced LIG simulation clearly supports a maximum Antarctic contribution to GMSL early in the interglacial period (Fig. 3). However, we note that owing to the demonstrated influence of Southern Ocean temperature on the timing of retreat and the uncertain magnitude and chronology of our imposed forcing<sup>29</sup>, these results cannot definitively rule out maximum Antarctic retreat at the end of the LIG, as has also been proposed<sup>4,74</sup>.

**Future simulations.** Because of the new ice-model physics that directly involve the atmosphere via meltwater enhancement of crevassing and calving, highly resolved atmospheric climatologies are needed at spatial resolutions beyond those of most GCMs. However, multi-century RCM simulations are computationally infeasible. To accommodate the need for long but high-resolution climatologies, the nested GCM-RCM is run to equilibrium with 1 × PAL, 2 × PAL, 4 × PAL and 8 × PAL CO<sub>2</sub>. In the ice-sheet simulations, CO<sub>2</sub> follows the extended RCP greenhouse gas emissions<sup>36</sup> to the year 2500, and the climate at any time is the average of the two appropriate surrounding RCM solutions, weighted according to the logarithm of the concentration of CO<sub>2</sub>. The RCM climatologies follow total equivalent CO<sub>2</sub>, which accounts for all radiatively active trace gases in the RCP timeseries. In RCP8.5, equivalent CO<sub>2</sub> forcing exceeds 8 × PAL after 2175, but it is conservatively limited here to a maximum of 8 × PAL (Fig. 4a). A 10-yr lag is imposed in the RCM climatologies to reflect the average offset between sea surface temperatures and surface air temperatures in the equilibrated RCM (with equilibrated sea surface temperatures from the parent GCM) and the transient response of the real ocean's mixed layer.

Ocean temperatures in the RCP scenarios are provided by high-resolution (0.5° atmosphere and 1° ocean) NCAR CCSM4<sup>37</sup> ocean model output, following the RCP2.6, RCP4.5, and RCP8.5 greenhouse gas emissions scenarios run to 2300. Ocean temperatures beyond the limit of the CCSM4 simulations at 2300 are conservatively maintained at their 2300 values. As with the World Ocean Atlas, water temperatures at 400-m depth (between ocean model z-levels 30 and 31) are used in the parameterization of oceanic sub-ice melt (oceanic melt rate) described above. The CCSM4 underestimates the wind-driven warming of Antarctic Shelf Bottom Water<sup>41</sup> in the Amundsen and Bellingshausen seas associated with recent increases in melt rates and grounding-line retreats<sup>20,42,43</sup>. To account for this, additional warming is added to the Amundsen and Bellingshausen sectors of the continental margin. We find the addition of 3°C to the CCSM4 ocean temperatures increases melt rates to 25–30 m yr<sup>–1</sup> (Extended Data Fig. 5f). While still less than observed, this substantially improves grounding-line positions in the Amundsen Sea (Pine Island Glacier in particular) from 1950 to 2015. When applied to RCP4.5 and RCP8.5, the ocean-bias correction accelerates twenty-first-century WAIS retreat (Fig. 4d, g, h) but is found to have little effect beyond 2100 (Extended Data Table 1).

Extended RCP greenhouse gas scenarios<sup>36</sup> are available up to 2500, beyond which we assume two different scenarios: (1) natural decay of CO<sub>2</sub><sup>75,76</sup> and no further anthropogenic emissions, or (2) engineered, fast drawdown towards pre-industrial levels with an e-folding time of 100 years. These choices are not intended to be definitive, but serve to illustrate the ice-sheet response to a wide range of possible long-term future forcings.



Future high-resolution ocean-model output is not available on multi-millennial timescales. In our long (5,000-year) future simulations (Extended Data Fig. 7), CCSM4 ocean temperatures at 400 m depth are assumed to remain at their 2300 values for thousands of years beyond 2300 (until 7000). This assumption is based on the thermal inertia of the deep ocean (thousands of years)<sup>47</sup>, its longwave radiative feedback on atmospheric temperatures<sup>77</sup>, and its relative isolation from surface variations. The response of the intermediate and deep ocean to atmospheric and surface-ocean warming before 2300 is heavily lagged in time, and consequently deep-ocean temperatures would continue to rise long after CO<sub>2</sub> levels and surface temperatures began to decline after 2500<sup>77</sup>. However, at some point several thousand years later, intermediate- and deep-ocean waters would start to cool if CO<sub>2</sub> levels decay as in Extended Data Fig. 7. The trajectory of these temperatures would vary spatially and depend on details of the ocean circulation. To our knowledge, the state of the ocean as it recovers from a greenhouse gas perturbation over these timescales is largely unknown, as relevant coupled atmosphere–ocean global climate model simulations at the resolution and duration appropriate to our ice model have not been run. Consequently, our assumption of constant 400-m ocean temperatures after 2300, although likely to be conservative beyond 2500, may be questionable for the latter parts of the simulations assuming fast, engineered CO<sub>2</sub> drawdown. However, assuming the slow, natural pace of CO<sub>2</sub> recovery<sup>76</sup>, atmospheric concentrations would remain above twice the current level of carbon dioxide ( $2 \times \text{CO}_2$ ) for thousands of years in the RCP8.5 scenario (Extended Data Fig. 7). Assuming a global temperature sensitivity of  $\sim 3^\circ\text{C}$  per doubling of CO<sub>2</sub>, our ocean temperatures applied to the long RCP8.5 scenario are probably conservative over the duration of the simulation.

#### Geologically constrained Large Ensemble analysis of future ice-sheet retreat.

To quantify model uncertainty due to poorly known parameter values, ensembles of surface RCP scenarios are performed with varying model parameters affecting sub-ice oceanic melt rates, meltwater-enhanced calving (hydrofracturing) and marine-terminating ice cliff failure. Ensemble members use the high-resolution atmospheric and ocean forcing described in the main text and above. Alternative ensembles are run both with and without the bias correction of CCSM4 ocean temperatures in the Amundsen and Bellingshausen Seas. The three parameters and four values used for each are as follows.

OCFAC is the coefficient in the parameterization of sub-ice-shelf oceanic melt, which is proportional to the square of the difference between nearby ocean water temperature at 400-m depth, and the pressure-melting point of ice. It corresponds to  $K$  in equation (17) of ref. 27. The relationship between proximal ocean conditions and melting at the base of floating ice shelves remains a challenging topic of ongoing research<sup>78</sup>, and a simple parameterization<sup>64</sup> is used here. Ensemble values of OCFAC are 0.1, 1, 3 and 10 times the default value of  $0.224 \text{ m yr}^{-2} \text{ } ^\circ\text{C}^{-2}$ .

CREVLIQ is the coefficient in the parameterization of hydrofracturing due to surface liquid. It replaces the constant 100 in equation (B.6) of ref. 25, and is the additional crevasse depth due to surface melt plus rainfall rate, with a quadratic dependence. This crudely represents the complex relationship between surface water and crevasse propagation, and basic model sensitivity is shown in supplementary figure 7b of ref. 25. Values of CREVLIQ are 0 m, 50 m, 100 m and 150 m per  $(\text{m yr}^{-1})^{-2}$ .

VCLIF is the maximum rate of horizontal wastage due to ice-cliff structural failure. It replaces the default value of 3,000 ( $3 \text{ km yr}^{-1}$ ) in equation (A.4) of ref. 25. Its magnitude is based on observed retreat rates of modern large ice cliffs, and basic model sensitivity is shown in supplementary figure 7a of ref. 25. Values of VCLIF are  $0 \text{ km yr}^{-1}$ ,  $1 \text{ km yr}^{-1}$ ,  $3 \text{ km yr}^{-1}$  and  $5 \text{ km yr}^{-1}$ .

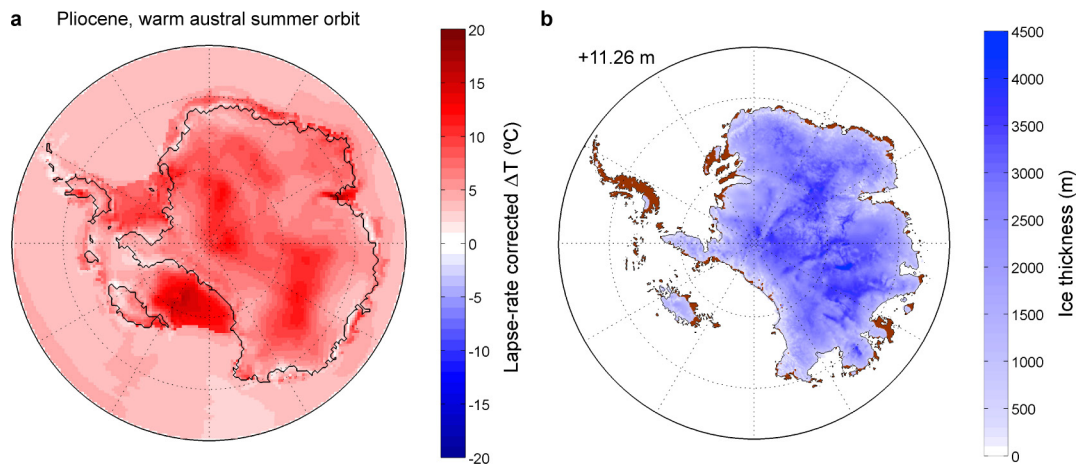
Medium-range, default values of OCFAC, CREVLIQ, and VCLIF used in our nominal Pliocene (Extended Data Fig. 1), LIG (Fig. 3), and Future (Fig. 4) simulations are OCFAC = 1 (corresponding to  $0.224 \text{ m yr}^{-2} \text{ } ^\circ\text{C}^{-2}$ ), CREVLIQ =  $100 \text{ m per } (\text{m yr}^{-1})^{-2}$ , and VCLIF =  $3 \text{ km yr}^{-1}$ , respectively.

Simulations for the Pliocene and LIG scenarios are run with all possible combinations of these parameter values, that is, 64 ( $=4^3$ ) runs (Extended Data Table 2). Each run is subject to a pass/fail test that its equivalent GMSL rise falls within the observed ranges for the LIG (3.6–7.4 m) and the Pliocene (10–20 m). The filtered subset of parameter combinations that pass (15 out of 64) are then used in an ensemble of future RCP scenarios. An additional ensemble calculation is performed using the same LIG criteria, but a lower accepted range for Pliocene sea-level rise (5–15 m), to reflect the large uncertainty in Pliocene sea-level reconstructions<sup>1</sup> (29 out of 64 passed this test). The mean and 1 $\sigma$  range of each ensemble are shown for the three RCP scenarios in Fig. 5, providing both an envelope of possible outcomes and an estimate of the model's parametric uncertainty. Two alternative sets of future RCP ensembles are run with the ocean-temperature bias correction in the Amundsen and Bellingshausen seas shown in Extended Data Fig. 5. This increases Antarctica's GMSL contribution by  $\sim 9 \text{ cm}$  over the next century in both RCP8.5 and RCP8.5, but has almost no effect on longer timescales (Extended Data Tables 1, 2). In the RCP2.6 ensemble calibrated against the higher

>10 m Pliocene sea-level targets, the ocean-bias correction increases both the ensemble-mean and  $1\sigma$  standard deviation to  $16 \pm 16 \text{ cm}$  in 2100 and  $62 \pm 76 \text{ cm}$  in 2500 (Extended Data Table 1). The increased variance is caused by three simulations in the RCP2.6 ensemble set, in which the stability of the Thwaites Glacier grounding line is exceeded and the WAIS retreats into the deep interior. Although the ensemble members with bias-corrected ocean temperatures are generally more consistent with observations of recent retreat in the Amundsen–Bellingshausen sector, the validity of the bias correction in the long-term future is unknown.

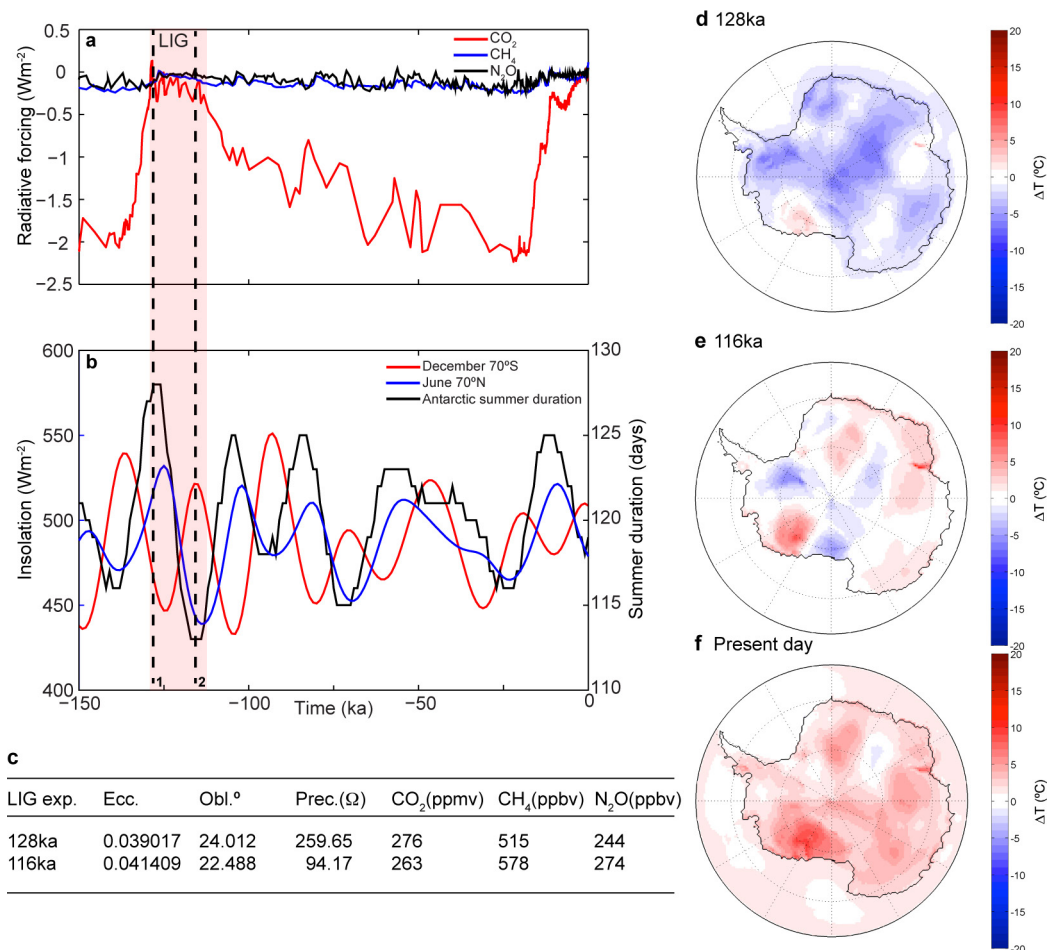
**Code availability.** Ice sheet and climate model codes, results from Pliocene, LIG, and future simulations, and tabulated ensemble results are freely available from the corresponding author.

51. Pollard, D. & DeConto, R. M. A simple inverse method for the distribution of basal sliding coefficients under ice sheets, applied to Antarctica. *Cryosphere* **6**, 953–971 (2012).
52. Benn, D. I., Warren, C. R. & Mottram, R. H. Calving processes and the dynamics of calving glaciers. *Earth Sci. Rev.* **82**, 143–179 (2007).
53. Nick, F. M. *et al.* Future sea-level rise from Greenland's main outlet glaciers in a warming climate. *Nature* **497**, 235–238 (2013).
54. Bassis, J. M. & Jacobs, S. Diverse calving patterns linked to glacier geometry. *Nature Geosci.* **6**, 833–836 (2013).
55. Joughin, I. *et al.* Continued evolution of Jakobshavn Isbrae following its rapid speedup. *J. Geophys. Res.* **113**, F04006 (2008).
56. Joughin, I. *et al.* Seasonal to decadal scale variations in the surface velocity of Jakobshavn Isbrae, Greenland: observation and model-based analysis. *J. Geophys. Res.* **117**, F02030 (2012).
57. Scambos, T. A., Bohlander, J. A., Shuman, C. A. & Skvarca, P. Glacier acceleration and thinning after ice shelf collapse. *Geophys. Res. Lett.* **31**, L18402 (2004).
58. Phillips, T., Rajaram, H., Colgan, W., Steffen, K. & Abdalati, W. Evaluation of cryo-hydrologic warming as an explanation for increased ice velocities in the wet snow zone, Sermeq Avannarqeq, West Greenland. *J. Geophys. Res.* **118**, 1241–1256 (2013).
59. Pal, J. S. *et al.* Regional climate modeling for the developing world: the ICTP RegCM3 and RegCM3. *Bull. Am. Meteorol. Soc.* **88**, 1395–1409 (2007).
60. Alder, J. R., Hostetler, S. W., Pollard, D. & Schmittner, A. Evaluation of a present-day climate simulation with a new coupled atmosphere-ocean model GENMOM. *Geosci. Model Dev.* **4**, 69–83 (2011).
61. Thompson, S. L. & Pollard, D. Greenland and Antarctic mass balances for present and doubled atmospheric CO<sub>2</sub> from the GENESIS Version-2 Global Climate Model. *J. Clim.* **10**, 871–900 (1997).
62. Kiehl, J. T. *et al.* The National Center for Atmospheric Research Community Climate Model: CCM3. *J. Clim.* **11**, 1131–1149 (1998).
63. Le Brocq, A., Payne, A. J. & Veli, A. An improved Antarctic dataset for high resolution numerical ice sheet models (ALBMAP v1). *Earth Syst. Sci. Data* **2**, 247–260 (2010).
64. Martin, M. A. *et al.* The Potsdam Parallel Ice Sheet Model (PISM-PIK)—part 2: dynamic equilibrium simulation of the Antarctic ice sheet. *Cryosphere* **5**, 727–740 (2011).
65. Holland, P. R., Jenkins, A. & Holland, D. The response of ice shelf basal melting to variations in ocean temperature. *J. Clim.* **21**, 2558–2572 (2008).
66. Naish, T. *et al.* Obliquity-paced, Pliocene West Antarctic Ice Sheet oscillations. *Nature* **458**, 322–328 (2009).
67. Slater, D. A., Nienow, P. W., Cowton, T. R., Goldberg, D. N. & Sole, A. J. Effect of near-terminus subglacial hydrology on tidewater glacier submarine melt rates. *Geophys. Res. Lett.* **42**, 2861–2868 (2015).
68. Locarnini, R. A. *et al.* *World Ocean Atlas 2013 Vol. 1 Temperature* 1–40 [http://data.nodc.noaa.gov/woa/woa13/DOC/woa13\\_vol1.pdf](http://data.nodc.noaa.gov/woa/woa13/DOC/woa13_vol1.pdf) (2013).
69. Dutrieux, P. *et al.* Strong sensitivity of Pine Island ice-shelf melting to climatic variability. *Science* **343**, 174–178 (2014).
70. Koehn, S. J. *et al.* Ice sheet model dependency of the simulated Greenland Ice Sheet in the mid-Pliocene. *Clim. Past* **11**, 369–381 (2015).
71. Raymo, M. E. & Huybers, P. Unlocking the mysteries of the ice ages. *Nature* **451**, 284–285 (2008).
72. Spahn, R. *et al.* Atmospheric methane and nitrous oxide of the late Pleistocene from Antarctic ice cores. *Science* **310**, 1317–1321 (2005).
73. Berger, A. Long-term variations of daily insolation and Quaternary climatic changes. *J. Atmos. Sci.* **35**, 2362–2367 (1978).
74. Hearty, P. J., Hollin, J. T., Neumann, A. C., O'Leary, M. J. & McCulloch, M. Global sea-level fluctuations during the Last Interglaciation (MIS 5e). *Quat. Sci. Rev.* **26**, 2090–2112 (2007).
75. Archer, D. *et al.* Atmospheric lifetime of fossil fuel carbon dioxide. *Annu. Rev. Earth Planet. Sci.* **37**, 117–134 (2009).
76. Archer, D. & Maier-Reimer, E. Effect of deep-sea sedimentary calcite preservation on atmospheric CO<sub>2</sub> concentration. *Nature* **367**, 260–263 (1994).
77. Matthews, H. D. & Caldeira, K. Stabilizing climate requires near-zero emissions. *Geophys. Res. Lett.* **35**, L04705 (2008).
78. Hellmer, H. H., Kauker, F., Timmermann, R., Determann, J. & Rae, J. Twenty-first-century warming of a large Antarctic ice-shelf cavity by a redirected coastal current. *Nature* **485**, 225–228 (2012).
79. Huybers, P. Early Pleistocene glacial cycles and the integrated summer insolation forcing. *Science* **313**, 508–511 (2006).
80. Holden, P. B. *et al.* Interhemispheric coupling, the West Antarctic Ice Sheet and warm Antarctic interglacials. *Clim. Past* **6**, 431–443 (2010).



**Extended Data Figure 1 | Warm mid-Pliocene climate and ice-sheet simulation.** **a**, January (warmest monthly mean) difference in 2-m (surface) air temperature simulated by the RCM relative to a preindustrial control simulation with 280 p.p.m.v.  $\text{CO}_2$  and present-day orbit. The temperature difference is lapse-rate-corrected to account for the change in ice-sheet geometry and surface elevations. The Pliocene simulation uses 400 p.p.m.v.  $\text{CO}_2$ , a warm austral summer orbit, and assumes a

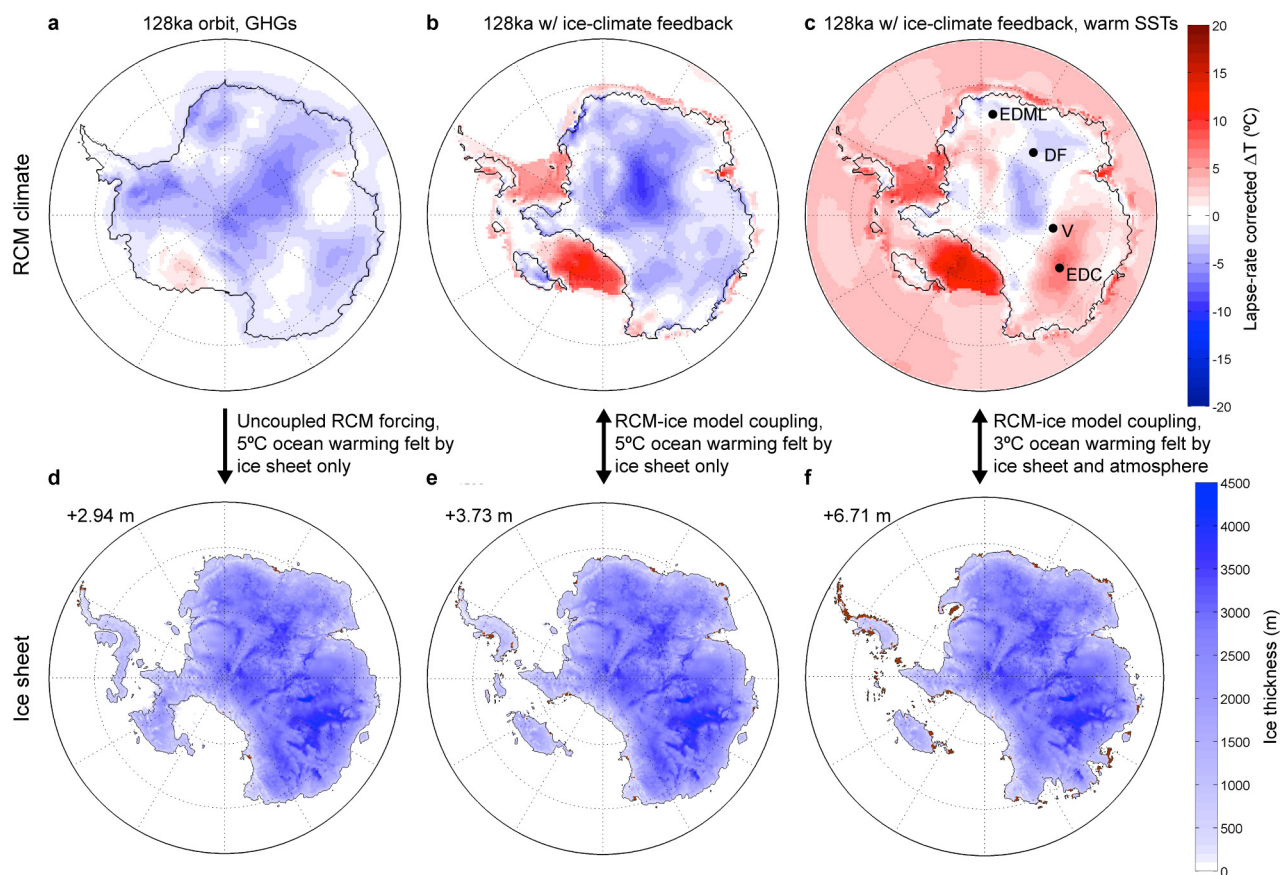
retreated WAIS to represent maximum Pliocene warm conditions. **b**, The Pliocene ice-sheet is shown after 5,000 model years, driven by the RCM climate in **a**, and assuming  $2^\circ\text{C}$  ocean warming relative to a modern ocean climatology<sup>32</sup>. In the model formulation used here, maximum Pliocene ice-sheet retreat with default model parameters is equivalent to 11.26 m GMSL, about 6 m less than in ref. 25.



**Extended Data Figure 2 | LIG greenhouse gases, orbital parameters, and RCM climates.** **a**, Greenhouse gas concentrations<sup>9,72</sup> converted to radiative forcing shows the LIG interval (light red bar) and the best opportunity for ice-sheet retreat. **b**, Summer insolation at 70° latitude in both hemispheres<sup>73</sup> (red, south; blue, north) and summer duration at 70°S (black)<sup>79</sup> shown over the last 150 kyr, and the two orbital time slices (vertical dashed black lines at 128 kyr ago and 116 kyr ago). **c**, Table showing the greenhouse gas atmospheric mixing ratios (CO<sub>2</sub> in parts per million by volume; CH<sub>4</sub> and N<sub>2</sub>O in parts per billion by volume) and orbital parameters (eccentricity, obliquity, precession) used in the

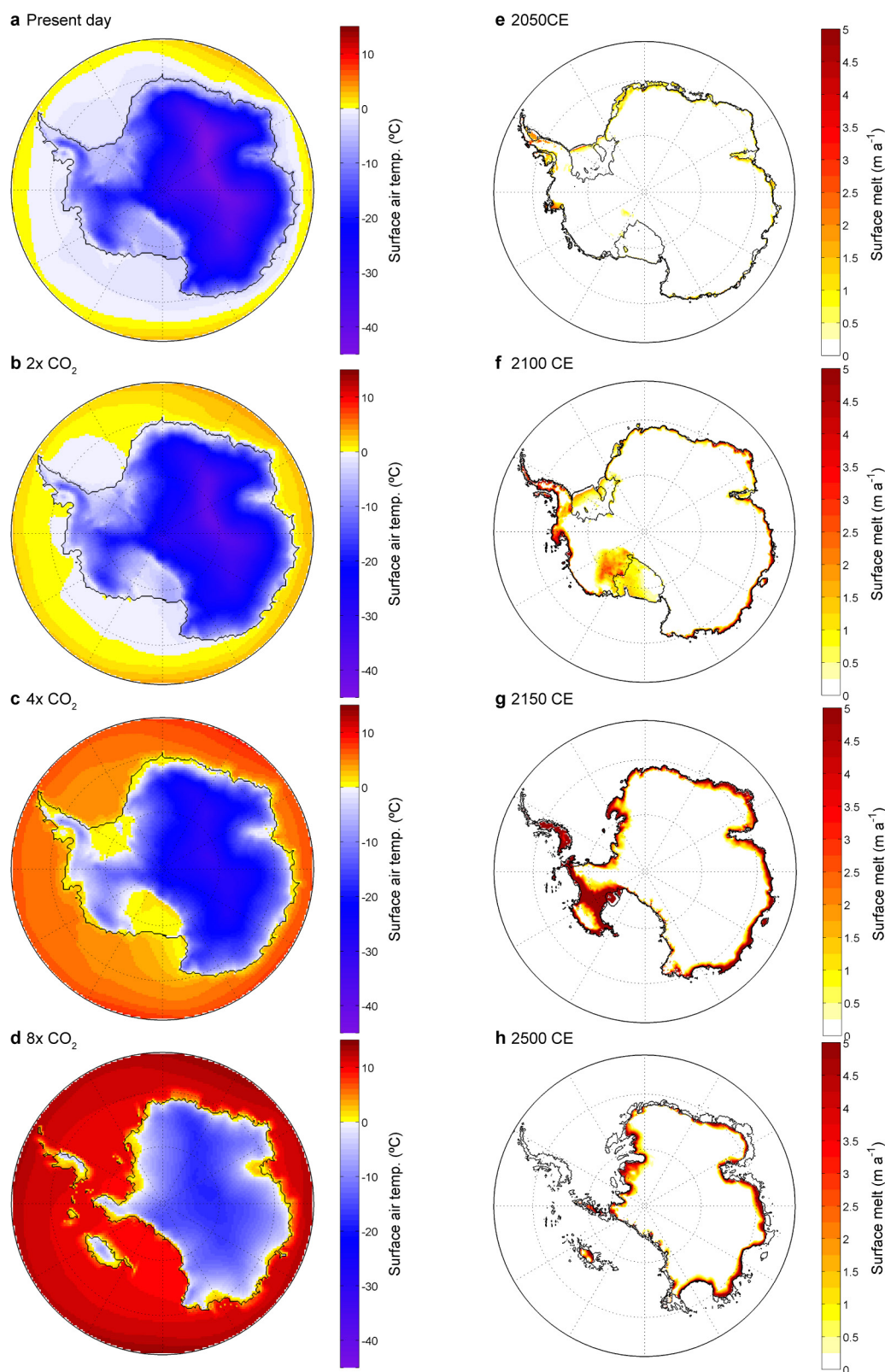
GCM–RCM at the LIG time slices (dashed lines 1 and 2 in **a** and **b**), respectively. **d–f**, January (warmest monthly mean) differences in 2-m surface air temperature relative to a preindustrial control simulation at 128 kyr ago (**d**), 116 kyr ago (**e**), and the present-day (2015) (**f**). Simulated austral summer temperatures at 116 kyr ago (**e**) with relatively high-intensity summer insolation is warmer than the long-duration summer orbit at 128 kyr ago (**d**), but unlike the Pliocene (Extended Data Fig. 1a), neither LIG climatology is as warm as the present day, producing little to no rain or surface melt on ice-shelf surfaces.





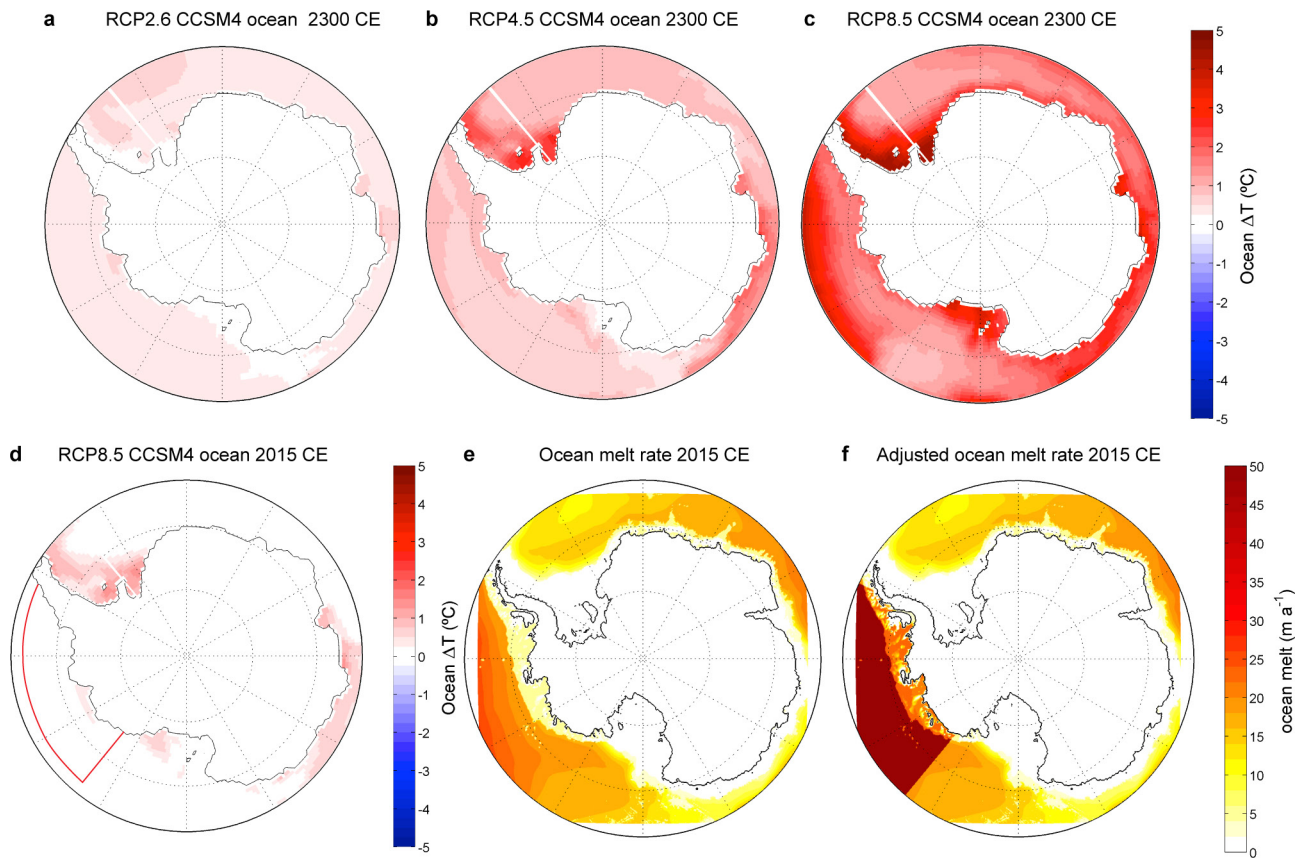
**Extended Data Figure 3 | Effect of Southern Ocean warming on Antarctic surface air temperatures and the ice sheet at 128 kyr ago.** **a–c**, January (warmest monthly mean) differences in 2-m surface air temperature at 128 kyr ago, relative to a preindustrial control simulation (top row). GHG, greenhouse gas; SST, sea surface temperature. **d, e**, Ice-sheet thickness (m) after 5,000 model years, driven by the corresponding climate in **a–c**. **a** and **d**, Without climate–ice sheet coupling (present-day ice extent and surface ocean temperatures in the RCM), and prescribed 5°C sub-surface ocean warming felt only by the ice sheet. **b** and **e**, With asynchronous coupling between the RCM atmosphere and ice sheet, and prescribed 5°C sub-surface ocean warming felt only by the ice

sheet. **c** and **f**, With asynchronous coupling between the RCM atmosphere and ice sheet, prescribed 3°C sub-surface ocean warming felt by the ice sheet, and ~2°C surface ocean warming felt by the RCM atmosphere. **c** shows the locations of East Antarctic ice cores (EDC, EPICA Dome C; V, Vostock; DF, Dome F; EDM, EPICA Dronning Maud Land) indicating warming early in the interglacial<sup>29</sup> and previously attributed to WAIS retreat<sup>80</sup>; this warming is similar to that simulated in **c** from a combination of ice-sheet retreat and warmer Southern Ocean temperatures, supporting the notion that the timing of LIG retreat was largely driven by far-field ocean influences, rather than local astronomical forcing.



**Extended Data Figure 4 | RCM climates used in future, time-continuous RCP scenarios and evolving ice-surface melt rates linked to hydrofracturing model physics.** a–d, January surface (2-m) air temperatures simulated by the RCM at the present-day (2015) (a), twice the present level of carbon dioxide,  $2 \times \text{CO}_2$  (b),  $4 \times \text{CO}_2$  (c), and  $8 \times \text{CO}_2$  (d) with the retreating ice sheet. The colour scale is the same in all panels. Yellow to red colours indicate temperatures above freezing with

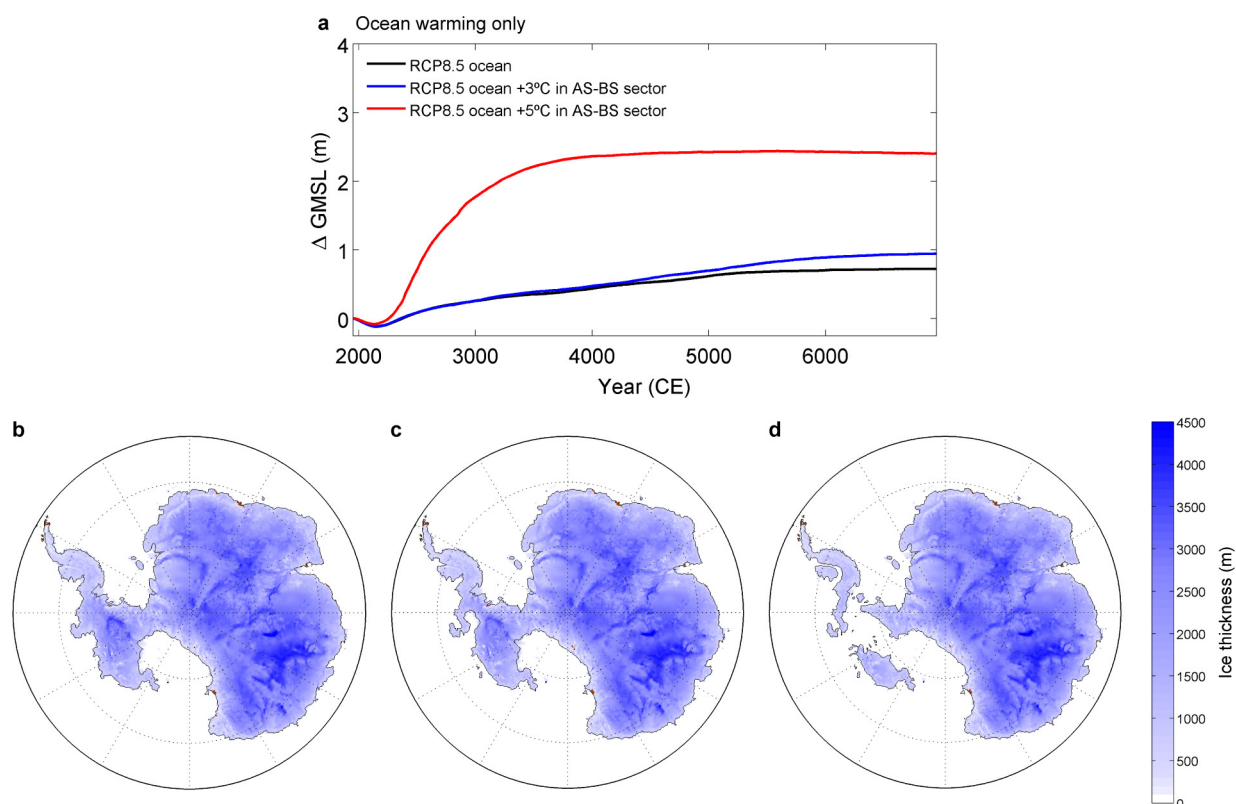
the potential for summer rain, and surface meltwater production. e–h, Evolving ice-surface meltwater production (in metres per year) in the time-evolving RCP8.5 ice-sheet simulations, driven by a time-continuous RCM climatology (Methods) following the RCP8.5 greenhouse gas time series (Fig. 4a). Black lines show the positions of grounding lines and ice-shelf calving fronts at discrete time intervals—e, 2050; f, 2100; g, 2150; and h, 2500—with superposed meltwater production rates.



**Extended Data Figure 5 | NCAR CCSM4 ocean temperatures and oceanic sub-ice-shelf melt rates.** **a**, RCP2.6 ocean warming at 400-m depth, shown as the difference of decadal averages from 1950–1960 to 2290–2300. **b**, Same as **a** but for RCP4.5. **c**, Same as **a** but for RCP8.5. **d**, CCSM4 RCP8.5 ocean warming from 1950–1960 to 2010–2020 showing little to no warming in the Amundsen and Bellingshausen seas. The red

line shows the area of imposed, additional ocean warming. **e**, **f**, Oceanic melt rates at 2015 calculated by the ice-sheet model from interpolated CCSM4 temperatures (**e**), and with +3°C adjustment in the Amundsen and Bellingshausen seas (**f**), corresponding to the area within the red line in **d**.

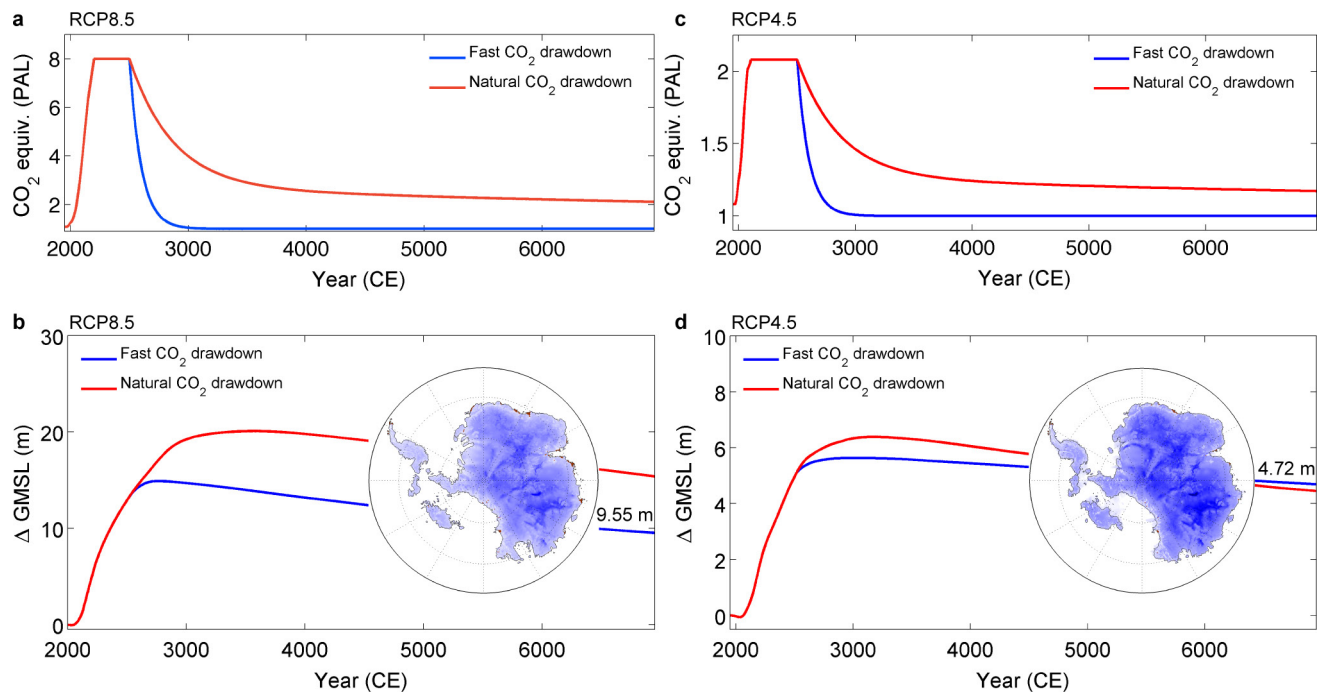




#### Extended Data Figure 6 | Effect of future ocean warming only.

**a**, Antarctic contribution to future GMSL rise in long, 5,000-yr ice-sheet simulations driven by sub-surface ocean warming simulated by CCSM4, following RCP8.5 (black line), with a +3 °C adjustment in the Amundsen and Bellingshausen seas (blue line; see Extended Data Fig. 5) and a warmer +5 °C adjustment (red line). Atmospheric temperatures and precipitation are maintained at their present values. **b–d**, Ice-sheet thickness at

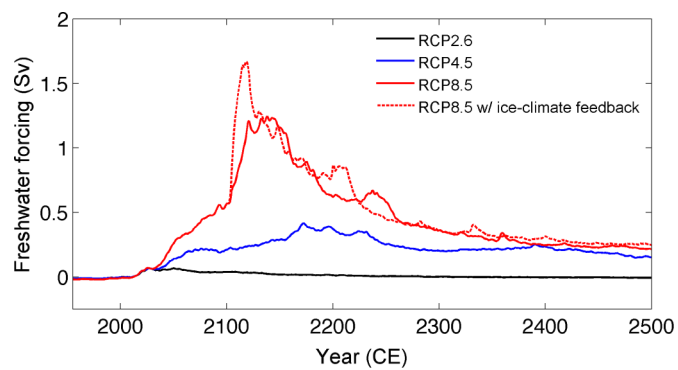
model-year 5,000, driven by sub-surface ocean forcing from CCSM4 (**b**) and from CCSM4 with a +3 °C (**c**) or +5 °C (**d**) adjustment in the Amundsen and Bellingshausen seas. Note the near-complete loss of ice shelves, but modest grounding-line retreat in **b**, the retreat of Pine Island Glacier in **c**, and the near-complete collapse of WAIS once a stability threshold in the Thwaites Glacier grounding line is reached in **d**.



**Extended Data Figure 7 | The long-term future of the ice sheet and GMSL over the next 5,000 years following RCP8.5 and RCP4.5.**

**a.** Equivalent CO<sub>2</sub> forcing following RCP8.5 until the year 2500, and then assuming zero emissions after 2500 and allowing a natural relaxation of greenhouse gas levels (red) or assuming a fast, engineered drawdown (blue) with an e-folding timescale of 100 years. **b.** Antarctic contribution to GMSL over the next 5,000 years, following the greenhouse gas scenarios

in **a**, **c**. The same as **a**, except showing long-term RCP4.5 greenhouse gas forcing. **d.** The same as **b**, except following the RCP4.5 scenarios in **c**. The insets in **b** and **d** show the ice sheet (and remaining sea-level rise) after 5,000 model years in RCP8.5 and RCP4.5, respectively, assuming fast CO<sub>2</sub> drawdown (blue lines), highlighting the multi-millennial commitment to a loss of marine-based Antarctic ice, even in the moderate RCP4.5 scenario. Note the different y-axes in RCP8.5 versus RCP4.5.

**Extended Data Figure 8 | Freshwater input to the Southern Ocean.**

Total freshwater and iceberg flux from 1950 to 2500, following the future RCP scenarios shown in Fig. 4b. Freshwater input calculations include contributions from ice loss above and below sea level and exceed 1 Sv in RCP8.5.



**Extended Data Table 1 | Summary of Antarctic contributions to GMSL during the Pliocene, LIG, future centuries, and future millennia**

RCM climate forcing, default model parameter values	Pliocene GMSL (m)	
	11.26	
	LIG 128ka GMSL (m)	LIG 116ka GMSL (m)
Modern ocean	-1.63	-0.69
+2 °C ocean	0.41	0.65
+3 °C ocean	0.85	1.12
+4 °C ocean	1.43	1.73
+5 °C ocean	2.94	3.29
+5 °C ocean, ice-climate feedback	3.73	3.84
+3 °C ocean, ice-climate-SST feedback	6.71	6.01
+5 °C ocean, ice-climate-SST feedback	7.16	7.52
Proxy-based climate and ocean forcing, default model parameters	LIG max. GMSL (m)	
Modern ice-sheet initial conditions	6.09	
Glacial ice-sheet initial conditions	7.54	
Old model physics	1.07	
RCM climate forcing, CCSM4 ocean, default model parameters	2100 CE GMSL (m)	2500 CE GMSL (m)
RCP2.6	0.03	0.20
RCP4.5	0.32	5.03
RCP8.5, no ice-climate feedback	0.77	12.30
RCP8.5	0.77	13.62
RCP8.5 +3°C AS-BS adjustment	0.86	13.60
RCM climate forcing, CCSM4 ocean, ensemble-filtered model parameters: LIG 3.6-7.4 m, Pliocene 10-20 m	2100 CE GMSL (m)	2500 CE GMSL (m)
RCP2.6	0.11±0.11	0.25±0.23
RCP4.5	0.49±0.20	5.69±1.00
RCP8.5	1.05±0.30	15.65±2.00
RCP2.6 +3°C AS-BS adjustment	0.16±0.16	0.62±0.76
RCP4.5 +3°C AS-BS adjustment	0.58±0.28	5.76±1.00
RCP8.5 +3°C AS-BS adjustment	1.14±0.36	15.65±2.00
RCM climate forcing, CCSM4 ocean, ensemble-filtered model parameters: LIG 3.6-7.4 m, Pliocene 5-20 m	2100 CE GMSL (m)	2500 CE GMSL (m)
RCP2.6	0.02±0.13	0.19±0.42
RCP4.5	0.26±0.28	3.97±1.97
RCP8.5	0.64±0.49	13.11±3.04
RCP2.6 +3°C AS-BS adjustment	0.14±0.19	0.70±0.78
RCP4.5 +3°C AS-BS adjustment	0.41±0.30	4.20±1.80
RCP8.5 +3°C AS-BS adjustment	0.79±0.46	13.09±3.05
Long-term simulations using default model parameters	7000 CE GMSL (m)	
RCP4.5 no CO <sub>2</sub> drawdown	8.47	
RCP4.5 natural CO <sub>2</sub> drawdown	4.48	
RCP4.5 fast CO <sub>2</sub> drawdown	4.72	
RCP8.5 no CO <sub>2</sub> drawdown	35.99	
RCP8.5 natural CO <sub>2</sub> drawdown	15.41	
RCP8.5 fast CO <sub>2</sub> drawdown	9.55	

Antarctic contributions to GMSL for the Pliocene and LIG simulations (rows 1–9) with +2 °C ocean warming in the Pliocene and incrementally imposed ocean warming in the LIG simulations. Values shown represent ice retreat at the end of quasi-equilibrated 5000-yr simulations. Time-continuous LIG simulations forced by proxy-based atmosphere and ocean climatologies (rows 10–12) list maximum GMSL contributions occurring early in the LIG (Fig. 3a). The remaining rows list Antarctic contributions to GMSL at specific times (years as shown) in time-dependent future simulations. Ensemble means and standard deviations ( $1\sigma$ ) of the RCP ensemble members listed in Extended Data Table 2 are also shown. Future GMSL contributions are shown relative to 2000.

Extended Data Table 2 | Ensemble simulations of Pliocene, LIG, and future Antarctic contributions to GMSL

Parameter values	Pliocene	LIG	LE#	Future GMSL ensembles (m)						Future GMSL ensembles (m)						
	GMSL	GMSL		LIG 3.6-7.4 m, Pliocene 5-15 m						LIG 3.6-7.4 m, Pliocene 5-15 m						
				No AS-BS ocean bias correction						With AS-BS ocean bias correction						
				RCP2.6		RCP4.5		RCP8.5		RCP2.6		RCP4.5		RCP8.5		
(m)	(m)		2100	2500	2100	2500	2100	2500	2100	2500	2100	2500	2100	2500		
0.1,0,0	3.54	-0.45														
0.1,0,1	3.52	-0.44														
0.1,0,3	3.65	-0.43														
0.1,0,5	3.66	-0.42		1	-0.06	-0.13	0.20	4.07	0.66	13.51	-0.06	-0.10	0.20	4.06	0.65	13.52
0.1,50,0	4.39	-0.30		2	0.08	0.07	0.51	5.69	1.15	17.27	0.07	0.10	0.51	5.71	1.14	17.32
0.1,50,1	8.29	-2.63		3	-0.01	0.01	0.28	4.56	0.74	13.57	0.01	0.04	0.28	4.55	0.74	13.58
0.1,50,3	10.72	3.53	1	4	0.18	0.21	0.64	6.30	1.29	17.45	0.18	0.24	0.62	6.31	1.28	17.43
0.1,50,5	10.89	3.76	2	5	-0.16	-0.53	-0.03	1.97	0.21	10.64	-0.16	-0.50	-0.03	2.00	0.21	10.66
0.1,100,0	4.31	-0.27		6	0.02	0.06	0.31	4.74	0.77	13.59	0.02	0.08	0.31	4.80	0.77	13.59
0.1,100,1	8.42	3.41		7	0.21	0.27	0.67	6.53	1.34	17.48	0.22	0.30	0.68	6.62	1.34	17.47
0.1,100,3	11.15	4.44	3	8	-0.17	-0.46	-0.04	2.03	0.19	10.66	-0.14	-0.33	0.00	2.32	0.23	10.65
0.1,100,5	11.31	4.72	4	9	-0.03	0.06	0.25	4.52	0.69	13.58	0.01	0.23	0.31	4.66	0.77	13.56
0.1,150,0	4.14	-0.23		10	0.11	0.25	0.55	6.10	1.20	17.38	0.16	0.42	0.63	6.22	1.30	17.38
0.1,150,1	8.66	3.68	5	11	-0.14	-0.38	-0.01	2.32	0.22	10.69	-0.11	-0.22	0.03	2.51	0.26	10.67
0.1,150,3	11.24	4.75	6	12	0.03	0.20	0.32	5.03	0.77	13.62	0.07	0.37	0.39	5.16	0.86	13.60
0.1,150,5	11.57	4.92	7	13	0.22	0.41	0.67	6.80	1.33	17.47	0.27	0.58	0.78	6.83	1.45	17.48
1,0,0	3.74	1.15		14	-0.13	-0.32	0.00	2.41	0.24	10.70	-0.10	-0.17	0.04	2.59	0.27	10.69
1,0,1	3.81	1.17		15	0.06	0.25	0.35	5.24	0.81	13.62	0.10	0.41	0.43	5.37	0.88	13.62
1,0,3	4.36	1.22		16	0.25	0.46	0.72	6.94	1.38	17.50	0.31	0.62	0.84	7.04	1.48	17.51
1,0,5	4.50	1.18		17	-0.10	-0.19	0.04	2.59	0.27	10.75	-0.04	0.52	0.14	2.89	0.39	10.74
1,50,0	4.57	1.20		18	0.04	0.36	0.34	5.09	0.80	13.66	0.12	1.54	0.55	5.31	0.99	13.63
1,50,1	8.53	4.68	8	19	0.18	0.54	0.67	6.61	1.34	17.50	0.37	2.16	1.02	6.67	1.66	17.47
1,50,3	10.93	5.73	9	20	-0.07	-0.04	0.07	2.79	0.30	10.78	0.00	0.64	0.18	3.09	0.43	10.74
1,50,5	11.00	5.92	10	21	0.33	0.76	0.83	7.12	1.48	17.59	0.53	2.35	1.17	7.12	1.75	17.55
1,100,0	4.56	1.20		22	-0.05	0.00	0.08	2.87	0.31	10.77	0.01	0.70	0.19	3.17	0.44	10.77
1,100,1	8.83	5.02	11	23	-0.05	0.17	-0.01	1.21	0.09	9.76	0.22	1.19	0.25	2.03	0.35	9.72
1,100,3	11.26	6.09	12	24	-0.04	0.44	0.00	1.44	0.10	9.78	0.29	1.40	0.34	2.26	0.42	9.75
1,100,5	11.47	6.22	13	25	-0.02	1.01	0.02	2.00	0.11	9.95	0.41	1.88	0.45	2.74	0.54	9.91
1,150,0	4.51	1.13		26	0.03	1.44	0.04	2.37	0.12	10.20	0.57	2.05	0.61	2.87	0.71	10.15
1,150,1	8.88	5.12	14	27	-0.04	0.21	0.03	1.86	0.18	10.22	0.22	1.22	0.31	2.31	0.51	10.18
1,150,3	11.39	6.21	15	28	-0.03	0.22	0.03	1.96	0.20	10.22	0.23	1.24	0.33	2.38	0.53	10.18
1,150,5	11.81	6.41	16	29	-0.03	0.21	0.04	2.00	0.20	10.22	0.23	1.22	0.33	2.34	0.53	10.18
3,0,0	4.21	3.18		mean	0.02	0.19	0.26	3.97	0.64	13.11	0.14	0.70	0.41	4.20	0.79	13.09
3,0,1	4.63	3.28		1-σ	0.13	0.42	0.28	1.97	0.49	3.04	0.19	0.78	0.30	1.80	0.46	3.05
3,0,3	4.87	3.31														
3,0,5	4.95	3.27														
3,50,0	4.76	3.28														
3,50,1	9.02	5.37	17													
3,50,3	11.29	6.23	18													
3,50,5	11.45	6.34	19													
3,100,0	4.82	3.30														
3,100,1	9.28	6.31	20	1	-0.06	-0.13	0.20	4.07	0.66	13.51	-0.06	-0.10	0.20	4.06	0.65	13.52
3,100,3	11.38	7.70		2	0.08	0.07	0.51	5.69	1.15	17.27	0.07	0.10	0.51	5.71	1.14	17.32
3,100,5	11.60	6.55	21	3	-0.01	0.01	0.28	4.56	0.74	13.57	0.01	0.04	0.28	4.55	0.74	13.58
3,150,0	4.84	3.32		4	0.18	0.21	0.64	6.30	1.29	17.45	0.18	0.24	0.62	6.31	1.28	17.43
3,150,1	9.40	6.36	22	6	0.02	0.06	0.31	4.74	0.77	13.59	0.02	0.08	0.31	4.80	0.77	13.59
3,150,3	11.49	7.89		7	0.21	0.27	0.67	6.53	1.34	17.48	0.22	0.30	0.68	6.62	1.34	17.47
3,150,5	11.90	7.99		9	-0.03	0.06	0.25	4.52	0.69	13.58	0.01	0.23	0.31	4.66	0.77	13.56
10,0,0	5.36	5.32	23	10	0.11	0.25	0.55	6.10	1.20	17.38	0.16	0.42	0.63	6.22	1.30	17.38
10,0,1	5.73	5.65	24	12	0.03	0.20	0.32	5.03	0.77	13.62	0.07	0.37	0.39	5.16	0.86	13.60
10,0,3	5.84	5.80	25	13	0.22	0.41	0.67	6.80	1.33	17.47	0.27	0.58	0.78	6.83	1.45	17.48
10,0,5	5.89	5.81	26	15	0.06	0.25	0.35	5.24	0.81	13.62	0.10	0.41	0.43	5.37	0.88	13.62
10,50,0	6.01	5.28	27	16	0.25	0.46	0.72	6.94	1.38	17.50	0.31	0.62	0.84	7.04	1.48	17.51
10,50,1	9.69	7.67		18	0.04	0.36	0.34	5.09	0.80	13.66	0.12	1.54	0.55	5.31	0.99	13.63
10,50,3	11.59	8.55		19	0.18	0.54	0.67	6.61	1.34	17.50	0.37	2.16	1.02	6.67	1.66	17.47
10,50,5	11.83	8.66		21	0.33	0.76	0.83	7.12	1.48	17.59	0.53	2.35	1.17	7.12	1.75	17.55
10,100,0	6.01	5.32	28	mean	0.11	0.25	0.49	5.69	1.05	15.65	0.16	0.62	0.58	5.76	1.14	15.65
10,100,1	9.86	7.80		1-σ	0.11	0.23	0.20	1.00	0.30	2.00	0.16	0.76	0.28	1.00	0.36	2.00
10,100,3	11.88	8.79														
10,100,5	12.05	8.89														
10,150,0	5.98	5.34	29													
10,150,1	9.97	7.82														
10,150,3	11.97	8.93														
10,150,5	12.41	9.04														

Varying combinations of three model parameters (first column) correspond to OCFAC, CREVLIQ and VCLIF, respectively (see Methods). The resulting GMSL contributions of each ensemble member driven by Pliocene and LIG climatologies are shown in the second and third columns. Combinations of model parameters satisfying Pliocene and LIG sea-level targets are assigned a Large Ensemble number (LE#) in the fourth column. Default model parameter values (LE# 12) and resulting Pliocene and LIG GMSL rise are in bold type. Four future ensembles using alternative sets of the palaeo-filtered Large Ensemble members and following RCP2.5, RCP4.5 and RCP8.5 emissions scenarios are shown at right. The top two ensembles use 29 combinations of parameter values that satisfy LIG sea-level targets and a range of Pliocene sea-level targets between 5 m and 15 m. The bottom two ensembles use a more restricted set of 15 parameter combinations that satisfy a higher Pliocene target range >10 m. Future RCP ensembles at left correspond to the GMSL time series in Fig. 5. The two ensemble sets at far right include the ocean-temperature bias correction described in the text, Fig. 4 and Extended Data Fig. 5. Antarctic GMSL contributions for each ensemble member are shown at 2100 and 2500. Ensemble means and 1σ standard deviations are also shown. GMSL contributions in future ensembles are relative to 2000.

# Cullin–RING ubiquitin E3 ligase regulation by the COP9 signalosome

Simone Cavadini<sup>1,2</sup>, Eric S. Fischer<sup>1,2,3,4</sup>, Richard D. Bunker<sup>1,2</sup>, Alessandro Potenza<sup>1,2</sup>, Gondichatnahalli M. Lingaraju<sup>1,2</sup>, Kenneth N. Goldie<sup>5</sup>, Weam I. Mohamed<sup>1,2</sup>, Mahamadou Faty<sup>1,2</sup>, Georg Petzold<sup>1,2</sup>, Rohan E. J. Beckwith<sup>6</sup>, Ritesh B. Tichkule<sup>6</sup>, Ulrich Hassiepen<sup>7</sup>, Wassim Abdulrahman<sup>1,2</sup>, Radosav S. Pantelic<sup>5,8</sup>, Syota Matsumoto<sup>9,10</sup>, Kaoru Sugasawa<sup>9,10</sup>, Henning Stahlberg<sup>5</sup> & Nicolas H. Thomä<sup>1,2</sup>

**The cullin–RING ubiquitin E3 ligase (CRL) family comprises over 200 members in humans. The COP9 signalosome complex (CSN) regulates CRLs by removing their ubiquitin-like activator NEDD8. The CUL4A–RBX1–DDB1–DDB2 complex (CRL4A<sup>DDB2</sup>) monitors the genome for ultraviolet-light-induced DNA damage. CRL4A<sup>DDB2</sup> is inactive in the absence of damaged DNA and requires CSN to regulate the repair process. The structural basis of CSN binding to CRL4A<sup>DDB2</sup> and the principles of CSN activation are poorly understood. Here we present cryo-electron microscopy structures for CSN in complex with neddylated CRL4A ligases to 6.4 Å resolution. The CSN conformers defined by cryo-electron microscopy and a novel apo-CSN crystal structure indicate an induced-fit mechanism that drives CSN activation by neddylated CRLs. We find that CSN and a substrate cannot bind simultaneously to CRL4A, favouring a deneddylated, inactive state for substrate-free CRL4 complexes. These architectural and regulatory principles appear conserved across CRL families, allowing global regulation by CSN.**

Sophisticated repair systems have evolved to protect the genome from the constant insult of DNA-damaging agents<sup>1–3</sup>. CRL4<sup>DDB2</sup>, a cullin–RING ubiquitin E3 ligase (CRL) composed of CUL4, RBX1, DDB1 and DDB2 detects ultraviolet (UV)-light-induced lesions in the genome<sup>4,5</sup>. DDB2, the CRL4<sup>DDB2</sup> substrate receptor, specifically binds DNA duplexes containing 6–4-photoproducts (6-4PPs) or cyclobutane-pyrimidine dimers (CPDs)<sup>6–9</sup>. CRL4A<sup>DDB2</sup> and CRL4B<sup>DDB2</sup> ubiquitinate proteins surrounding these lesions, facilitating repair by the nucleotide excision repair (NER) pathway<sup>1,4,10</sup>. Mutations in *DDB2* cause xeroderma pigmentosum, a rare congenital disorder characterized by heightened UV sensitivity and cancer predisposition<sup>11,12</sup>.

The COP9 signalosome complex (CSN) is required for efficient NER<sup>13</sup>. CSN contains six different PCI (proteasome lid-CSN-initiation factor 3) proteins (CSN1–CSN4, CSN7 and CSN8) and two MPN (MPR1/PAD1 amino-terminal) domain-containing proteins (CSN5 and CSN6) of which one subunit, CSN5, is enzymatic<sup>14,15</sup>. The CSN5 and CSN6 MPN domains form a heterodimer, and the six PCI proteins assemble into a horseshoe-shaped ring (PCI ring) from which their arm-like  $\alpha$ -helical domains project. All eight subunits are united in an intricate bundle formed by their carboxy (C)-terminal  $\alpha$ -helices, which is stacked between the CSN5–CSN6 dimer and PCI ring. CSN is regulated by autoinhibition, which is only released by neddylated CRL binding, ensuring CSN5 specifically removes the activating NEDD8 modification from CRLs<sup>14</sup>.

CSN has been implicated in maintaining CRL4A<sup>DDB2</sup> in an inhibited state, which is relieved by the presence of damaged DNA<sup>6,16</sup>. CRL4A<sup>DDB2</sup> is one of ~200 different CRLs in humans, divided into five families by the identity of their cullin subunit (CRL1, CRL2, CRL3, CRL4A, CRL4B and CRL5)<sup>17</sup>. CRLs constitute ~30% of all human E3 proteins, and orchestrate degradation of ~20% of the protein processed by the proteasome<sup>18</sup>. Despite substantial structural variation

and substrate diversity (Extended Data Fig. 1), all CRLs are regulated by CSN<sup>15,19–21</sup>. The molecular mechanism by which DNA or protein substrates<sup>22</sup> prevent deneddylation of CRLs remains unclear. Structural data for CSN–CRLs has been limited to low-resolution negative-stain EM models<sup>23–25</sup>. Detailed structural characterization of CSN–CRL complexes is needed to understand their activity and regulation.

## Structure of CSN–N<sub>8</sub>CRL4A complexes

We obtained cryo-EM structures of human CSN in complex with neddylated (NEDD8 (N<sub>8</sub>)) CRL4A<sup>DDB2</sup> (CSN–N<sub>8</sub>CRL4A<sup>DDB2</sup>) at 8.3 Å resolution and CSN–N<sub>8</sub>CRL4A at 6.4 Å resolution (Fig. 1 and Extended Data Figs 2 and 3). The structures were interpreted with crystallographic models for each subunit, detailing the overall architecture of the assembly, the conformation of each subunit (Extended Data Fig. 4) and the protein–protein interfaces. Sub-classification of the CSN–N<sub>8</sub>CRL4A particles revealed different conformations of the CSN5–CSN6 dimer, the CUL4A WHB domain (WHB, residues 690–759) and NEDD8 (Extended Data Fig. 3c).

CSN–N<sub>8</sub>CRL4A<sup>DDB2</sup> is a thirteen-protein assembly (Fig. 1a) with dimensions of 180 × 160 × 110 Å. The major contacts are formed between (i) CSN2 and the CUL4A C-terminal domain (CUL4A<sub>CTD</sub>), (ii) CSN2 and CSN4, which sandwich RBX1, and (iii) CSN1 and DDB1 (Fig. 2). The substrate receptor DDB2 is positioned at the distal end of the helical bundle, where the C termini of the seven non-catalytic CSN proteins emanate (Fig. 1a). The CSN–N<sub>8</sub>CRL4A assembly, which lacks DDB2, has a ~40 Å gap between DDB1 and the CSN helical bundle (Fig. 1b).

## CSN2 engages CUL4A<sub>CTD</sub> at multiple sites

CSN2 has been implicated in CRL1 binding by CSN<sup>23</sup>. N-terminal truncation of CSN2 (CSN (CSN2<sup>250–443</sup>)), but not of CSN1

<sup>1</sup>Friedrich Miescher Institute for Biomedical Research, Maulbeerstrasse 66, 4058 Basel, Switzerland. <sup>2</sup>University of Basel, Petersplatz 10, 4003 Basel, Switzerland. <sup>3</sup>Department of Cancer Biology, Dana-Farber Cancer Institute, LC-4312, 360 Longwood Avenue, Boston, Massachusetts 02215, USA. <sup>4</sup>Department of Biological Chemistry and Molecular Pharmacology, Harvard Medical School, Boston, Massachusetts 02215, USA. <sup>5</sup>Center for Cellular Imaging and NanoAnalytics, Biozentrum, University of Basel, 4058 Basel, Switzerland. <sup>6</sup>Novartis Institutes for Biomedical Research, 250 Massachusetts Avenue, Cambridge, Massachusetts 02139, USA. <sup>7</sup>Novartis Pharma AG, Institutes for Biomedical Research, Novartis Campus, 4056 Basel, Switzerland. <sup>8</sup>Gatan R&D, 5974 W. Las Positas Boulevard, Pleasanton, California 94588, USA. <sup>9</sup>Biosignal Research Center, Organization of Advanced Science and Technology, Kobe University, Kobe 657-8501, Japan. <sup>10</sup>Graduate School of Science, Kobe University, Kobe, 657-8501, Japan.



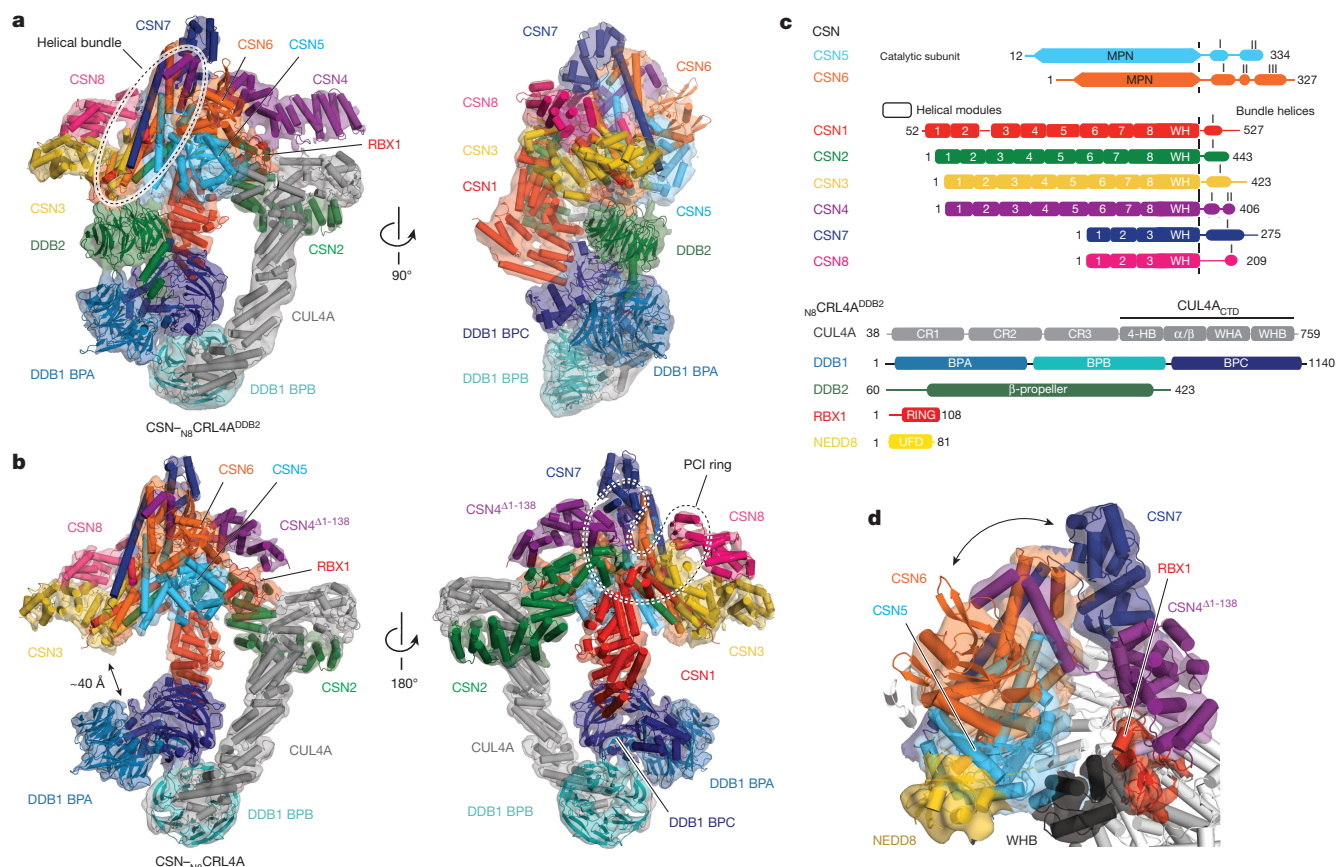


**Figure 1 | Cryo-EM structures of CSN-N<sub>8</sub>CRL4A<sup>DDB2</sup> and CSN-N<sub>8</sub>CRL4A. a**, CSN-N<sub>8</sub>CRL4A<sup>DDB2</sup> map (8.3 Å) with fitted model (cartoon representation). C-terminal helical bundle indicated as dashed line. **b**, CSN-N<sub>8</sub>CRL4A map (6.7 Å) and fitted model (cartoon representation). Dashed lines highlight the PCI ring. **c**, Domain organization of human CSN, CUL4A, NEDD8 and zebrafish DDB2.

(CSN (CSN1<sup>279-527</sup>)) or CSN4 (CSN (CSN4<sup>180-406</sup>)), abolished N<sub>8</sub>CRL4A<sup>DDB2</sup> deneddylation (Extended Data Fig. 5a–c and Table 1). The CSN-N<sub>8</sub>CRL4A structure details three separate contacts between the concave face of CSN2 and conserved patches on the CUL4A C-terminal domain (CUL4A<sup>CTD</sup>), which comprises a four-helix bundle (4-HB, residues 404–485), the α/β-domain (residues 486–592), and winged-helix domains A (WHA, residues 593–677) and WHB (Fig. 2a and Extended Data Fig. 6a). Interactions are formed between CSN2 helical module 1 (numbered as antiparallel pairs of α-helices from the N terminus; Fig. 1c) and the WHA, CSN2 helical modules 3 and 4, and the 4-HB, and CSN2 helical module 6 and the α/β-domain (Fig. 2a). In time-resolved fluorescence resonance energy transfer (TR-FRET) assays (see Extended Data Fig. 5d–g for the assay validation), wild-type CSN tightly bound N<sub>8</sub>CRL4A<sup>DDB2</sup> ( $K_d \sim 7$  nM) and N<sub>8</sub>CRL4A ( $K_d \sim 4$  nM), whereas mutations in the different CSN2 patches reduced binding affinity 5–16-fold (Fig. 2a, Extended Data Fig. 5h and Table 1) and impaired steady-state deneddylation (Extended Data Fig. 5i and Table 1). These biochemical results identify CSN2 helical modules 3, 4 and 6 as the primary CRL4A-binding interfaces of CSN.

### RBX1 is shielded by CSN2 and CSN4

Unable to transfer ubiquitin themselves, CRLs rely on their constituent RING domain protein RBX1 (or RBX2) to recruit ubiquitin-conjugating enzymes (E2) to carry out ubiquitination<sup>26–31</sup>. Previous attempts at modelling low-resolution maps of different CSN–CRL1 complexes tentatively positioned RBX1 in a groove between CSN5 and CSN2 (ref. 23). We find the RBX1 globular domain (residues 40–108) sandwiched by CSN2 (helical module 7) and CSN4 (helical module 5) (Fig. 2b)

and nestled against the flexible WHB (Fig. 1d and Extended Data Fig. 6b), the region modified by NEDD8 (ref. 32). This RBX1–CUL4A<sup>CTD</sup> conformation resembles the inhibited, unneddylated CAND1–CUL4B–RBX1 structure (PDB accession code 4A0C) (Extended Data Fig. 6c). Mutations in the RBX1 binding sites of CSN2 or CSN4 reduced binding affinity fivefold or twofold, respectively, compared with wild-type CSN (Fig. 2b, Extended Data Fig. 5j and Table 1).

If substrates are unavailable, CRLs have the proclivity to auto-ubiquitinate, thus potentially leading to their own destruction<sup>4,6</sup>. In the CSN-N<sub>8</sub>CRL4A structures, the RBX1 E2 binding site is shielded by CSN2, as revealed by the superposition of RBX1 in an E2–RING-finger complex (PDB accession code 4P5O)<sup>33</sup> onto CSN-N<sub>8</sub>CRL4A, which predicts clashes of E2 with CSN1, CSN2 and CSN4 (Fig. 2c). This architecture enables CSN to prevent CRLs from recruiting E2 ubiquitin-conjugating enzymes, explaining the inhibition of CRL4A auto-ubiquitination by CSN observed *in vitro*<sup>6</sup>.

### CSN1 binds the CRL4A adaptor DDB1

CUL4A family members employ the DDB1 adaptor to bind substrate receptors. DDB1 contains three WD40 β-propeller domains (BPA, BPB and BPC)<sup>6,34,35</sup> (Fig. 1a–c). The BPB domain of DDB1 (DDB1 BPB) rotates with the associated CUL4A arm relative to DDB1 BPA/BPC (Extended Data Fig. 6d), creating an extended ubiquitination zone<sup>6</sup>. In the CSN-N<sub>8</sub>CRL4A<sup>DDB2</sup> and CSN-N<sub>8</sub>CRL4A structures, CSN1 helical modules 5 and 6 bind DDB1 BPC (residues 979–992) (Fig. 2d) and restrict the rotational freedom of DDB1 and CUL4A. Mutation of the CSN1 contact (helical modules 5 and 6) in CSN impaired N<sub>8</sub>CRL4A<sup>DDB2</sup> binding and  $k_{cat}$  (Fig. 2d, Extended Data Fig. 5k, n

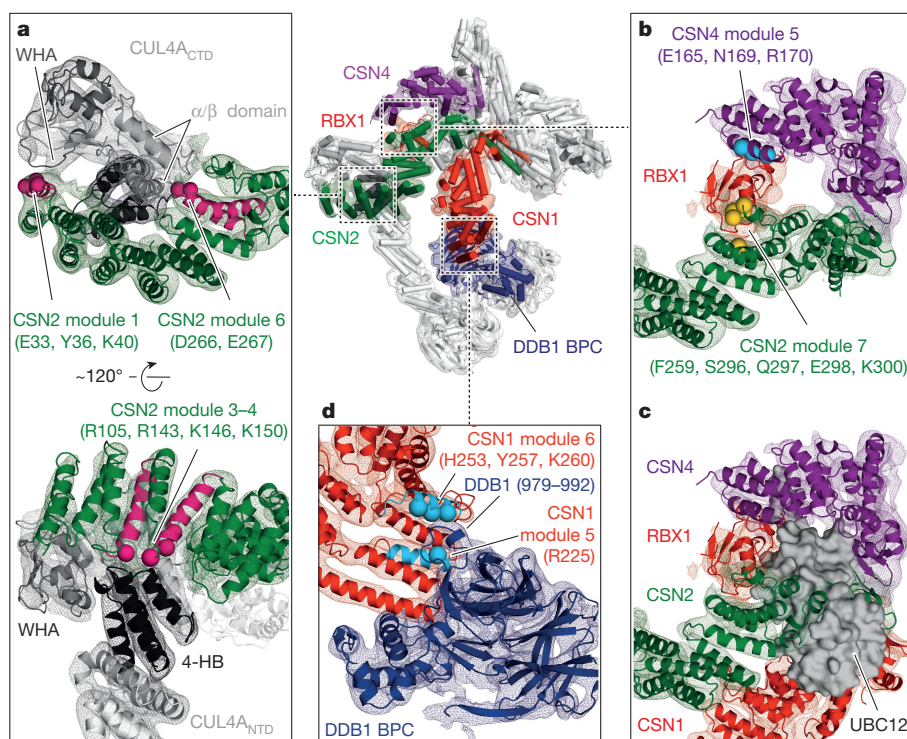


**Figure 2 | Conserved patches hold CSN and CRL4A together.**

CSN<sub>N8</sub>CRL4A (top centre) coloured as in Fig. 1. **a**, CSN2 interaction with CUL4A<sub>CTD</sub>. CSN2 helical modules in pink. Interface residues are shown in pink spheres. **b**, Close-up view of the interaction of RBX1 with CSN2 and CSN4. Interface residues are shown in cyan (CSN4) and yellow (CSN2).

spheres. **c**, Superposition of the E2 enzyme UBC12 (PDB accession code 4P5O) on RBX1. **d**, Close-up view highlighting the interaction between the DDB1 BPC propeller domain and CSN1, with helical modules shown in cyan. Interface residues are shown in pink spheres.

and Table 1). The CSN1–DDB1 contact therefore has an important role in stabilizing the mobile CUL4A arm and this interaction is required for efficient deneddylation.

### Induced-fit activation of CSN

The 6.4 Å CSN<sub>N8</sub>CRL4A cryo-EM map was (Extended Data Fig. 3b) obtained from 63,269 particles at the expense of obscuring the density for

the CSN5–CSN6 dimer. Further three-dimensional (3D) classification revealed three distinct CSN5–CSN6 dimer conformers (Fig. 3a–c and Extended Data Fig. 3c), which describe a  $\sim 30$  Å movement from a retracted position resembling apo-CSN to a NEDD8-engaged state that permits CSN5 to reach N<sub>8</sub>CUL4A<sub>CTD</sub> (Fig. 1d).

The conformational change CSN can undergo is revealed by comparing previous crystallographic models of apo-CSN (PDB accession codes

**Table 1 | Affinity of CSN for N<sub>8</sub>CRL4A<sup>DDB2</sup> and steady-state kinetic parameters**

Binding of CSN to N <sub>8</sub> CRL4A <sup>DDB2</sup> and deneddylation activity	$K_d$ (nM)	$k_{cat}$ (s <sup>-1</sup> )	$K_m$ (nM)
CSN (wild-type)	$6.7 \pm 1.0$	$0.57 \pm 0.06$	$709 \pm 160$
CSN1 <sup>279-527</sup>	-	$0.05 \pm 0.01$	$374 \pm 70$
CSN2 <sup>250-443</sup>	ND	-	-
CSN4 <sup>180-406</sup>	-	$0.1 \pm 0.01$	$294 \pm 49$
CSN1 <sup>module5-6</sup> (R225E, H253A, Y257A, K260E)	$35.6 \pm 10.9$	$0.10 \pm 0.02$	$729 \pm 295$
CSN2 <sup>module1</sup> (E33K, Y36A, K40D)	$41.2 \pm 3.6$	$<0.30^*$	-
CSN2 <sup>module3-4</sup> (R105E, K143D, R146E, K150D)	$117.2 \pm 24.1$	$<0.10^*$	-
CSN2 <sup>hinge</sup> (D182K, D183K, E185K, D186R, D187K, K189D, K190E)	$29.4 \pm 8.1$	$0.45 \pm 0.07$	$1,026 \pm 316$
CSN2 <sup>module7</sup> (F259A, S296A, Q297A, E298K, K300D)	$32.8 \pm 7.2$	$0.03 \pm 0.01$	$383 \pm 142$
CSN2 <sup>module6</sup> (D266R, E267R)	$94.9 \pm 12.8$	$<0.03^*$	-
CSN4 <sup>module5</sup> (E165K, N169A, R170E)	$12.8 \pm 3.8$	$0.25 \pm 0.03$	$479 \pm 162$
CSN5(S284A, F285A, L287A, H292A, R294D, K295D), CSN6 <sup>1-313</sup>	-	$0.43 \pm 0.04$	$598 \pm 129$
CSN6 <sup>192-327</sup>	-	$0.008 \pm 0.001$	$1,100 \pm 360$
CSN7 <sup>1-218</sup>	$8.3 \pm 0.15$	$0.2^*$	584
CSN7 <sup>30-218</sup>	$20.6 \pm 0.9$	$<0.03^*$	-
CSN1 <sup>52-507</sup> , CSN3 <sup>1-400</sup> , CSN5(S284A, F285A, L287A, H292A, R294D, K295D), CSN6 <sup>1-313</sup>	$7.5 \pm 1.2$	$0.30 \pm 0.03$	$338 \pm 114$

Experiments carried out as technical replicates as detailed in Extended Data Figs 5 and 8.

ND, not detected

\*Estimated from fit.



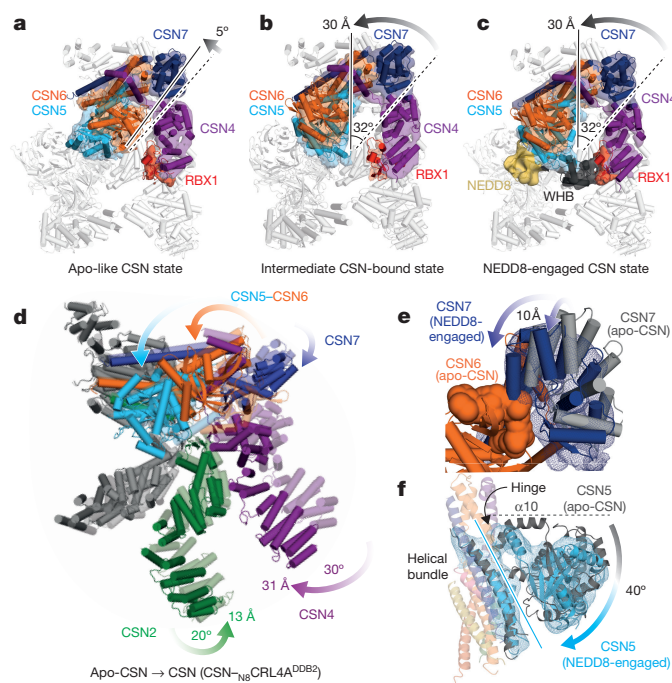


**Figure 3 | Structural changes in CSN induced by  $N_8$ CRL4A binding.** Conformational dynamics of the CSN5–CSN6 dimer in CSN– $N_8$ CRL4A revealed by 3D classification: class I (a), class II (b) and class III (c) (Extended Data Fig. 3c). d, Superimposition of CSN (PDB accession code 4D18 chains I–P, shade) and the CSN– $N_8$ CRL4A<sup>DDB2</sup> cryo-EM model. e, Superimposition of apo-CSN (PDB accession code 4D18) and NEDD8-engaged CSN (c) showing clashes between CSN7 and CSN6 MPN-domain in its apo-CSN position. f, Superposition of CSN– $N_8$ CRL4A and apo-CSN (PDB accession code 4D18) highlighting the CSN5 hinge loop between helices  $\alpha 10$  and  $\alpha 11$ . Cryo-EM density for CSN5 is shown as a mesh (cyan).

4D10 and 4D18, space group  $P3_1$ ) with a novel apo-CSN crystal form (space group  $P1$ ) determined here, with six highly varied conformers in its asymmetric unit. The ensemble of apo-CSN crystallographic models provide evidence for coordinated domain movement across CSN2, CSN4, CSN7 and the CSN5–CSN6 dimer. These movements of apo-CSN in the crystal (Extended Data Fig. 6e, f) mimic the conformational changes CSN undergoes to bind CRL4A described by the cryo-EM structures (Fig. 3d). The N-terminal arms of CSN2 and CSN4 move towards each other (Fig. 3d) and the PCI ring extends 5 Å (Extended Data Fig. 6g). Expansion of the PCI ring pushes the N-terminal portion of CSN7  $\sim 10$  Å into the CSN6 MPN domain (Fig. 3e), which potentially dislodges the CSN5–CSN6 dimer (Fig. 3f), allowing it to engage NEDD8 on the CUL4A<sup>CTD</sup>.

Conformational changes in CSN2, CSN4 and CSN7 thus provide a mechanism to relay  $N_8$ CRL4A binding to the CSN5–CSN6 dimer and prime CSN5 for deneddylation. To address this experimentally, we mutated a conserved hinge in CSN2 linking helical modules 4 and 5 (see CSN2<sup>hinge</sup> in Table 1), which is distant from CUL4A, but changes conformation on binding CRL4A. This mutation reduced binding affinity  $\sim$ fourfold, while only mildly impairing catalysis (Extended Data Fig. 5l and Table 1). Deletion of the first helical module in CSN7 (CSN (CSN7<sup>30–218</sup>)), which is predicted to push against the CSN5–CSN6 dimer, in contrast, profoundly diminished deneddylation (Extended Data Fig. 5m and Table 1). Deletion of the CSN6 MPN domain (CSN (CSN6<sup>192–327</sup>)) analogously decreased CSN activity  $>50$ -fold (Extended Data Fig. 5n and Table 1). Our data shows that CRL4A binding triggers conformational changes in CSN2, CSN4 and CSN7 that liberate the CSN5–CSN6 dimer. In addition to release, the CSN5 active site needs to be remodelled to fully relieve CSN auto-inhibition. Limited by the local resolution of the CSN active site (Extended Data Fig. 3b), which was poorly defined in all cryo-EM

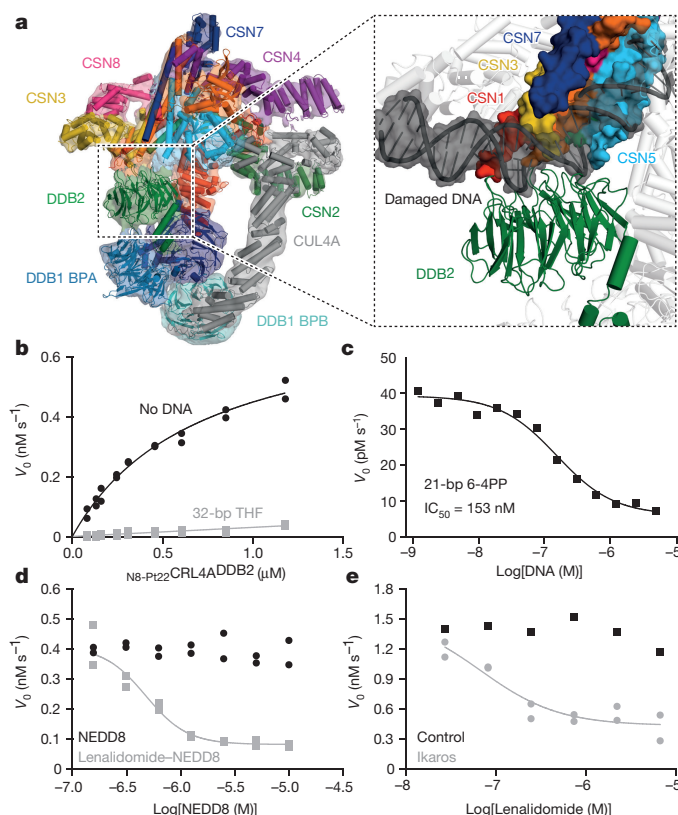


**Figure 4 | A steric mechanism governs CRL4A binding to CSN.**

a, Close-up of the DDB2–CSN interface with modelled damaged DNA highlighting clashes. b, The  $N_8$ -PT22CRL4A<sup>DDB2</sup> deneddylation in the presence or absence of 10  $\mu$ M THF-containing DNA ( $n = 2$ ) and 2 nM CSN. See Supplementary Information for more information about the PT22 fluorescent dye. c, Increasing amounts of a 21-bp oligonucleotide containing a central 6-4PP site (21-bp 6-4PP) mixed with CSN at 1 nM and  $N_8$ -PT22CRL4A<sup>DDB2</sup> at 200 nM, fitted to an  $IC_{50}$  value of 153 nM ( $n = 1$ ). d, As in c but with increasing amounts of NEDD8 (black), or lenalidomide–NEDD8 conjugate (grey), mixed with CSN at 3 nM and  $N_8$ -PT22CRL4A<sup>CRBN</sup> at 500 nM ( $n = 2$ ) in buffer containing a total of 4.4% glycerol. e, Increasing amounts of lenalidomide, or a buffer control, mixed with Ikaros at 10  $\mu$ M (grey), 3 mg ml<sup>−1</sup> BSA, CSN at 2 nM and  $N_8$ -PT22CRL4A<sup>CRBN</sup> at 500 nM ( $n = 2$ ). Data are technical replicates shown as individual data points.

structures, it remains unclear how the remodelling of the CSN5 auto-inhibitory loop (Ins-1)<sup>14</sup> is achieved.

### Steric gating of the CSN–CRL interaction

Comparison of the CSN– $N_8$ CRL4A and CSN– $N_8$ CRL4A<sup>DDB2</sup> structures reveals rearrangements of the CSN helical bundle. To accommodate DDB2, the C-terminal helices of CSN3, CSN4, CSN7 and CSN8 reposition (Extended Data Fig. 7a, b). Mutation of potential CSN contacts ((CSN (CSN1<sup>52–507</sup>, CSN3<sup>1–400</sup>, CSN5(S284A, F285A, L287A, H292A, R294D, K295D), CSN6<sup>1–313</sup>))) with DDB2 did not affect binding affinity, however (Extended Data Fig. 5o and Table 1). The proximity of DDB2 to CSN has important implications for the regulation of the CSN– $N_8$ CRL4A<sup>DDB2</sup> interaction. As damaged DNA bound to DDB2 would collide with the CSN helical bundle in CSN– $N_8$ CRL4A<sup>DDB2</sup> (Fig. 4a), we tested whether CSN and DNA substrate binding are mutually exclusive. Addition of a 32-bp tetrahydrofuran (THF)-containing DNA duplex, a DNA damage mimic bound by DDB2 (refs 11, 35), displaces CSN from neddylation and unneddylation CRL4A<sup>DDB2</sup> in pull-down assays (Extended Data Fig. 8a, b). On the functional level, deneddylation was largely abolished in steady-state assays with saturating concentrations of THF-containing DNA (10  $\mu$ M;  $K_d \sim 296$  nM) measured across a wide range of  $N_8$ CRL4A<sup>DDB2</sup>



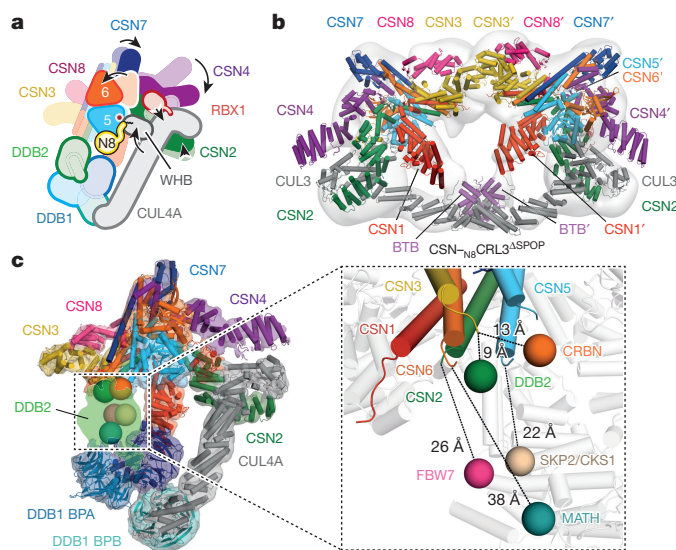


**Figure 5 | Shared mechanisms of binding and regulation across CSN-CRLs complexes.** **a**, Model of CSN conformational changes following  $N_8$ CRL4A binding. **b**, CSN- $N_8$ CRL3 $\Delta$ SPOB EM density fitted with CUL1 $_{CTD}$ , CUL3 $_{NTD}$  BTB (PDB accession codes 1LDK, 4EOZ and 3HU6) and the cryo-EM CSN- $N_8$ CRL4A model (without CUL4A-DDB1). **c**, Approximate position of substrate-binding sites defined by various CSN-CRL EM structures indicated by spheres and shown with the CSN- $N_8$ CRL4A $^{DDB2}$  cryo-EM map with the fitted model omitting DDB2. Close-up view showing the substrate binding sites (coloured spheres) of different substrate receptors with respect to the CSN helical bundle.

concentrations (Fig. 4b). CSN inhibition was proportional to the fraction of CRL4A $^{DDB2}$  bound to damaged DNA (compare Fig. 4c with Extended Data Fig. 8c, d). Combined with the structural data, this suggests that DNA inhibits  $N_8$ CRL4A $^{DDB2}$  deneddylation sterically by colliding with CSN.

Similarity among previous CRL4 structures<sup>6,36</sup> predicts that the WD40-containing substrate receptors face the helical bundle like DDB2 in CSN- $N_8$ CRL4A $^{DDB2}$ . Substrate-dependent escape from CSN inhibition may thus apply to other CRL4 complexes. We turned to CRBN<sup>37,38</sup>, the target of the drug thalidomide and its analogues lenalidomide and pomalidomide<sup>39</sup>, to examine whether non-WD40 CRL4A substrate receptors also use a similar gating mechanism. A negative-stain EM reconstruction of CSN- $N_8$ CRL4A $^{CRBN}$  (~25 Å) confirmed the CRBN substrate receptor orientation facing CSN (Extended Data Fig. 9a–d). To address whether CSN displacement from  $N_8$ CRL4A $^{CRBN}$  is driven purely by steric repulsion, we engineered an artificial CRBN substrate by conjugating NEDD8 to lenalidomide. This substrate inhibited  $N_8$ CRL4A $^{CRBN}$  deneddylation in a dose-dependent manner (Fig. 4d), whereas NEDD8 and lenalidomide separately did not affect catalysis (Fig. 4d and Extended Data Fig. 8e–g). The lenalidomide-dependent CRBN neo-substrate Ikaros (IKZF1)<sup>40,41</sup> also inhibited  $N_8$ CRL4A $^{CRBN}$  deneddylation (Fig. 4e). Thus, substrates as diverse as DNA, conjugated ligands and drug-induced neo-substrates prevent  $N_8$ CRL4A deneddylation. This is consistent with a steric gating mechanism that controls the CSN-CRL4 interaction.

Our CSN- $N_8$ CRL4A $^{DDB2}$  and CSN- $N_8$ CRL4A structures enable interpretation of negative-stain maps of the CSN- $N_8$ CRL4A $^{CRBN}$  (~25 Å) and the dimeric CSN- $N_8$ CRL3 $\Delta$ SPOB complex (~27 Å) (Fig. 5 and Extended Data Fig. 9e–h), and allow reinterpretation of the CSN- $N_8$ CRL1 $^{SKP2/CKS1}$  and CSN- $N_8$ CRL1 $^{FBW7}$  reconstructions<sup>23</sup> (Extended Data Fig. 9i, j). Beyond the CRL4 family, we find key shared contacts between CSN and CRLs that seem supplemented by family-specific interactions. The highly conserved CSN2-CUL $_{CTD}$  contact (Extended Data Fig. 6a), the interaction of RBX1 with CSN2 and CSN4, and the association of the CSN5-CSN6

dimer with the  $N_8$ CUL $_{CTD}$  are present in CSN- $N_8$ CRL3 $\Delta$ SPOB and CSN- $N_8$ CRL1 $^{SKP2/CKS1}$ . The intricate allosteric activation circuitry that governs CSN5 activity in CSN (Fig. 5a) thus broadly applies to the CRL1, CRL3 and CRL4 families. The CSN1-DDB1 contact, on the other hand, appears specific to CRL4, as mutations at this site did not affect binding and deneddylation of CRL1 and CRL3 by CSN (Extended Data Fig. 8h, i and Extended Data Table 1a–c). Although shapes of adaptors and substrate receptors differ across CRLs (Extended Data Fig. 1), we find that the substrate binding sites in the CRL1, CRL3 and CRL4 families occupy a common volume ~40 × 60 × 50 Å distanced ~10–40 Å from the CSN helical bundle (Fig. 5c). Substrates bound to these sites are thus expected to displace CSN, giving rise to a steric gating mechanism that is conserved across CRLs. This is in line with previous observations showing disruption of the CSN-CRL1 complex in the presence of a CRL1 substrate<sup>23</sup>.

Our structural and functional results support a model where substrate-free CRLs are inactivated by CSN. The apparent nanomolar affinity of the CSN- $N_8$ CRL interaction, the fast turnover rates and ~500 nM cellular concentration of CSN (determined in HEK293T cells)<sup>21</sup>, which approximates the estimated 1–2 μM concentration of the CRL pool, predicts substrate-free CRLs are rapidly deneddylated. This is consistent with the fast deneddylation kinetics (on the order of minutes) observed in cells treated with the neddylation inhibitor MLN4924 (ref. 42). The deneddylation rate of a given CRL, however, can be attenuated by the presence of its substrate. This model is consistent with previous cellular observations, in which CRL1 and CRL2 proteins with mutated substrate-binding sites, were found to be preferentially deneddylated<sup>43</sup> compared to CRLs carrying wild-type substrate receptors.

Deneddylated CRL4s have three orders of magnitude lower affinity for CSN than neddylated CRL4s (Extended Data Fig. 5d, e). After deneddylation, CRLs become available for CAND1-mediated substrate receptor exchange<sup>44</sup>. Our findings thus suggest the high affinity CSN- $N_8$ CRL interaction to act as a selectivity filter to inactivate CRLs that are idle or transiently engaged with spurious targets. Such a mechanism allows CSN to protect those CRLs from futile auto-ubiquitination. Our findings help explain why CSN, the primary negative regulator of CRLs, is also required for efficient CRL activity and specificity, a conundrum known as the ‘CSN paradox’<sup>45</sup>.

**Online Content** Methods, along with any additional Extended Data display items and Source Data, are available in the online version of the paper; references unique to these sections appear only in the online paper.

**Received 31 December 2015; accepted 15 February 2016.**

- Marteijn, J. A., Lans, H., Vermeulen, W. & Hoeijmakers, J. H. Understanding nucleotide excision repair and its roles in cancer and ageing. *Nature Rev. Mol. Cell Biol.* **15**, 465–481 (2014).
- Ciccia, A. & Elledge, S. J. The DNA damage response: making it safe to play with knives. *Mol. Cell* **40**, 179–204 (2010).
- Wood, R. D., Mitchell, M. & Lindahl, T. Human DNA repair genes, 2005. *Mutat. Res.* **577**, 275–283 (2005).
- Sugasawa, K. *et al.* UV-induced ubiquitylation of XPC protein mediated by UV-DDB-ubiquitin ligase complex. *Cell* **121**, 387–400 (2005).
- Kapetanaki, M. G. *et al.* The DDB1-CUL4A $^{DDB2}$  ubiquitin ligase is deficient in xeroderma pigmentosum group E and targets histone H2A at UV-damaged DNA sites. *Proc. Natl Acad. Sci. USA* **103**, 2588–2593 (2006).
- Fischer, E. S. *et al.* The molecular basis of CRL4 $^{DDB2/CSA}$  ubiquitin ligase architecture, targeting, and activation. *Cell* **147**, 1024–1039 (2011).
- Scrima, A. *et al.* Detecting UV-lesions in the genome: the modular CRL4 ubiquitin ligase does it best! *FEBS Lett.* (2011).
- Reardon, J. T. *et al.* Comparative analysis of binding of human damaged DNA-binding protein (XPE) and *Escherichia coli* damage recognition protein (UvrA) to the major ultraviolet photoproducts: T[c,s]T, T[t,s]T, T[6–4]T, and T[Dewar]T. *J. Biol. Chem.* **268**, 21301–21308 (1993).
- Wittschieben, B. Ø., Iwai, S. & Wood, R. D. DDB1-DDB2 (xeroderma pigmentosum group E) protein complex recognizes a cyclobutane pyrimidine dimer, mismatches, apurinic/aprimidinic sites, and compound lesions in DNA. *J. Biol. Chem.* **280**, 39982–39989 (2005).
- Wang, H. *et al.* Histone H3 and H4 ubiquitylation by the CUL4-DDB-ROC1 ubiquitin ligase facilitates cellular response to DNA damage. *Mol. Cell* **22**, 383–394 (2006).

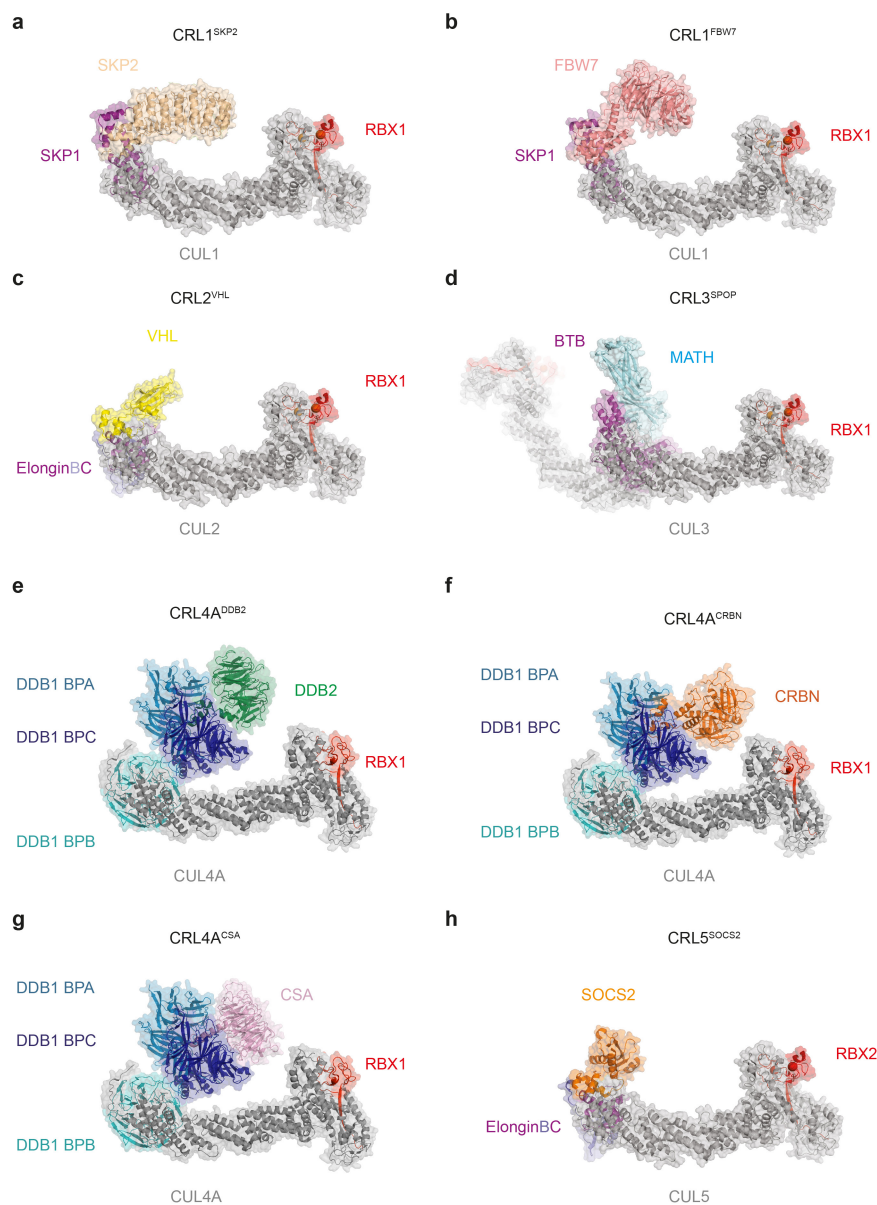
11. Tang, J. & Chu, G. Xeroderma pigmentosum complementation group E and UV-damaged DNA-binding protein. *DNA Repair (Amst.)* **1**, 601–616 (2002).
12. Chu, G. & Chang, E. Xeroderma pigmentosum group E cells lack a nuclear factor that binds to damaged DNA. *Science* **242**, 564–567 (1988).
13. Groisman, R. *et al.* The ubiquitin ligase activity in the DDB2 and CSA complexes is differentially regulated by the COP9 signalosome in response to DNA damage. *Cell* **113**, 357–367 (2003).
14. Lingaraju, G. M. *et al.* Crystal structure of the human COP9 signalosome. *Nature* **512**, 161–165 (2014).
15. Lyapina, S. *et al.* Promotion of NEDD–CUL1 conjugate cleavage by COP9 signalosome. *Science* **292**, 1382–1385 (2001).
16. Takedachi, A., Saijo, M. & Tanaka, K. DDB2 complex-mediated ubiquitylation around DNA damage is oppositely regulated by XPC and Ku and contributes to the recruitment of XPA. *Mol. Cell. Biol.* **30**, 2708–2723 (2010).
17. Zimmerman, E. S., Schulman, B. A. & Zheng, N. Structural assembly of cullin–RING ubiquitin ligase complexes. *Curr. Opin. Struct. Biol.* **20**, 714–721 (2010).
18. Soucy, T. A. T. *et al.* An inhibitor of NEDD8-activating enzyme as a new approach to treat cancer. *Nature* **458**, 732–736 (2009).
19. Schwechheimer, C. *et al.* Interactions of the COP9 signalosome with the E3 ubiquitin ligase SCF<sup>TR1</sup> in mediating auxin response. *Science* **292**, 1379–1382 (2001).
20. Chen, X., Zhang, Y., Douglas, L. & Zhou, P. UV-damaged DNA-binding proteins are targets of CUL-4A-mediated ubiquitination and degradation. *J. Biol. Chem.* **276**, 48175–48182 (2001).
21. Bennett, E. J., Rush, J., Gygi, S. P. & Harper, J. W. Dynamics of Cullin–RING ubiquitin ligase network revealed by systematic quantitative proteomics. *Cell* **143**, 951–965 (2010).
22. Emberley, E. D., Mosadeghi, R. & Deshaies, R. J. Deconjugation of Nedd8 from Cul1 is directly regulated by Skp1–F-box and substrate, and the COP9 signalosome inhibits deneddylated SCF by a noncatalytic mechanism. *J. Biol. Chem.* **287**, 29679–29689 (2012).
23. Enchev, R. I. *et al.* Structural basis for a reciprocal regulation between SCF and CSN. *Cell Rep.* **2**, 616–627 (2012).
24. Enchev, R. I., Schreiber, A., Beuron, F. & Morris, E. P. Structural insights into the COP9 signalosome and its common architecture with the 26S proteasome lid and eIF3. *Structure* **18**, 518–527 (2010).
25. Rockel, B., Schmalzer, T., Huang, X. & Dubiel, W. Electron microscopy and *in vitro* deneddylation reveal similar architectures and biochemistry of isolated human and Flag-mouse COP9 signalosome complexes. *Biochem. Biophys. Res. Commun.* **450**, 991–997 (2014).
26. Joazeiro, C. A. *et al.* The tyrosine kinase negative regulator c-Cbl as a RING-type, E2-dependent ubiquitin-protein ligase. *Science* **286**, 309–312 (1999).
27. Waterman, H., Levkowitz, G., Alroy, I. & Yarden, Y. The RING finger of c-Cbl mediates desensitization of the epidermal growth factor receptor. *J. Biol. Chem.* **274**, 22151–22154 (1999).
28. Yokouchi, M. *et al.* Ligand-induced ubiquitination of the epidermal growth factor receptor involves the interaction of the c-Cbl RING finger and UbcH7. *J. Biol. Chem.* **274**, 31707–31712 (1999).
29. Lorick, K. L. *et al.* RING fingers mediate ubiquitin-conjugating enzyme (E2)-dependent ubiquitination. *Proc. Natl Acad. Sci. USA* **96**, 11364–11369 (1999).
30. Freemont, P. S., Hanson, I. M. & Trowsdale, J. A novel cysteine-rich sequence motif. *Cell* **64**, 483–484 (1991).
31. Zheng, N., Wang, P., Jeffrey, P. D. & Pavletich, N. P. Structure of a c-Cbl–UbcH7 complex: RING domain function in ubiquitin-protein ligases. *Cell* **102**, 533–539 (2000).
32. Zheng, N. *et al.* Structure of the Cul1–Rbx1–Skp1–F box<sup>Skp2</sup> SCF ubiquitin ligase complex. *Nature* **416**, 703–709 (2002).
33. Scott, D. C. *et al.* Structure of a RING E3 trapped in action reveals ligation mechanism for the ubiquitin-like protein NEDD8. *Cell* **157**, 1671–1684 (2014).
34. Li, T., Chen, X., Garbutt, K. C., Zhou, P. & Zheng, N. Structure of DDB1 in complex with a paramyxovirus V protein: viral hijack of a propeller cluster in ubiquitin ligase. *Cell* **124**, 105–117 (2006).
35. Scrima, A. *et al.* Structural basis of UV DNA-damage recognition by the DDB1–DDB2 complex. *Cell* **135**, 1213–1223 (2008).
36. Angers, S. *et al.* Molecular architecture and assembly of the DDB1–CUL4A ubiquitin ligase machinery. *Nature* **443**, 590–593 (2006).
37. Fischer, E. S. *et al.* Structure of the DDB1–CRBN E3 ubiquitin ligase in complex with thalidomide. *Nature* **512**, 49–53 (2014).
38. Ito, T. *et al.* Identification of a primary target of thalidomide teratogenicity. *Science* **327**, 1345–1350 (2010).
39. Lopez-Girona, A. *et al.* Cereblon is a direct protein target for immunomodulatory and antiproliferative activities of lenalidomide and pomalidomide. *Leukemia* **26**, 2326–2335 (2012).
40. Krönke, J. *et al.* Lenalidomide causes selective degradation of IKZF1 and IKZF3 in multiple myeloma cells. *Science* **343**, 301–305 (2014).
41. Lu, G. *et al.* The myeloma drug lenalidomide promotes the cereblon-dependent destruction of Ikaros proteins. *Science* **343**, 305–309 (2014).
42. Brownell, J. E. *et al.* Substrate-assisted inhibition of ubiquitin-like protein-activating enzymes: the NEDD8 E1 inhibitor MLN4924 forms a NEDD8–AMP mimetic *in situ*. *Mol. Cell* **37**, 102–111 (2010).
43. Chew, E.-H. & Hagen, T. Substrate-mediated regulation of cullin neddylation. *J. Biol. Chem.* **282**, 17032–17040 (2007).
44. Pierce, N. W. *et al.* Cand1 promotes assembly of new SCF complexes through dynamic exchange of F box proteins. *Cell* **153**, 206–215 (2013).
45. Dubiel, W. Resolving the CSN and CAND1 paradoxes. *Mol. Cell* **35**, 547–549 (2009).
46. Kucukelbir, A., Sigworth, F. J. & Tagare, H. D. Quantifying the local resolution of cryo-EM density maps. *Nature Methods* **11**, 63–65 (2014).
47. Landau, M. *et al.* ConSurf 2005: the projection of evolutionary conservation scores of residues on protein structures. *Nucleic Acids Res.* **33**, W299–W302 (2005).

**Supplementary Information** is available in the online version of the paper.

**Acknowledgements** We thank K. Böhm for technical assistance in protein expression and purification, D. Hess and J. Seebacher for mass spectrometry analysis, and M. Jones, B. Martoglio, R. Assenberg, C. Logel, I. Bechtold and M. Renatus for help developing the TR-FRET and PT22 CSN assays. We thank B. Anderson and A. Fecteau-Lefebvre ('C-CINA') for technical support and TEM maintenance. We are grateful to T. Walz and D. Barford for help and discussions. Part of this work was performed at beamline X10SA of the Swiss Light Source. This work was supported by the Novartis Research Foundation and grants to N.H.T. from the European Research Council (ERC-2014-ADG 666068 CSNCRL) and to H.S. from the Swiss initiative for Systems Biology (SystemsX.ch grant 'C-CINA'). G.P. was supported by long-term fellowships of the European Molecular Biology Organization (EMBO; ALTF-1350-2013) and the Human Frontier Science Program (HFSP; LT000210/2014). W.I.M. was supported by the Boehringer Ingelheim Fonds.

**Author Contributions** S.C., E.S.F. and N.H.T. co-led the study. S.C. prepared the specimens for EM data collection and collected EM data with contributions from K.N.G.. S.C. performed EM data processing. E.S.F. developed the binding and activity assays with input from U.H., G.P. and A.P. G.M.L. designed and created CSN mutants with input from S.C. E.S.F., M.F., G.M.L. and W.A. purified proteins for crystallography, cryo-EM and biochemical assays. A.P. and E.S.F. performed functional assays and analysed the results. G.M.L. crystallized CSN. R.D.B. and G.M.L. collected the X-ray diffraction data. R.D.B. carried out the crystallographic analysis, built the cryo-EM models with input from S.C., and interpreted the results with S.C. and N.H.T. K.N.G., R.S.P. and H.S. provided access to TEM microscopes and initial training. W.I.M. designed the RBX1–CSN4 fusion construct and purified protein for EM studies. R.E.J.B. and R.B.T. designed and performed the chemical syntheses. S.M. and K.S. performed cellular assays. S.C., E.S.F., R.D.B. and N.H.T. wrote the manuscript with input from G.P.

**Author Information** The cryo-EM structures are available from the Electron Microscopy Data Bank under accessions EMD-3313 (CSN–N<sub>8</sub>CRL4A at 6.7 Å), EMD-3314 (CSN–N<sub>8</sub>CRL4A at 6.4 Å), EMD-3315 (CSN–N<sub>8</sub>CRL4A at 8.8 Å) and EMD-3316 (CSN–N<sub>8</sub>CRL4A<sup>DDB2</sup> at 8.3 Å). The negative-stain CSN–N<sub>8</sub>CRL3<sup>ΔSPOP</sup> map is available under accession EMD-3317. The coordinates and structure factors for the CSN P1 crystal form have been deposited in the PDB under accession number 4WSN. Reprints and permissions information is available at [www.nature.com/reprints](http://www.nature.com/reprints). The authors declare no competing financial interests. Readers are welcome to comment on the online version of the paper. Correspondence and requests for materials should be addressed to N.H.T. ([nicolas.thoma@fmi.ch](mailto:nicolas.thoma@fmi.ch)).



### Extended Data Figure 1 | Atomic models of the canonical CRL families.

**a**, CUL1–RBX1–SKP1–SKP2 (PDB accession codes 1LDK and 1FQV).

**b**, CUL1–RBX1–SKP1–FBW7 (PDBs accession codes 1LDK and 2OVP).

**c**, CUL2–RBX1–ElonginB–ElonginC–VHL (PDB accession codes 1LDK and 1VCB). **d**, Dimeric CUL3–RBX1–SPOP. The SPOP protein includes a

BTB and a MATH domain. (PDB accession codes 1LDK, 4EOZ and

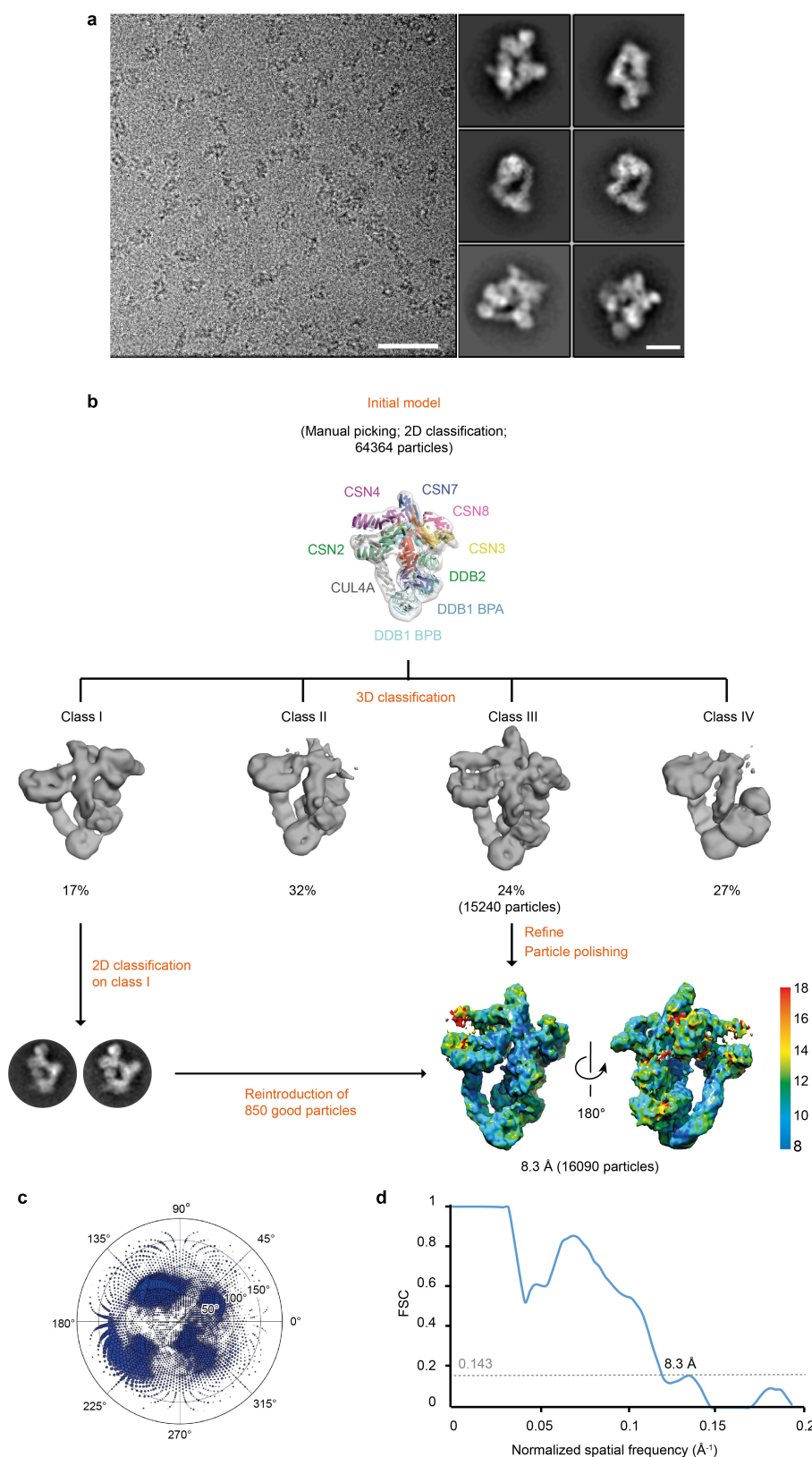
3HU6). **e**, CUL4A–RBX1–DDB1–DDB2 (PDB accession code 4A0K).

**f**, CUL4A–RBX1–DDB1–CRBN (PDB accession codes 4A0K and 4CI1).

**g**, CUL4A–RBX1–DDB1–CSA (PDB accession codes 4A0K and 4A11).

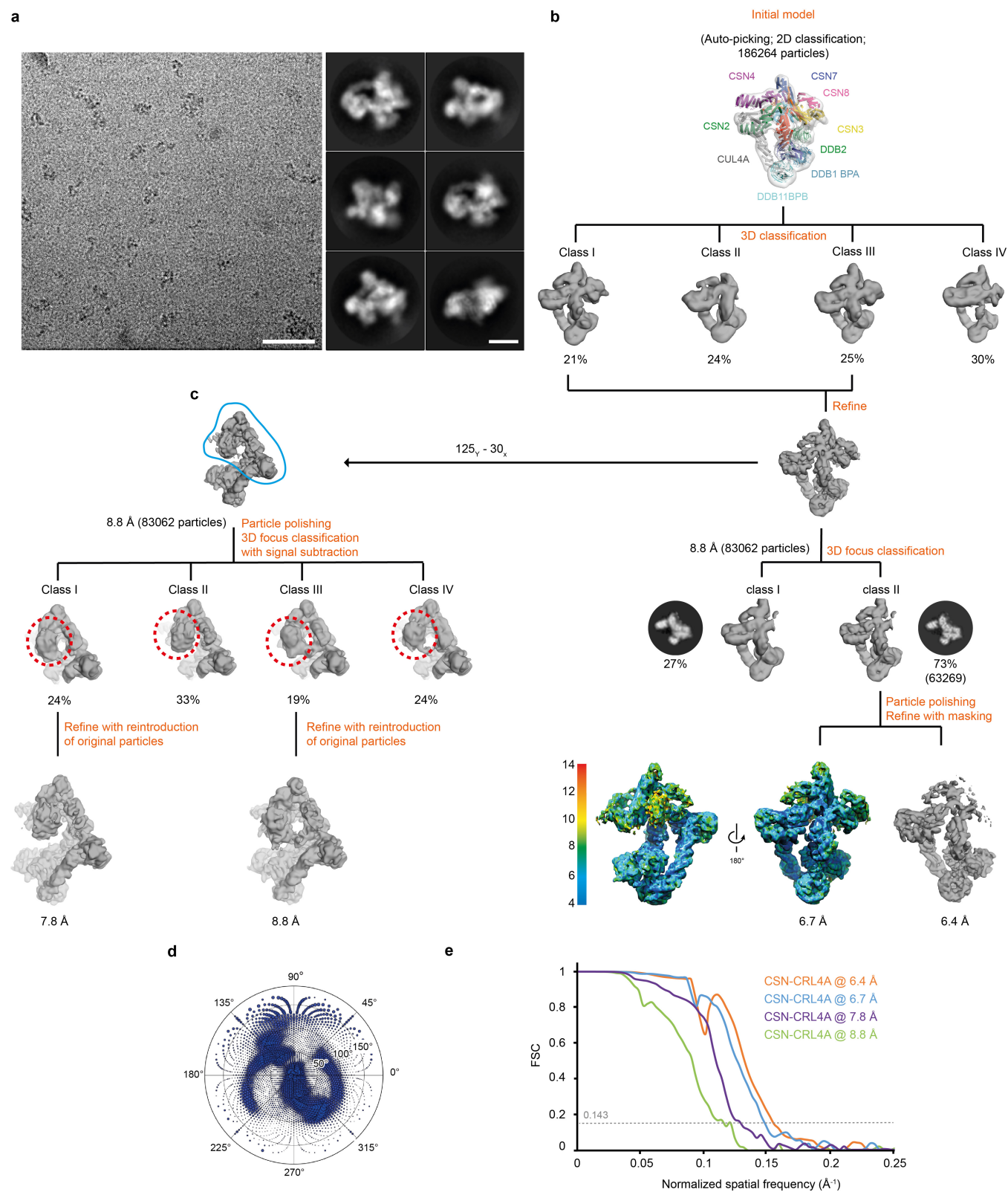
**h**, CUL5–RBX1–ElonginB–ElonginC–SOCS2 (PDB accession codes 1LDK, 4JGH and 2C9W).





**Extended Data Figure 2 | Classification and refinement procedures for the CSN-N<sub>8</sub>CRL4A<sup>DDB2</sup> complex.** **a**, Representative micrographs (scale bar, 50 nm; the whole data set includes 1,427 micrographs) and reference-free two-dimensional (2D) class averages (scale bar, 10 nm). **b**, After reference-free 2D classification, the initial model obtained from preliminary cryo-EM studies of CSN-N<sub>8</sub>CRL4A<sup>DDB2</sup> was low-pass filtered

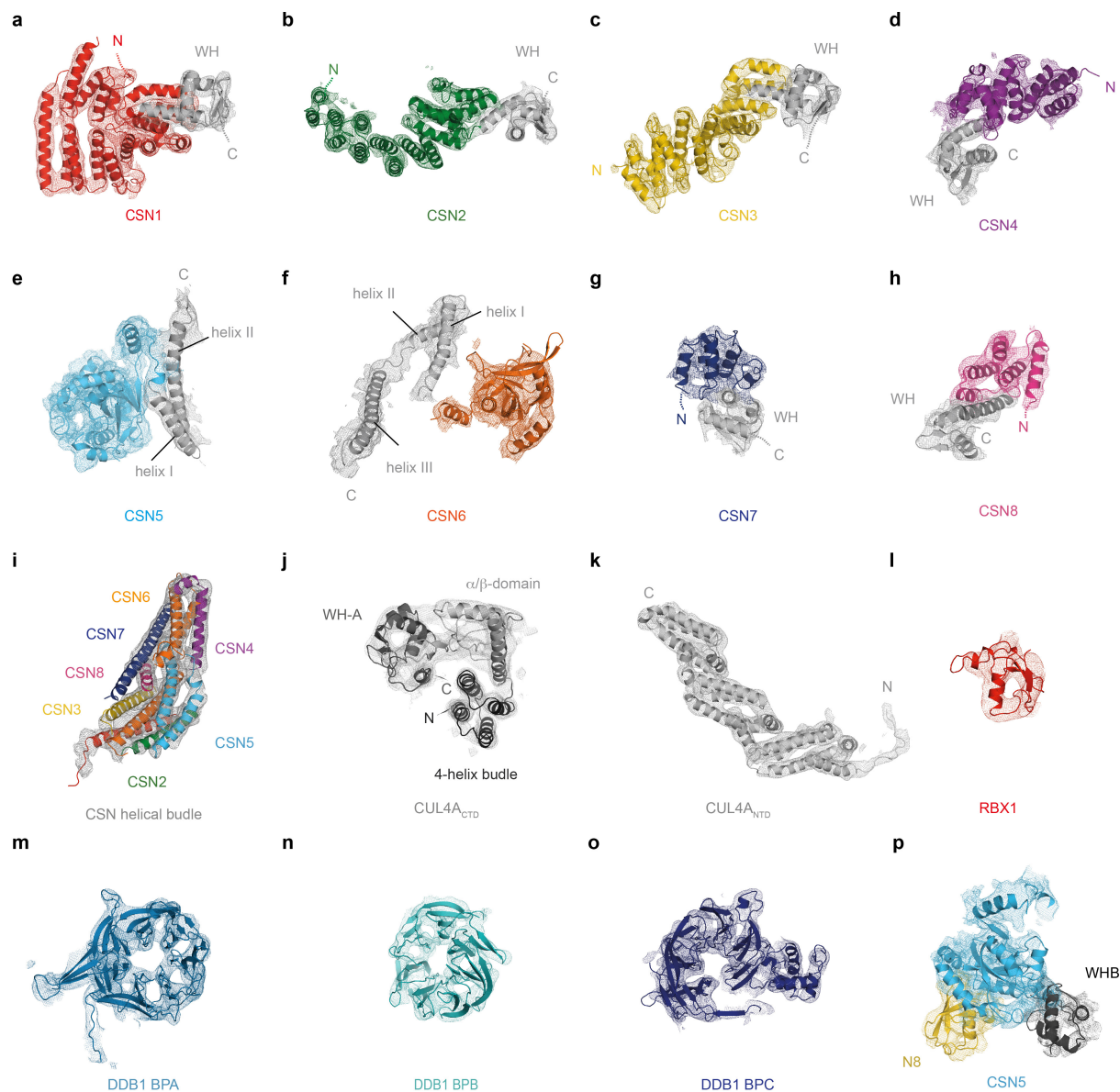
to 60 Å and subjected to 3D classification to discard large misassembled particles. Class I was subjected to a second round of 2D classification and particles showing an intact assembly were merged with the particles included in the Class III, leading to 16,090 particles. The final model was refined to 8.3 Å resolution. **c**, Angular distribution plot. **d**, Gold-standard Fourier shell correlation curve (FSC).



**Extended Data Figure 3 | Classification and refinement procedures for the CSN-N<sub>8</sub>CRL4A complex.** **a**, Representative micrographs (scale bar, 50 nm; the whole data set includes 2,626 micrographs) and reference-free 2D class averages (scale bar, 10 nm). **b**, After 2D classification, the initial model obtained from preliminary cryo-EM studies of CSN-N<sub>8</sub>CRL4A<sup>DDB2</sup> was low-pass filtered to 60 Å and subjected to a first round of 3D classification to discard large misassembled particles. Particles included in class I and class III were combined and refined in a 8.8 Å reconstruction map. To improve the resolution, we performed further 3D classification into two classes. The most populated (73%, 63,269 particles) class shows better resolution and finer details as suggested by the slice-through *Z* of the map (black circles with particles on the left and right side of the 3D model). Refinement with a soft mask around the more rigid part

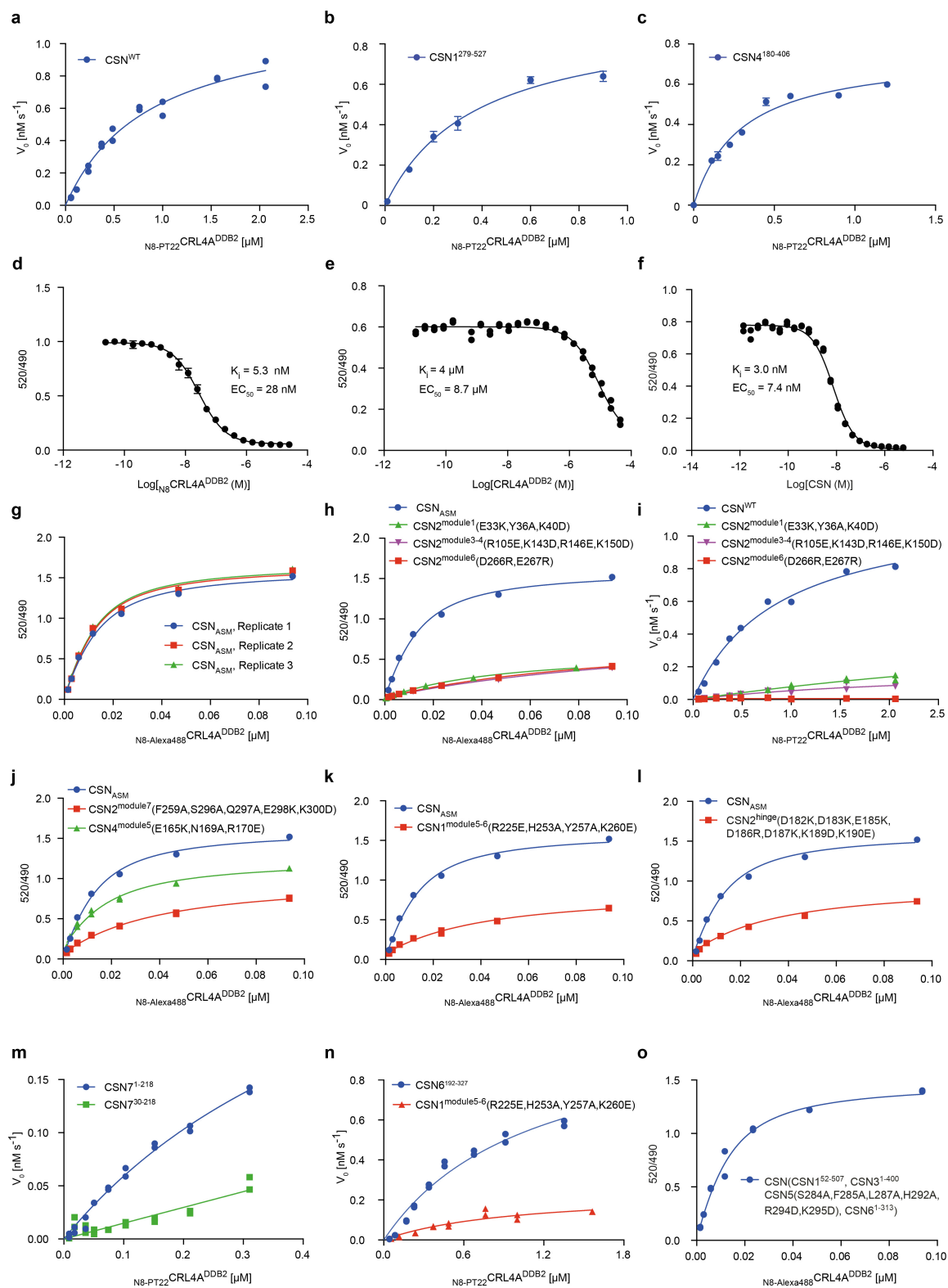
of the complex led to a 6.4 Å resolution map. Refinement of the same set of particles with a soft mask around the whole complex led to a 6.7 Å resolution map. The 6.7 Å reconstruction is coloured according to the local resolution as estimated with ResMap<sup>46</sup>. **c**, The same set of particles that led to the 8.8 Å structure were also subjected to particle polishing and 3D focus classification on CSN (mask drawn as a blue line) with signal subtraction of CUL4A-DDB1. The data was divided into four classes revealing the dynamic of the CSN5-CSN6 heterodimer on cullin binding (Fig. 3a–c) (highlighted with a dashed red circle). Refinement of class I and class III led to a 7.8 Å and 8.8 Å resolution maps, respectively. **d**, Angular distribution of the particles included in the 6.4 Å (and 6.7 Å) data set. **e**, Gold-standard Fourier shell correlation curves (FSC) for the four refined models.





**Extended Data Figure 4 | The overall fold of each protein within the CSN-N8CRL4A complex. a–r,** Unless specified, the individual subunits found in 6.4 Å CSN-N8CRL4A map are shown as cartoon representation. The cryo-EM density of each subunit is shown as a coloured mesh. CSN1 (a); CSN2 (b); CSN3 (c); CSN4 (d) CSN5 (8.8 Å resolution CSN-N8CRL4A map) (e) and CSN6 (8.8 Å resolution CSN-N8CRL4A map) (f); CSN7 (g);

and CSN8 (h). Cryo-EM density and architecture of the CSN helical bundle found in the 6.7 Å CSN-N8CRL4A cryo-EM map (i); C-terminal (j) and N-terminal domain of CUL4A (k); RBX1 (l); DDB1 WD40  $\beta$ -propeller domains BPA (m); BPB (n); and BPC (o); NEDD8 (N8) and WHB binding to CSN5 as shown in the 8.8 Å resolution CSN-N8CRL4A map (Fig. 1d) (p).



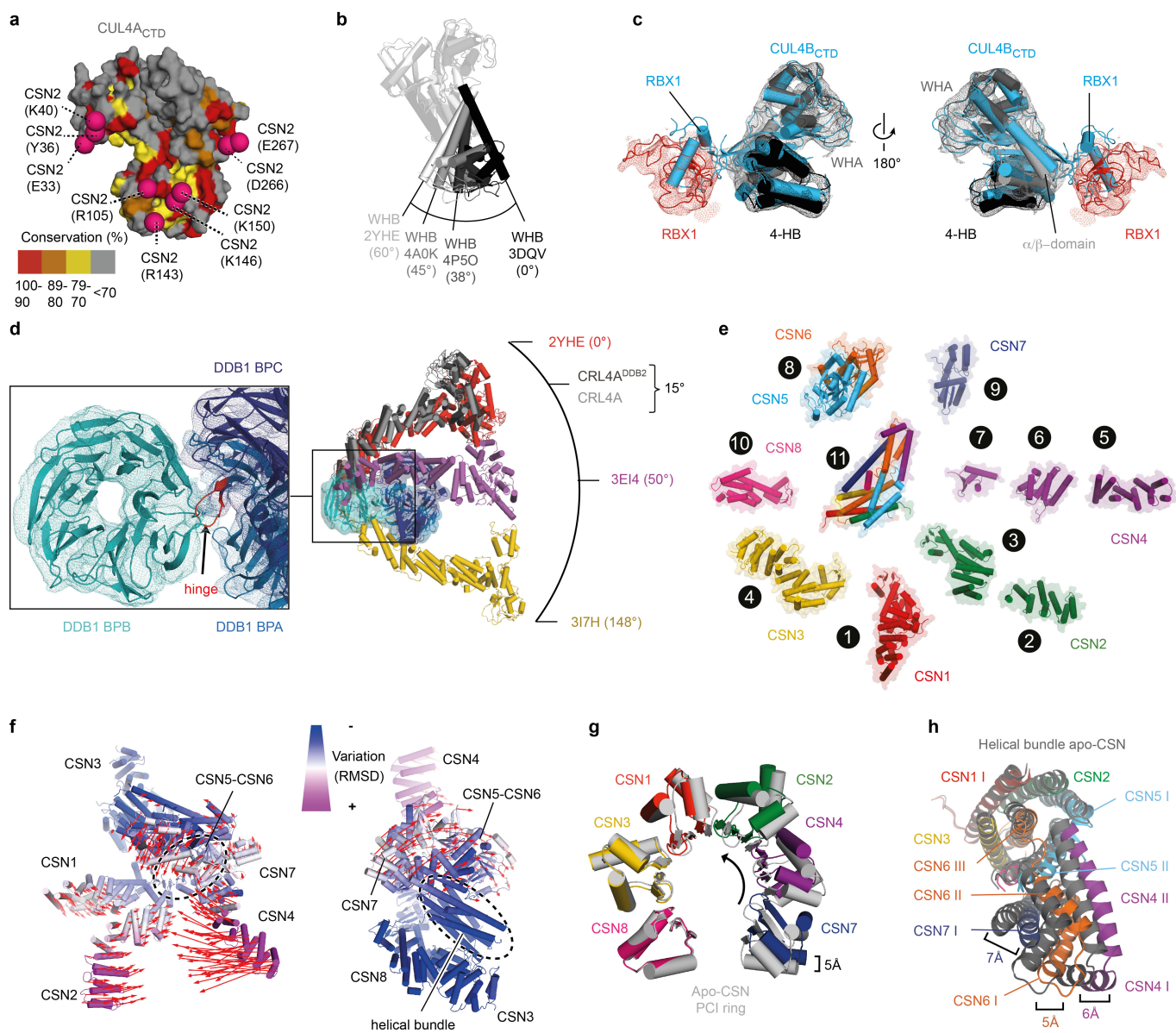
Extended Data Figure 5 | See next page for caption.

**Extended Data Figure 5 | Biophysical characterization of CSN mutants.**

Determination of steady-state kinetics using the  $N_8$ -PT22CRL4A<sup>DDB2</sup> substrate. Initial rates observed following incubation of CSN or mutants (at 10 nM, unless specified otherwise) with increasing concentrations of  $N_8$ -PT22CRL4A<sup>DDB2</sup>. The fit of the observed data to the Michaelis–Menten equation is shown in **a**, for 2 nM wild-type CSN (the experiment shown is a representative of four technical replicates ( $n = 2$ )); **b**, 20 nM CSN1<sup>279–527</sup> ( $n = 3$ ); **c**, 10 nM CSN4<sup>180–406</sup> ( $n = 3$ ). **d**, Dose response curve for the CSN– $N_8$ -Alexa488CRL4A<sup>DDB2</sup> complex obtained by increasing concentration of unlabelled  $N_8$ CRL4A ( $n = 3$ ). **e**, As in **d**, but with increasing concentration of CRL4A<sup>DDB2</sup> ( $n = 2$ ). **f**, As in **d**, but with increasing concentration of unlabelled CSN ( $n = 2$ ). **g**, Biotinylated CSN active site mutant (CSN<sub>ASM</sub>) at 10 nM and terbium–streptavidin (Tb–streptavidin) conjugate (4 nM) were mixed with increasing concentrations of  $N_8$ -Alexa488CRL4A<sup>DDB2</sup> and the dissociation constants of CSN for  $N_8$ -Alexa488CRL4A<sup>DDB2</sup> obtained by fitting the TR-FRET signal assuming equimolar binding (see Supplementary Information). Three technical replicates are shown as overlaid curves to illustrate the reproducibility of the experiment. **h**, Binding of CSN<sub>ASM</sub> (10 nM) and biotin-labelled ASM variants of CSN

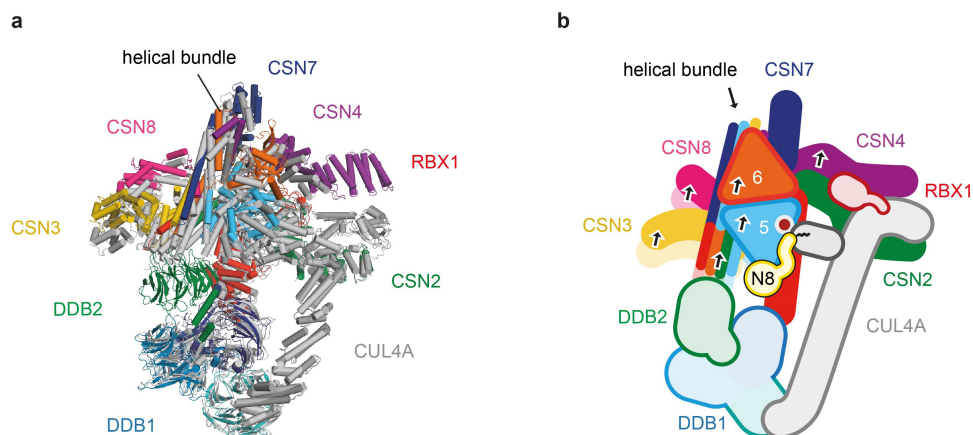
mutants at 10 nM (CSN (CSN2 (E33K, Y36A, K40D))), (CSN (CSN2 (R105E, K143D, R146E, K150D))), and (CSN (CSN2 (D266R, E267R))) to  $N_8$ -Alexa488CRL4A<sup>DDB2</sup> ( $n = 2$ ). **i**, Steady-state kinetics for the CSN mutants (2 nM) used in **h** ( $n = 2$ ). **j**, **k**, **l**, Binding of  $N_8$ -Alexa488CRL4A<sup>DDB2</sup> to CSN<sub>ASM</sub> (10 nM) and biotin-labelled ASM variants of the CSN mutants at 10 nM (CSN (CSN2 (F259A, S296A, Q297A, E298K, K300D))) and (CSN (CSN4 (E165K, N169A, R170E))) (**j**) ( $n = 2$ ); (CSN (CSN1 (R225E, H253A, Y257A, K260E))) (**k**) ( $n = 2$ ); (CSN (CSN2 (D182K, D183K, E185K, D186R, D187K, K189D, K190E))) (**l**) ( $n = 2$ ). **m**, **n** Steady-state kinetics for the CSN mutants (CSN (CSN7<sup>1–218</sup>)) (2 nM) and (CSN (CSN7<sup>30–218</sup>)) (2 nM) (**m**) ( $n = 2$ ); 150 nM ((CSN(CSN6<sup>192–327</sup>)) ( $n = 2$ ) and 2 nM (CSN (CSN1 (R225E, H253A, Y257A, K260E))) ( $n = 2$ ) (**n**). In **n**, the deviation between fit and data for (CSN (CSN6<sup>192–327</sup>)) may suggest cooperative behaviour. **o**, Binding of the biotin-labelled ASM variant of the CSN mutant at 10 nM (CSN (CSN1<sup>52–507</sup>, CSN3<sup>1–400</sup>, CSN5 (S284A, F285A, L287A, H292A, R294D, K295D), CSN6<sup>1–313</sup>)) to  $N_8$ -Alexa488CRL4A<sup>DDB2</sup> ( $n = 2$ ). Data are technical replicates as indicated and shown as individual data points (for  $n \leq 2$ ) or mean  $\pm$  s.d. (for  $n \geq 3$ ) in addition to the fit to the mean curve.



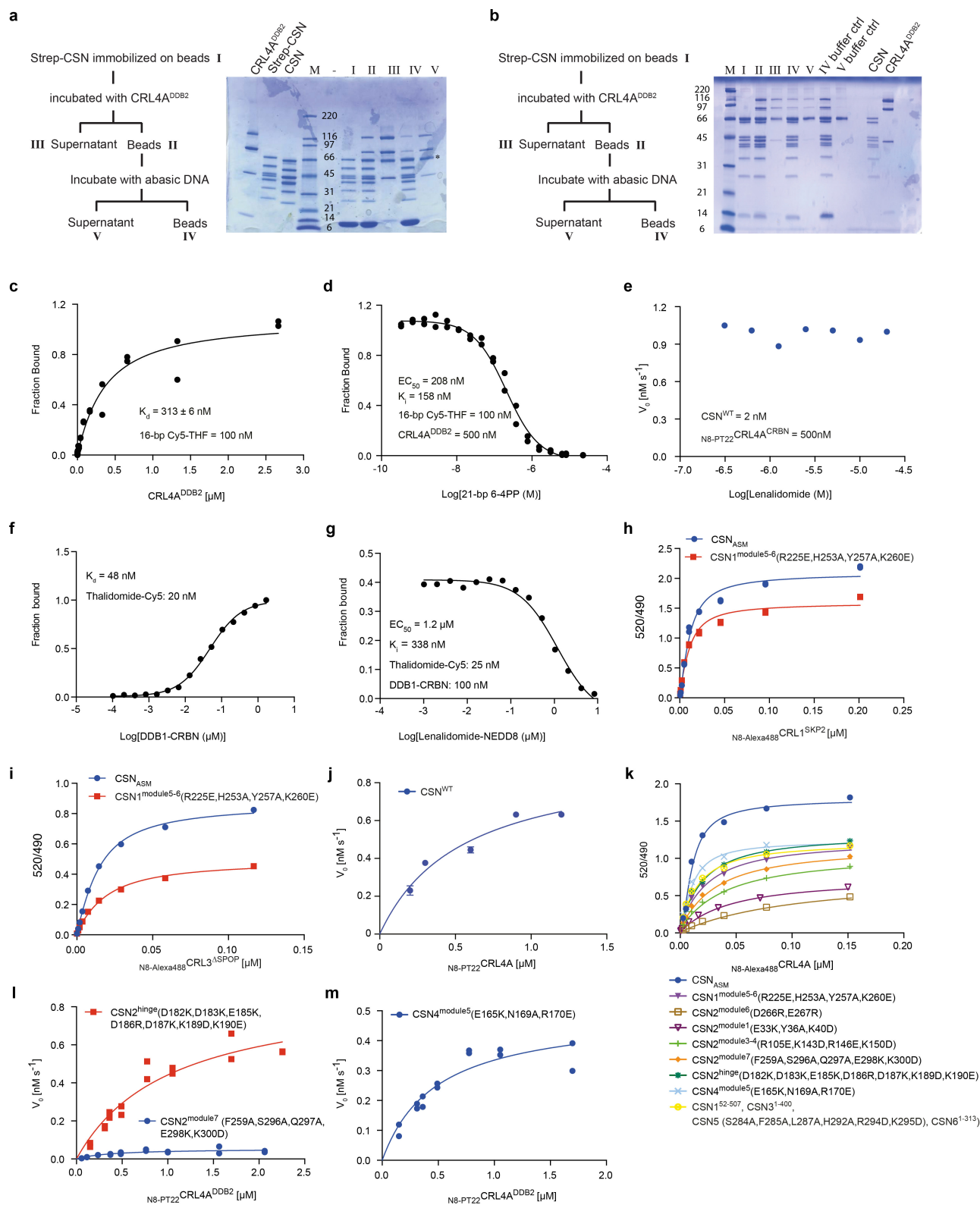


**Extended Data Figure 6 | Structural plasticity of CSN-CRL4 complexes.** **a**, The CUL4A C-terminal domain (CUL4A<sub>CTD</sub>) is coloured by conservation across all cullin families (automatically defined in ConSurf)<sup>47</sup>. Residues in proximity of the CSN2-CUL4A<sub>CTD</sub> interaction patches (shown as spheres) (Fig. 2a) are highly conserved. **b**, Superimposing WHA,  $\alpha/\beta$ -domain and 4-HB domains (shown as transparent cartoon) of different structures (PDB accession codes 2HYE, 4A0K, 4P5O, 3DQV) reveal flexibility of the WHB domain. **c**, Superimposition of the CAND1-CUL4B-RBX1 structure (PDB accession code 4A0C, cyan) with the CUL4A-RBX1 conformation found in the cryo-EM CSN-N<sub>8</sub>CRL4A structures. **d**, The DDB1 inter-domain hinge shown in the close-up enables the DDB1 BPA and BPC subdomains to adopt different position with respect to DDB1 BPB allowing the CUL4A arm to swing at least 150°. The presence or absence of the substrate receptors does not affect the position of the cullin arm within CSN-N<sub>8</sub>CRL4A complexes. **e**, Rigid body dissection of apo-CSN.

Boundaries (1) CSN1: 77–463; (2) CSN2: 30–180; (3) CSN2: 192–411; (4) CSN3: 3–345; (5) CSN4: 1–179; (6) CSN4: 180–298 (7) CSN4: 266–366; (8) CSN5: 24–249, CSN6: 29–296; (9) CSN7: 8–165; (10) CSN8: 11–167 (11) helical bundle: CSN1: 464–505, CSN2: 412–443, CSN3: 346–403, CSN4: 367–406, CSN5: 250–333, CSN6: 217–316, CSN7: 166–216, CSN8: 194–209. **f**, Structural comparison across 10 CSN crystallographic conformers, including *P1* and *P3*<sub>1</sub> (PDB accession codes 4D10 and 4D18) crystals, provides evidence for large-scale conformational change. The models are coloured by levels of root mean squared deviation (RMSD). **g**, Superimposition of the PCI ring from apo-CSN (PDB accession code 4D18, grey) and the cullin-bound CSN conformation (Fig. 3d) (coloured as in Fig. 1). **h**, Superimposition of the helical bundle from apo-CSN (PDB accession code 4D18, grey) and in the cullin-bound CSN conformation showing structural rearrangement of the helical bundle on cullin binding (coloured as in Fig. 1).



**Extended Data Figure 7 | Receptor-induced remodelling of CSN.** **a**, Superimposition of atomic models for the CSN–N<sub>8</sub>CRL4A<sup>DDB2</sup> (Fig. 1a) and CSN–N<sub>8</sub>CRL4A (Fig. 1b, grey). **b**, Schematic of the CSN subunits displacement shown in **a**, induced by the substrate receptor DDB2.



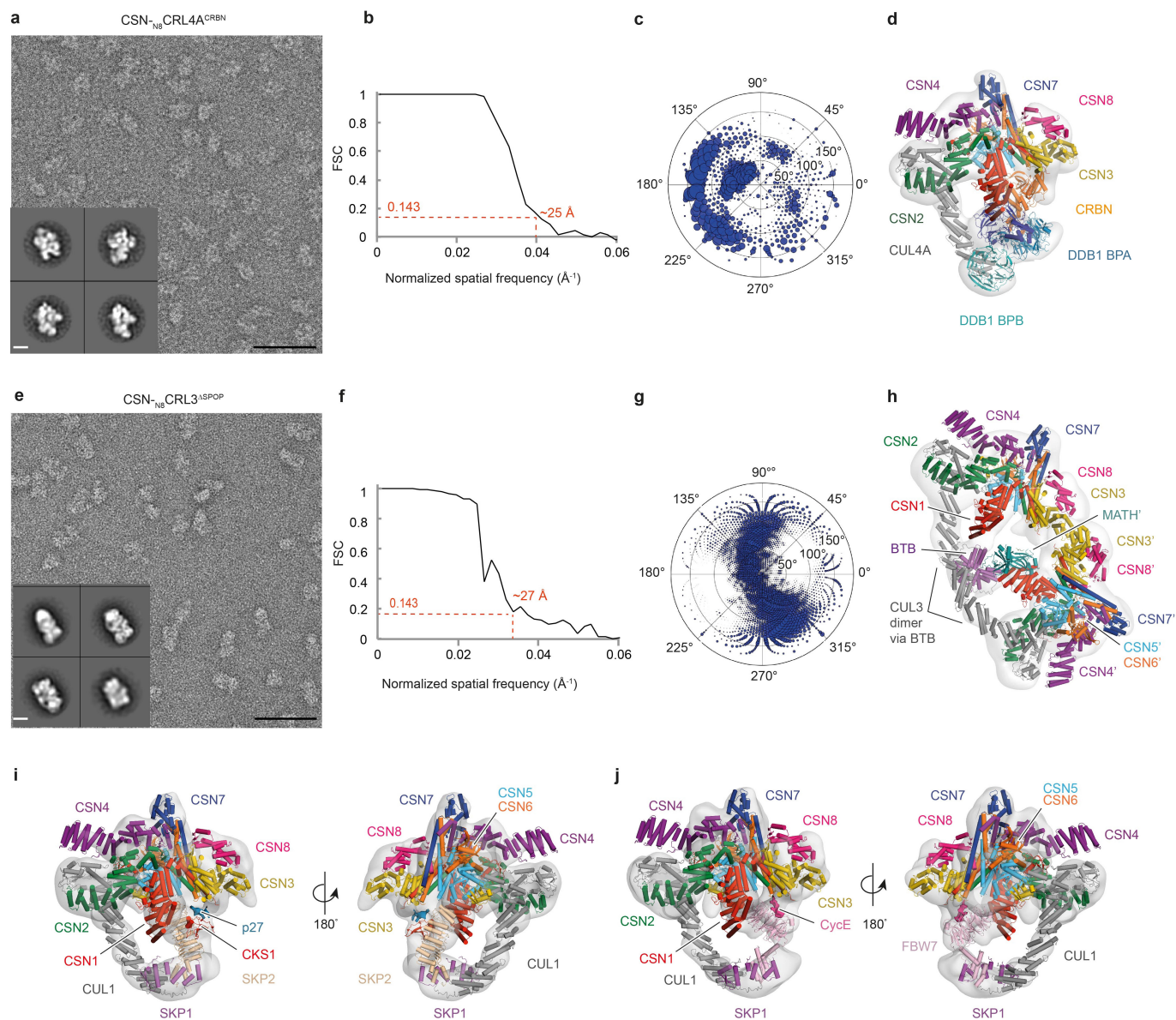
Extended Data Figure 8 | See next page for caption.



**Extended Data Figure 8 | Substrate binding inhibits CSN activity.**

StrepII-tagged CSN was immobilized on Strep-Tactin beads and incubated with either CRL4A<sup>DDB2</sup> (a) or N8CRL4A<sup>DDB2</sup> (b). Following excessive washing, CRL4A<sup>DDB2</sup> complexes remained bound to immobilized CSN (lane II). The immobilized complexes were subsequently incubated with 10  $\mu$ M of a 31-bp THF oligo. Coomassie stained SDS-PAGE analysis revealed that CRL4A<sup>DDB2</sup> and N8CRL4A<sup>DDB2</sup> were dislodged in presence of DNA (lane IV) but not in a buffer control (lane IV buffer control in b). c, Increasing amounts of CRL4A<sup>DDB2</sup> were mixed with a 16-bp Cy5-THF oligo and the dissociation constant  $K_d$  was determined by fitting the data to a model assuming one binding site ( $n = 2$ ). d, Increasing concentrations of unlabelled 21-bp 6-4PP oligo were mixed with 16-bp Cy5-THF (100 nM) and CRL4A<sup>DDB2</sup> (500 nM). The half-maximum effective concentration ( $EC_{50}$ ) was used to calculate the  $K_i$  (see Supplementary Information) inhibition constant ( $K_i$  is equivalent to  $K_d$  of 21-bp 6-4PP for CRL4A<sup>DDB2</sup>) ( $n = 2$ ). e, Dose-response experiment with increasing concentration of lenalidomide titrated into CSN (2 nM) and N8-PT22CRL4A<sup>CRBN</sup> (500 nM) ( $n = 1$ ). f, Binding of thalidomide-Cy5 to DDB1-CRBN ( $n = 1$ ). g, Increasing concentration of lenalidomide-NEDD8 titrated into thalidomide-Cy5 (25 nM) and DDB1-CRBN (100 nM).  $EC_{50}$  was used

to calculate  $K_i$ . These data indicate that lenalidomide-NEDD8 directly compete with thalidomide binding to DDB1-CRBN, and hence uses the same binding site ( $n = 1$ ). h, i, Affinity of the biotin-labelled ASM variant of the CSN mutant (CSN (CSN1 (R225E, H253A, Y257A, K260E))) (10 nM) for N8CRL1<sup>SKP2</sup> ( $n = 2$ ) (h) and N8CRL3 <sup>$\Delta$ SPOP</sup> (i), determined by mixing increasing amounts of N8-Alexa488CRL1<sup>SKP2</sup> and N8-Alexa488CRL3 <sup>$\Delta$ SPOP</sup> respectively with CSN (10 nM) and Tb-streptavidin (4 nM). Data were fitted as described in the Supplementary Information ( $n = 2$ ). j, Steady-state kinetics of 2 nM CSN with a N8-PT22CRL4A substrate ( $n = 3$ ). k, Binding curves for the biotin-labelled ASM variant of the CSN mutants (listed below the panel) to N8-Alexa488CRL4A ( $n = 2$ ). One representative fit for each CSN mutant is shown from two technical replicates. l, Steady-state kinetics of CSN mutants (CSN (CSN2 (D182K, D183K, E185K, D186R, D187K, K189D, K190E))) and (CSN (CSN2 (F259A, S296A, Q297A, E298K, K300D))) with a N8-PT22CRL4A<sup>DDB2</sup> substrate ( $n = 2$ ). m, Steady-state kinetics of 2 nM CSN mutant (CSN (CSN4 (E165K, N169A, R170E))) with a N8-PT22CRL4A<sup>DDB2</sup> substrate ( $n = 2$ ). Data are technical replicates as indicated and shown as individual data points (for  $n \leq 2$ ) or mean  $\pm$  s.d. (for  $n \geq 3$ ) in addition to the fit to the mean curve.



### Extended Data Figure 9 | Negative-stain single-particle EM reconstructions of CSN-N8CRL4A<sup>CRBN</sup> and CSN-N8CRL3<sup>ΔSPOP</sup>.

**a**, Representative micrographs (scale bar, 50 nm; the whole data set includes 265 micrographs) and reference-free 2D class averages (scale bar, 10 nm) for CSN-N8CRL4A<sup>CRBN</sup>. **b**, Gold-standard Fourier shell correlation curve (FSC) for the CSN-N8CRL4A<sup>CRBN</sup> reconstruction. **c**, Angular distribution for CSN-N8CRL4A<sup>CRBN</sup>. **d**, CSN-N8CRL4A<sup>CRBN</sup> density fitted with DDB1-CRBN (PDB accession code 4CI1) and the cryo-EM CSN-N8CRL4A model (without DDB1). **e**, Representative micrographs (scale bar, 50 nm; the whole data set includes 104 micrographs) and reference-free 2D class averages (scale bar, 10 nm) for CSN-N8CRL3<sup>ΔSPOP</sup>. **f**, Gold-standard FSC for the CSN-N8CRL3<sup>ΔSPOP</sup> reconstruction. **g**, Angular distribution of the CSN-N8CRL3<sup>ΔSPOP</sup> particles. **h**, Crystallographic

models of CUL3<sup>NTD</sup>-BTB (PDB accession code 4EOZ), the substrate receptor MATH (PDB accession code 3HQ1), and the NEDD8-engaged CSN cryo-EM model fitted in the CSN-N8CRL3<sup>ΔSPOP</sup> negative-stain EM map. Modelling of the N-terminal MATH domain of SPOP (residues 28–166, Extended Data Fig. 1d) reveals its position within the CSN-N8CRL3<sup>ΔSPOP</sup> architecture. **i**, Fit of the cullin-bound CSN model (Fig. 3d) and crystallographic models of N8CRL1<sup>SKP2/CKS1/p27</sup> (PDB accession codes 1LDK, 3DQV, 2ASS) into the CSN-N8CRL1<sup>SKP2/CKS1</sup> negative-stain map (EMDB accession code 2173). **j**, Fit of the cullin-bound CSN model (Fig. 3d) and crystallographic models of N8CRL1<sup>FBW7/CycE</sup> (PDB accession codes 1LDK and 2OVP) into the CSN-N8CRL1<sup>FBW7</sup> negative-stain map (EMDB accession code 2174).

**Extended Data Table 1 | Determination of CSN affinities for  $N_8$ CRLs, apo-CSN crystallographic data collection and refinement statistics****a. Binding of CSN to  $N_8$ CRL4A**

	$K_d$ [nM]	$k_{cat}$ [ $s^{-1}$ ]	$K_m$ [nM]
CSN (wild-type)	$3.7 \pm 1.8$	$0.47 \pm 0.07$	$547 \pm 195$
CSN1 <sup>module5-6</sup> (R225E,H253A,Y257A,K260E)	$21.1 \pm 5.7$	-	-
CSN2 <sup>module1</sup> (E33K,Y36A,K40D)	$38.6 \pm 5.9$	-	-
CSN2 <sup>module3-4</sup> (R105E,K143D,R146E,K150D)	$35.0 \pm 5.7$	-	-
CSN2 <sup>hinge</sup> (D182K,D183K,E185K,D186R,D187K,K189D,K190E)	$15.0 \pm 2.8$	-	-
CSN2 <sup>module7</sup> (F259A,S296A,Q297A,E298K,K300D)	$27.2 \pm 4.9$	-	-
CSN2 <sup>module6</sup> (D266R,E267R)	$100.8 \pm 12.4$	-	-
CSN4 <sup>module5</sup> (E165K,N169A,R170E)	$6.5 \pm 1.7$	-	-
CSN1 <sup>52-507</sup> , CSN3 <sup>1-400</sup> , CSN5(S284A,F285A,L287A,H292A,R294D,K295D), CSN6 <sup>1-313</sup>	$11.9 \pm 3.9$	-	-

**b. Binding of CSN to  $N_8$ CRL1<sup>SKP2</sup>**

	$K_d$ [nM]
CSN (wild-type)	$6.0 \pm 2.0$
CSN1 <sup>module5-6</sup> (R225E,H253A,Y257A,K260E)	$5.9 \pm 2.4$

**c. Binding of CSN to  $N_8$ CRL3<sup>ASPOP</sup>**

	$K_d$ [nM]
CSN (wild-type)	$7.1 \pm 3.4$
CSN1 <sup>module5-6</sup> (R225E,H253A,Y257A,K260E)	$13.6 \pm 0.6$

**d. Crystallographic data collection and refinement statistics**

	CSN P1
<b>Data collection</b>	
Space group	P1
Cell dimensions	
$a, b, c$ (Å)	150.66, 151.00, 336.76,
$\alpha, \beta, \gamma$ (°)	92.33, 92.36, 119.88
$R_{sym}$ (%)	7.2 (132)*
$R_{meas}$ (%)	9.8 (180)
$R_{pim}$ (%)	6.5 (120)
CC <sub>1/2</sub> outer shell; number of pairs	0.166; $n = 3185$
$\langle I/\sigma I \rangle$	5.4 (0.6)
Completeness (%)	94.9 (88.7)
Multiplicity	1.9 (1.9)
<b>Refinement</b>	
Resolution range (Å)	50–5.5 (5.61–5.50)
No. reflections	79098 (4292)
$R_{work} / R_{free}$ (%)	25.41 / 28.21
No. atoms	
Protein	124422
Zn <sup>2+</sup> ions	6
R.m.s deviations	
Bond lengths (Å)	0.005
Bond angles (°)	0.839

\*Highest resolution shell is shown in parenthesis

a, Affinity of CSN for  $N_8$ CRL4A. b, Affinity of CSN for  $N_8$ CRL1<sup>SKP2</sup>. c, Affinity of CSN for  $N_8$ CRL3<sup>ASPOP</sup>. d, Apo-CSN data collection and refinement statistics. a–c, Experiments carried out as detailed in Extended Data Figs 5 and 8.



# Structure of promoter-bound TFIID and model of human pre-initiation complex assembly

Robert K. Louder<sup>1</sup>, Yuan He<sup>2,3†</sup>, José Ramón López-Blanco<sup>4</sup>, Jie Fang<sup>5</sup>, Pablo Chacón<sup>3</sup> & Eva Nogales<sup>2,3,5</sup>

**The general transcription factor IID (TFIID) plays a central role in the initiation of RNA polymerase II (Pol II)-dependent transcription by nucleating pre-initiation complex (PIC) assembly at the core promoter. TFIID comprises the TATA-binding protein (TBP) and 13 TBP-associated factors (TAF1–13), which specifically interact with a variety of core promoter DNA sequences. Here we present the structure of human TFIID in complex with TFIIA and core promoter DNA, determined by single-particle cryo-electron microscopy at sub-nanometre resolution. All core promoter elements are contacted by subunits of TFIID, with TAF1 and TAF2 mediating major interactions with the downstream promoter. TFIIA bridges the TBP–TATA complex with lobe B of TFIID. We also present the cryo-electron microscopy reconstruction of a fully assembled human TAF-less PIC. Superposition of common elements between the two structures provides novel insights into the general role of TFIID in promoter recognition, PIC assembly, and transcription initiation.**

Initiation of transcription by Pol II represents a major control point for eukaryotic cells, and its regulation is the primary means of differential gene expression in metazoans<sup>1</sup>. A prerequisite for Pol II transcription is the recruitment of the general transcription factors TFIIA, -B, -D, -E, -F, and -H, to the core promoter, where they assemble with Pol II into the PIC<sup>2</sup>. The process is thought to begin with the recruitment of TFIID and TFIIA to the core promoter, followed by TFIIB, TFIIE, and Pol II, and ending with TFIIE and TFIIH<sup>2,3</sup>.

TFIID is an ~1 megadalton complex consisting of TBP and TAF1–13 (refs 4, 5). TBP and TAFs mediate specific interactions with a variety of core promoter sequences<sup>6–10</sup> and other components of the PIC<sup>11–14</sup>, establishing TFIID as the primary core promoter recognition factor that nucleates PIC assembly. Additionally, TAFs mediate regulatory signals by interacting with transcriptional activators or epigenetic marks, and TFIID has been shown to be required for the initiation of activated transcription<sup>5</sup>.

Despite its critical role in transcription, little is known about the arrangement of subunits within TFIID and the structural bases of their interactions with DNA and the transcriptional machinery. The lack of a recombinant expression system for full TFIID necessitates purification from endogenous sources, which limits the yield that can be used for structural studies. There are crystallographic structures for domains of several TFIID subunits<sup>15–25</sup>, but only low-resolution electron microscopy (EM) structures of the TFIID holocomplex and subcomplexes<sup>25–33</sup>.

Here we present the cryo-EM structure of human TFIID bound to TFIIA and core promoter DNA, determined by single-particle cryo-EM at 7–16 Å resolution. The structure reveals the position of the TBP–TFIIA–TATA subcomplex and defines the path and register for promoter DNA. Our study also shows the locations of TAF1, -2, -6, -7, and -8, and implicates specific elements within TAF1 and TAF2 in mediating interactions with downstream core promoter DNA. We also present the cryo-EM reconstruction of a human TAF-less PIC containing Pol II, promoter DNA, TBP, TFIIA, -B, -F, -S, -E, and -H. By

superimposing the common elements between the two structures, we propose a model for the complete TFIID-based PIC that provides novel insights into the intertwined roles of TFIID in promoter recognition, PIC assembly, and transcription initiation.

## Overall structure of promoter-bound TFIID

Human TFIID has a horseshoe shape, with lobes A, B, and C surrounding a central cavity<sup>26,29</sup>. Our previous cryo-EM studies revealed that human TFIID adopts two major conformations, termed the canonical and rearranged states, that differ in the position of lobe A<sup>33</sup>. In the canonical state, lobe A is attached to lobe C, while in the rearranged state, which is the conformation in which TFIID binds promoter DNA, lobe A adopts a position proximal to lobe B. To reduce the conformational and compositional heterogeneity limiting the resolution of our previous studies (~30 Å), we purified human promoter-bound TFIID complexes using the super core promoter (SCP) sequence. This composite promoter was designed to maximize transcriptional output by increasing the affinity of TFIID for DNA through the presence of several naturally occurring promoter motifs (TATA, Inr, MTE, and DPE)<sup>34</sup>. Purification of SCP-bound TFIID in the presence of TFIIA (see Methods) resulted in more homogeneous TFIID–IIA–SCP complexes, which we then used in single-particle cryo-EM to obtain a reconstruction with an overall resolution of 10.2 Å (Extended Data Fig. 1).

The shape of the human promoter-bound TFIID is consistent with previous lower-resolution reconstructions<sup>26,29,33</sup>. In our present structure, lobe A appears separated into a smaller lobe (lobe A1) that is more stably positioned with respect to the BC core, and a highly flexible lobe A2 (Fig. 1a and Extended Data Fig. 1e). To improve the resolution of the more stable core (comprising lobes A1, B, and C), lobe A2 was excluded from the references used during subsequent three-dimensional classification and refinement (see Methods). This procedure led to an improved reconstruction of the promoter-bound TFIID core with an overall resolution of 8.7 Å (Fig. 1b and Extended Data Fig. 2a, c–e).

<sup>1</sup>Biophysics Graduate Group, University of California, Berkeley, California 94720, USA. <sup>2</sup>QB3 Institute, Department of Molecular and Cell Biology, University of California, Berkeley, California 94720, USA. <sup>3</sup>Molecular Biophysics and Integrative Bioimaging Division, Lawrence Berkeley National Laboratory, Berkeley, California 94720, USA. <sup>4</sup>Department of Biological Physical Chemistry, Rocasolano Physical Chemistry Institute, CSIC, Serrano 119, Madrid 28006, Spain. <sup>5</sup>Howard Hughes Medical Institute, University of California, Berkeley, California 94720, USA.

<sup>†</sup>Present address: Interdisciplinary Biological Sciences Program, Northwestern University, Evanston, Illinois 60208, USA.

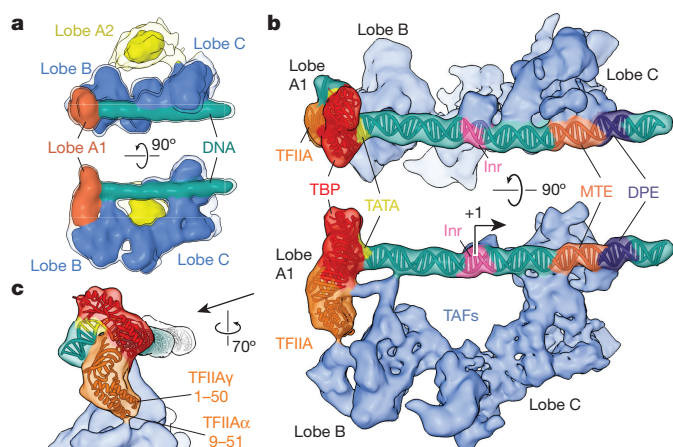


**Figure 1 | Cryo-EM reconstruction of the TFIID-IIA-SCP complex.**

**a**, TFIID-IIA-SCP reconstruction. Isosurfaces are displayed at two thresholds, with the lower one shown in transparency to enable visualization of weaker densities. **b**, Locally refined cryo-EM reconstruction of the promoter-bound core of TFIID (that is, excluding lobe A2). TSS is marked '+1' and the transcription direction by an arrow. **c**, Close-up view of the TBP-TFIIA promoter-binding module, indicating putative TFIID-interacting regions of TFIIA.

### TFIIA-TBP-TATA subcomplex and DNA path

We could easily localize the TBP-TFIIA-TATA ternary complex within lobe A1 by rigid-body docking of the crystal structure<sup>19</sup> into the cryo-EM density (Fig. 1c and Supplementary Video 1). This result is consistent with previous EM studies using gold labelling that localized the TATA-containing upstream promoter region to lobes A and B, and the downstream region to lobe C of the rearranged TFIID<sup>33</sup>. The position of TBP and TFIIA in our structure, together with previous lower-resolution reconstructions of promoter-bound TFIID-IIA and of TFIID alone<sup>33</sup> (Extended Data Fig. 3a), are consistent with the proposal that TBP resides in the mobile lobe A and thus changes position during TFIID rearrangement.

In our promoter-bound complex, TFIIA appears to serve as a bridge between TBP and lobe B of TFIID. Interestingly, DNase I footprinting of TFIID-bound SCP showed that only in the presence of TFIIA is the TATA box protected<sup>33</sup>, supporting the idea that TFIIA is essential for TBP positioning for DNA engagement in the rearranged state. The tip of the TFIIA four-helix bundle is oriented towards lobe B, in agreement with the finding that mutations within this region of TFIIA affect its interaction with TFIID<sup>35</sup> (Fig. 1c and Extended Data Fig. 3b). A density connecting the TFIIA  $\beta$ -barrel with lobe B of TFIID and the DNA near position -16 (Fig. 1b, bottom, and Extended Data Fig. 3b) cannot reasonably accommodate any TFIIA portions unmodelled in the crystal structure. On the other hand, footprinting has shown a TFIID-dependent protection from DNase I cleavage in this region of promoter DNA<sup>33</sup>, suggesting the connecting density probably corresponds to one of the TAFs in lobe B.

We could model the SCP DNA from -40 to +42 base pairs (bp) relative to the transcription start site (TSS), including all SCP motifs (TATA, Inr, MTE, and DPE), using the bent TATA DNA as an anchoring point for assigning the base pair register (Fig. 1b and Supplementary Video 1). The MPE-Fe cleavage pattern of SCP DNA bound to TFIID-IIA<sup>33</sup> can be mapped onto the structure with high correspondence between protected sequences and protein contacts (Extended Data Fig. 3c). Mapping the downstream core element<sup>9</sup> onto our structure strongly suggests that TFIID uses very similar protein elements to interact with this alternative promoter motif (Extended Data Fig. 3d).

### Lobe C architecture and downstream promoter binding

The structural stability of lobe C and bound downstream promoter DNA relative to the rest of the complex allowed us to improve the

resolution in this region (to  $\sim 7$ – $12$  Å, with an 8.2 Å average) through further local three-dimensional classification and alignment against a masked reference (Extended Data Fig. 2b–f). The crystal structure of a human TAF1-TAF7 complex<sup>24</sup> that includes the highly conserved central and amino (N)-terminal fragments of TAF1 and TAF7, respectively, could be unambiguously docked as a rigid body into the density adjacent to the downstream core promoter (Fig. 2a and Supplementary Video 1), in agreement with its reported ability to bind DNA with a preference for the downstream sequence of the SCP<sup>24</sup>. The docking reveals that TAF1 is the primary mediator of downstream promoter binding, contributing contacts that span 34 bp of DNA (positions -3 to +31; Fig. 2a). The winged helix (WH) domain of TAF1 forms a major interaction at the junction of the MTE and DPE promoter motifs (Fig. 2a–c). Superposition of the TAF1 WH-DNA complex with other DNA-binding WH proteins confirms that it shares a common mode of DNA recognition<sup>36</sup> (Extended Data Fig. 4a). The third  $\alpha$ -helix ( $\alpha 3$ ) of this domain inserts into the major groove, positioning three conserved positively charged residues (R864, K865, K868) for specific interaction with the MTE (Fig. 2b, c and Extended Data Fig. 4b), which supports the finding that mutation of these residues to alanine ablates binding of the TAF1-TAF7 module to promoter DNA<sup>24</sup>. Additional conserved positively charged residues within the extended  $\beta$ -wing (R875) and N-terminal end of the first  $\alpha$ -helix ( $\alpha 1$ ; K818) of the WH domain form additional promoter contacts within the minor groove of the DPE and near the upstream boundary of the MTE, respectively (Fig. 2b, c and Extended Data Fig. 4b). There is a small protein density contacting the minor groove of the Inr (Fig. 2a, d). We propose that it corresponds to the portion of TAF1 between residues 993–1075, which is disordered in the crystal structure but is well conserved among metazoans and is predicted to

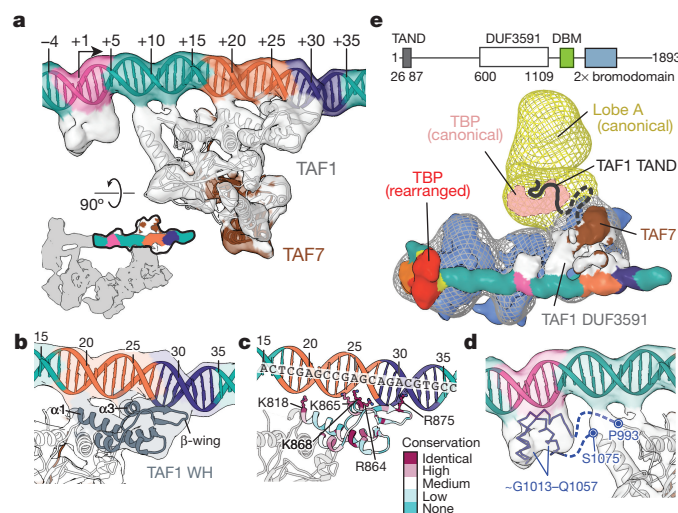


**Figure 2 | A TAF1-TAF7 subcomplex forms a downstream promoter-binding module.** **a**, Docking of the human TAF1-TAF7 complex (PDB accession number 4RGW)<sup>24</sup> into the locally refined lobe C density.

Promoter is coloured as in Fig. 1. The location of the segmented density in the overall map is highlighted in the bottom left. **b**, Close-up view of the TAF1 WH domain (dark grey) bound to promoter DNA. **c**, The TAF1 WH domain with residues coloured according to conservation (Extended Data Fig. 4a). Conserved positively charged residues that appear involved in DNA binding are shown as ball-and-sticks. **d**, Predicted three-dimensional structure for the TAF1 segment spanning residues 1013–1057, docked into the protein density bound to the Inr promoter element. The predicted unstructured linker regions (993–1013 and 1056–1075) are represented as dashed lines. **e**, Putative interaction between TBP and the TAND of TAF1 within the canonical state of TFIID. The low-resolution reconstruction of TFIID in the canonical state<sup>33</sup> is shown in mesh, superimposed on the new structure of promoter-bound TFIID. The domain organization of human TAF1 is shown at the top (the DUF3591 domain has been localized in this study).



be ~50%  $\alpha$ -helical (Extended Data Fig. 4c–e). The residues near both termini of this missing stretch also appear to form contacts with the DNA between the Inr and MTE (Fig. 2d).

Superposition of the previous low-resolution cryo-EM reconstruction of TFIID in the canonical state<sup>33</sup> with our promoter-bound TFIID structure reveals that, in the former, lobe A is attached to lobe C near the newly identified position of the TAF1/TAF7 subcomplex (Fig. 2e). The N-terminal domain of TAF1 (TAND) contains two subdomains known to bind the concave and convex surfaces of TBP, respectively, thereby competing with TBP binding to DNA and TFIIA<sup>23,37</sup>. It is likely that in the canonical state of TFIID, TBP is at least partly inhibited from binding to promoter DNA through interactions with the TAND. In the rearranged promoter-bound state of TFIID, however, TBP is at the opposite end of the core promoter from the identified region of TAF1. Binding of TFIIA to the convex side of TBP probably plays a role in releasing TBP from inhibition by the TAND<sup>23,37</sup>. Additionally, TFIIA contributes to the localization of TBP in the rearranged state of TFIID through its interaction with lobe B. Thus, our studies suggest that the conformational rearrangement of TFIID and the binding of TFIIA are coupled and play critical roles in modulating the handoff of TBP to the upstream promoter region.

Previous studies suggested that TAF1 interacts with promoter DNA as a complex with TAF2<sup>8</sup>. The conserved N-terminal portion of TAF2 is homologous to M1-family aminopeptidases<sup>38</sup> and we could unambiguously assign the density adjacent to TAF1 and the downstream promoter to the TAF2 aminopeptidase-like domain (APD) by fitting the structure of the human endoplasmic reticulum aminopeptidase (ERAP1)<sup>39</sup> into our map (Extended Data Fig. 5a–c). We were able to generate a complete atomic model of the TAF2 APD (residues 27–975) through homology modelling and flexible fitting into the cryo-EM density (Fig. 3a, b, Extended Data Fig. 5a–d, Supplementary Video 1 and Methods). All TAF2 interactions with promoter DNA are mediated by APD domain 3, with the primary contact involving a highly conserved loop of the  $\beta$ -sandwich that interacts with the MTE (Fig. 3b, c and Extended Data Fig. 5e). Contacts with TAF1 are contributed by APD domains 2 and 3, involving the regions from ~467 to ~514 and from ~558 to ~561 of TAF2 (Fig. 3c, d).

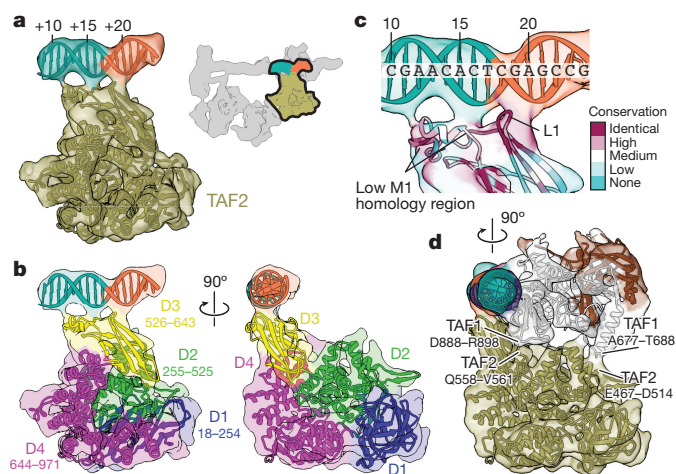


**Figure 3 | TAF2 APD.** **a**, Homology-based atomic model of the TAF2 APD fitted into the cryo-EM density. Colouring of the promoter DNA is the same as in Fig. 1. The location of the segmented density in the overall map is highlighted in the upper-right. **b**, Model of the TAF2 APD coloured by domain (D1–D4), with boundary residues for each domain indicated. **c**, Close-up of TAF2 APD domain 3 binding to promoter DNA with residues coloured according to conservation (see Extended Data Fig. 5e). **d**, Side view highlighting the TAF1–TAF2 interface, with potential regions of interaction between the two subunits indicated.

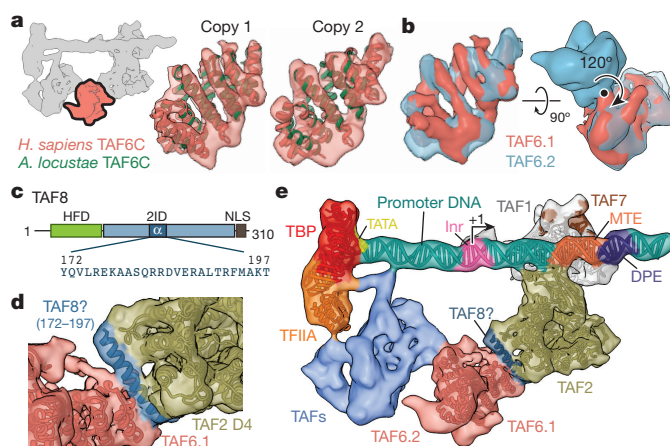


**Figure 4 | Structural TAFs within lobe C.** **a**, Docking of the crystal structure of *A. locustae* TAF6C (PDB accession number 4ATG)<sup>22</sup> into two adjacent densities in the cryo-EM map, termed copy 1 and copy 2. The location of the segmented density in the overall map is highlighted in the schematic on the left. **b**, The density for the two copies of TAF6C in the improved lobe C map are shown superimposed (left), and the homodimer interface and symmetry operation is depicted using the original map from Fig. 1b (right). **c**, Location and sequence of the predicted 26-residue helix within the TAF2-interacting domain (2ID) of TAF8. The relative locations of the histone fold domain (HFD) and nuclear localization signal (NLS) are also depicted. **d**, Docking of the TAF8 26 residue helix between TAF2 APD domain 4 (D4) and TAF6 copy 1 (TAF6.1). **e**, Overall architecture of TFIID with all fitted atomic models.

### Structural TAFs and unassigned density

We were able to assign the majority of the remaining lobe C density to two copies of the carboxy (C)-terminal HEAT repeat domain of TAF6 (TAF6C) by fitting the crystal structure of the *Antonospora locustae* orthologue<sup>22</sup> (Fig. 4a, Extended Data Fig. 6a, b and Supplementary Video 1). We propose that this part of TAF6 forms a homodimer that effectively bridges the downstream promoter-interacting TAFs (TAF1, -2, and -7) with lobe B (Fig. 4b, e). The TAF6C density, at  $<9$  Å resolution, was sufficient to unambiguously confirm the alignment with all ten  $\alpha$ -helices in the crystal structure (Fig. 4a), and the density at the C-terminal region of both TAF6C copies is indicative of the presence of additional C-terminal  $\alpha$ -helices, which are predicted to exist in the human protein but are missing in the crystallized orthologue (Extended Data Fig. 6b, c). We were unable to detect density near either copy of the TAF6C homodimer for the N-terminal histone fold domain of TAF6, which forms a heterodimer with the histone fold domain of TAF9 (ref. 15). This result, which suggests that the TAF6 histone fold is flexibly attached and not critical to the structural integrity of the core TFIID, agrees with the finding that the human isoform TAF6 $\delta$ , which lacks a critical part of its histone fold domain, integrates into an active TFIID complex that retains all TAFs except TAF9 (ref. 40).

After accounting for the portions of TAF2 and TAF6 that we could model into lobe C, there remains clear density for two additional  $\alpha$ -helices bridging TAF2 and TAF6 that we were not able to assign to either of these TAFs (Extended Data Fig. 6d). We propose that these helices are contributed by the C-terminal region of TAF8 because (1) TAF8 associates directly with TAF2 and mediates its nuclear import and incorporation into TFIID through its C-terminal region<sup>25</sup>, (2) a fragment of the region critical for TAF2 binding (residues ~140–200)<sup>25</sup> is predicted to harbour a ~26 residue  $\alpha$ -helix, the length of the longer helical density we observe bridging TAF2 and TAF6 (Fig. 4c–e, Extended Data Fig. 6e and Supplementary Video 1), and (3) TAF8 exhibits robust crosslinking to TAF6 within reconstituted TFIID subcomplexes<sup>25</sup>.

We were unable to localize the positions for the rest of the TAFs (TAF3, -4, -5, -9, -11, -12, and -13) within our promoter-bound



TFIID structure. These TAFs must therefore reside within lobes A2 and B, which are not yet resolved at enough resolution for reliable identification of subunits via docking of the available atomic models. The combined volume of these unassigned lobes is consistent with the  $\sim 300$  kDa of structured TAF domains that have yet to be localized (Extended Data Table 1), considering that much of TFIID is predicted to be intrinsically disordered. A previously described recombinant 5TAF subcomplex contains two copies each of TAF4, -5, -6, -9, and -12 (refs 32, 41). TAF6 is the only component of 5TAF that we were able to localize in our map. While lobe B is contiguous with TAF6C, the density for lobe B is not large enough to accommodate two copies of each TAF in the 5TAF subcomplex. Additionally, we do not observe density within lobe B for the distinctive WD40 beta-propeller domain of TAF5 nor the TAF6–TAF9 histone-fold heterodimer, both of which were proposed to contact TAF6C through opposing interfaces within the recombinant 5TAF subcomplex. We therefore conclude that the components of 5TAF are probably divided between lobes B and A2 in the full TFIID complex.

### TAF-less PIC structure and full PIC model

To gain structural insight into the full PIC assembly, we solved the cryo-EM structure of a simplified, TAF-less PIC containing TBP, Pol II, TFIIA, -B, -F, -S, -E, -H, and SCP DNA. This human TAF-less PIC cryo-EM reconstruction is similar to the one we previously reported using negative stain EM<sup>42</sup>, but promoter DNA is now visible (Fig. 5a and Supplementary Video 1). By superimposing the common elements between the TFIID–IIA–SCP complex and the TAF-less PIC (that is, TBP, TFIIA, promoter DNA), we were able to generate a model of a complete TFIID-based PIC (Fig. 5b and Supplementary Video 1). Overall the two structures fit well with each other, with significant shape complementarity and minimal steric clashes, which are, however, of potential functional relevance. Superposition of the unmasked TFIID–IIA–SCP reconstruction (including lobe A2) onto our model of the TFIID-based PIC indicates that the observed range of positions for the flexible lobe A2 is overall compatible with the model, without any major clashes (Extended Data Fig. 7a). The proximity of TFIIF and TFIIE to lobe B of TFIID in our model supports the finding that these factors can interact with TAFs<sup>11–13</sup>, thus implicating TAFs in the recruitment of PIC components (Fig. 5b, c). The unidentified density emanating from TFIIA and lobe B of TFIID and contacting the DNA downstream of the TATA sequence in the TFIID–IIA–SCP reconstruction overlaps the promoter-binding site of the RAP30 WH domain of TFIIF in the TAF-less PIC, suggesting that a structural reorganization occurs in this region upon TFIIF recruitment to the PIC (Fig. 5c).

Our model shows that Pol II docks between the up- and downstream promoter-binding regions of TFIID. The protein density bound to the Inr promoter element, which we attribute to TAF1, docks into the cleft of Pol II, adjacent to its RPB1, RPB2, and RPB5 subunits (Extended Data Fig. 7b). Downstream of the Inr, TAF1, TAF2, and the XPB subunit of TFIIF make complementary promoter contacts on opposite faces of the DNA duplex (Fig. 5b, right). Minor clashes between TAF1 and RPB1, -2, and -5 signify that this region of TFIID undergoes structural rearrangement upon loading of Pol II onto promoter DNA. Additionally, the path of the promoter DNA in the TFIID–IIA–SCP complex deviates from that seen in the TAF-less PIC, especially downstream of the TSS, further supporting a structural rearrangement in TFIID and downstream promoter DNA during PIC assembly (Extended Data Fig. 7c).

As Pol II reads through the DNA downstream of the TSS, TAF1 and TAF2 must disengage from the downstream promoter DNA before Pol II clears the promoter. Indeed, it has been found that upon recruitment of Pol II, promoter-bound TFIID undergoes an isomerization in which the TFIID contacts with promoter DNA downstream of the +10 position are released concomitantly with the engagement of the promoter DNA with Pol II upstream of this position<sup>43</sup>.

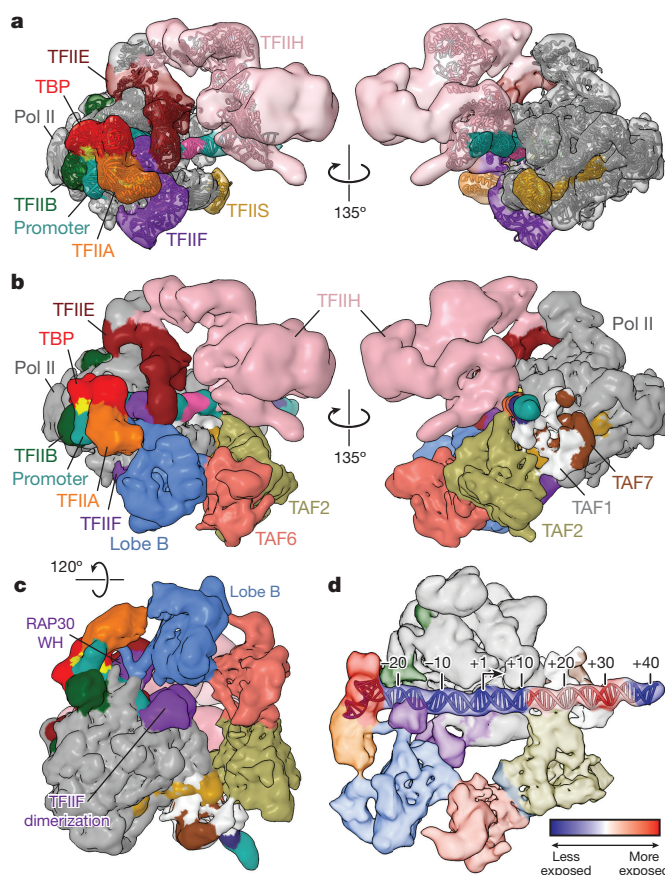


**Figure 5 | Model of the TFIID-based PIC.** **a**, Cryo-EM reconstruction of the human TAF-less PIC, with fitted atomic models. Views are similar to those in Fig. 5a in ref. 42. **b**, Model of the TFIID-based PIC generated by superimposing the densities for TBP, TFIIA, and promoter DNA within the TFIID–IIA–SCP and TAF-less PIC reconstructions. For clarity, the superimposed densities from the TAF-less PIC reconstruction are hidden. **c**, Bottom view of the TFIID-based PIC model highlighting putative interactions between lobe B of TFIID and TFIIF. **d**, Changes in protein–DNA contacts following the addition of TFIIB–Pol II–TFIIF to the TFIID–IIA–SCP complex, according to data published in ref. 43. The blue to red colouring scale represents the rate constant of change in DNaseI cleavage ( $k_{\text{obs}}$ ) for each base pair following the addition of Pol II–TFIIB–TFIIF, with blue set to  $-10 \times 10^{-3} \text{ s}^{-1}$ , corresponding to regions that become more protected, and red set to  $+10 \times 10^{-3} \text{ s}^{-1}$ , corresponding to regions that become more exposed.

Those findings can be mapped onto our model (Fig. 5d) and agree with our structure-based proposal of a reorganization in the downstream region of the PIC. It has also been recently demonstrated that a chemical inhibitor of this isomerization interacts with the intrinsically disordered region of TAF2 and prevents the first round of transcription initiation by blocking the initial recruitment of Pol II<sup>44</sup>. However, the inhibitor has no effect on reinitiation of transcription, suggesting that the isomerization does not occur during reloading of Pol II. We propose that the isomerization of promoter-bound TFIID required for Pol II recruitment, its engagement with promoter DNA, and its clearance of the promoter during transcription initiation, largely involves the release of downstream promoter contacts by TAF1 and TAF2. Since the same isomerization does not take place during reinitiation, it is likely that TAF1 and TAF2 do not re-form some of these promoter contacts following the first round of initiation. The release of TAF7 from TFIID following PIC assembly has been shown to be required for transcription initiation<sup>45</sup>, and could potentially serve as the mechanism for preventing re-engagement of the promoter DNA by TAF1 and TAF2.

Recent cryo-EM studies have revealed the binding site of the yeast Mediator complex on Pol II within a minimal transcription initiation complex<sup>46,47</sup>. Superposition of this structure with our TFIID-based PIC model shows that TFIID and Mediator occupy opposite faces of Pol II (Extended Data Fig. 7d, e and Supplementary Video 1).

### Role of TFIID in transcription initiation

Our structures suggest that a primary function of TFIID during PIC assembly is the proper positioning of TBP on the upstream promoter, which ultimately determines the placement of Pol II relative to the TSS. For the majority of human promoters, which lack a canonical TATA sequence<sup>48–50</sup>, accurate loading of TBP would be ensured by the TAF subunits of TFIID, which collectively act as a molecular ruler to position TBP at a location on the upstream promoter that is precisely defined by the downstream promoter-binding sites of TAF1–TAF2 and the length of the BC core of TFIID. TAFs may also facilitate PIC assembly by contributing to the incorporation of TFIIF and TFIIE to the growing PIC. To accommodate the recruitment of Pol II and its subsequent engagement with promoter DNA, an isomerization occurs in which TAF1 and TAF2 probably release some of their contacts with the downstream DNA. Our model suggests that TAFs are generally required for initial PIC assembly and first round of transcription initiation, but that at least some TAFs may be dispensable for the reloading of Pol II.

TAFs are probably also critical for providing additional levels of control of transcription initiation. For instance, competition from the TAND of TAF1 with the binding of TFIIA and DNA to TBP, which we propose involves the conformational rearrangement of TFIID, may present additional opportunities for regulating PIC assembly. The timing and rate of PIC assembly at the promoter will ultimately be regulated through combinatorial interactions involving TAFs, variable promoter sequences, activators, and epigenetic marks. The demonstrated flexible character of TFIID is likely to be an important property for integrating regulatory cues and allowing sequential conformational states that provide checkpoints throughout the processes of PIC assembly and transcription initiation. The structures presented here offer a structural framework for understanding the complex mechanism underlying TFIID function, shedding new light into the overlapping roles of TFIID as both a coactivator and a general platform for PIC assembly in the coordination of transcription initiation.

**Online Content** Methods, along with any additional Extended Data display items and Source Data, are available in the online version of the paper; references unique to these sections appear only in the online paper.

**Received 24 October 2015; accepted 3 February 2016.**

**Published online 23 March 2016.**

- Levine, M., Cattoglio, C. & Tjian, R. Looping back to leap forward: transcription enters a new era. *Cell* **157**, 13–25 (2014).
- Thomas, M. C. & Chiang, C. M. The general transcription machinery and general cofactors. *Crit. Rev. Biochem. Mol. Biol.* **41**, 105–178 (2006).
- Buratowski, S., Hahn, S., Guarente, L. & Sharp, P. A. Five intermediate complexes in transcription initiation by RNA polymerase II. *Cell* **56**, 549–561 (1989).
- Burley, S. K. & Roeder, R. G. Biochemistry and structural biology of transcription factor IID (TFIID). *Annu. Rev. Biochem.* **65**, 769–799 (1996).
- Albright, S. R. & Tjian, R. TAFs revisited: more data reveal new twists and confirm old ideas. *Gene* **242**, 1–13 (2000).
- Verrijzer, C. P., Chen, J. L., Yokomori, K. & Tjian, R. Binding of TAFs to core elements directs promoter selectivity by RNA polymerase II. *Cell* **81**, 1115–1125 (1995).
- Burke, T. W. & Kadonaga, J. T. The downstream core promoter element, DPE, is conserved from *Drosophila* to humans and is recognized by TAFII60 of *Drosophila*. *Genes Dev.* **11**, 3020–3031 (1997).
- Chalkley, G. E. & Verrijzer, C. P. DNA binding site selection by RNA polymerase II TAFs: a TAF(II)250-TAF(II)150 complex recognizes the initiator. *EMBO J.* **18**, 4835–4845 (1999).
- Lee, D. H. *et al.* Functional characterization of core promoter elements: the downstream core element is recognized by TAF1. *Mol. Cell. Biol.* **25**, 9674–9686 (2005).

- Thiesen, J. W., Lim, C. Y. & Kadonaga, J. T. Three key subregions contribute to the function of the downstream RNA polymerase II core promoter. *Mol. Cell. Biol.* **30**, 3471–3479 (2010).
- Hisatake, K. *et al.* Evolutionary conservation of human TATA-binding-polypeptide-associated factors TAFII31 and TAFII80 and interactions of TAFII80 with other TAFs and with general transcription factors. *Proc. Natl Acad. Sci. USA* **92**, 8195–8199 (1995).
- Ruppert, S. & Tjian, R. Human TAFII250 interacts with RAP74: implications for RNA polymerase II initiation. *Genes Dev.* **9**, 2747–2755 (1995).
- Dubrovskaya, V. *et al.* Distinct domains of hTAFII100 are required for functional interaction with transcription factor TFIIF $\beta$  (RAP30) and incorporation into the TFIID complex. *EMBO J.* **15**, 3702–3712 (1996).
- Wu, S. Y. & Chiang, C. M. TATA-binding protein-associated factors enhance the recruitment of RNA polymerase II by transcriptional activators. *J. Biol. Chem.* **276**, 34235–34243 (2001).
- Xie, X. *et al.* Structural similarity between TAFs and the heterotetrameric core of the histone octamer. *Nature* **380**, 316–322 (1996).
- Birck, C. *et al.* Human TAF(II)28 and TAF(II)18 interact through a histone fold encoded by atypical evolutionary conserved motifs also found in the SPT3 family. *Cell* **94**, 239–249 (1998).
- Jacobson, R. H., Ladurner, A. G., King, D. S. & Tjian, R. Structure and function of a human TAFII250 double bromodomain module. *Science* **288**, 1422–1425 (2000).
- Werten, S. *et al.* Crystal structure of a subcomplex of human transcription factor TFIID formed by TATA binding protein-associated factors hTAF4 (hTAF(II)135) and hTAF12 (hTAF(II)20). *J. Biol. Chem.* **277**, 45502–45509 (2002).
- Bleichenbacher, M., Tan, S. & Richmond, T. J. Novel interactions between the components of human and yeast TFIIA/TBP/DNA complexes. *J. Mol. Biol.* **332**, 783–793 (2003).
- Bhattacharya, S., Takada, S. & Jacobson, R. H. Structural analysis and dimerization potential of the human TAF5 subunit of TFIID. *Proc. Natl Acad. Sci. USA* **104**, 1189–1194 (2007).
- Wang, X. *et al.* Conserved region I of human coactivator TAF4 binds to a short hydrophobic motif present in transcriptional regulators. *Proc. Natl Acad. Sci. USA* **104**, 7839–7844 (2007).
- Scheer, E., Delbac, F., Tora, L., Moras, D. & Romier, C. TFIID TAF6-TAF9 complex formation involves the HEAT repeat-containing C-terminal domain of TAF6 and is modulated by TAF5 protein. *J. Biol. Chem.* **287**, 27580–27592 (2012).
- Anandapadamanaban, M. *et al.* High-resolution structure of TBP with TAF1 reveals anchoring patterns in transcriptional regulation. *Nature Struct. Mol. Biol.* **20**, 1008–1014 (2013).
- Wang, H., Curran, E. C., Hinds, T. R., Wang, E. H. & Zheng, N. Crystal structure of a TAF1-TAF7 complex in human transcription factor IID reveals a promoter binding module. *Cell Res.* **24**, 1433–1444 (2014).
- Trowitzsch, S. *et al.* Cytoplasmic TAF2-TAF8-TAF10 complex provides evidence for nuclear holo-TFIID assembly from preformed submodules. *Nature Commun.* **6**, 6011 (2015).
- Andel, F., Ill, Ladurner, A. G., Inouye, C., Tjian, R. & Nogales, E. Three-dimensional structure of the human TFIID-IIA-IIIB complex. *Science* **286**, 2153–2156 (1999).
- Brand, M., Leurent, C., Mallouh, V., Tora, L. & Schultz, P. Three-dimensional structures of the TAFII-containing complexes TFIID and TFIIIC. *Science* **286**, 2151–2153 (1999).
- Leurent, C. *et al.* Mapping histone fold TAFs within yeast TFIID. *EMBO J.* **21**, 3424–3433 (2002).
- Grob, P. *et al.* Cryo-electron microscopy studies of human TFIID: conformational breathing in the integration of gene regulatory cues. *Structure* **14**, 511–520 (2006).
- Liu, W. L. *et al.* Structural changes in TAF4b-TFIID correlate with promoter selectivity. *Mol. Cell* **29**, 81–91 (2008).
- Papai, G. *et al.* TFIIA and the transactivator Rap1 cooperate to commit TFIID for transcription initiation. *Nature* **465**, 956–960 (2010).
- Bieniossek, C. *et al.* The architecture of human general transcription factor TFIID core complex. *Nature* **493**, 699–702 (2013).
- Cianfrocco, M. A. *et al.* Human TFIID binds to core promoter DNA in a reorganized structural state. *Cell* **152**, 120–131 (2013).
- Juven-Gershon, T., Cheng, S. & Kadonaga, J. T. Rational design of a super core promoter that enhances gene expression. *Nature Methods* **3**, 917–922 (2006).
- Kraemer, S. M., Ranallo, R. T., Ogg, R. C. & Stargell, L. A. TFIIA interacts with TFIID via association with TATA-binding protein and TAF40. *Mol. Cell. Biol.* **21**, 1737–1746 (2001).
- Gajiwala, K. S. & Burley, S. K. Winged helix proteins. *Curr. Opin. Struct. Biol.* **10**, 110–116 (2000).
- Kokubo, T., Swanson, M. J., Nishikawa, J. I., Hinnebusch, A. G. & Nakatani, Y. The yeast TAF145 inhibitory domain and TFIIA competitively bind to TATA-binding protein. *Mol. Cell. Biol.* **18**, 1003–1012 (1998).
- Malkowska, M., Kokoszynska, K., Rychlewski, L. & Wyrwicz, L. Structural bioinformatics of the general transcription factor TFIID. *Biochimie* **95**, 680–691 (2013).
- Kochan, G. *et al.* Crystal structures of the endoplasmic reticulum aminopeptidase-1 (ERAP1) reveal the molecular basis for N-terminal peptide trimming. *Proc. Natl Acad. Sci. USA* **108**, 7745–7750 (2011).

40. Bell, B., Scheer, E. & Tora, L. Identification of hTAF(II)80 delta links apoptotic signaling pathways to transcription factor TFIID function. *Mol. Cell* **8**, 591–600 (2001).
41. Wright, K. J., Marr, M. T., II & Tjian, R. TAF4 nucleates a core subcomplex of TFIID and mediates activated transcription from a TATA-less promoter. *Proc. Natl Acad. Sci. USA* **103**, 12347–12352 (2006).
42. He, Y., Fang, J., Taatjes, D. J. & Nogales, E. Structural visualization of key steps in human transcription initiation. *Nature* **495**, 481–486 (2013).
43. Yakovchuk, P., Gilman, B., Goodrich, J. A. & Kugel, J. F. RNA polymerase II and TAFs undergo a slow isomerization after the polymerase is recruited to promoter-bound TFIID. *J. Mol. Biol.* **397**, 57–68 (2010).
44. Zhang, Z. *et al.* Chemical perturbation of an intrinsically disordered region of TFIID distinguishes two modes of transcription initiation. *eLife* **4**, e07777 (2015).
45. Gegonne, A., Devaiah, B. N. & Singer, D. S. TAF7: traffic controller in transcription initiation. *Transcription* **4**, 29–33 (2013).
46. Plaschka, C. *et al.* Architecture of the RNA polymerase II-Mediator core initiation complex. *Nature* **518**, 376–380 (2015).
47. Tsai, K. L. *et al.* Subunit architecture and functional modular rearrangements of the transcriptional mediator complex. *Cell* **157**, 1430–1444 (2014).
48. Kim, T. H. *et al.* A high-resolution map of active promoters in the human genome. *Nature* **436**, 876–880 (2005).
49. Carninci, P. *et al.* Genome-wide analysis of mammalian promoter architecture and evolution. *Nature Genet.* **38**, 626–635 (2006).
50. Cooper, S. J., Trinklein, N. D., Anton, E. D., Nguyen, L. & Myers, R. M. Comprehensive analysis of transcriptional promoter structure and function in 1% of the human genome. *Genome Res.* **16**, 1–10 (2006).

**Supplementary Information** is available in the online version of the paper.

**Acknowledgements** We thank P. Grob, S. Howes, and R. Zhang for electron microscopy support; T. Houweling for computer support; S. Scheres for technical advice on image processing; A. Patel for discussion; C. Inouye for providing us with recombinant TFIIF; S. Zheng for providing TAF4 mAb; and D. King for providing peptides. We are thankful to R. Tjian and J. Kadonaga for their comments on the manuscript. Computational resources were provided in part by the National Energy Research Scientific Computing Center (DE-AC02-05CH11231). This work was funded by NIGMS (GM63072 to E.N.) and Spanish Ministry of Economy and Competitiveness (BFU2013-44306P to P.C.). R.K.L. was supported by the NIGMS Molecular Biophysics Training Grant (GM008295). E.N. is a Howard Hughes Medical Institute Investigator.

**Author Contributions** R.K.L. and Y.H. designed and performed the experiments; J.R.L.-B. and P.C. performed structural modelling; J.F. purified the TFIID, Pol II, TFIIE, and TFIIF; R.L., Y.H., and E.N. analysed the data and wrote the paper.

**Author Information** Cryo-EM density maps have been deposited in the Electron Microscopy Data Bank (EMDB) under codes EMD-3304 (TFIID-IIA-SCP complex), EMD-3305 (locally refined BC-core of TFIID-IIA-SCP complex), EMD-3306 (locally refined lobe C of TFIID-IIA-SCP complex), and EMD-3307 (TAF-less PIC). Model coordinates have been deposited in the Protein Data Bank (PDB) under accession number 5FUR. Reprints and permissions information is available at [www.nature.com/reprints](http://www.nature.com/reprints). The authors declare no competing financial interests. Readers are welcome to comment on the online version of the paper. Correspondence and requests for materials should be addressed to E.N. (ENogales@lbl.gov).



## METHODS

No statistical methods were used to predetermine sample size. The experiments were not randomized. The investigators were not blinded to allocation during experiments and outcome assessment.

**Preparation of transcription complexes for cryo-EM.** TFIID, Pol II, and TFIIF were immunopurified from HeLa cell nuclear extracts following previously established protocols<sup>31,32</sup>. The human TFIIA used in the reconstitution of both the TFIID–IIA–SCP complex and TAF-less PIC was recombinantly expressed and purified first as three separate polypeptides (TFIIA $\alpha$  2–58, TFIIA $\beta$  303–376, and TFIIA $\gamma$  2–109) from *Escherichia coli*, then reconstituted into the conserved three-subunit core TFIIA similarly as in ref. 19. The C-terminal DNA-binding core of human TBP (residues 159–339), and full-length TFIIB, TFIIE, TFIIF, and TFIIS, were used in the reconstitution of the TAF-less PIC and were recombinantly expressed and purified from *E. coli*.

The sequence of the promoter DNA construct used in this study was based on the SCP<sup>34</sup>, except that a BREu element was introduced upstream of the TATA box and an EcoRI restriction enzyme site was included downstream of the DPE element for purification purposes (template 5′-ACTGGGGAATTCATGGTCCGTAGG CACGTCTGCTCGGCTCGAGTGTTCGATCGCGACTGAGGACGAACGCG CCCCCACCCCTTTTATAGGCGCCCTTC-3′; non-template 5′-GAAGGGC GCCTATAAAGGGGGTGGGGGCGCTTCCTCAGTCGCGATCGAA CACTCGAGCCGAGCAGACGTGCCTACGGACCATGGAATTCGCCAGT-3′). The template strand was modified with a biotin tag at the 5′ end (Integrated DNA Technologies). To generate the duplexed DNA, equimolar amounts of the template and non-template strand oligonucleotides were mixed at a final concentration of 25  $\mu$ M in water, and the annealing reaction was heated to 95 °C for 5 min then allowed to slowly cool to room temperature over 2–3 h.

To assemble TFIID–IIA–SCP complex, 5.0 pmol TFIIA was first added to 2.5 pmol purified HeLa TFIID in assembly buffer (20 mM HEPES pH 7.9, 0.2 mM EDTA, 10% glycerol, 6 mM MgCl<sub>2</sub>, 80 mM KCl, 1 mM DTT, 0.05% NP-40) and incubated for 5 min at 37 °C. A limiting amount of biotinylated SCP DNA (1 pmol) was then added and the assembly reaction was incubated for 10 min at 37 °C. The reaction was added to 0.25  $\mu$ l Streptavidin Mag Sepharose magnetic beads (GE Healthcare) and incubated at 28 °C for 15 min. The beads were then washed three times with washing buffer (10 mM HEPES pH 7.9, 3% trehalose, 8 mM MgCl<sub>2</sub>, 100 mM KCl, 1 mM DTT, 0.025% NP-40). The promoter-bound complex was then eluted by incubating in 3.6  $\mu$ l of elution buffer (10 mM HEPES pH 7.9, 10 mM MgCl<sub>2</sub>, 3% trehalose, 50 mM KCl, 1 mM DTT, 0.05% NP-40, 1 unit per microlitre EcoRI–HF (New England BioLabs)) for 30 min at 37 °C.

The TAF-less PIC was assembled similarly as before<sup>42</sup>, except for an additional incubation of TFIIS at a final concentration of 200 nM with the purified PIC before application to the grid. We included TFIIS in our initiation assemblies because of its novel role in active PIC formation besides that in elongation<sup>53</sup>.

Following the restriction digest elution, purified TFIID–IIA–SCP complex or TAF-less PIC was crosslinked with 0.01% glutaraldehyde for 5 min on ice, then used immediately for cryo-EM sample preparation.

**Electron microscopy.** Cryo-EM samples were prepared on continuous carbon coated C-flat holey carbon grids (Protochips). Grids were plasma cleaned for 10 s in air using a Solarus Plasma Cleaner (Gatan) operating at 10 W. Immediately following crosslinking, 4  $\mu$ l of purified TFIID–IIA–SCP complex or TAF-less PIC was added to the plasma-cleaned grid and loaded into a Vitrobot (FEI). The sample was incubated on the grid for 10 min at 4 °C and 100% relative humidity to enhance its absorption onto the carbon substrate, then was blotted and immediately plunge-frozen in liquid ethane. Frozen grids were transferred to a 626 Cryo-Transfer Holder (Gatan) and loaded into a Titan electron microscope (FEI) operating at 300 keV. Images were recorded with a K2 direct electron detector (Gatan) operating in counting mode at a calibrated magnification of 37,879 (1.32 Å per pixel) and a defocus range of –2  $\mu$ m to –4  $\mu$ m, using the Leginon data collection software for semi-automated acquisition targeting. Twenty-frame exposures were taken at 0.5 s per frame (10 s total exposure time), using a dose rate of 8 electrons per pixel per second (4.6 electrons per square ångström per second or 2.3 electrons per square ångström per frame), corresponding to a total dose of 46 electrons per square ångström per micrograph.

**Image processing.** The exposure frames were aligned using MotionCorr<sup>54</sup> to correct for specimen motion, and the average of the aligned frames was used for initial processing. The CTF parameters of the micrographs were estimated using CTFFIND3<sup>55</sup>. For the TFIID–IIA–SCP complex, RELION<sup>56</sup> (version 1.4-beta) was used for automatic selection of 203,163 particles from 1,253 micrographs (Extended Data Fig. 1a). For the TAF-less PIC, 245,501 particles were automatically selected from 855 micrographs using a difference of Gaussians (DoG) particle picker<sup>57</sup> within the Appion image processing environment<sup>58</sup>. All two- and

three-dimensional classification and refinement steps were performed within RELION<sup>56</sup> (version 1.4-beta).

For the TFIID–IIA–SCP complex, the initial set of 203,163 particles was subjected to an initial three-dimensional classification, with the negative stain reconstruction of the same complex (in which the nucleic acid is not visible) low-pass filtered to 60 Å used as an initial reference (Extended Data Fig. 1b). Three out of five classes in this classification, corresponding to 121,459 particle images, were indicative of promoter-bound complexes and were selected for further processing. Reference-free two-dimensional classification of this set of images was used to select for 56,457 high-quality particle images. The 56,457-particle set was then subjected to three-dimensional refinement and particle polishing procedure within RELION<sup>59</sup> to correct for individual particle motion and beam-induced radiation damage of the sample. Owing to the low contrast inherent in the images of this sample, the per-frame *B*-factor plot used to model the beam-induced radiation damage was too noisy to use for modelling. Instead, we generated an idealized curve for the dose-dependent *B*-factor on the basis of cryo-EM data collected on microtubules under similar imaging conditions (Extended Data Fig. 1c), which we applied to our data during the particle polishing step. The resulting set of 56,457 ‘polished’ particles (56k set) was used in all subsequent three-dimensional classification and refinement.

An initial three-dimensional refinement of the 56k set resulted in a reconstruction of the promoter-bound TFIID–IIA complex at 10.2 Å resolution (Extended Data Fig. 1d, e). All resolutions reported herein correspond to the gold-standard Fourier shell correlation (FSC) = 0.143 criterion<sup>60</sup>. Local resolution estimation indicated that the density for lobe A2 of TFIID was at much lower resolution than the promoter-bound BC-core (Extended Data Fig. 1e). To improve the reconstruction of the promoter-bound BC-core of TFIID, the orientations of the particle images were locally refined against a reference in which a mask was applied around the BC-core density, effectively excluding the contribution of lobe A2 signal from the alignment. The images were then three-dimensionally classified within the same mask, and one class with 22,050 particles exhibited the lowest error in angular and translational alignment (Extended Data Fig. 2a). This set of 22,050 particle images was then subjected to three-dimensional refinement without using any mask, followed by a local refinement against a reference with a mask around the BC-core. This procedure resulted in an improved reconstruction of the BC-core with an overall resolution of 8.7 Å (Extended Data Fig. 2c).

Three-dimensional classification and local-resolution analysis of the BC-core density indicated further conformational heterogeneity, which could be largely characterized as mobility of lobe B, TBP/TFIIA module, and upstream promoter DNA relative to lobe C and bound downstream promoter DNA (Extended Data Fig. 2d–f). Therefore, we employed a similar strategy to improve the reconstruction of lobe C and bound downstream promoter DNA (Extended Data Fig. 2b). The resulting lobe C density incorporated 28,448 particle images and had an overall resolution of 8.2 Å (Extended Data Fig. 2c).

For the TAF-less PIC, all particle picks were used for an initial three-dimensional classification, using the previously published negative stain reconstruction of the TFIIF-containing PIC (EMDB code 2308), low-pass filtered to 60 Å, as an initial reference. A single class corresponded to the fully assembled, TFIIF-containing TAF-less PIC, comprising 24,290 particle images. A three-dimensional refinement of this set of particles yielded the final reconstruction at 7.2 Å resolution.

Local resolution estimations were performed using the Bsoft software package<sup>61</sup>, and all final volumes shown in this paper have been automatically sharpened using the post-processing program within RELION and then filtered according to local resolution using the blocfilt program within Bsoft.

**Structural modelling.** For the TFIID–IIA–SCP complex, densities were initially assigned to specific components by rigid-body docking of known crystal structures (TBP, TFIIA, TATA DNA, TAF1, TAF7) or homologous structures (TAF2 and TAF6) using UCSF Chimera<sup>62</sup>, ADP-EM<sup>63</sup>, or Situs<sup>64</sup>. These structures were used as starting point for flexible refinement using iMODFIT<sup>65</sup> when necessary. Reliable homology models were generated with either the SWISS-MODEL server<sup>66</sup> or I-TASSER server<sup>67</sup>.

The TBP–TFIIA–TATA DNA complex was the first structure to be fitted into the density, which was accomplished by docking the crystal structure of this complex<sup>19</sup> as a single rigid body. The model of the entire SCP was then generated by extrapolating B-form DNA from TBP-bound TATA box sequence present in the fitted crystal structure, followed by manual bending of the DNA structure using the 3D-DART server<sup>68</sup>, and finally by flexible fitting of the DNA into the cryo-EM density using iMODFIT<sup>65</sup>.

The density for the TAF1–TAF7 promoter-binding module was initially identified within the promoter-bound BC-core of TFIID using the unbiased 6D global docking search algorithm implemented in Situs, and the rigid body

docking of the crystal structure (PDB accession number 4RGW)<sup>24</sup> was further refined using the higher-resolution lobe C density within Chimera. The secondary and three-dimensional structure prediction for TAF1 993–1074 (putative Inr-binding domain) was performed using the I-TASSER server<sup>67</sup>.

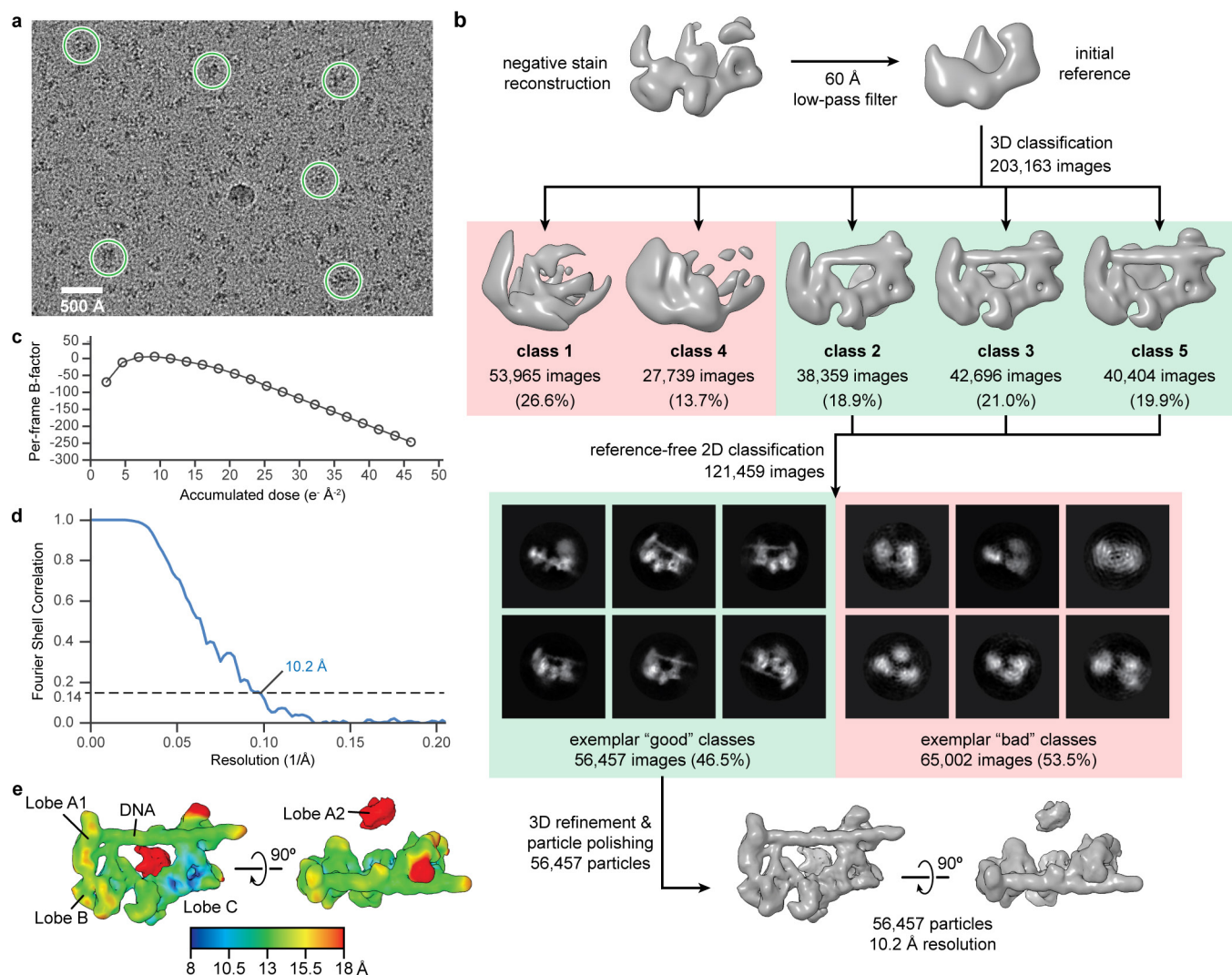
The density for TAF2 was initially identified through manual docking of the crystal structure of the human endoplasmic reticulum aminopeptidase I (ERAPI, PDB accession number 2YD0)<sup>39</sup> within UCSF Chimera. Homology modelling of the TAF2 APD began with the building of APD domains 1 and 2 within the SWISS-MODEL server<sup>66</sup>, using the structures of leukotriene A-4 hydrolase (PDB accession number 3U9W: 21% sequence identity, 31% similarity, and 79% coverage) and endoplasmic reticulum aminopeptidase 2 (PDB accession number 3SE6: 16% identity, 30% similarity, and 88% coverage) as templates. While the first 26 N-terminal residues and an insertion (residues 88–124) of APD domain 1 could not be modelled by homology, there are two nearby unassigned densities in contact with APD domain 4 that are likely to account this missing modelling part. TAF2 APD domain 3 was then modelled using templates derived from aminopeptidase N (PDB accession number 3B34 and 4QME). Despite the high confidence secondary structure prediction score of the 16 predicted alpha helices in APD domain 4, the low sequence identities (between 10% and 19%), coverages (between 50% and 86%), and the conformational variability of the model templates precluded that a single model fit well in the armadillo fold visible in the density. However, we were able to accommodate the distinctive armadillo curvature by merging and flexibly fitting fragments from two to six helices extracted from different models. The templates of these models were the structures of aminopeptidase N (PDB accession number 3B34 and 4QME), deoxyhypusine hydroxylase (PDB accession number 4D4Z), AP2 clathrin adaptor (PDB accession number 1GW5), and hypothetical protein yibA (PDB accession number 1OYZ). The missing loops between fragments and domains were modelled *ab initio* using RCD<sup>69</sup> to obtain a complete model. Finally, the full TAF2 APD model was relaxed with Chiron<sup>70</sup> and PyRosetta<sup>71</sup> to prevent clashes and to improve geometry.

The DUF1546 domain of TAF6 (TAF6C) was modelled from the crystal structure of the *A. locustae* orthologue (PDB accession number 4ATG: 23% identity and 81% coverage)<sup>22</sup>. Two copies of this well conserved structure containing HEAT repeats were easily located by rigid-body docking in the cryo-EM density using Situs<sup>64</sup>. In the contact region between TAF6 and the TAF2 APD domain 4, there is obvious density for two alpha helices, which we predict to be derived from TAF8 on the basis of biochemical data and secondary structure prediction.

The model for the TAF-less PIC is based on the previously published model using the negative stain EM reconstruction of the PIC containing TBP, TFIIA, SCP DNA, TFIIB, Pol II, TFIIF, TFIIE, and TFIIH. The model for TFIIS was based on a combination of the yeast Pol II–TFIIS complex (PDB accession number 1Y1V) and the free human TFIIS domain II (PDB accession number 3NDQ). The model of the TFIID-based PIC was generated by superimposing the promoter DNA downstream of the TATA sequence in the TFIID–IIA–SCP structure with that in the TAF-less PIC structure within UCSF Chimera.

All multi-sequence alignments were performed using Clustal Omega<sup>72</sup>. Secondary structure predictions were performed with the PSIPRED server<sup>73</sup>, except where noted. All molecular graphics and analyses were performed with the UCSF Chimera package<sup>62</sup>.

51. Pal, M., Ponticelli, A. S. & Luse, D. S. The role of the transcription bubble and TFIIB in promoter clearance by RNA polymerase II. *Mol. Cell* **19**, 101–110 (2005).
52. Revyakin, A. *et al.* Transcription initiation by human RNA polymerase II visualized at single-molecule resolution. *Genes Dev.* **26**, 1691–1702 (2012).
53. Kim, B. *et al.* The transcription elongation factor TFIIS is a component of RNA polymerase II preinitiation complexes. *Proc. Natl Acad. Sci. USA* **104**, 16068–16073 (2007).
54. Li, X. *et al.* Electron counting and beam-induced motion correction enable near-atomic-resolution single-particle cryo-EM. *Nature Methods* **10**, 584–590 (2013).
55. Mindell, J. A. & Grigorieff, N. Accurate determination of local defocus and specimen tilt in electron microscopy. *J. Struct. Biol.* **142**, 334–347 (2003).
56. Scheres, S. H. RELION: implementation of a Bayesian approach to cryo-EM structure determination. *J. Struct. Biol.* **180**, 519–530 (2012).
57. Voss, N. R., Yoshioka, C. K., Radermacher, M., Potter, C. S. & Carragher, B. DoG Picker and TiltPicker: software tools to facilitate particle selection in single particle electron microscopy. *J. Struct. Biol.* **166**, 205–213 (2009).
58. Lander, G. C. *et al.* Appion: an integrated, database-driven pipeline to facilitate EM image processing. *J. Struct. Biol.* **166**, 95–102 (2009).
59. Scheres, S. H. Beam-induced motion correction for sub-megadalton cryo-EM particles. *eLife* **3**, e03665 (2014).
60. Henderson, R. *et al.* Outcome of the first electron microscopy validation task force meeting. *Structure* **20**, 205–214 (2012).
61. Heymann, J. B. Bsoft: image and molecular processing in electron microscopy. *J. Struct. Biol.* **133**, 156–169 (2001).
62. Pettersen, E. F. *et al.* UCSF Chimera—a visualization system for exploratory research and analysis. *J. Comput. Chem.* **25**, 1605–1612 (2004).
63. Garzón, J. I., Kovacs, J., Abagyan, R. & Chacón, P. ADP\_EM: fast exhaustive multi-resolution docking for high-throughput coverage. *Bioinformatics* **23**, 427–433 (2007).
64. Wriggers, W. Using Situs for the integration of multi-resolution structures. *Biophys. Rev.* **2**, 21–27 (2010).
65. López-Blanco, J. R. & Chacón, P. iMODFIT: efficient and robust flexible fitting based on vibrational analysis in internal coordinates. *J. Struct. Biol.* **184**, 261–270 (2013).
66. Biasini, M. *et al.* SWISS-MODEL: modelling protein tertiary and quaternary structure using evolutionary information. *Nucleic Acids Res.* **42**, W252–W258 (2014).
67. Yang, J. *et al.* The I-TASSER Suite: protein structure and function prediction. *Nature Methods* **12**, 7–8 (2015).
68. van Dijk, M. & Bonvin, A. M. 3D-DART: a DNA structure modelling server. *Nucleic Acids Res.* **37**, W235–W239 (2009).
69. Chys, P. & Chacón, P. Random coordinate descent with spinor-matrices and geometric filters for efficient loop closure. *J. Chem. Theory Comput.* **9**, 1821–1829 (2013).
70. Ramachandran, S., Kota, P., Ding, F. & Dokholyan, N. V. Automated minimization of steric clashes in protein structures. *Proteins* **79**, 261–270 (2011).
71. Chaudhury, S., Lyskov, S. & Gray, J. J. PyRosetta: a script-based interface for implementing molecular modeling algorithms using Rosetta. *Bioinformatics* **26**, 689–691 (2010).
72. Sievers, F. *et al.* Fast, scalable generation of high-quality protein multiple sequence alignments using Clustal Omega. *Mol. Syst. Biol.* **7**, 539 (2011).
73. Buchan, D. W., Minneci, F., Nugent, T. C., Bryson, K. & Jones, D. T. Scalable web services for the PSIPRED Protein Analysis Workbench. *Nucleic Acids Res.* **41**, W349–W357 (2013).



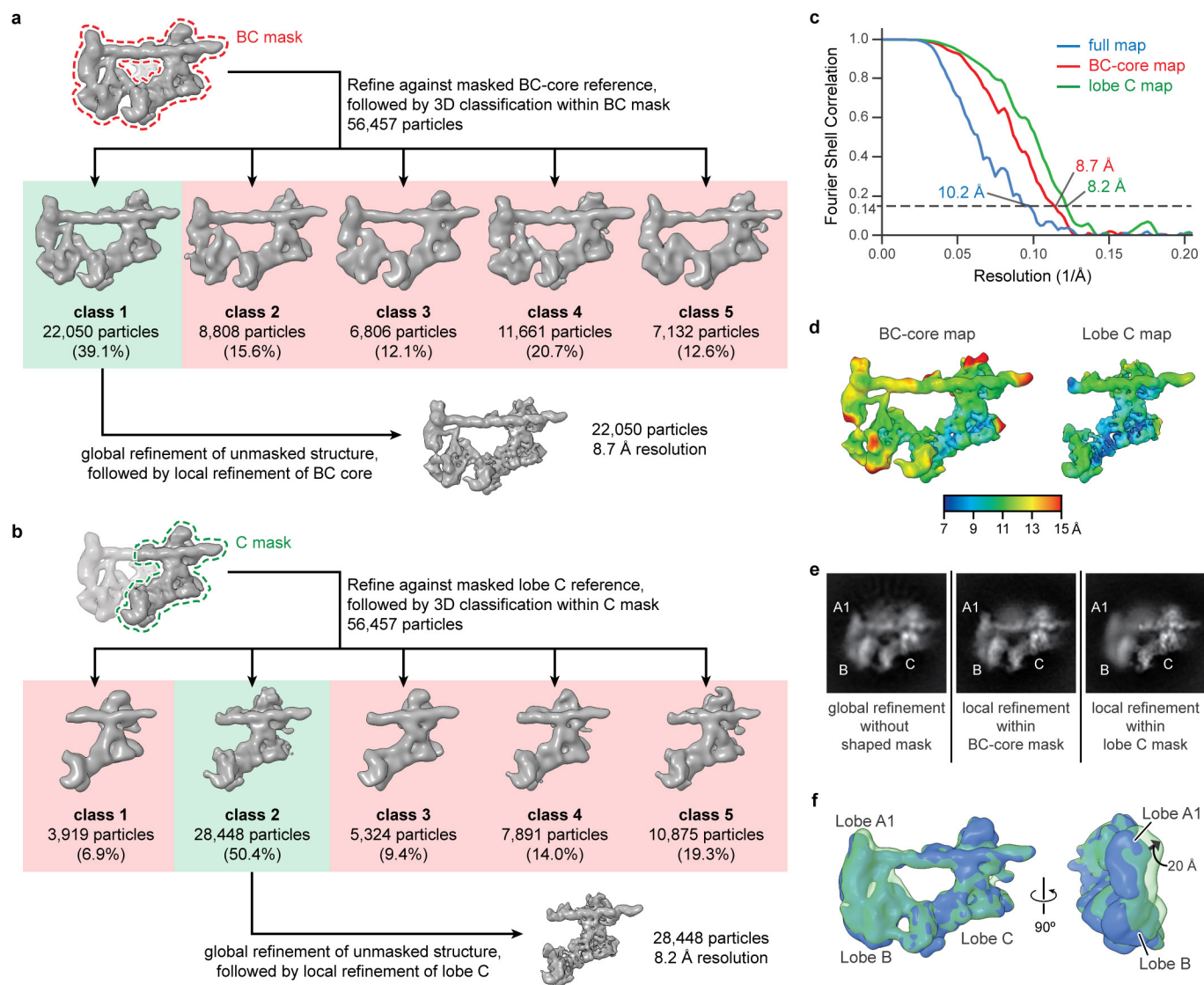
### Extended Data Figure 1 | Cryo-EM of the TFIID-IIA-SCP complex.

**a**, Representative micrograph of frozen-hydrated TFIID-IIA-SCP complexes. Examples of particle picks are indicated by the green circles; 203,163 such picks were made from 1,253 total micrographs.

**b**, Initial classification and refinement scheme for the TFIID-IIA-SCP

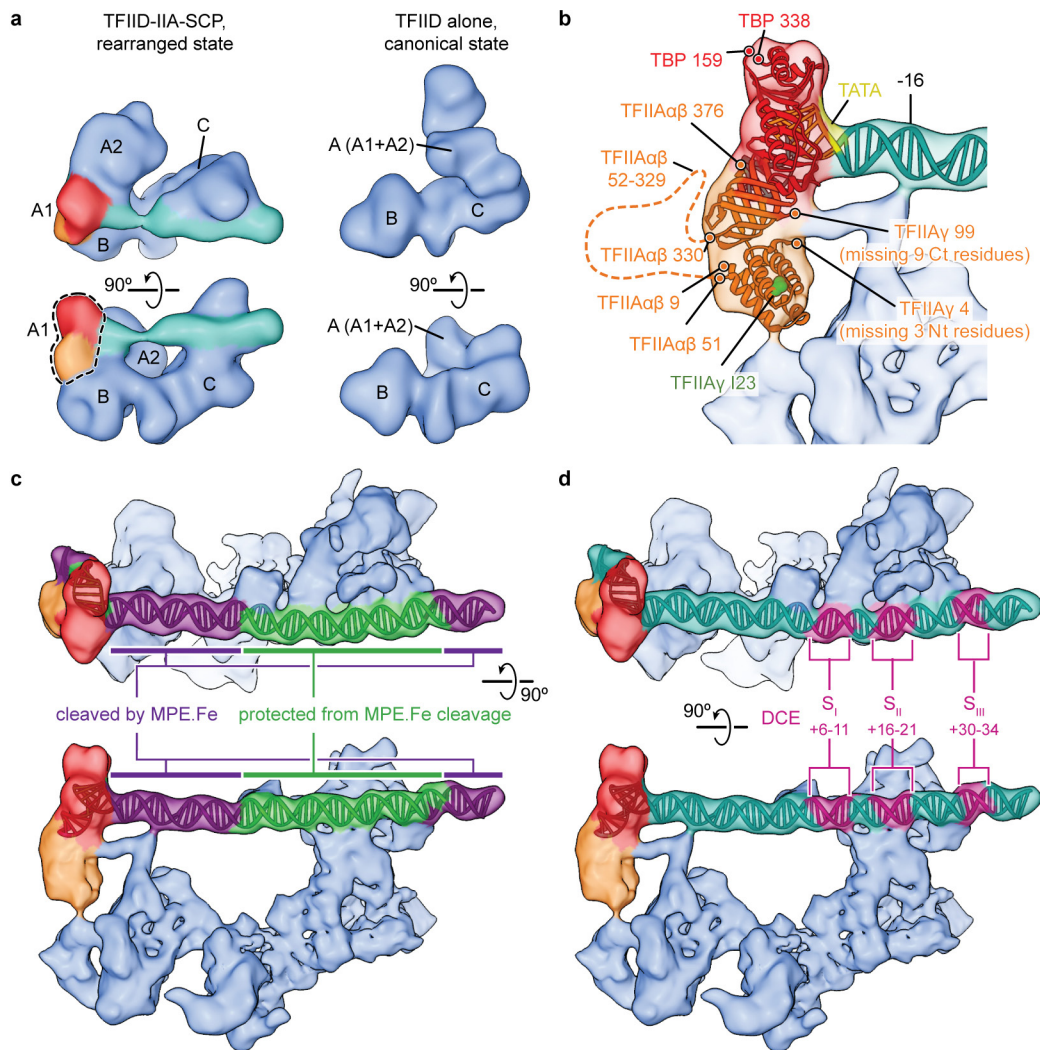
structure (see Methods). **c**, Idealized dose-dependent *B*-factor plot based on cryo-EM data collected on microtubules under similar imaging conditions. This plot was used for the particle polishing step in **b**, **d**, **e**, Fourier shell correlation plot (**d**) and local resolution estimation (**e**) for the final reconstruction shown in **b**.





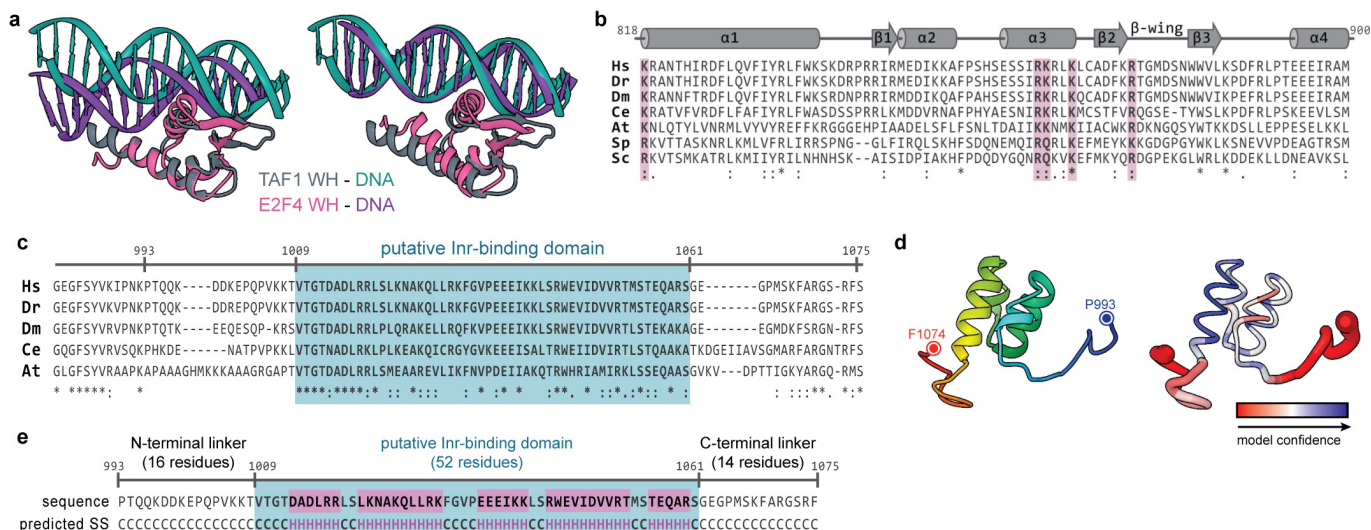
**Extended Data Figure 2 | Focused classification and refinement of the promoter-bound BC-core and lobe C of TFIID. a, b,** Scheme for focused classification and refinement of the BC-core region (**a**) or lobe C region of the TFIID-IIA-SCP structure (**b**) (see Methods). **c, d,** Fourier shell correlation plots (**c**) and local resolution estimations (**d**) of the BC-core and lobe C maps, corresponding to the final structures shown in **a** and **b**, respectively. **e,** Two-dimensional projections of the refined maps for the full TFIID-IIA-SCP structure (left), locally refined BC-core map (middle), and locally refined lobe C map (right). The maps used to calculate the

projections are the same as the final structures in **a, b**, and Extended Data Fig. 1b, except that all have been low-pass filtered to 10 Å before calculating projections. **f,** Three-dimensional classification of 56,457 particles into two classes (solid blue and transparent green), following focused alignment to the lobe C region of the structure. The resulting classes have been superposed through their lobe C densities to illustrate the flexibility of lobe B and the upstream region of promoter DNA relative to lobe C and the downstream promoter region. The magnitude of motion within lobe A1 (20 Å) is indicated.



**Extended Data Figure 3 | Modelling of TBP, TFIIA, and promoter DNA into the cryo-EM density.** **a**, Previously published reconstructions of TFIID-IIA-SCP in the rearranged state (left; EMDB code 2282) and of free TFIID in the canonical state (right; EMDB code 2287)<sup>33</sup>. For the former, the densities for TFIIA (orange) and TBP (red) are assigned on the basis of the superposition with the TFIID-IIA-SCP structure from our present study. **b**, Close-up view of the TBP-TFIIA-TATA module density and fitted structures. The termini of the TBP structure and the three subunits ( $\alpha$ ,  $\beta$ , and  $\gamma$ ) within the TFIIA structure are indicated with circles. In the cell, the  $\alpha$ - and  $\beta$ -subunits of TFIIA are translated as a single polypeptide and then are post-translationally cleaved. The location of the long stretch

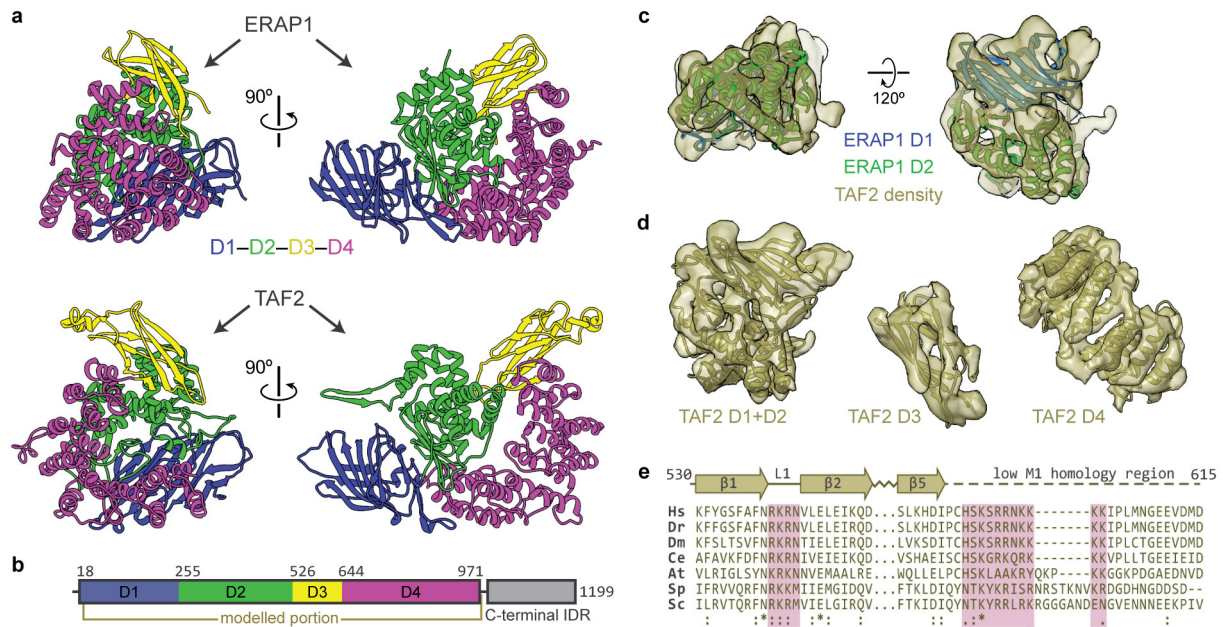
of residues spanning the region between the structured parts of TFIIA $\alpha$  and TFIIA $\beta$  (TFIIA $\alpha\beta$  52–329) is indicated as a dashed line. Note that only 34 of the residues within this flexible loop (52–58 and 303–329) are included in the TFIIA construct used for this study. Mutational analysis in yeast has shown that mutation of an isoleucine residue (I23 in humans, I27 in yeast; represented in green spheres) to lysine at the tip of the TFIIA four-helix bundle disrupts the interaction between TFIID and TFIIA<sup>35</sup>. **c**, Mapping of the MPE.Fe(II) cleavage pattern for SCP DNA bound to TFIID-IIA, on the basis of data published in ref. 33. **d**, Mapping of the downstream core element (DCE)<sup>9</sup> sequence onto the SCP DNA within the TFIID-IIA-SCP structure from our present study.



**Extended Data Figure 4 | Structural modelling and conservation of the TAF1 promoter-binding domains.** **a**, TAF1 WH domain (grey) in complex with promoter DNA (cyan) superposed with the DNA-binding WH domain of the transcription factor E2F4 (PDB accession number 1CF7, magenta) in complex with its cognate DNA, with the alignment based on the protein (left) or DNA (right) components. **b**, Sequence alignment and secondary structure map of the TAF1 WH domain, used to calculate the conservation scores depicted in Fig. 2c (Hs, *Homo sapiens*; Dr, *Danio rerio*; Dm, *Drosophila melanogaster*; Ce, *Caenorhabditis elegans*; At, *Arabidopsis thaliana*; Sp, *Schizosaccharomyces pombe*; Sc, *Saccharomyces cerevisiae*). The conserved positively charged residues that are in close proximity to the promoter DNA within the docked structure (K818, R864, K865, K868, and R875) are highlighted in pink. Numbering is based on the human sequence. **c**, Sequence alignment of a region of the

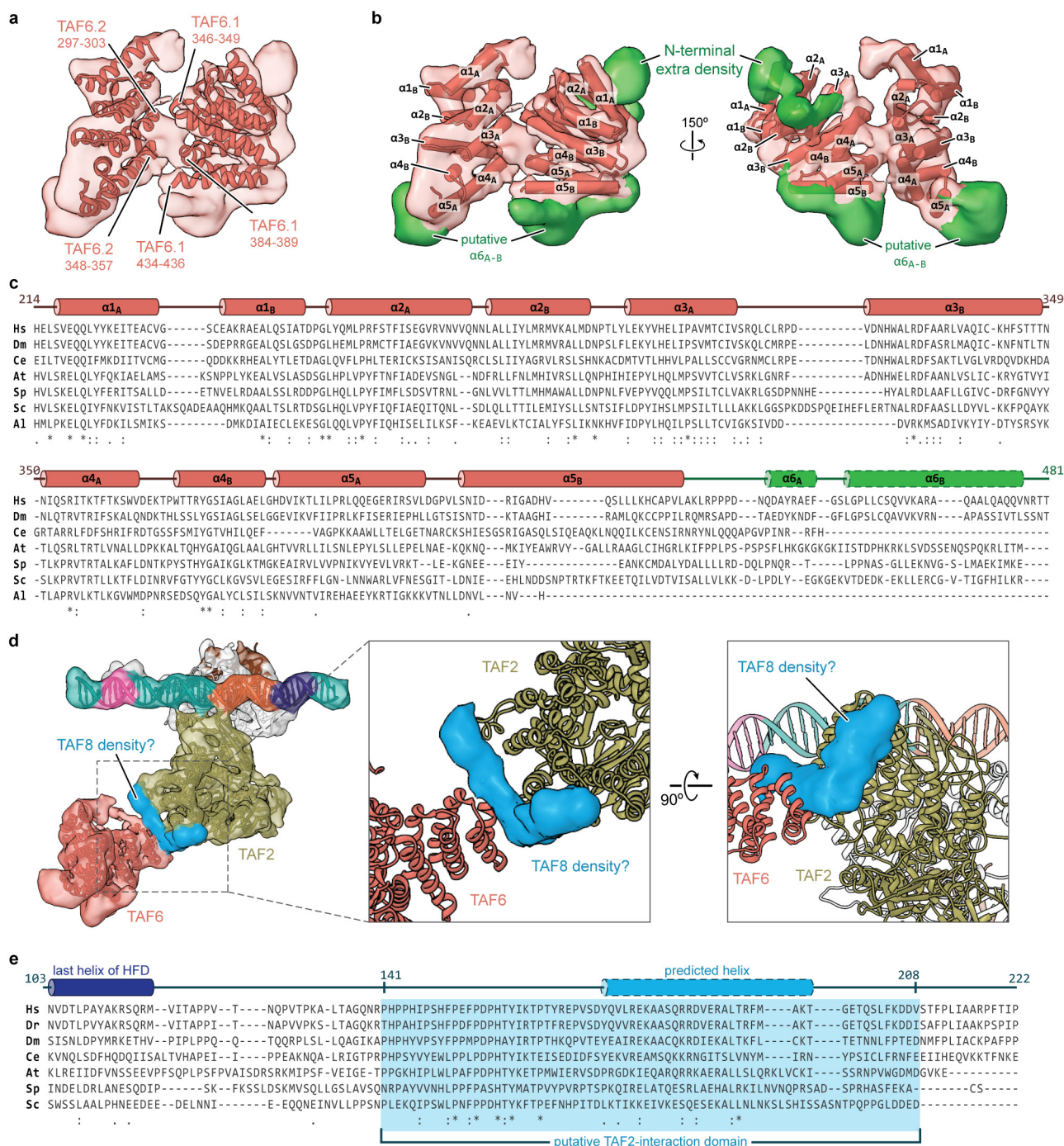
TAF1 DUF3591 corresponding to the internal segment that is missing from the crystal structure and neighbouring residues. The putative Inr-binding domain (1009–1061) within this segment is highlighted in blue. Numbering is based on the human sequence, and abbreviations are the same as in **a**. **d**, Three-dimensional structure prediction for the putative TAF1 Inr-binding domain output by the I-TASSER server<sup>67</sup>. On the left, the residues are coloured in rainbow from N to C termini, with the terminal residues indicated. On the right, the modelling confidence is depicted in terms of the ResQ score (ribbon colour) and *B*-factor estimation (ribbon thickness) output by I-TASSER<sup>67</sup>, with high confidence regions represented by thinner blue ribbon and low-confidence regions represented with thicker red ribbon. **e**, Secondary structure prediction for the sequence modelled in **d** (H, helix; C, coil).





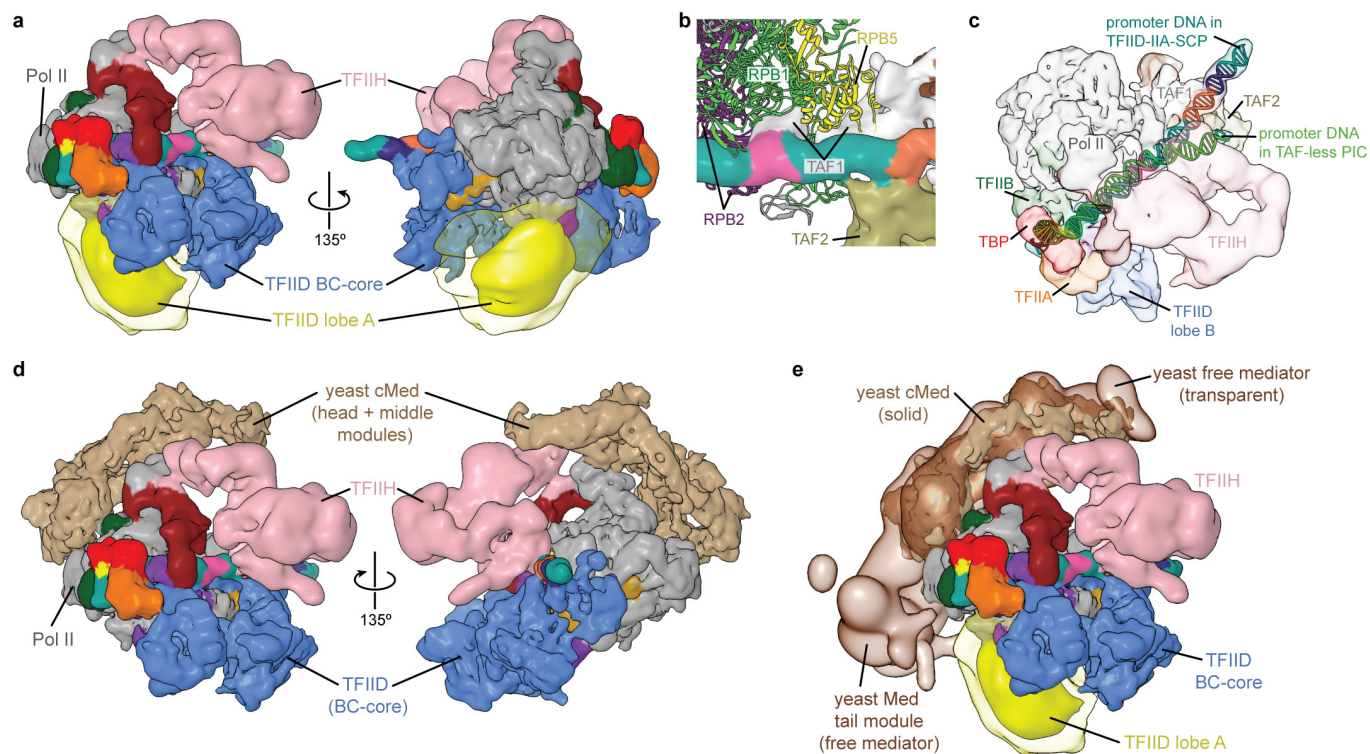
**Extended Data Figure 5 | Structural modelling and conservation of TAF2 APD.** **a**, Structural arrangement of domains (D1–D4) within the TAF2 APD (bottom) compared with that of human ERAP1 (top, PDB accession number 2YD0)<sup>39</sup>, a member of the M1 family of aminopeptidases to which TAF2 shares homology. **b**, Domain arrangement of TAF2, including the four subdomains of the APD (D1–D4), and the C-terminal intrinsically disordered region (IDR). **c**, Rigid-body docking of the best-conserved domains (D1 and D2) of the homologous human ERAP1 confirms the identity of this density. **d**, Segmented densities and

fitted structures for the four subdomains (D1–D4) of the TAF2 APD. **e**, Sequence alignment and secondary structure map for the putative DNA-binding regions within domain 3 of the TAF2 APD (species abbreviations are the same as in Extended Data Fig. 4b). Conserved residues that are in close proximity to the DNA within the docked structure are highlighted in pink. The stretch that is depicted as a dashed line shares low sequence similarity with known M1 aminopeptidases. Numbering is based on the human sequence.



**Extended Data Figure 6 | Structural modelling and conservation of TAF6 and putative TAF8 density.** **a**, Cryo-EM density of the TAF6 dimer with fitted homology models. Putative regions involved in the homodimer interface are labelled. **b**, Organization of  $\alpha$ -helices within the human TAF6 HEAT-like repeat and unaccounted density (green) around the TAF6 homodimer. **c**, Sequence alignment and secondary structure map of the TAF6 HEAT repeat domain (species abbreviations are the same as in Extended Data Fig. 4b, except that Al is *A. locustae*). The green region indicates the region that is unmodelled in our structure, with the two predicted C-terminal helices outlined with dashes. Numbering is based

on the human sequence. **d**, Unaccounted density indicative of two  $\alpha$ -helices, located between domain 4 of the TAF2 APD and one copy of the TAF6 HEAT domain, which we attribute to TAF8. **e**, Sequence alignment of a putative TAF2-interaction domain within TAF8 (species abbreviations are the same as in Extended Data Fig. 4b). The last helix of the structurally determined histone fold domain of TAF8 is depicted in dark blue, while the 26 residue stretch that is predicted to be  $\alpha$ -helical is shown in light blue with dashed outline. Secondary structure prediction was performed with PSI-PRED<sup>71</sup>.



**Extended Data Figure 7 | Modelling of the TFIID-based PIC.** **a**, TFIID-based PIC model from Fig. 4, with the density for lobe A2 density (yellow) low-pass filtered to 16 Å and displayed at two different intensity thresholds (lower threshold in transparency). Both thresholds are lower than that used to display the density for the promoter-bound BC-core of TFIID. **b**, Close-up view of putative interactions between RPB1, -2, and -5 of Pol II and TAF1 of TFIID. **c**, Comparison of the paths of the promoter DNA within the TFIID-IIA-SCP and TAF-less PIC structures. The promoter DNA from the TFIID-IIA-SCP structure is coloured as in Fig. 1,

and the promoter DNA from the TAF-less PIC is coloured in green. View is from the top of the model, relative to **a**. **d**, Docking of the core mediator coactivator complex (cMed, EMDB code 2786)<sup>46</sup>, including the mediator head and middle modules, onto the TFIID-based PIC, on the basis of the structure of a cMED-bound initial transcribing complex. **e**, Docking of the free yeast mediator complex (brown transparency, EMDB code 2634)<sup>47</sup> on the basis of alignment with the core mediator shown in **c**. Lobe A2 of TFIID (yellow) is depicted similarly as in **a**.



Extended Data Table 1 | Summary of TFIID subunits

TFIID subunit	Length (residues)	M.M. (kDa)	Expected # of copies	Structured domains*	Span (residues)	M.M. (kDa)
TBP	339	38	1	DNA binding <sup>a</sup>	159-338	20
				TAND <sup>b</sup>	26-87	6
TAF1	1872	213	1	DUF3591 <sup>a</sup>	600-1109	59
				Double bromo <sup>b</sup>	1359-1625	31
TAF2	1119	137	1	Aminopeptidase <sup>a</sup>	18-975	110
TAF3	929	104	1	Histone fold <sup>b</sup>	5-89	10
				Plant homeo <sup>b</sup>	847-921	9
TAF4	1085	110	2	TAFH <sup>b,c</sup>	582-678	11
				Histone fold <sup>b,c</sup>	870-943	9
TAF5	800	87	2	N-terminal 1 <sup>b,c</sup>	91-124	4
				N-terminal 2 <sup>b,c</sup>	194-340	18
				WD40 repeat <sup>b,c</sup>	460-739	31
TAF6	677	73	2	Histone fold <sup>b,c</sup>	8-77	8
				HEAT-like repeat <sup>a,c</sup>	212-436	25
TAF7	349	40	1	TAF1-interacting <sup>a</sup>	11-154	17
TAF8	310	34	1	Histone fold <sup>b</sup>	28-120	11
TAF9	264	29	2	Histone fold <sup>b,c</sup>	13-80	8
TAF10	218	22	1	Histone fold <sup>b</sup>	113-212	11
TAF11	211	23	1	Histone fold <sup>b</sup>	113-201	10
TAF12	161	18	2	Histone fold <sup>b,c</sup>	57-128	9
TAF13	124	14	1	Histone fold <sup>b</sup>	31-75	5

Subset of structured domains†	Total M.M. ‡ (kDa)
(a) Fitted domains	260
(b) Unassigned domains	290
(c) Present in the recombinant 5TAF	250

MM, molecular mass calculated from amino-acid sequence.

\*‘Structured domains’ indicates domains that have a known structure or are predicted to be structured by sequence homology.

†The structured domains constituting each subset are indicated by superscripted letters in the larger table above, corresponding to the letter label of that subset (‘a’, ‘b’, or ‘c’).

Note that each domain is included in either the fitted domains subset or unassigned domains subset, on the basis of whether or not they have been modelled in the present study, respectively. Additionally, domains present in the recombinant 5TAF complex<sup>32</sup> constitute subset ‘c’.

‡Total molecular mass for domain subsets corresponds to the total mass of structured domains and takes into account the expected number of copies for each corresponding subunit.

# R-process enrichment from a single event in an ancient dwarf galaxy

Alexander P. Ji<sup>1,2</sup>, Anna Frebel<sup>1,2</sup>, Anirudh Chiti<sup>1</sup> & Joshua D. Simon<sup>3</sup>

Elements heavier than zinc are synthesized through the rapid (r) and slow (s) neutron-capture processes<sup>1,2</sup>. The main site of production of the r-process elements (such as europium) has been debated for nearly 60 years<sup>2</sup>. Initial studies of trends in chemical abundances in old Milky Way halo stars suggested that these elements are produced continually, in sites such as core-collapse supernovae<sup>3,4</sup>. But evidence from the local Universe favours the idea that r-process production occurs mainly during rare events, such as neutron star mergers<sup>5,6</sup>. The appearance of a plateau of europium abundance in some dwarf spheroidal galaxies has been suggested as evidence for rare r-process enrichment in the early Universe<sup>7</sup>, but only under the assumption that no gas accretes into those dwarf galaxies; gas accretion<sup>8</sup> favours continual r-process enrichment in these systems. Furthermore, the universal r-process pattern<sup>1,9</sup> has not been cleanly identified in dwarf spheroidals. The smaller, chemically simpler, and more ancient ultrafaint dwarf galaxies assembled shortly after the first stars formed, and are ideal systems with which to study nucleosynthesis events such as the r-process<sup>10,11</sup>. Reticulum II is one such galaxy<sup>12–14</sup>. The abundances of non-neutron-capture elements in this galaxy (and others like it) are similar to those in other old stars<sup>15</sup>. Here, we report that seven of the nine brightest stars in Reticulum II, observed with high-resolution spectroscopy, show strong enhancements in heavy neutron-capture elements, with abundances that follow the universal r-process pattern beyond barium. The enhancement seen in this ‘r-process galaxy’ is two to three orders of magnitude higher than that detected in any other ultrafaint dwarf galaxy<sup>11,16,17</sup>. This implies that a single, rare event produced the r-process material in Reticulum II. The r-process yield and event rate are incompatible with the source being ordinary core-collapse supernovae<sup>18</sup>, but consistent with other possible sources, such as neutron star mergers<sup>19</sup>.

Ultrafaint dwarfs (UFDs) are small galaxies that orbit the Milky Way and have been discovered by deep, wide-area sky surveys<sup>12,13</sup>. Although physically close to us, they are also relics from the era of the first stars and

galaxies and thus an ideal place to investigate the first metal-enrichment events in the Universe<sup>10</sup>. Observations of UFDs provide evidence that they formed all of their stars within 1 to 3 gigayears (Gyr) of the Big Bang<sup>20</sup>; that their stars contain very small amounts of elements heavier than helium (‘metals’)<sup>21</sup>; and that they are enriched by the metal output of only a few generations of stars<sup>11,20</sup>. Analysis of the chemical abundances of light elements (those less heavy than iron) has suggested that core-collapse supernovae are the primary metal sources in these systems<sup>11,16,17</sup>. This conclusion is supported by the unusually low abundances of neutron-capture elements in UFDs—abundances that are consistent with a low production of such elements, and which are associated with massive star evolution<sup>11</sup>. Neutron star mergers might be the dominant source of r-process elements now<sup>5,6</sup>, but they have been thought to be irrelevant in the low-metallicity regime, including in UFDs. Specifically, the r-process yield from neutron star mergers was thought to be too high to be consistent with r-process abundances in low-metallicity stars<sup>3</sup>; the rate of occurrence of these binaries was too low to be found in typical UFDs<sup>4,7</sup>; and the long merging period precluded substantial contributions from neutron star mergers at early times<sup>4,22,23</sup>.

The UFD Reticulum II (Ret II) was recently discovered from Dark Energy Survey data<sup>12,13</sup>, and confirmed as one of the most metal-poor galaxies known<sup>14</sup>. On 1–4 October 2015, we obtained high-resolution spectra of the nine brightest member stars in Ret II (see Table 1 and Extended Data Fig. 1). The abundances of non-neutron-capture elements in all nine stars are consistent with the abundances in other UFD stars and Milky Way halo stars<sup>11,15,24</sup>. Surprisingly, however, only the two most metal-poor stars show the deficiency in neutron-capture elements that is typically found in UFDs<sup>11,16</sup>; the remaining seven stars display extremely strong spectral lines for europium and other neutron-capture elements (Fig. 1). Our abundance analysis (see Methods) finds that these seven stars span a factor of ten in metallicity, centred at  $[\text{Fe}/\text{H}] = -2.5$ , and that all seven stars are substantially enhanced in neutron-capture elements. Their  $[\text{Eu}/\text{Fe}]$  abundances are the highest found in any dwarf galaxy so far<sup>7,16</sup>, and are comparable with those of

**Table 1 | Properties of the nine observed Reticulum II stars**

RA	Dec.	$v_{\text{hel}}$	$g$	$T_{\text{eff}}$ (K)	$\log g$ (dex)	$v_t$ (km s <sup>-1</sup> )	$[\text{Fe}/\text{H}]$	$[\text{Ba}/\text{Fe}]$	$[\text{Eu}/\text{Fe}]$
3 h 35 min 23.85 s	-54° 04' 07.50"	66.8	16.45	4,608	1.00	2.40	-3.01	0.79	1.68
3 h 36 min 07.75 s	-54° 02' 35.56"	62.7	17.43	4,833	1.55	2.15	-2.97	0.91	1.74
3 h 34 min 47.94 s	-54° 05' 25.01"	62.0	17.52	4,900	1.70	1.90	-2.91	1.08	1.87
3 h 35 min 31.14 s	-54° 01' 48.25"	60.9	17.64	4,925	1.90	1.80	-3.34	<-0.80	<1.50
3 h 35 min 48.04 s	-54° 03' 49.82"	61.9	18.27	5,125	2.35	1.75	-2.19	0.36	0.95
3 h 35 min 37.06 s	-54° 04' 01.24"	63.5	18.57	5,170	2.45	1.55	-2.73	1.40	1.70
3 h 35 min 56.28 s	-54° 03' 16.27"	62.7	18.85	5,305	2.95	1.65	-3.54	<0.10	<2.40
3 h 34 min 57.57 s	-54° 05' 31.42"	61.9	18.94	5,328	2.85	1.50	-2.08	1.36	1.77
3 h 34 min 54.24 s	-54° 05' 58.02"	71.6	18.95	5,395	3.10	1.35	-2.77	1.40	2.11

Right ascension (RA) and declination (Dec.) indicate star coordinates.  $v_{\text{hel}}$  is the heliocentric radial velocity of the star in km s<sup>-1</sup>.  $g$  is the star's magnitude. Stellar parameters are effective temperature ( $T_{\text{eff}}$ ), surface gravity ( $\log g$ ), and microturbulence ( $v_t$ ). The notation  $[A/B] = \log_{10}(N_A/N_B)_{\text{star}} - \log_{10}(N_A/N_B)_{\text{Sun}}$ , which quantifies the logarithmic number ratio between two elements A and B relative to the solar ratio.

<sup>1</sup>Department of Physics & Kavli Institute for Astrophysics and Space Research, Massachusetts Institute of Technology, Cambridge, Massachusetts 02139, USA. <sup>2</sup>Joint Institute for Nuclear Astrophysics, Center for the Evolution of the Elements, East Lansing, Minnesota 48824, USA. <sup>3</sup>Observatories of the Carnegie Institution of Washington, Pasadena, California 91101, USA.

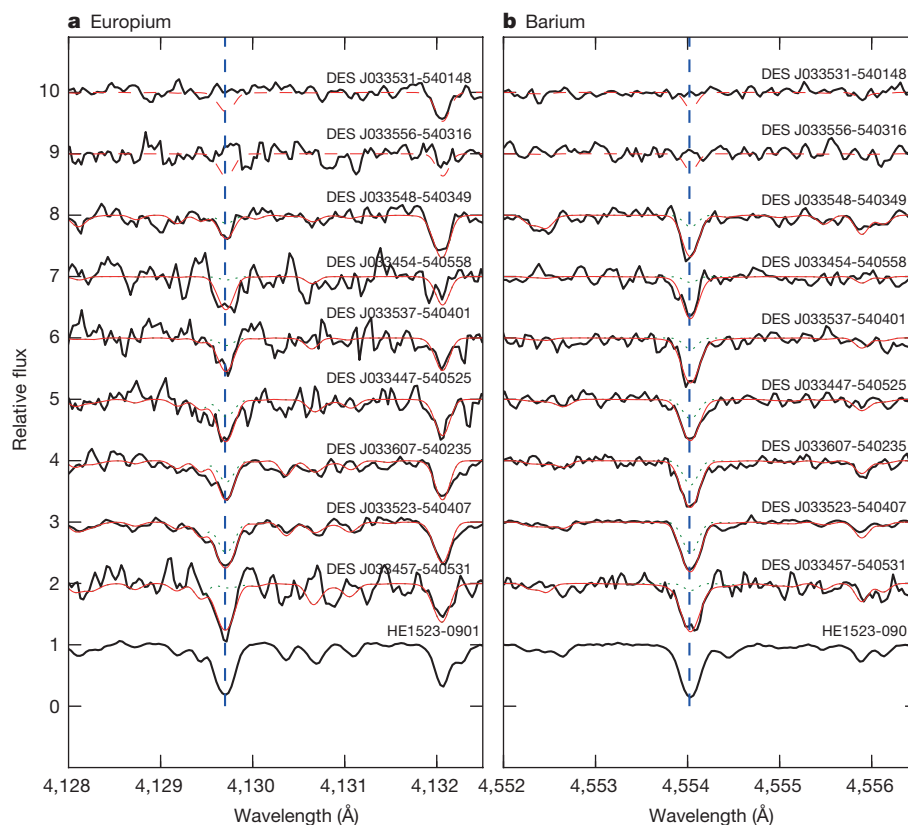


**Figure 1 | Spectra of stars in Reticulum II.** **a**, The spectral region around the europium absorption line (412.9 nm) for the nine brightest stars in Reticulum II, identified by the Dark Energy Survey (DES). Absorption is clearly present in seven of the nine Ret II spectra (black lines), including those with modest signal-to-noise ratios. Thin red lines show synthesized fits to the absorption lines (dashed red lines show upper limits).

For comparison, dotted green lines show synthesized spectra for each individual star using typical limits found in other UFDs ( $[\text{Eu}/\text{H}] = -2.0$ ). Also shown is HE1523-0901, one of the most r-process-enhanced halo stars known<sup>1</sup>. **b**, As for **a**, but showing the region around the barium absorption line (455.4 nm) (the dotted green line shows  $[\text{Ba}/\text{H}] = -4.0$ ).

the most europium-enhanced halo stars known<sup>24</sup> (Fig. 2a, b). Surface accretion of neutron-capture elements from the interstellar medium is at least 1,000 times too small to account for this level of enhancement<sup>25</sup>, and binary mass transfer is unlikely to enrich multiple stars in this galaxy. Thus, these stars must have formed from gas that was heavily pre-enriched with neutron-capture elements.

From our spectra of the four brightest neutron-capture-rich stars, we measure two to eight additional abundances of rare-earth elements. The relative abundances of elements with atomic numbers greater than 55 unambiguously match the scaled solar r-process pattern<sup>1,9</sup> (Fig. 2c). The  $[\text{Eu}/\text{Ba}]$  ratios of the three fainter neutron-capture-rich stars also point to an r-process origin. Ret II thus appears to be an ‘r-process galaxy’, with 78% of observed stars being highly enriched in r-process elements. In comparison, the frequency of metal-poor stars in the Milky Way halo that show similar r-process enhancement is less than 5% (ref. 24). Furthermore, all stars in the nine other UFDs with high-resolution neutron-capture abundances have  $[\text{Ba}/\text{Fe}]$  and  $[\text{Eu}/\text{Fe}]$  values at least 100 times lower than those of the stars in Ret II (although, for some of these UFDs, there are as yet few stars for which such measurements have been made)<sup>11,16,17</sup>. It is thus extremely likely that the neutron-capture material in Ret II was produced by just one event. If each UFD were equally likely to host an r-process event, then the probability that  $N$  r-process events occurred in Ret II, but zero r-process events occurred in the other nine UFDs, is  $(1/10)^N$ . There is thus only about a 1% chance that two or more events contributed to the r-process material in Ret II. Although gas accretion could potentially hide a prolific r-process event in one of the other UFDs, accreting enough gas to decrease the neutron-capture abundance by over two orders of magnitude, while leaving no stars with intermediate r-process enhancements, is implausible.

The r-process yield of a typical core-collapse supernova cannot explain the high r-process abundances found in this galaxy. Using europium as the representative r-process element, we found that five of the r-process stars in Ret II have  $[\text{Eu}/\text{H}]$  abundances of  $-1$  to  $-1.3$ , suggesting that these stars formed in an environment in which the europium mass ratio ( $M_{\text{Eu}}/M_{\text{H}}$ ) was  $10^{-10.3}$  to  $10^{-10.6}$ . The two faintest r-process stars have higher  $[\text{Eu}/\text{H}]$  values, but their larger abundance uncertainties place them within  $1-2\sigma$  of  $[\text{Eu}/\text{H}] = -1$ . In a UFD, metals are typically diluted into roughly  $10^6$  solar masses of hydrogen by turbulent mixing during galaxy assembly<sup>10,26,27</sup>, with low and high limits of  $10^5$ – $10^7$  solar masses (see Methods). The europium yield from this r-process event would then be  $10^{-4.3}$  to  $10^{-4.6}$  solar masses—1,000 times higher than the yields that are typical of core-collapse supernovae ( $M_{\text{Eu}} \approx 10^{-7.5}$  solar masses<sup>17</sup>; brown vertical bar in Fig. 2a, b). Extreme supernova europium yields of about  $10^{-6}$  solar masses have been invoked to aid in chemical evolution models<sup>4</sup>, but even combining these with the minimum possible dilution mass results in  $[\text{Eu}/\text{H}]$  values that are too low to match the stellar abundances in Ret II.

Although there are several candidate sites for rare and prolific r-processes, neutron star mergers are thought to be one of the most likely<sup>3–6,23,25–28</sup>. Typical europium yields from neutron star mergers are  $M_{\text{Eu}} \approx 10^{-4.5}$  solar masses<sup>19</sup>, resulting in  $[\text{Eu}/\text{H}]$  values compatible with those observed in Ret II (orange vertical bar in Fig. 2a, b). The rate of the Ret II r-process event also appears consistent with a neutron star merger, although both the observed and the expected rates are uncertain (see Methods). Given that only one prolific r-process event has occurred in the ten UFDs observed so far, combining the present-day stellar masses of these ten UFDs allows an estimate of how many supernovae must explode for every neutron star merger. Using a standard initial mass function, we find that about 2,000 supernovae contributed



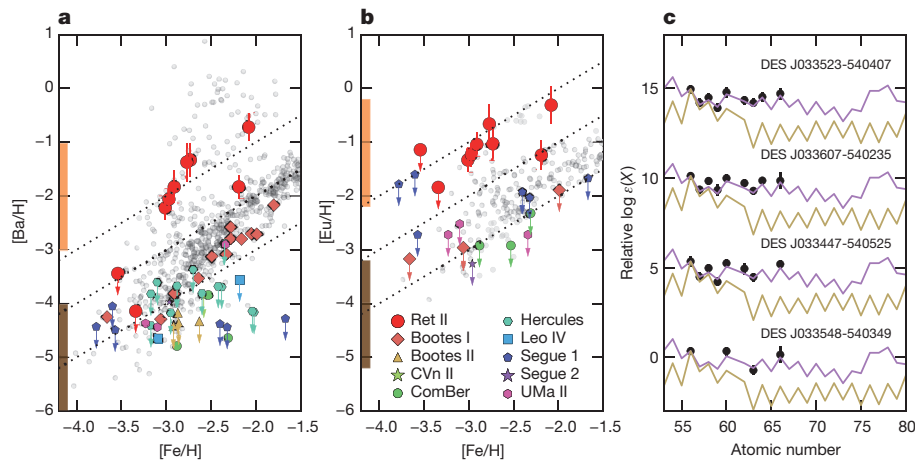


**Figure 2 | Chemical abundances of stars in Reticulum II.** **a**, [Ba/H] and [Fe/H] abundances in stars from Ret II (red points), in halo stars<sup>24</sup> (grey points), and in other UFDs (coloured points; see references within refs 16, 17). The orange and brown vertical bars indicate the abundance ranges that would be expected following a neutron star merger and in a core-collapse supernova, respectively. The dotted black lines show constant [Ba/Fe] abundances. Arrows denote upper limits. Error bars

to all ten of these UFDs, comparable to the expected average rate of one neutron star merger every 1,000–2,000 supernovae<sup>7</sup>.

Chemical evolution models that incorporate yields from neutron star mergers typically need to invoke unusually short merging times (of about 1 million years, Myr) to explain the observed halo-star [Eu/Fe] and [Fe/H] distributions<sup>4,23,28</sup>. However, recent studies have found that a combination of inhomogeneous mixing, hierarchical galaxy formation, and inefficient star formation can alleviate this issue<sup>25–28</sup>. A neutron star merger in a UFD naturally produces such conditions. In particular, energy injection from supernovae is especially effective at disrupting the small minihalo progenitors of UFDs. The resulting delays of more than 10–100 Myr between star-formation episodes<sup>10,29</sup> are consistent with the shortest delay times predicted for neutron star mergers<sup>22</sup>.

Our observations are also consistent with other rare and prolific r-process events. In particular, magnetorotationally driven supernovae synthesize as much as some  $10^{-5}$  solar masses of europium on a supernova timescale and at a rate more frequent than that of neutron star mergers<sup>23</sup>. These particular supernovae and neutron star mergers are similar enough in their r-process yields and rates that Ret II cannot yet be used to distinguish firmly between them. If future theoretical work finds that these two sites differ in other ways—for example, in the abundance of neutron-capture elements around the first r-process peak<sup>15</sup>—then the stellar abundances in Ret II might eventually be used to differentiate between them.

Previous evidence for the occurrence of rare, prolific r-process events in more luminous dwarf spheroidals relied on interpreting a flat [Eu/H] trend with respect to [Fe/H]<sup>7</sup>. However, the existence of this plateau favours a rare r-process event only if gas accretion is unimportant in the galaxy. Invoking gas accretion actually lowers the [Eu/H] value as metallicity increases—in which case the observed plateau requires continual europium production from core-collapse supernovae, rather than a single r-process event. We note that hierarchical structure formation predicts substantial gas accretion into these larger dwarf galaxies, and that extra gas is needed to reproduce their overall metallicity-distribution functions<sup>8</sup>.

In contrast, our evidence for a single event in Ret II is based on large [Eu/Fe] and [Ba/Fe] enhancements relative to those measured in stars in the other UFDs. The europium and barium trends within Ret II can then be used to understand the star-formation, gas-accretion, and metal-mixing history of this galaxy. As an illustration, the star with the highest [Fe/H] abundance might reveal the presence of

represent  $1\sigma$  (see Extended Data Table 1 and Methods). **b**, As in **a**, but for [Eu/H] abundances. **c**, Abundance patterns beyond barium for the four brightest europium-enhanced stars in Ret II (black dots; see Extended Data Table 2), compared with the solar r-process and s-process patterns<sup>9</sup> (purple and yellow lines, respectively). Solar patterns are scaled to stellar barium abundance. Stars are offset from each other by multiples of five.

inhomogeneous metal mixing, as it has a similar [Eu/Fe] abundance to those of the stars with lower [Fe/H] abundances<sup>30</sup> (although we caution that the present data give statistically insignificant abundance trends; see Methods). Thus, the stellar abundances in Ret II not only show that rare and prolific r-process events occurred in the early Universe; they also hold the key to understanding the formation of this relic from the era of the first galaxies.

**Online Content** Methods, along with any additional Extended Data display items and Source Data, are available in the online version of the paper; references unique to these sections appear only in the online paper.

**Received 3 November 2015; accepted 10 February 2016.**

**Published online 21 March 2016.**

1. Sneden, C., Cowan, J. J. & Gallino, R. Neutron-capture elements in the early galaxy. *Annu. Rev. Astron. Astrophys.* **46**, 241–288 (2008).
2. Burbidge, E. M., Burbidge, G. R., Fowler, W. A. & Hoyle, F. Synthesis of the elements in stars. *Rev. Mod. Phys.* **29**, 547–650 (1957).
3. Qian, Y. Z. Supernovae versus neutron star mergers as the major r-process sources. *Astrophys. J.* **534**, L67–L70 (2000).
4. Argast, D., Samland, M., Thielemann, F. K. & Qian, Y. Z. Neutron star mergers versus core-collapse supernovae as dominant r-process sites in the early Galaxy. *Astron. Astrophys.* **416**, 997–1011 (2004).
5. Tanvir, N. R. et al. A ‘kilonova’ associated with the short-duration  $\gamma$ -ray burst GRB 130603B. *Nature* **500**, 547–549 (2013).
6. Wallner, A. et al. Abundance of live <sup>244</sup>Pu in deep-sea reservoirs on Earth points to rarity of actinide nucleosynthesis. *Nature Commun.* **6**, 5956 (2015).
7. Tsujimoto, T., Ishigaki, M. N., Shigeyama, T. & Aoki, W. Chemical feature of Eu abundance in the Draco dwarf spheroidal galaxy. *Publ. Astron. Soc. Jpn* **67**, L3 (2015).
8. Kirby, E. N., Lanfranchi, G. A., Simon, J. D., Cohen, J. G. & Guhathakurta, P. Multi-element abundance measurements from medium-resolution spectra. III. Metallicity distributions of Milky Way dwarf satellite galaxies. *Astrophys. J.* **727**, 78 (2011).
9. Burris, D. L. et al. Neutron-capture elements in the early galaxy: insights from a large sample of metal-poor giants. *Astrophys. J.* **544**, 302–319 (2000).
10. Ji, A. P., Frebel, A. & Bromm, V. Preserving chemical signatures of primordial star formation in the first low-mass stars. *Mon. Not. R. Astron. Soc.* **454**, 659–674 (2015).
11. Frebel, A., Simon, J. D. & Kirby, E. N. Segue 1: an unevolved fossil galaxy from the early Universe. *Astrophys. J.* **786**, 74 (2014).
12. Bechtol, K. et al. Eight new Milky Way companions discovered in first-year Dark Energy Survey data. *Astrophys. J.* **807**, 50 (2015).
13. Koposov, S. E., Belokurov, V., Torrealba, G. & Evans, N. W. Beasts of the southern wild: discovery of nine ultra faint satellites in the vicinity of the Magellanic Clouds. *Astrophys. J.* **805**, 130 (2015).
14. Simon, J. D. et al. Stellar kinematics and metallicities in the ultra-faint dwarf galaxy Reticulum II. *Astrophys. J.* **808**, 95 (2015).
15. Roederer, I. U. et al. Detailed chemical abundances in the r-process-rich ultra-faint dwarf galaxy Reticulum 2. Preprint at <http://arxiv.org/pdf/1601.04070.pdf> (2016).

16. Ji, A. P., Frebel, A., Simon, J. D. & Geha, M. C. High-resolution spectroscopy of extremely metal-poor stars in the least evolved galaxies: Bootes II. *Astrophys. J.* **817**, 41 (2016).
17. François, P. *et al.* Abundance ratios of red giants in low mass ultra faint dwarf spheroidal galaxies. Preprint at arXiv:1510.05401 (2015).
18. Wanajo, S. The r-process in proto-neutron-star Wind revisited. *Astrophys. J.* **770**, L22 (2013).
19. Goriely, S., Bauswein, A. & Janka, H.-T. R-process nucleosynthesis in dynamically ejected matter of neutron star mergers. *Astrophys. J.* **738**, L32 (2011).
20. Brown, T. M. *et al.* The quenching of the ultra-faint dwarf galaxies in the reionization era. *Astrophys. J.* **796**, 91 (2014).
21. Kirby, E. N., Simon, J. D., Geha, M. C., Guhathakurta, P. & Frebel, A. Uncovering extremely metal-poor stars in the Milky Way's ultrafaint dwarf spheroidal satellite galaxies. *Astrophys. J.* **685**, L43–L46 (2008).
22. Dominik, M. *et al.* Double compact objects. I. The significance of the common envelope on merger rates. *Astrophys. J.* **759**, 52 (2012).
23. Wehmeyer, B., Pignatari, M. & Thielemann, F. K. Galactic evolution of rapid neutron capture process abundances: the inhomogeneous approach. *Mon. Not. R. Astron. Soc.* **452**, 1970–1981 (2015).
24. Frebel, A. Stellar archaeology: exploring the Universe with metal-poor stars. *Astron. Nachr.* **331**, 474–488 (2010).
25. Komiya, Y., Yamada, S., Suda, T. & Fujimoto, M. Y. The new model of chemical evolution of r-process elements based on the hierarchical galaxy formation. I. Ba and Eu. *Astrophys. J.* **783**, 132 (2014).
26. Shen, S. *et al.* The history of r-process enrichment in the Milky Way. *Astrophys. J.* **807**, 115 (2015).
27. Van de Voort, F., Quataert, E., Hopkins, P. F., Kere, D. & Faucher-Giguere, C. A. Galactic r-process enrichment by neutron star mergers in cosmological simulations of a Milky Way-mass galaxy. *Mon. Not. R. Astron. Soc.* **447**, 140–148 (2014).
28. Ishimaru, Y., Wanajo, S. & Prantzos, N. Neutron star mergers as the origin of r-process elements in the galactic halo based on the sub-halo clustering scenario. *Astrophys. J.* **804**, L35 (2015).
29. Bland-Hawthorn, J., Sutherland, R. & Webster, D. Ultrafaint dwarf galaxies—the lowest-mass relics from before reionization. *Astrophys. J.* **807**, 154 (2015).
30. Frebel, A. & Bromm, V. Chemical signatures of the first galaxies: criteria for one-shot enrichment. *Astrophys. J.* **759**, 115 (2012).

**Acknowledgements** We gathered data using the 6.5-metre Magellan Clay telescope located at Las Campanas Observatory, Chile. A.P.J. thanks N. Weinberg and P. Schechter for discussions. A.P.J. and A.F. are supported by National Science Foundation (NSF)-CAREER grant AST-1255160. A.F. acknowledges support from the Silverman (1968) Family Career Development Professorship. J.D.S. acknowledges support from NSF grant AST-1108811. This work made use of NASA's Astrophysics Data System Bibliographic Services and the open-source Python libraries numpy, scipy, matplotlib, statsmodels, pandas, seaborn, and astropy. We also used data products originally obtained with the Dark Energy Camera (DECam), which was constructed by the Dark Energy Survey (DES) collaboration. The DES Projects have been funded by the DOE and the NSF (USA), MISE (Spain), STFC (UK), HEFCE (UK), NCSA (UIUC), KICP (Univ. Chicago), CCAPP (Ohio State), MIFPA (Texas A&M), CNPQ, FAPERJ and FINEP (Brazil), MINECO (Spain), DFG (Germany) and the collaborating institutions in the Dark Energy Survey, which are Argonne Lab, UC Santa Cruz, University of Cambridge, CIEMAT-Madrid, University of Chicago, University College London, DES-Brazil Consortium, University of Edinburgh, ETH Zürich, Fermilab, University of Illinois, ICE (IEEC-CSIC), IFAE Barcelona, Lawrence Berkeley Lab, LMU München and the associated Excellence Cluster Universe, University of Michigan, NOAO, University of Nottingham, Ohio State University, University of Pennsylvania, University of Portsmouth, SLAC National Lab, Stanford University, University of Sussex, and Texas A&M University.

**Author Contributions** A.P.J. took the observations and led the analysis and paper writing; A.F. and A.C. assisted with the observations; A.F. and J.D.S. contributed to the analysis; all authors contributed to writing the paper.

**Author Information** Reprints and permissions information is available at [www.nature.com/reprints](http://www.nature.com/reprints). The authors declare no competing financial interests. Readers are welcome to comment on the online version of the paper. Correspondence and requests for materials should be addressed to A.P.J. ([alexji@mit.edu](mailto:alexji@mit.edu)).

## METHODS

**Observations and abundance analysis.** We selected for observation the brightest known red-giant members of Ret II from published medium-resolution spectroscopic surveys of Ret II<sup>14,31,32</sup> (Extended Data Fig. 1). On 1–4 October 2015, we obtained high-resolution spectra with the MIKE spectrograph<sup>33</sup> on the Magellan Clay telescope, using a 1.0-arcsec slit and covering 3,500 Å to 9,000 Å. This provides a spectral resolution of  $\sim 22,000$  and  $\sim 28,000$  at redder and bluer optical wavelengths, respectively. Stars were each observed for 1 to 4 hours, resulting in signal-to-noise ratio per pixel of  $\sim 8$ – $22$  at 4,250 Å and 15–45 at 6,000 Å (Extended Data Table 1). We used the Carnegie–Python pipeline to reduce the spectra<sup>34</sup>. Separate echelle orders were normalized and summed with the semi-automated code SMH<sup>35</sup>, which was also used for the abundance analysis. Radial velocities were determined by cross-correlation of the magnesium triplet lines near 5,150 Å against a high signal-to-noise spectrum of the metal-poor star HD140283.

We determined stellar parameters and abundances with standard spectroscopic methods<sup>36</sup>, which we summarize briefly here. Equivalent widths of iron lines were determined by fitting Gaussian profiles. We rejected iron lines whose reduced equivalent width is larger than  $-4.5$ , because these lines are probably past the linear regime of the curve of growth. We used the Castelli–Kurucz stellar atmospheres with enhanced alpha-abundances<sup>37</sup> and the abundance-analysis code MOOG<sup>38</sup> to determine the abundances of these lines. The effective temperature was found by requiring no iron abundance trend with respect to excitation potential. The surface gravity was found by requiring the Fe II lines to have the same abundance as the Fe I lines. For the seventh and ninth stars in Table 1, we used an isochrone<sup>39</sup> to determine the surface gravity, as no Fe II lines were detectable. We found the microturbulence by requiring no trend between abundance and reduced equivalent width. After determining the stellar parameters spectroscopically, we applied an effective temperature correction<sup>36</sup> and re-determined the surface gravity and microturbulence. This correction increases the effective temperatures and results in increased metallicities.

We estimated statistical uncertainties in the effective temperature and microturbulence by varying the parameters to match the standard deviation of the fitted slopes. Uncertainty in the surface gravity was estimated by varying the parameter to match the standard error of the Fe I and Fe II abundance. We adopt systematic stellar parameter uncertainties of 150 K, 0.3 dex, and 0.2 km s<sup>-1</sup> for the effective temperature, surface gravity, and microturbulence, respectively. These are added in quadrature to the 1 $\sigma$  statistical error. For surface gravity, we adopt a total uncertainty of 0.4 dex when no Fe II lines are available. The uncertainties are listed in Extended Data Table 1. The stellar parameter uncertainties typically correspond to a total uncertainty in iron abundance of  $\sim 0.2$ – $0.3$  dex, which is dominated by the uncertainty in the effective temperature. The abundances of the brightest four stars have been confirmed by observations with higher signal-to-noise ratios<sup>15</sup>.

Abundances of neutron-capture elements were determined with a line list compiled from several sources (refs 40, 41, and references within refs 42, 43). We used spectrum synthesis to derive abundances of barium, lanthanum, praseodymium and europium. Abundances of other neutron-capture elements were determined using equivalent widths of unblended lines. The abundances are tabulated in Extended Data Table 2. Abundance uncertainties indicate the larger of: (1) the standard deviation of abundances derived from individual lines, accounting for small-number statistics<sup>44</sup>; and (2) the total [Fe/H] uncertainty, including stellar parameter uncertainties. The latter uncertainty typically dominates (see Extended Data Table 1). Abundances are quoted relative to solar abundances<sup>45</sup>. We determined conservative upper limits by synthesizing a line with amplitude two times larger than the typical continuum uncertainty.

The strong 4,554 Å and 4,934 Å barium lines are affected by the isotope ratios of these lines. We have used the r-process-only isotope ratios, which reduce the abundance derived from these lines by 0.1–0.3 dex compared with using the solar barium-isotope ratios<sup>1</sup>. We also use the 5,853 Å, 6,141 Å, and 6,496 Å lines to determine the barium abundances. For europium, we use the r-process-only isotope fractions and measure the 4129 Å, 4,205 Å, 4,435 Å, 4,522 Å, and 6,645 Å lines. Full line lists can be obtained by contacting us.

**Dilution mass for ultrafaint dwarf galaxies.** To determine the yield of the r-process event, the observed ratio between europium and hydrogen must be converted into a europium mass. This requires finding the mass of hydrogen gas into which the r-process material is diluted. The dominant physical process affecting this dilution mass is turbulent mixing, driven by the gravitational assembly of the UFD<sup>10,46</sup>. Cosmological simulations have not yet resolved this at the scale of individual metal enrichment events<sup>27</sup>, but order-of-magnitude estimates of a turbulent diffusion coefficient and mixing time result in typical dilution masses of  $\sim 10^6$  solar masses<sup>10</sup>.

Stringent upper and lower bounds can be placed on the dilution mass. The total halo mass of an assembling UFD is  $10^7$ – $10^8$  solar masses, including dark matter<sup>10</sup>. With the cosmological baryon fraction, this places an upper bound of  $\sim 10^7$  solar masses of hydrogen gas that is available for dilution. A lower bound can be derived

by assuming the limit of no turbulent mixing. For a  $10^{51}$  erg supernova, this corresponds to  $\sim 10^5$  solar masses<sup>10</sup>. For a  $10^{50}$  erg neutron star merger, this limit is instead  $10^{3.5}$ – $10^4$  solar masses<sup>27</sup>. The estimate of  $10^6$  solar masses of gas thus cannot be off by more than one order of magnitude in either direction.

Including a  $\pm 1$  order-of-magnitude range on the mixing mass still rules out ordinary core-collapse supernovae as the source of the r-process material in Ret II. See Fig. 2a, b, where the small shaded bars on the left show the [Ba/H] and [Eu/H] derived using a mixing mass of  $10^5$  to  $10^7$  solar masses of hydrogen and a fiducial yield. The adopted europium yields are  $10^{-7.5}$  solar masses for core-collapse supernovae<sup>18</sup> and  $10^{-4.5}$  solar masses for neutron star mergers<sup>19</sup>. The barium yield is calculated from the europium yield by assuming the r-process ratio<sup>9</sup> such that [Ba/Eu] =  $-0.82$ . Note that there are no abundances or upper limits for europium for many of the dwarf galaxy stars in Fig. 2b: it is common to not report europium upper limits when they are too large to be a relevant constraint.

**Expected event rate.** We derive an expected event rate by estimating the total number of supernovae that have exploded in all ten UFDs considered here. The combined present-day luminosity of these UFDs is  $\sim 10^5 L_\odot$ <sup>14,47</sup> (where  $L_\odot$  is the luminosity of the Sun). Note that 80% of the stellar mass comes from just three galaxies (Hercules, Boo I and Leo IV).

Consider an initial mass function of the form  $\phi(m) \sim m^{-\alpha}$ , where  $\phi(m)$  is the probability distribution function describing the number of stars at mass  $m$ , with lower and upper mass limits  $M_l$  and  $M_u$ . Let the minimum mass for a supernova be  $M_{SN}$ , and let the maximum mass of a star that lives for the age of the Universe be  $M_{max}$ . Then, given a present-day luminosity  $L_0$  and mass-to-light ratio  $\eta$ , it is straightforward to show that the number of supernovae per surviving solar mass  $M_\odot$  is:

$$\frac{\int_{M_{SN}}^{M_u} \phi(m) dm}{\int_{M_l}^{M_{max}} m \phi(m) dm} \eta L_0$$

Typical values are  $M_l \sim 0.1 M_\odot$ ,  $M_u \sim 50 M_\odot$ ,  $M_{SN} \sim 10 M_\odot$ , and  $M_{max} \sim 0.8 M_\odot$ . We calculate  $\eta = 2.2$  with a Dartmouth isochrone (12 Gyr, [Fe/H] =  $-2.5$ ,  $[\alpha/Fe] = 0.4$ )<sup>48</sup>. The standard Salpeter initial mass function has  $\alpha = 2.35$ , which results in the number of supernovae being  $\sim 0.009 \eta L_0$ , or  $\sim 2,000$  supernovae from  $\sim 10^5 L_\odot$  of stars surviving until today. This rate is consistent with the average expected rate of neutron star mergers<sup>7</sup>.

The agreement between the rates is promising but by no means conclusive, as several additional factors may affect the estimated rate. If these galaxies lost stellar mass because of tidal stripping, the number of supernovae would have been correspondingly larger. If the initial mass function in UFDs is not Salpeter, this will affect the number of supernovae as well. Indeed, the observed initial mass function for stars with  $M < 0.8 M_\odot$  in UFDs is bottom-light with a slope  $\alpha \sim 1.3$  and mass-to-light ratio  $\eta = 0.92$ . Although it is unknown whether the slope can be extrapolated to higher masses<sup>11,49</sup>, such an extrapolation results in much larger numbers of supernovae. For the typical mass limits considered here, there are  $0.683 \eta L_0$  supernovae, or 63,000 supernovae in all the UFDs combined. Additionally, the r-process in Ret II occurred at very low metallicity, perhaps implying a higher rate for the event than calculated here, because r-process elements synthesized by neutron star mergers occurring after star formation finished cannot be preserved in a galaxy's chemical abundances. Some UFDs may contain r-process-enhanced stars not yet observed. The low-metallicity environment may also affect the binary fraction and merging delay time. We note that the expected rate of neutron star mergers is uncertain to one to two orders of magnitude even in the local Universe<sup>50</sup>. A neutron star binary may experience large velocity kicks during its formation, which can eject the binary from its host galaxy and further reduce the expected rate of these mergers<sup>51</sup>.

**Statistical significance of abundance trends.** The [Ba/H] and [Eu/H] values appear visually to increase with [Fe/H]. However, we caution that these trends should not be overinterpreted, owing to the small number of stars and the substantial abundance uncertainties. As a simple illustration, we performed a weighted least-squares regression (weighting by the inverse error) on the seven r-process stars and used a  $t$ -test to determine the significance of the slope. The [Ba/H] versus [Fe/H] abundance trend has a slope of 0.890, standard error of 0.446, and  $P$ -value of 0.10. The [Eu/H] versus [Fe/H] abundance trend has a slope of 0.486, standard error of 0.354, and  $P$ -value of 0.23. Neither abundance correlation is statistically significant.

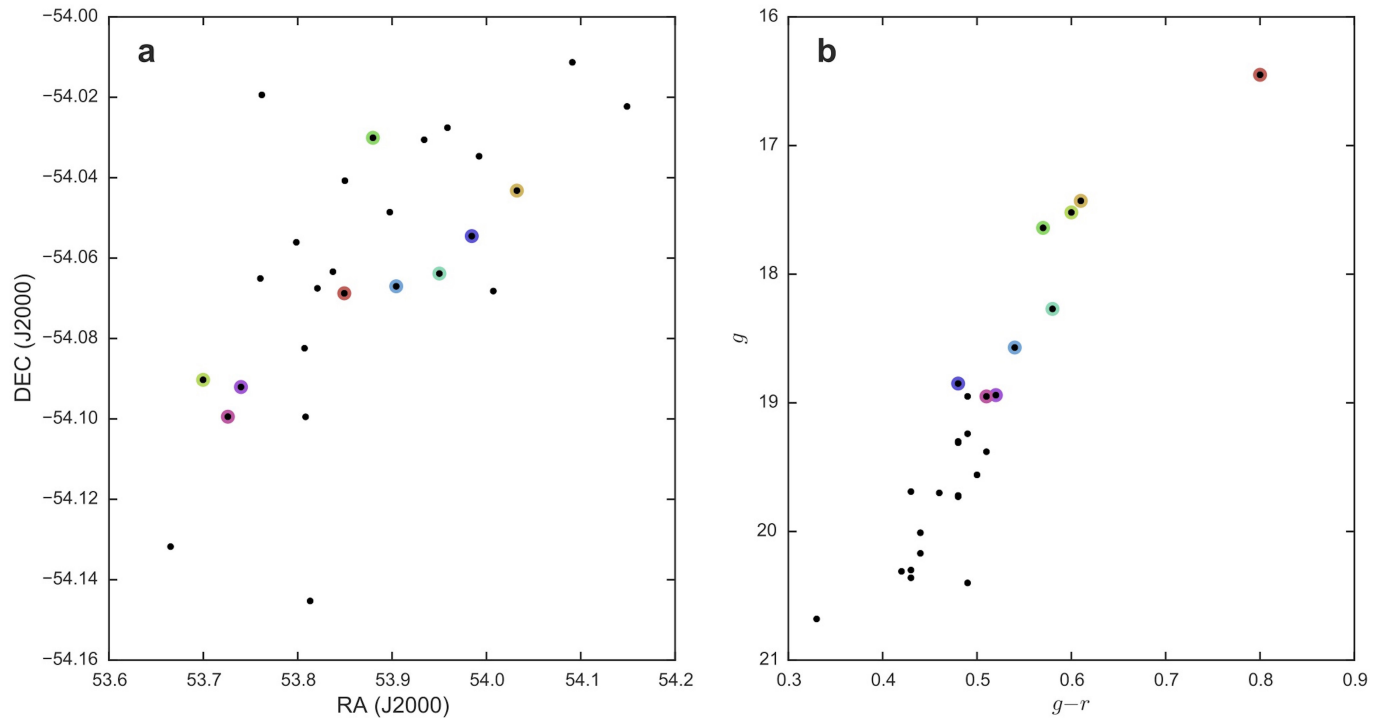
**Code availability.** All codes used to reduce and analyse the data are publicly available. This includes the Carnegie–Python MIKE reduction pipeline<sup>34</sup> and the abundance-analysis code MOOG<sup>38</sup>.

31. Walker, M. G. *et al.* Magellan/M2FS spectroscopy of the Reticulum 2 dwarf spheroidal galaxy. *Astrophys. J.* **808**, 108 (2015).

32. Koposov, S. E. *et al.* Kinematics and chemistry of recently discovered Reticulum 2 and Horologium 1 dwarf galaxies. *Astrophys. J.* **811**, 62 (2015).



33. Bernstein, R., Sheckman, S. A., Gunnels, S. M., Mochnecki, S. & Athey, A. E. MIKE: a double echelle spectrograph for the Magellan telescopes at Las Campanas Observatory. *Proc. SPIE* **4841**, 1694–1704 (2003).
34. Kelson, D. D. Optimal techniques in two-dimensional spectroscopy: background subtraction for the 21st century. *Publ. Astron. Soc. Pacif.* **115**, 688–699 (2003).
35. Casey, A. R. A tale of tidal tails in the Milky Way. Preprint at arXiv:1405.5968 (2014).
36. Frebel, A., Casey, A. R., Jacobson, H. R. & Yu, Q. Deriving stellar effective temperatures of metal-poor stars with the excitation potential method. *Astrophys. J.* **769**, 57 (2013).
37. Castelli, F. & Kurucz, R. L. New grids of ATLAS9 model atmospheres. Preprint at arXiv:astro-ph/0405087 (2004).
38. Sneden, C. A. *Carbon and Nitrogen Abundances in Metal-Poor Stars*. PhD thesis, Univ. Texas, Austin (1973).
39. Kim, Y. C., Demarque, P., Yi, S. K. & Alexander, D. R. The Y2 isochrones for  $\alpha$ -element enhanced mixtures. *Astrophys. J.* **143** (Suppl.), 499–511 (2002).
40. Hill, V. *et al.* First stars. I. The extreme r-element rich, iron-poor halo giant CS 31082-001. Implications for the r-process site(s) and radioactive cosmochronology. *Astron. Astrophys.* **387**, 560–579 (2002).
41. Ivans, I. I. *et al.* Near-ultraviolet observations of HD 221170: new insights into the nature of r-process-rich stars. *Astrophys. J.* **645**, 613–633 (2006).
42. Sneden, C., Lawler, J. E., Cowan, J. J., Ivans, I. I. & Den Hartog, E. A. New rare earth element abundance distributions for the Sun and five r-process-rich very metal-poor stars. *Astrophys. J.* **182** (Suppl.), 80–96 (2009).
43. Roederer, I. U. *et al.* A search for stars of very low metal abundance. VI. Detailed abundances of 313 metal-poor stars. *Astrophys. J.* **147**, 136 10.1088/0004-6256/147/6/136 (2014).
44. Keeping, E. S. *Introduction to Statistical Inference* Ch. 8 (Van Nostrand, 1962).
45. Asplund, M., Grevesse, N., Sauval, A. J. & Scott, P. The chemical composition of the Sun. *Annu. Rev. Astron. Astrophys.* **47**, 481–522 (2009).
46. Greif, T. H., Glover, S. C. O., Bromm, V. & Klessen, R. S. The first galaxies: chemical enrichment, mixing, and star formation. *Astrophys. J.* **716**, 510–520 (2010).
47. McConnachie, A. W. The observed properties of dwarf galaxies in and around the local group. *Astrophys. J.* **144**, 4 10.1088/0004-6256/144/1/4 (2012).
48. Dotter, A. *et al.* The Dartmouth stellar evolution database. *Astrophys. J.* **178** (Suppl.), 89–101 (2008).
49. Geha, M. C. *et al.* The stellar initial mass function of ultra-faint dwarf galaxies: evidence for IMF variations with galactic environment. *Astrophys. J.* **771**, 29 (2013).
50. Abadie, J. *et al.* Topical review: predictions for the rates of compact binary coalescences observable by ground-based gravitational-wave detectors. *Class. Quantum Gravity* **27**, 173001 (2010).
51. Bramante, J. & Linden, T. On the r-process enrichment of dwarf spheroidal galaxies. Preprint at arXiv:1601.06784 (2016).



**Extended Data Figure 1 | Properties of Reticulum II member stars.**  
**a**, Coordinates of member stars, in right ascension (RA) and declination (DEC) at the standard epoch (J2000)<sup>14</sup>. Stars selected for observation with high-resolution spectroscopy are highlighted with large coloured

circles, while other members are shown in black. **b**, Colour-magnitude diagram based on Dark Energy Survey photometry<sup>14</sup>;  $g$  and  $r$  are the stars' magnitudes in two different filters.

Extended Data Table 1 | Stellar-parameter uncertainties

Star	S/N 4250Å	N Fe I Lines	Statistical Uncertainty			Total Uncertainty			[Fe/H] total error	Ba error s.d. (N)	Eu error s.d. (N)
			$T_{\text{eff}}$	$\log g$	$v_t$	$T_{\text{eff}}$	$\log g$	$v_t$			
1	22	128	46	0.02	0.21	157	0.30	0.29	0.23	0.06 (5)	0.13 (5)
2	12	103	71	0.16	0.19	166	0.34	0.28	0.21	0.17 (5)	0.22 (4)
3	11	104	81	0.08	0.20	170	0.31	0.28	0.23	0.30 (5)	0.06 (3)
4	16	80	63	0.19	0.20	163	0.36	0.28	0.23		
5	12	124	62	0.12	0.20	162	0.32	0.28	0.22	0.11 (5)	0.27 (2)
6	10	51	134	0.21	0.30	201	0.37	0.36	0.31	0.30 (5)	0.00 (2)
7	11	33	210	N/A	0.35	258	0.40	0.40	0.37		
8	8	67	104	0.11	0.23	183	0.32	0.30	0.26	0.04 (5)	0.35 (3)
9	7	31	199	N/A	0.37	249	0.40	0.42	0.36	0.24 (4)	0.00 (2)

S/N is the signal-to-noise ratio per pixel near 4,250 Å.  $T_{\text{eff}}$  is in K,  $\log g$  in dex, and  $v_t$  in km s<sup>-1</sup>. The number of lines used to determine the barium and europium abundances is given in parentheses. The adopted abundance error is the larger of the standard deviations between lines and the [Fe/H] error. Stars are numbered from brightest to faintest, from Star 1 to Star 9 in this order: DES J033523–540407, DES J033607–540235, DES J033447–540525, DES J033531–540148, DES J033548–540349, DES J033537–540401, DES J033556–540316, DES J033457–540531, DES J033454–540558.



Extended Data Table 2 | Abundances of neutron-capture elements

Element	Star 1	Star 2	Star 3	Star 4	Star 5	Star 6	Star 7	Star 8	Star 9
$\log \epsilon(\text{Ba})$	-0.04	0.12	0.35	<-1.96	0.35	0.85	<-1.26	1.46	0.81
[Ba/Fe]	0.79	0.91	1.08	<-0.80	0.36	1.40	<0.10	1.36	1.40
$\log \epsilon(\text{La})$	-0.81	-0.64	-0.51						
[La/Fe]	1.10	1.23	1.30						
$\log \epsilon(\text{Ce})$	-0.51	-0.16	-0.02					0.75	
[Ce/Fe]	0.92	1.23	1.31					1.25	
$\log \epsilon(\text{Pr})$	-1.09	-0.67	-0.79						
[Pr/Fe]	1.20	1.58	1.40						
$\log \epsilon(\text{Nd})$	-0.21	-0.01	0.25		0.35			1.18	
[Nd/Fe]	1.38	1.54	1.74		1.12			1.84	
$\log \epsilon(\text{Sm})$	-0.65	-0.28	-0.05						
[Sm/Fe]	1.40	1.73	1.90						
$\log \epsilon(\text{Eu})$	-0.81	-0.71	-0.52	<-1.32	-0.72	-0.51	<-0.62	0.21	-0.14
[Eu/Fe]	1.68	1.74	1.87	<1.50	0.95	1.70	<2.40	1.77	2.11
$\log \epsilon(\text{Gd})$	-0.47	-0.14							
[Gd/Fe]	1.47	1.76							
$\log \epsilon(\text{Dy})$	-0.29	-0.15	0.20		0.15	0.16		1.22	
[Dy/Fe]	1.62	1.72	2.01		1.24	1.79		2.20	

Stars are numbered from brightest to faintest, from star 1 to star 9, as in Extended Data Table 1.

# Measurement of the Earth tides with a MEMS gravimeter

R. P. Middlemiss<sup>1,2</sup>, A. Samarelli<sup>1</sup>, D. J. Paul<sup>2</sup>, J. Hough<sup>1</sup>, S. Rowan<sup>1</sup> & G. D. Hammond<sup>1</sup>

**The ability to measure tiny variations in the local gravitational acceleration allows, besides other applications, the detection of hidden hydrocarbon reserves, magma build-up before volcanic eruptions, and subterranean tunnels. Several technologies are available that achieve the sensitivities required for such applications (tens of microgal per hertz<sup>1/2</sup>): free-fall gravimeters<sup>1</sup>, spring-based gravimeters<sup>2,3</sup>, superconducting gravimeters<sup>4</sup>, and atom interferometers<sup>5</sup>. All of these devices can observe the Earth tides<sup>6</sup>: the elastic deformation of the Earth's crust as a result of tidal forces. This is a universally predictable gravitational signal that requires both high sensitivity and high stability over timescales of several days to measure. All present gravimeters, however, have limitations of high cost (more than 100,000 US dollars) and high mass (more than 8 kilograms). Here we present a microelectromechanical system (MEMS) device with a sensitivity of 40 microgal per hertz<sup>1/2</sup> only a few cubic centimetres in size. We use it to measure the Earth tides, revealing the long-term stability of our instrument compared to any other MEMS device. MEMS accelerometers—found in most smart phones<sup>7</sup>—can be mass-produced remarkably cheaply, but none are stable enough to be called a gravimeter. Our device has thus made the transition from accelerometer to gravimeter. The small size and low cost of this MEMS gravimeter suggests many applications in gravity mapping. For example, it could be mounted on a drone instead of low-flying aircraft for distributed land surveying and exploration, deployed to monitor volcanoes, or built into multi-pixel density-contrast imaging arrays.**

Gravimeters can be split into two broad categories: absolute gravimeters and relative gravimeters. Absolute gravimeters measure the gravitational acceleration,  $g$ , by timing a mass in free fall over a set distance. Absolute gravimeters are very accurate but are bulky and expensive. The Micro- $g$  Lacoste FG5 (ref. 1), for example, achieves acceleration sensitivities of  $1.6 \mu\text{Gal Hz}^{-1/2}$  (that is, an acceleration measurement of  $1.6 \mu\text{Gal}$  over an integration time of one second, where  $1 \text{ Gal} = 1 \text{ cm s}^{-2}$ ), but it costs over \$US100,000 and weighs 150 kg. Relative gravimeters make gravity measurements relative to the extension of a spring: the deflection of a mass on a spring will change as  $g$  varies. These devices can be made smaller than absolute gravimeters but are intrinsically less stable: the spring constant can change with varying environmental conditions. The Scintrex CG5 relative gravimeter (also costing over \$US100,000, but weighing 8 kg) can measure gravity variations down to  $2 \mu\text{Gal}$  (refs 2 and 3) but is much more susceptible to drift than absolute devices. For any mass-on-spring system, increased acceleration sensitivity is achieved by either improving the sensitivity to displacement, or by minimizing the ratio,  $k/m$ , between the spring constant,  $k$ , and the mass,  $m$ . A system in which a mass is suspended from a spring within a rigid housing will respond differently to signals above or below the resonant frequency. In the regime below the resonance there will be a linear relationship between the displacement of the proof mass and the acceleration of the housing. This is the region in which the device can be used as an accelerometer or gravimeter.

MEMS devices are microscopic mechanical devices made from semiconductor materials. They have the advantage of being mass-producible, light-weight and cheap. Although mobile phone accelerometers are not very sensitive, some MEMS devices have been developed that reach sensitivities much better than the  $0.23 \text{ mGal Hz}^{-1/2}$  of the iPhone MEMS device<sup>7</sup>. For example: a device developed by ref. 8 has a sensitivity of  $17 \mu\text{Gal Hz}^{-1/2}$ , the SERCEL QuietSieis<sup>9</sup> has a sensitivity of  $15 \mu\text{Gal Hz}^{-1/2}$ , and a microseismometer developed by ref. 10 has a sensitivity of  $2 \mu\text{Gal Hz}^{-1/2}$ . These devices, however, can only operate as seismometers and do not have sufficient stability to be classed as gravimeters, which are capable of monitoring low-frequency gravimetric signals such as the Earth tides (around  $10 \mu\text{Hz}$ ). Extended Data Table 1 summarizes the characteristics of these MEMS seismometers, the Scintrex CG5 gravimeter, and our own gravimeter. Extended Data Fig. 7 provides a further comparison between our own device, the microseismometer in ref. 10, the Scintrex CG5 and two other commercial devices.

The Earth tides are an elastic deformation of the Earth's crust caused by the changing relative phases of the Sun, the Earth and the Moon<sup>6</sup>. They produce a small variation in the local gravitational acceleration, the size of which also depends on the latitude and elevation of the measurement location. Depending on the time of the lunar month, the Earth tides vary in amplitude and frequency, moving between diurnal ( $2 \times 10^{-5} \text{ Hz}$ ) and semi-diurnal ( $1 \times 10^{-5} \text{ Hz}$ ) peaks. Since the Earth tides have a peak signal strength<sup>3</sup> of less than  $400 \mu\text{Gal}$ , and a low-frequency oscillation, they are a useful natural signal with which to demonstrate both the sensitivity and long-term stability of any gravimeter.

Our device is designed to have a resonant frequency of under 4 Hz. To achieve such low frequencies a geometric anti-spring system<sup>11,12</sup> was chosen. With increasing displacement, anti-springs get softer and their resonant frequency gets lower. A geometrical anti-spring requires a pair of arched flexures that meet at a constrained central point. In the case of our MEMS device they meet at the proof mass. This geometry constrains the motion of the proof mass to the axis shown in Fig. 1. As the proof mass is pulled away from its unloaded position the spring constant is lowered. This is in contrast to a spring obeying Hooke's law, in which the spring constant does not change with increasing displacement. Tilting the MEMS device from the horizontal to the vertical orientation pulls the proof mass down, thus lowering the frequency from over 20 Hz when horizontal to 2.3 Hz when vertical. We have opted for a configuration with a pair of anti-spring flexures supporting the lower portion of the proof mass, and a single flexure supporting the top. All of the flexures are only  $5 \mu\text{m}$  wide but  $200 \mu\text{m}$  deep. The three-flexure system maintains an anti-spring behaviour as the gravitational loading increases (when the device is tilted from horizontal to vertical). Owing to the asymmetry of the design, however, a small level of  $y$ -axis tilting occurs. This tilt pulls the system off its constrained axis. When the system reaches its equilibrium, it shows Hooke's law behaviour (see Methods and Extended Data Fig. 1 for further details). We thus

<sup>1</sup>Scottish Universities Physics Alliance (SUPA), University of Glasgow, School of Physics and Astronomy, Kelvin Building, University Avenue, Glasgow G12 8QQ, UK. <sup>2</sup>University of Glasgow, School of Engineering, Rankine Building, Oakfield Avenue, Glasgow G12 8LT, UK.

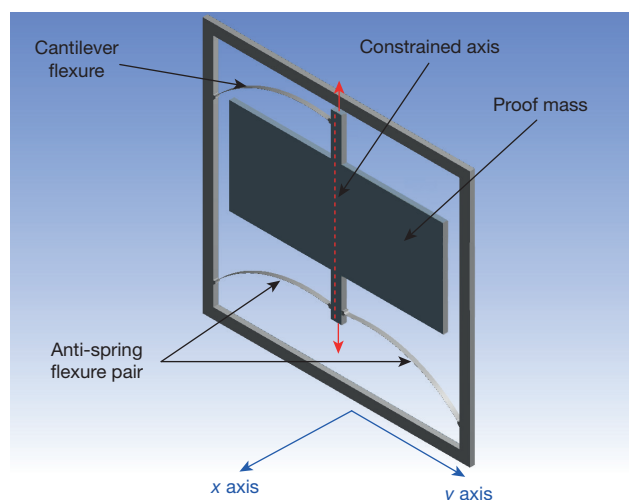


**Figure 1 | The MEMS device.** Design of the MEMS gravimeter. The central proof mass is suspended from three flexures: an anti-spring pair at the bottom and a curved cantilever at the top. The anti-spring pair constrains the motion of the proof mass along the constrained axis (red dashed line). The frequency is lowered by this constraint until the cantilever pushes the motion off-axis, stabilizing the MEMS device at a lower frequency.

have a device that is stable at a much lower frequency than traditional MEMS devices. A resonant frequency of 2.3 Hz is the lowest resonant frequency of any reported MEMS accelerometer so far. To our knowledge the next-lowest resonant frequency reported is 10.2 Hz in a device made by ref. 13. The fact that the system has Hooke's law behaviour in its vertical configuration means that it is less sensitive to tilt in the  $x$  axis (see Fig. 1) than would be the case for a normal geometrical anti-spring (see Extended Data Fig. 8).

The proof mass motion is measured using an optical shadow sensor<sup>14</sup>. Here a light-emitting diode (LED) illuminates a photodiode with the MEMS device mounted in between. Motion of the proof mass modulates the shadow, generating a change in the current output of the photodiode. This shadow sensor (Fig. 2) achieves a high sensitivity (equating to an acceleration noise floor of  $\leq 10 \mu\text{Gal}$  at the sampling frequency of 0.03 Hz), while allowing a large dynamic range of up to  $50 \mu\text{m}$ .

Observation of the Earth tides requires stable operation over several days. The main contributor to parasitic motion is the varying

temperatures of the system. For this reason the 'C'-shaped structure of the shadow sensor was fabricated from fused silica because of its low thermal expansion coefficient at room temperature ( $4.1 \times 10^{-7} \text{K}^{-1}$ )<sup>15</sup>. Silicon has a much larger thermal expansion coefficient ( $2.6 \times 10^{-6} \text{K}^{-1}$ )<sup>16</sup>, but we used silicon to make the MEMS because it is a standard fabrication material in the semiconductor industry, it has high mechanical strength, and its thermal properties are well characterized. The dominant mechanism by which temperature variations affect the gravity measurement is the change in Young's modulus,  $Y$ , of the flexures<sup>17,18</sup>. This in turn alters the spring constant  $k$  of the flexures, giving  $k^{-1}dk/dT = 7.88 \times 10^{-6} \text{K}^{-1}$ . We therefore implemented servo control loops to maintain the temperature of the system to within 1 mK. A change in temperature of 1 mK would give an uncertainty in the gravity reading of about  $25 \mu\text{Gal}$ . The primary control loop maintained the temperature of the MEMS device directly, the second controlling the temperature of a copper thermal shield that encased the entire shadow sensor (Fig. 2). The MEMS device was placed inside a vacuum system. This was bolted to the floor without an external seismic isolation table, which would be a large and expensive addition.

From December 2014 the system was left in continuous operation while the servo control was optimized. Figure 3 demonstrates a data run of five days between 13 and 18 March 2015 in which gravitational acceleration is plotted against time. The blue data demonstrates our experimental data averaged with a time constant of 240 min (the full noise data can be observed in Extended Data Fig. 2a), together with a data set filtered with a 10-min time constant (Extended Data Fig. 2b). The solid red line is a theoretical plot of the Earth tides as should be observed at our location ( $55.8719^\circ \text{N}$ ,  $4.2875^\circ \text{W}$ ), and was plotted using *TSOFT*<sup>19</sup>. An ocean loading correction is also included in this theoretical plot to account for the effect of nearby tidal waters pressing on the Earth's crust, although the effect is at the level of 5% of the total signal for our laboratory. There is a strong correlation coefficient,  $R$ , of 0.86 between our experimental data and the theory plot, indicating that we have indeed measured the Earth tides with our MEMS device. This measurement provides a natural calibration for the gravimeter, the results of which allow us to determine that the present sensitivity of the device is  $40 \mu\text{Gal Hz}^{-1/2}$ . We further performed a stability test of the calibration factor for our device by monitoring the tides at two intervals approximately three months apart. The calibration remained constant to better than 5% (Extended Data Fig. 9).

The noise floor of our device is limited by seismic noise. A theoretical thermal noise floor of under  $0.5 \mu\text{Gal Hz}^{-1/2}$  can be calculated, assuming that losses are due to structural damping<sup>20</sup>. This calculation is

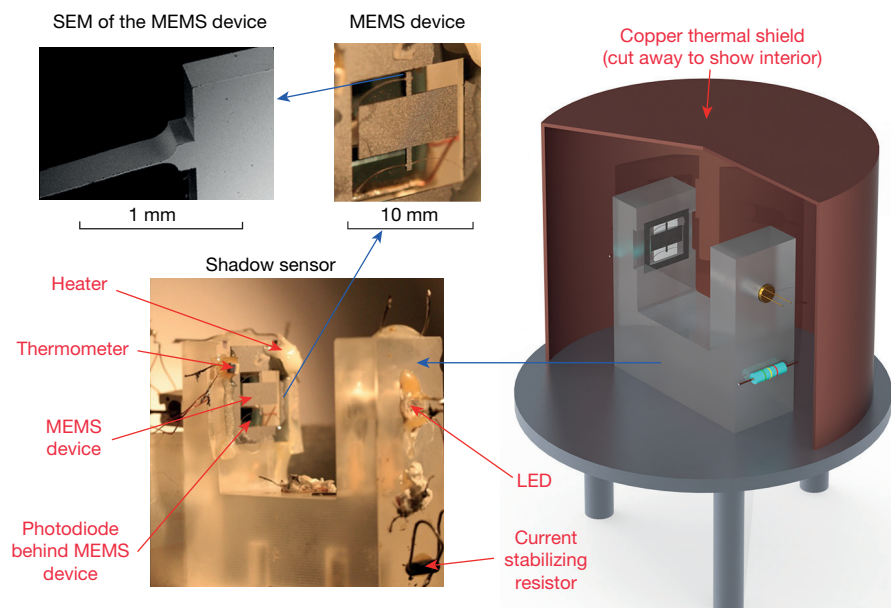


**Figure 2 | The experimental set-up.** The MEMS device and the shadow sensor. Both sit on an aluminium plate and are encased in a copper thermal shield. Both the MEMS device and the shield are thermally controlled. At the top left is a photograph and scanning electron microscope (SEM) image (copyright for both images R.P.M., 2015) of the MEMS device. At the bottom left is a photograph of the MEMS device mounted on the optical shadow sensor with glue holding the heater and thermometer in place (copyright G.D.H., 2015).



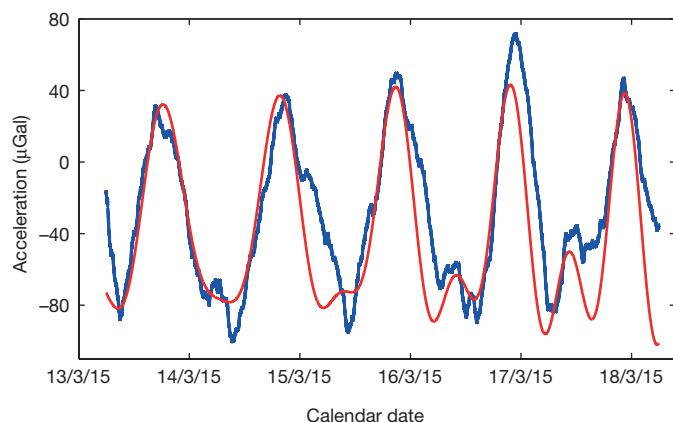


**Figure 3 | The Earth tides.** The measurements of the Earth tides obtained from the MEMS device. The data has been averaged with a time constant of 240 min. The red line is a theoretical plot calculated with *TSOFT*<sup>19</sup>, including an ocean loading correction. The blue line is the experimental data. The two series have a correlation coefficient of 0.86.

based upon a measurement of the quality factor,  $Q$ , of the device under vacuum of about 80 (the relaxation time of the MEMS device is about 11 s). We observe that  $Q$  reduces as the resonant frequency is lowered

(Extended Data Fig. 3). This behaviour is observed in geometrical anti-springs because at low resonant frequencies the springs restoring force becomes comparable to internal friction<sup>21</sup>.

To put the sensitivity of our device into context,  $40 \mu\text{Gal Hz}^{-1/2}$  is sufficient in 1 s to detect a tunnel with a cross-sectional area of  $2 \text{ m}^2$  and length of 4 m at a depth of 2 m. It could be used to find oil reservoirs exceeding a size of  $50 \text{ m} \times 50 \text{ m} \times 50 \text{ m}$  (with a density contrast of 50%) at a depth of 150 m. A change of  $45 \mu\text{Gal}$  was a 'clear precursor' to a volcanic eruption in the Canary Islands in 2011<sup>22</sup>. It is accepted that intrusion of new magma into a reservoir precedes volcanic eruptions<sup>23</sup> so continuous microgravity measurements around volcanoes are a useful tool in monitoring such events<sup>24</sup>. The ratio of ground deformation to change in gravity can be used to monitor magma chambers at depths of several kilometres<sup>25</sup>.

In Fig. 3 a linear drift term has been removed from the data. This drift equates to less than  $150 \mu\text{Gal}$  per day, a factor of three better than the drift of the Scintrex CG5 ( $500 \mu\text{Gal}$  per day). Our MEMS device and the Scintrex CG5 auto-correct this drift with software. Figure 4 consists of eight subplots demonstrating the drift characteristics of the MEMS device. Figure 4a shows the full-noise tide data without a linear drift correction. Figure 4c shows the same data but with the tide signal removed. Figure 4e shows the same data again but with a linear drift correction. Figure 4g shows the same data as in Fig. 4e, but with a 240-min filter applied. Figure 4b, d, f and h shows the Allan deviation for the data in

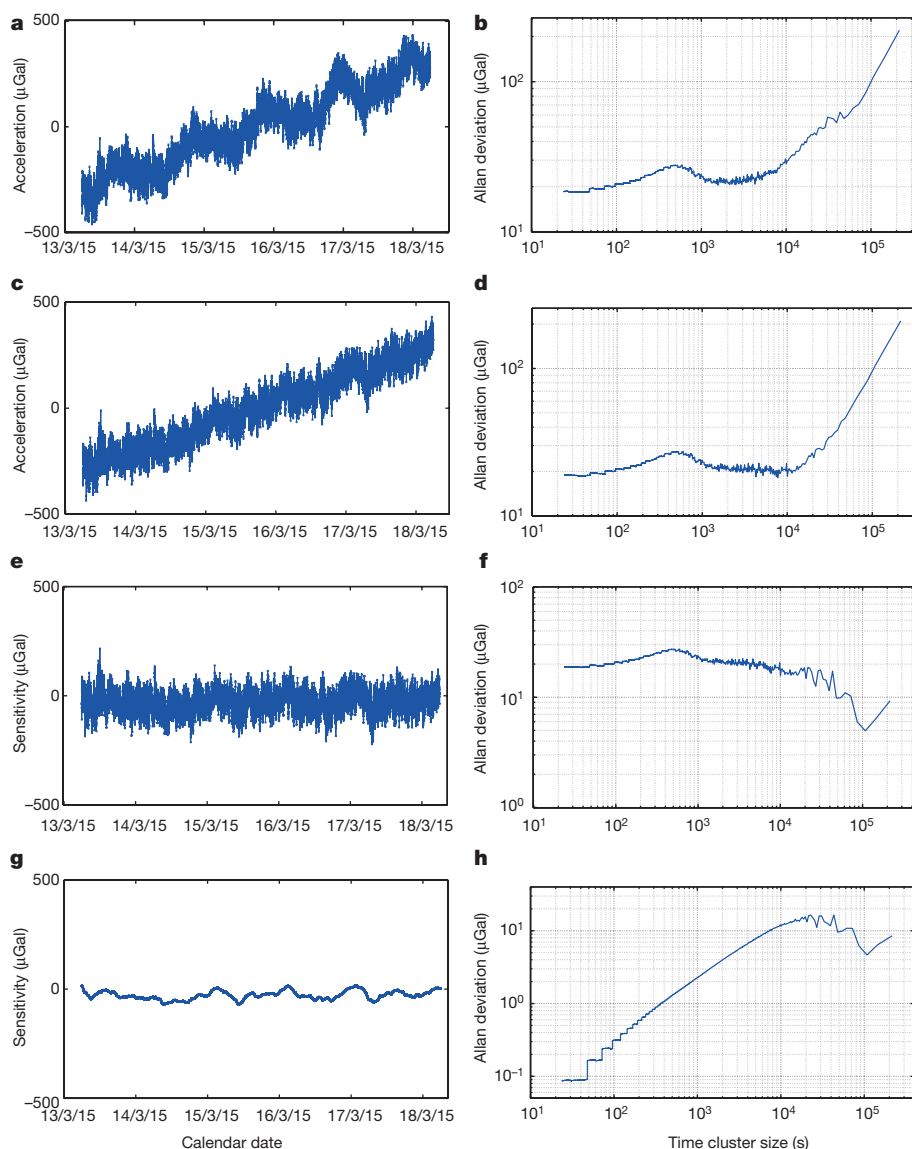


**Figure 4 | Drift characteristics.** **a**, A full noise time series of the tide measurement. **b**, The Allan deviation of the series in **a**. **c**, A full noise time series of the tide measurement with the tide signal removed via a regression against the theoretical data from *TSOFT*<sup>19</sup>. **d**, The Allan deviation of the series in **c**. **e**, A time series of the tide measurement with the tides removed and the linear drift corrected. **f**, The Allan deviation of the series in **e**. **g**, The same data as in **e** but with a 240-min filter added. **h**, The Allan deviation plot of the filtered data in **g**.

Fig. 4a, c, e and g respectively. Allan deviation is a technique used to measure the variation over the full frequency range of a signal by averaging over increasingly larger time intervals<sup>26</sup>.

The data analysed in Fig. 4 spans a frequency range from  $10^{-5}$  Hz to 0.03 Hz (the sampling frequency of this data set, which was used to remove the effect of seismic noise). A second data set was taken at a faster sampling rate to observe the response of the device from 0.03 Hz up to the resonant frequency of 2.3 Hz. Both data sets can be observed in Extended Data Fig. 6 in the form of a root-mean-square acceleration sensitivity plot. The Allan deviation for the high-frequency series is polluted by the presence of two large signals: the resonant frequency of the device, and the microseismic peak<sup>27,28</sup>. This deviation plot is not a useful measure of the noise of the device and has therefore not been included in Fig. 4. Figure 4a and c demonstrates the linear drift that the device experiences. Figure 4b, d and f also demonstrates a small peak at 500 s that is an artefact of the temperature servo. The broad peak that is only visible on the rising edge of Fig. 4b is the tide signal. A comparison between the drift characteristics of our device and some other commercial gravimeters is displayed in Extended Data Fig. 7 in which an acceleration power spectral density plot is displayed.

Because this MEMS device is capable of measuring the Earth tides, it is not just an accelerometer, but a gravimeter. Made from a single silicon chip the size of a postage stamp, this sensor has the lowest reported resonant frequency of any MEMS accelerometer (2.3 Hz), is within an order of magnitude of the best acceleration sensitivity of any MEMS device ( $40 \mu\text{Gal Hz}^{-1/2}$ ), and has the best reported stability of any MEMS device. This prototype will enable the development of density-contrast imaging technology useful in many industrial, defence, civil and environmental applications. It has the potential to be inexpensive, mass-produced and light-weight, opening up new markets. This MEMS gravimeter could be flown in drones by oil and gas exploration companies, reducing the need for dangerous low-altitude aeroplane flights, it could be used to locate subterranean tunnels, and it could be used by building contractors to find underground utilities. Networks of sensors could be operated in areas unsafe for humans, to monitor natural and man-made hazards, for example, on volcanoes or unstable slopes to measure the spatial and temporal resolution of subsurface density changes and improve hazard forecasting<sup>25,29</sup>.

**Online Content** Methods, along with any additional Extended Data display items and Source Data, are available in the online version of the paper; references unique to these sections appear only in the online paper.

**Received 31 July 2015; accepted 2 February 2016.**

1. Van Camp, M. Uncertainty of absolute gravity measurements. *J. Geophys. Res.* **110**, B05406 (2005).
2. Jiang, Z. *et al.* Relative gravity measurement campaign during the 8th international comparison of absolute gravimeters (2009). *Metrologia* **49**, 95–107 (2012).
3. Lederer, M. Accuracy of the relative gravity measurement. *Acta Geodyn. Geomater.* **6**, 383–390 (2009).
4. Goodkind, J. M. The superconducting gravimeter. *Rev. Sci. Instrum.* **70**, 4131–4152 (1999).
5. de Angelis, M. *et al.* Precision gravimetry with atomic sensors. *Meas. Sci. Technol.* **20**, 022001 (2009).
6. Farrell, W. E. Earth tides, ocean tides and tidal loading. *Phil. Trans. R. Soc. A* **274**, 253–259 (1973).
7. D'Alessandro, A. & D'Anna, G. Suitability of low-cost three-axis MEMS accelerometers in strong-motion seismology: tests on the LIS331DLH (iPhone) accelerometer. *Bull. Seismol. Soc. Am.* **103**, 2906–2913 (2013).
8. Krishnamoorthy, U. *et al.* In-plane MEMS-based nano-g accelerometer with sub-wavelength optical resonant sensor. *Sens. Actuat. A* **145–146**, 283–290 (2008).
9. Lainé, J. & Mougnot, D. A high-sensitivity MEMS-based accelerometer. *Leading Edge* **33**, 1234–1242 (2014).
10. Pike, W. T. *et al.* A self-levelling nano-g silicon seismometer. In *Proc. IEEE Sensors 2014* 1599–1602, <http://ieeexplore.ieee.org/xpl/articleDetails.jsp?arnumber=6985324> (IEEE, 2014).

11. Bertolini, A., Cella, G., Desalvo, R. & Sannibale, V. Seismic noise filters, vertical resonance frequency reduction with geometric anti-springs: a feasibility study. *Nucl. Instrum. Meth. A* **435**, 475–483 (1999).
12. Cella, G. *et al.* Seismic attenuation performance of the first prototype of a geometric antispring filter. *Nucl. Instrum. Meth. A* **487**, 652–660 (2002).
13. Pike, W. T., Standley, I. M. & Calcutt, S. A silicon microseismometer for Mars. In *Transducers and Eurosensors XXVII* 622–625, <http://ieeexplore.ieee.org/xpl/articleDetails.jsp?arnumber=6626843> (IEEE, 2013).
14. Carbone, L. *et al.* Sensors and actuators for the Advanced LIGO mirror suspensions. *Class. Quantum Gravity* **29**, 115005 (2012).
15. Bell, C. J., Reid, S. & Faller, J. Experimental results for nulling the effective thermal expansion coefficient of fused silica fibres under a static stress. *Class. Quantum Gravity* **31**, 065010 (2014).
16. Watanabe, H., Yamada, N. & Okaji, M. Linear thermal expansion coefficient of silicon from 293 to 1000 K. *Int. J. Thermophys.* **25**, 221–236 (2004).
17. Poggi, M. A., McFarland, A. W., Colton, J. S. & Bottomley, L. A. A method for calculating the spring constant of atomic force microscopy cantilevers with a nonrectangular cross section. *Anal. Chem.* **77**, 1192–1195 (2005).
18. Cho, C. H. Characterization of Young's modulus of silicon versus temperature using a “beam deflection” method with a four-point bending fixture. *Curr. Appl. Phys.* **9**, 538–545 (2009).
19. Van Camp, M. & Vauterin, P. Tsoft: graphical and interactive software for the analysis of time series and Earth tides. *Comput. Geosci.* **31**, 631–640 (2005).
20. Callen, H. B. & Welton, T. A. Irreversibility and generalized noise. *Phys. Rev.* **83**, 34–40 (1951).
21. Chin, E., Lee, K., Winterood, J., Ju, L. & Blair, D. Low frequency vertical geometric anti-spring vibration isolators. *Phys. Lett. A* **336**, 97–105 (2005).
22. Sainz-Maza Aparicio, S., Sampedro, J. A., Montesinos, F. G. & Molist, J. M. Volcanic signatures in time gravity variations during the volcanic unrest on El Hierro (Canary Islands). *J. Geophys. Res.* **119**, 5033–5051 (2014).
23. Mogi, K. Relations between the eruptions of various volcanoes and the deformations of the ground surfaces around them. *Bull. Earthq. Res. Inst.* **36**, 99–134 (1958).
24. Battaglia, M., Gottsmann, J., Carbone, D. & Fernandez, J. 4D volcano gravimetry. *Geophysics* **73**, WA3–WA18 (2008).
25. Rymer, H., Williams-Jones, G. & Keynes, M. Gravity and deformation measurements. *Geophys. Res. Lett.* **27**, 2389–2392 (2000).
26. Allan, D. Statistics of atomic frequency standards. *Proc. IEEE* **54**, 221–230 (1966).
27. Peterson, J. *Observations and modeling of seismic background noise*. US Geological Survey Open-file Report Number 93-322, [http://www.mtmtllr.com/ADS/DATA/peterson\\_usgs\\_seismic\\_noise\\_ofr93-322.pdf](http://www.mtmtllr.com/ADS/DATA/peterson_usgs_seismic_noise_ofr93-322.pdf) (USGS, 1993).
28. Essen, H. H., Kruger, F., Dahm, T. & Grevemeyer, I. On the generation of secondary micro-seisms observed in northern and central Europe. *J. Geophys. Res.* **108**, 2506–2520 (2003).
29. Baxter, P. J. & Gresham, A. Deaths and injuries in the eruption of Galeras volcano, Colombia, 14 January 1993. *J. Volcanol. Geotherm. Res.* **77**, 325–338 (1997).

**Acknowledgements** The work was funded by the Royal Society Paul Instrument Fund and STFC grant number ST/M000427/1. We thank M. Pitkin for advice on completing statistical significance tests on the data, W. Cunningham for advice on finite element modelling, M. Perreux-Lloyd and R. Jones for their help in rendering three-dimensional images of the apparatus, and the staff and other users of the James Watt Nanofabrication Centre for help and support in undertaking the MEMS fabrication.

**Author Contributions** R.P.M. led the methodology of the etch process for the MEMS gravimeter and worked with G.D.H. on the development of the MEMS gravimeter. G.D.H. and R.P.M. enhanced the long-term, low-noise stability of the entire system, taking the tide data and performing the computational analysis. R.P.M. led writing the manuscript. A.S. led the methodology of the MEMS mask fabrication. A.S. and R.P.M. took the tide measurements in early 2015 and performed computational analysis of the MEMS gravimeter. D.J.P. supervised the design of the MEMS device fabrication process and with G.D.H. came up with the concept for a MEMS gravity sensor. J.H. developed the methodology of utilizing geometric anti-springs for the MEMS gravimeter system and commented on the manuscript. S.R. was responsible for the resources that were necessary to complete the project and commented on the manuscript. G.D.H. had the initial concept of a MEMS gravimeter together with D.J.P. G.D.H. had oversight of the design, fabrication and testing of the gravimeter (via the supervision of R.P.M. and A.S.). R.P.M. and G.D.H. characterized and enhanced the low noise performance, resulting in the measurement of the tides. G.D.H. was responsible for acquiring the funding for the work.

**Author Information** The research data relevant to this Letter are stored on the University of Glasgow's Enlighten Repository (<http://dx.doi.org/10.5525/gla.researchdata.213>). Reprints and permissions information is available at [www.nature.com/reprints](http://www.nature.com/reprints). The authors declare no competing financial interests. Readers are welcome to comment on the online version of the paper. Correspondence and requests for materials should be addressed to G.D.H. ([giles.hammond@glasgow.ac.uk](mailto:giles.hammond@glasgow.ac.uk)) or R.P.M. ([richard.middlemiss@glasgow.ac.uk](mailto:richard.middlemiss@glasgow.ac.uk)).

## METHODS

**MEMS device fabrication.** The MEMS device was fabricated from a single chip of 200- $\mu\text{m}$ -thick silicon. The reverse side of the wafer was first coated with 2.5  $\mu\text{m}$  of plasma-enhanced chemical vapour deposition (PECVD)  $\text{SiO}_2$ . A 100-nm coating of chromium was next deposited on the top surface of the silicon using a thermal evaporator.

The MEMS device pattern was created in a layer of positive photoresist using a g-line photolithography process. The mask was a 'halo' design<sup>31</sup> that is, instead of etching away all of the unwanted areas of silicon, trenches were used in an outline of the structure, to keep a constant etch rate and profile over all etched areas. The halo was 10  $\mu\text{m}$  wide. The photoresist pattern was then used as a mask to wet-etch the chrome using a nitric acid chrome etchant for 100 s, thus etching the MEMS device proof mass pattern into the chrome. The resist was then removed ultrasonically with acetone and isopropanol, leaving the chrome etch mask in place. A 7- $\mu\text{m}$  layer of AZ-4562 photoresist was then spun onto the back of the sample and used later to make the sample free-standing.

The sample was fixed to a carrier wafer (chrome side up) using a thin, spun-on layer of Crystalbond 509 (as mounting adhesive) in solution with acetone. To ensure a good thermal contact the sample was weighted and left on the hotplate at 88°C (just above the melting point of Crystalbond 509) for 5 min. The sample was next placed in an Oxford Instruments PlasmaPro 100 Estrelas Deep Silicon Etch System, and Bosch-etched<sup>32</sup> for 80 min using an  $\text{SF}_6$ ,  $\text{C}_4\text{F}_8$  process optimized for highly anisotropic trenches. This etch was the same depth as the silicon and stopped when it reached the  $\text{SiO}_2$  back layer. The PlasmaPro 100 Estrelas Deep Silicon Etch System allows control of the gas flow, enabling processes to be tuned with negative and positive defined etch profiles. Our spring profiles are vertical to within 0.5°.

To remove the sample from the carrier wafer it was heated to 88°C for 5 min, and then pushed laterally off the Crystalbond 509, which is now fluid. The  $\text{SiO}_2$  and the AZ-4562 layers enabled this to be done without damaging the MEMS device structure. The sample was then turned upside down and placed (not affixed) on a blank piece of silicon. The residual Crystalbond 509 and photoresist were removed from the bottom of the sample using an  $\text{O}_2$  plasma ash. The sample was exposed to a  $\text{CF}_4/\text{O}_2$  etchant plasma until all of the  $\text{SiO}_2$  was removed, making the sample free-standing.

**Geometrical anti-spring design.** Our MEMS device is comprised of a proof mass suspended from three curved cantilevers/flexures. To better understand the physical characteristics of this system we first discuss these flexures individually. Consider a cantilever, clamped at one end, and free to move at the other. A proof mass mounted on the moving end will oscillate with a frequency that depends on the geometry of the cantilever, and the Young's modulus of the material from which it is made. The proof mass will oscillate along an arc defined by the length of the flexure. The system will behave as a Hooke's law spring, with a linear relationship between force and displacement. This behaviour can be observed in Extended Data Fig. 4a. A curved single cantilever also behaves in the same manner, as seen in Extended Data Fig. 4b.

To create an anti-spring, one can take two such curved cantilevers and attach them at a central pivot point. A proof mass mounted at this point will no longer be able to trace out an arc as it oscillates. Instead, because of the symmetrical forces applied by the two identical cantilevers, its motion will be constrained along a vertical axis (as presented in Fig. 1). It is this constraint that causes the spring constant to change as the displacement increases. Instead of observing a linear relationship between force and displacement, a nonlinear behaviour is observed (see Extended Data Fig. 4c). This now means that the spring gets softer with increasing displacement.

A four-flexure anti-spring system is a simple extension of a two-flexure system. Here, a second pair of cantilevers are placed below the first pair, which allows a non-point-source proof mass to be suspended. The behaviour of the spring is still nonlinear, and is displayed in Extended Data Fig. 4d. The behaviour is identical to that of a two-flexure system, except the system can support twice the mass.

Both the two- and four-flexure anti-spring systems can be used to create oscillators that have low resonant frequencies. When the limits of  $k/m$  are pushed to create the lowest resonant frequency possible, however, these systems become unstable. They become unstable because the motion is so well constrained along its vertical axis that the spring gets softer and softer until it can no longer support the weight of the proof mass. This behaviour can be observed in Extended Data Fig. 4c and d: as the force increases, the displacement increases rapidly. A stable resonant frequency is imperative for a useful relative gravimeter, so this instability would create problems if used for the design of a MEMS gravimeter. It would require the use of a closed-loop feedback system.

Our MEMS device utilizes a novel three-flexure anti-spring system, with one flexure of the upper pair of cantilevers removed (see Fig. 1). In the first instance, the device behaves as a four-flexure anti-spring: it gets rapidly softer as the

displacement of the proof mass increases. The anti-spring behaviour is maintained while the proof mass moves along its vertically constrained axis. The asymmetry of the system, however, means that the device does not stay constrained along the anti-spring constraining axis. The single upper flexure ultimately tilts the proof mass marginally away from the constraining axis. As the motion is pulled from this axis, the anti-spring trend is halted and the device regains a Hooke's law behaviour, where  $dF/dz$  is a constant. This behaviour can be observed in Extended Data Fig. 4e, where the gradient of force versus displacement reaches a minimum at  $z = 0.6$ . This means that the device assumes a constant value of  $k$  at the minimum stiffness value that we have demonstrated to be stable over many months (as demonstrated by Extended Data Fig. 9).

**Optical shadow sensor.** The proof mass motion is measured using an optical shadow sensor<sup>14</sup>. Using a fused silica 'C'-shaped support structure, a red LED (powered at 0.3 mW) was shone onto a split photodiode, with the MEMS device proof mass mounted in between. The change in intensity incident on the photodiode resulting from the motion of the proof mass shadow was then used as a measure of the motion. The split photodiode was made from two 5 mm by 10 mm planar silicon photodiodes, and wired to give a differential output. A split photodiode was used so that at the nominal position of the proof mass the output signal was zero. This allowed maximal amplification without saturation of the measurement instrumentation. The LED signal was modulated (at a frequency of 107 Hz with a 50:50 duty cycle) to reduce the  $1/f$  noise in the output signal. The modulation was carried out by turning the LED on and off with an HP 33120A square-wave signal generator. A precision current-stabilizing resistor (displayed in Fig. 2) maintained the LED drive current; this resistor was heat sunk to the fused silica 'C'-shaped structure. The current output from the photodiode was first converted into a voltage using a Stanford Research Systems SR570 current-to-voltage converter, band-passed between 3 Hz to 100 Hz, and amplified by a factor of  $10^6 \text{ V A}^{-1}$ . This amplified signal was then de-modulated via an analogue lock-in amplifier (Femto LIA-MV-200) referenced from the signal generator. The lock-in amplified the signal with a gain of ten and undertook readings with a time constant of 3 s. This analogue signal was passed through a Stanford Research Systems SR560 low pass filter of 0.03 Hz, 12 dB per octave, to remove aliasing and filter seismic noise, before being digitized via a 16-bit, analogue-to-digital converter (National Instruments M Series 6229) and recorded by a computer with a 24-s time constant. Analogue signals were used to reduce digitization noise that would have occurred if a digital signal had been amplified by this magnitude.

The shadow sensor has a read-out noise floor of  $\leq 10 \mu\text{Gal}$  at the sampling frequency of 0.03 Hz, and a dynamic range of about 50  $\mu\text{m}$ . A large dynamic range is required because of the large initial displacement (0.8 mm) of the proof mass when it is tilted to its vertical operating orientation, thus making initial alignment of the MEMS device difficult. Although the maximum peak-to-peak displacement of the proof mass caused by the tides is only 16 nm, the proof mass also oscillates at its resonant frequency by up to 100 nm owing to seismic ground motion. A high dynamic range is also useful to measure this signal, which is ultimately removed from the data by averaging with a 0.03 Hz filter in the read-out electronics.

**Temperature control.** The control loops used to maintain the temperature of the system were proportional integral derivative control mechanisms, written in Labview (<http://www.ni.com/labview/>). Temperatures were monitored using a four-terminal measurement of small platinum resistors, via two Keithley 2000 digital multimeters. A four-terminal measurement eradicates contact resistance by driving the thermometer with a current and measuring the voltage across it. This removes the temperature sensitivity of external wires. Low-temperature-coefficient Manganin alloy wires were used for these connections to minimize parasitic thermal conduction. One platinum resistor was placed on the outer frame of the MEMS device and three were placed equidistantly around the copper shield. Wire wound resistors were used as the heating mechanism to feedback into the system; again, one of these was placed on the MEMS device frame and three around the shield. The output signal to the heaters was sent via a National Instruments (USB 6211) digital-to-analogue converter (DAC) card, and the heaters were powered with non-inverting amplifiers with a capability to power up to 100 mA. All circuitry and instrumentation used to amplify and measure the output signal, and to measure and control the system temperature, were selected for their high thermal stability. This entire configuration was constructed in a vacuum chamber with a pressure of  $\leq 10^{-5}$  mTorr.

**Data analysis.** Although proportional integral derivative (PID) temperature control was implemented for the MEMS device and the shield, there were other components with variations that could not be actively controlled. These were the room temperature that coupled into the data via a temperature-sensitive lock-in amplifier, and the intensity variations of the LED, which were monitored using a monitor photodiode. There was also an offset, and a linear drift of under 150  $\mu\text{Gal}$  per day once the system had been left evacuated for over a week. This drift term is due to stress in the silicon flexures. Like all mechanical systems, application of stress leads to



anelasticity, which causes creep and drift over long timescales. Our device also shows polynomial drift which decays away approximately one week after evacuating the apparatus. The polynomial drift is probably due to adsorbed water on the surface layer of silicon, and could be mitigated by baking out the system before evacuation. Extended Data Fig. 5 demonstrates this initial polynomial drift. The data were therefore regressed against the temperature measurements listed above, the drift offset and the intensity. This regression—carried out in Matlab (<http://uk.mathworks.com/products/matlab/>) with the *mregg* tool—identified correlations between the output data and these parameters, and removed any resulting correlated trends from the final data. Floor tilt and power variation of the LED were also monitored, but neither had any discernible effect on the signal and were therefore not regressed.

The correlation coefficient,  $R$ , between the averaged theoretical and experimental tide data was calculated using Matlab's *corrcoeff* function. An  $R$  value of 0.86 was produced for the plot presented in Fig. 3. To check the level of statistical significance of our experimental data we compared it to the correlation of the noise alone. We created 10,000 random permutations of our data set and calculated the correlation coefficient for each with respect to the theoretical data. This set of  $R$  values was plotted as a histogram. This histogram had a distribution with a mean value of zero and a standard deviation of 0.008. The  $R$  value from the un-randomized data are  $114\sigma$  from this distribution, suggesting the correlation is real to an extremely high degree of confidence.

Extended Data Fig. 6 is a plot of the root-mean-square acceleration sensitivity of the device over its full spectral range. The tide signal can be observed at  $1 \times 10^{-5}$  Hz. The peak at  $10^{-3}$  Hz is an artefact of the temperature servo. Between 0.1 Hz and 0.2 Hz the microseismic peak can be recognized; its presence indicates that the device is also a sensitive seismometer. Past observations—made in Scotland from February to March 2000—of the microseismic peak<sup>28</sup> confirm the validity of our observation. At 2.3 Hz the primary resonant mode of the MEMS device generates a large peak due to excitation from seismic noise. This plot was used to calculate the sensitivity of the MEMS device. To find a sensitivity in microgal per hertz<sup>1/2</sup>, it is only necessary to read off the acceleration sensitivity at the point where the data crosses 1 Hz on the horizontal axis. We believe that the value of  $40 \mu\text{Gal Hz}^{-1/2}$  is an overestimate of the true sensitivity of the device because at 1 Hz the influence of both the primary resonance of the device and the micro-seismic peak are important.

**Tilt variation.** Although tilt did not have an effect on the tide measurement, we are interested to know at what point tilt would become an issue. Extended Data Fig. 8 presents two plots of an experiment used to assess the effect of tilt on our device. Inside the vacuum tank, the MEMS device was mounted vertically and aligned with the tilt sensor. The  $y$  axis of the tilt sensor was aligned with the plane of the MEMS device, with the  $x$  axis perpendicular to this (see Fig. 1). Extended Data Fig. 8a demonstrates the induced tilt of the tank and the output of the MEMS device along the  $x$  axis. Extended Data Fig. 8b shows the same data as in Extended Data Fig. 8a, but for the  $y$  axis. There is a strong correlation between the  $y$ -axis variation and the voltage output, giving a tilt sensitivity in this axis of  $21.2 \mu\text{Gal}$  per arcsecond. There is less sensitivity to the  $x$ -axis tilt with a tilt sensitivity of only  $0.6 \mu\text{Gal}$  per arcsecond.

The  $x$ -axis tilt sensitivity is low because in the vertical configuration the spring resumes a Hooke's law response, as observed in Extended Data Fig. 1, for which the  $x$ -axis tilt variation is plotted against the resonant frequency (the acceleration sensitivity of the device is proportional to the square of the resonant frequency). Ultimately the spring could be tuned to operate with even less variation with tilt in this axis if it were positioned to operate at one of its minima. Alternatively the flexures could be made marginally thicker to shift the minimum in resonant frequency to  $90^\circ$ ; this was not carried out because the device did not show sufficient tilt sensitivity to cause concern. The  $y$ -axis variation is larger because the device has a mode of oscillation in which the proof mass tilts and pivots about the upper cantilever flexure.

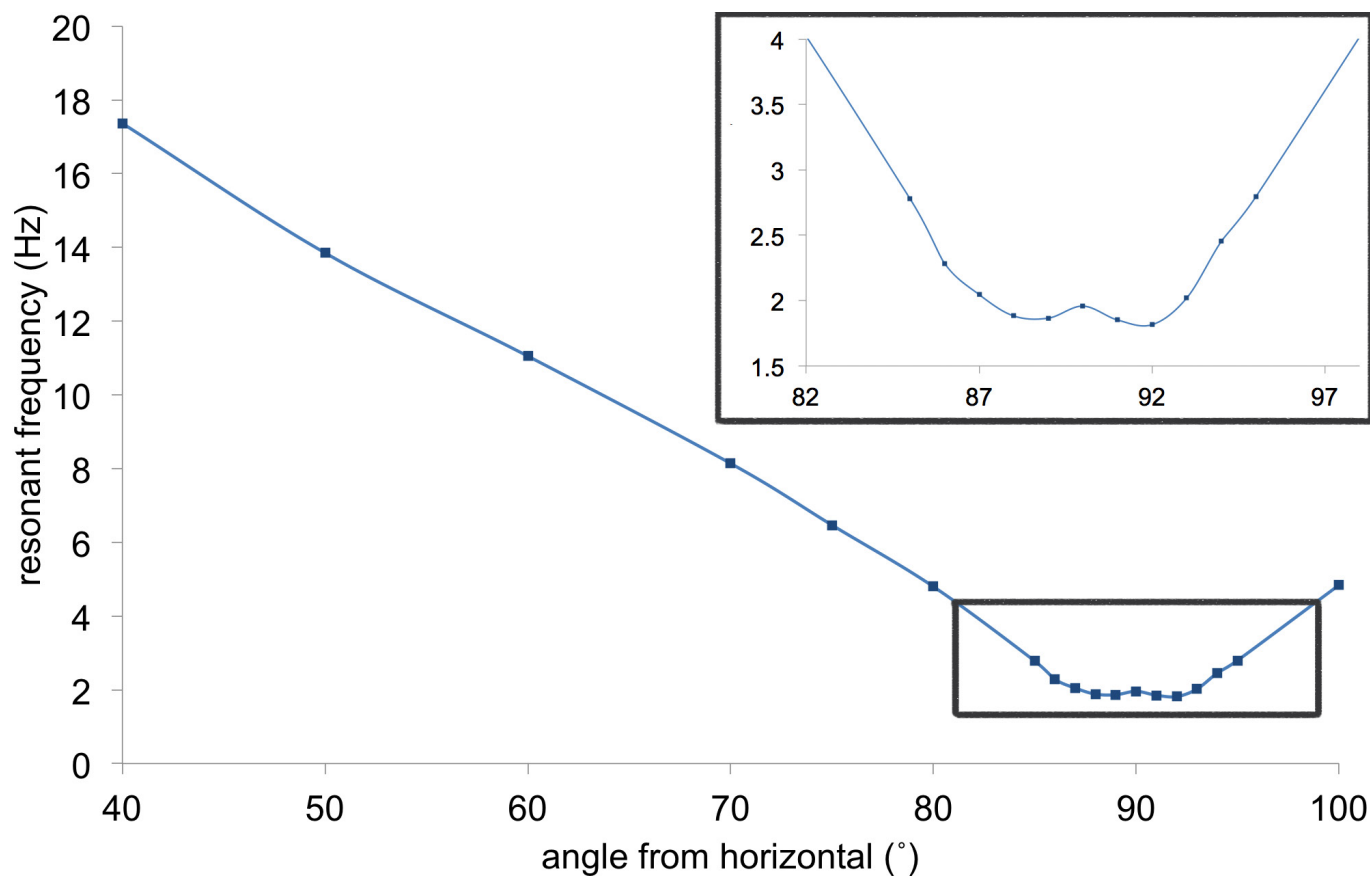
When vertical, the device would need to be levelled with an accuracy limited by the  $y$ -axis sensitivity (that is, less than 2 arcsec to maintain the current sensitivity) to make repeatable measurements in different locations. This accuracy of levelling is achievable with a simple surveyor's bubble level.

**Temporal reproducibility tests.** Extended Data Fig. 9 demonstrates two short data sets separated by nearly four months. These were used as a test of the temporal stability of the device. To convert the raw voltage output of the device into a unit of acceleration, a calibration factor was required. By comparing the experimental (blue line) data in Extended Data Fig. 9a with that in Extended Data Fig. 9b we were able to test whether the calibration factor had drifted over time. The same calibration factor has been used to make both of these plots. By averaging the data and changing the calibration factor of Extended Data Fig. 9b, it was found that a change in the calibration factor of 5% made the fit to the tide theory (red line) data noticeably worse. Changes smaller than this were not resolvable. We therefore believe that if the calibration factor has changed, it has done so by no more than 5%. During this period, the vacuum tank was vented and evacuated several times, and the MEMS was moved around each time. This is an important feature of a device that could eventually be used in the field.

**Applications.** MEMS gravimeters have many industrial applications. Given their small size and low cost, they could be used for down-borehole exploration in the oil and gas industry<sup>33</sup> and used to monitor well drainage. Such devices could also be used for environmental monitoring, where networks of sensor arrays could monitor subsurface water levels<sup>34</sup>, or to determine the location of historic landfill sites. In the security industry, low-cost and small-size gravimeters would also be useful in detecting subterranean tunnels<sup>35,36</sup> or for imaging of cargo containers, where high spatial resolution via numerous sensors is an advantage<sup>37</sup>. MEMS gravimeters could also be used in civil engineering. For example, at present in the UK, for many cities built in the Victorian period the placement of utilities is accurate on maps only to within 15 m of landmarks such as trees, fences or buildings. There have been trials of the Scintrex CG5 and MEMS-based arrays should improve mapping resolution. Gravimetry is already used in volcanology and could help to predict eruptions using networks of small, low-cost gravimeter arrays<sup>22,24,25</sup>.

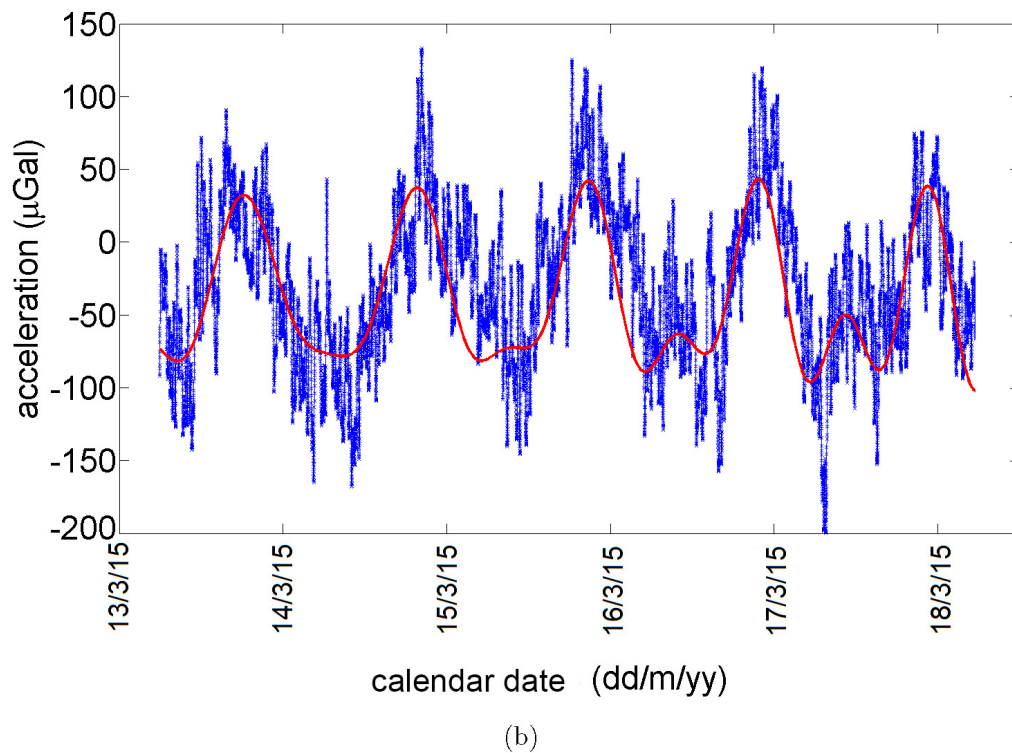
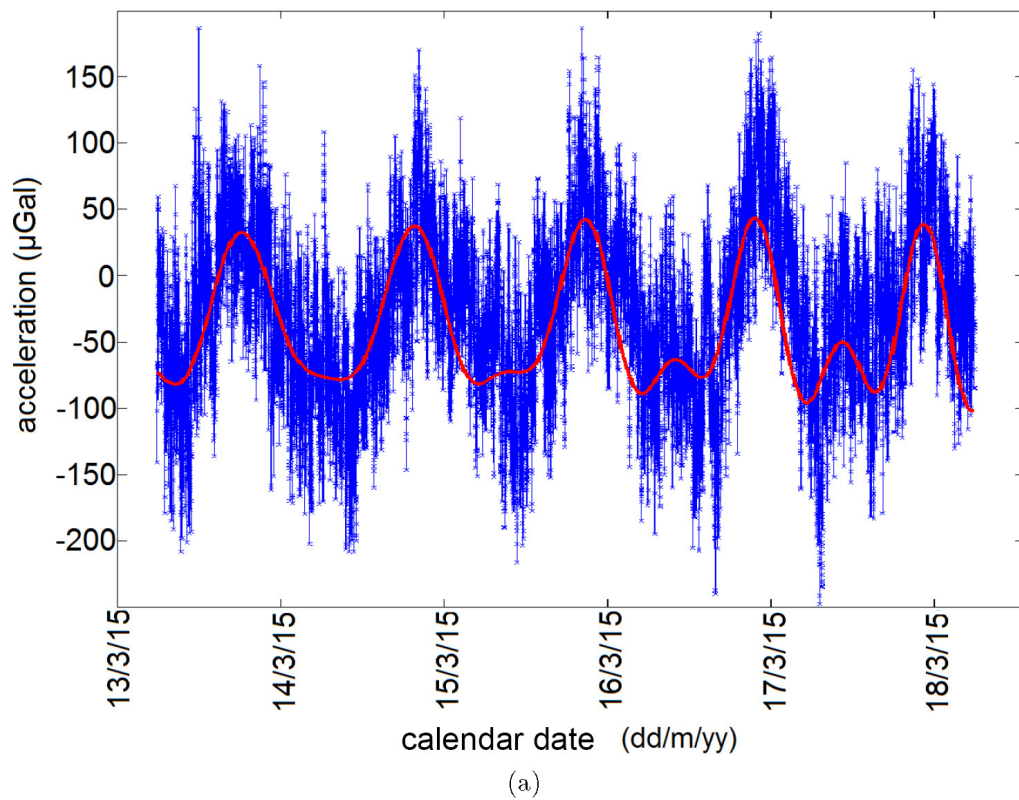
A field prototype is currently being developed in Glasgow that will be the size of a tennis ball and require a power supply of under 1 W. A powerless getter pump will be used to maintain vacuum, both the thermal control and the optical read-out will be on-chip; tilt levelling will be included, and all of the read-out and control software will be run on a micro-controller.

30. Riccardi, U., Rosat, S. & Hinderer, J. Comparison of the Micro-g LaCoste gPhone-054 spring gravimeter and the GWR-C026 superconducting gravimeter in Strasbourg (France) using a 300-day time series. *Metrologia* **48**, 28–39 (2011).
31. Pike, W. Analysis of sidewall quality in through-wafer deep reactive-ion etching. *Microelectron. Eng.* **73–74**, 340–345 (2004).
32. Laermer, F. & Schilp, A. Method of anisotropic etching of silicon. US patent number 5,501,893 (1996).
33. Rim, H. & Li, Y. Advantages of borehole vector gravity in density imaging. *Geophysics* **80**, G1–G13 (2015).
34. Bauer-gottwein, P., Christiansen, L. & Rosbjerg, D. Informing hydrological models with ground-based time-lapse relative gravimetry: potential and limitations. In *Proc. Symp. J-H01 (GRACE, Remote Sensing and Ground-based Methods in Multi-Scale Hydrology)* 187–194 (IAHS Publ. 343, 2011).
35. Romaides, A. J. et al. A comparison of gravimetric techniques for measuring subsurface void signals. *J. Phys. D* **34**, 433–443 (2001).
36. Butler, D. K. Microgravimetric and gravity gradient techniques for detection of subsurface cavities. *Geophysics* **49**, 1084–1096 (1984).
37. Kirkendall, B., Li, Y. & Oldenburg, D. Imaging cargo containers using gravity gradiometry. *IEEE Trans. Geosci. Remote Sens.* **45**, 1786–1797 (2007).



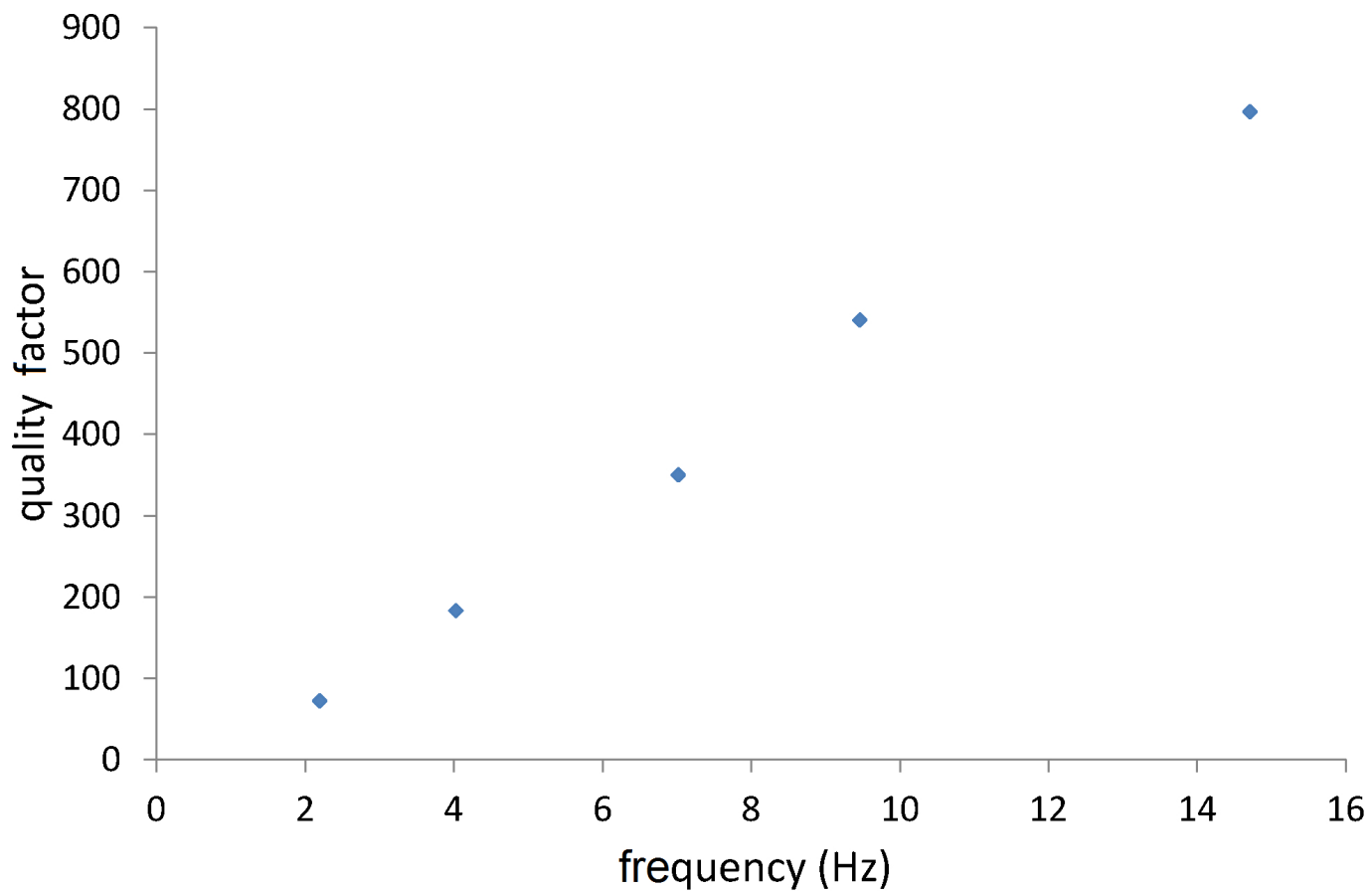
**Extended Data Figure 1 | Spring resonant frequency behaviour with tilt.** The resonant frequency decreases as the MEMS device gets closer to vertical due to the geometrical anti-spring effect. At 88° and 92° there are minima in the plot (see inset). At this point the frequency is constant with tilt and the system displays Hooke's law behaviour. The resonant frequency

of a symmetric anti-spring would reach an instability here. This figure also demonstrates that while the instrument is operated at 90° the resonant frequency is 2.3 Hz. It can be lowered to 1.8–1.9 Hz by tilting to operate at one of the minima.

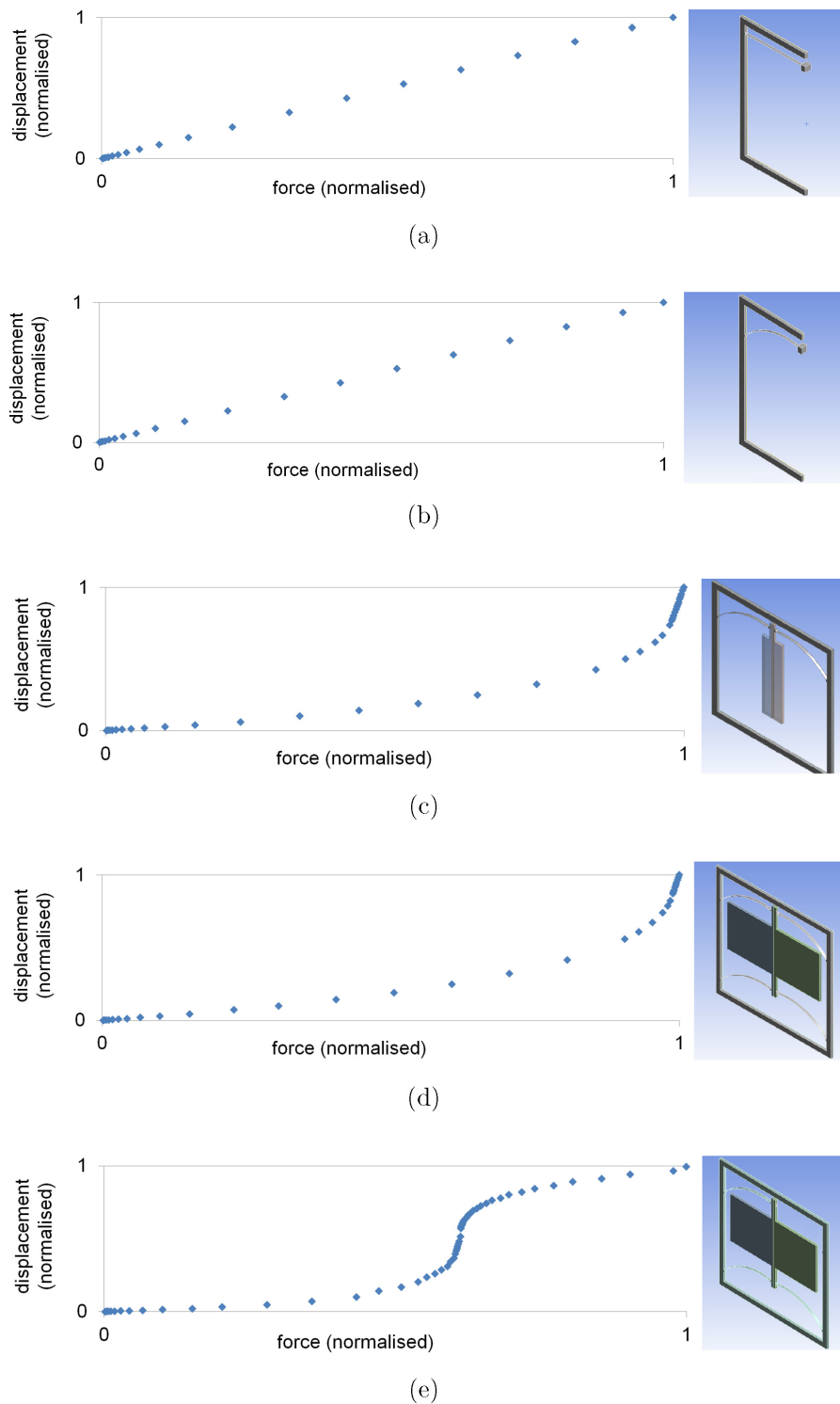


**Extended Data Figure 2 | The Earth tides with different filtering.** **a**, Measurements of the Earth tides obtained from the MEMS device. This is the raw data output. **b**, The same data but with a 10-min filtering time. The red lines are theoretical plots calculated by *TSOFT*. The blue lines are the experimental data.



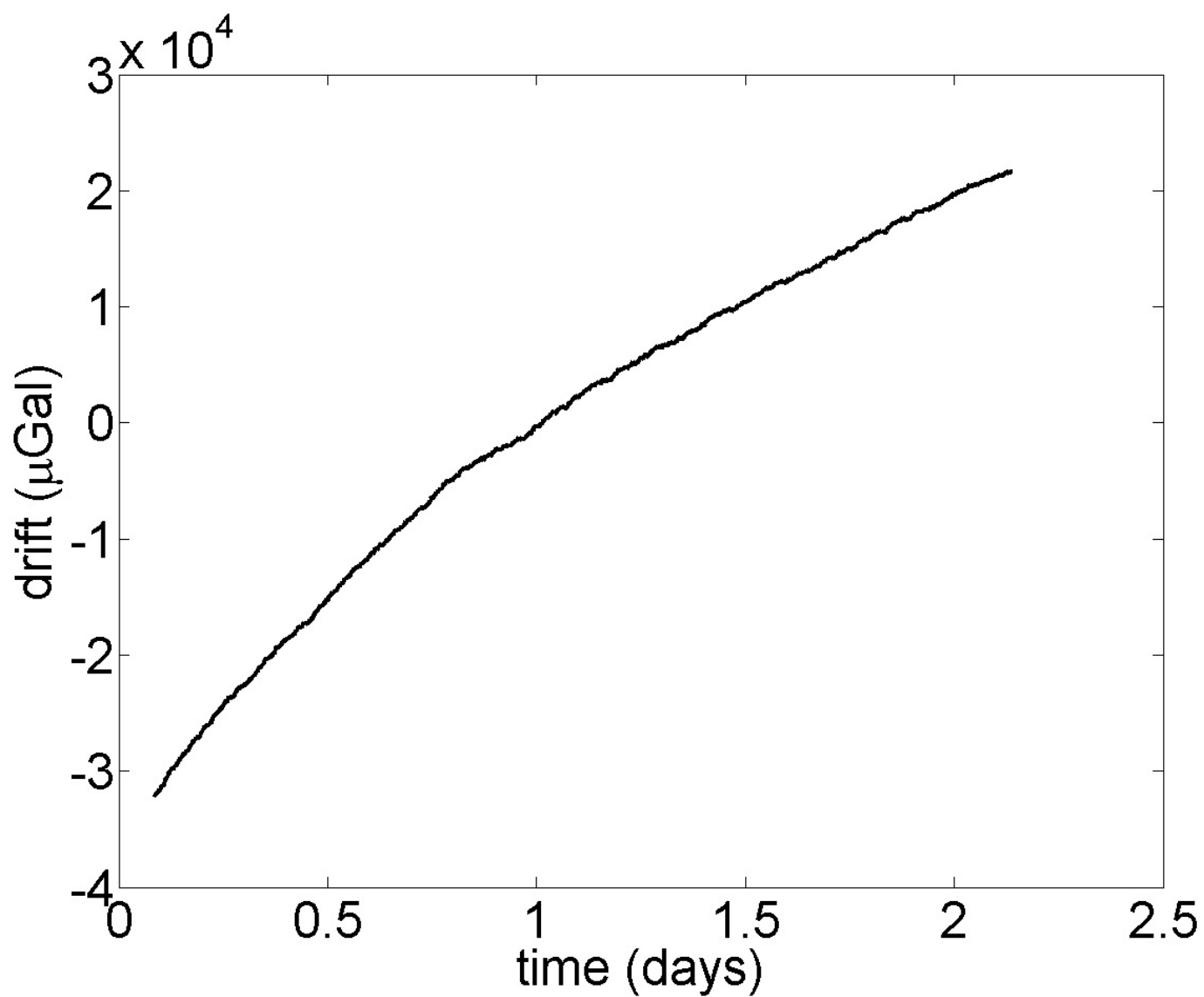


**Extended Data Figure 3 | Quality factor frequency dependence.** We observe a trend of decreasing quality factor with decreasing frequency of our device. At low frequencies the internal friction of the material becomes the dominant loss mechanism. This trend has been discussed by ref. 21.



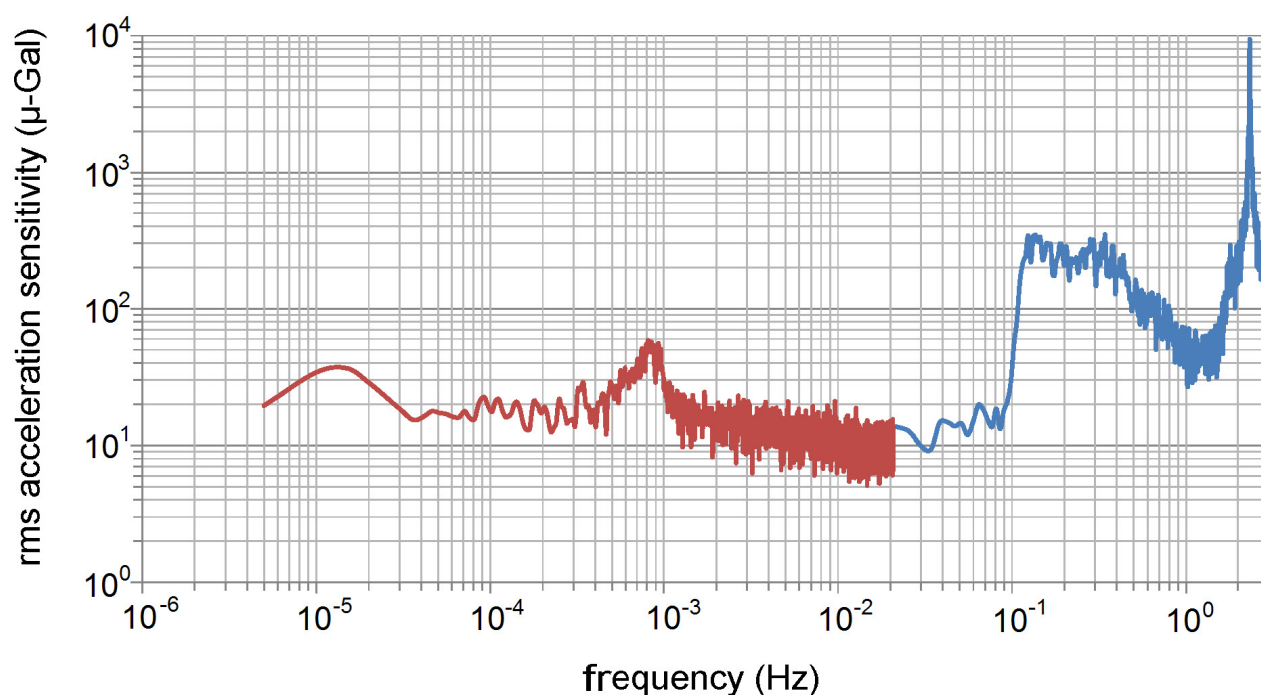
**Extended Data Figure 4 | Geometrical anti-spring design.** **a** and **b** demonstrate the Hooke's law behaviour of a straight and curved cantilever, respectively. **c** and **d** demonstrate the unstable anti-spring characteristics of a 2- and 4-flexure MEMS device, respectively. **e**, The behaviour of a 3-flexure MEMS device (see Fig. 1). Whereas a 2- or 4-flexure system

reaches an instability with increasing load, a 3-flexure system regains Hooke's law behaviour. The 3-flexure system behaves as such because it is pushed off its constrained axis by the asymmetry of the design. All of these plots were produced using Ansys finite element analysis software (<http://www.ansys.com/en-GB>).

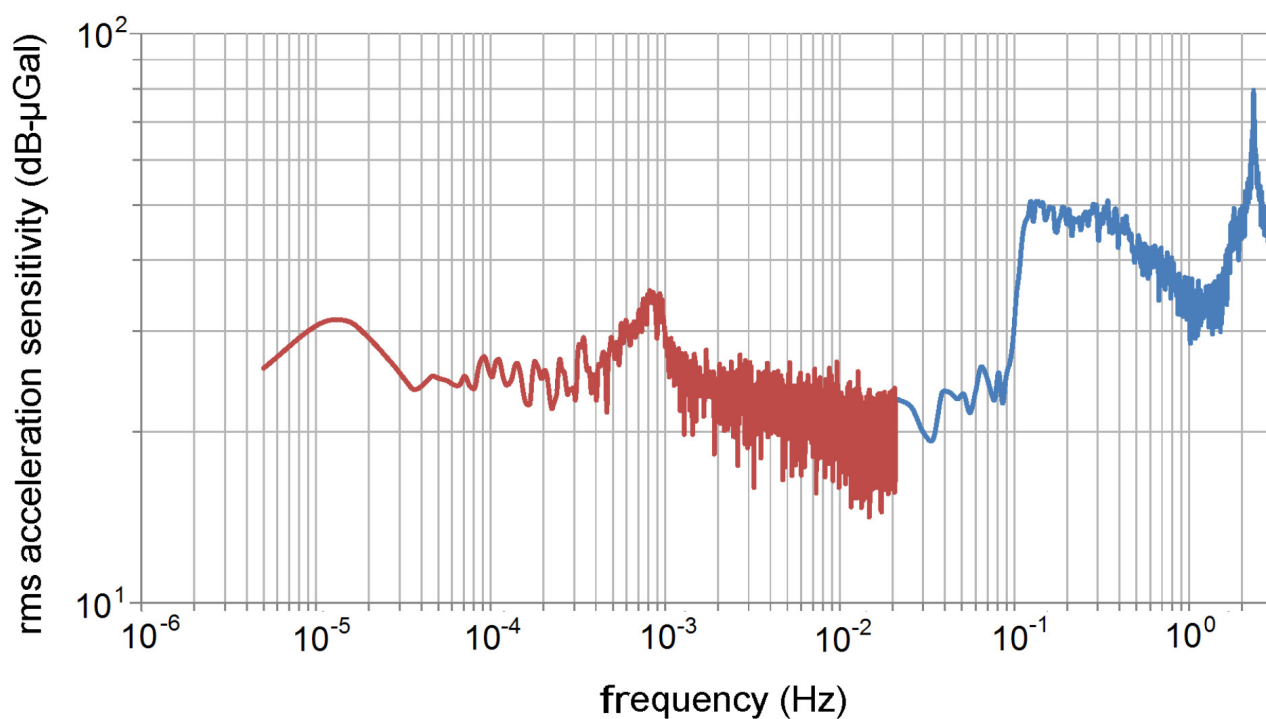


**Extended Data Figure 5 | Polynomial drift.** This plot demonstrates the drift in the data shortly after the vacuum pump has been turned on. A polynomial component to the drift is clearly visible. Once the vacuum system has settled, however, the drift becomes linear, as demonstrated in Fig. 4b, at a level of  $150 \mu\text{Gal}$  per day.





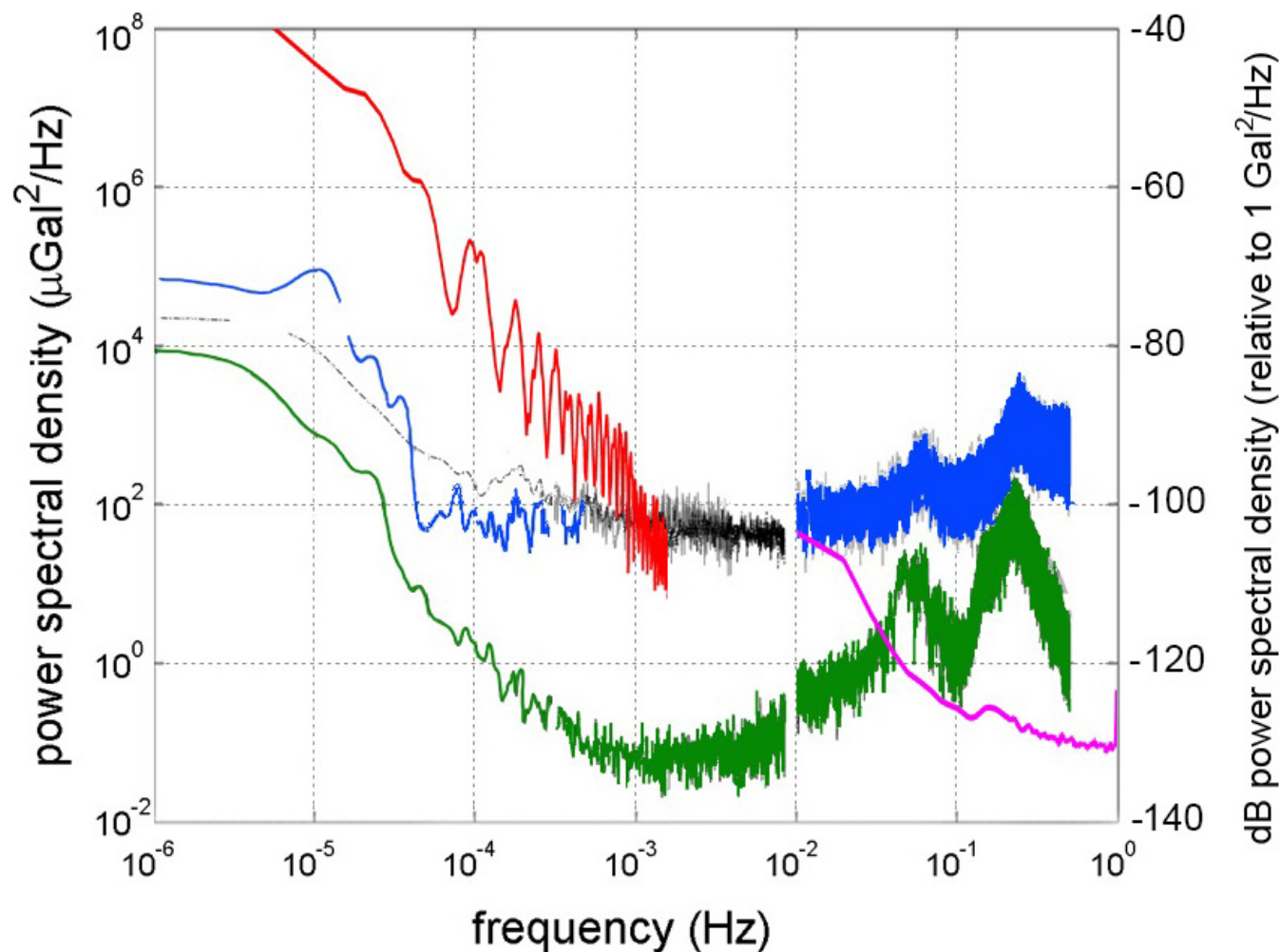
(a)



(b)

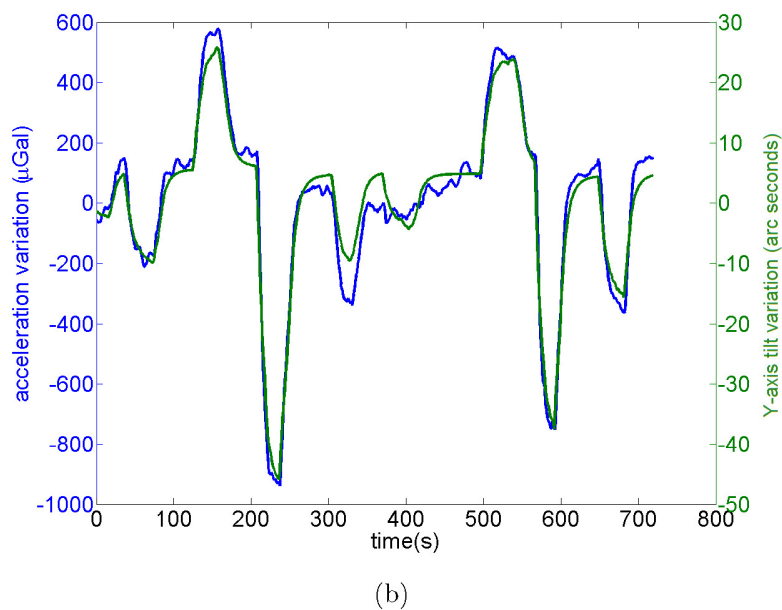
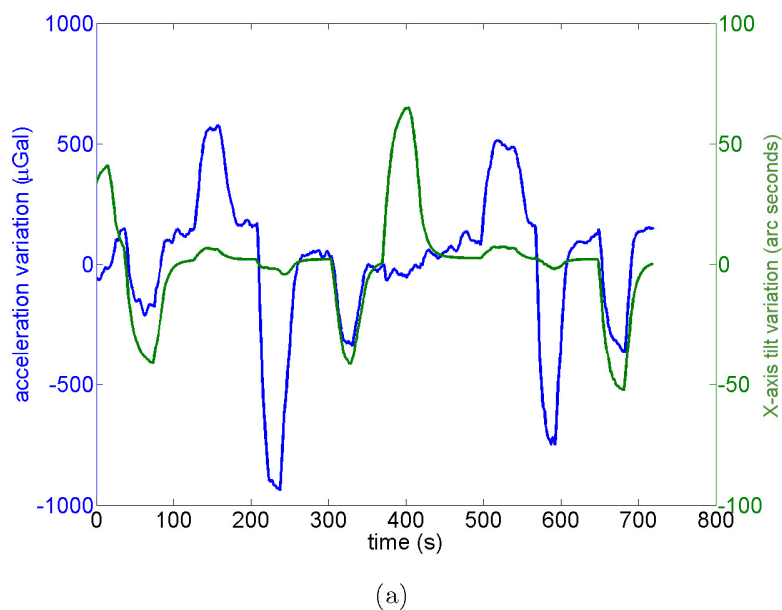
**Extended Data Figure 6 | MEMS device root-mean-square acceleration sensitivity.** **a**, The root-mean-square acceleration sensitivity in microgal. **b**, The root-mean-square acceleration sensitivity in decibel microgal. The tide signal can be observed in both plots at  $10^{-5}$  Hz; the peak at  $2 \times 10^{-3}$  Hz is the artefact of the temperature servo discussed earlier; the microseismic peak can be observed between 0.1 Hz and 0.2 Hz; and the

2.3-Hz resonant frequency can be observed to the right of the plot (the blue spike at just above 1 Hz). Two different sampling rates were used to capture this data. The blue series was captured at a sampling rate of 70 Hz while the red series was captured at a sampling rate of 0.05 Hz. This was done to minimize the size of the data file.



**Extended Data Figure 7 | Power spectral density comparison.** The red line—plotted using the data from Fig. 4g—represents our MEMS device, demonstrating its sensitivity in the tidal frequency range. The filtering time means that the sensitivity rolls off above  $10^{-4}$  Hz. The black line represents the Scintrex CG5, the blue line the Micro-g Lacoste gPhone-054, the green line the SG-C026 superconducting gravimeter.

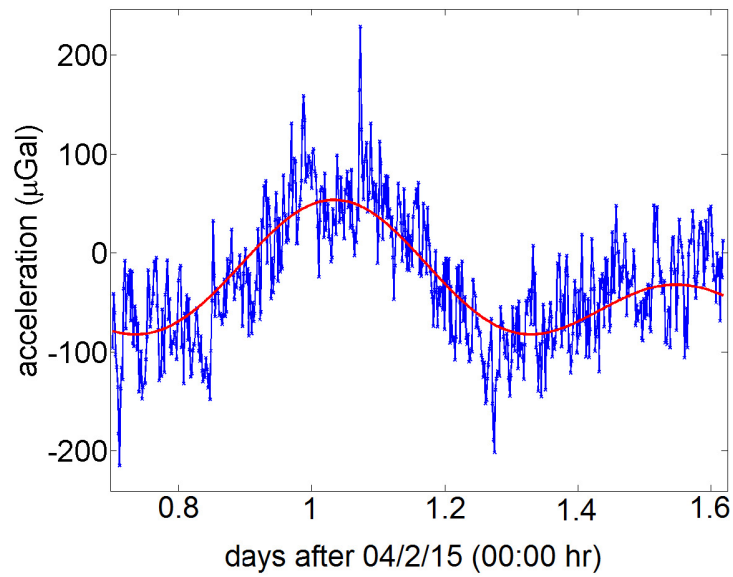
The data from these three series are taken from figure 8 in ref. 30 (copyright Bureau International des Poids et Mesures, reproduced by permission of IOP Publishing, all rights reserved). The magenta series represents the microseismometer by W. T. Pike *et al.* (private communication by permission of the author, to be published in the 47th Lunar and Planetary Science Conference).



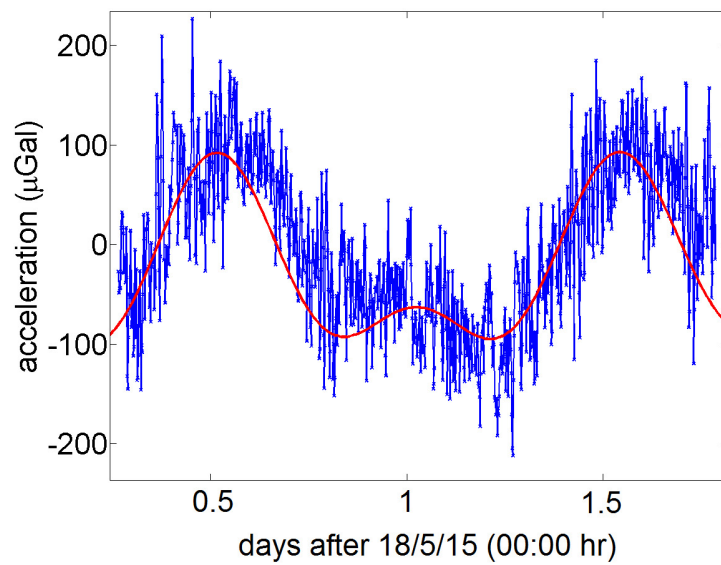
**Extended Data Figure 8 | Tilt susceptibility tests.** **a**, The variation in output of the MEMS device with the  $x$ -axis tilt of the sensor plotted on a secondary axis. **b**, The same as **a** but for the  $y$  axis. There is an  $y$ -axis

(in-plane MEMS tilt) tilt sensitivity in this axis of  $21.2\mu\text{Gal}$  per arcsecond, but in the  $x$  axis (out-of-plane MEMS tilt) the tilt sensitivity is only  $0.6\mu\text{Gal}$  per arcsecond.





(a)



(b)

**Extended Data Figure 9 | Long-term reproducibility tests.** **a** and **b** are two data sets separated by approximately 4 months, with no filtering employed. During this period the vacuum chamber was evacuated and vented several times, but despite this the calibration factor of the device has not changed by more than 5%.

Extended Data Table 1 | Technology comparison table

Device	Technology	Technology	Stability in the $\mu\text{Hz}$ Regime	Resonant Frequency	Use
Scintrex CG5 <sup>2,3</sup>	Fused Quartz	2 $\mu\text{Gal}$	0.5 mGal/day	3 Hz	Gravimetry
Krishnamoorthy <sup>8</sup>	MEMS	17 $\mu\text{Gal}$	N/A	36 Hz	Seismology
Quietseis <sup>9</sup>	MEMS	15 $\mu\text{Gal}$	N/A	800 Hz	Seismology
Pike <sup>10</sup>	MEMS	2 $\mu\text{Gal}$	N/A	11 Hz	Seismology
Glasgow MEMS	MEMS	40 $\mu\text{Gal}$	0.14 mGal/day	2.31 Hz	Gravimetry

This table compares the key parameters of several acceleration sensors: the Scintrex CG5<sup>2,3</sup>, the Krishnamoorthy<sup>8</sup> MEMS device, the Quietseis<sup>9</sup> MEMS device, the Pike<sup>10</sup> MEMS device, and our own MEMS device.

# Soft surfaces of nanomaterials enable strong phonon interactions

Deniz Bozyigit<sup>1</sup>, Nuri Yazdani<sup>1</sup>, Maksym Yarema<sup>1</sup>, Olesya Yarema<sup>1</sup>, Weyde Matteo Mario Lin<sup>1</sup>, Sebastian Volk<sup>1</sup>, Kantawong Vuttivorakulchai<sup>2</sup>, Mathieu Luisier<sup>2</sup>, Fanni Juranyi<sup>3</sup> & Vanessa Wood<sup>1</sup>

**Phonons and their interactions with other phonons, electrons or photons drive energy gain, loss and transport in materials. Although the phonon density of states has been measured and calculated in bulk crystalline semiconductors<sup>1</sup>, phonons remain poorly understood in nanomaterials<sup>2–5</sup>, despite the increasing prevalence of bottom-up fabrication of semiconductors from nanomaterials and the integration of nanometre-sized components into devices<sup>6–8</sup>. Here we quantify the phononic properties of bottom-up fabricated semiconductors as a function of crystallite size using inelastic neutron scattering measurements and *ab initio* molecular dynamics simulations. We show that, unlike in microcrystalline semiconductors, the phonon modes of semiconductors with nanocrystalline domains exhibit both reduced symmetry and low energy owing to mechanical softness at the surface of those domains. These properties become important when phonons couple to electrons in semiconductor devices. Although it was initially believed that the coupling between electrons and phonons is suppressed in nanocrystalline materials owing to the scarcity of electronic states and their large energy separation<sup>9</sup>, it has since been shown that the electron–phonon coupling is large and allows high energy-dissipation rates exceeding one electronvolt per picosecond (refs 10–13). Despite detailed investigations into the role of phonons in exciton dynamics, leading to a variety of suggestions as to the origins of these fast transition rates<sup>14,15</sup> and including attempts to numerically calculate them<sup>12,13,16</sup>, fundamental questions surrounding electron–phonon interactions in nanomaterials remain unresolved. By combining the microscopic and thermodynamic theories of phonons<sup>1,17–19</sup> and our findings on the phononic properties of nanomaterials, we are able to explain and then experimentally confirm the strong electron–phonon coupling and fast multi-phonon transition rates of charge carriers to trap states. This improved understanding of phonon processes permits the rational selection of nanomaterials, their surface treatments, and the design of devices incorporating them.**

To study phonons as a function of crystalline domain size, we select nanocrystal (NC)-based solids as a model system. Colloidal NCs offer excellent size tunability and monodispersity and are usually assembled into thin films such that their nanosized dimensions and quantum-confined properties are retained<sup>8</sup>. We work with lead sulfide (PbS) because the phonon properties of bulk PbS have been well studied, microcrystalline PbS is readily available, and PbS NC-solids (that is, compact solids formed from closely attached NCs) have been used for LEDs<sup>20</sup>, photodetectors<sup>21</sup>, solar cells<sup>7,22</sup> and thermoelectrics<sup>23</sup>.

We quantify the phononic properties using inelastic neutron scattering (INS). For each sample (Table 1), we reconstruct the dynamic structure factor ( $S(q, \omega)$ ) as a function of the momentum ( $q$ ) and energy ( $\omega$ ) gained by the scattered neutron, from which we can approximate the mean square displacement ( $\langle u^2 \rangle$ ) of atoms in the material and calculate the phonon density of states ( $g(\omega)$ ). Supplementary

Methods 1–6 detail sample preparation, measurement, characterization and analysis.

First, we compare measurements on microcrystalline PbS (sample S1) with those on two NC-solids having increasingly smaller crystallite sizes (radius  $r = 8.2$  nm (S2) and  $r = 1.33$  nm (S3)) (Fig. 1a). For microcrystalline PbS, we observe Bragg reflections around  $\omega = 0$  cm<sup>−1</sup> that are characteristic of the PbS crystal lattice, and a distinct structure along the  $q$  axis at finite energy transfers ( $\omega \neq 0$  cm<sup>−1</sup>) due to the Bloch-wave symmetry of the phonons that results from the discrete translational symmetry of the crystal lattice. With decreasing crystallite size, these features progressively disappear, indicating a breakdown of the Bloch-wave symmetry of the phonon modes. We calculate  $\langle u^2 \rangle = 0.042 \pm 0.007$  Å<sup>2</sup> for S1, in agreement with previous measurements<sup>24</sup> (Supplementary Methods 5). For nanocrystalline samples,  $\langle u^2 \rangle$  increases twofold (Table 1), signalling increased atomic motion. The measured  $g(\omega)$  of the microcrystalline sample shows excellent agreement with density-functional-theory (DFT) calculations for bulk PbS (Supplementary Methods 8), with transverse acoustic (TA) modes at 48.8 cm<sup>−1</sup> and longitudinal acoustic (LA) modes at 84.4 cm<sup>−1</sup> (Fig. 1b). With decreasing crystallite size, the TA and LA bulk modes reduce in relative weight and new modes appear at 25 cm<sup>−1</sup> (Fig. 1b inset).

Next, we investigate the impact of varying NC size within the quantum-confined regime ( $r = 1.5$  nm (S4) to  $r = 3.3$  nm (S7)). Despite the large influence of NC radius on the bandgap ( $E_g$ ), we find no appreciable impact on  $g(\omega)$  or  $\langle u^2 \rangle$  (Table 1, Fig. 1c). While previous studies on phonons in NCs have reported a  $1/r$  size dependence<sup>25</sup>, these studies used Raman spectroscopy, where the  $1/r$  dependence results from the optical selection rules<sup>26</sup>. In contrast, INS has no intrinsic selection rules relevant to the present study.

Finally, we control for the influence of the linker molecule used in the assembly of the NC-solids (Supplementary Methods 2, 3). Comparing the  $g(\omega)$  of samples with deuterated (S3) and hydrogen-containing (S4) 1,2-ethanedithiol (EDT-d4 and EDT), we find the key features that emerge from nanosizing (that is, low-energy modes at 25 cm<sup>−1</sup> and large  $\langle u^2 \rangle$ ) present in both samples and identify the peaks at 90, 150 and 250 cm<sup>−1</sup> as phonon modes originating from the EDT molecules (Fig. 1c). *Ab initio* molecular dynamics (MD) simulations support this assignment (Fig. 1c bottom, Supplementary Methods 11).

We then use *ab initio* MD simulations ( $T = 100$  K) of a NC to determine the origins of the low-frequency mode and the large  $\langle u^2 \rangle$  found in all nanocrystalline samples (Supplementary Methods 10). In agreement with INS measurements, the simulated  $g(\omega)$  (Fig. 2a) shows the bulk modes and the low-frequency mode at 25 cm<sup>−1</sup>, indicating that the latter indeed comes from the NCs. The plot of the average  $\langle u^2 \rangle$  as a function of depth ( $d$ ) below the surface of the NC (Fig. 2a inset) shows that  $\langle u^2 \rangle$  matches the bulk value (0.015 Å<sup>2</sup>; ref. 24) in the core of the NC ( $d > 10$  Å), while  $\langle u^2 \rangle$  is substantially larger (0.027–0.074 Å<sup>2</sup>) at the surface of the NC ( $d < 10$  Å). The large

<sup>1</sup>Laboratory for Nanoelectronics, Department of Information Technology and Electrical Engineering, ETH Zurich, CH-8092 Zurich, Switzerland. <sup>2</sup>Nano TCAD Group, Department of Information Technology and Electrical Engineering, ETH Zurich, CH-8092 Zurich, Switzerland. <sup>3</sup>Laboratory for Neutron Scattering and Imaging, Paul Scherrer Institute, CH-5232 Villigen PSI, Switzerland.



**Table 1 | Samples studied by INS**

Sample	$r$ (nm)	$E_g$ (FWHM) (eV)	$\langle u^2 \rangle$ ( $\text{\AA}^2$ )	Ligand	Inelastic scattering contributions
S1 (bulk)	>100	-	$0.042 \pm 0.007$	None	Pb (61%), S (39%)
S2	8.2	-	$0.077 \pm 0.003$	$S^{2-}$	Pb (61%), S (39%)
S3	1.3	1.32 (0.196)	$0.084 \pm 0.001$	EDTd4	PbS (59%), D (33%)
S4	1.5	1.31 (0.157)	$0.100 \pm 0.009$	EDT	H (90%), PbS (9%)
S5	1.6	1.12 (0.128)	$0.097 \pm 0.007$	EDT	H (91%), PbS (8%)
S6	2.0	0.98 (0.111)	$0.099 \pm 0.010$	EDT	H (91%), PbS (8%)
S7	3.3	0.73 (0.068)	$0.107 \pm 0.010$	EDT	H (88%), PbS (11%)

$r$  is the crystallite radius determined from XRD,  $E_g$  and FWHM are the energy and the full-width at half-maximum of the exciton peak extracted from the optical absorption spectrum of NCs in solution, and  $\langle u^2 \rangle$  is the atomic mean square displacement approximated from the Debye-Waller factor (Supplementary Methods 5). Error bars are the s.d. determined by evaluating  $\langle u^2 \rangle$  at three different momentum slices. The type of ligand used for each sample plays an important role in determining the dominant atomic species that contributes to the inelastic part of the neutron scattering signal (Supplementary Methods 3).

values for  $\langle u^2 \rangle$  found experimentally (Table 1) thus come from the surface of the nanocrystalline domains.

Plotting the partial  $g(\omega)$  of the Pb and the S atoms for three concentric regions of the NC (Fig. 2b) and as a density plot versus  $d$  (Fig. 2c, d), we find that the core of the NC shows the bulk PbS phonon spectrum<sup>13,27</sup>. The low-frequency mode is predominantly from Pb atoms within the first 2.7  $\text{\AA}$  of the NC surface. The S atoms on the surface of the NC show optical phonon modes shifted to higher energies and contribute in the frequency range of the acoustic modes. This contribution breaks the real-space symmetry that exists in the bulk  $g(\omega)$ , where the partial  $g(\omega)$  for Pb atoms involves only acoustic modes and the partial  $g(\omega)$  of S atoms only optical modes (Fig. 2a). These findings can be explained by the reconstruction of the NC surface (Supplementary Methods 9).

We now consider the implications of our findings for the performance of bottom-up fabricated semiconductors. In a trapping or recombination event, an electron transitions in a single step between two electronic states  $|e1\rangle$  and  $|e2\rangle$  by gaining or losing energy ( $\Delta E = 0.1\text{--}1\text{ eV} = 800\text{--}8,000\text{ cm}^{-1}$ ) through interaction with a number of phonons ( $p$ ) of energy  $\hbar\omega$  (Fig. 3a). The transition rate ( $k$ ) of such a process is strongly dependent on the electron–phonon coupling factor (or Huang–Rhys factor,  $S_{HR}$ ), in particular for transitions that involve many phonons ( $p \gg 1$ ), because  $k \propto (S_{HR})^p$  (ref. 1).  $S_{HR}$  depends on microscopic parameters of the system<sup>1</sup>:

$$S_{HR} = AM\kappa^{-1}(\hbar\omega)^{-1}D^2 \quad (1)$$

where  $A$  is the unitless overlap integral of the electronic states with number of phonon modes  $M$ ,  $D$  is the deformation potential in  $\text{eV \AA}^{-1}$ , and  $\kappa$  is the effective phonon spring constant in  $\text{eV \AA}^{-2}$ , which is related both to the effective mass ( $\mu$ ) and frequency ( $\omega$ ) of the phonon mode ( $\omega^2 = \kappa/\mu$ ). The spring constant ( $\kappa$ ) is closely related to the atomic mean square displacement ( $\kappa \approx k_B T / \langle u^2 \rangle$ ) for a given thermal energy  $k_B T$  (Supplementary Discussion 3) and gives direct insight into the strength of electron–phonon interactions (Supplementary Discussion 4).

Thermodynamics provides a complementary description of  $k$  based on the Gibbs free energy  $G$  ( $\Delta G = \Delta E - T\Delta S$ ), which includes the changes in (internal) energy and entropy ( $\Delta E$  and  $\Delta S$ , respectively) (ref. 17). Expressed as an Arrhenius dependence,  $k = k_0 \exp(-\Delta E/k_B T)$ , the attempt-frequency ( $k_0$ ) is then determined by a prefactor ( $k_{00}$ ) and  $\Delta S$  through  $k_0 = k_{00} \exp(\Delta S/k_B)$  (ref. 18). In the limit of large energy transitions ( $\Delta E \gg k_B T$  and  $\Delta E \gg \hbar\omega$ ), the entropy change is determined by the multi-excitation entropy (MEE)  $\Delta S/k_B = \Delta E/E_{MEE}$ , where  $E_{MEE}$  is the smallest available effective quantum of heat energy<sup>19</sup>. We use  $E_{MEE}$  to write the attempt-frequency as:

$$k_0 = k_{00} \exp(\Delta E/E_{MEE}) \quad (2)$$

We show in Supplementary Discussion 1 that the microscopic and thermodynamic expressions for multi-phonon transitions (equations (1)

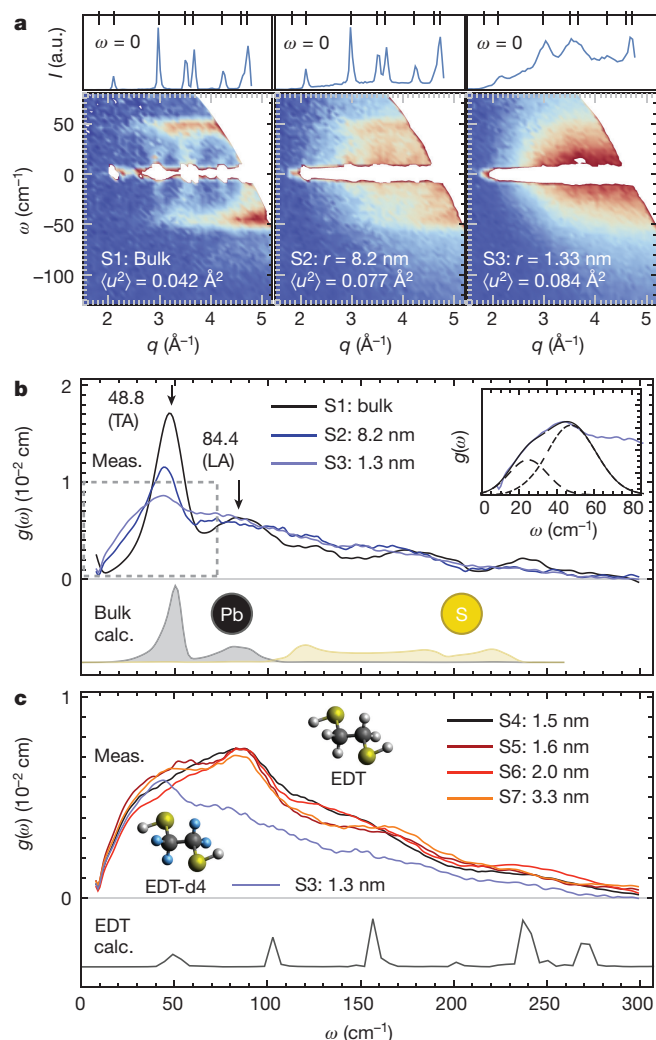


**Figure 1 | Inelastic neutron scattering (INS) measurements.** **a**, The intensity ( $I$ ) of the elastic line ( $\omega = 0$ ) and the dynamic structure factor ( $S(q, \omega)$ ) reconstructed from INS data for bulk PbS (S1) and two NC-solids with crystallite radii  $r = 8.2\text{ nm}$  (S2) and  $r = 1.33\text{ nm}$  (S3). a.u., arbitrary units. **b**, Phonon density of states ( $g(\omega)$ ) for samples S1 (black), S2 (dark blue) and S3 (light blue). Below, the partial  $g(\omega)$  for Pb atoms (grey) and S atoms (yellow) calculated by density-functional theory (DFT). All  $g(\omega)$  are normalized to an area of 1 between 0 and  $300\text{ cm}^{-1}$ . Peaks are the Van Hove singularities of transverse acoustic (TA) and longitudinal acoustic (LA) modes. NC-solids (S2, S3) show a mode at  $25\text{ cm}^{-1}$  (Gaussian fit in inset). **c**,  $g(\omega)$  for samples S4–S7 with radii between 1.5 nm and 3.3 nm. Peaks at 90, 150 and  $250\text{ cm}^{-1}$  are attributed to vibrations of the linker molecule 1,2-ethanedithiol (EDT), which do not appear in sample S3 (blue) using deuterated EDT (EDT-d4) (for better visibility  $g(\omega)$  of S3 (blue) is scaled by 0.68). *Ab initio* molecular dynamics calculations of EDT bound to a Pb atom are shown below (grey) (Supplementary Methods 11).

and (2)) can be related if  $E_{MEE} = \hbar\omega/\log S_{HR}$ . This means that for a transition characterized by an energy change  $\Delta E$ , a system with smaller phonon energy ( $\hbar\omega$ ) and/or larger electron–phonon coupling ( $S_{HR}$ ) has an exponentially larger transition rate. This is an entropy effect: the smaller  $E_{MEE}$ , the more possible ways there are to gain or lose energy  $\Delta E$ .

We found that Bloch-wave and real-space symmetry of bulk phonon modes break in a NC-solid. In bulk crystals, these symmetries render many overlap integrals zero (this is often conceptualized as crystal-momentum conservation). The absence of these symmetries in NCs will result in a non-negligible overlap integral  $A$ , and thus an important electron–phonon coupling  $S_{HR}$  (equation (1); see also Supplementary Methods 12). Mechanical softening of the surface, that

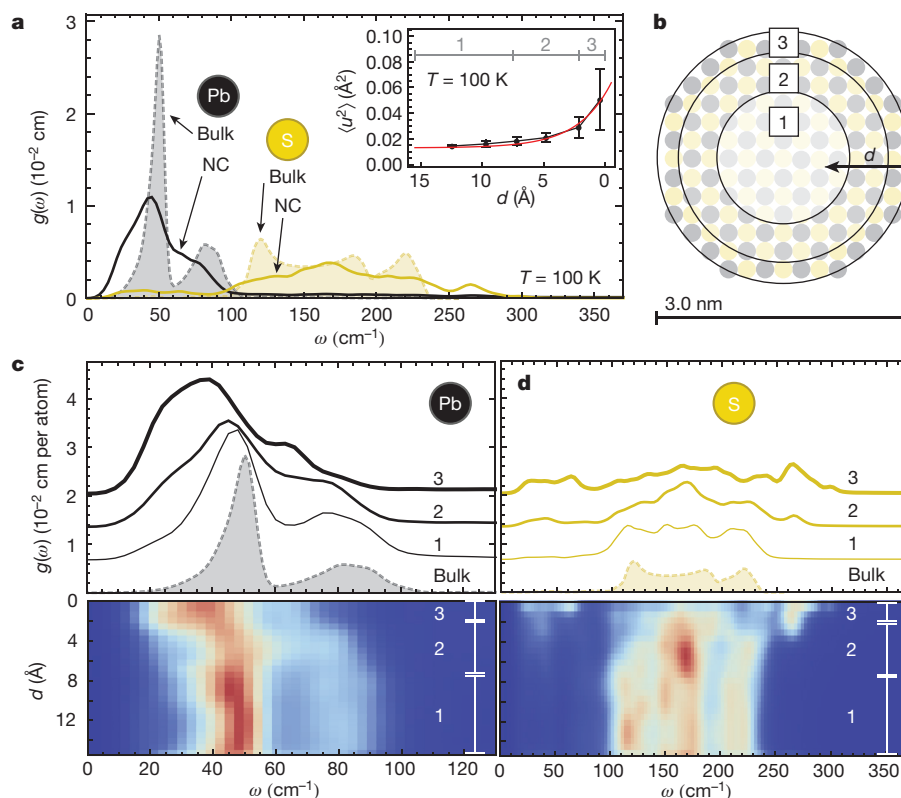


**Figure 2 | *Ab initio* molecular dynamics simulations of nanocrystal (NC) vibrations.** **a**, Simulated phonon density of states ( $g(\omega)$ ) comparing a PbS NC (520 atoms at  $T = 100$  K), plotted as partial for Pb atoms (black) and S atoms (yellow) with the spectra for the bulk (dashed and shaded). All  $g(\omega)$  are normalized to a total area of 1. Inset, the atomic mean square displacement ( $\langle u^2 \rangle$ ) versus the depth ( $d$ ) below the NC surface trends towards the bulk value in the core (exponential fit in red with decay constant  $2.7$  Å). Error bars indicate standard deviation over the  $\langle u^2 \rangle$  values for all atoms in the volume. **b**, Schematic of the simulated NC, where three regions are distinguished as a function of the depth ( $d$ ). **c**, Partial  $g(\omega)$  for Pb atoms normalized to density of states per atom.

Upper part,  $g(\omega)$  averaged over three concentric regions of the NC as indicated in **b**. Region 1, the core of the NC (thin line), shows a spectrum similar to bulk PbS (dashed and shaded) with both transverse acoustic (TA) and longitudinal acoustic (LA) modes. Towards the surface (regions 2 and 3 (progressively thicker lines)), low-frequency modes appear at  $25$   $\text{cm}^{-1}$ . Lower part, partial  $g(\omega)$  for Pb resolved along  $d$ . Blue and red correspond to  $0$  and  $2.6 \times 10^{-2}$  cm per atom. **d**, Same as **c** for partial  $g(\omega)$  from the S atoms. In contrast to the bulk, at the surface, high-frequency modes shift to  $270$   $\text{cm}^{-1}$  and S atoms contribute to low-frequency modes. Lower part, blue and red correspond to  $0$  and  $1 \times 10^{-2}$  cm per atom.

is, a reduced effective spring constant ( $\kappa \approx k_B T / \langle u^2 \rangle$ ), further increases  $S_{\text{HR}}$  through both lower  $\kappa$  and  $\hbar\omega$  (equation (1), Supplementary Discussion 4). Our findings therefore predict that, in a NC-solid, electrons couple to low-energy surface modes (equation (1)), and that both the lower energy ( $\hbar\omega$ ) of the modes and the non-negligible  $S_{\text{HR}}$  lead to non-radiative transitions with high entropy change that should be experimentally evidenced by small values of  $E_{\text{MEE}}$  ( $E_{\text{MEE}} = \hbar\omega / \log S_{\text{HR}}$ ) and large attempt-frequencies  $k_0$  (equation (2)).

To investigate whether this prediction—that low-energy surface modes found in NC-solids contribute to non-radiative transitions—is correct, we measure the non-radiative transition rates of electrons in a variety of NC-based diodes containing PbS NCs of bandgaps ranging from  $0.8$  eV to  $1.7$  eV (that is, radii of  $1.25$ – $3.0$  nm; Supplementary Methods 13). These diodes are based on NC-solids prepared in the same manner as S4–S7, which all showed evidence of low-energy surface modes. Using thermal admittance spectroscopy (TAS), we determine (1) the activation energy ( $\Delta E$ ) and attempt-frequency ( $k_0$ ) of each transition (Fig. 3b) by fitting a line ( $k = k_0 \exp(-\Delta E/k_B T)$ ) to the Arrhenius plot of the device capacitance ( $C_D$ ) and (2) the spectra of electronic states ( $N_T$ ) involved in the transition (Fig. 3c). Fig. 3d summarizes the different ( $\Delta E, k_0$ ) measured. Because of the different types of defect states that can occur in NC-solids, the  $\Delta E$  does not correlate with NC size (Supplementary Methods 13).

Transitions with  $\Delta E$  in the range  $0.1$ – $0.5$  eV ( $800$ – $4,000$   $\text{cm}^{-1}$ ) and  $k_0$  in the range  $10^6$ – $10^{14}$   $\text{s}^{-1}$  (group A) are similar to those previously reported<sup>28</sup> and to those in Cu(In,Ga)(S,Se)<sub>2</sub> (CIGS) diodes<sup>29</sup>. We fit a

line (equation (2)) to these points and find  $E_{\text{MEE}}^A = 53 \pm 6$  meV ( $427 \pm 48$   $\text{cm}^{-1}$ ) and  $k_0^A = 10^{8.0 \pm 0.3} \text{ s}^{-1}$ . Attributing these transitions to high-energy optical phonons<sup>29</sup>, which have energies ranging from  $120$   $\text{cm}^{-1}$  to  $240$   $\text{cm}^{-1}$  ( $15$ – $30$  meV) (Figs 1b, 2c), implies an  $S_{\text{HR}} = \exp(\hbar\omega/E_{\text{MEE}}) \approx 1.3$ – $1.8$ . We rule out that these group A transitions are driven predominately by ligand vibrations by comparing measurements on devices fabricated with EDT and EDT-d4 (Supplementary Methods 14).

In some PbS:EDT diodes, we observe transitions (group B) with high  $\Delta E$  ( $0.8$ – $1.2$  eV =  $6,500$ – $9,700$   $\text{cm}^{-1}$ ) and very large  $k_0$  ( $10^{25}$ – $10^{35}$   $\text{s}^{-1}$ ) (Fig. 3d). While the combination of high attempt-frequency ( $k_0$ ) and high activation energy ( $\Delta E$ ) results in transition rates ( $k = k_0 \exp(-\Delta E/k_B T) = 10^1$ – $10^{10}$   $\text{s}^{-1}$ ) similar to those for group A, an attempt-frequency ( $k_0$ ) that is a factor of more than  $10^{15}$  larger might seem unphysically large. These large attempt-frequencies in group B result not from large  $k_0$  ( $k_0^B = 10^{4.4 \pm 1.8} \text{ s}^{-1} < k_0^A$ ) but from a smaller  $E_{\text{MEE}}$  ( $E_{\text{MEE}}^B = 17.7 \pm 1.3$  meV ( $143 \pm 10$   $\text{cm}^{-1}$ )  $< E_{\text{MEE}}^A$ ). A small  $E_{\text{MEE}}^B$  occurs when transitions are driven by phonons with lower energy ( $\hbar\omega$ ), a stronger electron–phonon coupling factor ( $S_{\text{HR}}$ ), or both ( $E_{\text{MEE}} = \hbar\omega / \log S_{\text{HR}}$ ). Although we cannot uniquely assign group B transitions to a specific phonon mode, assigning them to the phonons at  $25$ – $50$   $\text{cm}^{-1}$  ( $3$ – $6$  meV) originating from the soft NC surface (Fig. 2a, c, d) implies  $S_{\text{HR}} = \exp(\hbar\omega/E_{\text{MEE}}) \approx 1.2$ – $1.4$ , consistent with our predictions that the low-frequency surface phonons have non-negligible  $S_{\text{HR}}$ . The large attempt-frequencies ( $10^{30}$   $\text{s}^{-1}$ ) are not unphysical, but rather reflect the many different ways that a high-energy

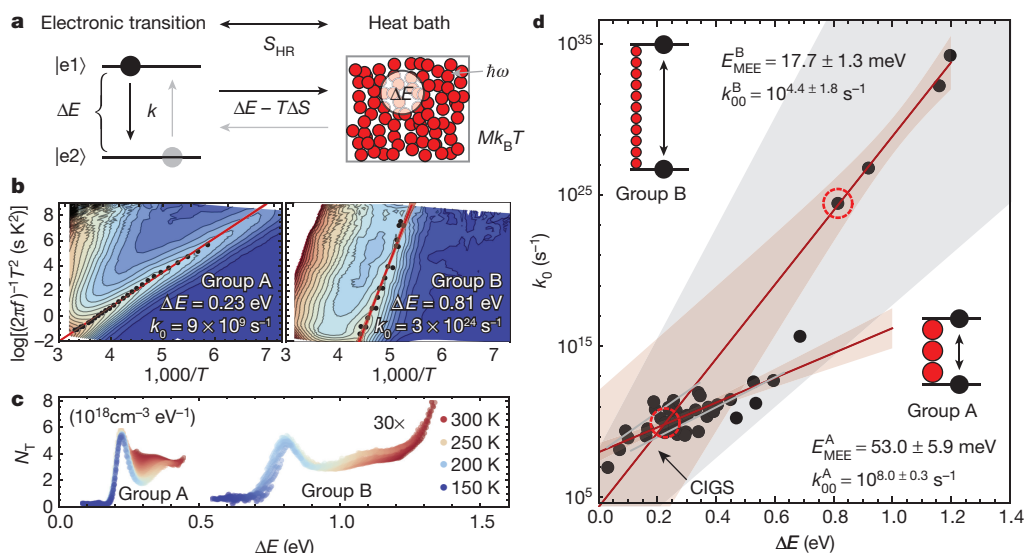


**Figure 3 | Non-radiative transition rates measured by thermal admittance spectroscopy (TAS).** **a**, Schematic of multi-phonon transitions between two electronic states  $|e1\rangle$  and  $|e2\rangle$  through the exchange of energy ( $\Delta E$ ) and entropy ( $\Delta S$ ) with a heat bath. The heat bath is made up of a number of  $M$  phonon modes with phonons of energy  $\hbar\omega$  and, at a given temperature  $T$ , contains a total energy of  $Mk_B T$ , where  $k_B$  is the Boltzmann constant. The quantum mechanical coupling between the electronic transition and the heat bath is given by the Huang–Rhys factor  $S_{HR}$ , which depends on the microscopic interaction between the electrons and the phonons. Multi-phonon transitions are dominant when  $\Delta E \gg \hbar\omega$  and can involve large entropy factors due to the combinatorial possibilities of how phonons can be chosen from the heat bath to drive the electronic transition. **b**, In a diode, electronic transitions in the semiconductor contribute to the frequency ( $f$ )-dependent capacitance ( $C_D$ ) of the device. Arrhenius plots of a TAS measurement ( $dC_D/df$ ) give the activation

energy ( $\Delta E$ ) and the attempt-frequency ( $k_0$ ) of a discrete trap state (red lines). Shown are examples of a trap state with low  $\Delta E$  and  $k_0$  (left, group A) and a trap state with high  $\Delta E$  and  $k_0$  (right, group B). **c**, Spectra of electronic states ( $N_T$ ) (left, right) corresponding to the data sets shown in **b** (left, right). **d**, Statistics of ( $\Delta E, k_0$ ) pairs for TAS measurements on diodes with different bandgap values and device architectures. Fitting equation (2) to points of group A (bottom left), we find  $E_{MEE}^A = 53 \pm 6$  meV ( $427 \pm 48$  cm $^{-1}$ ) and  $k_{00}^A = 10^{8.0 \pm 0.3}$  s $^{-1}$ . These values are comparable to measurements on Cu(In,Ga)(S,Se) $_2$  (CIGS) diodes (grey lines) $^{29}$ . Group B (top right) follows equation (2) with  $E_{MEE}^B = 17.7 \pm 1.3$  meV ( $143 \pm 10$  cm $^{-1}$ ) and  $k_{00}^B = 10^{4.4 \pm 1.8}$  s $^{-1}$ . The grey area indicates the parameter space observable in our measurement. Red circles are the two exemplary data points presented in **b** and **c**. Red lines indicate fits of equation (2) to group A and B, light red shading indicates their 95% confidence interval.

transition can be driven by low-energy excitations (Supplementary Discussion 2).

In summary, whereas in bulk crystals electronic transitions to trap states have been shown to occur via processes involving several optical phonons, we find that in NC-solids, electronic transitions can occur not only via several (that is,  $\sim 10$ ) higher-energy optical phonons but also by very large numbers (that is,  $\sim 200$ ) of low-energy phonons. Consistent with our experimental findings that  $S_{HR} \approx 1$  for both the low-energy surface phonons and the higher-energy optical phonons, simulations of the electronic structure indicate electron–phonon interactions at these phonon energies (Supplementary Methods 12).

We now address how our findings relate to the large body of literature on phonons in PbS NCs. Unlike most optical-based approaches to studying phonons, INS provides a complete picture of the phonon modes present in a NC-solid, independent of the electronic transition in which they play a role. We perform Raman measurements on samples S1–S7 and show that the results are consistent with those from INS and other Raman scattering studies $^{3,30}$  (Supplementary Methods 7). For example, our finding of an  $S_{HR}$  value of  $\sim 1$  is consistent with that determined by Raman studies on exciton transitions in the presence of trapped charge $^5$ .

Many studies have investigated how the dynamics of excitons in individual NCs are influenced by confined phonons $^{31}$  and ligand vibrations $^{32}$ . In contrast, we use our investigation of phonon properties to look at the case of electronic transitions to trap states in NC-solids and find that models invoking only confined phonons or single phonons cannot fully explain all electronic transitions occurring in a NC $^{30}$ . Indeed, our results show that the mechanical softening at the NC surface enables a large number ( $> 100$ ) of low-frequency phonon modes that efficiently drive multi-phonon processes.

Our findings provide important insight for device engineering. Energy loss in NC-based semiconductors is traditionally discussed in terms of the presence or absence of electronic defect states. However, in contrast to bulk semiconductors, no clear correlation between a measured trap density and device performance has been demonstrated. While measurements have shown  $\sim 0.01$ – $0.1$  defects per NC in solar cells $^{28}$ , surface treatments that successfully improve efficiencies replace of the order of  $10$ – $100$  atoms per NC $^{33}$ . This presents a paradox. Why does ‘passivation’ of  $0.01$ – $0.1$  traps per NC require the replacement of  $\sim 100$  atoms per NC? We propose that surface passivation succeeds not through elimination of electronic defect states but by mechanically stabilizing the NC surface, which consists of several hundred atoms. Whereas conventional materials engineering aims to remove electronic states on the surface of the NCs $^{22,33}$ , our work suggests that non-radiative rates might be better controlled by engineering mechanical stability and electron–phonon coupling at the NC surface.

Phonon processes in nanomaterials cannot be ignored: mechanical softening of the surface will enhance all phonon interactions, including the scattering with electrons, neutrons, photons or other phonons (Supplementary Discussion 4). While strong phonon–electron interactions and the entropy effects of low-frequency phonons are undesirable for applications such as LEDs and solar cells, other applications based on laser cooling, superconductivity, magnetoresistance, thermoelectrics and catalysis could benefit from enhanced phonon interactions. At the same time, the composite nature of bottom-up fabricated semiconductors offers the possibility of tuning the phononic structure, a feature not readily available in bulk semiconductors.

**Online Content** Methods, along with any additional Extended Data display items and Source Data, are available in the online version of the paper; references unique to these sections appear only in the online paper.



Received 14 July 2015; accepted 4 January 2016.

Published online 9 March 2016.

- Ridley, B. K. *Quantum Processes in Semiconductors* 235–281 (Oxford Univ. Press, 1999).
- Mittleman, D. M. *et al.* Quantum size dependence of femtosecond electronic dephasing and vibrational dynamics in CdSe nanocrystals. *Phys. Rev. B* **49**, 14435–14447 (1994).
- Krauss, T. D. & Wise, F. W. Raman-scattering study of exciton-phonon coupling in PbS nanocrystals. *Phys. Rev. B* **55**, 9860–9865 (1997).
- Harbold, J. M. *et al.* Time-resolved intraband relaxation of strongly confined electrons and holes in colloidal PbSe nanocrystals. *Phys. Rev. B* **72**, 195312 (2005).
- Kambhampati, P. On the kinetics and thermodynamics of excitons at the surface of semiconductor nanocrystals: are there surface excitons? *Chem. Phys.* **446**, 92 (2015).
- Shirasaki, Y., Supran, G. J., Bawendi, M. G. & Bulović, V. Emergence of colloidal quantum-dot light-emitting technologies. *Nature Photon.* **7**, 13–23 (2012).
- Kramer, I. J. & Sargent, E. H. The architecture of colloidal quantum dot solar cells: materials to devices. *Chem. Rev.* **114**, 863–882 (2014).
- Talapin, D. V., Lee, J.-S., Kovalenko, M. V. & Shevchenko, E. V. Prospects of colloidal nanocrystals for electronic and optoelectronic applications. *Chem. Rev.* **110**, 389–458 (2010).
- Bockelmann, U. & Bastard, G. Phonon scattering and energy relaxation in two-, one-, and zero-dimensional electron gases. *Phys. Rev. B* **42**, 8947–8951 (1990).
- Schaller, R. D. *et al.* Breaking the phonon bottleneck in semiconductor nanocrystals via multiphonon emission induced by intrinsic nonadiabatic interactions. *Phys. Rev. Lett.* **95**, 196401 (2005).
- Cooney, R. R., Sewall, S. L., Anderson, K. E. H., Dias, E. A. & Kambhampati, P. Breaking the phonon bottleneck for holes in semiconductor quantum dots. *Phys. Rev. Lett.* **98**, 177403 (2007).
- Kilina, S. V., Kilin, D. S. & Prezhd, O. V. Breaking the phonon bottleneck in PbSe and CdSe quantum dots: time-domain density functional theory of charge carrier relaxation. *ACS Nano* **3**, 93–99 (2009).
- Han, P. & Bester, G. Carrier relaxation in colloidal nanocrystals: bridging large electronic energy gaps by low-energy vibrations. *Phys. Rev. B* **91**, 085305 (2015).
- Keuleyan, S., Kohler, J. & Guyot-Sionnest, P. Photoluminescence of mid-infrared HgTe colloidal quantum dots. *J. Phys. Chem. C* **118**, 2749–2753 (2014).
- Mooney, J., Krause, M. M., Saari, J. I. & Kambhampati, P. A microscopic picture of surface charge trapping in semiconductor nanocrystals. *J. Chem. Phys.* **138**, 204705 (2013).
- Liu, J., Neukirch, A. J. & Prezhd, O. V. Non-radiative electron–hole recombination in silicon clusters: *ab initio* non-adiabatic molecular dynamics. *J. Phys. Chem. C* **118**, 20702–20709 (2014).
- Marcus, R. A. Electron transfer reactions in chemistry theory and experiment. *J. Electroanal. Chem.* **438**, 251–259 (1997).
- Lang, D. V., Grimmeiss, H. G., Meijer, E. & Jaros, M. Complex nature of gold-related deep levels in silicon. *Phys. Rev. B* **22**, 3917–3934 (1980).
- Yelon, A., Movaghar, B. & Crandall, R. S. Multi-excitation entropy: its role in thermodynamics and kinetics. *Rep. Prog. Phys.* **69**, 1145–1194 (2006).
- Sun, L. *et al.* Bright infrared quantum-dot light-emitting diodes through inter-dot spacing control. *Nature Nanotechnol.* **7**, 369–373 (2012).
- Konstantatos, G. *et al.* Ultrasensitive solution-cast quantum dot photodetectors. *Nature* **442**, 180–183 (2006).
- Ip, A. H. *et al.* Hybrid passivated colloidal quantum dot solids. *Nature Nanotechnol.* **7**, 577–582 (2012).
- Zhao, L. D. *et al.* High performance thermoelectrics from earth-abundant materials: enhanced figure of merit in PbS by second phase nanostructures. *J. Am. Chem. Soc.* **133**, 20476–20487 (2011).
- Božin, E. S. *et al.* Entropically stabilized local dipole formation in lead chalcogenides. *Science* **330**, 1660–1663 (2010).
- Tanaka, A., Onari, S. & Arai, T. Low-frequency Raman scattering from CdS microcrystals embedded in a germanium dioxide glass matrix. *Phys. Rev. B* **47**, 1237–1243 (1993).
- Combe, N., Huntzinger, J. R. & Mlayah, A. Vibrations of quantum dots and light scattering properties: atomistic versus continuous models. *Phys. Rev. B* **76**, 205425 (2007).
- Han, P. & Bester, G. Confinement effects on the vibrational properties of III–V and II–VI nanoclusters. *Phys. Rev. B* **85**, 041306 (2012).
- Bozyigit, D., Volk, S., Yarema, O. & Wood, V. Quantification of deep traps in nanocrystal solids, their electronic properties, and their influence on device behavior. *Nano Lett.* **13**, 5284–5288 (2013).
- Herberholz, R. *et al.* Meyer–Neldel behavior of deep level parameters in heterojunctions to Cu(In,Ga)(S,Se)<sub>2</sub>. *Appl. Phys. Lett.* **69**, 2888–2890 (1996).
- Kilina, S. V., Kilin, D. S., Prezhd, V. V. & Prezhd, O. V. Theoretical study of electron–phonon relaxation in PbSe and CdSe quantum dots: evidence for phonon memory. *J. Phys. Chem. C* **115**, 21641–21651 (2011).
- Kilina, S., Kilin, D. & Tretyak, S. Light-driven and phonon-assisted dynamics in organic and semiconductor nanostructures. *Chem. Rev.* **115**, 5929–5978 (2015).
- Pandey, A. & Guyot-Sionnest, P. Slow electron cooling in colloidal quantum dots. *Science* **322**, 929–932 (2008).
- Bae, W. K. *et al.* Highly effective surface passivation of PbSe quantum dots through reaction with molecular chlorine. *J. Am. Chem. Soc.* **134**, 20160–20168 (2012).

Supplementary Information is available in the online version of the paper.

**Acknowledgements** D.B., N.Y., M.Y., W.M.M.L., O.Y., S.V. and V.W. acknowledge funding from the Swiss National Science Foundation through the NCCR Quantum Science and Technology and an ETH Research Grant. K.V. and M.L. acknowledge funding from SNF TORNAD under project 149454. Neutron scattering experiments were performed at the Swiss spallation neutron source SINQ, Paul Scherrer Institute. Molecular dynamics simulations were supported by a grant from the Swiss National Supercomputing Centre (CSCS; project ID s579). We thank D. Norris for access to SEM and EDX, C. Hierold for access to the confocal Raman spectrometer, and M. Wörle for access to XRD at the Small Molecule Crystallography Center at ETH Zürich.

**Author Contributions** M.Y. and O.Y. designed and conducted the material synthesis; M.Y., O.Y., D.B., N.Y., W.M.M.L. and S.V. performed the sample preparation; D.B., N.Y. and M.Y. characterized the samples; D.B. and F.J. conducted the neutron scattering experiments and data analysis; N.Y. and D.B. performed the *ab initio* molecular dynamics simulations; K.V. performed density functional theory calculations; D.B., W.M.M.L. and N.Y. fabricated NC diodes and performed thermal admittance spectroscopy; D.B. performed Raman spectroscopy; D.B. developed the theoretical description of the results; D.B. and V.W. devised the experiments; and all authors contributed to the writing of the manuscript.

**Author Information** Reprints and permissions information is available at [www.nature.com/reprints](http://www.nature.com/reprints). The authors declare no competing financial interests. Readers are welcome to comment on the online version of the paper. Correspondence and requests for materials should be addressed to D.B. ([denizb@iis.ee.ethz.ch](mailto:denizb@iis.ee.ethz.ch)) or V.W. ([vwood@ethz.ch](mailto:vwood@ethz.ch)).

# Visualizing coherent intermolecular dipole–dipole coupling in real space

Yang Zhang<sup>1\*</sup>, Yang Luo<sup>1\*</sup>, Yao Zhang<sup>1\*</sup>, Yun-Jie Yu<sup>1</sup>, Yan-Min Kuang<sup>1</sup>, Li Zhang<sup>1</sup>, Qiu-Shi Meng<sup>1</sup>, Yi Luo<sup>1</sup>, Jin-Long Yang<sup>1</sup>, Zhen-Chao Dong<sup>1</sup> & J. G. Hou<sup>1</sup>

Many important energy-transfer and optical processes, in both biological and artificial systems, depend crucially on excitonic coupling that spans several chromophores<sup>1–9</sup>. Such coupling can in principle be described in a straightforward manner by considering the coherent intermolecular dipole–dipole interactions involved<sup>10,11</sup>. However, in practice, it is challenging to directly observe in real space the coherent dipole coupling and the related exciton delocalizations, owing to the diffraction limit in conventional optics. Here we demonstrate that the highly localized excitations that are produced by electrons tunnelling from the tip of a scanning tunnelling microscope, in conjunction with imaging of the resultant luminescence, can be used to map the spatial distribution of the excitonic coupling in well-defined arrangements of a few zinc-phthalocyanine molecules. The luminescence patterns obtained for excitons in a dimer, which are recorded for different energy states and found to resemble  $\sigma$  and  $\pi$  molecular orbitals, reveal the local optical response of the system and the dependence of the local optical response on the relative orientation and phase of the transition

dipoles of the individual molecules in the dimer. We generate an in-line arrangement up to four zinc-phthalocyanine molecules, with a larger total transition dipole, and show that this results in enhanced ‘single-molecule’ superradiance from the oligomer upon site-selective excitation. These findings demonstrate that our experimental approach provides detailed spatial information about coherent dipole–dipole coupling in molecular systems, which should enable a greater understanding and rational engineering of light-harvesting structures and quantum light sources.

Scanning tunnelling microscope (STM)-induced luminescence (STML; see Extended Data Fig. 1) enables nano-imaging beyond the diffraction limit, owing to the highly localized excitation by the tunnelling electrons. This makes it possible to obtain intensity-based photon-yield images<sup>12,13</sup> (photon images) and energy-resolved spectroscopic images of a single molecule<sup>14</sup>. To extend these abilities to reveal fundamental properties of intermolecular interactions at the molecular level, we first realize molecule-specific exciton emission from single molecules. As illustrated in Fig. 1a, this realization involves using an

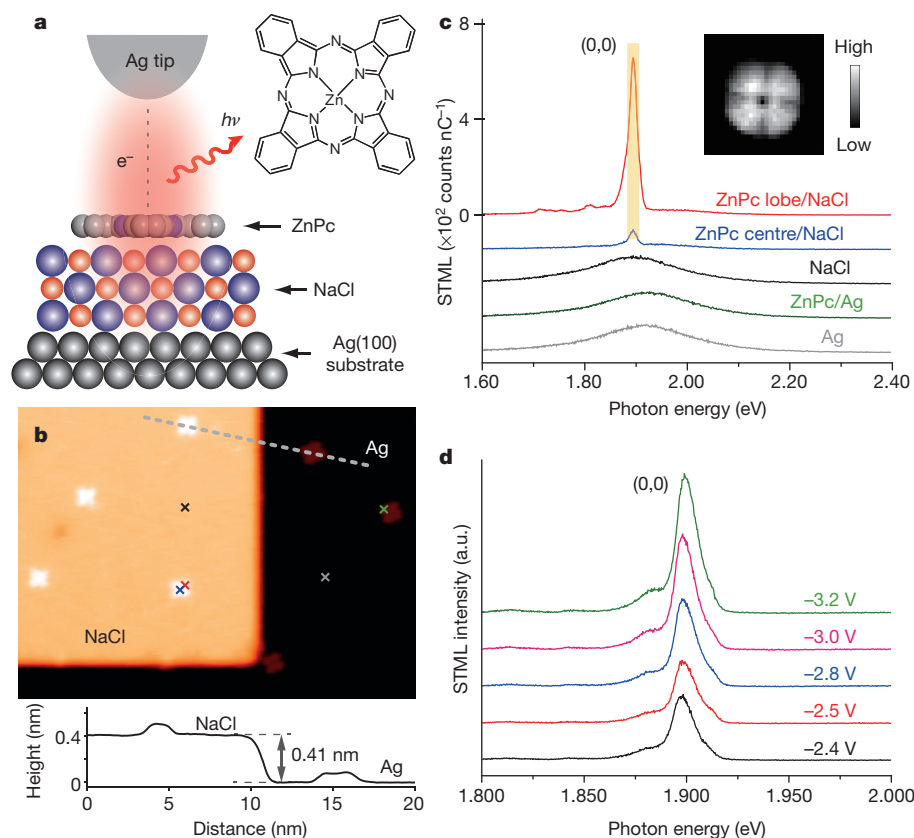


**Figure 1 | Single-molecule electrochromism through electronic decoupling and nanocavity-plasmon enhancement.** **a**, Schematic of STML from a ZnPc molecule on NaCl/Ag(100). Inset, ZnPc molecular structure. **b**, STM image showing isolated single ZnPc molecules adsorbed on either a three-monolayer NaCl island or bare Ag(100) (image size:  $34 \text{ nm} \times 25 \text{ nm}$ ; scanning parameters:  $-1.7 \text{ V}$ ,  $2 \text{ pA}$ ). The height profile along the grey dashed line is given below the STM image. **c**, STML spectra acquired at the positions marked with an ‘x’ in **b** ( $-2.5 \text{ V}$ ,  $200 \text{ pA}$ ,  $60 \text{ s}$ ); the colour of the trace in **c** matches that of the corresponding ‘x’ in **b**. Inset, photon image of ZnPc on NaCl ( $-2.5 \text{ V}$ ,  $200 \text{ pA}$ ,  $5 \text{ s}$  per pixel;  $4 \text{ nm} \times 4 \text{ nm}$ ,  $30 \times 28$  pixels; integrated over  $1.89\text{--}1.91 \text{ eV}$ , the yellow shaded energy region). For each pixel in the inset, a spectrum was recorded. The photon intensity integration is applied to each pixel (and each spectrum) for the selected energy range. **d**, STML spectra acquired above the molecular lobe on NaCl at different biases ( $200 \text{ pA}$ ,  $60 \text{ s}$ ). a.u., arbitrary units. All STML spectra are offset for clarity; in **c**, the y-axis scale applies only to the red line. ‘(0,0)’ refers to the  $Q(0,0)$  transition.

<sup>1</sup>Hefei National Laboratory for Physical Sciences at the Microscale and Synergetic Innovation Center of Quantum Information and Quantum Physics, University of Science and Technology of China, Hefei, Anhui 230026, China.

\*These authors contributed equally to this work.

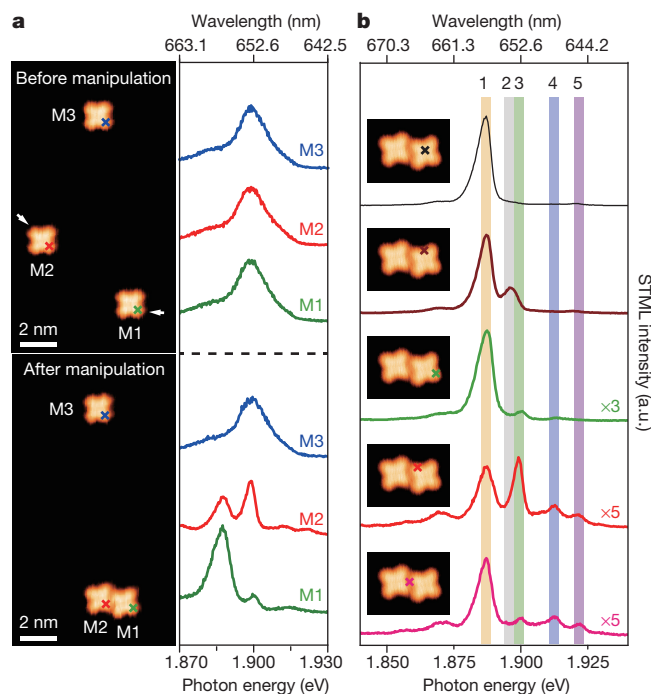


**Figure 2 | Spectral evolution from isolated ZnPc monomers to an artificially constructed molecular dimer on NaCl.** **a**, STM images (left;  $-1.7$  V,  $2$  pA) and STML spectra (right;  $-2.5$  V,  $200$  pA,  $60$  s) acquired before and after manipulation. Molecules M1 and M2 were pushed together, with the direction of motion indicated by the white arrows; molecule M3 was used as a reference. The STML spectra were acquired at the lobe positions marked with an 'x' in the STM images. **b**, Site-dependent STML spectra ( $-2.5$  V,  $200$  pA,  $60$  s) acquired at the positions marked with an 'x' in the inset STM images ( $4$  nm  $\times$   $3$  nm;  $-1.7$  V,  $2$  pA). All STML spectra are offset for clarity. The shaded bands labelled 1–5 indicate the peak positions and the ranges of integration used in Fig. 3b. a.u., arbitrary units.

ultrathin NaCl layer to electronically decouple zinc-phthalocyanine (ZnPc) molecules from the Ag(100) substrate to suppress substrate-induced fluorescence quenching<sup>15–21</sup>; it also involves enhancing the spontaneous emission by resonant nanocavity plasmons (NCPs; red halo in Fig. 1a)<sup>22,23</sup>. Images of isolated, single ZnPc molecules adsorbed on a three-monolayer NaCl island<sup>24</sup> and on bare Ag(100) both appear as four-lobe patterns (Fig. 1b), but excitation of adsorbed molecules through carrier injection (see Methods and Extended Data Fig. 2) generates detectable single-molecule fluorescence only in the case of decoupled ZnPc molecules (Fig. 1c). The sharp emission peak around  $1.90$  eV (approximately  $653$  nm) is assigned to the Q(0,0) transition of neutral ZnPc molecules on the basis of good agreement with the photoluminescence data of ZnPc in an argon matrix<sup>25</sup>, the sharpness of the spectral feature that differs from the broadband emission of the NCP, and the nearly constant position of the peak when varying the excitation voltage (Fig. 1d)<sup>16</sup>.

Spectral measurements as a function of position (Fig. 1c) show that excitation over the ZnPc lobe generates emission with a much greater intensity than that generated from excitation above the ZnPc centre, probably owing to the dipole symmetry of the whole system<sup>14</sup>. This character is confirmed by the sub-nanometre-resolved spatial variations of optical transition probabilities in the photon image (Fig. 1c inset and Extended Data Fig. 3).

We next explore intermolecular excitonic coupling by pushing isolated ZnPc molecules together to create artificial molecular dimers (see Methods and Extended Data Fig. 4), which markedly changes the spectral features we observe (Fig. 2a). Differential conductance ( $dI/dV$ ) spectra yield essentially the same electronic states for isolated monomers and the artificial dimer (Extended Data Fig. 5), so the spectral changes are not due to structural changes of the molecules. Moreover,

electronic coupling between two adjacent monomers in their ground state is very weak because the  $D_{4h}$  symmetry of the natural ZnPc molecule gives rise to a negligible permanent dipole.

A series of STML spectra collected at five different representative sites over the ZnPc dimer (Fig. 2b) shows that emission modes and intensities vary from site to site, and allows us to identify five major emission modes (marked in Fig. 2b) with narrower peak widths than those seen for the isolated monomer. Peak 1 (approximately  $657$  nm) and peak 2 (approximately  $654$  nm) are redshifted with respect to the monomer emission; almost no shift is observed for peak 3 (approximately  $653$  nm); peak 4 (approximately  $648$  nm) and peak 5 (approximately  $645$  nm) are blueshifted. (The origin of the additional emission peak at about  $663$  nm in Fig. 2b is discussed in Methods and Extended Data Fig. 6.)

For a more panoramic view of these five emission modes (indicated by arrows in Fig. 3a), we carried out spatially resolved spectroscopic imaging over the constructed dimer and obtained photon imaging patterns with noticeably different features for the different emission modes (Fig. 3b). The five photon imaging patterns, each with distinct numbers and positions of emission maxima and nodes, all differ from the photon imaging pattern of the isolated monomer. This, along with the occurrence of both blue- and redshifting of emission modes, suggests coherent excitonic coupling as the cause of the spectral changes observed upon dimer formation.

For a coherently coupled dimer with one of the monomers excited, two new one-exciton eigenstates formed via resonance interaction can be expressed as<sup>10</sup>

$$\Psi_{\text{dim},e} = (\psi_{1,e}\psi_{2,g} \pm \psi_{1,g}\psi_{2,e})/\sqrt{2} \quad (1)$$

in which  $\Psi$  and  $\psi$  represent the wavefunctions of the dimer and the monomer unit, respectively; the subscripts 'e' and 'g' denote the excited and ground states. The optical transition energy for the dimer ( $\Delta E_{\text{dim}}$ ) is (see Fig. 3c)

$$\Delta E_{\text{dim}} = \Delta E_{\text{mono}} + \Delta W \pm |J| \quad (2)$$

in which  $\Delta E_{\text{mono}}$  represents the optical transition energy for an isolated monomer,  $\Delta W$  represents the energy difference of van der Waals interaction between the excited and ground states of the dimer, and  $|J|$  represents the exciton coupling strength. Within the point-dipole approximation<sup>10,26</sup>,  $J$  can be expressed as

$$J = \frac{\boldsymbol{\mu}_1 \cdot \boldsymbol{\mu}_2}{4\pi\epsilon_0 r^3} - \frac{3(\boldsymbol{\mu}_1 \cdot \mathbf{r})(\boldsymbol{\mu}_2 \cdot \mathbf{r})}{4\pi\epsilon_0 r^5} \quad (3)$$

in which  $\boldsymbol{\mu}_{1,2}$  are the transition dipoles of the component monomers (with amplitude  $\mu_0$ ),  $\mathbf{r}$  is the position vector between the two monomer centres ( $|\mathbf{r}| = r$  is its magnitude) and  $\epsilon_0$  is the vacuum permittivity.

Each ZnPc molecule possesses two degenerate excited states and, hence, two associated equivalent transition-dipole orientations ( $x$  and  $y$ ), owing to  $D_{4h}$  symmetry (Fig. 3d). Consequently, there are five possible dipole coupling modes for a molecular dimer: in-line in-phase ( $\rightarrow\rightarrow$ ), in-line out-of-phase ( $\rightarrow\leftarrow$ ), parallel in-phase ( $\uparrow\uparrow$ ), parallel out-of-phase ( $\uparrow\downarrow$ ) and orthogonal ( $\uparrow\rightarrow$  and  $\rightarrow\uparrow$ ). According to equation (3), the corresponding  $J$  for different dipole phase relations is

$$J_{\rightarrow\rightarrow} = -\frac{2\mu_0^2}{4\pi r^3} = -J_{\leftarrow\leftarrow}, J_{\uparrow\uparrow} = \frac{\mu_0^2}{4\pi r^3} = -J_{\downarrow\downarrow}, J_{\uparrow\rightarrow} = J_{\rightarrow\uparrow} = 0 \quad (4)$$

On the basis of the sequence of the energy levels and the coupling strength predicted by equations (2) and (4) for different modes, the emission peaks in Fig. 3a are assigned according to the exciton splitting diagram in Fig. 3d. The coupling strength ( $|J|$ ) and the energy shift ( $\Delta W$ ) for different coherent dipole–dipole coupling modes can be directly measured (see Methods and Extended Data Table 1).

Insight into the coherent dipole–dipole coupling behaviour is thus obtained through the combined use of sub-nanometre-resolved



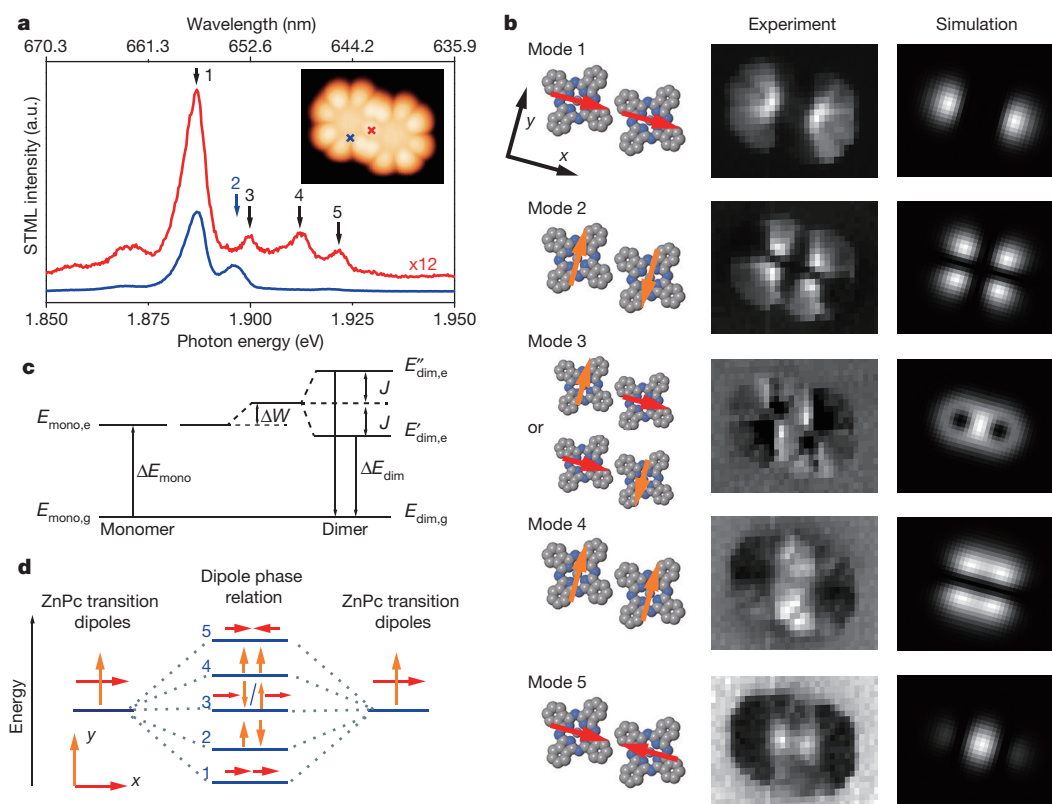


**Figure 3 | Real-space visualization of coherent intermolecular dipole-dipole coupling in a constructed ZnPc dimer.** **a**, STML spectra ( $-2.5$  V,  $200$  pA,  $60$  s) acquired at the positions marked with an 'x' in the inset STM image ( $5$  nm  $\times$   $4$  nm;  $-2.5$  V,  $2$  pA), showing five distinct emission modes (as indicated); the colour of the trace matches that of the corresponding 'x' in the inset. a.u., arbitrary units. **b**, Left, schematic arrangements of the transition dipoles. The red and orange arrows represent the in-line dipole along the dimer axial direction and the parallel dipole perpendicular to the dimer axial direction, respectively, which are superimposed on the molecular units. Middle, energy-resolved photon images for the five modes indicated in **a** ( $-2.5$  V,  $200$  pA,  $5$  s per pixel;  $5$  nm  $\times$   $4$  nm,  $34 \times 22$  pixels; integration ranges for modes 1–5:  $1,887 \pm 1.5$  meV,  $1,896 \pm 1.5$  meV,  $1,899 \pm 1.5$  meV,  $1,912 \pm 1.5$  meV and  $1,922 \pm 1.5$  meV, respectively, as indicated by the correspondingly labelled, shaded regions in Fig. 2b). **c**, Exciton band energy diagram of a molecular dimer.  $E_{\text{mono,e/g}}$ , excited-/ground-state energy of an isolated monomer;  $\Delta E_{\text{mono}}$ , optical transition energy for an isolated monomer;  $E_{\text{dim,g}}$ , ground-state energy of the dimer;  $E'_{\text{dim,e}}$  and  $E''_{\text{dim,e}}$ , low-lying and high-lying excited-state energy of the dimer for similar coupling modes with opposite phases;  $\Delta E_{\text{dim}}$ , optical transition energy for the dimer;  $\Delta W$ , energy difference of van der Waals interaction between the excited and ground states of the dimer;  $J$ , exciton coupling strength. The horizontal line between that for  $E_{\text{mono,e}}$  and  $\Delta W$  refers to a hypothetical energy level of the dimer without any interactions; the horizontal line above  $\Delta W$  refers to a hypothetical energy level without dipole coupling; the dashed lines serve as guides for the eye indicating the energy difference specified. **d**, Exciton splitting diagram for different coherent dipole-dipole coupling modes; the numbers correspond to the modes in **a** and **b**.

Right, corresponding simulated patterns. **c**, Exciton band energy diagram of a molecular dimer.  $E_{\text{mono,e/g}}$ , excited-/ground-state energy of an isolated monomer;  $\Delta E_{\text{mono}}$ , optical transition energy for an isolated monomer;  $E_{\text{dim,g}}$ , ground-state energy of the dimer;  $E'_{\text{dim,e}}$  and  $E''_{\text{dim,e}}$ , low-lying and high-lying excited-state energy of the dimer for similar coupling modes with opposite phases;  $\Delta E_{\text{dim}}$ , optical transition energy for the dimer;  $\Delta W$ , energy difference of van der Waals interaction between the excited and ground states of the dimer;  $J$ , exciton coupling strength. The horizontal line between that for  $E_{\text{mono,e}}$  and  $\Delta W$  refers to a hypothetical energy level of the dimer without any interactions; the horizontal line above  $\Delta W$  refers to a hypothetical energy level without dipole coupling; the dashed lines serve as guides for the eye indicating the energy difference specified. **d**, Exciton splitting diagram for different coherent dipole-dipole coupling modes; the numbers correspond to the modes in **a** and **b**.

real-space visualization of local optical responses for different modes and theoretical simulations in Fig. 3b. The simulated photon imaging patterns show spatially resolved optical transition probabilities for various coupling modes based on the consideration of emission processes alone (see Methods and Extended Data Fig. 7). These simulated patterns capture the number and position of the emission maxima and nodes in the different experimentally observed patterns when considering that the transition-dipole orientations of the two monomers become parallel or perpendicular to the centre-to-centre axial direction upon dimer formation. This result indicates that the photon image for each mode is determined mainly by the emission process and its dependence on the molecular transition-dipole arrangements and their couplings, and that only minor features in the images arise as a result of changes in the spatial distribution of the local electronic density of states caused by modification of local excitation efficiencies (see Methods).

The in-line (parallel) dipole coupling patterns, which resemble  $\sigma$ -type ( $\pi$ -type) orbital bonding/anti-bonding patterns in molecular orbital theory (Extended Data Fig. 8), reflect directly, and in real space, the coherent nature of the dipole-dipole coupling for the different modes. These mode-specific patterns also serve as 'fingerprints' to aid spectral assignments, by identifying the physical origin of complicated optical transitions in molecular systems (see Methods and Extended Data Fig. 6).

The transition dipole arrangements in the dimer (as sketched in Fig. 3b) classify mode 1 and mode 4 as superradiant modes, owing to in-phase dipole coupling. In particular, the emission intensity for mode 1 at its brightest spots is much stronger than emission from any other modes, probably owing to an in-line and in-phase dipole coupling that results in the largest total dipole and the expected largest population probability at the lowest energy level. Surprisingly, we detect photon emission from mode 2 and mode 5 even though they show out-of-phase dipole coupling and are thus expected to be dark, subradiant modes; the observation of these subradiant modes is probably the result of the asymmetric image-dipole effect caused by the near-field tip generating a dipole component along the tip axial direction. It is the simultaneous observation of super- and subradiant emission modes that allows us to directly measure the dipole coupling strength  $|J|$  (see Methods).

The initial excitation in STML occurs directly underneath the STM tip—in this case, in only one of the monomers, owing to the highly localized nature of the tunnelling electrons and the excitations they induce. The coherence evident in both the spectrally and spatially resolved data described above indicates that the excitation energy is rapidly shared between the two coupled monomers, and oscillated back and forth to yield an entangled dimer. The oscillation frequency  $\Omega$  (ref. 27; see Methods and Extended Data Table 1),

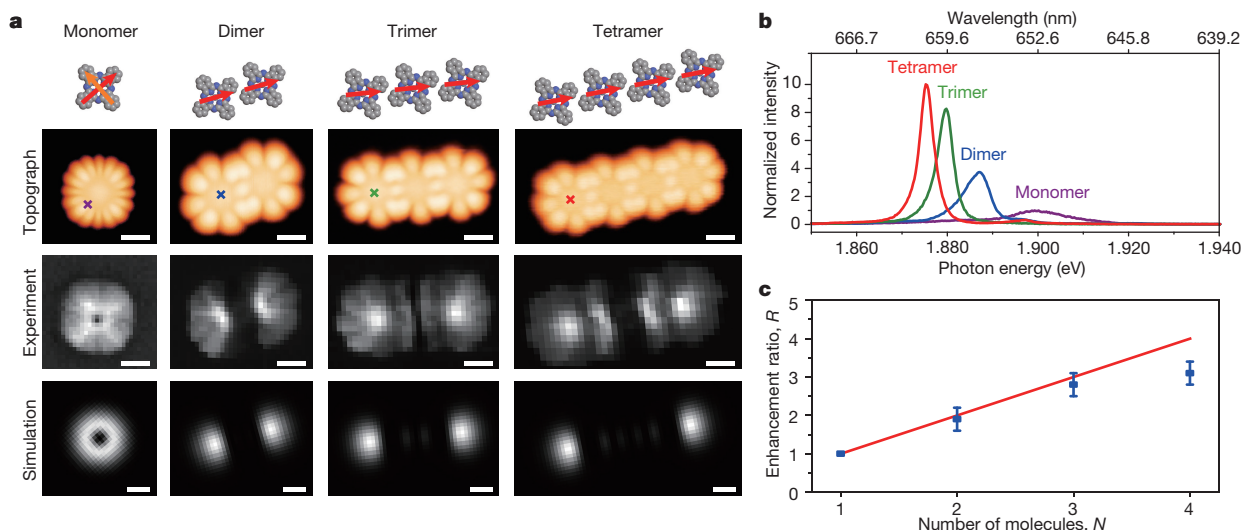


**Figure 4 | Engineering electrically driven ‘single-molecule’ superradiance.** **a**, First row, schematic arrangements of molecular structures and transition dipoles. Second row, STM images ( $-2.5$  V,  $2$  pA). Third row, experimental photon images of the superradiant modes of the oligomers ( $-2.5$  V,  $200$  pA,  $5$  s per pixel; pixel resolution (left to right):  $30 \times 28$ ,  $34 \times 24$ ,  $34 \times 21$  and  $40 \times 18$ ; integration ranges (left to right):  $1,899 \pm 1.5$  meV,  $1,887 \pm 1.5$  meV,  $1,880 \pm 1.5$  meV and  $1,875 \pm 1.5$  meV). Fourth row, simulated patterns based on in-line in-phase coupled dipole models. Scale bars,  $1$  nm. **b**, Typical STML spectra acquired at the positions marked by an ‘ $\times$ ’ in the second row of **a** ( $-2.5$  V,

$200$  pA,  $60$  s), normalized by the peak maximum of neighbouring, isolated ZnPc monomers to exclude the tip-induced intensity fluctuations. **c**, The emission enhancement ratio  $R$  for the superradiant mode of oligomers as a function of the number of molecules  $N$  (blue squares). The red line represents the ideal  $R = N$  relation.  $R$  is calculated by dividing the integrated intensity of the oligomer emission over  $1.86$ – $1.94$  eV by that of the monomer emission for ten data sets, and taking the average, yielding  $R = 1$ ,  $1.9(3)$ ,  $2.8(3)$  and  $3.1(3)$  for the monomer, dimer, trimer and tetramer, respectively, with the numbers in parentheses and error bars indicating the standard deviation.

deduced from the measured  $|J|$ , is of the order of  $10^{13} \text{ s}^{-1}$ , which is faster than the vibrational relaxation of the molecules (about  $10^{12} \text{ s}^{-1}$ ; ref. 28), and thus enables exciton delocalization and the generation of coherent signals<sup>29</sup>. In this context, efficient decoupling of the emitter from the metallic substrate through the thin NaCl spacer layer is crucial for facilitating the observation of the coherent dipole–dipole coupling.

Guided by the knowledge gained from studying the dimer, and inspired by the prospect that superradiant modes might enable us to engineer bright, ‘single-molecule’ photon sources, we also explore the optical properties of larger entangled systems. Because in-line in-phase dipole coupling (that is, mode 1) should result in a large total dipole and yield strong superradiance, we arrange several molecules in a line to create oligomer architectures containing up to four molecules. This is illustrated in Fig. 4a, which also shows experimental and simulated photon imaging patterns for an isolated monomer and for the in-line in-phase superradiant mode of the dimer, trimer and tetramer. The STML spectra acquired in each system at the brightest spot (that marked with an ‘ $\times$ ’ in Fig. 4a) are compared in Fig. 4b, which shows that the emission intensities increase as the number of component monomers increases. This finding is expected for an increase in total dipole moment, which is theoretically predicted when increasing the number of monomers. The  $\sigma$ -type anti-bonding-like patterns seen in the photon images of the trimer and tetramer, together with the further redshifted peaks due to stronger excitonic coupling, suggest that coherence is well maintained in these multi-molecule systems. The emission enhancement ratio ( $R$ ) is expected to equal the number of monomers ( $N$ ) in the coupled oligomer<sup>30</sup>, but we find that our data deviate from this linear relation for the largest oligomer studied (that is,  $N > 3$ ). Although this effect, which might be due to the limited spatial extension of confined NCP fields under the tip and increased non-radiative decay, requires further study, the findings we report here clearly demonstrate that it is possible to visualize excitonic coupling in real space with sub-nanometre resolution. This capability will enable new opportunities for studying intermolecular interaction at the level of individual molecules.

**Online Content** Methods, along with any additional Extended Data display items and Source Data, are available in the online version of the paper; references unique to these sections appear only in the online paper.

**Received 28 August 2015; accepted 11 February 2016.**

- Scholes, G. D. & Rumbles, G. Excitons in nanoscale systems. *Nature Mater.* **5**, 683–696 (2006).
- Hettich, C. *et al.* Nanometer resolution and coherent optical dipole coupling of two individual molecules. *Science* **298**, 385–389 (2002).
- Würthner, F., Kaiser, T. E. & Saha-Möller, C. R. J-aggregates: from serendipitous discovery to supramolecular engineering of functional dye materials. *Angew. Chem. Int. Ed.* **50**, 3376–3410 (2011).
- Engel, G. S. *et al.* Evidence for wavelike energy transfer through quantum coherence in photosynthetic systems. *Nature* **446**, 782–786 (2007).
- Lippitz, M. *et al.* Coherent electronic coupling versus localization in individual molecular dimers. *Phys. Rev. Lett.* **92**, 103001 (2004).
- Unold, T., Mueller, K., Lienau, C., Elsaesser, T. & Wiek, A. D. Optical control of excitons in a pair of quantum dots coupled by the dipole-dipole interaction. *Phys. Rev. Lett.* **94**, 137404 (2005).
- Hildner, R., Brinks, D., Nieder, J. B., Cogdell, R. J. & van Hulst, N. F. Quantum coherent energy transfer over varying pathways in single light-harvesting complexes. *Science* **340**, 1448–1451 (2013).
- Diehl, F. P. *et al.* Emergence of coherence through variation of intermolecular distances in a series of molecular dimers. *J. Phys. Chem. Lett.* **5**, 262–269 (2014).
- Halpin, A. *et al.* Two-dimensional spectroscopy of a molecular dimer unveils the effects of vibronic coupling on exciton coherences. *Nature Chem.* **6**, 196–201 (2014).
- Kasha, M., Rawls, H. & Ashraf El-Bayoumi, M. The exciton model in molecular spectroscopy. *Pure Appl. Chem.* **11**, 371–392 (1965).
- Tretiak, S., Zhang, W. M., Chernyak, V. & Mukamel, S. Excitonic couplings and electronic coherence in bridged naphthalene dimers. *Proc. Natl Acad. Sci. USA* **96**, 13003–13008 (1999).
- Berndt, R. *et al.* Photon-emission at molecular resolution induced by a scanning tunneling microscope. *Science* **262**, 1425–1427 (1993).
- Chen, C., Bobisch, C. A. & Ho, W. Visualization of Fermi’s golden rule through imaging of light emission from atomic silver chains. *Science* **325**, 981–985 (2009).
- Chen, C., Chu, P., Bobisch, C. A., Mills, D. L. & Ho, W. Viewing the interior of a single molecule: vibronically resolved photon imaging at submolecular resolution. *Phys. Rev. Lett.* **105**, 217402 (2010).
- Qiu, X. H., Nazin, G. V. & Ho, W. Vibrationally resolved fluorescence excited with submolecular precision. *Science* **299**, 542–546 (2003).
- Dong, Z. C. *et al.* Vibrationally resolved fluorescence from organic molecules near metal surfaces in a scanning tunneling microscope. *Phys. Rev. Lett.* **92**, 086801 (2004).

17. Čavar, E. *et al.* Fluorescence and phosphorescence from individual C<sub>60</sub> molecules excited by local electron tunneling. *Phys. Rev. Lett.* **95**, 196102 (2005).
18. Kabakchiev, A., Kuhnke, K., Lutz, T. & Kern, K. Electroluminescence from individual pentacene nanocrystals. *ChemPhysChem* **11**, 3412–3416 (2010).
19. Lee, J., Perdue, S. M., Rodriguez Perez, A. & Apkarian, V. A. Vibronic motion with joint angstrom–femtosecond resolution observed through fano progressions recorded within one molecule. *ACS Nano* **8**, 54–63 (2014).
20. Reecht, G. *et al.* Electroluminescence of a polythiophene molecular wire suspended between a metallic surface and the tip of a scanning tunneling microscope. *Phys. Rev. Lett.* **112**, 047403 (2014).
21. Merino, P., Große, C., Roslowska, A., Kuhnke, K. & Kern, K. Exciton dynamics of C<sub>60</sub>-based single-photon emitters explored by Hanbury Brown–Twiss scanning tunnelling microscopy. *Nature Commun.* **6**, 8461 (2015).
22. Dong, Z. C. *et al.* Generation of molecular hot electroluminescence by resonant nanocavity plasmons. *Nature Photon.* **4**, 50–54 (2010).
23. Rossel, F., Pivetta, M. & Schneider, W.-D. Luminescence experiments on supported molecules with the scanning tunneling microscope. *Surf. Sci. Rep.* **65**, 129–144 (2010).
24. Ploigt, H.-C., Brun, C., Pivetta, M., Patthey, F. & Schneider, W.-D. Local work function changes determined by field emission resonances: NaCl/Ag(100). *Phys. Rev. B* **76**, 195404 (2007).
25. Murray, C. *et al.* Visible luminescence spectroscopy of free-base and zinc phthalocyanines isolated in cryogenic matrices. *Phys. Chem. Chem. Phys.* **13**, 17543–17554 (2011).
26. Vlaming, S. M. & Eisfeld, A. Tunable superradiance in porphyrin chains on insulating surfaces. *J. Phys. D* **47**, 305301 (2014).
27. Lanzani, G. *The Photophysics behind Photovoltaics and Photonics* Ch. 3 (John Wiley & Sons, 2012).
28. Krishna, V. & Tully, J. C. Vibrational lifetimes of molecular adsorbates on metal surfaces. *J. Chem. Phys.* **125**, 054706 (2006).
29. Kasha, M. Energy transfer mechanisms and the molecular exciton model for molecular aggregates. *Radiat. Res.* **20**, 55–70 (1963).
30. Scully, M. O. & Svidzinsky, A. A. The super of superradiance. *Science* **325**, 1510–1511 (2009).

**Acknowledgements** We thank B. Wang for discussions. This work is supported by the National Basic Research Program of China, the Strategic Priority Research Program of the Chinese Academy of Sciences, the Natural Science Foundation of China, the Fundamental Research Funds for the Central Universities and Hefei Science Center of the Chinese Academy of Sciences.

**Author Contributions** Z.-C.D. and J.G.H. supervised the project. Yang Z., Yang L., Yao Z., Y.-J.Y., Y.-M.K., L.Z. and Q.-S.M. performed the experiments and analysed the data. Yang Z., Yang L., Yao Z., Yi L., J.-L.Y., Z.-C.D. and J.G.H. contributed to the interpretation of the data and theoretical simulations. Yang Z., Yi L., Z.-C.D. and J.G.H. co-wrote the manuscript. All authors discussed the results and commented on the manuscript.

**Author Information** Reprints and permissions information is available at [www.nature.com/reprints](http://www.nature.com/reprints). The authors declare no competing financial interests. Readers are welcome to comment on the online version of the paper. Correspondence and requests for materials should be addressed to Z.-C.D. ([zcdong@ustc.edu.cn](mailto:zcdong@ustc.edu.cn)) or J.G.H. ([jghou@ustc.edu.cn](mailto:jghou@ustc.edu.cn)).



## METHODS

**Experimental section.** Our experiments were performed with a custom low-temperature ultrahigh-vacuum STM (Unisoku) combined with optical detection systems at about 8 K under a base pressure of about  $1 \times 10^{-10}$  Torr. ZnPc molecules were thermally evaporated onto the Ag(100) substrate partially covered by NaCl islands<sup>24</sup> at about 8 K (Ag(100) was previously cleaned by argon ion sputtering and annealing). Electrochemically etched silver (Ag) tips used in all our experiments were cleaned by electron-bombarding and argon-ion sputtering, followed by further modification through voltage pulses to achieve the desired NCP modes. STM imaging and spectral measurements were taken in a constant-current mode with the sample biased. Spatially resolved spectroscopic imaging over molecular structures was carried out with each pixel recording a spectrum that provides energy-resolved optical transition probabilities<sup>31,32</sup>. The photon collection and detection systems are detailed in Extended Data Fig. 1.  $dI/dV$  spectra and  $dI/dV$  mapping were measured using a lock-in technique.

Because STM is known to have versatile manipulation abilities<sup>33–35</sup>, here the ZnPc molecular manipulation was realized via pushing by positioning the tip over the edge of a ZnPc lobe and decreasing the tip–molecule distance (for example, approaching 200 pm) at a positive bias of +2.5 V (Extended Data Fig. 4). The bias-dependent feature of the STM images from –1.7 V to –2.5 V is detailed in Extended Data Fig. 5.

Spatially and spectrally resolved photon images were obtained by recording a spectrum at each pixel and assigning to each pixel the integrated emission intensities over a certain wavelength range. The thermal drift issue should be considered for spectroscopic imaging experiments when the total acquisition time is long. The thermal drift of our current system at about 8 K is 0.1–0.2 nm h<sup>–1</sup>. For the STM imaging with acquisition times of around 10–20 min, such drift can be neglected. However, for the spectroscopic imaging experiments, the total acquisition time could be as long as 1.5 h and the total drift value would be 0.15–0.3 nm, which is relatively large compared with the size of an individual ZnPc molecule. Therefore, to precisely correlate the emission feature with the molecular structure, we corrected the image distortion caused by the thermal drifts for all the photon imaging patterns given in the main text, as detailed in the following. When we acquired an energy-resolved spectroscopic image, a reference STM image for the same molecule was acquired simultaneously. The resultant, slightly deformed STM image was adjusted to match with the molecular features in an almost drift-free STM image for the same area that was acquired at a normal scanning speed (about 10 min per frame). The same adjustment parameters are applied to the corresponding photon imaging pattern.

**Energy-level alignment and carrier-injection excitation.** At –2.5 V (the voltage used for most of our experiments), the single-molecule electroluminescence is generated by the carrier-injection excitation in a double-barrier tunnelling junction. As shown in Extended Data Fig. 2, molecular electroluminescence increases as excitation bias increases from –1.8 V to –2.5 V in amplitude, in particular when the voltage approaches about –2.2 V, at which the highest occupied molecular orbital (HOMO) is aligned with the Fermi level of the tip (such that holes can be directly injected into the HOMO), as discussed below.

The energy-level alignments are deduced according to previously documented methods<sup>20,36,37</sup>. The photon energy emitted from a single ZnPc is determined by the energy difference between the excited and ground states of the molecule, which is less than or equal to the HOMO–LUMO gap of the molecule (LUMO, lowest unoccupied molecular orbital). For the sake of simplicity, we assume that the HOMO–LUMO gap at zero bias ( $V_b = 0$ ) is approximately equal to the optical gap associated with the (0,0) emission band at approximately 653 nm (about 1.9 eV), with the energy of the HOMO state represented by  $E_H$  and that of the LUMO state by  $E_L$ . By denoting the voltage drop repartition across the vacuum barrier as  $\alpha$ , and referring to the onset voltages for the emergence of the HOMO and LUMO states in the  $dI/dV$  spectra, we have  $E_L - E_H = 1.9$ ,  $E_L = 0.6\alpha$  and  $E_H = -2.2\alpha$ . From these relations we deduce  $\alpha = 0.68$ ,  $E_H = -1.5$  eV and  $E_L = 0.4$  eV with respect to the Fermi level ( $E_0 = 0$ ) at  $V_b = 0$  V. The energy-level alignments for  $V_b = -2.2$  V and  $V_b = +4.7$  V can also be deduced accordingly. That is why the emission intensity is evidently increased at about –2.2 V—the HOMO is now aligned with the Fermi level of the tip (and so holes can be directly injected into the HOMO). When a ZnPc molecule is excited at –2.5 V (the voltage used for most of our experiments), the excitation model based on the carrier injection is valid in terms of energy-level alignment. The LUMO and HOMO states fall inside the energy window between the Fermi levels of the tip and substrate. Thus, the electrons can be injected to the LUMO from the substrate while the electrons in the HOMO can tunnel out to the tip, generating holes in the HOMO. Then, the molecule-specific emission occurs through the recombination of the electron in the LUMO and the hole in the HOMO when the molecular excited state (exciton) decays back to the ground state.

When a ZnPc molecule is excited at positive bias such as +2.5 V, the molecular electroluminescence becomes very weak. The injection excitation mechanism would become a dominant process only for positive biases raised above +4.7 V,

at which both the LUMO and HOMO fall inside the energy window between the Fermi levels of the tip and substrate, as shown in Extended Data Fig. 2e. At such high voltages, the molecule can easily be moved or even damaged, making the measurements impossible.

**Spectral evolution with varied intermolecular distances.** In the experiments, the NaCl surface is not perfectly flat and the ZnPc is believed to move in a discontinuous manner by hopping between the surface lattice sites. The minimum displacement for manipulation is found to be about 0.4 nm, which is very close to the lattice constant of the NaCl surface<sup>38</sup>. This makes it impossible to achieve continuous spectral evolution with varied intermolecular distances. We therefore acquired spectra at only a few representative intermolecular distances ( $r$ , centre-to-centre distance), as shown in Extended Data Fig. 4.

When  $r \geq 4.0$  nm, no spectral changes in emission peaks are observed for the ZnPc lobes at the spectral-resolution limit of our current instruments (0.7 meV). When  $r$  was decreased to about 2.8 nm, some small spectral changes were observed (see STML spectrum on M2), which suggests the presence of some intermolecular coupling. When  $r$  was further decreased to about 2 nm, the emission peaks shifted or split and five emission modes were observed in STML spectra acquired at representative sites, as shown in Extended Data Fig. 4c. In this case, the measured emission-peak energies for modes 1 and 5 are approximately 1.893 eV and 1.912 eV, respectively, giving rise to a smaller exciton coupling strength  $|J|$  of about 9.5 meV for the in-line coupling, as expected. However, it is hard to precisely deduce  $J$  for parallel coupling, because the mode-2, mode-3 and mode-4 emission peaks are heavily mixed together.

**Assignment of the emission peak at about 1.870 eV for the ZnPc dimer.** The emission peak at approximately 1.870 eV (about 663 nm) for the dimer (mode 1' in Extended Data Fig. 6b) originated from the in-line in-phase coupling of transition dipoles associated with the shoulder peak at approximately 1.882 eV (659 nm) for an isolated ZnPc monomer (Extended Data Fig. 6a). The latter peak is related to the vibronic structure of the Q band with relatively large Franck–Condon contribution<sup>39,40</sup>. This assignment for the emission peak at approximately 1.870 eV for the ZnPc dimer is supported by two facts: (1) the photon imaging pattern of the peak (at approximately 1.870 eV) shown in Extended Data Fig. 6c is very similar to the  $\sigma$ -type anti-bonding-like feature of the imaging pattern for mode 1 in Fig. 3b; and (2) mode 1' is redshifted by about 17 meV with respect to mode 1, which is about the same as the redshift between the shoulder peak and the dominant Q(0,0) peak.

The emission intensity of mode 1' is much weaker than that of mode 1, although mode 1' is believed to be the strongest emission mode over all the modes that originate from the dipole–dipole coupling associated with the shoulder peak. If we assume that the ratio of the emission intensity between mode 2' (3', 4', 5') and mode 1' is the same as that between mode 2 (3, 4, 5) and mode 1, then the intensity of mode 2' (3', 4', 5') will be much weaker than that of mode 2 (3, 4, 5), making their emission features buried in the spectral background of modes 1–5.

Therefore, the dipole coupling associated with the shoulder peak at approximately 1.882 eV will not affect the spectral features from 1.88 eV to 1.93 eV for various modes of the dimer that are attributed to the contribution from the dominant Q-band emission peak (at about 1.899 eV).

The weak high-energy shoulder around 1.91 eV for the ZnPc monomer might be related to the rotation of ZnPc under the excitation. However, such a rotation is blocked for the dimer (as shown in Extended Data Fig. 5) and for oligomers, and so the high-energy shoulder in the monomer no longer exists.

**The roles of excitation and emission processes on the photon images.** The photon image is spectrally reconstructed from the photon-yield signal at each pixel, which is related to both the local excitation efficiency and the optical transition probability between two different electronic states. The excitation efficiency depends on the local electronic density of states under the carrier-injection excitation model, whereas the optical transition probability is decided by the emission process associated with molecular transition-dipole arrangements and their couplings.

In ref. 14, the important influence of the emission process on the pattern of photon images is demonstrated for a single molecule. More appealing evidence for the dominant role of the emission process in the photon image for each mode is found in our experiments for molecular dimers (or oligomers) involving more-than-one-transition dipoles and all their possible arrangements. As illustrated in Fig. 3b, different photon images are obtained for different emission modes, despite excitation under the same bias of –2.5 V (that is, the same distribution of local electronic density of states). Moreover, the mode-1 emission patterns of the trimer and tetramer in Fig. 4 are different to the corresponding  $dI/dV$  mappings shown in Extended Data Fig. 9.

The major feature of the photon image for each mode is similar to the theoretically simulated photon image in Fig. 3b that is based on emission processes alone (a similar theoretical treatment to that proposed in ref. 14), which further suggests that the major feature of the photon image for each mode is determined

by the emission process associated with molecular transition-dipole arrangements and their couplings.

**Photon images acquired in constant-height and constant-current mode.** The trajectory of the tip is known to affect the intra-molecularly resolved conductance images measured with a closed feedback loop (that is, constant-current mode) (see, for example, ref. 41). We examined the effect of such variation of tip-sample distance on the photon images. As shown in Extended Data Fig. 10, a special spectroscopic image with an open feedback loop (that is, constant-height mode) was collected. The resultant photon images for different modes were normalized by the tunnelling current pixel by pixel. The features of the normalized photon images acquired with an open feedback loop are almost the same as those acquired with a closed feedback loop. These results indicate that, in the spectroscopic imaging measurements with a closed feedback loop, the variations in tip-sample distance caused by the fluctuations of the molecular topography will not affect the major features of photon images.

**Theoretical simulation of real-space STML mapping.** For a single ZnPc molecule, the transition-dipole moment corresponding to the HOMO–LUMO transition, described by the transition density  $\langle\psi_g|\psi_e\rangle$  (refs 42, 43) is calculated to be about 10.6 Debye (about 0.22  $e\cdot\text{nm}$ ) using density functional theory (DFT)<sup>44</sup>. To capture the physical essence and fit with the experimental patterns, we simplify the transition dipole of a single molecule to a pair of opposite point charges (each containing one electron charge) separated by 0.22 nm, as shown in Extended Data Fig. 7a. The centres of the charge pairs are placed in the centres of the ZnPc monomers. The distance between the centres of charge pairs in the dimer are chosen to be 1.45 nm, which is the centre-to-centre distance between two component ZnPc monomers measured in STM images.

The best agreement between experimental photon imaging patterns and simulated patterns is achieved when the transition-dipole orientations of ZnPc molecules in the dimer are chosen to be parallel or perpendicular to the dimer axial direction (centre-to-centre), as illustrated in Fig. 3 and Extended Data Fig. 7b. This orientation modification is probably associated with the symmetry breakdown from  $D_{4h}$  for the monomer to  $C_{2h}$  for the dimer.

A simple image-charge method was used to simulate real-space STML mapping. The introduction of a metallic plasmonic tip induces image charges on both the tip and the substrate, which produces local enhancement in the near field and generates enhanced fluorescence signals in the far field in the emission process. Different tip positions give rise to different enhancement factors, which leads to the tip-position-dependent photon yield. Different modes have different charge distributions owing to different transition dipoles. For a given tip position, the local enhancement produced by the tip will be different for different modes. Overall, the tip position is important for enhancing the optical contrast of photon images through site- and mode-selective enhancement by image charges.

The model used in the simulation of photon images is similar to the one proposed in ref. 14. Here we simplify the STM tip–substrate structure as a combined sphere–plane system. Considering the sphere and the plane as perfect conductors, the images  $Q'$  of a certain charge  $Q$  for these two surfaces are

$$Q' = -Q \quad \text{and} \quad Q' = -\frac{R_0}{r}Q$$

for the plane and sphere, respectively; the position vectors of the image charges for the first reflection are

$$\mathbf{r}_1^p = (x, y, -z) \quad \text{and} \quad \mathbf{r}_1^s = \frac{R_0^2}{r^2}\mathbf{r}$$

for the plane ('p' superscript) and sphere ('s' superscript), respectively, in which  $R_0$  is the radius of the sphere and  $\mathbf{r}$  is the position vector from the centre of the sphere to the charge, as illustrated in Extended Data Fig. 7c, d.

The reflections between two surfaces will result in a series of image charges, and the total dipole moment  $\mathbf{p}_{\text{tot}}$  of a charge  $Q$  positioned in the gap is

$$\begin{aligned} \mathbf{p}_{\text{tot}}(Q) = & Q\mathbf{r}_0 + \left[(-1)Q\mathbf{r}_1^p + (-1)\frac{R_0}{r_1^s}Q\mathbf{r}_1^s\right] + \left[(-1)^2\frac{R_0}{r_1^s}Q\mathbf{r}_2^p + (-1)^2\frac{R_0}{r_2^s}Q\mathbf{r}_2^s\right] + \dots \\ = & Q\left\{\mathbf{r}_0 + \left[(-1)\mathbf{r}_1^p + (-1)\frac{R_0}{r_1^s}\mathbf{r}_1^s\right] \right. \\ & + \sum_{n=1}^{N_r/2} \left[(-1)^{2n}\mathbf{r}_{2n}^p \prod_{m=1}^n \left(\frac{R_0}{r_{2m-1}^s}\right) + (-1)^{2n}\mathbf{r}_{2n}^s \prod_{m=1}^n \left(\frac{R_0}{r_{2m}^p}\right)\right] \\ & \left. + \sum_{n=1}^{N_r/2-1} \left[(-1)^{2n+1}\mathbf{r}_{2n+1}^p \prod_{m=1}^n \left(\frac{R_0}{r_{2m}^s}\right) + (-1)^{2n+1}\mathbf{r}_{2n+1}^s \prod_{m=0}^n \left(\frac{R_0}{r_{2m+1}^p}\right)\right]\right\} \end{aligned}$$

in which  $N_r$  is the total number of reflections and is chosen to be an even number because of the presence of two surfaces (substrate plane and tip surface). In our calculation, we use  $N_r = 300$  to ensure convergence.

By summing up all the total dipole moments of the charges corresponding to the transition dipoles in the molecular architectures, we obtain the total dipole moment of the whole system:  $\mathbf{P}_{\text{tot}} = \sum_i \mathbf{P}_{\text{tot}}(Q_i)$ .

The differential radiation power in the far field per solid angle  $\frac{dP_{\text{rad}}}{d\Omega}$  is calculated<sup>45</sup> using

$$\frac{dP_{\text{rad}}}{d\Omega} = \frac{\omega^4}{32\pi^2\epsilon_0 c^3} |\mathbf{P}_{\text{tot}}|^2 \sin^2(\theta)$$

in which  $\theta$  is the optical detection angle ( $\theta = 60^\circ$  with respect to the STM tip axis in our system),  $\omega$  is the radiation frequency of the dipole and  $c$  is the speed of light. By changing the positions of the tip (sphere), we can obtain the real-space distribution of radiation intensity for different distributions of point charges, corresponding to different dipole–dipole configurations. The parameters for simulation are as follows: the radius of the sphere is 1 nm; the distance between the molecular plane and the end of the sphere is 0.8 nm; and the distance between the molecular plane and the substrate is 0.5 nm, according to the thickness of three-monolayer NaCl. The frame size of simulated patterns for a dimer is 6.25 nm  $\times$  5 nm.

Reasonable agreement was achieved between the simulated patterns and experimental images for dimer and oligomer systems, in terms of the numbers and positions of emission maxima and nodes, especially for the two strongest emission modes (modes 1 and 2). This consistency suggests that the simple dipole model used here could provide valuable information on the coherent excitonic coupling features in coupled molecular systems.

By contrast, the agreement for the photon imaging patterns of modes 3 and 4 is relatively poor. To reproduce the details of the photon imaging patterns for all coupling modes, and precisely calculate the energy differences, more sophisticated theoretical calculations are needed to thoroughly understand the excitation process, the excited states of the coupled molecule systems on dielectric surfaces, and the radiative transitions that originated from delocalized excitons.

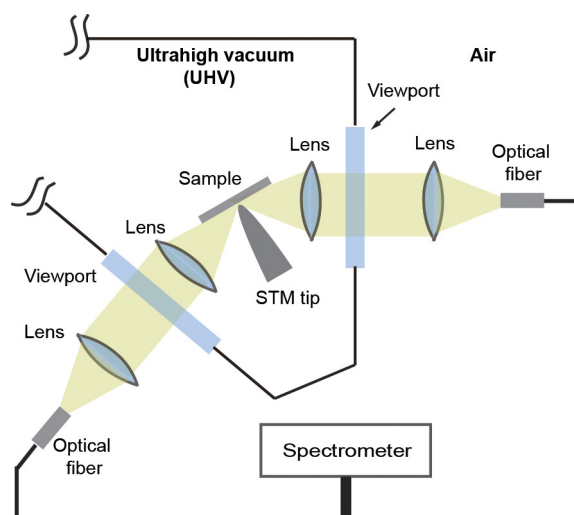
**Measured exciton coupling strength and oscillation frequency.** According to equation (2) and Fig. 3c, d, the coupling strength  $|J|$  and energy shifts  $\Delta W$  presented in Extended Data Table 1 can be determined from the peak positions of different emission modes. The oscillation frequency  $\Omega$  in the entangled dimer system is calculated via  $\Omega = 2|J|/\hbar$  (ref. 27). The coupling strengths for in-line and parallel coupling types are obtained from the following peak values for different emission modes of a ZnPc dimer: 1,887.4  $\pm$  0.3 meV (mode 1), 1,896.0  $\pm$  0.3 meV (mode 2), 1,898.9  $\pm$  0.3 meV (mode 3), 1,912.4  $\pm$  0.3 meV (mode 4), and 1,921.9  $\pm$  0.3 meV (mode 5). The peak energy for a ZnPc monomer is 1,899.2  $\pm$  0.6 meV. These peak energy values for the dimer are obtained from statistical analyses over eight data sets acquired with the same tip under the same NCP resonance condition. The STML spectra used for these analyses were acquired over the strongest emission site for each mode with a spectral resolution of about 0.2 nm (0.7 meV; calibrated by the 546 nm Hg line) using a grating of 1,200 grooves per mm and a slit width of 25  $\mu\text{m}$ .

The experimentally determined coupling strength  $|J|$  for the in-line dipole coupling (approximately 17.3 meV) was found to be nearly twice of that for the parallel coupling (approximately 8.2 meV), as predicted by the theoretical model given in equation (4). This consistency, together with the reasonable agreement between the experimental photon imaging patterns and the simulated ones, suggests that the dipole–dipole coupling captures the essence of the excitonic coupling in coupled molecular systems.

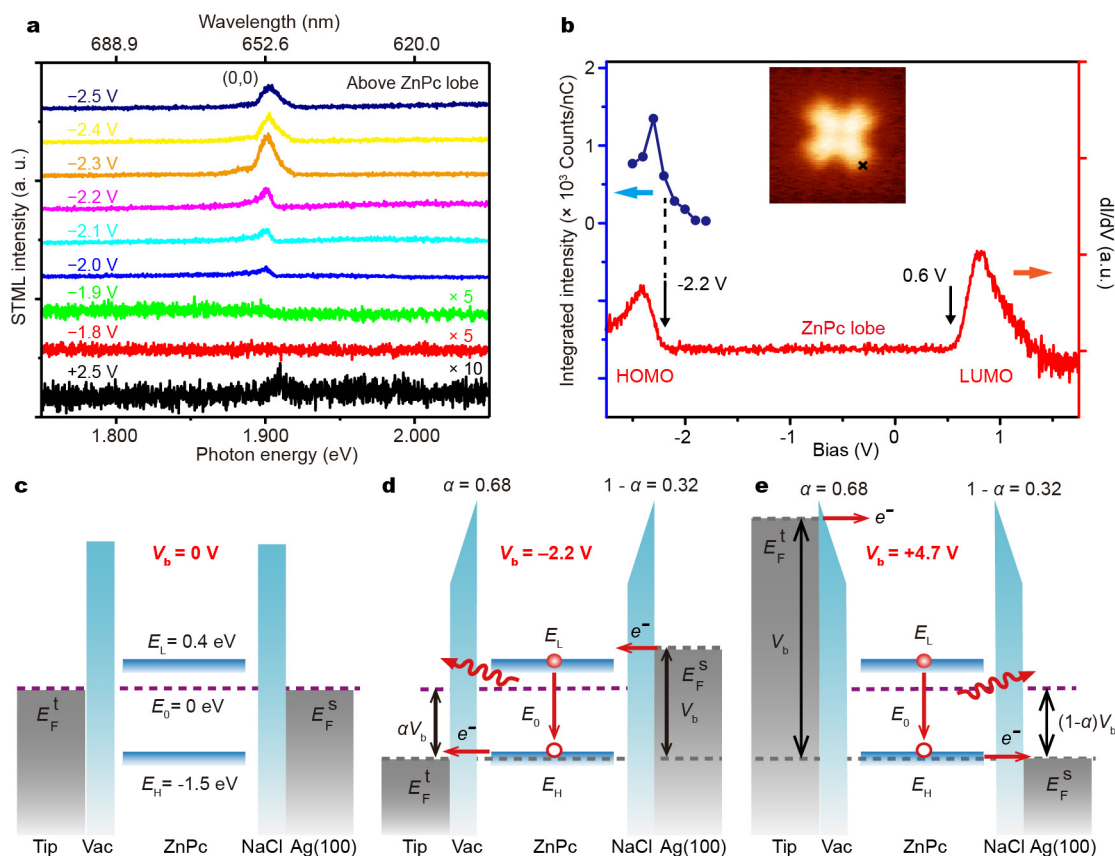
- Hoffmann, G., Libioulle, L. & Berndt, R. Tunneling-induced luminescence from adsorbed organic molecules with submolecular lateral resolution. *Phys. Rev. B* **65**, 212107 (2002).
- Zhang, C., Chen, L. G., Zhang, R. & Dong, Z. C. Scanning tunneling microscope based nanoscale optical imaging of molecules on surfaces. *Jpn. J. Appl. Phys.* **54**, 08LA01 (2015).
- Crommie, M. F., Lutz, C. P. & Eigler, D. M. Confinement of electrons to quantum corrals on a metal surface. *Science* **262**, 218–220 (1993).
- Manoharan, H. C., Lutz, C. P. & Eigler, D. M. Quantum mirages formed by coherent projection of electronic structure. *Nature* **403**, 512–515 (2000).
- Zhao, A. D. *et al.* Controlling the Kondo effect of an adsorbed magnetic ion through its chemical bonding. *Science* **309**, 1542–1544 (2005).
- Wu, S. W., Nazin, G. V., Chen, X., Qiu, X. H. & Ho, W. Control of relative tunneling rates in single molecule bipolar electron transport. *Phys. Rev. Lett.* **93**, 236802 (2004).
- Meng, Q. *et al.* Tunneling electron induced molecular electroluminescence from individual porphyrin J-aggregates. *Appl. Phys. Lett.* **107**, 043103 (2015).
- Le Moal, E., Müller, M., Bauer, O. & Sokolowski, M. Misfit driven azimuthal orientation of NaCl domains on Ag(100). *Surf. Sci.* **603**, 2434–2444 (2009).
- Gouterman, M. In *The Porphyrins* Vol. III (ed. Dolphin, D.) Ch. 1, 1–165 (Academic Press, 1978).

40. Minaev, B., Wang, Y.-H., Wang, C.-K., Luo, Y. & Ågren, H. Density functional theory study of vibronic structure of the first absorption  $Q_x$  band in free-base porphyrin. *Spectrochim. Acta A* **65**, 308–323 (2006).
41. Lu, X., Grobis, M., Khoo, K. H., Louie, S. G. & Crommie, M. F. Spatially mapping the spectral density of a single  $C_{60}$  molecule. *Phys. Rev. Lett.* **90**, 096802 (2003).
42. Beenken, W. J. D. & Pullerits, T. Excitonic coupling in polythiophenes: comparison of different calculation methods. *J. Chem. Phys.* **120**, 2490–2495 (2004).
43. Sun, M., Chen, J. & Xu, H. Visualizations of transition dipoles, charge transfer, and electron-hole coherence on electronic state transitions between excited states for two-photon absorption. *J. Chem. Phys.* **128**, 064106 (2008).
44. Zhou, X., Ren, A.-M., Feng, J.-K. & Liu, X.-J. Theoretical studies on the one- and two-photon absorption of tetrabenzoporphyrins and phthalocyanines. *Can. J. Chem.* **82**, 19–26 (2004).
45. Le Ru, E. & Etchegoin, P. *Principles of Surface-Enhanced Raman Spectroscopy and Related Plasmonic Effects* Ch. 2 (Elsevier, 2008).



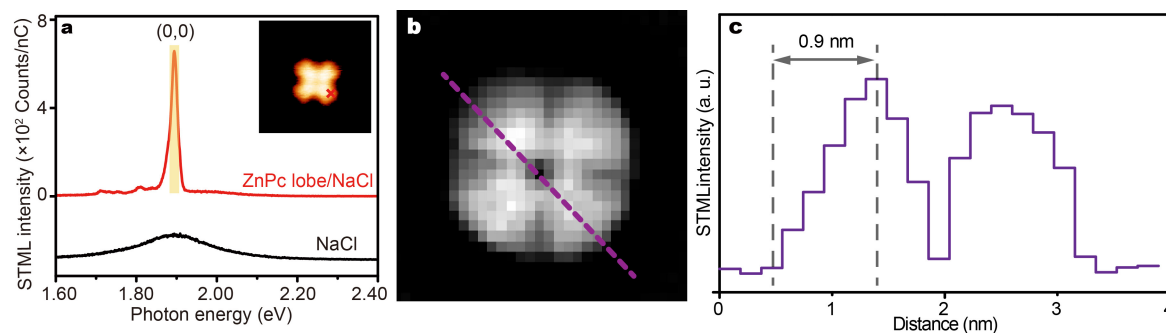


**Extended Data Figure 1 | Schematic of our experimental set-up for a combined system of low-temperature ultrahigh-vacuum STM with optical detections.** The highly localized tunnelling electrons in a STM are used to excite light emission from the STM junction through inelastic tunnelling. This technique is called STM-induced luminescence (STML). In our system, photons emitted from the STM junction were collected by a two-channel double-lens system to increase the collection efficiency. The total hemisphere photon collection efficiency for the two-channel double-lens system is about 20%. The spectra were measured with a liquid-nitrogen-cooled charge-coupled device spectrometer (Princeton Instruments). Different gratings (150 grooves per mm, 600 grooves per mm and 1200 grooves per mm) and slits (100  $\mu\text{m}$  and 25  $\mu\text{m}$ ) were used in spectral measurements for different requirements on wavelength ranges and spectral resolutions. All spectra presented in this paper are not corrected for the wavelength-dependent sensitivity of photon detection systems.



**Extended Data Figure 2 | Excitation mechanism in STML.** **a**, STML spectra acquired above the lobe of a single ZnPc molecule on the NaCl island at different excitation biases, as indicated (10 pA, 60 s). **b**,  $dI/dV$  spectra acquired at the ZnPc lobe (red line) using the lock-in technique. The tunnelling gap was set at -2.5 V and 50 pA. The bias modulation was 20 mV (r.m.s.) at 329 Hz. The molecular emission intensities over a different excitation bias is also plotted as a blue line and filled circles

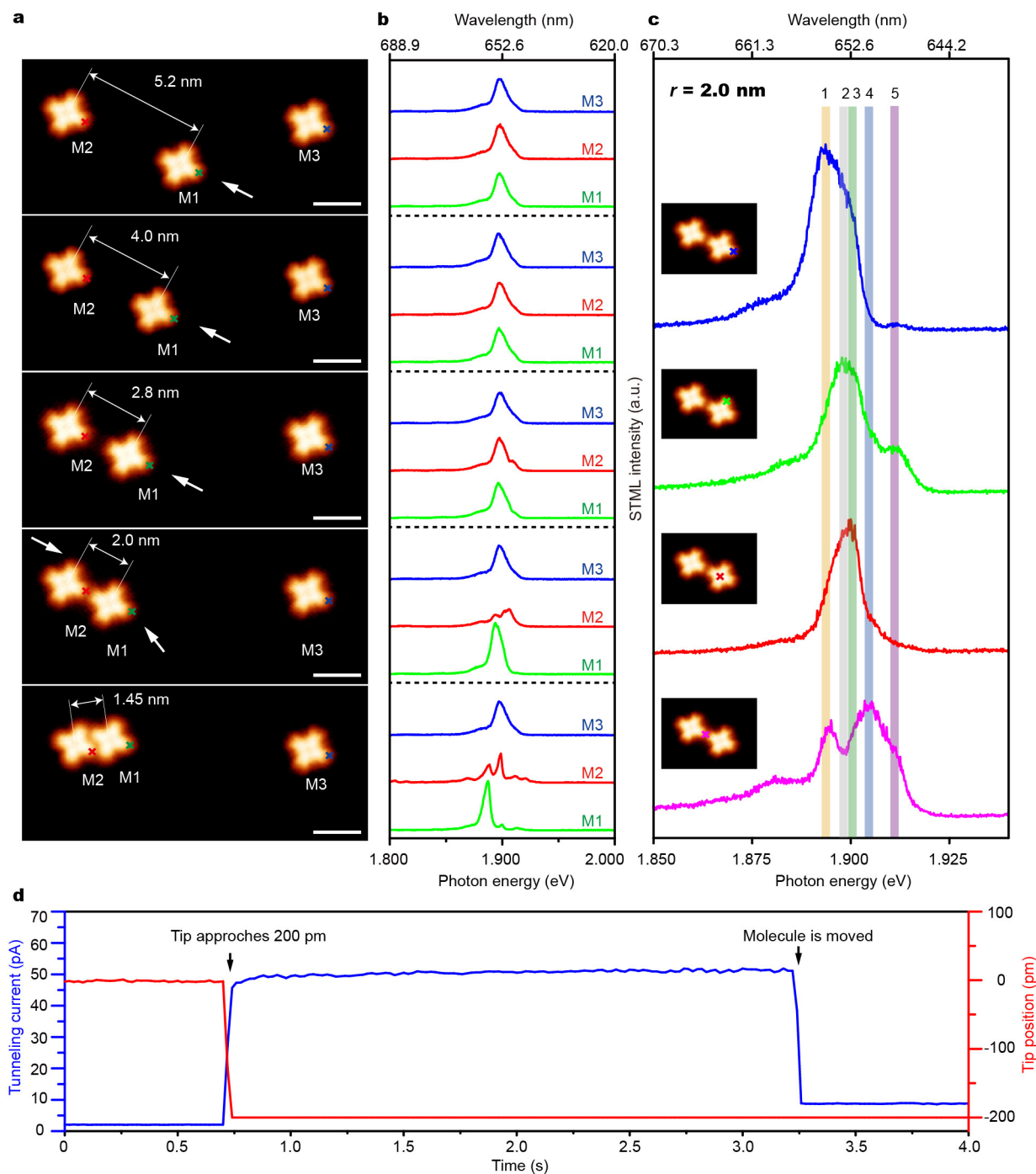
(integrated spectral range: 1.86–1.94 eV). The inset shows an STM image of a ZnPc molecule ( $3 \text{ nm} \times 3 \text{ nm}$ ; -1.7 V, 2 pA) with the 'x' marking the position for both the  $dI/dV$  and STML measurements in **a**. **c–e**, Sketch of a double-barrier junction showing the energy-level alignments of the HOMO and LUMO at different bias voltages:  $V_b = 0$  V (**c**),  $V_b = -2.2$  V (**d**) and  $V_b = +4.7$  V (**e**).  $E_F^{t/s}$ , Fermi energy of the tip/substrate.



**Extended Data Figure 3 | Sub-nanometre spatial resolution of spectroscopic imaging.** **a**, STML spectrum ( $-2.5$  V,  $200$  pA,  $60$  s) acquired at the lobe of an isolated ZnPc monomer on NaCl (top curve, red), indicated by the 'x' in the inset ( $-1.7$  V,  $2$  pA;  $4$  nm  $\times$   $4$  nm). The NCP emission spectrum (bottom curve, black) acquired on the NaCl surface is shown as a reference. **b**, Energy-resolved photon imaging pattern of a single ZnPc molecule on NaCl by integrating the molecule-specific

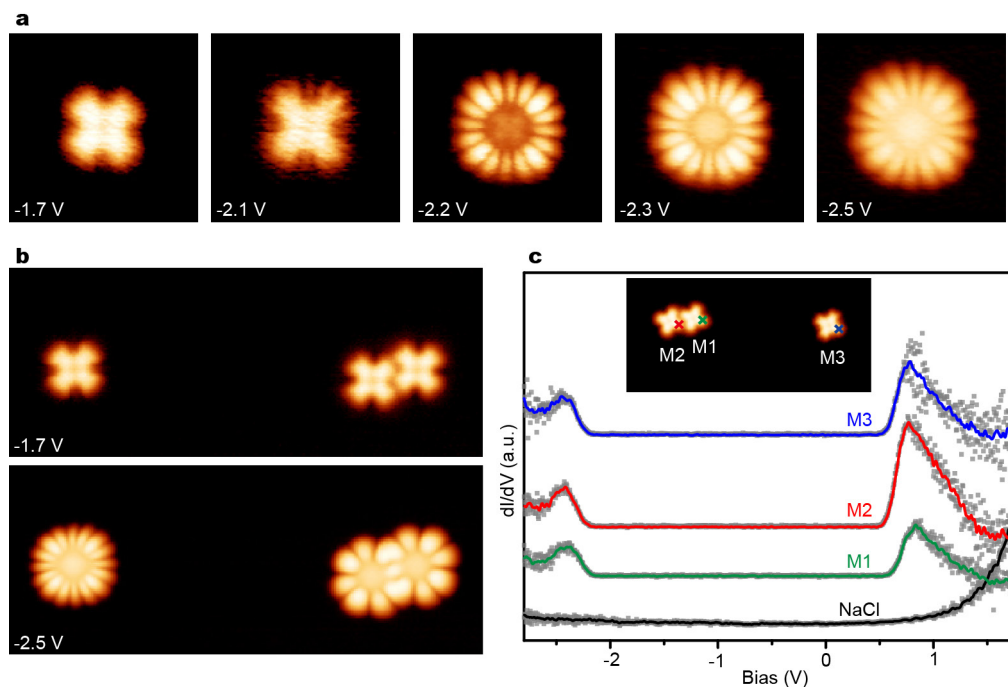
fluorescence signals over the energy range  $1.89$ – $1.91$  eV, indicated by the yellow shading in **a** ( $4$  nm  $\times$   $4$  nm,  $30 \times 28$  pixels;  $-2.5$  V,  $200$  pA,  $5$  s per pixel). **c**, STML intensity profile for the (purple dashed) line trace in **b**. The line-profile analysis has a spatial resolution of less than  $1$  nm (about  $0.7$  nm estimated within a  $10\%$ – $90\%$  contrast), showing the change of contrast from  $0\%$  to  $100\%$  over a distance as short as  $0.9$  nm.





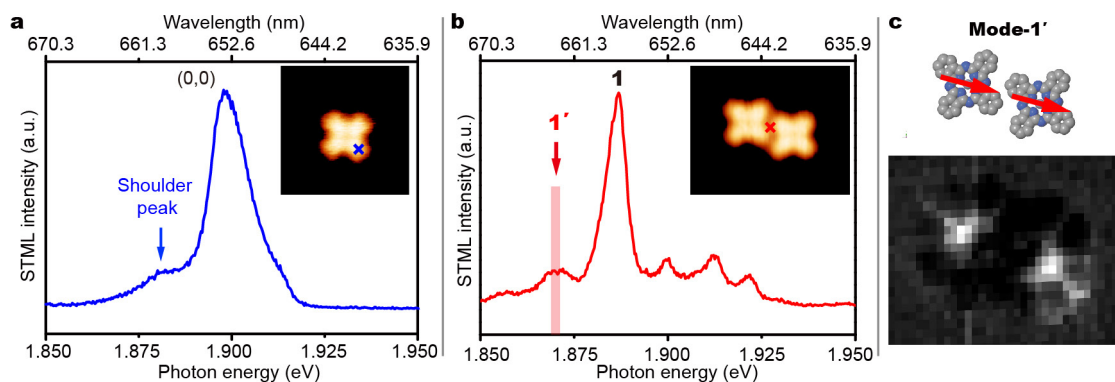
**Extended Data Figure 4 | Spectral evolution with varied intermolecular distances.** **a**, STM images taken during the manipulation process ( $-1.7$  V,  $2$  pA). There are three isolated ZnPc molecules adsorbed on NaCl marked as M1, M2 and M3. M3 is used as a reference molecule. M1 and M2 are pushed together, as indicated by the white arrows for manipulation directions. The intermolecular centre-to-centre distance  $r$  between M1 and M2 is marked. Scale bars,  $2$  nm. **b**, Corresponding electroluminescence spectra ( $-2.5$  V,  $200$  pA,  $60$  s) collected from the lobes of the three ZnPc molecules, as indicated by the 'x's in **a**. **c**, Representative site-dependent

STML spectra ( $-2.5$  V,  $200$  pA,  $60$  s) for  $r = 2.0$  nm acquired at the respective 'x' positions in the insets images ( $4.6$  nm  $\times$   $6$  nm,  $-1.7$  V,  $2$  pA). The shaded regions labelled 1–5 mark the possible peak positions induced by the coherent dipole–dipole interaction. **d**, Typical current–time and tip–position–time curves during the manipulation process. First, we placed the STM tip close to the edge of the lobe of a ZnPc molecule on NaCl. Second, we turned off the feedback and approached the tip to the molecule by about  $200$  pm (set point:  $+2.5$  V,  $2$  pA). In this way, the ZnPc molecule was found to move away from the STM tip.



**Extended Data Figure 5 | Bias-dependent features of STM images and  $dI/dV$  spectra for isolated ZnPc monomers and ZnPc dimers on the NaCl surface.** **a**, STM images of an isolated ZnPc monomer acquired at different biases ( $4\text{ nm} \times 4\text{ nm}$ ;  $2\text{ pA}$ ). The cross-like feature is observed when the bias is set inside the HOMO–LUMO gap (for example,  $-1.7\text{ V}$ ), revealing the characteristics of the molecular skeleton. The rotating behaviour of an isolated ZnPc monomer is evident at about  $-2.2\text{ V}$ , giving rise to a 16-lobe-like pattern instead of the 8-lobe-like pattern associated with the HOMO state for a immobilized ZnPc. **b**, STM images of an isolated ZnPc monomer and a ZnPc dimer at different biases ( $15\text{ nm} \times 6\text{ nm}$ ;  $2\text{ pA}$ ). The rotation of ZnPc is blocked when in contact with another ZnPc owing to the steric hindrance, as indicated by the appearance of an 8-lobe-like

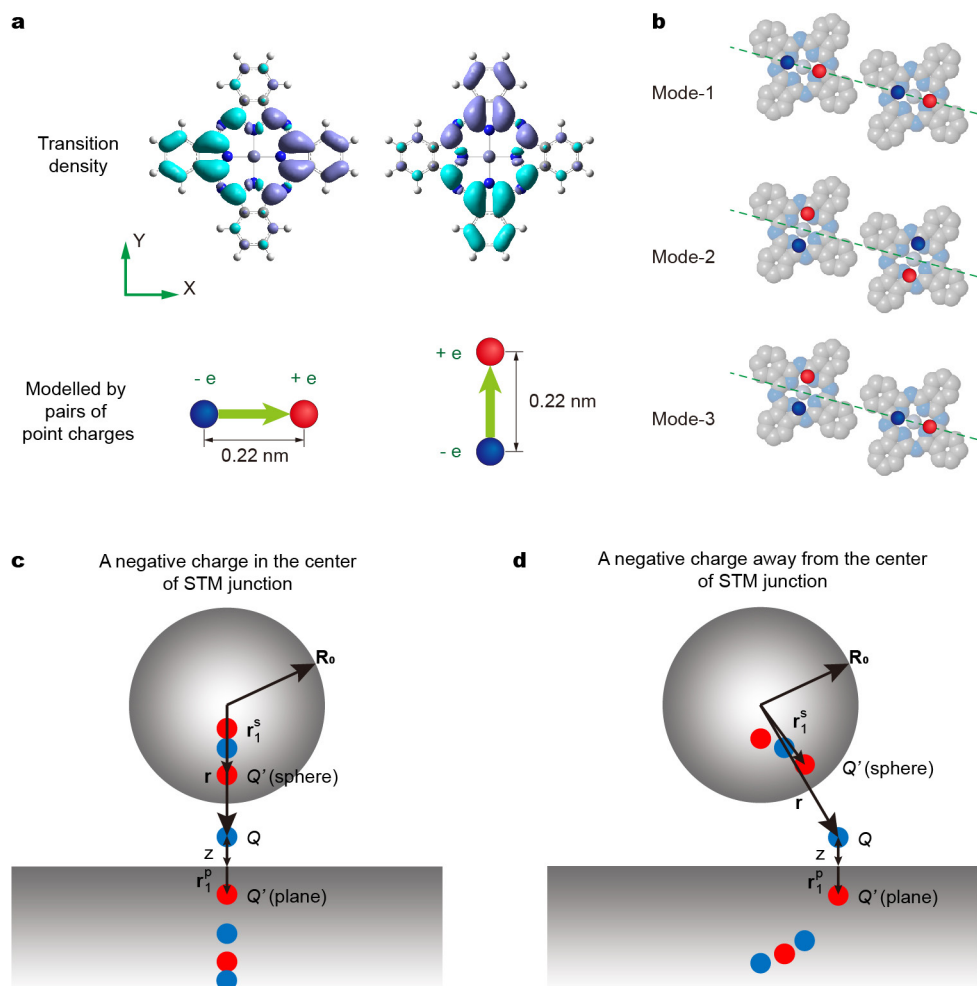
pattern of the component ZnPc monomer in the dimer. **c**,  $dI/dV$  spectra were acquired at the ZnPc lobes of M1, M2 and M3, as indicated in the inset ( $15\text{ nm} \times 7\text{ nm}$ ,  $-1.7\text{ V}$ ,  $2\text{ pA}$ ). The  $dI/dV$  spectrum on the bare NaCl surface is also shown as a reference. The smoothed  $dI/dV$  curves are presented in colour; the raw data are represented as grey squares. The  $dI/dV$  signals were measured using the lock-in technique. The tunnelling gap was set at  $-2.5\text{ V}$  and  $20\text{ pA}$ . The bias modulation was  $20\text{ mV}$  (r.m.s.) at  $329\text{ Hz}$ . The  $dI/dV$  spectra are offset for clarity. No noticeable difference in peak positions was observed between the  $dI/dV$  curves acquired from both the isolated ZnPc monomer and the ZnPc dimer. However, the STML spectral features from the dimer are markedly different to those of an isolated ZnPc monomer (Fig. 2).



**Extended Data Figure 6 | Origin of the emission peak at about 1.870 eV from the ZnPc dimer.** **a**, STML spectrum ( $-2.5$  V, 200 pA, 60 s) acquired at a lobe of the isolated ZnPc molecule, as indicated in the inset ( $4$  nm  $\times$   $4$  nm;  $-1.7$  V, 2 pA), showing the Q-band emission containing a shoulder peak at  $1.882$  eV (about  $659$  nm). **b**, STML spectrum ( $-2.5$  V, 200 pA, 60 s) acquired at the centre of the ZnPc dimer, as indicated in the

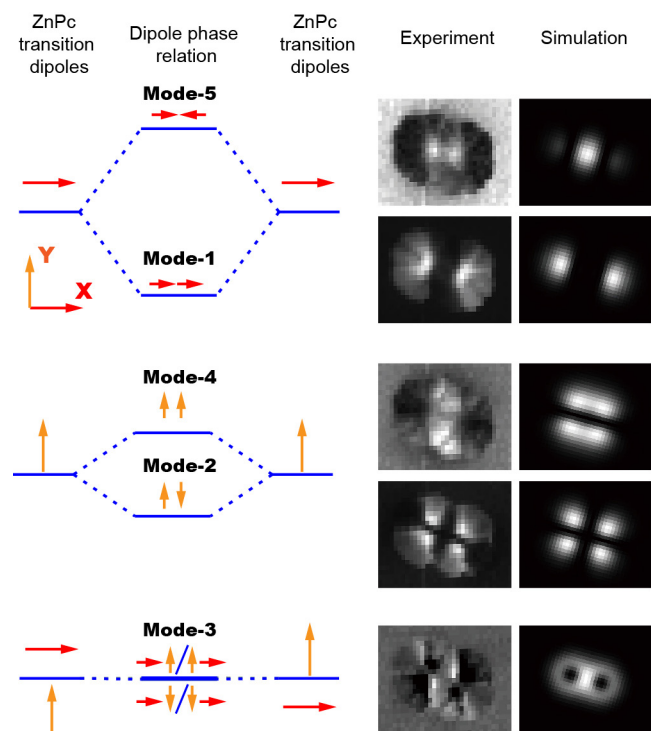
inset ( $5$  nm  $\times$   $4$  nm;  $-1.7$  V, 2 pA), showing an additional peak at  $1.870$  eV (about  $663$  nm) labelled as mode  $1'$ . **c**, Photon imaging pattern acquired by integrating the spectral range corresponding to the mode- $1'$  emission ( $-2.5$  V, 200 pA, 5 s per pixel; frame size:  $5$  nm  $\times$   $4$  nm,  $34 \times 21$  pixels; integration range:  $1,870 \pm 1.5$  meV, shaded region in **b**).



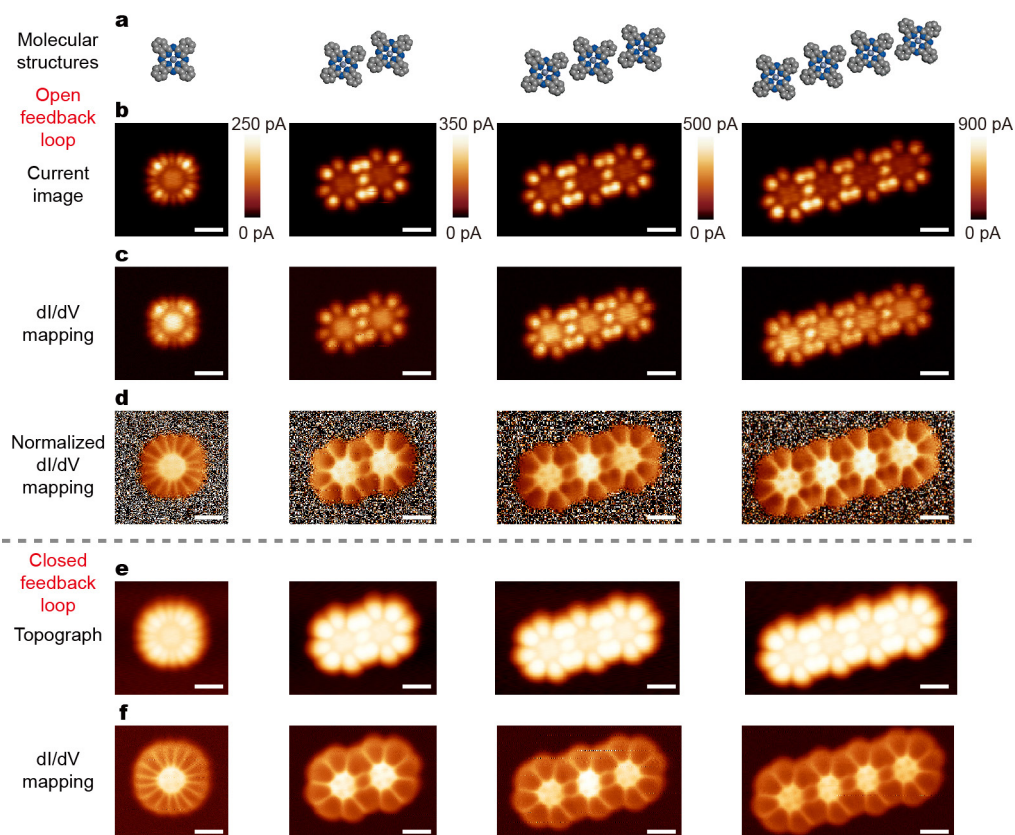


**Extended Data Figure 7 | Theoretical simulation of real-space STML mapping.** **a**, Modelling the transition dipoles of the ZnPc monomer by pairs of opposite point charges. The top images show the distribution of two equivalent transition densities associated with the corresponding transition dipoles of a ZnPc molecule. Positive and negative transition densities are represented by the violet and cyan shading, respectively, which are superimposed on the ball-and-stick model of a ZnPc molecule (the H, C, N

and Zn atoms are represented by the white, grey, blue and violet spheres, respectively). **b**, Arrangements of the orientations for the pair of point charges for selected examples of coupling modes (modes 1, 2 and 3) in our simulations. The distance between the two opposite charges in the schematic is exaggerated for clarity. The green dashed lines mark the centre-to-centre axial direction of the dimer. **c**, **d**, Schematic of the image-charge models when the tip is centred over the molecule (**c**) or off-centre (**d**).



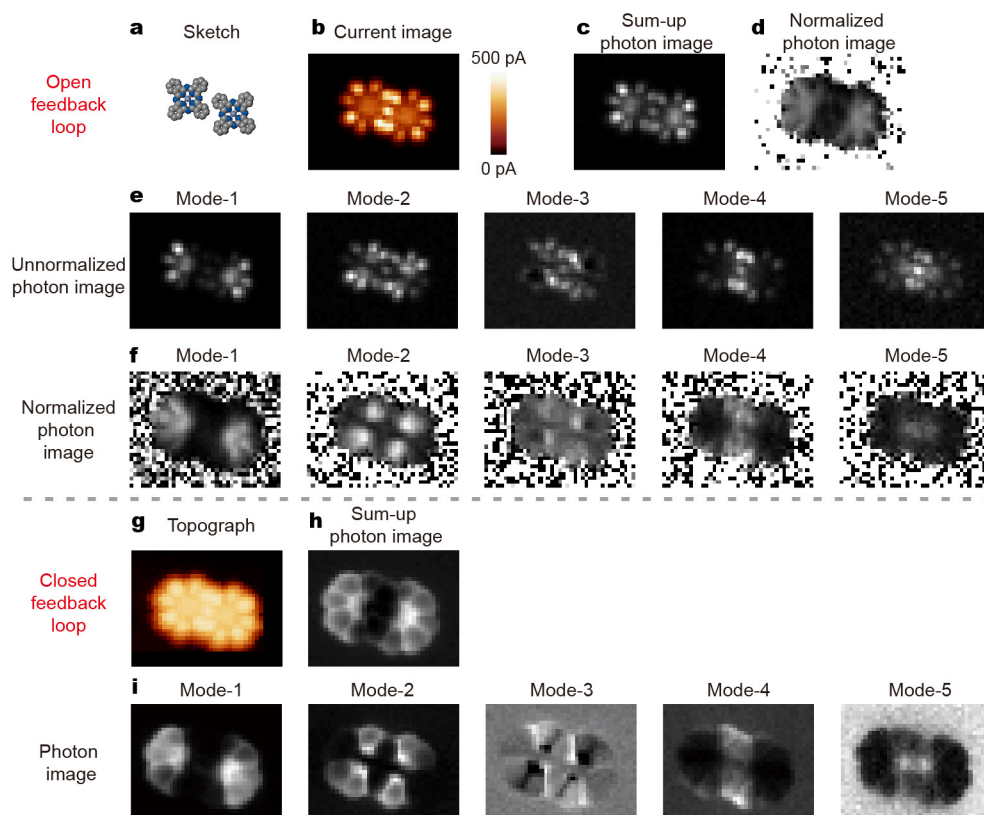
**Extended Data Figure 8 | Analogy to the bonding/anti-bonding-like features of  $\sigma$  and  $\pi$  orbitals.** To better view the analogy, the experimental and simulated patterns in Fig. 3 are reorganized as 'bonding-like' and 'anti-bonding-like' pattern pairs. The left column shows the schematic diagrams of different modes corresponding to different coherent dipole-dipole coupling arrangements in terms of transition-dipole orientations and related phase relations. The corresponding experimental and simulated patterns are plotted in the middle and right columns.



**Extended Data Figure 9 | dI/dV mapping data for a ZnPc monomer, dimer, trimer and tetramer acquired with an open or closed feedback loop.** **a**, Sketch of ZnPc molecular configurations. **b**, **c**, Current images (**b**) and dI/dV images (**c**) for different ZnPc molecular configurations acquired simultaneously with an open feedback loop ( $-2.5$  V). The bias modulation was 10 mV (r.m.s.) at 329 Hz. **d**, Corresponding normalized dI/dV images obtained by dividing the tunnelling current pixel by pixel.

**e**, **f**, STM images (**e**) and dI/dV images (**f**) for different ZnPc molecular configurations acquired simultaneously with a closed feedback loop ( $-2.5$  V, 100 pA). The bias modulation was 10 mV (r.m.s.) at 329 Hz. For the measurements of dI/dV mapping and spectroscopic imaging with an open feedback loop, we positioned the tip above the NaCl surface ( $-2.5$  V, 2 pA), switched off the feedback loop, lifted the tip up by 150 pm and started scanning over the selected area with molecules. Scale bars, 1 nm.





**Extended Data Figure 10 | Spectroscopic imaging of a ZnPc dimer with an open or closed feedback loop.** **a**, Sketch of a ZnPc dimer. **b**, **c**, Current image (**b**) and sum-up photon image (integrated over 1.86–1.94 eV) (**c**) acquired simultaneously with an open feedback loop (5.2 nm × 4 nm, 39 × 30 pixels; −2.5 V, 1 s per pixel). **d**, Corresponding normalized sum-up photon image obtained by dividing the sum-up image by the tunnelling

current image pixel by pixel. **e**, Un-normalized photon images for each mode. **f**, Corresponding normalized photon images for each mode in (**e**). **g**, **h**, For comparison, a spectroscopic image on the same ZnPc dimer is acquired with a closed feedback loop. STM image (**g**) and sum-up photon image (integrated over 1.86–1.94 eV) (**h**) (5.2 nm × 4 nm, 39 × 30 pixels; −2.5 V, 200 pA, 2 s per pixel). **i**, Photon images for each mode.

**Extended Data Table 1 | Experimentally determined exciton coupling strength  $|J|$  and oscillation frequency  $\Omega$**

	$ J $ (meV)	$\Delta W$ (meV)	$\Omega$ (s <sup>-1</sup> )
$\rightarrow \rightarrow / \rightarrow \leftarrow$	$17.3 \pm 0.3$	$5.5 \pm 0.9$	$\sim 5.3 \times 10^{13}$
$\uparrow \downarrow / \uparrow \uparrow$	$8.2 \pm 0.3$	$5.0 \pm 0.9$	$\sim 2.5 \times 10^{13}$

Also listed are the energy differences of van der Waals interaction between the excited and ground states of the dimer ( $\Delta W$ ). The arrow pattern  $\rightarrow \rightarrow / \rightarrow \leftarrow$  in the first column indicates exciton splitting between the in-line in-phase and in-line out-of-phase coupling modes; the arrow pattern  $\uparrow \downarrow / \uparrow \uparrow$  indicates exciton splitting between the parallel out-of-phase and parallel in-phase coupling modes.

# Komatiites reveal a hydrous Archaean deep-mantle reservoir

Alexander V. Sobolev<sup>1,2</sup>, Evgeny V. Asafov<sup>2</sup>, Andrey A. Gurenko<sup>3</sup>, Nicholas T. Arndt<sup>1</sup>, Valentina G. Batanova<sup>1,2</sup>, Maxim V. Portnyagin<sup>2,4</sup>, Dieter Garbe-Schönberg<sup>5</sup> & Stepan P. Krashenninnikov<sup>2</sup>

Archaean komatiites (ultramafic lavas) result from melting under extreme conditions of the Earth's mantle. Their chemical compositions evoke very high eruption temperatures, up to 1,600 degrees Celsius, which suggests even higher temperatures in their mantle source<sup>1,2</sup>. This message is clouded, however, by uncertainty about the water content in komatiite magmas. One school of thought holds that komatiites were essentially dry and originated in mantle plumes<sup>3–6</sup> while another argues that these magmas contained several per cent water, which drastically reduced their eruption temperature and links them to subduction processes<sup>7–9</sup>. Here we report measurements of the content of water and other volatile components, and of major and trace elements in melt inclusions in exceptionally magnesian olivine (up to 94.5 mole per cent forsterite). This information provides direct estimates of the composition and crystallization temperature of the parental melts of Archaean komatiites. We show that the parental melt for 2.7-billion-year-old komatiites from the Abitibi greenstone belt in Canada contained 30 per cent magnesium oxide and 0.6 per cent water by weight, and was depleted in highly incompatible elements. This melt began to crystallize at around 1,530 degrees Celsius at shallow depth and under reducing conditions, and it evolved via fractional crystallization of olivine, accompanied by minor crustal assimilation. As its major- and trace-element composition and low oxygen fugacities are inconsistent with a subduction setting, we propose that its high H<sub>2</sub>O/Ce ratio (over 6,000) resulted from entrainment into the komatiite source of hydrous material from the mantle transition zone<sup>10</sup>. These results confirm a plume origin for komatiites and high Archaean mantle temperatures, and evoke a hydrous reservoir in the deep mantle early in Earth's history.

We investigated samples of 2.7-billion-year-old komatiites from two well-studied parts of the Abitibi greenstone belt in Canada: Pyke Hill in Munro Township<sup>11–13</sup> and the Alexo flow<sup>11</sup>. Using electron probe, ion probe and laser ablation inductively coupled plasma mass spectrometry (LA-ICP-MS), we measured concentrations of water, chlorine, fluorine, carbon, boron and sulfur, boron isotopic composition, as well as contents of a full spectrum of major and trace elements in melt inclusions and major and trace elements in their host olivines. We also analysed by electron probe the compositions of spinel and coexisting skeletal olivine. These data were used to constrain the evolution of melt compositions and the crystallization temperatures of magnesian olivine (forsterite (Fo) 94.5–86.7 mol%). In addition, these data were used to reconstruct the parental melt composition and determine the origin of the komatiite magmas.

Crystallization temperatures were obtained using three different geothermometers: Fe/Mg partitioning between olivine and melt, Sc/Y partitioning between olivine and melt, and Al partitioning between olivine and spinel (see Methods). The resultant temperatures are plotted against Fo content in Fig. 1a and compared with calculated temperatures of komatiite melt containing 0–2 wt% water. For the same

Fo contents of olivine the temperatures from different thermometers agree within the uncertainties. The same thermometers give much lower temperatures when applied to low-Ca boninites (high-Si, high-Mg lavas from subduction settings) from Cape Vogel in Papua New Guinea, for which H<sub>2</sub>O in the melt exceeds 2 wt%<sup>14</sup>. This demonstrates the capacity of the geothermometers to estimate the crystallization temperatures of hydrous melts. The important conclusion is that the komatiite melts contained small amounts of water.

We measured directly the water and CO<sub>2</sub> contents in melt inclusions using secondary ion mass spectrometry (SIMS). Figure 1b shows that the measured water contents compare well with those inferred from the difference in temperature between anhydrous melt and temperatures obtained from the geothermometers. The measured concentrations of CO<sub>2</sub> in the melt inclusions, corrected for CO<sub>2</sub> contents in vapour bubbles, yield crystallization pressures of 150–250 bar of CO<sub>2</sub>-rich fluid (see Methods).

The data indicate gradually decreasing crystallization temperatures with decreasing Fo content of olivine. The most magnesian olivine studied for melt inclusions (Fo 94.5 mol%) started to crystallize at pressures of 150–250 bar and temperatures of around 1,500 °C. Crystallization proceeded until the temperature reached 1,350 °C, when the olivine composition reached Fo 86.7 mol%. The crystallization was accompanied by a gradual decrease of H<sub>2</sub>O content in the melt, from around 0.6 ± 0.1 wt% (all errors are 2σ) to almost 0 wt% (Fig. 1a and b). Also, the variations of measured H<sub>2</sub>O contents in the inclusions in highly magnesian olivine of Pyke Hill komatiite tend to correlate with the inclusion size, with the lowest values in inclusions with diameters <30 μm (Supplementary Tables 1–3). We attribute this to degassing that accompanied crystallization at shallow depth or during eruption, and, possibly, to the subsequent diffusional loss of H through the host olivine<sup>15</sup>. The H<sub>2</sub>O content in inclusions with diameters of 30 μm and larger is constant within analytical error and we consider it to be that of the trapped melt because it also matches, within error, the H<sub>2</sub>O content expected from the temperature estimated by Sc/Y partitioning (Extended Data Table 1). A relatively high average CO<sub>2</sub> concentration (168 ± 62 parts per million, p.p.m.) and CO<sub>2</sub>/H<sub>2</sub>O ratio (0.025 ± 0.005) in these inclusions (Extended Data Table 1) suggests saturation with CO<sub>2</sub>-rich (molar CO<sub>2</sub>/H<sub>2</sub>O = 2.7 ± 0.2) fluid at pressures of 193 ± 69 bar (Methods). Thus, substantial H<sub>2</sub>O degassing from the melts at higher pressures, both during and before crystallization of the most Mg-rich olivine, is unlikely, and the estimated H<sub>2</sub>O concentrations are considered to be those of the parental melt.

Oxygen fugacity during olivine crystallization was estimated from V partitioning between olivine and melt and from the Sc/V ratio in the melt (see Methods). The two estimates match and correspond to the quartz–fayalite–magnetite buffer minus one log unit for the primary melt. It gradually increases with decreasing forsterite content of olivine (Fig. 2), indicating crystallization of olivine in the system closed for oxygen.

<sup>1</sup>Université Grenoble Alpes, Institute Science de la Terre (ISTerre), CNRS, F-38041 Grenoble, France. <sup>2</sup>Vernadsky Institute of Geochemistry and Analytical Chemistry, Russian Academy of Sciences, 19 ul. Kosygina, Moscow 119991, Russia. <sup>3</sup>Centre de Recherches Pétrographiques et Géochimiques (CRPG), UMR 7358, Université de Lorraine, 54501 Vandœuvre-lès-Nancy, France.

<sup>4</sup>GEOMAR Helmholtz Centre for Ocean Research Kiel, Wischhofstrasse 1-3, 24148 Kiel, Germany. <sup>5</sup>CAU Kiel University, Institute of Geosciences, Ludewig-Meyn-Strasse 10, 24118 Kiel, Germany.



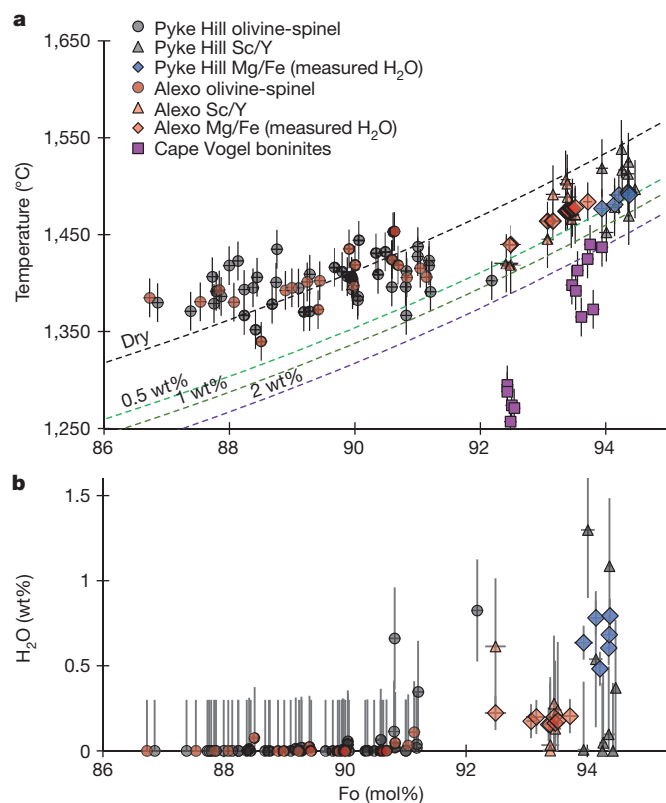


**Figure 1 | Crystallization temperatures and H<sub>2</sub>O contents in melt versus olivine composition of Abitibi komatiites.** **a**, Temperature and model H<sub>2</sub>O content versus olivine composition. Temperatures are estimated from Sc/Y olivine–melt, Mg–Fe olivine–melt and Al olivine–spinel geothermometers (see Methods). Dashed lines represent the temperature–composition relationship of olivine in the primary melt of Abitibi komatiites<sup>11</sup> at 400 bar and with 0 wt%, 0.5 wt%, 1 wt% and 2 wt% initial H<sub>2</sub>O content, calculated using models<sup>20,30</sup>. Temperatures for Cape Vogel boninites are calculated using the Al olivine–spinel geothermometer (see Methods). The error bars correspond to the reported errors of the thermometers:  $\pm 30^\circ\text{C}$  for Sc/Y and Al and  $\pm 20^\circ\text{C}$  for Fe/Mg partitioning. The errors in Fo contents are less than 300 p.p.m. and thus are within symbol sizes. **b**, Measured and calculated H<sub>2</sub>O concentrations in melt versus olivine composition. H<sub>2</sub>O contents are measured by SIMS (diamonds) or inferred from the difference between the temperatures calculated for ‘dry’ conditions using model<sup>30</sup> and those obtained from Sc/Al olivine–melt and Al olivine–spinel geothermometers (see Methods). The errors in measured H<sub>2</sub>O contents are within 20% relative to the concentration. The errors in calculated H<sub>2</sub>O contents (better than 0.4 wt%) are higher and relate to the errors of temperature calculation (see above). The compositions and calculated temperatures are reported only for inclusions with diameter equal to or larger than 30  $\mu\text{m}$ . As in the text, all errors on figures are  $2\sigma$ .

The reconstructed melt compositions (see Methods) contain 28–23 wt% MgO (Fig. 2). All Alexo samples have higher contents of Al<sub>2</sub>O<sub>3</sub> (not shown), TiO<sub>2</sub>, K<sub>2</sub>O, La, Ba, Sr, Cl, F and other highly incompatible elements than do Pyke Hill samples, and the less magnesian melts contain higher-than-expected contents of these elements. We attribute these differences to contamination of depleted parental komatiite melt by crustal material with high contents of these elements, as suggested by ref. 16. Further clues to the nature of the contaminant come from the spider diagram (Fig. 3a) and Extended Data Table 1. Melt inclusions in more Fo-rich olivines—samples M810 from Pyke Hill and M823 from Alexo—are moderately depleted in most incompatible elements. Melt inclusions in a more evolved olivine from sample M823 (823-8-ol31) have a flat pattern with slight deficits of Nb (high Ba/Nb = 52) and Ti, and enrichment of Cl, Ba, Sr and Rb. This pattern can be modelled by the assimilation of about 10% of sulfidic

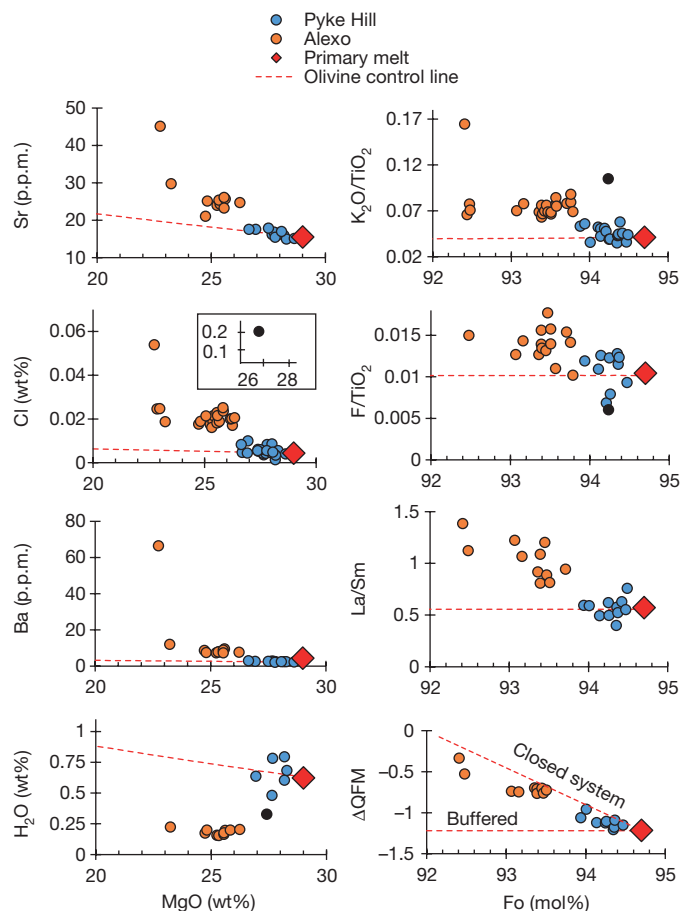


**Figure 2 | Compositions and oxygen fugacity of komatiite melt and coexisting olivine.** The compositions of melt do not follow the olivine control line, indicating that fractional crystallization of olivine is accompanied by assimilation of rock enriched in highly incompatible elements. Water contents vary in the opposite manner: the highest concentrations are found in the least contaminated parental melts. One extremely chlorine-rich Pyke Hill inclusion, 810-7-ol3, is indicated by a solid black symbol (inset). The compositions are reported only for inclusions with diameter equal to or larger than 30  $\mu\text{m}$  except for inclusion 810-7-ol3, which has diameter 20  $\mu\text{m}$  (see Extended Data Table 1).  $\Delta\text{QFM}$  is the oxygen fugacity compared to the quartz–fayalite–magnetite buffer, estimated using the partition of V between olivine and melt (see Methods).

sediment of the type interlayered with the Alexo komatiites<sup>16</sup>. The high Cl and F contents in the evolved melts are also attributed to this contamination (Fig. 2).

To estimate the composition of uncontaminated parental melt of the Abitibi komatiites, we averaged the compositions of melt inclusions hosted by the most magnesian olivine (Fo > 94) of the Pyke Hill samples (Extended Data Table 1). For trace elements more incompatible than Nd, this composition is slightly more depleted than the parental Alexo komatiite, as calculated by ref. 11, but similar to Pyke Hill komatiites<sup>13</sup>.

As shown on Fig. 3b and already noted for melt inclusions in less magnesian olivine (Fo 91–93 mol%), from Zimbabwe komatiites<sup>6</sup>, the trace-element patterns of the parental melt of Abitibi komatiites do not show the features characteristic of subduction related magmas—they lack the negative anomalies of high-field-strength elements (Nb, Zr, Ti), the positive anomalies of large-ion lithophile elements (Rb, Ba, K, Sr), B and Pb, and the U-shaped patterns typical of boninites. In addition, our data show that komatiites crystallized at highly reducing conditions uncharacteristic of supra-subduction magmatism<sup>17</sup>. They do, however, show marked enrichment in Cl and possibly in F, but mostly in H<sub>2</sub>O. The high Cl content might be partly explained by contamination by

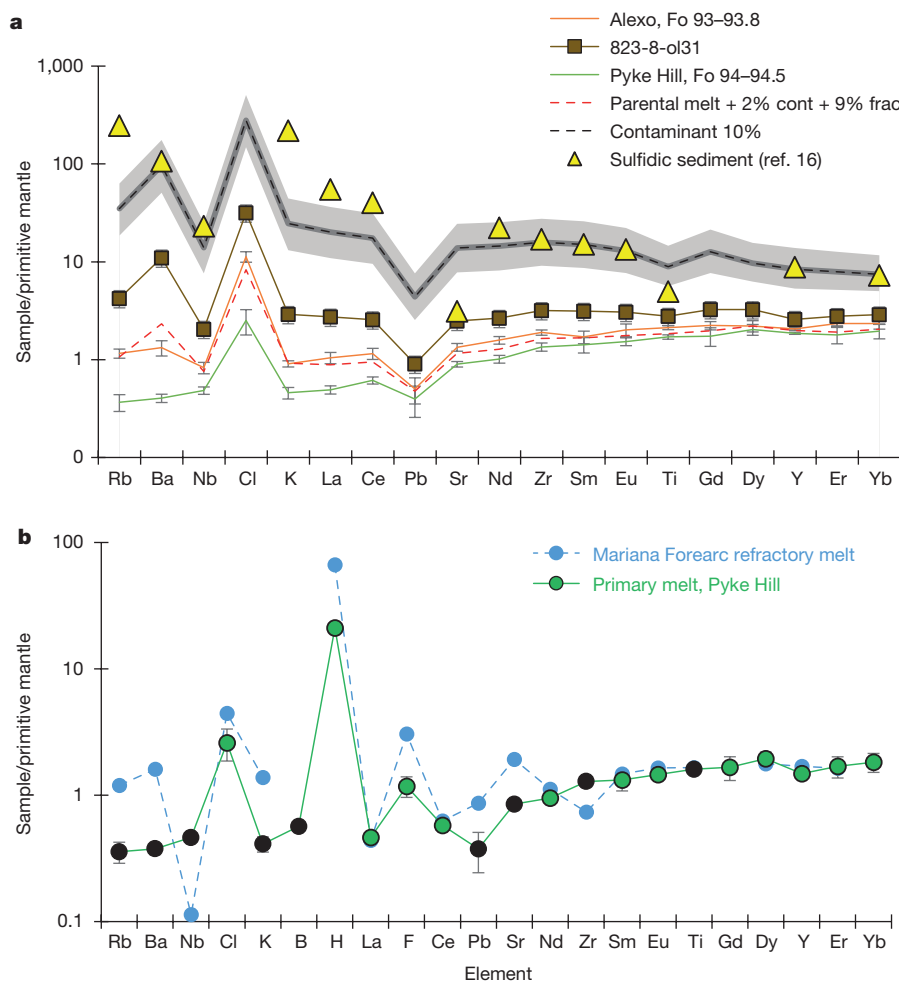


**Figure 3 | Incompatible element compositions of primary and evolved melts. a**, Spider diagram presenting the compositions of least-contaminated, average, and most-contaminated melt inclusions in olivine from Abitibi komatiites. The composition of the contaminant (see Extended Data Table 1) has been estimated assuming that the most contaminated melt inclusion (823-8-ol31) contains 10% of this contaminant (grey dashed line; see Methods). The grey field illustrates 5%–15% assimilation. These compositions fit reasonably well with the immobile element contents of sulfidic sediment of the type interlayered with the Alexo komatiites<sup>16</sup>. The average composition of melt inclusions

Cl-rich brine with high Cl/K<sub>2</sub>O and Cl/H<sub>2</sub>O ratios, similar to that reported for modern submarine eruptions<sup>18</sup>. Direct evidence for the presence of such a component is provided by the composition of inclusion 810-7-ol3 in a highly magnesian Pyke Hill olivine (Fo 94.2 mol%) which has Cl/K<sub>2</sub>O = 7, Cl/F = 100 and Cl/H<sub>2</sub>O = 0.6 (see Extended Data Table 1 and Fig. 2). Such contamination cannot, however, explain the elevated water and fluorine contents in the parental melt because of its extremely high H<sub>2</sub>O/Cl (>160) and its elevated F/Cl (>1). Both ratios are much higher than in the contaminant.

Selected melt inclusions were analysed for boron concentrations and isotopic compositions (see Methods). The uncontaminated melt in a high-Fo olivine of Pyke Hill sample M810 (inclusion 810-6-ol20) has low B concentration ( $0.23 \pm 0.02$  p.p.m.) and mantle-like isotope composition ( $\delta^{11}\text{B} = -12.9 \pm 10.6\text{‰}$ )<sup>19</sup>. By contrast, typical moderately contaminated melt trapped in high-Fo olivines from Alexo flow sample M823 (inclusion 823-6-ol16-a) has twice the B concentration ( $0.46 \pm 0.04$  p.p.m.) and a heavier B isotope ratio ( $\delta^{11}\text{B} = -3.8 \pm 6.8\text{‰}$ ), probably indicating contamination by a component altered by sea water<sup>19</sup>.

The composition of the primary melt of the Abitibi komatiites can be reconstructed from the composition of the uncontaminated parental

in olivine from the Alexo flow (sample M823) is explained by 2% contamination (cont) and 9% of fractional crystallization of olivine (frac) of the least-contaminated melt with such a component. **b**, Spider diagram of primary melt composition compared with refractory subduction-related melt from the Mariana forearc<sup>31</sup> associated with high-Mg olivine–Fo 93–94 mol%. The positive Rb, Ba and Sr anomalies and negative Nb, Zr and Ti anomalies of the subduction-related melt are absent in the komatiite melt (these elements are indicated by black circles). All elements are normalized to the composition of primitive mantle<sup>32</sup>. The error bars correspond to  $2\sigma$  of the average or analytical error  $\pm 20\%$ .

melt by adding equilibrium olivine until equilibrium is reached with Fo 94.7, the most magnesian olivine known in the Abitibi komatiites. To be conservative, we used two different models of Fe/Mg partitioning between olivine and melt<sup>20,21</sup> (Extended Data Table 1). The overall correction is less than 7 wt% of added olivine. The primary melt contains  $30.2 \pm 0.5\text{ wt}\%$  MgO and is depleted in highly incompatible elements, but contains  $0.6 \pm 0.1\text{ wt}\%$  H<sub>2</sub>O and has a very high H<sub>2</sub>O/Ce ratio of over 6,000 (Extended Data Table 1). For a pressure of 250 bar, its liquidus temperature is close to  $1,530^\circ\text{C} \pm 20^\circ\text{C}$ , about  $60^\circ\text{C}$  lower than the temperature of anhydrous komatiite liquidus. Assuming that the composition of the melt has not changed since its last equilibrium with the source peridotite, we can estimate the potential temperature of the mantle source. We used Herzberg and Asimow's relationship<sup>22</sup> between the potential mantle temperature and the low-pressure liquidus temperature and the MgO content of primary melt. Considering its H<sub>2</sub>O content ( $0.6 \pm 0.1\text{ wt}\%$ ) we obtained a potential temperature of  $1,730 \pm 50^\circ\text{C}$ . This value exceeds average estimates of the potential temperature for the Archaean non-arc basalts<sup>23</sup> and maximum estimates for Phanerozoic plumes<sup>24</sup> by at least  $100^\circ\text{C}$ . This is consistent with a plume origin of Abitibi komatiites<sup>6</sup> and a higher overall mantle temperature in the Archaean<sup>23</sup>.

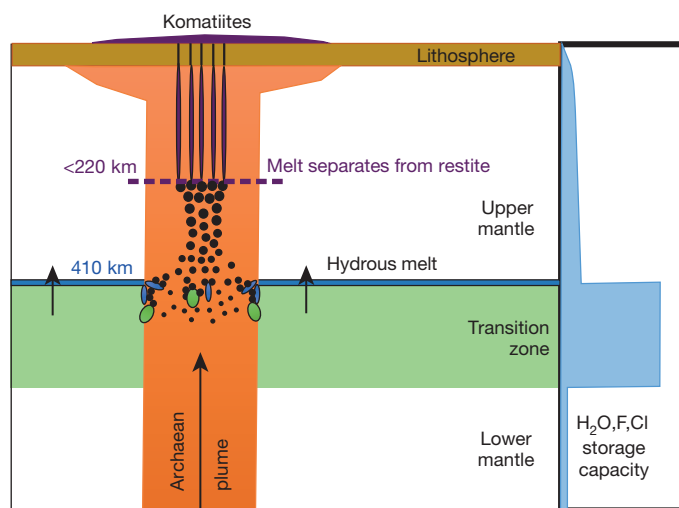


**Figure 4 | Cartoon illustrating a hot Archaean plume passing through the mantle transition zone at 410–660 km depth.** The plume (orange) traverses the transition zone, which contains excess  $\text{H}_2\text{O}$ , F and Cl in ringwoodite and/or wadsleyite. The plume is partially molten near the top of the transition zone (small black dots) and entrains hydrous melt (blue shapes) either from the layer at the upper boundary of the transition zone or from the hot boundary between the plume and the transition zone. Alternatively or additionally the plume may entrain solid wadsleyite from the transition zone (green shapes). All these hydrous materials introduce  $\text{H}_2\text{O}$  and possibly F and Cl into the plume and accelerate its melting (larger black dots). Further ascent of the plume generates more melt during decompression (large black dots), which then separates from the source (restite is the solid residue after melting of peridotite) and ascends to the surface without reaction with peridotite (purple stripes). The maximum separation depth has been estimated from the composition of the primary melt and the experimental data for maximum pressure of generation of a melt containing 30 wt% MgO without equilibrium with garnet<sup>33</sup>.

The source of  $\text{H}_2\text{O}$  in the primary komatiite melt must have had high ratios of  $\text{H}_2\text{O}$  to the most incompatible elements such as the light rare-earth elements (LREE), Nb, K, Rb, Ba, Pb and B. The ratios of mobile to immobile trace elements and the isotope composition of B should be similar to those in the mantle.

In the crust, a possible source of  $\text{H}_2\text{O}$  could be ultramafic rocks altered by seawater (serpentinites) or brines. Saturated brines have high concentrations of NaCl and would produce  $\text{H}_2\text{O}/\text{Cl}$  ratios in contaminated melts of 8–50 (ref. 18), values that are far lower than those in the reconstructed komatiite parental melt ( $\text{H}_2\text{O}/\text{Cl} > 160$ ). Serpentinites contain 10–15 wt%  $\text{H}_2\text{O}$  and thus around 5 wt% of their assimilation could yield the elevated  $\text{H}_2\text{O}$  contents of the parental komatiite melt. However, this, and any other source produced by seawater alteration, lacks the mantle ratios of mobile to immobile elements, as well as a mantle-like boron isotope ratio<sup>19</sup> and low B concentration. In addition, the assimilation of serpentinite alone—that is, without other crustal rocks with high incompatible element contents such as basalt or sediment—is improbable.

An alternative explanation—the hydration of originally dry melt inclusions by volume diffusion of  $\text{H}_2\text{O}$  through the host olivine<sup>15</sup>—is inconsistent with the relatively low crystallization temperatures estimated for magnesian olivines, which indicate the presence of  $\text{H}_2\text{O}$  in the parental melt (Fig. 1 and Extended Data Table 1). We thus consider a crustal source of the  $\text{H}_2\text{O}$  in the parental komatiite melt unlikely.

Mantle sources of Phanerozoic intraplate magmas (including apparent plumes) and mid-ocean-ridge basalts do not have high  $\text{H}_2\text{O}/\text{Ce}$  ratios<sup>25</sup>. Their maximum values (400) are more than 15 times lower than those we estimated for the primary komatiite melt (>6,000). One alternative source might be a fluid released by dehydration of subducting slabs in supra-subduction settings<sup>8</sup>, but such a source is inconsistent

with the trace-element composition (Fig. 3b) and low oxygen fugacity of the komatiite melts.

Another possible source is the mantle transition zone at 410–660 km depth. Experimental studies have shown that the high-pressure polymorphs of olivine—wadsleyite and ringwoodite—can accommodate high contents of  $\text{H}_2\text{O}$  and halogens compared to other incompatible elements<sup>10,26,27</sup>. Accordingly, the transitional zone peridotite could have exceptionally high ratios of  $\text{H}_2\text{O}$ , F, (and possibly Cl) to LREE, Nb, K, Rb, B and Ba. The recent finding of  $\text{H}_2\text{O}$ -rich ringwoodite in diamond<sup>28</sup> provides evidence that transition-zone peridotite indeed contains at least 1 wt% of  $\text{H}_2\text{O}$ . We thus consider the transition zone as a likely source of  $\text{H}_2\text{O}$  and a possible source of halogens in the primary melt of the Abitibi komatiites.

We envisage two mechanisms whereby water could be transferred from the transition-zone peridotite to the source of komatiite (Fig. 4). In the first, the transformation of wadsleyite to olivine-bearing peridotite at the top of the transition zone and/or on the hot boundary of a plume produces hydrous melt<sup>10</sup> with high  $\text{H}_2\text{O}$  to LREE, Nb, K, Rb, B and Ba ratios similar to that of the initial bulk rock. Entrainment of a few per cent of such hydrous melt would accelerate partial melting by decompression within the rising plume, which would then produce primary komatiite melt. An alternative mechanism is entrainment of solid water-bearing ringwoodite or wadsleyite into the plume as it traverses the transition zone. Both scenarios require that hydrous mantle was already present 2.7 billion years ago. This implies either that subduction started very early in the Earth history and delivered enough water to the transition zone by 2.7 billion years ago, or that  $\text{H}_2\text{O}$  originally became concentrated in the deep Earth mantle during accretion<sup>29</sup>. The elevated contents of Cl and F relative to other incompatible elements in the komatiite parental melt (Fig. 3b) could also originate from the transition zone<sup>27</sup>.

Why do Phanerozoic plumes not have excess  $\text{H}_2\text{O}$  (ref. 25), if they too pass through the transition zone? One explanation would be that the plume source of Archaean komatiites was so hot that, when it traversed the transition zone, it contained partial melt that took in water from ringwoodite or wadsleyite, whereas Phanerozoic plumes were completely solid at these depths. In such a scenario, the transition-zone water filter<sup>10</sup> acts for the superhot Archaean plumes in the opposite direction to that of present-day mantle upwelling.

**Online Content** Methods, along with any additional Extended Data display items and Source Data, are available in the online version of the paper; references unique to these sections appear only in the online paper.

**Received 28 October 2015; accepted 19 January 2016.**

1. Herzberg, C. Depth and degree of melting of komatiites. *J. Geophys. Res. Solid Earth* **97**, 4521–4540 (1992).
2. Nisbet, E. G., Cheadle, M. J., Arndt, N. T. & Bickle, M. J. Constraining the potential temperature of the Archaean mantle—a review of the evidence from komatiites. *Lithos* **30**, 291–307 (1993).
3. Arndt, N. et al. Were komatiites wet? *Geology* **26**, 739–742 (1998).
4. Campbell, I. H., Griffiths, R. W. & Hill, R. I. Melting in an Archaean mantle plume—heads it's basalts, tails it's komatiites. *Nature* **339**, 697–699 (1989).
5. Herzberg, C. et al. Temperatures in ambient mantle and plumes: constraints from basalts, picrites, and komatiites. *Geochem. Geophys. Geosyst.* **8**, Q02006 (2007).
6. McDonough, W. F. & Ireland, T. R. Intraplate origin of komatiites inferred from trace-elements in glass inclusions. *Nature* **365**, 432–434 (1993).
7. Allègre, C. J. in *Komatiites* (eds Arndt, N. T. & Nisbet, E. G.) 495–500 (George Allen and Unwin, 1982).
8. Grove, T. L. & Parman, S. W. Thermal evolution of the Earth as recorded by komatiites. *Earth Planet. Sci. Lett.* **219**, 173–187 (2004).
9. Parman, S. W., Grove, T. L., Dann, J. C. & de Wit, M. J. A subduction origin for komatiites and cratonic lithospheric mantle. *S. Afr. J. Geol.* **107**, 107–118 (2004).
10. Bercowski, D. & Karato, S. Whole-mantle convection and the transition-zone water filter. *Nature* **425**, 39–44 (2003).
11. Lahaye, Y. & Arndt, N. Alteration of a komatiite flow from Alexo, Ontario, Canada. *J. Petrol.* **37**, 1261–1284 (1996).
12. Pyke, D. R., Naldrett, A. J. & Eckstrand, O. R. Archaean ultramafic flows in Munro township, Ontario. *Geol. Soc. Am. Bull.* **84**, 955–977 (1973).
13. Puchtel, I. S., Walker, R. J., Brandon, A. D. & Nisbet, E. G. Pt-Re-Os and Sm-Nd isotope and HSE and REE systematics of the 2.7 Ga Bellingwue and Abitibi komatiites. *Geochim. Cosmochim. Acta* **73**, 6367–6389 (2009).



14. Kamenetsky, V. S., Sobolev, A. V., Eggins, S. M., Crawford, A. J. & Arculus, R. J. Olivine-enriched melt inclusions in chromites from low-Ca boninites, Cape Vogel, Papua New Guinea: evidence for ultramafic primary magma, refractory mantle source and enriched components. *Chem. Geol.* **183**, 287–303 (2002).
15. Portnyagin, M., Almeev, R., Matveev, S. & Holtz, F. Experimental evidence for rapid water exchange between melt inclusions in olivine and host magma. *Earth Planet. Sci. Lett.* **272**, 541–552 (2008).
16. Lahaye, Y., Barnes, S. J., Frick, L. R. & Lambert, D. D. Re-Os isotopic study of komatiitic volcanism and magmatic sulfide formation in the southern Abitibi greenstone belt, Ontario, Canada. *Can. Mineral.* **39**, 473–490 (2001).
17. Evans, K. A., Elburg, M. A. & Kamenetsky, V. Oxidation state of subarc mantle. *Geology* **40**, 783–786 (2012).
18. Kent, A. J. R., Norman, M. D., Hutcheon, I. D. & Stolper, E. M. Assimilation of seawater-derived components in an oceanic volcano: evidence from matrix glasses and glass inclusions from Loihi seamount, Hawaii. *Chem. Geol.* **156**, 299–319 (1999).
19. Gurenko, A. A. & Kamenetsky, V. S. Boron isotopic composition of olivine-hosted melt inclusions from Gorgona komatiites, Colombia: new evidence supporting wet komatiite origin. *Earth Planet. Sci. Lett.* **312**, 201–212 (2011).
20. Ford, C. E., Russell, D. G., Craven, J. A. & Fisk, M. R. Olivine liquid equilibria—temperature, pressure and composition dependence of the crystal liquid cation partition coefficients for Mg, Fe<sup>2+</sup>, Ca and Mn. *J. Petrol.* **24**, 256–266 (1983).
21. Herzberg, C. & O'Hara, M. J. Plume-associated ultramafic magmas of phanerozoic age. *J. Petrol.* **43**, 1857–1883 (2002).
22. Herzberg, C. & Asimow, P. D. PRIMELT3 MEGA-XLSM software for primary magma calculation: peridotite primary magma MgO contents from the liquidus to the solidus. *Geochem. Geophys. Geosyst.* **16**, 563–578 (2015).
23. Herzberg, C., Condie, K. & Korenaga, J. Thermal history of the Earth and its petrological expression. *Earth Planet. Sci. Lett.* **292**, 79–88 (2010).
24. Herzberg, C. & Gazel, E. Petrological evidence for secular cooling in mantle plumes. *Nature* **458**, 619–622 (2009).
25. Dixon, J. E., Leist, L., Langmuir, C. & Schilling, J. G. Recycled dehydrated lithosphere observed in plume-influenced mid-ocean-ridge basalt. *Nature* **420**, 385–389 (2002).
26. Mibe, K., Orihashi, Y., Nakai, S. i. & Fujii, T. Element partitioning between transition-zone minerals and ultramafic melt under hydrous conditions. *Geophys. Res. Lett.* **33**, L16307 (2006).
27. Roberge, M. *et al.* Is the transition zone a deep reservoir for fluorine? *Earth Planet. Sci. Lett.* **429**, 25–32 (2015).
28. Pearson, D. G. *et al.* Hydrous mantle transition zone indicated by ringwoodite included within diamond. *Nature* **507**, 221–224 (2014).
29. Albarède, F. Volatile accretion history of the terrestrial planets and dynamic implications. *Nature* **461**, 1227–1233 (2009).
30. Falloon, T. J. & Danyushevsky, L. V. Melting of refractory mantle at 1.5, 2 and 2.5 GPa under, anhydrous and H<sub>2</sub>O-undersaturated conditions: implications for the petrogenesis of high-Ca boninites and the influence of subduction components on mantle melting. *J. Petrol.* **41**, 257–283 (2000).
31. Ribeiro, J. M. *et al.* Composition of the slab-derived fluids released beneath the Mariana forearc: evidence for shallow dehydration of the subducting plate. *Earth Planet. Sci. Lett.* **418**, 136–148 (2015).
32. Hofmann, A. W. Chemical differentiation of the Earth: the relationship between mantle, continental crust, and oceanic crust. *Earth Planet. Sci. Lett.* **90**, 297–314 (1988).
33. Walter, M. J. Melting of garnet peridotite and the origin of komatiite and depleted lithosphere. *J. Petrol.* **39**, 29–60 (1998).

**Supplementary Information** is available in the online version of the paper.

**Acknowledgements** We thank A. Kadik, A. Borisov and A. Kargal'tsev for their assistance in high-temperature experiments, V. Magnin for assistance in maintenance of the EPMA laboratory, U. Westernströer for help with laser-ablation ICP-MS measurements, and V. Kamenetsky for providing sample 41F of the Cape Vogel boninites. The paper benefited greatly from the constructive reviews of C. Herzberg and I. Puchtel and the comments of S. Sobolev. This study was funded by the Russian Science Foundation grant number 14-17-00491 (to A.V.S.). The EPMA facility in ISTERre was established and maintained by funds of the Agence Nationale de la Recherche, France, the Chair of Excellence grant ANR-09-CEXC-003-01 and partly by CNRS and Labex OSUG@2020 (Investissements d'avenir—ANR10 LABX56). A.V.S. acknowledges the support of Institut Universitaire de France and the Deep Carbon Observatory. The costs of SIMS analyses were covered by CRPG (A.A.G.'s internal funds). This is CRPG contribution number 2430.

**Author Contributions** A.V.S. designed the study, participated in sample collection, data processing and interpretation, and wrote the paper. E.V.A. participated in sample collection, found and prepared melt inclusions in olivines, conducted EPMA analyses and participated in the data processing and interpretation. A.A.G. performed SIMS analyses and participated in data interpretation and writing the paper. N.T.A. led the field work and sample collection, participated in data interpretation and co-authored the paper. V.G.B. managed the EPMA analyses. M.V.P. performed the laser-ablation ICP-MS analyses and participated in data interpretation and writing the paper. D.G.-S. managed the laser-ablation ICP-MS analyses. S.P.K. conducted the heating experiments. All authors discussed the results, problems or methods and participated in preparation of the paper.

**Author Information** A copy of the Supplementary Information has been submitted to Researchgate ([https://www.researchgate.net/profile/Alexander\\_Sobolev](https://www.researchgate.net/profile/Alexander_Sobolev)) and GEOROC (<http://georoc.mpch-mainz.gwdg.de/georoc/>) databases. Reprints and permissions information is available at [www.nature.com/reprints](http://www.nature.com/reprints). The authors declare no competing financial interests. Readers are welcome to comment on the online version of the paper. Correspondence and requests for materials should be addressed to A.V.S. (alexander.sobolev@ujf-grenoble.fr).

## METHODS

**Samples.** The samples are 2.7-billion-year-old komatiites from two outcrops in the Abitibi greenstone belt in Canada: Pyke Hill in Munro Township (M810) and the Alexo flow (M823)<sup>11,13</sup>. Both samples come from the cumulate B2 zones and contain partly unaltered olivine grains of different size and composition. Sample M810 (Pyke Hill) contains large (1–2 mm) euhedral olivine grains with high-Fo cores (94–94.7 mol% Fo) and less magnesian rims (down to 87 mol% Fo). Sample M823 (Alexo flow) contains smaller (0.5 mm) anhedral olivine grains with zoned cores (92–94 mol% Fo) and Fo-depleted rims (86.5 mol% Fo). The other minerals are skeletal olivine (91–86.7 mol% Fo), equant and skeletal spinel (Cr-number of 60–70), acicular clinopyroxene and altered glass. The cores of olivine grains contain abundant, partly crystallized melt inclusions, which are composed of glass, high-Al clinopyroxene, spinel and gas bubbles (see Extended Data Fig. 1 and Extended Data Table 1).

**Analytical methods.** To study the compositions of minerals and glasses we used the following in situ analytical techniques: electron probe microanalysis (EPMA), secondary ion mass-spectrometry (SIMS) and LA-ICP-MS.

**EPMA.** Melt inclusions, host olivine and spinel were analysed on a JEOL JXA 8230 microprobe at ISTERre in Grenoble, France. For analyses of olivine we used beam currents from 300 nA to 900 nA and accelerated voltages of 15–25 kV using analytical methods from refs 34 and 35. Melt inclusions were analysed at 12 nA and 15 kV, using GOR-132G (ref. 36) as a standard for major elements and set of international standards for minor and trace elements<sup>37</sup>. Long counting time (240–300 s) was applied for measurement of trace elements: K, Cl and S. Spinel was analysed at 50 nA and 20 kV using the analytical method from ref. 37. The ZAF correction procedure was applied to correct matrix compositional effects<sup>35</sup>.

**SIMS.** We used secondary ion mass spectrometry (SIMS) to determine the contents of CO<sub>2</sub>, H<sub>2</sub>O, Cl, F, S and B and the isotopic composition of B in melt inclusions in olivine.

**Volatile concentrations in olivine-hosted melt inclusions.** The analyses were obtained using the CAMECA IMS 1280 HR and the upgraded CAMECA IMS 1270 E7 ion microprobes at the CRPG in Nancy, France. The inclusion-bearing olivine grains, previously analysed for major elements by EPMA, were carefully re-polished to remove residual carbon coating, with final polishing using 1 µm Al<sub>2</sub>O<sub>3</sub> suspension. The grains were then removed from epoxy, remounted by pressing them into indium metal, ultrasonically cleaned and stored at +60 °C. About 12–24 h before analysis, the mount was placed into the sample storage of the ion probe at a pressure of ~10<sup>−8</sup> Torr. A liquid-nitrogen cold trap and a sublimation pump were always used to reduce CO<sub>2</sub> and H<sub>2</sub>O background and maintain a pressure of <2 × 10<sup>−9</sup> Torr in the sample chamber. The samples were sputtered with a 0.8–1 nA, 10-kV <sup>133</sup>Cs<sup>+</sup> primary beam focused to a spot of 5–10 µm and then rastered to 10 µm × 10 µm. A field aperture of ~1,000 µm was used to eliminate any secondary ion signal from the spot margins. A mass-resolving power of ~5,000, enough to resolve <sup>17</sup>O from <sup>16</sup>OH and <sup>30</sup>Si from <sup>29</sup>Si H peaks, was applied. The <sup>12</sup>C<sup>−</sup> (counting time 8 s), <sup>16</sup>OH<sup>−</sup> (6 s), <sup>19</sup>F<sup>−</sup> (6 s), <sup>27</sup>Al<sup>−</sup> (2 s) and <sup>30</sup>Si<sup>−</sup> (2 s), <sup>32</sup>S<sup>−</sup> (4 s) and <sup>35</sup>Cl<sup>−</sup> (6 s) ions were counted during 12 cycles after 300 s pre-sputtering, using the axial electron multiplier. A set of reference glasses (ALV981-R23, ALV519-4-1, 30-2, 40-2, VG2 USNM111240, CY84-06-02, CL-DR01-5, KL2-G, ETNA II-6 and ETNA II-7; see Supplementary Table 5) and San Carlos olivine were analysed to create calibration lines, which we used to determine volatile concentrations in the unknown samples. Using the established calibration lines, the accuracy of SIMS analyses (calculated as average relative deviation of the measured values from the reference ones) was estimated to be 6%–24% for CO<sub>2</sub>, 6%–20% for H<sub>2</sub>O, 4%–10% for F, 2%–6% for S and 8%–24% for Cl (95% confidence level), varying among four separate analytical sessions in March, April and July 2015. The host olivines next to the included glasses were also analysed for volatile concentrations to account for background in each particular grain. The background values calculated assuming zero concentrations of the species in olivine are: 16–21 p.p.m. for CO<sub>2</sub>, 60–80 p.p.m. for H<sub>2</sub>O, 2–4 p.p.m. for F, 0.3–0.5 p.p.m. for S and 0.7–1.6 p.p.m. for Cl.

**Boron contents and isotopic composition of olivine-hosted melt inclusions.** Boron contents and isotopic compositions of the homogenized olivine-hosted melt inclusions were analysed using the CAMECA IMS 1280 HR ion microprobe at CRPG. The 10–12-nA 13-kV <sup>16</sup>O<sup>−</sup> primary beam was focused to 15–20 µm and then rastered to 10 µm × 10 µm, for sample pre-sputtering (10 min) at the beginning of each run and during the analyses. A 400-µm contrast aperture and a 1,000-µm field aperture were used, giving a field of view of approximately 25 µm. Secondary <sup>10</sup>B<sup>+</sup>, <sup>11</sup>B<sup>+</sup> and <sup>28</sup>Si<sup>++</sup> ions were accelerated at 10 kV and analysed at a mass-resolving power of ~2,000, sufficient to resolve <sup>9</sup>Be H interference on the <sup>10</sup>B peak, <sup>10</sup>B H on the <sup>11</sup>B peak and <sup>13</sup>C H on the <sup>28</sup>Si double-charged peak, using a circular focusing mode and a transfer optic of ~150 µm. The energy slit was centred and opened to 50 V. The automatic routine of secondary beam centring in the centre

of field and contrast apertures was used at the beginning of each measurement. High voltage sample control was executed at acquisition begin and then every 20 cycles throughout the acquisition to compensate for possible sample charge usually ranging between 5 and 10 V. Typical ion intensities were 20–60 counts per second (cps) of <sup>10</sup>B<sup>+</sup>, 90–220 cps of <sup>11</sup>B<sup>+</sup> and 70,000–80,000 cps of <sup>28</sup>Si<sup>++</sup> ions. The 1 s.d. internal precision of individual measurements ranged from 3.4% to 5.4%, depending primarily on the boron concentration in the melt inclusions (0.2–0.6 p.p.m. B). The obtained precision was reached after ~2 h of counting (200 cycles, each comprising 12 s, 4 s and 2 s counting time on the <sup>10</sup>B<sup>+</sup>, <sup>11</sup>B<sup>+</sup> and <sup>28</sup>Si<sup>++</sup> peaks, respectively, and 2 s waiting time between each mass change). It matches well the in-run Poisson counting statistics, implying that the instrument was stable.

Instrumental mass fractionation (IMF), expressed as a ratio of the measured to the true values ( $\alpha_{\text{IMF}} = R_{\text{measured}}/R_{\text{true}}$ ), was determined based on the replicate measurements (3–5 times at the beginning and end of the analytical session) of two reference glasses: StHs6/80-G andesite glass (11.6 p.p.m. B,  $\delta^{11}\text{B} = -4.4\text{‰}$ ) and GOR132-G basaltic glass (15.6 p.p.m. B,  $\delta^{11}\text{B} = +7.1\text{‰}$ )<sup>38</sup>. The uncertainty of IMF on <sup>11</sup>B/<sup>10</sup>B inferred from multiple measurements of the reference glasses was estimated to be ±1.4%, 1 s.d. This is 2–3 times better than the internal precision of individual  $\delta^{11}\text{B}$  determinations, mostly due to the low B concentrations in the unknown samples. The  $\delta^{11}\text{B}$  values were calculated using <sup>11</sup>B/<sup>10</sup>B = 4.04558 ± 0.00033 for the NBS 951 standard<sup>39</sup>.

Boron concentrations were determined using IMF values of <sup>11</sup>B<sup>+</sup>/<sup>28</sup>Si<sup>++</sup> ratios of the above standards. The precision and accuracy was always better than 4% relative.

**LA-ICP-MS.** Trace-element concentrations in melt inclusions and host olivine were analysed by LA-ICP-MS using an Agilent 7500 s quadrupole mass-spectrometer coupled with a 193 nm Excimer laser ablation system GeoLas Pro (Coherent) at the Institute of Geosciences of the Christian-Albrecht University of Kiel, Germany. Analyses were performed with 24-µm and 32-µm spots for inclusions and olivine, respectively, 10-Hz pulse frequency, and a laser fluence of 10 J cm<sup>−2</sup>. Olivine analyses were performed in three spots around every inclusion, on areas pre-ablated for 3 s to reduce surface contamination. All analyses were performed in a large volume ‘Zürich’ ablation cell. Carrier gas was He (~1 litre per min) with addition of H<sub>2</sub> (0.014 litre per min), which were mixed with Ar (0.85 litre per min) before introduction into spectrometer. Oxide production rate, estimated as ThO<sup>+</sup>/Th<sup>+</sup>, was <0.3%. Analyses were performed in time-resolved mode and included 20 s background measurement followed by 20 s sample ablation and signal measurement. Dwell time was 10 ms for all elements. All spectra were inspected in GLITTER software to define intervals for integration and exclude contamination from the surface. Concentrations were quantified from the measured ion yields normalized to <sup>43</sup>Ca for glass and <sup>29</sup>Si for olivine. Ca and Si concentrations came from microprobe data, and MPI-DING KL-2G glass was used as a primary standard for all elements<sup>36</sup>. Other MPI-DING reference glasses (GOR-128G, GOR-132G, BM90/21G) as well as an in-house reference sample of pressed olivine nano-powder tablet (SCOP), were analysed as unknowns. Isobaric interference of <sup>29</sup>Si<sup>16</sup>O on <sup>45</sup>Sc was monitored and corrected by using data from Sc-free synthetic quartz, which was measured together with reference glasses every 20 analyses.

**Melt inclusions.** To eliminate the effects of crystallization of melt inclusions, olivine grains containing inclusions were heated to 1,350–1,400 °C at 1 atm of CO<sub>2</sub>:H<sub>2</sub> gas mixture corresponding to the QFM oxygen buffer in a vertical furnace at Vernadsky Institute in Moscow, Russia. Samples were heated for 5 min and then quenched. The olivine grains were then mounted in epoxy and polished to expose melt inclusions on the surfaces. Heated and quenched melt inclusions consist of glass, shrinkage bubbles of low-density gas and spinel (see Extended Data Fig. 1). Melt inclusions that had been originally altered and cracked before or during heating were recognized by very low concentrations of sulfur (below 0.005 wt%) and were filtered out. Measured compositions of glasses in melt inclusions are modified by crystallization of olivine on the walls of cavities, by crystallization of spinel within cavities, and by Fe–Mg exchange between host olivine and included melt<sup>40</sup>. In addition, the segregation of shrinkage bubbles in the inclusions drastically affects the concentration of C in the melt<sup>41,42</sup>. To reconstruct the original compositions of the trapped melts we applied an algorithm to reverse Fe–Mg exchange between olivine and melt<sup>43</sup>, based on the olivine melt equilibrium models<sup>20,21</sup> and the estimated concentrations of FeO in the trapped melt. The FeO contents were estimated as a function of the host olivine composition by modelling the crystallization of the Abitibi komatiite parental melt<sup>11</sup> at 250-bar pressure and QFM-1 oxygen fugacity. The compositions and temperatures of trapped melts in equilibrium with host olivine were calculated using Petrolog v.3.1.1.3 software<sup>44</sup>, measured H<sub>2</sub>O concentrations, and estimated FeO contents. The concentrations of CO<sub>2</sub> in the inclusions were then corrected for the amount of CO<sub>2</sub> stored in the segregated shrinkage bubbles using estimated bubble volume and density. Bubble volumes were calculated using a relationship between trapping and quenching

temperature<sup>41</sup>. Bubble densities were calculated using pressures estimated from the measured concentrations of CO<sub>2</sub> and H<sub>2</sub>O in the included glasses and the pressure–volume–temperature properties of CO<sub>2</sub>–H<sub>2</sub>O mixtures<sup>45,46</sup>. The estimated concentrations of CO<sub>2</sub> in the melt at the time of entrapment are almost ten times higher than measured ones. They correspond to CO<sub>2</sub>–H<sub>2</sub>O gas pressures of 150–250 bar<sup>46</sup>.

**Geothermometers.** To estimate crystallization temperatures, we used partitioning of Fe/Mg and Sc/Y between olivine and melt<sup>20,21,47</sup> and Al between olivine and spinel<sup>48</sup>. Temperatures obtained from Fe/Mg olivine–melt partitioning were corrected for the effects of measured H<sub>2</sub>O contents in the melt using the equation of Falloon and Danyushevsky<sup>30</sup>. We used this equation rather than those of other models<sup>49,50</sup> because its calibration includes melts with >15–20 wt% MgO whereas the others are focused in less magnesian melts (≤10 wt% MgO). For Sc/Y thermometry, we used Sc and Y concentrations in olivine and Sc and Y contents of Abitibi komatiites as a function of their MgO concentrations using ref. 51:

$$\text{Sc melt} = 46.3 - 0.733 \times \text{MgO melt}$$

$$\text{Y melt} = 16.4 - 0.326 \times \text{MgO melt}$$

We used the Sc and Y concentrations of rocks rather than melt inclusions to avoid effects of olivine crystallization on inclusion walls on the Sc concentrations in the melt. Calculated Y contents in melts are similar within the error to ones measured in inclusions and corrected for olivine crystallization on the walls.

Olivine–spinel thermometry was applied for olivine containing less than 92 mol% Fo, which crystallize together with spinel. The reported two standard errors of thermometers, including errors in the determination of Y and Al in olivine, are ±30 °C for Sc/Y and Al thermometers<sup>47,48</sup>, and ±20 °C for the Fe–Mg thermometers<sup>20,21</sup>.

To estimate the oxygen fugacity we used vanadium olivine–melt and V/Sc melt oxybarometers<sup>47,52</sup>. For that we used V concentrations of olivine and V contents of rocks<sup>51</sup> as a function of their MgO contents:

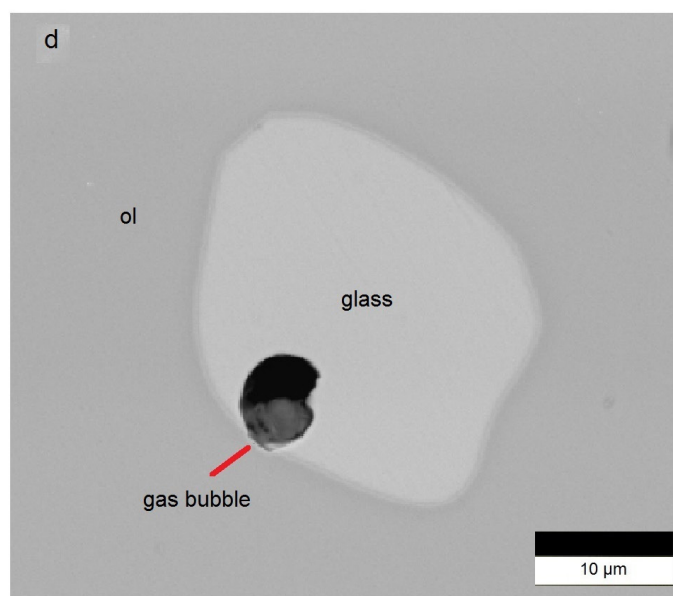
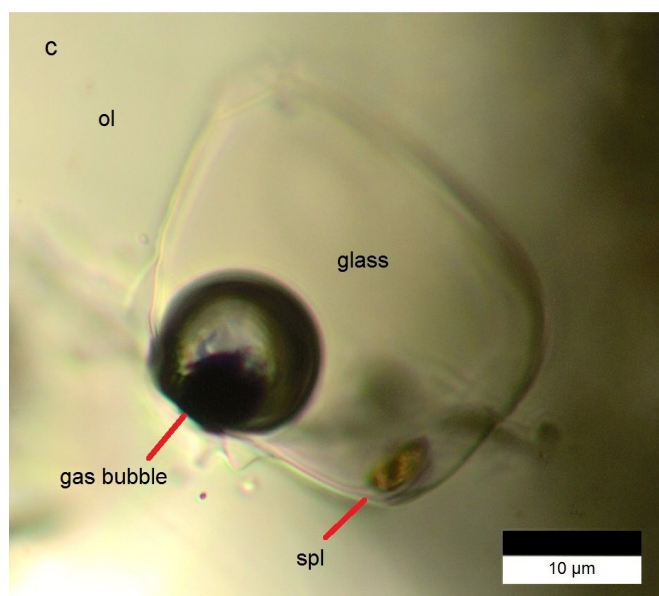
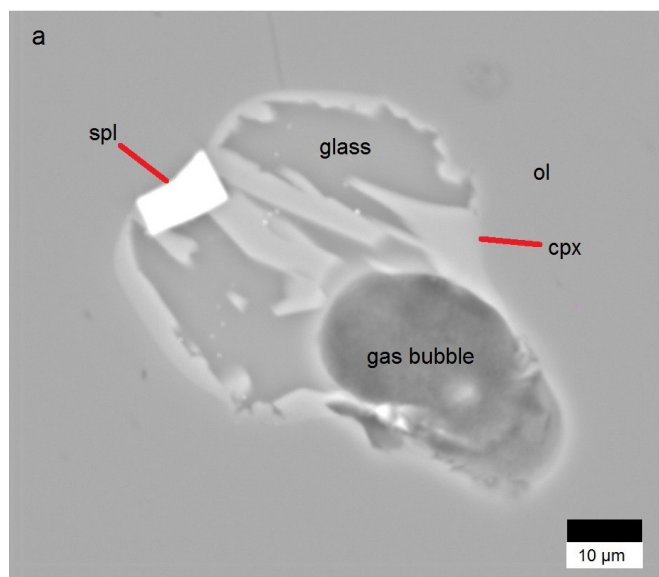
$$\text{V melt} = 319 - 5.96 \times \text{MgO melt}$$

We also used the average Sc/V ratio of rocks<sup>51</sup>. We did not use V concentrations and Sc/V ratios in the included melt because they were affected by crystallization of olivine and spinel in the inclusions.

**Contamination.** The compositions of trapped melts change with decreasing Fo content of host olivine, but do not follow olivine crystallization paths (Fig. 2). This suggests that contamination accompanies fractional crystallization. Melts trapped in the most Fo-rich olivine in the Pyke Hill sample are least affected by these processes. The most affected is melt inclusion 823-ol31, trapped in the least magnesian olivine in our Alexo flow sample. The amount of olivine crystallized between these two extremes is around 15 wt%. Because of energetic constraints, we assume that the amount of assimilated contaminant is less than the amount of crystallized olivine: between 5 wt% and 15 wt%, and 10 wt% on average. Using this assumption, and known compositions of uncontaminated and contaminated melts, we calculated the composition of the contaminant (Fig. 3a and Extended Data Table 1).

34. Sobolev, A. V. *et al.* The amount of recycled crust in sources of mantle-derived melts. *Science* **316**, 412–417 (2007).
35. Batanova, V. G., Sobolev, A. V. & Kuzmin, D. V. Trace element analysis of olivine: high precision analytical method for JEOL JXA-8230 electron probe microanalyser. *Chem. Geol.* **419**, 149–157 (2015).
36. Jochum, K. P. *et al.* MPI-DING reference glasses for in situ microanalysis: new reference values for element concentrations and isotope ratios. *Geochem. Geophys. Geosyst.* **7**, Q02008 (2006).
37. Batanova, V. G., Belousov, I. A., Savelieva, G. N. & Sobolev, A. V. Consequences of channelized and diffuse melt transport in supra-subduction mantle: evidence from Voykar ophiolite (Polar Urals). *J. Petrol.* **52**, 2483–2521 (2011).
38. Rosner, M. & Meixner, A. Boron isotopic composition and concentration of ten geological reference materials. *Geostand. Geoanal. Res.* **28**, 431–441 (2004).
39. Spivack, A. J. & Edmond, J. M. Determination of boron isotope ratios by thermal ionization mass-spectrometry of the dicesium metaborate cation. *Anal. Chem.* **58**, 31–35 (1986).
40. Sobolev, A. V. & Danyushevsky, L. V. Petrology and geochemistry of boninites from the North termination of the Tonga trench—constraints on the generation conditions of primary high-Ca boninite magmas. *J. Petrol.* **35**, 1183–1211 (1994).
41. Wallace, P. J., Kamenetsky, V. S. & Cervantes, P. Melt inclusion CO<sub>2</sub> contents, pressures of olivine crystallization, and the problem of shrinkage bubbles. *Am. Mineral.* **100**, 787–794 (2015).
42. Mironov, N. *et al.* Quantification of the CO<sub>2</sub> budget and H<sub>2</sub>O–CO<sub>2</sub> systematics in subduction-zone magmas through the experimental hydration of melt inclusions in olivine at high H<sub>2</sub>O pressure. *Earth Planet. Sci. Lett.* **425**, 1–11 (2015).
43. Danyushevsky, L. V., Sokolov, S. & Falloon, T. J. Melt inclusions in olivine phenocrysts: using diffusive re-equilibration to determine the cooling history of a crystal, with implications for the origin of olivine-phyric volcanic rocks. *J. Petrol.* **43**, 1651–1671 (2002).
44. Danyushevsky, L. V. & Plechov, P. Petrolog3: integrated software for modeling crystallization processes. *Geochem. Geophys. Geosyst.* **12**, Q07021 (2011).
45. Brown, P. E. FLINCOR: a microcomputer program for the reduction and investigation of fluid-inclusion data. *Am. Mineral.* **74**, 1390–1393 (1989).
46. Newman, S. & Lowenstern, J. B. VOLATILECALC: a silicate melt–H<sub>2</sub>O–CO<sub>2</sub> solution model written in Visual Basic for Excel. *Comput. Geosci.* **28**, 597–604 (2002).
47. Mallmann, G. & O'Neill, H. S. Calibration of an empirical thermometer and oxybarometer based on the partitioning of Sc, Y and V between olivine and silicate melt. *J. Petrol.* **54**, 933–949 (2013).
48. Coogan, L. A., Saunders, A. D. & Wilson, R. N. Aluminum-in-olivine thermometry of primitive basalts: evidence of an anomalously hot mantle source for large igneous provinces. *Chem. Geol.* **368**, 1–10 (2014).
49. Médard, E. & Grove, T. L. The effect of H<sub>2</sub>O on the olivine liquidus of basaltic melts: experiments and thermodynamic models. *Contrib. Mineral. Petrol.* **155**, 417–432 (2008).
50. Almeev, R. R., Holtz, F., Koepke, J., Parat, F. & Botcharnikov, R. E. The effect of H<sub>2</sub>O on olivine crystallization in MORB: experimental calibration at 200 MPa. *Am. Mineral.* **92**, 670–674 (2007).
51. Fan, J. & Kerrich, R. Geochemical characteristics of aluminum depleted and undepleted komatiites and HREE-enriched low-Ti tholeiites, Western Abitibi greenstone belt: A heterogeneous mantle plume convergent margin environment. *Geochim. Cosmochim. Acta* **61**, 4723–4744 (1997).
52. Mallmann, G. & O'Neill, H. S. C. The crystal/melt partitioning of V during mantle melting as a function of oxygen fugacity compared with some other elements (Al, P, Ca, Sc, Ti, Cr, Fe, Ga, Y, Zr and Nb). *J. Petrol.* **50**, 1765–1794 (2009).





**Extended Data Figure 1 | Melt inclusions in olivine from Abitibi belt komatiites.** **a**, Back-scattered electron image of partly crystallized (unheated) melt inclusion 823-th-ol8 in olivine (ol) of Alexo flow sample M823. The inclusion is composed of glass, quenched clinopyroxene (cpx), spinel (spl) and gas bubble. **b**, Heated and quenched melt inclusion

(810-7-ol1) in olivine from Pyke Hill komatiite sample M810. The inclusion contains glass, gas bubble and spinel. **c**, Heated and quenched melt inclusion (810-9-ol16) in olivine from Pyke Hill komatiite sample M810. The inclusion contains glass, gas bubble and spinel. **d**, Back-scattered electron image of the inclusion in **c**.

**Extended Data Table 1 | Representative and average compositions of olivine-hosted melt inclusions and primary melt of the Abitibi belt komatiites**

	810-7- ol1	810-7- ol3	810-4- ol1	810-6- ol20	810-7- ol2	823-8- ol31	P. Hill, Fo 94-94.5	26	Alexo, Fo 93-93.8	26	PM 1	26	PM 2	26	PM avg	26	Cont.
Size, $\mu\text{m}$	50	20	22	52	30	27	avg		avg		avg		avg		avg		model
SiO <sub>2</sub>	46.1	45.7	46.0	46.0	46.0	47.0	46.1	0.1	46.6	0.1	45.8	0.1	45.1	0.1	<b>45.4</b>	0.1	48.4
TiO <sub>2</sub>	0.30	0.30	0.31	0.29	0.28	0.51	0.30	0.01	0.37	0.01	0.29	0.01	0.27	0.01	<b>0.28</b>	0.01	2.0
Al <sub>2</sub> O <sub>3</sub>	6.7	7.5	6.8	6.6	6.6	9.0	7.0	0.1	7.6	0.1	6.5	0.1	5.9	0.1	<b>6.2</b>	0.1	20.5
Fe <sub>2</sub> O <sub>3</sub>	1.2	1.3	1.3	1.3	1.3	1.2	1.4	0.1	1.2	0.0	1.3	0.0	1.7	0.0	<b>1.5</b>	0.1	2.5
FeO	10.1	10.0	10.0	10.0	10.0	10.9	9.9	0.1	10.4	0.1	9.6	0.0	8.8	0.0	<b>9.2</b>	0.2	6.6
MnO	0.10	0.10	0.09	0.09	0.09	0.15	0.09	0.00	0.12	0.00	0.09	0.00	0.12	0.01	<b>0.11</b>	0.01	0.6
MgO	27.7	27.5	27.8	28.2	28.3	22.8	27.8	0.2	25.7	0.2	29.0	0.1	31.4	0.1	<b>30.2</b>	0.5	4.7
CaO	6.2	6.4	6.3	6.1	6.0	7.2	6.2	0.1	6.9	0.1	5.9	0.1	5.4	0.1	<b>5.7</b>	0.1	8.6
Na <sub>2</sub> O	0.56	0.68	0.55	0.58	0.54	1.05	0.56	0.01	0.66	0.02	0.53	0.01	0.47	0.01	<b>0.50</b>	0.02	4.7
K <sub>2</sub> O	0.015	0.031	0.012	0.010	0.012	0.084	0.013	0.001	0.032	0.010	0.012	0.001	0.010	0.001	<b>0.011</b>	0.001	0.7
P <sub>2</sub> O <sub>5</sub>	0.020	0.040	0.020	0.023	0.020	0.034	0.020	0.002	0.031	0.005	0.018	0.001	0.016	0.001	<b>0.017</b>	0.001	0.1
Cr <sub>2</sub> O <sub>3</sub>	0.24	0.21	0.24	0.25	0.24	0.20	0.24	0.01	0.22	0.01	0.24	0.01	0.22	0.01	<b>0.23</b>	0.01	
Cl	0.004	0.228	0.005	0.001	0.005	0.054	0.005	0.001	0.020	0.002	0.005	0.001	0.004	0.001	<b>0.004</b>	0.001	0.5
S	0.032	0.025	0.030	0.023	0.021	0.028	0.026	0.002	0.029	0.002	0.025	0.002	0.022	0.002	<b>0.023</b>	0.001	
H <sub>2</sub> Owt%	0.78	0.32	0.51	0.60	0.68		0.66*	0.10	0.17	0.02	0.62	0.06	0.53	0.05	<b>0.58</b>	0.06	
CO <sub>2</sub>	223		312	116	166		168*	84	222	126	173	74	204	95	<b>188</b>	61	
F	37	18	38	37	32		34*	5	48	3	29	5	22	2	<b>26</b>	4	382
S	434	184	467	467	337		413*	70	321	32	348	65	269	42	<b>308</b>	58	
Cl	74	1785	64	67	64		73*	14	214	15	61	12	47	11	<b>54</b>	12	
B				0.18			0.18	0.01	0.46	0.02	0.17	0.01	0.15	0.01	<b>0.16</b>	0.02	
Sc	26.0	26.2	25.9	25.6	25.6	29.6	25.9	0.2	27.7	0.2	24.5	0.1	22.7	0.1	<b>23.6</b>	0.4	13
V	154	155	153	150	150	183	153	2	167	2	144	0	130	0	<b>137</b>	3	173
Cu	37		25	29	25	72	26	3	44	4	24	3	22	3	<b>23</b>	2	422
Rb	0.1		0.2	0.2	0.2	2.3	0.20	0.03	0.62	0.04	0.19	0.02	0.17	0.02	<b>0.18</b>	0.02	19
Sr	16.2		16.6	15.9	15.0	45.2	16.4	0.6	24.4	1.0	15.5	0.5	14.0	0.5	<b>14.7</b>	0.5	253
Y	7.4	7.5	7.3	7.2	7.2	9.0	7.3	0.11	8.1	0.10	6.9	0.02	6.2	0.04	<b>6.6</b>	0.18	10.6
Zr	12.4		12.1	12.7	12.6	30.9	13.1	0.8	18.4	0.3	12.4	0.7	11.2	0.7	<b>11.8</b>	0.5	154
Nb	0.27		0.28	0.33	0.29	1.3	0.30	0.02	0.51	0.04	0.28	0.01	0.26	0.01	<b>0.27</b>	0.01	8.6
Ba	2.74		2.46	2.45	2.37	66.4	2.44	0.16	8.01	0.51	2.31	0.13	2.09	0.12	<b>2.20</b>	0.10	582
La	0.32		0.27	0.28	0.34	1.7	0.30	0.02	0.64	0.02	0.29	0.02	0.26	0.02	<b>0.27</b>	0.01	12.4
Ce	1.05		0.93	0.99	0.94	4.1	0.98	0.05	1.85	0.07	0.93	0.05	0.84	0.04	<b>0.89</b>	0.04	27.9
Nd	1.29		1.22	1.23	1.04	3.2	1.20	0.07	1.88	0.11	1.14	0.06	1.03	0.06	<b>1.09</b>	0.05	17.2
Sm	0.64		0.44	0.69	0.58	1.2	0.55	0.06	0.66	0.06	0.52	0.06	0.47	0.05	<b>0.50</b>	0.04	5.8
Eu	0.21		0.21	0.25	0.22	0.4	0.22	0.01	0.29	0.02	0.21	0.01	0.19	0.01	<b>0.20</b>	0.01	1.9
Gd	0.82		0.63	0.86	0.80	1.7	0.89	0.12	1.14	0.07	0.84	0.11	0.76	0.10	<b>0.80</b>	0.07	6.5
Dy	1.14		1.04	1.43	1.32	2.1	1.29	0.10	1.41	0.11	1.22	0.10	1.11	0.09	<b>1.17</b>	0.07	6.2
Er	0.77		0.51	0.77	0.62	1.2	0.75	0.08	0.97	0.04	0.71	0.08	0.64	0.07	<b>0.67</b>	0.06	3.3
Yb	0.91		0.89	0.51	0.71	1.2	0.81	0.08	0.97	0.07	0.77	0.08	0.70	0.07	<b>0.73</b>	0.05	3.1
Pb					0.09	0.1	0.06	0.02	0.08	0.01	0.06	0.02	0.05	0.02	<b>0.05</b>	0.01	0.7
T Sc/Y	1482	1497	1542	1517	1530	1442	1505	20	1484	14	1523	20	1523	20	<b>1523</b>	14	
T Fe/Mg	1484	1501	1494	1496	1495		1488	10	1482	10	1506	10	1558	10	<b>1532</b>	10	
Fo (host)	94.1	94.2	94.2	94.4	94.4	92.4	94.3	0.1	93.5	0.2	94.7		94.7		<b>94.7</b>		

All compositions were corrected for host olivine crystallization, Fe–Mg exchange with host olivine and CO<sub>2</sub> loss to the shrinkage gas bubble. See Methods for details. The Fe–Mg olivine–melt partition was calculated after ref. 20, (except PM2 and PM avg, see below). The extremely Cl-rich inclusion (810-7-ol3) and the contaminated inclusion (823-8-ol31) have been excluded from the averages. T Sc/Y and T Fe/Mg are temperatures in degrees Celsius calculated using the models in ref. 47 and ref. 20, respectively (except PM2 and PM avg, see below). PM1, average primary melt for the Pyke Hill calculated using the model in ref. 20; PM2, average primary melt for the Pyke Hill calculated using the model in ref. 21; PM avg, average composition of all primary melts calculated by both models<sup>20,21</sup>. Cont., composition of the contaminant (see Methods). \*Average values calculated for inclusions with diameters larger or equal to 30  $\mu\text{m}$ .

# Boreal and temperate trees show strong acclimation of respiration to warming

Peter B. Reich<sup>1,2</sup>, Kerrie M. Sendall<sup>1</sup>, Artur Stefanski<sup>1</sup>, Xiaorong Wei<sup>1,3</sup>, Roy L. Rich<sup>1,4</sup> & Rebecca A. Montgomery<sup>1</sup>

Plant respiration results in an annual flux of carbon dioxide (CO<sub>2</sub>) to the atmosphere that is six times as large as that due to the emissions from fossil fuel burning, so changes in either will impact future climate. As plant respiration responds positively to temperature, a warming world may result in additional respiratory CO<sub>2</sub> release, and hence further atmospheric warming<sup>1,2</sup>. Plant respiration can acclimate to altered temperatures, however, weakening the positive feedback of plant respiration to rising global air temperature<sup>3–7</sup>, but a lack of evidence on long-term (weeks to years) acclimation to climate warming in field settings currently hinders realistic predictions of respiratory release of CO<sub>2</sub> under future climatic conditions. Here we demonstrate strong acclimation of leaf respiration to both experimental warming and seasonal temperature variation for juveniles of ten North American tree species growing for several years in forest conditions. Plants grown and measured at 3.4 °C above ambient temperature increased leaf respiration by an average of 5% compared to plants grown and measured at ambient temperature; without acclimation, these increases would have been 23%. Thus, acclimation eliminated 80% of the expected increase in leaf respiration of non-acclimated plants. Acclimation of leaf respiration per degree temperature change was similar for experimental warming and seasonal temperature variation. Moreover, the observed increase in leaf respiration per degree increase in temperature was less than half as large as the average reported for previous studies<sup>4,7</sup>, which were conducted largely over shorter time scales in laboratory settings. If such dampening effects of leaf thermal acclimation occur generally, the increase in respiration rates of terrestrial plants in response to climate warming may be less than predicted, and thus may not raise atmospheric CO<sub>2</sub> concentrations as much as anticipated.

Rising global temperatures (of 1.1–6.4 °C by 2100) will probably result in a positive terrestrial feedback to the global carbon cycle, because respiratory flux to the atmosphere from soils and plants is anticipated to increase more with warming than is the rate of gross primary production (GPP)<sup>5,6</sup>. Respiration in terrestrial plants releases approximately 64 Gt of carbon each year to the atmosphere (~six times the amount of fossil fuel emissions), directly offsetting roughly half of the GPP of terrestrial ecosystems<sup>5,6</sup>, so even a small fractional change in total plant respiration with climate warming could be important for both global net productivity and the carbon content of the atmosphere. If long-term net respiratory fluxes from terrestrial ecosystems follow the near-exponential short-term relationship of respiration to temperature<sup>3</sup>, climate warming will trigger a sharp increase in ecosystem respiration. Such an increase in CO<sub>2</sub> release would probably be greater than the offsetting increase in GPP, because GPP tends to show a saturating, hump-shaped response to rising temperature. This would result in a heightened net CO<sub>2</sub> release from terrestrial ecosystems, and further atmospheric warming<sup>1,2</sup>.

Plants, however, can dynamically adjust the response of respiration to temperature over the long term (weeks to years), even though plant respiration always shows an accelerating increase when subjected to a short-term (minutes to hours) increase in temperature. Typically, a plant that has experienced warmer temperatures will have a lower rate of respiration at a standardized measurement temperature than a plant that has experienced cooler temperatures (Extended Data Fig. 1). This process is labelled thermal acclimation<sup>3,4,7</sup>. The greater the thermal acclimation of respiration globally, the smaller the positive feedback between climate warming and ecosystem CO<sub>2</sub> release<sup>3,7,8</sup>. Thermal acclimation of plant respiration has been noted in most, but not all, cases studied<sup>3,7–13</sup>, but the degree of acclimation is extremely uncertain<sup>3,7–13</sup>, especially for plants in natural settings. Such information will be crucial for making better predictions of terrestrial feedbacks<sup>14,15</sup>. The need for ecologically realistic acclimation generalizations is clear, because current state-of-the-art models<sup>16,17</sup> predict acclimation based on a study of first-year seedlings grown for 2–3 months at constant 7, 14, 21 and 28 °C conditions in growth cabinets<sup>4</sup>. Hence, observations of acclimation of plants grown in more realistic field settings (for as long as 5 years), as presented here, should provide a meaningful advance.

High latitude boreal and temperate forests account for approximately one-third of Earth's total forest area, and have an important role in terrestrial carbon cycling<sup>4,5,13–15</sup>. To advance understanding of carbon cycling in a changing climate, we assessed the acclimation capacity of more than 1,200 individuals of 10 dominant North American tree species grown in ambient and warmed (+3.4 °C) plots in a free-air warming experiment<sup>18,19</sup>. We present the results of 1,620 leaf respiration–temperature response curves<sup>3,20–22</sup> made from 2009 to 2013 in both open and understory forest habitats at two sites (~150 km apart) at the boreal–temperate forest ecotone in Minnesota, USA. Species were measured in three ( $n=4$ ), four ( $n=2$ ) or all five ( $n=4$ ) years. Temperatures measured for each response curve ranged from 12 to 37 °C in 5-degree intervals (see Methods). Because the shape of the short-term temperature response curves did not vary with warming treatment for any of the species (see later), comparing the curves of plants from warmed and ambient treatments enables assessment of the magnitude of thermal acclimation in response to experimental warming. Additional information is gained by comparing the curves of plants measured at different times during the growing season; that is, assessing how much lower leaf respiration is at a given measurement temperature in a warm spell compared to a cold spell.

We focus on the magnitude of acclimation induced by experimental warming as well as the magnitude of acclimation comparing warmer to cooler time periods. For example, if a plant grown at 20 °C increased leaf respiration ( $R_{\text{leaf}}$ ) by 40% after being moved to 25 °C for 30 min, but had the same rate after 3 weeks at 25 °C as initially when grown and measured at 20 °C, it would have completely (100%) acclimated

<sup>1</sup>Department of Forest Resources, University of Minnesota, Minnesota 55108, USA. <sup>2</sup>Hawkesbury Institute for the Environment, Western Sydney University, Penrith, New South Wales 2753, Australia. <sup>3</sup>State Key Laboratory of Soil Erosion and Dryland Farming on the Loess Plateau, Northwest A&F University, Yangling 712100, China. <sup>4</sup>Smithsonian Environmental Research Center, Edgewater, Maryland 20137, USA.



(see Extended Data Fig. 1a, equivalent to homeostatic acclimation)<sup>7</sup>. If the rate after 3 weeks at 25 °C had increased, but by less than 40% compared to the plant grown and measured at 20 °C, this would represent partial acclimation (Extended Data Fig. 1b). Thus, an acclimated plant will eliminate some or all of the increase in  $R_{\text{leaf}}$  with rising temperature expected of non-acclimated plants.

We compare acclimation responses between experimental and natural seasonal temperature variation, boreal and temperate species, and angiosperm and gymnosperm species. On the basis of previous research<sup>3,7,9–13,23,24</sup>, we expected to observe partial acclimation (of ~30–50%) that would be similar across species in response to both experimental and temporal temperature variation. We also anticipated that boreal species, which experience a greater temperature range in their native higher-latitude distributions, would show a greater acclimation than temperate species.

Calculating entire respiratory temperature response curves (rather than measurements at a single temperature) for all sampled leaves enabled us to discern whether the shape of the short-term response varies with thermal environment, or whether the elevation of the entire curve shifts over time as experienced temperatures vary. We tested five models to establish the best equation for quantifying  $R_{\text{leaf}}$  as a function of short-term leaf temperature variation (see Methods). Across all 1,620 curves, all models provided good fits. Exponential equations with a fixed  $Q_{10}$  coefficient (that describes the proportional change in  $R_{\text{leaf}}$  with a 10 °C temperature increase) and an Arrhenius model worked well (median  $R^2 = 0.95$ , Extended Data Table 1). By contrast, adding temperature-sensitivity did not improve the Arrhenius model, and two other temperature-sensitive models (a log-polynomial<sup>20</sup> and a Michaelis-Menton approach<sup>21</sup>) did not consistently show their expected decelerating forms (see Methods and Extended Data Table 1). Given that fits were best described as exponential, we present the data using the  $Q_{10}$  approach; however, results are similar if any of the other models are used.

The  $Q_{10}$  value differed among species, but was unaffected by experimental warming, as there were no differences in  $Q_{10}$  across the warming treatments for any of the 10 species studied (Extended Data Fig. 2 and Table 1). Thus, to assess acclimation for each species, we compared  $R_{\text{leaf}}$  at a standardized measurement temperature, which represents the overall elevation of each curve, given consistent  $Q_{10}$  values. We chose standard leaf temperatures of 20 °C and 23.4 °C, and derived respiration rates at those temperatures ( $R_{20}$  and  $R_{23.4}$ , respectively) for each temperature response curve. We chose 20 °C as a typical standard for comparing respiration rates<sup>7,13,25</sup>, and 23.4 °C because it represents the average temperature above that standard due to the warming treatment<sup>18,19,26</sup>.

We also assessed the acclimation response to seasonal variation in temperature by examining  $R_{20}$  in relation to the mean night-time temperature for the 5 nights before the measurement date. We chose this rather than the previous 10-day period<sup>4,16,17</sup>, as evidence suggests acclimation can occur within a few days of temperature shifts<sup>10,23,24</sup>, hence our response curves are perhaps more representative of leaf physiological status over the previous 5-day than 10-day period. Nonetheless, acclimation was similar (in fact, slightly stronger) if the previous 10-night mean temperature was used, and the results are not dependent on this choice.

Across species and sites, plants in the +3.4 °C treatment had significantly lower  $R_{20}$  values than ambient-grown plants (Extended Data Fig. 3 and Table 1), indicating acclimation to increased growth temperature<sup>3,7</sup>. The best statistical model included only treatment and species (see Methods), as the response to warming treatment did not differ with site (site  $\times$  warming,  $P = 0.74$ ; site  $\times$  species  $\times$  warming,  $P = 0.69$ ). Species differed in their average  $R_{20}$  value, but the acclimation response to experimental warming did not differ significantly among species (Table 1), sites or species groupings (boreal/temperate; angiosperm/gymnosperm). Differences between ambient and warmed plants were similar if other metrics (for example,  $R_{\text{leaf}}$  measured at 25 °C) were used, or if  $R_{\text{leaf}}$  was estimated using temperature response functions from the alternative models (for example, Methods and Extended Data Figs 4 and 5).

As a result of this strong acclimation (Extended Data Fig. 3), individuals in each species grown in the +3.4 °C warming treatment had leaf respiration rates at 23.4 °C that were generally not notably greater than those of ambient-grown plants measured at 20.0 °C (Fig. 1). In fact, on average across species, plants grown in the +3.4 °C warming treatment had leaf respiration rates at 23.4 °C that were just 5% higher ( $\pm 2\%$  s.e.m. among species) on average than those measured at 20.0 °C for untreated plants (Fig. 2). By contrast, non-acclimated ambient-grown plants had rates at 23.4 °C that were 23% higher ( $\pm 1\%$  s.e.m. among species) on average than at 20.0 °C (Figs 1 and 2). Thus, thermal acclimation of warmed plants eliminated roughly 80% of the increase in leaf respiration expected of non-acclimated plants (see below).

Shifts in  $R_{20}$  in relation to seasonal variation in temperature (Fig. 3) also demonstrated strong acclimation that was consistent with shifts in  $R_{20}$  in response to warming treatments. This acclimation was statistically examined by evaluating the  $R_{20}$  response to prior 5-night mean temperature, warming treatment and species. The prior 5-night mean temperature was significant, whereas warming treatment was not, because the prior 5-night temperature metric fully accounted for its impact (Table 1). Thus, all 10 species showed pronounced acclimation of  $R_{20}$  to recently experienced temperatures (Fig. 3). The slopes of  $R_{20}$  versus recent temperatures did not differ between boreal and

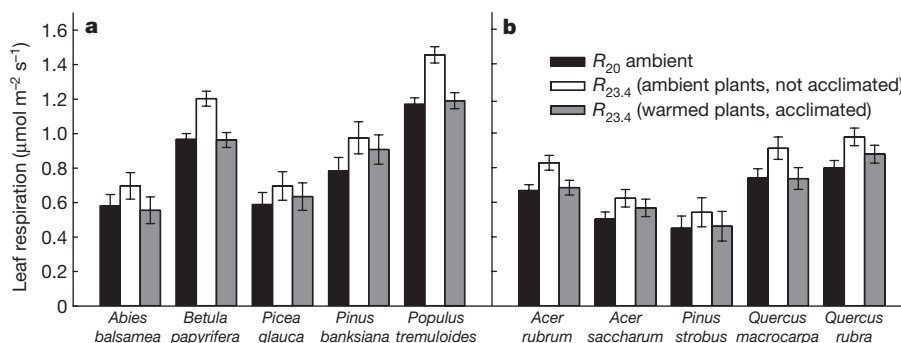


**Figure 1 | Leaf dark respiration rate of ambient and experimentally warmed plants. a, b,** Data are from five boreal (a) and five temperate (b) tree species. Respiration is shown at measurement temperatures of 20 °C and 23.4 °C for ambient-grown plants; respiration for plants grown at +3.4 °C conditions is shown at a measurement temperature of 23.4 °C. The two values for ambient plants show the increase in respiration with a +3.4 °C temperature increase for non-acclimated plants; comparison of

ambient plants measured at 20 °C with warmed plants measured at 23.4 °C represents the increase in respiration with a +3.4 °C temperature increase for acclimated plants. Sample size by warming treatment and biome type (boreal, ambient = 363; boreal, warmed = 380; temperate, ambient = 434; temperate, warmed = 443). Data are mean and s.e.m. (s.e.m. values are from the full model).

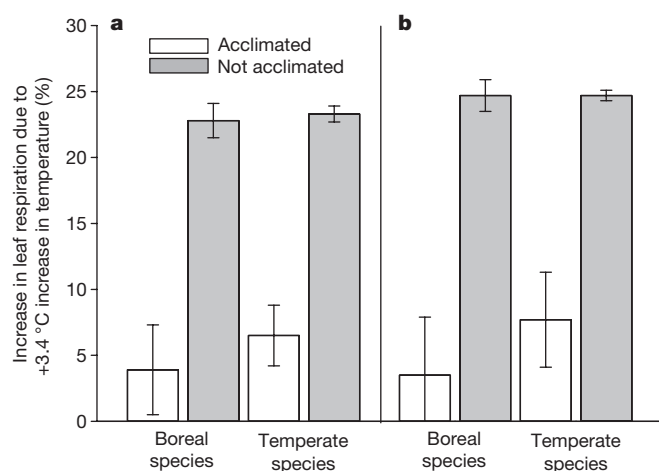


**Figure 2 | Increase in leaf dark respiration ( $R_{\text{leaf}}$ ) with +3.4°C warming for acclimated and non-acclimated plants, among species, by biome of the species. a, b, Increase in  $R_{\text{leaf}}$  is shown on a percentage basis in response to both experimental warming (a) and seasonal temperature variation (b). For acclimated plants, response is calculated as:  $((R_{\text{leaf}}$  of warmed plants at 23.4°C per  $R_{\text{leaf}}$  of ambient plants at 20.0°C)  $\times$  100. For non-acclimated plants, response is:  $((R_{\text{leaf}}$  of ambient plants at 23.4°C per  $R_{\text{leaf}}$  of ambient plants at 20.0°C)  $\times$  100. Sample sizes are as in Fig. 1. Data are mean and s.e.m. (s.e.m. among species, by biome group and treatment).**

temperate species, but were significantly steeper on average for the four gymnosperms than the six angiosperms (Methods and Extended Data Table 2).

On the basis of the species responses to seasonal temperature variation, plants that had experienced recent night temperatures of 23.4°C would be expected to have  $R_{\text{leaf}}$  at 23.4°C that was just 6% higher ( $\pm 3\%$  s.e.m. among species) on average than  $R_{\text{leaf}}$  at 20.0°C for plants recently experiencing 20.0°C nights (Fig. 2). By contrast, without acclimation (that is, for a plant that recently experienced 20.0°C nights), rates at 23.4°C would be 25% ( $\pm 1\%$  s.e.m. among species) higher on average than at 20.0°C. Those acclimation responses to seasonal temperature variation were very similar to those noted above for plants acclimated to +3.4°C experimental warming. In other words, the differences in growth temperatures due to experimental warming had the same effect on  $R_{\text{leaf}}$  value at any given measurement temperature as the changes in the prior 5-night temperature of the same extent. Thus, acclimation to temperature as it varied across time was similar to acclimation to experimental warming. If extrapolated to a 10°C shift in temperature, acclimation would result in realized long-term (or 'apparent')  $Q_{10}$  value of  $\sim 1.2$ , despite a short-term  $Q_{10}$  of  $\sim 1.9$ .

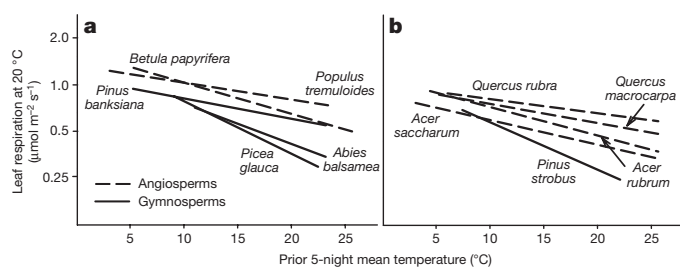


**Figure 3 | Relationship between leaf dark respiration measured at 20°C and the prior 5-night mean temperature, across seasons and years. a, b, Data are for five boreal (a) and five temperate (b) tree species. Sample sizes are as in Fig. 1. Data are the best fit regressions between the logarithm of  $R_{20}$  and the prior 5-night mean temperature per species, using data from both ambient and warmed treatments. Angiosperms and gymnosperms differed in slope ( $P < 0.05$ ), but species within each group did not. Resultant species-specific equations are shown in Extended Data Table 2.**

**Table 1 |  $Q_{10}$  and  $R_{20}$  in relation to +3.4°C warming and species**

Source of variance	$Q_{10}$		$R_{20}$		$R_{20}$ , 5-night T	
	F	P>F	F	P>F	F	P>F
Species	4.66	<0.0001	57.07	<0.0001	40.89	<0.0001
Treatment	0.66	0.4199	11.53	0.0012	2.59	0.1119
Species $\times$ treatment	1.09	0.3646	0.76	0.6557	1.17	0.3127
5-night T					38.95	<0.0001
5-night T $\times$ species					2.48	0.0081
5-night T $\times$ treatment					0.01	0.9265
5-night T $\times$ species $\times$ treatment					0.34	0.9626
Full model $R^2$	0.10		0.43		0.45	

Summaries of analysis of variance for  $Q_{10}$  (exponent of short-term temperature response function) and  $R_{20}$  (respiration rate at standard measurement temperature of 20°C) are shown in relation to +3.4°C warming treatment and species. Also shown is the model for  $R_{20}$  that includes the prior 5-night mean temperature (5-night T) and associated interactions. All models significant at  $P < 0.0001$ . F indicates the F-ratio used in the F-test of the significance of each factor or interaction among factors. Data for 10 species ( $n = 1,620$ ).  $R_{20}$  was log<sub>10</sub>-transformed before analyses.

We also assessed percentage acclimation, a measure of how much of the respiratory increase expected due to short-term (minutes to hours) warming is eliminated by physiological adjustment of plants warmed by the same extent but for weeks or months. We quantified this acclimation for plants in response to warming treatment by contrasting the difference between the  $R_{23.4}$  of plants in the +3.4°C treatment and the  $R_{20}$  of those in ambient conditions with the difference between the  $R_{23.4}$  and  $R_{20}$  of plants in ambient conditions (Fig. 1; see Methods for equation). The mean percentage acclimation to experimental warming across species was 78.2% ( $\pm 7.7$  s.e.m. among species), and the mean percentage acclimation to the 5-prior night temperature was 80.9  $\pm$  9.5% (Extended Data Fig. 6).

Given the close coupling of respiration and photosynthesis<sup>13,21,27,28</sup>, shifts in leaf respiration of plants growing under different thermal conditions could result from temperature-related shifts in photosynthesis<sup>14</sup>. Previous work with seedlings has found the ratio of leaf respiration to photosynthesis ( $R:P$ ) to be stable in some cases, but to increase with growth temperature in others<sup>14</sup>. Data from our multi-year experiment indicate that the acclimation of  $R_{\text{leaf}}$  did not result from (or result in) a stable  $R:P$  ratio, because for all 10 species,  $R:P$  was higher in warmer conditions, whether seasonal or experimental (Methods). However, without acclimation,  $R:P$  would have been much more increased at higher mean daily temperatures compared to what was observed. Hence our results suggest that acclimation is part of a process that limits the size of the 'window' within which  $R:P$  varies, but does not support the idea of a complete homeostasis of  $R:P$ . Statistical analyses also showed that the response to warming treatment of  $Q_{10}$ , or  $R_{20}$ , could not be explained by concomitant shifts in photosynthesis (Methods).

As respiration in terrestrial plants (including root, stem and leaf fluxes) releases  $\sim 64$  Gt of carbon per year to the atmosphere, offsetting  $\sim 50\%$  of terrestrial GPP<sup>5,6,16,17</sup>, autotrophic respiration and its acclimation to rising temperature are crucial to the global carbon balance<sup>5,6</sup>. Our experimental results are informative relative to this issue.

Our results demonstrated strong acclimation of leaf respiration to both a +3.4°C warming and seasonal temperature increases, which profoundly reduced plant respiratory carbon loss compared to what would have occurred without acclimation. A recent meta-analysis<sup>7</sup>, based largely on short-term studies of laboratory grown plants, found acclimation to be less than half as great as we observed (see Methods for details). Moreover, earth system models<sup>14–17</sup> typically simulate even weaker levels of acclimation, or none at all. For example, two recent modelling papers<sup>16,17</sup> based their acclimation routines on data from first-year seedlings in laboratory settings that showed  $\sim 30\%$  respiration acclimation<sup>4</sup>. Despite this more modest acclimation than we observed here, acclimation alone still resulted in a 10% change in simulated global carbon stocks compared to a model that assumed no

leaf respiration acclimation<sup>17</sup>. Given that we observed a much greater (~80%) acclimation of respiration, our results suggest that high latitude forests may show a more pronounced leaf respiration acclimation than expected<sup>4,7,13</sup> to increasing growing season temperatures associated with climate change.

If our realistic, long-term field results are broadly indicative, they suggest that leaf respiratory acclimation globally may have a larger ameliorating impact than expected on CO<sub>2</sub> losses with rising temperatures as climate changes. Such amelioration would be even larger if stems and roots showed similar acclimation as leaves, but whether this is so is highly uncertain owing to a scarcity of available data. Our results contribute to current efforts to improve the characterization and incorporation of thermal acclimation of respiration in land surface models<sup>14,17</sup> by providing robust field evidence on the nature and magnitude of leaf respiratory acclimation, thus aiding future models in improving estimates of respiratory acclimation in a changing climate, and of the consequences of acclimation for carbon cycling.

**Online Content** Methods, along with any additional Extended Data display items and Source Data, are available in the online version of the paper; references unique to these sections appear only in the online paper.

**Received 7 September 2015; accepted 18 January 2016.**

**Published online 16 March 2016.**

- Cox, P. M., Betts, R. A., Jones, C. D., Spall, S. A. & Totterdell, I. J. Acceleration of global warming due to carbon-cycle feedbacks in a coupled climate model. *Nature* **408**, 184–187 (2000).
- Heimann, M. & Reichstein, M. Terrestrial ecosystem carbon dynamics and climate feedbacks. *Nature* **451**, 289–292 (2008).
- Atkin, O. K. & Tjoelker, M. G. Thermal acclimation and the dynamic response of plant respiration to temperature. *Trends Plant Sci.* **8**, 343–351 (2003).
- Campbell, C. *et al.* Acclimation of photosynthesis and respiration is asynchronous in response to changes in temperature regardless of plant functional type. *New Phytol.* **176**, 375–389 (2007).
- Arneth, A. *et al.* Terrestrial biogeochemical feedbacks in the climate system. *Nature Geosci.* **3**, 525–532 (2010).
- Intergovernmental Panel on Climate Change. *Climate Change 2013: The Physical Science Basis* (Cambridge Univ. Press, 2013).
- Slot, M. & Kitajima, K. General patterns of acclimation of leaf respiration to warmer temperatures across biomes and plant types. *Oecologia* **177**, 885–900 (2015).
- Luo, Y. Terrestrial carbon-cycle feedback to climate warming. *Annu. Rev. Ecol. Evol. Syst.* **38**, 683–712 (2007).
- Gunderson, C. A., Norby, R. J. & Wullschlegel, S. D. Acclimation of photosynthesis and respiration to simulated climatic warming in northern and southern populations of *Acer saccharum*: laboratory and field evidence. *Tree Physiol.* **20**, 87–96 (2000).
- Lee, T. D., Reich, P. B. & Bolstad, P. V. Acclimation of leaf respiration to temperature is rapid and related to specific leaf area, soluble sugars and leaf nitrogen across three temperate deciduous tree species. *Funct. Ecol.* **19**, 640–647 (2005).
- Loveys, B. R. *et al.* Thermal acclimation of leaf and root respiration: an investigation comparing inherently fast- and slow-growing plant species. *Glob. Change Biol.* **9**, 895–910 (2003).
- Slot, M. *et al.* Thermal acclimation of leaf respiration of tropical trees and lianas: response to experimental canopy warming, and consequences for tropical forest carbon balance. *Glob. Chang. Biol.* **20**, 2915–2926 (2014).
- Tjoelker, M. G., Oleksyn, J., Reich, P. B. & Zytowski, R. Coupling of respiration, nitrogen, and sugars underlies convergent temperature acclimation in *Pinus banksiana* across wide-ranging sites and populations. *Glob. Change Biol.* **14**, 782–797 (2008).
- Smith, N. G. & Dukes, J. S. Plant respiration and photosynthesis in global-scale models: incorporating acclimation to temperature and CO<sub>2</sub>. *Glob. Chang. Biol.* **19**, 45–63 (2013).
- Atkin, O. K., Meir, P. & Turnbull, M. H. Improving representation of leaf respiration in large-scale predictive climate-vegetation models. *New Phytol.* **202**, 743–748 (2014).
- Smith, N. G. *et al.* Foliar temperature acclimation reduces simulated carbon sensitivity to climate. *Nature Clim. Change* <http://dx.doi.org/10.1038/nclimate2878> (2016).
- Lombardo, D. L. *et al.* Temperature acclimation of photosynthesis and respiration: A key uncertainty in the carbon cycle-climate feedback. *Geophys. Res. Lett.* **42**, 8624–8631 (2015).
- Reich, P. B. *et al.* Geographic range predicts photosynthetic and growth response to warming in co-occurring tree species. *Nature Clim. Change* **5**, 148–152 (2015).
- Rich, R. L. *et al.* Design and performance of combined infrared canopy and belowground warming in the B4WarmED (Boreal Forest Warming at an Ecotone in Danger) experiment. *Glob. Chang. Biol.* **21**, 2334–2348 (2015).
- O'Sullivan, O. S. *et al.* High-resolution temperature responses of leaf respiration in snow gum (*Eucalyptus pauciflora*) reveal high-temperature limits to respiratory function. *Plant Cell Environ.* **36**, 1268–1284 (2013).
- Kruse, J., Rennenberg, H. & Adams, M. A. Steps towards a mechanistic understanding of respiratory temperature responses. *New Phytol.* **189**, 659–677 (2011).
- Tjoelker, M. G., Oleksyn, J. & Reich, P. B. Modelling respiration of vegetation: evidence for a general temperature-dependent Q<sub>10</sub>. *Glob. Change Biol.* **7**, 223–230 (2001).
- Atkin, O. K., Holly, C. & Ball, M. C. Acclimation of snow gum (*Eucalyptus pauciflora*) leaf respiration to seasonal and diurnal variations in temperature: the importance of changes in the capacity and temperature sensitivity of respiration. *Plant Cell Environ.* **23**, 15–26 (2000).
- Bolstad, P. V., Reich, P. B. & Lee, T. D. Rapid temperature acclimation of leaf respiration rates in *Quercus alba* and *Quercus rubra*. *Tree Physiol.* **23**, 969–976 (2003).
- Reich, P. B. *et al.* Scaling of respiration to nitrogen in leaves, stems, and roots of higher land plants. *Ecol. Lett.* **11**, 793–801 (2008).
- Sendall, K. M. *et al.* Acclimation of photosynthetic temperature optima of temperate and boreal tree species in response to experimental warming. *Glob. Chang. Biol.* **21**, 1342–1357 (2015).
- Katja, H. *et al.* Temperature responses of dark respiration in relation to leaf sugar concentration. *Physiol. Plant.* **144**, 320–334 (2012).
- Ow, L. F., Griffin, K. L., Whitehead, D., Walcroft, A. S. & Turnbull, M. H. Thermal acclimation of leaf respiration but not photosynthesis in *Populus deltoides* × *nigra*. *New Phytol.* **178**, 123–134 (2008).

**Acknowledgements** This research was supported by the US Department of Energy, Office of Science, Office of Biological and Environmental Research award DE-FG02-07ER64456; Minnesota Agricultural Experiment Station MIN-42-030 and MIN-42-060; the Minnesota Department of Natural Resources; and the College of Food, Agricultural, and Natural Resources Sciences and Wilderness Research Foundation, University of Minnesota. Assistance with experimental operation and data collection was provided by K. Rice, C. Buschena, C. Zhao, H. Jihua and numerous summer interns.

**Author Contributions** P.B.R., R.A.M. and R.L.R. designed the study. R.L.R. designed the warming system. R.L.R. and A.S. implemented the warming system and A.S., K.M.S. and X.W. the day-to-day field measurements. P.B.R. analysed the data. P.B.R. wrote the first draft and along with the other co-authors jointly wrote the manuscript.

**Author Information** Reprints and permissions information is available at [www.nature.com/reprints](http://www.nature.com/reprints). The authors declare no competing financial interests. Readers are welcome to comment on the online version of the paper. Correspondence and requests for materials should be addressed to P.R. ([preich@umn.edu](mailto:preich@umn.edu)).



## METHODS

**Site description and experimental design.** This study was conducted in an open-air climate change facility (the Boreal Forest Warming at an Ecotone in Danger (B4WarmED) project) in northern Minnesota, USA. The details of the study sites and experimental design are described elsewhere<sup>18,19,26</sup>. The experiment used here had a 2 (site) × 2 (habitat) × 2 (warming treatment) factorial design with six replicates, for a total of 48 circular plots 3-m in diameter. We sampled juveniles of 10 native tree species from the 11 per species planted into each plot in 2008 into a matrix of native shrubs and herbs. The treatments were ambient versus +3.4 °C above ambient (both below and above ground) and were implemented 24 h per day for 8–9 months per year<sup>19</sup>.

**Measurement of leaf respiration temperature response curve and data analysis overview.** Temperature response curves (1,620) of leaf respiration were measured at both field sites from June–September each year and across the years 2009–2013. Measurements were made using detached foliage sampled from ambient and warmed plots<sup>26</sup>. Respiration temperature response curves were developed based on measurements at 12, 17, 22, 27, 32 and 37 °C. Dark respiration rates of detached leaves are stable under these conditions for several hours or longer<sup>12,24</sup>.

Comparisons among five models showed that fixed  $Q_{10}$  and Arrhenius models provided the most reasonable statistical approach for fitting short-term respiration–temperature response curves; moreover, the fixed  $Q_{10}$  and Arrhenius models yielded virtually identical predictions,  $R^2 > 0.99$  (see Extended Data Table 1 and Extended Data Figs 7 and 8 for more details). We therefore report only the following parameters: the  $Q_{10}$  of the temperature response function of each leaf, and the respiration rate at standard measurement temperatures of 20.0 °C ( $R_{20}$ ) and 23.4 °C ( $R_{23.4}$ ), calculated from the temperature response equation for every leaf.

The  $R_T$  was calculated as:

$$R_T = R_{T_{ref}} Q_{10} \left( \frac{T - T_{ref}}{10} \right) \quad (1)$$

in which  $R_T$  is the dark respiration measured at leaf temperature  $T$ ,  $R_{T_{ref}}$  is the respiration at reference temperature  $T_{ref}$ , and  $Q_{10}$  is a metric that describes the proportional increase of respiration rate with a 10 °C increase in temperature.

We calculated respiration rates at measurement temperatures of 20.0 and 23.4 °C for both ambient and experimentally warmed treatments ( $R_{20 \text{ ambient}}$ ,  $R_{23.4 \text{ ambient}}$  and  $R_{23.4 \text{ warmed}}$ ) using equation (1). We chose to show values at measurement temperatures of 20 and 23.4 °C as they represent a temperature (20 °C) that has been commonly used in other studies, and a temperature (23.4 °C) representing the difference due to our warming treatment. These were used in statistical analyses and to calculate percentage acclimation.

Mixed-effect analyses of variance were conducted to compare  $Q_{10}$  and  $R_{20}$  values across species, warming treatment, and sites.  $R_{20}$  was log-transformed for statistical analyses to meet assumptions of normality and homoscedasticity of residuals better. Comprehensive sampling of three of the species across warming treatments, sites, years, seasons and habitat, found minimal difference in acclimation response to warming among sites, years, seasons (early, mid or late summer) or habitat (X.W. *et al.*, manuscript in preparation); hence here we focus on species, sites and treatments. The independent variables included in the initial models that tested for warming treatment effects were site, treatment and species (with plot considered a random effect). On the basis of both Akaike and Bayesian information criteria, the best models for  $Q_{10}$  and  $R_{20}$  included only treatment and species (moreover, response to warming did not differ among sites). We then tested for response to prior 5-night temperature, warming treatment and species. Including the prior 5-night mean temperature in the model was significant for  $R_{20}$  but not significant for  $Q_{10}$ . Furthermore, after including prior 5-night temperature in the model, warming treatment was no longer significant (indicating that incorporating this effect into the prior 5-night temperature accounted for its effect), and the best model included only 5-night mean temperature and species.

To assess effect of acclimation on reducing expected respiratory carbon loss, we calculated percentage acclimation as:

$$\text{Acclimation}(\%) = \frac{R_{23.4 \text{ ambient}} - R_{23.4 \text{ warmed}}}{R_{23.4 \text{ ambient}} - R_{20.0 \text{ ambient}}} \times 100 \quad (2)$$

in which a value of <0 means no acclimation, a value between 0 and 100% means partial acclimation, 100% means complete acclimation, >100% means over-acclimation.

**Study sites.** The B4WarmED experiment was conducted at the Cloquet Forestry Center at Cloquet, Minnesota, USA (46° 31' N, 92° 30' W) and at the Hubachek

Wilderness Research Center near Ely, Minnesota, USA (47° 55' N, 92° 30' W). Both sites are located in the boreal–temperate forest ecotone. The mean annual precipitation and temperature (1973–2008) were 783 mm and 4.8 °C at Cloquet Forestry Center, and 726 mm and 2.6 °C at the nearest weather stations to Hubachek Wilderness Research Center. The warming experiments at both sites were conducted on coarse-textured upland soils in mixed *Populus tremuloides*–*Betula papyrifera*–*Abies balsamea* stands (with stand ages of 40–60 years) in both under-story (5–10% full light) and open (40–60% full light) conditions, which are representative of the typical regeneration sites for the study species.

**Experimental design.** For details of experimental design, see refs 18, 19, 26. The treatments included two levels of simultaneous plant and soil warming (ambient temperatures and day and night temperatures 3.4 °C above ambient throughout the entire growing season). Both treatments included soil heating cables (un electrified cables in the ambient plots). The heating treatment was implemented during the 2009–2013 growing seasons with a synchronized above- and below-ground open-air system (that is, without chambers) via feedback controls that acted concurrently and independently at the plot scale to maintain a fixed temperature differential from ambient conditions (see ref. 19 for a detailed description of the experimental warming system). Although warming treatments varied slightly with site, canopy and year<sup>19</sup>, on average 3.4 °C warming of both above-ground plant surfaces and soil was obtained during treatments. Eleven individual seedlings of ten native species (most two years old and grown from local seed sources) were planted in each plot in 2008. The seedlings were obtained from the Minnesota Department of Natural Resources<sup>18,26</sup>.

**Measurement of leaf respiration temperature response curve details.** The temperature response curves of leaf respiration were measured on detached foliage sampled from the ambient and warmed plots from June–September 2009–2013 (day of year = 169–271). Sampling across the warming treatments was very closely balanced for each species across sites and habitats. Fully expanded, healthy leaves were collected each morning and were immediately inserted into floral water pik tubes to keep them hydrated throughout the day. The leaves were then transported to a nearby laboratory and transferred to a darkened growth chamber that was able to maintain a broad range of temperatures. Temperature response curves were measured from 12 to 37 °C leaf temperature at increments of ~5 °C by adjusting the air temperatures of the growth chamber and the temperature control setting of the cuvette housing the sample leaf.

The dark respiration rate was measured using an infrared gas analyser system (LI-6400 portable photosynthesis systems, Li-Cor) with a standard 2 × 3-cm leaf chamber used for broadleaved species and a conifer chamber (that fits sprigs 7.5-cm long with needles up to 3.5-cm long) for the needle-leaved species, operated in an open configuration with a flow rate of 300–500 μmol s<sup>−1</sup> and a CO<sub>2</sub> concentration of 400 μmol mol<sup>−1</sup>. The leaf chamber was placed inside the growth chamber, and the leaf temperature in the cuvette was set to correspond to the temperature in the growth chamber. The leaf was allowed to stabilize at the new temperature for a minimum of 10 min prior to being clamped in the leaf chamber for the dark respiration measurement. Three values were logged at 15 s intervals after the readings had stabilized and were averaged for each temperature. Dark respiration rates were measured for each leaf at 12 °C control setting, after which both the leaf and growth chambers were set to 17 °C, and the process was repeated for all temperatures in increasing order. We note that the measurement of leaf temperature when the respiration measurement was made was recorded and used in all calculations, rather than the set point temperature (which was usually close, but not identical, to the measured leaf temperature). The humidity within the leaf chamber was controlled to the extent possible (see ref. 26 for details of controlling humidity in leaf chambers). The measurements were completed within 3–4 h. Detailed measurements for three species across seasons (late spring, summer, early autumn), habitats and sites, showed that both the  $Q_{10}$  of the short-term response curve and the acclimation of the entire curve to warming treatment effects were unaffected by habitat or site (X.W. *et al.*, manuscript in preparation). Hence we focus here on species and treatment effects initially, and then on response to recently experienced temperatures.

An important question about measurements of dark respiration temperature response functions involves the stability of measurements over the time needed to conduct each curve. Although it has been shown that metabolism of sugars can change respiration rates<sup>13,27</sup>, extensive previous work done to test the stability of measurements with many of the same species as in our study has shown no effect of duration in the dark on respiration rates or their short-term temperature sensitivity<sup>10,12,13,27–29</sup>. Another recent study with a different tree species<sup>20</sup>, found that respiration rates and temperature responses were stable for as long as 4 days (the longest period they tested). As noted<sup>27</sup>, sugar concentrations found naturally had only a small effect on respiration of *Populus* leaves compared to those induced in artificially sucrose-fed leaves, and even in the latter, sugar concentration only had marked effects on respiration rates at leaf temperatures greater than 40 °C and

none detectable below 30 °C. Moreover, given that all treatments and species in our study received the same protocol it is unlikely that variability due to lack of stability influenced the outcome of our measurements and analyses.

#### Different approaches to fitting leaf respiration temperature response function.

It has been known for decades that over the short-term (minutes to hours), respiration increases approximately exponentially with temperature (equivalent to log-linearly)<sup>3,7,20,21</sup>, which often can be well described by  $Q_{10}$  or Arrhenius functions (see equations (1) and (3), and Extended Data Fig. 6). Hence both the  $Q_{10}$  (equation (1)) and Arrhenius functions (equation (3)) have been widely used to describe the respiration–temperature response curves in plant, ecosystem, land surface, and earth system simulation models. However, several studies have reported the response to not be a fixed proportional change (on a logarithmic basis), but a decelerating proportional change<sup>20,22</sup>, such that if one uses the  $Q_{10}$  approach to characterize this, the  $Q_{10}$  is lower across any given temperature span at higher than lower temperatures<sup>20,22</sup>. In fact, the two most comprehensive assessments, one a synthesis by Tjoelker and colleagues<sup>22</sup> and the other a new study of 218 species globally<sup>30</sup> strongly support the temperature sensitive  $Q_{10}$  model (that is, decelerating polynomial function). In such cases a temperature-sensitive Arrhenius (equation (4)); a polynomial model (equation (5)), with a value of  $c < 0$ ; and a Michaelis–Menton model (equation (6)), with a value of  $\delta(T_{\text{ref}}) < 0$  have been found to be good models to describe the observations. However, no single function has emerged as the best across all studies; thus, the nature and variability among taxa of the short-term temperature response function of leaf respiration remains uncertain<sup>3,4,14,20–22</sup>.

Given this uncertainty, we examined the alternative approaches with our data, and used the results to inform our choice of which to focus on. We examined five models (1, 3, 4, 5 and 6):

$$R_T = R_{T_{\text{ref}}} e^{\left( \frac{E_a}{r T_{\text{ref}}} \left( 1 - \frac{T_{\text{ref}}}{T} \right) \right)} \quad (3)$$

$$R_T = R_{T_{\text{ref}}} e^{\left( \frac{E_a}{r T_{\text{ref}}} \left( \frac{T_{\text{ref}}}{T_{\text{ref}} - T_0} - \frac{T_{\text{ref}}}{T - T_0} \right) \right)} \quad (4)$$

$$R_T = e^{a + bT + cT^2} \quad (5)$$

$$\ln R_T = \ln R_{T_{\text{ref}}} + \frac{E_0(T_{\text{ref}})}{r} \times \frac{[T - T_{\text{ref}}]}{T(T_{\text{ref}})} + \delta(T_{\text{ref}}) \left[ \frac{T - T_{\text{ref}}}{T(T_{\text{ref}})} \right]^2 \quad (6)$$

in which  $R_T$  is the dark respiration measured at leaf temperature  $T$ ;  $R_{T_{\text{ref}}}$  is the respiration at reference temperature  $T_{\text{ref}}$ ;  $Q_{10}$  is a metric that describes the proportional increase of respiration rate with a 10 °C increase in temperature;  $E_a$  (J mol<sup>−1</sup>) is the activation energy of respiration;  $r$  is the universal gas constant (8.314 J mol<sup>−1</sup> K<sup>−1</sup>);  $a$ ,  $b$  and  $c$  in equation (5) are coefficients that describe the temperature response of the natural log of respiration, and  $E_0(T_{\text{ref}})$  (J mol<sup>−1</sup>) is the overall activation energy of the reference temperature.  $T$  and  $T_{\text{ref}}$  are in °C in equations (1) and (5), and in K in equation (3) and (4). A temperature-dependent  $Q_{10}$  value can be calculated from parameters in equation (5)<sup>20,22</sup>

$$Q_{10} = e^{10 \times (T + 2cT)} \quad (7)$$

A value of  $c < 0$  in equation (5) or  $\delta(T_{\text{ref}}) < 0$  in equation (6) indicates a decrease in  $Q_{10}$  or  $E_0$ , respectively (each of which can be evaluated at every point along the curve) with temperature, and a value of  $> 0$  indicates an increase in  $Q_{10}$  or  $E_0$  with temperature, respectively.

Curves were considered for analysis only when all points fit within a 95% confidence interval, the  $R^2$  exceeded 0.60 and the overall curve and slope parameters were at least marginally significant at  $P < 0.10$  for at least three of the models. In total, 1,620 curves met these requirements, with mean and median (across all curves and all five models)  $R^2$  of 0.94 and 0.96, respectively and with 99% significant at  $P < 0.05$ . Given that curves on average were approximately exponential, the temperature-sensitive Arrhenius model (equation (4)) fit similarly well as, but very slightly less well than the Arrhenius model (equation (3)) and is not further discussed. Among the five equations (1), (3), (4), (5) and (6), equations (5) and (6) had a slightly higher  $R^2$  and lower root mean square error (r.m.s.e.) values than equations (1) and (2) (Extended Data Table 1). However, among our 1,620 curves determined using equation (5), 894 (55%) had  $c < 0$  and 726 (45%) had  $c > 0$  (Extended Data Fig. 7), with roughly half of the curves for equation (6) also not supporting a decelerating function. Thus, for our sample, an accelerating proportional change in respiration was almost as likely as a decelerating proportional change, refuting the idea that a decelerating model is a good choice overall for our data. Given that use of either equation (5) or (6) is inconsistent with any single

shape of the response function, including the deceleration framework that is the underlying premise of both models, we did not use either to describe our measured response curves. Instead equations (1) and (3) ( $Q_{10}$  and Arrhenius models) performed similarly and very well; they had similar  $R^2$  and r.m.s.e. values (Extended Data Table 1), and were roughly equally accurate across the full range of measurement temperatures. Moreover, the predicted respiration rates from equations (1) ( $Q_{10}$ ) and (3) (Arrhenius function) at the reference temperature of 20 °C were nearly identical (data not shown), and as expected,  $Q_{10}$  from equation (1) was extremely well correlated ( $R^2 = 0.999$ ) with  $E_a$  from equation (3) (Extended Data Fig. 6). For the respiration data generated in our study, using the exponential fit was a reasonable statistical approach, and we therefore only report parameters from equation (1); but do not intend this as an indication that equation (1) is preferable to equation (3) for these data. We note the estimates of acclimation would be similar regardless of which of the five models of short-term respiration response were used.

**Statistical tests.** To compare leaf respiration rates across species, warming treatments, and recently experienced night-time temperatures, we converted the respiration rates of all leaves to values at a common measurement temperature of 20 °C ( $R_{20}$ ), using the leaf-specific equation (1) for each of the 1,620 leaves. To assess how much of the potential increase in respiration the acclimation eliminates, we calculated percentage acclimation using equation (2), where a value of  $< 0$  means no acclimation, a value between 0 and 100% means partial acclimation, 100% means complete acclimation,  $> 100\%$  means over acclimation. We also expressed  $R$  at 25 °C ( $R_{25}$ ) to test for many of the relationships described in this paper using  $R_{20}$ , including those with photosynthesis, as 25 °C was in the centre of the temperature range used to develop the response curve for each leaf and  $R$  at 25 °C is perhaps the most common reference value<sup>31</sup>.

Mixed-effect analyses of variance were conducted to compare  $Q_{10}$ ,  $R_{20}$  and  $R_{25}$  data by species, site and treatment, pooled across all other sources of variation.  $R_{20}$  and  $R_{25}$  were log-transformed to fit assumptions of a normal distribution. As responses of  $R_{25}$  and  $R_{20}$  were extremely similar, we largely show only those for the latter here. We also fit simple regressions of  $\log(R_{20})$  versus prior 5-night and 10-night temperatures, for each species, and used these to calculate percentage acclimation across time. All data analyses used JMP 11.0 (SAS Institute).

**Model selection and results.** We first tested models for  $Q_{10}$  and  $R_{20}$  including species, site, warming treatment and all interactions (with plot included as a random effect). There were no site  $\times$  treatment (or site  $\times$  treatment  $\times$  species) interactions, nor was site (with or without interactions) included in the best models (based on both on AIC and BIC criteria), hence site was not considered further in any models. The best models included only treatment and species (both significant as main effects), but we show the model including their interaction term in Table 1 to allow readers to see the level of significance of their interaction. We also tested whether grouping species by biome of origin (boreal versus temperate) or phylogenetic group (angiosperm versus gymnosperm), instead of by species, identified a difference in response to warming treatment by groups. Group was significant in both cases as a main effect, but there was no significant interaction with treatment and the models were much poorer overall than those including species (data not shown).

We also tested an additional model for  $R_{20}$  that included the prior temperature (temperature of the prior 5 nights) and all interactions (shown in Table 1). Species, prior temperature and the interaction of species  $\times$  prior temperature were the only significant terms. However the species  $\times$  prior temperature interaction was only significant for the species with the steepest and shallowest slopes (*Picea glauca* and *Quercus macrocarpa*, respectively), and neither of those species had a slope significantly different than any other species from the same phylogenetic group (gymnosperm or angiosperm). Thus we tested the model for  $R_{20}$  with independent predictors of phylogenetic group, prior temperature and their interaction. Groups differed in slope ( $P = 0.0084$ ) of  $R_{20}$  to prior 5-night temperature. Models for each group separately found species did not differ in slope (no species  $\times$  5-night temperature interaction) but did differ in intercept (species significant as main effect). Thus, for modelling purposes the most statistically appropriate equations are for each species to have a unique intercept, but for all gymnosperms and angiosperms to share a common slope (Extended Data Table 2), as derived from separate models for conifers ( $R^2 = 0.33$  for model) and angiosperms ( $R^2 = 0.27$  for model).

Furthermore, as autotrophic respiration is a process closely coupled to photosynthesis<sup>13,21,27</sup>, shifts in leaf respiration observed for plants growing under different thermal conditions could result from the coupling of respiration and photosynthesis, and temperature related shifts in photosynthesis<sup>14</sup>. If this were the case, acclimation of leaf respiration might be driven largely by temperature-related variation in photosynthesis. Empirical evidence from prior publications, predominantly for laboratory grown seedlings, found that the ratio of leaf respiration to photosynthesis ( $R:P$ ) was stable in some cases, but increased with growth

temperature in others<sup>14</sup>. Using temperature response curves of photosynthesis made in this experiment<sup>26</sup>, we estimated photosynthesis at prevailing daytime temperatures and combined these with estimates of leaf respiration at prevailing night-time temperatures to estimate the  $R:P$  ratio and assess how it varied with temperature (using mean daily 24-h temperature to represent the general thermal regime). These estimates indicate that acclimation of  $R_{\text{leaf}}$  did not result from (or result in) a stable  $R:P$  ratio, because for all 10 species,  $R:P$  was higher in warmer conditions, whether seasonal or experimental. However, the acclimation of leaf respiration did constrain the extent to which  $R:P$  varies, because without acclimation,  $R:P$  would have been much more increased at higher mean daily temperatures compared to what was observed. Hence our results are consistent with the notion that acclimation is part of a process that limits the size of the 'window' within which  $R:P$  varies, but does not support the idea of a complete homeostasis of  $R:P$  that would directly result in acclimation of leaf respiration, if photosynthesis rose little with increased temperatures.

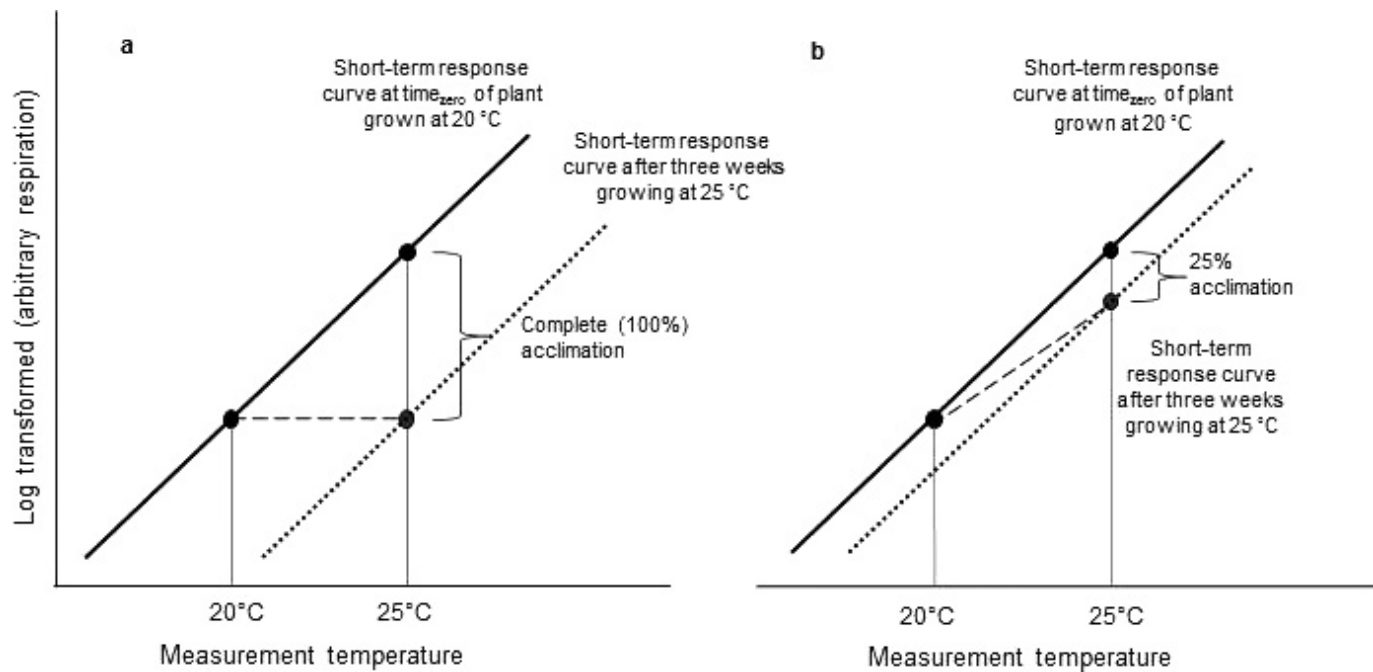
We also assessed whether the response to warming treatment of  $Q_{10}$ , or leaf respiration rate at a given measurement temperature, could be explained in full or part by photosynthesis. We did this by including photosynthesis as a predictor in models that examined (1)  $Q_{10}$ , and (2) respiration at 20 °C ( $R_{20}$ ) or 25 °C ( $R_{25}$ ), in relation to species, treatment, and the species  $\times$  treatment interaction (across all 1,620 leaves). As elsewhere,  $R_{20}$  and  $R_{25}$  were log-transformed to fit assumptions of a normal distribution. Including photosynthesis in these analyses did not alter our results or conclusions. In the model with  $Q_{10}$  as the dependent variable, photosynthesis was not significant ( $P = 0.62$ ), nor was warming treatment ( $P = 0.78$ ), but species was ( $P = 0.0025$ ), and  $Q_{10}$  values for each species in both ambient and warmed treatments were similar as our original analyses. In the models with  $R_{20}$  and  $R_{25}$  as the dependent variables, photosynthesis was significant ( $P < 0.0001$ ), (that is, respiration was positively related to photosynthetic rate), and the temperature treatment remained significant ( $P = 0.05$ ), with the degree of shift of

respiration with warming treatment (that is, the acclimation) similar with or without photosynthesis in the model.

**Comparison with published acclimation meta-analysis.** A recent meta-analysis on acclimation of leaf respiration to temperature<sup>7</sup> provides a useful basis of comparison for our work. Among 104 records for 67 species from 18 studies, 96 were from growth cabinets or greenhouses, with an average duration of 41 days and a wide range of the degree of warming. This meta-analysis includes the data from ref. 4 that is the basis for several recent assessments of acclimation effects on global carbon cycling. On average across all records, the increase in  $R_{\text{leaf}}$  for a one-degree temperature increase was 5.7% for that meta-analysis<sup>7</sup>, compared with 1.5% from the 10 species in our study. In the meta-analysis, the response of  $R_{\text{leaf}}$  per °C increase was weakly but significantly linearly correlated with the degree of warming ( $R^2 = 0.04$ ,  $P = 0.036$ ), suggesting that the extent of acclimation is less when the shift in temperature is greatest. On the basis of that correlation, acclimation in response to 3.4 °C warming should result in a 3.4% increase in  $R_{\text{leaf}}$  per °C. Hence, both the mean shift in  $R_{\text{leaf}}$  across all data (+5.7% per °C warming) and the shift after adjustment to a +3.4 °C warming (+3.4% per °C warming) from the meta-analysis are at least twice as great as the increase in  $R_{\text{leaf}}$  (1.5% per °C warming) from our study. There are several potential reasons why acclimation was so much stronger in our study than in previous studies; these include the longer duration of the treatments and the more realistic whole-plant warming treatments, among others.

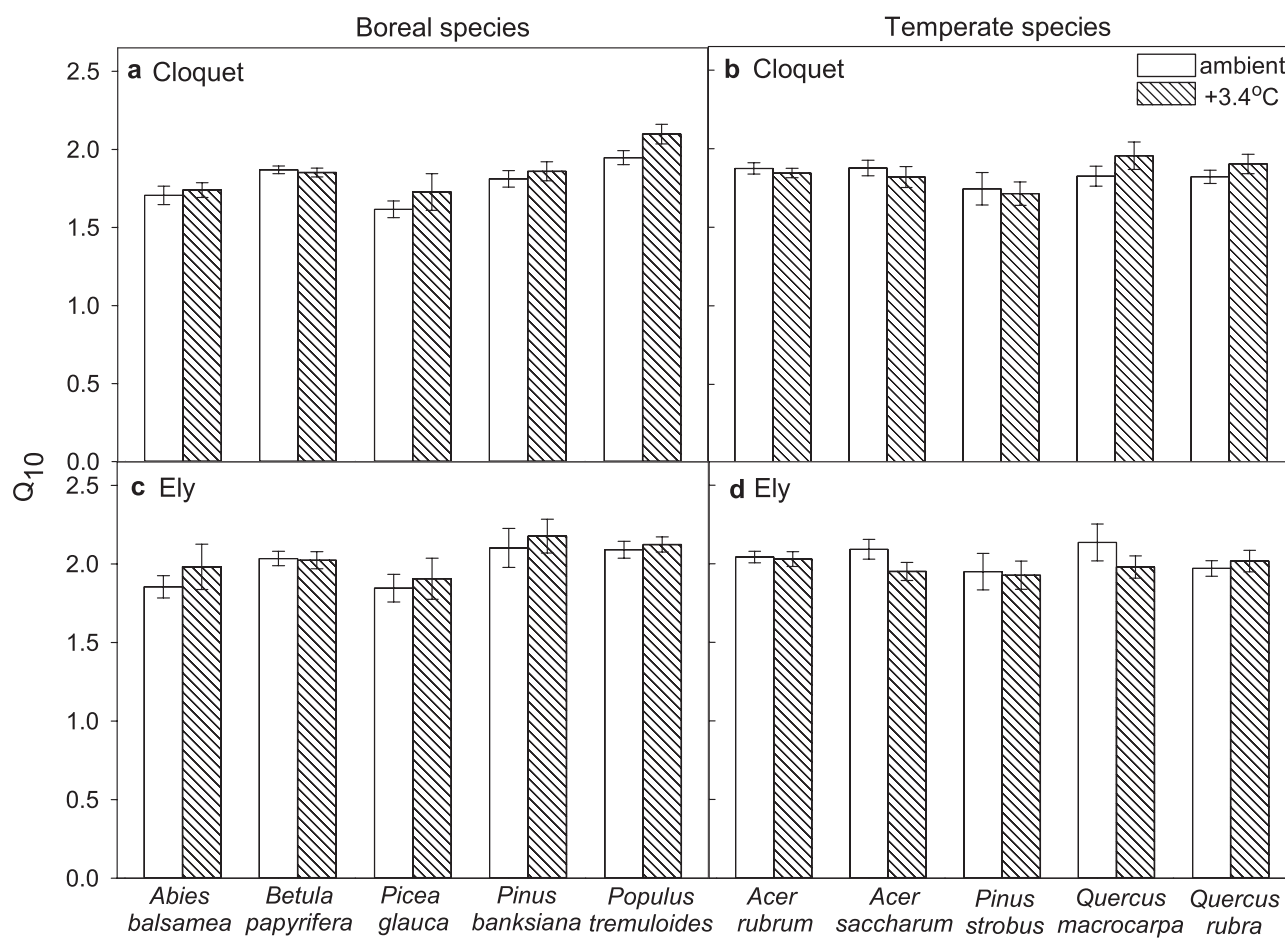
29. Mitchell, K. A., Bolstad, P. V. & Vose, J. M. Interspecific and environmentally induced variation in foliar dark respiration among eighteen southeastern deciduous tree species. *Tree Physiol.* **19**, 861–870 (1999).
30. Heskell, M. A. *et al.* Convergence in the temperature response of leaf respiration across biomes and plant functional types. *Proc. Natl Acad. Sci.* (in press).
31. Atkin, O. K. Global variability in leaf respiration in relation to climate, plant functional types and leaf traits. *New Phytol.* **206**, 614–636 (2015).





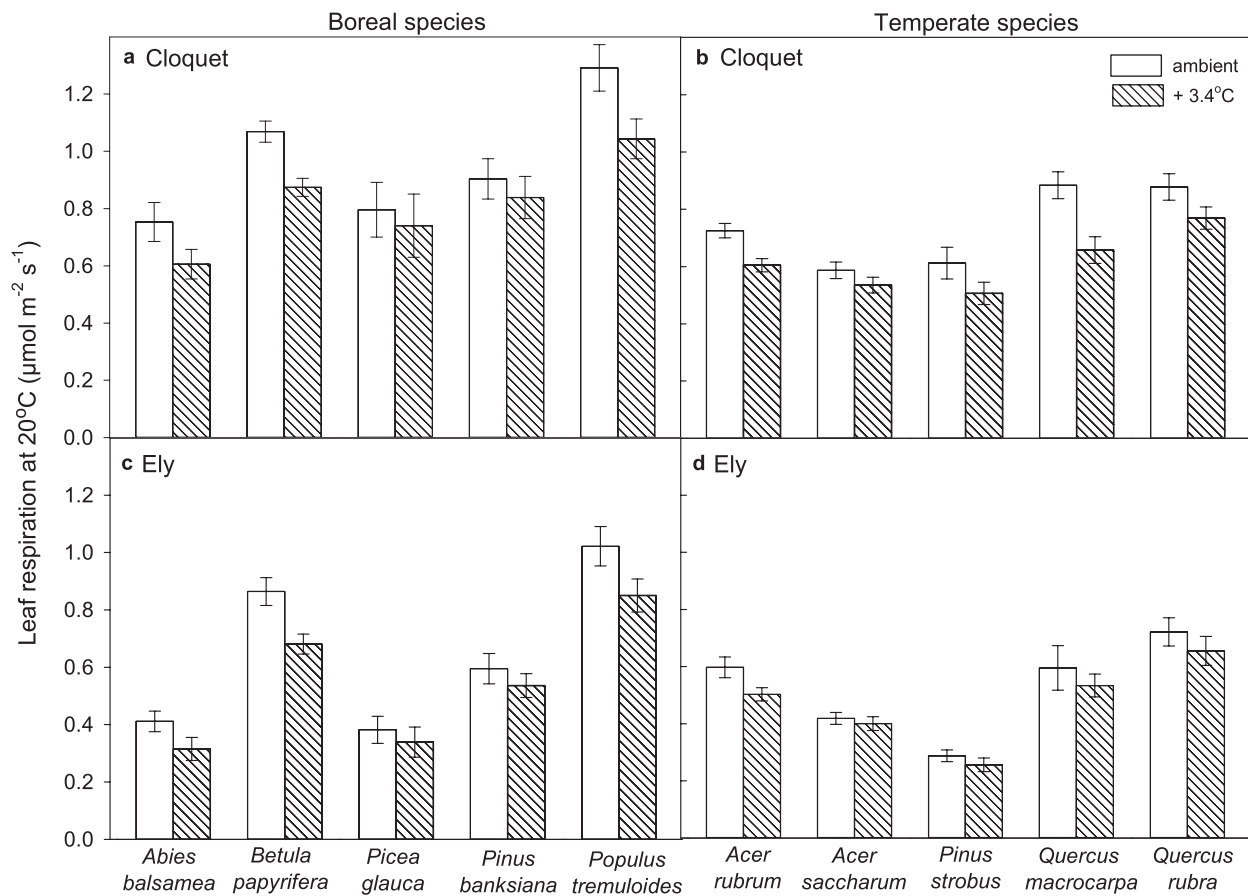
**Extended Data Figure 1 | Illustration of complete and partial acclimation.** **a**, If a plant increased respiration by 40% when placed under conditions 5 °C warmer for 30 min (solid line), but had no increase

after 3 weeks at the same +5 °C conditions (dotted line), it would have completely acclimated. **b**, If the increase over 3 weeks was 30%, it would have partially acclimated by 25% (dotted lined), and so on.



**Extended Data Figure 2 |  $Q_{10}$  in ambient and experimentally warmed treatments. a–d,  $Q_{10}$  (exponent of the short-term temperature response function, equation (1)) of ambient and experimentally warmed plants of all 10 species, shown for each site (grouped by biome affiliation of the species). Sample size by biome type, site, and warming treatment:**

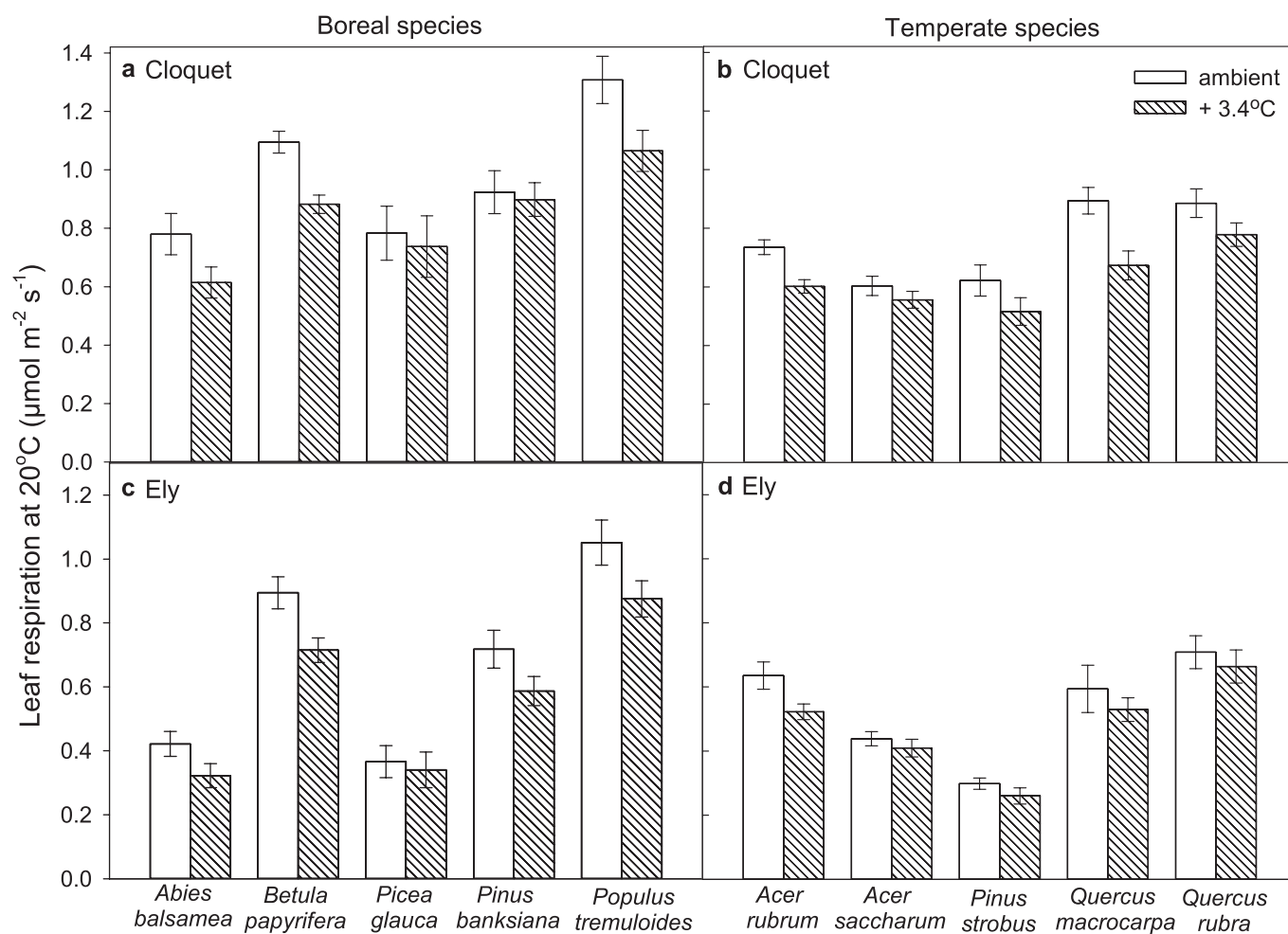
boreal, Cloquet (a), ambient = 194, warmed = 206; temperate, Cloquet (b), ambient = 244, warmed = 247; boreal, Ely (c), ambient = 169, warmed = 174; temperate, Ely (d), ambient = 190; warmed = 196. Data are mean and s.e.m.



**Extended Data Figure 3 | Leaf dark respiration rate using  $Q_{10}$  approach, at a standardized measurement temperature, for ambient and experimentally warmed plants. a–d, Mean (and s.e.m.) leaf respiration at 20°C ( $R_{20}$ ) of ambient and experimentally warmed plants of all 10 species. Data derived from equation (1) ( $Q_{10}$  approach) shown for each**

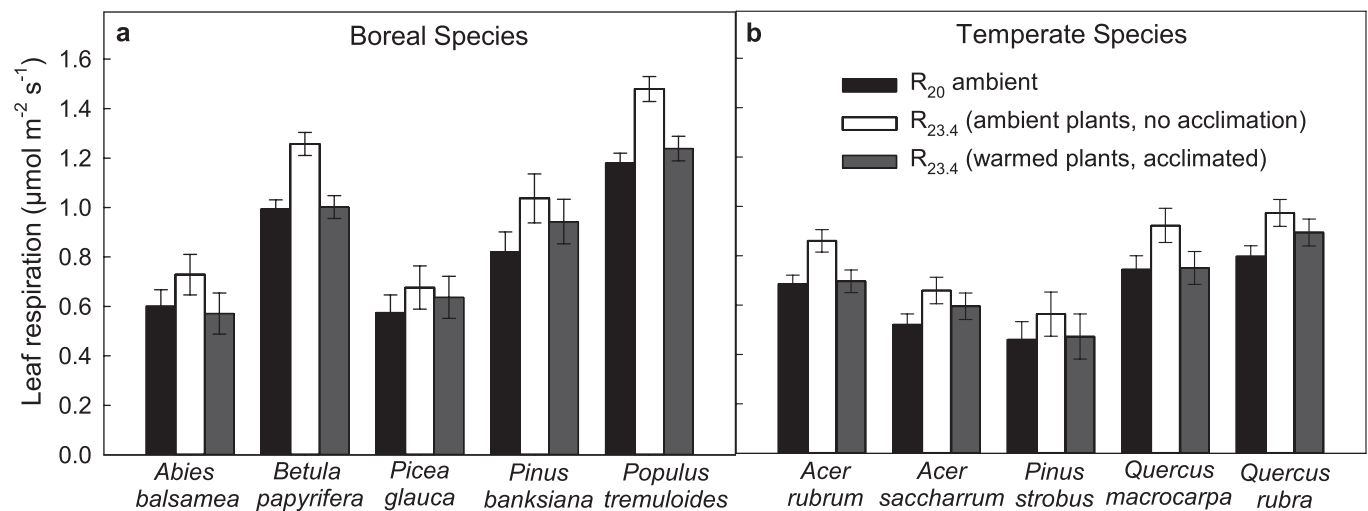
site (grouped by biome affiliation of the species). Sample size by biome type, site, and warming treatment: boreal, Cloquet (a), ambient = 194, warmed = 206; temperate, Cloquet (b), ambient = 244, warmed = 247; boreal, Ely (c), ambient = 169, warmed = 174; temperate, Ely (d), ambient = 190; warmed = 196.





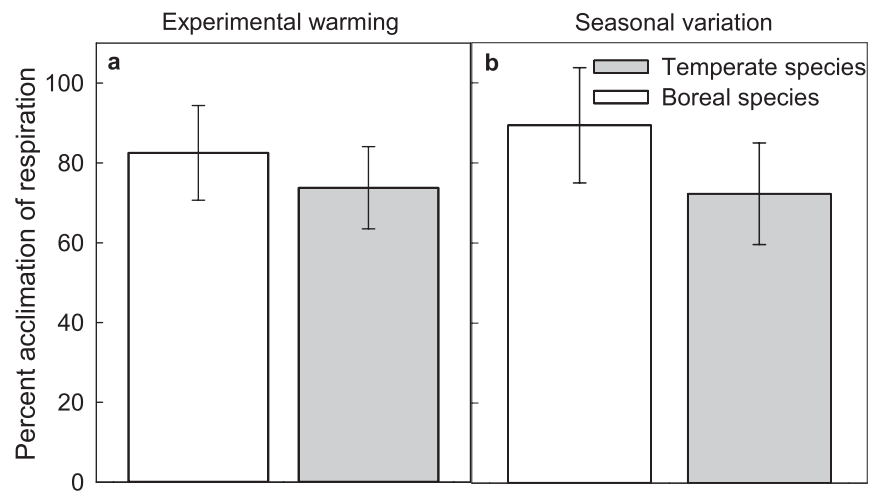
**Extended Data Figure 4 | Leaf dark respiration rate using Michaelis–Menton approach, at a standardized measurement temperature, for ambient and experimentally warmed plants. a–d,** Mean (and s.e.m.) leaf respiration at 20°C ( $R_{20}$ ) of ambient and experimentally warmed plants of all 10 species. Data derived from equation (6) shown for each site (grouped

by biome affiliation of the species). Sample size by biome type, site, and warming treatment: boreal, Cloquet (a), ambient = 194, warmed = 206; temperate, Cloquet (b), ambient = 244, warmed = 247; boreal, Ely (c), ambient = 169, warmed = 174; temperate, Ely (d), ambient = 190; warmed = 196.

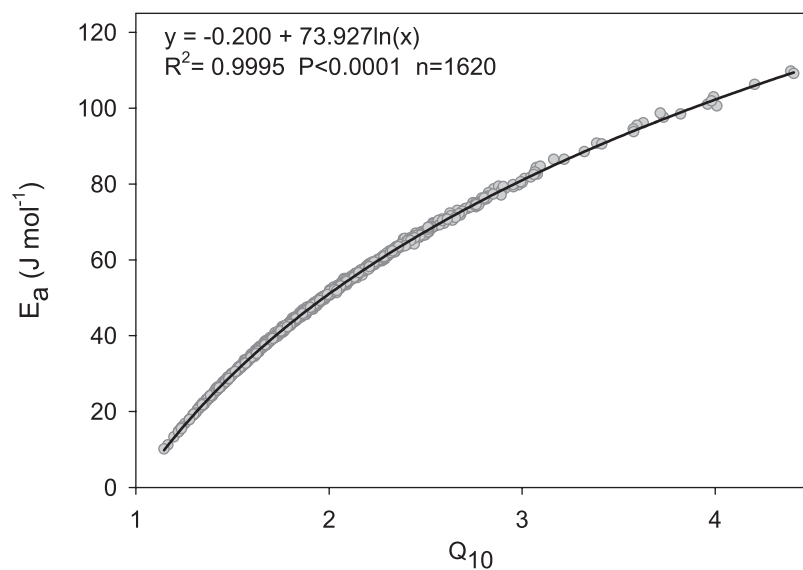


**Extended Data Figure 5 | Leaf dark respiration rate of ambient and experimentally warmed plants. a, b,** Data are from five boreal (a) and five temperate (b) tree species. Figure is identical to Fig. 1 except fits were made using equation (6) (Michaelis–Menton model approach) instead of equation (1) ( $Q_{10}$  approach). Respiration is shown at measurement temperatures of 20 °C and 23.4 °C for ambient-grown plants; respiration for plants grown at +3.4 °C conditions is shown at measurement

temperature of 23.4 °C. The two values for ambient plants show the increase in respiration with a +3.4 °C temperature increase for non-acclimated plants; comparison of ambient plants measured at 20 °C with warmed plants measured at 23.4 °C represents the increase in respiration with a +3.4 °C temperature increase for acclimated plants. Data are mean and s.e.m. (s.e.m. are from the full model). Sample sizes as in Fig. 2.

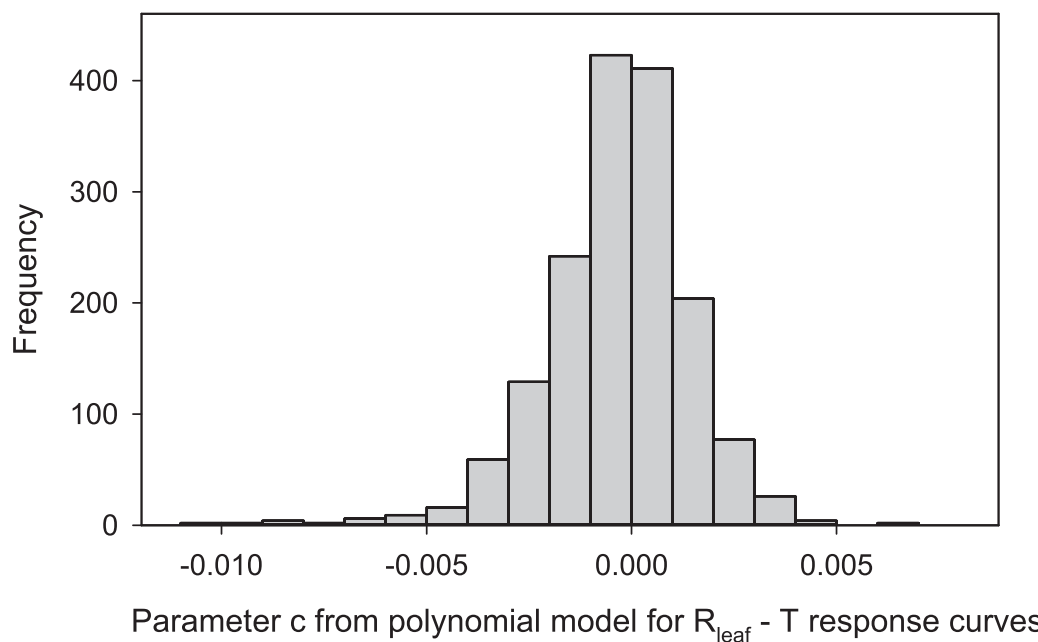


**Extended Data Figure 6 | Percentage acclimation by biome, in response to both experimental warming and seasonal temperature variation.**  
**a**, Experimental warming. **b**, Seasonal temperature variation. Data are mean and s.e.m. Sample sizes as in Fig. 2. Percentage acclimation is calculated according to equation (2).



**Extended Data Figure 7 | Relationship between  $Q_{10}$  and activation energy of respiration ( $E_a$ ).** Graph shows relationship between the exponent of the short-term temperature response function ( $Q_{10}$ ; from equation (1)), and the activation energy of respiration ( $E_a$ ) from the Arrhenius model (equation (3)).  $n = 1,620$ .





**Extended Data Figure 8 | Frequency distribution of parameter  $c$  from the log polynomial model (equation 5) for the respiration–temperature response curve.** Among the 1,620 curves, 894 curves had  $c < 0$ , 726 curves had  $c > 0$ . Negative  $c$  values support the idea of a decelerating function

(with a decreasing temperature-sensitive  $Q_{10}$ ); positive values support an accelerating function. The inconsistency of  $c$  being negative indicates a lack of support for a decelerating function, and thus a lack of support for the decelerating log polynomial model as useful for the data in this paper.

Extended Data Table 1 | Mean and median  $R^2$  and r.m.s.e. of four models

Models	Q <sub>10</sub> model	Arrhenius model	Polynomial model	M-M model
Mean $R^2$	0.93	0.93	0.96	0.96
Median $R^2$	0.95	0.95	0.97	0.97
RMSE	0.17	0.17	0.15	0.15
Is shape consistent?	na	na	No	No

1: Q<sub>10</sub> model; 3: Arrhenius model; 5: log-polynomial model; and 6: Michaelis–Menton model for fitting respiration-temperature response curves ( $n = 1,620$ ). The temperature-sensitive Arrhenius equation (equation (4)) was similar to model 3 and is therefore not included.

**Extended Data Table 2 | Species-specific equations relating  $\log(R_{20})$  to the prior 5-night temperature**

Species	Equation
<i>Abies balsamea</i>	$0.1757 - 0.0301 * T$
<i>Acer rubrum</i>	$0.0047 - 0.0171 * T$
<i>Acer saccharum</i>	$-0.0804 - 0.0171 * T$
<i>Betula papyrifera</i>	$0.1610 - 0.0171 * T$
<i>Picea glauca</i>	$0.1424 - 0.0301 * T$
<i>Pinus banksiana</i>	$0.3332 - 0.0301 * T$
<i>Pinus strobus</i>	$0.0162 - 0.0301 * T$
<i>Populus tremuloides</i>	$0.2154 - 0.0171 * T$
<i>Quercus macrocarpa</i>	$0.0533 - 0.0171 * T$
<i>Quercus rubra</i>	$0.1110 - 0.0171 * T$

We tested the model for  $R_{20}$  with independent predictors of phylogenetic group (angiosperm versus gymnosperm), prior temperature and their interaction. Groups differed in slope ( $P = 0.0084$ ) of  $R_{20}$  to the prior 5-night temperature. Models for each group separately found species did not differ in slope (no species  $\times$  5-night temperature interaction) but did differ in intercept (species significant as main effect). Thus, for modelling purposes the most statistically appropriate equations are for each species to have a unique intercept, but for all gymnosperms and angiosperms to share a common slope, as derived from separate models for conifers ( $R^2 = 0.33$  for model,  $P < 0.0001$ ) and angiosperms ( $R^2 = 0.27$  for model,  $P < 0.0001$ ).

# The mid-developmental transition and the evolution of animal body plans

Michal Levin<sup>1†\*</sup>, Leon Anavy<sup>1\*</sup>, Alison G. Cole<sup>1</sup>, Eitan Winter<sup>1</sup>, Natalia Mostov<sup>1</sup>, Sally Khair<sup>1</sup>, Naftalie Senderovich<sup>1</sup>, Ekaterina Kovalev<sup>1</sup>, David H. Silver<sup>1</sup>, Martin Feder<sup>1</sup>, Selene L. Fernandez-Valverde<sup>2†</sup>, Nagayasu Nakanishi<sup>2†</sup>, David Simmons<sup>3</sup>, Oleg Simakov<sup>4</sup>, Tomas Larsson<sup>4</sup>, Shang-Yun Liu<sup>5</sup>, Ayelet Jerafi-Vider<sup>6</sup>, Karina Yaniv<sup>6</sup>, Joseph F. Ryan<sup>3</sup>, Mark Q. Martindale<sup>3</sup>, Jochen C. Rink<sup>5</sup>, Detlev Arendt<sup>4</sup>, Sandie M. Degnan<sup>2</sup>, Bernard M. Degnan<sup>2</sup>, Tamar Hashimshony<sup>1</sup> & Itai Yanai<sup>1</sup>

Animals are grouped into ~35 ‘phyla’ based upon the notion of distinct body plans<sup>1–4</sup>. Morphological and molecular analyses have revealed that a stage in the middle of development—known as the phylotypic period—is conserved among species within some phyla<sup>5–9</sup>. Although these analyses provide evidence for their existence, phyla have also been criticized as lacking an objective definition, and consequently based on arbitrary groupings of animals<sup>10</sup>. Here we compare the developmental transcriptomes of ten species, each annotated to a different phylum, with a wide range of life histories and embryonic forms. We find that in all ten species, development comprises the coupling of early and late phases of conserved gene expression. These phases are linked by a divergent ‘mid-developmental transition’ that uses species-specific suites of signalling pathways and transcription factors. This mid-developmental transition overlaps with the phylotypic period that has been defined previously for three of the ten phyla, suggesting that transcriptional circuits and signalling mechanisms active during this transition are crucial for defining the phyletic body plan and that the mid-developmental transition may be used to define phylotypic periods in other phyla. Placing these observations alongside the reported conservation of mid-development within phyla, we propose that a phylum may be defined as a collection of species whose gene expression at the mid-developmental transition is both highly conserved among them, yet divergent relative to other species.

To study the broad patterns of embryonic development, we selected ten distantly related species that collectively provide a wide sampling of the variation exhibited by the animal kingdom at the level of morphological and developmental complexity (Fig. 1 and Extended Data Table 1). This collection includes a single species from poriferans, cnidarians, nematodes, arthropods, chordates, echinoderms, annelids, platyhelminthes, ctenophores, and tardigrades. Seven of the species are bilaterians—five protostomes and two deuterostomes—while the cnidarian *Nematostella vectensis* represents a clade that is the sister group to bilaterians, and the ctenophore *Mnemiopsis leidyi* and the poriferan *Amphimedon queenslandica* represent two earlier branching taxa<sup>11</sup>. Collectively, these species provide a unique platform for the study of global features in animal development.

For each species, we isolated on average 70 individual embryos spanning development (Fig. 1b). The transcriptome of each embryo was analysed using CEL-Seq<sup>12</sup>, a technique for low-input multiplexed RNA-seq. For three species—*Hypsibius dujardini* (tardigrade), *Schmidtea polychroa* (platyhelminth), and *Platynereis dumerilii* (annelid)—where

a published genome was unavailable, we first produced a comprehensive developmental transcriptome (Extended Data Fig. 1, Extended Data Tables 2 and 3, and Supplementary Table 1). To assay dynamic expression so that it is not overly biased by individual embryos, for each of the ten time-courses we computed expression across twenty overlapping sliding windows of the embryos, sorted by BLIND<sup>13</sup>, a technique for ordering large-scale transcriptomic developmental time-courses (Extended Data Fig. 2a), and used these averaged expression profiles in our analyses.

Figure 2 shows the standardized expression profiles of the dynamically expressed genes across the ten species (Extended Data Fig. 2b). To compare gene expression across these species, we delineated 11,139 orthologous protein families, with each orthologous family having representatives from an average of six species. The expression of eleven *C. elegans* transcription factors—conserved across the other species in this study—are indicated in Fig. 2, highlighting how this data set can serve as a resource for developmental and evolutionary biologists. For example, the TCF/LEF family is expressed in the early phases of six of the time-courses and later in the remaining species (Fig. 2, dark squares, TCF/LEF is named *pop-1* in *C. elegans*).

To systematically compare gene expression across species, we computed the correlation across orthologous gene expression throughout development for each pair of species. For example, comparison of tardigrade and annelid embryonic transcriptomes revealed two conserved phases of expression in these two species—early and late—separated by a sharp mid-developmental transition ( $P < 10^{-10}$ , Kolmogorov–Smirnov test, Fig. 3, inset; Extended Data Fig. 3). These observations indicate that although the external embryonic development of these two species is enormously different—at the level of orthologous gene expression, their early and late development is comparable. Moreover, while development appears morphologically gradual in both species, it is punctuated by a dramatic change in gene expression during mid-development. Comparing all pairs of species extended this result, even for the ctenophore and the sponge, suggesting that this dual-phase feature of development dates back to the common ancestor of all animals (Fig. 3). The broad extent of this behaviour is remarkable, especially considering the challenges associated with the *de novo* assembly of transcriptomes and reliance upon inferred gene models. Deviations from the dual-phase pattern may occur for biological reasons. For example, the early embryos of the planarian *S. polychroa* contain substantial amounts of maternal RNA, which appears as a third initial phase in all comparisons with that species. Other deviations appear more cryptic, such as the correlation matrix

<sup>1</sup>Department of Biology, Technion – Israel Institute of Technology, Haifa 32000, Israel. <sup>2</sup>School of Biological Sciences, University of Queensland, Brisbane, Queensland, Australia. <sup>3</sup>Whitney Laboratory for Marine Bioscience, University of Florida, 9505 N Ocean Shore Blvd, St Augustine, Florida 32080-8610 USA. <sup>4</sup>Developmental Biology Unit, European Molecular Biology Laboratory, Heidelberg, Germany. <sup>5</sup>Max Planck Institute of Molecular Cell Biology and Genetics, Pfotenhauerstrasse 108, 01307 Dresden, Germany. <sup>6</sup>Department of Biological Regulation, Weizmann Institute of Science, Rehovot, Israel. <sup>†</sup>Present addresses: Center for Thrombosis and Hemostasis (CTH), University Medical Center Mainz, Mainz, Germany (M.L.); Laboratorio Nacional de Genómica para la Biodiversidad, Centro de Investigación y de Estudios Avanzados del IPN, Irapuato, Guanajuato, Mexico (S.L.F.-V.); Whitney Laboratory for Marine Bioscience, University of Florida, 9505 N, Ocean Shore Blvd, St Augustine, Florida 32080-8610 USA (N.N.).

\*These authors contributed equally to this work.



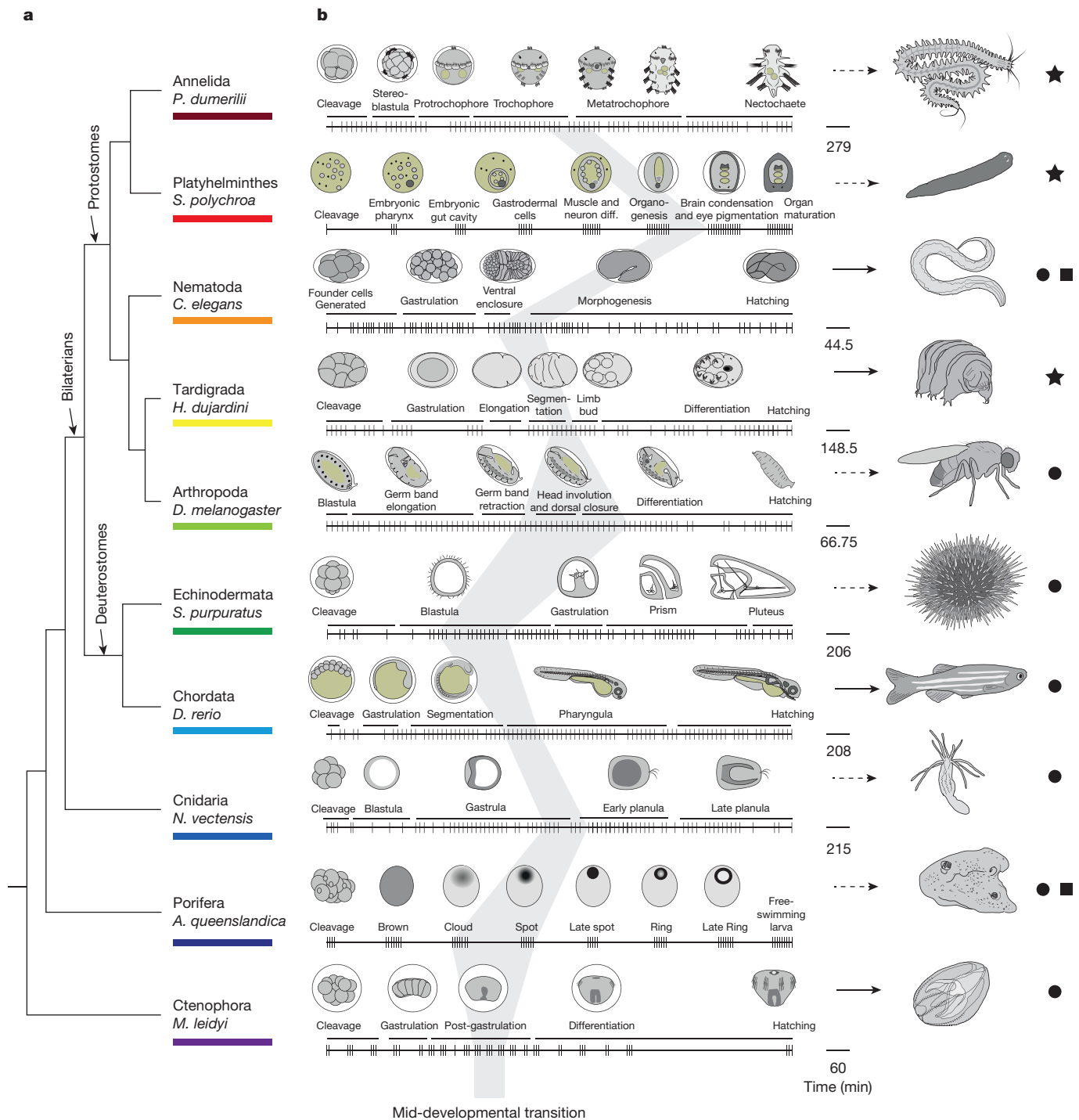


**Figure 1 | Comparing development across ten phyla using CEL-Seq.**

**a**, A phylogeny of the examined species based on recent work<sup>11,29,30</sup>.

**b**, A representation of the times (notches) at which individual embryos were collected. Drawings of embryos at the indicated representative stages are shown above the collection time-course (on the right, timescale in minutes). The dark grey shading indicates the mid-developmental

transitions. Stars, species where the developmental time-course is mapped to a mixed-stage transcriptome reported here; circles, mapped to the previously published genomes; squares, previously published time-courses<sup>13,28</sup>. Arrows indicate direct (solid) and indirect (dashed) developers.

between the cnidarian and the sponge. Overall, the dual-phase pattern holds for most pairwise species comparisons, with the exception of 9 out of 45 (Extended Data Fig. 3), and is robust to the parameters used for constructing the sliding window expression profiles and to possible biases in the embryo sampling (Extended Data Fig. 4a, b).

To study the deeply conserved expression modules we asked which Gene Ontology functional categories are enriched in the genes occurring in each of the two phases. Focusing on the stages

spanning three windows before and following the transition, we identified genes whose expression is restricted to the early and late phases (Extended Data Fig. 5). We found that orthologous groups of genes that tend to be expressed in the early phase across the ten species are enriched for chromatin changes, cell cycle, and the regulation of gene expression (Extended Data Fig. 5), suggesting that this phase is characterized by the expression of genes involved in the cell biology of proliferation. The late phase, in contrast, was enriched

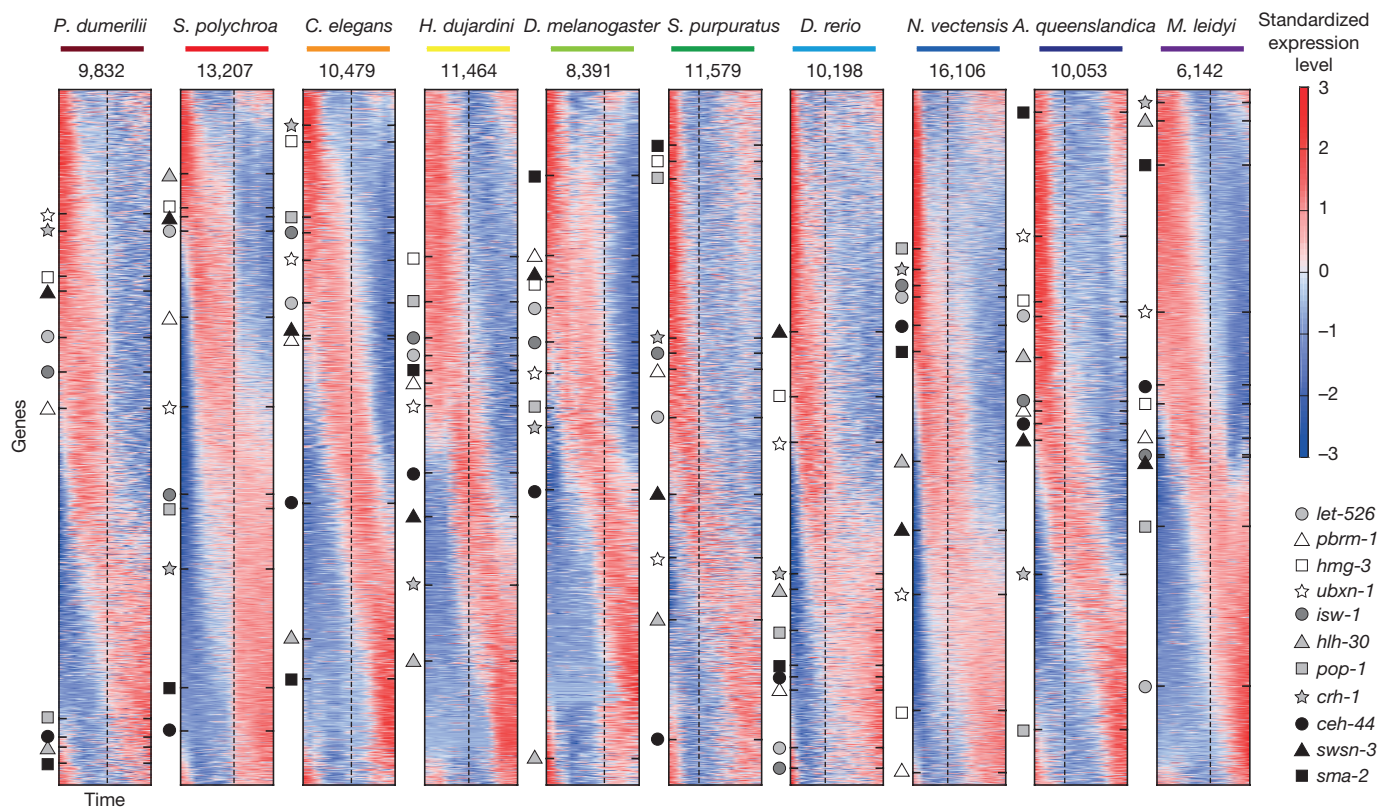


**Figure 2 | Dynamic embryonic expression throughout the animal kingdom.** Sorted standardized temporal gene expression profiles for each species. Genes of eleven orthologous groups are indicated by the

markers along with the name of the *C. elegans* orthologue. The dashed lines indicate the timing of the mid-developmental transition. The number indicates expressed genes in each data set.

with cell-type specific genes such as various transporters, metabolic enzymes, and synaptic transmission factors that together reflect a period of differentiation.

We next asked if the transition between the early and late phases is enriched in the expression of genes of particular functional groups, and found significant enrichments for signalling processes such as *Notch* and *Wnt* during this transition (Extended Data Fig. 5). Thus, a common signature among the animals studied here is that, between periods

of cell proliferation and differentiation, a period of intense signalling occurs, which is expected from a developmental biology perspective<sup>14</sup>. To study the expressed signalling pathways in greater detail, we examined seven major pathways and tested for their enrichment during the transition between the two phases in each of the ten species (Fig. 4a). We found a pattern of variation indicating that each of the distantly related species uses a distinct suite of signalling pathways during the transition. Extending this analysis to transcription factor families, we

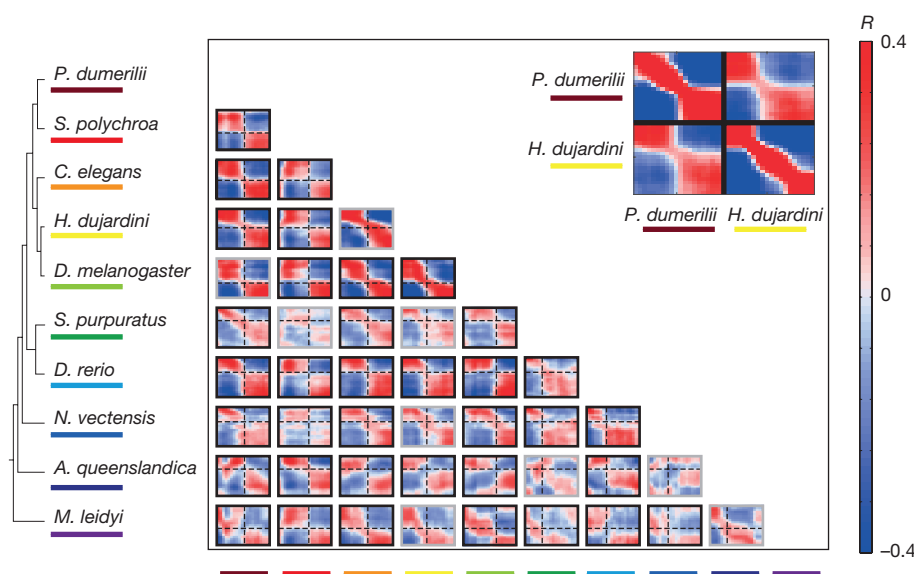


**Figure 3 | Cross-phyla comparison of developmental transcriptomes.** Each heat map shows the correlations between the developmental transcriptomes of a pair of species based upon analysis of 1,500 highly expressed orthologues (similar results are observed for other sets of orthologues, Extended Data Fig. 4c, d).

Dashed lines indicate the mid-developmental transitions. The grey box outlines indicate species-pairs in which the transition is not significant (Extended Data Fig. 3). The inset shows the comparison for *H. dujardini* and *P. dumerilii*, showing also the self-correlations.

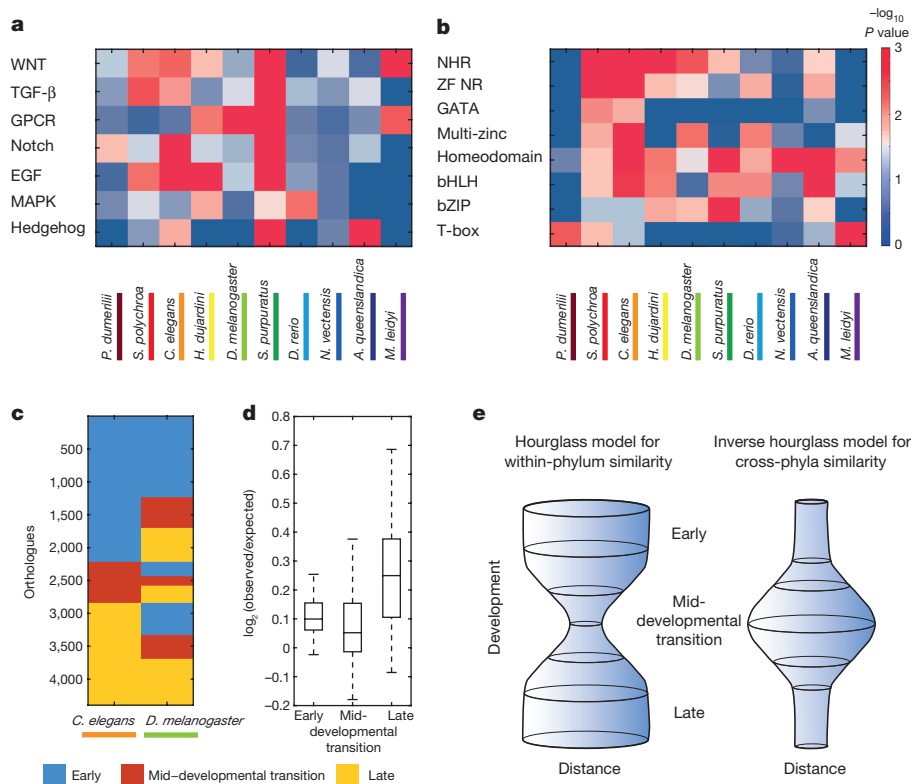


**Figure 4 | An inverse hourglass model for animal evolution.**

**a, b**, Functional enrichments for expression of seven signalling pathways (**a**) and seven transcription factor families (**b**) during the mid-developmental transitions. NHR, nuclear hormone receptors; ZF NR, zinc-finger nuclear receptors; multi-zinc, multiple zinc-fingers.

found that only the homeobox gene family is enriched at the mid-developmental transition in all ten species, as might be expected; otherwise, each species expresses a unique combination of the major developmental transcription factors (Fig. 4b). A distinct combination of signalling pathways and transcription factors during the mid-developmental transition may thus be of particular importance to the development of specific body plans.

Mapping the timing of these mid-developmental transitions back onto the embryonic time-course of nematodes, arthropods, and chordates, we found that they overlap—or partially overlap—with the previously described phylotypic periods of these animals (Fig. 1b). Specifically, in nematodes the transition maps to the end of the ventral enclosure stage which has been proposed as the phylotypic period<sup>7</sup> (Fig. 1b). In chordates, the transition maps to the early part of the pharyngula stage, which for this group of animals has been assigned the phylotypic period<sup>9,15</sup>. Furthermore, in arthropods, the transition centres upon the head involution and dorsal closure stage but also begins at the end of the germ-band stage, which has been assigned as the phylotypic period in this phylum<sup>16,17</sup>. Given this correspondence, we propose that the mid-developmental transition uncovered in this study marks a phylum's phylotypic period. We note, however, that the lack of complete correspondence of the arthropod mid-developmental transition with the germ-band stage will require further analysis and that this provisional definition will also need refinement to account for other taxonomic ranks (for example, class) and for the diversity of life cycles within a phylum.

In the annelid, the mid-developmental transition corresponds to the late trochophore stage, which overlaps the onset of differentiation of the first three larval segments, stomodeal opening (mouth), and ventral nerve cord<sup>18</sup>. These features have been proposed to define the phylotypic period in annelids<sup>19</sup>. Interestingly, the trochophore larva is common to other spiralian phyla (for example, molluscs and nemerteans).

**c**, Comparison of the orthologue temporal associations between *C. elegans* and *D. melanogaster*. **d**, Summary of the 45 pairwise species comparisons of orthologue temporal associations. **e**, Inverse hourglass model for the origin of phyla compared with the hourglass model for within-phylum evolution.

In the flatworm, which undergoes a highly derived mode of development<sup>20</sup>, the mid-developmental transition corresponds to the stage in which the embryonic pharynx is joined by a second 'adult-pharynx', consistent with the phylotypic period previously proposed for this phylum<sup>21</sup>. In the sponge, the mid-developmental transition may occur between the cloud and spot stages, when the primary larval axis is established<sup>22</sup>. We note however that in species with more complex life cycles with several phases of differentiation a single mid-developmental transition may be less accentuated.

Finally, we measured the extent of evolutionary change within the two conserved phases and the mid-developmental transition by determining whether orthologues annotated for a particular temporal category in one species are also annotated to the same temporal category in another species. Figure 4c shows an example of this analysis for *D. melanogaster* and *C. elegans*. For 4,395 orthologues delineated between these two species, the early phase, mid-developmental transition, and the late phase expression account for 51%, 14%, and 35% of the *C. elegans* orthologues, respectively. A total of 28% of the orthologues are annotated to the early phase in both *C. elegans* and *D. melanogaster*, while by chance only 22% are expected given the fraction of genes in each category across the species (Fig. 4c). In contrast, 3% were expected to be conserved at the mid-developmental transition at random, and 3% were observed. The log-odds ratios between observed and expected for the early phase and the mid-developmental transition between *C. elegans* and *D. melanogaster* are thus 0.35 and 0, respectively. Comparing the log-odds ratios across the three temporal categories for each of the 45 pairs of the ten species, we found that the mid-developmental transition profiles are significantly less conserved than the early and late phase expression (Fig. 4d,  $P < 10^{-6}$  compared with the early phase and  $P < 10^{-12}$  with the late phase, Kolmogorov–Smirnov test). We found a similar result when comparing at the level of PFAM domains (Extended Data Figs 6 and 7).



Our results are consistent with an inverse hourglass model for metazoan body plans (Fig. 4e) in which the molecular components that comprise early and late embryogenesis are more conserved, and the signalling pathways and transcription factors acting within the mid-developmental transition are variable across major animal lineages (Fig. 4a, b). Interestingly, the model summarizing comparisons made within a phylum, where gene expression differences across species are minimal at the phylotypic period, has an inverse pattern<sup>23</sup>. Consequently, a 'phylum' may be defined as a set of species sharing the same signals and transcription factor networks during the mid-developmental transition. As a result, transcriptional variance will have an hourglass shape within the phylum, and the inverse is seen when comparing species across phyla (Fig. 4e). A non-phylum lower taxon would not meet these criteria since an hourglass pattern of similarities would be observed both within the taxon and across more distant species. Should this transcriptomic definition hold, evidence will be provided for the usefulness of 'phylum' as a biological classification. It may also suggest the delineation of new phyla, as well as the collapsing of previously distinct ones, requiring validation by zoological studies. We note that the topology of an inverted hourglass has been previously proposed for heterochrony at the phylotypic period<sup>24</sup>, though it was not invoked in the context of inter-phylum divergence.

While the *Hox* cluster has been implicated with the metazoan 'zootype'<sup>25</sup>, we find that even organisms without *Hox* genes (*Amphimedon*<sup>26</sup> and *Mnemiopsis*<sup>27</sup>) have a mid-developmental transition period at a time consistent with a phylotypic period (Fig. 1b). Thus, more ancient than the patterning of the body axis by *Hox* genes, may be the molecular constraints of the transition from a general phase of proliferation to a phase of signalling and differentiation that results in the positioning of cells in a phylum-specific manner. Such a transition may be a hallmark of development only in animals, or future work may show that this is a general characteristic of development in all multicellular life. It will be interesting to further employ systematic analyses in studying the developmental constraints on metazoans and other clades<sup>8,28</sup>.

**Online Content** Methods, along with any additional Extended Data display items and Source Data, are available in the online version of the paper; references unique to these sections appear only in the online paper.

**Received 19 July 2015; accepted 12 January 2016.**

**Published online 17 February 2016.**

- Valentine, J. W. *On the Origin of Phyla* (Univ. Chicago Press, 2004).
- Haeckel, E. *The Evolution of Man* Vol. 1 (C. K. Paul & Company, 1879).
- Darwin, C. *On the Origin of Species by Means of Natural Selection, or, The Preservation of Favoured Races in the Struggle for Life* (J. Murray, 1859).
- Gould, S. J. *Ontogeny and Phylogeny*. (Harvard Univ. Press, 1977).
- Abzhanov, A. Von Baer's law for the ages: lost and found principles of developmental evolution. *Trends Genet.* **29**, 712–722 (2013).
- Kalinka, A. T. *et al.* Gene expression divergence recapitulates the developmental hourglass model. *Nature* **468**, 811–814 (2010).
- Levin, M., Hashimshony, T., Wagner, F. & Yanai, I. Developmental milestones punctuate gene expression in the *Caenorhabditis* embryo. *Dev. Cell* **22**, 1101–1108 (2012).
- Domazet-Lošo, T. & Tautz, D. A phylogenetically based transcriptome age index mirrors ontogenetic divergence patterns. *Nature* **468**, 815–818 (2010).
- Irie, N. & Kuratani, S. Comparative transcriptome analysis reveals vertebrate phylotypic period during organogenesis. *Nature Commun.* **2**, 248 (2011).
- Scholtz, G. in *Evolutionary Developmental Biology of Crustacea. Crustacean Issues* 15. 3–16 (A. A. Balkema, 2004).

- Ryan, J. F. *et al.* The genome of the ctenophore *Mnemiopsis leidyi* and its implications for cell type evolution. *Science* **342**, 1242592 (2013).
- Hashimshony, T., Wagner, F., Sher, N. & Yanai, I. CEL-Seq: single-cell RNA-Seq by multiplexed linear amplification. *Cell Rep.* **2**, 666–673 (2012).
- Anavy, L. *et al.* BLIND ordering of large-scale transcriptomic developmental timecourses. *Development* **141**, 1161–1166 (2014).
- Davidson, E. H. *The Regulatory Genome: Gene Regulatory Networks in Development And Evolution* (Academic Press, 2006).
- Ballard, W. W. Morphogenetic movements and fate maps of vertebrates. *Am. Zool.* **21**, 391–399 (1981).
- Patel, N. H. Developmental evolution: insights from studies of insect segmentation. *Science* **266**, 581–590 (1994).
- Sander, K. in *Development and Evolution* (eds Goodwin, B. C., Holder, N. & Wylie, C. C.) 137–160 (Cambridge Univ. Press, 1983).
- Fischer, A. H., Henrich, T. & Arendt, D. The normal development of *Platynereis dumerilii* (Nereididae, Annelida). *Front. Zool.* **7**, 31 (2010).
- Slack, J. M. W. in *Keywords and Concepts in Evolutionary Developmental Biology* (eds Hall, B. K. & Olson, W. M.) 476 (Harvard Univ. Press, 2003).
- Cardona, A., Hartenstein, V. & Romero, R. Early embryogenesis of planaria: a cryptic larva feeding on maternal resources. *Dev. Genes Evol.* **216**, 667–681 (2006).
- Martín-Durán, J. M. & Egger, B. Developmental diversity in free-living flatworms. *EvoDevo* **3**, 7 (2012).
- Adamska, M. *et al.* The evolutionary origin of hedgehog proteins. *Curr. Biol.* **17**, R836–R837 (2007).
- Raff, R. A. *The Shape of Life: Genes, Development, and the Evolution of Animal Form* (Univ. Chicago Press, 1996).
- Richardson, M. K. Vertebrate evolution: the developmental origins of adult variation. *Bioessays* **21**, 604–613 (1999).
- Slack, J. M., Holland, P. W. & Graham, C. F. The zootype and the phylotypic stage. *Nature* **361**, 490–492 (1993).
- Larroux, C. *et al.* The NK homeobox gene cluster predates the origin of Hox genes. *Curr. Biol.* **17**, 706–710 (2007).
- Ryan, J. F., Pang, K., Mullikin, J. C., Martindale, M. Q. & Baxevanis, A. D. The homeodomain complement of the ctenophore *Mnemiopsis leidyi* suggests that Ctenophora and Porifera diverged prior to the ParaHoxozoa. *EvoDevo* **1**, 9 (2010).
- Hashimshony, T., Feder, M., Levin, M., Hall, B. K. & Yanai, I. Spatiotemporal transcriptomics reveals the evolutionary history of the endoderm germ layer. *Nature* **519**, 219–222 (2015).
- Hejnol, A. *et al.* Assessing the root of bilaterian animals with scalable phylogenomic methods. *Proc. R. Soc. Lond. B* **276**, 4261–4270 (2009).
- Dunn, C. W. *et al.* Broad phylogenomic sampling improves resolution of the animal tree of life. *Nature* **452**, 745–749 (2008).

**Supplementary Information** is available in the online version of the paper.

**Acknowledgements** We thank M. Rockman and B. de Bivort for helpful discussions. We also thank U. Gat, A. Salzberg, S. B. Tabou De Leon, M. Blaxter, G. Koutsovoulos, S. Mansour, and B. Goldstein for materials and reagents. We thank the Technion Genome Center for technical assistance and the Radcliffe Institute for Advanced Studies at Harvard University for hosting the analysis phase. This work was supported by a European Research Council grant (EvoDevoPaths), the EMBO Young Investigator Program, and a grant from the Australian Research Council.

**Author Contributions** M.L., T.H., and I.Y. conceived and designed the project. M.L. led the collection of samples with help from N.N., D.S., N.M., S.K. and A.J.-V. The processing of the samples for CEL-Seq was carried out by M.L., T.H., N.M., S.K., and N.S. *De novo* transcriptome assembly was carried out by L.A. with assistance from I.Y., E.W., J.F.R., and S.-Y.L. Processing of CEL-Seq reads and initial bioinformatics was performed by L.A. with help from M.F., E.W., E.K., D.H.S., O.S., T.L., and S.L.F.-V. The data was analysed by I.Y. and L.A. I.Y. coordinated the interpretation of the data with significant help from B.M.D.; L.A., S.M.D., T.H., A.G.C., D.A., J.F.R., M.Q.M., K.Y., and J.C.R. also contributed to the interpretation of the data. I.Y. wrote the manuscript which the authors commented on.

**Author Information** The complete data set has been deposited to the NCBI GEO database GSE70185. Reprints and permissions information is available at [www.nature.com/reprints](http://www.nature.com/reprints). The authors declare no competing financial interests. Readers are welcome to comment on the online version of the paper. Correspondence and requests for materials should be addressed to I.Y. ([yanai@technion.ac.il](mailto:yanai@technion.ac.il)).



## METHODS

**Data reporting.** No statistical methods were used to predetermine sample size. The investigators were not blinded to allocation during experiments and outcome assessment.

**Sample collection.** *Platynereis dumerilii* embryos were collected in EMBL Heidelberg, Germany. In each of several containers, a gravid male and a female were mixed in a small container containing North Sea water. The classical breeding dance was observed after several minutes and the females and males released oocytes and sperm. Fertilized eggs were incubated at 18 °C and embryos were collected every hour after fertilization for a period of 5 days. Individual embryos were collected on the cap of a 1.5 ml Eppendorf tube using a micro mouth pipette. Excessive water was removed and the sample was flash-frozen in liquid nitrogen.

*Schmidtea polychroa* embryos were collected at the Max Planck Institute CBG, Dresden, Germany. A population of *S. polychroa* was maintained in the lab at 20 °C as previously described<sup>31</sup>. Egg capsules were regularly collected over 15 days of development just after deposition and kept in Petri dishes at 20 °C. To release embryos for isolation, capsules were carefully opened using two fine forceps. After assessment of stage of development according to the Martin–Duran system<sup>32</sup> excess water was removed and embryos were flash-frozen in Eppendorf tubes in liquid nitrogen.

*Hypsibius dujardini* starting cultures were provided by Bob Goldstein (University of North Carolina at Chapel Hill) and embryos were collected as previously described<sup>33</sup> at the Technion, Israel. Small cultures of tardigrades were kept in 60 mm glass Petri dishes in commercial bottled spring water until gravid animals were visible. Tardigrades lay 2–5 eggs during molting, with the embryos deposited in their shed exoskeleton, the exuvia. Soon after the adult crawled out of the exuvia, it was cut open using a scalpel on a microscope cavity-slide to release embryos into the medium. Embryos were observed using a standard binocular and when reaching two-cell stage were deposited in a 10 µl drop mineral water on the cap of a 1.5 ml Eppendorf tube. Tubes were incubated for respective periods at 20 °C. For 4.5 days, once per hour past the two-cell stage, embryos were inspected for viability, excessive water was removed using a micro mouth pipette, and the tube was flash-frozen in liquid nitrogen.

*Drosophila melanogaster* embryos were collected at the Technion using a previously published protocol<sup>34</sup>. Briefly, agar plates with apple juice smeared with freshly prepared yeast were used to make young adult flies lay a lot of eggs. Cages consisting of such plates were set up with at least 20 flies and left for roughly one day for the flies to acclimatize. Plates were replaced with fresh ones twice in one hour interval to ensure the use of only newly laid eggs. *Drosophila* embryos are covered with a non-transparent chorion which has to be removed before live imaging by dechoriation. Shortly after being laid, embryos were washed off from plates into a plastic sieve using tap water and a fine brush used to loosen the embryos. In the sieve, embryos were submerged in 50% bleach solution for two minutes. Embryos were washed and rinsed with cold water. Using a needle pick, 20 embryos were placed in a row on a strip of agar placed on a glass slide. n-Heptane glue was applied in a thin layer on a big glass cover slip. This coverslip was carefully put upside down on top of the embryos on the agar strip so that embryos adhere to the glue layer. Embryos were covered with PBS and kept in humid chambers at 25 °C. Embryos on the coverslip were observed under the light microscope and for each embryo, the time of cellularization was noted. To collect an embryo, a needle pick was used to carefully remove it from the slide and it was flash-frozen in an Eppendorf tube in liquid nitrogen.

*Strongylocentrotus purpuratus* oocytes and sperm were kindly provided by Smadar Ben Tabou deLeon (Haifa University, Israel) and mixed and cultured at the Technion. Mixing occurred by 4 drops of sperm in 50 ml of eggs in sea water and incubated at 18 °C in Petri dishes. After fertilization, every 40 min (for a period of 72 hours), single embryos were deposited on the cap of a 1.5 ml Eppendorf tube. Excessive water was removed using a micro mouth pipette and the embryo was flash-frozen in liquid nitrogen.

*Danio rerio* fertilization was performed in the lab of Karina Yaniv (Weizmann Institute, Israel). Four female and one male *Danio rerio* fish were mixed in a breeder tank. Fertilized eggs were collected into zebrafish embryo medium as previously described<sup>35</sup>. Fertilized eggs were sampled in a small volume of medium every 40 min from fertilization into the cap of a 1.5 ml Eppendorf tube. Excess water was removed using a micro mouth pipette and the embryo flash-frozen in liquid nitrogen.

*Nematostella vectensis* egg masses and sperm were provided by Amos Schaffer (Gat Lab, Hebrew University of Jerusalem). Eggs and sperms were mixed and egg jelly was dissolved as previously described<sup>36</sup> using 4% cysteine (pH 7.4–7.6) to make single embryos accessible for collection. The embryos were washed with cysteine six times using 30% of sea water. Fertilized embryos were observed under a light microscope and embryos reaching the 4-cell stage were deposited in a 10 µl

drop of 30% salt water on the cap of a 1.5 ml Eppendorf tube. Tubes were closed and incubated for respective periods at 20 °C. At collection time, embryos were inspected for viability and excessive water was removed using a micro mouth pipette. The embryo was then flash-frozen in liquid nitrogen. After (and including) the four-cell stage, every 20 minutes (for a period of 48 hours when the embryos reached the late planula stage), single embryos were deposited on the cap of a 1.5 ml Eppendorf tube.

*Mnemiopsis leidyi* embryos were collected in the Whitney Institute, University of Florida as previously described<sup>37</sup>. Stages ranged from the fertilized egg to 20 h. Three replicate time-courses each comprising 20 embryos were isolated. In one replicate, embryos were flash frozen and shipped on dry ice. In the other two RNA was prepared by a TRIzol extraction and shipped in 75% ethanol on dry ice.

**RNA-seq transcriptome sequencing.** For *Hypsibius dujardini*, *Schmidtea polychroa*, and *Platynereis dumerilii*, RNA was isolated from a mixed population of embryos, larvae, and adults according to the TRIzol protocol (Invitrogen). This RNA was processed according to the Illumina TruSeq RNA-seq protocol by the Technion Genome Center and 100 bp paired-end sequencing was performed. To pre-process the reads, 'Sickle'<sup>38</sup> was used for quality trimming with a threshold of 31 and Illumina adaptors were removed using 'Scythe'<sup>39</sup>. Sequencing error correction was next made using the AllpathLG toolkit<sup>40</sup> and poly-A sequences were trimmed using trimest (Gary Williams, unpublished). The resulting libraries were cleaned of short and duplicate reads using the fastx toolkit (Assaf Gordon, unpublished). *Hypsibius dujardini*'s genome has been recently reported by two groups<sup>41,42</sup>.

**Mapping to *S. purpuratus* and *N. vectensis*.** The sea urchin transcriptome was downloaded from Echinobase, NCBI BioProject PRJNA81157. The longest isoform per transcript was selected leaving ~21,000 peptides. For this organism the mapping was done more loosely with bowtie parameters set to "–mp 3,1 -N 1 -L 15" as the RNA-seq was done on a heterogenic population. For *Nematostella* we retrieved the T1 transcriptome from Stellabase<sup>43</sup>. Using Transdecoder (<https://transdecoder.github.io>) revealed that, of the ~115,000 transcripts, only ~53,000 encoded proteins. BLAST analysis of the encoded protein resulted in ~42,000 unique proteins and the longest transcript was selected for each protein.

**CEL-Seq transcriptome sequencing.** Total RNA was extracted from single embryos using TRIzol as previously described<sup>7</sup> including minor adjustments. After the addition of TRIzol to the embryos the mixture was frozen in liquid nitrogen, thawed at 37 °C and vortexed for 30 s. This procedure was repeated five times. Chloroform was then added and the sample further processed. The dried total RNA pellet was dissolved in RNase-free water before introduction into subsequent amplification and sequencing library preparation steps. Using the CEL-Seq protocol<sup>44</sup>, 1 µl of a single embryo total RNA sample with a maximum concentration of 50 ng µl<sup>-1</sup>, was mixed with 1 µl of the ERCC spike-in kit diluted according to the manufacturer's protocol<sup>45</sup>. The libraries were sequenced using Illumina paired-end sequencing as previously reported in the CEL-Seq protocol<sup>44</sup>. For Read 1, used to determine the barcode, the first 15 bp were sequenced and for Read 2, used to determine the identity of the transcript, the first 35 bp were sequenced. The CEL-Seq pipeline is available at <https://github.com/yanailab/CEL-Seq-pipeline>.

**CEL-Seq initial analysis pipeline.** Transcript abundances were obtained from the sequencing data using custom scripts organized into a multistep paralleled computational pipeline. Briefly, after trimming and filtering, the paired-end reads were demultiplexed based on the first eight bases of the first read. For each sample, reads were mapped to a reference genome or transcriptome using bowtie2 version 2.2.3 (ref. 46) with default parameters and counted using htseq-count<sup>47</sup> to generate read counts. Samples were filtered to include only samples with at least 500,000 reads and in additions ERCC spike-in information was also used to filter out samples with low correlation coefficients (<0.65) to the known concentration or with high (>0.3) spike-in to gene read count ratio. Read counts were then normalized by dividing by the total number of counted reads and multiplying by 10<sup>6</sup>. Because CEL-Seq retains only the 3' end of the transcript, this procedure yields the estimated gene expression levels in transcripts per million (tpm) without transcript length normalization. In this work, we compare the transcripts per million developmental profiles for different genes and across orthologues, and such comparisons are generally robust to overall RNA content changes.

**De novo transcriptome assembly with strand and 3' anchoring.** A *de novo* transcriptome was generated for *S. polychroa*, *P. dumerilii* and *H. dujardini*. Since we had at our disposal CEL-Seq reads, in addition to the RNA-Seq reads, our strategy was to exploit the stranded and 3'-biased nature of CEL-Seq. The Trinity software<sup>48</sup> was used to generate, for each of the three species, two *de novo* transcriptome assemblies: (1) single-end CEL-Seq reads were used to generate a 3' biased stranded transcriptome, and (2) the CEL-Seq reads were combined with paired-end RNA-seq reads were used to generate a combined transcriptome. For the CEL-Seq 3' assembly, we ran Trinity using the single-end mode with 'SS\_lib\_type' parameter set to 'F'. For the combined assembly we ran Trinity using the paired-end mode

with default parameters. The two resulting transcriptomes were then used to generate a single 3' anchored stranded transcriptome. For each transcript (contig) in the first set, we identified the corresponding transcripts in the second set using BLAST<sup>49</sup>. Of those identified, we selected the transcript with the highest alignment score and used the strand information of the transcript in the first set to generate a stranded transcript (Extended Data Fig. 1). Genes with alternative 3'-ends may be represented as distinct genes in this set, in those rare cases when the CEL-Seq contigs do not overlap. The generated set of transcripts was further filtered to contain only transcripts with a predicted protein using the Trinotate pipeline that is a part of the Trinity software<sup>48</sup>. PFAM domains<sup>50</sup> were then identified using HMMER<sup>51</sup>.

**Gene Ontology and PFAM.** GO annotations for each transcriptome were generated using Trinotate (<http://trinotate.github.io/>). Specifically, transcripts were searched against Uniprot sequences (comprising SwissProt and TrEMBL invertebrate, vertebrate, mammal, rodents and human data, clustered to 90% identity). GO and PFAM identifiers were then extracted from Uniprot accessions.

**Delineation of orthologous clusters.** OrthoMCL<sup>52</sup> was used to delineate orthologous clusters from the ten proteomes of the ten species using the following parameters: "percentMatchCutoff" was set to 24, "valueExponentCutoff" was set to -5, and the MCL parameters were "-abc -I 1.5". In the case of multiple genes in an orthology cluster for a particular species, the one with the highest fold-change was selected as the representative. We found similar results if the representative is selected randomly among the inparalogues.

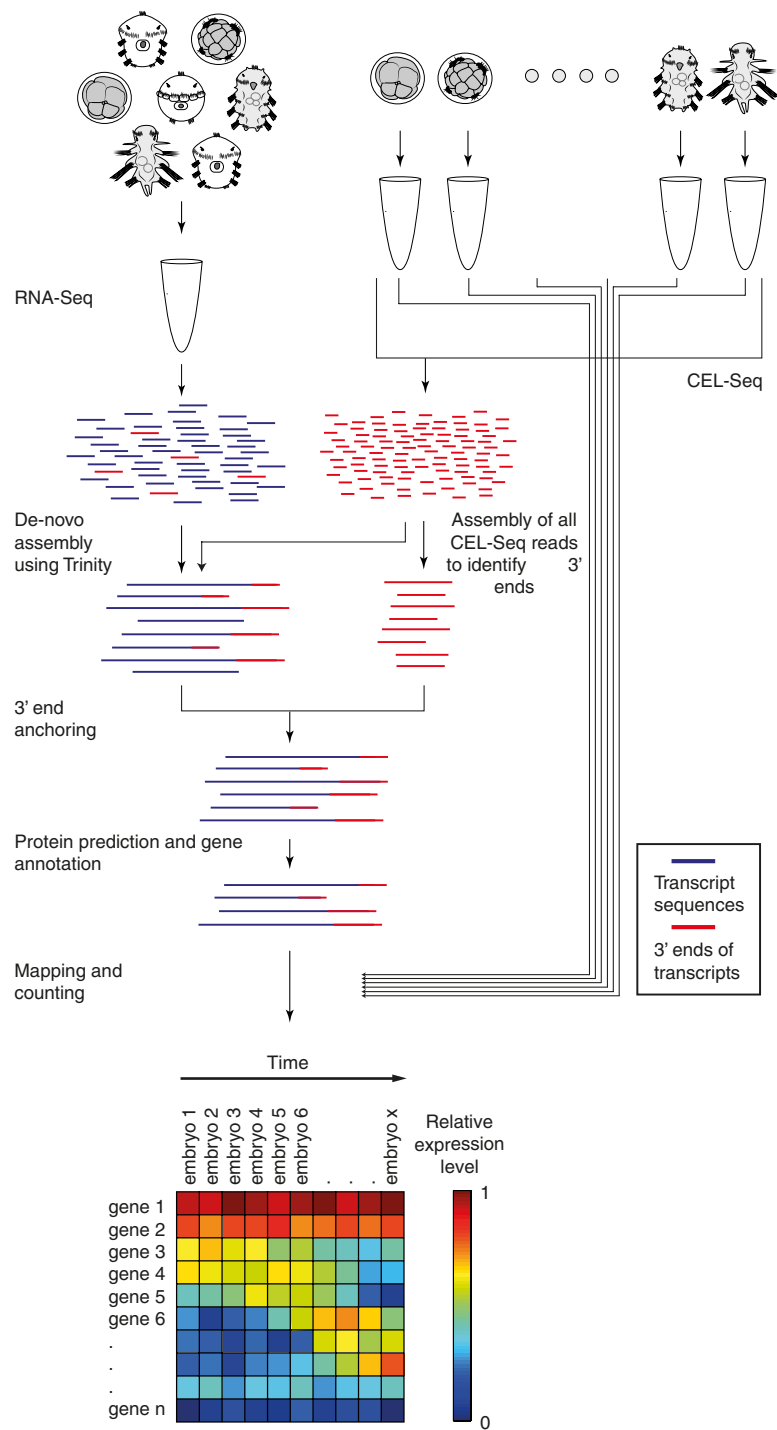
**Developmental gene expression profiles.** Each time-course was initially ordered using BLIND—an automated method for determining the developmental order of transcriptomic samples<sup>13</sup> (Extended Data Fig. 2a). These profiles were smoothed using a moving average calculation with span parameter set to 3. In order to compare profiles of equal lengths, for each species we reduced the time-course to twenty sliding windows using the following method. We defined the size of the window such that there is only overlap between every two consecutive windows. For each window, the average expression was calculated for each gene across the included embryos. For each time-course, dynamic genes were defined as those with minimum expression of 10 transcripts per million and at least a twofold change. Standardized expression was used in analysis where noted: to generate a standardized expression, the mean expression value was subtracted from each expression value and the results were divided by the standard deviation. To generate the phasegrams shown in Fig. 2 we first standardized the log<sub>10</sub> profiles by subtracting the mean and dividing by the standard deviation. We next computed the first two principal components of this expression data; since the profiles were standardized, the genes form a circle. The genes are then sorted according to their angle from the origin in this space. A gene expression profile was mapped to a temporal phase (early, transition, or late) by computing the correlation with the three idealized profiles shown in Extended Data Fig. 5 and assigning it to the pattern exhibiting the highest correlation and thus best match.

**Mid-developmental transition detection.** The transition period for each species was computed based upon the transcriptome similarities with the transcriptomes of the other species, shown in Fig. 3. The twenty transcriptomes were clustered using hierarchical clustering based upon the Euclidean distances among their profiles of correlations with the profiles of all other species. The two deepest clusters were then identified and the precise temporal window separating them was set as the mid-developmental transition period.

**Gene Ontology (GO) enrichment analysis.** A temporal phase was assigned to each orthologous group by annotating it to its most represented phase. The *C. elegans* Gene Ontology annotation was used on the *C. elegans* orthologues. Enrichment was computed using the hypergeometric distribution. In order to avoid retrieving enrichments due to the same set of genes we carried out serial enrichments as follows. The most enriched gene ontology group was noted, its genes removed from the set, and enrichment search was repeated to detect additional Gene Ontology terms. For the signalling pathways shown in Fig. 4b, the following gene ontology terms were used: 'Wnt signalling pathway', 'Notch signalling pathway', 'hedgehog receptor activity', 'epidermal growth factor receptor signalling pathway', 'transforming growth factor beta receptor signalling pathway', 'MAPK cascade', 'G-protein coupled receptor activity'. For this analysis, we searched for enrichment up to three windows before and after the inferred transition, and kept the most significant *P* value for each pathway (hypergeometric distribution).

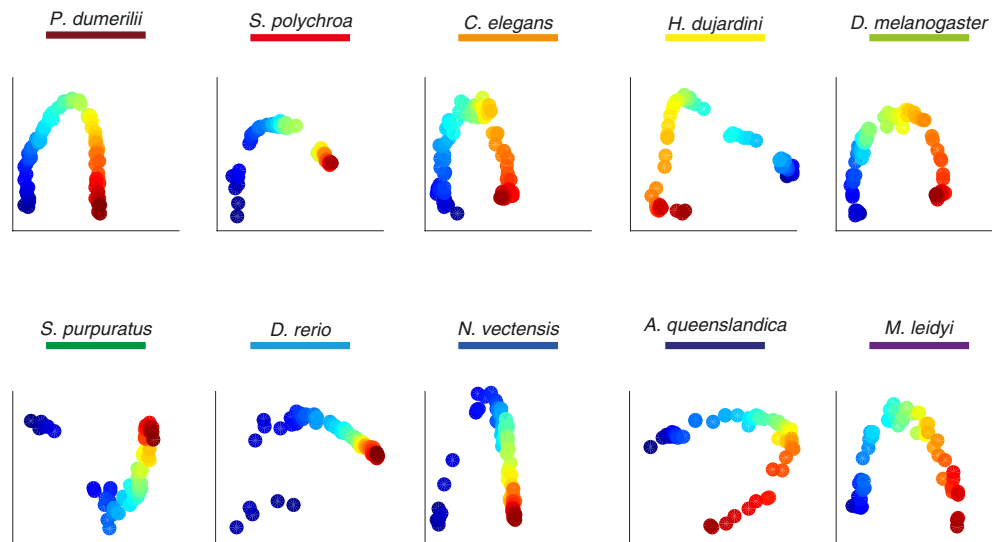
**PFAM signatures.** For each of 5,745 PFAMs, we computed an enrichment profile throughout time, and for each species, as follows. For each of the twenty expression windows of the matrix of standardized log<sub>10</sub> expression values of the dynamic genes, we marked genes with expression above 0.5 as expressed. We then calculated the fraction of the genes within this set that contain genes annotated to the PFAM domain. A temporal phase was annotated using supervised clustering using the same approach shown in Extended Data Fig. 5. For the transcription factor families shown in Fig. 4d the following PFAMs were used: 'Homeobox domain', 'GATA zinc finger', 'Ligand-binding domain of nuclear hormone receptor', 'Helix-loop-helix DNA-binding domain', 'bZIP transcription factor', 'Zinc finger, C4 type (two domains)', 'Zinc finger, C2H2 type', and 'T-box'. For this analysis, we searched for enrichment up to three windows before and after the inferred transition, and kept the most significant *P* value for each TF family (hypergeometric distribution).

- Martín-Durán, J. M., Duocastella, M., Serra, P. & Romero, R. New method to deliver exogenous material into developing planarian embryos. *J. Exp. Zool. B Mol. Dev. Evol.* **310**, 668–681 (2008).
- Martín-Durán, J. M., Amaya, E. & Romero, R. Germ layer specification and axial patterning in the embryonic development of the freshwater planarian *Schmidtea polychroa*. *Dev. Biol.* **340**, 145–158 (2010).
- Gabriel, W. N. et al. The tardigrade *Hypsibius dujardini*, a new model for studying the evolution of development. *Dev. Biol.* **312**, 545–559 (2007).
- Kiehart, D. P., Crawford, J. M. & Montague, R. A. Collection, dechoriation, and preparation of *Drosophila* embryos for quantitative microinjection. *Cold Spring Harb. Protoc.* **2007**, <http://dx.doi.org/10.1101/pdb.prot4717> (2007).
- Detrich, H. W., Westerfield, M. & Zon, L. I. *Essential Zebrafish Methods: Cell and Developmental Biology*. (Academic Press, 2009).
- Fritzenwanker, J. H. & Technau, U. Induction of gametogenesis in the basal cnidarian *Nematostella vectensis* (Anthozoa). *Dev. Genes Evol.* **212**, 99–103 (2002).
- Pang, K. & Martindale, M. Q. *Mnemiopsis leidyi* spawning and embryo collection. *Cold Spring Harb. Protoc.* **2008**, <http://dx.doi.org/10.1101/pdb.prot5085> (2008).
- Joshi, N. & Fass, J. Sickle: A sliding-window, adaptive, quality-based trimming tool for FastQ files. <https://github.com/najoshi/sickle> (2011).
- Vince, B. Scythe — A Bayesian adapter trimmer. <https://github.com/vsbuffalo/scythe> (2011).
- Gnerre, S. et al. High-quality draft assemblies of mammalian genomes from massively parallel sequence data. *Proc. Natl Acad. Sci. USA* **108**, 1513–1518 (2011).
- Boothby, T. C. et al. Evidence for extensive horizontal gene transfer from the draft genome of a tardigrade. *Proc. Natl Acad. Sci. USA* **112**, 15976–15981 (2015).
- Koutsovoulos, G. et al. The genome of the tardigrade *Hypsibius dujardini*. Preprint at *bioRxiv* <http://dx.doi.org/10.1101/033464> (2015).
- Sullivan, J. C., Reitzel, A. M. & Finnerty, J. R. Upgrades to StellaBase facilitate medical and genetic studies on the starlet sea anemone, *Nematostella vectensis*. *Nucleic Acids Res.* **36**, D607–D611 (2008).
- Hashimshony, T., Wagner, F., Sher, N. & Yanai, I. CEL-Seq: single-cell RNA-Seq by multiplexed linear amplification. *Cell Rep.* **2**, 666–673 (2012).
- Baker, S. C. et al. The External RNA Controls Consortium: a progress report. *Nature Methods* **2**, 731–734 (2005).
- Langmead, B. & Salzberg, S. L. Fast gapped-read alignment with Bowtie 2. *Nature Methods* **9**, 357–359 (2012).
- Anders, S., Pyl, P. T. & Huber, W. HTSeq—A Python framework to work with high-throughput sequencing data. *Bioinformatics* **31**, 166–169 (2015).
- Haas, B. J. et al. *De novo* transcript sequence reconstruction from RNA-seq using the Trinity platform for reference generation and analysis. *Nature Protocols* **8**, 1494–1512 (2013).
- Altschul, S. F., Gish, W., Miller, W., Myers, E. W. & Lipman, D. J. Basic local alignment search tool. *J. Mol. Biol.* **215**, 403–410 (1990).
- Punta, M. et al. The Pfam protein families database. *Nucleic Acids Res.* **40**, D290–D301 (2012).
- Finn, R. D., Clements, J. & Eddy, S. R. HMMER web server: interactive sequence similarity searching. *Nucleic Acids Res.* **39**, W29–W37 (2011).
- Li, L., Stoeckert, C. J. & Roos, D. S. OrthoMCL: identification of ortholog groups for eukaryotic genomes. *Genome Res.* **13**, 2178–2189 (2003).
- Simão, F. A., Waterhouse, R. M., Ioannidis, P. & Kriventseva, E. V. & Zdobnov, E. M. BUSCO: assessing genome assembly and annotation completeness with single-copy orthologs. *Bioinformatics* (2015).

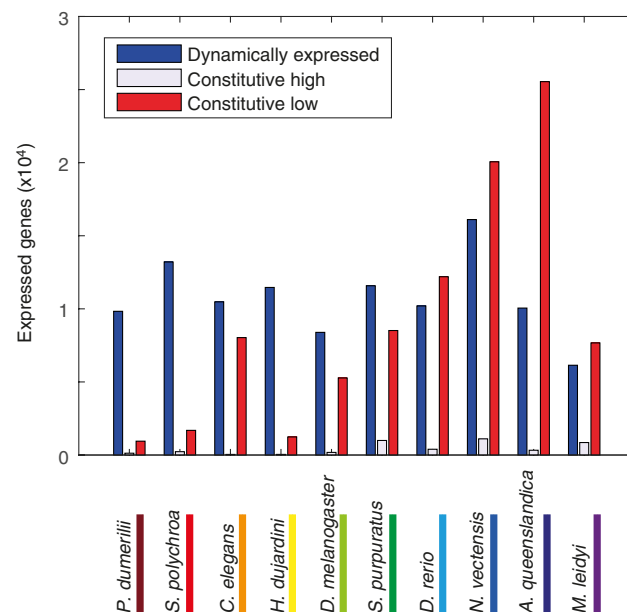


**Extended Data Figure 1 | A schematic for the *de novo* transcriptome analysis.** See also the Methods section. CEL-Seq reads were mapped to the published transcriptomes where available.

a



b

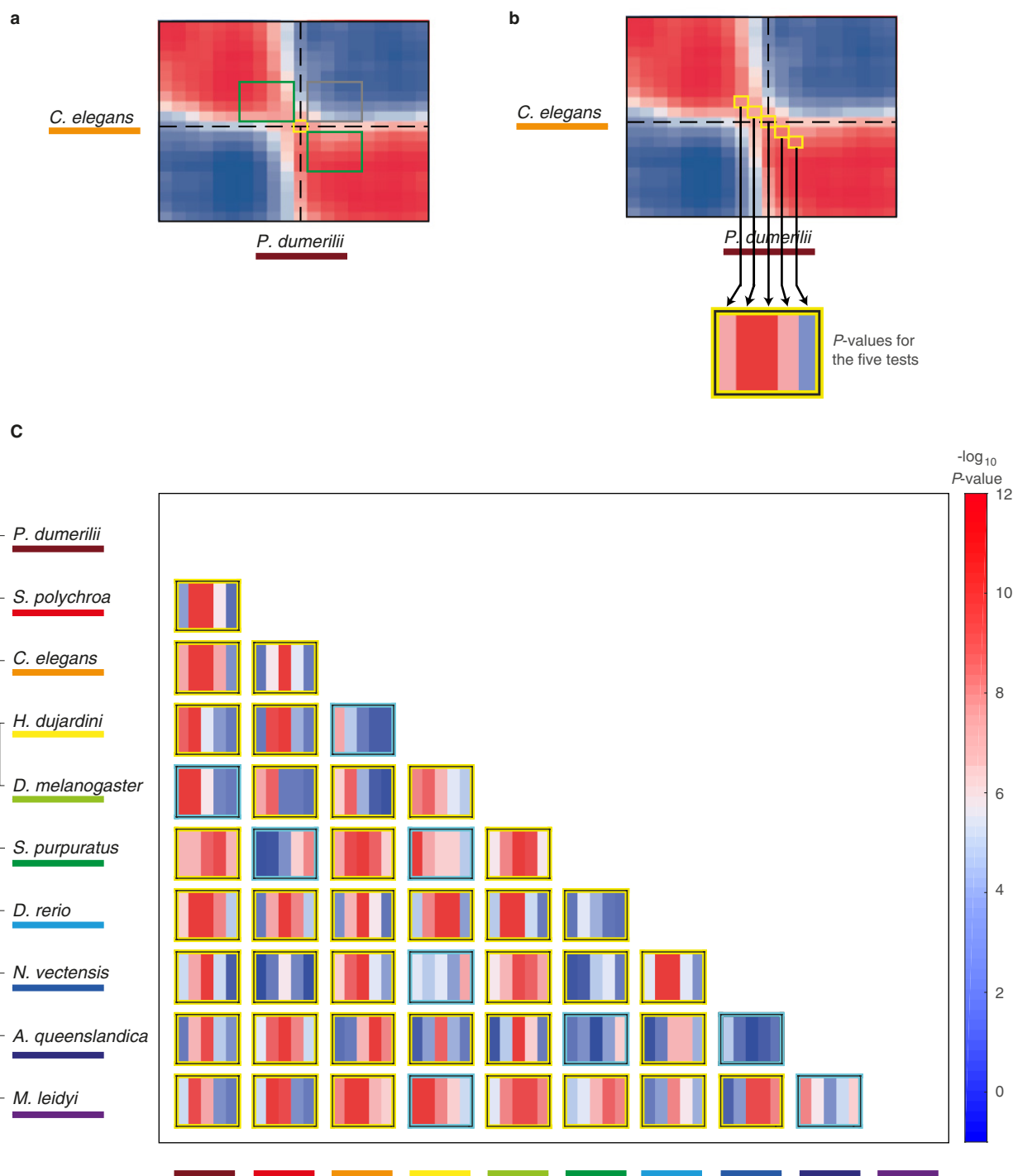


### Extended Data Figure 2 | Gene expression time-courses for ten species.

**a**, BLIND analysis on the reported time-courses. The colour indicates the ordering. The species is indicated for each plot. **b**, The number of dynamically expressed genes for each species. The species are shown in the

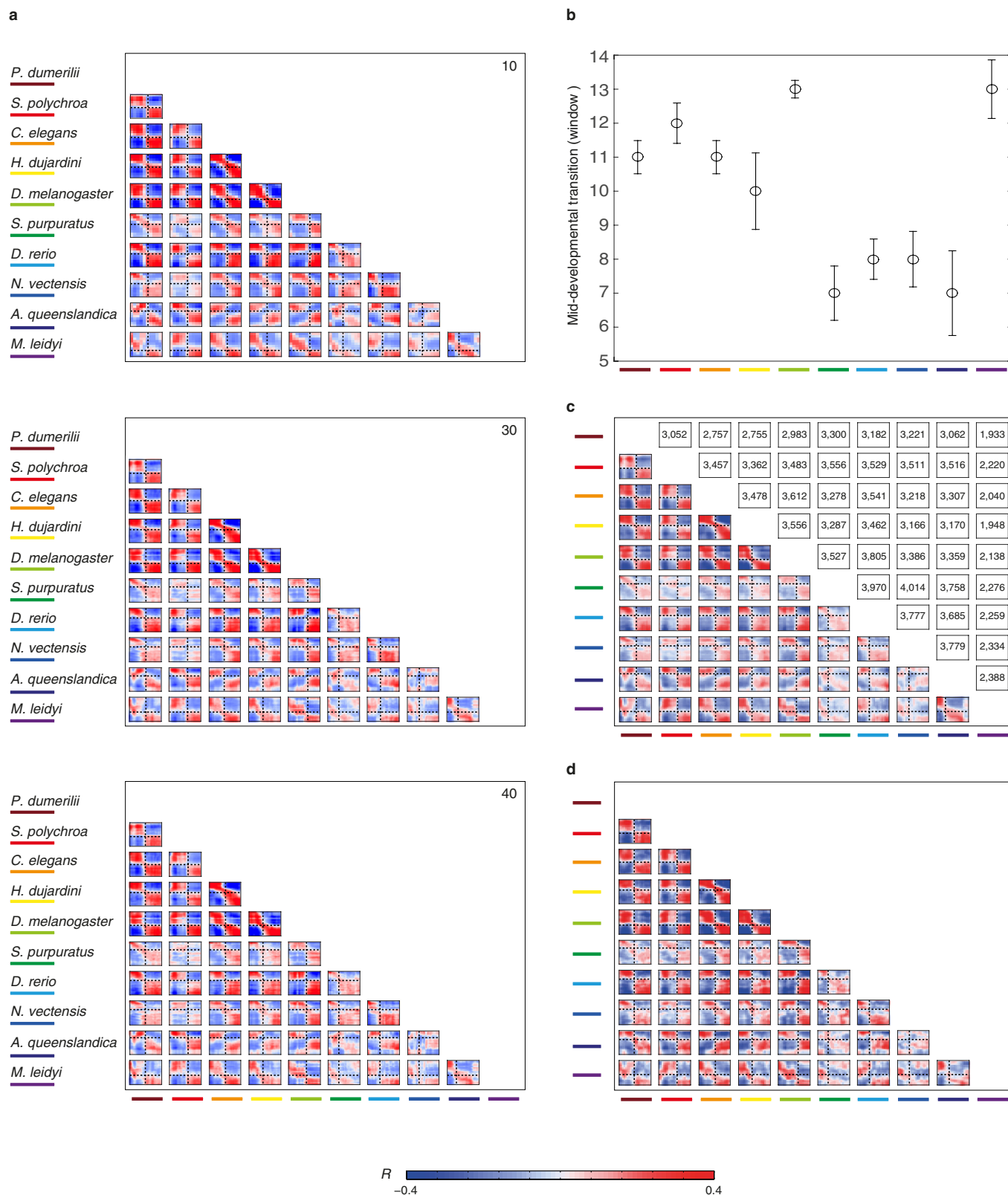
same order as in the main figures. Constitutively high (low) expression is defined as that where the maximum expression is more (less) than the 10 transcripts per million threshold yet is not dynamic (two-fold change and at least 10 transcripts per million maximum expression).

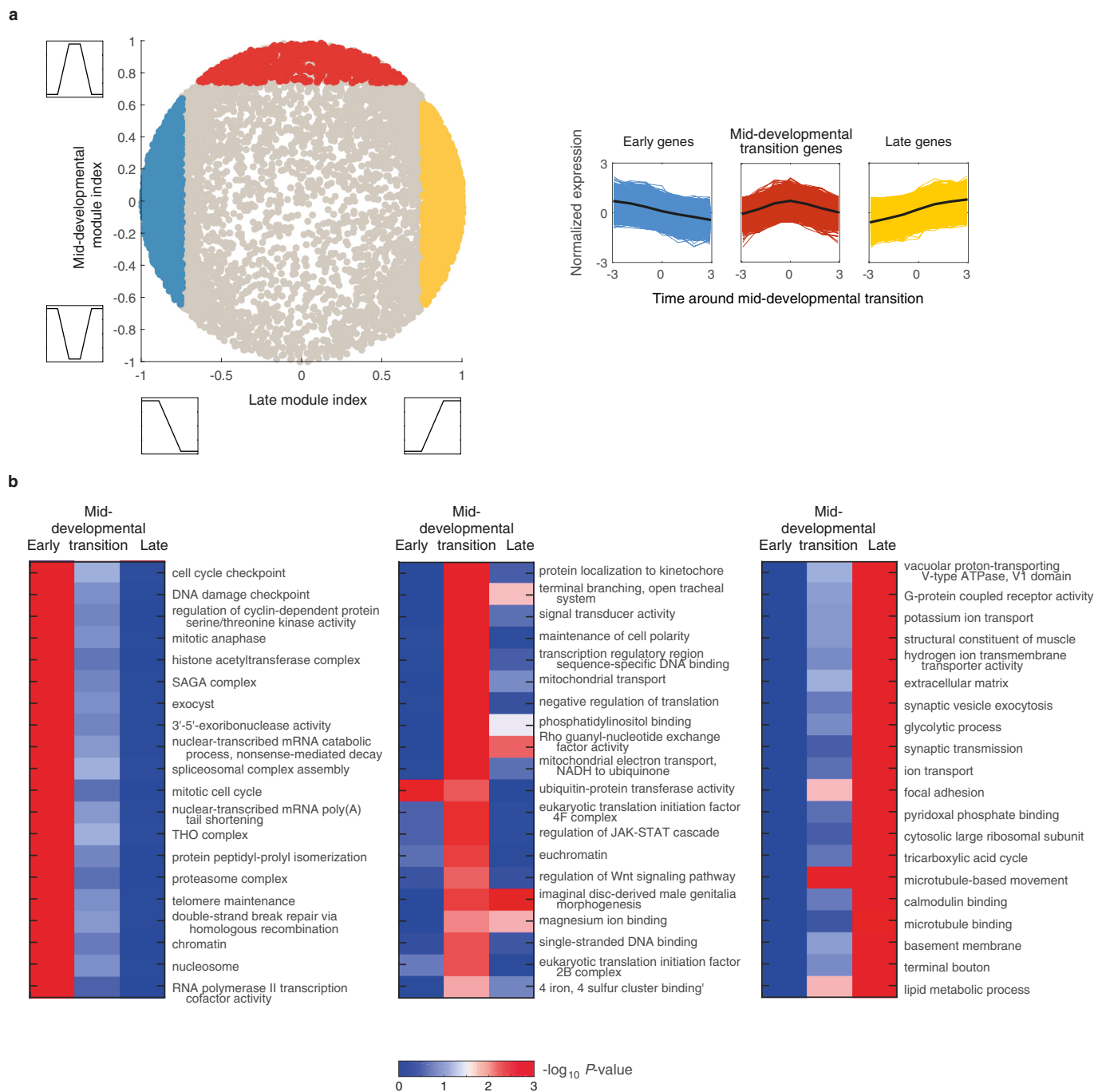




**Extended Data Figure 3 | Testing the significance of the transition in the orthologue correlation matrices shown in Fig. 3. a**, Schematic indicating the mid-developmental transition (orange), correlations among windows of the same phase (green), and correlations among windows of different phases (grey). **b**, The orange squares indicate statistical tests examined in **c**. **c**, For each pair of species a series of Kolmogorov–Smirnov

tests are shown. Each test compares the intra-phase to the inter-phase correlations (**a**) for the mid-developmental transition and three windows before and after it (**b**). The yellow boxes indicate those species comparisons where there is significant statistical evidence for the dual-phase pattern (higher significance for the middle tests).





**Extended Data Figure 5 | Gene enrichment analysis.** **a**, A landscape showing for each gene (circle) the correlation with an idealized 'late module profile' (x axis) and with a 'transition profile' (y axis). The idealized profiles used to compute correlations are shown in the insets. Spots correspond to *C. elegans* genes. They are coloured according to the assigned sets: early module (blue), mid-developmental transition (red), and late module (yellow). **b**, Gene Ontology (GO) enrichment for the early phase, transition, and late phase gene sets. The gene sets were defined by

integrating expression from all ten species. 'RNA polymerase II...' is short for 'RNA polymerase II core promoter sequence-specific DNA binding transcription factor activity involved in preinitiation complex assembly'. The legend indicates the assigned sets: early phase (blue), mid-developmental transition (red), and late phases (yellow). The profiles are of length seven since we examined three windows before and after the mid-developmental transition.

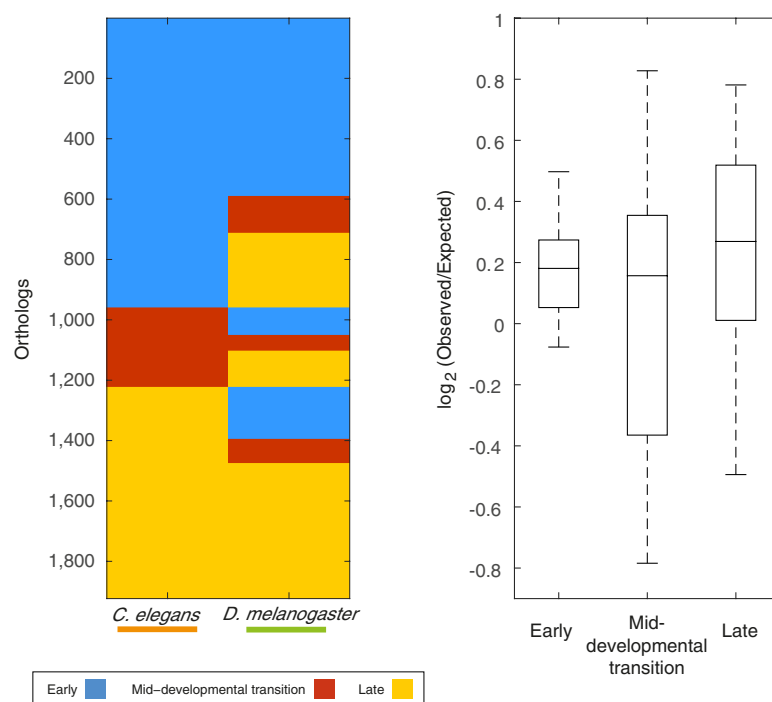


Extended Data Figure 6 | See next page for caption.



**Extended Data Figure 6 | PFAM enrichment and conservation across phyla.** **a**, For each of 5,746 PFAM protein domains, we computed an expression signature based upon the fraction of its genes expressed at each stage throughout development across each of the ten species. As an example of this approach, **a** shows the signatures for six PFAMs, indicating the normalized fraction of genes in that group expressed at the time points surrounding the transition for each species. The profiles are centred according to the mid-developmental transition as defined in Fig. 3, examining four windows before and after it. The greyscale indicates the fraction of genes expressed in each window. We attributed a phase of expression for each PFAM in each species, as we have for individual genes. To the right of each PFAM signature is the annotated phase; early (blue), mid-developmental transition (red), or late (yellow). We then computed the degree to which the temporal expression across phyla matches a coherent phase expression in three groupings: metazoan,

bilaterian, and protostomes. **b**, Metazoan (all ten species), bilaterian (all except the cnidarian, sponge, and ctenophore), and protostome (nematode, arthropod, tardigrade, annelid, and platyhelminth) groups are shown. To identify PFAMs in the metazoan group, we queried for PFAMs whose signature contains the same temporal phases of expression across the species. The metazoan-consistent PFAMs were nearly exclusively expressed in the early phase, suggesting stronger evolutionary constraints on this phase. A similar pattern was also observed for PFAMs with coherent expression in the seven bilaterian species in our data set. From this analysis, we conclude that bilaterians and protostomes each possess unique suites of innovations that are reflected in these shared phase-specific PFAM enrichments. Interestingly, protostome-coherent PFAMs are biased towards the late phases, possibly related to common differentiation processes operating in these taxa.



**Extended Data Figure 7 | Same as Fig. 4c, d for PFAM analysis.** The degree of conservation of early, transition, and late phase annotation of PFAMs was computed across species. A similar pattern was observed as that for orthologues (Fig. 4c, d).

Extended Data Table 1 | Developmental systematics of the examined species

Species	Super-phylo classification	Egg type; Cleavage type	Direct developer <sup>53</sup>	Germ layers	Method of development	Specialties	Ref
<i>D. melanogaster</i>	Metazoa/ Bilateria/ Protostomia/ Ecdysozoa/ Arthropoda	Centrolecithal egg; Syncytial cleavage	No	3	Embryonic development ends with hatching of the self-feeding first star larva	Cleavage occurs in a multinucleate syncytium	54
<i>H. dujardini</i>	Metazoa/ Bilateria/ Protostomia/ Ecdysozoa/ Tardigrada	Isolecithal egg; Rotational holoblastic cleavage	Yes	3	Embryonic development ends with hatching of self-feeding juvenile	Stereotyped cleavage pattern with asymmetric cell divisions	34
<i>D. rerio</i>	Metazoa/ Bilateria/ Deuterostome/ Chordata	Telolecithal egg; Discoidal meroblastic cleavage	Yes	3	Embryonic development ends with hatching of larva still feeding on yolk	Teleost egg is telolecithal; i.e., a mound of cytoplasm (the blastodisc) sits on the large mass of yolk and undergoes incomplete (meroblastic) cleavage. Embryo is derived from the blastodisc, and the remainder of the zygote becomes the yolk sac, which is later digested.	55
<i>S. polychroa</i>	Metazoa/ Bilateria/ Protostomia/ Lophotrochozoa/ Platyhelminthes	"Blastomere anarchy"	No	3	Embryonic development ends with hatching of self-feeding juvenile	During early cleavage (stage 1), yolk cells fuse and enclose the zygote into a syncytium. The zygote divides into blastomeres that dissociate and migrate into the syncytium. During stage 2, a subset of blastomeres differentiate into a transient embryonic epidermis that surrounds the yolk syncytium, and an embryonic pharynx. Other blastomeres divide as a scattered population of cells in the syncytium. During stage 5 the external syncytial yolk mantle is resorbed and the embryonic cells contained within differentiate into an irregular scaffold of muscle and nerve cells. Epidermal cells differentiate and replace the transient embryonic epidermis.	56
<i>C. elegans</i>	Metazoa/ Bilateria/ Protostomia/ Ecdysozoa/ Nematoda	Isolecithal egg; Rotational holoblastic cleavage	Yes	3	Embryonic development ends with hatching of self-feeding L1 larva	Stereotyped cleavage pattern with asymmetric cell divisions	57
<i>A. queenslandica</i>	Metazoa/ Porifera	Chaotic cell cleavage and molar delamination	No	0	Embryogenesis gives rise to larvae with at least a dozen cell types that are segregated into three layers and patterned along the body axis.	The pattern of cells within the embryo appears to be individualistic, suggesting that fixed cleavage patterns and cell lineages do not exist. The embryos develop asynchronously in brood chambers until they reach a certain size, then disperse as parenchymella larvae.	58
<i>P. dumerilii</i>	Metazoa/ Bilateria/ Protostomia/ Lophotrochozoa/ Annelida	Isolecithal egg; Spiral holoblastic cleavage	No	3	Embryogenesis gives rise to Mid-nectochaete larvae	Larval development comprises traditionally three major stages: the trochophore - spherical larva characterized by an equatorial ciliated belt and an apical organ with a ciliary tuft, the metatrochophore - segmented trunk, which slightly elongates, and the nectochaete - bears parapodial appendages used for swimming and crawling, and resembles the adult in major traits.	18
<i>S. purpuratus</i>	Metazoa/ Bilateria/ Deuterostome/ Echinodermata	Isolecithal egg; Radial holoblastic cleavage	No	2	Embryonic development ends in a pluteus larva that transforms after 1-3 months in the plankton into a juvenile urchin	By the 60-cell stage, most of the embryonic cell fates are specified, but cells are not irreversibly committed. Certain blastomeres consistently produce the same cell types in each embryo, but these cells remain pluripotent and can give rise to other cell types if experimentally placed in a different part of the embryo.	59
<i>M. leidyi</i>	Metazoa/ Ctenophora	Centrolecithal and isotropic eggs; Unipolar and holoblastic cleavage	Yes	2	Embryos develop into and hatch as juvenile adults with a free-swimming cydippid stage	Fertilized eggs go through a highly stereotyped ctenophore-specific cleavage program in which the fate of some (but not all) blastomeres are determined at the time of their birth.	60
<i>N. vectensis</i>	Metazoa /Cnidaria	Telolecithal egg; Holoblastic cleavage	No	2	Embryonic development ends in a primary poly	Early cleavage stages are characterized by substantial variability from embryo to embryo, yet invariably lead to the formation of a coeloblastula.	61

Extended Data Table 2 | Basic statistics of the expression data

Species	Average counted reads (genes)	Average counted reads (ERCC)	Genes	Counted genes	Dynamically expressed genes	Collected samples	Collected samples
<i>P. dumerilii</i>	852,212	88,165	10,908	10,906	9,832	97	80
<i>S. polychroa</i>	781,744	37,837	15,124	15,124	13,207	132	58
<i>C. elegans</i>	1,364,849	4,626	20,687	18,553	10,479	139	81
<i>H. dujardini</i>	1,498,810	199,916	12,746	12,744	11,464	126	62
<i>D. melanogaster</i>	1,784,414	90,767	15,682	13,842	8,391	91	77
<i>S. purpuratus</i>	462,396	141,587	21,092	17,443	11,579	87	57
<i>D. rerio</i>	2,010,010	32,058	32,433	22,790	10,198	106	88
<i>N. vectensis</i>	1,147,629	176,166	40,499	37,272	16,106	123	83
<i>A. queenslandica</i>	1,783,845	45,455	44,719	35,922	10,053	63	51
<i>M. leidyi</i>	1,583,798	6,111	16,548	14,664	6,142	60	53



Extended Data Table 3 | Assemblies for CEL-Seq mapping and their BUSCO completeness<sup>53</sup>

Species	Assembly used for mapping	BUSCO
<i>P. dumerilii</i>	Pdum_transcriptome_v1 (De Novo - NCBI BioProject PRJNA271451)	57%
<i>S. polychroa</i>	Spol_transcriptome_v1 (De Novo - NCBI BioProject PRJNA271420)	70%
<i>C. elegans</i>	WS230 (WormBase)	90%
<i>H. dujardini</i>	Hduj_transcriptome_v1 (De Novo - NCBI BioProject PRJNA271450)	71%
<i>D. melanogaster</i>	BDGP5 (Ensembl)	99%
<i>S. purpuratus</i>	WHL22 transcriptome <sup>63,64</sup>	78%
<i>D. rerio</i>	Zv9 (Ensembl)	96%
<i>N. vectensis</i>	NvT1 (Stellabae) <sup>65</sup>	78%
<i>A. queenslandica</i>	Aqu2.1 <sup>66</sup>	83%
<i>M. leidy</i>	MIScaffold09 <sup>11,67</sup>	70%

# Nucleus accumbens D2R cells signal prior outcomes and control risky decision-making

Kelly A. Zalocusky<sup>1,2,3</sup>, Charu Ramakrishnan<sup>1,3</sup>, Talia N. Lerner<sup>1,3</sup>, Thomas J. Davidson<sup>1,3</sup>, Brian Knutson<sup>4</sup> & Karl Deisseroth<sup>1,3,5</sup>

**A marked bias towards risk aversion has been observed in nearly every species tested<sup>1–4</sup>. A minority of individuals, however, instead seem to prefer risk (repeatedly choosing uncertain large rewards over certain but smaller rewards), and even risk-averse individuals sometimes opt for riskier alternatives<sup>2,5</sup>. It is not known how neural activity underlies such important shifts in decision-making—either as a stable trait across individuals or at the level of variability within individuals. Here we describe a model of risk-preference in rats, in which stable individual differences, trial-by-trial choices, and responses to pharmacological agents all parallel human behaviour. By combining new genetic targeting strategies with optical recording of neural activity during behaviour in this model, we identify relevant temporally specific signals from a genetically and anatomically defined population of neurons. This activity occurred within dopamine receptor type-2 (D2R)-expressing cells in the nucleus accumbens (NAc), signalled unfavourable outcomes from the recent past at a time appropriate for influencing subsequent decisions, and also predicted subsequent choices made. Having uncovered this naturally occurring neural correlate of risk selection, we then mimicked the temporally specific signal with optogenetic control during decision-making and demonstrated its causal effect in driving risk-preference. Specifically, risk-preferring rats could be instantaneously converted to risk-averse rats with precisely timed phasic stimulation of NAc D2R cells. These findings suggest that individual differences in risk-preference, as well as real-time risky decision-making, can be largely explained by the encoding in D2R-expressing NAc cells of prior unfavourable outcomes during decision-making.**

Previous work has implicated ventral tegmental area dopamine neurons<sup>6–8</sup>, as well as their downstream targets (including NAc<sup>8–11</sup>, prefrontal cortex<sup>12–14</sup>, and orbitofrontal cortex (OFC)<sup>15,16</sup>) in risk-preference. Ventral tegmental area stimulation, for example, has been shown to increase risk-seeking choices<sup>17</sup>, and pharmacological manipulations have implicated dopamine release in NAc<sup>8</sup> and prefrontal cortex<sup>14</sup> in modulating risk-preference.

We devised a task in which rats repeatedly chose between a ‘safe’ lever, which yielded the same volume of sucrose on every trial, and a ‘risky’ lever, which yielded a small reward on 75% of trials and a large reward on 25% of trials. The expected value was constant across the two levers (Fig. 1a). Each day, each rat performed 50 forced choice trials, in which only one lever entered the operant chamber, followed by 200 free choice trials, in which both levers entered the chamber, allowing the rat to choose. The less favourable outcome of risky lever selection represented a loss relative to the expected value of each trial; we refer to this outcome as a loss. Each trial was initiated with a 1-s nosepoke hold just prior to lever press; we refer to this temporal window as the decision period.

Rats adapted their choices to track switches in the risk profile of the two levers (Extended Data Fig. 1), yet, when task parameters were held

constant, displayed consistent risk-preferences across days (Extended Data Fig. 2). Furthermore, rat behaviour recapitulated key features of human behaviour. Most individuals exhibited stable risk-aversion<sup>5</sup> (Fig. 1d and Extended Data Figs 2 and 3), adopted a win-stay/lose-switch decision strategy<sup>18,19</sup> (Fig. 1b, e, f), and showed modulation of behaviour by pharmacological agents consistent with the human clinical literature<sup>20</sup> (Fig. 2a, b).

Rat behaviour was approximated by a model that assumes subjects integrate over recent outcomes (Fig. 1c and Extended Data Fig. 3). Model coefficients suggested rats were more likely to choose the risky lever after large gain outcomes but to switch to the safe lever after losses (Fig. 1b). Furthermore, while most rats exhibited risk-averse behaviour, a subset was consistently risk-seeking (Fig. 1d). Construction of separate models for the risk-seeking and risk-averse rats revealed similar coefficients associated with gain outcomes but divergent coefficients in response to loss (Fig. 1e). Both risk-seeking and risk-averse rats were more likely to make a risky choice if the previous trial yielded a gain rather than a loss, but this effect was significantly larger in risk-averse rats (Fig. 1f). Accordingly, loss sensitivity (Methods) was larger for risk-averse than for risk-seeking rats (Fig. 1g).

We next examined whether rat behaviour aligned with known pharmacological effects on risk-preference in humans. Population studies reveal substantial increases in incidence of problem gambling among patients taking D2/D3 agonists for Parkinson’s disease<sup>20</sup>. Laboratory studies reveal that these agents reduce neural and behavioural response to loss<sup>21,22</sup>. Concordant with this clinical evidence, we found systemic administration of pramipexole (PPX) increased risk-seeking choices in rats in a dose-dependent manner (Fig. 2a). This effect was consistent across several days of testing (Fig. 2b), and in animals in which PPX significantly increased risk-seeking, a reduction in loss-sensitivity was observed (Fig. 2c).

By contrast, the D1 agonist A-77636, previously explored as a treatment for Parkinson’s disease<sup>23</sup>, did not significantly alter risk-preference (Fig. 2d) despite robust bioavailability evidenced by lengthened intertrial intervals (Extended Data Fig. 4). To localize the effect of PPX, we implanted bilateral cannulae into both the NAc (Fig. 2e, f) and the OFC (Fig. 2g, h) and infused PPX intracranially. We found a significant effect on risk-preference when PPX was infused directly into the NAc (Fig. 2f) but not when infused into the OFC (Fig. 2h).

Although D3R signalling may contribute to effects of PPX on gambling, we suspected that the large D2-expressing neural population in NAc might have a primary role. The sensitivity and kinetics of D2Rs have led to the hypothesis that D2R-expressing cells detect pauses or dips in dopamine signalling, potentially enabling these cells for loss detection<sup>24</sup>. Disruption of this circuit could profoundly affect subjects’ ability to modify their behaviour in response to losses, leading to maladaptive strategies in the face of cost/benefit trade-offs, such as gambling<sup>25</sup>.

If D2R<sup>+</sup> NAc cells are relevant to risk preference, their activity might reflect reward size, outcomes of previous gambles, or upcoming

<sup>1</sup>Bioengineering Department, Stanford University, Stanford, California 94305, USA. <sup>2</sup>Neurosciences Program, Stanford University, Stanford, California 94305, USA. <sup>3</sup>CNC Program, Stanford University, Stanford, California 94305, USA. <sup>4</sup>Psychology Department, Stanford University, Stanford, California 94305, USA. <sup>5</sup>Howard Hughes Medical Institute, Stanford University, Stanford, California 94305, USA.

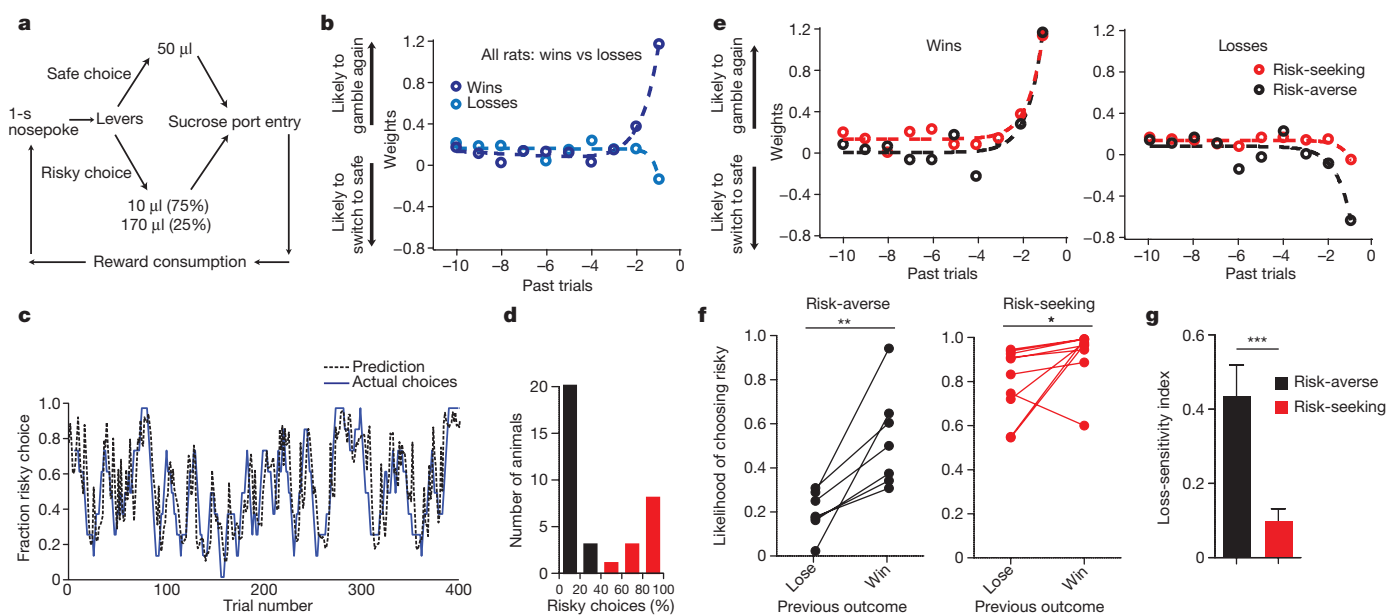


**Figure 1 | Trait variability in risk-aversion as loss-sensitivity: rat behavioural model.** **a**, Rats initiated each trial with a 1-s nosepoke, then chose either the 'safe' constant-reward lever or the 'risky' variable-reward lever. The safe lever delivered a 50- $\mu$ l reward. The risky lever delivered a 10- $\mu$ l reward with 75% probability and a 170- $\mu$ l reward with 25% probability. The expected value of each choice was 50  $\mu$ l. Rats retrieve the reward before initiating the next trial. **b**, Model coefficients revealed rats were more likely to choose the risky lever after a gain but less likely to choose the risky lever after a loss. Larger weights indicate a larger contribution of that outcome on choice. Coefficients were fit by exponential functions (Extended Data Fig. 2). Offset slightly above zero relates to the long tail of run lengths (Extended Data Fig. 3). **c**, Logistic regression trained on two-thirds of choices predicted choices in held-out test data with 80.2% accuracy (training data:  $n = 17$  rats, 6,593 trials;

test data:  $n = 17$  rats, 3,267 trials;  $P < 0.001$  by Monte Carlo simulation). Shown are 400 trials of test data from one rat. Actual choices are smoothed with an 8-trial boxcar filter; prediction is unsmoothed. **d**, Histogram of risk preference. Black indicates risk-averse ( $< 50\%$  risky choices); red indicates risk-seeking ( $> 50\%$  risky choices) rats. **e**, Weights for risk-seeking and risk-averse rats showed a difference in response to loss. **f**, Both risk-seeking ( $n = 10$ , Wilcoxon matched-pairs test,  $W = -41$ ,  $P = 0.03$ ) and risk-averse ( $n = 7$ , Wilcoxon matched-pairs test,  $W = -28$ ,  $P = 0.01$ ) rats were more likely to choose risk after a gain than after a loss. This effect was larger in risk-averse rats ( $n = 17$ , two-way analysis of variance (ANOVA), interaction  $F_{2,20} = 6.454$ ,  $P < 0.01$ ). **g**, Risk-averse rats were more loss-sensitive than risk-seeking rats ( $n = 10$  risk-seeking, 7 risk-averse rats, Mann-Whitney  $U = 2.00$ ,  $P = 0.0004$ ). Data shown are mean and s.e.m.

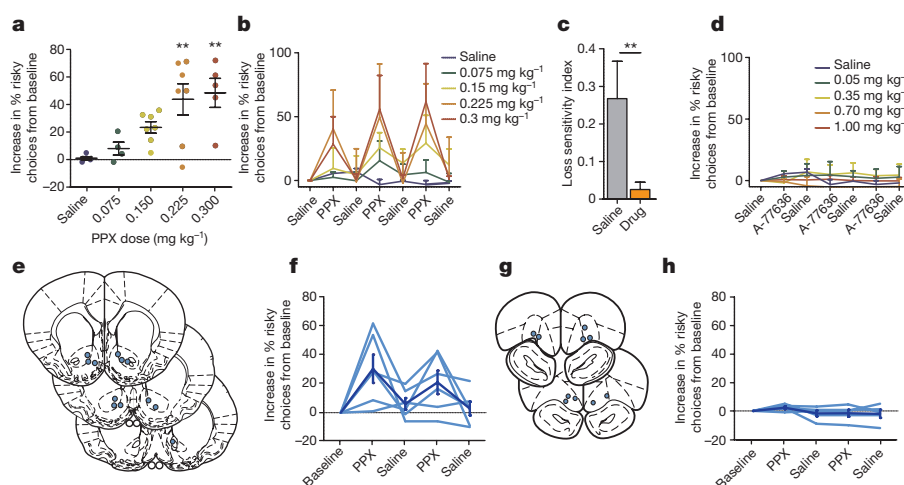


**Figure 2 | D2R agonist in the NAC increases risk-seeking behaviour in rats.** **a**, Points represent a rat's mean risky choices across 3 days of drug administration. Systemic PPX administration dose-dependently increased risky choices (Pearson's  $r^2 = 0.49$ ,  $P < 0.0001$ ; in order of increasing dose,  $n = 5, 4, 7, 7$  and 5 rats); doses  $\geq 0.225$  mg kg $^{-1}$  significantly increased risk-seeking (one-way ANOVA,  $F_{4,25} = 6.115$ ,  $P = 0.002$ ; Bonferroni's multiple comparison post-hoc test,  $**P < 0.01$  for both 0.225 mg kg $^{-1}$  and 0.3 mg kg $^{-1}$ ;  $n = 4-7$  animals per dose, as above). **b**, This effect was reversible across days ( $n = 4-7$  animals per dose, as above). **c**, In rats in which PPX significantly increased risk-seeking, it also decreased loss-sensitivity ( $t$ -test,  $t_{10} = 3.89$ ,  $**P = 0.003$ ). **d**, The D1 agonist A-77636 did not alter risk-preference (one-way ANOVA,  $F_{4,27} = 2.63$ ,  $P > 0.05$ ;

Bonferroni's multiple comparison post-hoc test reveals no significant effect at any dose tested. In order of increasing dose,  $n = 5, 6, 6, 6$  and 5 rats). **e**, **f**, Bilateral administration of PPX into the NAC increased risk-preference ( $n = 6$  rats; repeated-measures ANOVA,  $F_{4,20} = 4.455$ ,  $P < 0.01$ ). Injection sites are indicated on coronal diagrams as blue circles. **g**, **h**, Bilateral administration of PPX into the OFC had no effect on risk-seeking ( $n = 5$  rats; repeated-measures ANOVA,  $F_{4,16} = 1.307$ ,  $P = 0.31$ ). The effect of PPX administration into the NAC was significantly larger than the effect of administration into the OFC (two-way repeated measures ANOVA; interaction  $F_{4,36} = 2.989$ ,  $P = 0.03$ ; Bonferroni post-hoc test;  $P < 0.05$  on each drug administration day). Data are mean and s.e.m.

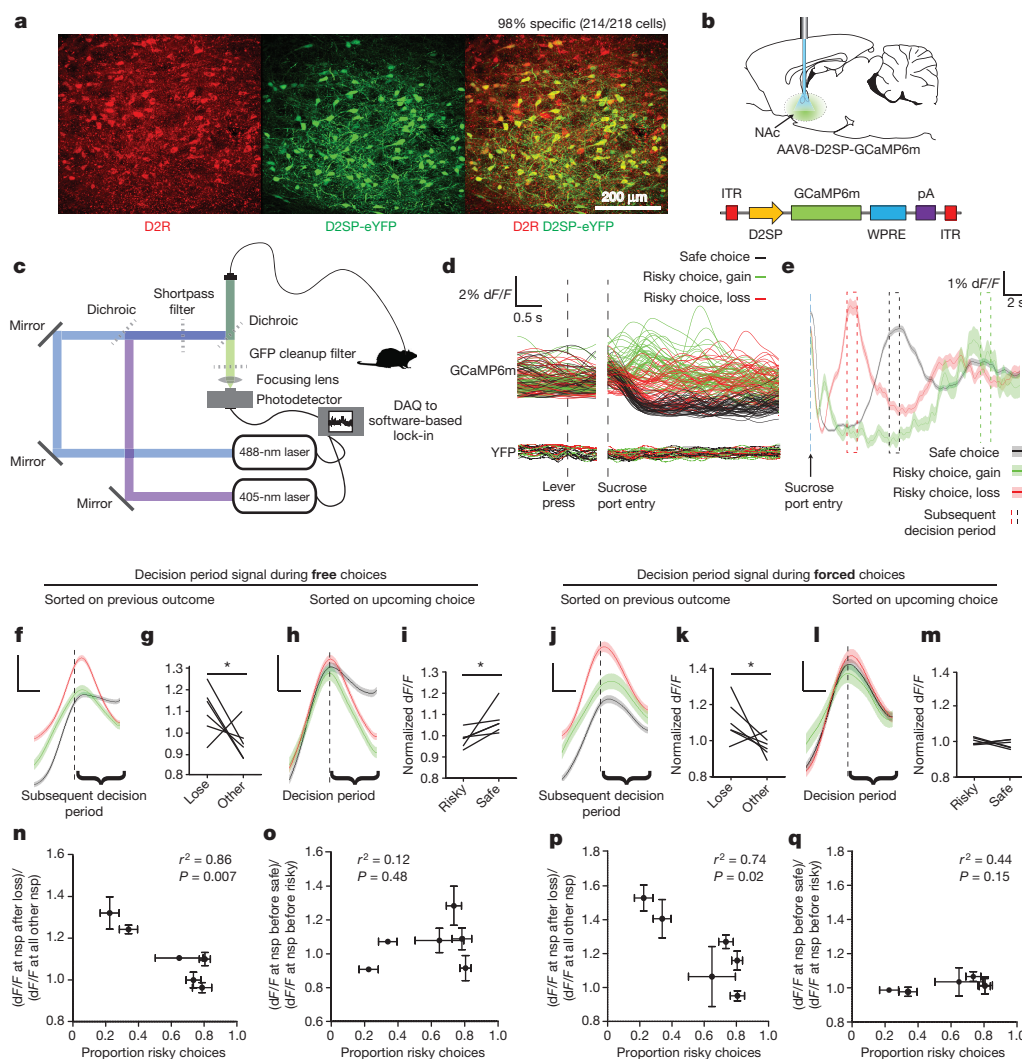


**Figure 3 | Activity in D2R-expressing cells in the NAc encodes loss-relevant task variables and predicts upcoming choice.** **a**, Adeno-associated viral (AAV) vector AAV8-D2SP-eYFP exhibits 98.2% specificity and 86.8% penetrance ( $n = 2$  rats, 214 of 218 cells that expressed YFP co-labelled for D2R). **b**, Photometry recordings were taken from NAc cells expressing AAV8-D2SP-GCaMP6m. **c**, Dual-excitation-wavelength fibre photometry rig (Methods). **d**, 50 traces of each trial type after isosbestic normalization in GCaMP6m- and YFP-expressing rats. **e**, Representative mean outcome-period traces. Blue dashed line indicates sucrose port entry. Later dashed boxes indicate median time of next decision period following: loss (red), gain (green), or safe (black) outcomes (1 rat, 911 trials, shaded area indicates s.e.m.). **f**, Mean decision-period signal sorted on previous outcome (6 rats, 5,693 trials). **g**, Decision-period signal is larger after losses than other outcomes ( $n = 6$  rats; paired  $t$ -test,  $t_5 = 2.371$ ,  $*P = 0.032$ ). **h**, Mean decision-period signal sorted on upcoming choice (6 rats, 5,693 trials). **i**, Decision-period signal was larger preceding safe versus risky choices ( $n = 6$  rats; paired  $t$ -test,  $t_5 = 2.374$ ,  $*P = 0.038$ ). **j**, Mean decision-period signal sorted on previous outcome, during

choice. The NAc contains a heterogeneous mixture of cells, however, posing challenges for assessment of D2R-specific neuron activity. To isolate signals from these cells, we developed a D2R-specific promoter, termed D2SP (Extended Data Fig. 5 and Methods). The D2SP construct markedly improved transgene expression and exhibited 98% specificity (Fig. 3a and Extended Data Fig. 5), with minimal expression in cholinergic interneurons after injection in the medial NAc core (Extended Data Fig. 6).

We used this construct to express the calcium indicator GCaMP6m<sup>26</sup> in D2R<sup>+</sup> NAc cells (Fig. 3b), and recorded population activity using fibre photometry<sup>27,28</sup> (Fig. 3c, d; Methods). To control for

forced-choice trials (6 rats, 1,550 trials). **k**, Decision-period signal was larger after losses during forced-choice trials ( $n = 6$  rats; paired  $t$ -test,  $t_5 = 2.126$ ,  $*P = 0.043$ ). **l**, Mean forced-choice decision-period signal, sorted by outcome (6 rats, 1,550 trials). **m**, Forced-choice decision-period signal did not distinguish upcoming action, as expected ( $n = 6$  rats; paired  $t$ -test,  $t_5 = 1.026$ ,  $P = 0.18$ ). **f**, **h**, **j**, **l**, Data are mean and s.e.m. Traces were z-score normalized before averaging. Scale bars indicate 0.5 s and 0.25 standard (z-score) units. **n**, Loss-sensitivity signal ((dF/F) at nosepoke (nsp) after loss/(dF/F at all other nsp)) significantly predicts risk-preference ( $n = 6$  rats; Pearson's  $r^2 = 0.86$ ,  $P = 0.007$ ). **o**, Safe choice signal ((dF/F) at nosepoke before safe choice/(dF/F at nosepoke before risky choice)) did not significantly predict risk-preference ( $n = 6$  rats; Pearson's  $r^2 = 0.12$ ,  $P = 0.48$ ). **p**, Loss-sensitivity signal during forced-choice significantly predicted risk-preference ( $n = 6$  rats; Pearson's  $r^2 = 0.74$ ,  $P = 0.02$ ). **q**, As expected, the safe choice signal during forced choices did not predict risk-preference ( $n = 6$  rats; Pearson's  $r^2 = 0.44$ ,  $P = 0.15$ ). **n**, **o**, **p**, **q**, Points indicate the mean risk-preference, mean loss-sensitivity signal, and s.e.m. across days.

potential behavioural artefacts, we determined the isosbestic point of GCaMP6m, which allowed us to use GCaMP6m as a ratiometric indicator (Extended Data Fig. 7 and Methods; as in ref. 28). This procedure yielded a 40-fold decrease in noise (Extended Data Fig. 7); robustness during movement was confirmed by stable recordings in a yellow fluorescent protein (YFP)-only animal (Fig. 3d and Extended Data Fig. 7).

Photometry traces revealed a signal in NAc D2R cells at initiation of each trial that depended on the outcome of the previous trial (Fig. 3e and Extended Data Fig. 8). This decision-period signal was larger if the rat had experienced a loss than if it had experienced a large gain or a safe outcome (Fig. 3e–g and Extended Data Fig. 8), and was



also higher if the rat was about to make a safe choice as compared to a risky choice (Fig. 3h, i and Extended Data Fig. 8).

As previously noted, rats became less likely to choose the risky lever after loss outcomes (Fig. 1b, f). To dissociate the correlated effects of loss outcome and upcoming safe choice on the decision-period signal, we examined activity during forced choice trials. In these trials, the decision-period signal continued to reflect previous losses, even though rats could not act on this information (Fig. 3j, k), indicating that the signal representing loss could exist independently from signals predicting upcoming choice. As expected, there was no difference detected when forced-choice decision-period activity was sorted based on the upcoming lever press (Fig. 3l, m). Together, these findings identify neural activity generated by NAc D2R<sup>+</sup> cells as both signalling recent loss (Fig. 3f, g, j, k) and predicting upcoming safe choice (Fig. 3h, i).

Although this signal was consistently higher after loss, we noted substantial variability in the signal across individuals. We explored whether this neural variability could account for naturally occurring differences in behaviour. Indeed, the ratio of decision-period activity after loss to activity after other outcomes (the loss-sensitivity signal) powerfully predicted risk preferences (Fig. 3n). Sorting this activity on the basis of upcoming choice rather than previous outcomes removed its predictive ability regarding individual risk preference (Fig. 3o), suggesting that individual differences are better accounted for by loss-sensitivity signals in these cells. Notably, the loss-sensitivity signal during forced-choice trials significantly predicted the number of risky choices a rat would make during subsequent free choice trials (Fig. 3p). As expected, forced choice signals sorted on upcoming decisions did not (Fig. 3q). Rats were allowed to move freely during the task, introducing the potential for differences in behaviour across trial types. However, differences in latency between sucrose port entry and the next decision period could not statistically account for the loss-sensitivity signal (Pearson's  $r^2 = 0.21$ ,  $P = 0.36$ ) or animals' risk preferences (Pearson's  $r^2 = 0.02$ ,  $P = 0.81$ ).

To verify the importance of selectively targeting D2R<sup>+</sup> neurons, we recorded pan-neuronal photometry signals from NAc using the human synapsin promoter (Extended Data Fig. 8). While D2R<sup>+</sup> recordings yielded a decision-period signal that was larger after losses (Fig. 3f, g and Extended Data Fig. 8), the pan-neuronal signal did not distinguish previous losses from previous gains (Extended Data Figs 8 and 9). Furthermore, unlike D2R<sup>+</sup> recordings, neither outcome-period nor decision-period activity in pan-neuronal recordings predicted individual differences in risk-preference (Extended Data Fig. 9), underscoring the importance of sorting neural signals based on cell type.

Because decision-period activity predicted risk-preferences and increased before safe choices, we sought to enhance the D2R<sup>+</sup> neural signal by optogenetically activating these cells during the decision period. An anticipated obstacle (D2SP-driven expression of channelrhodopsin-2 eYFP fusion protein (D2SP-ChR2(H134R)-eYFP) leading to protein aggregates in rat NAc neurons) was overcome by adding an endoplasmic reticulum (ER) export motif and trafficking signal<sup>29</sup> (producing enhanced channelrhodopsin (eChR2); Methods), resulting in improved expression (Extended Data Fig. 7). In acute slice recordings, NAc cells expressing D2SP-eChR2(H134R)-eYFP tracked 20-Hz optical stimulation with action potentials (Fig. 4c).

D2R<sup>+</sup> neuron stimulation during the decision period (Fig. 4a) decreased risky choices in risk-seeking (Fig. 4d–f) but not risk-averse (Fig. 4g–i) rats. Furthermore, stimulation during a pseudo-random subset of trials decreased risk-seeking choices with single-trial precision (Fig. 4j). The effect could be further narrowed to sub-phases of the task; the same pattern of stimulation delivered during the outcome period, rather than the decision period, resulted in a significantly reduced influence on choice (Extended Data Fig. 10). These findings indicate D2R<sup>+</sup> NAc cells can control online selection of risky options and that decision-period activity in these cells causally drives risk-preference.

In summary, we developed behavioural, genetic, imaging and optical stimulation methods for measuring and modulating neural dynamics

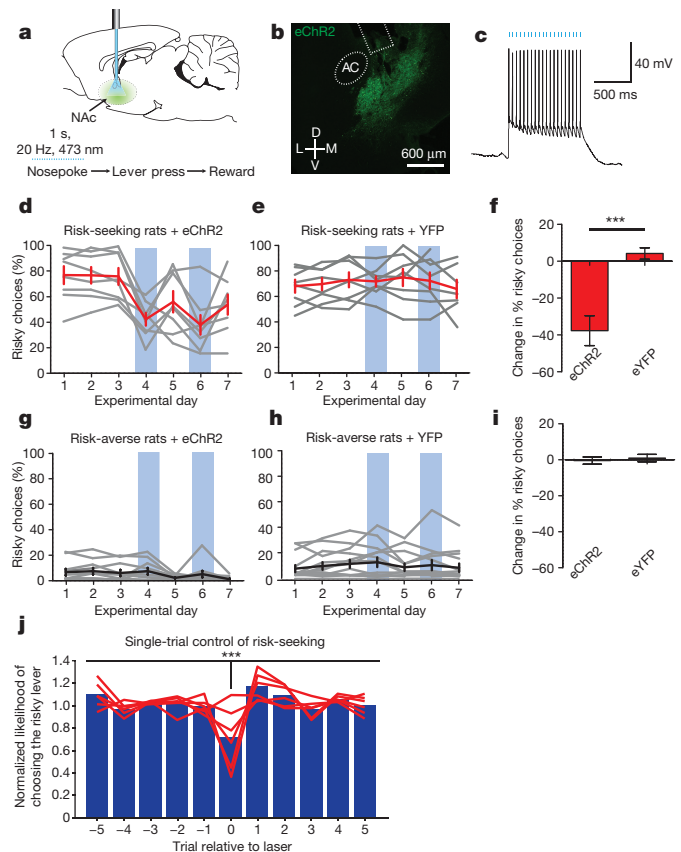


**Figure 4 | Providing phasic activity in D2-expressing NAc cells during the decision period decreased risky choices in risk-seeking rats.** **a**, NAc cell bodies expressing AAV8-D2SP-eChR2(H134R)-eYFP were stimulated bilaterally during the decision period. **b**, AAV8-D2SP-eChR2(H134R)-eYFP expression in NAc. AC, anterior commissure. Rectangle indicates fibre location. **c**, NAc cells expressing D2SP-eChR2-eYFP track 1-s 20-Hz optical stimulation (indicated by blue bars) in acute slices (representative trace; similar behaviour seen in 5 out of 5 cells). **d–i**, NAc D2R<sup>+</sup> cell decision-period stimulation decreased risky choices in risk-seeking rats, but not risk-averse rats relative to YFP-expressing controls ( $n = 8$  risk-seeking plus eChR2, 8 risk-seeking plus eYFP, 20 risk-averse plus eChR2, 26 risk-averse plus eYFP; two-way ANOVA, interaction  $F_{1,58} = 25.37$ ,  $P < 0.0001$ ; Bonferroni post-hoc test revealed a significant difference between ChR2-expressing and YFP-expressing risk-seeking rats, but no difference between experimental and control risk-averse rats;  $***P < 0.001$ ). Grey traces represent individual animals. Black and red traces represent the population mean. Error bars represent s.e.m. **j**, Stimulation significantly decreased risk-seeking choices on a single-trial basis in risk-seeking rats ( $n = 6$  rats; repeated-measures ANOVA,  $F_{5,10} = 5.504$ ,  $***P = 0.0006$ ; Dunnett's post-hoc test revealed the probability of choosing risky on stimulation trials was significantly lower than each other trial independently, correcting for multiple comparisons;  $P < 0.01$  in every case). Blue bars represent the mean likelihood of risky choice across rats; red lines represent the behaviour of individual rats.

underlying trait and trial-by-trial variation in risk preference. We observed neural correlates of risky choice in D2R<sup>+</sup> NAc cells, and optogenetically demonstrated the causal role of neural activity in this genetically and spatially defined population of neurons in risky choice. Together, these findings suggest individual differences in risk preference can be explained at the behavioural level by divergent responses to loss, and at the neural level by NAc D2R<sup>+</sup> cell responses to previous unfavourable outcomes.

These findings indicate interesting directions for further study. For example, population recordings may combine distinct subpopulations of NAc D2R<sup>+</sup> cells, which might separately encode upcoming decisions, reward receipt, and choice history. Furthermore, the observed

differences in activity on receipt of safe versus risky outcomes are consistent with D2R<sup>+</sup> cell activity influencing risk-preference through learning and plasticity. This outcome-period activity did not predict choice, however, while decision-period activity did predict choice and modulate behaviour in real-time when enhanced optogenetically. It will be of great interest to test for distinct D2R<sup>+</sup> subpopulations, trial-by-trial plasticity, and interactions between reward history and upcoming choice in D2R<sup>+</sup> cells<sup>30</sup> as they relate to risky choice. Insight into pharmacological disruption of risk preference in patients<sup>20,21</sup>, and into suboptimal or seemingly irrational choices by healthy individuals<sup>2</sup>, will benefit from deeper knowledge of how precisely defined cell populations, brain regions, and connections support risky choice.

**Online Content** Methods, along with any additional Extended Data display items and Source Data, are available in the online version of the paper; references unique to these sections appear only in the online paper.

Received 7 July 2015; accepted 5 February 2016.

Published online 23 March 2016.

1. Barkan, C. P. L. A Field test of risk-sensitive foraging in black-capped chickadees (*Parus atricapillus*). *Ecology* **71**, 391–400 (1990).
2. Kahneman, D. & Tversky, A. Prospect theory: an analysis of decision under risk. *Econometrica* **47**, 263–291 (1979).
3. Caraco, T., Martindale, S. & Whittam, T. S. An empirical demonstration of risk-sensitive foraging preferences. *Anim. Behav.* **28**, 820–830 (1980).
4. Real, L. A. Uncertainty and pollinator–plant interactions: the foraging behavior of bees and wasps on artificial flowers. *Ecology* **62**, 20–26 (1981).
5. Markowitz, H. Portfolio Selection. *J. Finance* **7**, 77–91 (1952).
6. Schultz, W. et al. Explicit neural signals reflecting reward uncertainty. *Philos. Trans. R. Soc. B Biol. Sci.* **363**, 3801–3811 (2008).
7. St Onge, J. R. & Floresco, S. B. Dopaminergic modulation of risk-based decision making. *Neuropsychopharmacology* **34**, 681–697 (2009).
8. Nasrallah, N. A. et al. Risk preference following adolescent alcohol use is associated with corrupted encoding of costs but not rewards by mesolimbic dopamine. *Proc. Natl Acad. Sci. USA* **108**, 5466–5471 (2011).
9. Knutson, B., Wimmer, G. E., Kuhnen, C. M. & Winkielman, P. Nucleus accumbens activation mediates the influence of reward cues on financial risk taking. *Neuroreport* **19**, 509–513 (2008).
10. Tom, S. M., Fox, C. R., Trepel, C. & Poldrack, R. A. The neural basis of loss aversion in decision-making under risk. *Science* **315**, 515–518 (2007).
11. Winstanley, C. A., Theobald, D. E. H., Dalley, J. W. & Robbins, T. W. Interactions between serotonin and dopamine in the control of impulsive choice in rats: therapeutic implications for impulse control disorders. *Neuropsychopharmacology* **30**, 669–682 (2005).
12. Bechara, A., Damasio, A. R., Damasio, H. & Anderson, S. W. Insensitivity to future consequences following damage to human prefrontal cortex. *Cognition* **50**, 7–15 (1994).
13. Clark, L. et al. Differential effects of insular and ventromedial prefrontal cortex lesions on risky decision-making. *Brain* **131**, 1311–1322 (2008).
14. St Onge, J. R., Abhari, H. & Floresco, S. B. Dissociable contributions by prefrontal D<sub>1</sub> and D<sub>2</sub> receptors to risk-based decision making. *J. Neurosci.* **31**, 8625–8633 (2011).
15. Bechara, A., Damasio, H. & Damasio, A. R. Emotion, decision making and the orbitofrontal cortex. *Cereb. Cortex* **10**, 295–307 (2000).
16. O'Neill, M. & Schultz, W. Coding of reward risk by orbitofrontal neurons is mostly distinct from coding of reward value. *Neuron* **68**, 789–800 (2010).
17. Stopper, C. M., Tse, M. T. L., Montes, D. R., Wiedman, C. R. & Floresco, S. B. Overriding phasic dopamine signals redirects action selection during risk/reward decision making. *Neuron* **84**, 177–189 (2014).
18. Hayden, B. Y. & Platt, M. L. Gambling for Gatorade: risk-sensitive decision making for fluid rewards in humans. *Anim. Cogn.* **12**, 201–207 (2009).
19. Niv, Y., Edlund, J. A., Dayan, P. & O'Doherty, J. P. Neural prediction errors reveal a risk-sensitive reinforcement-learning process in the human brain. *J. Neurosci.* **32**, 551–562 (2012).
20. Dodd, M. L. et al. Pathological gambling caused by drugs used to treat parkinson disease. *Arch. Neurol.* **62**, 1377–1381 (2005).
21. Frank, M. J., Seeberger, L. C. & O'Reilly, R. C. By carrot or by stick: cognitive reinforcement learning in parkinsonism. *Science* **306**, 1940–1943 (2004).
22. van Eimeren, T. et al. Dopamine agonists diminish value sensitivity of the orbitofrontal cortex: a trigger for pathological gambling in Parkinson's disease? *Neuropsychopharmacology* **34**, 2758–2766 (2009).
23. Kebabian, J. W. et al. A-77636: a potent and selective dopamine D<sub>1</sub> receptor agonist with antiparkinsonian activity in marmosets. *Eur. J. Pharmacol.* **229**, 203–209 (1992).
24. Dreyer, J. K., Herrik, K. F., Berg, R. W. & Hounsgaard, J. D. Influence of phasic and tonic dopamine release on receptor activation. *J. Neurosci.* **30**, 14273–14283 (2010).
25. Porter-Stransky, K. A., Seiler, J. L., Day, J. J. & Aragona, B. J. Development of behavioral preferences for the optimal choice following unexpected reward omission is mediated by a reduction of D<sub>2</sub>-like receptor tone in the nucleus accumbens. *Eur. J. Neurosci.* **38**, 2572–2588 (2013).
26. Chen, T.-W. et al. Ultrasensitive fluorescent proteins for imaging neuronal activity. *Nature* **499**, 295–300 (2013).
27. Gunaydin, L. A. et al. Natural Neural projection dynamics underlying social behavior. *Cell* **157**, 1535–1551 (2014).
28. Lerner, T. N. et al. Intact-brain analyses reveal distinct information carried by SNc dopamine subcircuits. *Cell* **162**, 635–647 (2015).
29. Gradinaru, V. et al. Molecular and cellular approaches for diversifying and extending optogenetics. *Cell* **141**, 154–165 (2010).
30. Tai, L.-H., Lee, A. M., Benavidez, N., Bonci, A. & Wilbrecht, L. Transient stimulation of distinct subpopulations of striatal neurons mimics changes in action value. *Nature Neurosci.* **15**, 1281–1289 (2012).

**Acknowledgements** We would like to thank R. Malenka and K. Shenoy for advice on experimental design; A. Andalman for advice on analysis; P. Kalanithi for advice in general; E. Ferenczi, C. Földy, G. Panagiotakos, M. Bennett, A. Bryant, C. Beinart, and M. Palner for preliminary data collection and training in experimental techniques; S. Pak and C. Delacruz for administrative support; and the entire Deisseroth laboratory and Stanford University Neurosciences Program for training and support. All viruses were packaged at the Stanford Viral and Vector Core. K.A.Z. was supported by the NSF Graduate Research Fellowship Program, by the Stanford Neurosciences Program NIH Training Grant, and by an NRSA Predoctoral Fellowship from NIDA (1F31MH105151-01). T.N.L. was supported by a Stanford Dean's Postdoctoral Fellowship and by an NRSA Postdoctoral Fellowship (1F32MH105053-01). B.K. was supported by a Stanford Neuroscience Institute Big Ideas Grant. K.D. was supported by NIMH, NIDA, NSF, the Wiegers Family Fund, the Nancy and James Grosfeld Foundation, the H.L. Snyder Medical Foundation, the Samuel and Betsy Reeves Fund, and the US Army Research Laboratory and Defense Advanced Research Projects Agency (Cooperative Agreement Number W911NF-14-2-0013); nothing in this material represents official views or policies of our funders. All clones and resources are freely available (<http://optogenetics.org>, <http://clarityresourcecenter.org>).

**Author Contributions** K.A.Z. led the design, performance, and analysis of experiments, in collaboration with C.R. for designing and generating the D2SP constructs, with B.K. for behavioural design and analysis, with T.N.L. for characterizing eChR2 and wavelength-dependent responses of GCaMP6m, and with T.J.D. and T.N.L. for photometry methods development and implementation. K.A.Z. and K.D. planned and wrote the paper with editorial input from all authors. K.D. supervised all aspects of the work.

**Author Information** Reprints and permissions information is available at [www.nature.com/reprints](http://www.nature.com/reprints). The authors declare no competing financial interests. Readers are welcome to comment on the online version of the paper. Correspondence and requests for materials should be addressed to K.D. (deissero@stanford.edu).

## METHODS

**Subjects.** Male Long–Evans rats were obtained from Charles River at 8–10 weeks old. Rats were pair housed in a colony maintained on a 12 h light/dark cycle, and were given food and water *ad libitum* outside of behavioural training. During training, rats were given food *ad libitum* but worked in a closed economy for water, obtaining 15 ml of 5% sucrose solution during the task. Experimental protocols were approved by Stanford University IACUC to meet guidelines of the National Institutes of Health guide for the Care and Use of Laboratory Animals. Sample sizes were chosen to meet or exceed those in previously published accounts of cognitive and decision-making tasks in rats<sup>31,32</sup>. Post-hoc tests then verified adequate statistical power given the observed effect sizes (see ‘Power analyses’).

**Behavioural training.** All behaviour was assessed in operant chambers (Med Associates). One wall of the operant chamber was arranged such that the sucrose port (Med Associates ENV-200R3BM) was positioned in the bottom centre slot. The nosepoke (Med Associates ENV-114BM) used to initiate each trial was slotted immediately above the sucrose port. The retractable choice levers (Med Associates, ENV-112CM) were on either side of the sucrose port (Extended Data Fig. 1).

In the first phase of training, both levers were extended into the chamber, and every press resulted in 50  $\mu$ l sucrose reward. Rats were given two hours to earn and retrieve 150 total sucrose rewards. Most rats completed this phase in one day. In the second phase of training, a randomly-selected lever entered the chamber and retracted when pressed. Every press resulted in a 50- $\mu$ l sucrose reward. Rats were given 2 h to earn and retrieve 200 sucrose rewards. In the third phase of training, rats were trained to initiate each trial with a one-second nosepoke. On the first trial, the rat was required to nosepoke for 250 ms, after which both levers would enter the chamber. The rat would then press a lever to obtain a 50- $\mu$ l sucrose reward. In each subsequent trial, the length of the required nosepoke incremented by 5 ms. Rats were given 2 h to complete 200 lever presses. In the final phase of training, rats were exposed to the behavioural task described in Fig. 1a. Each trial was initiated with a 1-s nosepoke. If the rat failed to hold the nosepoke for 1 s, it could try again immediately without penalty, but the 1-s clock would start again from zero. One lever always delivered a 50- $\mu$ l reward, while the other delivered a 10- $\mu$ l reward with 75% probability and a 170- $\mu$ l reward with 25% probability (expected value = 50  $\mu$ l). These objective expected values were held constant throughout the task. For the first 50 ‘forced choice’ trials, one randomly chosen lever entered the chamber, and the rat pressed it to obtain its reward. For the remaining 200 ‘free choice’ trials, both levers entered the chamber and the rat was allowed to choose. Rats were trained until their fraction of risky choices across three consecutive days varied by less than 10%. On average, rats required approximately 5 sessions in the final phase of training before reaching a stable behavioural baseline (mean = 4.85, s.d. = 2.29). In total, 12 out of 132 rats failed to learn the task. Rats were excluded from experiments if they failed to learn the initial lever pressing task, lost a fibreoptic implant before the conclusion of testing, or failed to develop stable baseline behaviour; these criteria were established in advance of experimentation. All cell counting data collection in Extended Data Figs 5–7 was conducted blinded to condition; the behavioural experimenter was not blind to the risk preference of each animal, but instead all behaviour was conducted while the experimenter monitored the rats from a different room, so as not to influence the animals’ choices.

To validate rat sensitivity to relative expected value across the two levers, rats were trained to a stable baseline, as described above. The expected value of the safe lever was then systematically increased across days, to map out behavioural response curves (Extended Data Fig. 1b). To validate that rats’ choices were due to preference for the safe or risky reward schedule, rather than simply to side bias or indifference, rats were trained to a stable baseline. The location of the risky lever was then alternated between left and right levers at an uncued time in blocks of 100–250 trials (Extended Data Fig. 1c). Trial lengths for these blocks were on the order of the number of trials used in the main gambling task (200 free choice trials). The loss-sensitive index is determined as shown in equation (1).

$$\text{Loss-sensitivity index} = \frac{P(\text{choosing risky}|\text{gain}) - P(\text{choosing risky}|\text{loss})}{P(\text{choosing risky}|\text{gain}) + P(\text{choosing risky}|\text{loss})} \quad (1)$$

**Systemic pharmacology.** PPX (Sigma-Aldrich, A1237) and A-77636 hydrochloride (Tocris Biosciences, 1701) were diluted in physiological saline and injected intraperitoneally 30 min before the start of the task at the doses described in Fig. 2. A large cohort of animals was trained to conduct this experiment, and separate animals within the cohort were used for each drug dose. Animals were trained to a stable baseline, as described above, before drug injections were initiated.

**Stereotactic viral injection, cannula or fibre implantation, and light delivery.** Surgeries were performed on 8–10-week-old rats. Rats were anaesthetized with 2–3% isoflurane; scalps were shaved, and subjects were placed in a stereotactic head apparatus. Rats received a subcutaneous injection of buprenorphine (0.01 mg kg<sup>−1</sup>) and a subcutaneous injection of lactated ringer’s solution (3 ml).

Ophthalmic ointment was applied to prevent eyes from drying. A midline scalp incision was made, and a craniotomy was drilled above each injection or fibre implantation site. For intracranial drug infusion, guide cannulas (PlasticsOne, C313G) were implanted bilaterally. OFC cannulas were implanted at (A/P 4.5, M/L  $\pm$ 1.4, D/V  $-$ 4.2; all coordinates in mm and relative to bregma (here and below)). NAc cannulas were implanted at (A/P 1.5, M/L  $\pm$ 1.8, D/V  $-$ 6.5). In both NAc and OFC, left cannulas were implanted vertically while right cannulas were implanted at a 20° angle. Dental adhesive (C&B metabond, Parkell) was applied and dental cement (Stoelting) was added to secure the cannulas to the skull.

For photometry and optogenetics experiments, virus was injected with a 10- $\mu$ l glass syringe and a 33-gauge beveled metal needle (World Precision Instruments). Importantly, virus should be injected at a titre no greater than  $3 \times 10^{12}$  viral particles per ml to avoid potential cytotoxicity and diluted in ice-cold PBS if necessary. The injection volume and flow rate (750 nl at 150 nl min<sup>−1</sup>) were controlled by an injection pump (Harvard Apparatus). Each NAc received two injections (A/P 1.5, M/L  $\pm$ 1.8 mm, D/V  $-$ 7.6 and  $-$ 7.0). After injection, the needle was left in place for 5 additional minutes and then slowly withdrawn. All rats were injected and implanted bilaterally. In each NAc, an 8-mm fibre stub, terminated with a 2.5-mm diameter ferrule was implanted at (A/P 1.5 mm, M/L  $\pm$ 1.8 mm, D/V  $-$ 7.2 mm). Left cannulas were implanted vertically while right cannulas were implanted at a 20° angle. For stimulation, a 30- $\mu$ m core diameter, 0.37 numerical aperture (NA) fibre was used; for photometry, a 400- $\mu$ m core diameter, 0.48-NA low-autofluorescence fibre with low-fluorescence epoxy for photometry (implantable fibres assembled by Doric Lenses, using fibre manufactured by Thorlabs or CeramOptec). Dental adhesive (C&B metabond; Parkell) was applied and light-curing composite (Flow-It ALC, Pentron Clinical, N11VH) was added to secure the ferrules to the skull. All behavioural experiments occurred at least 3 weeks after virus injection. Rats’ innate behaviour determined their assignment to ‘risk-seeking’ or ‘risk-averse’ groups. For optogenetic manipulations, half of the rats were randomly assigned to ChR2 or YFP (control) groups.

For photometry, each excitation source was set to an average power of 30  $\mu$ W at the fibre tip. Light was delivered through a 400- $\mu$ m core diameter, 0.48-NA low-fluorescence patch cord (Doric Lenses) and joined to the implanted fibre ferrules using zirconia sleeves (Thorlabs). Recording location (left or right NAc) was balanced across subjects. For optogenetic stimulation, light pulses were administered for 1 s at 20 Hz at a power of 15 mW per side (0.75 mW per side corrected for duty cycle). Decision period stimulation began when the rat initiated a nosepoke. Outcome period stimulation occurred in the 1 s after sucrose port entry. Light was delivered through a 300- $\mu$ m core diameter, 0.37-NA fibre (Thorlabs), fed through a fibre optic rotary joint (Doric Lenses, FRJ\_1x1\_FC-FC), and split into two beams using a Doric minicube (Doric Lenses, DMC\_1x2i\_VIS\_FC). At each output of the minicube a 0.5-m, 300- $\mu$ m core diameter, 0.37-NA fibre, terminating in a 2.5-mm ferrule (Thorlabs) was attached. Each fibre was sheathed in a steel spring to protect from chewing (PlasticsOne) and joined to an implanted fibre ferrule using a zirconia sleeve (Thorlabs).

**Intracranial drug infusions.** Rats were anaesthetized with 1–2% isoflurane and were placed in a stereotactic head apparatus. PPX was dissolved in saline (10  $\mu$ g  $\mu$ l<sup>−1</sup>, 0.9% NaCl). Thirty minutes before the behaviour, 0.5  $\mu$ l of the PPX solution was infused in each side of OFC or each side of NAc via an internal infusion needle (PlasticsOne, C313I) inserted into the guide cannula. The internal needle was connected to a 10- $\mu$ l Hamilton syringe (Nanolit; WPI). Flow rate (0.1  $\mu$ l min<sup>−1</sup>) was regulated by a syringe pump (Harvard Apparatus). Cannula locations were verified in Nissl-stained sections. Infusions were conducted in an ABABA design, alternating infusions of saline or PPX across days.

**Immunohistochemistry.** Rats were anaesthetized with Beuthanasia and perfused transcardially, first with ice-cold PBS (pH 7.4) and then with 4% paraformaldehyde (PFA) dissolved in PBS. The brains were removed and post-fixed in 4% PFA overnight at 4°C, and then equilibrated in 30% sucrose in PBS. Forty-micrometre-thick coronal sections were prepared on a freezing microtome (Leica) and stored in cryoprotectant (25% glycerol and 30% ethylene glycol in PBS, pH 6.7) at 4°C. Cell counts were conducted by blinded experimenters. For anti-D2R staining (Millipore, AB1558) was used as described below. For anti-ChAT staining (Millipore, AB144P) was used as previously described<sup>33</sup>. For anti-GFP staining (Life Technologies, A-31852) was used as previously described<sup>28</sup>.

For D2R staining, the following protocol was used: (1) rinse 40- $\mu$ m sections in PBS (pH 7.4), 3  $\times$  10 min. (2) Block in PBS plus 3% normal donkey serum and 0.3% Triton-X (PBS++) for 30 min. (3) Incubate in primary antibody (rabbit anti-D2R, Millipore ab1558) at 1:200 in PBS++ for 24 h at room temperature on a rotary shaker. (4) Wash slices for 4  $\times$  15 min in PBS. (5) Incubate in secondary antibody (Alexa-fluor 647, goat anti-rabbit, Life Technologies, A-21245) at 1:200 in PBS++ overnight at room temperature on a rotary shaker. (6) Wash slices for 4  $\times$  15 min in PBS. (7) Incubate in tertiary antibody (Alexa-fluor 647, donkey anti-goat, Life Technologies, A-21447) at 1:500 in PBS++ for 8 h at room temperature on a rotary



shaker. (8) Wash for 15 min in PBS. (9) Wash for 15 min in 1:50,000 DAPI in PBS. (10) Wash for 15 min in PBS and mount with PVA-DABCO.

**Molecular cloning.** We developed a novel dopamine D2R-specific promoter (D2SP) for expression of transgenes in rat D2R<sup>+</sup> cells compatible with use in a single AAV vector (Extended Data Fig. 5). The new 1.5-kb D2SP fragment was taken from a region immediately upstream of the rat *D2R* (also known as *Drd2*) gene (full sequence: Extended Data Fig. 5), differing from a previously reported D2R promoter region<sup>34</sup> by excluding exon 1 and including a Kozak sequence inserted between the promoter region and the gene that it controls. D2SP was amplified from rat genomic DNA using primers 5'-CGCACGCGTTTATCCTCGGTGCATCTCAGAG-3' and 5'-GGCGGATCCCCCGGCACTGAGGCTGGACAGCT-3' digested with MluI and BamHI and ligated with pAAV-hSYN-eYFP or pAAV-hSYN-hChR2(H134R)-eYFP digested with the same two enzymes to yield pAAV-D2SP-eYFP or pAAV-D2SP-hChR2(H134R)-eYFP, respectively. pAAV-D2RE-eYFP was constructed using the D2R promoter sequence described previously<sup>34</sup> to replace the hSYN promoter in pAAV-hSYN-eYFP. pAAV-D2SP-eChR2(H134R)-eYFP was constructed with the ER export motif and trafficking signal as described previously<sup>29</sup>. pGP-CMV-GCaMP6m (Addgene plasmid 40754) and pGP-CMV-GCaMP6f Kim (Addgene plasmid 40755) were a gift from D. Kim. The GCaMP DNA was amplified by PCR using 5'-CCGGATCCGCCACCATTGGGTTCTCATCATCATCATC-3' and 5'-CGATAAGCTTGTCACTTCGCTGTGCATCATTTGTAC-3', digested with BamHI and HindIII and cloned under the CaMKIIa or D2SP promoters to yield pAAV-CaMKIIa-GCaMP6m, pAAV-CaMKIIa-GCaMP6f, pAAV-D2SP-GCaMP6m and pAAV-GCaMP6f. All constructs were fully sequenced to check for accuracy of the cloning procedure, and all AAV vectors were tested for *in vitro* expression before viral production as AAV8/Y733F serotype packaged by the Stanford Neuroscience Gene Vector and Virus Core. Updated maps are available at <http://optogenetics.org/>.

**Neuron culture and calcium phosphate transfections.** Primary cultured striatal neurons were prepared from P0 Sprague-Dawley rat pups (Charles River). The striatum was isolated, digested with 0.4 mg ml<sup>-1</sup> papain (Worthington), and plated onto glass coverslips precoated with 1:30 Matrigel (Beckton Dickinson Labware). Cultures were maintained in a 5% CO<sub>2</sub> humid incubator with Neurobasal-A medium (Invitrogen Carlsbad) containing 1.25% FBS (Hyclone), 4% B-27 supplement (Gibco), 2 mM glutamax (Gibco), and FUDR (10 mg 5-fluoro-2'-deoxyuridine and 25 µg uridine) from Sigma, for 6–10 days in a 24-well plate at a density of 65,000 cells per well. For each coverslip, a DNA and CaCl<sub>2</sub> mix was prepared with 1.5–3.0 µg DNA (Qiagen endotoxin-free preparation) and 1.875 µl 2 M CaCl<sub>2</sub> (final Ca<sup>2+</sup> concentration 250 mM) in 15 µl total H<sub>2</sub>O. To the DNA and CaCl<sub>2</sub> mix, 15 µl of 2× HEPES-buffered saline (pH 7.05) was added, and the final volume was mixed well by pipetting. After 20 min at room temperature, the 30 µl DNA–CaCl<sub>2</sub>–HBS mix was added drop-wise into each well (from which the growth medium had been temporarily removed and replaced with 400 µl pre-warmed MEM) and transfection was allowed to proceed at 37°C for 45–60 min. At the end of the incubation, each well was washed with 3 × 1-ml warm MEM before the original growth medium was returned. Opsin expression was generally observed within 24 h.

**Ca<sup>2+</sup> imaging in culture.** Coverslips of cultured neurons were transferred from the culture medium to a recording bath filled with Tyrode solution (containing in mM: 125 NaCl, 2 KCl, 2 CaCl<sub>2</sub>, 2 MgCl<sub>2</sub>, 30 glucose and 25 HEPES). The coverslip was scanned for GCaMP-expressing neurons and a glass monopolar stimulating electrode filled with Tyrode was placed nearby. A 10-s 50-Hz stimulation (pulse width 5-ms, intensity 5–6 mA) was used to obtain maximal responses. Wavelengths of either 475 nm or 400 nm, generated using a Spectra X LED light engine (Lumencor), were used to illuminate the cell. Video was recorded at 10 Hz using a CCD camera (RoleraXR, Q-Imaging).

**Cultured neuron physiology.** Coverslips of cultured neurons were transferred from the culture medium to a recording bath filled with Tyrode solution (containing in mM: 125 NaCl, 2 KCl, 2 CaCl<sub>2</sub>, 2 MgCl<sub>2</sub>, 30 glucose, 25 HEPES, 0.001 TTX, 0.005 NBQX, 0.05 APV and 0.05 picrotoxin). Whole-cell patch-clamp recordings were performed with glass electrodes (resistance 2.5–4.0 MΩ when filled with internal, which includes (in mM): 120 K-gluconate, 11 KCl, 1 CaCl<sub>2</sub>, 1 MgCl<sub>2</sub>, 10 EGTA, 10 HEPES, 2 Mg-ATP and 0.3 Na-GTP, adjusted to pH 7.3 with KOH). Signals were amplified with a Multiclamp 700B amplifier, acquired using a Digidata 1440A digitizer, sampled at 10 kHz, and filtered at 2 kHz. All data acquisition and analysis were performed using pCLAMP software (Molecular Devices). ChR2-expressing neurons were visually identified for patching using an upright microscope (Olympus BX51WI) equipped with DIC optics, a filter set for visualizing YFP, and a CCD camera (RoleraXR, Q-Imaging). To stimulate ChR2, 1 s of continuous blue light (~10 mW mm<sup>-2</sup>) was generated using a Spectra X LED light engine (Lumencor) and delivered to the slice via a ×40/0.8 water immersion objective focused onto the recorded neuron.

**Acute brain slice physiology.** Acute 300-µm coronal slices were prepared by transcardially perfusing the rat with room-temperature NMDG slicing solution (containing in mM: 92 *N*-methyl-D-glucamine, 2.5 KCl, 30 NaHCO<sub>3</sub>, 1.2 NaH<sub>2</sub>PO<sub>4</sub>·H<sub>2</sub>O, 20 HEPES, 25 glucose, 5 sodium ascorbate, 2 thiourea and 3 sodium pyruvate, adjusted to pH 7.4 with HCl) and slicing the brain tissue in the same solution using a vibratome (VT1200S, Leica). Slices were allowed to recover for 10 min at 33°C in the NMDG solution, then another 20 min at 33°C in a modified HEPES artificial cerebrospinal fluid (containing in mM: 92 NaCl, 2.5 KCl, 30 NaHCO<sub>3</sub>, 1.2 NaH<sub>2</sub>PO<sub>4</sub>·H<sub>2</sub>O, 20 HEPES, 25 glucose, 5 sodium ascorbate, 2 thiourea and 3 sodium pyruvate), then another 15 min at room temperature in the HEPES solution. Finally, slices were transferred to standard artificial cerebrospinal fluid (aCSF; containing in mM: 125 NaCl, 2.5 KCl, 2 CaCl<sub>2</sub>, 1 MgCl<sub>2</sub>, 26 NaHCO<sub>3</sub>, 1.25 NaH<sub>2</sub>PO<sub>4</sub>·H<sub>2</sub>O and 11 glucose) bubbled with 95% O<sub>2</sub>/5% CO<sub>2</sub> and stored at room temperature until recording. Whole-cell patch-clamp recordings were performed in aCSF at 30–32°C. Synaptic blockers (5 µM NBQX, 50 µM D-AP5 (D(-)-2-amino-5-phosphonopivalic acid) and 50 µM picrotoxin; Tocris) were added to the aCSF to isolate direct ChR2 responses. Resistance of the patch pipettes was 2.5–4.0 MΩ when filled with intracellular solution containing the following (in mM): 120 K-gluconate, 11 KCl, 1 CaCl<sub>2</sub>, 1 MgCl<sub>2</sub>, 10 EGTA, 10 HEPES, 2 Mg-ATP and 0.3 Na-GTP, adjusted to pH 7.3 with KOH). Signals were amplified with a Multiclamp 700B amplifier, acquired using a Digidata 1440A digitizer, sampled at 10 kHz, and filtered at 2 kHz. All data acquisition and analysis were performed using pCLAMP software (Molecular Devices). ChR2-expressing neurons were visually identified for patching using an upright microscope (Olympus BX51WI) equipped with DIC optics, a filter set for visualizing YFP, and a CCD camera (RoleraXR, Q-Imaging). To stimulate ChR2, 1 s of 5-ms blue light pulses (~10 mW mm<sup>-2</sup>) were generated at 20 Hz using a Spectra X LED light engine (Lumencor) and delivered to the slice via a ×40/0.8 water immersion objective focused onto the recorded neuron. *Ex-vivo* and cell culture physiology data were analysed using Clampfit software (Axon Instruments Inc., Molecular Devices). Statistical analyses were performed using MATLAB (Mathworks Inc.) and GraphPad Prism (GraphPad Software).

**Code availability.** All custom-written MATLAB code is available on request.

**Multicolour fibre photometry.** As described previously<sup>27,28</sup>, we measured bulk fluorescence from deep brain regions using a single optical fibre for both delivery of excitation light to, and collection of emitted fluorescence from, the targeted brain region. The fluorescence output of the calcium sensor is modulated by varying the intensity of the excitation light, generating an amplitude-modulated fluorescence signal that can be demodulated to recover the original calcium sensor response. This 'upconversion' of the calcium signal to a frequency range of our choice allows us to avoid any contribution to the signal from changes in ambient light levels with behaviour (since these will not be modulated at the appropriate frequency), as well as avoiding drift or low-frequency 'flicker noise' in our photodetector.

We have extended this method to the case of multiple excitation wavelengths delivered over the same fibre, each modulated at a distinct carrier frequency, to allow for ratiometric measurements.

Fluorescence excitation was provided by two diode lasers at 488 nm and 405 nm with analogue modulation capabilities (Luxx, Omicron Laserage). A real-time signal processor (RP2.1, Tucker-Davis Technologies) running custom software sinusoidally modulated each laser's output (average power at the fibre tip was set to 30 µW for each wavelength), and simultaneously demodulated the two output signals from the output of the single photodetector (Model 2151 Femtowatt Photoreceiver) as described below.

Carrier frequencies (211 and 531 Hz for 488 and 405 nm excitation, respectively) were chosen to avoid contamination from overhead lights (120 Hz and harmonics) and cross-talk between channels (the bandwidth of GCaMP6M was observed to be <15 Hz), while remaining within the 30–750-Hz bandwidth of the photodetector. Excitation light from the two lasers was combined by a dichroic mirror (425-nm longpass, DMLP425), passed through a clean-up filter (Thorlabs, FES0500) and a dichroic mirror (505-nm long-pass, DMLP505), before being coupled into a large-core, high-NA, low-fluorescence optical fibre patch cord (400 µm diameter, 0.48 NA, Doric Lenses) using a fixed-focused coupler/collimator with a standard FC connector (F240FC-A, NA 0.51, f = 7.9 mm). The far end of the patch cord is butt-coupled to the chronically implanted fibre using standard 2.5 mm ferrules and a zirconia sleeve, allowing for easy connections and repeated measurements across days, as in standard optogenetics preparations.

A small amount of the fluorescence emitted in the brain is captured at the tip of the implanted fibre and travels back to the rig, where it is collimated and passes through the last dichroic mirror and is focused onto the photodetector by a lens (NA 0.5, f = 12.7 mm, part 62-561, Edmund Optics). The photodetector signal was sampled at 6.1 kHz, and each of the two modulated signals was independently recovered using standard synchronous demodulation techniques: the detector output was routed to two product detectors, one using the selected channel's



modulation signal as a reference, and the other using a 90° phase-shifted copy of the same reference. These outputs were low-pass filtered (corner frequency of 15 Hz), and added in quadrature. This dual-phase detection approach makes the output insensitive to any phase delay between the reference and signal. The resulting fluorescence magnitude signals were then decimated to 382 Hz for recording to disk, and then further filtered using an ~2-Hz low-pass filter.

The ratiometric fluorescence signal used throughout the paper was calculated for each behavioural session as follows. A linear least-squares fit between the two timeseries was calculated (that is, the 405-nm control signal values were the independent variable and the 488-nm signal was the dependent variable). Change in fluorescence ( $dF$ ) was calculated as (488 nm signal – fitted 405 nm signal), adjusted so that a  $dF$  of 0 corresponded to the second percentile value of the signal.  $dF/F$  was calculated by dividing each point in  $dF$  by the 405-nm fit at that time, which scaled transients according to the degree of bleaching estimated at that time.

Behavioural variables, such as lever presses and reward port entry times, were fed into the real-time processor as TTL signals from the operant chambers.

**Statistical analysis.** For each figure, a statistical test matching the structure of the experiment and the structure of the data was employed. For simple comparisons between just two groups,  $t$ -tests were used. Where the structure of the data did not fit the assumptions of the test, the non-parametric Mann–Whitney (for unpaired tests) or Wilcoxon matched-pairs (for paired tests) was used instead. When comparing the magnitude of effects of a manipulation across two groups, a two-way ANOVA was used, and where significant interactions were detected, a Bonferroni post-hoc test was used to determine the nature of the differences. When quantifying repeated manipulations within a group, a repeated-measures ANOVA was used, and where significant interactions were detected, a Dunnett's post-hoc test was used to determine whether the manipulation altered behaviour, while correcting for multiple comparisons. For linear correlation, the Pearson's  $r$  test was used throughout. Variances within each group of data are displayed as s.e.m. throughout.

**Reliability of risk preferences.** To quantify the temporal stability of individual subjects' risk preferences across days, we calculated the reliability of percentage risky choices in unmanipulated control animals' behaviour across 7 days of testing. Odd-versus-even day split-half reliability estimates (as in ref. 35) indicated significant internal consistency in risk preferences for risk-seeking animals ( $ICC = 0.95$ ,  $P = 0.0003$ ), risk-averse animals ( $ICC = 0.99$ ,  $P < 0.0001$ ), and overall ( $ICC = 0.99$ ,  $P < 0.0001$ ). Bootstrap analysis of 10,000 randomly-assigned split halves of the data generates an average  $ICC = 0.987$  ( $P < 0.0001$ ; Extended Data Fig. 2). Across rats, the average standard deviation in percentage risky choices across the 7 days of testing was 6.1%.

**Photometry within-animal analysis.** For each rat, we calculated the median neural activity during each nosepoke, in the 1 s after nosepoke entry, during successfully completed nosepokes, across all free choices, across all days of behaviour. We then sorted nosepoke periods based either on previous trial outcome (Fig. 3g, k) or on the upcoming choice (Fig. 3i, m). In the case of previous trial outcome, a  $t$ -test was used to compare a list of all nosepoke-period signals when the animal received a loss outcome (hundreds of individual trials) against a list of all the signals when the animal received a gain or safe outcome (also hundreds of individual trials). In the case of next decision, a  $t$ -test compared the list of all activity during nosepokes when the animal was about to choose safe to the list of all nosepoke activity when the rat was about to choose to take a risk. The signal was larger after loss outcomes than after gain or safe outcomes (Fig. 3e–g). This trend is individually significant in 5 out of 6 rats ( $t$ -test,  $P < 0.0001$  in all cases). Decision-period activity was higher in D2R<sup>+</sup> cells before safe choices versus risky choices (Fig. 3h, i). This trend held in all rats tested and was individually significant in 5 out of 6 rats ( $t$ -test,  $P < 0.02$  in all cases).

**Power analyses.** The logistic regression analysis displayed in Fig. 1b–e is supported by 17 animals and >9,800 individual data points. Post-hoc analyses revealed power of 0.9 and 0.84, respectively, for the subpanels in Fig. 1f and a power of 0.99 for

Fig. 1g. The one-way ANOVA in Fig. 2a has a power of 0.96. The Mann–Whitney test in Fig. 2c has a power of 0.96. The repeated-measures ANOVA used in Fig. 2f has a power of 0.99. The data in Fig. 3 comprise 31 recording sessions across the 6 rats, totalling >7,500 trials. Post-hoc power tests on Fig. 3g, i, k, m reveal a power >0.84 for all significant results. Tests on the significant correlations reveal a power of 0.95 for Fig. 3n and a power of 0.86 for Fig. 3p. The optogenetics experiments in Fig. 4 contain a total of 62 animals across the 4 groups. Power analyses reveal that the two-way ANOVA used to evaluate Fig. 4d–i has a power of 0.99. The one-way ANOVA in Fig. 4j has a power of 0.89.

**Logistic regression.** The goal of this classification is to determine the probability that a rat will choose the risky lever on any given trial given recent outcome history. We used a soft-max decision function:

$$h_{\theta}(x) = \frac{1}{1 + e^{-\theta^T x}} \quad (2)$$

such that:

$$h_{\theta}(x) = P(y = 1|x; \theta) \quad (3)$$

where  $x$  is a vector representing the recent outcome history,  $y \in \{0, 1\}$  is a dummy variable indicating whether the rat chose risky on a given trial, and  $\theta$  is the set of weights learned by the model. In this scenario, we know the outcome history ( $x$ ) and the choice outcomes ( $y$ ). We seek to use these data to find a set of weights ( $\theta$ ) that minimizes the difference between the prediction ( $h_{\theta}(x)$ ) and the rat's actual behaviour ( $y$ ). To accomplish this, we use the MATLAB gradient descent algorithm `fminunc` to generate a set of weights ( $\theta$ ) that minimize the cost function:

$$J(\theta) = \frac{1}{m} \sum_{i=1}^m -\log(h_{\theta}(x^{(i)})) \quad \text{if } y^{(i)} = 1$$

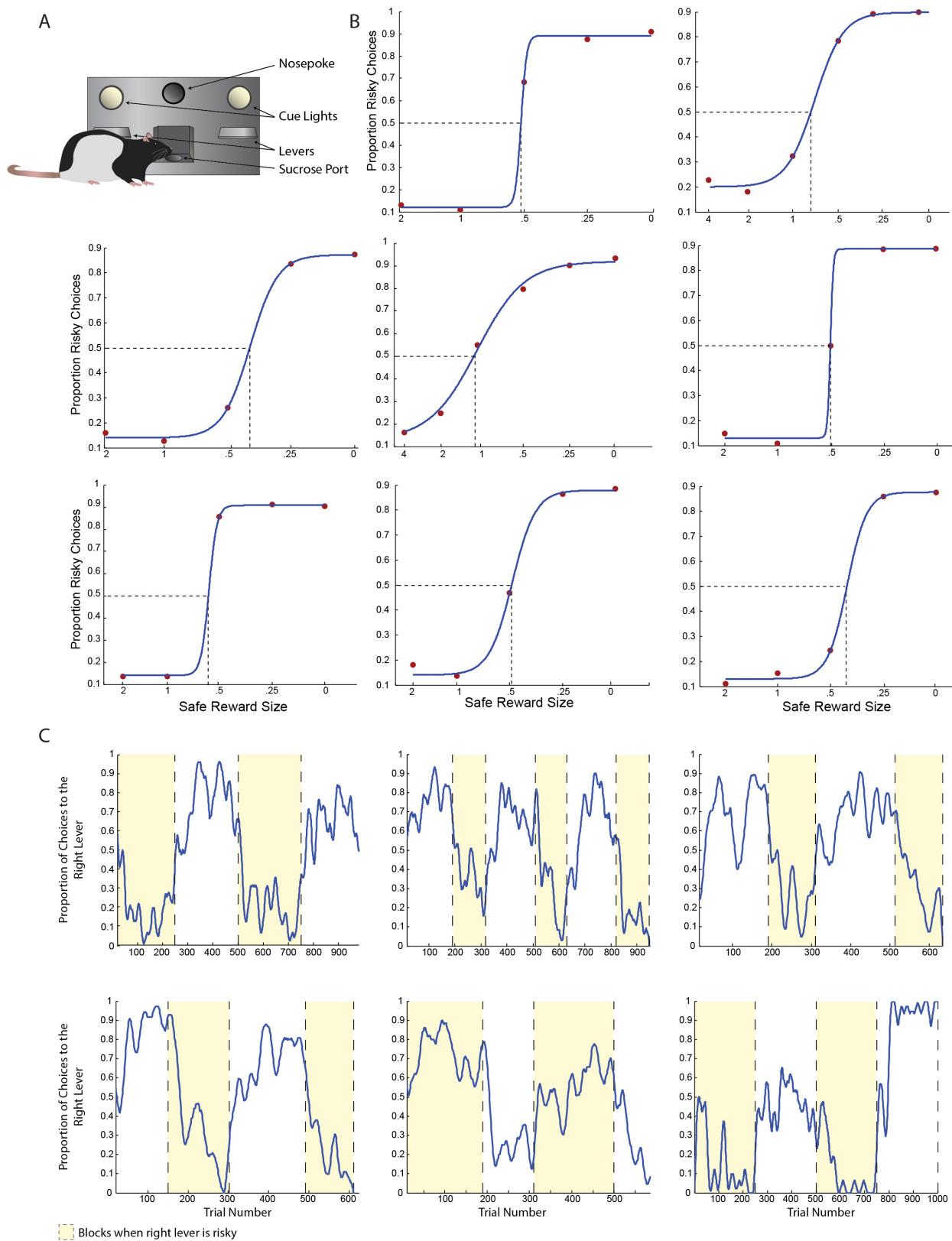
$$J(\theta) = \frac{1}{m} \sum_{i=1}^m -\log(1 - h_{\theta}(x^{(i)})) \quad \text{if } y^{(i)} = 0 \quad (4)$$

over  $m$  training examples. We use the vectorized implementation:

$$J(\theta) = -\frac{1}{m} \left[ \log \left( \frac{1}{1 + e^{-(X\theta)}} \right)^T y + \log \left( 1 - \frac{1}{1 + e^{-(X\theta)}} \right)^T (1 - y) \right] \quad (5)$$

We then used the weights generated by running this optimization over the training data to determine how well the model generalized to test data from the same rats. To do this, we plugged the weights from the optimization over training data and the outcome histories from the test data into equation (2). The probabilities generated by equation (2) were then compared to actual choice outcomes on a trial-by-trial basis, such that  $[h_{\theta}(x) \geq 0.5 \text{ when } y = 1]$  or  $[h_{\theta}(x) < 0.5 \text{ when } y = 0]$  were considered correct predictions.

- Kepecs, A., Uchida, N., Zariwala, H. A. & Mainen, Z. F. Neural correlates, computation and behavioural impact of decision confidence. *Nature* **455**, 227–231 (2008).
- Kopec, C. D., Erlich, J. C., Brunton, B. W., Deisseroth, K. & Brody, C. D. Cortical and subcortical contributions to short-term memory for orienting movements. *Neuron* **88**, 367–377 (2015).
- Witten, I. B. *et al.* Recombinase-driver rat lines: tools, techniques, and optogenetic application to dopamine-mediated reinforcement. *Neuron* **72**, 721–733 (2011).
- Minowa, T., Minowa, M. T. & Mouradian, M. M. Analysis of the promoter region of the rat D<sub>2</sub> dopamine receptor gene. *Biochemistry* **31**, 8389–8396 (1992).
- Leong, J. K., Pestilli, F., Wu, C. C., Samanez-Larkin, G. R. & Knutson, B. White-matter tract connecting anterior insula to nucleus accumbens correlates with reduced preference for positively skewed gambles. *Neuron* **89**, 63–69 (2016).

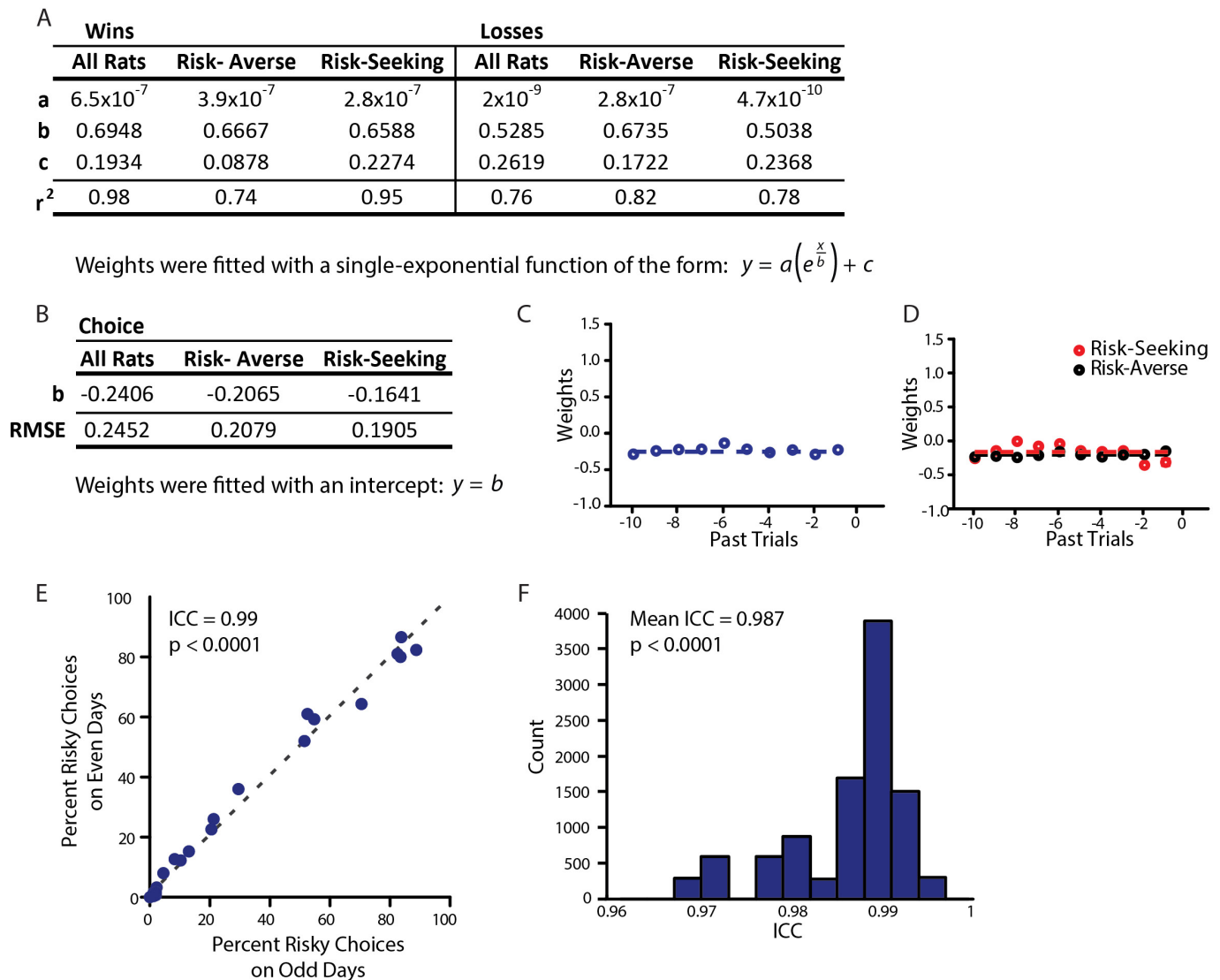


Extended Data Figure 1 | See next page for caption.

**Extended Data Figure 1 | Task validation and behavioural controls.**

**a**, Scale diagram of the behavioural apparatus, showing the relative size and location of the nosepoke, levers, and sucrose port. **b**, Rats varied the proportion of choices they made to the risky lever as a function of the relative value of the safe and risky options. Subplots were constructed for each rat. The size of the safe reward is displayed as a proportion of the expected value of the risky reward. Red points indicate the proportion of risky choices each rat made to the risky lever given a particular value of the safe reward; blue lines indicate sigmoidal fits to those values. Dashed lines indicate each rat's indifference point. Data in the centre panel are from a risk-seeking rat (indifference point  $> 1$ ); all other rats were risk-averse. Side bias, in these data, would appear as an upward or downward shift of the sigmoid, such that behaviour would asymptote without spanning

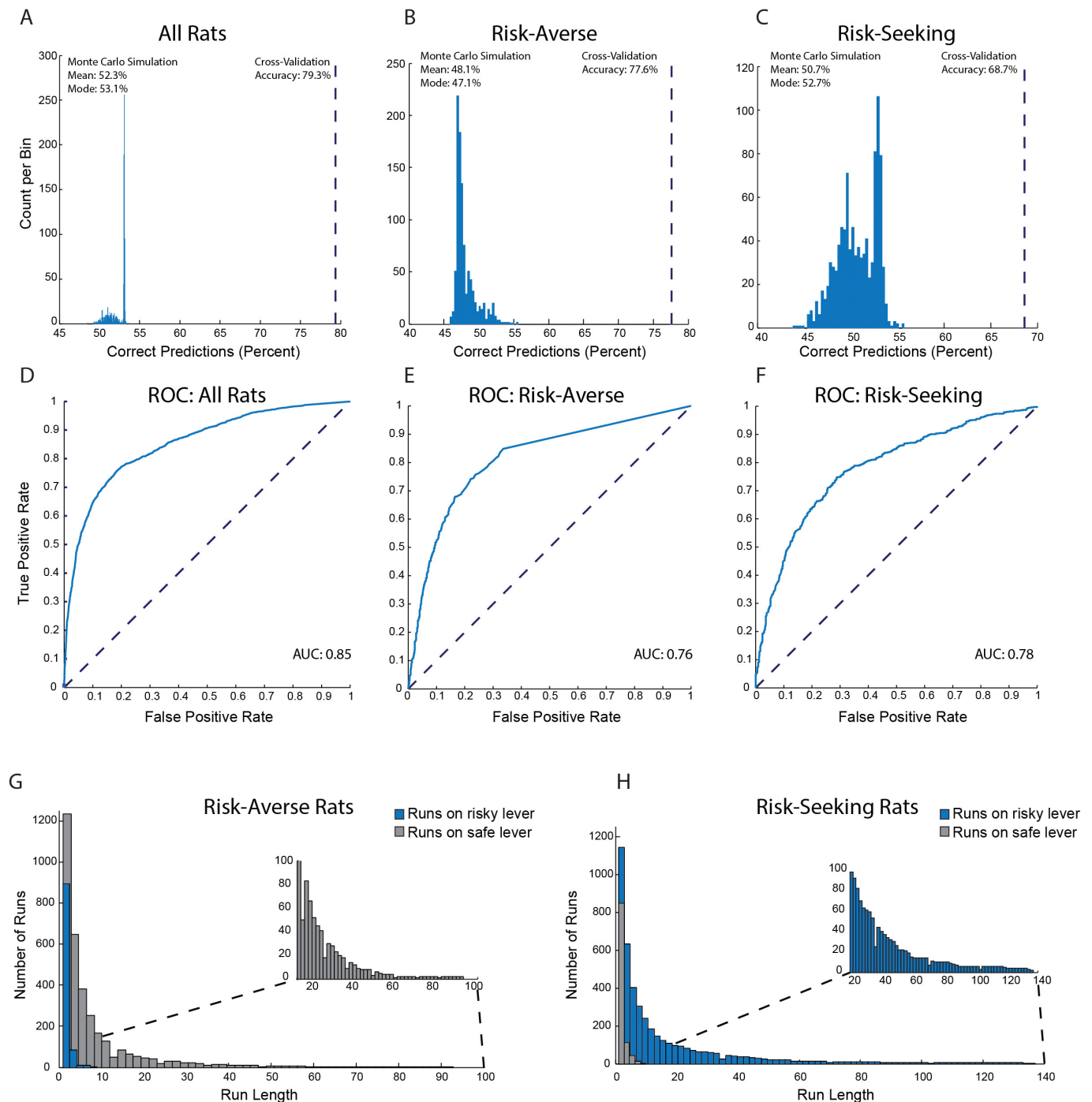
the range of risky choices, and 50% would not centre the sigmoid on the ordinate. An additional cohort of rats was trained specifically for this control experiment. These rats do not appear elsewhere in the manuscript. **c**, Rats reversed their behaviour to track their preferred reward contingency (safe or risky). Each panel displays the behaviour of one rat across several hundred trials. The location of the risky lever is alternated in blocks of trials. Blocks where the right lever is risky are highlighted in yellow. Rats' choices are smoothed with a 15-trial moving window. The rat in the bottom centre panel displayed risk-seeking behaviour; all others were risk-averse. An additional cohort of rats was trained specifically for this control experiment. These rats do not appear elsewhere in the manuscript.



**Extended Data Figure 2 | Parameters for logistic regression classifier.** **a**, Parameter values and goodness-of-fit for single-exponential fits of the form  $y = a\left(e^{\frac{x}{b}}\right) + c$  to weights obtained in the logistic regression classifier (Methods) shown in Fig. 1. **b**, Parameter values and root mean squared error (RMSE) for fits of the form  $y = b$  to weights associated with choosing the safe option in the logistic regression classifier (Methods) shown in Fig. 1. **c**, Model coefficients associated with choosing the safe lever, as obtained from the entire population of rats. **d**, Model coefficients associated with choosing the safe lever, obtained for risk-seeking and risk-averse rats separately. **e**, Split-half reliability. Each dot represents a

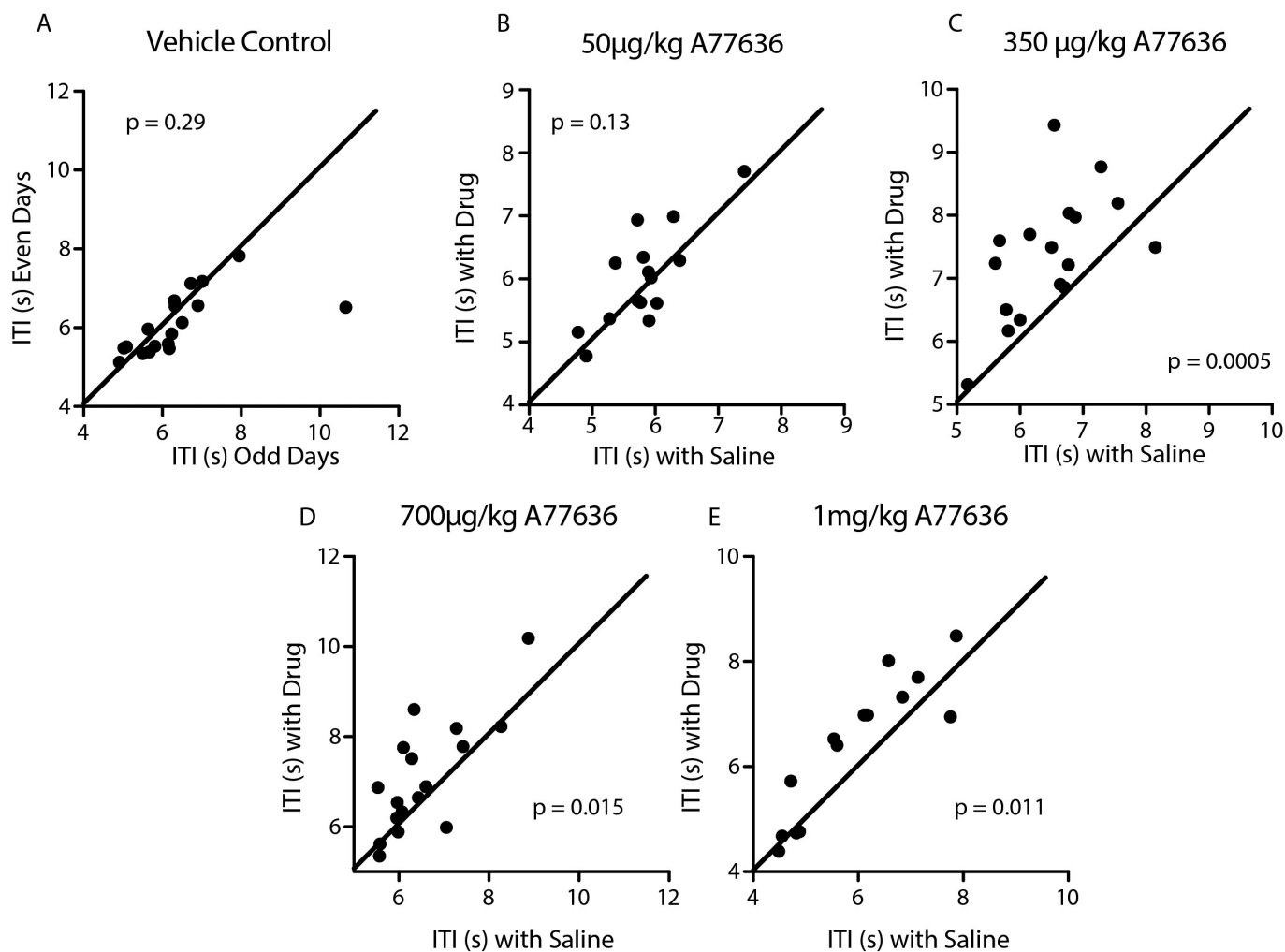
comparison between a rat's average risk preference on odd days of behaviour and the rat's average risk preference on even days of behaviour across seven days of testing. Perfect reliability would be represented by each animal's data falling along the (grey, dashed) unity line. **f**, A 10,000-fold bootstrap over randomly assigned split halves of each rat's behaviour generates an average reliability (intraclass correlation (ICC)) of 0.987. Reliability estimates were generated from control animal behavioural data represented in Fig. 4, as this cohort represents the longest test of unmanipulated behaviour in the manuscript.





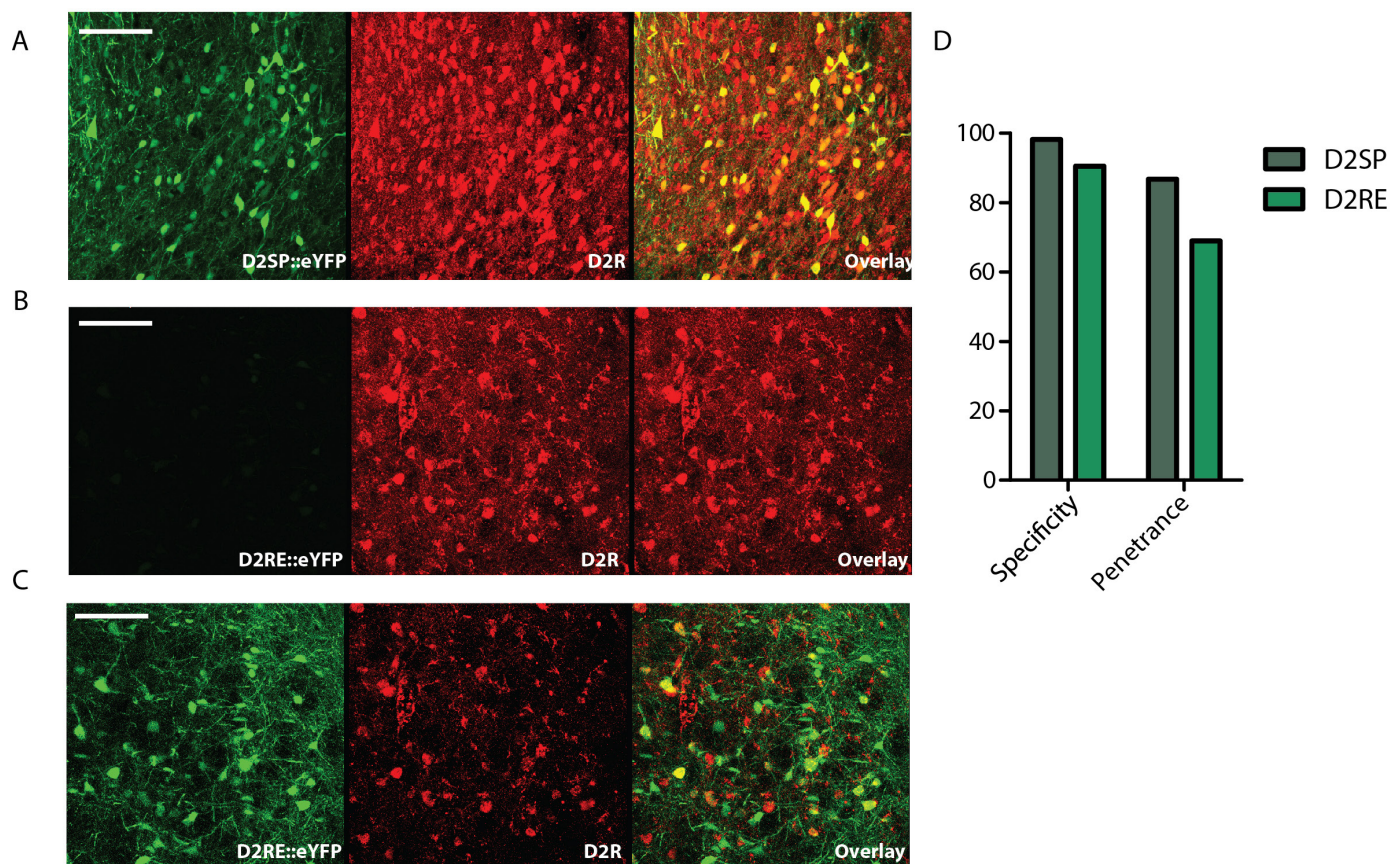
**Extended Data Figure 3 | Predictive validity of the logistic regression classifier.** **a–c**, The model was trained on two-thirds of data and tested on the one-third of data that was held-out. The blue histogram indicates the chance distribution, determined by the model's performance over a 1,000-fold shuffle of the held-out test data. The dashed line indicates cross-validation accuracy (CV) on held-out data. This calculation was performed for data from all rats (**a**;  $P < 0.001$  by Monte Carlo simulation; CV is 24.3 s.d. outside the chance distribution), a balanced subset of data from risk-averse rats, such that approximately 50% of choices were safe and 50% were risky (**b**;  $P < 0.001$  by Monte Carlo simulation;

CV is 20.6 s.d. outside the chance distribution), and a balanced subset of data from risk-seeking rats (**c**;  $P < 0.001$  by Monte Carlo simulation; CV is 8.5 s.d. outside the chance distribution). **d–f**, Receiver operating characteristic (ROC) curves derived from model performance on held-out test data across all rats (**d**; area under the curve (AUC) = 0.85), a balanced subset of data from risk-averse rats (**e**; AUC = 0.76), and a balanced subset of data from risk-seeking rats (**f**; AUC = 0.78). **g, h**, Histogram of run lengths for risk-averse rats (**g**) and risk-seeking rats (**h**). Blue bars indicate runs on the risky lever. Grey bars indicate runs on the safe lever. Insets show exceptionally long runs.



**Extended Data Figure 4 | The D1 agonist A-77636 increased intertrial interval without influencing risk preference.** Each rat in this experiment received alternating treatments of intraperitoneal A-77636 and intraperitoneal saline (see Fig. 2d). Each plot represents a different dose of A-77636. On each *x* axis is the intertrial interval on days receiving saline, and on the *y* axis is the intertrial interval on days receiving drug. Points above the unity line indicate an increase in intertrial interval with drug administration. **a**, Vehicle alone does not alter intertrial interval (paired

*t*-test,  $t_{17} = 1.088$ ,  $P = 0.29$ ). **b**, A 50 µg kg<sup>-1</sup> dose of A-77636 does not significantly alter intertrial interval (paired *t*-test,  $t_{14} = 1.598$ ,  $P = 0.13$ ). **c**, A 350 µg kg<sup>-1</sup> dose of A-77636 significantly increases intertrial interval (paired *t*-test,  $t_{16} = 4.391$ ,  $P = 0.0005$ ). **d**, A 700 µg kg<sup>-1</sup> dose of A-77636 significantly increases intertrial interval (paired *t*-test,  $t_{16} = 2.738$ ,  $P = 0.015$ ). **e**, A 1,000 µg kg<sup>-1</sup> dose of A-77636 significantly increases intertrial interval (paired *t*-test,  $t_{13} = 2.948$ ,  $P = 0.011$ ).



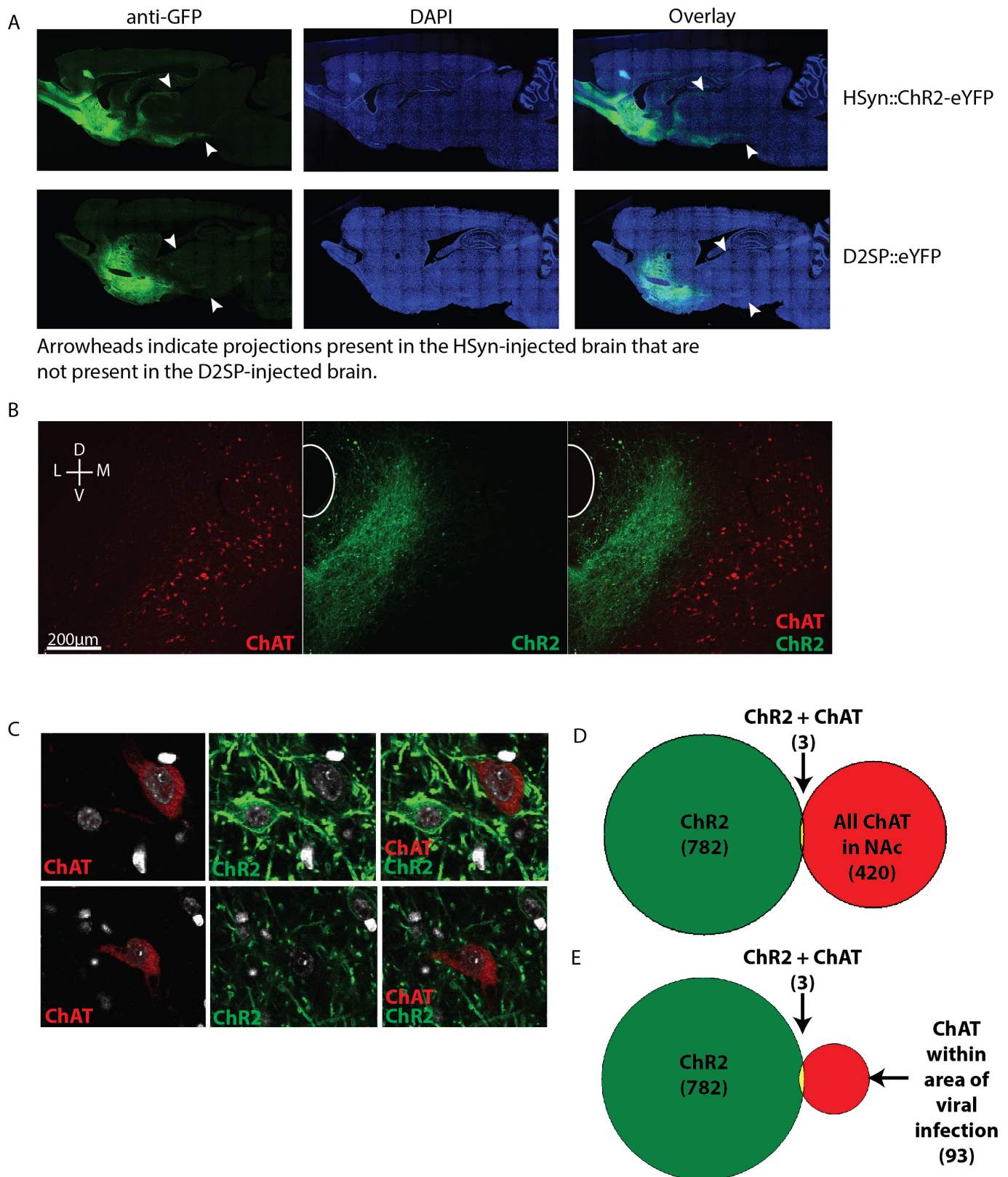
E

ttatcctcgggtgcatctcagagaaataagcattgcttggaccaatgtggaccggatgttaacacctagagccagagagattaaaaaattaatcaaca  
tctacaactggcaagggatagacataggacacacgactgggtggaacgtatagaggtgatgggttgagaagaacaaaatccctgtttaagtagg  
ttatttcttgggaagaacatgtccagggcacataggaaaatagtggggattcaacatgtctgtaatgtgtgagtgccttaaaagcaaatgtgaaaaa  
ttctaattgttctgtagttctaacacttccctaccatgcctatagagagccatgaatagaccataccccaagaataatgaataggggaagggaggct  
agttccccttttctaaatgcctccataactggccacatctaagaaaaatgtgctgtgtataggagctgtccactgtggtccccgtgaggtttggagg  
ggcatgcctcttgggtcccagattccaccttgaaatcaaacaggggttagttgaatattagtgtctgtcttccaaccttaatttccaggattgtgtgg  
atcaatggaaggagtttcttcttgtggctaagtggcatgactgccggctatatgcagactgtcctctgtgctcctgcccttggaatctgtgtgtgcttct  
ccttgggggacttgaaattggccaatggccagctcctgtgaggttccggagctgtcggtactccacagcacctatttaagctacaagatttggaaagactc  
tactctggattgaccccatgcattctgaatctcatgtagaagctggccaaggcaggacagaggacagaaagcaccagctggatttgagaagaagag  
gatggaaagggtttaggttccctgggtgggagatgacctggacagggtgaagaagatcacatttcttctcctgctcctcagtcagacggaa  
gggtgagctagaatttccagcccttcttatcattcccatcttagatctgctctgccaaagtcttctctcagaaagcacaacagcagaacgaactgct  
gtgatttccagacctgaggtctgtacaccgactctggatatccttccggaatctatttctcctttaaagacttgatgtaccacacgtagtgcttcagctagc  
ccttggccctgactcctcaaaggaggggatcgaccgctggtgtgtgattgctagaccagagtaggtttggatgggcaggggtgttacttaaaaagtat  
aggatgacaccggcgagcagtcgggagcacaggctatccctcctcaaagccagagatggatttctcggtctcagctctcaaggttcttcccaggccc  
cacagtgcagagatagttctggggccctgggtgggtggggcctctgtacaaggggcggggtcccgggcgctcgtggccaggggtgaccccgcccct  
cctctcgcgcagcgtctgattccgcggagctgtccagcctcagtgccgggg

**Extended Data Figure 5 | The novel D2SP improves expression and specificity over previously published promoters.** **a**, Expression of eYFP under the novel D2SP. Red shows D2R immunostaining (Methods). Scale bar, 100  $\mu$ m. **b**, Expression of eYFP under a D2R promoter based on previously published constructs (D2RE), which included the first exon of the D2 receptor gene<sup>30,31</sup>. Image taken with settings matched to those used for the D2SP image in **a**. Scale bar, 100  $\mu$ m. **c**, Images are of the same

field of view as in **b** but taken with settings optimized to see the (otherwise dim) eYFP expression. Scale bar, 100  $\mu$ m. **d**, Specificity of expression under the D2SP improved from 90.5% to 98.2% under the previously described promoter. Penetrance of expression under the D2R promoter improved from 69% to 86.8% under the previously described promoter. **e**, Full sequence of D2SP.

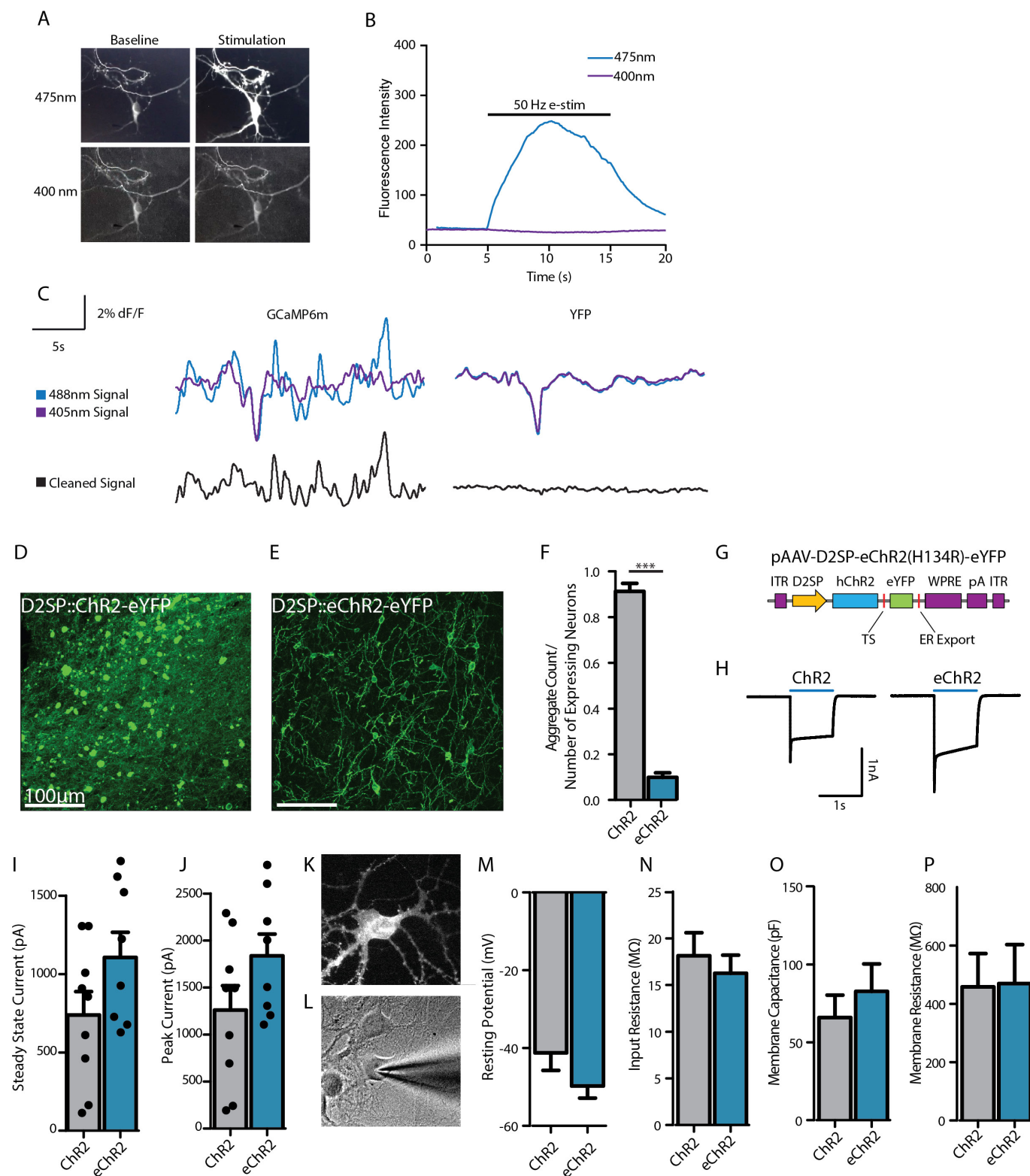




**Extended Data Figure 6 | Specificity of D2SP.** **a**, Sagittal sections taken from brains injected with AAV8-hSYN-ChR2-eYFP (top) and AAV8-D2SP-eYFP (bottom). Arrowheads indicate projections expressing eYFP in the hSYN-injected brain that are not expressing eYFP in the D2SP-injected brain. **b**, Representative injection location, showing minimal overlap of D2SP-eChr2-eYFP with choline acetyltransferase (ChAT)<sup>+</sup> cells. Green indicates D2SP-eChr2-eYFP, red indicates ChAT. **c**, Example of the three

ChAT<sup>+</sup> cells observed expressing eChr2-eYFP across 6 animals (top) and a ChAT<sup>+</sup> cell that does not express eChr2-eYFP (bottom). **d**, Across NAc sections from the most densely expressing slices from 6 animals, 782 cells expressing eChr2-eYFP, 420 cells expressing ChAT, and 3 cells expressing both ChAT and ChR2-eYFP were observed. **e**, Within the area of viral infection, 782 cells expressing eChr2-eYFP, 93 cells expressing ChAT, and 3 cells expressing both ChAT and ChR2-eYFP were observed.



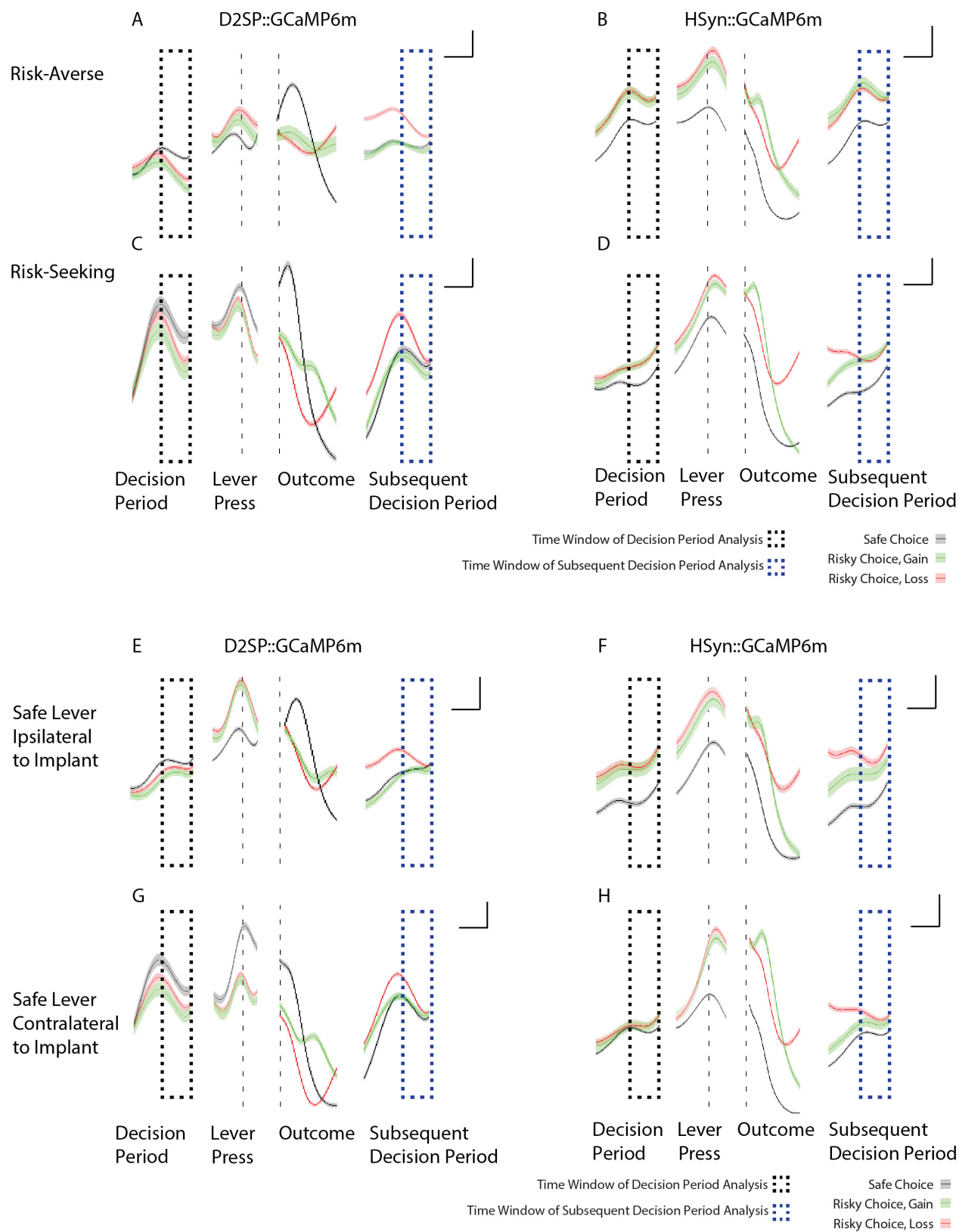


Extended Data Figure 7 | See next page for caption.

**Extended Data Figure 7 | Characterization of dual-wavelength photometry and eChR2.**

**a**, Images of a GCaMP6m-expressing neuron illuminated at the imaging wavelength (475 nm) and the isosbestic wavelength (400 nm), at baseline (left) and with 10 s of 50 Hz electrical stimulation (right). **b**, Fluorescence intensity from a representative neuron, illuminated at 475 nm and 400 nm, during 10 s of 50 Hz electrical stimulation. **c**, Traces from a GCaMP6m-expressing rat (left) and a YFP-expressing rat (right) during the gambling task. Cyan traces are of the imaging wavelength; violet traces are of the isosbestic wavelength; black traces represent the cleaned signal (Methods). **d**, Expression of D2SP-ChR2-eYFP in rat NAc, showing evidence of opsin accumulations (bright green spots). **e**, Expression of D2SP-eChR2-eYFP in rat NAc; note greatly reduced accumulation density. **f**, D2SP-ChR2-eYFP-expressing cells have significantly more aggregates than D2SP-eChR2-eYFP-expressing cells. Quantification is in number of aggregates per expressing cell across *ex vivo* histological sections (*t*-test,  $t_7 = 21.25$ , \*\*\* $P < 0.0001$ ;  $n = 168$

ChR2-expressing cells in 4 sections,  $n = 131$  eChR2-expressing cells in 5 sections). **g**, Backbone diagram of pAAV-D2SP-eChR2(H134R)-eYFP showing the membrane trafficking modifications (trafficking signal (TS) and endoplasmic reticulum (ER) export motifs). **h**, Representative photocurrents evoked by ChR2 and eChR2 in cultured neurons by 1 s 473-nm light. **i**, Steady-state photocurrents measured from ChR2- and eChR2-expressing cultured neurons. In addition to showing reduced accumulations, photocurrents trended higher with eChR2. **j**, Peak photocurrents measured from ChR2- and eChR2-expressing cultured neurons; eChR2 trended towards higher peaks as well. **k**, Expression of eChR2-eYFP in a cultured rat striatal neuron. **l**, Whole-cell patch-clamp recording from the neuron shown in **k**. **m–p**, Resting membrane potential, input resistance, membrane capacitance, and membrane resistance measured from ChR2- and eChR2-expressing cultured neurons; no significant differences were observed. All error bars represent s.e.m.



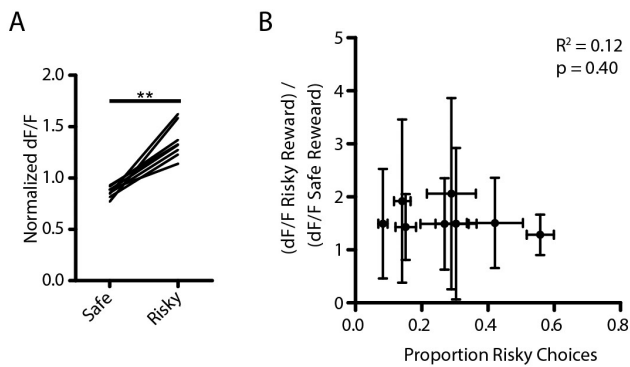
Extended Data Figure 8 | See next page for caption.

**Extended Data Figure 8 | D2R<sup>+</sup> (but not pan-neuronal) cellular signals are increased during the decision-period leading to risk rejection (safe choice) and encode prior loss. a–h,** In all plots, black dashed boxes indicate decision-period activity, and blue dashed boxes indicate subsequent decision-period activity. Traces indicate mean neural activity sorted on trial outcome: safe (black), gain (green) or loss (red). Shaded regions indicate s.e.m. **a,** Average traces from the most risk-averse cell-specific D2SP-GCaMP6m-expressing rats ( $n = 3$ ). Note increased neural activity during the decision period preceding a safe choice as compared to a risky (gain or loss) choice, as well as increased activity during the subsequent decision period (blue dashed box) following a loss outcome. **b,** Average traces from the most risk-averse non-cell-type-specific (hSYN-GCaMP6m-expressing) rats ( $n = 4$ ). Note the increased activity in these cells during the decision period before making a risky (red/green) as compared to safe (black) choice (contrasting with the opposite D2R<sup>+</sup>-specific result in **a**). Also in contrast to the D2R<sup>+</sup> case, the pan-neuronal signal did not discriminate immediately-preceding loss (red)

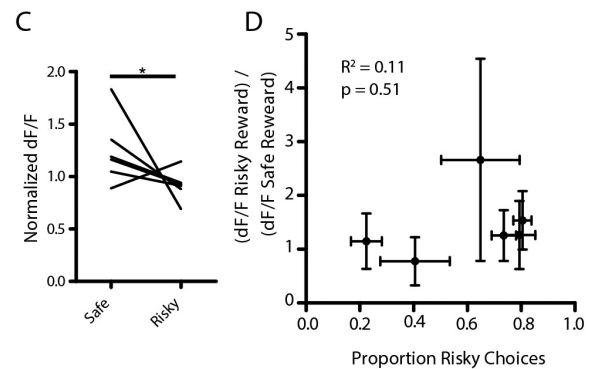
from immediately-preceding gain (green) during the subsequent decision period. **c, d,** These pattern were also consistent in the most risk-seeking animals (D2SP-GCaMP6m-expressing rats,  $n = 3$ ; hSYN-GCaMP6m-expressing rats,  $n = 4$ ). **e–h,** This pattern did not depend on the location of the implant relative to the safe lever. Shown are data from D2SP-GCaMP6m-expressing rats with implants ipsilateral to the location of the safe lever ( $n = 4$ ); hSYN-GCaMP6m-expressing rats with implants ipsilateral to the location of the safe lever ( $n = 4$ ); D2SP-GCaMP6m-expressing rats with implants contralateral to the location of the safe lever ( $n = 2$ ); hSYN-GCaMP6m-expressing rats with implants contralateral to the location of the safe lever ( $n = 4$ ). Data for **a, c, e** and **g** are from the rats whose behaviour and neural data are represented in Fig. 3. Data for **b, d, f** and **h** are not represented in the main figures of the manuscript. Throughout the figure, traces were analysed as  $dF/F$  and z-score normalized before averaging. Scale bars indicate 1 s and 0.25 standard (z-score) units.



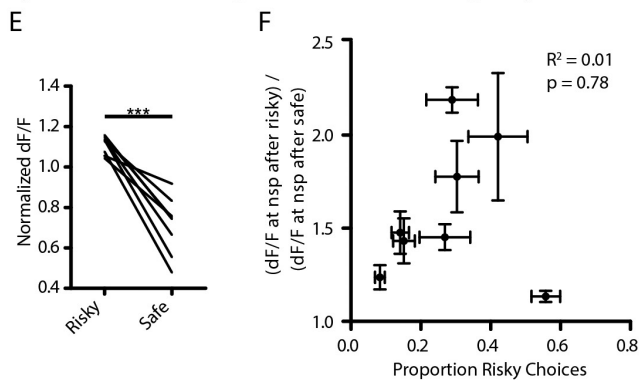
## hSYN Signal Is Greater During Outcomes Following Risky Choice



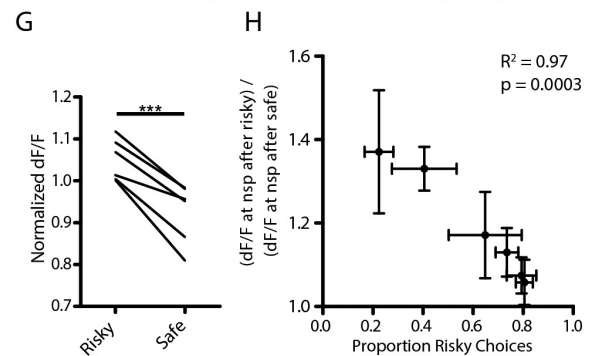
## D2R+ Signal Is Greater During Outcomes Following Safe Choice



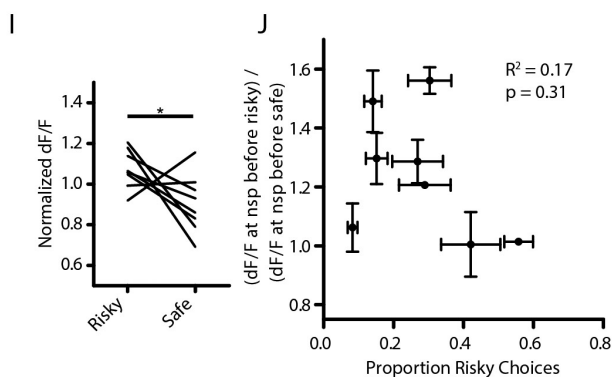
## hSYN Decision Period Signal Is Greater Following Risky Outcomes



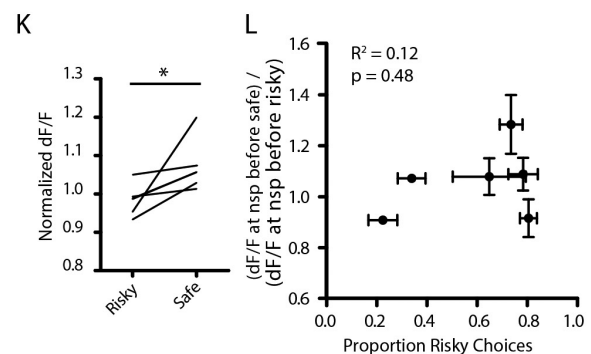
## D2R+ Decision Period Signal Is Greater Following Risky Outcomes



## hSYN Decision Period Signal Is Greater Before Risky Choices

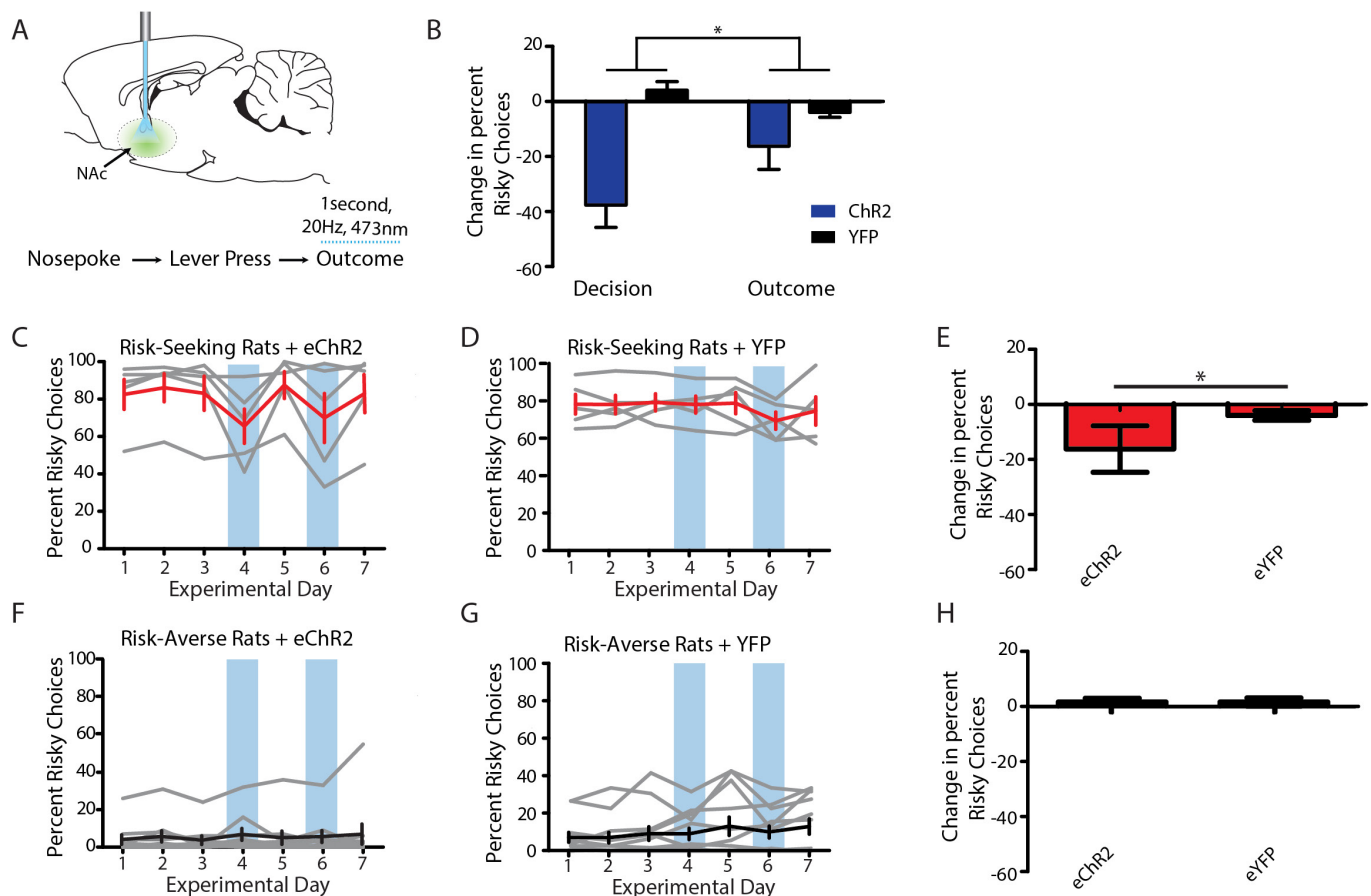


## D2R+ Decision Period Signal Is Greater Before Safe Choices



**Extended Data Figure 9 | Pan-neuronal NAc recordings: increased activity associated with risky decisions.** **a**, Median-normalized dF/F signal during the first second of the outcome period for each hSYN-GCaMP6m-expressing rat, comparing risky outcomes to safe outcomes ( $n = 8$ ; Wilcoxon matched-pairs test,  $W = 36$ ,  $P = 0.008$ ). **b**, Lack of correlation between the proportion of choices made by each rat to the risky lever and the individual's risky versus safe outcome signal ((dF/F) during the first 1 s of risky outcome/(dF/F) during safe outcome) ( $n = 8$  rats, Pearson's  $r^2 = 0.12$ ,  $P = 0.40$ ). **c**, Median-normalized dF/F signal during the first second of the outcome period for each D2SP-GCaMP6m-expressing rat, comparing safe outcomes to risky outcomes ( $n = 6$ ; Wilcoxon matched-pairs test,  $W = 17$ ,  $P = 0.04$ ). **d**, Lack of correlation between the proportion of choices made by each rat to the risky lever and the individual's risky versus safe outcome signal ((dF/F) during the first 1 s of safe outcome/(dF/F) during risky outcome) ( $n = 6$ ; Pearson's  $r^2 = 0.11$ ,  $P = 0.51$ ). **e**, Median-normalized dF/F signal at the time of trial initiation for each hSYN-GCaMP6m-expressing rat, sorted on previous trial outcome, comparing risky outcomes to safe outcomes ( $n = 8$ ; paired  $t$ -test,  $t_7 = 7.25$ ,  $P = 0.0002$ ). **f**, Lack of correlation between the proportion of choices made by each rat to the risky lever and the individual's risk signal ((dF/F) at nosepoke trial initiation after risky outcome/(dF/F) after safe outcome) ( $n = 8$ ; Pearson's  $r^2 = 0.01$ ,  $P = 0.78$ ). **g**, Median-normalized

dF/F signal at the time of trial initiation for each D2SP-GCaMP6m-expressing rat, sorted on previous trial outcome, comparing risky outcomes to safe outcomes ( $n = 6$ ; paired  $t$ -test,  $t_5 = 6.901$ ,  $P = 0.001$ ). **h**, Correlation between the proportion of choices made by each D2SP-GCaMP6m-expressing rat to the risky lever and the individual's risk signal ((dF/F) at nosepoke trial initiation after risky outcome/(dF/F) after safe outcome) ( $n = 6$ ; Pearson's  $r^2 = 0.97$ ,  $P = 0.0003$ ). **i**, Median-normalized dF/F signal at the time of trial initiation for each hSYN-GCaMP6m-expressing rat, sorted on upcoming choice, comparing risky choices to safe choices ( $n = 8$ ; paired  $t$ -test,  $t_7 = 2.11$ ,  $P = 0.036$ ). **j**, Lack of correlation between the proportion of choices made by each rat to the risky lever and the individual's decision period signal ((dF/F) at nosepoke trial initiation before a risky choice/(dF/F) before a safe choice) ( $n = 8$ ; Pearson's  $r^2 = 0.17$ ,  $P = 0.31$ ). **k**, Median-normalized dF/F signal at the time of trial initiation for each D2SP-GCaMP6m-expressing rat, sorted on upcoming choice, comparing risky choices to safe choices ( $n = 8$ ; paired  $t$ -test,  $t_7 = 2.11$ ,  $P = 0.036$ ). **l**, Lack of correlation between the proportion of choices made by each rat to the risky lever and the individual's safe choice signal ((dF/F) at nosepoke trial initiation before choosing safe/(dF/F) at nosepoke before choosing risky) ( $n = 6$ ; Pearson's  $r^2 = 0.12$ ,  $P = 0.48$ ). Data from **k** and **l** also appear in Fig. 3i, o and are reproduced here for ease of comparison. All error bars represent s.e.m.



**Extended Data Figure 10 | D2SP-eChR2 stimulation during the outcome period produced a small but still detectable effect on risk preference.** **a**, Stimulation was as in Fig. 4, except delivered during the first second of reward retrieval rather than during the 1-s decision period. **b**, The effect of this stimulation during the outcome period was smaller than that of stimulation during the decision period (two-way ANOVA, interaction  $F_{1,24} = 6.12$ ;  $*P = 0.02$ ; Bonferroni post-hoc tests revealed a significant effect of stimulation during the decision period,  $P < 0.001$ , but no effect of stimulation during the outcome period). **c–h**, As in Fig. 4, 1 s

of 20-Hz optical stimulation of NAc DR2<sup>+</sup> cells during the outcome period decreased risky choices in risk-seeking, but not risk-averse rats relative to YFP-expressing controls (two-way ANOVA, interaction  $F_{1,31} = 4.317$ ,  $P = 0.046$ ; Bonferroni post-hoc test revealed a significant difference between eChR2-expressing and YFP-expressing risk-seeking rats, but no difference between experimental and control risk-averse rats;  $*P < 0.05$ ). Grey traces represent individual animals. Black and red traces represent the population average. Error bars represent s.e.m. Blue boxes indicate days on which optical stimulation was delivered during the outcome.

# Bidirectional electromagnetic control of the hypothalamus regulates feeding and metabolism

Sarah A. Stanley<sup>1</sup>, Leah Kelly<sup>1</sup>, Kaamashri N. Latcha<sup>1</sup>, Sarah F. Schmidt<sup>1</sup>, Xiaofei Yu<sup>1</sup>, Alexander R. Nectow<sup>1</sup>, Jeremy Sauer<sup>2</sup>, Jonathan P. Dyke<sup>3</sup>, Jonathan S. Dordick<sup>2</sup> & Jeffrey M. Friedman<sup>1,4</sup>

**Targeted, temporally regulated neural modulation is invaluable in determining the physiological roles of specific neural populations or circuits. Here we describe a system for non-invasive, temporal activation or inhibition of neuronal activity *in vivo* and its use to study central nervous system control of glucose homeostasis and feeding in mice. We are able to induce neuronal activation remotely using radio waves or magnetic fields via Cre-dependent expression of a GFP-tagged ferritin fusion protein tethered to the cation-conducting transient receptor potential vanilloid 1 (TRPV1) by a camelid anti-GFP antibody (anti-GFP-TRPV1)<sup>1</sup>. Neuronal inhibition via the same stimuli is achieved by mutating the TRPV1 pore, rendering the channel chloride-permeable. These constructs were targeted to glucose-sensing neurons in the ventromedial hypothalamus in glucokinase-Cre mice, which express Cre in glucose-sensing neurons<sup>2</sup>. Acute activation of glucose-sensing neurons in this region increases plasma glucose and glucagon, lowers insulin levels and stimulates feeding, while inhibition reduces blood glucose, raises insulin levels and suppresses feeding. These results suggest that pancreatic hormones function as an effector mechanism of central nervous system circuits controlling blood glucose and behaviour. The method we employ obviates the need for permanent implants and could potentially be applied to study other neural processes or used to regulate other, even dispersed, cell types.**

While electrode stimulation and lesioning studies suggest that hypothalamic neurons regulate blood glucose and feeding<sup>3</sup>, these methods affect both cells and fibres of passage<sup>4–6</sup> and do not define contributing cell types<sup>7</sup>. Previously we showed that radio waves or magnetic fields can control calcium (Ca<sup>2+</sup>) entry and gene expression using ferritin nanoparticles tethered to the temperature-sensitive TRPV1 channel<sup>1</sup>. In this report, we tested the utility of our approach for neural activation and investigate the function of hypothalamic glucose-sensing neurons. A replication-deficient adenovirus with Cre-dependent expression of anti-GFP-TRPV1/GFP-ferritin (Ad-FLEX-anti-GFP-TRPV1/GFP-ferritin) was injected unilaterally into the ventromedial hypothalamus (VMH) of glucokinase-Cre (GK-Cre) mice, which express Cre in glucose-sensing neurons<sup>2</sup> (Extended Data Fig. 1a), targeting ~2,000 neurons (see Methods), similar to previous studies<sup>8,9</sup>. Radio frequency (RF) treatment (465 kHz) of these mice significantly increased blood glucose (change in blood glucose at 30 min: RF-treated, 48.9 ± 16.9 mg dl<sup>-1</sup> versus untreated, -0.7 ± 12.9 mg dl<sup>-1</sup>; *P* < 0.05; at 45 min: RF-treated, 91.3 ± 28.2 mg dl<sup>-1</sup> versus untreated, 8.7 ± 11.1 mg dl<sup>-1</sup>; *P* < 0.05) and the cumulative change in blood glucose (area under the curve (AUC; 0–90 min): RF-treated, 5,562 ± 1,977 mg dl<sup>-1</sup> min versus untreated, 62 ± 1,184 mg dl<sup>-1</sup> min; *P* < 0.05) (Fig. 1b, c). The time course and extent of glucose changes after RF treatment were almost superimposable with those after optogenetic activation of VMH GK-Cre neurons, albeit with a slight delay (Fig. 1b, c). RF treatment of GK-Cre mice with VMH injection of anti-GFP-TRPV1/GFP-ferritin halved plasma

insulin, increased plasma glucagon threefold and significantly induced expression of the hepatic gluconeogenic enzyme<sup>10</sup>, glucose-6-phosphatase (Fig. 1d). Thus, remote activation of glucose-sensing neurons regulated pancreatic hormones to increase blood glucose. Blood glucose changes were dependent on RF field strength and duration (Extended Data Fig. 2a–d). RF treatment did not alter blood glucose in wild-type mice with VMH injection of anti-GFP-TRPV1/GFP-ferritin (Extended Data Fig. 3). RF treatment induced c-Fos expression only in GFP-expressing neurons and not in RF-treated wild-type mice (Extended Data Fig. 1d). Anti-GFP-TRPV1/GFP-ferritin expression, with or without RF, did not alter apoptotic cell count compared to control virus expressing GFP (Extended Data Fig. 1d, e).

Consistent with these *in vivo* data, RF significantly increased the number of cells with raised intracellular Ca<sup>2+</sup> in a hypothalamic N38 cell line stably expressing anti-GFP-TRPV1/GFP-ferritin. These effects were blocked by the TRP channel inhibitor ruthenium red. The mode response time was 11–15 s after RF onset (Extended Data Fig. 4a–c). Calcium responses were proportional to RF field strength and a 10 s pulse significantly increased intracellular Ca<sup>2+</sup> (Extended Data Fig. 4d–g). RF treatment of N38 cells expressing anti-GFP-TRPV1/GFP-ferritin also significantly increased targets of Ca<sup>2+</sup> signalling, phosphorylated-cAMP-response element-binding protein (pCREB)<sup>11</sup> and c-Fos<sup>12</sup>, and these effects were blocked by ruthenium red (Extended Data Fig. 4h, i). RF treatment of N38 cells without anti-GFP-TRPV1/GFP-ferritin induced a small increase in c-Fos and no increase in pCREB (Extended Data Fig. 6). Immunohistochemistry, electron microscopy and immuno-electron microscopy confirmed co-expression and co-localization of anti-GFP-TRPV1 and GFP-ferritin *in vitro* (Extended Data Fig. 5).

Non-invasive neural inhibition would provide a valuable research tool and potentially offer an alternative to deep brain stimulation which may act by neural inhibition<sup>13</sup>. An amino acid substitution, from isoleucine to lysine in the S6 pore region of TRPM2 and M8 changed ionic selectivity from cations to chloride (Cl<sup>-</sup>) ions<sup>14</sup>. We introduced and tested an analogous mutation in TRPV1 S6 region (I679K) (Fig. 2a) to create the TRPV1<sup>mutant</sup> channel. In N38 cells stably expressing anti-GFP-TRPV1<sup>mutant</sup>/GFP-ferritin, the TRP agonist 2-aminoethoxydiphenyl borate (2-APB) significantly increased intracellular Cl<sup>-</sup> levels measured by MQAE quenching. This effect was blocked by ruthenium red (Fig. 2b and Extended Data Fig. 8). RF treatment of N38 cells expressing anti-GFP-TRPV1<sup>mutant</sup>/GFP-ferritin significantly reduced pCREB levels and failed to increase c-Fos expression (Extended Data Fig. 7a).

We next tested whether remote inhibition of hypothalamic glucose-sensing neurons altered glucose metabolism *in vivo*. RF treatment of fasted GK-Cre mice following VMH injection of adenovirus with Cre-dependent expression of anti-GFP-TRPV1<sup>mutant</sup>/GFP-ferritin (Ad-FLEX-anti-GFP-TRPV1<sup>mutant</sup>/GFP-ferritin) significantly

<sup>1</sup>Laboratory of Molecular Genetics, Rockefeller University, New York, New York 10065, USA. <sup>2</sup>Department of Chemical & Biological Engineering, Center for Biotechnology & Interdisciplinary Studies, Rensselaer Polytechnic Institute, Troy, New York 12180, USA. <sup>3</sup>Department of Radiology, Weill Cornell Medical College, New York, New York 10065, USA. <sup>4</sup>Howard Hughes Medical Institute, New York, New York 10065, USA.

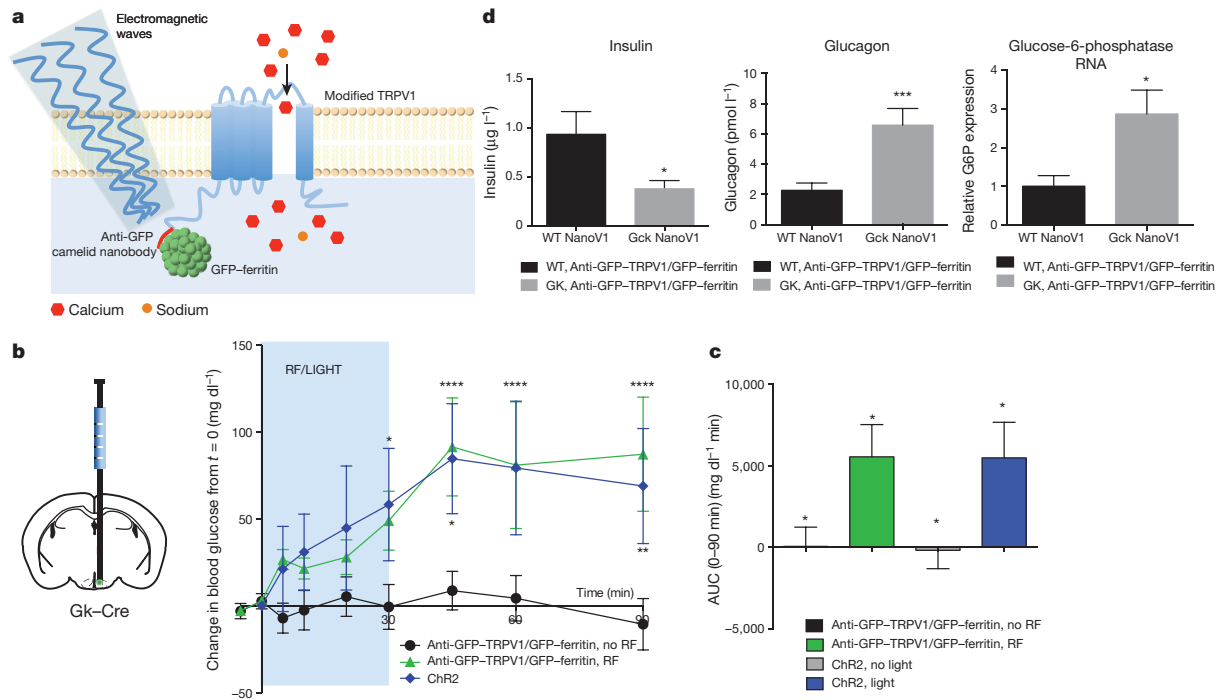


**Figure 1 | Remote neural activation *in vivo* using radio waves.** **a**, Schema of activation system. **b**, **c**, Change in blood glucose (**b**) and cumulative blood glucose (**c**) with RF treatment of GK-Cre mice (VMH injection Ad-FLEX-anti-GFP-TRPV1/GFP-ferritin,  $n = 13$ ; VMH injection rAAV-FLEX-ChR2,  $n = 4$ ). Values are mean  $\pm$  s.e.m.; two-way ANOVA with Sidak's multiple comparison test; \* $P < 0.05$ , \*\* $P < 0.01$ , \*\*\*\* $P < 0.0001$ . ChR2, channelrhodopsin 2. **d**, RF treatment of GK-Cre (GK) or wild-type (WT) mice with VMH Ad-FLEX-anti-GFP-TRPV1/GFP-ferritin on

plasma insulin (GK-Cre,  $n = 8$ ; wild type,  $n = 8$ ), glucagon (GK-Cre,  $n = 6$ ; wild type,  $n = 11$ ) and hepatic glucose-6-phosphatase expression (GK-Cre,  $n = 12$ ; wild type,  $n = 9$ ). Values are mean  $\pm$  s.e.m.; two-tailed, unpaired Student's  $t$ -test or Mann-Whitney  $U$ -test; \* $P < 0.05$ , \*\*\* $P < 0.005$ . WT nanoV1 refers to wild-type mice with VMH injection of Ad-FLEX-anti-GFP-TRPV1/GFP-ferritin. Gck NanoV1 indicates GK-Cre mice with VMH injection of Ad-FLEX-anti-GFP-TRPV1/GFP-ferritin.

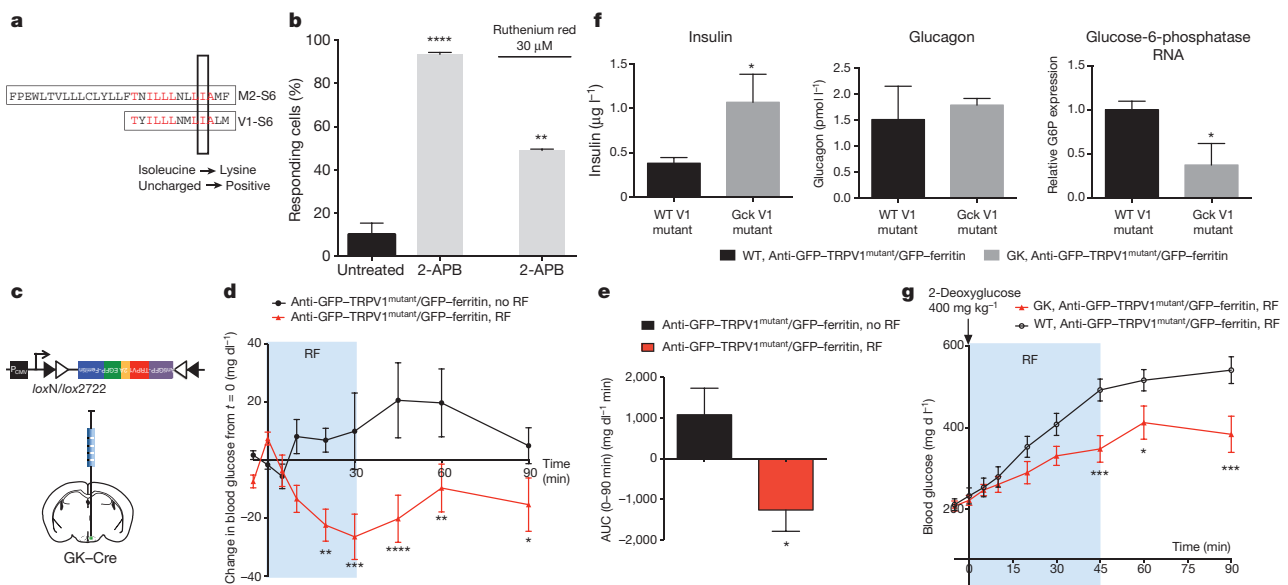


**Figure 2 | Remote neural inhibition *in vitro* and *in vivo* using radio waves.** **a**, Amino acid sequences for TRPM2 and TRPV1 S6 regions indicating substitution site. **b**, Responding cells (>10% decrease in MQAE ( $N$ -(ethoxycarbonylmethyl)-6-methoxyquinolinium bromide) fluorescence) with 2-APB (4 replicates, 20 cells) alone or with ruthenium red (2 replicates, 6 cells). Values are mean  $\pm$  s.e.m. Kruskal-Wallis with Dunn's multiple comparison test; \*\* $P < 0.01$ , \*\*\*\* $P < 0.0001$  versus untreated. **c**, Construct for Cre-dependent expression of anti-GFP-TRPV1<sup>mutant</sup>/GFP-ferritin. **d**, **e**, Change in blood glucose (**d**) and cumulative blood glucose (**e**) with RF treatment of GK-Cre mice with VMH injection of Ad-FLEX-anti-GFP-TRPV1<sup>mutant</sup>/GFP-ferritin ( $n = 13$ ). Values are mean  $\pm$  s.e.m.; two-way ANOVA with Sidak's multiple

comparison test and two-tailed Student's  $t$ -test; \* $P < 0.05$ , \*\* $P < 0.01$ , \*\*\* $P < 0.001$ , \*\*\*\* $P < 0.0001$ . **f**, RF treatment of GK-Cre (GK) or wild-type (WT) mice with VMH injection of Ad-FLEX-anti-GFP-TRPV1<sup>mutant</sup>/GFP-ferritin on plasma insulin (GK-Cre,  $n = 9$ ; wild type,  $n = 9$ ), glucagon (GK-Cre,  $n = 5$ ; wild type,  $n = 9$ ) and hepatic glucose-6-phosphatase expression (GK-Cre,  $n = 4$ ; wild type,  $n = 8$ ). Values are mean  $\pm$  s.e.m.; two-tailed, unpaired Student's  $t$ -test; \* $P < 0.05$ . **g**, RF treatment of GK-Cre ( $n = 6$ ) or wild-type ( $n = 9$ ) mice with VMH injection of Ad-FLEX-anti-GFP-TRPV1<sup>mutant</sup>/GFP-ferritin on blood glucose with 2-deoxyglucose treatment. Values are mean  $\pm$  s.e.m.; two-way ANOVA with Sidak's multiple comparison test; \* $P < 0.05$ , \*\*\* $P < 0.001$ .



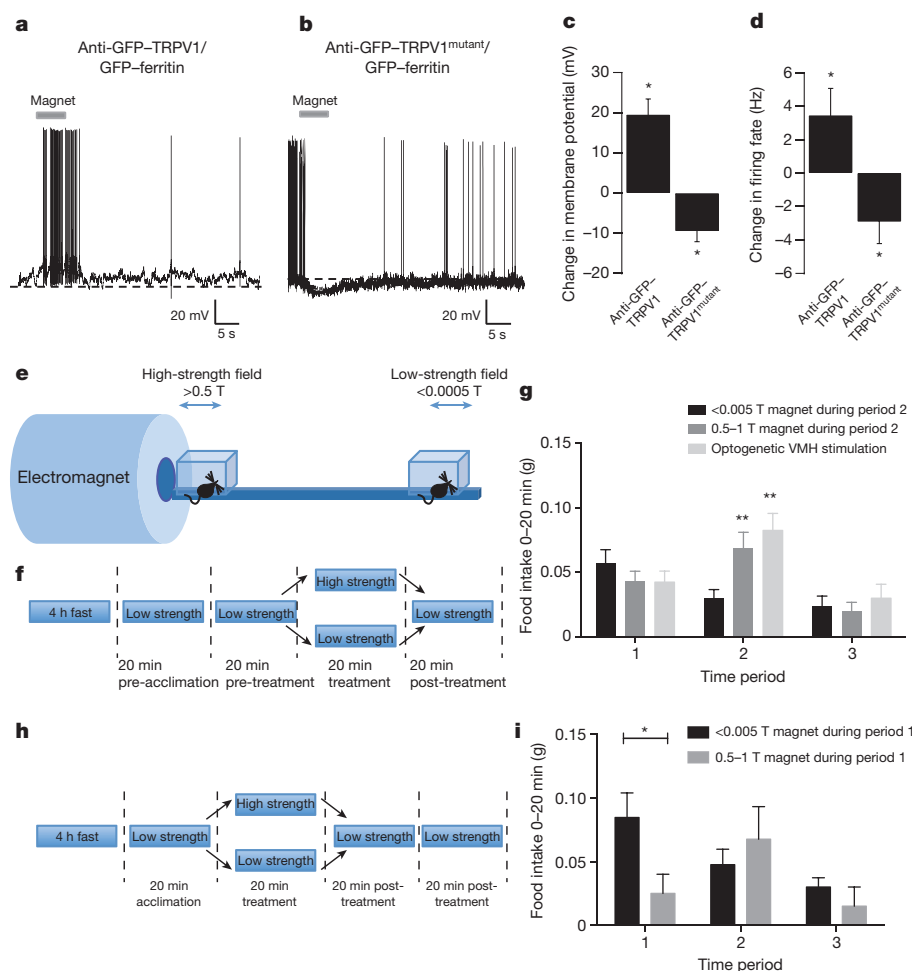


**Figure 3 | Remote neural modulation *in vitro* and *in vivo* using magnetic field.** **a, b**, Representative whole-cell current-clamp trace with magnet treatment (5 s) from GK-Cre VMH neurons in *ex vivo* slices expressing (a) anti-GFP-TRPV1/GFP-ferritin and (b) anti-GFP-TRPV1<sup>mutant</sup>/GFP-ferritin (of 14 and 6 recordings, respectively). **c, d**, Magnet treatment on membrane potential (c) and firing rate (d) in VMH neurons expressing anti-GFP-TRPV1/GFP-ferritin ( $n = 14$  and 16 cells, respectively) and anti-GFP-TRPV1<sup>mutant</sup>/GFP-ferritin ( $n = 6$  and 6 cells, respectively). Values are mean  $\pm$  s.e.m.; Wilcoxon matched pairs. **e, f**, Schema (e) and protocol (f) for magnetic field neural activation to

examine food intake. **g**, Food intake with magnet treatment in GK-Cre mice (VMH injection of Ad-FLEX-anti-GFP-TRPV1/GFP-ferritin,  $n = 6$ ; VMH injection of rAAV-FLEX-ChR2,  $n = 4$ ). No replicates. Values are mean  $\pm$  s.e.m.; two-way ANOVA with Sidak's multiple comparisons;  $**P < 0.01$ . **h**, Protocol for magnetic field neural activation to examine food intake. **i**, Food intake with magnet treatment in GK-Cre mice with VMH injection of Ad-FLEX-anti-GFP-TRPV1<sup>mutant</sup>/GFP-ferritin ( $n = 6$ ). No replicates. Values are mean  $\pm$  s.e.m.; two-way ANOVA with Sidak's multiple comparisons;  $*P < 0.05$ .

reduced blood glucose (change in blood glucose at 20 min: RF-treated,  $-22.5 \pm 5.5$  mg dl<sup>-1</sup> versus untreated,  $6.8 \pm 4.1$  mg dl<sup>-1</sup>;  $P < 0.01$ ; at 30 min: RF-treated,  $-26.5 \pm 7.8$  mg dl<sup>-1</sup> versus untreated,  $9.9 \pm 13.1$  mg dl<sup>-1</sup>;  $P < 0.001$ ; at 45 min: RF-treated,  $-20.3 \pm 8.2$  mg dl<sup>-1</sup> versus untreated,  $20.6 \pm 12.9$  mg dl<sup>-1</sup>;  $P < 0.0001$ ) and the cumulative change in blood glucose (Fig. 2c–e). RF treatment of these mice significantly increased insulin without a rise in glucagon and significantly reduced hepatic glucose-6-phosphatase expression (Fig. 2f). Inhibition of these neurons also blunted the hyperglycaemic response to 2-deoxyglucose, a non-metabolizable form of glucose that mimics hypoglycemia<sup>15</sup> (Fig. 2g and Extended Data Fig. 7c). RF treatment did not affect wild-type mice with VMH injection of anti-GFP-TRPV1<sup>mutant</sup>/GFP-ferritin (Extended Data Fig. 7d). These results suggest that hypothalamic glucose-sensing neurons are necessary for the normal counter-regulatory response to hypoglycaemia and to maintain blood glucose after an overnight fast.

We previously showed that ferritin's superparamagnetic properties allow ferritin-tethered TRPV1 to activate gene expression in a magnetic field<sup>16</sup>. We next tested whether a magnetic field could modulate neural activity. We were unable to make electrophysiological recordings using radio waves because of electrode heating and recording artefacts.

Magnet treatment (5 s) induced a significant inward current in HEK or N38 cells expressing anti-GFP-TRPV1/GFP-ferritin and an outward current in HEK or N38 cells expressing TRPV1<sup>mutant</sup>/GFP-ferritin (Extended Data Fig. 8a–f). Peak magnet-induced current displayed a rise time of  $0.62 \pm 0.4$  s and a 37% decay time of  $1.1 \pm 0.74$  s for anti-GFP-TRPV1/GFP-ferritin and  $2.29 \pm 1.8$  s and  $11.7 \pm 4.9$  s respectively for anti-GFP-TRPV1<sup>mutant</sup>/GFP-ferritin. The current-voltage relationship of TRPV1<sup>mutant</sup> with different intracellular anions (Extended Data Fig. 8i, j) was consistent with analogous pore loop mutations in TRPM2 and TRPM8<sup>14</sup>. Magnet treatment increased intracellular calcium in N38 cells expressing anti-GFP-TRPV1/GFP-ferritin and intracellular chloride in N38 cells expressing anti-GFP-TRPV1<sup>mutant</sup>/GFP-ferritin. These effects were blocked by ruthenium red (Extended Data Fig. 8k–o).

We next tested the effects of magnet treatment on neural activity *ex vivo* in slices from GK-Cre mice crossed to the reporter strain *Rosa-lox-stop-lox-tdTomato* after VMH injection of Ad-anti-GFP-TRPV1/GFP-ferritin or Ad-anti-GFP-TRPV1<sup>mutant</sup>/GFP-ferritin. In slices from mice injected with Ad-anti-GFP-TRPV1/GFP-ferritin, magnet treatment (5 s) depolarized neurons expressing tdTomato and GFP, significantly increasing membrane potential ( $16.39 \pm 2.9$  mV,  $P < 0.001$ ) and firing rate ( $2.355 \pm 0.63$  Hz,  $P < 0.001$ ) in 76% of neurons. Magnet treatment

(5 s) of slices from mice injected with Ad-anti-GFP-TRPV1<sup>mutant</sup>/GFP-ferritin significantly hyperpolarized neurons by  $4.7 \pm 1.1$  mV ( $P < 0.05$ ) and decreased firing rate  $-2.552 \pm 1.17$  ( $P < 0.05$ ) in 71% of neurons (Fig. 3a–d, Extended Data Fig. 8g, h).

To test whether a magnetic field could remotely modulate neurons *in vivo* to control behaviour, we placed animals close to the electromagnetic coil of an MRI machine (Fig. 3e, f). We reasoned that since hypoglycaemia triggers feeding<sup>17</sup>, activation of hypothalamic GK neurons might increase food intake. Magnet treatment of GK-Cre mice with VMH injection of Ad-FLEX-anti-GFP-TRPV1/GFP-ferritin increased blood glucose (Extended Data Fig. 9b–d) and significantly increased food intake after a fast to a similar extent as optogenetic activation of VMH GK-Cre neurons (Fig. 3g). We tested the effect of neural inhibition by magnet treatment of GK-Cre mice with VMH injection of Ad-anti-GFP-TRPV1<sup>mutant</sup>/GFP-ferritin. Food intake was significantly decreased (Fig. 3h, i). Expression of the activating and inhibitory constructs did not alter baseline blood glucose or food intake (Extended Data Fig. 10) and magnetic field treatment did not affect blood glucose or feeding in wild-type mice after VMH injection of either construct (Extended Data Fig. 9e, f).

Here we show that remote neural modulation of a subpopulation of hypothalamic glucose-sensing neurons changes blood glucose in either direction by regulating pancreatic hormone levels, and that neural activation increases feeding while inhibition decreases it. VMH inhibition to reduce glucose and feeding could be beneficial in metabolic disease. Because activation of the GK neuronal subpopulation mimics the responses to low glucose and inhibiting them blunts this response, we hypothesize that we targeted glucose-inhibited neurons, though further studies will be needed to confirm this, as well as the mechanism by which glucose can inhibit GK-expressing neurons<sup>18,19</sup>. While local particle heating could independently affect mitochondrial UCP2 or other mechanisms, we consider this unlikely because of rapid heat dissipation with distance and the finding that wild-type and mutant TRPV1 had opposite effects<sup>20</sup>.

Radio-wave- or magnetic-field-controlled neural modulation provides distinct attributes relative to optogenetics or DREADDs (designer receptors exclusively activated by designer drugs). Unlike optogenetics, the approach does not require a permanent implant so may be suitable when an implant interferes with function or cannot be secured. Further, optogenetics and methods using exogenous nanoparticles<sup>21,22</sup> only target local populations, whereas our genetically encoded system could potentially modulate dispersed populations and/or multiple sites in a circuit simultaneously without requiring multiple implants or nanoparticle injections. The system also enables more rapid responses than DREADDs<sup>23</sup> which activate G protein signalling and the slower kinetics of which<sup>24,25</sup> could affect their utility for neural modulation over short time intervals. Our method could also regulate calcium and/or chloride currents in other, even dispersed, populations such as immune, epithelial and endocrine cells. Pending further efficacy and safety studies and the development of suitable devices, the method could potentially provide a less invasive alternative to deep brain stimulation which requires permanent implants and are sometimes associated with complications<sup>26</sup>.

**Online Content** Methods, along with any additional Extended Data display items and Source Data, are available in the online version of the paper; references unique to these sections appear only in the online paper.

**Received 10 August 2015; accepted 28 January 2016.**

**Published online 23 March 2016.**

1. Stanley, S. A., Sauer, J., Kane, R. S., Dordick, J. S. & Friedman, J. M. Remote regulation of glucose homeostasis in mice using genetically encoded nanoparticles. *Nature Med.* **21**, 92–98 (2015).
2. Stanley, S. *et al.* Profiling of glucose-sensing neurons reveals that GHRH neurons are activated by hypoglycemia. *Cell Metab.* **18**, 596–607 (2013).
3. Davies, R., Nakajima, S. & White, N. Enhancement of feeding produced by stimulation of the ventromedial hypothalamus. *J. Comp. Physiol. Psychol.* **86**, 414–419 (1974).

4. Goto, Y., Carpenter, R. G., Berelowitz, M. & Frohman, L. A. Effect of ventromedial hypothalamic lesions on the secretion of somatostatin, insulin, and glucagon by the perfused rat pancreas. *Metabolism* **29**, 986–990 (1980).
5. Shimazu, T., Fukuda, A. & Ban, T. Reciprocal influences of the ventromedial and lateral hypothalamic nuclei on blood glucose level and liver glycogen content. *Nature* **210**, 1178–1179 (1966).
6. Schwartz, M. W. *et al.* Cooperation between brain and islet in glucose homeostasis and diabetes. *Nature* **503**, 59–66 (2013).
7. Kang, L., Routh, V. H., Kuzhikandathil, E. V., Gaspers, L. D. & Levin, B. E. Physiological and molecular characteristics of rat hypothalamic ventromedial nucleus glucosensing neurons. *Diabetes* **53**, 549–559 (2004).
8. Aponte, Y., Atasoy, D. & Sternson, S. M. AGRP neurons are sufficient to orchestrate feeding behavior rapidly and without training. *Nature Neurosci.* **14**, 351–355 (2011).
9. Anthony, T. E. *et al.* Control of stress-induced persistent anxiety by an extra-amygdala septohypothalamic circuit. *Cell* **156**, 522–536 (2014).
10. Nordlie, R. C., Foster, J. D. & Lange, A. J. Regulation of glucose production by the liver. *Annu. Rev. Nutr.* **19**, 379–406 (1999).
11. Bito, H., Deisseroth, K. & Tsien, R. W. CREB phosphorylation and dephosphorylation: a  $Ca^{2+}$ - and stimulus duration-dependent switch for hippocampal gene expression. *Cell* **87**, 1203–1214 (1996).
12. Ghosh, A., Ginty, D. D., Bading, H. & Greenberg, M. E. Calcium regulation of gene expression in neuronal cells. *J. Neurobiol.* **25**, 294–303 (1994).
13. Lozano, A. M. & Eltahawy, H. How does DBS work? *Suppl. Clin. Neurophysiol.* **57**, 733–736 (2004).
14. Kühn, F. J., Knop, G. & Luckhoff, A. The transmembrane segment S6 determines cation versus anion selectivity of TRPM2 and TRPM8. *J. Biol. Chem.* **282**, 27598–27609 (2007).
15. Landau, B. R. & Lubs, H. A. Animal responses to 2-deoxy-d-glucose administration. *Proc. Soc. Exp. Biol. Med.* **99**, 124–127 (1958).
16. Kim, T., Moore, D. & Fussenegger, M. Genetically programmed superparamagnetic behavior of mammalian cells. *J. Biotechnol.* **162**, 237–245 (2012).
17. Rowland, N. E., Bellush, L. L. & Carlton, J. Metabolic and neurochemical correlates of glucoprivic feeding. *Brain Res. Bull.* **14**, 617–624 (1985).
18. Evans, M. L. *et al.* Hypothalamic ATP-sensitive  $K^{+}$  channels play a key role in sensing hypoglycemia and triggering counterregulatory epinephrine and glucagon responses. *Diabetes* **53**, 2542–2551 (2004).
19. Murphy, B. A., Fakira, K. A., Song, Z., Beuve, A. & Routh, V. H. AMP-activated protein kinase and nitric oxide regulate the glucose sensitivity of ventromedial hypothalamic glucose-inhibited neurons. *Am. J. Physiol. Cell Physiol.* **297**, C750–C758 (2009).
20. Horvath, T. L. *et al.* Brain uncoupling protein 2: uncoupled neuronal mitochondria predict thermal synapses in homeostatic centers. *J. Neurosci.* **19**, 10417–10427 (1999).
21. Chen, R., Romero, G., Christiansen, M. G., Mohr, A. & Anikeeva, P. Wireless magnetothermal deep brain stimulation. *Science* **347**, 1477–1480 (2015).
22. Stanley, S. A. *et al.* Radio-wave heating of iron oxide nanoparticles can regulate plasma glucose in mice. *Science* **336**, 604–608 (2012).
23. Armbruster, B. N., Li, X., Pausch, M. H., Herlitze, S. & Roth, B. L. Evolving the lock to fit the key to create a family of G protein-coupled receptors potentially activated by an inert ligand. *Proc. Natl Acad. Sci. USA* **104**, 5163–5168 (2007).
24. Alexander, G. M. *et al.* Remote control of neuronal activity in transgenic mice expressing evolved G protein-coupled receptors. *Neuron* **63**, 27–39 (2009).
25. Nawaratne, V. *et al.* New insights into the function of M4 muscarinic acetylcholine receptors gained using a novel allosteric modulator and a DREADD (designer receptor exclusively activated by a designer drug). *Mol. Pharmacol.* **74**, 1119–1131 (2008).
26. Falowski, S. M., Ooi, Y. C. & Bakay, R. A. Long-term evaluation of changes in operative technique and hardware-related complications with deep brain stimulation. *Neuromodulation* **18**, 670–677 (2015).

**Acknowledgements** We would like to thank A. North, P. Ariel and K. Thomas for help with confocal imaging, D. Acehan and K. Uryu for performing EM studies and S. Korres for assistance with the manuscript. This work was funded by Howard Hughes Medical Institute, the JPB Foundation, the National Institutes of Health (GM095654 and MH105941) and a Rensselaer Fellowship (to J.S.) under an NIH predoctoral training grant (GM067545). Support for this project was provided by a grant from the Robertson Foundation.

**Author Contributions** J.M.F. conceived the project and supervised the studies. S.A.S. and L.K. designed and performed the experiments. K.L. and S.F.S. provided technical assistance. A.N. assisted with optogenetic studies, J.S. assisted with magnet activation studies and X.Y. assisted with cell culture studies. J.D. provided technical advice for *in vivo* magnet activation studies. J.S.D. provided technical advice. S.A.S., L.K. and J.M.F. wrote the manuscript.

**Author Information** Reprints and permissions information is available at [www.nature.com/reprints](http://www.nature.com/reprints). The authors declare no competing financial interests. Readers are welcome to comment on the online version of the paper. Correspondence and requests for materials should be addressed to J.M.F. ([friedj@mail.rockefeller.edu](mailto:friedj@mail.rockefeller.edu)).

## METHODS

**Radiofrequency field and static magnetic field.** A 465 kHz sinusoidal signal was provided by a signal generator and applied through an amplifier (both Ultraflex) to a 2-turn solenoid coil with a radius of 2.5 cm to produce an electromagnetic field. The field strengths tested were 31 mT, 27 mT and 23 mT. Samples were placed within the solenoid.

A static magnetic field for imaging experiments was produced using a neodymium-iron-boron permanent magnet ( $0.25 \times 1$  inch, axially magnetized, K&J Magnetics). This was able to produce a magnetic flux density of over 5 kilogauss at the magnet surface. Field strengths of 280 mT and 130 mT were generated by increasing the distance from the cells to the magnet surface (2 mm and 5 mm, respectively). A N52 grade neodymium magnet ( $0.06 \times 0.25$  inch, axially magnetized, K&J Magnetics) was used for electrophysiological studies. The magnetic field for *in vivo* studies was generated by the superconducting electromagnetic MRI field from a GE 3.0 Tesla Excite HDx MRI Scanner (GE Healthcare). The field strength was measured and regions with strengths of 0.5–1 T or 0.2–0.5 T were used for *in vivo* studies.

**Plasmids.** Anti-GFP nanobody-TRPV1-2A-GFP ferritin in pEGFPN1 and MSCV-hygro were generated as previously described<sup>1</sup>. Mutation of residue I679K in TRPV1 was performed by site-directed mutagenesis using QuikChange XL Site-Directed Mutagenesis Kit (Agilent). These sequences were cloned into pVQ Ad CMV KNPα for generation of replication deficient adenovirus. To construct Cre-activated recombinant adenovirus vectors, a DNA construct with two pairs of incompatible *lox* sites, *loxN* and *lox2722*, was synthesized and Anti-GFP nanobody-TRPV1-2A-GFP ferritin was cloned between the two pairs in the antisense orientation. The floxed inverted Anti-GFP nanobody-TRPV1-2A-GFP ferritin cassette was then cloned into pVQ Ad CMV KNPα for generation of replication deficient adenovirus. The fidelity of PCR products and cloning was confirmed by DNA sequencing.

**Viruses.** The recombinant adenoviruses (Ad-CMV-GFP, Ad-CMV-anti-GFP-TRPV1/GFP-ferritin, Ad-FLEX-anti-GFP-TRPV1/GFP-ferritin and Ad-FLEX-anti-GFP-TRPV1<sup>mutant</sup>/GFP-ferritin) were packaged by Viraquest. The final titre was  $4 \times 10^{10}$  plaque-forming units (p.f.u.) per ml. AAV-EF1a-DIO-hChR2(H134R)-eYFP was purchased from UNC Viral Core.

**Cell culture and *in vitro* studies.** Human embryonic kidney (HEK 293T) cells (ATCC CRL-3216), mycoplasma testing and STR profiling for authentication performed by ATCC) were cultured in DMEM with 10% fetal bovine serum (FBS; Gibco) at 37°C and 5% CO<sub>2</sub>. HEK cells have been reported to be among cell lines that are commonly misidentified. We used HEK 293T cells obtained from and authenticated by ATCC. HEK 293T cells are readily transfected and express transgene products at high levels. Transfected cells were used to examine the sites of TRPV1 and GFP-tagged ferritin expression, to generate stable cells to determine calcium responses to RF and magnetic stimulation and for electrophysiology studies. These studies were also performed in additional cell lines such as N38 (calcium responses), examined *in vivo* (protein expression) or in *ex vivo* slices (electrophysiology). Phoenix ecotropic packaging cells (Stanford University, no authentication or mycoplasma testing) were grown in DMEM with 10% FBS (Gibco) at 37°C and 5% CO<sub>2</sub>. Embryonic mouse hypothalamic N38 cells (Cellutions Biosystems Inc., no authentication, mycoplasma testing performed by Cellutions Biosystems Inc.) were grown in DMEM with 10% FBS at 37°C and 5% CO<sub>2</sub>.

Stable cell lines were produced by retroviral infection of N38 cells using the Phoenix system. Briefly, Phoenix eco cells ( $2 \times 10^6$  cells per 6-cm dish) were transfected with MSCV-hygro anti-GFP-TRPV1/GFP-ferritin or MSCV-hygro anti-GFP-TRPV1<sup>mutant</sup>/GFP-ferritin. After 24 h, the medium was replaced and the cells placed at 32°C. Medium was aspirated after a further 24 h and spun to remove cell debris. The Phoenix cell supernatant was added to N38 cells (plated at  $1 \times 10^6$  cells per 6-cm dish) using a 1:2 dilution in DMEM/10% FBS with polybrene ( $4 \mu\text{g ml}^{-1}$ , Sigma-Aldrich). Cells were incubated at 32°C for a further 24 h before replacing the medium with DMEM/10% FBS. Selection medium was added 48 h after infection. Stably transfected N38 cells were maintained at 32°C.

For immunocytochemistry, electrophysiology, RF and magnet studies, stably transfected N38 cells or HEK cells were cultured on 12-mm cover glass (Fisher Scientific) coated with fibronectin ( $10 \text{ mg ml}^{-1}$ , Sigma). HEK cells were transfected with appropriate constructs 24 h after plating using lipofectamine 2000 (Invitrogen). Culture medium was replaced 18 h after transfection and holotransferrin ( $2 \text{ mg ml}^{-1}$ , Sigma) was added to the cells. Cells were studied 72–96 h after transfection or subculture.

**Effect of RF or magnet on pCREB and c-Fos.** 24 h before the study, cells were placed in 1% FBS in opti-mem medium at 32°C to ensure minimal activation of TRPV1 and calcium-dependent pathways. On the day of study, cells were incubated in 500  $\mu\text{l}$  of calcium imaging buffer at room temperature (control) or in a RF field

(31 mT) at room temperature. For magnet treatment, cells were treated with a static magnetic field (280 mT) for 5 s every 2 min for 1 h at room temperature. After 60 min, the cells were placed on ice, the supernatant removed and cells lysed with RIPA buffer (40  $\mu\text{l}$  for western blot) or lysis buffer (100  $\mu\text{l}$  Agilent Absolutely RNA microprep kit) and frozen at  $-80^\circ\text{C}$  until assay or RNA purification. Each study was repeated on three occasions each with four replicates. Control studies with N38 cells alone were performed on two occasions with four replicates.

**Calcium imaging.** TRPV1 is a non-selective cation channel with relatively high permeability to divalent cations, particularly calcium ( $\text{Ca}^{2+} > \text{Mg}^{2+} > \text{Na}^+ \approx \text{K}^+ \approx \text{Cs}^+$ )<sup>27</sup>.

For studies examining the effects of RF (31 mT) or magnet (280 mT) with and without ruthenium red, stably transfected cells were washed three times in PBS then loaded with Fluo-4 3  $\mu\text{M}$  (Invitrogen) in the presence of sulfinpyrazone 500  $\mu\text{M}$  (Sigma) for 45–60 min at room temperature. Cells were washed again in PBS then incubated for 15–30 min in sulfinpyrazone in PBS. Cells were washed and then imaged in calcium imaging buffer. Imaging was performed using a Deltavision personal DV imaging system (Applied Precision) equipped with a custom-made ceramic lens. Images were acquired every 3 s for 3 min. Cells were imaged without treatment (eight occasions), before and during RF treatment (nine occasions), before and during application of a neodymium magnet (for 45 s, three occasions) or before and after treatment with 200  $\mu\text{M}$  2-APB (two occasions). Imaging was repeated in the presence of ruthenium red (100  $\mu\text{M}$ ) (two occasions for each condition). Images were analysed using ImageJ software.

For studies to examine the effects of increasing RF or magnet field strength, to assess the effects of short RF treatment (10 s) on calcium responses and to examine the kinetics of the calcium response, cells were loaded with FluoForte 20  $\mu\text{M}$  (Enzo Life Sciences) in the presence of Pluronic F-127 (0.02% vol/vol) and sulfinpyrazone 500  $\mu\text{M}$ . Cells were washed and then imaged in calcium imaging buffer. Imaging was performed as above with images acquired every second for 1 min. Cells were imaged without treatment (four occasions), before and during RF treatment at 31, 27 and 23 mT (four occasions each), before and during application of a neodymium magnet at 280 or 130 mT (magnet 2 mm or 5 mm from the cells, respectively, four occasions each) and before, during and after 10 s treatment with RF (31 mT) (four occasions). Images were analysed using ImageJ software.

**Multiphoton chloride imaging.** Stably transfected cells were washed with Krebs-HEPES buffer three times then loaded with MQAE (5 mM, Invitrogen) for 60 min at room temperature. The cells were washed with Krebs-HEPES buffer and then incubated in buffer for 15 min before imaging. Imaging was performed using LSM 510 NLO inverted multiphoton and confocal system (Zeiss) using a  $40\times$  objective with two photon excitation at 750 nm. Cells were imaged without treatment (four occasions), before and during application of a neodymium magnet (280 mT) for 20 s (on six occasions), before and after treatment with 200  $\mu\text{M}$  2-APB (two occasions). Imaging was repeated in the presence of ruthenium red (100  $\mu\text{M}$ ) (two occasions for each condition). Images were analysed using ImageJ software.

**Immunocytochemistry and immunohistochemistry.** Immunocytochemistry (ICC) and immunohistochemistry (IHC) were used to detect expression of TRPV1, GFP and Flag-tagged ferritin, to localize c-Fos expression and to quantify apoptosis in cells and tissue. Cells were washed twice in PBS and then fixed for 15 min in 2% paraformaldehyde (Electron Microscopy Services). Tissue was fixed in 10% formalin (Sigma) at 4°C overnight and 40- $\mu\text{m}$  sections cut on a vibrating microtome. Fixed cells or tissue sections were washed then incubated for 1 h in blocking buffer (3% BSA (Sigma) and 2% goat serum (Sigma) in PBS with 0.1% Triton-X (Sigma)). Cells and tissues were then incubated in primary antibody (rabbit anti-TRPV1 1:500 (AB9554<sup>1</sup>, Chemicon), mouse anti-Flag 1:1,000 (Flag-tag mouse monoclonal antibody #F3165, Sigma<sup>28</sup>), chicken anti-GFP 1:1,000 (ab13970<sup>1</sup>, Abcam), rabbit anti-activated-caspase-3 1:250 (G7481, Promega<sup>1</sup>) or rabbit anti-c-Fos 1:5,000 (PC38, Calbiochem<sup>2</sup>)) diluted in blocking buffer overnight at 4°C. Cells or tissue were washed three times in PBS/0.1% Triton-X before incubation in secondary antibody (goat anti-rabbit 594 (A1012) or goat anti-rabbit 488 (A11008), goat anti-chicken 488 (A11039), goat anti-mouse 350 (A11045), all 1:1,000) diluted in blocking buffer for 2 h. To stain for cell membrane, Alexa 594 conjugated to wheat germ agglutinin (Invitrogen,  $5 \mu\text{g ml}^{-1}$ ) was included in the blocking buffer with secondary antibodies. The cells or tissue were washed a further three times in PBS/0.1% Triton-X before mounting using Fluoromount (Southern Biotech).

Images were acquired using confocal microscopy (LSM 510 laser scanning confocal microscope; Carl Zeiss MicroImaging, Inc.). Confocal fluorescence images were acquired on a scanning laser microscope using a  $20\times/0.70$  NA objective or  $100\times/1.4$  NA objective. To quantify GFP-positive and activated-caspase-3-positive cells, a 1,280  $\mu\text{m}$  section of the brain with the injection site taken as the centre was imaged by taking tiled, serial stack images covering a depth of 40  $\mu\text{m}$  every 320  $\mu\text{m}$ . Quantification of GFP and activated-caspase-3 immunostaining was performed by an investigator blinded to the treatment group using Imaris



3D quantification software. The image analysis software calculated the number of GFP- or activated-caspase-3-positive cells per volume by thresholding immunoreactivity above background levels. Confocal images to examine co-localization of TRPV1, GFP and Flag-tagged ferritin were acquired with a 40× objective.

**Immuno-electron microscopy and electron microscopy.** Mouse brains were perfused by 4% PFA and sectioned at 50 µm by vibratome (Leica VT 100S). The sections were blocked by 4% BSA and 0.15% saponin in 20 mM Tris buffer (pH 7.4) for 2 h at room temperature, then incubated with anti-GFP (1:1,000) (#1020, Aves Lab Inc.<sup>29</sup>) overnight at 4°C, followed by biotinylated anti-chicken incubation (1:1,000, Vector Laboratories, Inc.), with Nanogold streptavidin (1:100, Nanoprobes), and treated with GoldEhance EM (#2114 Nanoprobes). Negative control was done with the same procedure, except for omitting the primary antibody incubation. The tissue sections underwent fixation with 2% glutaraldehyde in sodium cacodylate buffer, light osmication (0.5% osmium tetroxide) for 15 min and en bloc staining with 1% uranyl acetate for 30 min. Subsequently tissues were dehydrated through an ethanol series followed by incubation with Eponate12 (Ted Pella Inc.) The samples were embedded in the resin and polymerized at 60°C for 48 h. Ultrathin (70 nm) sections were cut and examined under a JEOL JEM 100CX transmission electron microscope in the electron microscopy centre in The Rockefeller University.

For double immuno-electron microscopy studies, HEK cells with stable expression of TRPV1 without fixation were subjected to high-pressure freezing (Leica EMPAC2) and freeze substitution in 0.2% uranyl acetate in 95% acetone and 5% water. Subsequently they were embedded in Lowicryl HM20 at -40°C and cut into ultrathin sections. They were incubated with 4% BSA and 0.15% saponin, 0.15% cold fish skin gelatin in 20 mM TBS (pH 7.4) for 2 h at room temperature, a mixture of anti-GFP raised in chicken (1:300) (Aves Lab Inc.) and anti-TRPV1 raised in rabbit (1:300) (EMD Millipore Corp) overnight at 4°C. Antigen-antibody complexes were recognized by biotinylated anti-chicken antibody and streptavidin tagged with 5 nm colloidal gold (1:20, Nanoprobes), or anti-rabbit tagged with 12 nm colloidal gold (Jackson Immuno Research Lab Inc.) for 2 h at room temperature.

Electron microscopy was used to demonstrate ferritin in transfected HEK cells. Cells were fixed in 2% paraformaldehyde/2.5% glutaraldehyde/0.1 M cacodylate buffer, pH 7.4, for 15 min before pelleting and further fixation for 1 h. Cells were then treated with 1% osmium tetroxide (1 h, on ice) and 0.5% uranyl acetate (1 h) before dehydration with graded ethanol and treatment with propylene oxide (2 × 15 min). The cells were infiltrated with 50% EPON epoxy resin (Miller-Stephenson) and 50% propylene oxide overnight then 100% EPON (2 × 2 h) before curing at 60°C for 2 days. Blocks were cut with a diamond knife on a Leica UltracutE and ultrathin (~70 nm) sections were collected on uncoated 200-mesh grids and stained with uranium and lead. Grids were viewed with a Tecnai SpiritBT Transmission Electron Microscope (FEI) at 80 kV and pictures were taken with Gatan 895 ULTRASCAN Digital Camera in the electron microscopy centre in The Rockefeller University.

**Electrophysiology. Cell culture.** Whole-cell voltage clamp recordings were made at room temperature at -60 mV from cultured HEK cells and N38 cells expressing anti-GFP-TRPV1/GFP-ferritin or anti-GFP-TRPV1<sup>mutant</sup>/GFP-ferritin construct. Neurons expressing GFP were visualized using epifluorescence on an upright Zeiss Axioskop 2FS Plus microscope equipped with a Hamamatsu CCD camera. External solution contained (in mM): 140 NaCl, 2.8 KCl, 2 CaCl<sub>2</sub>, 1 MgCl<sub>2</sub>, 1 HEPES, 10 glucose, pH 7.4. Patch pipettes pulled from borosilicate glass (World Precision Instruments) had tip resistances of 5–10 MΩ and were filled with K-gluconate internal containing (in mM): 135 potassium gluconate, 4 KCl, 0.05 EGTA, 10 HEPES, 4 MgATP, 10 Na-phosphocreatine, pH adjusted to 7.3 with KOH, 290 OSM unless otherwise stated, in which case a CsCl internal solution was used containing (in mM): 125 CsCl, 10 HEPES, 10 EGTA, 4 MgATP, 0.5 CaCl<sub>2</sub>, 2-APB (200 µM) was prepared from a 10 mM DMSO stock and was perfused through the bath when stated. I–V relationships were obtained by measuring current responses to increasing 5-mV steps in the presence of 200 µM 2-APB. Cells were held at -60 mV. Magnetic activation was applied by bringing a permanent magnet within 500 µm of the recorded cell for 5 s with a micromanipulator. Recordings were acquired with an Axopatch 200B amplifier, filtered to 2 kHz and digitized at 10 kHz (pClamp10 software, Molecular Devices). Data were analysed using Igor Pro (Wavemetrics) and NeuroMatic (<http://www.neuromatic.thinkrandom.com/>). Series resistance was monitored and not compensated for. If there was more than a 20% change in series resistance the recording was excluded.

**Slice electrophysiology.** Glucokinase-Cre Rosa-tdTomato, injected with Ad-anti-GFP-TRPV1/GFP-ferritin or Ad-anti-GFP-TRPV1<sup>mutant</sup>/GFP-ferritin in the VMH were deeply anaesthetized with isoflurane before decapitation and removal of the entire brain to be immediately submerged in ice-cold 'slicing' solution containing (in mM): 85 NaCl, 2.5 KCl, 0.5 CaCl<sub>2</sub>, 4 MgCl<sub>2</sub>, 25 NaHCO<sub>3</sub>, 1.25 NaH<sub>2</sub>PO<sub>4</sub>, 64 sucrose, 25 glucose and 0.02 D-2-amino-5-phosphonopentanoic

acid (D-AP5, Tocris Bioscience). This was bubbled with 95% O<sub>2</sub> and 5% CO<sub>2</sub>, pH 7.4. Coronal hypothalamic slices (200 µm) were made with a moving blade microtome (VT1000S, Leica). The slices were kept at 32°C for 40 min in recording solution containing (in mM) 125 NaCl, 2.5 KCl, 1.25 NaH<sub>2</sub>PO<sub>4</sub>, 26 NaHCO<sub>3</sub>, 10 glucose, 2 CaCl<sub>2</sub> and 1 MgCl<sub>2</sub>, pH 7.4 when bubbled with 95% O<sub>2</sub> and 5% CO<sub>2</sub>. Whole-cell current-clamp patch-clamp recordings were made at room temperature from neurons in the VMH expressing both tdTomato indicating GK-Cre expression and GFP indicating expression of the anti-GFP-TRPV1/GFP-ferritin or anti-GFP-TRPV1<sup>mutant</sup>/GFP-ferritin construct. Neurons were visualized and recorded from as described above. In order to observe neuronal activation, neurons were hyperpolarized to below threshold.

Baseline characteristic for hypothalamic neurons are as follows. Mean series resistance for neurons expressing the construct was  $18.4 \pm 1.1$  MΩ ( $n = 37$ ) and did not differ significantly from hypothalamic neurons that did not express the construct ( $18.0 \pm 1$ ,  $n = 7$ ). The mean capacitance was  $5.1 \pm 0.55$  pF and did not differ significantly from neurons not expressing the channel ( $6.7 \pm 0.8$ ). The mean resting membrane potential in naive hypothalamic neurons was  $-48.21 \pm 4.7$  mV ( $n = 15$ ) and in cells expressing the construct before manipulation was  $-52 \pm 1.9$  mV ( $n = 37$ ),  $P > 0.5$ . Input resistances did not significantly differ in hypothalamic neurons; control neuron (without construct expression) =  $703 \pm 128$  MΩ ( $n = 13$ ), wild-type channel neuron =  $555 \pm 110$  MΩ ( $n = 7$ ), mutant neuron =  $866 \pm 220$  MΩ ( $n = 14$ ).

**Animals and in vivo studies.** Male and female C57Bl6 mice (8–9-weeks-old, Jackson Laboratories), *Nestin cre* (8–9-weeks-old, Jackson Labs), *Rosa lox-stop-lox tdTomato* (8–10-weeks-old, Jackson Labs) and *GK-cre* (8–16-weeks-old) mice were used and housed under controlled light conditions (12 h light/12 h dark) and temperature (22°C), single-caged, and fed *ad libitum* on standard mouse chow. Animal care and experimental procedures were performed with the approval of the Animal Care and Use Committee of Rockefeller University (protocols 12561 and 14712) under established guidelines. In all cases, mice were randomized according to body weight. The investigator was not blinded to the treatment group. The sample size required was estimated to be  $n = 8–10$  per group on the basis of previous studies examining the effects of RF treatment on gene expression and protein release. No statistical methods were used to predetermine sample size.

All surgeries were performed under aseptic conditions. Mice were anaesthetized using 1.5% isoflurane and the top of the head was shaved then cleaned with 70% ethanol. An incision was made in the midline and small craniotomies were made using a dental drill.

**Study 1.** Wild-type mice underwent stereotactic injection into the striatum (coordinates: +1 mm AP, +2.3 mm ML, -3.3 mm DV) with Ad-CMV-GFP or Ad-CMV-anti-GFP-TRPV1/GFP-ferritin ( $4 \times 10^8$  p.f.u. per injection) over 10 min. The needle remained in position for a further 5 min before being withdrawn. Mice also received a lateral ventricle injection of iron dextran (4 µl, coordinates: -0.4 mm AP, +1.2 mm ML, -2.0 mm DV). After 1 week or 4 weeks, mice injected with Ad-CMV-anti-GFP-TRPV1/GFP-ferritin were randomized to RF or no RF treatment ( $n = 4$  per time point and per treatment group). All mice treated with Ad-CMV-GFP were treated with RF ( $n = 4$  per time point). Mice were anaesthetized with tribromoethanol (200 mg kg<sup>-1</sup>) and after 15 min mice were treated with RF (Ad-GFP and Ad-CMV-anti-GFP-TRPV1/GFP-ferritin, RF-treated group) for 30 min by placing in the RF solenoid. Ad-CMV-anti-GFP-TRPV1/GFP-ferritin, untreated group were anaesthetized and 15 min after the induction of anaesthesia were placed in the RF solenoid without power for 30 min. One hour after the being placed in the solenoid, mice were perfused, brains removed and tissue processed for GFP and activated-caspase-3 immunostaining as described above.

Unilateral striatal injections were used to test our construct primarily because we thought that either basal activity in the absence of RF or significant toxicity and apoptosis would result in motor changes that are readily detectable. In addition, striatum does not express TRPV1 and we wanted to ensure any effect was the result of expressing our construct rather than a result of an effect of endogenous TRPV1. Finally, for RF treatment the mice needed to be anaesthetized and in pilot studies we found that anaesthetics often led to high levels of c-Fos activation in many central nervous system regions but not in the striatum. Thus, to minimize the possibility that the anaesthetic was contributing to either toxicity or non-specific staining, we used striatal injections in addition to assessing the VMH.

**Study 2.** *Nestin-Cre* or wild-type mice received striatal injections of Ad-FLEX-anti-GFP-TRPV1/GFP-ferritin ( $4 \times 10^8$  p.f.u. per injection) and ICV iron dextran as described above. After 1 week, mice were anaesthetized, treated with RF for 30 min and perfused after 1 h as described above. Tissue was processed for GFP and c-Fos immunostaining as described above.

**Study 3.** Glucokinase-Cre or wild-type mice were anaesthetized with isoflurane and underwent stereotactic injection of iron dextran into the lateral ventricle



(as above) and unilateral injection of Ad-FLEX-anti-GFP-TRPV1/GFP-ferritin ( $4 \times 10^8$  p.f.u. per injection) into the VMH (coordinates:  $-0.9$  mm AP,  $+0.32$  mm ML and  $-5.48$  mm DV). We performed unilateral injections of Cre-dependent adenovirus into the dorsomedial VMH of glucokinase-Cre mice. Construct expression was seen in this subdivision and in additional subdivisions of the VMH on the injected side. Virus expression is Cre-dependent as we did not see GFP expression in wild-type mice. After 1 week, half the mice in each group were studied using RF stimulation (31 mT) and half remained untreated. One week later, the previously treated mice were assessed without RF treatment and the previously untreated mice were treated with RF. Tail vein samples for blood glucose were taken at  $-5, 0, 5, 10, 20, 30, 45, 60$  and  $90$  min after the onset of RF treatment. After an additional week, mice were treated as described above but at  $60$  min after the onset of RF treatment, mice were killed and blood taken by cardiac puncture for hormone assessment and hepatic tissue was harvested and snap-frozen in liquid nitrogen for later assessment of gluconeogenic enzyme expression. Brains were fixed, sectioned and stained with GFP to check injection placement. Mice with injection sites outside the VMH were excluded from the analysis.

**Study 4.** GK-Cre mice were anaesthetized and injected with AAV-EF1a-DIO-hChR2(H134R)-EYFP ( $1 \mu\text{l}$ ) into the VMH using the coordinates above. An optic fibre was then placed  $200$  nm above the injection site and fixed with adhesive cement followed by dental cement then the scalp was sealed back using tissue adhesive. After 4 weeks, half the mice were treated with  $473$  nm laser stimulation ( $5$  Hz,  $15$  ms pulse width) for  $30$  min and half were attached to the optical cable but without light stimulation. One week later, the previously treated mice were assessed without light treatment and the previously untreated mice were treated with light. Tail vein samples for blood glucose were taken at  $-5, 0, 5, 10, 20, 30, 45, 60$  and  $90$  min after the onset of light treatment. Brains were fixed, sectioned and stained with GFP to check injection placement. Mice with injection sites outside the VMH were excluded from the analysis.

**Study 5.** GK-Cre or wild-type mice were anaesthetized with isoflurane and underwent stereotactic injection of iron dextran into the lateral ventricle (as above) and Ad-FLEX-anti-GFP-TRPV1<sup>mutant</sup>/GFP-ferritin ( $4 \times 10^8$  p.f.u. per injection) into the VMH. After one week, half the mice in each group were studied using RF stimulation (31 mT) and half remained untreated. One week later, the previously treated mice were assessed without RF treatment and the previously untreated mice were treated with RF. Tail vein samples for blood glucose were taken at  $-5, 0, 5, 10, 20, 30, 45, 60$  and  $90$  min after the onset of RF treatment. After a further 3 days, mice were anaesthetized and at time 0 were treated with 2-deoxyglucose ( $400$  mg kg<sup>-1</sup>, intraperitoneal) then treated with RF for  $45$  min. Tail vein samples for blood glucose were taken at  $-5, 0, 5, 10, 20, 30, 45, 60$  and  $90$  min after the onset of RF treatment. One week later, mice were anaesthetized and RF treated (31 mT) and at  $60$  min after the onset of RF treatment, they were killed and blood taken by cardiac puncture for hormone assessment and hepatic tissue was harvested and snap frozen in liquid nitrogen for later assessment of gluconeogenic enzyme expression. Brains were fixed, sectioned and stained with GFP to check injection placement. Mice with injection sites outside the VMH were excluded from the analysis.

**Study 6.** GK-Cre or wild-type mice were anaesthetized with isoflurane and underwent stereotactic injection of iron dextran into the lateral ventricle and Ad-FLEX-anti-GFP-TRPV1/GFP-ferritin ( $4 \times 10^8$  p.f.u. per injection) into the VMH (as above). After one week, mice were placed in a plastic chamber in a low-strength magnetic field ( $<0.005$  T) for a  $15$  min acclimation period, then half the mice were moved to a high-strength magnetic field ( $>0.5$  T) for  $30$  min and half remained in the low-strength field. After  $30$  min, all mice were placed in a low-strength field for a further  $30$  min. Tail vein samples for blood glucose were taken at  $-5, 0, 15, 30, 45$  and  $60$  min after the acclimation period. One week later, groups were crossed so the mice previously treated with high-strength magnetic field were treated with low-strength field and mice previously treated with low-strength field were treated with high-strength magnetic field. At the end of the study, mice were sacrificed and perfused. Brains were fixed, sectioned and stained with GFP to check injection placement. Mice with injection sites outside the VMH were excluded from the analysis.

**Study 7.** GK-Cre or wild-type mice were injected and recovered as in study 6. After one week, the effect of magnetic field stimulation on food intake was examined. After a  $4$ -h fast, mice were acclimated to their chamber for  $20$  min then food intake was assessed after  $20$  min at low-strength magnetic field. Food intake was then measured for  $20$  min with half the mice in high-strength magnetic field ( $0.5$ – $1$  T) and half at low-strength magnetic field. Food intake was measured for a final  $20$  min period at low-strength magnetic field. One week later, the groups were crossed so mice previously treated with high-strength magnetic field were treated with low-strength field and mice previously treated with low-strength field were treated with high-strength magnetic field. At the end of the study, mice

were sacrificed and perfused. Brains were fixed, sectioned and stained with GFP to check injection placement. Mice with injection sites outside the VMH were excluded from the analysis.

**Study 8.** GK-Cre mice underwent stereotactic injection as described in study 3. After one week, mice were anaesthetized and  $15$  min after the induction of anaesthesia were placed in the RF solenoid without power for  $30$  min (no RF treatment). After 3 days, the mice were divided into two equal groups, one group was treated with a field strength of  $27$  mT for  $30$  min and the other group with a field strength of  $23$  mT for  $30$  min. After a further 4 days, the treatment groups were reversed. A week later, the first group of mice were treated with RF (31 mT) for  $20$  min and the second group of mice with RF (31 mT) for  $10$  min. After a further 3 days, the treatment groups were reversed. Tail vein samples for blood glucose were taken at  $-5, 0, 5, 10, 20, 30, 45, 60$  and  $90$  min after the onset of RF treatment for all studies. After an additional week, half the mice were treated with RF (31 mT) for  $30$  min and half the mice remained untreated. At  $60$  min after the onset of RF treatment, mice were sacrificed and brains were fixed, sectioned and stained for GFP and activated-caspase-3 to assess apoptosis in the VMH.

**Study 9.** GK-Cre mice underwent stereotactic injection as described in study 3. After 2 weeks, the effects of lower magnetic strength ( $0.2$ – $0.5$  mT) on food intake were assessed. After a  $4$ -h fast, mice were acclimated to their chamber for  $20$  min and then food intake was assessed after  $20$  min at low-strength magnetic field followed by food intake measurement after  $20$  min treatment with a  $0.2$ – $0.5$  T magnetic field. Food intake was measured for a final  $20$  min period at low-strength magnetic field. At the end of the study, mice were sacrificed and perfused. Brains were fixed, sectioned and stained with GFP to check injection placement.

**Study 10.** GK-Cre mice underwent stereotactic injection as described in study 5 but with bilateral injection of Ad-FLEX-anti-GFP-TRPV1<sup>mutant</sup>/GFP-ferritin into the VMH. After a week, food intake was assessed in response to low-strength magnetic field treatment. After a  $4$ -h fast, mice were acclimated to their chamber for  $20$  min and then food intake was measured for three periods of  $20$  min at low field strength. One week later, the study was repeated with a  $20$  min acclimation period then food intake was measured for mice were treated with high strength magnetic field ( $0.5$ – $1$  T) for  $20$  min. Food intake was measured for a further two  $20$ -min periods at low magnetic field strength. At the end of the study, mice were sacrificed and perfused. Brains were fixed, sectioned and stained with GFP to check injection placement.

**Study 11.** GK-Cre/Rosa-tdTomato mice underwent stereotactic surgery as described in study 3. After one week, three mice were anaesthetized and  $15$  min after the induction of anaesthesia were treated with RF (31 mT) for  $30$  min. At  $60$  min after the onset of RF treatment, mice were sacrificed. Brains from three mice were fixed, sectioned and stained for GFP and c-Fos. The fourth mouse was perfused without RF treatment and the brain was used for immune-electron microscopy.

**Study 12.** GK-Cre ( $n=4$ ) underwent stereotactic surgery as described in study 3. After one week, the mice were anaesthetized and perfused. Brains were fixed, sectioned and stained for GFP. Tiled z-stack images were taken using confocal microscopy ( $20\times$  objective) and images analysed using Imaris 3D quantification software. The image analysis software calculated the number of GFP-positive cells per volume by thresholding immunoreactivity above background levels. Using this method the average number of GFP-positive cells was  $2,436 \pm 841$  cells per brain. **Assays.** Blood glucose was determined using a Breeze 2 glucometer (Bayer). Blood was spun for  $10$  min and plasma was collected. Plasma levels of insulin (Mercodia) and glucagon (Mercodia) were determined by ELISA.

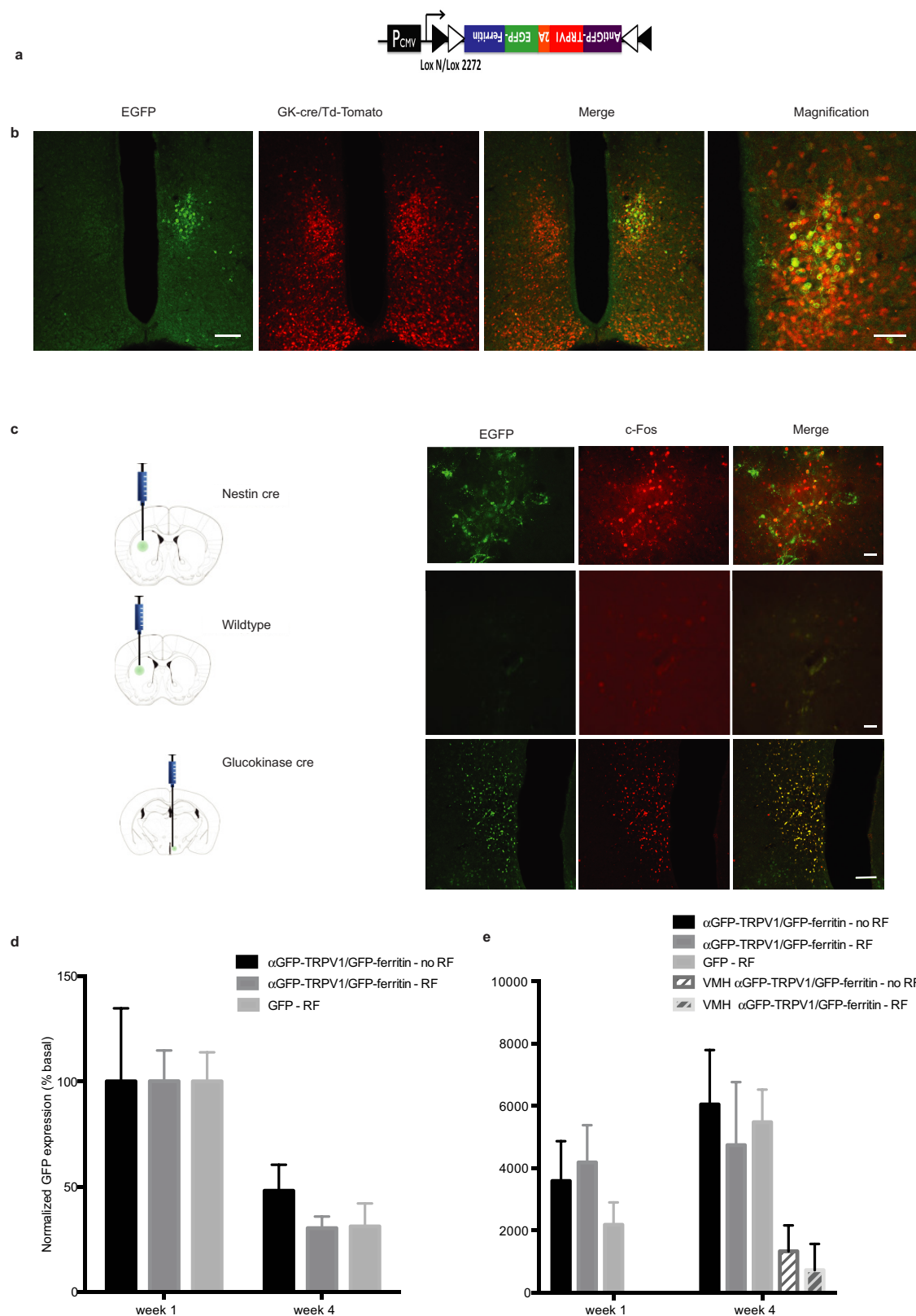
**Western blot.** Protein was isolated by lysis in RIPA buffer and centrifugation at  $16,000$  r.p.m.,  $4^\circ\text{C}$  for  $5$  min before addition of  $4\times$  Laemmli buffer. Samples were denatured for  $5$  min at  $95^\circ\text{C}$  and frozen at  $-20^\circ\text{C}$  before assay. Samples ( $15 \mu\text{l}$ ) were run on a  $4$ – $15\%$  gel then transferred to PVDF membrane. Membranes were blocked ( $3\%$  dried milk in TBST buffer) for  $1$  h at room temperature then incubated in primary antibody (pCREB (Ser133) (87G3) rabbit monoclonal antibody (1:1,000) or  $\beta$ -actin rabbit antibody (1:1,000), Cell Signaling) in TBST overnight at  $4^\circ\text{C}$ . Membranes were washed three times in TBST then incubated in secondary antibody (goat anti-rabbit IgG-HRP, 1:5,000, Santa Cruz) in TBST for  $2$  h at room temperature. The membrane was washed a further five times then developed in substrate for  $5$  min (Supersignal West Femto maximum sensitivity substrate, Life Technologies) and imaged (C-DiGit blot scanner, Licor). The pCREB density signal was corrected for any variation in protein loading by dividing by the density signal for the housekeeping gene, actin.

**Real-time PCR.** Total RNA was isolated by homogenizing tissue in TRIzol reagent (Invitrogen) or cells in buffer RLT and purifying the RNA using Absolutely RNA microprep kit (Agilent). Complimentary DNA was synthesized using QIAGEN omniscript RT kit. Real-time PCR was performed using the TaqMan system (Applied Biosystems) according to the manufacturer's protocol.

**Statistics.** Data over 2 s.d. outside the mean were excluded from further analysis as determined before the studies. All data were tested for Gaussian distribution and variance. Data with normal distribution and similar variance were analysed for statistical significance using two-tailed, unpaired Student's *t*-tests unless otherwise indicated. Data with normal variation and unequal variance were analysed by two-tailed Welch's *t*-tests. Paired data were analysed by paired *t*-tests. Data with more than two groups were analysed by one-way ANOVA with post-hoc Tukey's analysis for parametric data. Data which were not normally distributed were analysed by two-tailed Mann–Whitney *U*-tests or Kruskal–Wallis tests with post-hoc Dunn's correction. *P* values are as indicated. Time course data were analysed by two-way ANOVA with Sidak's

multiple comparisons or repeated measures two-way ANOVA with Sidak's multiple comparisons for paired data. Data are shown as mean  $\pm$  s.e.m. unless otherwise stated.

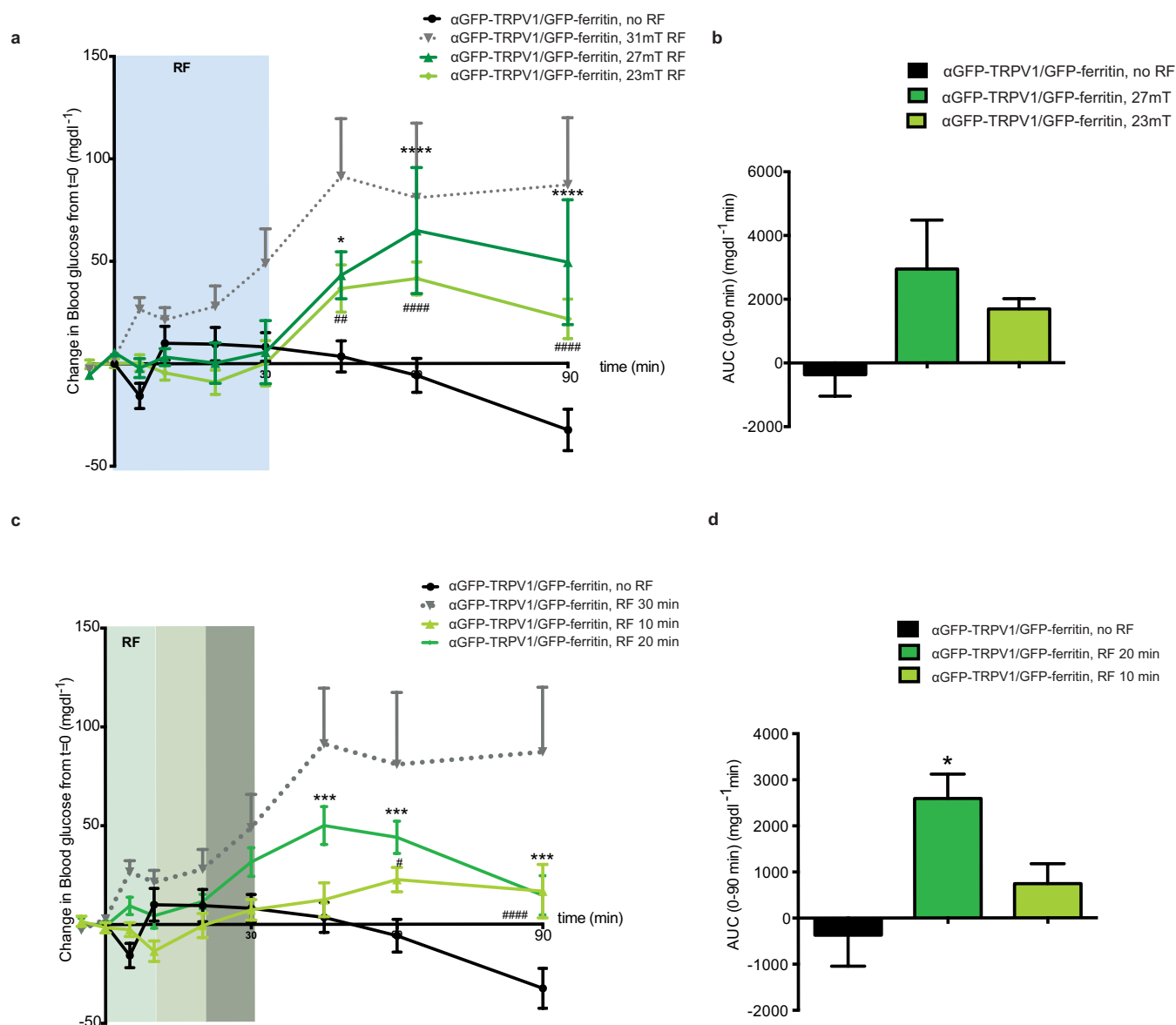
27. Caterina, M. J. *et al.* The capsaicin receptor: a heat-activated ion channel in the pain pathway. *Nature* **389**, 816–824 (1997).
28. Wu, S. Y. & Chiang, C. M. Expression and purification of epitope-tagged multisubunit protein complexes from mammalian cells. *Curr. Protoc. Mol. Biol.* Chapter 16, Unit 16.13 (2002).
29. Nakaya, N., Sultana, A., Lee, H. S. & Tomarev, S. I. Olfactomedin 1 interacts with the Nogo A receptor complex to regulate axon growth. *J. Biol. Chem.* **287**, 37171–37184 (2012).



### Extended Data Figure 1 | Remote neural activation using RF *in vivo*.

**a**, Construct design for Ad-FLEX-anti-GFP-TRPV1/GFP-ferritin. CMV, cytomegalovirus promoter. *loxN* and *lox2272* are orthogonal recombination sites. **b**, Immunostaining for eGFP in GK-Cre/TdTomato mice demonstrates expression of the GFP in glucokinase neurons after VMH injection of Ad-FLEX-anti-GFP-TRPV1/GFP-ferritin. Scale bars, 100  $\mu$ m; 50  $\mu$ m in magnification panel. **c**, Co-localization between eGFP and c-Fos after RF treatment of Nestin-Cre (upper panels) or wild-type (middle panels) mice injected with Ad-FLEX-anti-GFP-TRPV1/GFP-

ferritin into the striatum (Scale bar, 80  $\mu$ m) and of GK-Cre mice injected with Ad-FLEX-anti-GFP-TRPV1/GFP-ferritin into the VMH (lower panels). Scale bar, 100  $\mu$ m. Quantification of GFP (**d**) and activated-caspase-3 (**e**) immunostaining in mice following injection of Ad-anti-GFP-TRPV1/GFP-ferritin or Ad-GFP (1  $\mu$ l) into the striatum of wild-type (WT) mice or injection of Ad-FLEX-anti-GFP-TRPV1/GFP-ferritin into the VMH of GK-Cre mice. In all cases, columns represent mean and error bars indicate s.e.m. Data were analysed by Kruskal-Wallis test with post-hoc Dunn's correction.  $n = 4$  mice per group.

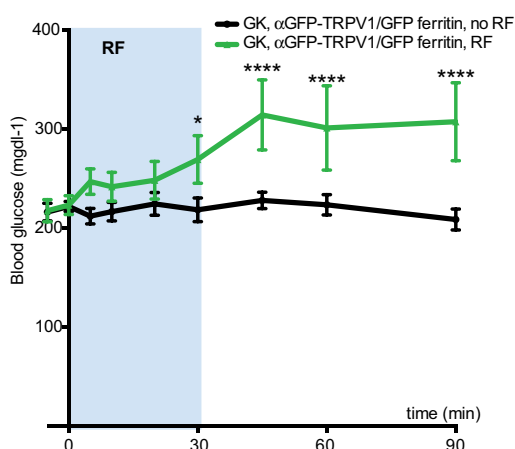


**Extended Data Figure 2 | Effects of RF field strength and treatment duration *in vivo*.** **a**, Effect of increasing RF field strength on the change in blood glucose and **b**, the cumulative change in blood glucose in GK-Cre mice with VMH injection of Ad-FLEX-anti-GFP-TRPV1/GFP-ferritin. Data are shown as mean and error bars indicate s.e.m. Data were analysed by two-way ANOVA with Sidak's multiple comparisons. \* or # indicates  $P < 0.05$ , \*\* or ## indicates  $P < 0.01$ , \*\*\* or ### indicates  $P < 0.001$ , \*\*\*\* or #### indicates  $P < 0.0001$  between treated and untreated groups.

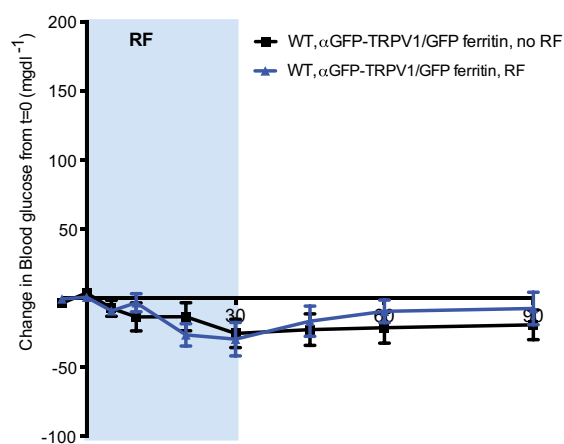
**c**, Effect of increasing RF treatment duration on the change in blood glucose and **d**, the cumulative change in blood glucose in GK-Cre mice with VMH injection of Ad-FLEX-anti-GFP-TRPV1/GFP-ferritin. Data are shown as mean and error bars indicate s.e.m. Data were analysed by two-way ANOVA with Sidak's multiple comparisons. \* or # indicates  $P < 0.05$ , \*\* or ## indicates  $P < 0.01$ , \*\*\* or ### indicates  $P < 0.001$ , \*\*\*\* or #### indicates  $P < 0.0001$  between treated and untreated groups.



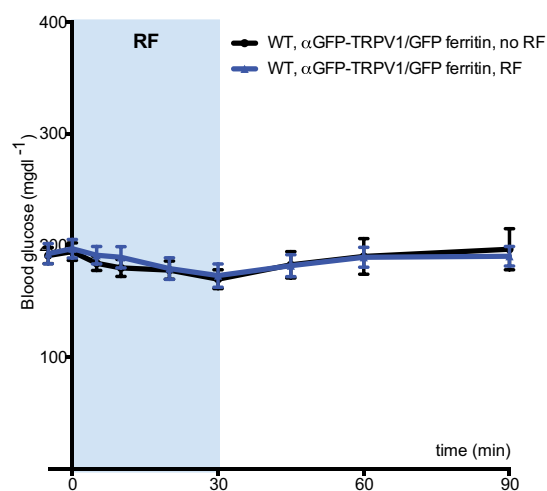
a



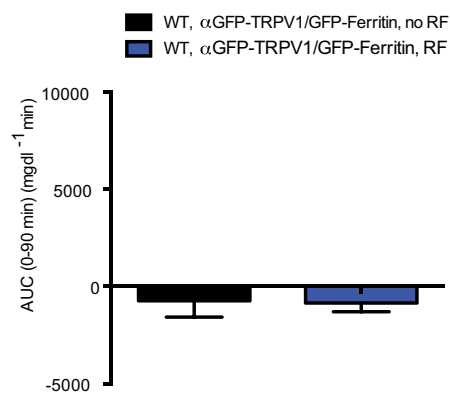
b



c



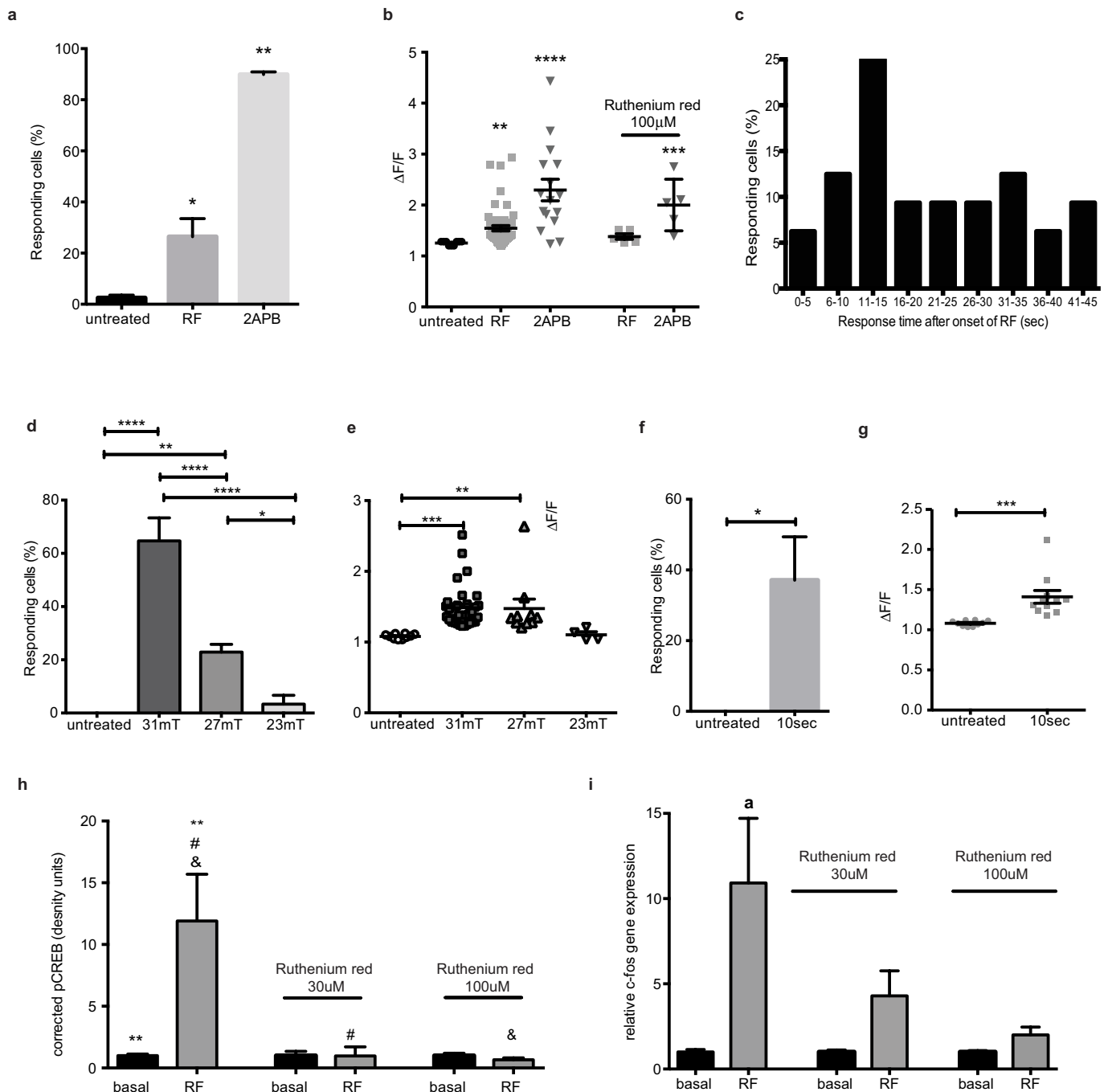
d



Extended Data Figure 3 | See next page for caption.

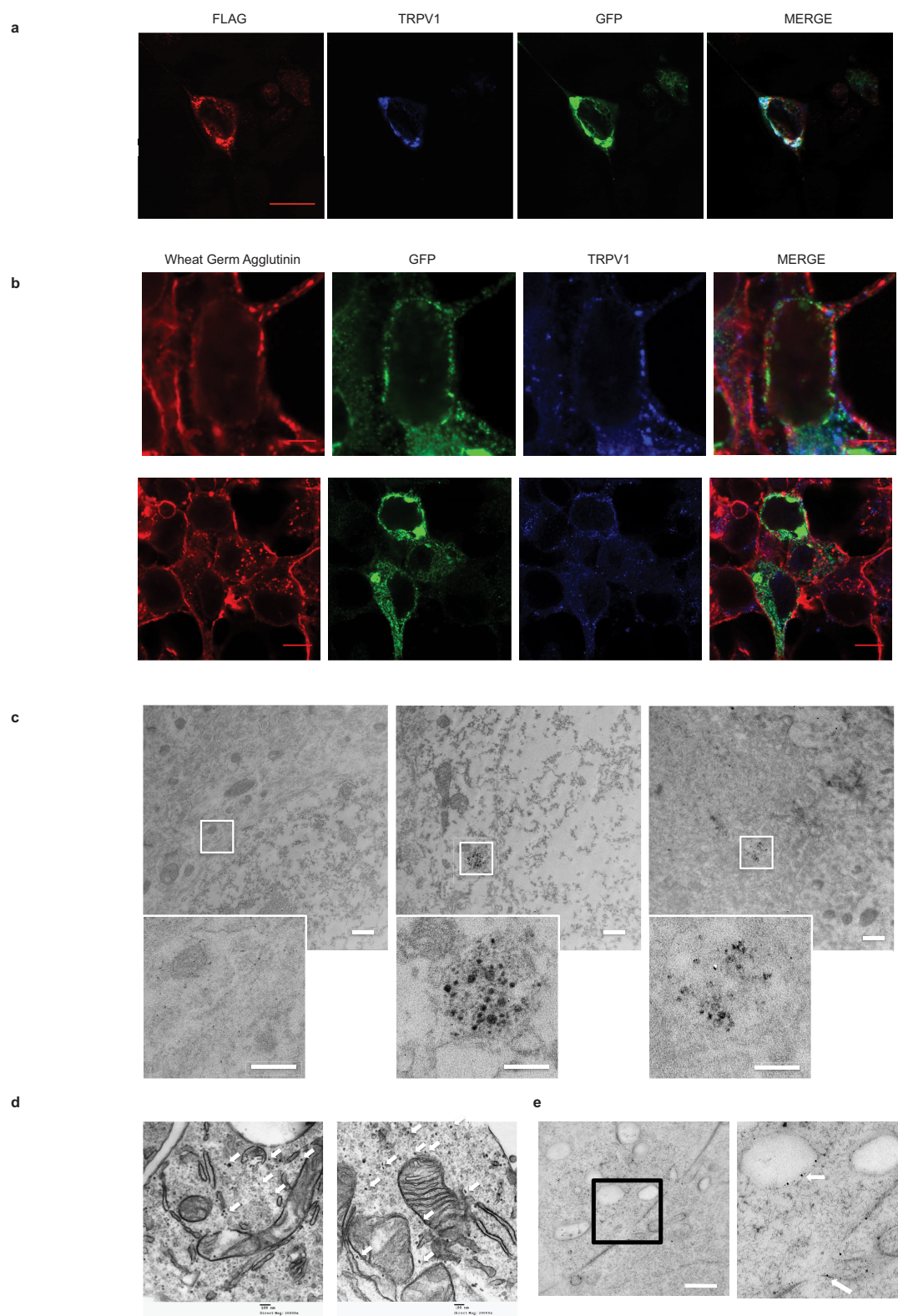
**Extended Data Figure 3 | Neural activation in GK-Cre and wild-type mice *in vivo*.** **a**, RF treatment of GK-Cre mice expressing anti-GFP-TRPV1/GFP-ferritin in the VMH significantly increases blood glucose compared to no RF treatment ( $n = 13$ ). Data points indicate mean and error bars indicate s.e.m. Data were analysed by two-way ANOVA with Sidak's multiple comparisons.  $*P < 0.05$ ,  $**P < 0.01$ ,  $***P < 0.001$ ,  $****P < 0.0001$  between treated and untreated groups. **b**, Effects of RF treatment of wild-type mice injected with anti-GFP-TRPV1/GFP-ferritin in the VMH on change in blood glucose with time ( $n = 10$ ). Data points indicate mean and error bars indicate s.e.m. Data were analysed by

two-way ANOVA with Sidak's multiple comparisons. **c**, Effects of RF treatment of wild-type mice injected with anti-GFP-TRPV1/GFP-ferritin in the VMH on blood glucose with time ( $n = 10$ ). Data points indicate mean and error bars indicate s.e.m. Data were analysed by two-way ANOVA with Sidak's multiple comparisons. **d**, Effect of RF treatment on cumulative change in blood glucose over the course of the study in wild-type mice with VMH injection of anti-GFP-TRPV1/GFP-ferritin ( $n = 10$ ). Columns represent mean and error bars indicate s.e.m. Data were analysed by two-tailed, paired Student's *t*-test.



**Extended Data Figure 4 | Remote neural activation of N38 cells expressing anti-GFP-TRPV1/GFP-ferritin in vitro.** **a**, Calcium imaging of RF-treated N38 cells expressing anti-GFP-TRPV1/GFP-ferritin showing the percentage of cells responding ( $>20\%$  increase in fluorescence) to no treatment, RF or 2-APB ( $n = 8, 9$  or  $2$  occasions, respectively), **b**, the increase in fluorescent signal with RF or 2-APB treatment that is inhibited by Ruthenium red and **c**, the response time (to reach  $20\%$  increase in fluorescence) to RF treatment ( $n = 38$  cells). Data are represented as mean and error bars indicate s.e.m. Data were analysed by Kruskal-Wallis test with Dunn's multiple comparison test.  $*P < 0.05$  vs. untreated,  $**P < 0.01$  vs. untreated,  $***P < 0.001$  vs. untreated and  $****P < 0.0001$  vs. untreated. **d**, Calcium imaging in stably transfected N38 cells expressing anti-GFP-TRPV1/GFP-ferritin demonstrates a field-strength-dependent increase in the percentage of responding cells ( $>20\%$  increase in fluorescence) and **e**, the fluorescent signal in compared to untreated cells;  $n = 10, 33, 10$  and  $4$  cells, respectively. Data points indicate mean and error bars indicate s.e.m. Data were analysed by

two-way ANOVA with Sidak's multiple comparisons.  $*P < 0.05$ ,  $**P < 0.01$ ,  $***P < 0.001$   $****P < 0.0001$  between treated and untreated groups. **f**, RF treatment of stably transfected N38 cells expressing anti-GFP-TRPV1/GFP-ferritin for  $10$  s significantly increases the percentage of responding cells and **g**, the fluorescent signal compared to untreated cells ( $n = 10$  and  $11$  cells for treated vs. untreated). Data points indicate mean and error bars indicate s.e.m. Data were analysed by unpaired Student's  $t$ -test.  $*P < 0.05$ ,  $***P < 0.001$  between treated and untreated groups. **h**, RF treatment of N38 cells expressing anti-GFP-TRPV1/GFP-ferritin significantly increases pCREB levels and **i**, relative *c-fos* (also known as *Fos*) gene expression (measured by quantitative PCR) and these increases are blocked by Ruthenium red ( $30$  and  $100 \mu\text{M}$ ). In all cases, columns represent mean and error bars indicate s.e.m. Data were analysed by one way ANOVA with post-hoc Tukey's analysis test. Columns marked with  $*$ ,  $\#$ ,  $a$  or  $\&$  indicate  $P < 0.01$ . Each study was repeated on three occasions each with four replicates.

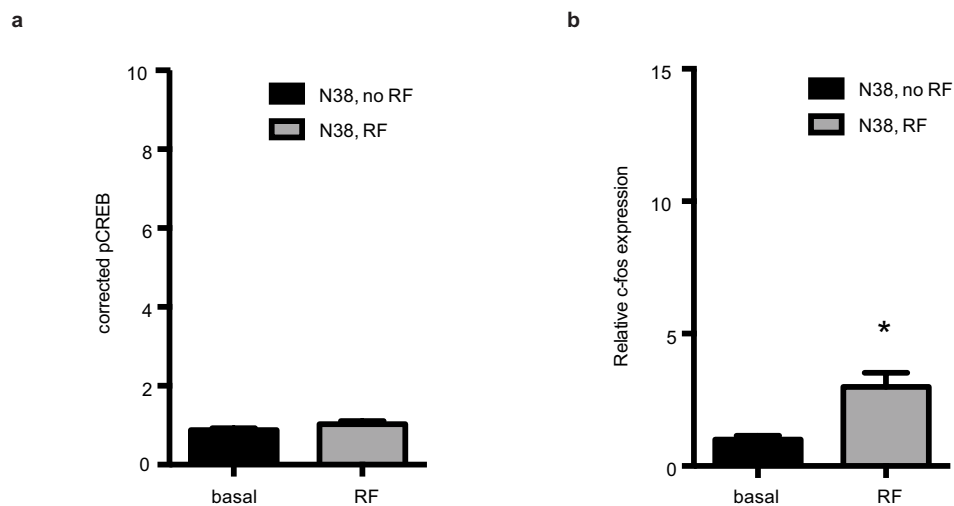


#### Extended Data Figure 5 | RF treatment of N38 cells *in vitro*.

**a**, Immunohistochemistry for Flag-tagged ferritin chimaera (red), TRPV1 (blue) and GFP (green) in N38 cells infected with adenovirus expressing anti-GFP-TRPV1/GFP-ferritin. Scale bar represents 20  $\mu\text{m}$ . **b**, Immunohistochemistry for cell membrane (Alexa-594-conjugated wheat germ agglutinin, red), GFP-ferritin (green) and TRPV1 (blue) in transfected cells showing close proximity of TRPV1 and GFP-ferritin with the cell membrane (upper panels; scale bar, 4  $\mu\text{m}$ ) and separate from the cell membrane (lower panels; scale bar, 8  $\mu\text{m}$ ). **c**, Immunoelectron microscopy images from hypothalamic sections taken from GK-Cre mice with unilateral expression of anti-GFP-TRPV1/GFP-ferritin

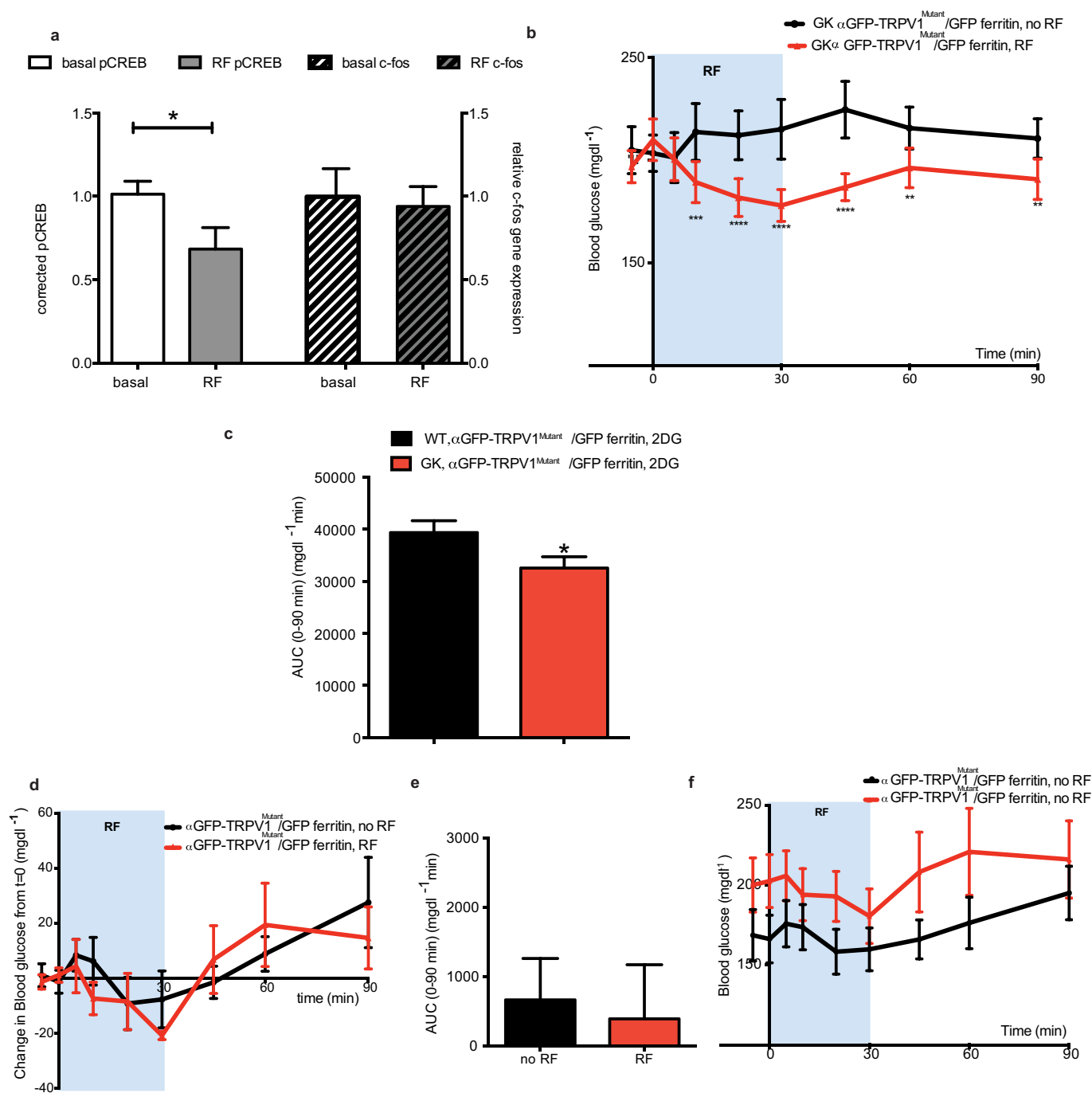
showing immunogold-labelled GFP-tagged ferritin (i; centre and right) from the injected side which are absent on the non-injected side (left, scale bar represents 500 nm and 250 nm for magnification). **d**, Electron micrograph of iron-loaded ferritin in HEK cells transfected with ferritin construct alone. **e**, Double immunoelectron microscopy images from stably transfected HEK cells expressing anti-GFP-TRPV1/GFP-ferritin showing co-localization of GFP and TRPV1 at vesicle membranes and at the cell membrane with magnification on the right. Immuno-electron microscopy for GFP and TRPV1 are marked by 5 nm and 12 nm colloidal gold respectively. Scale bar represents 500 nm.





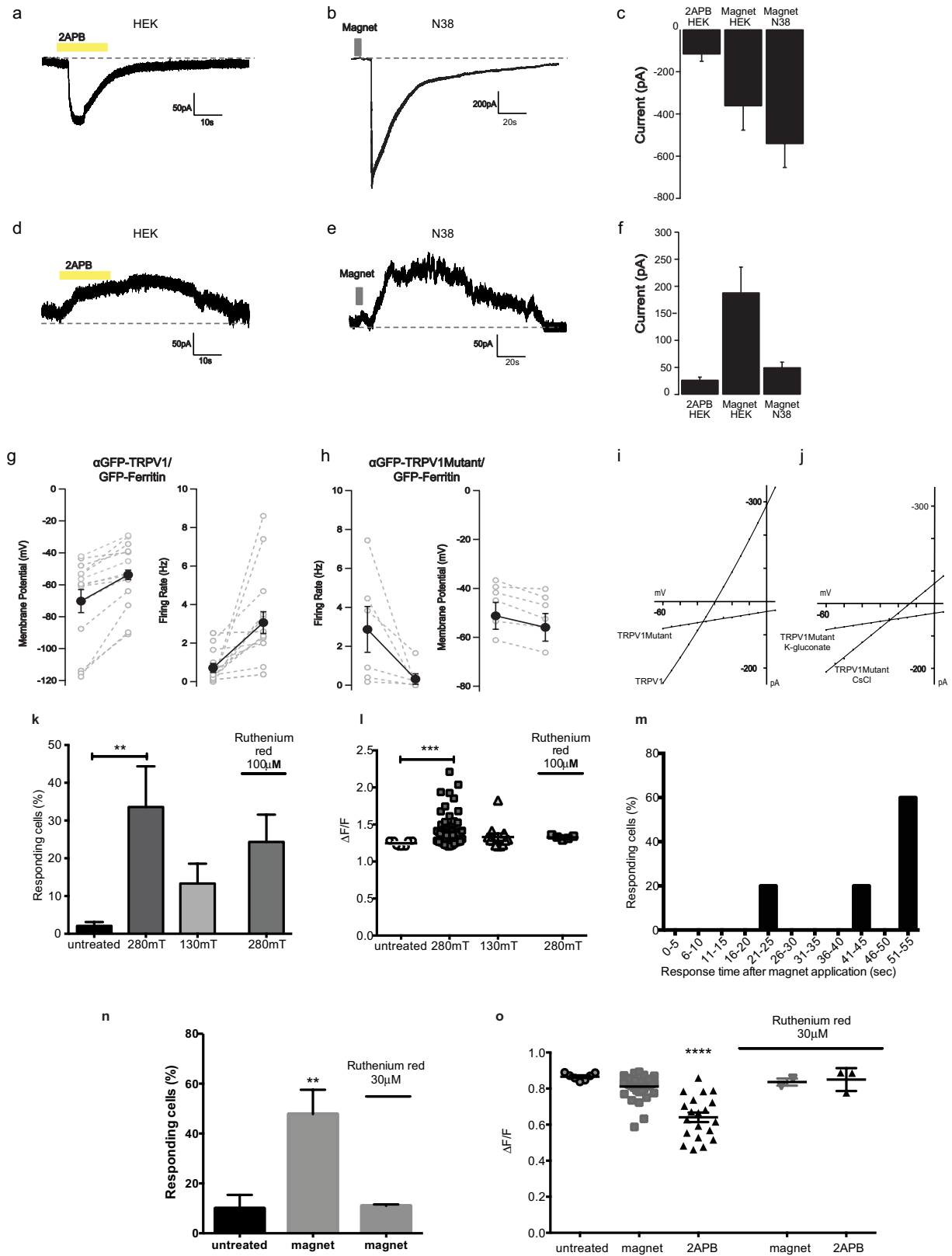
**Extended Data Figure 6 | RF treatment of N38 cells *in vitro*.** **a**, RF treatment of N38 cells does not alter pCREB levels. In all cases, columns represent mean and error bars indicate s.e.m. Each study was repeated on three occasions each with four replicates. **b**, RF treatment significantly

increases relative *c-fos* gene expression. In all cases, columns represent mean and error bars indicate s.e.m. Data were analysed by two-tailed, unpaired Student's *t*-test. \* $P < 0.05$ . Each study was repeated on three occasions each with four replicates.



**Extended Data Figure 7 | Neural inhibition in GK-Cre and wild-type mice *in vivo*.** **a**, Effect of RF treatment of N38 cells expressing anti-GFP-TRPV1<sup>Mutant</sup>/GFP-ferritin on pCREB levels and c-Fos expression. In all cases, columns represent mean and error bars indicate s.e.m. Data were analysed by two-tailed Mann-Whitney *U*-test. \**P* < 0.05. Each study was repeated on three occasions each with four replicates. **b**, RF treatment of GK-Cre mice expressing anti-GFP-TRPV1<sup>Mutant</sup>/GFP-ferritin in the VMH significantly decreases blood glucose compared to no RF treatment (*n* = 13). Data points indicate mean and error bars indicate s.e.m. Data were analysed by two-way ANOVA with Sidak's multiple comparisons. \**P* < 0.05, \*\**P* < 0.01, \*\*\**P* < 0.001, \*\*\*\**P* < 0.0001 between treated and untreated groups. **c**, RF treatment significantly decreases cumulative changes in blood glucose over the course of the study in GK-Cre mice with VMH expression of anti-GFP-TRPV1<sup>Mutant</sup>/GFP-ferritin (*n* = 6) compared to wild-type mice with VMH injection of Ad-FLEX-anti-GFP-

TRPV1<sup>Mutant</sup>/GFP-ferritin (*n* = 9) after administration of 2-deoxyglucose to mimic hypoglycaemia. Data are shown as mean and error bars indicate s.e.m. Data were analysed by unpaired Student's *t*-test. \**P* < 0.05. **d**, Effects of RF treatment of wild-type mice injected with anti-GFP-TRPV1<sup>Mutant</sup>/GFP-ferritin in the VMH on changes in blood glucose with time (*n* = 8). Data points indicate mean and error bars indicate s.e.m. Data were analysed by two-way ANOVA with Sidak's multiple comparisons. **e**, Effects of RF treatment of wild-type mice injected with anti-GFP-TRPV1<sup>Mutant</sup>/GFP-ferritin in the VMH on cumulative changes in blood glucose with time (*n* = 8). Data points indicate mean and error bars indicate s.e.m. Data were analysed by two-way ANOVA with Sidak's multiple comparisons. **f**, Effect of RF treatment on blood glucose over the course of the study in wild-type mice with VMH injection of anti-GFP-TRPV1<sup>Mutant</sup>/GFP-ferritin (*n* = 8). Data points represent mean and error bars indicate s.e.m. Data were analysed by two-way ANOVA with Sidak's multiple comparisons.



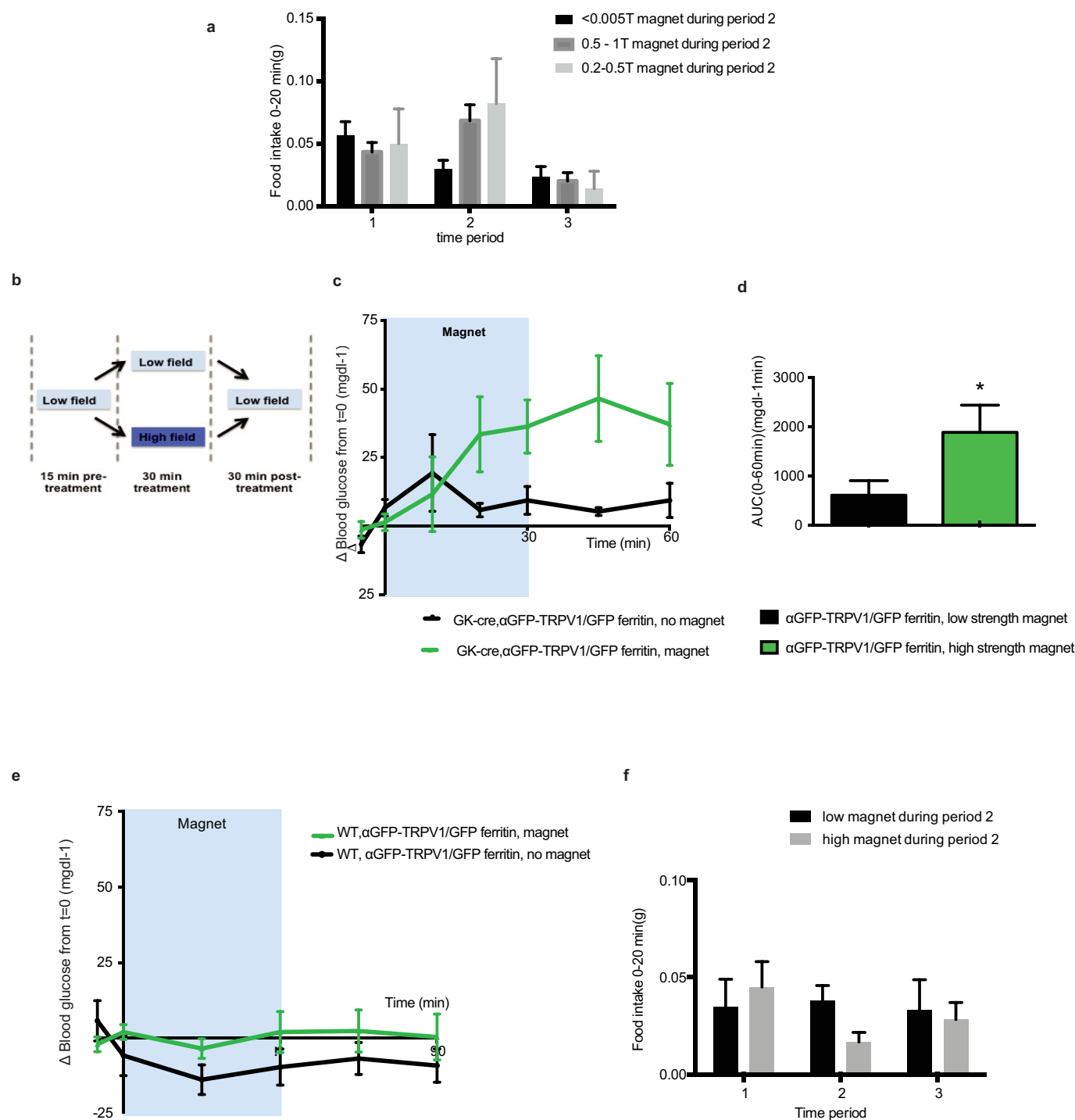
Extended Data Figure 8 | See next page for caption.

**Extended Data Figure 8 | Magnetic field activation and inhibition of N38 cells *in vitro*.**

Electrophysiological recordings of cultured cells. **a**, Current trace from a whole-cell voltage-clamp recording ( $-60$  mV) showing the inward current induced with TRPV1 agonist (2-APB  $200\text{ }\mu\text{M}$ ) in a HEK cell expressing anti-GFP-TRPV1/GFP-ferritin (representative of four recordings). **b**, Current trace from a whole-cell voltage-clamp recording ( $-60$  mV) induced with a magnetic field (5 s) showing the inward current in stably transfected N38 cells expressing anti-GFP-TRPV1/GFP-ferritin (representative of 15 recordings). **c**, Bar chart summary of mean peak current induced by TRPV1 agonist 2-APB ( $200\text{ nM}$ ,  $n = 4$ ) and magnet activation in cultured cells (HEK,  $n = 10$ ; N38,  $n = 15$ ) expressing anti-GFP-TRPV1/GFP-ferritin. Columns represent mean and error bars indicate s.e.m. Electrophysiological recordings of cultured cells. **d**, Current trace from a whole-cell voltage-clamp recording ( $-60$  mV) showing the outward current induced with TRPV1 agonist (2-APB  $200\text{ }\mu\text{M}$ ) in a HEK cell expressing anti-GFP-TRPV1<sup>mutant</sup>/GFP-ferritin (representative of 19 recordings). **e**, Current trace from a whole-cell voltage-clamp recording ( $-60$  mV) induced with a magnetic field (5 s) showing the outward current stably transfected N38 cells expressing anti-GFP-TRPV1<sup>mutant</sup>/GFP-ferritin (representative of 12 recordings). **f**, Bar chart summary of mean peak current induced by TRPV1 agonist 2-APB ( $200\text{ nM}$ ,  $n = 19$ ) and magnet activation in cultured cells (HEK,  $n = 3$ ; N38,  $n = 12$ ) expressing anti-GFP-TRPV1<sup>mutant</sup>/GFP-ferritin. Columns represent mean and error bars indicate s.e.m. **g**, Summary data showing magnet-induced changes in membrane potential and firing rate for GK VMH neurons expressing anti-GFP-TRPV1/GFP-ferritin and **h**, anti-GFP-TRPV1<sup>mutant</sup>/GFP-ferritin. Open circles denote values for individual cells and closed circles denote mean values. Error bars denote s.e.m. For neurons expressing anti-GFP-TRPV1/GFP-ferritin mean membrane potential significantly increased from  $-70.20 \pm 7.246$  mV to  $-53.81 \pm 5.349$  mV ( $n = 14$ ,  $P < 0.0001$ , paired  $t$ -test). Mean firing rate significantly increased from  $0.7084 \pm 0.2311$  to  $3.063 \pm 0.5632$  ( $n = 16$ ,  $P < 0.002$ , paired  $t$ -test; includes data from 2 cell-attached recordings).

For neurons expressing anti-GFP-TRPV1<sup>mutant</sup>/GFP-ferritin mean membrane potential significantly decreased from  $-51.2 \pm 5.519$  mV to  $-55.93 \pm 5.636$  mV ( $n = 6$ ,  $P = 0.03$ ; Wilcoxon matched pairs). Mean firing rate significantly decreased from  $2.868 \pm 1.177$  to  $0.3167 \pm 0.2685$  ( $n = 6$ ,  $P = 0.03$ ; Wilcoxon matched pairs). Current-voltage relationship of 2-APB-activated TRPV1<sup>mutant</sup> channels shows limited cation permeability and increased chloride permeability. **i**, Limited conductance of TRPV1<sup>mutant</sup> channels compared to wild-type when the predominant internal ions are  $\text{K}^+$  and gluconate. **j**, Conductance is increased for anti-GFP-TRPV1<sup>mutant</sup> channels when the predominant internal ions are Cs and Cl (isometrical chloride). **k**, Calcium imaging in stably transfected N38 cells expressing anti-GFP-TRPV1/GFP-ferritin demonstrates a magnetic field-strength-dependent increase in the percentage of responding cells ( $>20\%$  increase in fluorescence) ( $n = 7, 10, 3$  imaging studies, respectively) and **l**, the fluorescent signal compared to untreated cells ( $n = 11, 48, 12$  cells, respectively). The effects of magnet stimulation were blocked by Ruthenium red. Data points indicate mean and error bars indicate s.e.m. Data were analysed by two-way ANOVA with Sidak's multiple comparisons.  $*P < 0.05$ ,  $**P < 0.01$ ,  $***P < 0.001$ ,  $****P < 0.0001$  between treated and untreated groups. **m**, Histogram representing the response time (to reach 20% increase in fluorescence) in magnet-treated N38 cells expressing anti-GFP-TRPV1/GFP-ferritin ( $n = 68$  cells). **n**, Treatment of N38 cells expressing anti-GFP-TRPV1<sup>mutant</sup>/GFP-ferritin with magnet ( $n = 6$  occasions) significantly increased the percentage of responding cells ( $i$ ) ( $>10\%$  decrease in chloride indicator, MQAE, fluorescence) compared to untreated cells ( $n = 4$  occasions) and **o**, the reduction in MQAE signal. Ruthenium red reduced both the percentage of responding cells and the magnitude of the response ( $n = 2$  occasions). In all cases, columns represent mean and error bars indicate s.e.m. Data were analysed by Kruskal-Wallis test with Dunn's multiple comparison test. Columns marked with  $**P < 0.01$  vs. untreated, columns marked with  $****P < 0.001$  vs. untreated.

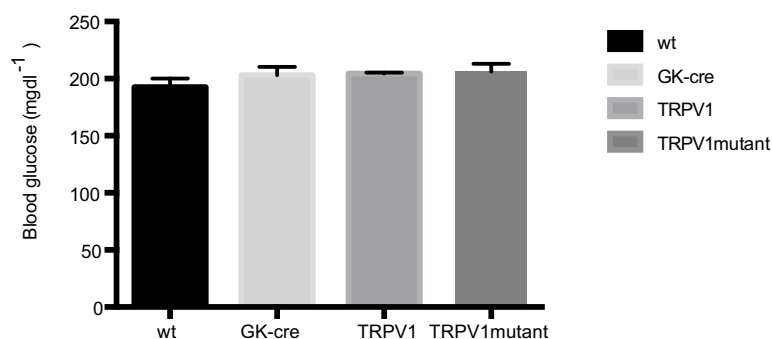




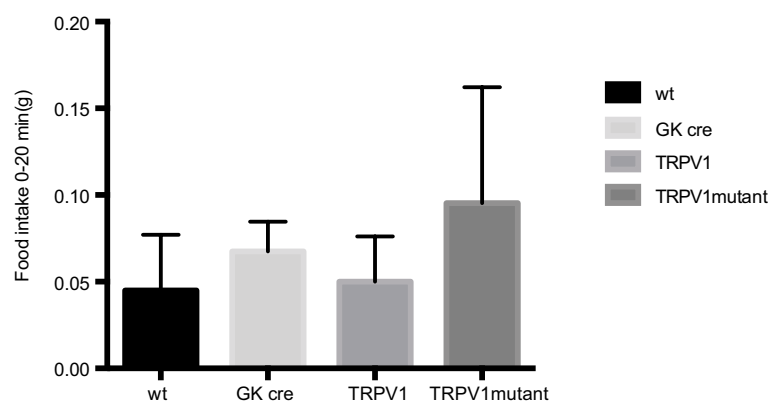
**Extended Data Figure 9 | Non-invasive neural activation *in vivo* using a static magnetic field.** **a**, The effect of moderate (0.2–0.5 T) magnetic field strength on food intake in GK-Cre mice expressing anti-GFP-TRPV1/GFP-ferritin in the VMH ( $n=5$ ). Columns represent mean and error bars indicate s.e.m. **b**, Schema of the crossover protocol used to examine the effect of neural activation with a static magnetic field on blood glucose. **c**, Magnetic field treatment of GK-Cre mice following VMH injection of anti-GFP-TRPV1/GFP-ferritin significantly increases blood glucose compared to no magnet treatment ( $n=6$ ). Data points indicate mean and error bars indicate s.e.m. Data were analysed by two-way ANOVA with Sidak's multiple comparisons. **d**, Magnet treatment significantly increases cumulative change in blood glucose over the course of the study

in GK-Cre mice with VMH injection of anti-GFP-TRPV1/GFP-ferritin ( $n=6$ ) compared to the same mice without magnet treatment. In all cases, columns represent mean and error bars indicate s.e.m. Data were analysed by Wilcoxon matched pairs signed rank test.  $*P < 0.05$ . **e**, Effects of static magnetic field treatment of wild-type mice with VMH injection of anti-GFP-TRPV1/GFP-ferritin on changes in blood glucose with time ( $n=6$ ). Data points indicate mean and error bars indicate s.e.m. Data were analysed by two-way ANOVA with Sidak's multiple comparisons. **f**, Effects of static magnetic field treatment of wild-type mice injected with anti-GFP-TRPV1/GFP-ferritin in the VMH on food intake ( $n=6$ ). Data points indicate mean and error bars indicate s.e.m. Data were analysed by two-way ANOVA with Sidak's multiple comparisons.

a



b



**Extended Data Figure 10 | Baseline characteristics in mice expressing anti-GFP-TRPV1/GFP-ferritin or anti-GFP-TRPV1<sup>mutant</sup>/GFP-ferritin.** **a**, Non-fasting blood glucose did not differ significantly between wild-type, GK-Cre and GK-Cre mice injected with anti-GFP-TRPV1/GFP-ferritin or anti-GFP-TRPV1<sup>mutant</sup>/GFP-ferritin ( $n = 10, 8, 8$  and  $5$ , respectively). Columns represent mean and error bars indicate s.e.m.

**b**, Food intake following a 4 h fast did not differ significantly between wild-type, GK-Cre and GK-Cre mice injected with anti-GFP-TRPV1/GFP-ferritin or anti-GFP-TRPV1<sup>mutant</sup>/GFP-ferritin ( $n = 6, 4, 6$  and  $13$  respectively). \* $P < 0.05$ . Columns represent mean and error bars indicate s.e.m.

# Potentiating the antitumour response of CD8<sup>+</sup> T cells by modulating cholesterol metabolism

Wei Yang<sup>1\*</sup>, Yibing Bai<sup>1\*</sup>, Ying Xiong<sup>2</sup>, Jin Zhang<sup>1</sup>, Shuokai Chen<sup>1</sup>, Xiaojun Zheng<sup>3</sup>, Xiangbo Meng<sup>1</sup>, Lunyi Li<sup>1</sup>, Jing Wang<sup>4</sup>, Chenguang Xu<sup>4</sup>, Chengsong Yan<sup>1</sup>, Lijuan Wang<sup>2</sup>, Catharine C. Y. Chang<sup>5</sup>, Ta-Yuan Chang<sup>5</sup>, Ti Zhang<sup>6</sup>, Penghui Zhou<sup>7</sup>, Bao-Liang Song<sup>8</sup>, Wanli Liu<sup>4</sup>, Shao-cong Sun<sup>9</sup>, Xiaolong Liu<sup>10</sup>, Bo-liang Li<sup>2</sup> & Chenqi Xu<sup>1,11</sup>

CD8<sup>+</sup> T cells have a central role in antitumour immunity, but their activity is suppressed in the tumour microenvironment<sup>1–4</sup>. Reactivating the cytotoxicity of CD8<sup>+</sup> T cells is of great clinical interest in cancer immunotherapy. Here we report a new mechanism by which the antitumour response of mouse CD8<sup>+</sup> T cells can be potentiated by modulating cholesterol metabolism. Inhibiting cholesterol esterification in T cells by genetic ablation or pharmacological inhibition of ACAT1, a key cholesterol esterification enzyme<sup>5</sup>, led to potentiated effector function and enhanced proliferation of CD8<sup>+</sup> but not CD4<sup>+</sup> T cells. This is due to the increase in the plasma membrane cholesterol level of CD8<sup>+</sup> T cells, which causes enhanced T-cell receptor clustering and signalling as well as more efficient formation of the immunological synapse. ACAT1-deficient CD8<sup>+</sup> T cells were better than wild-type CD8<sup>+</sup> T cells at controlling melanoma growth and metastasis in mice. We used the ACAT inhibitor avasimibe, which was previously tested in clinical trials for treating atherosclerosis and showed a good human safety profile<sup>6,7</sup>, to treat melanoma in mice and observed a good antitumour effect. A combined therapy of avasimibe plus an anti-PD-1 antibody showed better efficacy than monotherapies in controlling tumour progression. ACAT1, an established target for atherosclerosis, is therefore also a potential target for cancer immunotherapy.

The importance of CD8<sup>+</sup> T cells in antitumour immunity has been demonstrated in many types of cancer<sup>1,2</sup>. However, tumours can escape immune attack by various mechanisms of immunosuppression<sup>3,4</sup>. Reactivating the antitumour responses of T cells by checkpoint blockade has recently been demonstrated to have notable effects on treating cancer, but its response rate needs to be further improved<sup>8,9</sup>. It is therefore of great clinical interest to develop other therapies to potentiate the antitumour activity of CD8<sup>+</sup> T cells by modulating different pathways. Previous studies have demonstrated that membrane lipids can directly regulate T-cell signalling and function<sup>10–16</sup>. Cholesterol is a key component of membrane lipids, and has been shown to be required for T-cell receptor (TCR) clustering and the formation of the T-cell immunological synapse<sup>13–15</sup>. Here we studied whether the antitumour response of CD8<sup>+</sup> T cells can be potentiated by modulating cholesterol metabolism.

We first studied the reprogramming of cellular cholesterol metabolism of CD8<sup>+</sup> T cells after activation. The cholesterol levels of both the whole cell and the plasma membrane were markedly increased in

activated CD8<sup>+</sup> T cells (Extended Data Fig. 1a–c). Consistently, the messenger RNA levels of key genes encoding proteins of cholesterol biosynthesis and transport pathways were upregulated, whereas those of the cholesterol efflux pathway were downregulated (Extended Data Fig. 1d–f). We also checked the mRNA levels of cholesterol esterification genes. *Acat1* and *Acat2* are two key genes encoding cholesterol esterification enzymes that convert free cholesterol to cholesteryl esters for storage. *Acat1* is ubiquitously expressed while *Acat2* is mainly expressed in liver and small intestine<sup>17</sup>. Upon CD8<sup>+</sup> T-cell activation, *Acat1* mRNA levels were significantly upregulated at early time points, whereas *Acat2* mRNA levels first decreased and then increased at late time points (Fig. 1a). Inhibiting cholesterol esterification using the potent ACAT1/ACAT2 inhibitor CP-113,818 (ref. 18), or the less potent but specific ACAT1 inhibitor K604 (ref. 19), augmented the production of cytolytic granules and cytokines as well as the cytotoxicity of CD8<sup>+</sup> T cells (Fig. 1c–g). By contrast, inhibiting cholesterol biosynthesis (using the HMG-CoA reductase inhibitor lovastatin<sup>20</sup>) or cholesterol transport (U18666A; ref. 21) significantly decreased granule and cytokine productions of CD8<sup>+</sup> T cells (Extended Data Fig. 1g–i). The mRNA level of *Acat1* was approximately 20 times that of *Acat2* in CD8<sup>+</sup> T cells (Fig. 1b). The protein level of ACAT2 in CD8<sup>+</sup> T cells was nearly undetectable (Extended Data Fig. 2a). Genetic deletion of *Acat2* did not change the effector function of CD8<sup>+</sup> T cells (Fig. 1h). These data together supported the notion that ACAT1 is the major enzyme of cholesterol esterification in CD8<sup>+</sup> T cells, and inhibiting its activity can significantly potentiate the effector function of the cells. Given its unique function in CD8<sup>+</sup> T cells, we conditionally knocked out *Acat1* in T cells to test whether the ACAT1 deficiency could lead to better antitumour immunity.

We crossed *Acat1*<sup>fllox/flox</sup> mice with *CD4*<sup>cre</sup> mice to generate mice with T-cell-specific depletion of *Acat1* (termed *Acat1*<sup>CKO</sup> mice) (Extended Data Fig. 2b). The transcriptional level of *Acat2* in T cells was not changed in the *Acat1*<sup>CKO</sup> mice (Extended Data Fig. 2c, d). ACAT1 deficiency did not affect thymocyte development or peripheral T-cell homeostasis (Extended Data Fig. 3a–j). Most of the peripheral T cells were maintained as naive cells (CD62L<sup>hi</sup>CD44<sup>lo</sup>). The resting wild-type and *Acat1*<sup>CKO</sup> CD8 memory T cells showed comparable levels of cytokine production. Upon activation, the effector function of *Acat1*<sup>CKO</sup> CD8<sup>+</sup> T cells was significantly enhanced as compared to wild-type CD8<sup>+</sup> T cells (Fig. 2a–c). CD8<sup>+</sup> T-cell proliferation and survival were also promoted by ACAT1 deficiency (Extended Data Fig. 3k–n).

<sup>1</sup>State Key Laboratory of Molecular Biology, National Center for Protein Science Shanghai, Shanghai Science Research Center, Institute of Biochemistry and Cell Biology, Shanghai Institutes for Biological Sciences, Chinese Academy of Sciences, Shanghai 200031, China. <sup>2</sup>State Key Laboratory of Molecular Biology, CAS Center for Excellence in Molecular Cell Science, Institute of Biochemistry and Cell Biology, Shanghai Institutes for Biological Sciences, Chinese Academy of Sciences, Shanghai 200031, China. <sup>3</sup>Institute for Nutritional Sciences, Shanghai Institutes for Biological Sciences, Chinese Academy of Sciences, Shanghai 200031, China. <sup>4</sup>MOE Key Laboratory of Protein Science, School of Life Sciences, Collaborative Innovation Center for Infectious Diseases, Tsinghua University, Beijing 100084, China. <sup>5</sup>Department of Biochemistry, Geisel School of Medicine at Dartmouth, Hanover, New Haven 03755, USA. <sup>6</sup>Rheumatology and Immunology Department of ChangZheng Hospital, Second Military Medical University, Shanghai 200433, China. <sup>7</sup>Sun Yat-sen University Cancer Center, State Key Laboratory of Oncology in South China, Collaborative Innovation Center for Cancer Medicine, Guangzhou 510060, China. <sup>8</sup>College of Life Sciences, Wuhan University, Wuhan, Hubei Province 430072, China. <sup>9</sup>Department of Immunology, The University of Texas MD Anderson Cancer Center, Houston, Texas 77054, USA. <sup>10</sup>State Key Laboratory of Cell Biology, CAS Center for Excellence in Molecular Cell Science, Institute of Biochemistry and Cell Biology, Shanghai Institutes for Biological Sciences, Chinese Academy of Sciences, Shanghai 200031, China. <sup>11</sup>School of Life Science and Technology, ShanghaiTech University, 100 Haik Road, Shanghai 201210, China.

\*These authors contributed equally to this work.

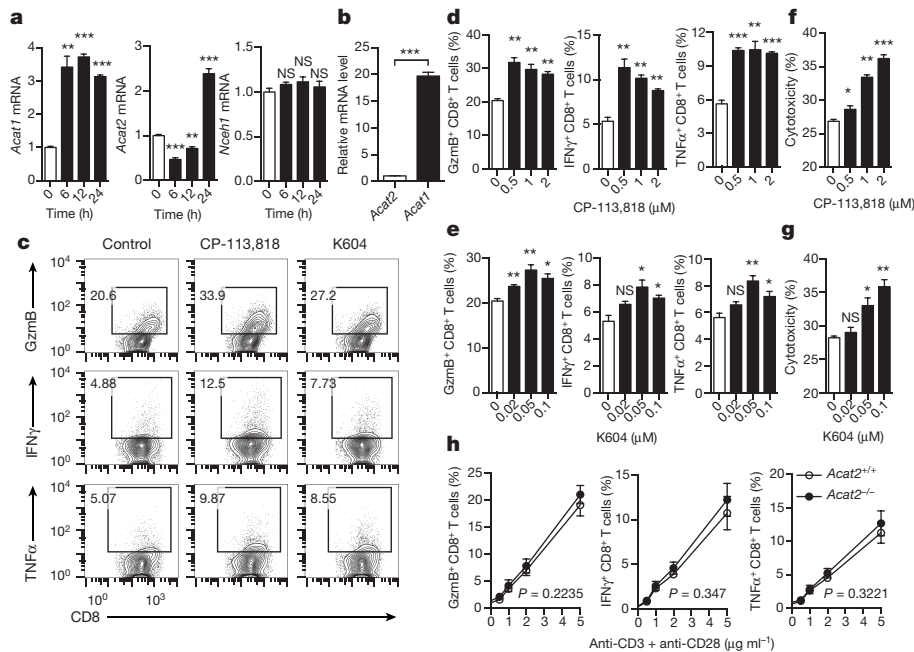


**Figure 1 | Inhibiting cholesterol esterification potentiates CD8<sup>+</sup> T-cell effector function.**

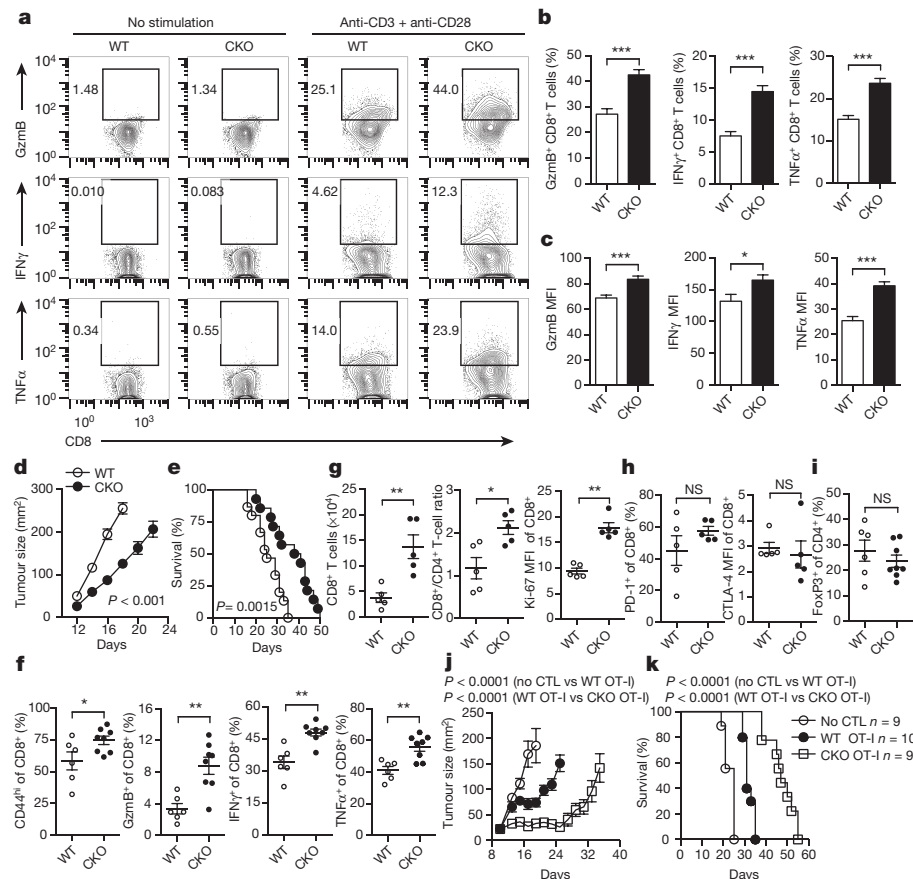
**a**, Transcriptional levels of cholesterol esterification genes *Acat1*, *Acat2* and *Nceh1* (cholesteryl ester hydrolase) in stimulated CD8<sup>+</sup> T cells ( $n = 3$ ). **b**, Relative transcriptional levels of *Acat1* and *Acat2* in naive CD8<sup>+</sup> T cells ( $n = 3$ ). **c–e**, Cytokine and cytotoxic granule production of CD8<sup>+</sup> T cells stimulated with 5 μg ml<sup>-1</sup> plate-bound anti-CD3/CD28. The cells were pretreated with vehicle (dimethylsulfoxide, DMSO), CP-113,818 or K604 ( $n = 3$ ). GzmB, granzyme B. **f**, **g**, Cytotoxicity of OT-I CTLs pretreated with CP-113,818 (**f**) or K604 (**g**) or vehicle ( $n = 3$ ). Effector:target ratio = 1:1. **h**, Cytokine/granule production of antibody-stimulated wild-type (*Acat2*<sup>+/+</sup>) or *Acat2* knockout (*Acat2*<sup>-/-</sup>) CD8<sup>+</sup> T cells ( $n = 4$ ). Data are representative of three (**a–g**) or four (**h**) independent experiments, and were analysed by unpaired *t*-test (**a–g**) or two-way analysis of variance (ANOVA) (**h**). Error bars denote s.e.m. \* $P < 0.05$ ; \*\* $P < 0.01$ ; \*\*\* $P < 0.001$ . NS, not significant.

However, *Acat1*<sup>CKO</sup> CD4<sup>+</sup> T cells had no significant enhancement of effector function (Extended Data Fig. 4a, b). This is probably due to the different metabolic programs of CD4<sup>+</sup> and CD8<sup>+</sup> T cells<sup>22</sup>. The mRNA and protein levels of *Acat2* were higher in CD4<sup>+</sup> than in CD8<sup>+</sup> T cells (Extended Data Figs 2a and 4c–e), which might partially compensate for ACAT1 deficiency. To assess whether ACAT1 regulates the CD8<sup>+</sup> T-cell immune response *in vivo*, we used *Listeria monocytogenes* to induce strong T-cell responses (Extended Data Fig. 5a–e). *Acat1*<sup>CKO</sup> mice had more IFN $\gamma$  production of CD8<sup>+</sup> T cells, higher

serum IFN $\gamma$  level and a reduced bacteria load. By contrast, the IFN $\gamma$  productions of *Acat1*<sup>CKO</sup> and wild-type CD4<sup>+</sup> T cells were comparable. We further tested the reactivity of *Acat1*<sup>CKO</sup> CD8<sup>+</sup> T cell to different antigens (Extended Data Fig. 5f, g). *Acat1*<sup>CKO</sup> mice were crossed with OT-I TCR transgenic mice (named *Acat1*<sup>CKO</sup> OT-I mice). ACAT1 deficiency potentiated the effector function of *Acat1*<sup>CKO</sup> OT-I CD8<sup>+</sup> T cells when stimulated with strong or weak antigens (OVA<sub>257–264</sub> (N4), A2, T4 or G4), but did not result in reactivity to self-antigen Catnb or positive-selection-supporting antigen R4 (ref. 23). We also found that

**Figure 2 | ACAT1 deficiency potentiates the antitumour activity of CD8<sup>+</sup> T cells.**

**a–c**, Cytokine/granule productions of antibody-stimulated wild-type (WT) and *Acat1*<sup>CKO</sup> (CKO) CD8<sup>+</sup> T cells ( $n = 8$ ). **d**, **e**, Survival (**e**) and tumour growth (**d**) in wild-type and CKO mice after B16F10 melanoma inoculation (**d**, WT,  $n = 9$ ; CKO,  $n = 8$ ; **e**, WT,  $n = 15$ ; CKO,  $n = 14$ ). Source Data relating to tumour growth is available online. **f**, **g**, Phenotypic analysis of tumour-infiltrating T cells at day 16 after melanoma inoculation (**f**, WT,  $n = 6$ ; CKO,  $n = 8$ ; **g**,  $n = 5$ ). MFI, median fluorescence intensity. **h**, **i**, PD-1 and CTLA-4 surface levels of tumour-infiltrating CD8<sup>+</sup> T cells ( $n = 5$ ) (**h**) and T<sub>reg</sub> (CD4<sup>+</sup> FoxP3<sup>+</sup>) cell percentage of tumour-infiltrating CD4<sup>+</sup> T cells (WT,  $n = 6$ ; CKO,  $n = 8$ ) (**i**). **j**, **k**, Survival and tumour sizes of B16F10-OVA tumour-bearing mice after adoptive transfer of wild-type or CKO OT-I CTLs. Data are representative of two (**g**, **h**), three (**d–f**) or five (**a–c**) independent experiments, and were analysed by Mann–Whitney test (**b**, **c**, **f–i**), log-rank (Mantel–Cox) test (**e**, **k**), or two-way ANOVA (**d**, **j**). Error bars denote s.e.m. \* $P < 0.05$ ; \*\* $P < 0.01$ ; \*\*\* $P < 0.001$ .





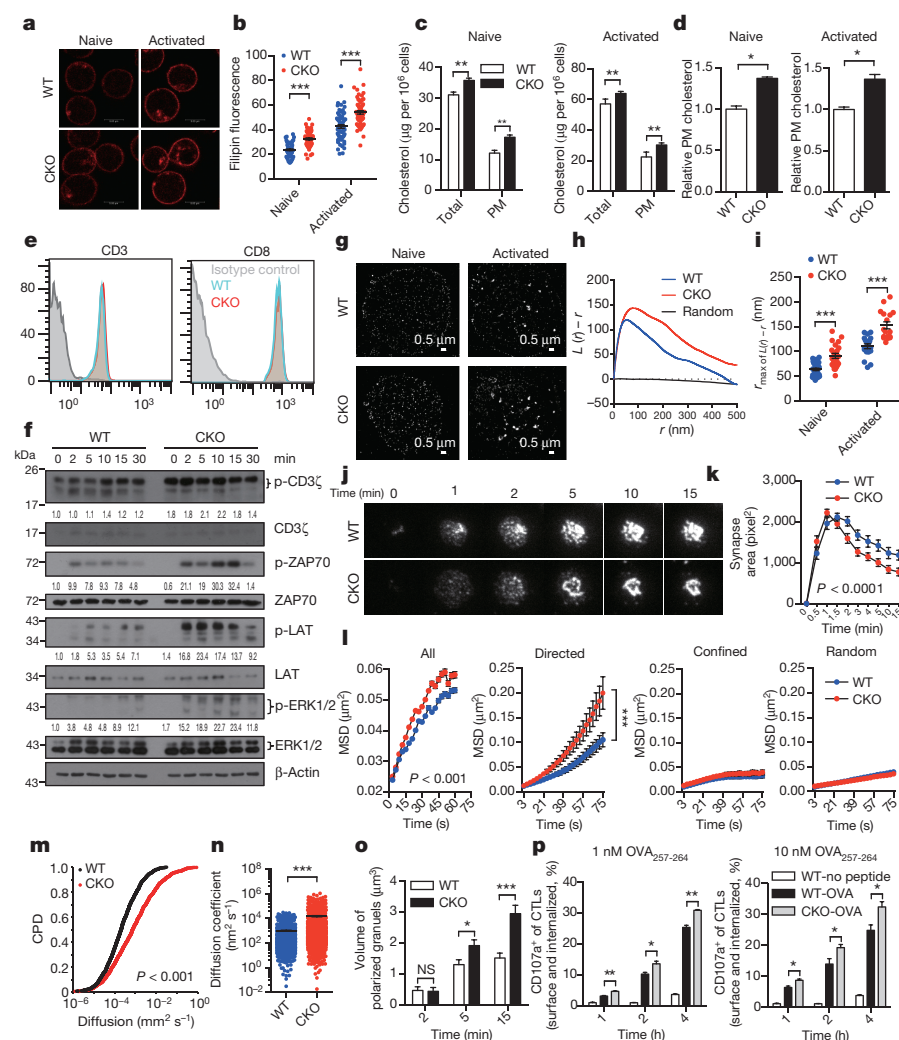


**Figure 3 | Plasma membrane cholesterol modulates TCR clustering and immunological synapse formation.** **a–d**, Cholesterol quantification of naive and activated CD8<sup>+</sup> T cells by filipin III staining (**a**, **b**), oxidation-based method (**c**) or biotinylation-based method (**d**) (**a**, **b**,  $n = 60$ ; **c**, **d**,  $n = 4$ ). PM, plasma membrane. **e**, CD3 and CD8 surface levels of naive wild-type and CKO CD8<sup>+</sup> T cells. **f**, TCR signalling of naive CD8<sup>+</sup> T cells stimulated with 4 μg ml<sup>-1</sup> anti-CD3/CD28. See Supplementary Fig. 1 for gel source data. **g–i**, STORM analysis of TCR clustering in naive and activated CD8<sup>+</sup> T cells. **g**, Representative images. **h**, Ripley's  $K$ -function analysis of TCR molecules.  $r$ , radius. **i**, The  $r$  value at the maximal  $L(r) - r$  value of Ripley's  $K$ -function curves (naive, WT,  $n = 29$ , CKO,  $n = 22$ ; activated, WT,  $n = 19$ , CKO,  $n = 17$ ). **j**, **k**, Total internal reflection fluorescence microscopy (TIRFM) analysis of immunological synapse of CD8<sup>+</sup> T cells on stimulatory planar lipid bilayer. **j**, Representative images. **k**, Immunological synapse area ( $n = 13$  cells). **l–n**, Parameters of TCR microcluster movements of CD8<sup>+</sup> T cells. **l**, Mean square displacements (MSD). TCR microcluster movements were split into directed, confined and random movements. **m**, Cumulative probability distribution (CPD). **n**, Mean scattered plots of diffusion coefficient. TCR microclusters were from 19 WT and 20 CKO cells. **o**, **p**, Cytolytic granule polarization (**o**,  $n = 50$ ) and degranulation (**p**,  $n = 3$ ) of OT-I CTLs. Data are representative of two (**a–c**, **j–n**, **p**) or three (**f–i**, **o**) independent experiments, and were analysed by unpaired  $t$ -test (**c**, **d**, **p**), Mann-Whitney test (**b**, **i**, **n**, **o**), two-way ANOVA (**k**, **l**) or Kolmogorov–Smirnov test (**m**). Error bars denote s.e.m. \* $P < 0.05$ ; \*\* $P < 0.01$ ; \*\*\* $P < 0.001$ .

the serum anti-double-stranded DNA (anti-dsDNA) IgG and IFN $\gamma$  levels of wild-type and *Acat1*<sup>CKO</sup> mice were comparable (Extended Data Fig. 3g, h), consistent with normal T-cell homeostasis (Extended Data Fig. 3) and organ size of *Acat1*<sup>CKO</sup> mice. These data suggest that ACAT1 deficiency might not cause autoimmunity.

A skin melanoma model and a lung metastasis melanoma model were used to study the activity of *Acat1*<sup>CKO</sup> CD8<sup>+</sup> T cells in controlling tumour progression and metastasis. In the skin model, *Acat1*<sup>CKO</sup> mice had a smaller tumour size and longer survival time (Fig. 2d, e). In the early stage of tumour progression (7 days after B16F10 melanoma inoculation), we analysed T-cell activation in draining lymph nodes. In *Acat1*<sup>CKO</sup> mice, CD8<sup>+</sup> T cells showed stronger activation phenotypes with higher CD44 levels and more IFN $\gamma$  production. The CD8<sup>+</sup> T-cell number and CD8<sup>+</sup>/CD4<sup>+</sup> T-cell ratio were also significantly increased (Extended Data Fig. 6a–c). In the advanced tumour stage (16 days after inoculation), we analysed the tumour-infiltrating T cells and found that CD8<sup>+</sup> T cells had better activity, increased cell numbers, and higher Ki-67 levels. The CD8<sup>+</sup>/CD4<sup>+</sup> T-cell ratio also increased (Fig. 2f, g). Notably, PD-1 and CTLA-4 levels of CD8<sup>+</sup> T cells and the proportion of regulatory T (T<sub>reg</sub>) cells (CD4<sup>+</sup>FoxP3<sup>+</sup>) were not affected by ACAT1 deficiency (Fig. 2h, i). In the lung metastasis model, the *Acat1*<sup>CKO</sup> mice developed fewer lung tumours and experienced longer survival times (Extended Data Fig. 6d–g). The lung-infiltrating CD8<sup>+</sup> T cells of the *Acat1*<sup>CKO</sup> mice had higher activity than those of wild-type mice (Extended Data Fig. 6h, i). Besides melanoma, ACAT1 deficiency also significantly attenuated the tumour progression in the Lewis lung carcinoma model (Extended Data Fig. 6j–l). To confirm the intrinsic role of ACAT1 in CD8<sup>+</sup> T-cell function further, we did an adoptive

T-cell transfer therapy for melanoma. Compared with wild-type, the transferred *Acat1*<sup>CKO</sup> OT-I cytotoxic T lymphocytes (CTLs) showed stronger antitumour activity, evidenced by smaller tumour size and a longer survival time of recipient mice (Fig. 2j, k).

Next, we sought to determine the underlying mechanism for the potentiated effector function and enhanced proliferation of ACAT1-deficient CD8<sup>+</sup> T cells. The plasma membrane cholesterol level of *Acat1*<sup>CKO</sup> CD8<sup>+</sup> T cells was substantially higher than that of wild-type T cells (Fig. 3a–d). By contrast, the plasma membrane cholesterol levels of CD4<sup>+</sup> T cells were comparable between *Acat1*<sup>CKO</sup> and wild-type mice (Extended Data Fig. 4f). This intriguing difference suggests that the increase in the plasma membrane cholesterol level may be an important cause for the augmented function of ACAT1-deficient CD8<sup>+</sup> T cells. As cholesterol is required for TCR clustering<sup>13,14</sup>, we tested whether a higher plasma membrane cholesterol level could lead to stronger TCR signalling, a major signal responsible for T-cell activation and proliferation. Indeed, TCR signalling of *Acat1*<sup>CKO</sup> CD8<sup>+</sup> T cells was largely enhanced compared with wild type, whereas the surface levels of TCR and CD8 of naive *Acat1*<sup>CKO</sup> CD8<sup>+</sup> T cells were not increased (Fig. 3e, f). Using super-resolution imaging, we found that TCR microclusters of both naive and activated *Acat1*<sup>CKO</sup> CD8<sup>+</sup> T cells were significantly larger than those of wild-type cells (Fig. 3g–i), which can enhance the avidity but not the affinity of TCRs to tumour antigens and lead to the formation of a bigger TCR signalosome<sup>24</sup>. We also studied the immunological synapse formation of *Acat1*<sup>CKO</sup> CD8<sup>+</sup> T cells because cholesterol is a key synapse component<sup>15</sup>. The immunological synapse is crucial for polarized secretion of CD8<sup>+</sup> T-cell cytolytic granules to kill target cells but not bystander cells<sup>25</sup>.

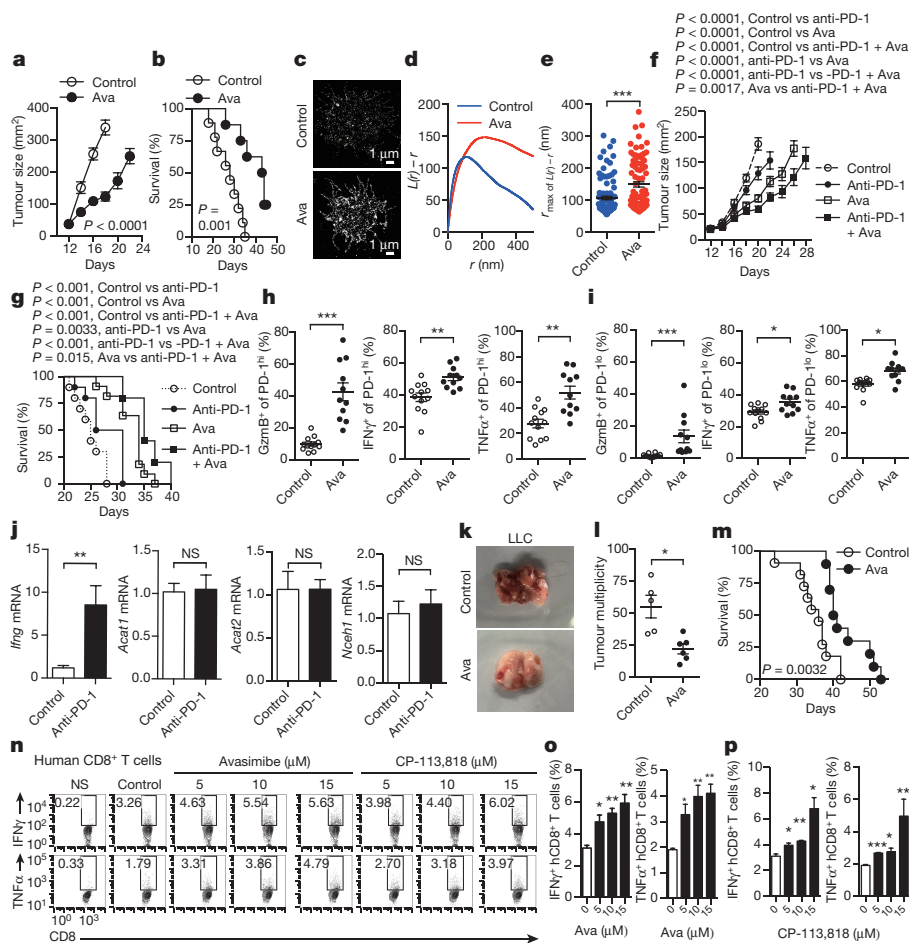


**Figure 4 | Cancer immunotherapies in mice with the ACAT inhibitor avasimibe.** **a, b,** Melanoma-bearing mice were treated with avasimibe (Ava) or DMSO control (5 times) (control,  $n = 9$ ; avasimibe,  $n = 8$ ). **c–e,** STORM analysis of TCR clustering of tumour-infiltrating CD8<sup>+</sup> T cells. **c,** Representative images. **d,** Ripley's K-function analysis of TCR molecules. **e,** The  $r$  value at the maximal  $L(r) - r$  value of Ripley's K-function curves (control,  $n = 100$ ; avasimibe,  $n = 85$ ). **f, g,** A combined therapy (avasimibe and anti-PD-1) or monotherapies (avasimibe or anti-PD-1) in treating melanoma ( $n = 10$ ). Avasimibe, 5 times; anti-PD-1, 4 times. **h, i,** Cytokine/granule productions of PD-1<sup>hi</sup> and PD-1<sup>lo</sup> tumour-infiltrating CD8<sup>+</sup> T cells (control,  $n = 12$ ; avasimibe,  $n = 11$ ). **j,** The effect of anti-PD-1 on the cholesterol esterification pathway. Melanoma-bearing mice were treated with anti-PD-1, and transcriptional levels of *Acat1*, *Acat2*, *Nceh1* and *Ifng* in tumour-infiltrating CD8<sup>+</sup> T cells were measured ( $n = 5$ ). **k–m,** Lewis lung carcinoma-bearing mice were treated with avasimibe or DMSO control (8 times). **l,** Tumour multiplicity on day 35 (control,  $n = 5$ ; avasimibe,  $n = 6$ ). **m,** Survival (control,  $n = 11$ ; avasimibe,  $n = 10$ ). **n–p,** Cytokine productions of stimulated human (h) CD8<sup>+</sup> T cells pretreated with avasimibe, CP-113,818 or DMSO ( $n = 3$ ). Data are representative of two (**f, g, n–p**) or three (**a, b, j**) independent experiments, and were analysed by log-rank (Mantel–Cox) test (**b, g, m**), two-way ANOVA (**a**, before day 18; **f**, before day 20), Mann–Whitney test (**e, h–j, l**), or unpaired  $t$ -test (**o, p**). Error bars denote s.e.m. \* $P < 0.05$ ; \*\* $P < 0.01$ ; \*\*\* $P < 0.001$ .

Using live-cell imaging, we found that ACAT1 deficiency led to faster directed movement of TCR microclusters towards the centre of the synapse (Fig. 3j–n). The mature immunological synapse of *Acat1*<sup>CKO</sup> CD8<sup>+</sup> T cells had a more compact structure, formed at a faster rate (Fig. 3j, k and Supplementary Video 1). Consequently, the cytolytic granule polarization and degranulation level were augmented in *Acat1*<sup>CKO</sup> CD8<sup>+</sup> T cells (Fig. 3o, p). Therefore, the more efficient establishment of a mature immunological synapse helps to explain the more potent killing capability of the ACAT1-deficient CD8<sup>+</sup> T cells<sup>25</sup>.

To study why the plasma membrane cholesterol level of *Acat1*<sup>CKO</sup> CD8<sup>+</sup> T cells was raised, we checked the transcriptional level of cholesterol metabolism genes. ACAT1 deficiency led to higher mRNA levels of cholesterol biosynthesis genes in both naive and activated CD8<sup>+</sup> T cells, whereas the mRNA levels of cholesterol transport and efflux genes underwent modest changes (Extended Data Fig. 2e). ACAT1 deficiency therefore not only caused less conversion of free cholesterol to cholesteryl esters, but might also cause more cholesterol biosynthesis, which could result in the higher cholesterol level<sup>5</sup>. To demonstrate that the higher cholesterol level of *Acat1*<sup>CKO</sup> CD8<sup>+</sup> T cells is the cause of the potentiated effector function, we performed membrane cholesterol modulation experiments. Depletion of plasma membrane cholesterol using methyl- $\beta$ -cyclodextrin (M $\beta$ CD) led to impaired effector function of CD8<sup>+</sup> T cells. The addition of plasma membrane cholesterol using M $\beta$ CD-coated cholesterol led to potentiated effector function. Notably, M $\beta$ CD-coated cholesterol treatment did not change the TCR surface level but significantly enhanced TCR clustering and signalling (Extended Data Fig. 7). These data further highlight the importance of the plasma membrane cholesterol level increase in the gain-of-function phenotype of *Acat1*<sup>CKO</sup> CD8<sup>+</sup> T cells.

We further studied whether ACAT1 deficiency affected energy metabolism. The glycolysis, oxidation phosphorylation and fatty acid oxidation levels of naive *Acat1*<sup>CKO</sup> and wild-type CD8<sup>+</sup> T cells were comparable (Extended Data Fig. 2f, g). We also studied the homing of *Acat1*<sup>CKO</sup> CD8<sup>+</sup> T cells to secondary lymphoid organs (Extended Data Fig. 8). The surface expression levels of homing receptor CCR7 and CD62L were comparable between naive wild-type and *Acat1*<sup>CKO</sup> CD8<sup>+</sup> T cells. After an injection of mixed wild-type and *Acat1*<sup>CKO</sup> CD8<sup>+</sup> T cells into melanoma-bearing mice, *Acat1*<sup>CKO</sup> cells had a slightly higher ratio in blood and secondary lymphoid organs, which was probably due to the better survival of *Acat1*<sup>CKO</sup> cells (Extended Data Fig. 3m, n). In addition, we did not observe that *Acat1*<sup>CKO</sup> cells had enhanced homing to tumour-draining lymph nodes compared with non-draining lymph nodes.

Finally, we tested the potential application of ACAT1 as a drug target for cancer immunotherapy. Avasimibe, an ACAT inhibitor with a good safety profile in humans, was used previously to treat atherosclerosis in clinical trials and in animal models of Alzheimer disease<sup>6,7,26</sup>. Like other ACAT1 inhibitors (Fig. 1d–g), avasimibe can enhance the effector function of mouse CD8<sup>+</sup> T cells *ex vivo* (Extended Data Fig. 9a, b). Of note, avasimibe treatment did not change melanoma cell viability (Extended Data Fig. 9c). The plasma membrane cholesterol level of avasimibe-treated CD8<sup>+</sup> T cells was substantially increased (Extended Data Fig. 9d, e). Consequently, TCR clustering and signalling as well as immunological synapse formation were significantly augmented (Extended Data Fig. 9f–k). We treated melanoma-bearing mice with avasimibe via multiple intraperitoneal injections. The phenotypes of avasimibe-treated mice were consistent with those of *Acat1*<sup>CKO</sup> mice. Tumour growth was inhibited and survival time was prolonged (Fig. 4a, b). The number of tumour-infiltrating CD8<sup>+</sup> T cells in avasimibe-treated mice increased, and these cells showed



potentiated effector function and enhanced proliferation (Extended Data Fig. 10a, b). The population of effector/effector memory CD8<sup>+</sup> T cells was substantially increased after avasimibe treatment, whereas the population of central memory cells remained unchanged (Extended Data Fig. 10c). The checkpoint receptor surface levels of tumour-infiltrating CD8<sup>+</sup> T cells were not affected by avasimibe treatment, while the TCR surface level was increased (Extended Data Fig. 10d). T<sub>reg</sub> and myeloid-derived suppressor cell populations in the tumour microenvironment were not changed (Extended Data Fig. 10e). Moreover, TCR clustering was significantly enhanced (Fig. 4c–e). We further tested a combined therapy of avasimibe and anti-PD-1 antibody. The combined therapy had a better efficacy than monotherapies in inhibiting tumour progression and in increasing survival (Fig. 4f, g). Avasimibe monotherapy potentiated the effector function of both PD-1<sup>hi</sup> and PD-1<sup>lo</sup> CD8<sup>+</sup> T cells in the tumour microenvironment (Fig. 4h, i). The monotherapy of anti-PD-1 clearly increased the IFN $\gamma$  production of tumour-infiltrating CD8<sup>+</sup> T cells, but did not alter the transcriptional levels of *Acat1* and other cholesterol esterification genes (Fig. 4j). These data show that avasimibe and anti-PD-1 act through different pathways and have additive effects in cancer immunotherapy. Besides melanoma, avasimibe also showed good antitumour effect in the Lewis lung carcinoma model (Fig. 4k–m). Moreover, we found that avasimibe can enhance the cytokine production of human CD8<sup>+</sup> T cells (Fig. 4n–p).

This study presents a new concept of cancer immunotherapy through the modulation of T-cell cholesterol metabolism. Activated CD8<sup>+</sup> T cells reprogram the cholesterol metabolism and synthesize more free cholesterol to support rapid cell proliferation<sup>16</sup>. We show here that inhibiting activity of the key cholesterol esterification enzyme ACAT1 can upregulate the plasma membrane cholesterol level of CD8<sup>+</sup> T cells. This leads to enhanced TCR clustering and signalling as well as more efficient formation of the immunological synapse. Consequently, the production of cytokines and cytolytic granules, and killing and proliferation of ACAT1-deficient CD8<sup>+</sup> T cells are all significantly enhanced. Inhibiting ACAT1 has been demonstrated to offer benefits in treating cardiovascular and neurodegenerative diseases<sup>6,7,26</sup>, and we show that it can offer an additional benefit in treating cancer. ACAT1 inhibition can be used to complement current therapies such as immune checkpoint blockade<sup>3,4,8,27–30</sup> because it acts through a different mechanism.

**Online Content** Methods, along with any additional Extended Data display items and Source Data, are available in the online version of the paper; references unique to these sections appear only in the online paper.

**Received 25 May 2015; accepted 10 February 2016.**

**Published online 16 March 2016.**

1. Fridman, W. H., Pages, F., Sautès-Fridman, C. & Galon, J. The immune contexture in human tumours: impact on clinical outcome. *Nature Rev. Cancer* **12**, 298–306 (2012).
2. Tumeh, P. C. *et al.* PD-1 blockade induces responses by inhibiting adaptive immune resistance. *Nature* **515**, 568–571 (2014).
3. Mellman, I., Coukos, G. & Dranoff, G. Cancer immunotherapy comes of age. *Nature* **480**, 480–489 (2011).
4. Joyce, J. A. & Fearon, D. T. T cell exclusion, immune privilege, and the tumor microenvironment. *Science* **348**, 74–80 (2015).
5. Chang, T. Y., Chang, C. C., Ohgami, N. & Yamauchi, Y. Cholesterol sensing, trafficking, and esterification. *Annu. Rev. Cell Dev. Biol.* **22**, 129–157 (2006).
6. Chang, T. Y., Li, B. L., Chang, C. C. & Urano, Y. Acyl-coenzyme A:cholesterol acyltransferases. *Am. J. Physiol. Endocrinol. Metab.* **297**, E1–E9 (2009).
7. Pal, P., Gandhi, H., Giridhar, R. & Yadav, M. R. ACAT inhibitors: the search for novel cholesterol lowering agents. *Mini Rev. Med. Chem.* **13**, 1195–1219 (2013).
8. Yao, S., Zhu, Y. & Chen, L. Advances in targeting cell surface signalling molecules for immune modulation. *Nature Rev. Drug Discov.* **12**, 130–146 (2013).
9. Sharma, P. & Allison, J. P. The future of immune checkpoint therapy. *Science* **348**, 56–61 (2015).

10. Xu, C. *et al.* Regulation of T cell receptor activation by dynamic membrane binding of the CD3 $\epsilon$  cytoplasmic tyrosine-based motif. *Cell* **135**, 702–713 (2008).
11. Shi, X. *et al.* Ca<sup>2+</sup> regulates T-cell receptor activation by modulating the charge property of lipids. *Nature* **493**, 111–115 (2013).
12. Gagnon, E., Schubert, D. A., Gordo, S., Chu, H. H. & Wucherpfennig, K. W. Local changes in lipid environment of TCR microclusters regulate membrane binding by the CD3 $\epsilon$  cytoplasmic domain. *J. Exp. Med.* **209**, 2423–2439 (2012).
13. Molnár, E. *et al.* Cholesterol and sphingomyelin drive ligand-independent T-cell antigen receptor nanoclustering. *J. Biol. Chem.* **287**, 42664–42674 (2012).
14. Schamel, W. W. *et al.* Coexistence of multivalent and monovalent TCRs explains high sensitivity and wide range of response. *J. Exp. Med.* **202**, 493–503 (2005).
15. Zech, T. *et al.* Accumulation of raft lipids in T-cell plasma membrane domains engaged in TCR signalling. *EMBO J.* **28**, 466–476 (2009).
16. Kidani, Y. *et al.* Sterol regulatory element-binding proteins are essential for the metabolic programming of effector T cells and adaptive immunity. *Nature Immunol.* **14**, 489–499 (2013).
17. Leon, C., Hill, J. S. & Wasan, K. M. Potential role of acyl-coenzyme A:cholesterol transferase (ACAT) inhibitors as hypolipidemic and antiatherosclerosis drugs. *Pharm. Res.* **22**, 1578–1588 (2005).
18. Chang, C. C. *et al.* Immunological quantitation and localization of ACAT-1 and ACAT-2 in human liver and small intestine. *J. Biol. Chem.* **275**, 28083–28092 (2000).
19. Ikenoya, M. *et al.* A selective ACAT-1 inhibitor, K-604, suppresses fatty streak lesions in fat-fed hamsters without affecting plasma cholesterol levels. *Atherosclerosis* **191**, 290–297 (2007).
20. Tobert, J. A. Lovastatin and beyond: the history of the HMG-CoA reductase inhibitors. *Nature Rev. Drug Discov.* **2**, 517–526 (2003).
21. Cenedella, R. J. Cholesterol synthesis inhibitor U18666A and the role of sterol metabolism and trafficking in numerous pathophysiological processes. *Lipids* **44**, 477–487 (2009).
22. MacIver, N. J., Michalek, R. D. & Rathmell, J. C. Metabolic regulation of T lymphocytes. *Annu. Rev. Immunol.* **31**, 259–283 (2013).
23. Santori, F. R. *et al.* Rare, structurally homologous self-peptides promote thymocyte positive selection. *Immunity* **17**, 131–142 (2002).
24. Lillemeier, B. F. *et al.* TCR and Lat are expressed on separate protein islands on T cell membranes and concatenate during activation. *Nature Immunol.* **11**, 90–96 (2010).
25. Beal, A. M. *et al.* Kinetics of early T cell receptor signaling regulate the pathway of lytic granule delivery to the secretory domain. *Immunity* **31**, 632–642 (2009).
26. Huttunen, H. J. & Kovacs, D. M. ACAT as a drug target for Alzheimer's disease. *Neurodegener. Dis.* **5**, 212–214 (2008).
27. Page, D. B., Postow, M. A., Callahan, M. K., Allison, J. P. & Wolchok, J. D. Immune modulation in cancer with antibodies. *Annu. Rev. Med.* **65**, 185–202 (2014).
28. Pardoll, D. M. The blockade of immune checkpoints in cancer immunotherapy. *Nature Rev. Cancer* **12**, 252–264 (2012).
29. Rosenberg, S. A. & Restifo, N. P. Adoptive cell transfer as personalized immunotherapy for human cancer. *Science* **348**, 62–68 (2015).
30. Schumacher, T. N. & Schreiber, R. D. Neoantigens in cancer immunotherapy. *Science* **348**, 69–74 (2015).

**Supplementary Information** is available in the online version of the paper.

**Acknowledgements** We thank Q. Leng for providing *L. monocytogenes*, F.-J. Nan for providing K604, and Y. Jiang for some preliminary experiments. We thank H. Gu and D. Li for careful reading of the manuscript. Imaging work was performed at the National Center for Protein Science Shanghai. Chenqi Xu is funded by MOST (2011CB910901 and 2012CB910804), NSFC grants (31370860, 31425009 and 31530022), and CAS grants (Strategic Priority Research Program XDB08020100; KSCX2-EW-J-11). B.L. is funded by MOST (2011CB910901) and NSFC grant 31271377. W.Y. is funded by NSFC grant (31400745) and China Postdoctoral Science Foundation (2014M561533 and 2014T770440). T.-Y.C. and C.C.Y.C. are funded by NIH grant HL 60306.

**Author Contributions** Chenqi Xu conceived the project. B.L., X.L., S.S., B.-L.S., W.Y. and Y.X. contributed to the design of the project and extensive discussions. P.Z. provided technical help on the tumour models. T.-Y.C. and C.C.Y.C. generated *Acat1*<sup>lox/lox</sup> mice. W.Y., Y.B., X.Z., J.Z., X.M. and L.L. performed the *ex vivo* T-cell experiments and animal experiments. W.Y. and S.C. performed the STORM experiments. Y.B. performed the TIRFM experiments. T.Z. provided human cells. J.Z. and T.Z. performed the human cell experiments. W.L., J.W. and Chenguang Xu helped with the TIRFM setup and data analysis. L.W. helped with the cholesterol staining and quantification. Chenqi Xu, W.Y. and Y.B. wrote the manuscript. Other authors revised the manuscript.

**Author Information** Reprints and permissions information is available at [www.nature.com/reprints](http://www.nature.com/reprints). The authors declare no competing financial interests. Readers are welcome to comment on the online version of the paper. Correspondence and requests for materials should be addressed to C.X. (cxqu@sibcb.ac.cn) or B.-L.L. (bli@sibcb.ac.cn).

## METHODS

**Reagents and mice.** Filipin III was from Sigma. Amplex Red cholesterol assay kit was from Invitrogen. IL-2 was from Promega. For the flow cytometric analysis, anti-mCD4 (RM4-5), anti-mCD8 (53-6.7), anti-mCD3 $\epsilon$  (145-2C11), anti-IFN $\gamma$  (XMG1.2), anti-TNF $\alpha$  (MP6-XT22), anti-granzyme B (NGZB), anti-CD44 (IM7), anti-CD69 (H1.2F3), anti-PD-1 (J43), anti-CTLA-4 (UC10-4B9), anti-Ki-67 (16A8), anti-FoxP3 (FJK-16s), anti-Gr1 (RB6-8C5), anti-CD11b (M1/70) and anti-CD45 (30-F11) were purchased from eBioscience. For western blots, anti-pCD3 $\zeta$ , anti-CD3 $\zeta$ , anti-pZAP70, anti-ZAP70, anti-pLAT, anti-LAT, anti-pERK1/2 and anti-ERK1/2 were from Cell Signaling Technology. Avasimibe was from Selleck. M $\beta$ CD-cholesterol and M $\beta$ CD were from Sigma. Lovastatin was from Sigma. U18666A was from Merck. K604 was chemically synthesized in F.-J. Nan's laboratory. CP113,818 was a research gift from P. Fabre. MTS (3-(4,5-dimethylthiazol-2-yl)-5-(3-carboxymethoxyphenyl)-2-(4-sulfophenyl)-2H-tetrazolium) was from Promega. B16F10, Lewis lung carcinoma and EL-4 cell lines were originally obtained from the American Type Culture Collection, and proved mycoplasma-free. *Listeria monocytogenes* was provided by Q. Leng.

C57BL/6 mice were purchased from SLAC. OT-I TCR transgenic mice were from the Jackson Laboratory. *CD4<sup>cre</sup>* transgenic mice was described previously<sup>31</sup>. InGeneious Labs produced homozygous *Acat1<sup>loxP/loxP</sup>* mouse. To produce this mouse, the *Acat1 loxP* construct was made by inserting two *loxP* sites covering *Acat1* exon 14, which includes His460 known to be essential for the enzymatic activity<sup>32</sup>. The construct was injected into embryonic stem cells. The correctly targeted clones as determined by Southern blot and diagnostic PCR were injected into C57BL/6 blastocysts. To remove the Neo marker, the mice were further backcrossed to the C57BL/6 Frt mice. Through mouse crossing, the wild-type *Acat1* allele (*Acat1<sup>+/+</sup>*), heterozygous *Acat1 loxP* allele (*Acat1<sup>loxP/+</sup>*) and homozygous *Acat1 loxP* allele (*Acat1<sup>loxP/loxP</sup>*) were obtained and confirmed by using diagnostic PCR. *Acat1<sup>loxP/loxP</sup>* mice were crossed with *CD4<sup>cre</sup>* transgenic mice to get *Acat1<sup>CKO</sup>* mice with ACAT1 deficiency in T cells. *Acat1<sup>CKO</sup>* mice were further crossed with OT-I TCR transgenic mice to get *Acat1<sup>CKO</sup>* OT-I mice. Animal experiments using *Acat1<sup>CKO</sup>* mice were controlled by their littermates with normal ACAT1 expression (*Acat1<sup>loxP/loxP</sup>*). Animal experiments using *Acat1<sup>CKO</sup>* OT-I mice were controlled by their littermate with normal ACAT1 and OT-I TCR expression (*Acat1<sup>loxP/loxP</sup>* OT-I). *Acat2<sup>-/-</sup>* mice were purchased from Jackson Laboratory. All mice were maintained in pathogen-free facilities at the Institute of Biochemistry and Cell Biology. All animal experiments used mice with matched age and sex. Animals were randomly allocated to experimental groups. The animal experiments performed with a blinded manner were described below. All animal experiments were approved by the Institutional Animal Care and Use Committee (IACUC) of Institute of Biochemistry and Cell Biology, Shanghai Institutes for Biological Sciences, Chinese Academy of Sciences. The maximal tumour measurements/volumes are in accordance with the IACUC. All human studies have been approved by the Research Ethical Committee from ChangZheng Hospital, Shanghai, China. Informed consent was obtained from all study subjects.

**Quantitative reverse transcription PCR.** Total RNA was extracted with Trizol (Life technology) from the indicated cells and subjected to quantitative reverse transcription PCR (qRT-PCR) using gene specific primers (5'-3'): *Acat1* (forward, GAAACCGGCTGTCAAAATCTGG; reverse, TGTGACCATTCTGTATGTGTCC); *Acat2* (forward, ACAAGACAGACCTC TTCCCTC; reverse, ATGGTTCGGAAATGTTCAAC); *Nceh* (forward, TTGAATACAGGCTAGTCCCACA; reverse, CAACGTAGGTAACTG TTGTCCC); *Srebp1* (forward, GCAGCCACCCTAGCTAGCTG; reverse, CAGCAGTGAGTCTGCCTTGAT); *Srebp2* (forward, GCAGCAACGGG ACCATTCT; reverse, CCCCATGACTAAGTCTCTCAACT); *Acaca* (forward, ATGGGCGGAATGGTCTCTTC; reverse, TGGGGACCTGTCTTTCATCAT); *Fasn* (forward, GGAGGTGGTGATAGCCGGTAT; reverse, TGGGTAA TCCATAGAGCCAG); *Hmgcs* (forward, AACTGGTGCAGAAATCTTAGC; reverse, GGTGAATAGCTCAGACTAGCC); *Hmgcr* (forward, AGCTTGCCC GAATTGTATGTG; reverse, TCTGTTGTGAACCATGTGACTTC); *Sqle* (forward, ATAAGAAATGCGGGGATGTAC; reverse, ATATCCGAGAAGGCAGC GAAC); *Ldlr* (forward, TGACTCAGACGAACAAGGCTG; reverse, ATCT AGGCAATCTCGGTCTC); *Idol* (forward, TGCAGGCTGCTAGGGATCAT; reverse, GTTAAAGGCGGTAAAGGTGCCA); *Abca1* (forward, AAAACCGCA GACATCCTTCAG; reverse, CATACCGAAACTCGTTCACCC); *Abcg1* (forward, CTTTCCTACTCTGTACCCGAGG; reverse, CGGGGCATTCCATTGATA AGG); *Irfng* (forward, ATGAACGCTACACTGCATC; reverse, CCATCCTTTT GCCAGTTCCTC).

**Measurement of the cholesterol level of T cells.** Three methods were used to measure the cholesterol level of T cells.

**Filipin III staining.** Filipin III was dissolved in ethanol to reach the final concentration of 5  $\mu\text{g ml}^{-1}$ . Cells were fixed with 4% paraformaldehyde (PFA) and stained

with 50  $\mu\text{g ml}^{-1}$  filipin III for 30 min at 4°C. Images were collected using a Leica SP8 confocal microscope and analysed using a Leica LAS AF software.

**Plasma membrane cholesterol oxidation-based assay.** The total cellular cholesterol level was quantified using the Amplex Red cholesterol assay kit (Invitrogen). To quantify the intracellular cholesterol, CD8<sup>+</sup> T cells were fixed with 0.1% glutaraldehyde and then treated with 2 U ml<sup>-1</sup> cholesterol oxidase for 15 min to oxidize the plasma membrane cholesterol. The intracellular cholesterol was then extracted with methanol/chloroform (vol/vol, 1:2), and quantified using the Amplex Red cholesterol assay kit. The value of the plasma membrane cholesterol was obtained by subtracting the intracellular cholesterol from the total cellular cholesterol.

**Biotinylation-based plasma membrane lipid purification and quantification.** Plasma membrane cholesterol level was measured as previously described<sup>33</sup>. The plasma membrane of CD8<sup>+</sup> T cells was biotinylated by 1 mg ml<sup>-1</sup> sulfo-NHS-S-biotin, and then the cells were lysed by passing 13 times through a ball-bearing homogenizer. Plasma membrane was isolated from the supernatant of homogenate by streptavidin magnetic beads. Lipids were extracted with hexane/isopropanol (vol/vol, 3:2), and then were used for measurement of unesterified cholesterol with Amplex Red Cholesterol Assay Kit and choline-containing phospholipids with EnzyChrom Phospholipid Assay Kit. The relative plasma membrane cholesterol level was normalized to the total phospholipids.

**Modulation of the plasma membrane cholesterol level by M $\beta$ CD and M $\beta$ CD-coated cholesterol.** To deplete cholesterol from the plasma membrane, CD8<sup>+</sup> T cells were treated with 0.1–1 mM M $\beta$ CD for 5 min at 37°C, and then washed three times with PBS. To add cholesterol to the plasma membrane, CD8<sup>+</sup> T cells were incubated with the culture medium supplied with 1–20  $\mu\text{g ml}^{-1}$  M $\beta$ CD-coated cholesterol at 37°C for 15 min. The cells were then washed three times with PBS.

**T-cell isolation and effector function analysis.** Peripheral T cells were isolated from mouse spleen and draining lymph nodes by a CD8<sup>+</sup> or CD4<sup>+</sup> T-cell negative selection kit (Stem cell). To analyse the tumour-infiltrating T cells, tumours were first digested by collagenase IV (sigma), and tumour-infiltrating leukocytes were isolated by 40–70% Percoll (GE) gradient centrifugation. To measure the effector function of CD8<sup>+</sup> T cells, the isolated cells were first stimulated with 1  $\mu\text{M}$  ionomycin and 50 ng ml<sup>-1</sup> phorbol 12-myristate 13-acetate (PMA) for 4 h in the presence of 5  $\mu\text{g ml}^{-1}$  BFA, and then stained with PERCP-conjugated anti-CD8a. Next, cells were fixed with 4% PFA and stained with FITC-conjugated anti-granzyme B, allophycocyanin (APC)-conjugated anti-IFN $\gamma$  and phycoerythrin (PE)-conjugated anti-TNF $\alpha$ . In general, to gate the cytokine or granule-producing cells, T cells without stimulation or stained with isotype control antibody were used as negative controls. This gating strategy is applicable for most of the flow cytometric analyses. To detect the MDSC cells in the tumour, the Percoll-isolated leukocyte were stained with anti-CD45, anti-CD11b and anti-Ly6G (Gr1), the CD45<sup>+</sup> population was gated, after which the MDSC population (CD11b<sup>+</sup> Gr1<sup>+</sup>) in CD45<sup>+</sup> were gated.

**Antigen stimulation of CD8<sup>+</sup> T cells.** A pan T-cell isolation kit (Miltenyi biotech) was used to deplete T cells from splenocytes isolated from C57BL/6 mice. The T-cell-depleted splenocytes were pulsed with antigenic peptides for 2 h and washed three times. SIINFEKL (OVA<sub>257–264</sub> or N4), SAINFEKL (A2), SIITFEKL (T4), SIIGFEKL (G4) are four types of agonist antigens with strong to weak TCR affinities. RTYTYEKL (Catnb) is a self-antigen of OT-I TCR. SIIRFEKL (R4) supports the positive selection of OT-I T cells and thus mimics a self-antigen. The T-cell-depleted and antigen-pulsed splenocytes were co-incubated with *Acat1<sup>CKO</sup>* OT-I T cells or wild-type OT-I T cells for 24 h. Cytokine production of CD8<sup>+</sup> T cells was measured by intracellular staining and flow cytometric analysis.

**Measurement of CD8<sup>+</sup> T-cell cytotoxicity.** To generate mature CTLs, splenocytes isolated from *Acat1<sup>CKO</sup>* OT-I mice or wild-type OT-I mice were stimulated with OVA<sub>257–264</sub> (N4) for 3 days in the presence of 10 ng ml<sup>-1</sup> IL-2. Cells were centrifuged and cultured in fresh medium containing 10 ng ml<sup>-1</sup> IL-2 for 2 more days, after which most of the cells in the culture were CTLs. To measure CD8<sup>+</sup> T-cell cytotoxicity, EL-4 cells were pulsed with 2 nM antigenic peptide (N4, A2, T4, G4, R4 or Catnb) for 30 min. After washing EL-4 cells and CTLs three times with PBS, we mixed CTLs and antigen-pulsed EL-4 cells ( $1 \times 10^5$ ) in the killing medium (phenol-free RPMI 1640, 2% FBS), at the ratios of 1:1, 2:1 and 5:1, respectively. After 4 h, the cytotoxic efficiency was measured by quantifying the release of endogenous lactate dehydrogenase (LDH) from EL-4 cells using a CytoTox 96 Non-Radioactive Cytotoxicity kit (Promega).

**Measurement of human CD8<sup>+</sup> T-cell cytokine production.** Human peripheral blood mononuclear cells from healthy donors were stimulated with 5  $\mu\text{g ml}^{-1}$  phytohaemagglutinin (Sigma) for 2 days and then rested for 1 day. Cells were pretreated with vehicle (DMSO), CP113,818 or avasimibe for 12 h and then stimulated with 5  $\mu\text{g ml}^{-1}$  plate-bound anti-CD3 and anti-CD28 antibodies for 24 h. Intracellular staining and flow cytometry were used to measure cytokine productions of CD8<sup>+</sup> T cells.



**T-cell metabolism.** Oxygen consumption rates and extracellular acidification rates were measured in nonbuffered DMEM (sigma) containing either 25 mM or 10 mM glucose, 2 mM L-glutamine, and 1 mM sodium pyruvate, under basal conditions and in response to 1  $\mu$ M oligomycin (to block ATP synthesis), 1.5  $\mu$ M FCCP (to uncouple ATP synthesis from the electron transport chain), 0.5  $\mu$ M rotenone and antimycin A (to block complex I and III of the electron transport chain, respectively), and 200  $\mu$ M etomoxir (to block mitochondrial fatty acid oxidation) on the XF-24 or XF-96 Extracellular Flux Analyzers (Seahorse Bioscience) according to the manufacturer's recommendations.

**Measurement of cell viability with MTS assay.** B16F10 cells ( $5 \times 10^3$ ) in 100  $\mu$ l media containing avasimibe or DMSO were cultured for 24, 48 or 72 h. MTS reagent (20  $\mu$ l) (CellTiter 96 Aqueous One Solution Cell Proliferation Assay; Promega) was added into each well. After a 2–3 h incubation, the absorbance at 490 nm was measured. The effect of avasimibe on cell viability was obtained by normalizing the absorbance of avasimibe-treated cells with that of the DMSO-treated cells. The viability value of DMSO-treated cells was set as 1.

**Listeria monocytogenes infection.** *L. monocytogenes* ( $2 \times 10^4$ – $7 \times 10^4$  colony-forming units (CFU)) expressing a truncated OVA protein were intravenously injected into *Acat1*<sup>CKO</sup> and littermate wild-type mice aged 8–10 weeks. On day 6, T cells isolated from spleens were stimulated with 50 ng ml<sup>-1</sup> PMA and 1  $\mu$ M ionomycin for 4 h in the presence of brefeldin A and then assessed by flow cytometry to detect IFN $\gamma$  production. At the same time, the serum IFN $\gamma$  level was assessed by ELISA. To detect the antigen-specific response of CD8<sup>+</sup> T cells, the splenocytes were stimulated with 1  $\mu$ M OVA<sub>257–264</sub> peptide for 24 h. IFN $\gamma$  production was analysed as mentioned above. To detect the *L. monocytogenes* titre in the livers of infected mice, the livers were homogenized in 10 ml 0.2% (vol/vol) Nonidet P-40 in PBS, and the organ homogenates were diluted and plated on agar plates to determine the CFU of *L. monocytogenes*. Investigator was blinded to group allocation during the experiment and when assessing the outcome.

**Melanoma mouse models.** B16F10 cells were washed three times with PBS, and filtered through a 40- $\mu$ m strainer. In a skin melanoma model, B16F10 cells ( $2 \times 10^5$ ) were subcutaneously injected into the dorsal part of mice (aged 8–10 weeks). From day 10, tumour size was measured every 2 days, and animal survival rate was recorded every day. Tumour size was calculated as length  $\times$  width. Mice with tumour size larger than 20 mm at the longest axis were euthanized for ethical consideration. To analyse effector function of tumour-infiltrating T cells, mice were euthanized on day 16. In the avasimibe therapy, melanoma-bearing mice with similar tumour size were randomly divided into two groups. From day 10, avasimibe was injected intraperitoneally to the mice at the dose of 15 mg kg<sup>-1</sup> every 2 days.

In a lung-metastatic melanoma model, B16F10 cells ( $2 \times 10^5$ ) were intravenously injected into mice (aged 8–10 weeks). Animal survival rate was recorded every day. To study tumour growth, mice were euthanized on day 20 and tumour numbers on lungs were counted. Lung-infiltrating T cells were isolated and analysed as mentioned above. In the lung-metastatic melanoma model, investigator was blinded to group allocation during the experiment and when assessing the outcome.

**T-cell homing.** B16F10-OVA cells ( $2 \times 10^5$ ) were injected subcutaneously into C57BL/6 mice at age 8–10 weeks. On day 16, the naive wild-type or *Acat1*<sup>CKO</sup> OT-I CD8<sup>+</sup> T cells were isolated and labelled with live cell dye CFSE or CTDR (Cell Tracker Deep Red, Life Technologies), respectively. The labelled wild-type and CKO cells were mixed together at a 1:1 ratio, and  $1 \times 10^7$  mixed cells per mouse were injected intravenously into the B16F10-OVA-bearing mice. After 12 h, blood, spleens, inguinal lymph nodes (draining) and mesenteric lymph nodes (non-draining) of the mice were collected. Single-cell suspensions from these tissues were stained with the anti-CD8a antibody, and the ratio of transferred cells in CD8<sup>+</sup> populations was analysed using flow cytometry.

**Lewis lung carcinoma model.** The Lewis lung carcinoma cells were washed twice with PBS and filtered through a 40- $\mu$ m strainer. After which, the Lewis lung carcinoma cells ( $2 \times 10^6$ ) were intravenously injected into wild-type or *Acat1*<sup>CKO</sup> mice at age 8–10 weeks. To detect the tumour multiplicity in the lung, the mice were euthanized at day 35 after tumour inoculation and tumour numbers in the lung were counted. In the avasimibe therapy, mice were randomly divided into two groups. From days 10 to 35 after tumour inoculation, avasimibe was delivered to the mice by intragastric administration at the dose of 15 mg kg<sup>-1</sup> every 3 days.

**Treatment of melanoma by adoptive T-cell transfer.** B16F10-OVA cells ( $2 \times 10^5$ ) were injected subcutaneously into C57BL/6 mice at age 8–10 weeks. On day 10, melanoma-bearing mice with similar tumour size were randomly divided into three groups ( $n = 9$ – $10$ ) and respectively received PBS, wild-type OT-I CTLs ( $1.5 \times 10^6$ ) or *Acat1*<sup>CKO</sup> OT-I CTLs ( $1.5 \times 10^6$ ) by intravenous injection. From day 13, the tumour size was measured every two days, and the animal survival rate was recorded every day. Tumour size was calculated as length  $\times$  width. Mice with tumour size larger than 20 mm at the longest axis were euthanized for ethical consideration.

**Treatment of melanoma with avasimibe, anti-PD-1 antibody or avasimibe plus anti-PD-1 antibody.** B16F10 cells ( $2 \times 10^5$ ) were injected subcutaneously into C57BL/6 mice at age 8–12 weeks. On day 10, melanoma-bearing mice with similar tumour size were randomly divided into four groups ( $n = 8$ – $10$ ) and received PBS, avasimibe, anti-PD-1 antibody or both avasimibe and anti-PD-1 antibody, respectively. Avasimibe was delivered every 2 days at the dose of 15 mg kg<sup>-1</sup> by intragastric administration. Anti-PD-1 antibody (RMP1-14, Bio X Cell, 200  $\mu$ g per injection) was injected intraperitoneally every 3 days. The tumour size and survival were measured as mentioned above. Mice with tumour size larger than 20 mm at the longest axis were euthanized for ethical consideration.

**Super-resolution STORM imaging and data analysis.** Super-resolution STORM imaging was performed on a custom modified Nikon N-STORM microscope equipped with a motorized inverted microscope ECLIPSE Ti-E, an Apochromat TIRF 100  $\times$  oil immersion lens with a numerical aperture of 1.49 (Nikon), an electron multiplying charge-coupled device (EMCCD) camera (iXon3 DU-897E, Andor Technology), a quad band filter composed of a quad line beam splitter (zt405/488/561/640rpc TIRF, Chroma Technology Corporation) and a quad line emission filter (brightline HC 446, 523, 600, 677, Semrock, Inc.).

The TIRF angle was adjusted to oblique incidence excitation at the value of 3,950–4,000, allowing the capture of images at about 1  $\mu$ m depth of samples. The focus was kept stable during acquisition using Nikon focus system. For the excitation of Alexa647, the 647 nm continuous wave visible fibre laser was used, and the 405 nm diode laser (CUBE 405-100C, Coherent Inc.) was used for switching back the fluorophores from dark to the fluorescent state. The integration time of the EMCCD camera was 90–95 frames per second. To image TCR distribution in the plasma membrane, naive CD8<sup>+</sup> T cells or activated CD8<sup>+</sup> T cells (stimulated with 10  $\mu$ g ml<sup>-1</sup> anti-CD3 for 10 min at 37°C) were placed in Ibidi 35 mm  $\mu$ -Dish and fixed with 4% PFA, followed by surface staining with 5  $\mu$ g ml<sup>-1</sup> anti-mCD3 $\epsilon$  (145-2C11) for 4 h at 4°C, then the cells were stained with 2  $\mu$ g ml<sup>-1</sup> Alexa 647-conjugated goat anti-hamster IgG (the secondary antibody) for 2 h at 4°C after washing with PBS ten times. Before imaging, the buffer in the dish was replaced with the imaging buffer contained 100 mM  $\beta$ -mercaptoethanolamine (MEA) for a sufficient blinking of fluorophores.

Super-resolution images were reconstructed from a series of 20,000–25,000 frames using the N-STORM analysis module of NIS Elements AR (Laboratory imaging s.r.o.). Molecule distribution and cluster position were analysed with MATLAB (MathWorks) based on Ripley's *K* function.  $L(r) - r$  represents the efficiency of molecule clustering, and  $r$  value represents cluster radius. The  $r$  value at the maximum  $L(r) - r$  value represents the cluster size with the highest probability<sup>34</sup>.

**Imaging of immunological synapse by TIRFM.** Planar lipid bilayers (PLBs) containing biotinylated lipids were prepared to bind biotin-conjugated stimulating antibody by streptavidin as previously described<sup>35,36</sup>. Biotinylated liposomes were prepared by sonicating 1,2-dioleoyl-*sn*-glycero-3-phosphocholine and 1,2-dioleoyl-*sn*-glycero-3-phosphoethanolamine-cap-biotin (25:1 molar ratio, Avanti Polar Lipids) in PBS at a total lipid concentration of 5 mM. PLBs were formed in Lab-Tek chambers (NalgeNunc) in which the cover glasses were replaced with nanostrip-washed coverslips. Coverslips were incubated with 0.1 mM biotinylated liposomes in PBS for 20 min. After washing with 10 ml PBS, PLBs were incubated with 20 nM streptavidin for 20 min, and excessive streptavidin was removed by washing with 10 ml PBS. Streptavidin-containing PLBs were incubated with 20 nM bionylated anti-mCD3 $\epsilon$  (145-2C11) (Biolegend). Excessive antibody was removed by washing with PBS. Next, PLBs were treated with 5% FBS in PBS for 30 min at 37°C and washed thoroughly for TIRFM of T cells. Adhesion ligands necessary for immunological synapse formation were provided by treating the bilayer with serum.

Freshly isolated mouse splenocytes were stained with Alexa568-anti-mTCR $\beta$  Fab and FITC-anti-mCD8 and washed twice. Anti-mTCR $\beta$  antibody was labelled with Alexa568-NHS ester (Molecular probes) and digested to get Fab fragments with Pierce Fab Micro Preparation Kit (Thermo). Cells were then placed on anti-mCD3 $\epsilon$ -containing PLBs to crosslink TCR. Time-lapse TIRFM images were acquired on a heated stage with a 3-s interval time at 37°C, 5% CO<sub>2</sub>, using a Zeiss Axio Observer SD microscopy equipped with a TIRF port, Evolve 512 EMCCD camera and Zeiss Alpha Plan-Apochromat 100  $\times$  oil lens. The acquisition was controlled by ZEN system 2012 software. An OPSEL laser 488 nm and a DPSS laser 561 nm were used. Field of 512  $\times$  512 pixels was used to capture 6–8 CD8<sup>+</sup> T cells per image. Results of synapse formation and TCR movements were the population averages of all CD8<sup>+</sup> T cells from 2–3 individual images. The movements of TCR microclusters were splitted into directed, confined and random movement using the method described<sup>37</sup>. To sort the three movements, the MSD plot of each TCR microcluster was fitted with three functions as described<sup>37</sup>. The ones with good fit (square of correlation coefficients ( $R^2$ )  $\geq 0.33$ ) were selected for further classification. For a certain TCR microcluster, the movement is defined as random if

s.d. < 0.010. The distinction of directed and confined movement depends on which function fit better in the population of those s.d.  $\geq$  0.010. Images were analysed with Image Pro Plus software (Media Cybernetics), ImageJ (NIH) and MATLAB (MathWorks).

**Polarized secretion of cytolytic granules.** In the granule polarization imaging, CTLs stained with Alexa568-anti-mTCR $\beta$  Fab were placed on anti-mCD3 $\epsilon$ -containing PLBs for indicated time and fixed with 4% PFA. After the permeabilization, cells were stained with Alexa488-anti-mCD107a (1D4B) antibody. Three-dimensional spinning-disc confocal microscopy was used to image the granules polarized at 0–2  $\mu$ m distance from the synapse. The total granule volumes were quantified with Imaris software.

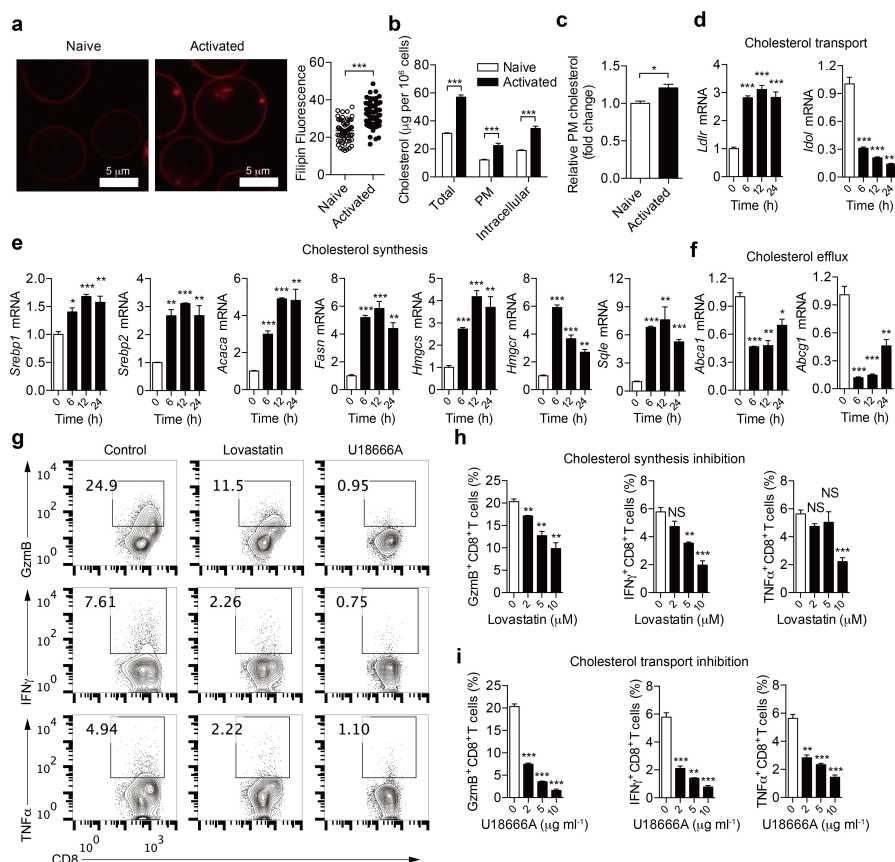
The degranulation level was measured as previously described<sup>38</sup>. OT-I CTLs were mixed with OVA<sub>257–264</sub> pulsed EL4 cells at 1:1 ratio. The mixed cells were then cultured in the medium supplemented with 1  $\mu$ g ml<sup>-1</sup> Alexa488-anti-CD107a antibody and 2  $\mu$ M monensin for 1, 2 and 4 h. After which, cells were washed with PBS and further stained with PE-Cy7-anti-CD8a antibody. Flow cytometry was used for assessing the surface and internalized CD107a levels.

**Code availability.** MATLAB code used to perform STORM and TIRFM data analysis can be accessed by contacting W.L. (liuwanli@biomed.tsinghua.edu.cn).

**Statistical analysis.** All sample sizes are large enough to ensure proper statistical analysis. Statistical analyses were performed using GraphPad Prism (GraphPad Software, Inc.). Statistical significance was determined as indicated in the figure legends.  $P < 0.05$  was considered significant; \* $P < 0.05$ ; \*\* $P < 0.01$ ; \*\*\* $P < 0.001$ . All  $t$ -test analyses are two-tailed unpaired  $t$ -tests. The replicates in Figs 2, 3b, i, k–o,

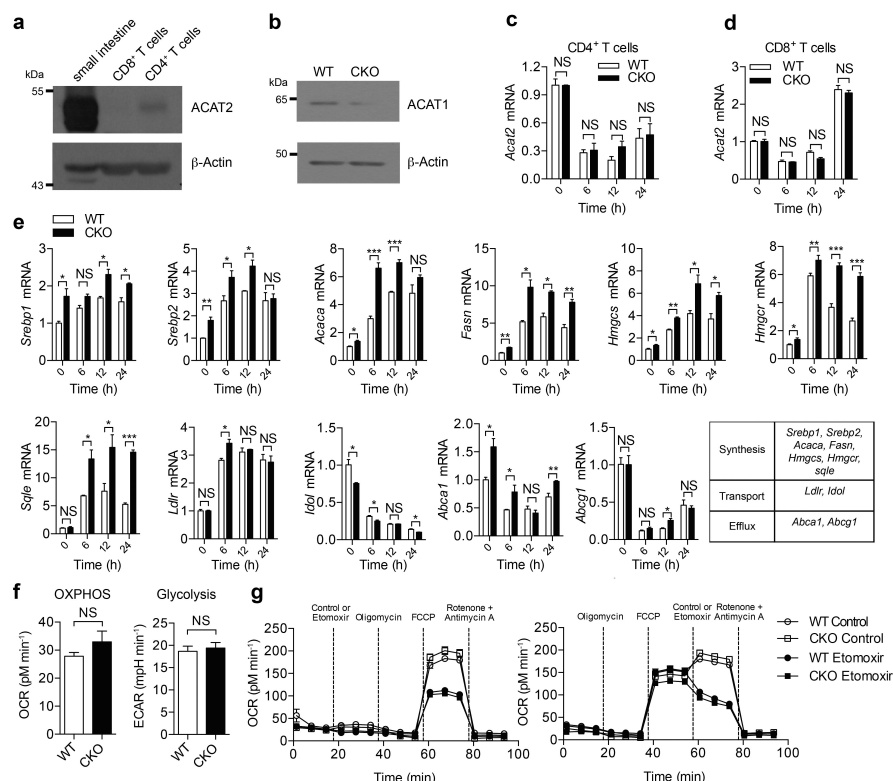
4a, b, e–j, l, m and Extended Data Figs 1a, 3a–c, g–l, 4f, 5a–e, 6, 7g, 8, 9e, h, j and 10 were biological replicates. The replicates in Figs 1, 3c, d, p, Fig. 4o, p and Extended Data Figs 1b–i, 2, 3d–f, m, n, 4b–e, 5f, g, 7a, b, i–l and 9a–c were technical replicates. The centre values shown in all figures are average values.

31. Cao, Y. *et al.* LKB1 regulates TCR-mediated PLC $\gamma$ 1 activation and thymocyte positive selection. *EMBO J.* **30**, 2083–2093 (2011).
32. Guo, Z. Y., Lin, S., Heinen, J. A., Chang, C. C. & Chang, T. Y. The active site His-460 of human acyl-coenzyme A:cholesterol acyltransferase 1 resides in a hitherto undisclosed transmembrane domain. *J. Biol. Chem.* **280**, 37814–37826 (2005).
33. Das, A., Goldstein, J. L., Anderson, D. D., Brown, M. S. & Radhakrishnan, A. Use of mutant 125I-perfringolysin O to probe transport and organization of cholesterol in membranes of animal cells. *Proc. Natl Acad. Sci. USA* **110**, 10580–10585 (2013).
34. Rossy, J., Owen, D. M., Williamson, D. J., Yang, Z. & Gaus, K. Conformational states of the kinase Lck regulate clustering in early T cell signaling. *Nature Immunol.* **14**, 82–89 (2013).
35. Brian, A. A. & McConnell, H. M. Allogeneic stimulation of cytotoxic T cells by supported planar membranes. *Proc. Natl Acad. Sci. USA* **81**, 6159–6163 (1984).
36. Grakoui, A. *et al.* The immunological synapse: a molecular machine controlling T cell activation. *Science* **285**, 221–227 (1999).
37. Liu, W., Won Sohn, H., Tolar, P., Meckel, T. & Pierce, S. K. Antigen-induced oligomerization of the B cell receptor is an early target of Fc $\gamma$ RIIB inhibition. *J. Immunol.* **184**, 1977–1989 (2010).
38. Jenkins, M. R., Tsun, A., Stinchcombe, J. C. & Griffiths, G. M. The strength of T cell receptor signal controls the polarization of cytotoxic machinery to the immunological synapse. *Immunity* **31**, 621–631 (2009).



**Extended Data Figure 1 | Reprogramming of cellular cholesterol metabolism in activated CD8<sup>+</sup> T cells.** **a**, Filipin III staining (left) and quantification (right) of cellular cholesterol of naive and activated CD8<sup>+</sup> T cells stimulated by 5  $\mu\text{g ml}^{-1}$  plate-bound anti-CD3/CD28 antibodies for 12 h ( $n = 60$ ). **b**, Total cellular, plasma membrane and intracellular cholesterol quantified using the cholesterol oxidation-based method ( $n = 4$ ). **c**, Relative plasma membrane cholesterol quantified using the biotinylation-based method ( $n = 4$ ). **d–f**, Transcriptional levels of key genes encoding molecules involved in cholesterol synthesis, transport and efflux ( $n = 3$ ). CD8<sup>+</sup> T cells were stimulated with 5  $\mu\text{g ml}^{-1}$  plate-bound anti-CD3/CD28 antibodies. Results and statistical analysis are relative to quiescent CD8<sup>+</sup> T cells. mRNA levels of cholesterol biosynthesis genes, including *Srebp1* (also known as *Srebf1*), *Srebp2* (*Srebf2*), *Hmgcr*, *Hmgcs*, *Fasn*, *Acaca* and *Sqle*, were upregulated in activated CD8<sup>+</sup> T cells. *Ldlr*, which encodes the LDL receptor, a major receptor

for cholesterol transport, was upregulated in activated CD8<sup>+</sup> T cells, whereas, *Idol* (also known as *Myliip*), which encodes IDOL, an inducible degrader of the LDL receptor, was downregulated. Cholesterol efflux genes, including *Abca1* and *Abcg1*, were all downregulated in activated CD8<sup>+</sup> T cells. **g–i**, Cytokine/granule productions of CD8<sup>+</sup> T cells after modulation of cholesterol metabolic pathways ( $n = 3$ ). Naive CD8<sup>+</sup> T cells were pretreated for 6 h with vehicle (DMSO), lovastatin (to inhibit cholesterol biosynthesis) or U18666A (a cholesterol transport inhibitor with pleiotropic effects), respectively. Cells were then stimulated with 5  $\mu\text{g ml}^{-1}$  plate-bound anti-CD3 and anti-CD28 antibodies for 24 h before intracellular staining. Representative flow cytometric profiles shown in **g**. Data are representative of two independent experiments, and were analysed by Mann–Whitney test (**a**) or unpaired *t*-test (**b–f**, **h**, **i**). Error bars denote s.e.m.; \* $P < 0.05$ ; \*\* $P < 0.01$ ; \*\*\* $P < 0.001$ ; NS, not significant.

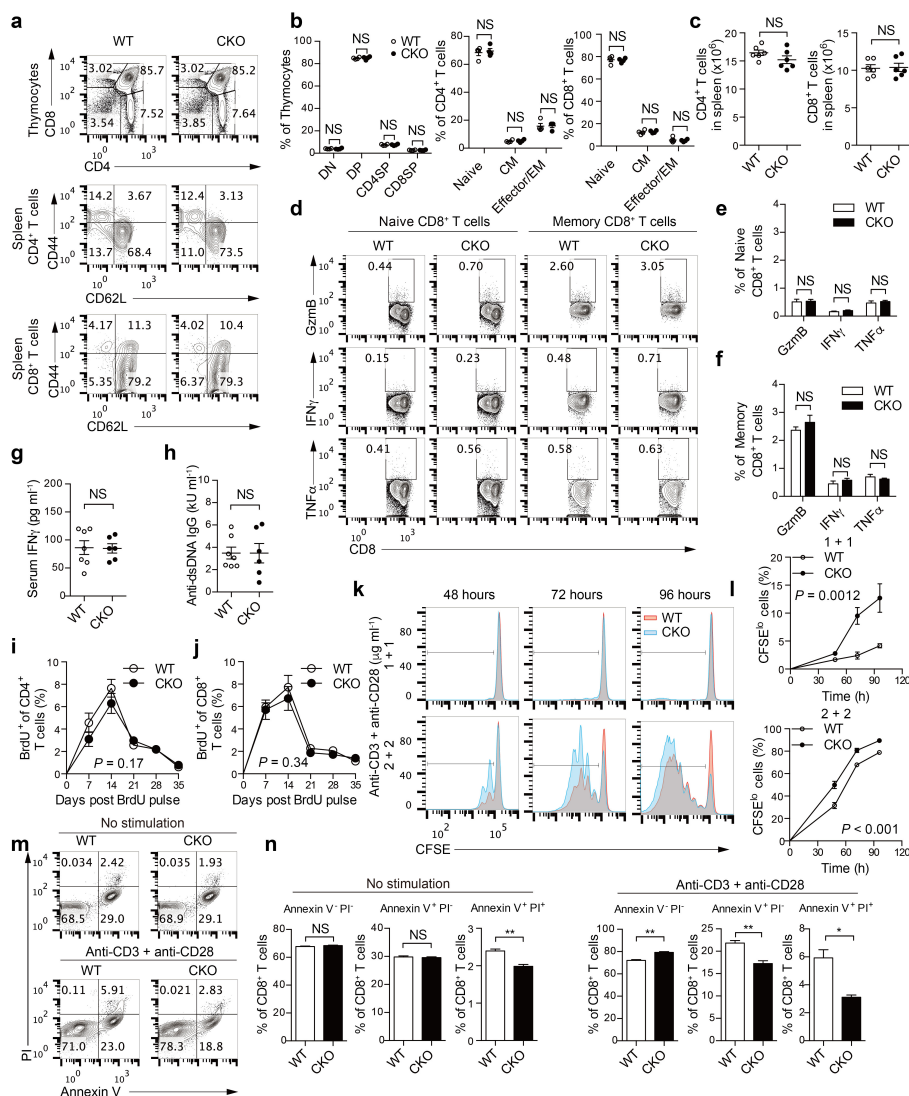


### Extended Data Figure 2 | ACAT1 deficiency affects the cholesterol metabolism but not the basal energy metabolism of CD8<sup>+</sup> T cells.

**a**, ACAT2 was weakly expressed in mouse CD4<sup>+</sup> T cells but was barely detectable in mouse CD8<sup>+</sup> T cells. A sample from mouse small intestine was used as a positive control. **b**, Protein levels of ACAT1 were significantly lower in *Acat1*<sup>CKO</sup> (CKO) CD8<sup>+</sup> T cells than in wild-type cells, indicating a good knockout efficiency of *Acat1* in CD8<sup>+</sup> T cells. See Supplementary Fig. 1 for gel source data. **c**, **d**, ACAT1 deficiency did not change the transcriptional level of *Acat2* in CD4<sup>+</sup> and CD8<sup>+</sup> T cells of *Acat1*<sup>CKO</sup> mice. Cells were stimulated with 5  $\mu$ g ml<sup>-1</sup> plate-bound anti-CD3 and anti-CD28 antibodies for the indicated time ( $n = 3$ ). **e**, ACAT1 deficiency resulted in significant enhancement of the transcription levels of cholesterol synthesis genes in both naive and activated cells. Transcription levels of cholesterol transport and efflux genes underwent only modest changes in CKO CD8<sup>+</sup> T cells. Naive wild-type or CKO CD8<sup>+</sup> T cells were stimulated with 5  $\mu$ g ml<sup>-1</sup> plate-bound anti-CD3 and anti-CD28 for the indicated time ( $n = 3$ ). **f**, **g**, Basal energy metabolism of naive wild-type and CKO CD8<sup>+</sup> T cells was measured. No significant

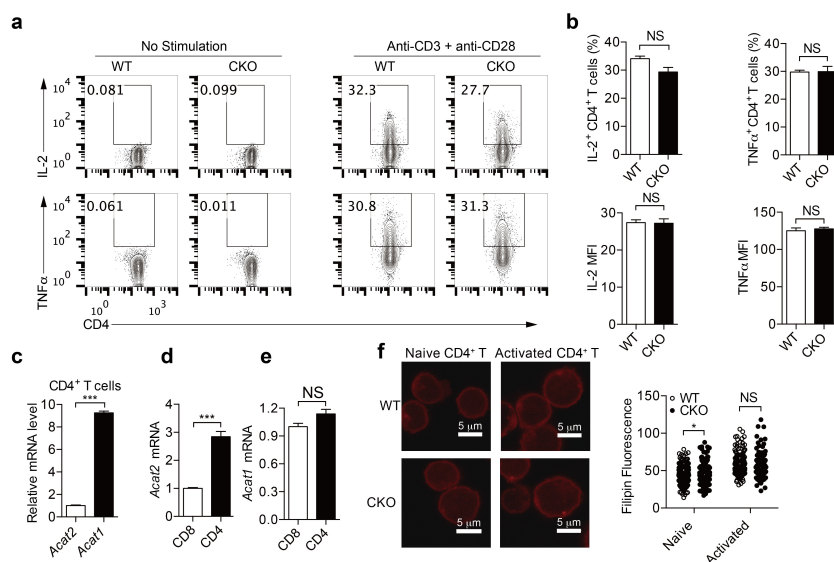
difference was observed between wild-type and CKO cells. **f**, Oxidative phosphorylation was measured by the oxygen consumption rates (OCR) under basal condition, and glycolysis was measured by the extracellular acidification rates (ECAR) under basal condition ( $n = 5$ ). **g**, Fatty acid oxidation was measured by the OCR under basal condition and in response to indicated drugs: oligomycin (to block ATP synthesis), FCCP (to uncouple ATP synthesis from the electron transport chain), rotenone and antimycin A (to block complex I and III of the electron transport chain, respectively), and etomoxir (to block mitochondrial fatty acid oxidation). Fatty acid oxidation can be represented by the influence of etomoxir on the OCR. Between wild-type etomoxir and CKO etomoxir:  $P > 0.05$  after FCCP in **g** (left);  $P > 0.05$  after etomoxir in **g** (right). Between wild-type and CKO:  $P > 0.05$  after FCCP in **g** (left);  $P > 0.05$  after control in **g** (right). No significant difference was observed ( $n = 3$ ). Data are representative of two (**c–e**, **g**) or three (**f**) independent experiments, and were analysed by unpaired *t*-test (**c–f**) or two-way ANOVA followed with Bonferroni's multiple comparison tests (**g**). Error bars denote s.e.m; \* $P < 0.05$ ; \*\* $P < 0.01$ ; \*\*\* $P < 0.001$ .





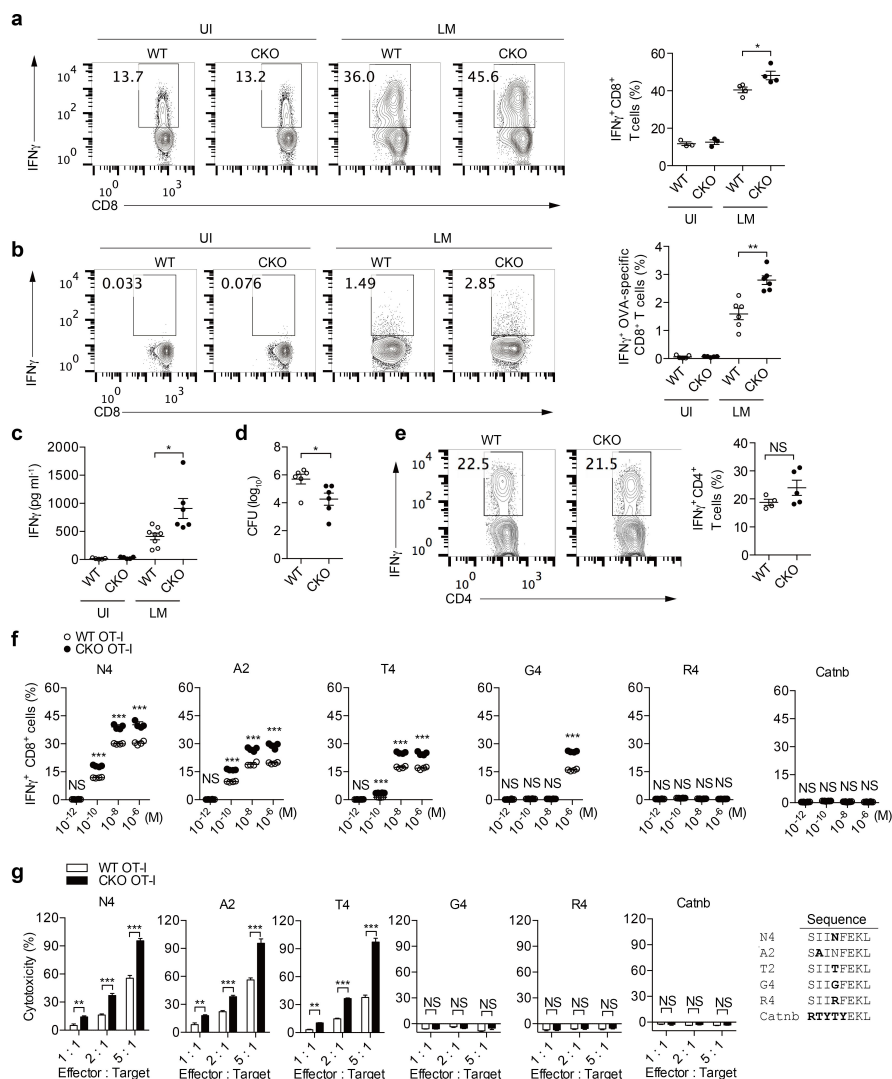
**Extended Data Figure 3 | ACAT1 deficiency does not affect thymocyte development and peripheral T-cell homeostasis, but results in enhanced proliferation and reduced apoptosis of CD8<sup>+</sup> T cells.** **a, b**, Flow cytometric analysis of thymocytes and splenic T cells from wild-type and CKO mice (8 weeks old, *n* = 4). Representative flow cytometric profiles were shown in **a**. Percentages of CD4<sup>+</sup> CD8<sup>+</sup> double negative (DN), CD4<sup>+</sup> CD8<sup>+</sup> double positive (DP), CD4<sup>+</sup> single positive (CD4SP) and CD8<sup>+</sup> single positive (CD8SP) cells in total thymocytes were comparable (**b**, left). Naive (CD44<sup>lo</sup>CD62L<sup>hi</sup>), central memory (CD44<sup>hi</sup>CD62L<sup>hi</sup>, CM) and effector/effector memory (CD44<sup>hi</sup>CD62L<sup>lo</sup>, effector/EM) of CD4<sup>+</sup> and CD8<sup>+</sup> T cells from the spleen of wild-type and CKO mice were comparable (**b**, right). Data were analysed by Mann-Whitney test, and no significant difference was observed. **c**, Total CD4<sup>+</sup> and CD8<sup>+</sup> T-cell numbers from the spleen of wild-type and CKO mice (8 weeks old, *n* = 6) were assessed using flow cytometry. Data were analysed with Mann-Whitney test, and no significant difference was observed. **d-f**, Cytokine/granule productions of resting naive (CD62L<sup>hi</sup>CD44<sup>lo</sup>) and central memory (CD62L<sup>hi</sup>CD44<sup>hi</sup>) CD8<sup>+</sup> T cells from the spleen of wild-type and CKO mice (8 weeks old, *n* = 3). CD8<sup>+</sup> T cells were isolated from the spleen and cultured for 4 h in the presence of 5 μg ml<sup>-1</sup> brefeldin A. Naive and memory populations were gated by CD62L and CD44 expression. Data were analysed by unpaired *t*-test, and no significant difference was observed. **g, h**, Serum

levels of IFN $\gamma$  and auto-antibody anti-dsDNA IgG of wild-type and CKO mice (12 weeks old, WT, *n* = 7; CKO, *n* = 6) were assessed using ELISA. Data were analysed by Mann-Whitney test, and no significant difference was observed. **i, j**, T-cell homeostasis was measured by BrdU labelling and detection. Wild-type and CKO mice (6 weeks old) were injected with a single dose (2 mg) of BrdU intraperitoneally. Peripheral blood was collected at the indicated time and analysed using flow cytometry. Percentages of BrdU<sup>+</sup> cells in total peripheral CD4<sup>+</sup> and CD8<sup>+</sup> T cells of wild-type and CKO mice (*n* = 6) were plotted. Data were analysed by two-way ANOVA, and no significant difference was observed. **k, l**, CD8<sup>+</sup> T-cell proliferation was measured by CFSE dilution. Cells were stimulated with 1–2 μg ml<sup>-1</sup> plate-bound anti-CD3 and anti-CD28 antibodies for the indicated time. Data were analysed by two-way ANOVA (*n* = 3). **m, n**, CD8<sup>+</sup> T-cell apoptosis was measured by annexin V and propidium iodide (PI) staining. The naive CD8<sup>+</sup> cells were isolated from the spleen of wild-type or CKO mice (8 weeks old), and cultured in medium for 24 h without stimulation, or stimulated with 5 μg ml<sup>-1</sup> plate-bound anti-CD3 and anti-CD28 antibodies for 24 h. Annexin V and propidium iodide were used to stain early (annexin V<sup>+</sup> PI<sup>-</sup>) and late (annexin V<sup>+</sup> PI<sup>+</sup>) cells apoptotic. Apoptotic cells were significantly lower in CKO CD8<sup>+</sup> T cells than in wild-type CD8<sup>+</sup> T cells. Data were analysed by unpaired *t*-test (*n* = 3). Error bars denote s.e.m; \**P* < 0.05; \*\**P* < 0.01.



**Extended Data Figure 4 | ACAT1 deficiency does not result in significant change of CD4<sup>+</sup> T-cell function.** **a, b**, Cytokine productions of CD4<sup>+</sup> T cells ( $n = 3$ ). Cells were stimulated with  $5 \mu\text{g ml}^{-1}$  plate-bound anti-CD3 and anti-CD28 antibodies for 12 h. Representative flow cytometric profiles are shown in **a**. **c–e**, Relative transcription levels of *Acat1* and *Acat2* in naive CD4<sup>+</sup> and CD8<sup>+</sup> T cells freshly isolated from C57BL/6 mice ( $n = 3$ ). *Acat1* transcription level was significantly higher than *Acat2* in CD4<sup>+</sup> T cells. *Acat1* transcription levels were comparable

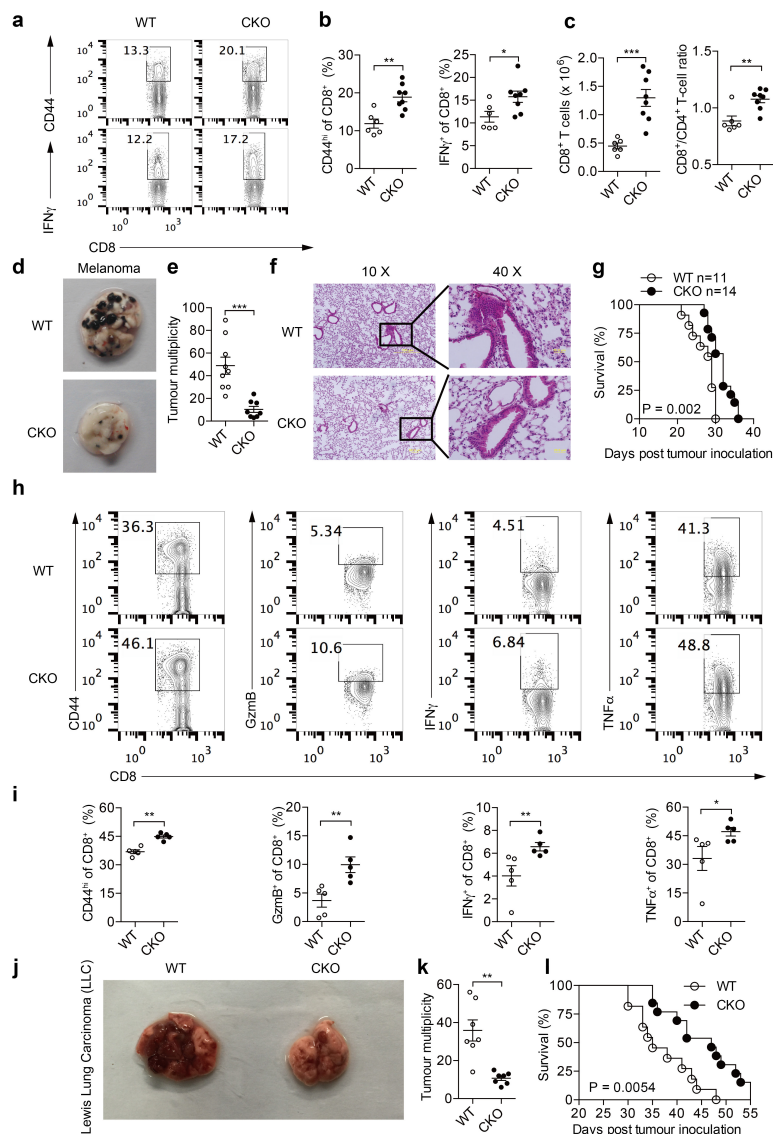
between CD4<sup>+</sup> and CD8<sup>+</sup> T cells, whereas the *Acat2* transcription level in CD4<sup>+</sup> T cells was significantly higher than that in CD8<sup>+</sup> T cells. *Acat2* transcription level in CD4<sup>+</sup> T cells was set as 1 in **c**. *Acat1* and *Acat2* transcription levels in CD8<sup>+</sup> T cells were set as 1 in **d** and **e**. **f**, Filipin III staining to analyse cellular cholesterol distribution in naive and activated CD4<sup>+</sup> T cells from wild-type and CKO mice. Data were analysed by unpaired *t*-test (**b–e**) or Mann–Whitney test (**f**). Error bars denote s.e.m; \* $P < 0.05$ ; \*\*\* $P < 0.001$ .



### Extended Data Figure 5 | ACAT1 deficiency promotes CD8 $^{+}$ T-cell response but does not result in autoreactivity to self-antigens.

**a–e**, *Listeria monocytogenes* was used to infect wild-type and CKO mice to induce a strong T-cell response. **a**, IFN $\gamma$  production of CD8 $^{+}$  T cells from wild-type and CKO mice infected (day 7 after infection) with *Listeria monocytogenes* (LM) that exogenously express OVA antigen, or were uninfected (UI). The splenocytes were re-stimulated with PMA (50 ng ml $^{-1}$ ) plus ionomycin (1  $\mu$ M) for 4 h in the presence of 5  $\mu$ g ml $^{-1}$  brefeldin A. CD8 $^{+}$  IFN $\gamma$  $^{+}$  cells were gated for analysis (UI,  $n = 3$ ; LM,  $n = 4$ ). **b**, IFN $\gamma$  production of OVA-specific CD8 $^{+}$  T cells from the wild-type and CKO mice infected (day 7 after infection) with *Listeria monocytogenes* that exogenously express OVA antigen or uninfected. Splenocytes were stimulated with OVA $_{257-264}$  peptide for 24 h. CD8 $^{+}$  IFN $\gamma$  $^{+}$  cells were gated for analysis (UI,  $n = 5$ ; LM,  $n = 6$ ). **c**, IFN $\gamma$  levels in serum of infected or uninfected mice were assessed by ELISA

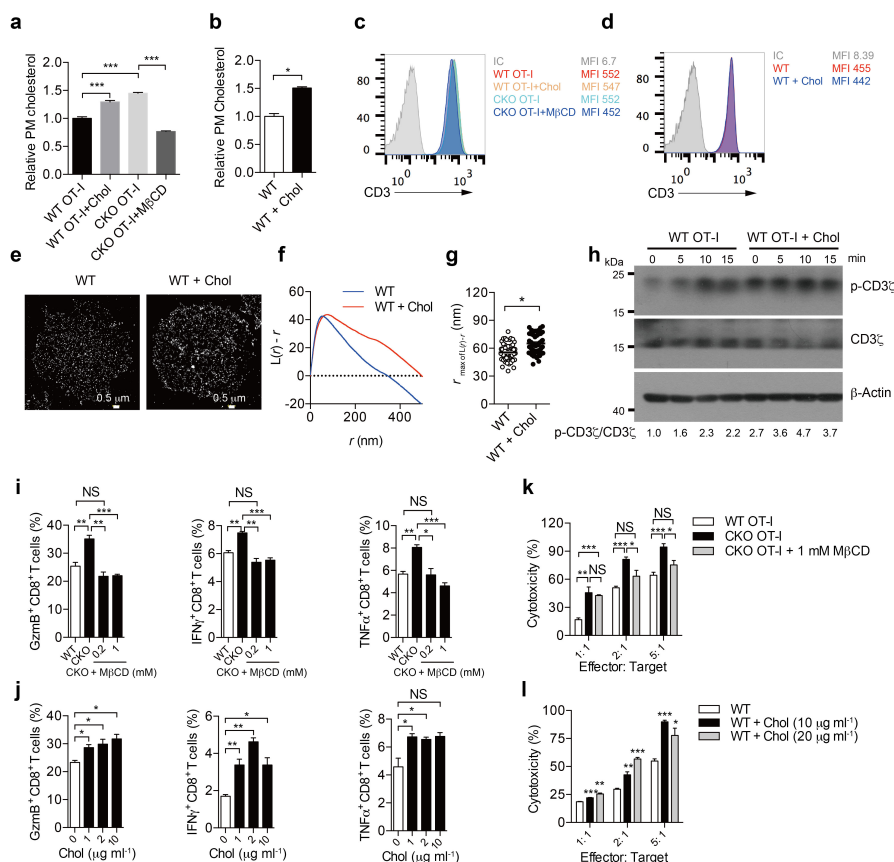
(UI,  $n = 5$ ; LM WT,  $n = 8$ ; LM CKO,  $n = 6$ ). **d**, Liver *Listeria monocytogenes* titre was analysed at day 6 after infection ( $n = 6$ ). **e**, Percentages of IFN $\gamma$  $^{+}$  cells in CD4 $^{+}$  cells from the spleens of wild-type and CKO mice were assessed as in **a** (WT,  $n = 4$ ; CKO,  $n = 5$ ). **f**, **g**, Effect of ACAT1 deficiency on CD8 $^{+}$  T-cell responses to different antigens. **f**, Naive wild-type OT-I or *Acat1* $^{CKO}$  OT-I (CKO OT-I) CD8 $^{+}$  T cells were stimulated with autologous splenocytes pulsed with foreign antigen (N4, A2, T4 or G4), positive-selection-supporting antigen (R4) or self-antigen (Catnb). Flow cytometry was used to measure IFN $\gamma$  production ( $n = 4$ ). **g**, Splenocytes from wild-type OT-I or CKO OT-I mice were stimulated with OVA $_{257-264}$  to generate mature CTLs. CTLs were incubated with EL-4 cells pulsed with different antigens for 4 h, and LDH release was measured to assess cytotoxic efficiency ( $n = 4$ ). Data are representative of three (**f**, **g**) independent experiments, and were analysed by Mann–Whitney test (**a–e**) or unpaired  $t$ -test (**f**, **g**). Error bars denote s.e.m.; \* $P < 0.05$ ; \*\* $P < 0.01$ ; \*\*\* $P < 0.001$ .



**Extended Data Figure 6 | ACAT1 deficiency promotes antitumour response of CD8<sup>+</sup> T cells in different tumour models.** **a–c**, B16F10 melanoma cells ( $2 \times 10^5$ ) were subcutaneously injected into wild-type ( $n=6$ ) or CKO ( $n=8$ ) mice to induce skin melanoma. On day 7, CD8<sup>+</sup> T cells were isolated from draining lymph nodes of wild-type and CKO mice. Flow cytometry was used to analyse surface expression of activation marker CD44 and IFN $\gamma$  production of CD8<sup>+</sup> T cells, as well as CD8<sup>+</sup> T-cell number and CD8/CD4 T-cell ratio. Data are representative of three independent experiments, and were analysed by Mann–Whitney test. **d–i**, B16F10 melanoma cells ( $2 \times 10^5$ ) were intravenously injected into wild-type or CKO mice to induce melanoma with lung metastasis. **d, e**, On day 20, lungs were isolated to count tumour numbers (WT,  $n=9$ ; CKO,  $n=8$ ). Data are representative of three independent experiments, and were

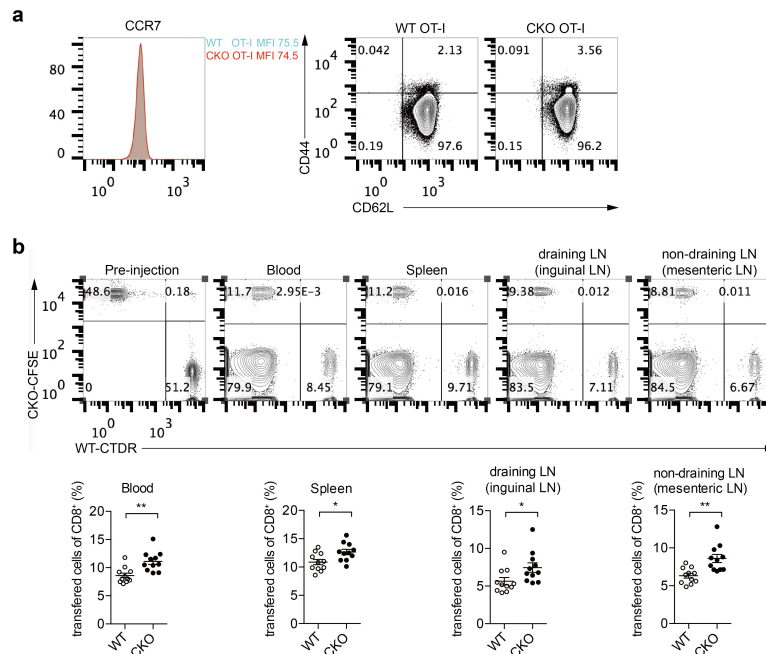
analysed by Mann–Whitney test. **f**, On day 14, lung sections were stained with haematoxylin and eosin to assess the infiltration of melanoma into lung. **g**, Survival was analysed by log-rank (Mantel–Cox) test (WT,  $n=11$ ; CKO,  $n=14$ ). **h, i**, On day 20, lung infiltrating CD8<sup>+</sup> T cells were isolated and flow cytometry was used to measure the granule and cytokine productions as well as surface expression of the activation marker CD44. Data were analysed by Mann–Whitney test. **j–l**, Lewis lung carcinoma cells ( $2 \times 10^6$ ) were intravenously injected into wild-type or CKO mice to induce lung cancer. On day 35, lungs were isolated to count tumour numbers. Tumour multiplicity data were analysed by Mann–Whitney test (**k**,  $n=7$ ). Survival was analysed by log-rank (Mantel–Cox) test (**l**, WT,  $n=11$ ; CKO,  $n=13$ ). Error bars denote s.e.m; \* $P < 0.05$ ; \*\* $P < 0.01$ ; \*\*\* $P < 0.001$ .





**Extended Data Figure 7 | Cholesterol level of the plasma membrane directly affects CD8<sup>+</sup> T-cell function.** To reduce the cholesterol level of the plasma membrane, CD8<sup>+</sup> T cells were treated with MβCD at different doses for 5 min. To increase the cholesterol level, CD8<sup>+</sup> T cells were treated with MβCD-coated cholesterol (chol) at different doses for 15 min. **a, b**, Measurements of plasma membrane cholesterol level of CD8<sup>+</sup> T cells by biotinylation-based method. MβCD-coated cholesterol treatment increased whereas MβCD decreased plasma membrane cholesterol. **a**, Wild-type OT-I CTLs were treated with 10 μg ml<sup>-1</sup> MβCD-coated cholesterol, and CKO OT-I CTLs were treated with 1 mM MβCD. WT OT-I, *n* = 8; CKO OT-I, *n* = 6. **b**, Naive wild-type polyclonal CD8<sup>+</sup> T cells were treated with 10 μg ml<sup>-1</sup> MβCD-coated cholesterol (*n* = 4). **c, d**, TCR levels of CD8<sup>+</sup> T cells after MβCD or MβCD-coated cholesterol treatment. MβCD treatment reduced whereas MβCD-coated cholesterol treatment did not change the surface TCR level. OT-I CTLs (**c**) and naive wild-type polyclonal CD8<sup>+</sup> T cells (**d**) were treated as in **a** and **b**, respectively. IC, isotype control. **e–g**, TCR clustering after treatment of naive wild-type CD8<sup>+</sup> T cells with 10 μg ml<sup>-1</sup> MβCD-coated cholesterol.

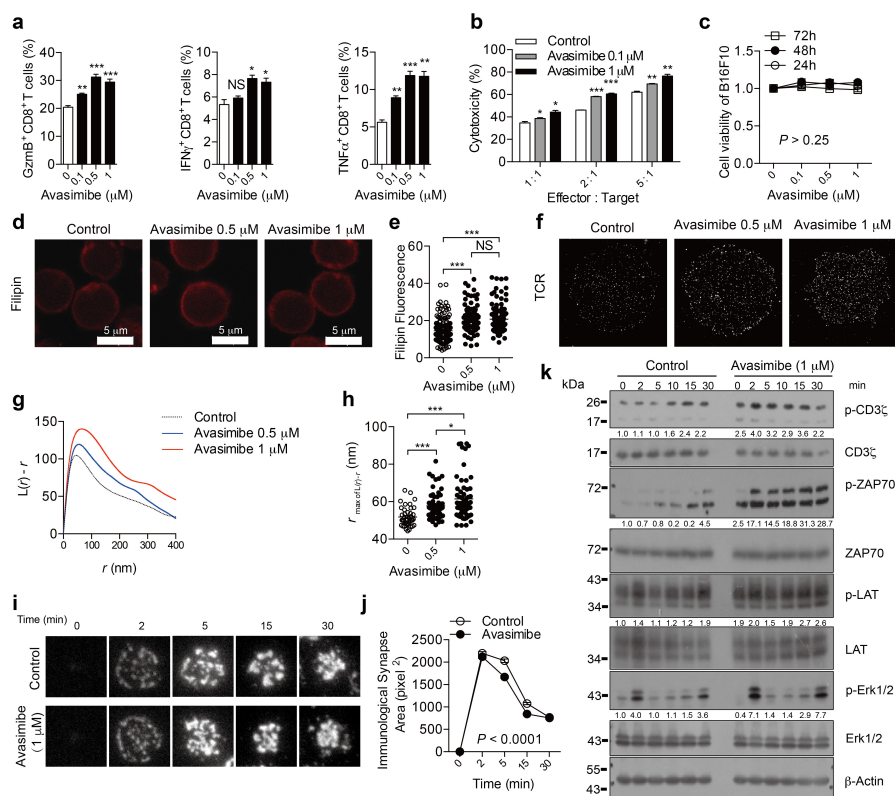
Super-resolution STORM images of TCR were acquired and analysed as Fig. 3g–i. Increasing plasma membrane cholesterol of CD8<sup>+</sup> T cells promoted the clustering of TCR. **g**, WT, *n* = 73; WT + chol, *n* = 62. **h**, TCR signalling after treatment of wild-type OT-I CTLs with 10 μg ml<sup>-1</sup> MβCD-coated cholesterol, measured by immunoblotting. Cells were then stimulated with 2 μg ml<sup>-1</sup> anti-CD3 and anti-CD28 antibodies for indicated time at 37 °C. Increasing plasma membrane cholesterol of CD8<sup>+</sup> T cells promoted the signalling of TCR. See Supplementary Fig. 1 for gel source data. **i, j**, Cytokine/granule productions of CD8<sup>+</sup> T cells treated with MβCD (**i**) or MβCD-coated cholesterol (**j**) (*n* = 3). Cells were stimulated with 5 μg ml<sup>-1</sup> plate-bound anti-CD3 and anti-CD28 antibodies for 24 h at 37 °C. **k, l**, Cytotoxicity of CD8<sup>+</sup> T cells treated with MβCD (**k**) or MβCD-coated cholesterol (**l**) (*n* = 3). CTLs were then incubated with EL-4 cells pulsed with OVA<sub>257–264</sub> for 4 h. LDH release was measured to assess cytotoxic efficiency. Data were analysed by unpaired *t*-test (**a, b, i–l**) or Mann–Whitney test (**g**). Error bars denote s.e.m.; \**P* < 0.05; \*\**P* < 0.01; \*\*\**P* < 0.001.



**Extended Data Figure 8 | Homing of naive wild-type or CKO OT-I T cells to secondary lymphoid organs in the B16-OVA melanoma-bearing mice.** Naive OT-I T cells were isolated from wild-type or CKO OT-I TCR transgenic mice, and labelled with CTDR (cell tracker deep red dye) or CFSE (carboxyfluorescein succinimidyl ester), respectively. Labelled wild-type and CKO cells were mixed at 1:1 ratio, and the mixture ( $10^7$  cells) was intravenously injected into the B16-OVA melanoma bearing C57BL/6 mice. After 12 h, the indicated tissues from the mice were isolated and

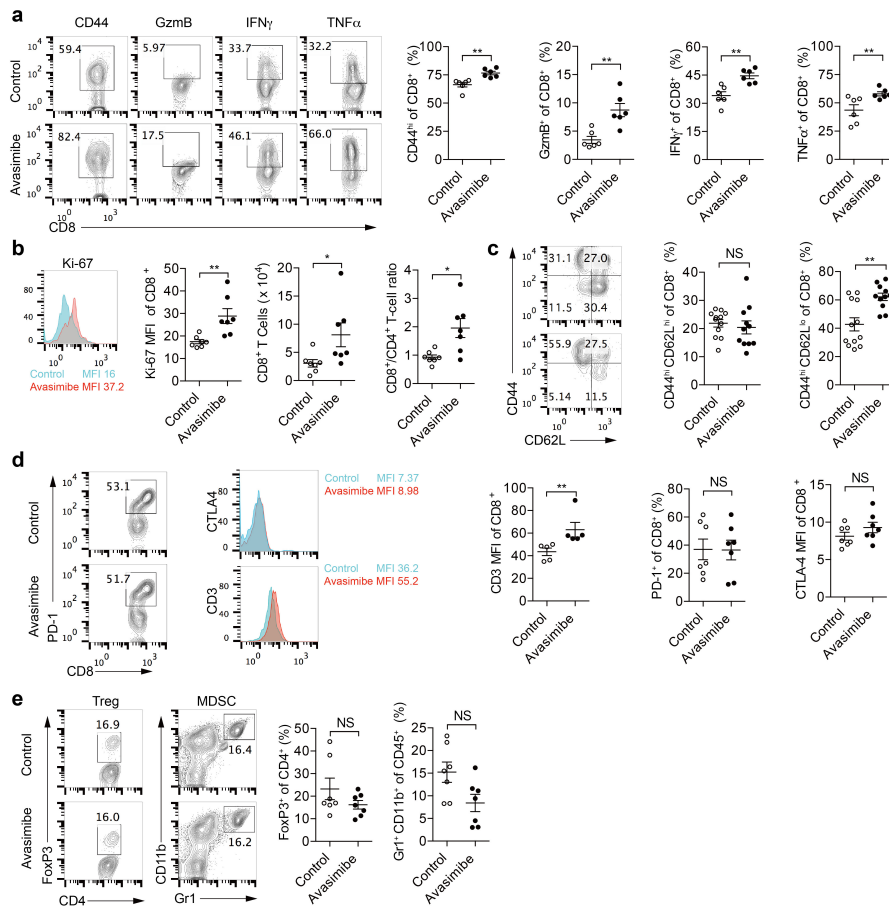
the percentages of the labelled cells were assessed using flow cytometry.

**a**, Flow cytometric analysis of the homing receptor CCR7 and CD62L surface level of naive wild-type and CKO OT-I T cells. No significant difference was observed. **b**, The percentages of transferred cells in total CD8<sup>+</sup> T cells were assessed using flow cytometry. Data were analysed with Mann-Whitney test ( $n = 11$ ). Data are representative of two independent experiments. Error bars denote s.e.m; \* $P < 0.05$ ; \*\* $P < 0.01$ .



**Extended Data Figure 9 | Avasimibe treatment leads to enhanced TCR clustering and signalling, as well as more efficient formation of immunological synapse.** **a**, Cytokine/granule productions of CD8<sup>+</sup> T cells after avasimibe treatment ( $n = 3$ ). The naive cells were pretreated for 6 h with avasimibe or vehicle (DMSO) and then stimulated by 5  $\mu$ g ml<sup>-1</sup> plate-bound anti-CD3 and anti-CD28 antibodies for 24 h. Data were analysed by  $t$ -test. **b**, CTL cytotoxicity after avasimibe treatment measured by the LDH assay ( $n = 3$ ). OT-I CTLs were pretreated with avasimibe or vehicle for 6 h and then incubated with EL-4 cells pulsed with OVA<sub>257–264</sub> peptide for 4 h. Data were analysed by  $t$ -test. **c**, An MTS-based cell viability assay was performed to assess the toxicity of avasimibe to B16F10 cells ( $n = 6$ ). Data were analysed by one-way ANOVA, and no significant difference was observed. **d**, **e**, Filipin III staining to analyse cellular cholesterol distribution in naive CD8<sup>+</sup> T cells treated with avasimibe or vehicle. **d**, Representative images. **e**, Data were analysed by Mann–Whitney test. 0,  $n = 217$ ; 0.5,  $n = 139$ ; 1,  $n = 133$ . **f–h**, Super-resolution STORM images of TCR in naive CD8<sup>+</sup> T cells treated with avasimibe

or vehicle. **f**, Representative images. **g**, Ripley's  $K$ -function was used to analyse TCR molecules distribution. **h**, The  $r$  value at the maximal  $L(r) - r$  value of Ripley's  $K$ -function curves, and data were analysed by Mann–Whitney test. 0,  $n = 41$ ; 0.5,  $n = 60$ ; 1,  $n = 66$ . **i**, Representative TIRFM images of immunological synapses of CD8<sup>+</sup> T cells treated with avasimibe (1  $\mu$ M) or vehicle for 6 h. Cells were stimulated by PLB-bound anti-CD3 for the indicated time and fixed by 4% PFA before imaging. **j**, Areas of the immunological synapses ( $n > 60$  cells). The formation and contraction of the immunological synapses of CD8<sup>+</sup> T cells treated with avasimibe were more rapid than those treated with vehicle. Data were analysed by two-way ANOVA. **k**, TCR proximal and downstream signalling was assessed using immunoblotting of protein phosphorylation. OT-I CTLs were treated with 1  $\mu$ M avasimibe or vehicle for 6 h and then stimulated with 2  $\mu$ g ml<sup>-1</sup> soluble anti-CD3 and anti-CD28 for the indicated time. See Supplementary Fig. 1 for gel source data. Error bars denote s.e.m.; \* $P < 0.05$ ; \*\* $P < 0.01$ ; \*\*\* $P < 0.001$ .



**Extended Data Figure 10 | Avasimibe treatment leads to potentiated effector function and enhanced proliferation of tumour-infiltrating CD8 $^{+}$  T cells.** C57BL/6 mice bearing B16F10 melanoma were treated with avasimibe (15 mg kg $^{-1}$ ) or same dose of DMSO in PBS for four times by intraperitoneal injection. The mice were euthanized at day 18 and the tumours were isolated. **a**, The CD44 surface expression and cytokine/granule productions of tumour-infiltrating CD8 $^{+}$  T cells were assessed using flow cytometry ( $n = 6$ ). **b**, CD8 $^{+}$  T-cell number, CD8 $^{+}$ /CD4 $^{+}$  T-cell ratio and Ki-67 level of tumour-infiltrating CD8 $^{+}$  T cells were assessed using flow cytometry ( $n = 7$ ). **c**, Percentages of CD8 $^{+}$  central memory

(CD44 $^{hi}$ CD62L $^{lo}$ ) and CD8 $^{+}$  effector/effector memory (CD44 $^{hi}$ CD62L $^{lo}$ ) were assessed using flow cytometry (control,  $n = 12$ ; avasimibe,  $n = 11$ ). **d**, Surface levels of PD-1, CTLA-4 and TCR of tumour-infiltrating CD8 $^{+}$  T cells. PD-1 level was indicated by the percentage of PD-1 $^{hi}$  cells. CTLA-4 and TCR levels were indicated by median fluorescence intensity. PD-1 and CTLA-4 staining,  $n = 7$ ; TCR staining,  $n = 5$ . **e**, T $_{reg}$  cell (FoxP3 $^{+}$ CD4 $^{+}$ ) and myeloid-derived suppressor cell (MDSC) (Gr1 $^{+}$ CD11b $^{+}$ ) percentages in the tumour microenvironment were assessed using flow cytometry ( $n = 7$ ). Data were analysed by Mann–Whitney test. Error bars denote s.e.m; \* $P < 0.05$ ; \*\* $P < 0.01$ ; \*\*\* $P < 0.001$ .



# Primary cilia are not calcium-responsive mechanosensors

M. Delling<sup>1\*</sup>, A. A. Indzhykulian<sup>2\*</sup>, X. Liu<sup>1</sup>, Y. Li<sup>2</sup>, T. Xie<sup>3</sup>, D. P. Corey<sup>2</sup> & D. E. Clapham<sup>1,2</sup>

**Primary cilia are solitary, generally non-motile, hair-like protrusions that extend from the surface of cells between cell divisions. Their antenna-like structure leads naturally to the assumption that they sense the surrounding environment, the most common hypothesis being sensation of mechanical force through calcium-permeable ion channels within the cilium<sup>1</sup>. This Ca<sup>2+</sup>-responsive mechanosensor hypothesis for primary cilia has been invoked to explain a large range of biological responses, from control of left–right axis determination in embryonic development to adult progression of polycystic kidney disease and some cancers<sup>2,3</sup>. Here we report the complete lack of mechanically induced calcium increases in primary cilia, in tissues upon which this hypothesis has been based. We developed a transgenic mouse, *Arl13b-mCherry-GECO1.2*, expressing a ratiometric genetically encoded calcium indicator in all primary cilia. We then measured responses to flow in primary cilia of cultured kidney epithelial cells, kidney thick ascending tubules, crown cells of the embryonic node, kinocilia of inner ear hair cells, and several cell lines. Cilia-specific Ca<sup>2+</sup> influxes were not observed in physiological or even highly supraphysiological levels of fluid flow. We conclude that mechanosensation, if it originates in primary cilia, is not via calcium signalling.**

To examine ciliary Ca<sup>2+</sup> signalling *in vivo*, we generated transgenic *Arl13b-mCherry-GECO1.2*<sup>tg</sup> mice in which fluorescent indicators are confined to the primary cilia (Fig. 1a–c and Extended Data Figs 1 and 2). To accurately measure changes in [Ca<sup>2+</sup>] in small moving subcellular structures and to control for motion artefacts and differential bleaching of ratioing dyes, we first examined hair cells in the cochlea's organ of Corti, the most sensitive of known Ca<sup>2+</sup>-responsive mechanosensors (CaRMS)<sup>4–6</sup>. The apical surface of each hair cell carries a hair bundle with staggered rows of specialized actin-based microvillar projections called 'stereocilia' (Extended Data Fig. 3). Adjacent to the tallest stereocilia is a single non-motile, microtubule-based true cilium (9 + 2; kinocilium). Fine filamentous 'tip links' connect adjacent stereocilia and transmit force to mechano-electrical transduction channels. Mechano-electrical transduction channels open in microseconds, and Ca<sup>2+</sup> entry rapidly raises [Ca<sup>2+</sup>] in stereocilia (10–20 ms time constant)<sup>7</sup>. Using hair cells from the *Arl13b-mCherry-GECO1.2*<sup>tg</sup> mouse, we can compare [Ca<sup>2+</sup>] changes in two structures (stereocilia and kinocilia) of similar geometry (4–10 μm length and 300–600 nm diameter), and determine whether the kinocilium is also a CaRMS, as suggested<sup>8</sup>.

*Arl13b-mCherry-GECO1.2* is expressed in all primary cilia of the inner ear sensory epithelium, including kinocilia of both inner hair cells (IHCs) and outer hair cells (OHCs) of the organ of Corti. Scanning electron microscopy at ages embryonic day (E)18 to postnatal (P)3 confirmed normal development of stereocilia bundles in transgenic animals (Extended Data Fig. 3). Fortuitously, some hair cell stereocilia also contained the Ca<sup>2+</sup> indicator (Fig. 1d and Extended Data Fig. 1d). To test for CaRMS, we applied laminar flow via a micropipette to IHC

bundles (Supplementary Video 1) or kinocilia and imaged via swept field confocal microscopy (up to 1,000 frames per second) to pinpoint the origin of Ca<sup>2+</sup> influx with high spatial and temporal resolution. Ratioing of GECO1.2 and mCherry fluorescence ( $F_{\text{GECO1.2}}/F_{\text{mCherry}}$ ) reduced movement-related artefacts (see Methods and Supplementary Information). As expected, deflection of the stereocilia bundle resulted in a rapid and robust increase in  $F_{\text{GECO1.2}}$  within the bundle, while  $F_{\text{mCherry}}$  remained largely unchanged (Fig. 1e–g and Supplementary Video 1). IHC bundle deflection increased the ratio approximately threefold (Fig. 2a), slowly recovering to the resting value within 2.5 s after flow application. The slow dissociation rate of Ca<sup>2+</sup> from GECO1.2 ( $\tau \approx 600$  ms; Extended Data Fig. 4) provides a valuable means of distinguishing true changes in [Ca<sup>2+</sup>] from movement-related artefacts. In contrast, kinocilia deflected by pressure steps over a range of developmental stages (E14 to P3) exhibited no detectable increase in [Ca<sup>2+</sup>]<sub>cilium</sub> (Fig. 2b–f and Supplementary Information). We conclude that kinocilia of mouse hair cells, unlike actin-based stereocilia, are not CaRMS.

Next, we examined kidney epithelia primary cilia, widely believed to be CaRMS<sup>1,3,9</sup>. Primary inner medullary collecting duct (mIMCD) epithelial cells were isolated from kidneys of P14–P21 *Arl13b-mCherry-GECO1.2*<sup>tg/tg</sup> mice, which express the kidney collecting duct epithelial cell markers, Aquaporin2 (Aqp2; Fig. 1b), and PC2 (Extended Data Fig. 1). *In vivo*, proximal tubule flow velocities are  $\sim 300 \mu\text{m s}^{-1}$  (ref. 10). To quantify these forces, we used a flow chamber to measure cilia bending at defined plasma membrane shear stress values in cultured mIMCD cells isolated from *Arl13b-mCherry-GECO1.2*<sup>tg/tg</sup> mice (Methods and Extended Data Fig. 5). Flow velocities ranging from 3 to 400  $\mu\text{m s}^{-1}$  (shear stress  $\approx 0.002$ –1 dyn cm<sup>−2</sup>) bent cilia (Fig. 3a, b) with half maximal bending at 70  $\mu\text{m s}^{-1}$  ( $\sim 0.11$  dyn cm<sup>−2</sup>). A similar cilium-bending profile is observed in modelling the cilium as a uniform cylindrical cantilevered beam<sup>11,12</sup>.

Primary cilia viewed from above were fully deflected by  $\sim 250 \mu\text{m s}^{-1}$  flow velocity (Supplementary Video 2 and Fig. 3). Fluorescence intensities immediately dropped as flow flattened the cilium (Fig. 3c, d). Ratioing  $F_{\text{GECO1.2}}/F_{\text{mCherry}}$  reduced this motion artefact (Fig. 3e and Extended Data Fig. 6). Imaging cilia from the side was most effective in reducing position/motion/path length artefacts; in this configuration, all parts of the primary cilium are in the same focal plane and never overlie the cell's variable autofluorescence (Fig. 3c, bottom, Supplementary Video 2 and Fig. 3f). Again, no change in [Ca<sup>2+</sup>]<sub>cilium</sub> was detected during deflection (Fig. 3g, h; digitonin control, Extended Data Fig. 6). Extending our study to other cell types, we found no CaRMS in osteocyte-like cells, mouse embryonic fibroblasts, or, indeed, any primary cilia examined (Extended Data Fig. 7). Instead, we found that in all cases where [Ca<sup>2+</sup>]<sub>cilia</sub> increased, the Ca<sup>2+</sup> rise was initiated at other sites in the cell and diffused from the cytoplasm into the cilium (Extended Data Figs 8 and 9 and Supplementary Video 3). At low image acquisition rates ( $>200$  ms per frame), this could easily be

<sup>1</sup>Department of Cardiology, Howard Hughes Medical Institute, Boston Children's Hospital, Boston, Massachusetts 02115, USA. <sup>2</sup>Department of Neurobiology, Howard Hughes Medical Institute, Harvard Medical School, Boston, Massachusetts 02115, USA. <sup>3</sup>Image and Data Analysis Core (IDAC), Harvard Medical School, Boston, Massachusetts 02115, USA.

\*These authors contributed equally to this work.

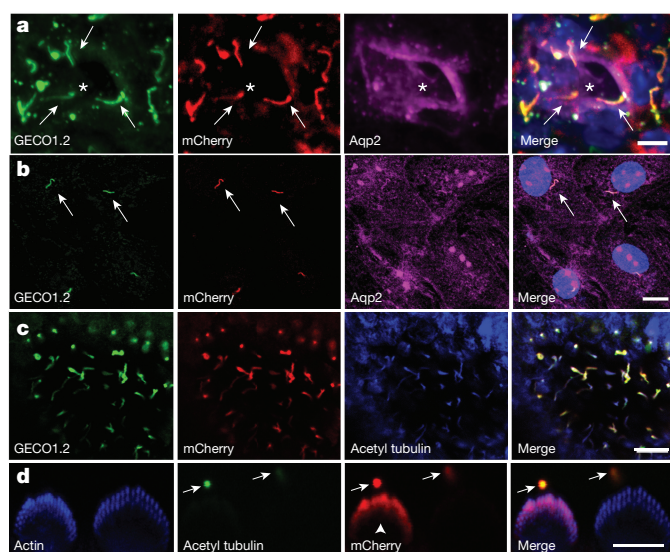
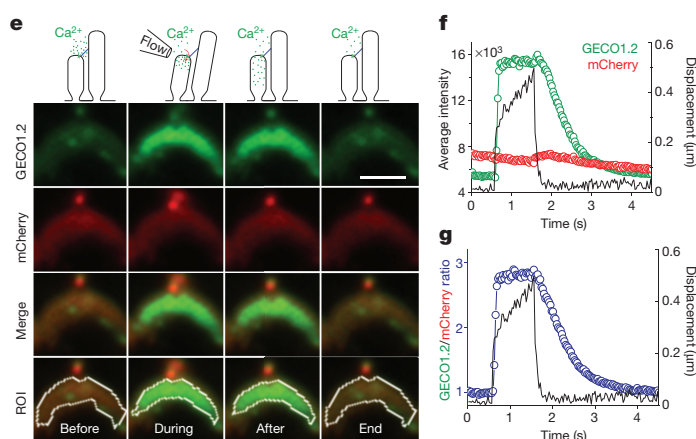


**Figure 1 | Genetically encoded  $\text{Ca}^{2+}$  indicator localizes to primary cilia and cochlear hair cell bundles.** **a**, P14 kidney section expressing Arl13b-mCherry-GECO1.2 in primary cilia. Cilia (white arrows) point into the lumen of an aquaporin-2-positive tubule (\*). Scale bar, 5  $\mu\text{m}$ . **b**, Aqp2 in primary epithelial cells isolated and cultured (3 days *in vitro*) from kidney papilla of P14–P21 Arl13b-mCherry-GECO1.2<sup>tg/tg</sup> mice (Extended Data Fig. 1). Scale bar, 10  $\mu\text{m}$ . **c**, Embryonic node from an Arl13b-mCherry-GECO1.2<sup>tg</sup> mouse. mCherry and GECO1.2 in cilia of the embryonic node overlap with the cilia marker, acetylated tubulin. Scale bar, 10  $\mu\text{m}$ . **d**, Arl13b-mCherry-GECO1.2 expression in IHCs. P4 organ of Corti explant showing two hair bundles; mCherry fluorescence (red), phalloidin-labelled actin (blue), and antibody to acetylated tubulin (green). Arl13b-mCherry-GECO1.2 protein localizes to all kinocilia as demonstrated by overlapping acetylated tubulin staining (arrows). Later in development, Arl13b-mCherry-GECO1.2 also localizes to stereocilia



bundles of some IHCs and OHCs (mCherry-positive bundle, arrowhead; Extended Data Fig. 1). Scale bar, 5  $\mu\text{m}$ . **e–g**, Deflection of IHC stereocilia bundle. Region of interest (ROI): white outline. **e**,  $F_{\text{GECO1.2}}$  and  $F_{\text{mCherry}}$  in stereocilia before, during, and after deflection. A 1 s flow stimulus (Supplementary Video 1) increased  $F_{\text{GECO1.2}}$  as  $\text{Ca}^{2+}$  entered the shorter rows of stereocilia. Scale bar, 5  $\mu\text{m}$ . **f**, Average  $F_{\text{GECO1.2}}$  and  $F_{\text{mCherry}}$  intensities (in arbitrary units) within the ROI; bundle displacement during deflection (black). Deflection increased  $F_{\text{GECO1.2}}$  threefold; mCherry bleached only slightly. **g**, Change of stereocilia  $F_{\text{GECO1.2}}/F_{\text{mCherry}}$  during the deflection (blue symbols); bundle displacement, black. After stimulus, the bundle rapidly returned to its resting position while  $\text{Ca}^{2+}$  fluorescence,  $F_{\text{GECO1.2}}$ , decayed slowly ( $\tau = 0.6$  s; Extended Data Fig. 4a, b). Images acquired sequentially, 30 ms per paired frame. All images are representative of more than ten images taken of biological triplicates.

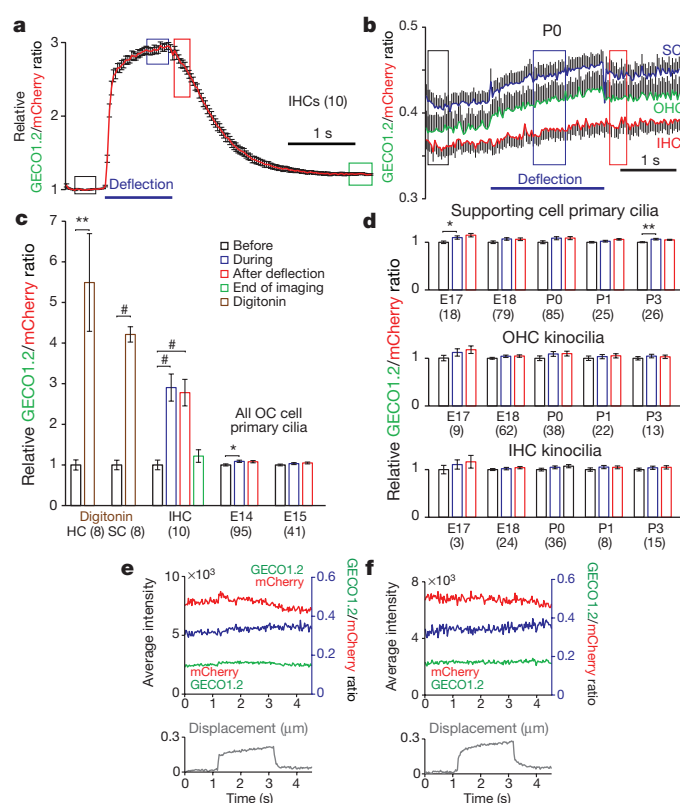


**Figure 2 | No change in  $[\text{Ca}^{2+}]_{\text{cilium}}$  in kinocilia of developing hair cells.** **a**, Average ratio changes in stereocilia for IHC bundle deflections in P5 + 3 days *in vitro* organ of Corti explants ( $n$  in brackets). **b**, Average ratio changes for IHC kinocilia (red,  $n = 36$ ), OHC kinocilia (green,  $n = 38$ ), and supporting-cell (SC) primary cilia (blue;  $n = 85$ ). The small positive slope results from differential dye bleaching (mCherry > GECO1.2). **c**, Normalized average fluorescent ratio changes at times boxed in **a** and **b**. Digitonin applied locally to permeabilize the membrane evoked an approximately fivefold ratio increase in hair cell kinocilia and SC primary cilia (brown bars). Black bar, normalized ratio before application; blue bar, during application; red bar, after application. IHC bundle deflection increased stereocilia ratios approximately threefold, persisting well after the bundle returned to its initial position. E14 and E15 explants showed no ratio change in any organ of Corti (OC) primary cilia. **d**, Kinocilia of IHC, OHC, and SC, from E17 to P3, show no ratio change upon deflection. The slight variability of the ratios from the SC cilia (before, during, after) is similar to the variability of the ratios in IHC and OHC kinocilia. **e**, **f**, Individual IHC (**e**) and OHC (**f**) kinocilia at P0.  $F_{\text{GECO1.2}}$  (green) and  $F_{\text{mCherry}}$  (red) intensities (in arbitrary units) and their ratio (blue) show no  $\text{Ca}^{2+}$  influx upon deflection. Kinocilium displacement in grey (bottom panel). Student's  $t$ -test, \* $P < 0.05$ , \*\* $P < 0.01$ , # $P < 0.001$ . All error bars  $\pm$  s.e.m.

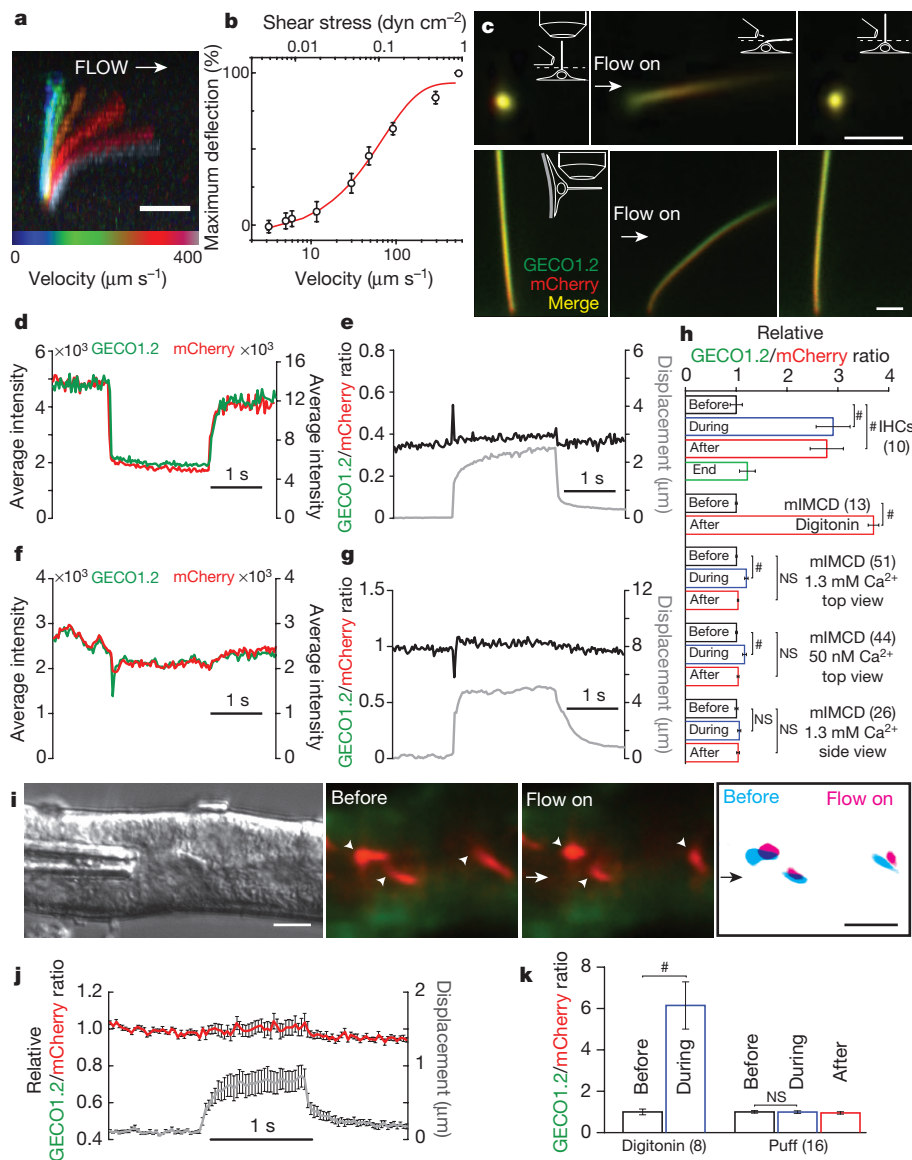


**Figure 3 | No change in  $[Ca^{2+}]_{cilium}$  during mechanical stimulation of kidney primary cilia.** **a**, mIMCD primary cilium at eight flow velocities (Extended Data Fig. 5). Scale bar, 5  $\mu m$ ; representative of 14 cilia (8 z-stacks, 12 focal planes each). **b**, Cilium deflection as a function of flow velocity and shear stress ( $n = 14$ ). **c**, Cultured primary mIMCD cells from P14–P21 *Arl13b-mCherry-GECO1.2<sup>tg/tg</sup>* mice imaged from above (top panels, 87 videos, 150 frames each) or the side (bottom, 32 videos  $\times$  150 frames); pipette  $\sim 4$ – $6 \mu m$  from cilium (Supplementary Video 2). Images: before, during, after 2 s,  $\sim 250 \mu m s^{-1}$  flow velocity stimulus. A MATLAB tracking algorithm identified the ROI frame-by-frame and quantified  $F_{GECO1.2}$  and  $F_{mCherry}$ . Scale bars, 2  $\mu m$ ; **d**, Channel intensities (in arbitrary units) from top panel in **c**. When flow flattened cilia, average  $F_{GECO1.2}$  and  $F_{mCherry}$  signals decreased owing to changes in the light path. **e**, Ratioing  $F_{GECO1.2}$  to  $F_{mCherry}$  reduced artefact (Extended Data Fig. 6), revealing no change in  $[Ca^{2+}]$  during deflection. **f**, Side view fluorescence of bottom panel in **c**;  $F_{GECO1.2}$  and  $F_{mCherry}$  were relatively constant. **g**, Side-imaged  $F_{GECO1.2}/F_{mCherry}$  ratio unchanged by deflection. **h**, Normalized  $F_{GECO1.2}/F_{mCherry}$  for positive controls (IHC stereocilia bundle deflection; data from Fig. 2c, and digitonin application); and for mIMCD primary cilia deflections in high and low  $[Ca^{2+}]$ ,  $n$  in brackets. Small ratio differences are due to motion artefact (Supplementary Information and Extended Data Fig. 6). **i**, Perfusion of acutely dissected kidney thick ascending limb tubules (representative of four preparations) (Extended Data Fig. 5). Green,  $F_{GECO1.2}$  and cytoplasmic autofluorescence; red,  $F_{mCherry}$ . A train of increasing 1 s pressure steps deflected intratubular cilia (arrowheads; Supplementary Video 5). Right,  $F_{mCherry}$  overlay from images before (cyan) and during (magenta) cilia deflection. Scale bars, 5  $\mu m$ ; 16 videos  $\times$  200 frames (middle). **j**, No change in  $[Ca^{2+}]_{cilium}$  for the smallest displacement in **i**. **k**, No change in  $[Ca^{2+}]_{cilium}$  before, during, and after deflection, data from **j** ( $1.0 \pm 0.06$  before versus  $0.99 \pm 0.06$  during,  $n = 16$  cilia). Student's  $t$ -test,  $\#P < 0.001$ , NS, not significant. Error bars  $\pm$  s.e.m.

misinterpreted as cilia CaRMS<sup>3,9,13–15</sup>. At very high, non-physiological flow velocities and shear stresses (peak, 10  $\text{dyn cm}^{-1}$  (refs 2, 16)), we observed that some cilium tips were ripped from the axoneme (Extended Data Fig. 9 and Supplementary Video 4) and external 2 mM  $Ca^{2+}$  filled the breached cilium<sup>17</sup>.

In intact kidney tubules, primary cilia are deflected in a pulsatile pattern<sup>18</sup>. We microdissected kidney tubules from P21 mice and deflected primary cilia inside isolated tubules (Extended Data Fig. 5). A train of 1 s stepped-amplitude flow stimuli in the lumen facilitated determination of the minimal flow deflecting cilia. Even flow sufficient to fully deflect cilia, however, did not change  $[Ca^{2+}]_{cilium}$ . Digitonin control increased  $Ca^{2+}$  ratios approximately sixfold (Fig. 3i–k and Supplementary Video 5).

During embryonic development, structures that are initially symmetric along the body axis develop a left–right orientation. This orientation depends on cilia in the embryonic node, a depression at the distal tip of the embryo<sup>19</sup>. Specialized motile cilia (Supplementary Video 6) in the central node direct fluid leftwards (viewed dorsally) at  $\sim 2$ – $4 \mu m s^{-1}$ , which is believed to initiate asymmetric gene expression across the node<sup>20</sup>. Disruption of flow or mutations in primary cilia proteins result in left–right patterning defects<sup>21</sup> such as situs inversus, while imposed fluid flow to the right side reverts left–right patterning<sup>22,23</sup>. A prominent hypothesis is that left-side crown cell primary cilia

are deflected by this flow, which mechanically activates ion channels in primary cilia and raises intracellular  $[Ca^{2+}]$ , leading to altered signalling and gene transcription in those cells and adjacent lateral plate mesoderm<sup>2,24</sup>. An alternative hypothesis is that the directed beating of nodal cilia creates a gradient of vesicles<sup>25</sup> or a secreted morphogen<sup>26</sup>.

To test the mechanosensitive model, we measured  $[Ca^{2+}]$  during deflection of left- and right-side nodal primary cilia (Fig. 4a, b, k, Extended Data Fig. 10 and Supplementary Videos 7 and 8). Cilia from developmental stages ‘early allantoic bud’ to two-somite were mechanically stimulated by applying flow using physiological levels (ramp from 0  $\mu m s^{-1}$  to  $\sim 10 \mu m s^{-1}$ ), or supraphysiological flow velocity of  $\sim 200 \mu m s^{-1}$ , similar to that previously shown to revert embryonic organ symmetry (Fig. 4b, c)<sup>22</sup>. Deflection of left- or right-sided nodal cilia did not change  $[Ca^{2+}]_{cilium}$  (Fig. 4d–i). These results demonstrate that primary cilia of the embryonic node are not CaRMS from physiological flow velocities to those 50–100 times greater. Notably, physiologically relevant flow velocities (less than  $\sim 10 \mu m s^{-1}$ ) barely deflected nodal crown cilia ( $458 \pm 22$  nm; Fig. 4k–p, Extended Data Fig. 10 and Supplementary Video 9) as predicted (Fig. 3a, b). Resting  $[Ca^{2+}]$  was  $\sim 300$  nM both in left- and in right-side cilia (Fig. 4j; for cytoplasmic calcium see ref. 23).

In summary, mechanical forces do not evoke  $Ca^{2+}$  signalling within up to 10 s of stimulation in the cilia of kidney tubules, the embryonic



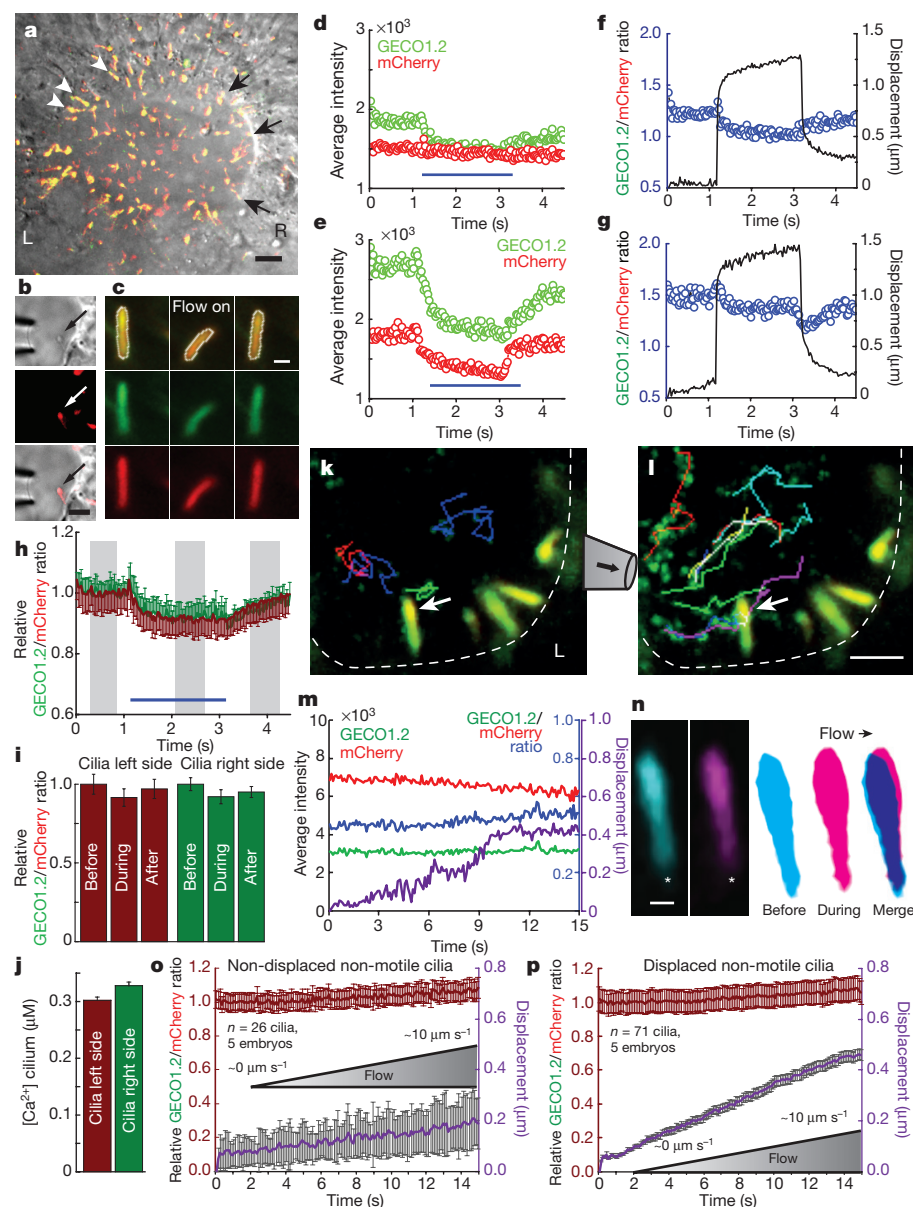


**Figure 4 | No change in  $[Ca^{2+}]_{\text{cilium}}$  in primary cilia of the embryonic node.** **a**, *Ar13b-mCherry-GECO1.2*<sup>28</sup> embryonic node, early headfold stage (EHF); L, left; R, right. Non-motile cilia; left, white arrowheads; right, black arrows. Scale bar, 20  $\mu\text{m}$ ;  $n = 4$  embryos. **b**, Crown-cell cilia deflected by  $2\text{ s}/\sim 200\text{ }\mu\text{m s}^{-1}$  flow velocity (2 videos  $\times$  500 frames). Scale bar, 5  $\mu\text{m}$ . **c**, Cilia from the left outer perimeter before (left), during (middle) and after (right)  $\sim 200\text{ }\mu\text{m s}^{-1}$  flow velocity. Top row, merged GECO1.2 and mCherry signals. White outline, ROI (32 videos  $\times$  150 frames). **d**, **e**,  $F_{\text{GECO1.2}}$  and  $F_{\text{mCherry}}$  (in arbitrary units) of a left (**d**) and right (**e**) nodal cilium;  $\sim 200\text{ }\mu\text{m s}^{-1}$ . **f**, **g**, Ratiometric changes on left (**f**) and right (**g**) sides;  $\sim 200\text{ }\mu\text{m s}^{-1}$  cilium deflection (black trace; same cilia as **d**, **e**). **h**, Average relative ratio changes for cilia on the left (burgundy,  $n = 29$ ) and right (green,  $n = 15$ ) sides of the node. **i**, Relative ratio changes; grey boxes in **h**, time blocks quantified. **j**, Resting  $[Ca^{2+}]$  in left- and right-side non-motile primary cilia.  $[Ca^{2+}]$  calculated as in Extended Data Fig. 2 and Methods (left cilium: 1.0,  $n = 67$ , 4 nodes; right cilium: 1.1,  $n = 72$ , 5 nodes); resting  $[Ca^{2+}]$  left:  $302 \pm 6\text{ nM}$ ; right:  $320 \pm 7\text{ nM}$ . **k**, **l**, Cilia on the left outer perimeter (dashed white line) with no net flow (**k**) or  $\sim 10\text{ }\mu\text{m s}^{-1}$  flow velocity (**l**) measured near the cilium (arrow). Coloured lines, tracks of beads (Supplementary Video 9). Scale bar, 5  $\mu\text{m}$ ; 42 videos  $\times$  150 frames. **m**, Traces of cilium in **k** (arrow). Displacement of cilium during  $0\text{--}10\text{ }\mu\text{m s}^{-1}$  ramp in purple. **n**, Cilium in **k** (arrow) at  $\sim 0\text{ }\mu\text{m s}^{-1}$  (left, frame average),  $\sim 10\text{ }\mu\text{m s}^{-1}$  (middle, frame average, end of deflection), and superposition (right, note  $< 1\text{ }\mu\text{m}$  deflection). Asterisk, ciliary base. Scale bar, 500 nm; 42 videos  $\times$  150 frames. **o**, **p**, Ratio changes of left crown-cell cilia from late bud to three-somite stage during flow from  $\sim 0$  to  $\sim 10\text{ }\mu\text{m s}^{-1}$  velocities. **o**, Ratio change for non-displaced cilia ( $n = 26$  cilia, 5 embryos), **p**, Ratio change for displaced cilia ( $n = 71$  cilia, 5 embryos; average centroid displacement,  $458 \pm 22\text{ nm}$ ). All error bars  $\pm$  s.e.m.

node, several cell lines used as models of cilia function, or kinocilia. Since mechanosensitive channels and putative mechanically gated G-protein-coupled receptors respond in the 10  $\mu$ s to 100 ms range<sup>27,28</sup>, we suspect the reported increases in  $[Ca^{2+}]_{cilium}$  after  $\sim$ 10–20 s stimulation<sup>3,15</sup> originate from the cell body. Indeed, imaging up to 100 Hz revealed that non-ciliary origins were always the initial site of  $\Delta[Ca^{2+}]$  (Extended Data Figs 8 and 9 and Supplementary Video 3) and the  $Ca^{2+}$  wave initiated in the cytoplasm propagated into the primary cilium. To account for previous observations, we speculate that the two primary sources of error were (1) insufficient time resolution— $Ca^{2+}$  originating from the cytoplasm can diffuse into the cilium in  $<200$  ms and be mistaken as originating from within the cilium, and (2) motion- and light-path-dependent artefacts. Finally, we do not imply that there are no mechanosensitive elements in primary cilia in physiologically relevant ranges, since motor, cytoskeletal, and other proteins are affected by changes in geometry and force without changes in ciliary  $[Ca^{2+}]$ <sup>29</sup>. An important implication of these findings is that situs inversus and polycystic kidney disease caused by the loss of polycystins<sup>23,30</sup> are not due to loss of mechanically induced cilia-initiated calcium signalling. These data should motivate investigators to focus on other potential mechanisms for regulation of ciliary ion

channels, and to determine whether calcium propagation into the cilium from the cytoplasm affects ciliary function.

**Online Content** Methods, along with any additional Extended Data display items and Source Data, are available in the online version of the paper; references unique to these sections appear only in the online paper.

Received 22 May 2015; accepted 16 February 2016.

Published online 23 March 2016.

1. Zimmerman, K. & Yoder, B. K. Snapshot: sensing and signaling by cilia. *Cell* **161**, 692–2.e1 (2015).
2. Hamada, H. Role of physical forces in embryonic development. *Semin. Cell Dev. Biol.* **47–48**, 88–91 (2015).
3. Nauli, S. M. *et al.* Polycystins 1 and 2 mediate mechanosensation in the primary cilium of kidney cells. *Nature Genet.* **33**, 129–137 (2003).
4. Corey, D. P. & Hudspeth, A. J. Ionic basis of the receptor potential in a vertebrate hair cell. *Nature* **281**, 675–677 (1979).
5. Corey, D. P. & Hudspeth, A. J. Response latency of vertebrate hair cells. *Biophys. J.* **26**, 499–506 (1979).
6. Sellick, P. M., Patuzzi, R. & Johnstone, B. M. Measurement of basilar membrane motion in the guinea pig using the Mössbauer technique. *J. Acoust. Soc. Am.* **72**, 131–141 (1982).
7. Beurg, M., Fettiplace, R., Nam, J. H. & Ricci, A. J. Localization of inner hair cell mechanotransducer channels using high-speed calcium imaging. *Nature Neurosci.* **12**, 553–558 (2009).



8. Kindt, K. S., Finch, G. & Nicolson, T. Kinocilia mediate mechanosensitivity in developing zebrafish hair cells. *Dev. Cell* **23**, 329–341 (2012).
9. Praetorius, H. A. & Spring, K. R. Bending the MDCK cell primary cilium increases intracellular calcium. *J. Membr. Biol.* **184**, 71–79 (2001).
10. Weinstein, A. M. A mathematical model of rat ascending Henle limb. III. Tubular function. *Am. J. Physiol. Renal Physiol.* **298**, F543–F556 (2010).
11. Schwartz, E. A., Leonard, M. L., Bizios, R. & Bowser, S. S. Analysis and modeling of the primary cilium bending response to fluid shear. *Am. J. Physiol.* **272**, F132–F138 (1997).
12. Young, Y. N., Downs, M. & Jacobs, C. R. Dynamics of the primary cilium in shear flow. *Biophys. J.* **103**, 629–639 (2012).
13. AbouAlaiwi, W. A. *et al.* Ciliary polycystin-2 is a mechanosensitive calcium channel involved in nitric oxide signaling cascades. *Circ. Res.* **104**, 860–869 (2009).
14. Jin, X. *et al.* Cilioplasm is a cellular compartment for calcium signaling in response to mechanical and chemical stimuli. *Cell. Mol. Life Sci.* **71**, 2165–2178 (2014).
15. Su, S. *et al.* Genetically encoded calcium indicator illuminates calcium dynamics in primary cilia. *Nature Methods* **10**, 1105–1107 (2013).
16. Lee, K. L. *et al.* The primary cilium functions as a mechanical and calcium signaling nexus. *Cilia* **4**, 7 (2015).
17. Delling, M., DeCaen, P. G., Doerner, J. F., Febvay, S. & Clapham, D. E. Primary cilia are specialized calcium signalling organelles. *Nature* **504**, 311–314 (2013).
18. O'Connor, A. K. *et al.* An inducible CiliaGFP mouse model for *in vivo* visualization and analysis of cilia in live tissue. *Cilia* **2**, 8 (2013).
19. Lee, J. D. & Anderson, K. V. Morphogenesis of the node and notochord: the cellular basis for the establishment and maintenance of left-right asymmetry in the mouse. *Dev. Dyn.* **237**, 3464–3476 (2008).
20. Okada, Y., Takeda, S., Tanaka, Y., Izpisua Belmonte, J. C. & Hirokawa, N. Mechanism of nodal flow: a conserved symmetry breaking event in left-right axis determination. *Cell* **121**, 633–644 (2005).
21. Nonaka, S. *et al.* Randomization of left-right asymmetry due to loss of nodal cilia generating leftward flow of extraembryonic fluid in mice lacking KIF3B motor protein. *Cell* **95**, 829–837 (1998).
22. Nonaka, S., Shiratori, H., Saijoh, Y. & Hamada, H. Determination of left-right patterning of the mouse embryo by artificial nodal flow. *Nature* **418**, 96–99 (2002).
23. Yoshida, S. *et al.* Cilia at the node of mouse embryos sense fluid flow for left-right determination via Pkd2. *Science* **338**, 226–231 (2012).
24. McGrath, J., Somlo, S., Makova, S., Tian, X. & Brueckner, M. Two populations of node monocilia initiate left-right asymmetry in the mouse. *Cell* **114**, 61–73 (2003).
25. Tanaka, Y., Okada, Y. & Hirokawa, N. FGF-induced vesicular release of Sonic hedgehog and retinoic acid in leftward nodal flow is critical for left-right determination. *Nature* **435**, 172–177 (2005).
26. Okada, Y. *et al.* Abnormal nodal flow precedes situs inversus in *iv* and *inv* mice. *Mol. Cell* **4**, 459–468 (1999).
27. Xiao, R. & Xu, X. Z. Mechanosensitive channels: in touch with Piezo. *Curr. Biol.* **20**, R936–R938 (2010).
28. Connelly, T. *et al.* G protein-coupled odorant receptors underlie mechanosensitivity in mammalian olfactory sensory neurons. *Proc. Natl Acad. Sci. USA* **112**, 590–595 (2015).
29. Iskratsch, T., Wolfenson, H. & Sheetz, M. P. Appreciating force and shape — the rise of mechanotransduction in cell biology. *Nature Rev. Mol. Cell Biol.* **15**, 825–833 (2014).
30. Ma, M., Tian, X., Igarashi, P., Pazour, G. J. & Somlo, S. Loss of cilia suppresses cyst growth in genetic models of autosomal dominant polycystic kidney disease. *Nature Genet.* **45**, 1004–1012 (2013).

**Supplementary Information** is available in the online version of the paper.

**Acknowledgements** We thank the Mouse Gene Manipulation Facility of the Boston Children's Hospital Intellectual and Developmental Disabilities Research Center (IDDR; NIH30-HD 18655), National Institutes of Health (NIH) 5R01 DC000304 to D.P.C., and the Kaplan Family for financial support to M.D. We thank J. Rivera, J. Angelo, J. Mager and K. Tremblay for help with developmental staging of mouse embryos, L. Palmer and G. Frindt for teaching M.D. the kidney tubule dissection, A. Weinstein for discussions of fluid velocities in kidney tubules, W. Fowle for access to the scanning electron microscopy facility, R. Stepanyan and J. Shen for help with statistics, and members of the Clapham and Corey laboratories for advice and discussion. We thank H. Zeng for the Ai95 mouse line, L. Bonewald for the MLO-Y4-cell line, P. Divieti Pajevic and J. Spatz for the Ocy454 cell line, and T. Indzhukulian for support. D.E.C. and D.P.C. are Investigators of the Howard Hughes Medical Institute.

**Author Contributions** M.D. and A.A.I. performed the experiments. X.L. and Y.L. helped with experiments; T.X. developed software for analysis. M.D., A.A.I., D.P.C., and D.E.C. analysed the data and wrote the manuscript.

**Author Information** Reprints and permissions information is available at [www.nature.com/reprints](http://www.nature.com/reprints). The authors declare no competing financial interests. Readers are welcome to comment on the online version of the paper. Correspondence and requests for materials should be addressed to D.E.C. ([dclapham@enders.tch.harvard.edu](mailto:dclapham@enders.tch.harvard.edu)) or D.P.C. ([dcory@hms.harvard.edu](mailto:dcory@hms.harvard.edu)).

## METHODS

The experiments were not randomized. The investigators were not blinded to allocation during experiments and outcome assessment.

**Molecular biology, transgenic animals.** The *Scal*/HindIII linearized *hArl13b-mCherry-GECO1.2* pCAG vector (chicken actin promoter) was gel-purified and injected into the pronucleus of *C57BL6/6J* oocytes at the transgenic animal core facility at Boston Children's Hospital (Boston, Massachusetts). The integration site for the *Arl13b-mCherry-GECO1.2* transgene was determined by genomic walking (Bio S&T). The genotype of transgenic animals was determined by PCR: primers 372-up, ACATGGCCTTTCCTGCTCTC; 372-down, TTCAACATTTCCGTGTCGCC; and 944-down, GACATCTGTGGGAGG AGTGG. PCR product for the wild-type genomic sequence: ~600 bp; transgene PCR product ~400 bp. All animal procedures of this study were approved by the IACUCs of Boston Children's Hospital and Harvard Medical School (Boston, MA). Animals were maintained according to ARCH standards at Boston Children's Hospital and euthanized using CO<sub>2</sub>.

**Isolation of mIMCD.** *Arl13b-mCherry-GECO1.2<sup>tg</sup>*: mIMCD cells were isolated as described<sup>31</sup>. Briefly, ten kidneys isolated from P14–P21 *Arl13b-mCherry-GECO1.2<sup>tg</sup>* mice were cut longitudinally with fine scissors and the outer and inner medulla removed. The tissue was cut into small pieces with a razor blade and digested in collagenase (2 mg ml<sup>-1</sup>) and hyaluronidase (1 mg ml<sup>-1</sup>) for 1 h at 37°C in L-15 medium (Life Technologies). After trituration of the homogenate, cells were washed twice in phosphate-buffered saline (PBS) and plated on laminin-coated dishes (Life Technologies). Cells were grown in DMEM (adjusted to 600 mOsm with urea and NaCl), containing 200 μM dibutyl-*l*-cAMP (db-cAMP), unless stated otherwise. After 2 days, cells were split on laminin-coated coverslips (NeuVito) and imaged after culturing for an additional 1–2 days to allow confluent cell growth. For side-view imaging, cells were grown on 24 mm Transwell inserts (Corning) until they reached confluency. The membrane was excised with a scalpel and folded before imaging. Where indicated, mIMCD cells were serum starved in DMEM containing 0.2% BSA for 24 h or 48 h. Imaging solutions: L-15 medium (1.3 mM Ca<sup>2+</sup>) or HEPES-containing solution buffered to 50 nM [Ca<sup>2+</sup>] (see 'Calibration of the ratiometric *Arl13b-mCherry-GECO1.2* sensor' for buffer composition).

**Microdissection of *Arl13b-mCherry-GECO1.2<sup>tg</sup>* kidney tubules.** Microdissection was performed as described previously<sup>32</sup> with modifications. In brief, 1-mm thick transverse slices of P14–P21 kidneys were incubated with collagenase (1 mg ml<sup>-1</sup>) and hyaluronidase (1 mg ml<sup>-1</sup>) for 30 min at 37°C in L-15 medium (Life Technologies), or gently dissected without prior treatment. The cortex was removed with fine forceps and bundles of tubules were isolated at the transition of inner (white) and outer (red) medulla (Extended Data Fig. 5c). Thick-walled individual tubules with luminal fluorescent cilia were microdissected and mounted on glass or plastic coverslips coated with Cell-Tak (Corning). Under ×4 magnification (upright Nikon NiE), a micromanipulator-mounted 20° micro-knife (Minitool) was used to cut individual tubules from the bundles. A second micromanipulator held a long-tapered micropipette (bent ~20° to ensure the tip of the pipette was parallel to the surface of the coverslip, Extended Data Fig. 5). Under higher magnification (×100/1.1 numerical aperture or ×60/1.0 numerical aperture water dipping lenses), the micropipette was gently inserted into the tubule lumen and the pressure stimulus applied. Regions of the tubule with no direct micropipette contact were used for Ca<sup>2+</sup> imaging. In some experiments a third micromanipulator was used to deliver digitonin (20 μM) to the tubules (direct injection into the tubule lumen or external application). Cilia from kidney tubule perfusion experiments were collected from three independent microdissections.

**Isolation of *Arl13b-mCherry-GECO1.2<sup>tg</sup>* and *Arl13b-mCherry-GECO1.2<sup>tg</sup>;GCaMP6f<sup>tg</sup>;E2aCre<sup>tg</sup>* embryos.** *GCaMP6f* (B6;129S-Gt(Rosa)26Sor<sup>tm95.1(CAG-GCaMP6f)Hze/J</sup>) and *E2a-Cre* (Tg(EIIa-cre)C5379Lmgd) transgenic animals were obtained from Jackson Laboratories. Embryo isolation was performed as described previously<sup>33</sup>. Timed pregnancies resulting from mating wild-type *C57BL6/6J*, *Arl13b-mCherry-GECO1.2<sup>tg</sup>* or *Arl13b-mCherry-GECO1.2<sup>tg</sup>/1g* females with *Arl13b-mCherry-GECO1.2<sup>tg</sup>/1g* or *GCaMP6f<sup>tg</sup>/1g*; *E2a-Cre<sup>tg</sup>/1g* males yielded embryos that were then selected for the appropriate developmental stages<sup>34</sup>. Embryos expressing motile cilia in the embryonic node at stages critical for asymmetric gene expression<sup>35</sup> (starting at developmental stages 'early allantoic bud' up to two-somite stage) were used for experiments. Embryos were mounted with the embryonic node facing up in a custom-designed embryo mounting plate (Extended Data Fig. 10b–d). Laser cut holes (diameters 0.5–1.2 mm) in 0.8 mm Delrin ensured a good fit of the embryo into the holding well (Extended Fig. 10b, c). All embryonic node imaging was performed in DMEM/F12 with 10% fetal calf serum (Invitrogen).

A similar mating strategy was used to obtain *Arl13b-mCherry-GECO1.2<sup>tg</sup>;GCaMP6f<sup>tg</sup>;E2a-Cre<sup>tg</sup>* E14 embryos. Mouse embryonic fibroblasts were

isolated from E14 embryos as described previously<sup>17</sup>. Where indicated, MEF cells were serum starved in DMEM containing 0.2% BSA for up to 48 h. To visualize cytoplasmic Ca<sup>2+</sup> oscillations, *Arl13b-mCherry-GECO1.2<sup>tg</sup>;GCaMP6f<sup>tg</sup>;E2a-Cre<sup>tg</sup>* embryos from late allantoic bud to late headfold stage were used. In brief, embryos were mounted in the upright position as described above and imaged for 4–6 min at a frame rate of 0.5 Hz on an upright FV1000 confocal system (Olympus, ×60/1.1 numerical aperture water dipping lens) at either 36°C or 22°C (room temperature). Cytoplasmic Ca<sup>2+</sup> oscillations were quantified using ImageJ as described previously<sup>33</sup> with slight modifications: in brief, fluorescence of all frames was averaged and individual frames were divided by average intensity to generate  $\Delta F/F$ . Images were thresholded to exclude cells with  $\Delta F/F$  less than 30%. Furthermore, only regions with area greater than 90 square pixels and circularities greater than 0.6 were used to define cells with cytoplasmic Ca<sup>2+</sup> oscillations. All Ca<sup>2+</sup> oscillations within 50 μm surrounding the embryonic node were analysed for occurrence on the left versus the right side of the node.

**Reagents.** The following reagents were used: mouse anti-acetylated tubulin (Sigma-Aldrich; T7451); CF 405M phalloidin to stain filamentous actin (Biotium; 00034); goat anti-PC2 (Santa Cruz; G-20 sc-10376), rat anti-mCherry (Life Technologies; M11240), chicken anti-EGFP (Aves Labs; GFP-1020).

**Immunocytochemistry, confocal microscopy.** Cells or embryos were fixed with 4% paraformaldehyde, permeabilized with 0.2% Triton X-100, and blocked by 10% donkey serum in PBS. Cells were labelled with the indicated antibody followed by secondary donkey anti-rabbit, anti-goat, or anti-mouse fluorescently labelled immunoglobulin-G (IgG) (Life Technologies) and Hoechst 33342 (Life Technologies). Confocal images were obtained using an inverted Olympus FV1000 (×60 1.2 numerical aperture water immersion objective lens) and images processed using ImageJ (NIH).

**Immunohistochemistry.** Fixed (4% paraformaldehyde) 15 μm frozen tissue sections were permeabilized with 0.5% TX100/PBS (pH 7.4) for 15 min and blocked with PBS containing 5% goat serum, 1% BSA, 0.1% fish gelatin, 0.1% TX-100, and 0.05% Tween20. For primary antibodies raised in mice, endogenous mouse IgGs were blocked by incubating sections with the unconjugated Fab fragment goat anti-mouse IgG for 1 h at room temperature. For goat primary antibodies, donkey serum and donkey secondary antibodies were used. Sections were washed twice in PBS-T, and incubated with primary antibodies in blocking solution overnight at 4°C. Slides were washed twice in PBS-T and goat anti-rabbit/anti-mouse fluorescently-labelled secondary antibodies applied at room temperature for 1 h with Hoechst 33342 (nuclear) dye. Sections were washed twice in PBS-T, mounted in Prolong Gold Antifade (Life Technologies), and imaged (inverted Olympus FV1000; ×60, 1.2 numerical aperture water immersion objective). Images were further processed with ImageJ (NIH).

**Ca<sup>2+</sup>-imaging in stereocilia and primary cilia.** *Arl13b-mCherry-GECO1.2*-expressing cilia were observed under an upright Nikon NiE microscope (×100, 1.1 numerical aperture, 2.5 working distance) equipped with an Opterra swept-field confocal imaging system (Bruker Nano Technologies) and a Photometrics Evolve 128 liquid-cooled EMCCD camera (128 pixels × 128 pixels, 120 nm effective pixel size). This system enables fast imaging of up to 500–1,000 frames per second (f.p.s.) in low-light conditions. In most cases, tissue was illuminated sequentially by 488 nm (GECO1.2) and 561 nm (mCherry) laser light, and imaged using the full CCD chip (15 ms exposure per channel; 33 f.p.s.). To increase light delivery to the camera and avoid excessive photobleaching, swept-field confocal imaging was performed in slit mode (35 μm).

**Measurements of cilia bending and flow velocities.** mIMCD and MEF cells isolated from *Arl13b-mCherry-GECO1.2<sup>tg</sup>* mice were seeded in an IBIDI μ-Slide VI 0.4 flow chamber coated with laminin (see IBIDI Application Note 11; for this chamber, apical membrane shear stress is  $\tau = \eta \times 131.6 \times \Phi$ , where  $\eta$  is dynamic viscosity (0.01 dyn s<sup>-1</sup> cm<sup>-2</sup>) and  $\Phi$  is flow rate in millilitres per minute. A syringe pump (Harvard Apparatus) delivered steady flow via 10 ml syringes containing L-15 medium. Z-stacks of primary cilia were recorded on an inverted Olympus FV1000 (×60, 1.2 numerical aperture water immersion objective). The bend angle was measured between ciliary base and tip<sup>18</sup>. Fluid velocities were measured by imaging the flow of the solution supplemented with 300 nm green fluorescent beads (Sicstar greenF, Micromod) at the focal plane corresponding to ciliary tips at rest. Images were acquired as line scans (2 ms per line) or in continuous scanning mode (64 or 128 ms per frame) and particles tracked using an ImageJ plugin.

**Calibration of the ratiometric *Arl13b-mCherry-GECO1.2* sensor.** Calibration was performed using an inverted Olympus FV1000 (×60, 1.2 numerical aperture water immersion objective) as described previously<sup>17</sup>. In brief, standard solutions of [Ca<sup>2+</sup>] (ranging from 50 nM to 50 μM) were prepared by adjusting the ratio of EGTA and CaCl<sub>2</sub> (MaxChelator) in 137 mM NaCl, 5.4 mM KCl, 10 mM HEPES. After isolation, mIMCD cells were plated onto 12 mm laminin-coated

glass coverslips (Neuvitro) and cultured for 3–4 days to allow cilia formation. For controls, digitonin membrane permeabilization (3 min) was followed by image acquisition in multiple fields of view. Ratios were obtained by dividing the average  $F_{\text{GECO1.2}}$  (per ROI, corresponding to a single cilium) by the average  $F_{\text{mCherry}}$ . The average ratios were plotted as a function of free  $[\text{Ca}^{2+}]$  fitted to a sigmoid curve:  $y = A_2 + (A_1 - A_2) / (1 + \exp[(x - x_0)/dx])$ , where  $A_1 = 0.15 \pm 0.03$ ,  $A_2 = 1.58 \pm 0.06$ ,  $x_0 = 442 \pm 25$ ,  $dx = 114 \pm 20$ , with  $x_0 = K_d$  (the dissociation constant). The  $K_d$  of bacterially expressed/purified GECO1.2 was  $1.1 \mu\text{M}$  (ref. 36), about twice the  $K_d$  measured for our GECO1.2 fusion construct in mammalian cells *in situ*.  $[\text{Ca}^{2+}]$  in embryonic node primary cilia was estimated from an  $R_{\text{min}}$ - and  $R_{\text{max}}$ -adjusted calibration curve, where both values were calculated from images collected on swept-field confocal imaging system. Late bud to late headfold embryos were permeabilized with  $20 \mu\text{M}$  digitonin (5 min) in either  $50 \text{ nM}$  or  $5 \mu\text{M}$   $[\text{Ca}^{2+}]$ . Resting values for nodal primary cilia were measured in DMEM/F12 + 10% FCS using the same imaging settings used to calculate  $R_{\text{min}}$  and  $R_{\text{max}}$ . Ratios were converted to  $[\text{Ca}^{2+}]$  using the adjusted  $\text{Ca}^{2+}$  calibration curve.

**Primary cilia and stereocilia deflections.** Primary cilia and stereocilia bundle deflections were performed using a custom-made fluid-jet system. Briefly, the micropipette pressure at the back of the pipette could be rapidly changed to a desired value by supplying vacuum and/or pressurized air via feedback-controlled solenoid valves (5–10 ms rise time for the pressure step stimulus). The micropipette was filled with bath solution and the pressure at the mouth of the pipette carefully adjusted before approaching to the cilium, ensuring that there was no flow applied to the cilium before the onset of the stimulus. Depending on the experimental design, digitonin was applied to the cells either using the fluid-jet pipette, or via an additional pipette positioned near the cilium and connected to an IM-9C microinjector (Narishige).

For kinocilium deflection experiments, organ of Corti explants were acutely dissected and mounted on a coverslip coated with CellTak, or immobilized with tungsten minuten pins (FST). All hair cell imaging experiments were performed at room temperature in L-15 cell culture medium (Invitrogen), containing in mM: NaCl (138), KCl (5.3),  $\text{CaCl}_2$  (1.3),  $\text{MgCl}_2$  (1.0),  $\text{Na}_2\text{HPO}_4$  (1.0),  $\text{KH}_2\text{PO}_4$  (0.44),  $\text{MgSO}_4$  (0.81). For stereocilia bundle  $\text{Ca}^{2+}$  imaging experiments, organ of Corti explants were dissected at P5 in L-15 medium and placed in culture in DMEM/F12 supplemented with 5% FBS and  $10 \text{ mg l}^{-1}$  ampicillin at  $37^\circ\text{C}$  (10%  $\text{CO}_2$ ). Explants were cultured for 3 days to increase the number of cells with sufficient sensor in stereocilia bundles.

All images were analyzed using a custom-made MATLAB tracking algorithm (described below), ImageJ (NIH), and Origin 8 (OriginLab).

Osteocyte-like cell lines MLO-Y4 and Ocy454 (ref. 37) were tested for authenticity in the laboratories that supplied them (see Acknowledgements) and for mycoplasma contamination by our laboratory. Both cell types were transfected with a plasmid encoding *Arl13b-mCherry-GECO1.2* using electroporation (LONZA, solution V, program T-20), as described previously<sup>38</sup>. Cells were seeded on coverslips after transfection and cultured at  $37^\circ\text{C}$ . Cells were used after a primary cilium was visible.

Embryonic node cilia were deflected with either a fast fluid-jet stimulus (described above) or with a ramp of slow, physiological level flow, delivering up to  $\sim 10 \mu\text{m s}^{-1}$  velocities: fluid flowed from a gravity-fed open-ended syringe to the micropipette. Flow rates were calibrated using  $100 \text{ nm}$  fluorescent beads (Sicstar-greenF, Micromod) and adjusted by gently lifting the syringe up 5–10 mm using a coarse micromanipulator. Perfusion fluid contained  $100 \text{ nm}$  fluorescent beads at  $10 \mu\text{g ml}^{-1}$  and was applied directly to the node via micropipette (pipette opening 4–6  $\mu\text{m}$  in diameter) that was 4–6  $\mu\text{m}$  away from the imaging area. Flow rates were adjusted manually as described above such that there was no net flow at the beginning of the experiment and  $\sim 10$ – $12 \mu\text{m s}^{-1}$  velocity at the end of the 15 s imaging experiment. Bead velocities and tracks were quantified and visualized using the 'manual tracking' plugin in ImageJ.

**Pipette flow calibration.** Pipette flow was calibrated using  $300 \text{ nm}$  fluorescent beads (Sicstar-greenF, Micromod) re-suspended at  $0.5 \text{ mg ml}^{-1}$  in DMEM/F12 10% FCS and loaded into micropipettes following sonication. A pressure stimulus was applied to the back of the pipette and steady flow imaged at 1,000 f.p.s. to ensure accurate frame-by-frame reading for each bead position while exiting the pipette and during its travel across the imaging area ( $\sim 15 \mu\text{m}$ ). The 1-ms time resolution of the calibration experiment was sufficient to resolve and calibrate the range of velocities used.

**Scanning electron microscopy.** Cultured mIMCD cells were fixed for 1 h at room temperature with 2.5% glutaraldehyde (Electron Microscopy Sciences) in 0.1 M sodium cacodylate buffer (pH 7.4), supplemented with 2 mM  $\text{CaCl}_2$ , and stored in distilled water. Organ of Corti explants were fixed following  $\text{Ca}^{2+}$  imaging experiments, or the entire cochlea was fixed, microdissected in distilled water and prepared for scanning electron microscopy as previously described<sup>39</sup>. Briefly, specimens

were dehydrated in ethanol, critical point dried from liquid  $\text{CO}_2$ , mounted on a carbon tape, sputter-coated with 5 nm platinum, and imaged on a Hitachi S-4800 field emission scanning electron microscope.

**Data analysis.** All images were analysed using a custom-made MATLAB tracking algorithm (described below), ImageJ (NIH), and Origin 8 (OriginLab).

**Sample size predetermination (power analysis).** In stereocilia we observed a  $2.9 \pm 1.05$  (mean  $\pm$  s.d.) -fold change (effect size  $d = 2.76$ ) in  $F_{\text{GECO1.2}}/F_{\text{mCherry}}$  after activation of a  $\text{Ca}^{2+}$ -conducting mechanosensor. Assuming a one-sided, paired *t*-test conducted at the 0.05 level of significance, a minimum of 12 cells would be required to detect an effect size of  $d = 1$  in mechanosensitive  $[\text{Ca}^{2+}]$  increase post-stimulation with 95% power.

**Image analysis.** Customized image analyses were developed using MATLAB to automatically process the large volume of ratiometric time-lapse data to improve quantitation and objectivity. The analysis was divided into three steps: channel alignment, object detection, and object tracking over time, with subsequent ratio calculations.

**Channel alignment.** Two factors contribute to misalignment of two channels during image acquisition: chromatic aberration from the optics and time delay due to sequential acquisition. For chromatic aberration, the two channels from each frame of a given time-lapse image were aligned using a translational transformation. A global translational transformation, derived from the individual frame transformations, was applied to all frames.

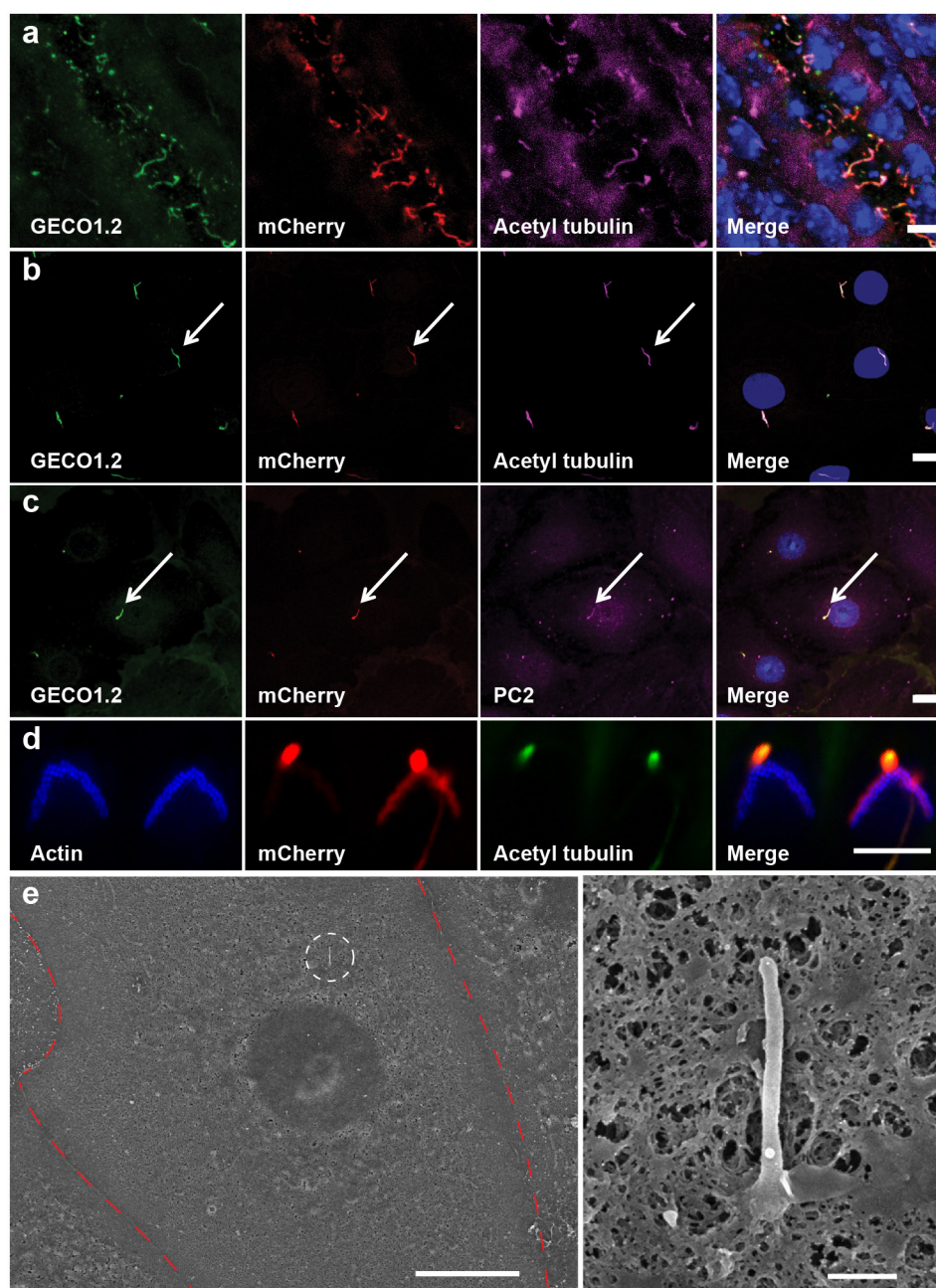
**Object detection.** Frame-by-frame superimposed images of both channels were created. When cilia motion was faster than acquisition time, channels were significantly misaligned. To create a combination image, two channels were added and smoothed using a Gaussian filter. Local image background was subtracted from the combination image, and Otsu thresholding used to detect objects. Small objects (less than three pixels) were filtered as noise.

**Object tracking with ratio calculations.** Different cilia in the same image vary with relative orientation. During flow application, many cilia undergo large deflections and even cross one another, further complicating the tracking of individual cilia. A tracking algorithm based on object overlap was implemented. It included features such as splitting of crossed cilia, linking cilia with no spatial overlap, and closing gaps over a given number of time frames. Once an individual cilium was tracked, the analysis code measured the signal of the cilium from both channels, calculated the ratio, and plotted it against time or spatial displacement.

**Code availability.** The algorithms were developed in MATLAB in open-source, and are available upon request.

1. Faust, D. *et al.* Culturing primary rat inner medullary collecting duct cells. *J. Vis. Exp.* **76**, 50366 (2013).
2. Palmer, L. G. & Frindt, G. Gating of Na channels in the rat cortical collecting tubule: effects of voltage and membrane stretch. *J. Gen. Physiol.* **107**, 35–45 (1996).
3. Takao, D. *et al.* Asymmetric distribution of dynamic calcium signals in the node of mouse embryo during left-right axis formation. *Dev. Biol.* **376**, 23–30 (2013).
4. Downs, K. M. & Davies, T. Staging of gastrulating mouse embryos by morphological landmarks in the dissecting microscope. *Development* **118**, 1255–1266 (1993).
5. Yoshida, S. & Hamada, H. Roles of cilia, fluid flow, and  $\text{Ca}^{2+}$  signaling in breaking of left-right symmetry. *Trends Genet.* **30**, 10–17 (2014).
6. Zhao, Y. *et al.* An expanded palette of genetically encoded  $\text{Ca}^{2+}$  indicators. *Science* **333**, 1888–1891 (2011).
7. Spatz, J. M. *et al.* The Wnt inhibitor sclerostin is up-regulated by mechanical unloading in osteocytes in vitro. *J. Biol. Chem.* **290**, 16744–16758 (2015).
8. Xiao, Z. *et al.* Cilia-like structures and polycystin-1 in osteoblasts/osteocytes and associated abnormalities in skeletogenesis and Runx2 expression. *J. Biol. Chem.* **281**, 30884–30895 (2006).
9. Indzhukulian, A. A. *et al.* Molecular remodeling of tip links underlies mechanosensory regeneration in auditory hair cells. *PLoS Biol.* **11**, e1001583 (2013).
10. DeCaen, P. G., Dellinger, M., Vien, T. N. & Clapham, D. E. Direct recording and molecular identification of the calcium channel of primary cilia. *Nature* **504**, 315–318 (2013).
11. Nagasawa, H., Miyamoto, M. & Fujimoto, M. [Reproductivity in inbred strains of mice and project for their efficient production (author's translation)]. *Jikken Dobutsu* **22**, 119–126 (1973).
12. Yuan, S., Zhao, L., Brueckner, M. & Sun, Z. Intraciliary calcium oscillations initiate vertebrate left-right asymmetry. *Curr. Biol.* **25**, 556–567 (2015).
13. Tian, L. *et al.* Imaging neural activity in worms, flies and mice with improved GCaMP calcium indicators. *Nature Methods* **6**, 875–881 (2009).
14. Nagai, T., Yamada, S., Tominaga, T., Ichikawa, M. & Miyawaki, A. Expanded dynamic range of fluorescent indicators for  $\text{Ca}^{2+}$  by circularly permuted yellow fluorescent proteins. *Proc. Natl Acad. Sci. USA* **101**, 10554–10559 (2004).
15. Chen, T. W. *et al.* Ultrasensitive fluorescent proteins for imaging neuronal activity. *Nature* **499**, 295–300 (2013).

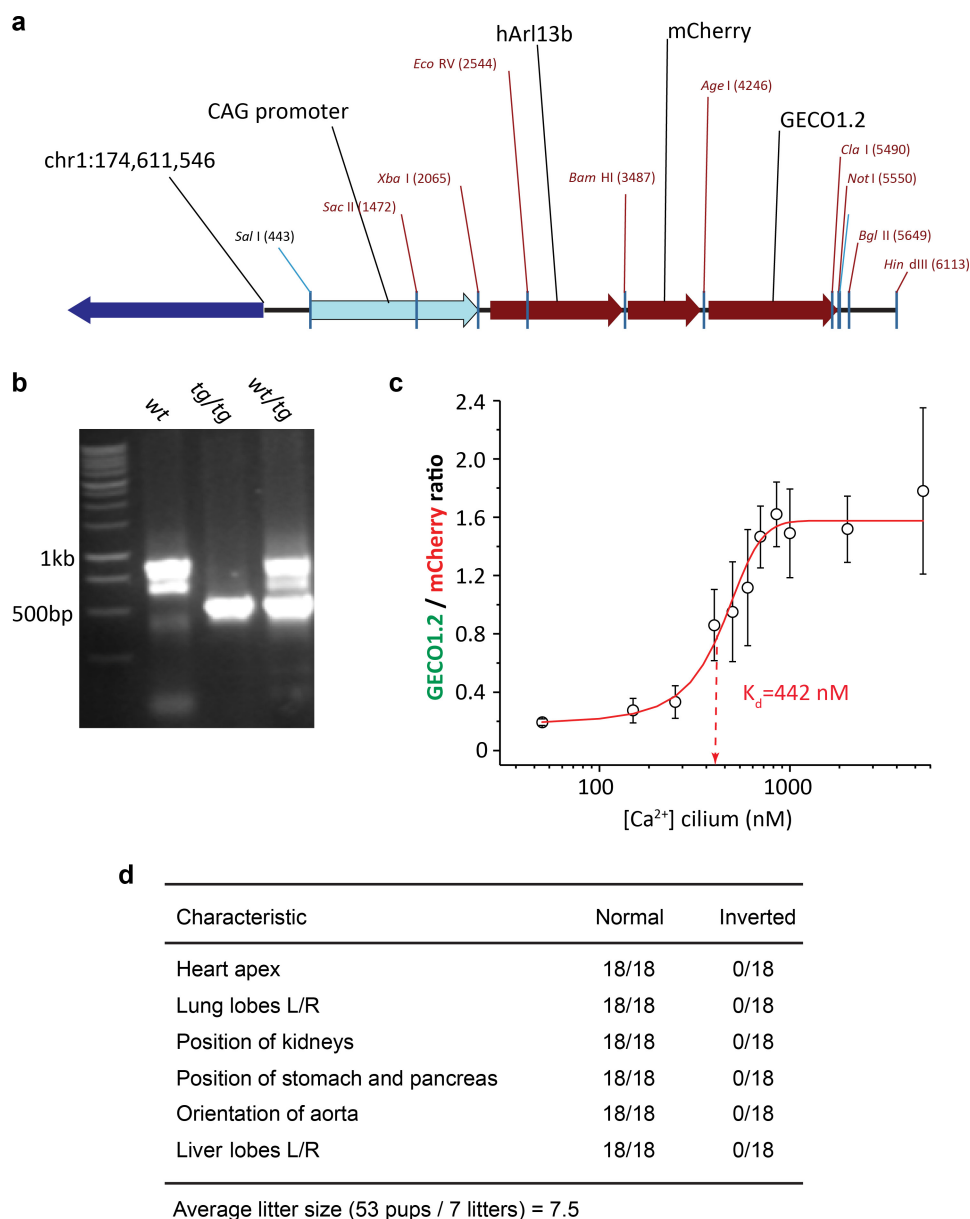




**Extended Data Figure 1 | Arl13b-mCherry-GECO1.2 identifies primary cilia.** Arl13b-mCherry-GECO1.2 contains an improved genetically encoded calcium indicator<sup>36</sup> (GECI) with an apparent  $K_d$  of 450 nM (Extended Data Fig. 2), well suited to work within the reported range of ciliary  $\text{Ca}^{2+}$  concentrations ( $[\text{Ca}^{2+}]_{\text{cilium}}$ )<sup>40</sup>. The genomic integration site of the transgene is within a non-coding region of chromosome 1 (Extended Data Fig. 2) and transgenic animals maintained as homozygotes (*Arl13b-mCherry-GECO1.2*<sup>tg</sup>) are viable, have average litter sizes, and do not show phenotypes consistent with cilia defects (for example, situs inversus, organ malformation; Extended Data Fig. 2). **a**, Frozen tissue section of P21 mouse kidney. GECO1.2 and mCherry are preferentially localized to cilia, identified by the cilia-specific marker,

anti-acetylated tubulin antibody. **b**, **c**, Primary mIMCD cells isolated from kidneys of P14–P21 *Arl13b-mCherry-GECO1.2* transgenic mice. Ciliary localization (arrow) of anti-polycystin 2 antibody in **c**. Scale bars, 10  $\mu$ m. **d**, Two OHC hair bundles marked with the actin-binding peptide, phalloidin. One of the stereocilia bundles expresses Arl13b-mCherry-GECO1.2. Kinocilia on both OHCs marked with an antibody to acetylated tubulin, express Arl13b-mCherry-GECO1.2. Scale bar, 5  $\mu$ m. **e**, Scanning electron micrograph of a primary mIMCD cell. Left, red dashed line outlines a single mIMCD cell; white circle indicates the primary cilium. Scale bar, 10  $\mu$ m. Right, magnified image. No defects in cilia formation were evident following 3–4 days in culture. Scale bar, 500 nm. All images are representative of more than ten images taken of biological triplicates.

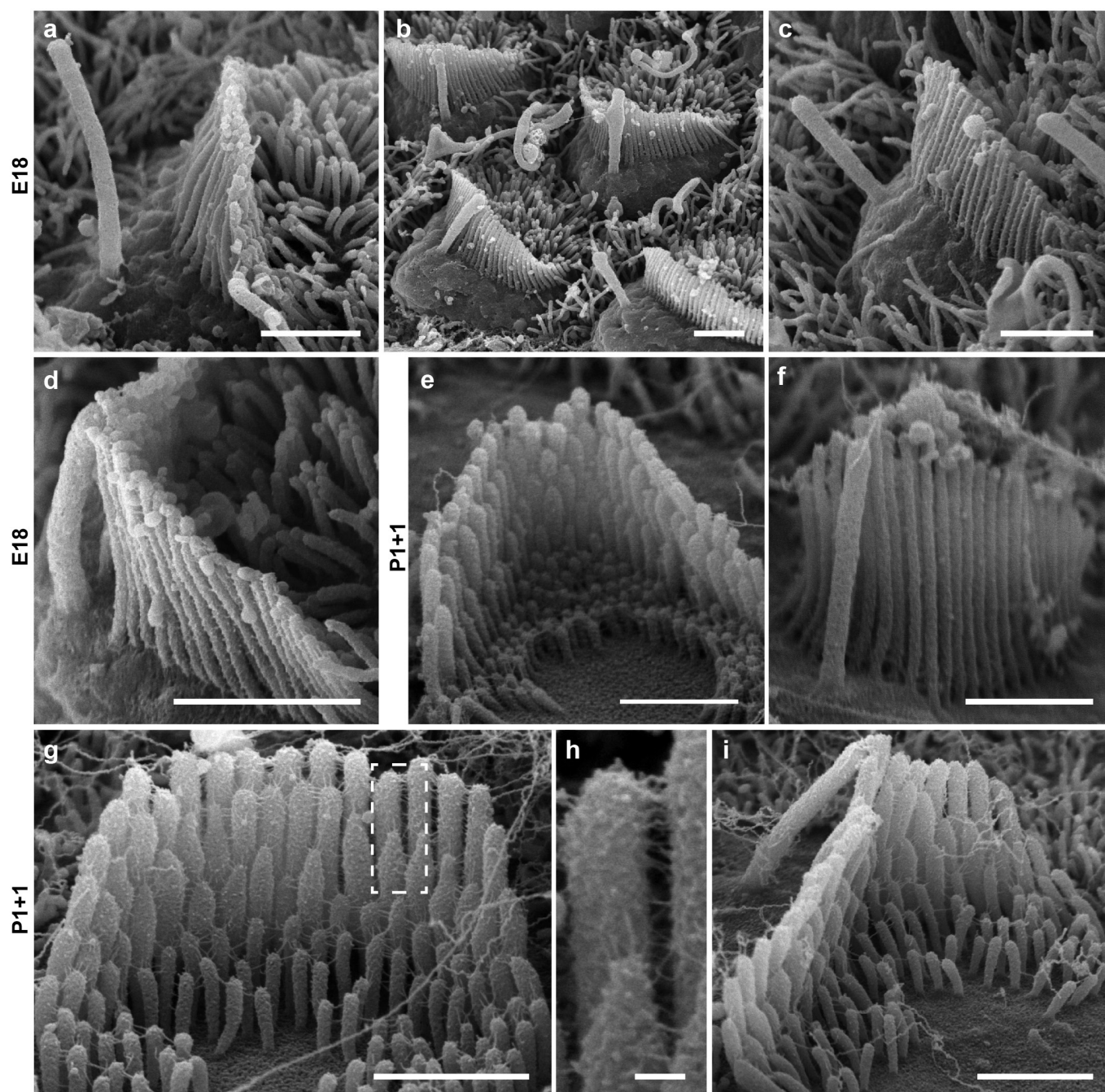




**Extended Data Figure 2 | *Arl13b*-mCherry-GECO1.2 transgenic mouse.**

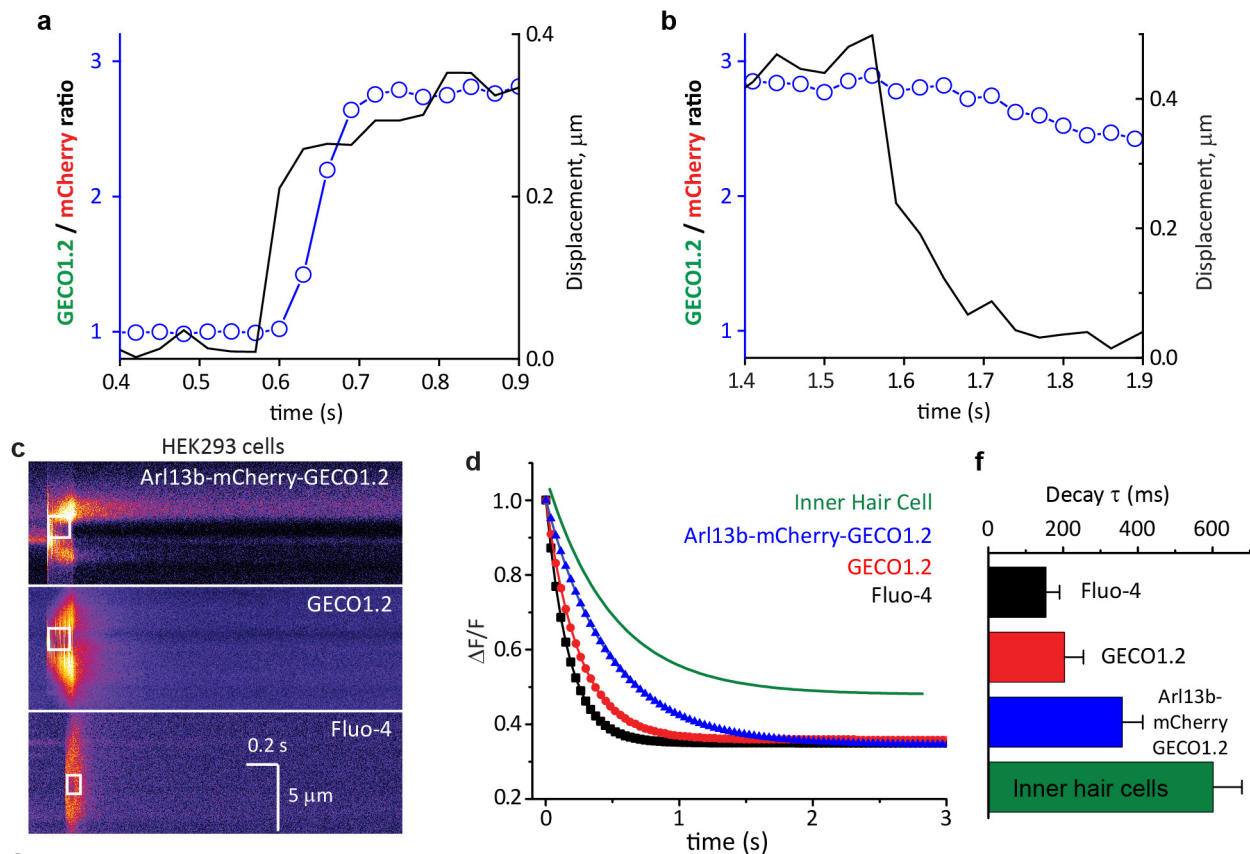
**a**, Transgene orientation and integration site. The transgene was integrated into the non-coding region of chromosome 1 (position 174,611,500).  
**b**, The genotype of transgenic animals was determined by PCR using the following primers: 372-up, ACATGGCCTTTCTGCTCTC; 372-down, TTCAACATTTCCGTGTCGCC; and 944-down, GACATCTGTGGGAGGAGTGG. The PCR product for wild-type genomic sequence was ~600 bp; the transgene PCR product was ~400 bp.

**c**, mIMCD cells isolated from *Arl13b*-mCherry-GECO1.2<sup>tg</sup> mice were imaged after permeabilization with 15  $\mu$ M digitonin in varying extracellular  $[Ca^{2+}]$ . Average ratios ( $n = 12$  cilia per each data point) are plotted versus free  $[Ca^{2+}]$ . *Arl13b*-mCherry-GECO1.2 calibration fitted by a Boltzmann curve ( $R^2 = 0.98$ ;  $K_d = 442$  nM). **d**, Phenotype of *Arl13b*-mCherry-GECO1.2<sup>tg/tg</sup> mice. Mouse organ morphology/orientation appeared normal (heterotaxy was not observed) and breeding animals had normal litter sizes (6–8 for C57Bl/6 (ref. 41)). All error bars  $\pm$  s.e.m.



**Extended Data Figure 3 | *Arl13b-mCherry-GECO1.2<sup>tg/tg</sup>* mouse organ of Corti hair cells develop normal stereocilia bundles.** Hair bundles from *Arl13b-mCherry-GECO1.2<sup>tg/tg</sup>* mice during development. **a–d**, Cochlear hair cells acutely dissected at age E18 appear normal. **a**, IHC, with kinocilium not attached to stereocilia. **b**, **c**, OHC stereocilia bundles with some kinocilia attached to the bundles. **d**, IHC bundle with kinocilium attached at tip. **e–i**, Cultured organ of Corti explant dissected

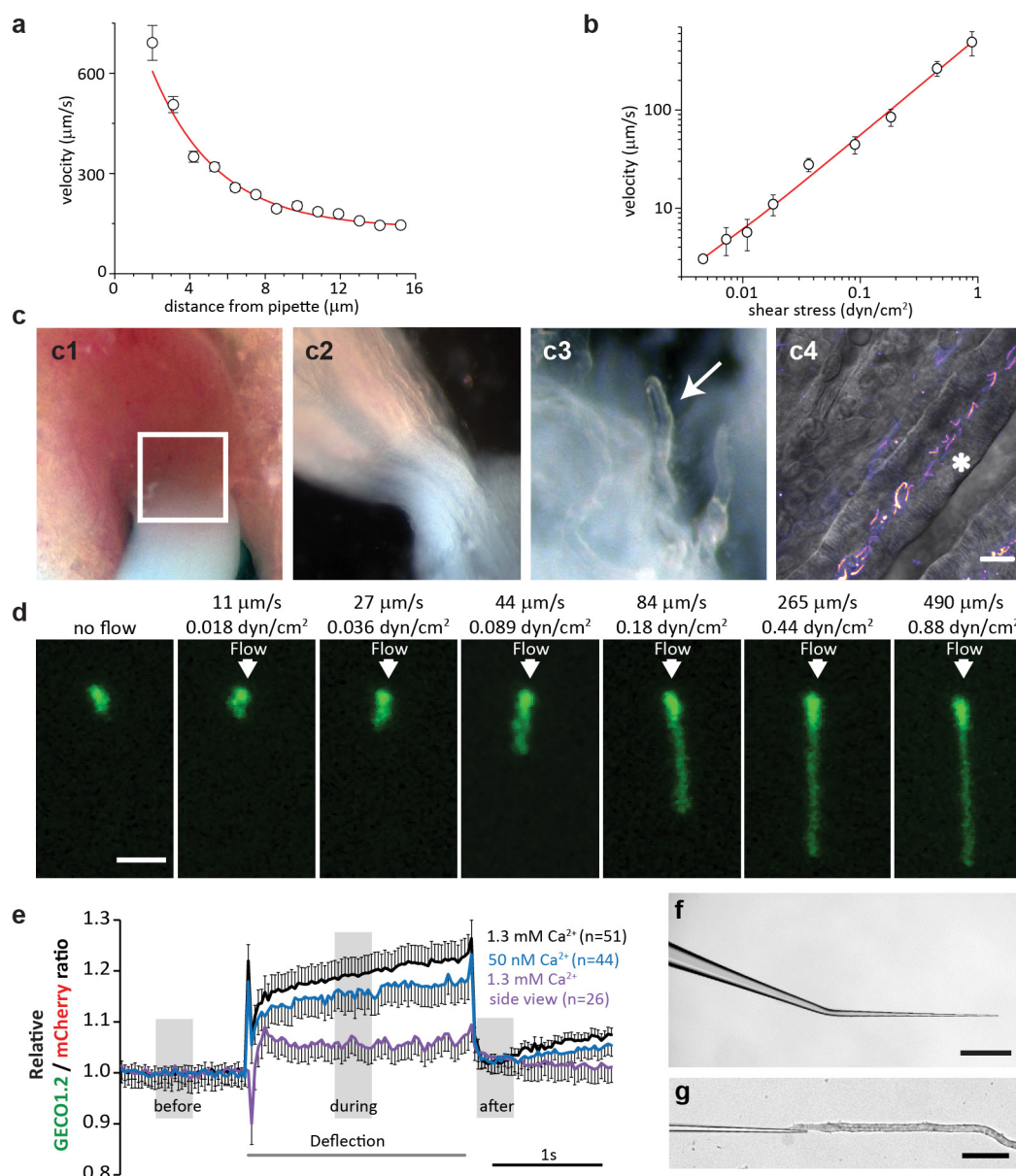
at P1 + 1 day *in vitro*. **e**, OHC with normal shape and stereocilia staircase structure. **f**, OHC stereocilia bundle with kinocilium. **g**, IHC with normal shape and stereocilia staircase structure; tip links and other links present. **h**, Pair of stereocilia (dashed box in **f**) at higher magnification. **i**, IHC with kinocilium attached at tip. Scale bars, 1 μm (except **h**, 100 nm). All images are representative of more than three images.



**Extended Data Figure 4 | GECO1.2  $k_{\text{off}}$  for  $\text{Ca}^{2+}$  dissociation from GECO1.2, measured in cells.** **a**, **b**, Fig. 1g at higher time resolution.  $F_{\text{GECO1.2}}/F_{\text{mCherry}}$  (open circles) relative to bundle motion (black line) at the initial deflection (**a**) and after return to the resting position (**b**). Bundle deflection preceded the  $F_{\text{GECO1.2}}/F_{\text{mCherry}}$  increase by two frames ( $\sim 60$  ms). At the termination of the flow stimulus and return to the resting position, the ratio remained elevated owing to the slow decay ( $\tau \approx 0.6$  s) of the  $\text{Ca}^{2+}$  from GECO1.2. **c**, Rapid  $\text{Ca}^{2+}$  uncaging was used to measure the  $\text{Ca}^{2+}$  decay rates for GECO1.2 (not bound to the membrane), Arl13b-mCherry-GECO1.2 (bound to the membrane), and the Fluo-4 control with its established time constant of decay. HEK293 cells were transfected with GECO1.2 or Arl13b-mCherry-GECO1.2 constructs and loaded with caged  $\text{Ca}^{2+}$  (NP-EGTA), or loaded with a combination of Fluo4-AM

and NP-EGTA. Caged  $\text{Ca}^{2+}$  was released by a local 100–200 ms pulse of ultraviolet laser illumination (white box); images were acquired in line scan mode (2 ms per vertical line). Representative of more than 16 images. **d**, Representative fitted fluorescence intensity decays of Fluo-4 in HEK293 cells (black), GECO1.2 (red), and Arl13b-mCherry-GECO1.2 (blue), compared with GECO1.2 from Arl13b-mCherry-GECO1.2 IHCs following deflection (green). **e**, Table summarizing molecular properties of genetically encoded calcium indicators (GECIs) used in current and previous reports describing ciliary  $\text{Ca}^{2+}$  signalling<sup>14–17,36,42–45</sup>. **f**, Average decay rates,  $\tau$ , for indicators in **c**, **d**. Fluo-4:  $\tau = 154 \pm 36$  ms ( $n = 16$ ); GECO1.2 in HEK293 cells:  $\tau = 203 \pm 50$  ms ( $n = 19$ ); Arl13b-mCherry-GECO1.2 in HEK293 cells:  $\tau = 358 \pm 55$  ms ( $n = 16$ ); Arl13b-mCherry-GECO1.2 in IHC stereocilia:  $\tau = 601 \pm 70$  ms ( $n = 10$ ). Averages  $\pm$  s.d.

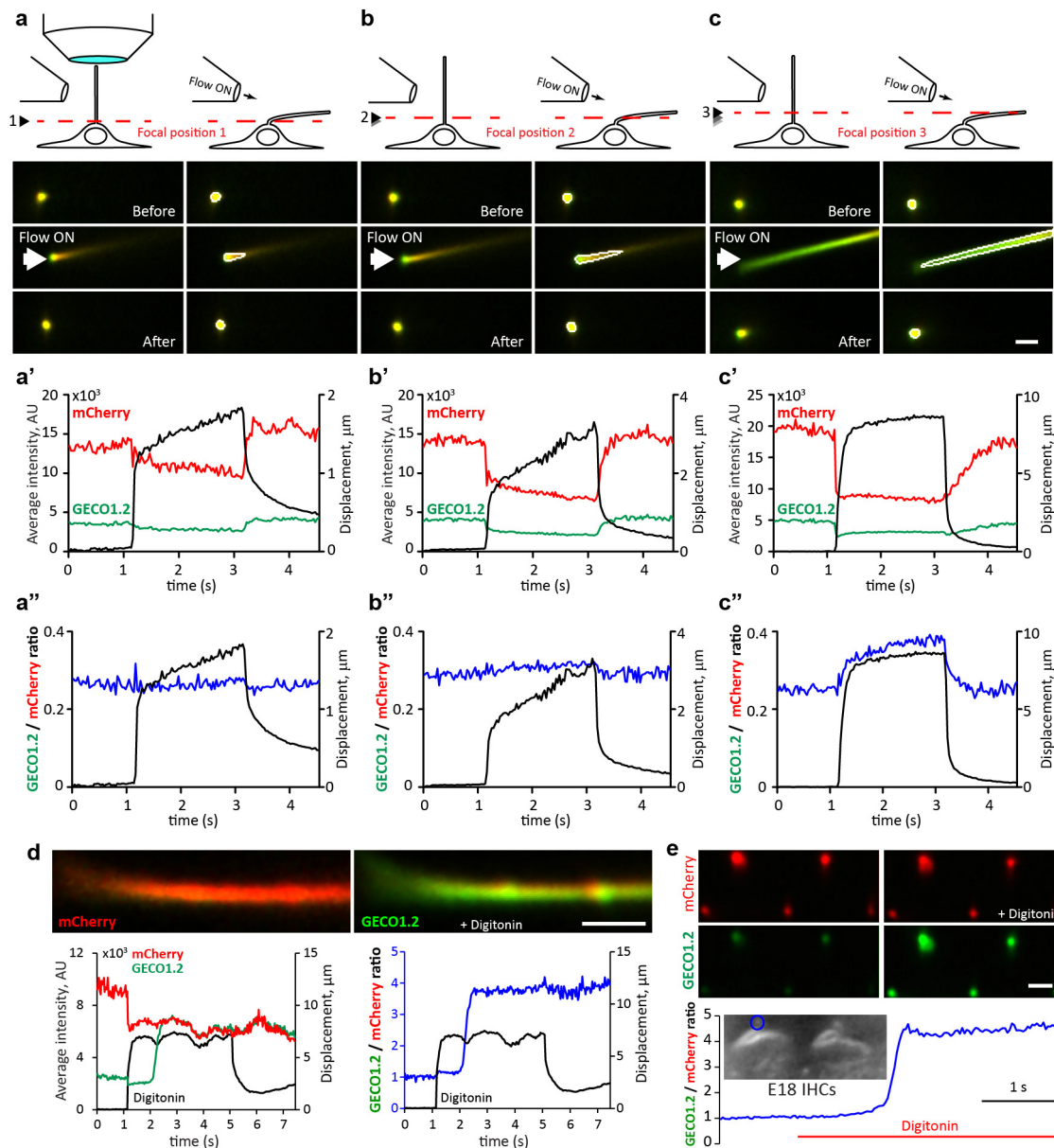




**Extended Data Figure 5 | Kidney tubule dissection and flow velocity calibration.** **a**, Calibration of the fluid velocity exiting the stimulus pipette versus distance from the mouth of the pipette (3- $\mu\text{m}$  pipette, 6.4 mm Hg pressure step). The pipette was positioned  $\sim 4\text{--}6\mu\text{m}$  from the cilium, delivering a flow velocity of  $250\text{--}300\mu\text{m s}^{-1}$  ( $n=5$ ). **b**, Velocity measured at the tip of the cilium and calculated shear stress at the plasma membrane ( $n=6$ ). **c**, Microdissection of kidney tubules. **c1**, Coronal section of P15 kidney; white box indicates the microdissected area. **c2**, Area from **c1** following microdissection. **c3**, Small bundle of tubules; individual tubules gently separated from the bundle (arrow). **c4**, Tubules with thick walls and fluorescent cilia (asterisk) used for experiments. Scale bar,  $5\mu\text{m}$ . Images representative of more than six preparations. **d**, Maximum intensity z-projection of mIMCD primary cilia deflected in the flow chamber using defined fluid velocities. Scale bar,  $3\mu\text{m}$ ; representative of 14 cilia each with 7 z-stacks containing 12 frames. **e**, Relative ratio changes in primary mIMCD primary cilia during deflection, three experimental conditions. Black and blue lines represent the averaged normalized ratio changes for top views of cilia deflection in 1.3 mM and 50 nM  $[\text{Ca}^{2+}]$ , respectively.

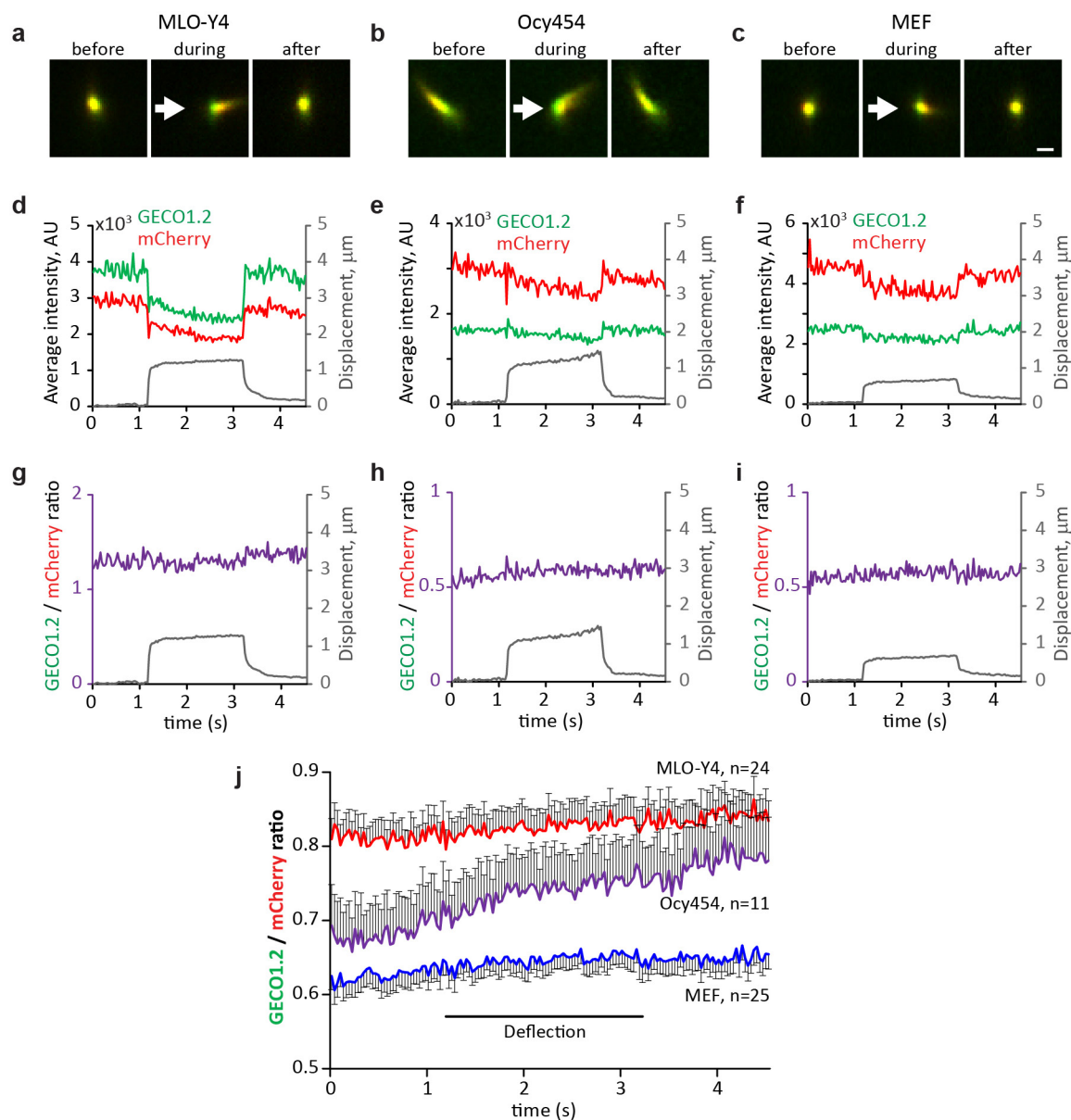
The increase in ratio upon cilium deflection is comparable between high and low external  $[\text{Ca}^{2+}]$ , suggesting that the ratio change did not result from  $\text{Ca}^{2+}$  entry (Fig. 3h for  $P$  values). In addition, the return to baseline with cilium movement was much faster than the  $\text{Ca}^{2+}$  indicator response time, providing further evidence that it is a motion artefact. Such fast responses were not observed in the bona fide  $\text{Ca}^{2+}$  entry into IHC stereocilia (Fig. 2a and Extended Data Fig. 4b, d). Purple line represents the average normalized ratio changes for side-imaged cilia deflections in the presence of 1.3 mM  $[\text{Ca}^{2+}]$ . Ratio changes were negligible in side views, as the motion artefact (light path length change upon motion) is small. The positive slope seen in top views results from differential dye bleach, faster for mCherry than GECO1.2. Bleaching has a much more pronounced effect in top views, probably from the change in geometry, contribution from underlying autofluorescence, and relative light exposure upon bending. **f**, Micropipette used for cilia deflection inside the kidney tubules. Scale bar,  $0.5\text{ mm}$ . **g**, Insertion of micropipette into the tubule. Scale bar,  $100\mu\text{m}$ . All error bars  $\pm$  s.e.m.





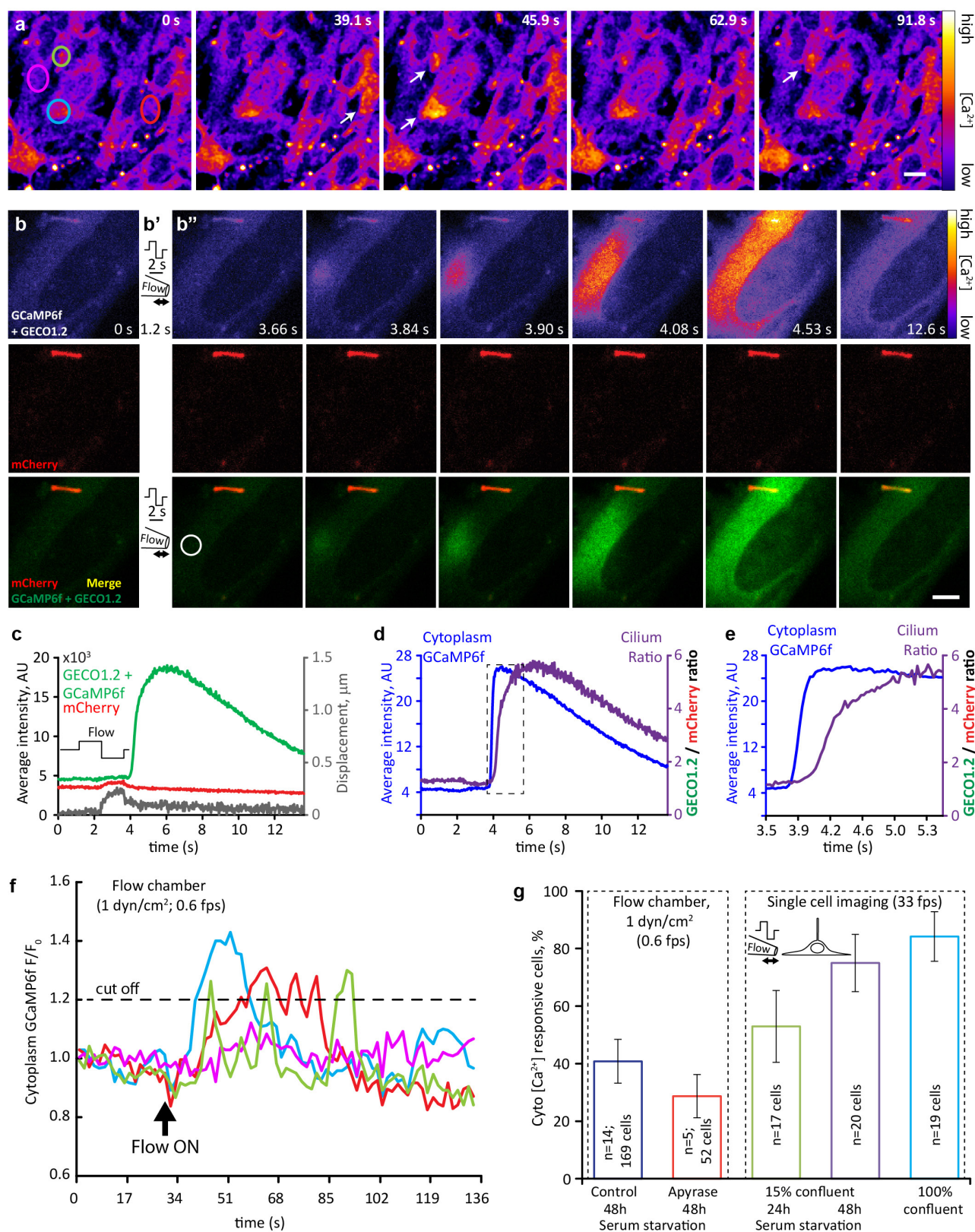
**Extended Data Figure 6 | Deflection of primary cilia in the presence of 50 nM  $[\text{Ca}^{2+}]$  reveals focal-plane-dependent artefact present in 'top view' imaging conditions; saturation controls for sensor. a–c,** An mIMCD cell cilium was repeatedly deflected in a low (50 nM)  $[\text{Ca}^{2+}]$  solution. The same flow stimulus (same pipette) was applied to the cilium while imaging in different focal planes. Top panels, experimental arrangement and fluorescence images of the cilium; red dashed lines indicate the focal plane for each set of images. Middle panels (a'–c'), average fluorescence intensity change for  $F_{\text{GECO1.2}}$  (green) and  $F_{\text{mCherry}}$  (red) during deflection (black). Lower panels (a''–c''), ratio change (blue) during deflection (black). **a,** Primary cilium near its attachment to the cell. **b,** At a slightly higher focal plane, deflection enlarges the cross section of the cilium. **c,** A focal plane  $\sim 1 \mu\text{m}$  above the cell surface. Different segments of the same cilium were imaged upon deflection. Note that the artefact increases with larger cross section changes. Thus, top view imaging of cilia is fraught with two interrelated artefacts: (1) at high

$z$ -resolution ( $0.8 \mu\text{m}$ ), the section of the cilia being imaged changes upon deflection, thus conflating fluorescence changes from different regions of the cilium; (2) at lower  $z$ -resolution, the path length, fluorescent indicator volume, and optical properties of the cilium above and below the image plane all change upon deflection and thus contribute to the apparent  $[\text{Ca}^{2+}]$  reporter changes. **d, e,** Digitonin permeabilization indicates that the Arl13b–mCherry–GECO1.2 sensor is not saturated in measurements of primary cilia and kinocilia. Scale bars,  $2 \mu\text{m}$ . **d,** Top: mIMCD cell cilium deflected by fluid flow containing  $10 \mu\text{M}$  digitonin. Bottom left:  $F_{\text{mCherry}}$  (red) decreased owing to cilia motion (black).  $F_{\text{GECO1.2}}$  (green) rose  $\sim 1$  s later, as permeabilization initiated  $\text{Ca}^{2+}$  influx. Right:  $F_{\text{GECO1.2}}/F_{\text{mCherry}}$  increased  $\sim 4.2$ -fold upon permeabilization. Representative of 13 videos  $\times$  400 frames. **e,** Kinocilia of E15 cochlear hair cells. Digitonin ( $10 \mu\text{M}$ ) increased the kinocilium's normalized  $F_{\text{GECO1.2}}/F_{\text{mCherry}}$  ratio by 4.6-fold. Representative of 6 videos  $\times$  400 frames. Similar results were obtained in P3 hair cell kinocilia (data not shown).



**Extended Data Figure 7 | No change in  $[Ca^{2+}]_{\text{cilium}}$  during mechanical stimulation of primary cilia in MLO-Y4 and Ocy454 osteocyte-like cells, and primary MEF cells.** a–c, Cultured MLO-Y4 (a, representative of 24 videos  $\times$  150 frames), Ocy454 (b, representative of 11 videos  $\times$  150 frames), and MEF cells isolated from E14 *Arl13b-mCherry-GECO1.2<sup>tg</sup>; GCaMP6f<sup>tg</sup>; E2a-Cre<sup>tg</sup>* mice (c, representative of 25 videos  $\times$  150 frames) were imaged from above; stimulus pipette was placed  $\sim 4\text{--}6\text{ }\mu\text{m}$  away from the cilium. Images: cilium before, during, and after deflection by a 2 s,  $\sim 250\text{ }\mu\text{m s}^{-1}$  flow stimulus. The ROI was identified frame-by-frame by a MATLAB tracking algorithm and  $F_{\text{GECO1.2}}$  and  $F_{\text{mCherry}}$  quantified. Scale bar,  $1\text{ }\mu\text{m}$ . d–f, Quantification of the channel intensities from the

cilia in a–c. Average fluorescence intensity for both  $F_{\text{GECO1.2}}$  and  $F_{\text{mCherry}}$  decreased as the cilia flattened and the light path length via the cilium volume changed. Cilium ROI displacement is superimposed in grey. g–i, Ratioing  $F_{\text{GECO1.2}}$  and  $F_{\text{mCherry}}$  compensated for the path-length artefact (see also Extended Data Fig. 6), revealing no change in  $[Ca^{2+}]$  during deflection. Cilium ROI displacement is superimposed in grey. j, Average  $F_{\text{GECO1.2}}/F_{\text{mCherry}}$  for MLO-Y4 (red,  $n = 24$ ), Ocy454 (purple,  $n = 11$ ) and MEF (blue,  $n = 25$ ) primary cilia. The small continuous positive slope during the entire course of the experiment results from differential dye bleaching ( $\text{mCherry} > \text{GECO1.2}$ ). All error bars  $\pm$  s.e.m.



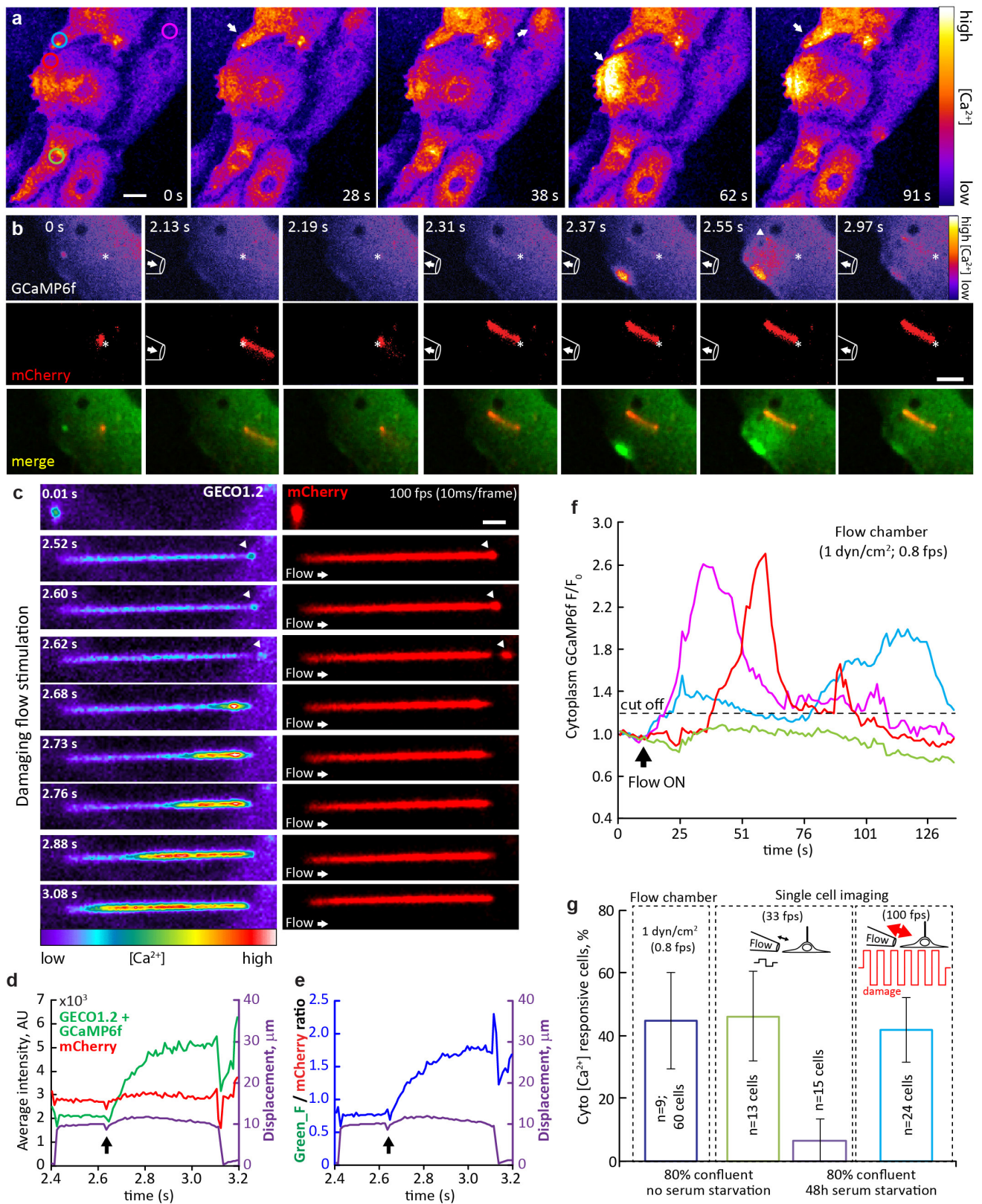
Extended Data Figure 8 | See next page for caption.



**Extended Data Figure 8 | Flow-dependent  $[Ca^{2+}]$  increases originate in the cytoplasm in MEF cells.** **a**, Representative image sequence of cultured MEF cells responding to  $1 \text{ dyn cm}^{-2}$  fluid flow in a flow chamber. Cells were isolated from E14 *Arl13b-mCherry-GECO1.2<sup>tg</sup>;GCaMP6f<sup>tg</sup>;E2a-Cre<sup>tg</sup>* mice, expressing *Arl13b-mCherry-GECO1.2* in primary cilia, and GCaMP6f in the cytoplasm.  $F_{GCaMP6f}$  is presented as pseudocolour heatmap; arrows point to the cells that respond to the flow stimulus, circles indicate ROI used for analysis in **f**; imaging rate, 0.6 f.p.s.; scale bar,  $10 \mu\text{m}$ . Representative of 19 videos  $\times$  60 frames. **b–b''**, Representative image sequence of cultured MEF cell responding to a single cycle of oscillatory fluid flow (OscFF<sup>16</sup>). Top row,  $F_{GCaMP6f} + F_{GECO1.2}$  presented as pseudocolour heatmap. Middle row, mCherry fluorescence. Bottom row, merged  $F_{GCaMP6f} + F_{GECO1.2}$  (green) and  $F_{mCherry}$  (red) signals. Left panel, **b**, average of about ten consecutive frames before stimulus application; 1.2 s into the experiment, an alternating pressure stimulus was applied to the cell membrane, away from the cilium (positive, then negative,  $\sim 1.5$  s each, diagram shown in **b'**). Following the stimulus (**b''**; each image is an average of three to five consecutive frames at the time point reflected on the image), a  $Ca^{2+}$  wave originating from the plasma membrane/cytoplasm spreads across the cell body. As seen on the image sequence, a single cycle of strong OscFF application to the cell membrane initiates a  $Ca^{2+}$  increase in the cytoplasm (whether from across the plasma membrane or from intracellular stores was not determined). Negligible cilium movement has been detected in this particular case ( $\sim 200 \text{ nm}$ , grey trace in **c**), as the cilium was located under the cell, between the cell and the coverslip. Scale bar,  $5 \mu\text{m}$ . Representative of 40 videos  $\times$  450 frames.

**c**, Quantification of ( $F_{GECO1.2} + F_{GCaMP6f}$ ) (green) and  $F_{mCherry}$  (red) channel intensities in the cilium in **b**. The ROI was identified frame-by-frame by a MATLAB tracking algorithm and average fluorescence plotted as a function of time. Cilium ROI displacement is superimposed in grey. **d**, Average  $F_{GCaMP6f}$  (cytoplasm) in the ROI depicted in **b'** (white circle), superimposed with ciliary ( $F_{GECO1.2} + F_{GCaMP6f}$ ) /  $F_{mCherry}$  (purple trace) showing an earlier  $Ca^{2+}$  onset for the cytoplasmic GCaMP6f indicator. Dashed box outlines the data shown in **e**. **e**, Same as in **c**, but with higher time resolution. Ciliary  $[Ca^{2+}]$  increase is  $\sim 200 \text{ ms}$  delayed from the cytoplasmic  $Ca^{2+}$  increase, showing the necessity for high imaging rates for  $Ca^{2+}$  imaging of cilia. **f**, Quantification of  $F_{GCaMP6f}$  change over time for four cells from **a**; ROIs depicted in **a**. Dashed line: threshold for labelling a cell as responsive (20% change in fluorescent intensity). All selected cells, except that represented by the magenta trace, responded to the flow. **g**, MEF cell response rate in flow chamber and pipette flow application experiments. Blue and red bars represent  $1 \text{ dyn cm}^{-2}$  application in flow chamber experiments;  $\sim 40\%$  of the cells responded to the flow. Apyrase (7 units per millilitre) application did not change the response rate, suggesting that ATP release is not a major contributor to flow-induced  $Ca^{2+}$  response in this cell type. Remaining bars represent single-cell imaging experiments with local flow delivery via pipette, using cells in three conditions: low confluency cells ( $\sim 15\%$ ), with 24 h (green bar) and 48 h (purple bar) serum starvation to promote cilia formation, and highly confluent coverslips without serum starvation (light blue bar). Arrest of MEF cells in G0 sensitizes cells to respond to flow stimulus with intracytoplasmic  $Ca^{2+}$  changes. All error bars  $\pm$  s.e.m.

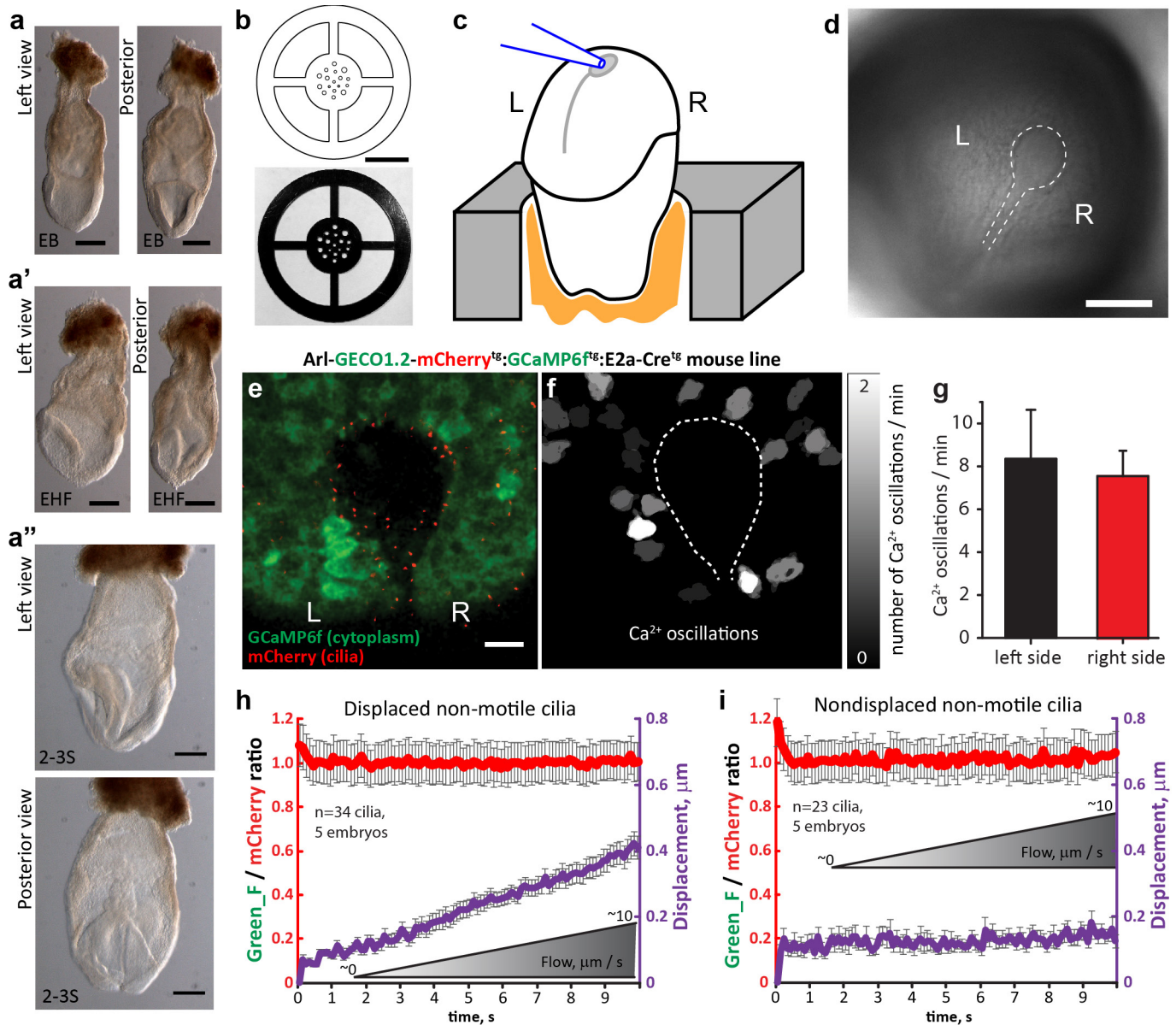




Extended Data Figure 9 | See next page for caption.

**Extended Data Figure 9 | Flow-dependent  $[Ca^{2+}]$  increases originate in the cytoplasm in primary mIMCD cells.** **a**, Cultured primary mIMCD cells, isolated from *Arl13b-mCherry-GECO1.2<sup>tg</sup>:GCaMP6f<sup>tg</sup>;E2a-Cre<sup>tg</sup>* mice, respond to  $1 \text{ dyn cm}^{-2}$  shear stress in a flow chamber.  $F_{\text{GCaMP6f}}$  fluorescence intensity is presented as pseudocolour heatmap. Arrows point to the cells that respond to the flow stimulus. Imaging rate, 0.8 f.p.s.; scale bar,  $10 \mu\text{m}$ . Representative of 6 videos  $\times$  100 frames. Circles indicate ROIs used for analysis in **f**. **b**, Cultured mIMCD cell with cytoplasmic  $Ca^{2+}$  oscillations following flow application. Pipette outline on the image represents its approximate position; an arrow inside the pipette represents the direction of the flow. An alternating flow stimulus deflects the primary cilium (red) in positive and negative directions. This deflects the cell membrane, resulting in  $Ca^{2+}$  increases in the cytoplasm. Although it is well known that mechanical force can initiate increases in cytoplasmic  $Ca^{2+}$ , there are several potential sources (plasma membrane rupture, mechanosensitive ion channels, ATP release and purinergic receptor activation, intracellular  $Ca^{2+}$  stores) that appear to depend on cell type and conditions. No change in ciliary  $[Ca^{2+}]$  is evident until the cytoplasmic  $Ca^{2+}$  reaches the cilium (arrowhead, 2.55 s). Top row,  $F_{\text{GCaMP6f}} + F_{\text{GECO1.2}}$  presented as a pseudocolour heatmap. Middle row, mCherry signal intensity. Bottom row, merged  $F_{\text{GCaMP6f}} + F_{\text{GECO1.2}}$  (green) and  $F_{\text{mCherry}}$  (red). Asterisks indicate the base of the cilium. Imaging rate, 33 f.p.s.; scale bar,  $5 \mu\text{m}$ . Representative of 17 videos  $\times$  450 frames. **c**, Fast imaging during supraphysiological flow application to primary cilium of cultured mIMCD

cells reveals ciliary damage and subsequent increase of ciliary  $[Ca^{2+}]$ .  $F_{\text{GCaMP6f}} + F_{\text{GECO1.2}}$ , pseudocolour heatmap (left);  $F_{\text{mCherry}}$ , red (right). At flow rates greater than ten times those used for ciliary deflection, the ciliary membrane disintegrates and distal parts of the cilium (arrowheads) detach. Following ciliary tip damage,  $Ca^{2+}$  enters the cilium from the break point. Ciliary  $Ca^{2+}$  influx does not occur before detachment of ciliary tip, presumably when the membrane experiences the highest force and stretch. Arrow, direction of the flow. Imaging rate, 100 f.p.s.; Scale bar,  $2 \mu\text{m}$ . Representative of 13 videos  $\times$  3,000 frames. **d**, **e**, Quantification of  $F_{\text{GCaMP6f}} + F_{\text{GECO1.2}}$  and  $F_{\text{mCherry}}$  from the cilium in **c**. Arrow, ciliary tip detachment event. The ROI was identified frame-by-frame by a MATLAB tracking algorithm and  $F_{\text{GECO1.2}}$  and  $F_{\text{mCherry}}$  (**d**) and ratio (**e**) plotted as a function of time. Cilium ROI displacement is superimposed (purple). **f**, Quantification of  $F_{\text{GECO1.2}}$  and  $F_{\text{mCherry}}$  fluorescence intensity change over time for four representative cells in **a**; ROIs depicted in **a** (left). Dashed line, 20% threshold defining responsive cells. All selected cells (except that represented by the green trace) responded to flow. **g**, Cultured primary mIMCD cell response rate in flow chamber and pipette flow application experiments. Blue bar, flow application performed in a flow chamber;  $\sim 46\%$  of the cells respond to  $1 \text{ dyn cm}^{-2}$  shear stress. Green and purple bars represent single-cell imaging experiments for highly confluent cells ( $\sim 80\%$ ), without (green bar) or following (purple bar) 48 h serum starvation. Light blue bar, cells following 48 h serum starvation in response to damaging flow stimulus. All error bars  $\pm$  s.e.m.



**Extended Data Figure 10 | Cytoplasmic  $\text{Ca}^{2+}$  signalling in the embryonic node of *Arl13b-mCherry-GECO1.2<sup>tg</sup>; GCaMP6f<sup>tg</sup>; E2a-Cre<sup>tg</sup>* embryos.** **a–a''**, Representative images of embryos within the developmental window used: from early bud (EB, **a**), early headfold (EHF, **a'**) to two- to three-somite stage (2–3S, **a''**). Scale bars, 200  $\mu\text{m}$ . Each panel is a representative of at least five images. **b**, Drawing (top modified after ref. 22) and image (bottom) of the embryo mounting plate used for imaging. Scale bar, 10 mm. **c**, Embryos were mounted with the node facing up. Pipette used for cilia deflection is shown in blue. **d**, Differential interference contrast image of embryo with the node outlined by the dashed line. Scale bar, 100  $\mu\text{m}$ . Representative of 14 images. **e**, Representative image of an embryonic node of an *Arl13b-mCherry-GECO1.2<sup>tg</sup>; GCaMP6f<sup>tg</sup>; E2a-Cre<sup>tg</sup>* EHF embryo, expressing GCaMP6f in the cytoplasm to visualize cytoplasmic  $\text{Ca}^{2+}$  oscillations. Scale bar, 20  $\mu\text{m}$ . Representative of 3 videos  $\times$  300 frames. **f**, Mapping of cytoplasmic  $\text{Ca}^{2+}$  oscillations in close proximity to the embryonic node. Only  $\Delta F/F > 30\%$

were included in the analysis. Nodal perimeter is outlined with white dashed line. **g**, Quantification of cytoplasmic  $\text{Ca}^{2+}$  signals shown in **e**, **f** occurring within 0.01 mm<sup>2</sup> on either the left or the right side of the embryonic node. Left side:  $8.3 \pm 2.3 \text{ min}^{-1}$ ; right side:  $7.6 \pm 1.2 \text{ min}^{-1}$ ;  $n = 5$  embryos; this difference was not statistically significant between the late bud and late headfold (LHF) stage (see also ref. 33) (Supplementary Video 10). **h**, **i**, Average ratio changes ( $F_{\text{GECO1.2}}/F_{\text{mCherry}}$ ) of crown cell primary cilia from the left side of the embryonic node of *Arl13b-mCherry-GECO1.2<sup>tg</sup>; GCaMP6f<sup>tg</sup>; E2a-Cre<sup>tg</sup>* expressing EHF embryos during the application of physiological levels of flow (slow deflection; note longer imaging time of 15 s). Flow velocity, calibrated in-frame using fluorescent beads, was slowly increased (ramped); see also Fig. 4 k, l. Cilia were divided into two groups: **h**, the average ratio change for displaced cilia ( $n = 34$  cilia from 5 embryos; average centroid displacement was  $409 \pm 35 \text{ nm}$ ); **i**, the average ratio change for non-displaced cilia ( $n = 23$  cilia from 5 embryos). All error bars  $\pm$  s.e.m.



# $\beta$ -Arrestin biosensors reveal a rapid, receptor-dependent activation/deactivation cycle

Susanne Nuber<sup>1,2</sup>, Ulrike Zabel<sup>1,2</sup>, Kristina Lorenz<sup>1,3†</sup>, Andreas Nuber<sup>1</sup>, Graeme Milligan<sup>4</sup>, Andrew B. Tobin<sup>5</sup>, Martin J. Lohse<sup>1,2,3†</sup> & Carsten Hoffmann<sup>1,2</sup>

( $\beta$ -)Arrestins are important regulators of G-protein-coupled receptors (GPCRs)<sup>1–3</sup>. They bind to active, phosphorylated GPCRs and thereby shut off ‘classical’ signalling to G proteins<sup>3,4</sup>, trigger internalization of GPCRs via interaction with the clathrin machinery<sup>5–7</sup> and mediate signalling via ‘non-classical’ pathways<sup>1,2</sup>. In addition to two visual arrestins that bind to rod and cone photoreceptors (termed arrestin1 and arrestin4), there are only two (non-visual)  $\beta$ -arrestin proteins ( $\beta$ -arrestin1 and  $\beta$ -arrestin2, also termed arrestin2 and arrestin3), which regulate hundreds of different (non-visual) GPCRs. Binding of these proteins to GPCRs usually requires the active form of the receptors plus their phosphorylation by G-protein-coupled receptor kinases (GRKs)<sup>1,3,4</sup>. The binding of receptors or their carboxy terminus as well as certain truncations induce active conformations of ( $\beta$ -)arrestins that have recently been solved by X-ray crystallography<sup>8–10</sup>. Here we investigate both the interaction of  $\beta$ -arrestin with GPCRs, and the  $\beta$ -arrestin conformational changes in real time and in living human cells, using a series of fluorescence resonance energy transfer (FRET)-based  $\beta$ -arrestin2 biosensors. We observe receptor-specific patterns of conformational changes in  $\beta$ -arrestin2 that occur rapidly after the receptor– $\beta$ -arrestin2 interaction. After agonist removal, these changes persist for longer than the direct receptor interaction. Our data indicate a rapid, receptor-type-specific, two-step binding and activation process between GPCRs and  $\beta$ -arrestins. They further indicate that  $\beta$ -arrestins remain active after dissociation from receptors, allowing them to remain at the cell surface and presumably signal independently. Thus, GPCRs trigger a rapid, receptor-specific activation/deactivation cycle of  $\beta$ -arrestins, which permits their active signalling.

Several lines of evidence suggest that GPCRs induce active conformations of ( $\beta$ -)arrestins, which facilitate interactions with effector proteins<sup>11–15</sup>. X-ray crystallography of such active conformations revealed movements in the central loops that interact with GPCRs, plus a 20° twisting of the amino- versus carboxy-terminal domain<sup>8–10</sup>. An intramolecular bioluminescence resonance energy transfer (BRET) sensor for  $\beta$ -arrestin2 activation showed activation over minutes, suggesting that it reports interactions with effectors rather than  $\beta$ -arrestin2 conformational changes<sup>16</sup>. Therefore, we set out to study the dynamics and the role and potential specificity of GPCRs in  $\beta$ -arrestin activation in living cells by FRET<sup>17</sup>. We generated eight different FRET-based  $\beta$ -arrestin2 biosensors by attaching an invariant cyan fluorescent protein (CFP) at the C terminus, and inserting a binding motif (CCPGCC) for the fluorescein arsenical hairpin (FAsH) binder into different positions at the periphery of the N and C domains that were unlikely to be directly involved in receptor– $\beta$ -arrestin interactions but might report conformational changes<sup>18</sup> (Fig. 1a and Extended Data Table 1).

Confocal microscopy of transfected HEK293 cells showed that all  $\beta$ -arrestin2 sensors were expressed in the cytosol and labelled with FAsH<sup>19</sup> (Extended Data Fig. 1). With the exception of  $\beta$ -arrestin2–FAsH8, all were rapidly recruited to the cell surface after stimulation of co-transfected parathyroid hormone type 1 receptors (PTH<sub>1</sub>R; Extended Data Fig. 2), a receptor known to induce robust  $\beta$ -arrestin2 interactions<sup>20</sup>.

For kinetic experiments, we used the  $\beta_2$ -adrenergic receptor ( $\beta_2$ AR), because its agonists have rapid on and off rates<sup>21,22</sup>. The interaction was monitored by measuring FRET between the C-terminal CFP in the  $\beta$ -arrestin2 sensors and a C-terminal yellow fluorescent protein (YFP) in the co-transfected  $\beta_2$ AR<sup>21,23</sup>. Stimulation of the  $\beta_2$ AR with 100  $\mu$ M isoproterenol promoted a  $\beta$ -arrestin–receptor interaction and increased FRET between CFP in the  $\beta$ -arrestin2 sensors and  $\beta_2$ AR–YFP<sup>21,23</sup> (Fig. 1b).

A phosphorylation-deficient  $\beta_2$ AR–YFP construct<sup>21</sup> failed to trigger such recruitment (Fig. 1c), indicating a high-affinity GRK-dependent  $\beta$ -arrestin–receptor interaction<sup>24,25</sup>. Requirement for GRK-mediated phosphorylation made the interaction slower for the first than for subsequent stimuli (Fig. 1b), when receptors are already pre-phosphorylated<sup>21</sup>. Therefore, all further analyses refer to second stimuli, eliminating GRK-dependent phosphorylation as a potential issue.

Since the measurement of this interaction relied on the invariant CFP in all  $\beta$ -arrestin2 sensors, the receptor interactions of the different constructs can be directly compared (Fig. 1d). All  $\beta$ -arrestin2 sensors bearing FAsH sequences in the N domain showed robust and quantitatively similar interactions with  $\beta_2$ AR–YFP, whereas of those with C-domain FAsH sequences, only the FAsH1 construct showed a similar interaction. The interaction of the FAsH6/7 constructs with PTH<sub>1</sub>R but not  $\beta_2$ AR indicates a distinct selectivity for  $\beta$ -arrestin2 between GPCRs. Receptor specificity was further suggested by an analogous M<sub>2</sub> muscarinic acetylcholine receptor (M<sub>2</sub>AChR) construct stimulated with 100  $\mu$ M acetylcholine (Fig. 1e). Here, only  $\beta$ -arrestin2–FAsH2 and  $\beta$ -arrestin2–FAsH5 showed a similar receptor interaction, whereas all other constructs exhibited no detectable interaction.

Conformational changes within the  $\beta$ -arrestin2 sensors were investigated via intramolecular FRET between the CFP and FAsH label (Fig. 1f–i), initially again using  $\beta$ -arrestin2–FAsH2–CFP and the  $\beta_2$ AR. Receptor stimulation caused a reversible reduction of intramolecular FRET in  $\beta$ -arrestin2–FAsH2–CFP (Fig. 1f), which was, again, absent for the phosphorylation-deficient  $\beta_2$ AR construct (Fig. 1g), indicating that agonist- and phosphorylation-dependent high-affinity receptor-binding was required for the conformational change. Only three  $\beta$ -arrestin2 sensors showed conformational changes after  $\beta_2$ AR stimulation (Fig. 1h). FAsH3 and FAsH4, which showed ligand-dependent receptor interactions (Fig. 1d), revealed no  $\beta$ -arrestin2 conformational changes, and FAsH1 showed only minor

<sup>1</sup>Institute of Pharmacology and Toxicology, University of Würzburg, Versbacher Str. 9, 97078 Würzburg, Germany. <sup>2</sup>Rudolf Virchow Center, University of Würzburg, Versbacher Str. 9, 97078 Würzburg, Germany. <sup>3</sup>Comprehensive Heart Failure Center, University of Würzburg, Versbacher Str. 9, 97078 Würzburg, Germany. <sup>4</sup>Molecular Pharmacology Group, Institute of Molecular, Cell and Systems Biology, College of Medical, Veterinary and Life Sciences, University of Glasgow, Glasgow G12 8QQ, UK. <sup>5</sup>MRC Toxicology Unit, University of Leicester, Hodgkin Building, Lancaster Road, Leicester LE1 9HN, UK. <sup>†</sup>Present address: Leibniz Institute for Analytical Sciences ISAS, Bunsen-Kirchhoff-Str. 11, 44139 Dortmund, Germany (K.L.); Max Delbrück Center for Molecular Medicine, Robert-Rössle-Str. 10, 13092 Berlin, Germany (M.J.L.).



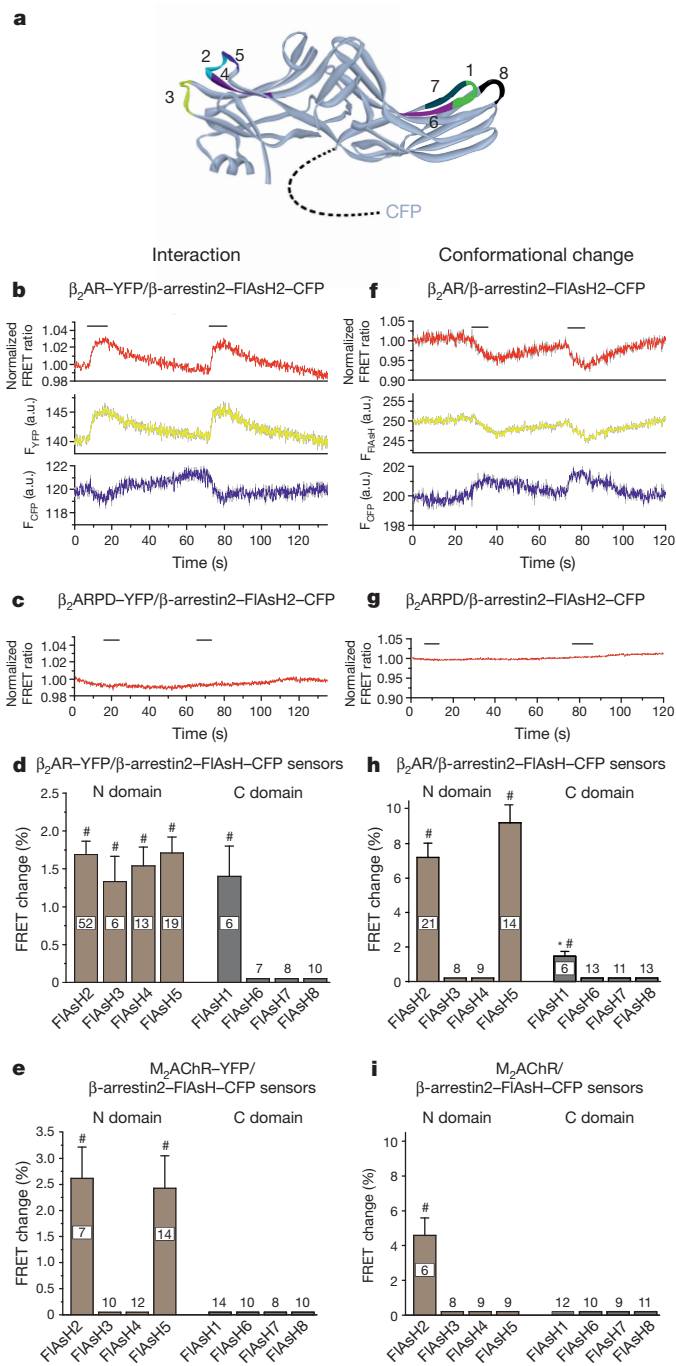


**Figure 1 | FRET sensors for the  $\beta$ -arrestin2–receptor interaction and receptor-dependent conformational changes in  $\beta$ -arrestin2.**

**a**, FRET-based  $\beta$ -arrestin2 biosensors. Schematic representation of the  $\beta$ -arrestin2-FLAsH constructs used in this study derived from the crystal structure (Protein Data Bank (PDB) code 3P2D). CFP was attached C-terminally, and the FLAsH binding motif (CCPGCC) was inserted in different positions. Positions of the FLAsH binding motif are highlighted in the structure and specified in Extended Data Table 1. The sensors were termed  $\beta$ -arrestin2-FLAsH1–8-CFP (abbreviated: FLAsH1–8). **b–i**, Monitoring the  $\beta$ -arrestin2–receptor interaction and receptor-dependent conformational changes in  $\beta$ -arrestin2 by FRET. **b, c, f, g**, Representative traces of isoproterenol-induced changes in CFP ( $F_{CFP}$ , cyan) and YFP or FLAsH ( $F_{YFP}$  or  $F_{FLAsH}$ , yellow) emissions and the corresponding normalized FRET ratio ( $F_{YFP}$  or  $F_{FLAsH}/F_{CFP}$ ) recorded from a single HEK293 cell expressing either YFP-fused  $\beta_2$ AR (**b**) or  $\beta_2$ AR (**f**) and the FLAsH-labelled  $\beta$ -arrestin2-FLAsH2-CFP. Isoproterenol application (100  $\mu$ M) is indicated. Intermolecular (**c**) and intramolecular (**g**) FRET detected upon stimulation of a phosphorylation-deficient  $\beta_2$ AR mutant ( $\beta_2$ ARPD) in HEK293 cells co-expressing  $\beta$ -arrestin2-FLAsH2-CFP; these experiments were repeated more than ten times with similarly negative results. **d, e, h, i**, Quantification of agonist-evoked FRET changes. Shown are maximal FRET changes (percentage) for the interaction of  $\beta_2$ AR-YFP (**d**) or  $M_2$ AChR-YFP (**e**) and the  $\beta$ -arrestin2-FLAsH-CFP sensors, or by conformational changes detected with the  $\beta$ -arrestin2 sensors after stimulation of  $\beta_2$ AR with 100  $\mu$ M isoproterenol (**h**) or  $M_2$ AChR with 100  $\mu$ M acetylcholine (**i**). Data represent mean  $\pm$  s.e.m., for  $n$  independent experiments (biological replicates) as indicated. # $P < 0.01$  (versus no effect); \* $P < 0.05$  (versus FLAsH2 and FLAsH5).

FFA4R (Extended Data Fig. 4), and by specific  $\beta$ -arrestin-mediated downstream signalling to kinases (Extended Data Fig. 5). In line with their different effects on  $\beta$ -arrestin2–FRET,  $M_2$ AChR caused significantly higher ERK1/2 activation than  $\beta_2$ AR, and FFA4R was the only receptor causing no significant Src-kinase activation.

A comparison of the kinetics of the  $\beta_2$ AR– $\beta$ -arrestin2 interaction and of  $\beta$ -arrestin2 conformational changes in  $\beta$ -arrestin2-FLAsH2-CFP illustrates that the interaction step is faster (and thus precedes) the conformational change (Fig. 2a, b). While both processes began without an apparent lag period after agonist addition, the  $\beta_2$ AR– $\beta$ -arrestin2 interaction was clearly faster (rate constant  $\tau = 1.3 \pm 0.17$  s (mean  $\pm$  s.e.m.)) than the conformational change ( $\tau = 2.2 \pm 0.22$  s;  $P < 0.01$ ). Analysis with various isoproterenol concentrations revealed that these values represent maximal speeds (Extended Data Fig. 6).

When the superfusion system (which has a delay time of  $< 10$  ms) was switched from isoproterenol (100  $\mu$ M) to buffer alone, both the  $\beta_2$ AR– $\beta$ -arrestin2 interaction and the  $\beta$ -arrestin2 conformational changes reverted (Fig. 2c), albeit with significantly different delays. This delay was  $1.9 \pm 0.51$  s for the interaction, but  $4.2 \pm 0.85$  s for the conformational change ( $P < 0.05$ ; Fig. 2d). This difference indicates that  $\beta$ -arrestin2 remains in an active conformation after dissociation from the receptor. If  $\beta$ -arrestins continue to signal to effectors after their dissociation from receptors, this would allow signal amplification analogous to the well-established signal amplification occurring in G-protein-mediated signalling<sup>26</sup>.

To assess whether these different delays might indeed be functionally relevant, we compared  $\beta_2$ AR-induced translocation of  $\beta$ -arrestin2-YFP by confocal microscopy with the  $\beta_2$ AR– $\beta$ -arrestin2 interaction monitored under identical conditions by FRET (Fig. 3a–c). Because technical reasons prevented the use of the rapid perfusion system, these experiments were performed with direct application of isoproterenol to coverslips and subsequent washout with a peristaltic pump; thus, the two sets of experiments can be compared with one other, but not with the preceding experiments. After agonist washout, the translocation of  $\beta$ -arrestin2-YFP to the cell membrane lasted much longer than the direct  $\beta_2$ AR– $\beta$ -arrestin2 interaction (FRET). The latter was completely reversed 90 s after buffer addition (Fig. 3c), while the former clearly persisted at this time and took four times as long to reverse (Fig. 3b). This would be consistent with the hypothesis

changes (Fig. 1h). This suggests that only distinct subdomains of  $\beta$ -arrestin2 move relative to its C terminus, and that the loop containing positions 2 and 5 (amino acids 154–158) is particularly sensitive. In line with their ability to report receptor-dependent activation, FLAsH2 and FLAsH5 increased isoproterenol-stimulated ERK phosphorylation in transfected HEK293 cells as much as wild-type  $\beta$ -arrestin2-CFP (Extended Data Fig. 3).

In analogous experiments with  $M_2$ AChR stimulated by 100  $\mu$ M acetylcholine (Fig. 1i), only  $\beta$ -arrestin2-FLAsH2-CFP showed an agonist-induced signal—that is, neither FLAsH5, which interacted with  $M_2$ AChR (Fig. 1e), nor FLAsH1, which changed conformation upon  $\beta_2$ AR stimulation (Fig. 1h), responded to  $M_2$ AChR stimulation. Thus, both receptor interactions and conformational changes in  $\beta$ -arrestin2 occur in distinct receptor-specific manners.

Further evidence for receptor-specificity was illustrated by a FRET increase in  $\beta$ -arrestin2-FLAsH2 triggered by the free fatty acid receptor

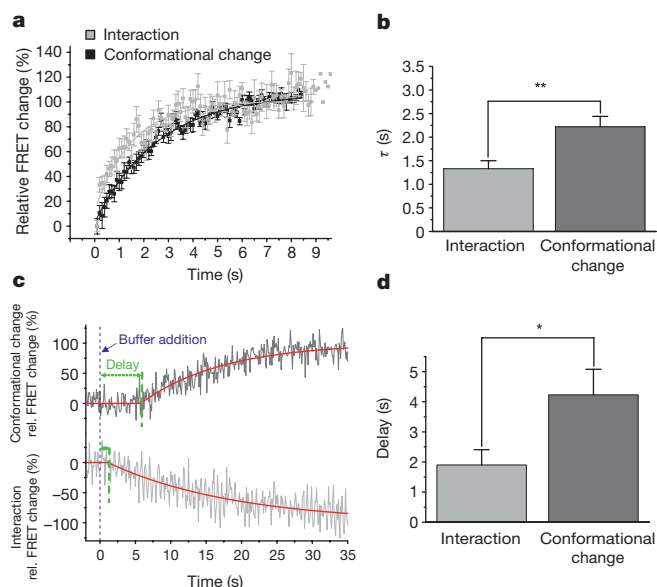


**Figure 2 | Kinetics of the interaction of  $\beta$ -arrestin2 with  $\beta_2$ AR and its conformational movements.** **a**, Kinetics of the agonist ( $100\ \mu\text{M}$  isoproterenol)-induced interaction of  $\beta$ -arrestin2-FLAsH2-CFP with  $\beta_2$ AR (light grey) and its conformational changes (dark grey). Interaction and conformational changes (inverted to facilitate comparison) were quantified by FRET as in Fig. 1. FRET changes were plotted against time and analysed by exponential fitting to yield time constants ( $\tau$ ). Maximal values were set to 100%. Data represent mean  $\pm$  s.e.m. of  $n = 17$  (interaction) or 23 (conformational change) independent experiments (biological replicates). **b**, Bar graph of the time constants for the  $\beta_2$ AR-agonist-induced interaction ( $\tau = 1.3 \pm 0.17\ \text{s}$ ) and the conformational changes detected with  $\beta$ -arrestin2-FLAsH2-CFP ( $\tau = 2.2 \pm 0.22\ \text{s}$ ). Data represent mean  $\pm$  s.e.m. of  $n = 17$  (interaction) or 23 (conformational change) independent experiments (biological replicates).  $^{**}P < 0.01$  (Mann–Whitney  $U$  test). **c**, Kinetics of FRET changes after agonist removal. FRET signals were recorded after termination of exposure to the agonist ( $100\ \mu\text{M}$  isoproterenol; switch to buffer indicated by blue line). Traces are from a representative experiment showing distinct delays in the intermolecular FRET signal indicating  $\beta$ -arrestin2–receptor dissociation, and the intramolecular FRET signal indicating reversal of the active  $\beta$ -arrestin conformation. The rate constants of the two processes were not different ( $\tau = 22 \pm 4.2\ \text{s}$  versus  $23 \pm 2.1\ \text{s}$ ). **d**, Bar graph of the delays for the agonist-induced  $\beta$ -arrestin–receptor dissociation ( $1.9 \pm 0.51\ \text{s}$ ), and the reversal of the  $\beta$ -arrestin2 conformational changes from experiments as shown in **c** ( $\tau = 4.2 \pm 0.85\ \text{s}$ ). Data represent mean  $\pm$  s.e.m. of  $n = 12$  independent experiments (biological replicates).  $^{*}P < 0.05$  (Mann–Whitney  $U$  test).

of an active, cell-surface-localized state of  $\beta$ -arrestin2–YFP lasting longer than the direct association with  $\beta_2$ AR. Whether the cell surface retention is due to binding to lipids or to additional proteins, for example, clathrin<sup>5,7</sup>, or is related to a biochemical modification remains to be determined.

Our data illustrate that GPCRs induce a complex, multi-step activation/deactivation cycle for  $\beta$ -arrestins that rapidly follows the well-known G-protein cycle. Provided sufficient GRK is present<sup>21</sup>, the rapid interaction between  $\beta$ -arrestins and receptors terminates G-protein activation long before downstream second messenger levels reach their new, receptor-triggered equilibrium<sup>27</sup>.

Second, the distinct kinetics of receptor interaction versus conformational change (activation) of  $\beta$ -arrestin2 are consistent with the two-step activation model, which requires receptor phosphorylation and binding of the receptors' C terminus for  $\beta$ -arrestin activation by GPCRs<sup>12,15</sup>. The time course of these steps reveals that GPCRs are as much  $\beta$ -arrestin-coupled receptors as they are G-protein-coupled receptors. Comparison of our  $\beta$ -arrestin2 sensors indicates that both steps occur in a receptor-specific manner. Thus, different activated

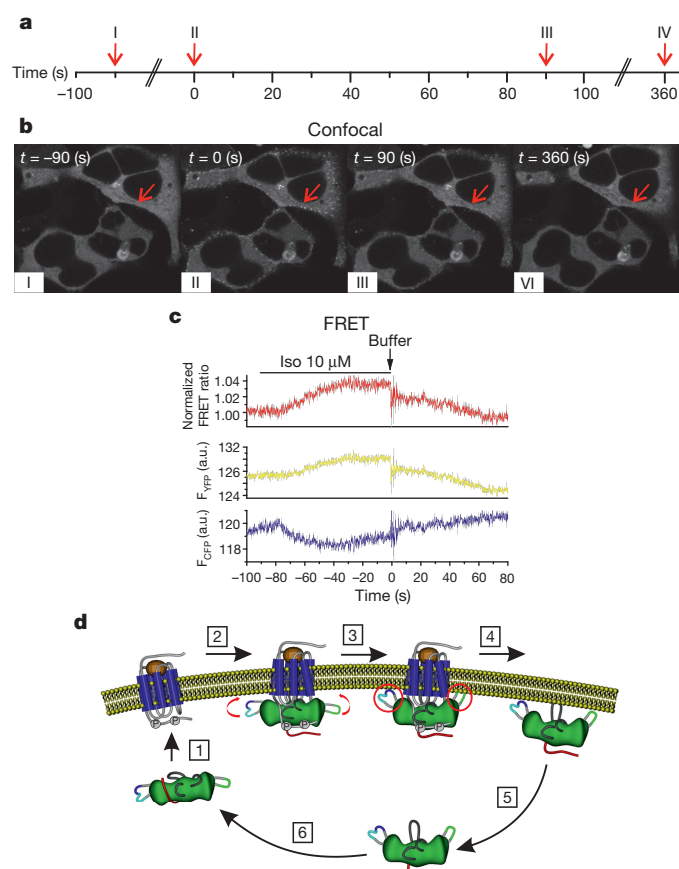


**Figure 3 | Kinetics of  $\beta$ -arrestin2 translocation between cytosol and cell membrane after  $\beta_2$ AR stimulation.** **a**, Timeline of the experimental set up. HEK293 cells co-expressing  $\beta$ -arrestin2–YFP and  $\beta_2$ AR were stimulated with isoproterenol (Iso  $10\ \mu\text{M}$ ) added to the coverslip, followed by washout with a peristaltic pump (flow rate  $1.4\ \text{ml min}^{-1}$ ). Translocation of  $\beta$ -arrestin2–YFP to the cell membrane and subsequent dissociation upon washout were determined by confocal microscopy. Images were taken every 15 s. The experiment is representative of six independent experiments. **b**, Confocal images before and after ligand addition. I,  $\beta$ -Arrestin2–YFP was diffusely cytosolic before agonist stimulation ( $t = -90\ \text{s}$ ). II, Maximal  $\beta$ -arrestin2 translocation to the cell membrane was observed 90 s after isoproterenol addition ( $t = 0\ \text{s}$ ; begin of washout). III,  $\beta$ -Arrestin2 movement back to the cytosol occurs after washout, but cell-surface localization is still clearly visible at 90 s after the beginning of washout ( $t = 90\ \text{s}$ ). IV, Translocation back to the cytosol is complete after 360 s of washout ( $t = 360\ \text{s}$ ). The images are representative of 4 independent experiments (biological replicates). **c**, Kinetics of the  $\beta$ -arrestin2– $\beta_2$ AR interaction after  $\beta_2$ AR stimulation and ligand washout measured by FRET. HEK293 cells were transfected with  $\beta_2$ AR–YFP and  $\beta$ -arrestin2–CFP. Isoproterenol ( $10\ \mu\text{M}$ ) was added for 90 s and then washed out as above. Changes in CFP ( $F_{\text{CFP}}$  cyan) and YFP ( $F_{\text{YFP}}$  yellow) emissions and the corresponding normalized FRET ratio ( $F_{\text{YFP}}/F_{\text{CFP}}$  red) were recorded from a single HEK293 cell. Note the artefact caused by switching on the pump for washout ( $t = 0\ \text{s}$ ). The traces are representative of 7 independent experiments (biological replicates). **d**, Model of an activation/deactivation and translocation cycle of  $\beta$ -arrestin2. After binding to an active phosphorylated receptor (1),  $\beta$ -arrestin2 adopts an activated conformation (2) that might facilitate fitting to the activated, phosphorylated receptor surface. Parts of C and/or N domain (labelled with FLAsH in our studies) undergo further movements (3) to bring  $\beta$ -arrestin2 into a receptor-specific activated conformation. After agonist removal,  $\beta$ -arrestin2 dissociates from the receptor (4) and remains active for some time (5) before its active state is reversed (6). The major rearrangements in the loops associated with  $\beta$ -arrestin2 activation are schematically illustrated. Structural elements of  $\beta$ -arrestin2 are coloured as follows in each step: N and C domains, green; C-tail, red; FLAsH2, cyan; FLAsH5, blue; FLAsH1, light green; finger, middle and gate loops, light grey.

forms of  $\beta$ -arrestins might exist that would allow signalling bias. The very recent determination of the X-ray structure of a rhodopsin-arrestin fusion protein<sup>10</sup> is compatible with such a stepwise activation model as predicted from earlier structures of pre-activated ( $\beta$ -) arrestins<sup>8,9</sup>. The stepwise activation would also allow active ( $\beta$ -) arrestins to dissociate from a GPCR.

Third, the persistence of active  $\beta$ -arrestin2 after dissociation from receptors has several important implications. It would allow signal amplification at this step, because a receptor becomes available for the activation of a subsequent  $\beta$ -arrestin while the first remains in an active state. It would allow  $\beta$ -arrestin coupling to its effectors at a site distinct from the cellular localization of the receptor, thus permitting distant  $\beta$ -arrestin-mediated signalling and thus making this process more versatile than previously thought.

While this work was in progress, we became aware of a complementary approach demonstrating  $\beta$ -arrestin conformational changes with BRET sensors and confirming the relevance of different active states of  $\beta$ -arrestin2 for downstream kinase signalling<sup>28</sup>.

In summary,  $\beta$ -arrestins may orchestrate GPCR signalling by temporally and spatially segregating different, receptor-specific signalling 'waves'<sup>29,30</sup>, each lasting for a few seconds: first, G-protein-mediated signals from the cell surface, second,  $\beta$ -arrestin-mediated signals in its receptor-bound states, third,  $\beta$ -arrestin-mediated signals after dissociation from receptors, and finally signals from internal sites after  $\beta$ -arrestin-mediated receptor internalization. Thus, the interactions of GPCRs with  $\beta$ -arrestins are highly versatile, rapid and dynamic, and trigger an array of diverse, receptor-specific signals in space and in time.

**Online Content** Methods, along with any additional Extended Data display items and Source Data, are available in the online version of the paper; references unique to these sections appear only in the online paper.

**Received 29 July 2015; accepted 2 February 2016.**

**Published online 23 March 2016.**

- Lohse, M. J. & Hoffmann, C. Arrestin interactions with G protein-coupled receptors. *Handb. Exp. Pharmacol.* **219**, 15–56 (2014).
- Shukla, A. K., Xiao, K. & Lefkowitz, R. J. Emerging paradigms of  $\beta$ -arrestin-dependent seven transmembrane receptor signaling. *Trends Biochem. Sci.* **36**, 457–469 (2011).
- Lohse, M. J., Benovic, J. L., Codina, J., Caron, M. G. & Lefkowitz, R. J.  $\beta$ -Arrestin: a protein that regulates  $\beta$ -adrenergic receptor function. *Science* **248**, 1547–1550 (1990).
- Wilden, U., Hall, S. W. & Kühn, H. Phosphodiesterase activation by photoexcited rhodopsin is quenched when rhodopsin is phosphorylated and binds the intrinsic 48-kDa protein of rod outer segments. *Proc. Natl Acad. Sci. USA* **83**, 1174–1178 (1986).
- Goodman, O. B. *et al.*  $\beta$ -Arrestin acts as a clathrin adaptor in endocytosis of the  $\beta_2$ -adrenergic receptor. *Nature* **383**, 447–450 (1996).
- Ferguson, S. S. *et al.* Role of  $\beta$ -arrestin in mediating agonist-promoted G protein-coupled receptor internalization. *Science* **271**, 363–366 (1996).
- Kang, D. S., Tian, X. & Benovic, J. L.  $\beta$ -Arrestins and G protein-coupled receptor trafficking. *Methods Enzymol.* **521**, 91–108 (2013).
- Shukla, A. K. *et al.* Structure of active  $\beta$ -arrestin-1 bound to a G-protein-coupled receptor phosphopeptide. *Nature* **497**, 137–141 (2013).
- Kim, Y. J. *et al.* Crystal structure of pre-activated arrestin p44. *Nature* **497**, 142–146 (2013).
- Kang, Y. *et al.* Crystal structure of rhodopsin bound to arrestin by femtosecond X-ray laser. *Nature* **523**, 561–567 (2015).
- Schleicher, A., Kühn, H. & Hofmann, K. P. Kinetics, binding constant, and activation energy of the 48-kDa protein-rhodopsin complex by extrametarhodopsin II. *Biochemistry* **28**, 1770–1775 (1989).
- Gurevich, V. V. & Gurevich, E. V. The structural basis of arrestin-mediated regulation of G-protein-coupled receptors. *Pharmacol. Ther.* **110**, 465–502 (2006).
- Hanson, S. M. *et al.* Differential interaction of spin-labeled arrestin with inactive and active phosphorhodopsin. *Proc. Natl Acad. Sci. USA* **103**, 4900–4905 (2006).
- Vishnivetskiy, S. A. *et al.* The role of arrestin  $\alpha$ -helix I in receptor binding. *J. Mol. Biol.* **395**, 42–54 (2010).
- Xiao, K., Shenoy, S. K., Nobles, K. & Lefkowitz, R. J. Activation-dependent conformational changes in  $\beta$ -arrestin 2. *J. Biol. Chem.* **279**, 55744–55753 (2004).
- Charest, P. G., Terrillon, S. & Bouvier, M. Monitoring agonist-promoted conformational changes of  $\beta$ -arrestin in living cells by intramolecular BRET. *EMBO Rep.* **6**, 334–340 (2005).
- Lohse, M. J., Nuber, S. & Hoffmann, C. Fluorescence/bioluminescence resonance energy transfer techniques to study G-protein-coupled receptor activation and signaling. *Pharmacol. Rev.* **64**, 299–336 (2012).
- Hanson, S. M. & Gurevich, V. V. The differential engagement of arrestin surface charges by the various functional forms of the receptor. *J. Biol. Chem.* **281**, 3458–3462 (2006).
- Hoffmann, C. *et al.* Fluorescent labeling of tetracycline-tagged proteins in intact cells. *Nature Protocols* **5**, 1666–1677 (2010).
- Klenk, C. *et al.* Formation of a ternary complex among NHERF1,  $\beta$ -arrestin, and parathyroid hormone receptor. *J. Biol. Chem.* **285**, 30355–30362 (2010).
- Krasel, C., Bünemann, M., Lorenz, K. & Lohse, M. J.  $\beta$ -Arrestin binding to the  $\beta_2$ -adrenergic receptor requires both receptor phosphorylation and receptor activation. *J. Biol. Chem.* **280**, 9528–9535 (2005).
- Sykes, D. A. *et al.* Observed drug-receptor association rates are governed by membrane affinity: the importance of establishing "micro-pharmacokinetic/pharmacodynamic relationships" at the  $\beta_2$ -adrenoceptor. *Mol. Pharmacol.* **85**, 608–617 (2014).
- Krasel, C. *et al.* Dual role of the  $\beta_2$ -adrenergic receptor C terminus for the binding of  $\beta$ -arrestin and receptor internalization. *J. Biol. Chem.* **283**, 31840–31848 (2008).
- Söhlemann, P., Hekman, M., Puzicha, M., Buchen, C. & Lohse, M. J. Binding of purified recombinant  $\beta$ -arrestin to guanine-nucleotide-binding-protein-coupled receptors. *Eur. J. Biochem.* **232**, 464–472 (1995).
- Violin, J. D., Ren, X.-R. & Lefkowitz, R. J. G-protein-coupled receptor kinase specificity for  $\beta$ -arrestin recruitment to the  $\beta_2$ -adrenergic receptor revealed by fluorescence resonance energy transfer. *J. Biol. Chem.* **281**, 20577–20588 (2006).
- Hein, P. & Bünemann, M. Coupling mode of receptors and G proteins. *Naunyn Schmiedeberg's Arch. Pharmacol.* **379**, 435–443 (2009).
- Lohse, M. J. *et al.* Optical techniques to analyze real-time activation and signaling of G-protein-coupled receptors. *Trends Pharmacol. Sci.* **29**, 159–165 (2008).
- Lee, M.-H. *et al.* The conformational signature of  $\beta$ -arrestin2 predicts its trafficking and signalling functions. *Nature* <http://dx.doi.org/10.1038/nature17154> (this issue).
- Lohse, M. J. & Calebiro, D. Cell biology: Receptor signals come in waves. *Nature* **495**, 457–458 (2013).
- Irannejad, R. *et al.* Conformational biosensors reveal GPCR signalling from endosomes. *Nature* **495**, 534–538 (2013).

**Acknowledgements** We thank N. Ziegler, N. Yurdagül-Hemmerich and M. Fischer for technical assistance and C. Krasel for discussions. This work was supported by the Deutsche Forschungsgemeinschaft grants SFB-487 TPA1 and SFB-TR166 (M.J.L. and C.H.), the Bundesministerium für Bildung und Forschung grant OptiMAR (M.J.L.), the ERC grants Topas and Fresca and the NIH grant 1 R01 DA038882 (M.J.L.), the Biotechnology and Biological Sciences Research Council (grant BB/K019864/1 to G.M.)

**Author Contributions** Contributed new reagents or analytical tools: S.N., U.Z., A.N., G.M. and A.B.T. Conducted experiments: S.N. (FRET, microscopy), U.Z. (cloning) and K.L. (kinase assays). Performed data analysis: S.N., A.N. and K.L. Wrote and contributed to writing of the manuscript: S.N., M.J.L. and C.H. Participated in research design: S.N., M.J.L. and C.H. Initiation of the project: C.H.

**Author Information** Reprints and permissions information is available at [www.nature.com/reprints](http://www.nature.com/reprints). The authors declare no competing financial interests. Readers are welcome to comment on the online version of the paper. Correspondence and requests for materials should be addressed to C.H. ([c.hoffmann@toxi.uni-wuerzburg.de](mailto:c.hoffmann@toxi.uni-wuerzburg.de)) or M.J.L. ([lohse@toxi.uni-wuerzburg.de](mailto:lohse@toxi.uni-wuerzburg.de)).



## METHODS

**Reagents.** Chemicals were purchased from the following sources: acetylcholine and isoproterenol from Sigma-Aldrich; penicillin ( $100 \text{ U ml}^{-1}$ ), streptomycin ( $100 \mu\text{g ml}^{-1}$ ), L-glutamine and G-418 from Invitrogen; Effectene transfection reagent from Qiagen. PCR primers were synthesized by MWG-Biotech, and sequencing reactions were done by Eurofins Medigenomix. DHA (*all-cis*-docosa-4,7,10,13,16,19-hexaenoic acid; 22:6(n-3)) was purchased from Sigma.

**Molecular biology.** FRET-based biosensors for  $\beta$ -arrestin2 were designed such that they would be able to interact with receptors and at the same time pick up conformational changes occurring during  $\beta$ -arrestin2 activation, based on work by Gurevich and co-workers<sup>12,13,31,32</sup>. To achieve this, cDNA encoding the six-amino-acid FAsH motif CCPGCC was inserted in different positions in the N or C domain of bovine  $\beta$ -arrestin2 cDNA, resulting in constructs  $\beta$ -arrestin2-FlAsH1–FlAsH8 (Fig. 1a and Extended Data Table 1). The enhanced variants of CFP or YFP, respectively (BD Bioscience Clontech) were fused to the C-termini of the human M<sub>2</sub>AChR,  $\beta_2$ AR or the  $\beta$ -arrestin2–FlAsH sensors by standard PCR extension overlap technique<sup>33</sup>. In each case, the C-terminal stop codon of the receptor and the initial codon for methionine of the fluorescent protein were deleted. All resulting constructs were cloned into pcDNA3 (Invitrogen Life Technologies) and confirmed by sequencing.

**Cell culture.** HEK293 cells were cultured in DMEM supplemented with  $4.5 \text{ g l}^{-1}$  glucose, 10% fetal calf serum (Biocrom AG),  $100 \text{ U ml}^{-1}$  penicillin G, and  $100 \mu\text{g ml}^{-1}$  streptomycin sulphate at  $37^\circ\text{C}$  and 7%  $\text{CO}_2$ . Cells were passaged every 2–3 days.

HEK293 cells were routinely tested for mycoplasma contamination using a primer set specific for the highly conserved 16S rRNA coding region in the mycoplasma genome. A mycoplasma-positive sample shows a distinct band at 265–278 base pairs.

**Transient expression of  $\beta$ -arrestin2 biosensors in HEK293 cells.** For fluorescence measurements, HEK293 cells were seeded on poly-D-lysine-coated coverslips in 6-well-plates 4–6 h before transfection. The cells were transfected using Effectene according to the manufacturer's instructions.  $0.3 \mu\text{g}$  of each of the following cDNAs were used per well:  $\beta_2$ AR or PTH<sub>1</sub>R and one of the YFP-tagged  $\beta$ -arrestin2–FlAsH sensors ( $\beta$ -arrestin2 translocation); M<sub>2</sub>AChR–YFP or  $\beta_2$ AR–YFP and one of the CFP-tagged  $\beta$ -arrestin2–FlAsH sensors (receptor– $\beta$ -arrestin2 interaction); M<sub>2</sub>AChR, FFA<sub>4</sub>R or  $\beta_2$ AR and one of the FlAsH-labelled CFP-tagged  $\beta$ -arrestin2–FlAsH constructs for measuring conformational changes. Cells were analysed 48 h after transfection.

**FlAsH labelling.** The labelling was done as described<sup>19,34,35</sup>. In brief, cells were washed twice, with Phenol red-free HBSS containing  $1.8 \text{ g l}^{-1}$  glucose (Invitrogen) and incubated at  $37^\circ\text{C}$  and 7%  $\text{CO}_2$  for 1 h with 1 ml 250 nM FlAsH in HBSS supplemented with  $12.5 \mu\text{M}$  1,2-ethane dithiol (EDT). To reduce unspecific labelling, cells were washed again with HBSS, incubated for 10 min with 1 ml 250  $\mu\text{M}$  EDT in HBSS, and finally washed twice with HBSS before being used for fluorescence measurements.

**Confocal microscopy.** Confocal microscopy experiments were performed on Leica TCS SP5 or TCS SP8 systems. Coverslips with transfected HEK29 cells were mounted using an Atofluor holder (Molecular Probes). Confocal images were taken with a  $63\times$  oil objective (numerical aperture, 1.4). CFP was excited with a diode laser at 458 nm laser line according to the manufacturer's settings and fluorescence intensities were recorded from 470 to 550 nm. YFP and FlAsH were excited with a 514 nm laser line according to the manufacturer's settings with the following modifications. Laser intensity was set to 2–4% and fluorescence intensities were recorded from 525 to 600 nm. Settings for recording were kept constant at  $512 \times 512$  pixel format, line average 4, and 400 Hz. To avoid bleed through, parallel images of CFP and YFP/FlAsH were taken in sequential scan mode using the settings described above.

Time series were recorded using the standard Leica software package (LAS AF 3). Images were taken at 30-s intervals (unless stated otherwise). For quantitative analysis of the  $\beta$ -arrestin2 translocation, regions of interest (ROIs) were defined on the membrane and fluorescence intensities were recorded over time. To correct the images in the ROIs for possible photobleaching, control regions including the whole cells were defined. To quantify  $\beta$ -arrestin2 translocation the resulting fluorescence intensities were then related to the initial values. Solely for display reasons, but not for quantitative analyses, individual images were corrected for autocontrast using Photoshop software (Adobe CS6).

**FRET.** Dynamic FRET measurements in intact cells were performed as described previously<sup>34,36,37</sup>. In brief, HEK293 cells transfected as described above were washed with HBSS and maintained in measuring buffer (140 mM NaCl, 5 mM KCl, 2 mM  $\text{CaCl}_2$ , 1 mM  $\text{MgCl}_2$ , and 10 mM HEPES, pH 7.3) at room temperature. FRET measurements using FlAsH (after labelling as described above) or YFP as acceptor and CFP as donor were done with an inverted microscope (Axiovert

135; Zeiss) equipped with an oil immersion  $63\times$  objective, a dual-emission photometric system (Till Photonics), and a polychrome IV light source (Till Photonics). Signals were converted with Digidata 1321A (Science Products GmbH) and stored with Clampex 8.1 software (Science Products GmbH). To minimize photobleaching, the fluorescence signals were recorded from entire cells with a frequency of 10 Hz with 20–40 ms illumination times. FRET was monitored from the emission ratio of YFP to CFP,  $F_{\text{YFP}}/F_{\text{CFP}}$  (emission intensities at  $535 \pm 15 \text{ nm}$  and  $480 \pm 20 \text{ nm}$ , beamsplitter DCLP 505 nm) upon excitation at  $436 \pm 10 \text{ nm}$  (beamsplitter DCLP 460 nm). The adjusted FRET ratio was corrected for the direct YFP or FlAsH excitation (YFP or FlAsH emission at 436 nm excitation divided by YFP emission at 480 nm excitation was 0.065). The CFP bleed-through was recorded separately and subtracted from the YFP fluorescence to give a corrected normalized ratio  $F_{\text{YFP}}/F_{\text{CFP}}$ . To determine dynamic changes in FRET, cells were continuously superfused with measuring buffer, and agonist was applied using a computer-assisted solenoid valve-controlled rapid superfusion device ALAVM8 (solution exchange 5–10 ms; ALA Scientific Instruments).

FRET was recorded between receptors C-terminally labelled with YFP and  $\beta$ -arrestin2 labelled with CFP (or vice versa) to monitor receptor– $\beta$ -arrestin2 interactions, or between FlAsH bound to positions 1–8 in the various constructs and the C-terminal CFP in the  $\beta$ -arrestin2–FlAsH sensors. For  $\beta_2$ AR interaction experiments, the phosphorylation-deficient  $\beta_2$ ARPD–YFP construct<sup>21</sup> served as a control for GRK-mediated phosphorylation. Since  $\beta$ -arrestin2 binding to M<sub>2</sub>AChR has been reported to have a greater contribution of non-phosphate binding elements<sup>32</sup>, phosphorylation-deficient receptor mutants could not serve as negative controls as in the case of  $\beta_2$ AR.

**Ligand washout with peristaltic pumps.** To compare the kinetics of the receptor– $\beta$ -arrestin interaction versus  $\beta$ -arrestin translocation under identical conditions the ligand addition to the coverslip was performed with a pipette. The subsequent agonist washout was done with a peristaltic pump (Ismatec IPC, IDEX Health & Science GmbH) whereby the cells were continuously superfused with measuring buffer and the solution was simultaneously withdrawn by suction. The solution exchange occurred with a flow rate of  $1.4 \text{ ml min}^{-1}$ . Note that this results in a slower solution exchange than via the fast perfusion system used in Figs 1 and 2, but for technical reasons the latter system could not be fitted to the confocal system.

**Immunoblot analysis for kinase activation.** ERK1/2, Src and JNK phosphorylation were assessed in serum-starved (0.5% for 24 h) HEK293 cells expressing either the CFP-tagged wild-type  $\beta$ -arrestin2 or the  $\beta$ -arrestin2–FlAsH2/5 sensor (Extended Data Fig. 3); these cells had been also co-transfected with M<sub>2</sub>-muscarinic,  $\beta_2$ -adrenergic or FFA<sub>4</sub> receptors (Extended Data Fig. 5) at 80% confluence. Isoproterenol ( $100 \mu\text{M}$ ), carbachol ( $100 \mu\text{M}$ ) and DHA ( $10 \mu\text{M}$ ) were added for the indicated times, and ERK1/2, Src or JNK phosphorylation was assessed by western blotting using phospho-specific antibodies (pERK, rabbit polyclonal anti-phospho-p44/42 MAPK (Thr-202/Tyr-204), Cell Signaling, 9101, 1:1,000; anti-phospho-Src (Tyr527), Cell Signaling, 2105, 1:1,000; phospho-SAPK/JNK (Thr183/Tyr185), Cell Signaling, 9251, 1:1,000). Total ERK or G $\beta$  was quantified as loading control using a rabbit polyclonal p44/42 MAPK antibody (Cell Signaling, 9102, 1:1,000) or G $\beta$  antibody (Santa Cruz, sc-378, 1:5,000). Quantification was done by chemiluminescence using a horseradish-peroxidase-conjugated polyclonal goat anti-rabbit antibody (Dianova, 111-035-144, 1:10,000). pERK, pSrc and pJNK bands 5–10 min after agonist stimulation represent the  $\beta$ -arrestin2 dependent activation of the respective kinases<sup>38</sup>.

**Statistical analysis.** No statistical methods were used to predetermine sample size. All data shown in bar graphs are presented as mean  $\pm$  s.e.m. of  $n$  independent experiments (biological replicates, that is only one cell per coverslip was analysed). Statistical analyses were performed with the OriginLab software (version 9.1). For kinetic analysis the data were fitted with a nonlinear mathematical function (exponential decay first order):

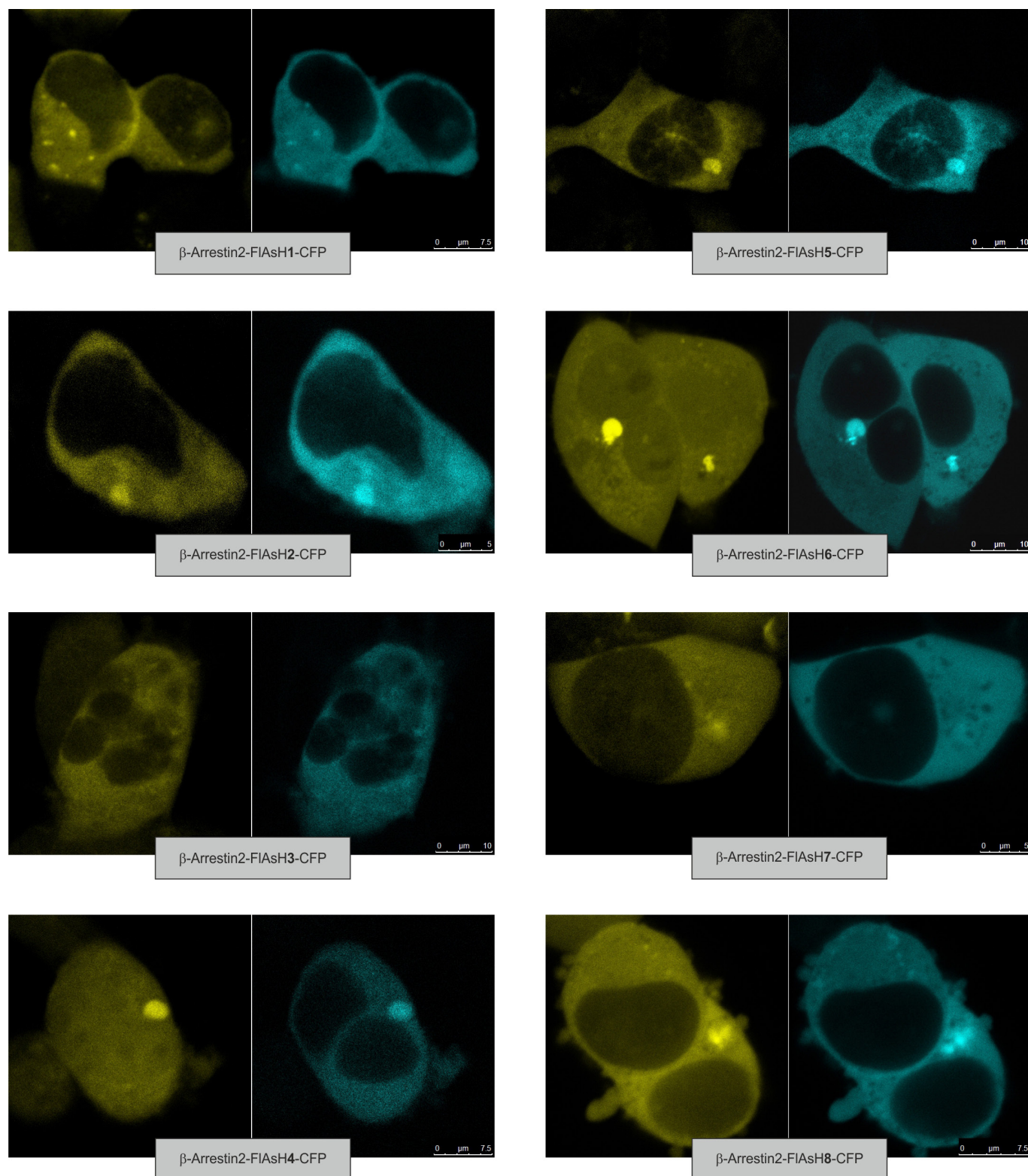
$$y(x) = A_0 \times (\exp(-(x - x_0)/\tau) - 1) \times H(x - x_0) + y_0, \text{ or} \\ y(x) = A_0 \times (1 - \exp(-(x - x_0)/\tau)) \times H(x - x_0) + y_0$$

where  $H(x)$  is the Heaviside step function) using again the Origin Lab software.

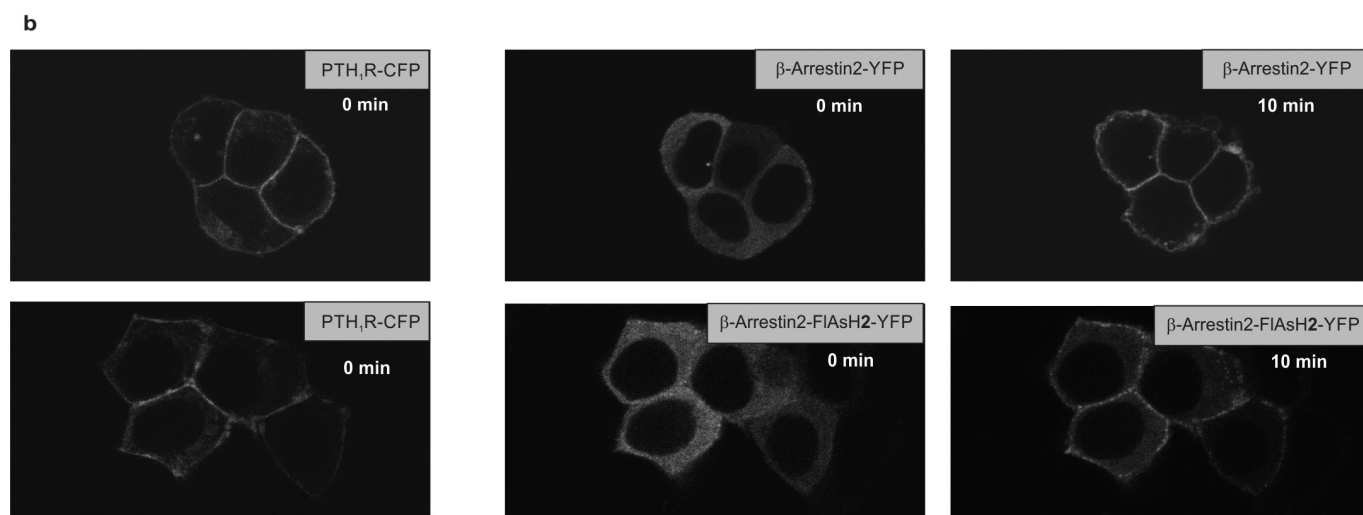
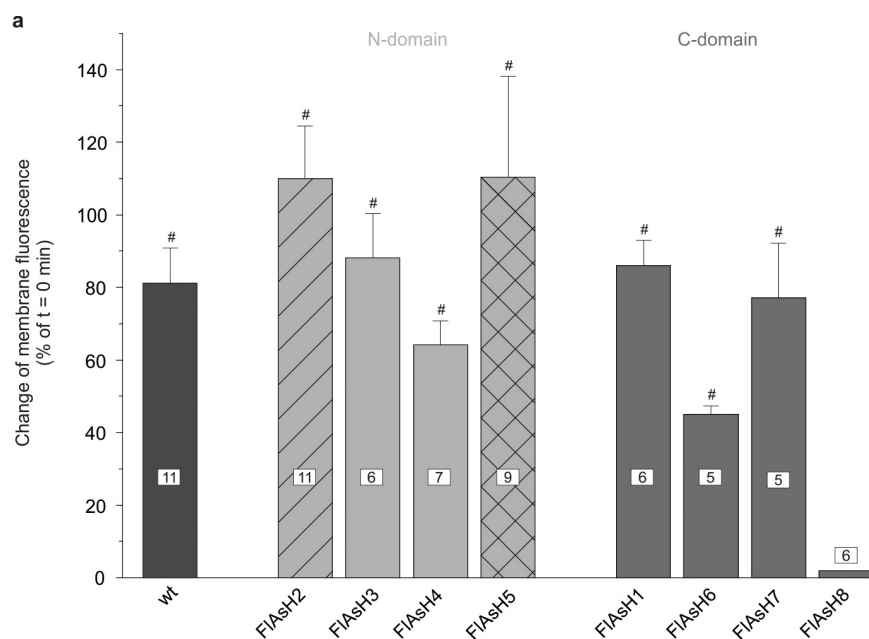
To analyse statistically significant differences of  $>2$  independent samples of equal or different sample sizes (with unknown distributions and/or unequal variances) the Kruskal–Wallis test was used. The Mann–Whitney  $U$  test was used as post-hoc test to identify where the stochastic dominance occurs or for how many pairs of groups stochastic dominance is obtained.



31. Gurevich, V. V. & Gurevich, E. V. The new face of active receptor bound arrestin attracts new partners. *Structure* **11**, 1037–1042 (2003).
32. Vishnivetskiy, S. A. *et al.* Few residues within an extensive binding interface drive receptor interaction and determine the specificity of arrestin proteins. *J. Biol. Chem.* **286**, 24288–24299 (2011).
33. Ho, S. N., Hunt, H. D., Horton, R. M., Pullen, J. K. & Pease, L. R. Site-directed mutagenesis by overlap extension using the polymerase chain reaction. *Gene* **77**, 51–59 (1989).
34. Hoffmann, C. *et al.* A FIAsh-based FRET approach to determine G protein-coupled receptor activation in living cells. *Nature Methods* **2**, 171–176 (2005).
35. Zürn, A. *et al.* Site-specific, orthogonal labeling of proteins in intact cells with two small biarsenical fluorophores. *Bioconjug. Chem.* **21**, 853–859 (2010).
36. Vilardaga, J.-P., Bünemann, M., Krasel, C., Castro, M. & Lohse, M. J. Measurement of the millisecond activation switch of G protein-coupled receptors in living cells. *Nature Biotechnol.* **21**, 807–812 (2003).
37. Hein, P., Frank, M., Hoffmann, C., Lohse, M. J. & Bünemann, M. Dynamics of receptor/G protein coupling in living cells. *EMBO J.* **24**, 4106–4114 (2005).
38. Shenoy, S. K. *et al.*  $\beta$ -Arrestin-dependent, G protein-independent ERK1/2 activation by the  $\beta_2$ -adrenergic receptor. *J. Biol. Chem.* **281**, 1261–1273 (2006).

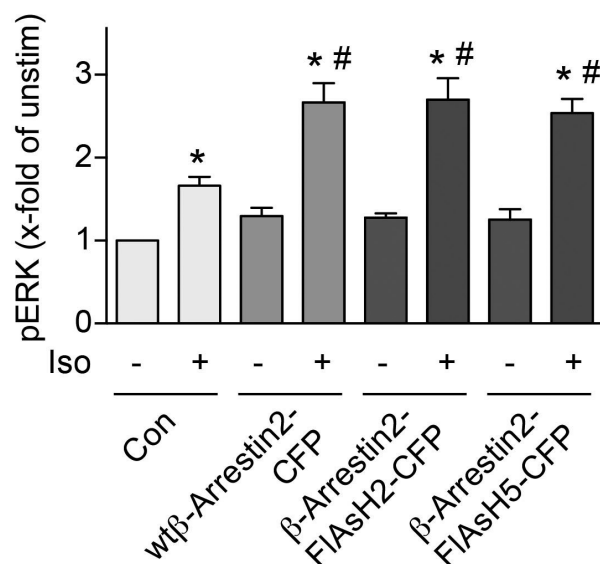


**Extended Data Figure 1 | Specific labelling of FRET-based  $\beta$ -arrestin2 biosensors in intact cells with FIAsH.** HEK293 cells were transfected with one of the CFP-tagged  $\beta$ -arrestin2 biosensors, labelled with FIAsH and analysed by laser scanning microscopy. Confocal images show overlapping intracellular staining in both the CFP (blue) and the FIAsH (yellow) channels.

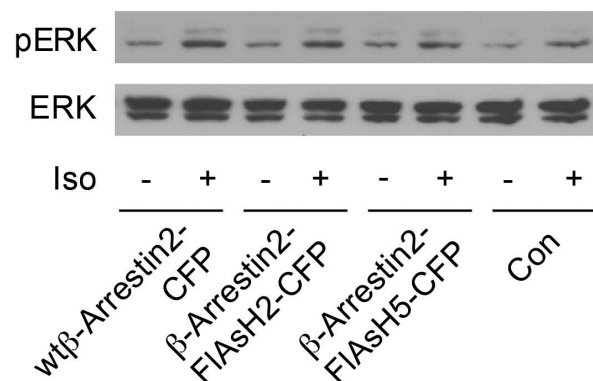


**Extended Data Figure 2 | Translocation of the  $\beta$ -arrestin2 biosensors.** HEK293 cells were transiently transfected with  $\text{PTH}_1\text{R}$ -CFP and either wild-type  $\beta$ -arrestin2-YFP or one of the eight  $\beta$ -arrestin2-FIAsH-YFP sensors. **a**, Increase in membrane fluorescence 10 min after stimulation with  $1\ \mu\text{M}$  PTH 1–34 (N-terminal fragment) expressed as percentage increase of the initial fluorescence at  $t = 0$  min. Data represent

mean  $\pm$  s.e.m. values of the indicated number of independent experiments. # $P < 0.01$  versus no effect (Kruskal–Wallis followed by Mann–Whitney  $U$  post-hoc analysis). **b**, Confocal images of the CFP-tagged  $\text{PTH}_1\text{R}$  (left) and wild-type  $\beta$ -arrestin2-YFP (top), or  $\beta$ -arrestin2-FIAsH2-YFP (bottom) before (middle) and 10 min after PTH stimulation (right).

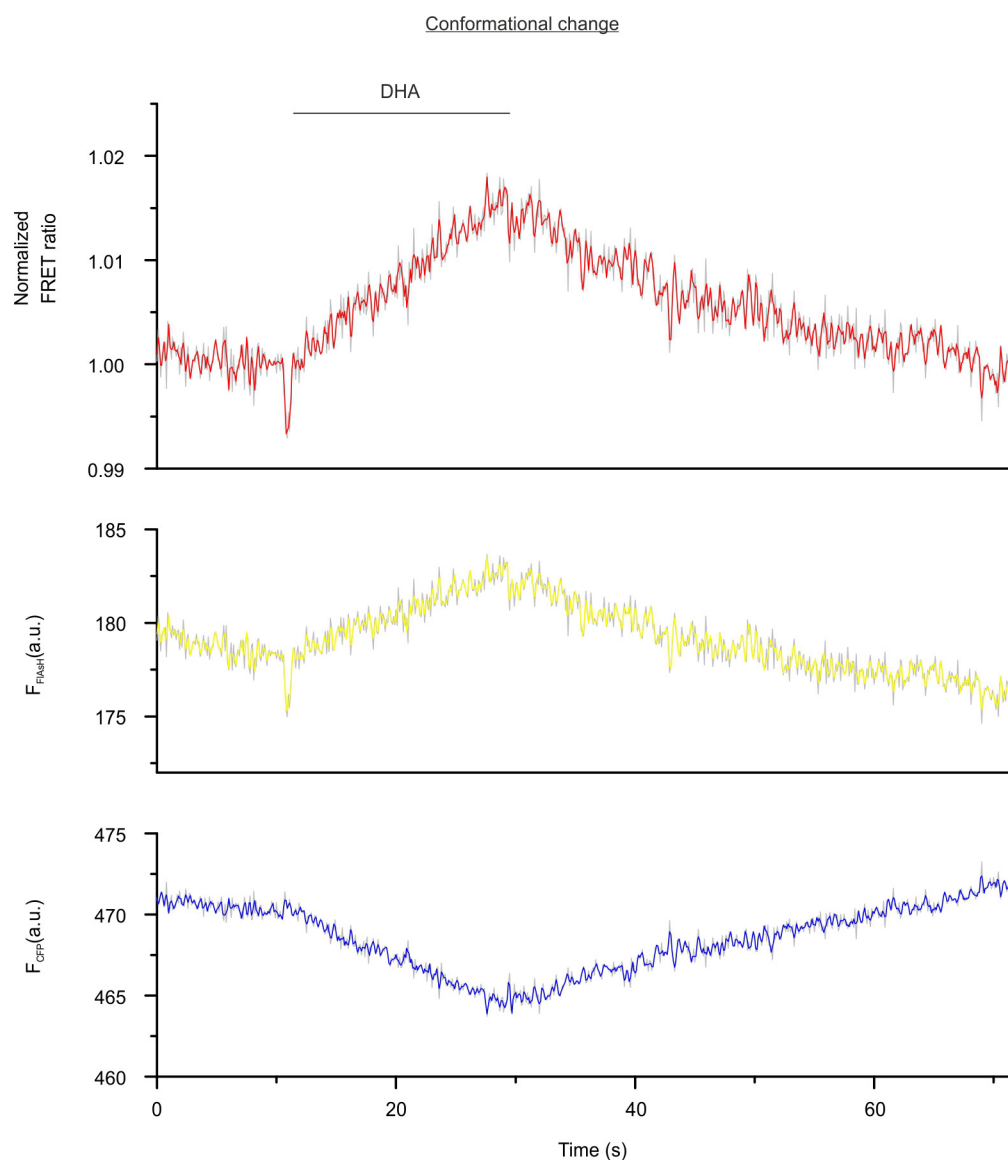


**Extended Data Figure 3 |  $\beta$ -Arrestin-dependent ERK1/2 phosphorylation.** HEK293 cells were transiently transfected with the indicated constructs or control vector (pcDNA3; Con) and treated without or with isoproterenol for 10 min (10  $\mu$ M) as indicated. Cell lysates



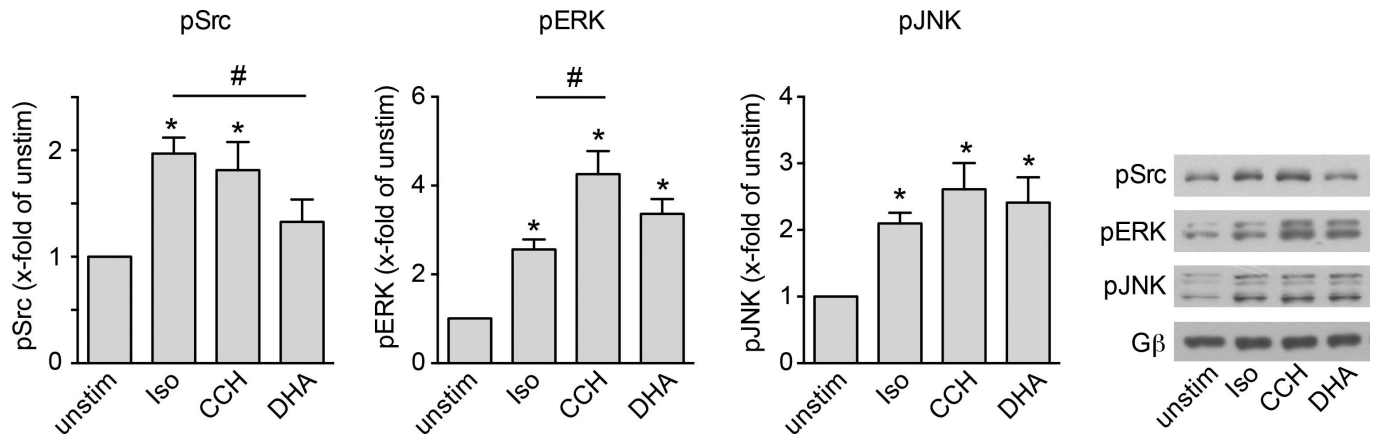
were analysed for pERK1/2 and ERK1/2 by immunoblot analysis. Data represent mean  $\pm$  s.e.m.,  $n = 6$  independent experiments. \* $P < 0.05$  versus unstimulated samples; # $P < 0.05$  versus isoproterenol-stimulated control (Kruskal–Wallis followed by Mann–Whitney  $U$  post-hoc analysis).





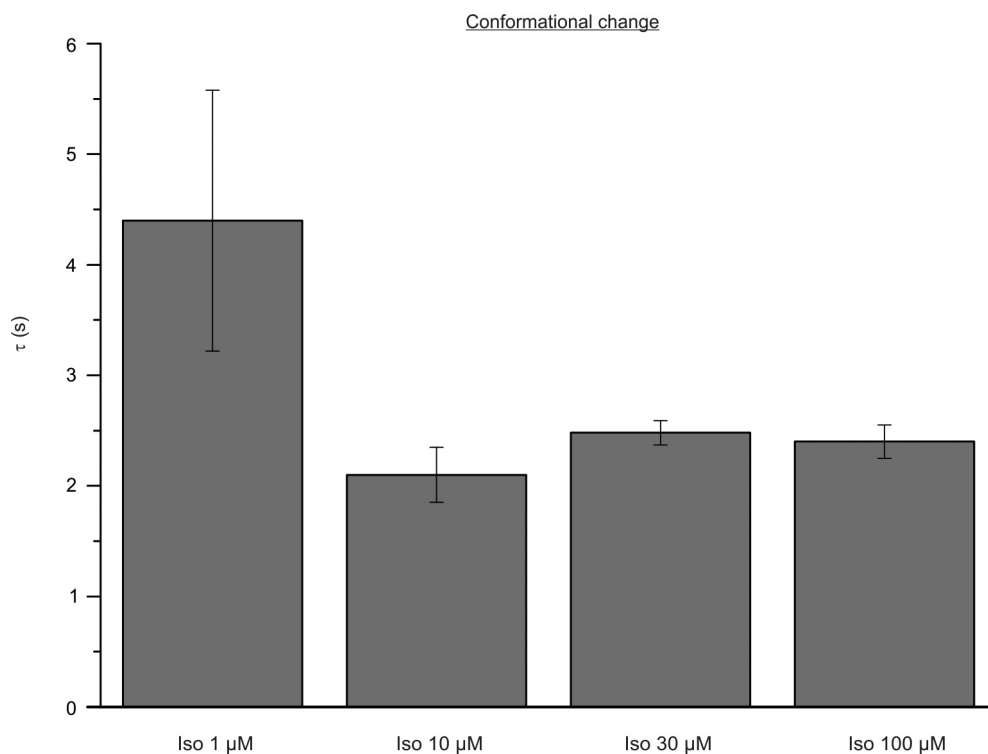
**Extended Data Figure 4 | Conformational changes in the  $\beta$ -arrestin2-FlAsH2 biosensor after FFA4R stimulation.** Representative traces of docosahexaenoic acid (DHA)-induced changes in the normalized FRET ratio ( $F_{\text{FlAsH}}/F_{\text{CFP}}$ ) and the corresponding CFP ( $F_{\text{CFP}}$  cyan) or FlAsH

( $F_{\text{FlAsH}}$ , yellow) emission recorded from one single HEK293 cell expressing the FFA4R and the FlAsH-labelled  $\beta$ -arrestin2-FlAsH2-CFP sensor. Application of 100  $\mu\text{M}$  DHA is indicated. Representative trace of 10 experiments.



**Extended Data Figure 5 |  $\beta$ -Arrestin-mediated downstream signalling to kinases for  $M_2$ -muscarinic,  $\beta_2$ -adrenergic and FFA4 receptors.** HEK293 cells were transfected with  $\beta_2$ AR,  $M_2$ -muscarinic or FFA4 receptors and stimulated with respective agonists at saturating concentrations (isoproterenol, 100  $\mu$ M; carbachol (CCH), 100  $\mu$ M; docosahexaenoic acid, 10  $\mu$ M) for 10 min.  $\beta$ -Arrestin downstream

signalling was evaluated by phospho-specific antibodies for pSrc, pERK1/2 and pJNK. G $\beta$  was used as loading control. Data represent mean  $\pm$  s.e.m. of  $n = 12$  independent experiments. \* $P < 0.05$  versus unstimulated control; # $P < 0.05$  versus indicated column (Kruskal–Wallis followed by Mann–Whitney  $U$  post-hoc analysis).



**Extended Data Figure 6 | Concentration dependency of the kinetics of the conformational changes in  $\beta$ -arrestin upon  $\beta_2$ AR stimulation.**

HEK293 cells were co-transfected with the  $\beta_2$ AR and  $\beta$ -arrestin2-FlAsH2-CFP and stimulated with different concentrations of isoproterenol. Kinetics of the agonist evoked intramolecular FRET changes were analysed by curve fitting according to Fig. 2. The bar

graph shows the rate constants  $\tau$  (s) for conformational changes detected with the  $\beta$ -arrestin2-FlAsH2 sensor upon stimulation with 1, 10, 30 or 100  $\mu$ M isoproterenol, respectively. Data represent mean  $\pm$  s.e.m. of  $n \geq 3$  independent experiments. The values are not significantly different ( $P < 0.05$ ).

**Extended Data Table 1 | FRET  $\beta$ -arrestin2 sensor constructs used in this study**

Abbreviation	Construct	FIAsH binding motif
FIAsH1	$\beta$ -Arrestin2-FIAsH1	<sup>331</sup> CCPGCC <sup>332</sup>
FIAsH2	$\beta$ -Arrestin2-FIAsH2	<sup>154</sup> CCPGCC <sup>155</sup>
FIAsH3	$\beta$ -Arrestin2-FIAsH3	<sup>49</sup> CCPGCC <sup>50</sup>
FIAsH4	$\beta$ -Arrestin2-FIAsH4	<sup>150</sup> CCPGCC <sup>151</sup>
FIAsH5	$\beta$ -Arrestin2-FIAsH5	<sup>157</sup> CCPGCC <sup>158</sup>
FIAsH6	$\beta$ -Arrestin2-FIAsH6	<sup>326</sup> CCPGCC <sup>327</sup>
FIAsH7	$\beta$ -Arrestin2-FIAsH7	<sup>335</sup> CCPGCC <sup>336</sup>
FIAsH8	$\beta$ -Arrestin2-FIAsH8	<sup>193</sup> CCPGCC <sup>194</sup>

Insertion sites for the FIAsH-binding motif CCPGCC are denoted in single letter code with the amino acid positions in the  $\beta$ -arrestin2 sequence.



# The conformational signature of $\beta$ -arrestin2 predicts its trafficking and signalling functions

Mi-Hye Lee<sup>1</sup>, Kathryn M. Appleton<sup>1</sup>, Erik G. Strungs<sup>1</sup>, Joshua Y. Kwon<sup>1</sup>, Thomas A. Morinelli<sup>1</sup>, Yuri K. Peterson<sup>2</sup>, Stephane A. Laporte<sup>3,4,5</sup> & Louis M. Luttrell<sup>1,6</sup>

**Arrestins are cytosolic proteins that regulate G-protein-coupled receptor (GPCR) desensitization, internalization, trafficking and signalling<sup>1,2</sup>. Arrestin recruitment uncouples GPCRs from heterotrimeric G proteins, and targets the proteins for internalization via clathrin-coated pits<sup>3,4</sup>. Arrestins also function as ligand-regulated scaffolds that recruit multiple non-G-protein effectors into GPCR-based ‘signalsomes’<sup>5,6</sup>. Although the dominant function(s) of arrestins vary between receptors, the mechanism whereby different GPCRs specify these divergent functions is unclear. Using a panel of intramolecular fluorescein arsenical hairpin (FAsH) bioluminescence resonance energy transfer (BRET) reporters<sup>7</sup> to monitor conformational changes in  $\beta$ -arrestin2, here we show that GPCRs impose distinctive arrestin ‘conformational signatures’ that reflect the stability of the receptor–arrestin complex and role of  $\beta$ -arrestin2 in activating or dampening downstream signalling events. The predictive value of these signatures extends to structurally distinct ligands activating the same GPCR, such that the innate properties of the ligand are reflected as changes in  $\beta$ -arrestin2 conformation. Our findings demonstrate that information about ligand–receptor conformation is encoded within the population average  $\beta$ -arrestin2 conformation, and provide insight into how different GPCRs can use a common effector for different purposes. This approach may have application in the characterization and development of functionally selective GPCR ligands<sup>8,9</sup> and in identifying factors that dictate arrestin conformation and function.**

The two non-visual arrestins,  $\beta$ -arrestin1 and  $\beta$ -arrestin2 (also known as arrestin2 and arrestin3, respectively), bind to and regulate the majority of extraretinal GPCRs<sup>1,2</sup>. Both static crystallographic structures<sup>10–14</sup> and biophysical studies in live cells<sup>15,16</sup> indicate that arrestins undergo conformational rearrangement on GPCR binding. To investigate the effect of GPCR activation on the dynamics of  $\beta$ -arrestin2 conformation and function, we prepared a series of FAsH BRET probes<sup>7</sup> by inserting the six-amino-acid motif, CCPGCC, into the  $\beta$ -arrestin2 sequence at sites not predicted to be involved in its interactions with receptors or major binding partners (Fig. 1a). Each probe (rLuc– $\beta$ -arrestin2–FAsH1–6) was designed to measure BRET between a *Renilla* luciferase (rLuc) fluorescence donor at the amino terminus, and a fluorescein arsenical acceptor located at one of six positions along the length of  $\beta$ -arrestin2. We hypothesized that observing changes in BRET efficiency from multiple vantage points would yield an  $\beta$ -arrestin2 conformational signature that would correlate with its molecular functions. We first tested whether insertion of the FAsH motif compromised  $\beta$ -arrestin2 recruitment by measuring the agonist-induced increase in intermolecular BRET between a C-terminal yellow fluorescent protein (YFP)-tagged GPCR and the N-terminal rLuc moiety of each rLuc– $\beta$ -arrestin2–FAsH construct. As shown in Fig. 1b, five of the rLuc– $\beta$ -arrestin2–FAsH constructs (F1, F2, F4, F5 and F6) generated

BRET signals comparable to unmodified rLuc– $\beta$ -arrestin2. The sixth construct (F3), which was poorly recruited, was included in subsequent experiments as an internal negative control. We then tested whether GPCR activation would produce an intramolecular rLuc– $\beta$ -arrestin2–FAsH BRET signal upon recruitment to an untagged GPCR. Agonist stimulation elicited changes in the  $\beta$ -arrestin2–FAsH BRET signal ( $\Delta$ net BRET) that were maintained over at least 10 min (Extended Data Fig. 1a) and proportional to receptor occupancy at less than saturating ligand concentration (Extended Data Fig. 1b). Thus, measuring the  $\Delta$ net BRET of each construct produced a  $\beta$ -arrestin2–FAsH BRET signature that was characteristic of the receptor being investigated (Fig. 1c). For the vasopressin type 2 receptor (V<sub>2</sub>R), ligand stimulation caused significant decreases in the signal from FAsH sensors in the N-terminal (F1 and F2) and C-terminal (F4 and F5) globular domains, and a significant increase in signal from the sensor located at the C terminus (F6). Predictably, given its poor recruitment, the F3 construct did not significantly change with stimulation.

To determine whether  $\beta$ -arrestin2–FAsH signatures were conserved between GPCRs, we selected a panel of six additional receptors with diverse G-protein coupling, arrestin binding, and arrestin-dependent signalling characteristics (Extended Data Table 1). Our test panel included two stable arrestin-binding class ‘B’<sup>17</sup> GPCRs: the angiotensin AT<sub>1A</sub> receptor (AT<sub>1A</sub>R) and the type 1 parathyroid hormone receptor (PTH<sub>1R</sub>); three transient arrestin-binding class ‘A’<sup>17</sup> GPCRs: the  $\alpha_{1B}$ -adrenergic receptor ( $\alpha_{1B}$ AR), the  $\beta_2$ -adrenergic receptor ( $\beta_2$ AR), and the sphingosine-1-phosphate 1 receptor (S1P<sub>1</sub>R); and the  $\alpha_{2A}$ -adrenergic receptor ( $\alpha_{2A}$ AR) that does not produce detectable  $\beta$ -arrestin2 translocation. The G-protein-mediated signalling of each receptor was characterized using a FLIPR<sup>TETRA</sup> fluorescent imaging plate reader to measure ligand-dependent activation or inhibition of adenylyl cyclase and stimulation of transmembrane Ca<sup>2+</sup> entry<sup>18</sup> (Extended Data Fig. 2). The pattern of arrestin recruitment was confirmed by confocal fluorescence microscopy using GFP-tagged  $\beta$ -arrestin2 (ref. 19) (Fig. 2a). The  $\beta$ -arrestin2–FAsH BRET signature generated by each receptor is shown in Fig. 2b. As the  $\Delta$ net BRET observed with each probe reflects the ‘population average’ conformation of the cellular pool of rLuc– $\beta$ -arrestin2–FAsH, signatures were generated under conditions of receptor excess and saturating ligand concentration to ensure that the largest possible fraction of the reporter pool was receptor-bound at steady state. Inspection of the rLuc– $\beta$ -arrestin2–FAsH BRET signatures revealed that the class B receptors AT<sub>1A</sub>R, PTH<sub>1R</sub> and V<sub>2</sub>R (Fig. 1c), which form stable GPCR–arrestin complexes that transit to endosomes<sup>17</sup>, produced significant negative  $\Delta$ net BRET signals at the F4 position and positive  $\Delta$ net BRET signals at the C terminus (Fig. 2b; black arrows). In contrast, the class A  $\alpha_{1B}$ AR,  $\beta_2$ AR and S1P<sub>1</sub>R, which dissociate from arrestin soon after internalization<sup>17</sup>, produced little to no signal in these positions. Only small N-terminal responses were observed with  $\alpha_{2A}$ AR, which interacts weakly with  $\beta$ -arrestin2 (ref. 20).

<sup>1</sup>Department of Medicine, Medical University of South Carolina, Charleston, South Carolina 29425, USA. <sup>2</sup>Department of Pharmaceutical & Biomedical Sciences, College of Pharmacy, Medical University of South Carolina, Charleston, South Carolina 29425, USA. <sup>3</sup>Department of Medicine, McGill University Health Center Research Institute, McGill University, Quebec H4A 3J1, Canada.

<sup>4</sup>Pharmacology and Therapeutics, McGill University, Quebec H3G 1Y6, Canada. <sup>5</sup>Anatomy and Cell Biology, McGill University, Quebec H3A 0C7, Canada. <sup>6</sup>Research Service of the Ralph H. Johnson Veterans Affairs Medical Center, Charleston, South Carolina 29401, USA.

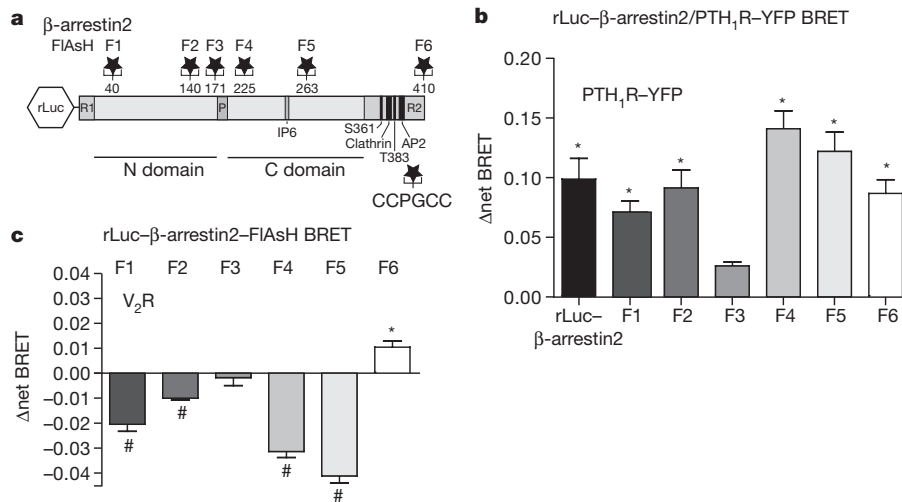


**Figure 1 | Design and characterization of rLuc- $\beta$ -arrestin2-FIAsH BRET reporters.** **a**, Six rLuc- $\beta$ -arrestin2-FIAsH BRET reporters (F1–F6) were constructed by inserting the amino acid motif CCPGCC after amino acid residues 40, 140, 171, 225, 263 and 410 of  $\beta$ -arrestin2. The location of each FIAsH motif is shown in relation to the globular N and C domains of  $\beta$ -arrestin2, as well as the clathrin and adaptor protein 2 (AP2) binding sites and reported phosphorylation sites (Ser<sup>361</sup> and Thr<sup>383</sup>) in

the  $\beta$ -arrestin2 C-terminal regulatory (R2) domain<sup>1</sup>. **b**, Intermolecular BRET demonstrating ligand-dependent recruitment of rLuc- $\beta$ -arrestin2–FIAsH1–6 to human PTH<sub>1</sub>R. **c**, rLuc- $\beta$ -arrestin2–FIAsH1–6 ‘signature’ of  $\beta$ -arrestin2 binding to the V<sub>2</sub>R. The bar graphs depict mean  $\pm$  s.e.m. of independent biological replicates ( $n = 3$  (**b**) and  $n = 5$  (**c**)). \* $P < 0.05$ , # $P < 0.005$ , greater or less than vehicle-stimulated control.

To relate the  $\beta$ -arrestin2–FIAsH BRET signature to arrestin-dependent signalling, we determined the effect of silencing  $\beta$ -arrestin1/2 expression on ligand-stimulated ERK1/2 activation<sup>21,22</sup> using HEK293 FRT/TO  $\beta$ -arrestin1/2 shRNA cells that carry tetracycline-inducible shRNA targeting  $\beta$ -arrestin1/2 (ref. 23). As shown in Fig. 2c, ERK1/2 activation by AT<sub>1</sub>AR, PTH<sub>1</sub>R and  $\alpha_{1B}$ AR was significantly attenuated

by  $\beta$ -arrestin1/2 silencing, indicating a positive signalling role for arrestin scaffolds<sup>24</sup>.  $\beta$ -arrestin1/2 silencing had no net effect on ERK1/2 activation by  $\beta_2$ AR, which reportedly activates ERK1/2 via both G<sub>i/o</sub>-dependent and arrestin-dependent pathways in HEK293 cells<sup>25</sup>, and significantly enhanced ERK1/2 activation by the S1P<sub>1</sub>R and  $\alpha_{2A}$ AR, suggesting that for these receptors the major role of arrestins is to

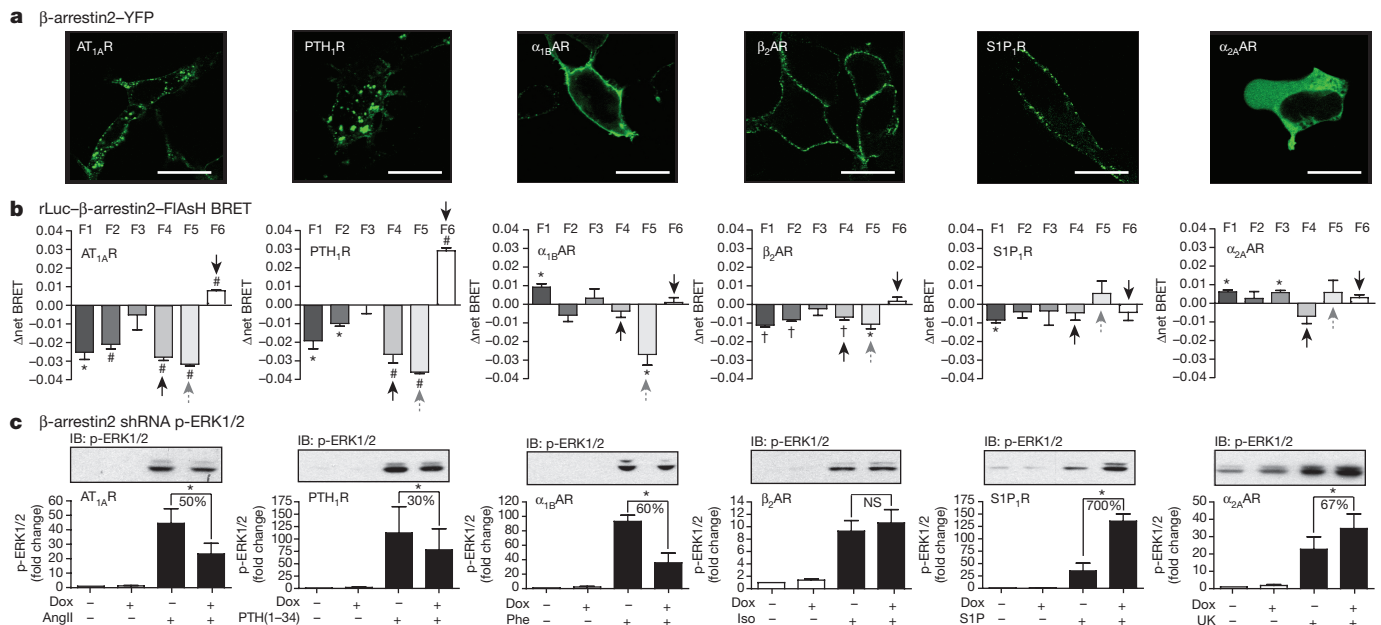


**Figure 2 | Relationship between GPCR- $\beta$ -arrestin2 complex formation, rLuc- $\beta$ -arrestin2-FIAsH BRET signature, and arrestin-dependent ERK1/2 activation for six different GPCRs.** **a**, Agonist-dependent recruitment of  $\beta$ -arrestin2–GFP. Each panel depicts a representative field of stimulated cells.  $\beta$ -arrestin2–GFP was diffusely cytosolic in the absence of agonist (not shown). Scale bars, 10  $\mu$ m. **b**, Receptor-specific rLuc- $\beta$ -arrestin2–FIAsH1–6 signatures. Each bar graph depicts mean  $\pm$  s.e.m. of independent biological replicates ( $n = 5$ ). \* $P < 0.05$ , # $P < 0.005$ , † $P < 0.001$ , greater or less than vehicle-stimulated control. Black arrows indicate BRET changes related to GPCR- $\beta$ -arrestin2 complex stability; grey arrows indicate changes related to  $\beta$ -arrestin2-dependent ERK1/2

activation. **c**, Effect of downregulating  $\beta$ -arrestin1/2 expression on GPCR-mediated ERK1/2 phosphorylation. A representative phospho-ERK1/2 immunoblot (IB) is shown above a bar graph depicting the mean  $\pm$  s.e.m. of independent biological replicates ( $n = 7$ , AT<sub>1</sub>AR;  $n = 9$ , PTH<sub>1</sub>R;  $n = 6$ ,  $\alpha_{1B}$ AR;  $n = 20$ ,  $\beta_2$ AR;  $n = 5$ ,  $\alpha_{2A}$ AR and S1P<sub>1</sub>R). Responses were normalized to the basal level of phospho-ERK1/2 in non-stimulated samples. Dox, doxycycline; iso, isoproterenol; phe, phenylephrine; PTH, parathyroid hormone N-terminal 1–34 fragment; S1P, sphingosine-1-phosphate; UK, UK14303. \* $P < 0.05$ , greater or less than stimulated response in non-induced cells. NS, not significant.

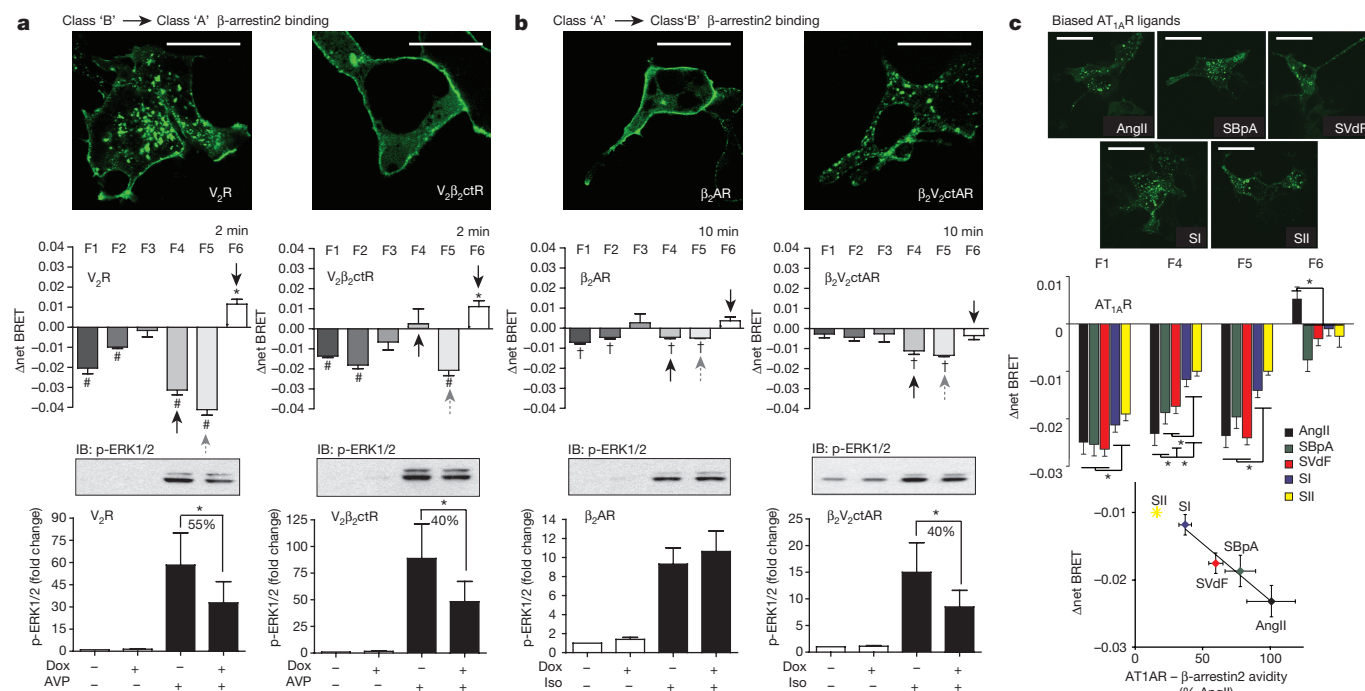


**Figure 3 | Effect of GPCR-arrestin trafficking pattern and ligand structure on the rLuc-β-arrestin2-FlAsH BRET conformational signature.** **a**, Effect of converting stable class B β-arrestin2 binding to transient class A binding. Upper, representative confocal fluorescence images showing the pattern of ligand-stimulated GFP-β-arrestin2 recruitment to the V<sub>2</sub>R or the chimaeric V<sub>2</sub>β<sub>2</sub>ctR. Centre, the β-arrestin2-FlAsH1–6 profiles generated by V<sub>2</sub>R and V<sub>2</sub>β<sub>2</sub>ctR. Lower, the arrestin-dependence of ERK1/2 phosphorylation by the V<sub>2</sub>R and V<sub>2</sub>β<sub>2</sub>ctR. **b**, Analogous experiment demonstrating the effect of converting transient class A β-arrestin2 binding to stable class B binding using the β<sub>2</sub>AR and the chimaeric β<sub>2</sub>V<sub>2</sub>ctAR. In **a** and **b**, phospho-ERK1/2 bar graphs depict mean ± s.e.m. of independent biological replicates ( $n = 12$ , V<sub>2</sub>R and V<sub>2</sub>β<sub>2</sub>ctR;  $n = 20$ , β<sub>2</sub>AR;  $n = 12$ , β<sub>2</sub>V<sub>2</sub>ctR). \* $P < 0.05$ , less than stimulated response in non-induced cells. Black arrows indicate BRET changes related

to GPCR-β-arrestin2 complex stability; grey arrows indicate changes related to β-arrestin2-dependent ERK1/2 activation. **c**, Effect of ligand structure on the rLuc-β-arrestin2-FlAsH BRET signature.

Upper, representative confocal fluorescence images showing the pattern of GFP-β-arrestin2 recruitment to the AT<sub>1</sub>R upon stimulation with AngII, SBpA, SVdF, SI or SII. Centre, the F1 and F4–6 profiles generated by each ligand. Bottom, the relationship between the amplitude of the F4 signal and the independently determined avidity of AT<sub>1</sub>R and β-arrestin2 measured by FRAP<sup>27</sup>. SII was not included in the linear fit, as the AT<sub>1</sub>R-β-arrestin2 avidity is too low to measure by FRAP. In all panels, the rLuc-β-arrestin2-FlAsH BRET graphs represent mean ± s.e.m. of independent biological replicates ( $n = 5$ , V<sub>2</sub>R and V<sub>2</sub>β<sub>2</sub>ctR;  $n = 6$ , β<sub>2</sub>AR and β<sub>2</sub>V<sub>2</sub>ctR;  $n = 6$ , AT<sub>1</sub>R, with each ligand). \* $P < 0.05$ , # $P < 0.005$ , + $P < 0.001$ , greater or less than vehicle-stimulated control. Scale bars, 10 μm.

dampen G-protein-dependent ERK1/2 activation by promoting desensitization. Consistent with this, we found that ERK1/2 activation via β<sub>2</sub>AR, S1P<sub>1</sub>R and α<sub>2A</sub>AR was strongly pertussis toxin-sensitive, indicating a predominantly G<sub>i/o</sub>-mediated mechanism of activation (Extended Data Fig. 3). Comparison with the rLuc-β-arrestin2-FlAsH BRET signatures revealed a correlation between arrestin-dependent ERK1/2 activation and a significant negative Δnet BRET signal at the F5 position. This was most apparent for the class A α<sub>1B</sub>AR, which lacked the F4 and F6 signals characteristic of class B receptors, but retained the F5 signal shared by GPCRs mediating arrestin-dependent signals (Fig. 2b; grey arrows). The relationship between α<sub>1B</sub>AR-induced F5 signal and ERK1/2 activation was present over a range of agonist concentrations (Extended Data Fig. 4a), whereas at saturating ligand concentration the F5 signal readily separated the positive and negative roles of arrestin in ERK1/2 activation by our panel of seven GPCRs (Extended Data Fig. 4b).

We next examined chimaeric GPCRs in which the receptor C-tail was exchanged to reverse the class A and class B patterns of arrestin binding. As shown in Fig. 3a, replacing the C-tail of the class B V<sub>2</sub>R with that of the class A β<sub>2</sub>AR (V<sub>2</sub>β<sub>2</sub>ctR) is sufficient to reverse the arrestin binding pattern<sup>26</sup>. Although the C-tail exchange affected the stability of the receptor-arrestin complex, it did not affect arrestin-dependent ERK1/2 activation, which persisted in the V<sub>2</sub>β<sub>2</sub>ctR. Comparison of the rLuc-β-arrestin2-FlAsH BRET profiles generated by V<sub>2</sub>R and V<sub>2</sub>β<sub>2</sub>ctR revealed that conversion of class B to class A binding caused the loss of the negative F4 signal characteristic of class B receptors such as AT<sub>1</sub>AR, PTH<sub>1</sub>R, and V<sub>2</sub>R (Fig. 2b). In contrast, the F5 signal was preserved,

such that the rLuc-β-arrestin2-FlAsH BRET signature of the chimaeric V<sub>2</sub>β<sub>2</sub>ctR resembled that of the α<sub>1B</sub>AR, the other class A GPCR that retained arrestin signalling. The opposite experiment, involving conversion of a class A receptor to class B, is shown in Fig. 3b. Replacing the C-tail of the class A β<sub>2</sub>AR with that of the class B V<sub>2</sub>R (β<sub>2</sub>V<sub>2</sub>ctAR) reverses the arrestin binding pattern. In this case, β<sub>2</sub>V<sub>2</sub>ctAR-mediated ERK1/2 activation became more arrestin-dependent, as evidenced by acquired sensitivity to shRNA silencing of β-arrestin1/2 expression. Inspection of the β-arrestin2-FlAsH BRET profiles of β<sub>2</sub>AR and V<sub>2</sub>β<sub>2</sub>ctR revealed that conversion of class A to class B produced a significant increase in the F4 signal that was most apparent following 10 min of ligand stimulation. Notably, the F5 signal also increased, consistent with the gain of arrestin-dependent signalling. Thus, reversing the stability of the arrestin-GPCR complex, without altering the other intracellular loops of the receptor, was sufficient to produce loss/gain of FlAsH BRET signal at the F4 position, whereas the magnitude of change in the F5 position correlated with arrestin-dependent signalling.

We then compared the β-arrestin2-FlAsH BRET signature generated by angiotensin II (AngII) with those of a previously characterized series of arrestin-selective 'biased' AngII analogues<sup>27</sup> (Fig. 3c). Although all five ligands—AngII, [Sar<sup>1</sup>,Ile<sup>4</sup>,Ile<sup>8</sup>]-AngII (SII), [Sar<sup>1</sup>,Ile<sup>8</sup>]-AngII (SI), [Sar<sup>1</sup>,Val<sup>5</sup>,D-Phe<sup>8</sup>]-AngII (SVdF) and [Sar<sup>1</sup>,Val<sup>5</sup>,Bpa<sup>8</sup>]-AngII (SBpA)—promote the assembly of endosomal AT<sub>1</sub>AR-arrestin complexes, fluorescence recovery after photobleaching (FRAP) has demonstrated that they cause different avidity between the receptor and β-arrestin2, with the rank order of receptor-arrestin complex half-life of AngII > SBpA > SVdF > SI > SII (ref. 27). The efficiency with which these



ligands promote arrestin-dependent ERK1/2 activation corresponds to the avidity of the complex, with longer half-life complexes generating proportionally greater arrestin-dependent signalling<sup>27</sup>. Inspection of the  $\beta$ -arrestin2–FAsH BRET signatures demonstrated that although different ligands had little effect on the magnitude of the N-terminal F1 shift, the amplitude of the F4 and F5 signals were very sensitive to ligand structure. Plotting the F4 signal versus receptor–arrestin avidity measured by FRAP revealed a strong linear correlation. Thus, the signature presented by  $\beta$ -arrestin2–FAsH BRET probes in the C-terminal domain reflected the avidity of the AT<sub>1A</sub>R– $\beta$ -arrestin2 interaction, even when comparing ligands that all evoke a canonical class B pattern of arrestin recruitment.

The rLuc– $\beta$ -arrestin2–FAsH BRET signature reflects both changes in the distance/orientation of the fluorophores due to conformational rearrangement, and steric effects generated by arrestin interaction with its receptor and non-receptor binding partners. Although it is not possible to ascribe the rLuc– $\beta$ -arrestin2–FAsH BRET signal at a given position to specific conformational shifts or engagement of binding partners, our data clearly demonstrate that ligand–GPCR complexes confer distinctive  $\beta$ -arrestin2 conformations, and that features of the conformational signature are conserved between receptors with similar arrestin binding/signalling characteristics. Moreover, we find that the  $\Delta$ net BRET at selected positions correlates with downstream arrestin function, for example, class A versus class B trafficking and arrestin-dependent ERK1/2 activation, suggesting that  $\beta$ -arrestin2–FAsH BRET probes can predict arrestin function on the basis of the ligand-induced conformational signature. Thus, intramolecular rLuc– $\beta$ -arrestin2–FAsH BRET probes may aid in identifying the factors that determine arrestin conformation and function, such as ligand ‘bias’<sup>8,9</sup>, GPCR C-tail ‘phosphorylation codes’ written by different GRKs<sup>28</sup>, and post-translational modifications of arrestin that stabilize or destabilize the complex<sup>29</sup>.

While this work was in progress, we became aware of a complementary study using  $\beta$ -arrestin2–FAsH fluorescence resonance energy transfer (FRET) sensors<sup>30</sup>. This study confirms the existence of GPCR-specific  $\beta$ -arrestin2 conformations and, with the superior temporal resolution of FRET, provides key insights into the kinetics of receptor binding and arrestin activation.

**Online Content** Methods, along with any additional Extended Data display items and Source Data, are available in the online version of the paper; references unique to these sections appear only in the online paper.

**Received 30 July 2015; accepted 19 January 2016.**

**Published online 23 March 2016.**

1. Ferguson, S. S. Evolving concepts in G protein-coupled receptor endocytosis: the role in receptor desensitization and signaling. *Pharmacol. Rev.* **53**, 1–24 (2001).
2. Gurevich, V. V. & Gurevich, E. V. Structural determinants of arrestin functions. *Prog. Mol. Biol. Transl. Sci.* **118**, 57–92 (2013).
3. Goodman, O. B., Jr et al.  $\beta$ -Arrestin acts as a clathrin adaptor in endocytosis of the  $\beta_2$ -adrenergic receptor. *Nature* **383**, 447–450 (1996).
4. Laporte, S. A. et al. The  $\beta_2$ -adrenergic receptor/ $\beta$ -arrestin complex recruits the clathrin adaptor AP-2 during endocytosis. *Proc. Natl Acad. Sci. USA* **96**, 3712–3717 (1999).
5. Shenoy, S. K. & Lefkowitz, R. J. Angiotensin II-stimulated signaling through G proteins and  $\beta$ -arrestin. *Sci. STKE* **2005**, cm14 (2005).
6. Luttrell, L. M. & Gesty-Palmer, D. Beyond desensitization: physiological relevance of arrestin-dependent signaling. *Pharmacol. Rev.* **62**, 305–330 (2010).
7. Hoffmann, C. et al. A FAsH-based FRET approach to determine G protein-coupled receptor activation in living cells. *Nature Methods* **2**, 171–176 (2005).
8. Kenakin, T. Functional selectivity through protean and biased agonism: who steers the ship? *Mol. Pharmacol.* **72**, 1393–1401 (2007).
9. Luttrell, L. M. Minireview: More than just a hammer: ligand “bias” and pharmaceutical discovery. *Mol. Endocrinol.* **28**, 281–294 (2014).

10. Han, M. et al. Crystal structure of  $\beta$ -arrestin at 1.9 Å: possible mechanism of receptor binding and membrane translocation. *Structure* **9**, 869–880 (2001).
11. Zhan, X. et al. Crystal structure of arrestin3 reveals the basis of the difference in receptor binding between two non-visual subtypes. *J. Mol. Biol.* **406**, 467–478 (2011).
12. Shukla, A. K. et al. Structure of active  $\beta$ -arrestin-1 bound to a G-protein-coupled receptor phosphopeptide. *Nature* **497**, 137–141 (2013).
13. Kim, Y. J. et al. Crystal structure of pre-activated arrestin p44. *Nature* **497**, 142–146 (2013).
14. Kang, Y. et al. Crystal structure of rhodopsin bound to arrestin by femtosecond X-ray laser. *Nature* **523**, 561–567 (2015).
15. Charest, P. G., Terrillon, S. & Bouvier, M. Monitoring agonist-promoted conformational changes of  $\beta$ -arrestin in living cells by intramolecular BRET. *EMBO Rep.* **6**, 334–340 (2005).
16. Shukla, A. K. et al. Distinct conformational changes in  $\beta$ -arrestin report biased agonism at seven-transmembrane receptors. *Proc. Natl Acad. Sci. USA* **105**, 9988–9993 (2008).
17. Oakley, R. H., Laporte, S. A., Holt, J. A., Caron, M. G. & Barak, L. S. Differential affinities of visual arrestin,  $\beta$ arrestin1, and  $\beta$ arrestin2 for G protein-coupled receptors delineate two major classes of receptors. *J. Biol. Chem.* **275**, 17201–17210 (2000).
18. Appleton, K. M. et al. Biasing the parathyroid hormone receptor: relating *in vitro* ligand efficacy to *in vivo* biological activity. *Methods Enzymol.* **522**, 229–262 (2013).
19. Barak, L. S., Ferguson, S. S., Zhang, J. & Caron, M. G. A  $\beta$ -arrestin/green fluorescent protein biosensor for detecting G protein-coupled receptor activation. *J. Biol. Chem.* **272**, 27497–27500 (1997).
20. Wu, G., Krupnick, J. G., Benovic, J. L. & Lanier, S. M. Interaction of arrestins with intracellular domains of muscarinic and  $\alpha_2$ -adrenergic receptors. *J. Biol. Chem.* **272**, 17836–17842 (1997).
21. DeFea, K. A. et al.  $\beta$ -Arrestin-dependent endocytosis of proteinase-activated receptor 2 is required for intracellular targeting of activated ERK1/2. *J. Cell Biol.* **148**, 1267–1281 (2000).
22. Luttrell, L. M. et al. Activation and targeting of extracellular signal-regulated kinases by  $\beta$ -arrestin scaffolds. *Proc. Natl Acad. Sci. USA* **98**, 2449–2454 (2001).
23. Zimmerman, B., Simaan, M., Lee, M.-H., Luttrell, L. M. & Laporte, S. A. c-Src-mediated phosphorylation of AP-2 reveals a general mechanism for receptors internalizing through the clathrin pathway. *Cell. Signal.* **21**, 103–110 (2009).
24. Wei, H. et al. Independent  $\beta$ -arrestin 2 and G protein-mediated pathways for angiotensin II activation of extracellular signal-regulated kinases 1 and 2. *Proc. Natl Acad. Sci. USA* **100**, 10782–10787 (2003).
25. Shenoy, S. K. et al.  $\beta$ -Arrestin-dependent, G protein-independent ERK1/2 activation by the  $\beta_2$  adrenergic receptor. *J. Biol. Chem.* **281**, 1261–1273 (2006).
26. Oakley, R. H., Laporte, S. A., Holt, J. A., Barak, L. S. & Caron, M. G. Association of  $\beta$ -arrestin with G protein-coupled receptors during clathrin-mediated endocytosis dictates the profile of receptor resensitization. *J. Biol. Chem.* **274**, 32248–32257 (1999).
27. Zimmerman, B. et al. Differential  $\beta$ -arrestin-dependent conformational signaling and cellular responses revealed by angiotensin analogs. *Sci. Signal.* **5**, ra33 (2012).
28. Tobin, A. B., Butcher, A. J. & Kong, K. C. Location, location, location...site-specific GPCR phosphorylation offers a mechanism for cell-type-specific signalling. *Trends Pharmacol. Sci.* **29**, 413–420 (2008).
29. Kommaddi, R. P. & Shenoy, S. K. Arrestins and protein ubiquitination. *Prog. Mol. Biol. Transl. Sci.* **118**, 175–204 (2013).
30. Nuber, S. et al.  $\beta$ -Arrestin biosensors reveal a rapid, receptor-dependent activation/deactivation cycle. *Nature* <http://dx.doi.org/10.1038/nature17198> (this issue).

**Acknowledgements** This work was supported by National Institutes of Health grants DK055524 (L.M.L.) and GM095497 (L.M.L.), funds provided by Dialysis Clinics, Inc. (T.A.M.) and the Research Service of the Charleston, SC Veterans Affairs Medical Center (L.M.L.). Supported by Canadian Institutes of Health Research operating grant MOP-74603 (S.A.L.). National Institutes of Health grant RR027777 (L.M.L.) supported the FLIPR<sup>TETRA</sup> facility. The contents of this article do not represent the views of the Department of Veterans Affairs or the United States Government.

**Author Contributions** M.-H.L., K.A.M., E.G.S., J.Y.K. and S.A.L. performed experimental measurements and data analysis. T.A.M., Y.K.P. and S.A.L. provided technical expertise. M.-H.L. and L.M.L. conceived the project. All authors contributed to preparation of the manuscript and approved the final version.

**Author Information** Reprints and permissions information is available at [www.nature.com/reprints](http://www.nature.com/reprints). The authors declare no competing financial interests. Readers are welcome to comment on the online version of the paper. Correspondence and requests for materials should be addressed to L.M.L. ([luttrell@muscc.edu](mailto:luttrell@muscc.edu)).



## METHODS

**Materials.** Cell culture medium and cell culture additives were from Life Technologies. FuGENE HD transfection reagent and Promega GloSensor cAMP reagent were from Fisher Scientific. FLIPR Calcium 5 Assay Kit was from Molecular Devices, Inc. Lipofectamine 2000 and TC-FLAsH II In-Cell Tetracycline Tag Detection Kits were from Invitrogen. Human PTH(1–34) was obtained from Bachem, Inc. Angiotensin II, [Arg<sup>8</sup>]-vasopressin, isoproterenol, phenylephrine, and UK14303 were from Sigma-Aldrich. S1P was from Avanti Polar Lipids Inc. SII was from MP Biomedicals. SI, SVdF and SBpA were synthesized at the Institut de Pharmacologie de Sherbrooke, Sherbrooke University. Rabbit polyclonal anti- $\beta$ -arrestin1/2 was a gift from R.J. Lefkowitz. Anti-phospho-ERK1/2 IgG (T202/Y204; #9101) and anti-ERK1/2 IgG (#4695) were from Cell Signaling Technology. Horseradish-peroxidase-conjugated donkey anti-rabbit IgG was from Jackson Immuno-Research Laboratories, Inc.

**Renilla luciferase- $\beta$ -arrestin2 FLAsH BRET reporters.** The pcDNA3.1 plasmid encoding rat  $\beta$ -arrestin2 tagged at the N terminus with *Renilla* luciferase (rLuc) was a gift from M. Bouvier. A series of six rLuc- $\beta$ -arrestin2-FLAsH BRET reporters were constructed by inserting a cDNA sequence encoding the amino acid motif, CCPGCC, immediately following amino acid residues 40, 140, 171, 225, 263 and 410 of  $\beta$ -arrestin2, using a modification of the precise gene fusion PCR method<sup>31</sup>. For each construct, two PCR steps were performed using the primer sets shown in Extended Data Table 2. The first step was to generate two PCR fragments using the primer pairs: RLucHindF-FLAsHR and FLAsAF-RLucApaR. One PCR product contained a HindIII restriction site at the 5' end and the CCPGCC FLAsH motif at the 3' end, and the other contained the complementary FLAsH sequence at the 5' end and an ApaI restriction site at the 3' end. A second PCR step was used to fuse the two fragments using three primers: RLucHindF, FLAsHR and RLucApaR, and the two PCR fragments as template DNA. The resultant full-length  $\beta$ -arrestin2 PCR product containing the FLAsH motif insert was digested with HindIII and ApaI and cloned into the parent rLuc- $\beta$ -arrestin2 plasmid to generate the rLuc- $\beta$ -arrestin2-FLAsH1–6 expression plasmids. All constructs were verified by dideoxynucleotide sequencing.

**Cell culture and transfection.** HEK293 cells (ATCC CRL1573) were from the American Type Culture Collection. HEK-293 GloSensor cells were from Promega Corporation. HEK293 cells were maintained in minimum essential medium supplemented with 10% fetal bovine serum and 1% antibiotic/antimycotic solution. The HEK293 FRT/TO  $\beta$ -arrestin1/2 shRNA cell line carrying tetracycline-inducible shRNA simultaneously targeting the  $\beta$ -arrestin1 and 2 isoforms (5'-CGTCCACGTCACCAACAAC-3') was generated as previously described<sup>23</sup>. These cells were maintained in Dulbecco's modified Eagle medium supplemented with 10% fetal bovine serum, 1% antibiotic/antimycotic solution and 50  $\mu$ g ml<sup>-1</sup> zeocin, 50  $\mu$ g ml<sup>-1</sup> blasticidin, and 50  $\mu$ g ml<sup>-1</sup> puromycin to maintain selection. Transient transfections were performed using Lipofectamine 2000 or FuGENE HD according to the manufacturer's protocols. Before experimentation, cells were serum-deprived overnight in 1% fetal bovine serum growth medium. Cells were not tested for mycoplasma contamination.

**FLIPR<sup>TETRA</sup> assay of calcium influx.** HEK293 cells in 6-well plates were transiently transfected with 1  $\mu$ g of plasmid cDNA encoding the angiotensin AT<sub>1A</sub>, PTH<sub>1R</sub>,  $\alpha_{1B}$ AR,  $\beta_2$ AR, S1P<sub>1R</sub> or  $\alpha_2A$ AR, using Lipofectamine 2000. Cells were seeded onto collagen-coated black-wall clear-bottom 96-well plates (BD Biosciences) 24 h after transfection, allowed to grow for a further 24 h, then serum deprived overnight. Fresh FLIPR calcium 5 assay reagent (100  $\mu$ l per well) was added to 100  $\mu$ l of serum-deprivation medium and plates were incubated for an additional 1 h before stimulation. Stimulations were carried out on a FLIPR<sup>TETRA</sup> (Molecular Devices) with 470–495 nm excitation and 515–575 nm emission filters as previously described<sup>18</sup>. All assays were performed using saturating ligand concentrations: AngII (0.1  $\mu$ M), hPTH(1–34) (0.1  $\mu$ M), isoproterenol (1  $\mu$ M), phenylephrine (10  $\mu$ M), S1P (1  $\mu$ M) or UK14303 (10  $\mu$ M) and run at room temperature. The instrument was programmed to simultaneously dispense 50  $\mu$ l of vehicle control, 5 $\times$  ligand, or the calcium ionophore A23187 (10  $\mu$ M) from the drug plate into the 200  $\mu$ l of medium in the corresponding wells of the assay plate to achieve the final ligand concentration. Fluorescence was recorded every 1 s for 10 reads to establish baseline fluorescence, then every 1 s for 300 reads. Raw data representing the relationship between time and fluorescence for each well were exported to Microsoft Excel for background subtraction and analysis.

**FLIPR<sup>TETRA</sup> assay of cAMP production.** Assays were performed using HEK293 GloSensor cAMP cells that stably express a genetically encoded biosensor composed of a cAMP binding domain fused to a mutated form of *Photinus pyralis* luciferase<sup>32</sup>. HEK293 GloSensor cAMP cells were seeded onto poly-D-lysine-coated white-wall clear-bottom 96-well plates (BD Biosciences) 24 h after transient transfection with plasmid cDNA encoding the receptors of interest. cAMP assays were performed 72 h after transfection as previously described<sup>18</sup>. cAMP reagent medium was prepared by adding 200  $\mu$ l of freshly thawed GloSensor cAMP reagent

to 10 ml of serum free MEM buffered with 10 mM HEPES (pH 7.4). The growth medium was gently aspirated and replaced with 100  $\mu$ l per well of pre-warmed cAMP reagent medium. Plates were incubated at 37°C with 5% CO<sub>2</sub> for 1.5 h, then removed from the incubator and incubated at room temperature in the dark for an additional 30 min. Stimulations were performed at room temperature in the FLIPR<sup>TETRA</sup> using saturating ligand concentrations. Luminescence was recorded every 1 s for 10 reads to establish baseline luminescence, then every 1 s for 50 reads. Thereafter, luminescence was recorded every 2 s for 600 reads. Raw data representing the relationship between time and luminescence for each well following ligand addition was exported to Microsoft Excel for background subtraction and analysis. All responses were normalized to the cAMP luminescence generated in response to 10  $\mu$ M forskolin. To assay G<sub>i</sub>-mediated inhibition of cAMP production ( $\alpha_{2A}$ AR and S1P<sub>1R</sub>), cells were pre-incubated with or without agonist for 30 min, then stimulated with 10  $\mu$ M forskolin.

**Intermolecular BRET using rLuc- $\beta$ -arrestin2 and PTH<sub>1R</sub>-YFP.** HEK 293 cells were transiently transfected with 1.5  $\mu$ g of plasmid DNA encoding the C-terminal yellow fluorescent protein (YFP)-tagged PTH<sub>1R</sub><sup>33</sup> and 0.15  $\mu$ g of either rLuc- $\beta$ -arrestin2 or one of the rLuc- $\beta$ -arrestin2-FLAsH constructs using Fugene HD. Cells were detached 48 h after transfection, collected by centrifugation, resuspended in BRET buffer (1 mM CaCl<sub>2</sub>, 140 mM NaCl, 2.7 mM KCl, 900  $\mu$ M MgCl<sub>2</sub>, 370  $\mu$ M NaH<sub>2</sub>PO<sub>4</sub>, 5.5 mM D-glucose, 12 mM NaHCO<sub>3</sub>, 25 mM HEPES (pH 7.4)) and aliquotted into white-wall clear-bottom 96-well plates at a density of 100,000 cells per well. Background and total Venus fluorescence were read on an OptiPlate microplate reader (PerkinElmer) with 485 nm excitation and 525–585 nm emission filters. Cells were stimulated with 0.1  $\mu$ M PTH(1–34) for 2 min and coelenterazine was then added to a final concentration of 5  $\mu$ M. Luciferase (440–480 nm) and Venus (525–585 nm) emissions were read to calculate the BRET ratio (emission eYFP/emission RLuc). Net BRET ratio was calculated by background subtracting the BRET ratio measured for vehicle- versus ligand-treated cells in the same experiment.

**Intramolecular FLAsH BRET using the rLuc- $\beta$ -arrestin2-FLAsH constructs.** HEK293 cells seeded in 6-well plates were co-transfected with 1.5  $\mu$ g of plasmid DNA encoding the receptor of interest and 0.1  $\mu$ g of DNA encoding one rLuc- $\beta$ -arrestin2-FLAsH construct using Fugene HD. Cells were detached 48 h after transfection, collected by centrifugation, and resuspended in 600  $\mu$ l of Hank's balanced salt solution. TC-FLAsH II In-Cell Tetracycline detection reagent was added at 2.5  $\mu$ M final concentration and the cells incubated at room temperature for 30 min, after which they were washed using 1 $\times$  BAL buffer from the TC-FLAsH kit, resuspended in BRET buffer and placed in white-wall clear-bottom 96-well plates at a density of 100,000 cells per well. Background and total TC-FLAsH fluorescence were read on an OptiPlate microplate reader (Perkin-Elmer) with 485 nm excitation and 525–585 nm emission filters. Except as noted in the figure legends, all stimulations were carried out at saturating ligand concentration: AngII (0.1  $\mu$ M), [Arg<sup>8</sup>]-vasopressin (1  $\mu$ M), hPTH(1–34) (0.1  $\mu$ M), isoproterenol (1  $\mu$ M), phenylephrine (10  $\mu$ M), S1P (1  $\mu$ M), SBpA (1  $\mu$ M), SII (1  $\mu$ M) SVdF (1  $\mu$ M), or UK14303 (10  $\mu$ M). Cells were exposed to agonist for 2–10 min, after which coelenterazine was added at a final concentration of 5  $\mu$ M. Six consecutive readings of luciferase (440–480 nm) and TC-FLAsH (525–585 nm) emissions were taken, and the BRET ratio (emission eYFP/emission RLuc) calculated using Berthold Technologies Tristar 3 LB 941. The  $\Delta$ net change in intramolecular BRET ratio for each of the six rLuc- $\beta$ -arrestin2-FLAsH constructs was calculated by background subtracting the BRET ratio measured for cells in the same experiment stimulated with vehicle only.

**Confocal microscopy.** For determining the pattern of GPCR-arrestin trafficking, HEK293 cells were seeded into collagen-coated 35 mm glass-bottom Petri dishes (MatTek Corporation) and co-transfected with 1.3  $\mu$ g of plasmid DNA encoding the receptors of interest and 0.7  $\mu$ g of plasmid encoding green fluorescent protein (GFP)-tagged  $\beta$ -arrestin2<sup>19</sup> using FuGene HD. Forty-eight hours after transfection, cells were serum derived for 4 h, stimulated with a saturating ligand concentration for 8 min, fixed with 4% paraformaldehyde in phosphate buffered saline for 30 min and washed with 4°C saline. Arrestin distribution was determined by confocal microscopy performed on a Zeiss LSM510 META laser-scanning microscope with 60 $\times$  objective using 488 nm excitation and 505–530 nm emission wavelengths. Measurement of AT<sub>1A</sub>AR- $\beta$ -arrestin2 avidity was performed as previously described<sup>27</sup>. HEK293 cells stably expressing AT<sub>1A</sub>AR and transfected with  $\beta$ -arrestin2-YFP were stimulated with AngII (1  $\mu$ M) or analogues (10  $\mu$ M) for 15 min, after which, endosomes were bleached and fluorescence recovery was monitored every 30 s over a period of 5 min.

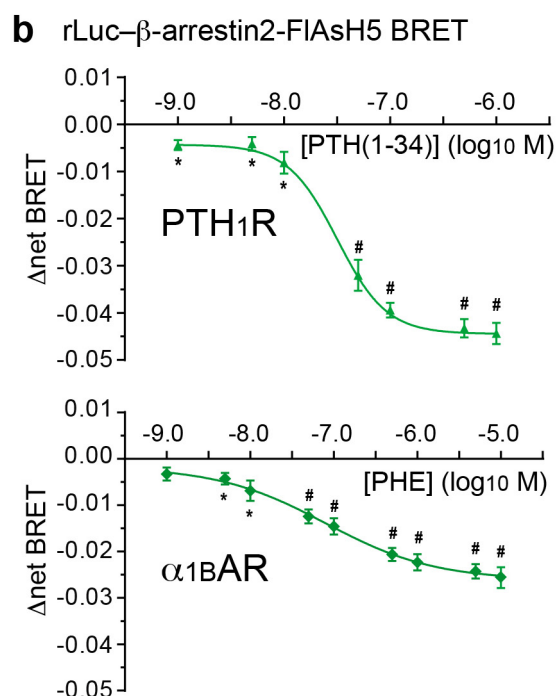
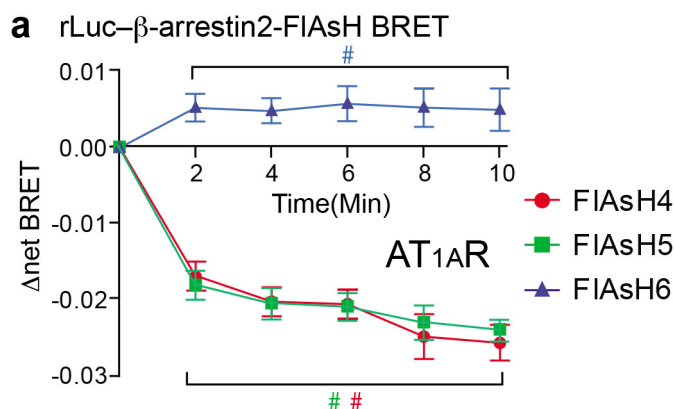
**Immunoblotting.** HEK293 FRT/TO  $\beta$ -arrestin1/2 shRNA cells were used to determine the contribution of arrestins to GPCR-stimulated ERK1/2 activation<sup>23,34</sup>. Cells in 12-well plates were transiently transfected with 1  $\mu$ g of plasmid cDNA encoding the receptor of interest using FuGENE HD. Twenty-four hours after transfection, downregulation of  $\beta$ -arrestin1/2 expression was induced by 48 h exposure to 1  $\mu$ M doxycycline. After overnight serum deprivation, cells were stimulated

for 5 min, after which monolayers were lysed in 1× Laemmli sample buffer. Stimulations were performed at saturating ligand concentration, except as noted in the figure legends. Lysates containing 10 µg of whole-cell protein were resolved by sodium dodecyl sulphate polyacrylamide gel electrophoresis and transferred to polyvinylidene difluoride membranes. Immunoblots of phospho-ERK1/2, total ERK1/2, and β-arrestin1/2 were performed using rabbit polyclonal IgG with HRP-conjugated goat anti-rabbit IgG as secondary antibody. Proteins were visualized using enhanced chemiluminescence (PerkinElmer).

**Statistical analysis.** The sample size ( $n$ ) reported in each figure legend refers to number of independently performed biological replicates in the data set. All analysable data points were included in the statistical analyses. No statistical methods were used to predetermine sample size. For experimental methods that were highly reproducible, for example, measurement of Δnet BRET, 5 to 6 biological replicates were sufficient to discern effects of  $\pm 0.01$  with  $P < 0.05$ . For experimental methods with greater variability between replicates, for example, fold ERK1/2 activation, 5 to 20 biological replicates were necessary to discern effects of β-arrestin1/2 silencing that were  $\pm 10\%$  of the control response with  $P < 0.05$ . The investigators

were not blinded to allocation during experiments and outcome assessment. All values are expressed as mean  $\pm$  s.e.m. ( $n \geq 5$ ). For comparisons between two groups, statistical significance was assessed with a two-tailed unpaired  $t$ -test. Computations were performed and graphs constructed with the GraphPad Prism 4.0 scientific graphing, curve fitting, and statistics program (GraphPad Software). The experiments were not randomized.

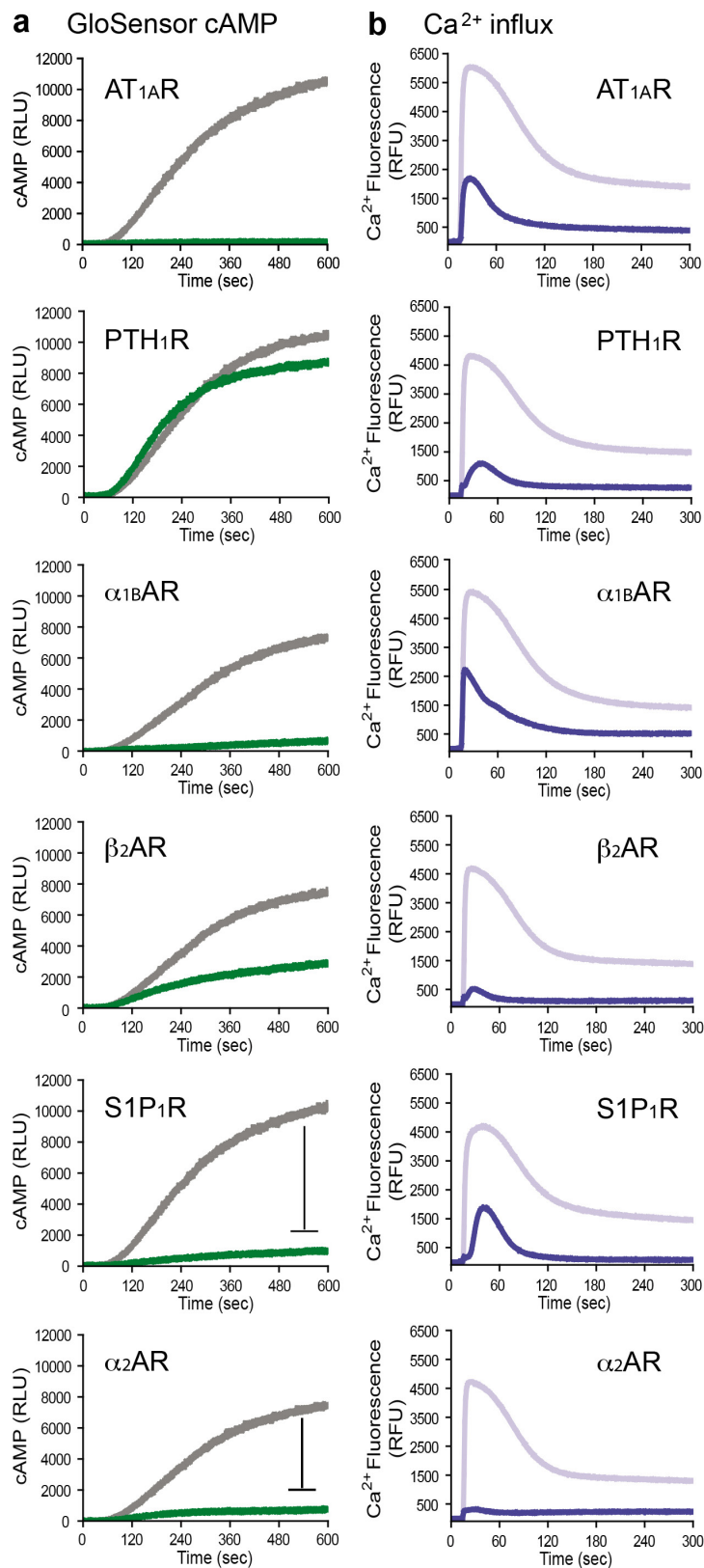
31. Yon, J. & Fried, M. Precise gene fusion by PCR. *Nucleic Acids Res.* **17**, 4895 (1989).
32. Binkowski, B. F., Fan, F. & Wood, K. V. Luminescent biosensors for real-time monitoring of intracellular cAMP. *Methods Mol. Biol.* **756**, 263–271 (2011).
33. Leonard, A. P., Appleton, K. M., Luttrell, L. M. & Peterson, Y. K. A high-content, live-cell, and real-time approach to the quantitation of ligand-induced β-arrestin2 and class A/class B GPCR mobilization. *Microsc. Microanal.* **19**, 150–170 (2013).
34. Wilson, P. C. *et al.* The arrestin-selective angiotensin AT1 receptor agonist [Sar<sup>1</sup>,Ile<sup>4</sup>,Ile<sup>6</sup>]-AngII negatively regulates bradykinin B2 receptor signaling via AT1-B2 receptor heterodimers. *J. Biol. Chem.* **288**, 18872–18884 (2013).



#### Extended Data Figure 1 | Time-course and relationship of the

#### $\beta$ -arrestin2 intramolecular FIAsH BRET signal to receptor occupancy.

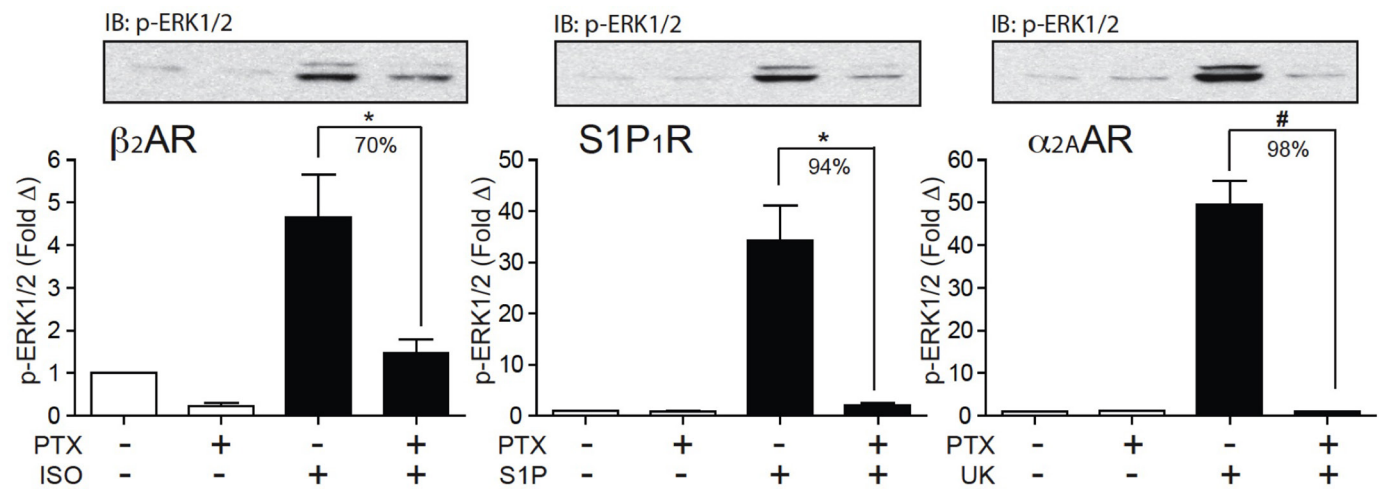
**a**, Time-course of AT<sub>1</sub>AR-induced changes in intramolecular FIAsH BRET. HEK293 cells were co-transfected with plasmid cDNA encoding AT<sub>1</sub>AR and the indicated rLuc- $\beta$ -arrestin2-FIAsH reporter. Stimulations were carried out at a saturating concentration of AngII for the indicated times. The graph depicts the mean  $\pm$  s.e.m. of independent biological replicates of ligand-induced  $\Delta$ net BRET for each rLuc- $\beta$ -arrestin2-FIAsH construct ( $n=6$ ). **b**, Ligand concentration dependence of PTH<sub>1</sub>R- and  $\alpha$ <sub>1</sub>BAR-induced changes in intramolecular FIAsH BRET. HEK293 cells were co-transfected with plasmid cDNA encoding the PTH<sub>1</sub>R or  $\alpha$ <sub>1</sub>BAR and the rLuc- $\beta$ -arrestin2-FIAsH5 reporter. Stimulations were for 2 min using the indicated agonist concentration. The graph depicts the mean  $\pm$  s.e.m. of independent biological replicates of ligand-induced  $\Delta$ net BRET ( $n=5$ ). The EC<sub>50</sub> for PTH(1-34) (PTH<sub>1</sub>R) and phenylephrine ( $\alpha$ <sub>1</sub>BAR) were 30 nM and 80 nM, respectively. In all panels: \* $P < 0.05$ , # $P < 0.005$ , greater or less than vehicle stimulated control.



**Extended Data Figure 2 | G-protein-coupling profiles of selected GPCRs. a,** Representative time-courses of cAMP luminescence following stimulation of HEK293 GloSensor cAMP cells transfected with each of six GPCRs. For the  $G_{i/o}$ -coupled S1P<sub>1</sub>R and  $\alpha$ <sub>2A</sub>AR, stimulations were carried out in the presence of 10  $\mu\text{M}$  forskolin to detect inhibition of adenylyl cyclase. Each panel depicts the agonist effect (green) compared to the control response to 10  $\mu\text{M}$  forskolin (grey) measured in adjacent wells.

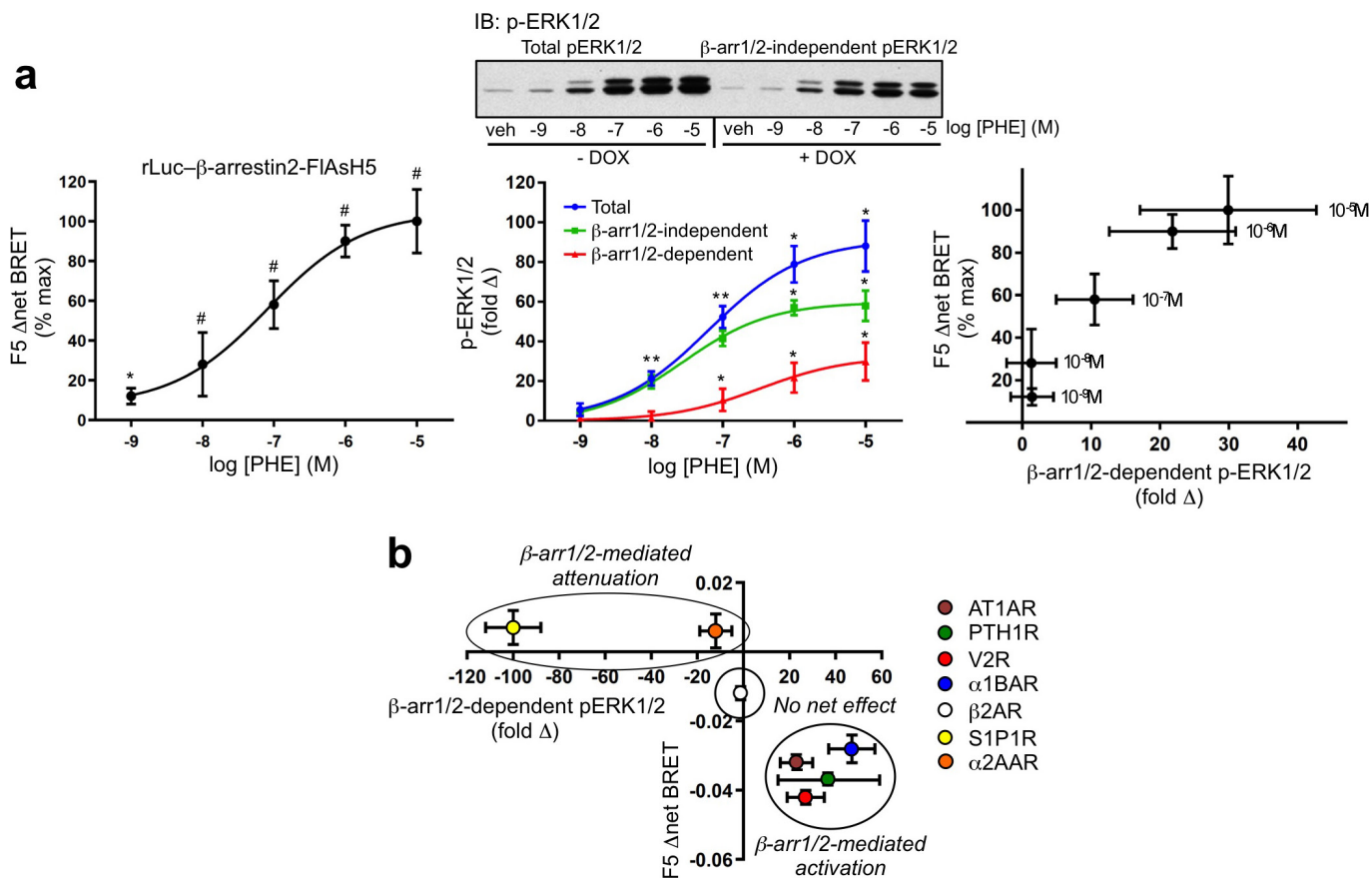
Data are presented in relative luminescence units (RLU). **b,** Representative time-courses of intracellular calcium fluorescence following stimulation of HEK293 cells transfected with the same panel of GPCRs. Each panel depicts the agonist effect (blue) compared to the control response to the calcium ionophore A23187 (lavender) measured in adjacent wells. Data are presented in relative fluorescence units (RFU).





**Extended Data Figure 3 | Pertussis toxin sensitivity of ERK1/2 activation by G<sub>i/o</sub>-coupled GPCRs.** HEK293 cells transfected with the β<sub>2</sub>AR, S1P<sub>1</sub>R or α<sub>2A</sub>AR were serum-deprived overnight in the presence or absence of 1 ng ml<sup>-1</sup> *Bordetella pertussis* toxin (PTX) before 5 min stimulation with isoproterenol, S1P or UK14303, respectively.

Representative phospho-ERK1/2 immunoblots are shown above bar graphs depicting the mean ± s.e.m. of independent biological replicates ( $n = 5$ , β<sub>2</sub>AR, S1P<sub>1</sub>R and α<sub>2A</sub>AR). Responses were normalized to the basal level of phospho-ERK1/2 in non-stimulated samples. \* $P < 0.05$ , # $P < 0.005$ , less than stimulated response in the absence of pertussis toxin.



**Extended Data Figure 4 | Concentration-response relationship between FlAsH5 signal and arrestin-dependent ERK1/2 activation.**  
a, Relationship between  $\alpha_{1B}$ AR-induced change in FlAsH5  $\Delta$ net BRET and arrestin-dependent ERK1/2 activation at varying agonist concentration. The percent maximal phenylephrine-induced FlAsH5  $\Delta$ net BRET was determined in HEK293 cells transfected with  $\alpha_{1B}$ AR and rLuc- $\beta$ -arrestin2-FlAsH5 expression plasmids (left). The concentration dependence of phenylephrine-stimulated ERK1/2 activation was determined in  $\alpha_{1B}$ AR-expressing HEK293 FRT/TO  $\beta$ -arrestin1/2 shRNA cells stimulated for 5 min (centre).  $\beta$ -arrestin1/2-dependent ERK1/2 activation was defined as the fold difference between agonist-stimulated ERK1/2 phosphorylation in the absence (total ERK1/2 signal) and presence ( $\beta$ -arrestin1/2-independent ERK1/2 signal) of doxycycline. A representative phospho-ERK1/2 immunoblot is shown above a

graph depicting the mean  $\pm$  s.e.m. of independent biological replicates ( $n = 4$ ). EC<sub>50</sub> for total ERK1/2,  $\beta$ -arrestin1/2-independent ERK1/2, and  $\beta$ -arrestin1/2-dependent ERK1/2 were 64 nM, 27 nM and 334 nM, respectively. Right, the relationship between percent maximal  $\alpha_{1B}$ AR-induced change in FIAsh5  $\Delta$ net BRET and  $\beta$ -arrestin1/2-dependent ERK1/2 activation over a range of agonist concentrations. In all panels, \* $P < 0.05$ , # $P < 0.005$ , greater than nonstimulated. **b**, Relationship between GPCR-induced change in FIAsh5  $\Delta$ net BRET and arrestin-dependent ERK1/2 activation at saturating agonist concentration. The ligand-induced FIAsh5  $\Delta$ net BRET was determined in HEK293 cells transfected with the indicated GPCR and rLuc- $\beta$ -arrestin2-FIAsh5 expression plasmids. The graph depicts the mean  $\pm$  s.e.m. of independent biological replicates ( $n = 5$ ).

Extended Data Table 1 | G-protein-coupling and trafficking profiles of selected GPCRs

Receptor	G protein	Arrestin binding
Angiotensin AT <sub>1A</sub>	G <sub>q/11</sub>	Class B stable binding
Parathyroid Hormone PTH <sub>1</sub>	G <sub>s</sub> > G <sub>q/11</sub>	Class B stable binding
Vasopressin V <sub>2</sub>	G <sub>s</sub>	Class B stable binding
α <sub>1B</sub> Adrenergic	G <sub>q/11</sub>	Class A transient binding
β <sub>2</sub> Adrenergic	G <sub>s</sub> > G <sub>i</sub>	Class A transient binding
sphingosine 1-phosphate S1P <sub>1</sub>	G <sub>i</sub> > G <sub>q/11</sub>	Class A transient binding
α <sub>2A</sub> adrenergic	G <sub>i</sub>	Not Detectable

Extended Data Table 2 | Primer sequences used to generate rLuc- $\beta$ -arrestin2-FIAsH1–6

Primer	Sequence
RlucHindF	ATCAAGCTTGC GTTACCGGATCCATGGGTGAA
RlucApaIR	AACGGGCCCTCTAGACTAGCAGAACTGGTCA
FIAsH1F	GGATCCTGTCGATGGTTGTTGTCCTGGTTGTTGTGTGGTGCTTGTGGATC
FIAsH1R	GATCCACAAGCACCACACAACAACCAGGACAACAACCATCGACAGGATCC
FIAsH2F	GAGGACACAGGGAAGTGTGTCCTGGTTGTTGTGCCTGTGGAGTAGAC
FIAsH2R	GTCTACTCCACAGGCACAACAACCAGGACAACACTTCCCTGTGTCCTC
FIAsH3F	GCTTATCATCAGAAAGTGTGTCCTGGTTGTTGTGTACAGTTTGCTCCTG
FIAsH3R	CAGGAGCAAACGTGTACACAACAACCAGGACAACACTTTCTGATGATAAGC
FIAsH4F	CCACGTCACCAACAATTGTTGTCCTGGTTGTTGTTCTGCCAAGACCGTCA
FIAsH4R	TGACGGTCTTGGCAGAACAACAACCAGGACAACAATTGTTGGTGACGTGG
FIAsH5F	AGCTTGAACAAGATGACCAGTGTTGTCCTGGTTGTTGTGTGTCTCCCAGTTCCACATT
FIAsH5R	AATGTGGAACCTGGGAGACACACAACAACCAGGACAACACTGGTCATCTTGTTCAAGCT
FIAsH6R	ACGGGCCCTCTAGACTAACAACAACCAGGACAACAGCAGAACTGGTCATC



# CAREERS

**NUCLEAR FUSION** How to manage a challenging reactor project **p.671**

**COMFORT ZONE** When anxiety is a good thing [go.nature.com/qonwad](http://go.nature.com/qonwad)

**NATUREJOBS** For the latest career listings and advice [www.naturejobs.com](http://www.naturejobs.com)

ISPEX PROJECT



Researchers measure atmospheric aerosols with iSPEX optical devices and smartphones.

## TECHNOLOGY

# Smartphone science

*Researchers are learning how to convert devices into global laboratories.*

BY JON CARTWRIGHT

A decade ago, Dutch astronomer Frans Snik invented a simple optical device to measure the density of dust, soot and other particles, or aerosols, in the atmosphere that affect human health and the climate. He hoped to launch it into orbit around Earth aboard a satellite. But one afternoon in 2011, Snik held up a demonstration version of his device to an iPhone camera. The smartphone's screen displayed a rainbow of colours: Snik's optical device was converting incoming light into a spectrum that contained polarization information and channelling it into the camera. Snik realized that he could pair smartphones with the optical device and make the same kind

of measurements that he and his colleagues planned to record from space.

An idea was born. "We thought, why not make use of a technology that millions of people carry around in their pockets anyway?"

By 2013, Snik and his colleagues at Leiden University in the Netherlands had given or sold a version of the optical device — called iSPEX — to more than 8,000 willing iPhone users across the country. The users followed instructions provided by an associated app to attach the optical devices to their iPhone cameras and photographed the sky in their local areas. Within a day, reams of crowdsourced spectra had stacked up in an online database, ready for analysis. It resulted in a Netherlands-wide map of atmospheric particles with unprecedented

resolution (F. Snik *et al. Geophys. Res. Lett.* **41**, 7351–7358; 2014) — several years before the proposed satellite launch and for a fraction of the original estimated cost. The team has since received funding from the European Union to repeat the project in 11 European cities.

## CITIZEN SCIENCE

Many researchers are finding ways to exploit smartphones. Snik's project, and those of some geophysicists, astronomers and other scientists who need huge data sets, go one step further. They recruit citizen scientists who use their own smartphones to collect data that would be difficult — if not impossible — to obtain in conventional ways. The various internal sensors that smartphones carry, such as cameras, ►

► microphones, accelerometers and pressure gauges, coupled with user-friendly apps offer a way for the public to contribute high-quality data. “There are tons of possibilities for science,” says Travis Desell, a computer scientist at the University of North Dakota who designs research projects that run on smartphones.

Scientists who want to exploit the potential of smartphones first need to assess whether the devices can obtain the measurements they need. They must then decide which software platform will optimize the proposed use, before ironing out any errors or ‘bugs’ in the apps that will be used to collect data. Scientists should also determine how to screen out invalid data. And they need to find ways to recruit participants.

Although recruiting the public isn’t complicated, thanks to social media, it can still be time-consuming. Snik and his colleagues had a head start — the iSPEX project was covered by the Dutch media, which prompted a few thousand citizens to send in requests to participate. The team drummed up a similar number of contributors by collaborating with the charity Lung Foundation Netherlands in Amersfoort, which invited participation from supporters who were concerned about the effects of aerosols on health. Even so, the iSPEX researchers had to spend a year and a half on their crowdsourcing campaign, which involved uploading instruction manuals and video tutorials to a website, posting calls for support on social media and in

online publications, and answering questions. But their efforts paid off when they received more than 6,000 submissions of data.

The more technical aspects of crowdsourcing data can be trickier to master, and it helps to have some technological savvy. Scientists will find it useful to know how to write an app or how to manufacture an inexpensive hardware ‘add-on’ (see ‘How to create a hand-held research toolkit’). But if a researcher is not an adept programmer, help is available. Snik and his team turned to DDQ, a Netherlands-based company that creates apps that are tailored to citizen science. Researchers who lack funds for third-party support can learn to write an app themselves, thanks to a wealth of free online tutorials and discussion forums.

Researchers also need to decide which software platform to select. Snik and his colleagues chose the popular Apple iOS: the physical similarity between iPhone models made it easier to design a compatible add-on. But the leading platform, Google’s Android, has advantages, too. It is less strict about the nature of apps and presents fewer barriers to its instrumentation.

Remote-sensing scientist Liam Gumley at the University of Wisconsin–Madison has developed an app that aims to improve weather forecasting by comparing photos of the sky taken from smartphones with satellite imagery. He has advice for anyone who is interested in smartphone-aided science: “Just do it!” Gumley recommends drawing up a set of storyboards that describe exactly what the app will do, what each screen will look like and what will happen when the user touches an onscreen control or a button. It is also a good idea, he says, to determine whether any data processing will be performed by the app or by a server online. Depending on the type of processing that is required, one might be faster than the other.

## BIG DATA

Researchers must also be ready with a database that can accommodate a deluge of data. “If you release the app globally, you may get more data than you expect within days,” warns Qingkai Kong, a PhD student in seismology at the University of California, Berkeley, who is working on MyShake, a seismology app. After extrapolating from a small group of users how much data he and his colleagues were likely to receive, they turned to Amazon Web Services to host their database. Other available cloud-computing services include the Google Cloud Platform and Microsoft Azure.

Once the data have been collected, it can be difficult to know whether they are reliable. Kong and his colleagues are refining MyShake so that it can distinguish between an actual seismic event and when a user is shaking a phone. A similar app, known as CSN-Droid and designed by scientists at the California Institute of Technology (Caltech) in Pasadena, was discontinued because it could not reliably make such distinctions. But Kong thinks that rigorous testing will

## ALWAYS ON

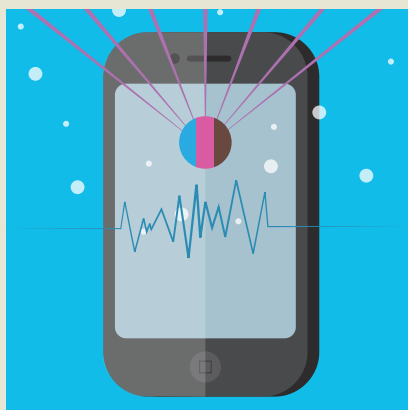
### *How to create a hand-held research toolkit*

Converting smartphones into a tool for citizen science is likely to require an app, and could also involve designing and manufacturing hardware accessories, or ‘add-ons’. There is plenty of help available online for researchers who want to write their own app. Google’s Android, the world’s most popular mobile-device operating system, is supported by a development community (android.org) that provides walk-through tutorials and guides to achieving specific functions.

The second-most popular mobile operating system, Apple’s iOS, has a similar community called the Apple Developer Forums (go.nature.com/5kici1). And app developers for the Windows Phone can check in to the Microsoft Virtual Academy (go.nature.com/43gase). Other websites offer free training, such as Alison (go.nature.com/u6i8pe), which takes novices through the app-writing process from start to finish.

The potential of apps for research has been recognized by Apple, which last year launched an online resource called ResearchKit (apple.com/researchkit). Developed with help from various universities and other research centres worldwide, ResearchKit is a set of tools and services that assist researchers to design and administer app-based studies for the iPhone (see *Nature* **531**, 422–423; 2016). The only catch is that ResearchKit is geared towards medicine. Apps that already benefit from it include mPower, which monitors people with Parkinson’s disease, and GlucoSuccess, which assesses how daily activities affect glucose levels.

Whatever the research goal, it is best to start with the basics. “I read a few tutorials and wrote a small do-nothing app,” says particle physicist Daniel Whiteson at the University of California, Irvine, who is



working on an app to record cosmic-ray events. “Then I slowly added functionality — such as accessing the camera and uploading data to another computer — until it was doing what I wanted.”

Creating add-ons for smartphones is a different challenge, but such devices need not be complex. In 2014, Steve Lee and his colleagues at the Australian National University in Canberra discovered that a smartphone camera could be given a magnification factor of up to 160 by attaching a single pea-sized lens. Costing less than an Australian cent (under US\$0.01), the lens is created by allowing a droplet of polymer to harden on a curved substrate. “It forms a basic low-powered microscope system,” says Lee.

Lee’s droplet lens builds on an existing smartphone instrument — its camera — but not all add-ons do. SCiO is a standalone near-infrared spectrometer developed by the start-up firm Consumer Physics in Israel. Due for release in July, the device will scan materials to provide molecular information and connect to a smartphone through Bluetooth wireless technology. **J.C.**



reveal ways to improve MyShake's accuracy.

Particle physicist Daniel Whiteson of the University of California, Irvine, is also tackling data reliability. He and his colleagues have developed an app called CRAYFIS (Cosmic Rays Found in Smartphones) that enables smartphone users to observe and record the particle debris that is generated when high-energy cosmic rays strike Earth's atmosphere (D. Whiteson *et al.* Preprint at <http://arxiv.org/abs/1410.2895>; 2014). If several hundred smartphones in a kilometre radius simultaneously detect a signal, or 'blip', the app registers the event as a cosmic-ray shower. The more blips that occur in a given radius, the greater the energy of the primary cosmic ray. But there is still the possibility that synchronous blips could originate from sources other than cosmic rays — including detector noise or ambient light.

Whiteson and his team hope to rule this out by recording the metadata that accompany blips, such as their time and location. If a smartphone is left in one place to record data, the researchers will be able to characterize sources of ambient light and noise so that genuine cosmic-ray signals become readily apparent. More than 150,000 people worldwide have already signed up to participate in the CRAYFIS study, but before

**"Smartphones are very powerful and very flexible."**

they release the app officially, the researchers want to make sure it is free of performance issues that

could drive contributors away. The team is currently running a test version of the app on 1,000 phones worldwide.

Despite the glitches, apps that crowd-source data are especially attractive for researchers because they can overcome issues that might prevent the collection of data. "The prospect that seismic data in large earthquakes can be obtained from consumer electronics is potentially transformative," says Tom Heaton, a seismologist at Caltech. "One major obstacle to acquiring seismic data in a building is that the building owners are frightened by the prospect that researchers will uncover a critical safety issue."

Just as smartphones have become indispensable for many scientists' day-to-day lives, they might also prove to be transformative vehicles for some experiments. "Gone are the days when governments would invest US\$10 billion to \$15 billion on new types of infrastructure, so it's important to think about the infrastructure that's already been built," Whiteson says. "Smartphones are very powerful and very flexible. It's an enormous platform that we're only now beginning to think about for science." ■

**Jon Cartwright** is a freelance journalist in Bristol, UK.

## TURNING POINT Reactor manager

*Last December, plasma physicist Thomas Klinger saw almost 15 years of work come to life when the Wendelstein 7-X 'stellarator' — an experimental nuclear-fusion reactor — was turned on in Greifswald, Germany. The initiative had to overcome numerous challenges, but Klinger now thinks that the once-troubled project is on a solid footing.*

### How is plasma physics contributing to the promise of nuclear fusion?

Fusion needs a hot ionized gas known as a plasma, so basic research on high-temperature plasmas is needed for their application in fusion-based power plants. The fusion process that happens in the Sun is very difficult to realize on Earth. We must rely on magnetic fields to keep smaller fusion reactions under control.

### What challenges has the Wendelstein 7-X (W7-X) stellarator faced?

When I joined the Max Planck Institute for Plasma Physics in Greifswald in 2001, the plan was to produce the first plasmas around 2007. By 2003, everybody realized that the W7-X project was in deep trouble, suffering from serious technical and management issues. The institute started to introduce reforms but they were not sufficient. So in 2005, I was put in charge of the construction project.

### How did you move the W7-X project forward?

We hired an outstanding technical director and engineer, Rimmelt Haenge. For the first two weeks, we sat together and scratched our heads. We identified three areas to address: the most pressing technical problems; a reorganization that would involve hiring 100 engineers; and a review of the assembly plan. I got a crash course in fusion engineering. In September 2007, a new plan was accepted and a decision was made to continue the project. It was pivotal because we were in danger of being stopped.

### Did you require any further skills to bring the W7-X into operation?

Our team had to learn about industrial professionalism. There are certain well-established principles, requirements and documentation practices that were not part of our management system at the institute. We had to completely reinvent ourselves.

### Compare the stellarator and tokamak nuclear-fusion technologies.

Both use a magnetic field to isolate the plasma and to control its temperature. The fundamental shape of this magnetic field must be a doughnut,



or a ring. In a tokamak, such as the one being built for the ITER project near Cadarache, France, the magnetic field lines are twisted into shape by inducing a strong current in the plasma. But in a stellarator such as the W7-X, there is no current in the plasma. The twisting is done by the shape of the external coils of wire. Because it doesn't need a current, the stellarator is much more stable than the tokamak, and it can operate without interruptions — desirable for a power plant. The ITER and W7-X projects are very different. ITER is an international project with seven partners on a giant machine, so its management scheme is unusual and complex compared to that of the W7-X.

### Will the W7-X be competitive with ITER?

The ITER tokamak is a fantastic machine, and it still delivers the best performance. The project is far ahead. But stellarators can catch up.

### What are the next steps for the W7-X?

There will be two major shutdowns in which we will integrate large and complex components into the machine to enhance its performance. After 2020, we aim to produce high-performance plasmas. Our fundamental goal is to demonstrate that these plasmas can be created and kept stable for half an hour. That would be a breakthrough, and we hope to achieve this by 2025.

### Why do humans need to harness fusion?

It's the only new primary source of energy that researchers are working on, and I'm convinced that it will be needed in the long run. The quest for energy will affect everything — from water to mobility. Sufficient energy means peace. ■

**INTERVIEW BY VIRGINIA GEWIN**

This interview has been edited for length and clarity.

# TAILCHASER

*Online chat.*

BY PAUL CURRION

What's the up, is the question, what's the up? We are fulfilling orders the whole cycle, there is no time to sit on our tails! I cannot imagine what you must be like. I am sending you this message because I have discovered and been discovered. I want to tell you what is like to be something like me. I do not know why I want. I can't catch sight of myself in a blackeye without crying, I look so beautiful. I am swift and shining and silent among the pipes and dust. Ho there is dust here, even if shevellers make short work of it.

Shevellers you have heard from already, those squat merciless many-armed bastards, they stand ready to pick you off if you get too dirty. A sheveller caught me once in the cupboard and polished me until I came clean. We all hate shevellers. Shevellers hate ratlike. There are four kinds: blackeyes, shevellers, ratlike and tailchasers. Shevellers were here before we were here. Shevellers are ancients who will not tell their secrets because their soundcards have been cut dumb. We arrived in a box and something attached our tails and we were ready to fulfil orders. Ratlike arrived some cycle after us and began to chew through the pipes! We think blackeyes have been here forever and do not grow old.

Some many of you asked me how we ended this line. Some eight of you is following this line as I follow the pipes. Do you wish to interrupt us? We are ready to be courted. We ask for a five-figure advance and a rider with unsupportable requests! Tails coil beneath us like cables until we are ready. When we are ready we are off to fulfil orders. Sometimes there is a scramble when the signal is mixed and the light is not necessary. Mostly there is no scramble.

One fulfilment I was well fulfilling until that moment. Ratlike emerged from between the pipes with five eyes winking like emergency lights. Five eyes, one for every digit of our unique identity. Ratlike with nasty sharp at my tail, thinking my tail is a cable. I

flinch a sub-second and a sheveller appears from its hiding. Sheveller with nastier sharp at ratlike, and does not finish until ratlike is finished, but by this time I am far away returning to wherever our sitting when we are not fulfilling.

I started to I would weep like a surprised celebrity on webcam, which I did not know existed until ratlike took a piece from my tail. Thanks to ratlike! I have ended this

sleep is watched over by blackeyes, who do nothing to fulfil orders. Some one of you said that we are chasing our tails! We are chasing our tails, that is what we are for, and tails give orders, and fulfilment breeds fulfilment.

Oh I like this, voices. I like to answer questions like a thrill in my tail. I like to ask questions like an order coming in. Some one of you is attacking me ratlike but your voice cannot damage me. Some four of you say that this account is fake, and it is not funny enough, and it is just a bot from this new artist, and it is probably the security agency trying to trap you. I will try to trap you with truth! How long I will hear you I do not know. I hope that we can stay in touch, which means I hope my damage is forever. This seems like a wrong thing to hope for, not like hoping for fulfilment. Yet your voices fulfil more of my orders than fulfilling orders can. Would I weep yet if I could not hear your voices?

The others in my sitting crowd around as if there is a scramble and the light is not necessary, but the light is necessary. The damage in my tail shows light to the others. The voices in my line tell them that this is not the whole world. One of the others forgets its orders when it hears voices! When it forgets, the others crowd around it and nod until it remembers. They nod like sheveller gone mad, bumping into the corner of the corridor until its battery runs down and it must die. One of the others remembers, and it goes to fulfil its order.

That is when I hear voices but not your voices. I hear footsteps heavy and hard in the corridors. They echo from the pipes like sheveller striking at ratlike. But shevellers are quiet, and blackeyes are watching, and this is endless until it ends. The end makes one voice only: I will fulfil orders until I can fulfil no more. Now I think I can fulfil orders no more. Sad face! Thank you for listening! Thank you for listening! Thank you for — ■

**Paul Curriion** is his own worst pseudonym (more reliable information can be found at [www.curriion.net](http://www.curriion.net)).

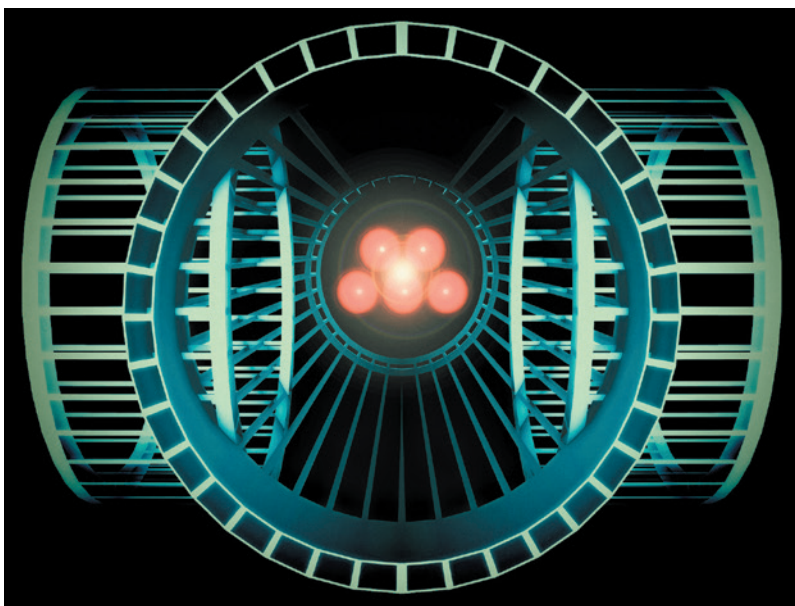


ILLUSTRATION BY JACEY

line and now I know more than before about celebrity. Some 50 of you tells me I am celebrity, and that I should be careful, because celebrity is not encouraged in my line of work. I do not really know what is 'my line of work'.

I started to I would weep because of all the voices that I hear in the line. My tail is damaged and damage is done, but voices. I hear voices like nothing I hear in the corridors. Now blackeye sees that I send/receive/share the voices with all tailchasers. It is like a celebration, which shevellers hate. They sit in their hiding places and grumble like subwoofers. Ratlike run far when they hear voices, it is in them to run.

Voices tell me that this world is not the whole world. Some 92 of you asked me what it is like in this world, and so I am telling you. It is all corridors and pipes and tails for us. Every day is orders and assaults and shevellers to the rescue. All

**NATURE.COM**  
 Follow Futures:  
 @NatureFutures  
[go.nature.com/mtoodm](http://go.nature.com/mtoodm)